NASA Technical Memorandum 4632 USAATCOM Technical Report 94-A-011

2-D and 3-D Oscillating Wing Aerodynamics for a Range of Angles of Attack Including Stall

R. A. Piziali

September 1994

National Aeronautics and
Space Administration

US Army
Aviation and Troop Command

NASA Technical Memorandum 4632 USAATCOM Technical Report 94-A-011

2-D and 3-D Oscillating Wing Aerodynamics for a Range of Angles of Attack Including Stall

R. A. Piziali, *Aeroflightdynamics Directorate, U.S. Army Aviation and Troop Command, Ames Research Center, Moffett Field, California*

September 1994

National Aeronautics and
Space Administration

Ames Research Center
Moffett Field, CA 94035-1000

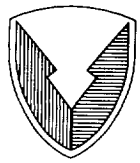

US Army
Aviation and Troop Command

Aeroflightdynamics Directorate
Moffett Field, CA 94035-1000

CONTENTS

LIST OF TABLES

LIST OF FIGURES

2-D AND 3-D OSCILLATING WING AERODYNAMICS FOR A RANGE OF ANGLES OF ATTACK INCLUDING STALL

R. A. Piziali*
Ames Research Center

SUMMARY

A comprehensive experimental investigation of the pressure distribution over a semispan wing undergoing pitching motions representative of a helicopter rotor blade was conducted. Testing the wing in the nonrotating condition isolates the three-dimensional (3-D) blade aerodynamic and dynamic stall characteristics from the complications of the rotor blade environment. The test has generated a very complete, detailed, and accurate body of data. These data include static and dynamic pressure distributions, surface flow visualizations, two-dimensional (2-D) airfoil data from the same model and installation, and important supporting blockage and wall pressure distributions. This body of data is sufficiently comprehensive and accurate that it can be used for the validation of rotor blade aerodynamic models over a broad range of the important parameters including 3-D dynamic stall. This data report presents all the cycle-averaged lift, drag, and pitching moment coefficient data versus angle of attack obtained from the instantaneous pressure data for the 3-D wing and the 2-D airfoil. Also presented are examples of the following: cycle-to-cycle variations occurring for incipient or lightly stalled conditions; 3-D surface flow visualizations; supporting blockage and wall pressure distributions; and underlying detailed pressure results.

INTRODUCTION

Dynamic stall produces a significant limitation on the operation and performance of rotorcraft at high speed. Current helicopter rotor computational simulations do not accurately predict the resulting vibratory loads of the rotor blades. The aerodynamic models used in these simulations to represent rotor blades must accurately predict the section aerodynamic forces and moments over a wide range of reduced frequencies, angles of attack including deep stall, flow conditions from nearly two-dimensional (2-D) to the highly three-dimensional (3-D) flow near the tip, and Mach numbers from low subsonic to those approaching sonic. Validations of these aerodynamic models are usually made on the basis of the local section aerodynamic coefficients over the above range of rotor blade operating conditions. The source of any resulting discrepancies, and thus direction for improvement of the models, cannot be determined without the availability of the underlying pressure distributions and time histories. While there have been experimental investigations of dynamic stall (e.g., refs. 1–3), most have not been of sufficient underlying detail and scope, particularly within one consistent data set, to validate and provide direction for development and improvement of the aerodynamic models. The test objective was to produce a data base adequate to satisfy this requirement over a major portion of the multiparameter operating environment.

For this test, a rectangular semispan wing and a 2-D configuration of the same installed model were used to obtain both static and dynamic pressure distributions, surface flow visualizations, and supporting blockage and wall static pressure distributions. To encompass the range of flow states encountered by rotor blades, a moderately high aspect ratio of 10 (full span) was selected for the wing. Using this aspect ratio allowed data to be obtained in relatively 2-D flow of the inboard regions and in the highly 3-D flow existing over the outer portions and near the tip. The same model and installation obtained the 2-D data by adding an outboard splitter plate to the semispan wing installation, assuring consistency between 2-D data and 3-D data. The 2-D data, useful in developing aerodynamic computational models, are also required to calibrate some of the semiempirical models.

These data were taken with and without an upper surface leading edge boundary layer trip (BL-trip) installed. The pressures were measured at 100 locations distributed over 9 span stations. The dynamic data were taken for a reduced frequency (ν) range from 0.04 to 0.20 for several amplitudes of pitch oscillation ($\Delta\alpha$) about the quarter chord and over the full mean angle of attack (α) range including both the incipient and deep stall conditions. The steady data presented were obtained in a quasi-steady manner (i.e., by very slowly changing the angle of attack) to obtain a very fine angle of attack resolution (256 points over the full mean angle range). Steady-state data were also taken to confirm negligible unsteady effects in the quasi-steady data and to document the chaotic nature of stall.

*Aeroflightdynamics Directorate, U.S. Army Aviation and Troop Command.

Rather than attempt to apply blockage and wind tunnel wall corrections to the aerodynamic data, local static pressure measurements were made about the wing as described in the Test Procedures section, Steady-Boundary Value Measurements. Hence, data users have the option of applying this information to make the corrections of their choice. Furthermore, those users developing theories to predict the aerodynamics and employing these data for correlation could use these measurements as boundary conditions for the computations.

The vertical displacement, cross sectional shape, and velocity defect of the near wing wake were measured for several angles of attack to provide the potential for validating the wake aspects of those aerodynamic models utilizing a free wake.

The instantaneous stalled upper surface flow patterns were obtained, along with the corresponding instantaneous pressure distributions, at equally spaced pitch cycle phase angles by the use of micro-tufts for a few operating conditions. Cycle-averaged flow patterns were also taken at the same phase angles. These results are useful in establishing the extent of the separated region and its variation through the pitch cycle. They also document the chaotic variations of the separated surface flow about the underlying cycle-averaged pattern and can be used to validate those higher ordered models yielding similar patterns and variations.

This report presents a description of the test, observations and comments concerning the data, and a compendium of all the reduced test results presented as lift (C_l), drag (C_d) and pitching moment (C_m) coefficients versus angle of attack. The list of figures and table 1 serve as an index of these results as described in the Data Presentation section of the report.

The Test Description section of this report contains a very detailed documentation of the test to aid in answering any questions arising about the data and their reliability. The Observations and Comments section presents examples of the cycle-to-cycle variations observed to occur for incipient or lightly stalled conditions. These demonstrate the chaotic nature of the separated flow (analogous to fixed wing stall buffeting) over a partially stalled wing or airfoil for both the steady-state and dynamic pitch conditions. This section also discusses some apparent anomalies observed in the data. Presented in the Basic Data Set are the cycle-averaged lift, drag, and pitching moment coefficient data versus angle of attack obtained for each span station of the 3-D wing and for the 2-D airfoil.

The appendix describes the archived data base from which the reduced results presented in this report were obtained. It also contains examples of the underlying data detail accessible via interactive software. This data base satisfies the objectives of this effort: first, to produce a comprehensive, consistent, accurate set of 2-D and 3-D static and dynamic data accessible in its underlying detail; second, to provide the overall integrated results for use in validating aerodynamic computational models while giving direction for their improvement. The scope of this test effort encompasses a significant portion of the multi-parameter operating environment of helicopter rotor blades; however, the important higher Mach number portion is not included and needs to be documented in a similar manner.

NOMENCLATURE

c	wing chord length, feet
C_d	drag coefficient, section drag/cq
C_l	lift coefficient, section lift/cq
C_m	moment coefficient, section moment/cq
C_p	pressure coefficient, pressure/q
Mn	Mach number
q	free stream dynamic pressure, $\frac{1}{2}\rho V^2$, psf
Re	Reynolds number
V	test section freestream velocity, fps
$\bar{x}$	distance from leading edge, chord lengths
$\bar{X}$	distance aft from wing trailing edge, chord lengths
$\bar{y}$	distance outward from wing root, span lengths

Symbols

α	wing mean angle of attack, deg
$\Delta\alpha$	pitch oscillation amplitude, deg
α_i	wing instantaneous angle of attack, deg
ρ	air density, slugs/ft^3
ω	pitch oscillation frequency, radians/sec
ν	reduced frequency, $\omega c/2V$

TEST DESCRIPTION

Facility

The test was conducted in the U.S. Army Aeroflightdynamics Directorate 7- by 10-Foot Subsonic Wind Tunnel at the NASA Ames Research Center.

Model

Wing– The model is a 60.0 in. semispan wing with a 12.0 in. chord (c), a NACA 0015 airfoil section, and zero twist. This wing served as the model for both the 2-D and 3-D testing as described in the installation subsection below. A single piece, machined out of aluminum, and an upper surface access cover plate (fig. 1) comprise the wing and shaft. The wing was designed to have its lowest natural frequency well above the highest test frequency of 20 Hz, assuring that the structural dynamic response would be negligible. To attain this objective, a 15% thick airfoil for increased torsional stiffness and outboard wire supports for increased bending stiffness were used. The measured fundamental natural frequency of the wing installed in the test section is 58.1 Hz for a torsion vibration mode with some bending.

Tip caps– The wing was tested with a round tip cap and with a square tip cap. Each of these tip caps extend beyond the 60.0 in. semispan of the wing. The round tip cap is 1/2 of a body of revolution formed by rotating the airfoil section profile about its chordline so that in a front elevation view this tip cap has a semicircular profile. The square tip cap is a simple spanwise extension (by 0.62 in.) of the wing airfoil; its projected planform area is equal to that of the round tip cap (i.e., 7.40 in.^{2}) and its front elevation view has a rectangular profile.

Boundary layer trip (BL-trip)– The wing was tested with and without a leading edge upper surface BL-trip to document the effect of a higher effective Reynolds number. The BL-trip consisted of a spanwise row of triangular shaped pieces of tape, 0.003 in. thickness. The triangular pieces, each side approximately 3/32 in. long, were spaced at equal intervals of about 1/8 in. and located 3/16 in. (measured along the upper surface) above the leading edge (i.e., at about 0.5% of the chord) as shown in figure 2. This trip was experimentally determined by surface oil flow studies to be the minimum disturbance required to assure consistent laminar to turbulent transition of the boundary layer and elimination of the laminar leading edge bubble over the angle of attack range of the test.

Location of the pressure taps– The wing was instrumented with 100 pressure transducers located at nine spanwise locations selected to measure (a) the spanwise load distribution, (b) the pressure distribution about the highly 3-D tip region, and (c) the pressure distribution of the relatively 2-D inboard region of the 3-D wing. The locations of the pressure transducers also allowed the wing model to be used to obtain 2-D airfoil data.

To maximize the amount of pressure information collected within a limited number of available data channels, differential pressure transducers were used at three span locations where the absolute pressures were of less importance. Thus, 10 differential pressure transducers were used at the inboard 25% span station and at the intermediate 80% and 90% span stations. Twenty absolute pressure transducers were used at the midspan 47.5% station that also served as the 2-D data station. The remaining 50 absolute pressure transducers were distributed over the 5 equally spaced span stations in the tip region (34 located on the upper surface and 16 on the lower surface) to define the pressure field in this highly 3-D flow region. On the upper surface of this tip region, 30 of these transducers were positioned to provide spanwise slices of this pressure field at 6 chordwise positions, thereby revealing the chordwise development of the tip vortex spanwise pressure field. The remaining 4 upper surface transducers were distributed at the 98.6% span station to fill in the definition of the chordwise pressure distribution at that tip span location. A similar strategy was used for the 16 lower surface transducers in this region. The locations of all the pressure transducers are presented in table 2, and these locations are shown on the wing outline in figure 3.

Installation

The installation of the model for the 2-D and 3-D testing is shown in the photos of figures 4–6 and described in the following sections.

3-D configuration– The wing was mounted horizontally in the test section by cantilevering it from the combination of test section wall and wall boundary layer splitter plate, shown in figure 4(a). Use of the splitter plate eliminates the wind tunnel wall boundary layer. To increase the installed bending frequency of the wing, an additional wing support was used consisting of a crossed pair of floor to ceiling streamlined aircraft flying wires, shown in figures 4(a) and 5. These wire supports were attached to the wing quarter chord at the 70% span station via a pitch bearing inside the wing, shown in figure 6. The supports were installed at 20 deg from the vertical and had an elliptical cross section measuring 0.087 in. thick and 0.348 in. long. The support wire attachment to the wing was sealed to prevent leakage between the upper and lower surfaces and had a sliding fairing flush with the wing surface. The cross section of the streamlined wires caused the only disturbance to the flow. Surface oil flow observations provided verification. A pressure seal consisting of a 22 in. circular disc attached to the wing root and centered on the quarter chord with a sliding seal between the disc and the splitter plate prevented leakage at the junction between the wing and the splitter plate.

2-D configuration– A splitter plate and wing seal identical to the wall splitter plate were added to the 3-D installation at the wing 95% span location to obtain the

2-D configuration (fig. 4(b)). This addition allowed the 20 absolute pressure transducers located at the 47.5% span station in the 3-D configuration, now located at the 50% span station in the 2-D configuration, to function as the primary 2-D data station.

Oscillating drive mechanism– The pitch drive system provides sinusoidal pitching motion about the quarter chord with less than 1.0% kinematic distortion at the second harmonic. The pitch oscillation of the wing was generated by a crank mechanism consisting of a variable speed feedback-controlled DC motor driving a flywheel and crank pin (with an adjustable offset for setting the oscillating amplitude), a connecting rod, and a pitch arm attached to the wing shaft at the quarter chord. Thus, the frequency, the amplitude of oscillation, and the mean angle were all infinitely adjustable within their design ranges. The amplitude of oscillation was adjustable from 0.0 to 10.0 deg and mean angle adjustable to accommodate instantaneous angles (α_i) over a 39 deg range from −12 deg to +27 deg.

Splitter plates (2-D and 3-D)– The wall splitter plate was installed 1 foot from the test section wall. It was 0.5 in. thick, with a NACA 0012 leading edge, and extended from the floor to the ceiling. The splitter plate extended from 3 chords downstream of the wing trailing edge to 1-1/2 chords upstream of the wing leading edge. Identical to the wall splitter plate and installed at the wing 95% span location, the outboard splitter plate was used to convert the 3-D configuration to the 2-D configuration.

Instrumentation

Pressure transducers– State-of-the-art miniature strain gage temperature-compensated differential pressure transducers with a pressure range of ±10 psid were used. For the absolute pressure measurements, the reference side of these differential pressure transducers were connected to the wind tunnel static pressure. The design natural frequency of the installed pressure transducers, with wing orifice diameters of 0.020 in., was 15 kHz.

Three of the transducers failed during the test and have been deleted from the data results. Two of the failed transducers were at span location 0.475 and one was at span location 0.966. These are noted by an asterisk in table 2.

Angle of attack– The wing angle of attack was measured at the wing root by a custom designed mechanism utilizing a "fast linear displacement transducer" installed in the splitter plate behind the wing root pressure seal disc.

Oscillation frequency– Frequency of oscillation was obtained from the pulse rate output of the data acquisition shaft encoder installed on the motor/flywheel shaft of the pitch drive system.

Wing temperature– Thermocouples were used to measure the temperature of the wing at span locations 0.25 and 0.70.

Wind tunnel operating parameters– Test section static and total pressures were obtained from a pitot-static probe located 34 in. ahead of the wing leading edge, 36 in. outboard of the wing tip, and 28 in. above the wing quarter chord.

Wind tunnel "standard" pressure sensing system (its calibration traceable to the National Bureau of Standards) measured the test section static pressure. The vibrating quartz crystal absolute pressure transducer system with digital output and a built-in microprocessor converts the frequency of vibration to units of pressure. Digital output was converted to analog by a D/A converter, enabling the static pressure to be recorded as instantaneous dynamic data.

The test section dynamic pressure was determined from the difference between the static and total pressures using a capacitive type differential pressure transducer.

The test section total temperature was obtained with a thermocouple located in the wind tunnel settling chamber.

Data Acquisition

Hardware– The automated data acquisition system had 64 channels for analog dynamic data and 6 channels for static data. Each dynamic channel consisted of signal conditioning, a sample and hold amplifier, and an analog to digital converter, all under the control of a large mainframe digital computer. A 1 and 256 pulse/rev shaft encoder, mounted on the motor/flywheel shaft of the wing pitch drive system, supplied the timing and rate for the acquisition of the dynamic data. Each of the static data channels utilized an off-the-shelf individual transducer-to-computer interface module that applied the appropriate calibration factor and supplied a digital output. The test engineer controlled this data acquisition system with menu-driven software via a computer terminal.

Dynamic data acquired– The dynamic data, consisting of the 100 pressure transducers on the wing, had to be acquired in 2 groups (A and B as described under Data Acquisition Process) of 50 channels plus 2 duplicate pressure channels. In addition to these 52 channels of wing dynamic pressure data, each group also contained the following dynamic data:

Test section static pressure
Test section dynamic pressure
Angle of attack
Torsion strain gage at wing root
Torsion strain gage on wing pitch shaft

A strain gage on each of the four support wires

Static data acquired– The static data consisted of the following data:

Shaft encoder pulse rate for frequency evaluation
Test section total temperature
Temperature of the wing at 25% span
Temperature of the wing at 70% span
48 scani-valve static pressures from wake or walls
Group A/B data switch position

Data acquisition process– Each data run, consisting of a number of data points, is preceded and followed by the acquisition of wind-off "zeros" for all channels.

A data point consists of a number of repeated data acquisition sequences allowing for evaluation of average results. Each individual data acquisition sequence begins with the static data, follows with the dynamic data, and concludes with the static data again. Thus, a data point with 20 repeats (or 20 cycles, in the case of pitching data) has 20 sets of dynamic data and 21 sets of static data.

Because there were more data channels to acquire than the 64 available data acquisition channels, the dynamic data for each data acquisition sequence were acquired in 2 sequential groups, A and B. The group-A data consist of all 50 pressure transducers at the spanwise locations of 0.25, 0.475, 0.80, and 0.90. In addition, the duplication of 2 transducers from the group-B data serves as a check of consistency between these 2 groups of data. The B-group data consist of the remaining 50 pressure transducers located in the tip region (outboard from span location 0.957). The duplication of 2 transducers from the group-A data serves as an additional consistency check between the groups of data. Thus, 4 duplicate channels exist, 2 in each group, to check the consistency of the 2 data groups, for a total of 52 wing dynamic pressure channels in each group.

Three types of tests were conducted with the 2-D and 3-D configurations of the model, the pitch oscillation test, the quasi-steady test, and the steady-state test. The data acquisition process for each is as follows.

Pitch oscillation test: For these data points, 20 cycles (i.e., 20 repeated data sequences) were acquired. Each of these repeats is 1 cycle of 256 samples of dynamic data. Because the dynamic data are acquired in 2 groups as described above, the cycles of data are not contiguous, but rather a collection of individual cycles automatically acquired from the continuous stream of data. The sampling rate is proportional to the frequency of oscillation for the pitch oscillation test data because the number of samples per cycle is constant (i.e., 256).

Steady-state test: These data points consist of 3 repeated data sequences of 12 sec duration per sequence. Each sequence contains 256 samples, resulting in 36 seconds of data and a sampling rate of about 21 samples per sec.

Quasi-steady test: These data points are actually pitch oscillation test data where the oscillation frequency is set very low, at 1 cycle per minute, and generally only 1 cycle of data is acquired. A few quasi-steady data points were acquired for 2 cycles to access repeatability. This allows the acquisition of instantaneous pressure data at 256 closely spaced angles of attack over the range from 0 to 20 deg.

Filtering– All the dynamic data passed through low pass filters set at 500 Hz for the pitch oscillation test data and 10 Hz for the quasi-steady test and steady-state test data.

Data storage– The raw data acquired for each data point were stored on optical disks as a collection of individual unformatted files. These raw data are the archived data base (described in the appendix) from which the reduced data presented in the report were derived. The reduced data of this report and the cycle-averaged pressures from which they were obtained are also archived with the raw data.

Acquisition software– The menu-driven data acquisition software controlled the data acquisition process, the calibration of the pressure transducers, and the recording of zeros and gain calibrations. This software also allowed the test engineer to reduce and plot online the results of the current data point at any level of detail desired prior to accepting it or to view any prior data point in a similar manner. For example, it is possible to plot anything from one of the single repeat cycles of an individual data channel to the average, over all cycles, of the integrated aerodynamic coefficients at each spanwise location.

Data Reduction

The zero drift with temperature for some of the pressure transducers exceeded the transducer specifications. Therefore, a linear interpolation is utilized to apply a temperature correction to all the transducer zeros by using the model temperature at each data point, the beginning and end zeros, and the model temperature at each zero. This procedure minimizes the zero drift problem. The instantaneous pressure coefficients, C_p, are then evaluated using the instantaneous value of the dynamic pressure, q, prior to computing their mean value and standard deviation at each phase angle.

A few data points evidenced noise spikes and/or 60 Hz noise in the chordwise integrated results. For those data points with noise spikes, the instantaneous C_p time history data were scanned and stripped of these spurious spikes by a procedure developed to discriminate these spikes from the actual data. A discrete digital filter scanned and stripped the C_p time history data of those data points with 60 Hz noise. This noise processing is a

data reduction optional procedure that does not alter the raw pressure data in the data base files.

A specially developed interpolation integrates the chordwise distribution of C_p. This procedure is carried out in an airfoil surface coordinate system divided into three regions: the leading edge region, and a region for each surface aft of the leading edge (i.e., the upper and lower surfaces).

For the leading edge region, the interpolation utilizes two basis functions which naturally span the space of solutions for the leading edge problem. They are derived from a second order airfoil theory (ref. 4) uniformly valid at the stagnation point and the suction peak. This leading edge fit procedure implicitly locates the stagnation point and assures that the fit of C_p always passes through the value of 1.0 at the stagnation point. Aft of the leading edge region on each surface, this procedure utilizes a spline function with the constraint that it match the amplitude and slope of the leading edge fit at the splice points. These splice points are positioned relative to and aft of the stagnation point and pressure peak obtained from the leading edge fit. The leading edge fit procedure only uses the upper and lower surface data points within 2.5% of the leading edge. At the trailing edge, the upper surface measured pressures at the two most aft chord locations are extrapolated to the trailing edge and used as the trailing edge value for both the upper and lower surfaces. This trailing edge procedure was used because the upper surface pressure transducers were located close to the trailing edge.

As evidence of the consistency of the interpolation procedure for the leading edge pressures, the resulting implicitly located stagnation point location versus the section C_l is plotted in figure 7 along with a linear regression to these results. These results are for the sequence of 2-D steady data points obtained below stall over the angle of attack range from −11 deg to +13 deg. This interpolation procedure yields a smooth linear variation of the stagnation with C_l. The stagnation point location is given in the airfoil surface coordinate system of the fit procedure.

Test Procedures

Calibrations– The transducer calibrations were periodically performed and checked via menu-driven software. The software compared the new results for all channels with previous results and flagged those data channels whenever a change in the calibration factor exceeded a prescribed tolerance. Results could then be corrected or accepted. Upon acceptance, the new calibrations were appended to a master file and recorded in the header of each subsequent data point file for use in data reduction. The procedures specific to each type of calibration are described below.

Data channel gains: The data channel gains were calibrated by shorting the inputs to all channels and applying a precisely measured voltage to all the inputs. Performed periodically, this calibration provided the first step in the wing pressure transducer calibration procedure. The gains calibration used a tolerance of 1% change.

Wing pressure transducers: A gains calibration always preceded calibration of the wing pressure transducers. The pressure transducers were calibrated in four groups. One group consisted of all the absolute pressure transducers calibrated by applying pressure to the manifold of the common reference side. The remaining three groups consisted of three span stations with differential pressure transducers. All the differential transducers at each span station were calibrated as a group. A fixture attached to the wing, enclosing all the pressure orifices at that span station, applied the necessary pressure.

Incrementally stepping the applied pressure through a full cycle over the range of –6 psi to +6 psi provided transducer calibration in each group. The pressure was measured by the wind tunnel "standard" pressure transducer used for the measurement of the test section static pressure. The output of all the transducers in the group was recorded and plotted versus the calibration pressure along with the linear regression used to determine the calibration factors. The change tolerance used for these pressure calibrations was 1%.

Wing angle of attack: The wing angle of attack was calibrated from −12 deg to +27 deg in incremental steps of approximately 2 deg for both increasing and decreasing angle of attack. An inclinometer on an airfoil contoured fixture, mounted at wing 20% span location, measured the angle of attack at each step. Operators manually recorded the measured angle and the output voltage for each calibration step.

To confirm the results, calibration was repeated once prior to the test. Thereafter, a three point calibration check was performed periodically at the positive and negative angle of attack limit stops and at +7.50 deg set by use of a stop-block inserted into the pitch drive mechanism.

Test section static pressure: Static pressure, measured by the wind tunnel "standard" with calibration traceable to the National Bureau of Standards, was not calibrated per se. However, the calibration factor for this data acquisition channel resulted from a linear regression of the digital output of this "standard" transducer versus the digital output of the data channel for incremental steps of about 1 psi over the range of 0.0 to 15.0 psi. Throughout the test, a two point calibration check was performed periodically by using the current atmospheric pressure and the transducer zero.

Test section dynamic pressure: Test section dynamic pressure calibrations spanned the range from 0.0 to 1.0 psi in steps of about 0.1 psi. A linear regression of the digital output of the standard transducers versus the digital output of the data channel provided the channel calibrations. This calibration was repeated once during the test.

Zeros– Prior to each data run, data channel beginning zeros were taken under computer control via the menu-driven software. The software compared the new results for all channels with the previous results and flagged those data channels where the change exceeded a prescribed tolerance. Results could then be corrected or accepted. The new accepted zeros, appended to a master file and recorded in the header of each subsequent data point file, were used for data reduction. A tolerance of 1% was used for the zeros.

Temperature sensitivity of some of the pressure transducers required stabilizing the model temperature prior to taking the zeros by running the wind tunnel at the test dynamic pressure and monitoring the temperature of the model. When model temperature approached equilibrium, the tunnel speed was quickly brought down to zero, the zeros taken, the speed resumed, and the data acquisition commenced.

End zeros were recorded to enable the data reduction correction for any possible zero drift occurring during the run. This required immediately taking zeros at the end of a run and recording them via the file header of a dummy data point taken at zero wind speed.

Pitch oscillation test– Changing the mean angle of attack and the oscillating amplitude required mechanical adjustments to the pitch drive mechanism. These were manually set with the wind off prior to a data run. Beginning run zeros were then acquired, the wind tunnel brought up to test speed, and 20 cycles of data acquired via the menu-driven software for each frequency of oscillation. The wind tunnel was shut down and run end zeros recorded via a dummy data point. The mean angle of attack was changed and the above run process repeated for each mean angle of the test matrix for the fixed oscillating amplitude.

Steady-state test– These data were obtained using the 3-D configuration with the round tip and the 2-D configuration with and without the leading BL-trip. The steady-state test did not employ the square tip 3-D configuration. The fixed angles of attack were set using the pitch oscillation mechanism to cover a 20 deg angle of attack range for each run. An electrically operated brake on the pitch oscillation mechanism held the pitch setting while data were acquired. At each angle of attack, 36 sec of data were acquired in three 12 sec repeats of 256 samples. Beginning and end zeros were acquired for each run.

Quasi-steady test– The relatively long time required to cover the 20 deg angle of attack range during the steady-state test created a concern about the potential for pressure transducer temperature drift. Therefore, the following procedure was tried and found to quickly acquire pseudo-steady-state data while minimizing the potential temperature drift effects. This test procedure also yields a finer angle of attack resolution. It is similar to the pitch oscillation test, except that it is conducted with a very low frequency oscillation and an angle of attack range from 0 to 20 deg (i.e., the angle of attack and the amplitude were both set at 10 deg). Generally, only 1 cycle of data was acquired for each data point, yielding data at 256 instantaneous angles of attack (i.e., 128 each for increasing and decreasing angles of attack). A few quasi-steady test data points, taken at a frequency of 1/2 cycle per minute, confirmed that the frequency of 1 cycle per minute was low enough to reduce unsteady effects to an imperceptible level.

2-D test– The 2-D testing only involves a configuration change. Thus, the test procedures for each of the above three test types are unchanged.

Micro-tuft surface flow visualization– About 1500 micro-tufts (1/2 in. long) were installed on the entire upper surface of the wing using a rectangular grid spacing of 1/2 in. The tufts were of 0.0019 in. diameter monofilament nylon treated to fluoresce under ultraviolet illumination. Two high intensity (2,000 joule) studio xenon strobe lamps, mounted above the wing outside the test section, illuminated the tufts. To photograph the model, a 70 mm remotely operated camera using high speed black and white film was mounted above the wing outside the test section. The strobe lamps were fitted with narrow-band-pass filters to allow only ultraviolet wavelengths, λ, of about 360 nm. A low-pass camera filter blocked the reflected wavelengths below about 430 nm. In other words, λ = 360 nm illumination caused fluorescence in the visible range, and any illumination reflected from the model and background below λ = 430 nm was blocked. Thus, with the test section dark, the strobe illuminated tufts photographed white on a totally black background.

The strobe lamps, camera, and data acquisition system were synchronized and triggered by an electronic controller circuit by the 1 and 256 per rev data acquisition shaft encoder pulses. With this system, the test engineer set the desired phase angle (pulse number) within the periodic pitching cycle and initiated the process via the controller start button. The controller opened the camera shutter and, at the selected pulse number following the next one-per-rev pulse, triggered the strobe units and data acquisition system and closed the shutter. Thus, a photograph recorded the upper surface tuft flow pattern, and the data system acquired the corresponding instantaneous pressure distribution at the selected phase angle.

A group of these visualization runs was made at the end of the test after removing the data acquisition system. For these runs there are no pressure data. To obtain a photo of the average tuft pattern rather than the instantaneous pattern at each phase angle, another group of visualization runs was made where the exposure was reduced by a factor of 30 (by reducing the lens aperture) and then 30 repeat exposures were made on a single frame of film for each phase angle.

Steady-boundary value measurements– For static angles of attack of 0.0 deg, 7.5 deg, 13 deg, and 15 deg, the static pressure distribution was measured around the 2-D and 3-D wing configurations (with the BL-trip installed) on a rectangular boundary in vertical planes aligned with the flow. The test section dynamic pressure was also measured on the fore and aft segments of this boundary. These measurements, made at midspan for the 2-D configuration and at four spanwise locations for the 3-D configuration (fig. 8), used the static pressure plates (fig. 9) on the ceiling and floor for top and bottom of the measurement boundary and pitot-static rakes (fig. 10) for the fore and aft segments of the boundaries. For the 3-D configuration, the static pressure was also measured along the wall centerline opposite the wing tip. This was accomplished by moving the ceiling static pressure plate to the wall, removing the front pitot-static rake, and leaving the rear rake and floor pressure plate in span position number four. Physical interference of the front pitot-static rake assembly with the floor and ceiling static pressure plates required this assembly to be offset five inches to one side.

These measurements were not made simultaneously at all span stations. Rather, the above apparatus was moved spanwise from station to station and the computer data acquisition process initiated after setting each of four steady angles of attack. The steady-state wing pressure distribution was recorded as one sequence of dynamic data consisting of 256 samples over a 12 sec period. The pressures on the measurement boundary were taken with two scani-valve systems and recorded by the data acquisition system as static data at each scani-valve step, following a 1.5 sec delay to allow for pressure equalization.

Dynamic pressure survey– This investigation measured the dynamic pressure in front of the 2-D and 3-D configurations for static angles of attack using a pitot-static probe installed on a traverse mechanism. Three measurement locations were 21 in. above the wing, midway between the wing and the ceiling, and 3 were 21 in. below the wing, midway between the wing and the floor. The spanwise probe locations were at midspan and 18.5 in. either side of the 3-D configuration midspan. For the 2-D configuration, these locations are midspan and 10 in. from each splitter plate. These measurement locations are all 9.5 in. ahead of the wing leading edge.

The dynamic pressure from the traverse probe, along with the test section dynamic pressure and the steady-state wing pressure distribution, were recorded as one sequence of dynamic data consisting of 256 samples over a 12 sec period.

Steady-state wake measurements– This test used a wake rake with 14 total head probes and 3 static pressure probes equally spaced vertically over about 2-1/4 in. (as seen in fig. 5). This rake was mounted on a traverse mechanism downstream of the 3-D wing configuration. The measurements were made for 3 static angles of attack at 1.5 and 3.0 chord lengths aft of the wing trailing edge and at spanwise locations of 25%, 47%, and 80%. The rake was centered vertically on the wake defect by observing the pressure pattern on a manometer board. These pressures were measured using the scani-valve system and recorded by the data acquisition system as static data at each scani-valve step, following a 1.5 sec delay to allow for pressure equalization.

Test Conditions

Primary operating conditions– The primary operating condition for the test was a nominal Reynolds number of 2.0×10^6 yielding the following corresponding nominal values:

Test section wind speed	≈ 313 fps
Dynamic pressure	≈ 117 psf
Mach number	≈ 0.278

Pitch oscillation test– Data for this test were acquired at the primary operating conditions with and without the leading edge BL-trip for the 2-D configuration, and with the round and the square tip caps for the 3-D wing configuration. This test covers a range of mean angles of attack up through stall and includes several amplitudes and frequencies of oscillation. Table 3 summarizes the test matrix for these data.

Steady-state test– This test was conducted at the primary operating conditions with and without the leading edge BL-trip for the 2-D configuration and the 3-D configuration (round tip cap). This test covers the angle of attack range from –11 deg to +20 deg with 2 overlapping runs. One run covered the range from –11 deg to +9 deg, and a second run, the range from 0 to +20 deg. The angle of attack range was covered in 1 deg increments, except in the vicinity of stall (12 deg to 17 deg), where an increment of 1/2 deg was used.

Quasi-steady test– Data for this test were acquired at the primary operating conditions with and without the leading edge BL-trip for the 2-D configuration, and with the round and the square tip caps for the 3-D wing

configuration. A few secondary quasi-steady test data points were taken at a reduced nominal Reynolds number of 1.4×10^6, yielding the following corresponding nominal values:

Test section wind speed	≈ 230 fps
Dynamic pressure	≈ 60 psf
Mach number	≈ 0.2

Oscillation frequency for the quasi-steady test was 1 cycle per minute (reduced frequency, $\nu = 0.00017$). The mean angle of attack and the amplitude were set at 10 deg to acquire data over the angle of attack range from 0 to 20 deg.

Micro-tuft surface flow visualization– Visualizations were made for both the pitch oscillation test and steady-state test, but only with the 3-D round tip configuration. They covered a range of free stream speeds and reduced frequencies. Clear tuft patterns were difficult to obtain at the primary test condition ($q \approx 117$ psf); thus, most visualizations were obtained at lower speeds. Table 4 summarizes the conditions covered.

Steady-boundary value measurements– These measurements were made at the primary operating conditions with the 2-D configuration and the 3-D configuration (round tip cap). Both configurations were tested only with the leading edge BL-trip. These measurements were made with the wing angle of attack set at 0.0 deg, 7.5 deg, 13.0 deg, and 15.0 deg for each configuration.

Dynamic pressure survey– This survey was made at the primary operating conditions with the 2-D configuration and the 3-D configuration (round tip cap). The 2-D configuration was tested with and without the leading edge BL-trip; the 3-D configuration was tested only with the trip. These measurements were made with the wing angle of attack set at 0.0 deg and 13.0 deg for each configuration.

Steady-state wake measurements– These measurements were made at the primary operating conditions using the 3-D round tip cap configuration without the leading edge BL-trip. They were taken with the wing angle of attack set at 5.0, 10.0, and 13.0 deg.

DISCUSSION

Experimental Accuracy

Although unattainable, ±1% accuracy in each of the measured quantities was sought. In so doing it was believed that the attained accuracy would be the best possible under the circumstances. Following is a brief discussion of equipment accuracy and an estimate of the accuracy of the resulting measurements.

Model– The machining tolerance for the airfoil section was ±0.002 in. The wing, designed to have zero twist, was found to have a very small positive twist (leading edge up), outboard of span station 0.30 (maximum of 0.065 deg at span station 0.51 and a distribution as shown in table 5).

Pressure transducers– Table 6 presents specifications for the pressure transducers. As described under Test Procedures, the tolerance used for the transducer calibrations and zeros was 1%. However, the zero drift with temperature for some of the pressure transducers exceeded specifications. As described in the Data Reduction section, a correction procedure minimized this problem.

Angle of attack– The mechanism for measuring the angle of attack had a resolution of better than 0.04 deg over a 39 deg angle of attack range from –12 deg to +27 deg. The kinematics of this mechanism produced a slightly nonlinear output. The output had a maximum deviation of 0.26 deg from a linear regression to the calibration results over the 39 deg range. The deviation was corrected by applying a seventh order polynomial calibration curve fit to these results. This procedure reduced the maximum resulting deviation to 0.03 deg over this 39 deg operating range.

Based on the above discussion, the angle of attack measurement appears to have been taken to an accuracy of about 1.0 to 1.5%. However, C_l does not always equal zero exactly at an angle of attack of zero as it should for a symmetrical airfoil. In some cases, it deviates by as much as 0.3 deg. Investigation of this problem led to the conclusion that it is, in part, due to the unsteadiness of the flow in the wind tunnel. Thus, the instantaneous angle of attack may have a deviation of as much as 0.3 deg. However, averaged values should be somewhat better.

Frequency– Frequency of oscillation was obtained from the 256 per rev pulse output of the shaft encoder by an off-the-shelf transducer-to-computer interface module having a resolution of 0.01 Hz and an accuracy of ±0.01%.

Test conditions– The wind tunnel "standard" pressure measuring system used to measure the test section static pressure has an accuracy of 0.015% full scale and a repeatability of 0.005% full scale with a calibration traceable to the Bureau of Standards. The capacitive type differential pressure transducer measured the test section dynamic pressure. It was calibrated against the wind tunnel standard pressure sensing system and has a linearity of 0.5% full scale and a repeatability of 0.01% full scale.

Structural dynamics– Investigation of the torsional dynamic response of the wing over the test frequency range used a state-of-the art video-based motion measurement system. The investigation confirmed that the response was closely approximated by a undamped second order system. The ratio of the tip motion to the root motion varies as the transmissibility, $1/(1 - \varpi,^2)$, where

ϖ is the forcing frequency ratio. If necessary for any application, this information can be used to account for the spanwise distribution of the small dynamic response. For example, the measured fundamental natural frequency was 58.1 Hz. Thus, at the highest test frequency of 20 Hz, where the dynamic response is the maximum (worst case), the transmissibility has a value of 1.13 (i.e., the tip pitching amplitude will be 13% greater than the root amplitude). For an oscillating pitch amplitude of 2 deg, the tip amplitude will be 2.26 deg. The spanwise distribution of this structural torsional response can be closely approximated by the first cantilever torsional mode shape of a uniform beam (i.e., a quarter sine wave).

Differential pressures cause errors– Use of differential pressures to obtain the section aerodynamic coefficients introduces an error in the lift (C_l) and moment (C_m) coefficients. The absence of the chordwise component of the surface pressures causes this error. The error was investigated by evaluating the C_l and C_m using the absolute pressure measurements obtained with the 2-D configuration with and without the chordwise component of the pressures included. The resultant error in C_l versus α is presented in figure 11, where it reaches a maximum of about 5% at an angle of attack of 16 deg. The curve of C_m versus α evaluated with and without the chordwise component of the pressures included is presented in figure 12. Here it is noted that neglecting the chordwise component of the pressures has increased the slope, $dC_m/d\alpha$, by about 50%.

Section aerodynamic coefficients– Test and data reduction procedures were generally adequate to minimize the influence of pressure transducer zero drift on the integrated results. However, occasionally the influence on the pitching C_m due to transducers near the trailing edge results in a small shift of the curve of C_m versus α. Except for this occasional shift in the C_m curve, the maximum errors in the integrated coefficients are probably ± 0.01.

Observations and Comments

The chaotic nature of stall– The fundamental nature of the flow about a stalling wing is one of chaos. There is a general overall flow state with pseudo-random variations about it varying with the depth of the stall. (On fixed wing aircraft, this is the source of the buffeting associated with stall.) Thus, when using the data to validate computational predictions, the chaotic aspect of the phenomenon should be considered. The results as presented in the Basic Data Set are cycle-averaged. This may or may not be representative of the individual cycles. In many cases, the cycle-to-cycle variation can be significant. It may be useful to look at individual cycles or delete a few cycles from the average when in the minority, i.e., non-representative. A computational procedure precisely modeling the stalling wing should, of course, also reproduce this variability as well as the mean.

Examples of the chaotic nature of stall for the steady-state and the oscillating pitch conditions are selected from the Basic Data Set and the underlying detail data. Figure 13(a) shows the cycle-averaged section coefficient results for the wing pitching about a mean angle of 13 deg with an amplitude of 4 deg at a reduced frequency of 0.04. Viewing the pressure on the airfoil upper surface at chord station 0.275 (a concatenation of the individual repeat cycle time histories) reveals the cycle-to-cycle variations for this case (fig. 13(b)). A closer look at the pressure time histories for repeat cycles numbers 7 and 12 is presented in figure 13(c). Comparing the section coefficient results for these two selected repeat cycles reveals (fig. 13(d)) the relatively extreme variation concealed in the cycle-averaged results.

The chaotic nature of the stalled flow about the wing operating at a constant angle of attack is evident in figure 14 for the condition of incipient to moderate stall. Here the pressure time history on the airfoil upper surface at the 5% chord station is presented for 4 angles of attack from 13.5 deg to 15.0 deg in 0.5 increments. The reduction in upper surface leading edge suction associated with the trailing edge type of stall occurs in a pseudo-random manner with increasing frequency as the angle of attack increases.

Nonclosure of coefficient loops– For a few data points, the loop formed by the plot of the section coefficients versus angle of attack does not close (e.g., fig. 15 for the wing oscillating at 10 Hz about a mean angle of 15 deg with an amplitude of 2 deg). This nonclosure only occurs for the relatively deep stall operating conditions. It is the result of averaging over noncontiguous cycles. Due to the stall, the flow state does not necessarily repeat at the start and end points of the cycle, as it does for the non-stalled condition.

Pitching moment variation with angle of attack– The section pitching moments increase with angle of attack, implying that the aerodynamic center is ahead of the airfoil quarter chord, contrary to what might be expected for a symmetrical section. This result is evident in other measurements made on the NACA 0015 airfoil section (e.g., see refs. 5 and 6). Increasing the trailing edge included angle of an airfoil section moves the aerodynamic center ahead of the quarter chord (ref. 7). Data for the NACA 0010-34 and NACA 0010-35 airfoils display this effect (ref. 8). Evidently the trailing edge angle of the NACA 0015 gives rise to this effect.

Stalled surface flow pattern– When stall occurs, the upper surface flow tends to separate in spanwise cells as shown in figure 16, although it is not always as well

defined and symmetrical as in this example. These cells become less prevalent as the Reynolds number is increased. In this example, α_i = 17.7 deg and is increasing while operating at a Reynolds number of 1.06×10^6 and oscillating with an amplitude of 4 deg about a mean angle of 15 deg at $\nu \approx 0.04$. The surface flow of each of these cells resembles that of a pair of counterrotating vortices, with the flow between them from the trailing edge to the leading edge, producing a mushroom-shaped surface pattern. This phenomenon has been investigated for 3-D wings at a constant angle of attack (refs. 9 and 10) where the number of spanwise cells was found to depend on the wing aspect ratio. However, the results reported herein are the first known observation of this phenomenon for dynamic stall of a wing.

DATA PRESENTATION

In addition to the Basic Data Set, this report presents some secondary data, and the supporting data. The Basic Data Set is a compendium of all the results (i.e., for all angles of attack, amplitudes, and frequencies—for each model configuration) obtained from the pitch oscillation test and the quasi-steady test. It is presented as plots of cycle-averaged aerodynamic section coefficients versus angle of attack. The secondary data consist of (1) a few data points taken to document the spanwise progression of stall, and (2) a few taken at lower Reynolds numbers. The supporting data consist of the steady-boundary value measurements, the dynamic pressure survey, the surface flow visualization, and the steady-state wake measurements. Each of these data sets is described below.

Basic Data Set

Description– The Basic Data Set is presented in figures 17–92. For each data point, the results are presented as plots of cycle-averaged C_l, C_d, and C_m, versus α_i at each span station with the data point ID and a list of all the test parameters characterizing the data point. The data point ID has the following four sequential parts:

(a) Model configuration
- 2-D = two-dimensional
- RT = 3-D with round tip cap
- ST = 3-D with square tip cap

(b) Test type
- POT = pitch oscillation test
- QST = quasi-steady test
- SST = steady-state test

(c) Boundary layer trip
- 1 = trip was used
- N = no trip used

(d) Sequential data point acquisition number
Four digits prefixed with the letter "D" for raw data file or "R" for reduced data file

For example, RTPOT1.D0845 is the data point for the RT configuration obtained from the POT with the BL-trip installed and a data point number of 845.

Below are the test parameters (cycle-average values) listed on each plot characterizing the data point:

- α = pitch mean angle of attack ± oscillation amplitude
- freq. = pitch frequency
- ν = reduced frequency
- vel. = test section wind speed
- Mn = Mach number
- Re = Reynolds number

Organization– The Basic Data Set is organized and presented as follows. First, all the results obtained with the leading edge BL-trip installed are presented, followed by all results obtained without the BL-trip. Each of these two sets of data is divided into three configuration groups: first, the 2-D results; second, the round tip 3-D results; and third, the square tip results. Within each configuration group, the results appear in four subgroups: first, the quasi-steady test results, followed by the three groups of pitch oscillation test results in ascending order of pitch amplitude (i.e., the 2 deg, 4 deg, and 5 deg results). Within each of the pitch oscillation test pitch amplitude subgroups, results are arranged in ascending order of the mean angle of attack. For each mean angle, the results are arranged in increasing magnitude of the pitch oscillation frequency. The list of figures and table 1 provide a useful guide to this body of data and its organization. Repeated data points are included as sub-figures (labeled as repeat) following the initial data point.

2-D configuration– 2-D airfoil results are presented at the following four span stations:

$$\bar{y} = 0.263, 0.500, 0.842, \text{and } 0.947$$

The 2-D data are defined as those at the midspan, 0.500, station having 20 absolute pressure transducers (also the 3-D span station 0.475). The additional 3 off-center span stations having 10 differential transducers (the 3-D span stations at 0.250, 0.800, and 0.900) are included to provide an assessment of the two-dimensionality for each data point. Noteworthy is a small error inherent in the use of differential pressures for calculating section lift and moment, as discussed in the prior Experimental Accuracy section.

3-D configuration– For 3-D wing configurations, results are presented at the following seven span stations:

$$\bar{y} = 0.250, 0.475, 0.800, 0.900, 0.986, 0.966, \text{and } 0.995$$

The data at span stations 0.957 and 0.976 are omitted because they consist only of upper surface pressures at six chord locations; thus, evaluation of the aerodynamic coefficients is not possible. These data are intended to be used together with the upper surface pressures at span stations 0.986, 0.966, and 0.995 to define the highly 3-D upper surface tip pressure distribution as influenced by the vortex formation.

Secondary Data

Three additional sets of data were obtained in addition to the Basic Data Set. The first set of data points documents the variation of the spanwise extent of the dynamic stall region with frequency. It was obtained with the 3-D round tip configuration by a frequency sweep over the range from 3.0 to 6.0 Hz for 13 deg mean angle of attack with an oscillating amplitude of 2 deg. This data set, taken without the use of the BL-trip (figs. 93 and 94), was obtained at the primary test condition (Reynolds number 2.0×10^6) and at the reduced nominal Reynolds number (1.4×10^6). A set of frequency sweep data was also taken at this reduced Reynolds number with the BL-trip installed (fig. 95).

The second additional set is quasi-steady test data taken at the above reduced Reynolds number. These data were obtained for the round tip configuration with and without the BL-trip installed (figs. 96 and 97) and for the 2-D configuration without the BL-trip installed (fig. 98).

The third additional set of data, presented in figure 99, was taken at the nominal operating conditions matching those used for some of the stalled surface flow visualizations. This operating condition was at a lower nominal Reynolds number of 1.06×10^6 corresponding to the following nominal values:

Test section wind speed	$\approx$ 162 fps
Dynamic pressure	$\approx$ 30 psf
Mach number	$\approx$ 0.15

Supporting Data

Steady-boundary values– Rather than attempt to apply blockage and wind tunnel wall corrections to the aerodynamic data, it was decided to make local static pressure measurements at four steady state angles of attack on a rectangular boundary surface about the wing (described under Test Procedures). Thus, users of the aerodynamic data have the option of applying this information to corrections of their choice. Those developing theories to predict the aerodynamics and using the data for correlation can apply these measurements as boundary conditions for the computations.

These results for the 2-D configuration are presented in figure 100, followed by the 3-D configuration results presented in figures 101–105. For the 3-D configuration, these results are presented in groups based on span location of the survey from wing root to tip. Within each group the results are presented in ascending order of angle of attack. These results are presented as the relative static pressure deviation—i.e., the local static pressure difference from the test section static pressure divided by the test section static pressure. Vertical distributions are plotted versus the distance from the floor; horizontal distributions are plotted versus the distance from the wing quarter chord. These distances are non-dimensionalized by chord length. Each plot contains three repeat measurements.

An anomaly occurs in the horizontal static pressure distributions on the floor and ceiling due to aerodynamic interference from the strut of the front pitot static rake. The strut location is 5 in. off to the side from the static pressure orifice located 1.67 chord lengths ahead of the wing quarter chord. The source of this anomaly is confirmed by the measurements presented in figure 105. With the front rake removed to make the wall static pressure measurements and the floor static pressure plate left in span location 1.67, the anomaly disappeared from the floor static pressure distribution.

These local boundary value static pressure distributions for each span location and the chordwise pressure distributions over the wing were obtained simultaneously. Except for small experimental variations, these steady-state chordwise pressure distributions are the same for each span location. Thus, the wing chordwise pressure distributions obtained at each angle of attack for the boundary value static pressure survey at span location 0.479 (fig. 106) represent those obtained for the static pressure survey at all span locations.

Dynamic pressure survey– The maximum peak-to-peak variation observed in the dynamic pressure survey was about 1% and that magnitude was aft of the wing for the high angle of attack measurements. Because of the relatively insignificant variations observed, plots of these results are omitted.

Micro-tuft surface flow visualization– Examples of the instantaneous and cycle-averaged micro-tuft surface flow visualizations are presented for the operating condition with a pitching amplitude of 4 deg about a mean angle of attack of 15 deg.

The instantaneous visualizations of the stalled surface flow pattern at 4 phase angles through the stall cycle were selected from the set obtained at a reduced frequency of 0.04 and are presented in figure 107(a). A repeat set of these visualizations at the same phase angles (fig. 107(b)) demonstrates the variations occurring in the stall separated surface flow from cycle to cycle. The instantaneous

pressures on the wing, taken simultaneously with the photos of the instantaneous surface flow patterns of figure 107(a), are presented in figure 108.

The cycle-averaged visualizations at a sequence of eight phase angles through the stall cycle are presented in figure 109 for a reduced frequency of 0.04 and in figure 110 for a reduced frequency of 0.20. These illustrate the change in the stalled surface flow pattern with reduced frequency.

Steady-state wake measurements– These measurements determine the approximate displacement and cross sectional shape (i.e., vertical location of the wake at several span stations) of the near wing wake and its velocity defect. Figures 111 and 112 present an example of these results obtained at 1.5 and 3.0 chords aft of the wing trailing edge for the wing operating at an angle of attack of 13 deg.

REFERENCES

1. Lorber, P. F.; Carta, F. O.; and Covino, A. F., Jr.: An Oscillating Three-Dimensional Wing Experiment: Compressibility, Sweep, Rate, Waveform, and Geometry Effects on Unsteady Separation and Dynamic Stall. UTRC Report R92-958325-6, 1992.
2. Costes, J. J.: Unsteady Three-dimensional Stall on a Rectangular Wing. Paper No. 30. Twelfth European Rotorcraft Forum, Garmisch-Partenkirchen, West Germany, 1986.
3. Wagner, Wolfgang J.: Comparative Measurement of the Unsteady Pressures and the Tip-Vortex Parameters on Four Oscillating Wing Tip Models. Paper No. 9. Tenth European Rotorcraft Forum, The Hague, The Netherlands, Aug. 28–31, 1984.
4. Roshko, Anatol: Pressure Distribution at the Nose of a Thin Airfoil. Douglas Aircraft Co. Report No. SM-23368, 1958.
5. McAlister, K. W.; and Takahashi, R. K.: NACA 0015 Wing Pressure and Trailing Vortex Measurements. NASA TP-3151, 1991.
6. Pope, A.: The Forces and Moments Over an NACA 0015 Airfoil. Aero Digest, vol. 58, no. 4, 1949, pp. 76, 78, and 100.
7. Seckel, E.: Stability and Control of Airplanes and Helicopters. Academic Press, 1964, p. 8.
8. Abbott, I. H.; and Von Doenhoff, A. E.: Theory of Wing Sections – Including a Summary of Airfoil Data. Dover Publications, 1949, pp. 456–459.
9. Winkelmann, A. E.; and Barlow, J. B.: Flowfield Model for a Rectangular Planform Wing Beyond Stall. AIAA J., vol. 18, no. 8, 1980, pp. 1006–1008.
10. Winkelman, A. E.: An Experimental Study of Mushroom Shaped Stall Cells. AIAA/ASME Third Joint Thermophysics, Fluids, Plasma, and Heat Transfer Conference, St. Louis, Mo., AIAA Preprint No. 82-0942, 1982.

Table 1. Test condition figure numbers

a. Pitch oscillation data

α	config. / ν / Δα	2-D .04	2-D .10	2-D .14	2-D .20	3-D Round tip .04	3-D Round tip .10	3-D Round tip .14	3-D Round tip .20	3-D Square tip .04	3-D Square tip .10	3-D Square tip .14	3-D Square tip .20
4	2	18/56	18/56	18/56	18/56	33/72	33/72	33/72	33/72	–/–	–/–	–/–	–/–
9	2	19/57	19/57	19/57	19/57	34/73	34/73	34/73	34/73	49/87	49/87	49/87	49/87
11	2	20/58	20/58	20/58	20/58	35/74	35/74	35/74	35/74	50/88	50/88	50/88	50/88
13	2	21/59	21/59	21/59	21/59	36/75	36/75	36/75	36/75	51/89	51/89	51/89	51/89
15	2	22/60	22/60	22/60	22/60	37/76	37/76	37/76	37/76	–/–	–/–	–/–	–/–
17	2	23/61	23/61	23/61	23/61	38/77	38/77	38/77	38/77	–/–	–/–	–/–	–/–
1	4	–/62	–/62	–/62	–/–	39/78	39/78	39/78	–/–	52/90	52/90	52/90	–/–
4	4	24/63	24/63	24/63	–/–	40/79	40/79	40/79	–/–	53/91	53/91	53/91	–/–
9	4	25/64	25/64	25/64	–/–	41/80	41/80	41/80	–/–	54/92	54/92	54/92	–/–
11	4	26/65	26/65	26/65	–/–	42/81	42/81	42/81	–/–	–/–	–/–	–/–	–/–
13	4	27/66	27/66	27/66	–/–	43/82	43/82	43/82	–/–	–/–	–/–	–/–	–/–
15	4	28/67	28/67	28/67	–/–	44/–	44/–	44/–	–/–	–/–	–/–	–/–	–/–
17	4	29/68	29/68	29/68	–/–	45/83	45/83	45/83	–/–	–/–	–/–	–/–	–/–
13	5	30/69	30/69	–/–	–/–	46/84	46/84	–/–	–/–	–/–	–/–	–/–	–/–
17	5	31/70	31/70	–/–	–/–	47/85	47/85	–/–	–/–	–/–	–/–	–/–	–/–

b. Quasi-static data

α	config. / Δα	2-D	3-D Round tip	3-D Square tip
10	10	17/55	32/71	48/86

Legend

Trip

No trip

Table 2. Pressure transducers locations on wing. (a) Spanwise locations: $\bar{y} = 0.25$, $\bar{y} = 0.80$, $\bar{y} = 0.90$ differential pressure transducers

Position no.	$\bar{x}$
1	0.010
2	0.025
3	0.050
4	0.125
5	0.225
6	0.325
7	0.450
8	0.600
9	0.750
10	0.900

Table 2. Continued. (b) Spanwise location: $\bar{y} = 0.475$ absolute pressure transducers

Upper position no.	$\bar{x}$	Lower position no.	$\bar{x}$
Leading edge	0.000	1	0.010
1	0.010	2	0.025
2	0.025	3	0.050*
3	0.050	4	0.150
4	0.100	5	0.300
5	0.175	6	0.500
6	0.275	7	0.700
7	0.400	8	0.900
8	0.550		
9	0.700*		
10	0.850		
11	0.975		

*Failed during test and deleted from results.

Table 2. Continued. (c) Spanwise locations: $\bar{y} = 0.957$, $\bar{y} = 0.976$ absolute pressure transducers

Upper position no.	$\bar{x}$
1	0.010
2	0.100
3	0.400
4	0.600
5	0.800
6	0.975

Table 2. Continued. (d) Spanwise location: $\bar{y} = 0.986$ absolute pressure transducers

Upper position no.	$\bar{x}$	Lower position no.	$\bar{x}$
Leading edge	0.000	1	0.010
1	0.010	2	0.025
2	0.025	3	0.050
3	0.050	4	0.150
4	0.100	5	0.300
5	0.250	6	0.500
6	0.400	7	0.700
7	0.600	8	0.900
8	0.800		
9	0.975		

Table 2. Concluded. (e) Spanwise locations: $\bar{y} = 0.966$, $\bar{y} = 0.995$ absolute pressure transducers

Upper position no.	$\bar{x}$	Lower position no.	$\bar{x}$
Leading edge	0.000	1	0.050
1	0.010	2	0.300
2	0.010	3	0.700
3	0.400	4	0.900
4	0.600		
5	0.800		
6	0.975*		

*Failed at span 0.966 during test and deleted from results.

Table 3. Test matrix for pressure measurements

α, deg	Δα, deg	Frequency, Hz	q, psf	Round tip	Square tip	2-D
4	2	4, 10, 14, 20	117	✓		✓
9	2	4, 10, 14, 20	117	✓	✓	✓
11	2	4, 10, 14, 20	117	✓	✓	✓
13	2	4, 10, 14, 20	117	✓	✓	✓
15	2	4, 10, 14, 20	117	✓		✓
17	2	4, 10, 14, 20	117	✓		✓
1	4	4, 10, 14	117	✓		✓*
4	4	4, 10, 14	117	✓	✓	✓
9	4	4, 10, 14	117	✓	✓	✓
11	4	4, 10, 14	117	✓	✓	✓
13	4	4, 10, 14	117	✓	✓	✓
15	4	4, 10, 14	117	✓*		✓
17	4	4, 10, 14	117	✓		✓
13	5	4, 10	117	✓		✓
17	5	4, 10	117	✓		✓
13	2	Sweep; 3–6	117	✓		
13	2	Sweep; 3–6	60	✓		
10	10	0.0167	117	✓	✓	✓
10	10	0.0167	60	✓		✓

*There is no data for the round tip no BL-trip case at $\alpha = 15$ deg or for the 2-D with BL-trip case at $\alpha = 1$ deg. The figure numbers for these cases are summarized in table 1.

Table 4. Test matrix for micro-tuft surface flow visualization

$\alpha/\Delta\alpha$, deg	q, psf	Frequency, Hz	Reduced frequency	B/L-trip Y or N	Average/ instantaneous A or I	Pressure data Y or N
13/4	117	4	0.04	Y	I	Y
13/4	117	10	0.10	Y	I	Y
13/4	117	14	0.14	Y	I	Y
15/4	30	2	0.04	Y	I	Y
15/4	30	5	0.10	Y	I	Y
15/4	30	10	0.20	Y	I	Y
15/4	30	2	0.04	Y	I	Y
15/4	30	2	0.04	N	I	Y
13/4	60	4	0.056	N	I	Y
$11 \le \alpha \le 15$	30	SST	0	N	I	N
$11 \le \alpha \le 20$	30	SST	0	N	A	N
$11 \le \alpha \le 19$	117	SST	0	N	I	N
$12 \le \alpha \le 20$	117	SST	0	N	A	N
$12 \le \alpha \le 21$	117	SST	0	N	I	N
15/4	30	2	0.04	N	A	N
15/4	30	5	0.10	N	A	N
15/4	30	10	0.20	N	A	N
13/4	60	4	0.056	N	A	N

Table 5. Residual wing twist due to manufacturing

Span, $\bar{y}$	Twist, deg
0.33	+0.012
0.51	+0.065
0.67	+0.030
0.83	+0.060
1.00	+0.024

Table 6. Pressure transducer specifications

Sensitivity	5 mv/psi
Nonlinearity and hysteresis	<0.5% FS
Repeatability	< 0.1% FS
Compensated temperature range	60 - 120 deg F
Zero change with temperature	< 0.5% FS/100 deg F
Sensitivity change with temperature	< 1% FS/100 deg F
Resonant frequency	150 K Hz
Acceleration sensitivity	0.0005% FS/G

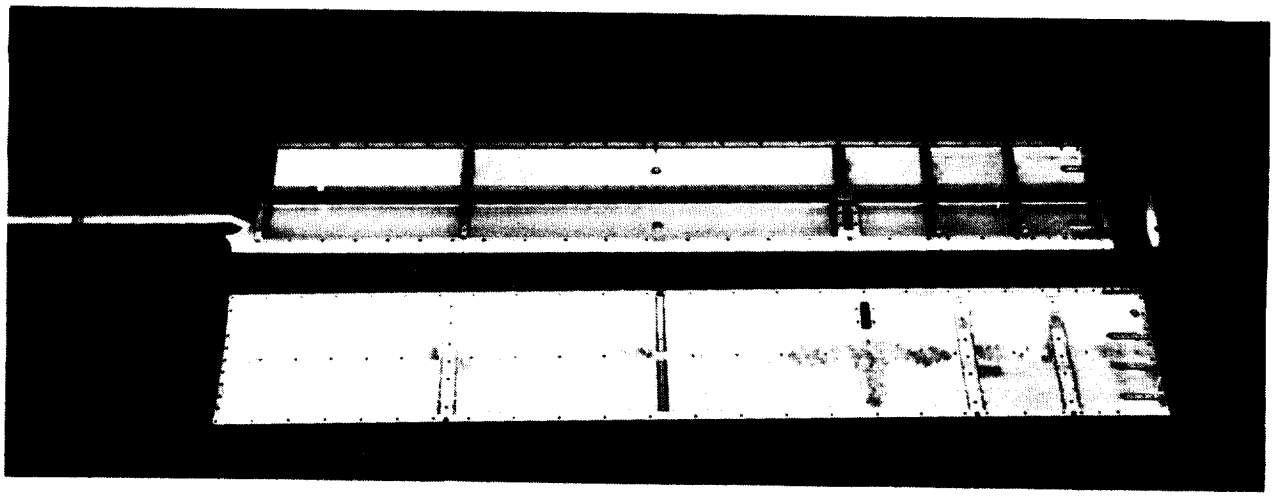

(a) Structural components

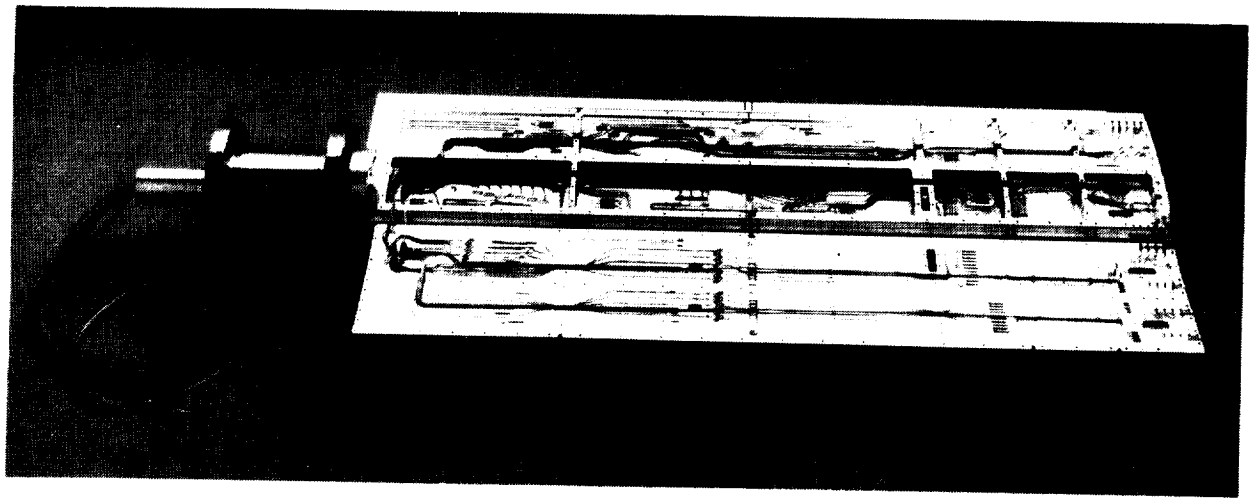

(b) Instrumented wing with bearing

Figure 1. Wing photos.

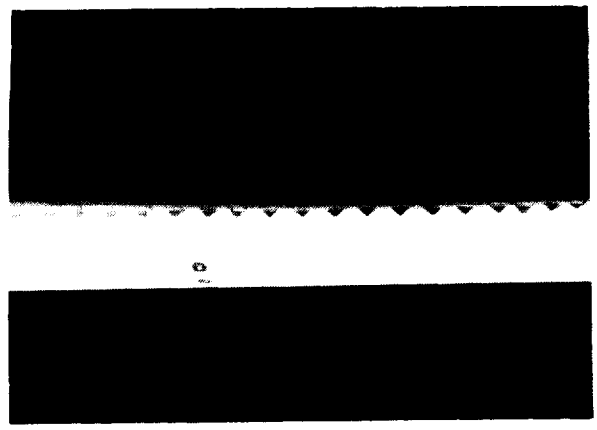

Figure 2. Upper surface leading edge BL-trip; installation photo.

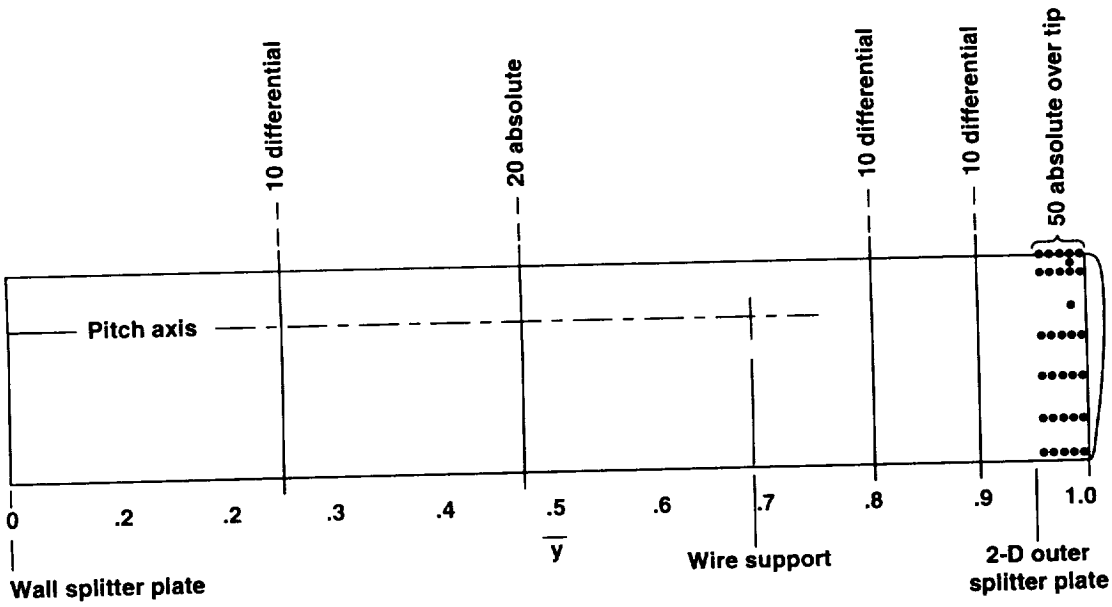

Figure 3. Locations of pressure taps, wing supports, and splitter plates.

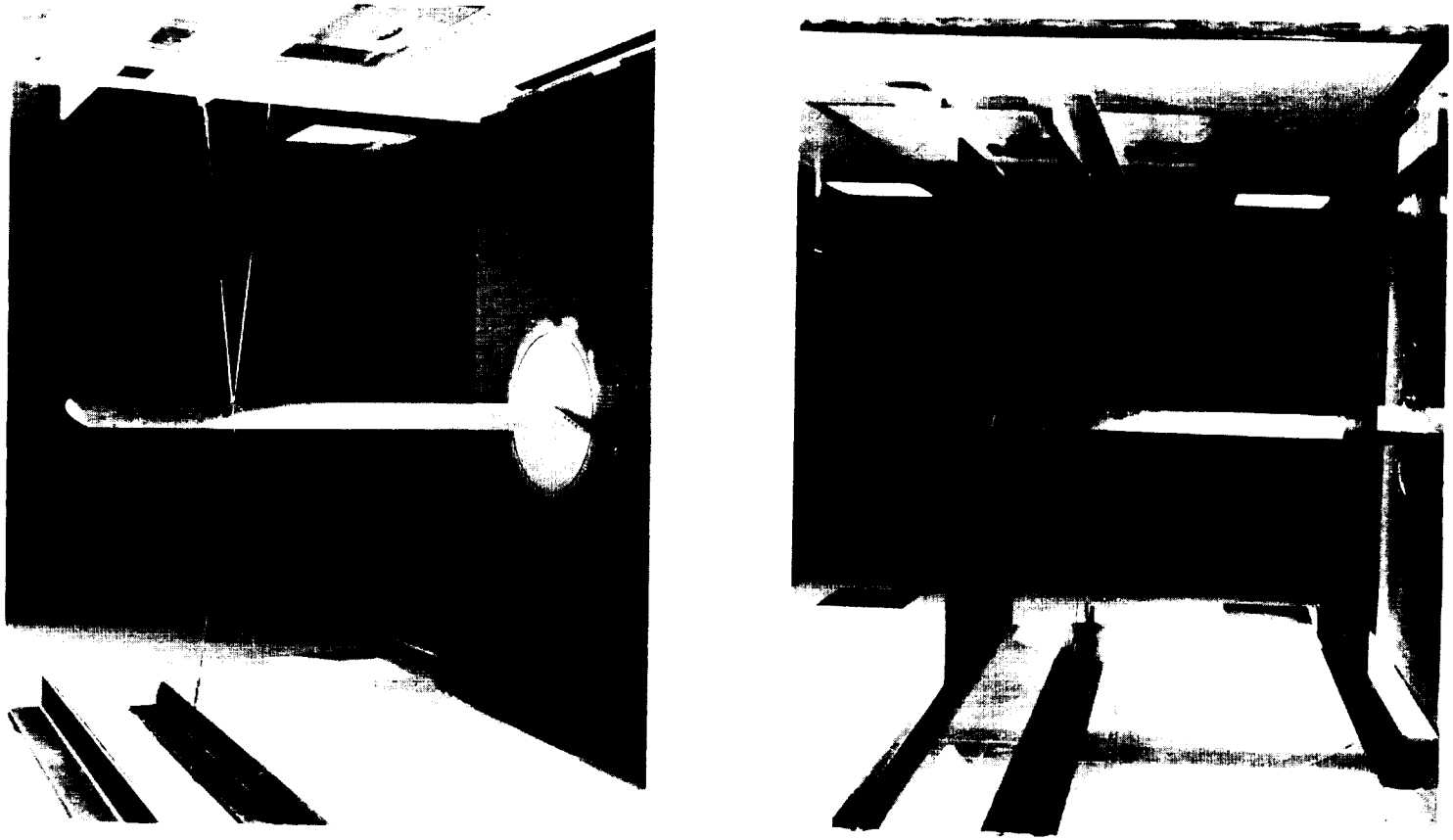

(a) The 3-D wing configuration

(b) The 2-D configuration

Figure 4. Installation photos of model in test section.

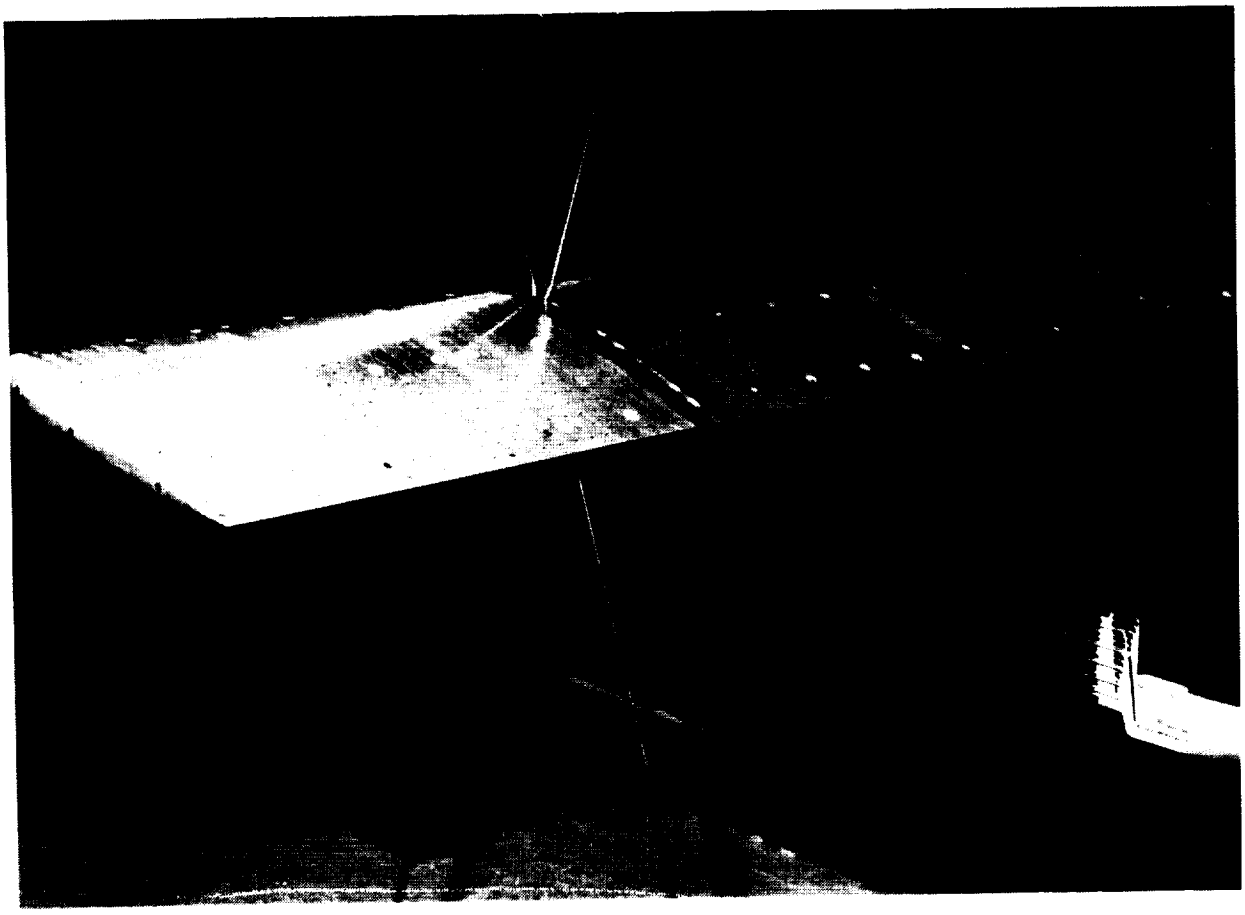

Figure 5. Photo of wire supports and wake rake installation.

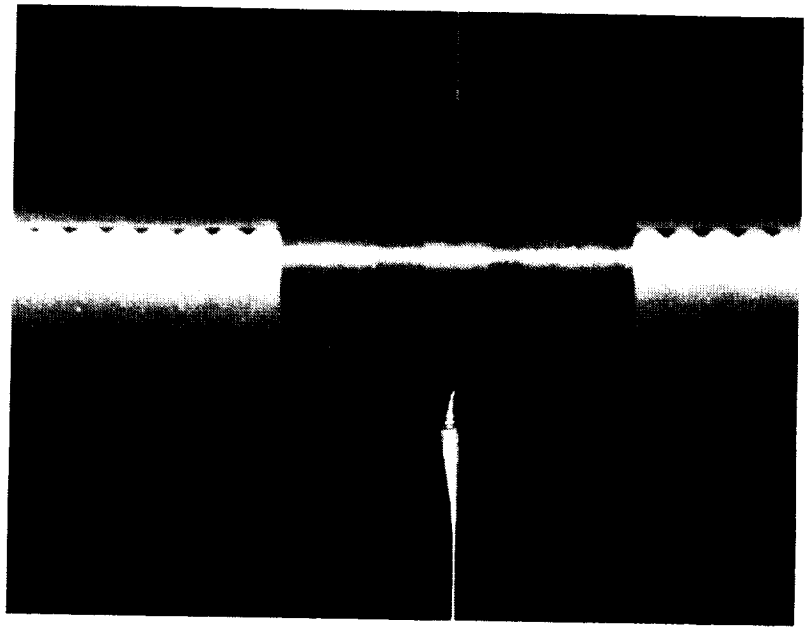

(a) Front view

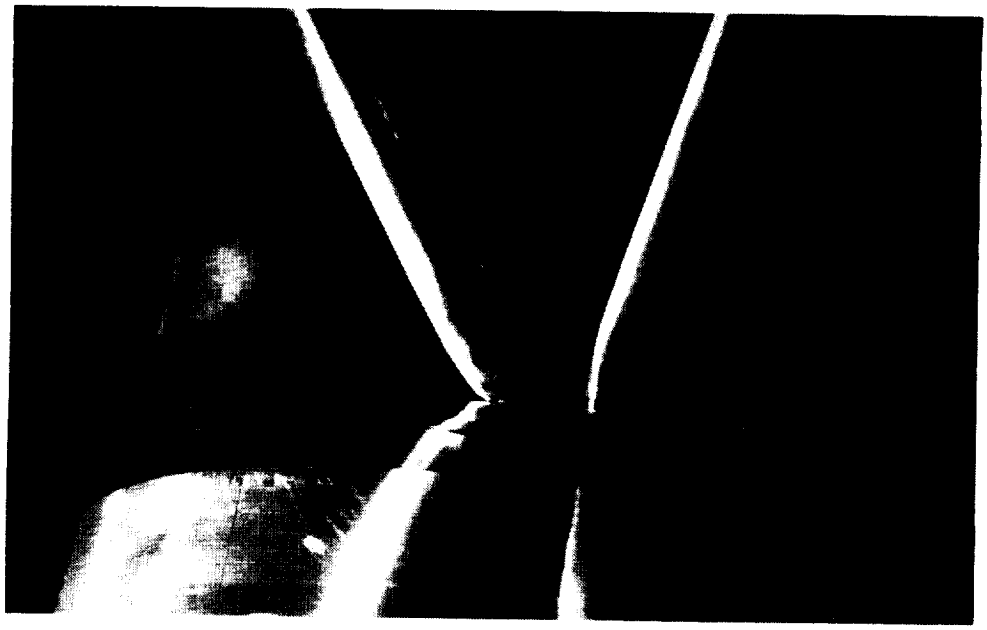

(b) Top/side view

Figure 6. Photos of wire support attachment to wing.

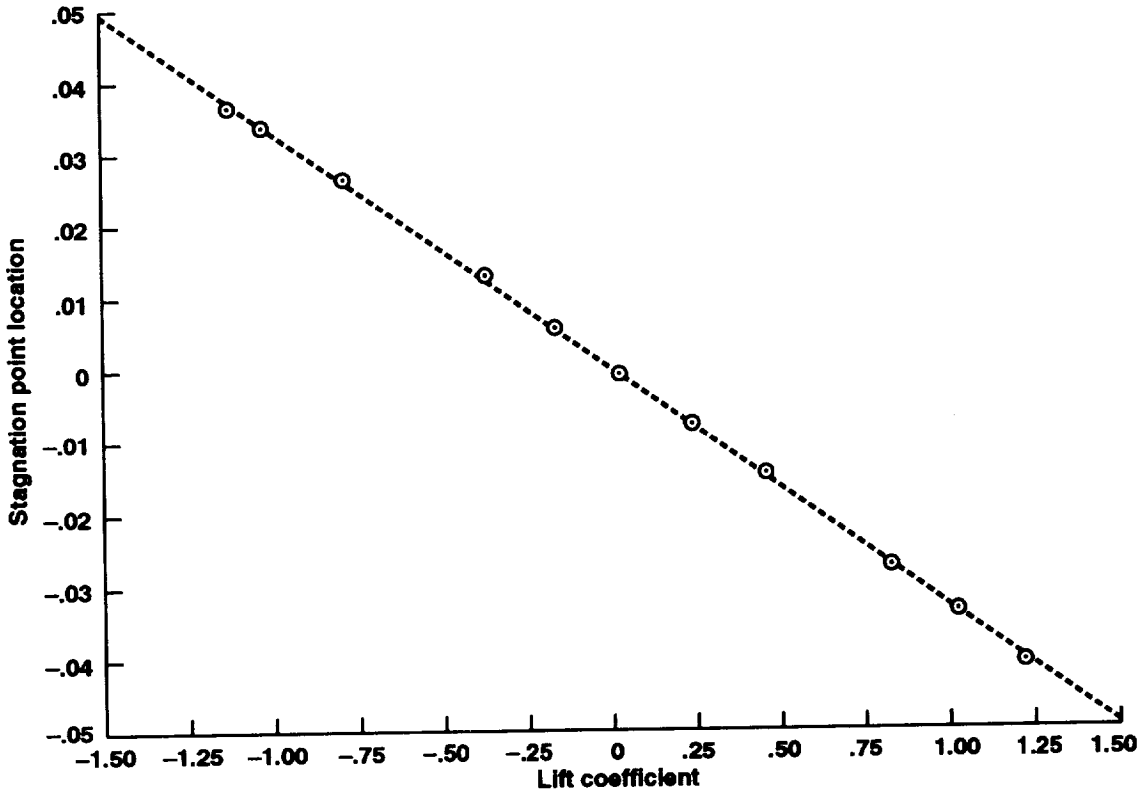

Figure 7. Stagnation point location versus lift coefficient.

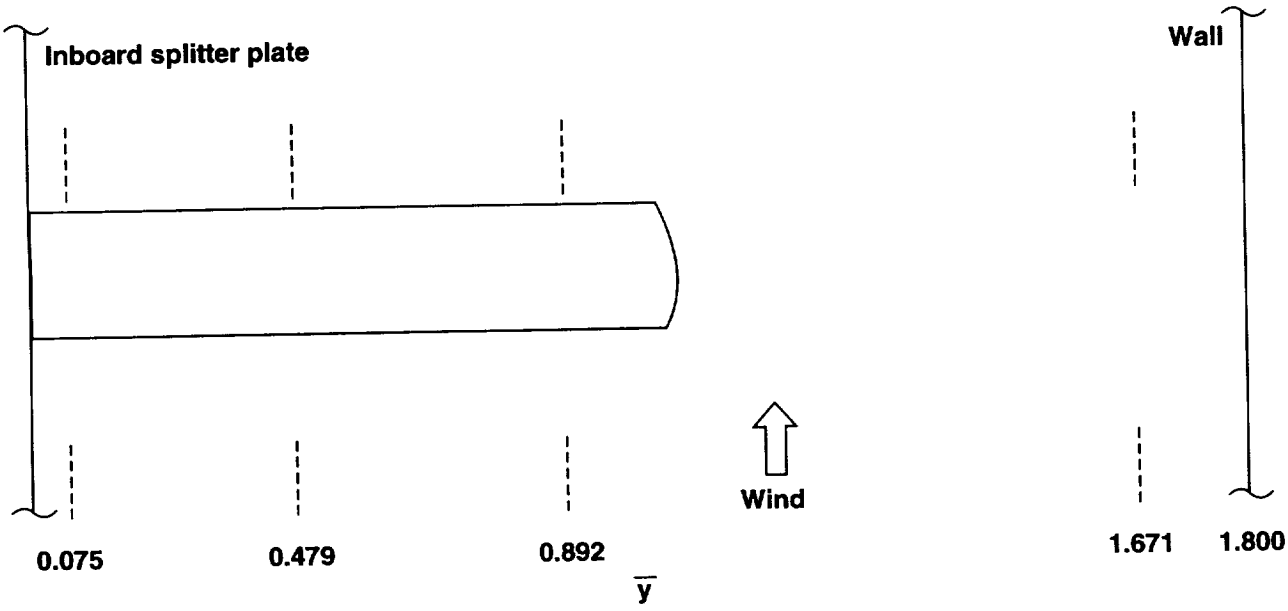

Figure 8. Spanwise locations for boundary value measurements.

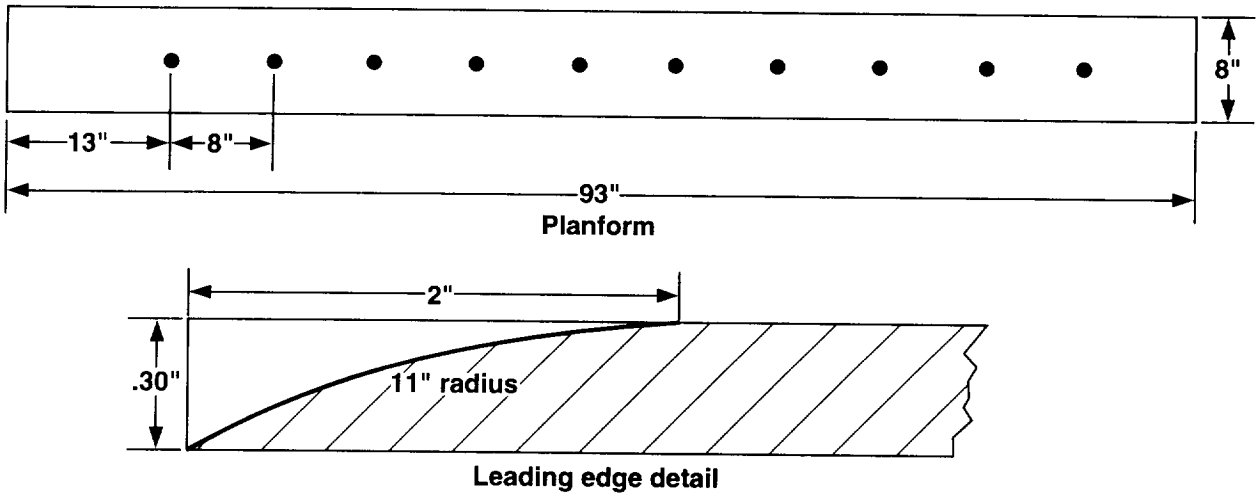

Figure 9. Static pressure plate for boundary value measurements.

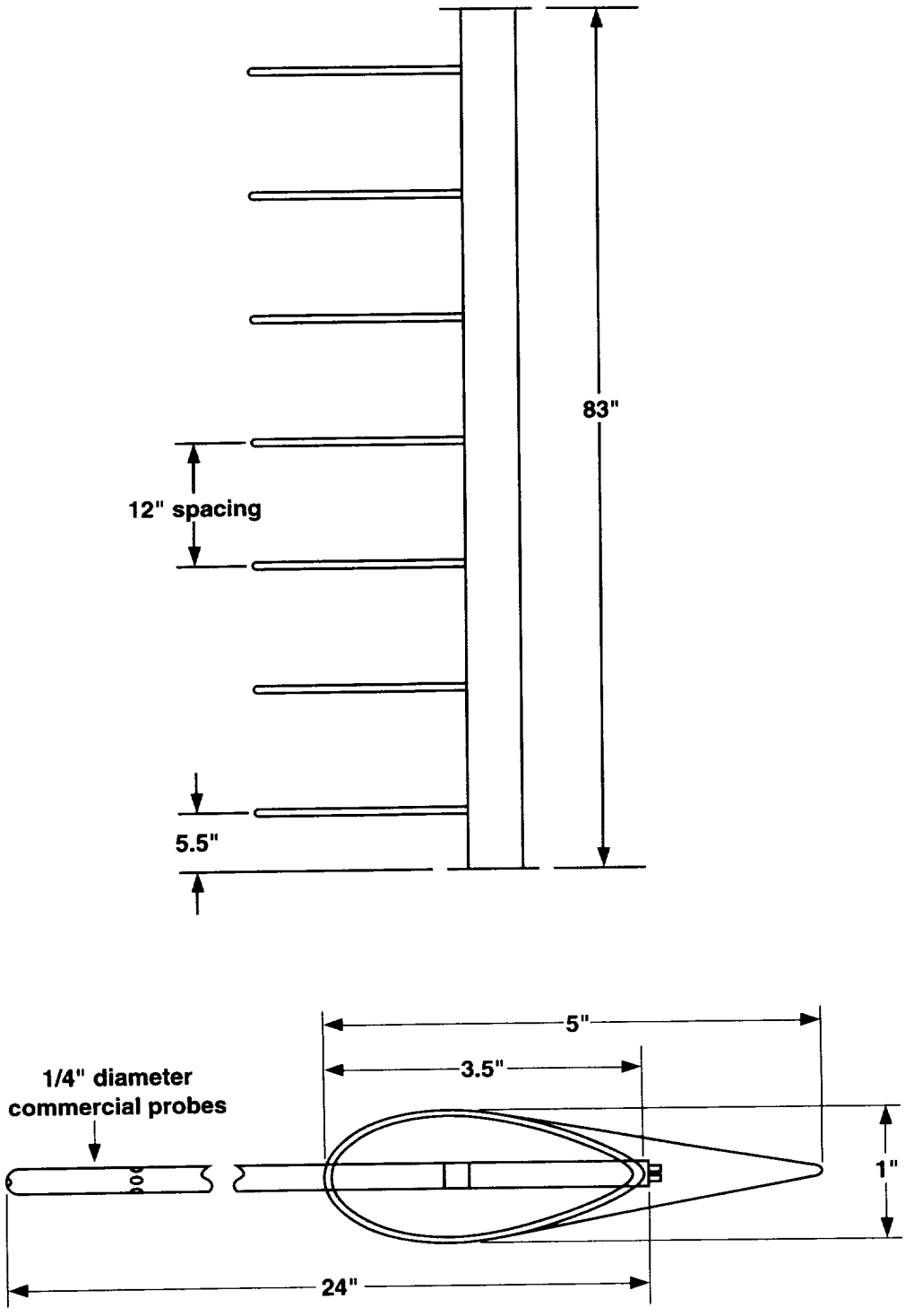

Figure 10. Pitot-static rake for boundary value measurements.

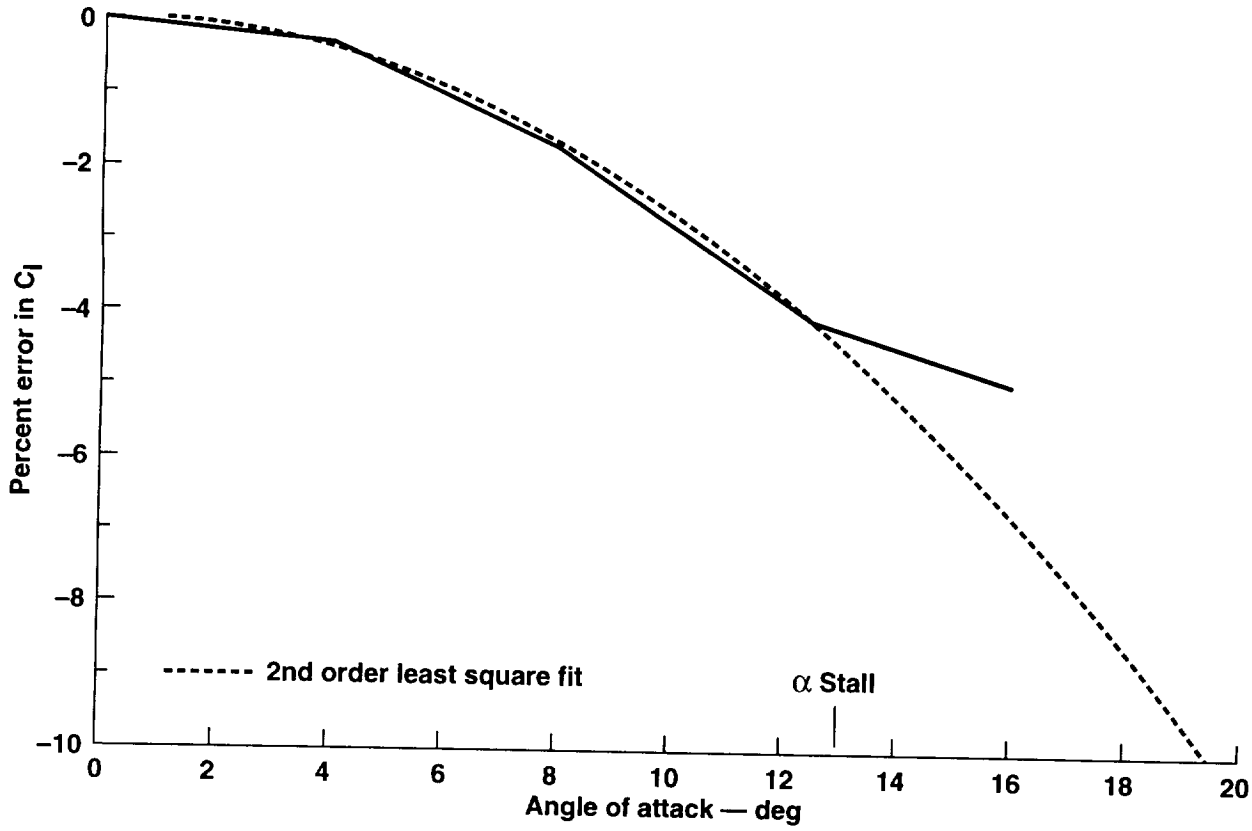

Figure 11. Error in C_l due to use of differential pressures.

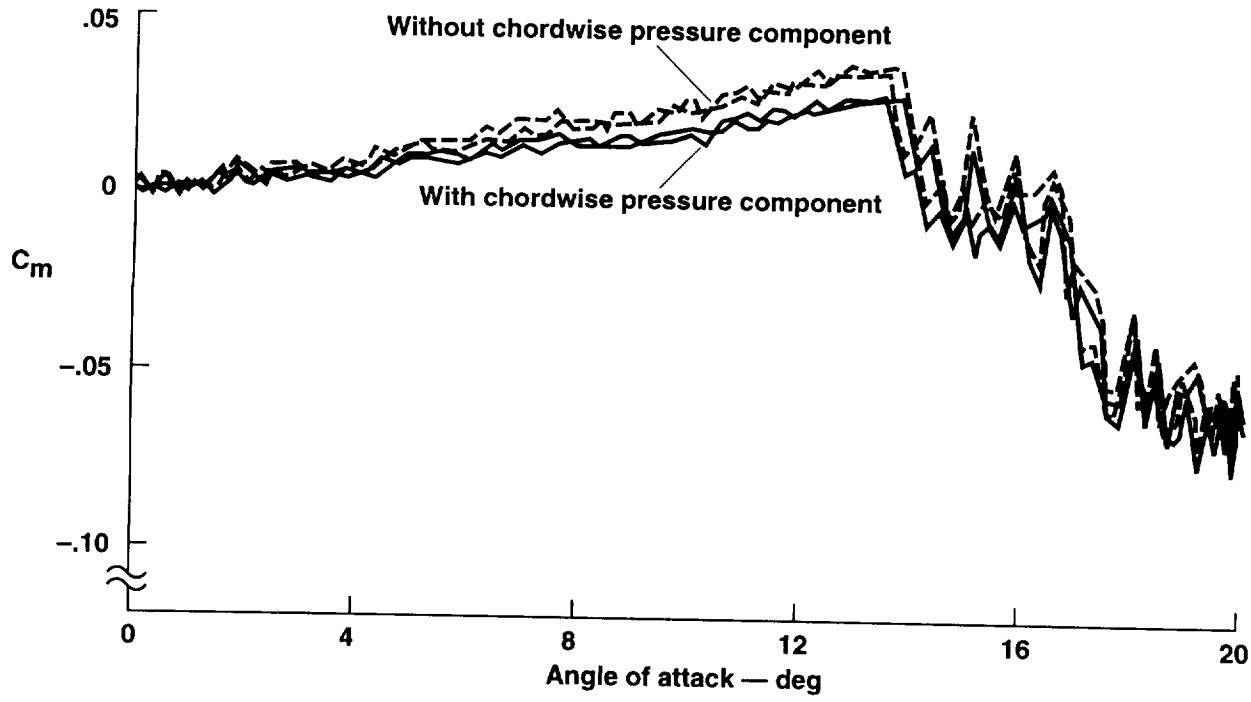

Figure 12. Error in C_m due to use of differential pressures.

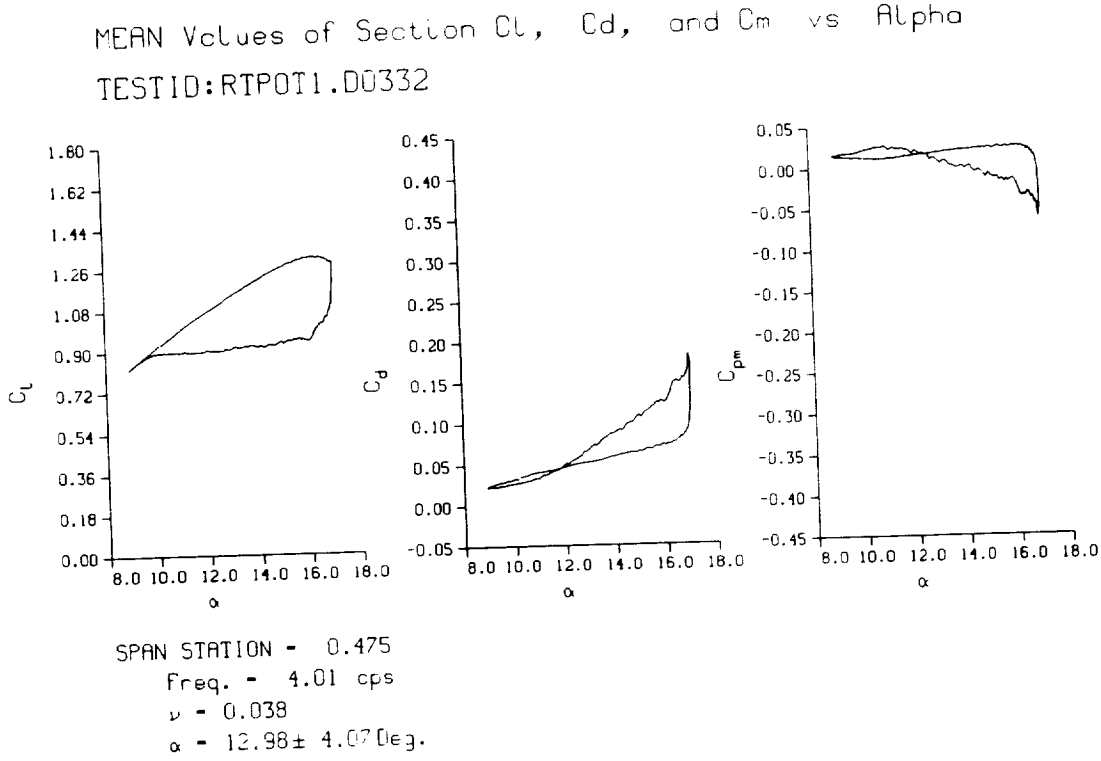

(a) Cycle-average section coefficient loops

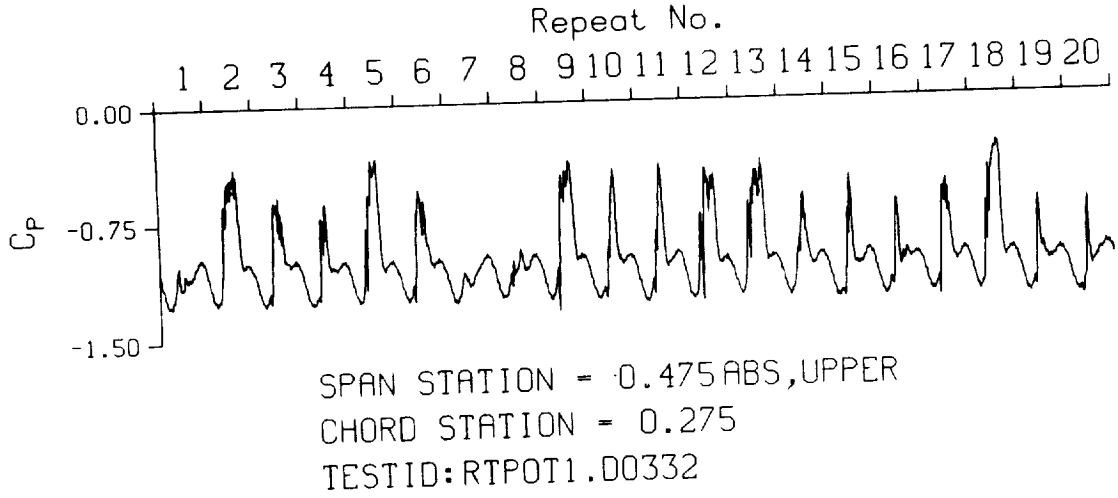

(b) Cycle-to-cycle airfoil section pressure variations

Figure 13. Example of the chaotic nature of stall during pitch oscillation.

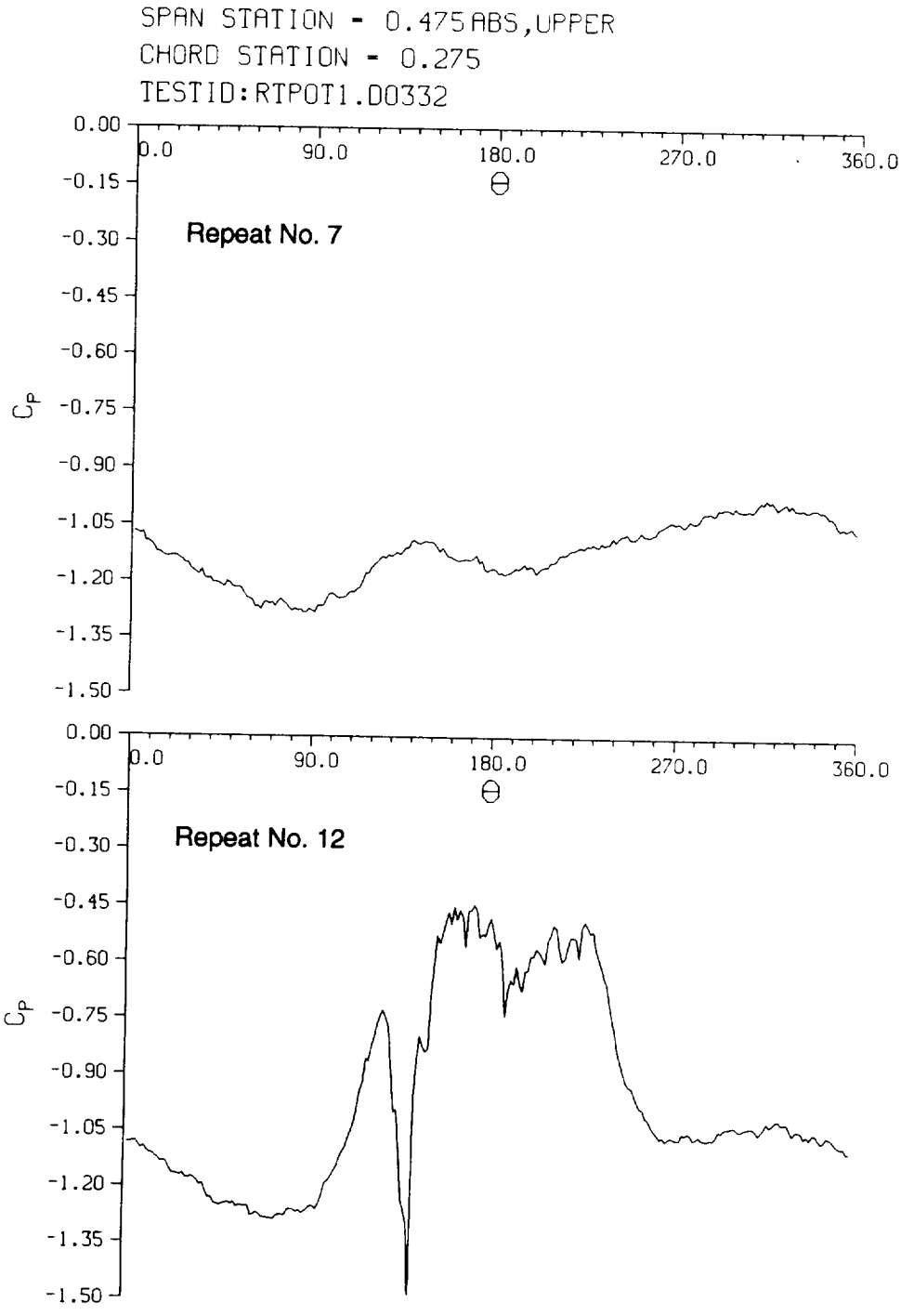

(c) Airfoil pressure time histories for cycle numbers 7 and 12

Figure 13. Continued.

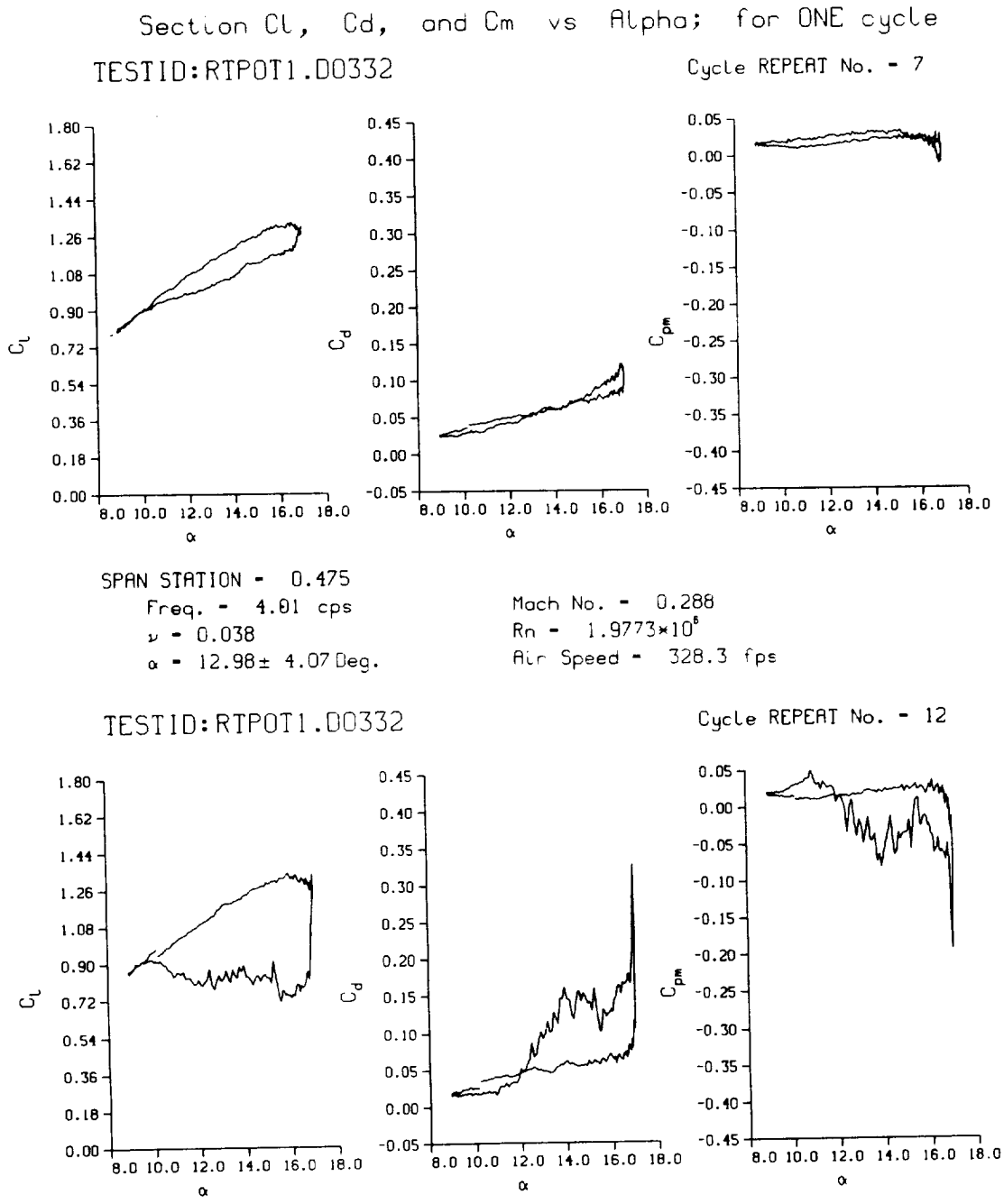

(d) Section coefficient loops for cycle numbers 7 and 12

Figure 13. Concluded.

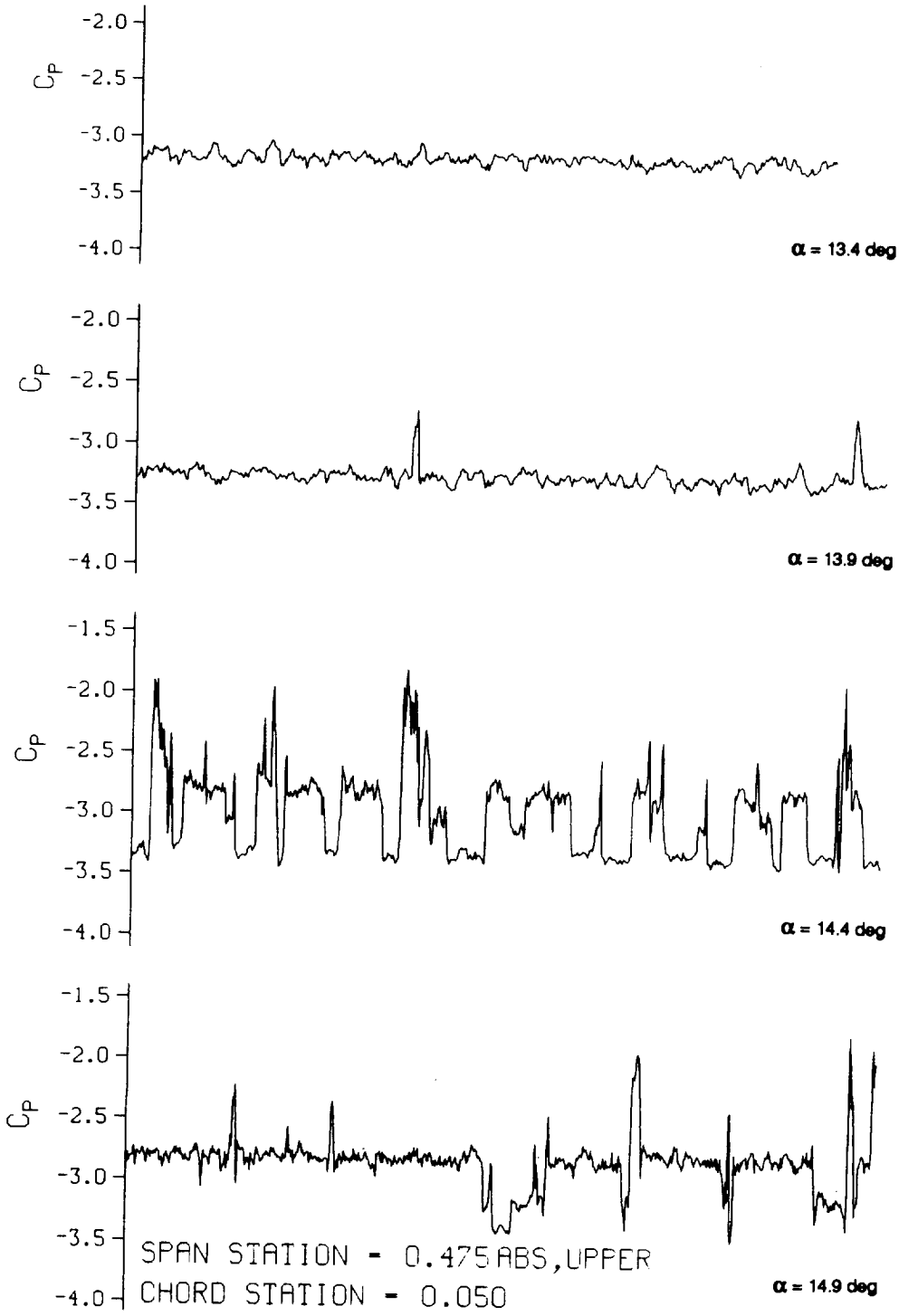

Figure 14. Example of the chaotic nature of stall at constant angle of attack.

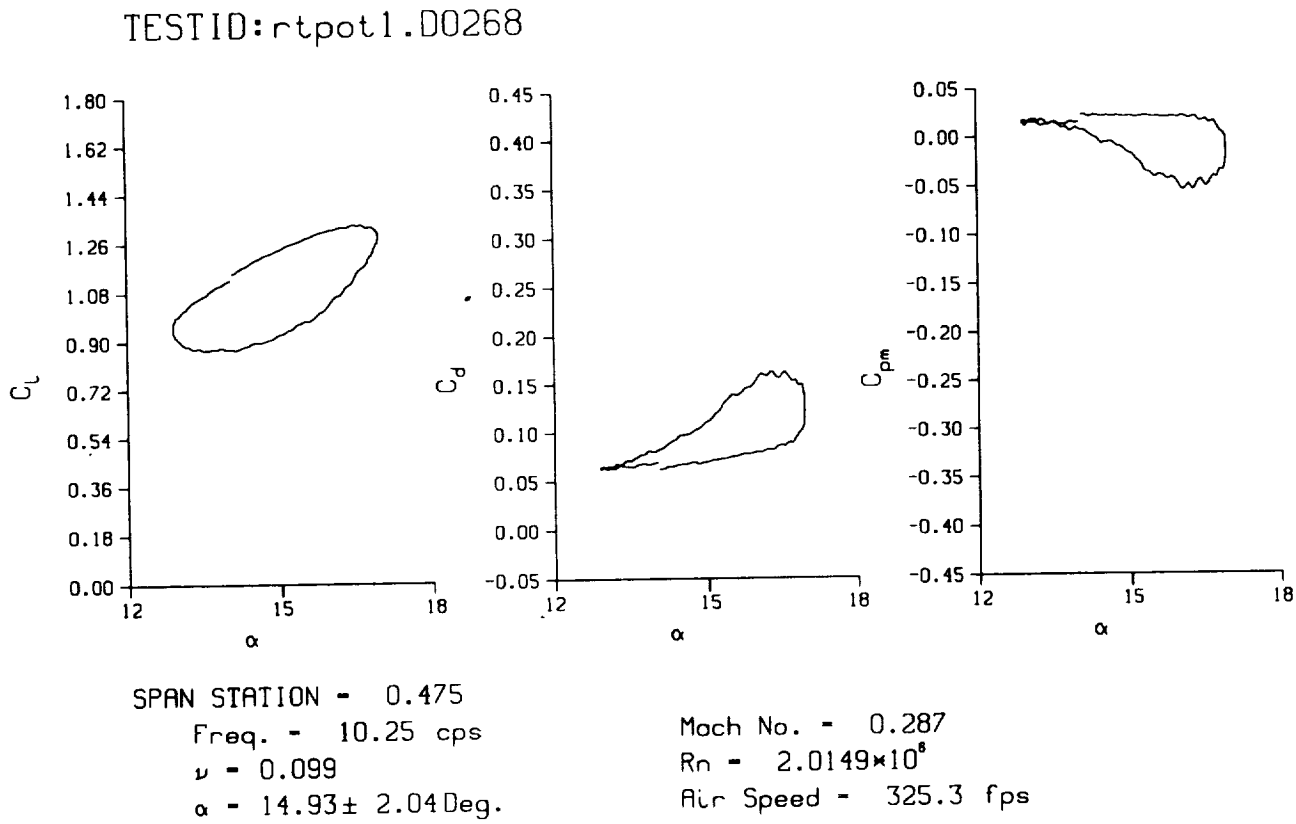

Figure 15. Example of nonclosure of the aerodynamic coefficient loops.

Figure 16. Stall cell surface flow pattern; α = 15 deg ± 4 deg; α_i = 17.6 deg ↑ ; ν = 0.04.

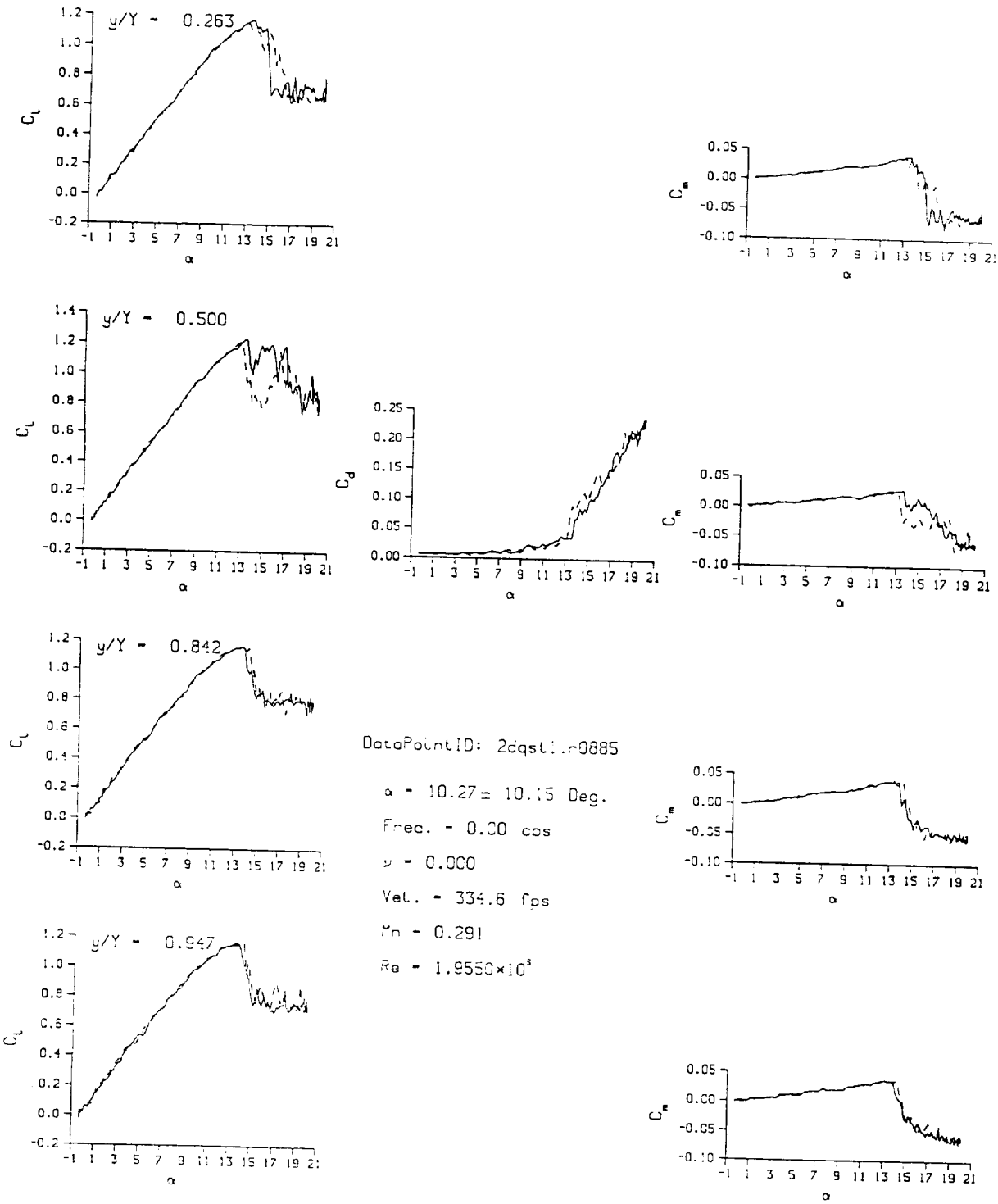

(a) Repeat no. 1

Figure 17. 2-D quasi-steady data; BL-trip; $0 \leq \alpha \leq 20$ deg.

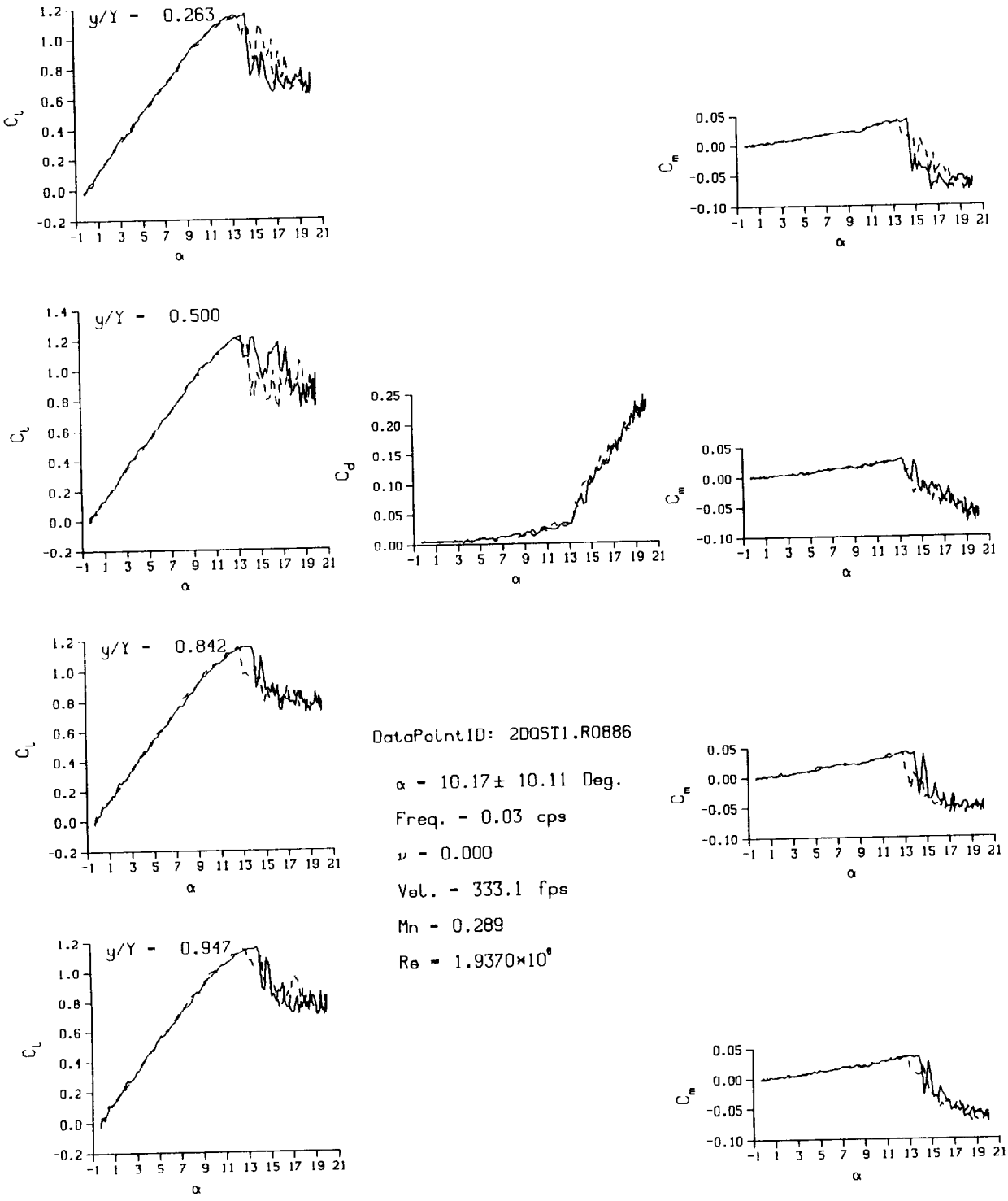

(b) Repeat no. 2

Figure 17. Continued.

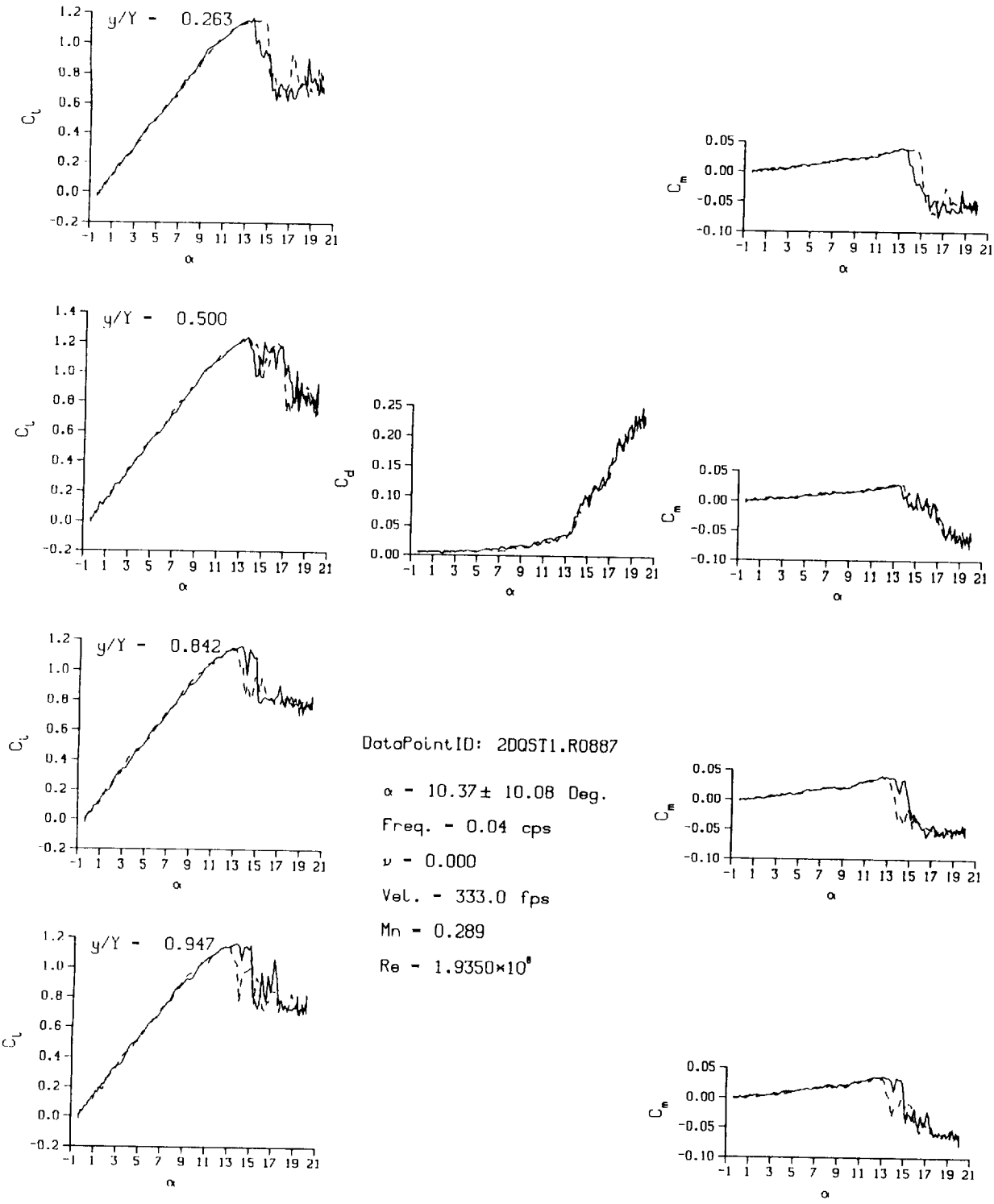

(c) Repeat no. 3

Figure 17. Concluded.

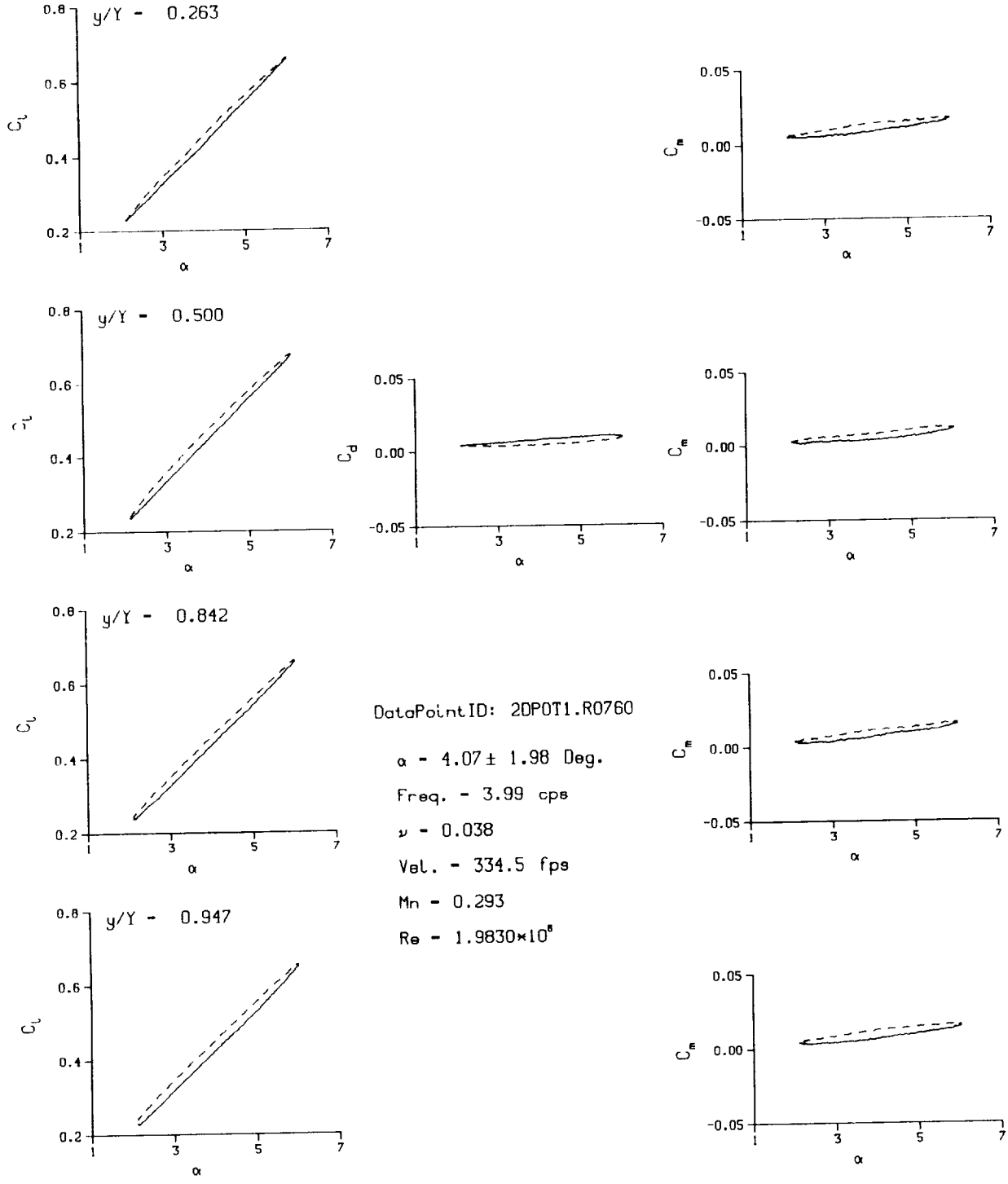

(a) v = 0.04

Figure 18. 2-D pitch oscillation data; BL-trip; α = 4 ± 2 deg.

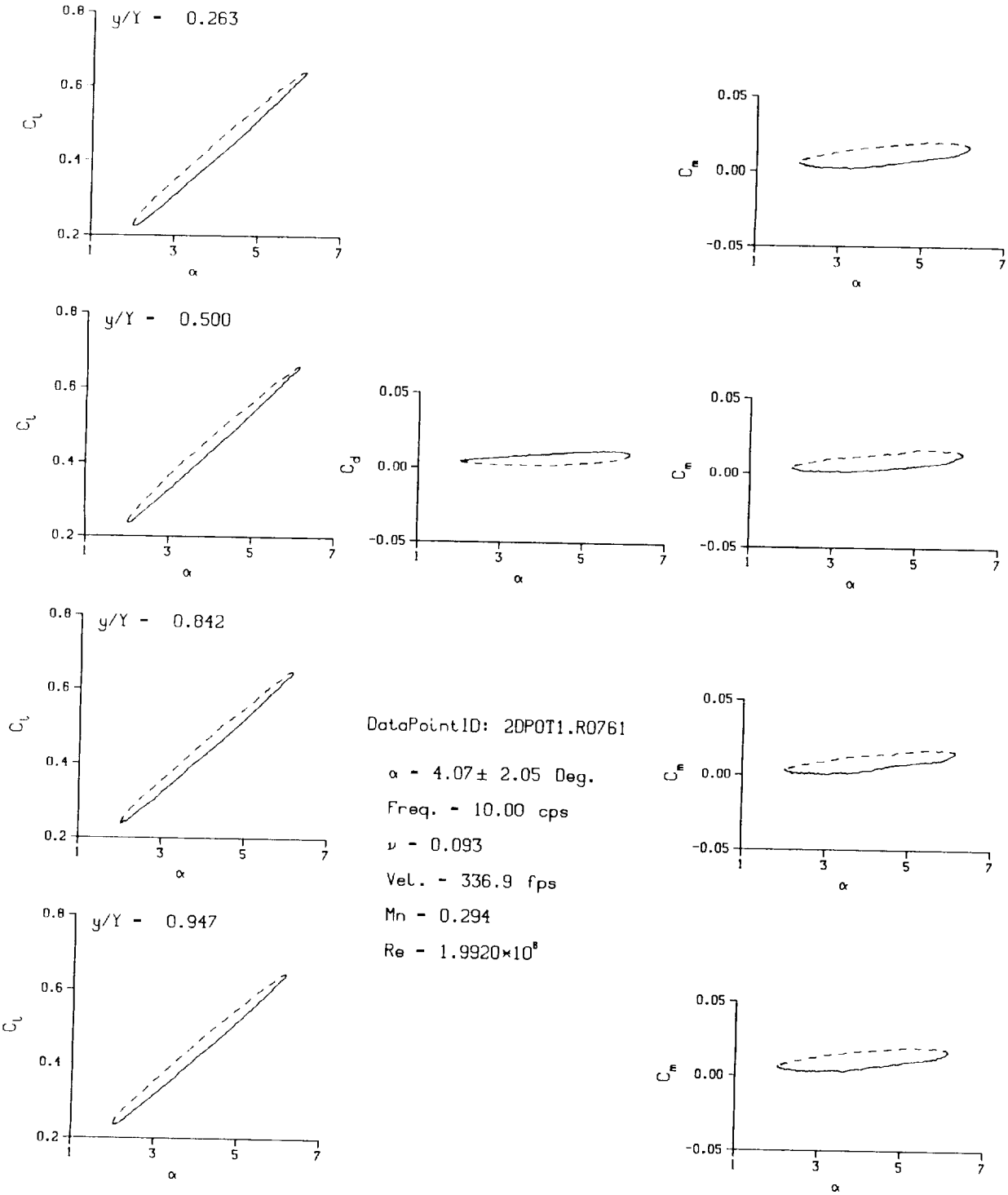

(b) v = 0.10

Figure 18. Continued.

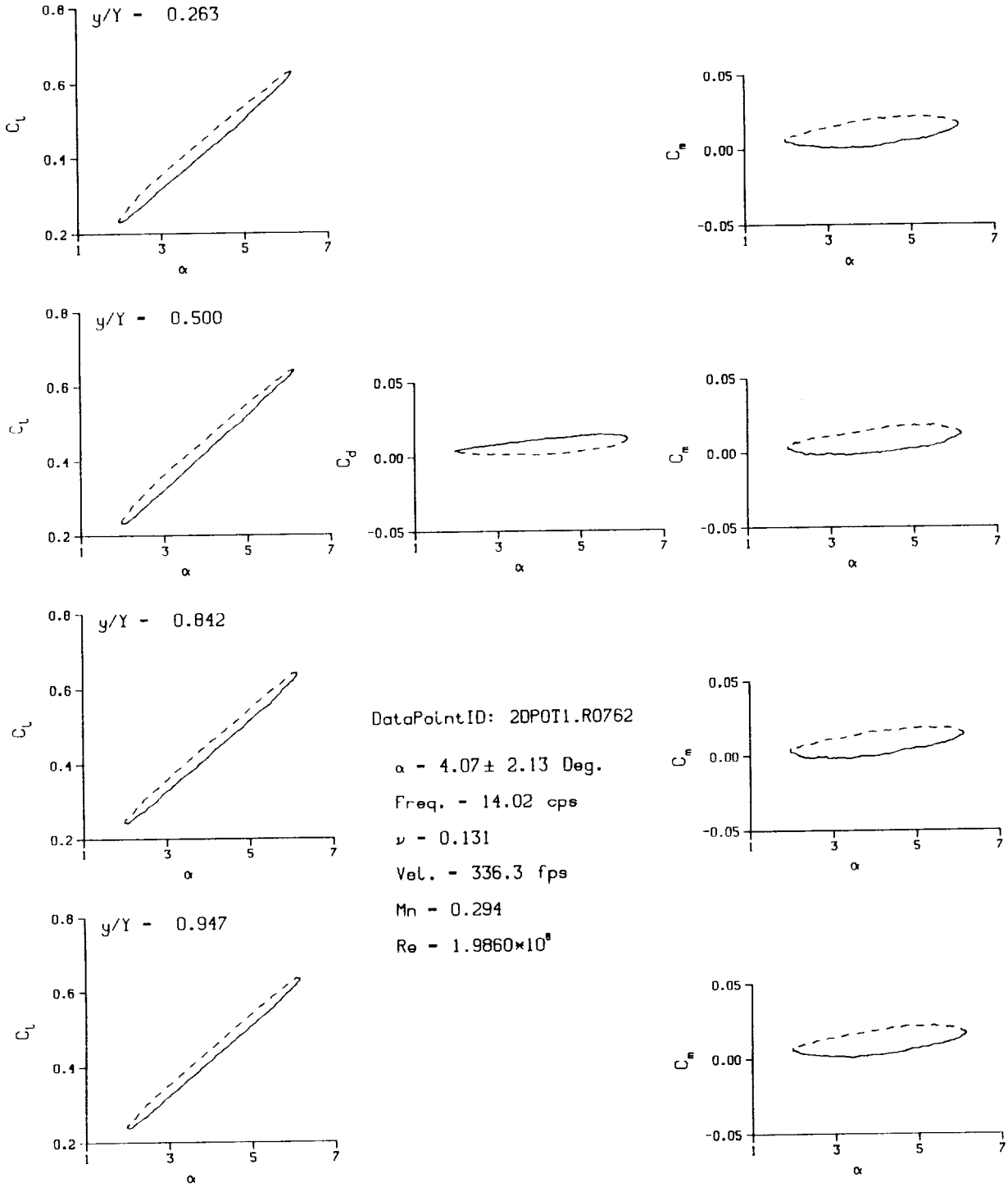

(c) ν = 0.14

Figure 18. Continued.

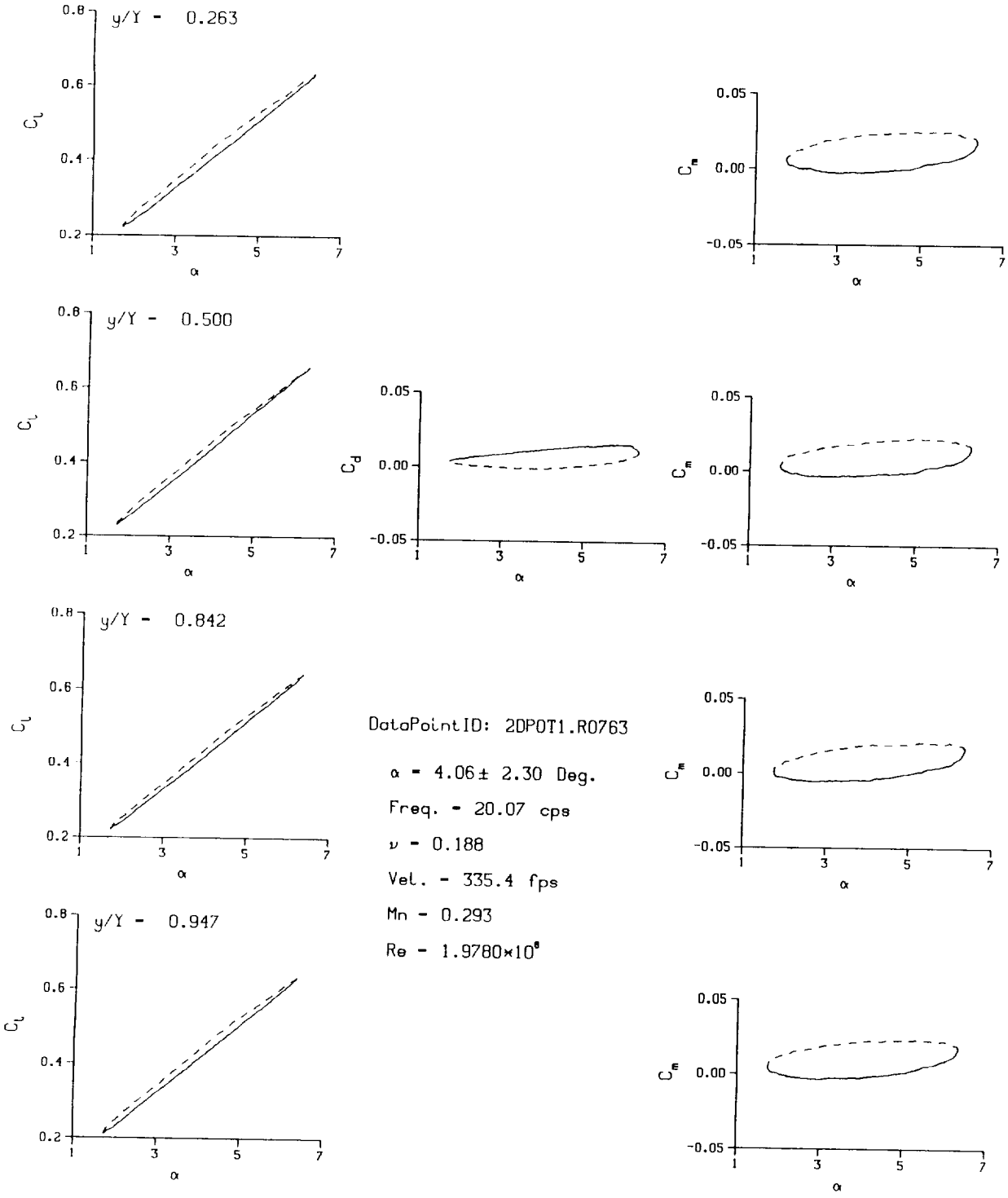

(d) v = 0.20

Figure 18. Concluded.

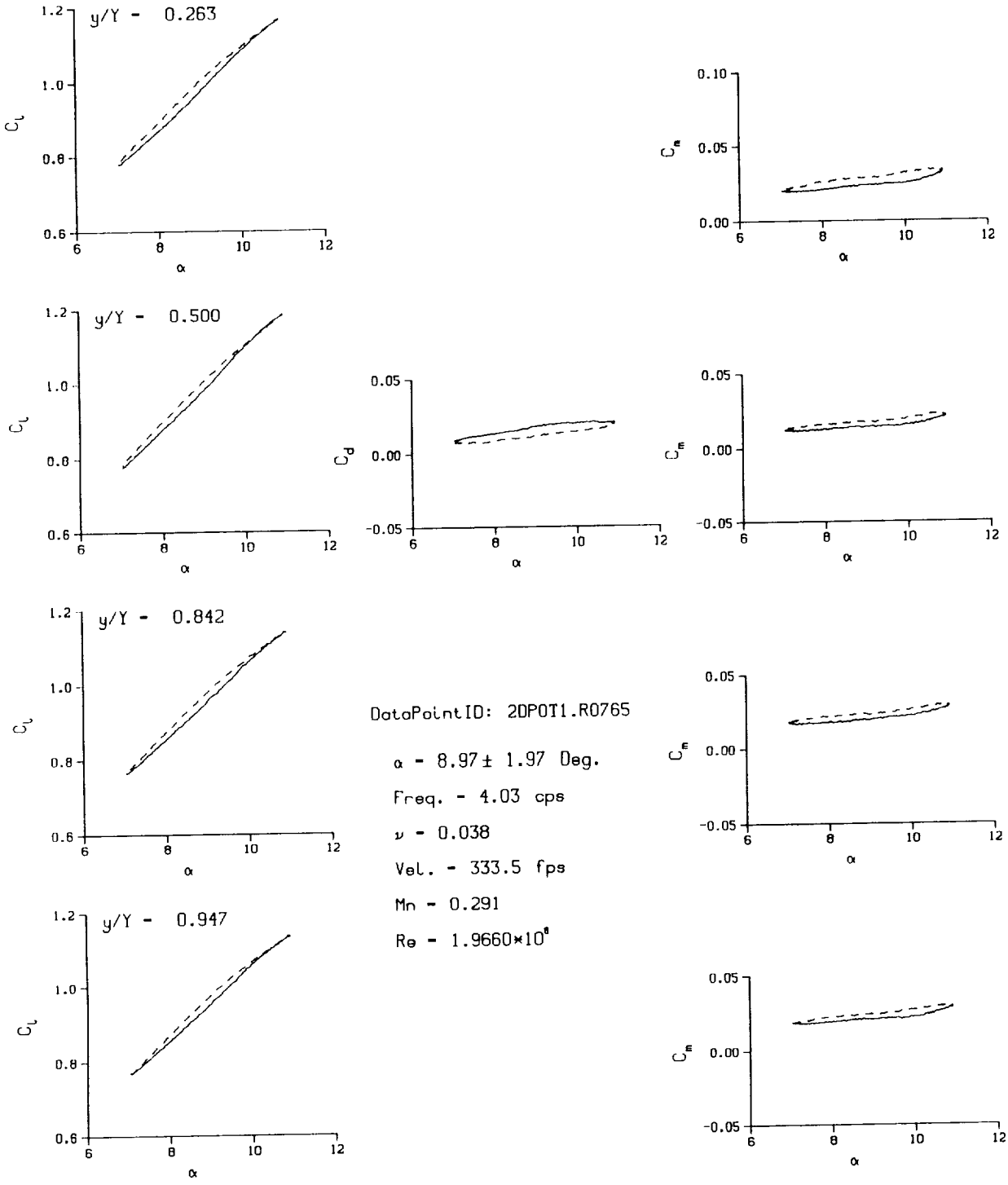

(a) v = 0.04

Figure 19. 2-D pitch oscillation data; BL-trip; α = 9 ± 2 deg.

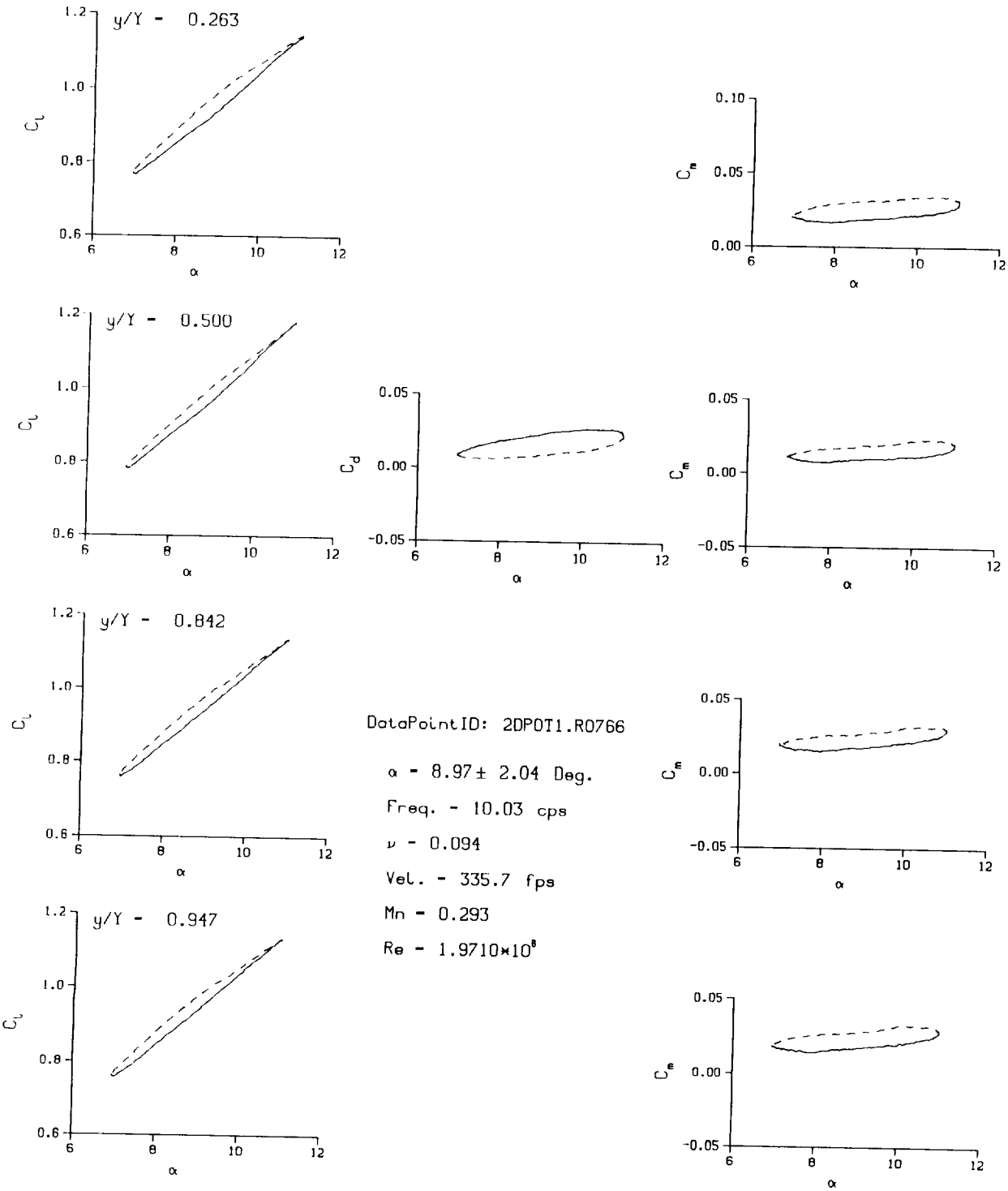

(b) v = 0.10

Figure 19. Continued.

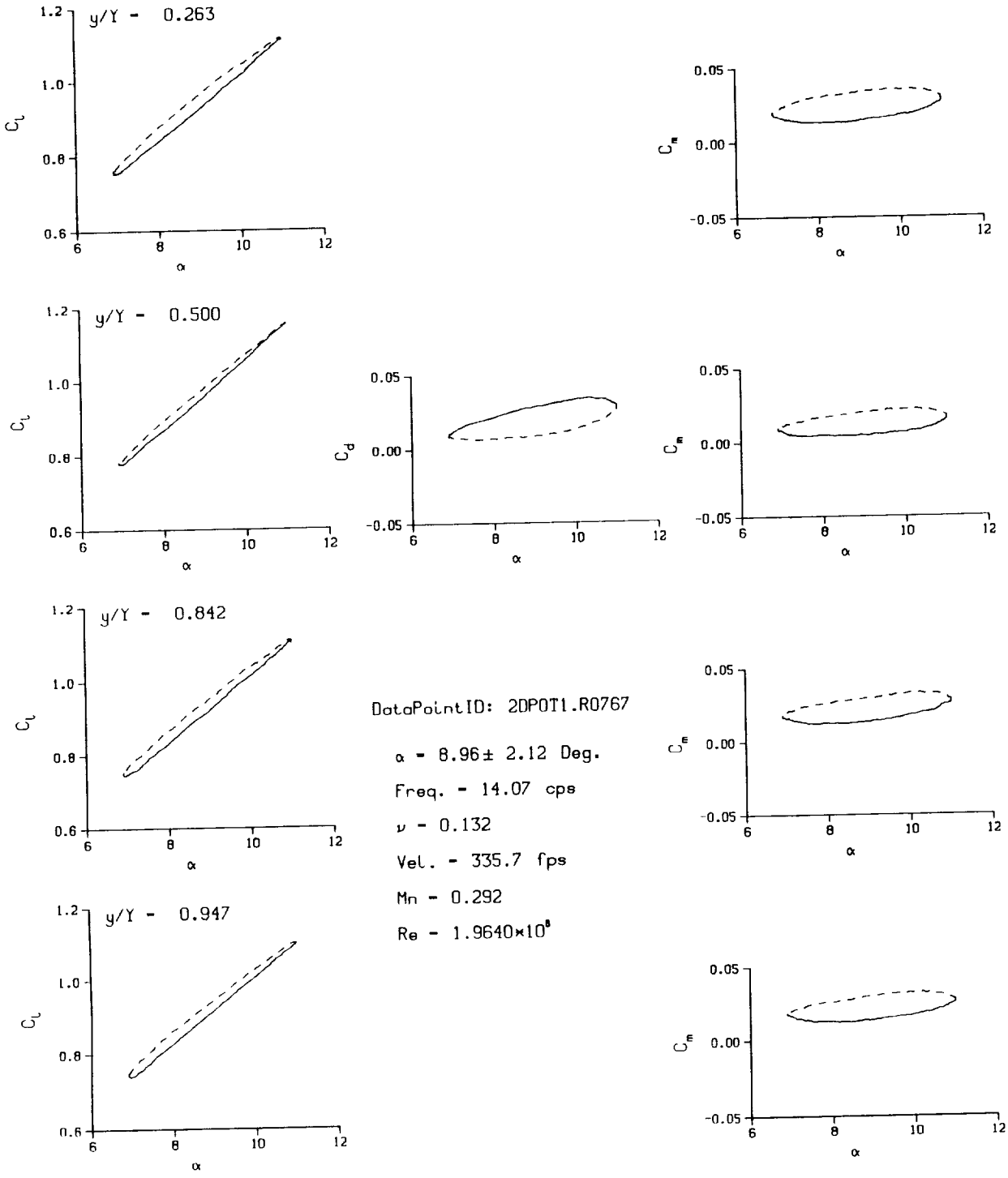

(c) $\nu = 0.14$

Figure 19. Continued.

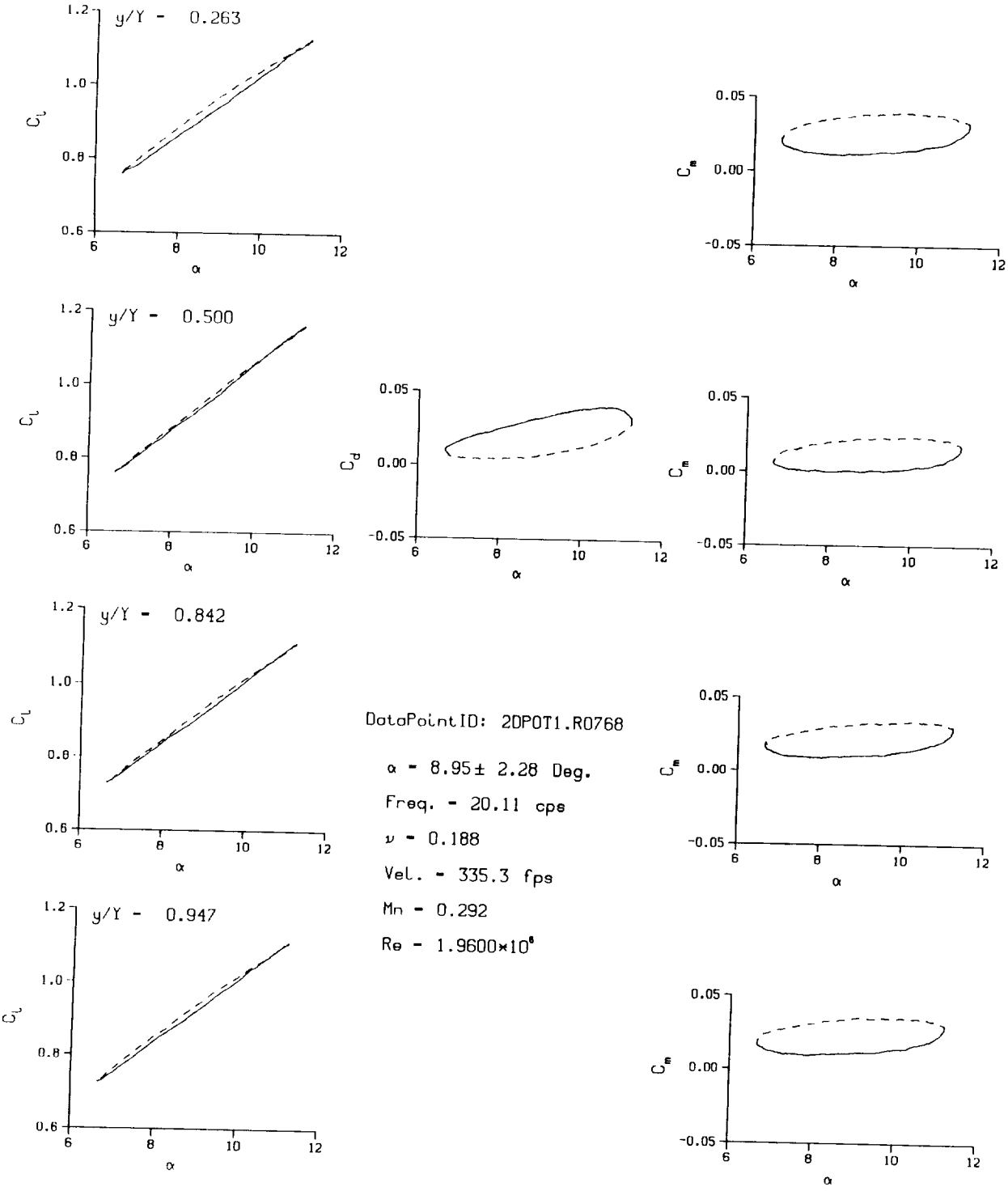

(d) v = 0.20

Figure 19. Concluded.

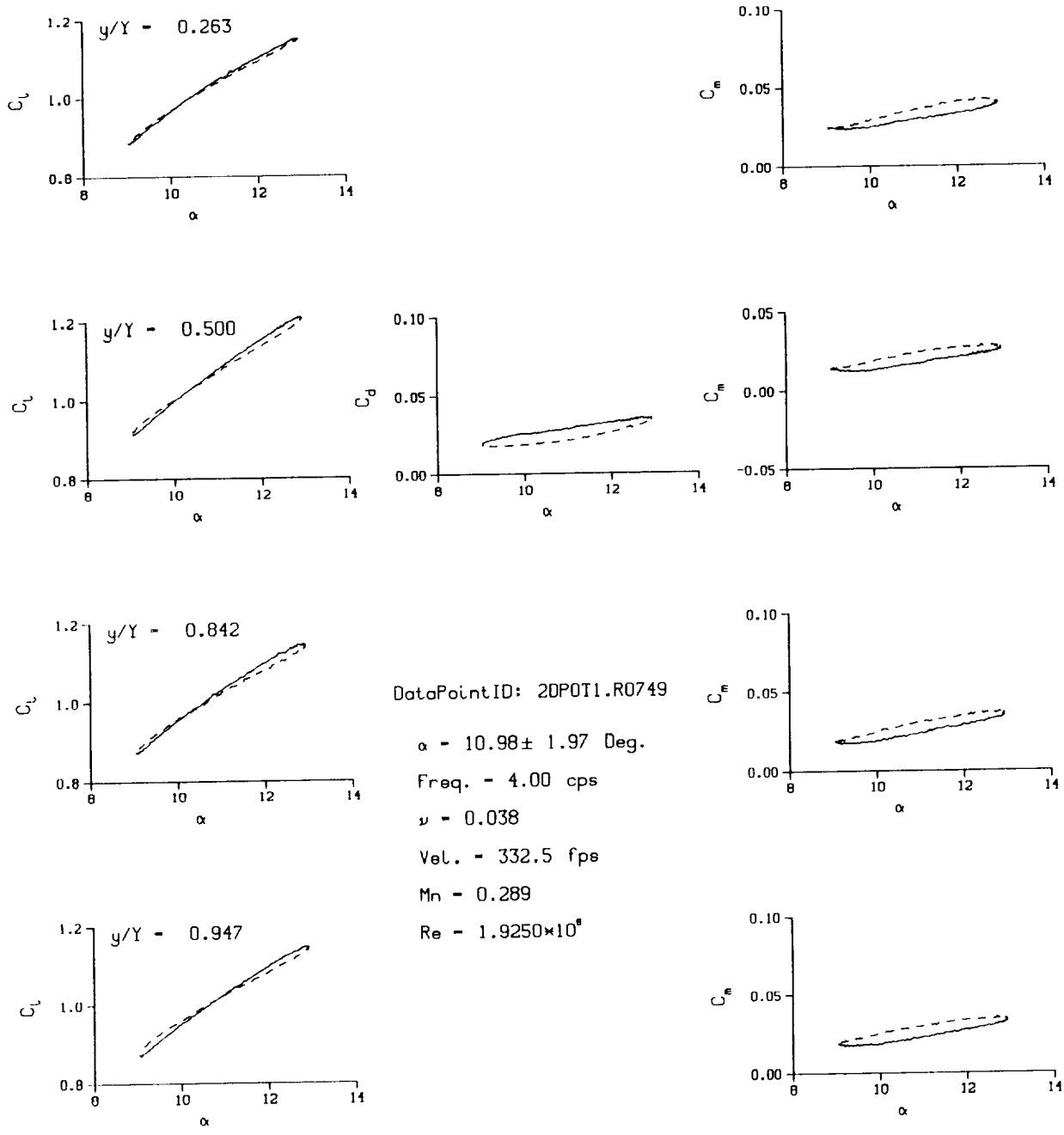

(a) v = 0.04

Figure 20. 2-D pitch oscillation data; BL-trip; α = 11 ± 2 deg.

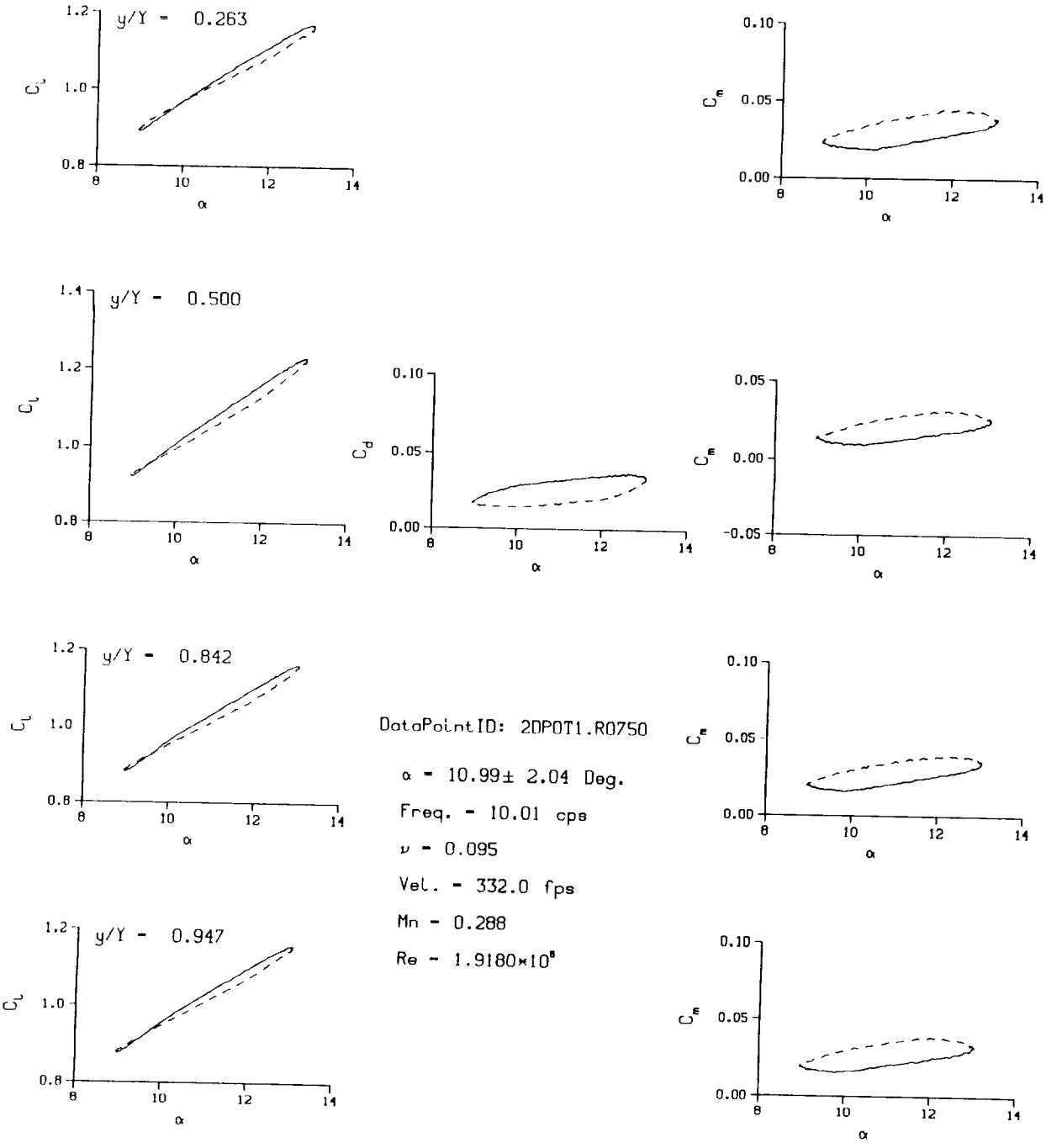

(b) v = 0.10

Figure 20. Continued.

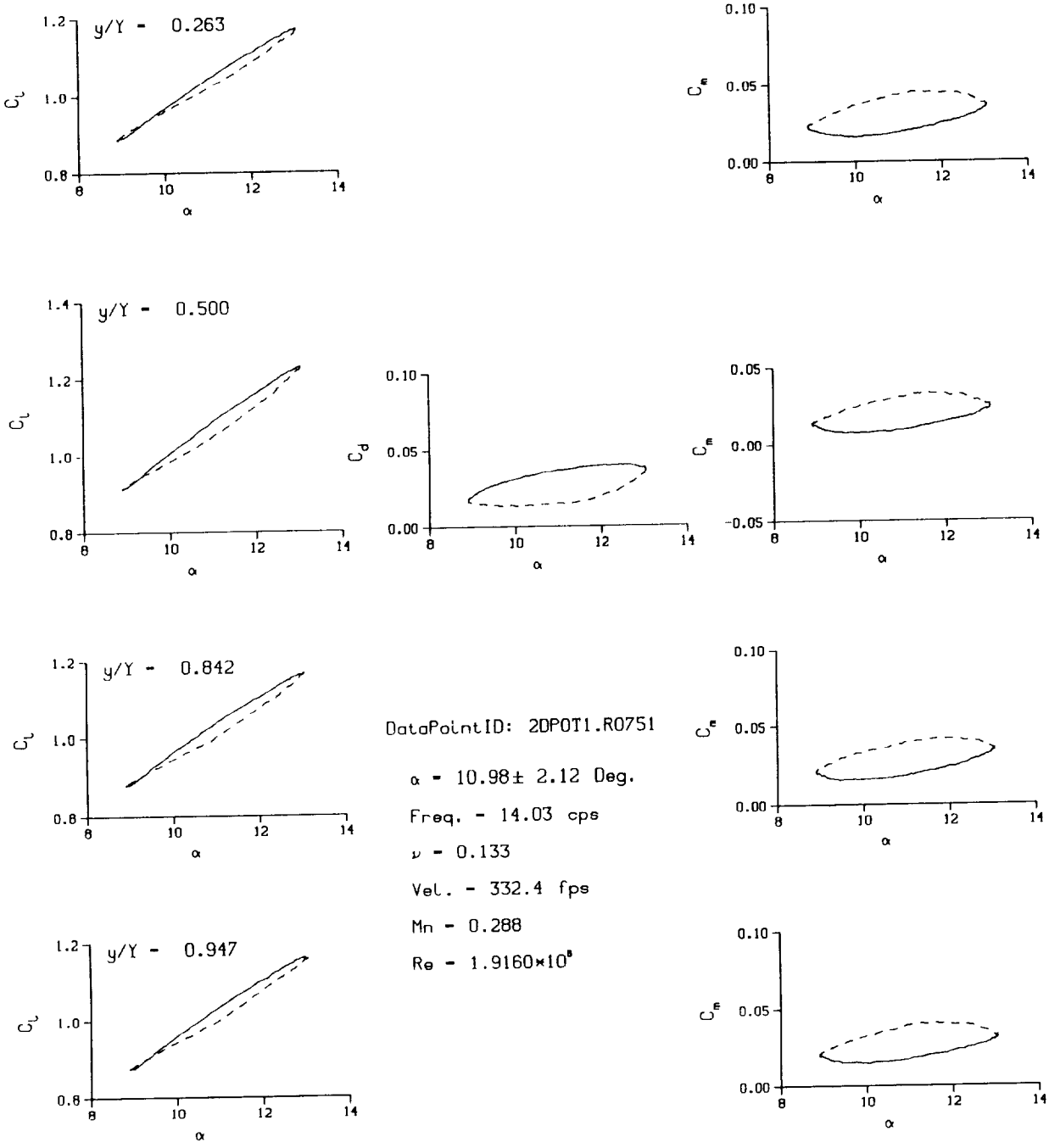

(c) v = 0.14

Figure 20. Continued.

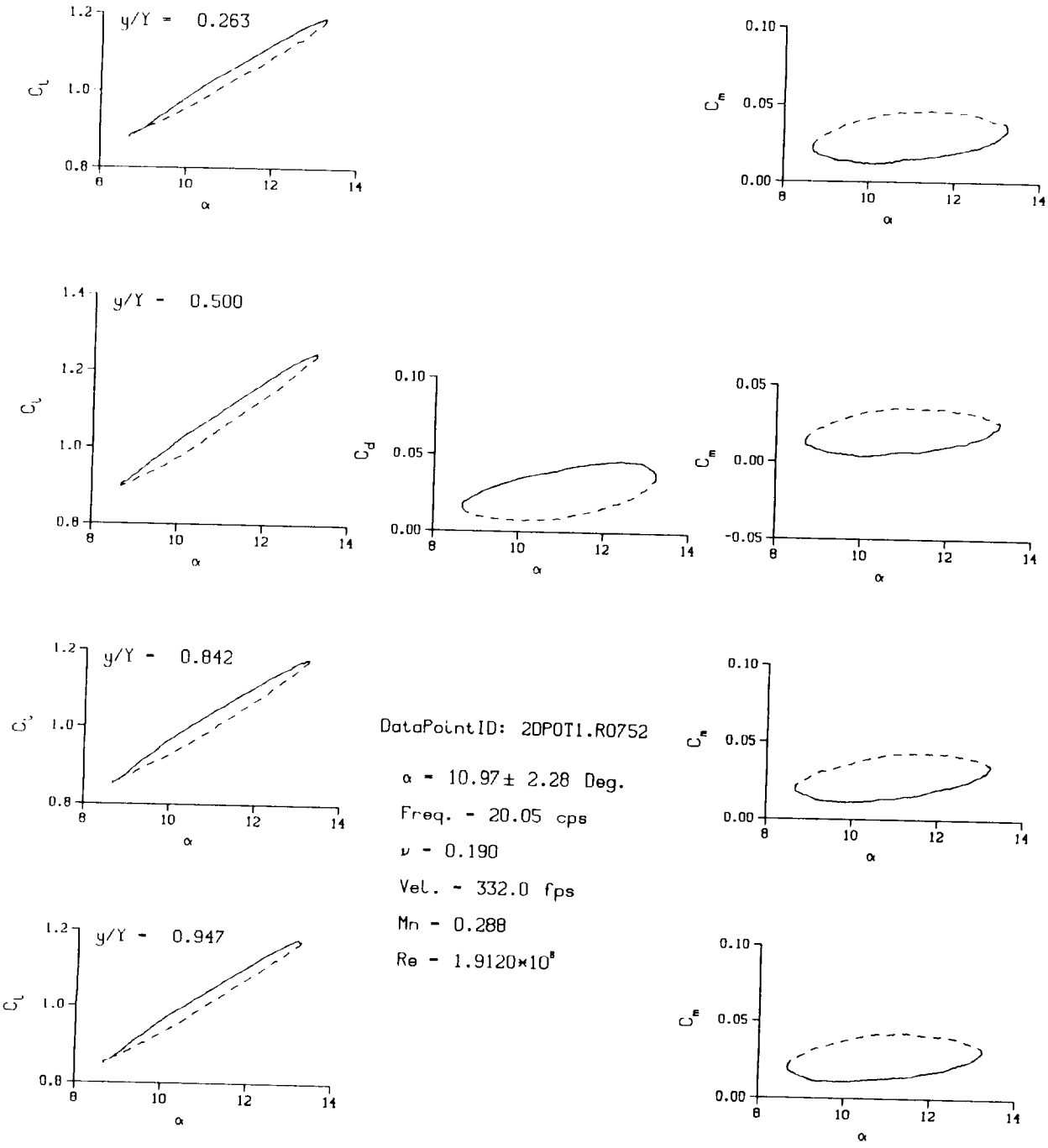

(d) ν = 0.20

Figure 20. Concluded.

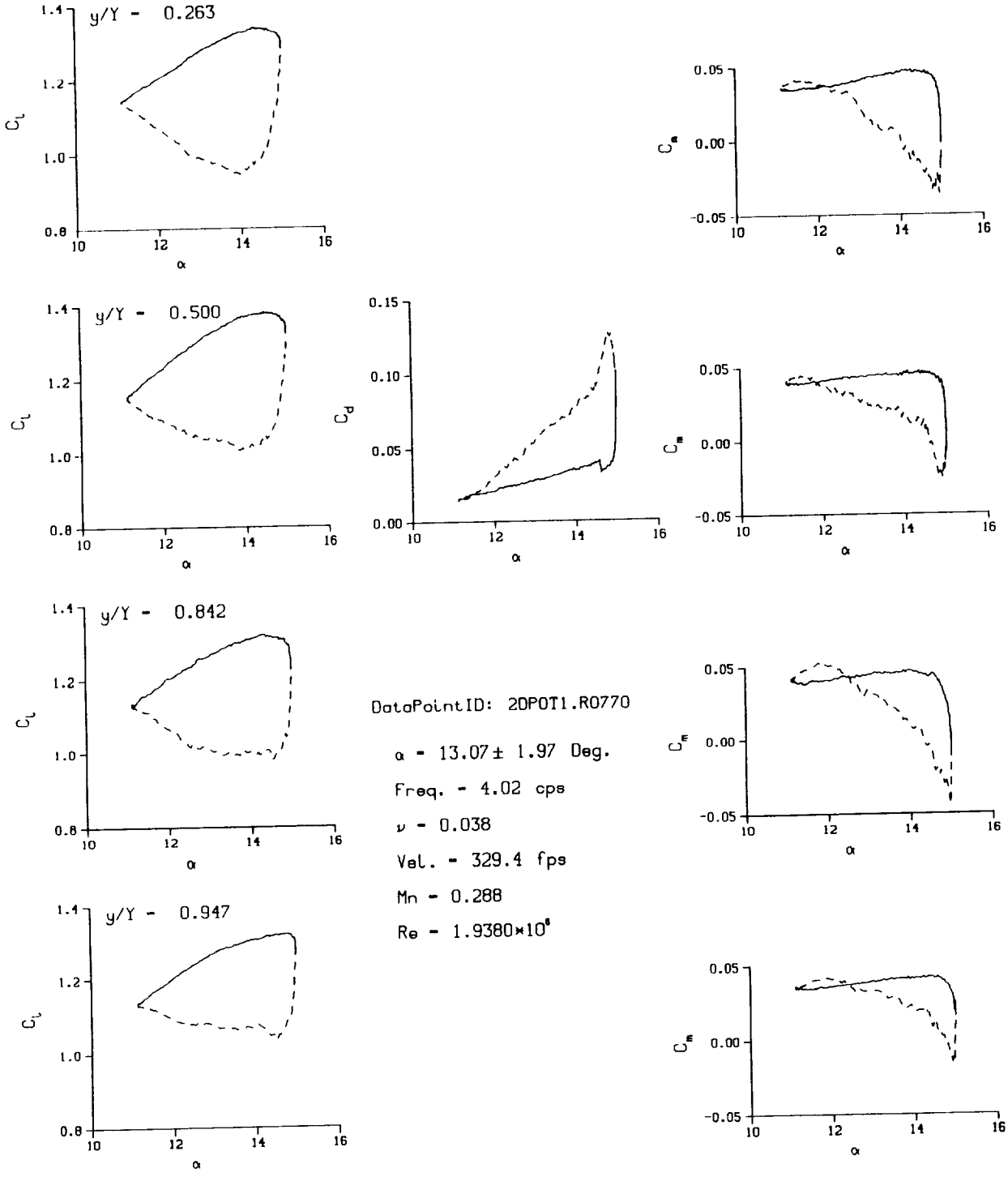

(a) v = 0.04

Figure 21. 2-D pitch oscillation data; BL-trip; α = 13 ± 2 deg.

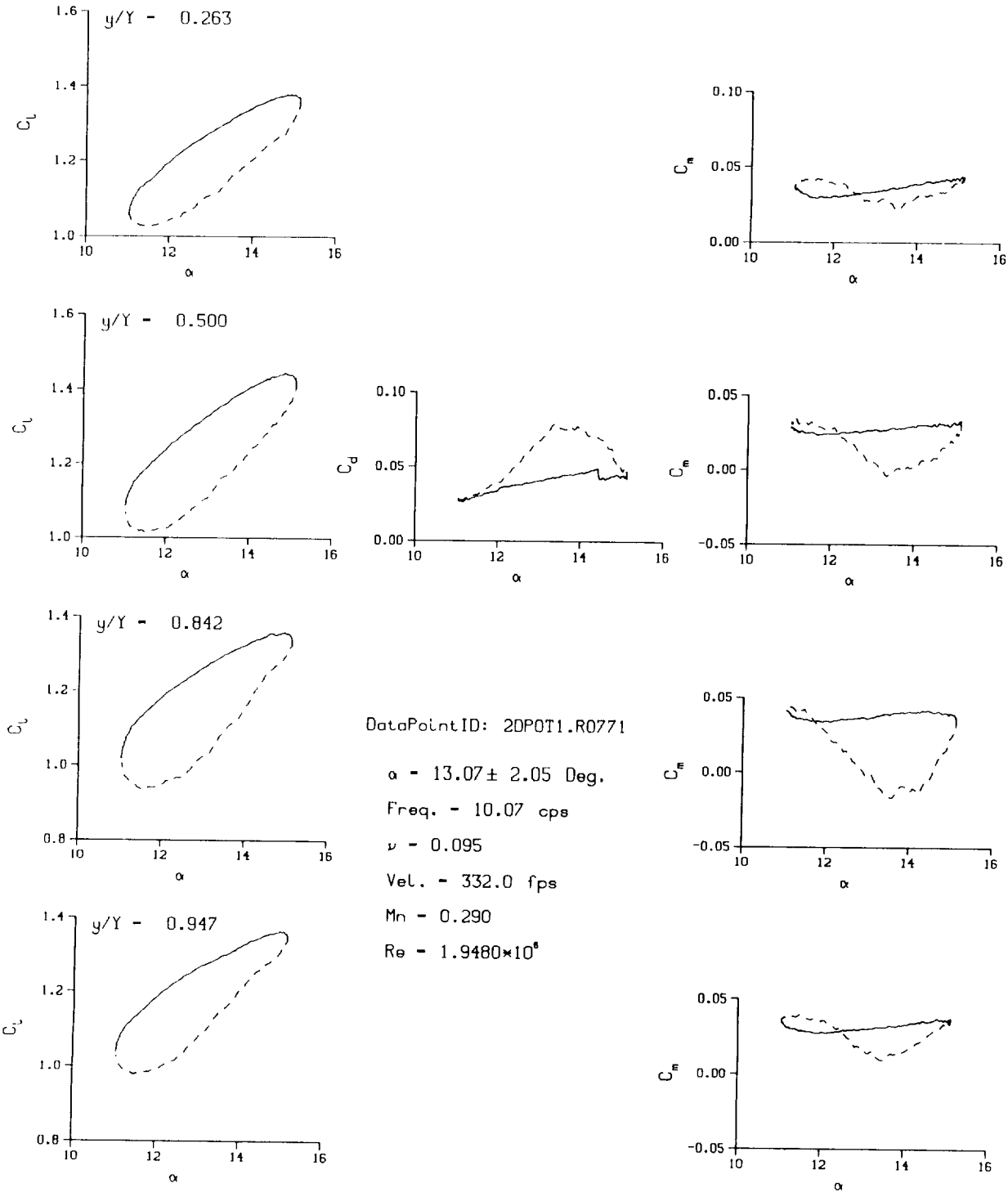

(b) v = 0.10

Figure 21. Continued.

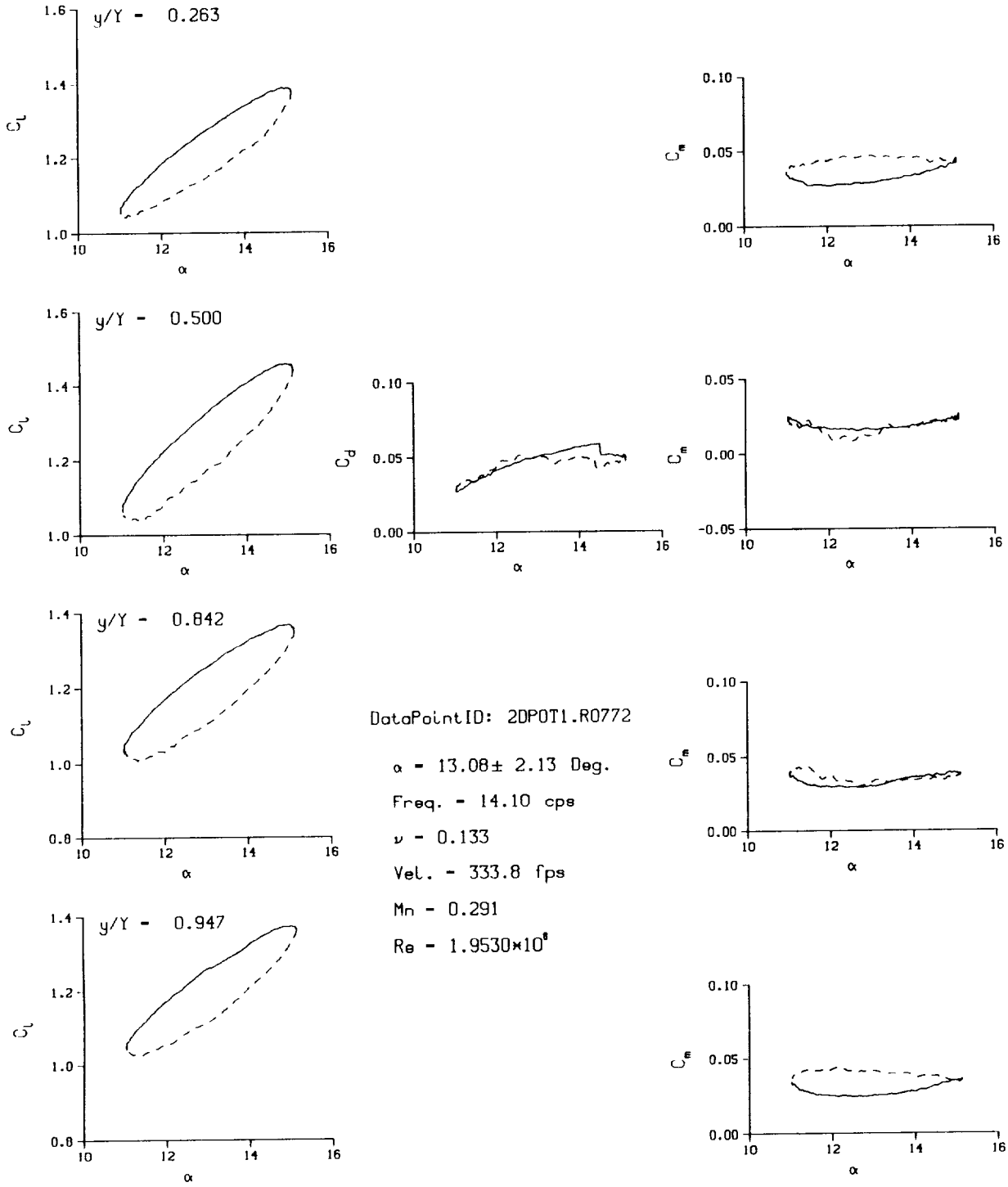

(c) v = 0.14

Figure 21. Continued.

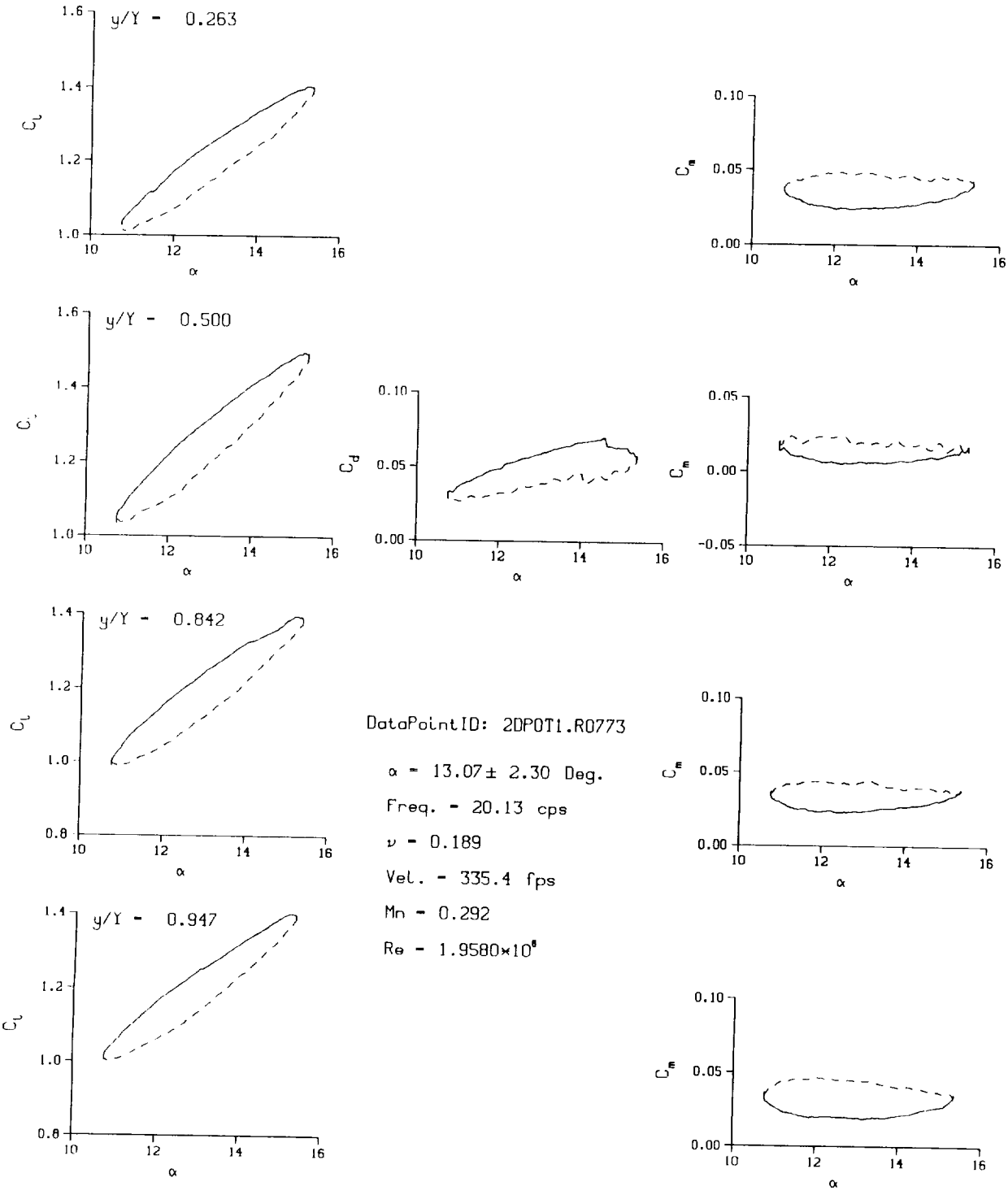

(d) ν = 0.20

Figure 21. Concluded.

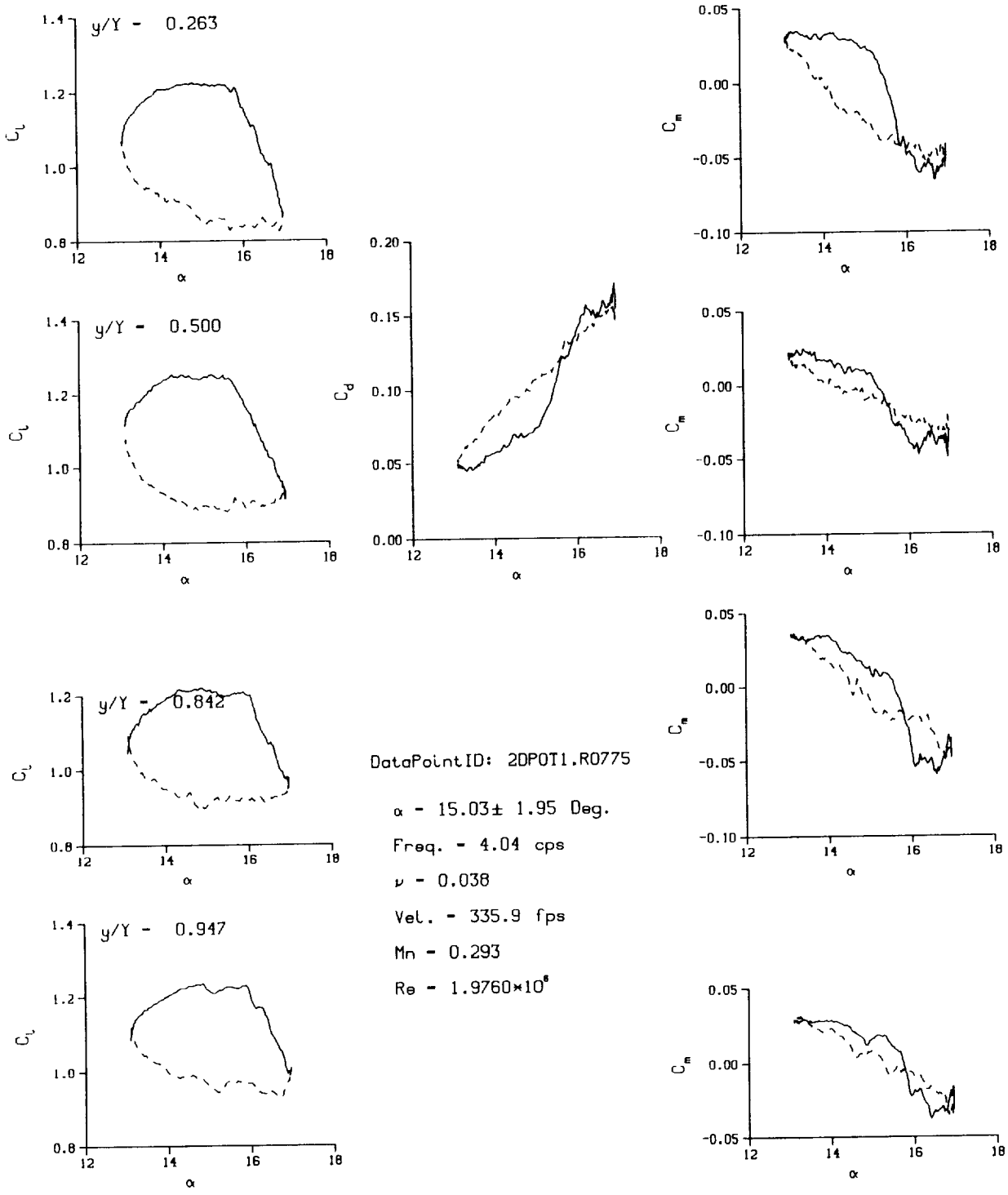

(a) v = 0.04

Figure 22. 2-D pitch oscillation data; BL-trip; α = 15 ± 2 deg.

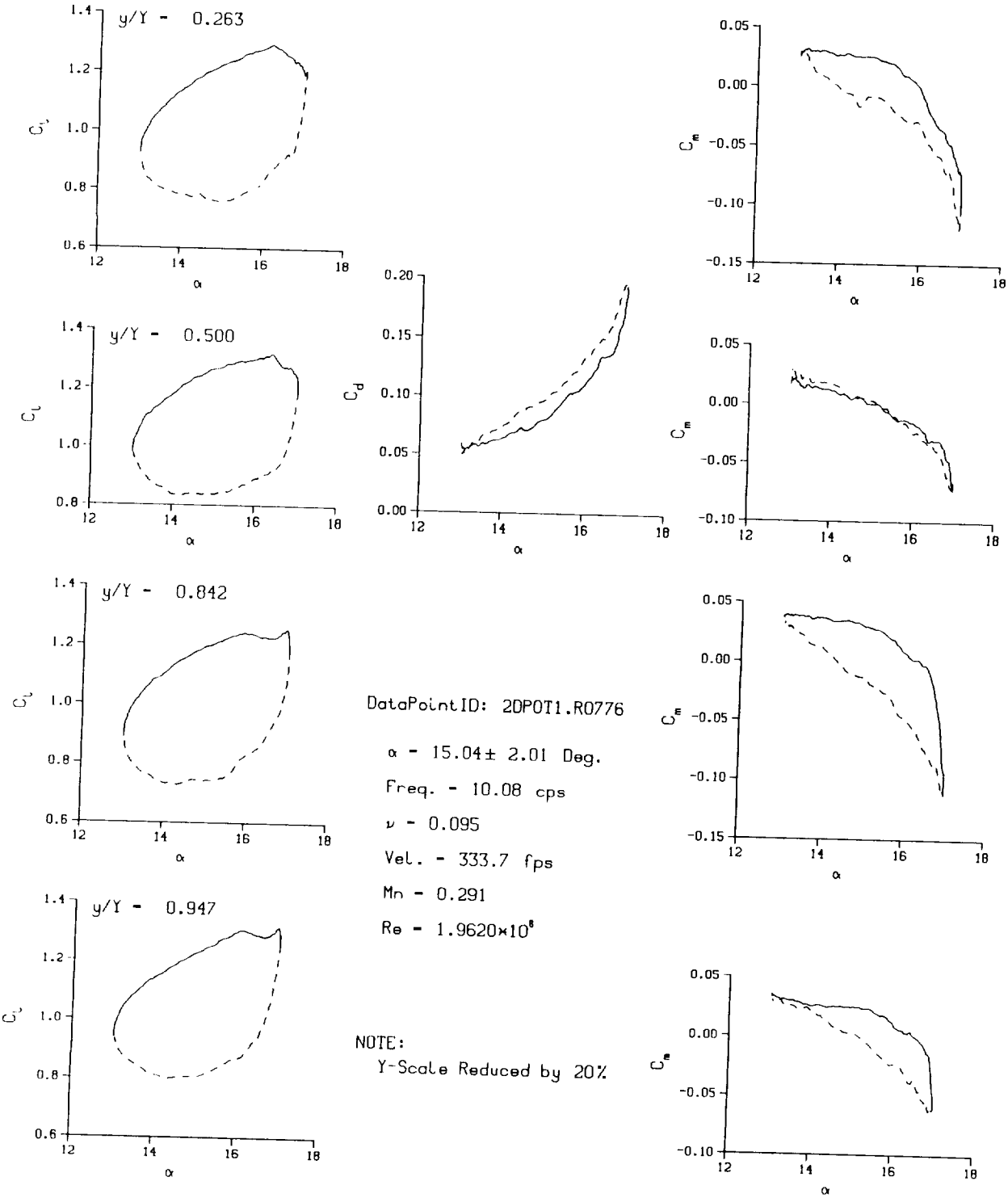

(b) ν = 0.10

Figure 22. Continued.

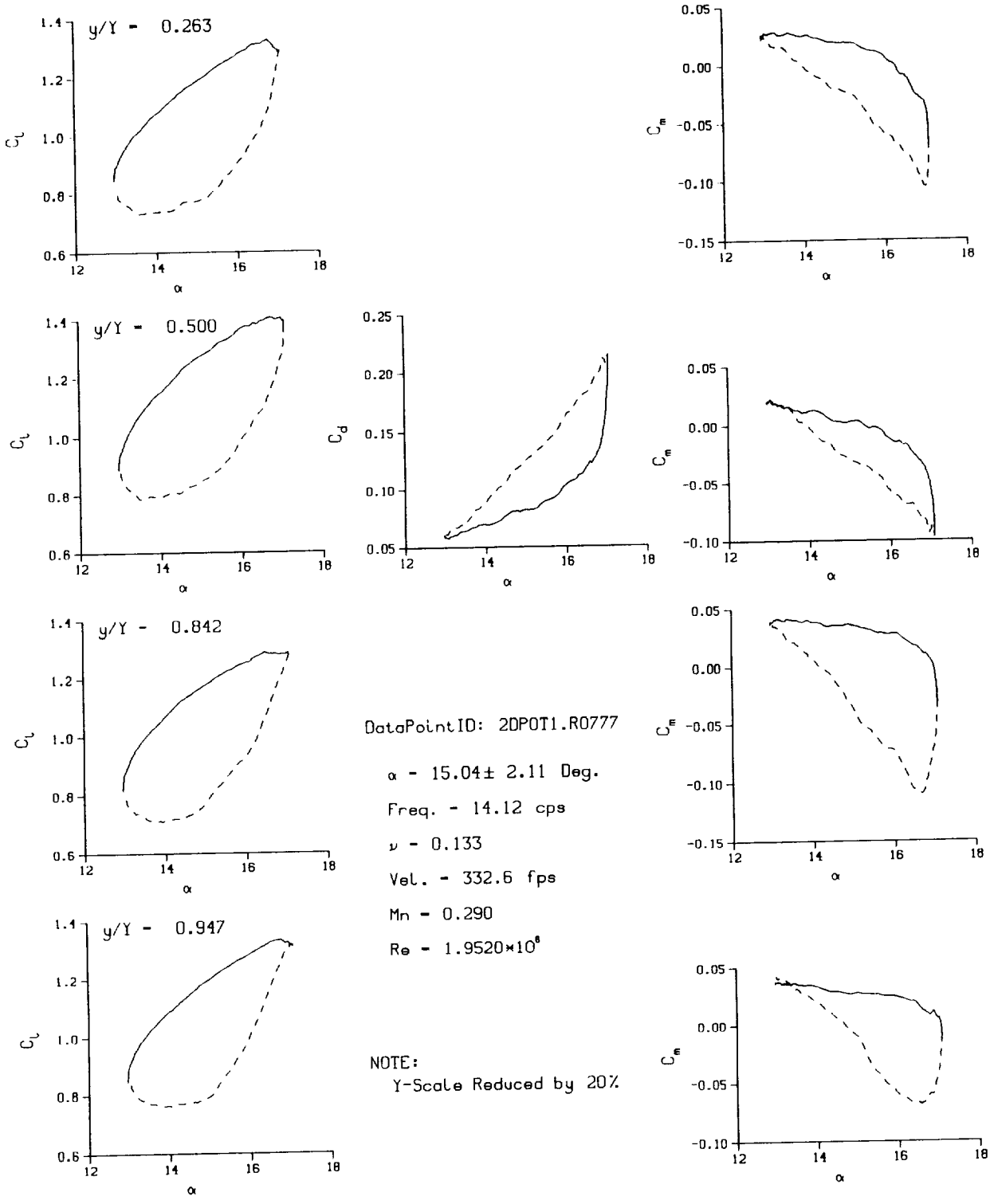

(c) v = 0.14

Figure 22. Continued.

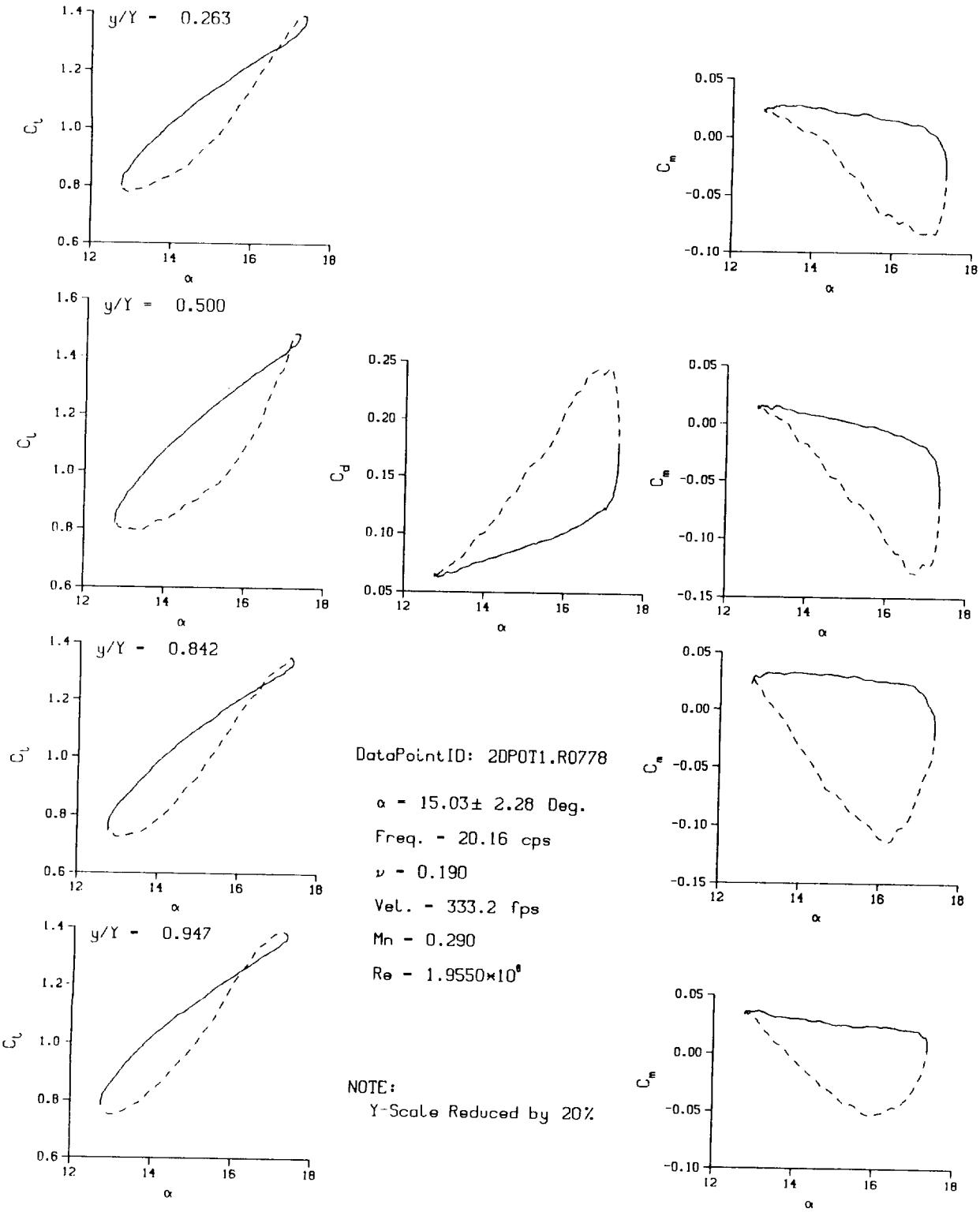

(d) ν = 0.20

Figure 22. Concluded.

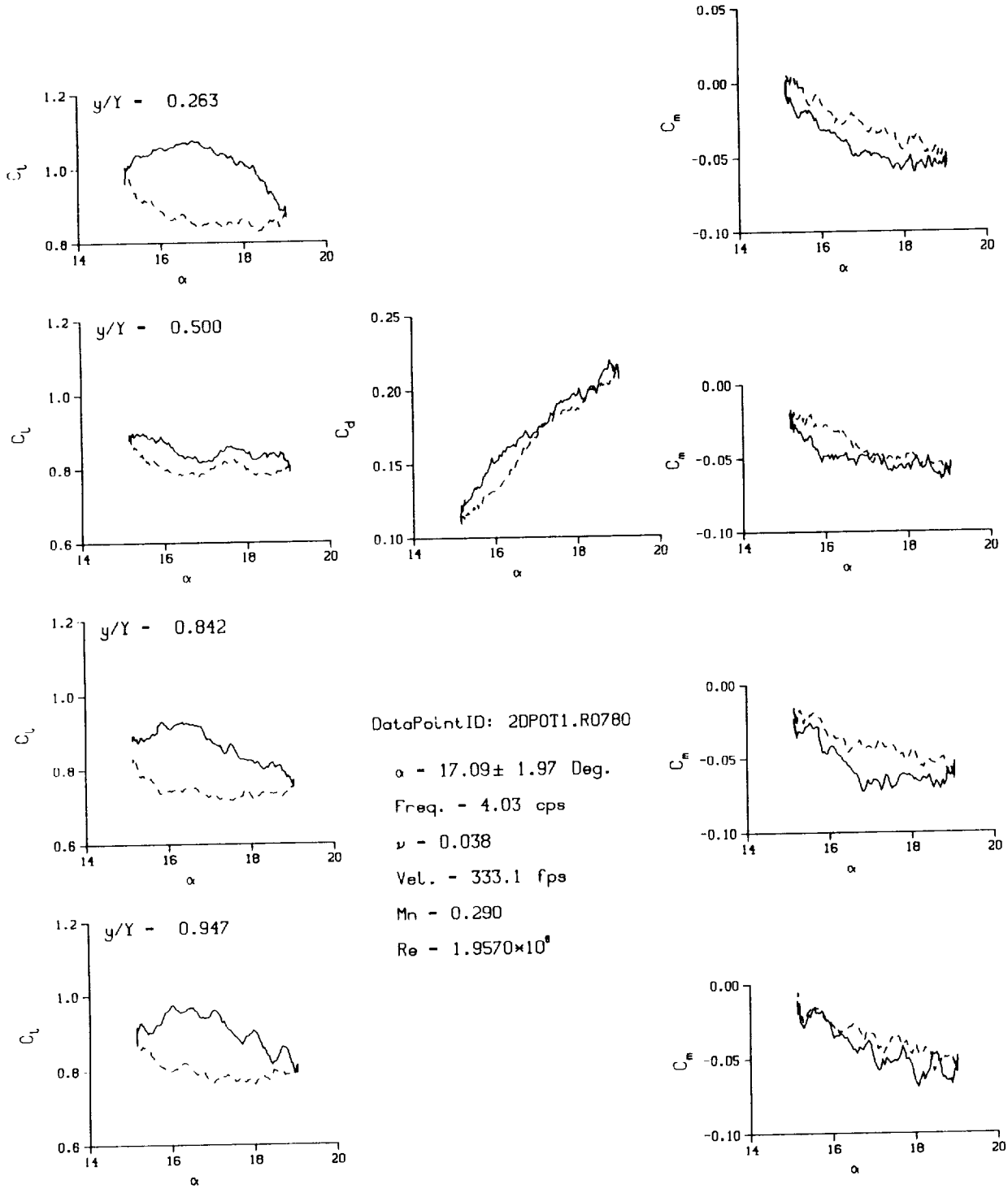

(a) v = 0.04

Figure 23. 2-D pitch oscillation data; BL-trip; α = 17 ± 2 deg.

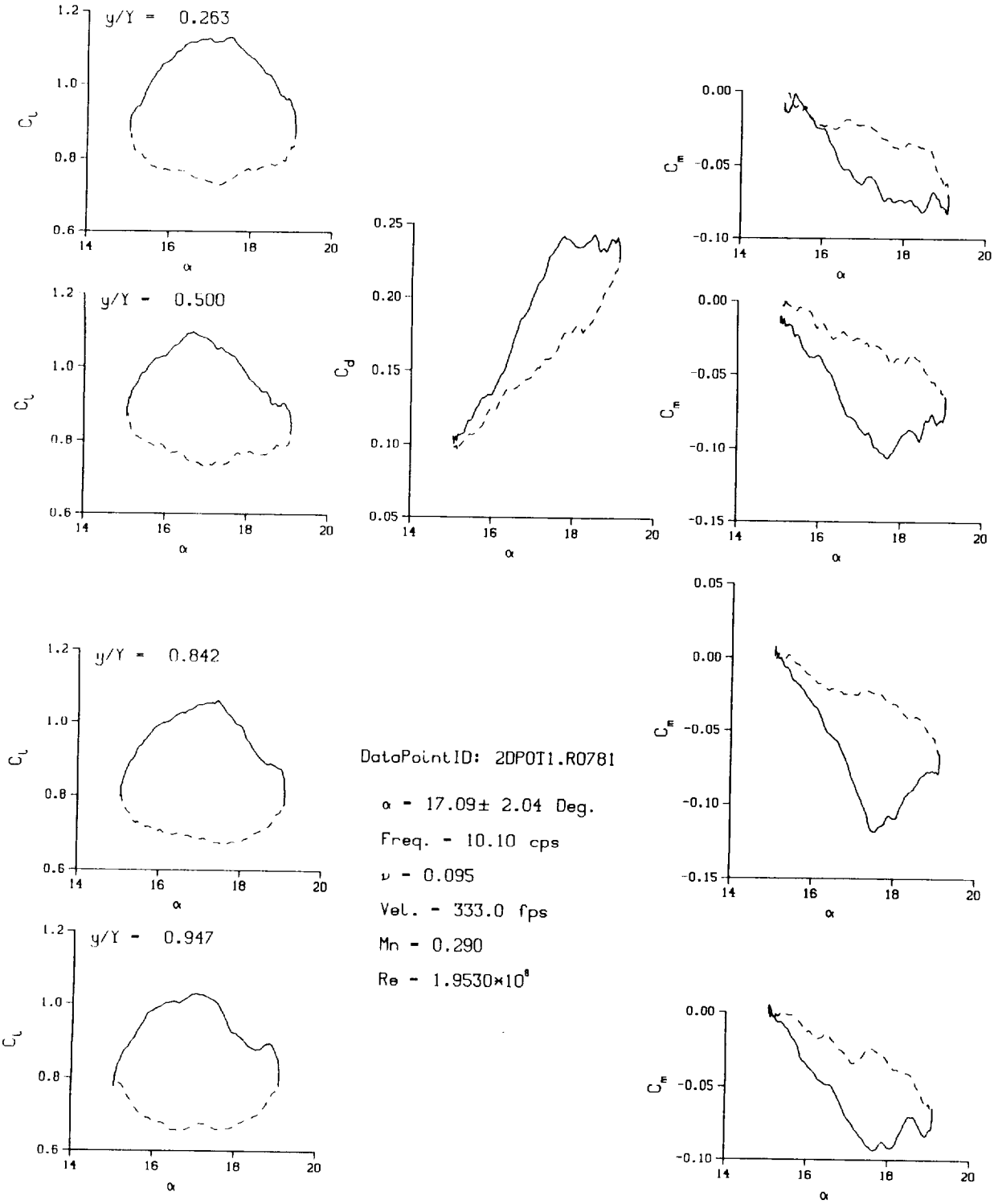

(b) v = 0.10

Figure 23. Continued.

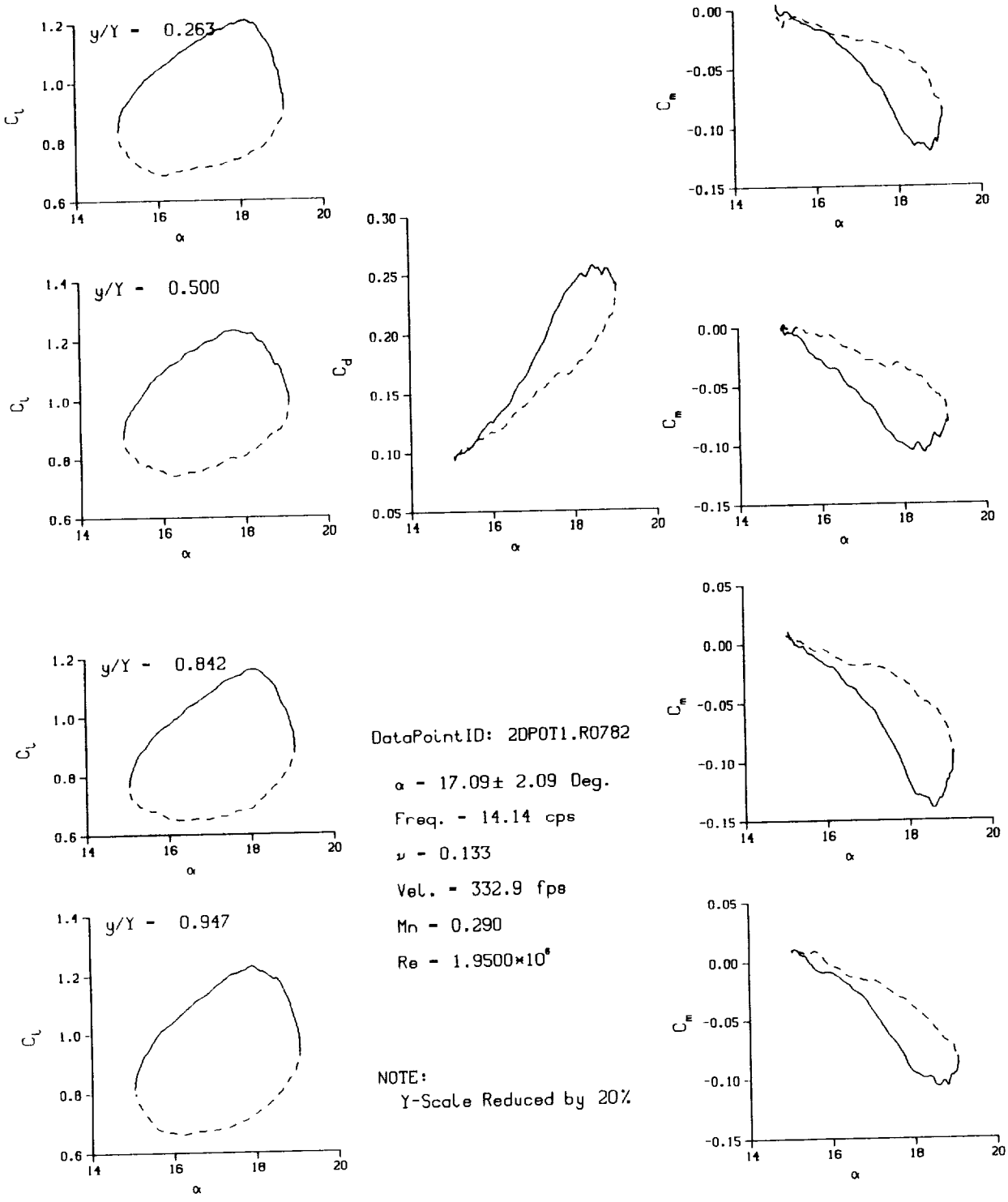

(c) v = 0.14

Figure 23. Continued.

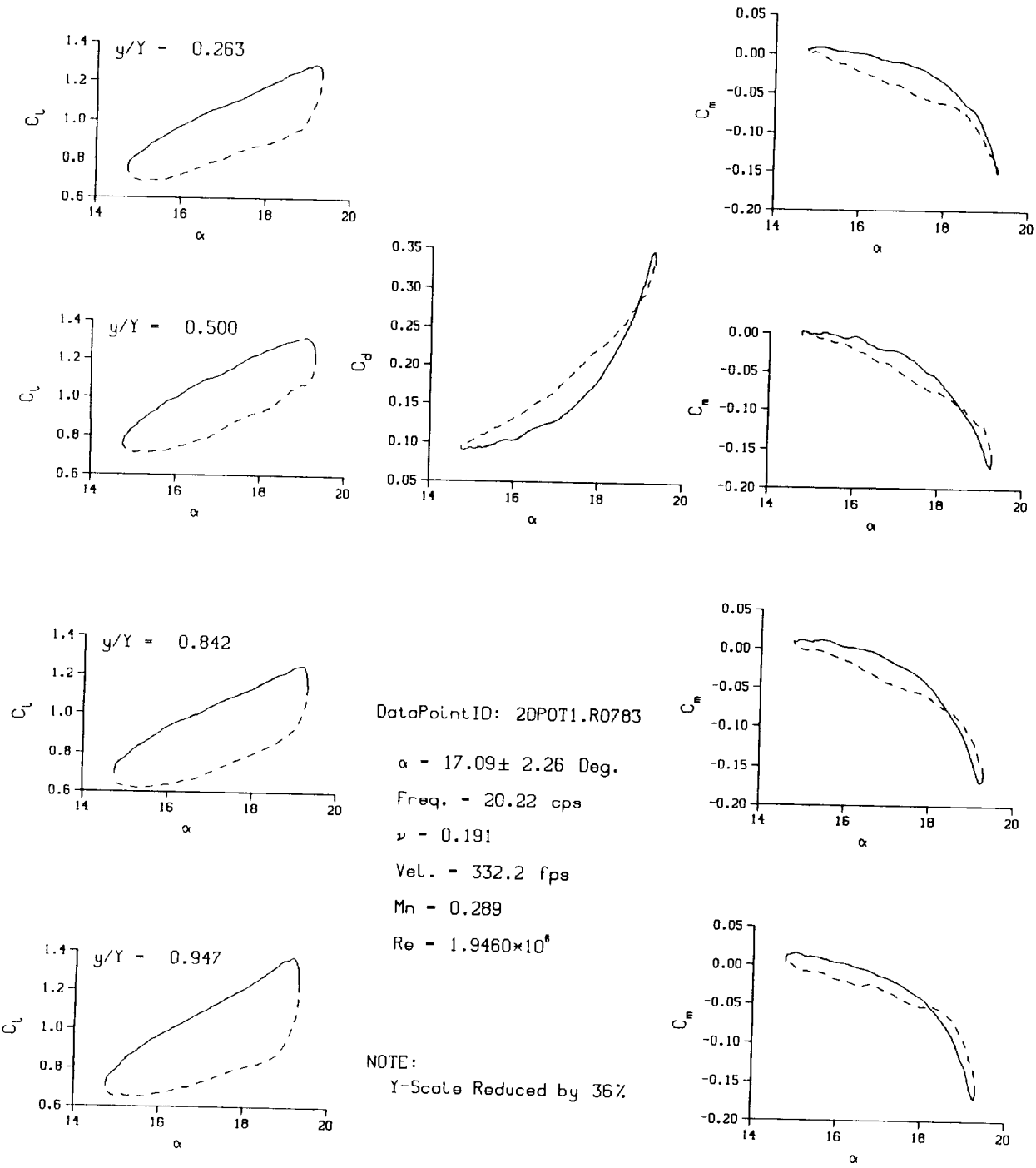

(d) ν = 0.20

Figure 23. Concluded.

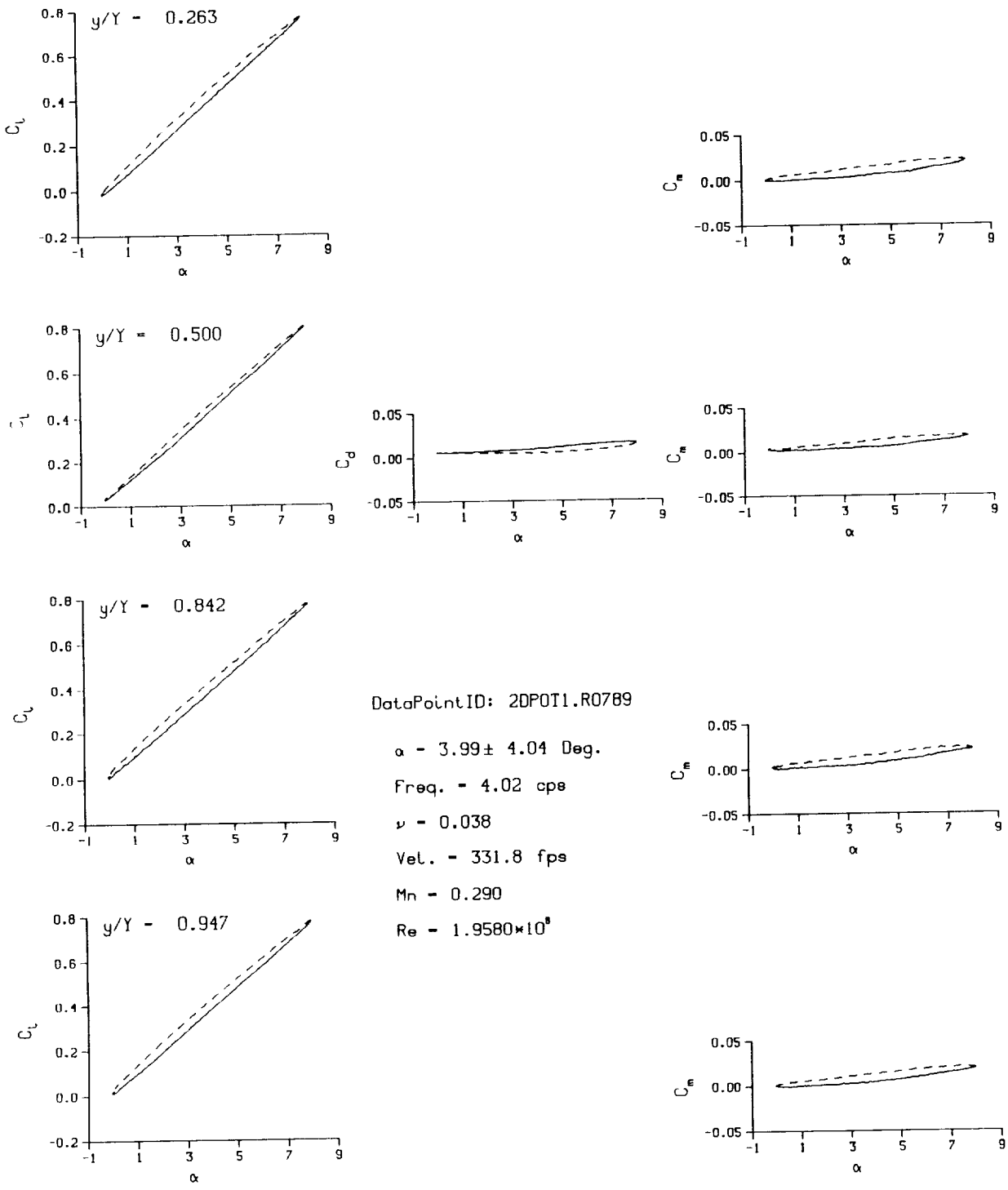

(a) ν = 0.04

Figure 24. 2-D pitch oscillation data; BL-trip; α = 4 ± 4 deg.

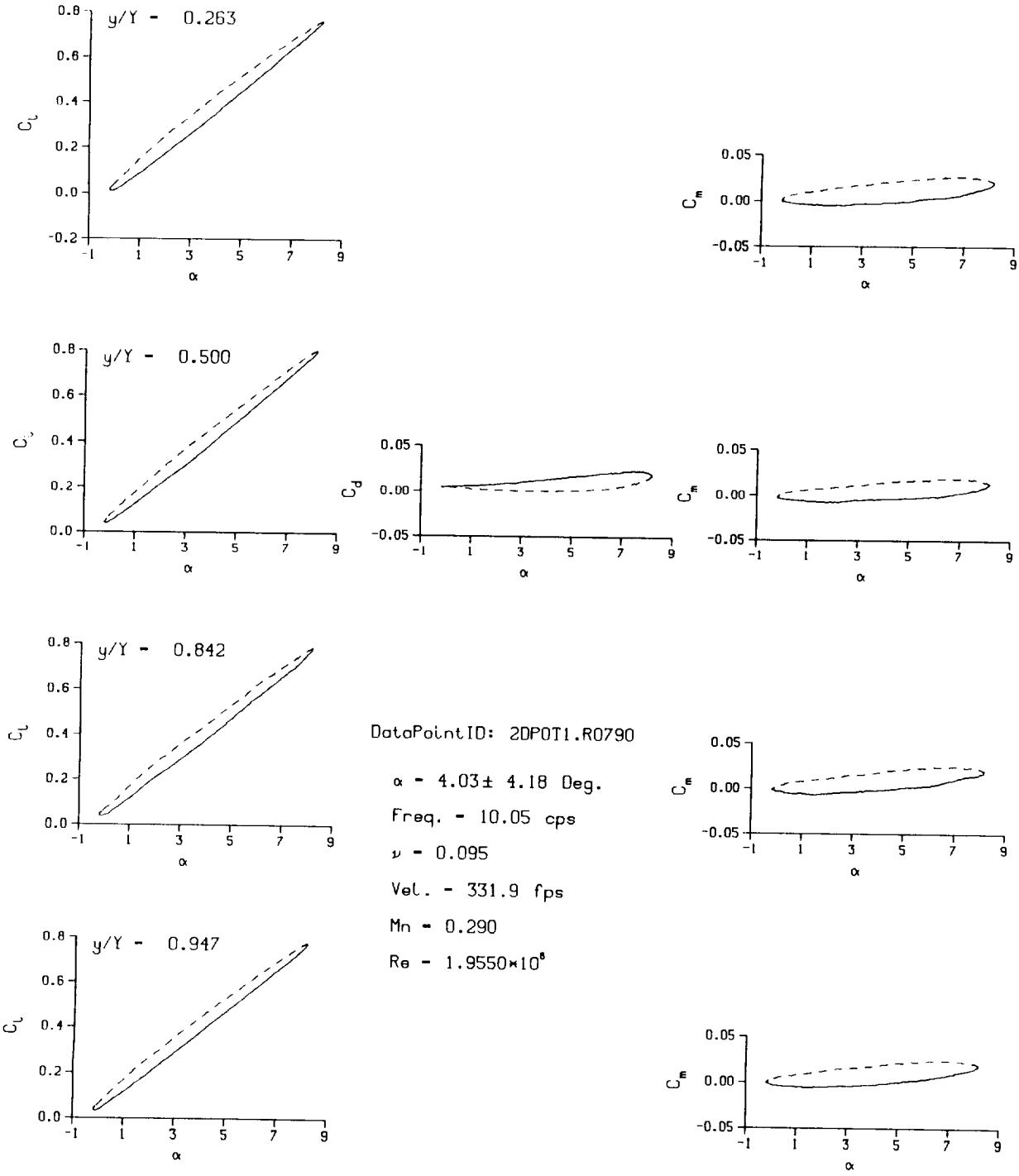

(b) v = 0.10

Figure 24. Continued.

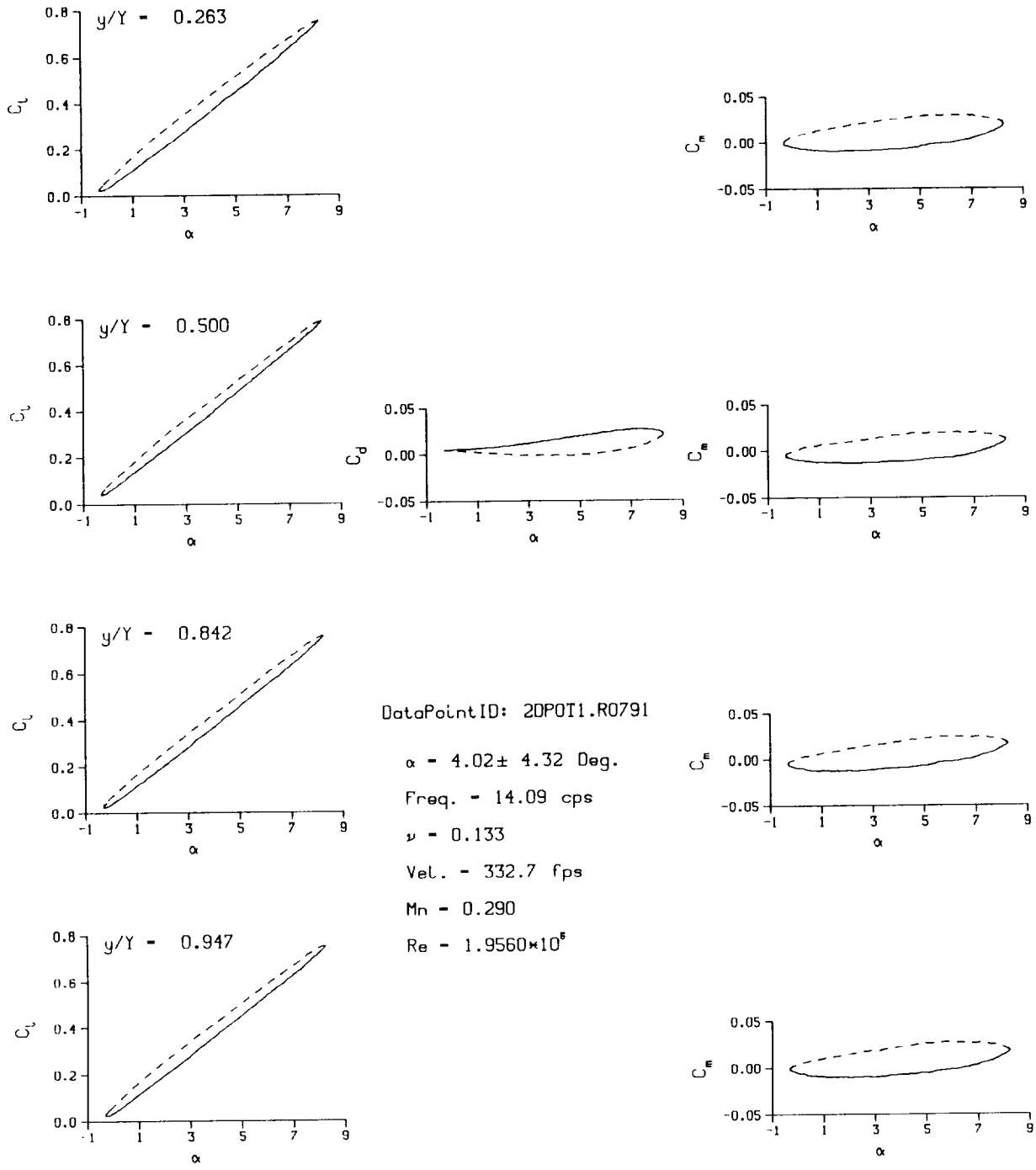

(c) v = 0.14

Figure 24. Concluded.

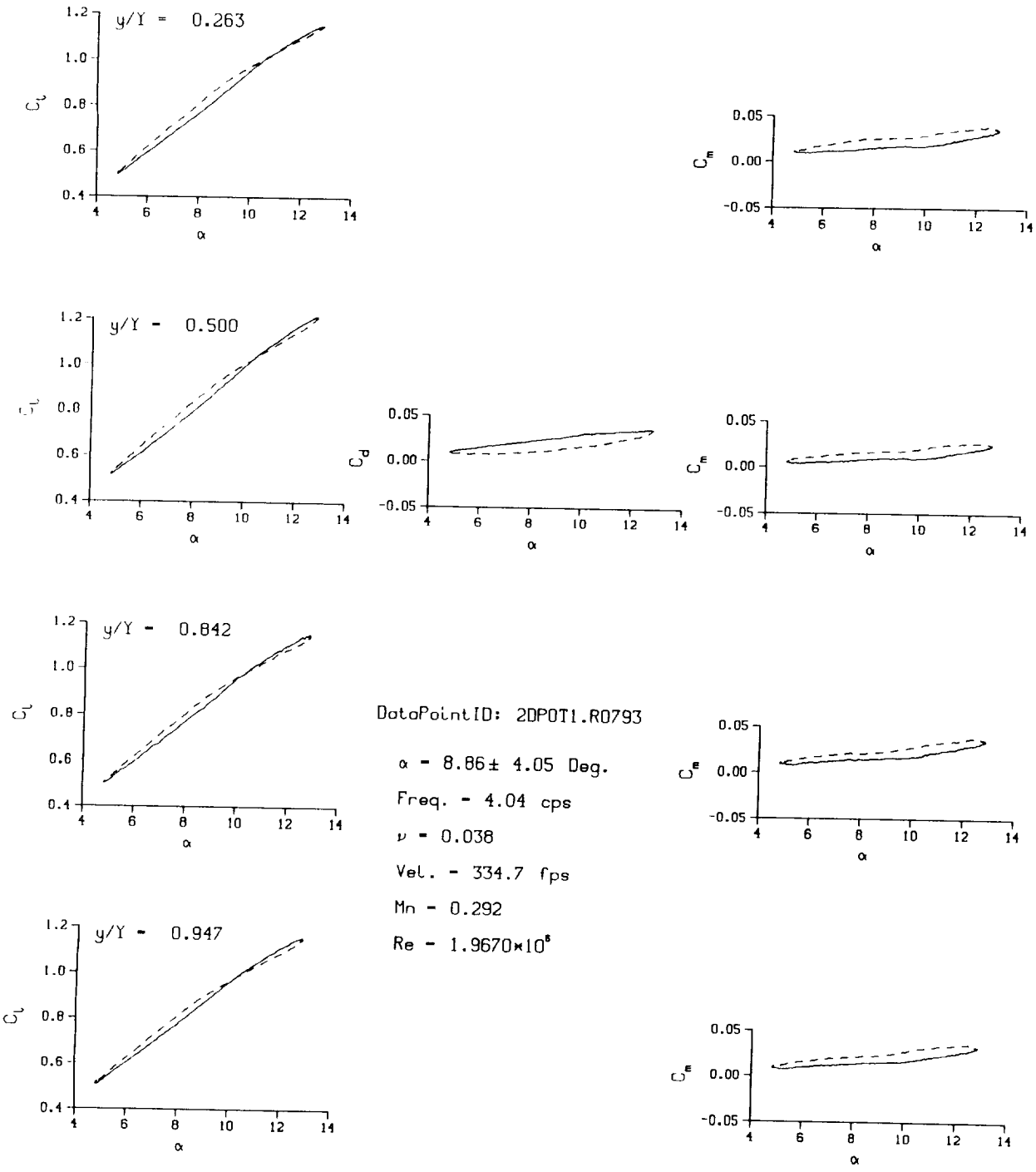

(a) v = 0.04

Figure 25. 2-D pitch oscillation data; BL-trip; α = 9 ± 4 deg.

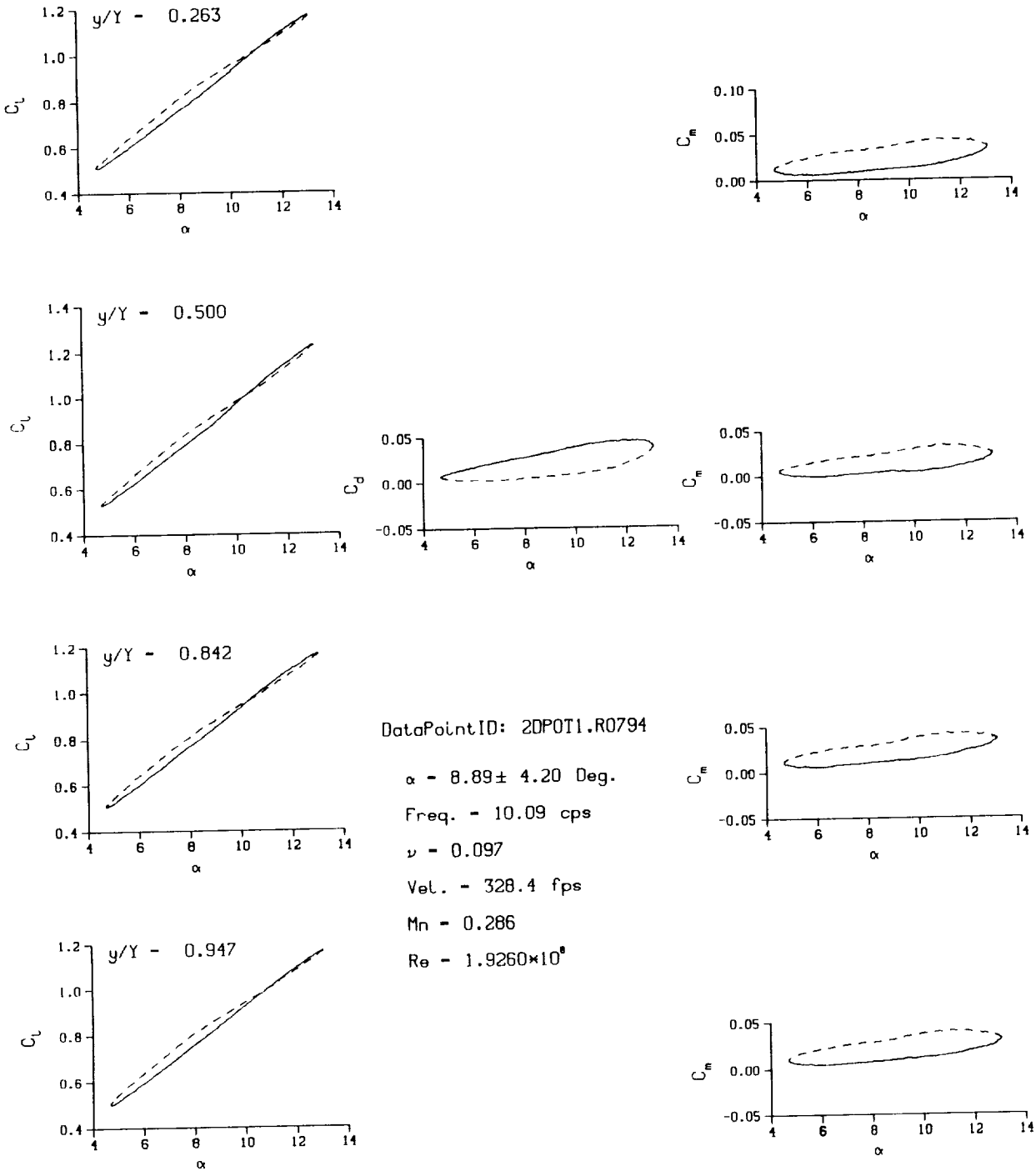

(b) ν = 0.10

Figure 25. Continued.

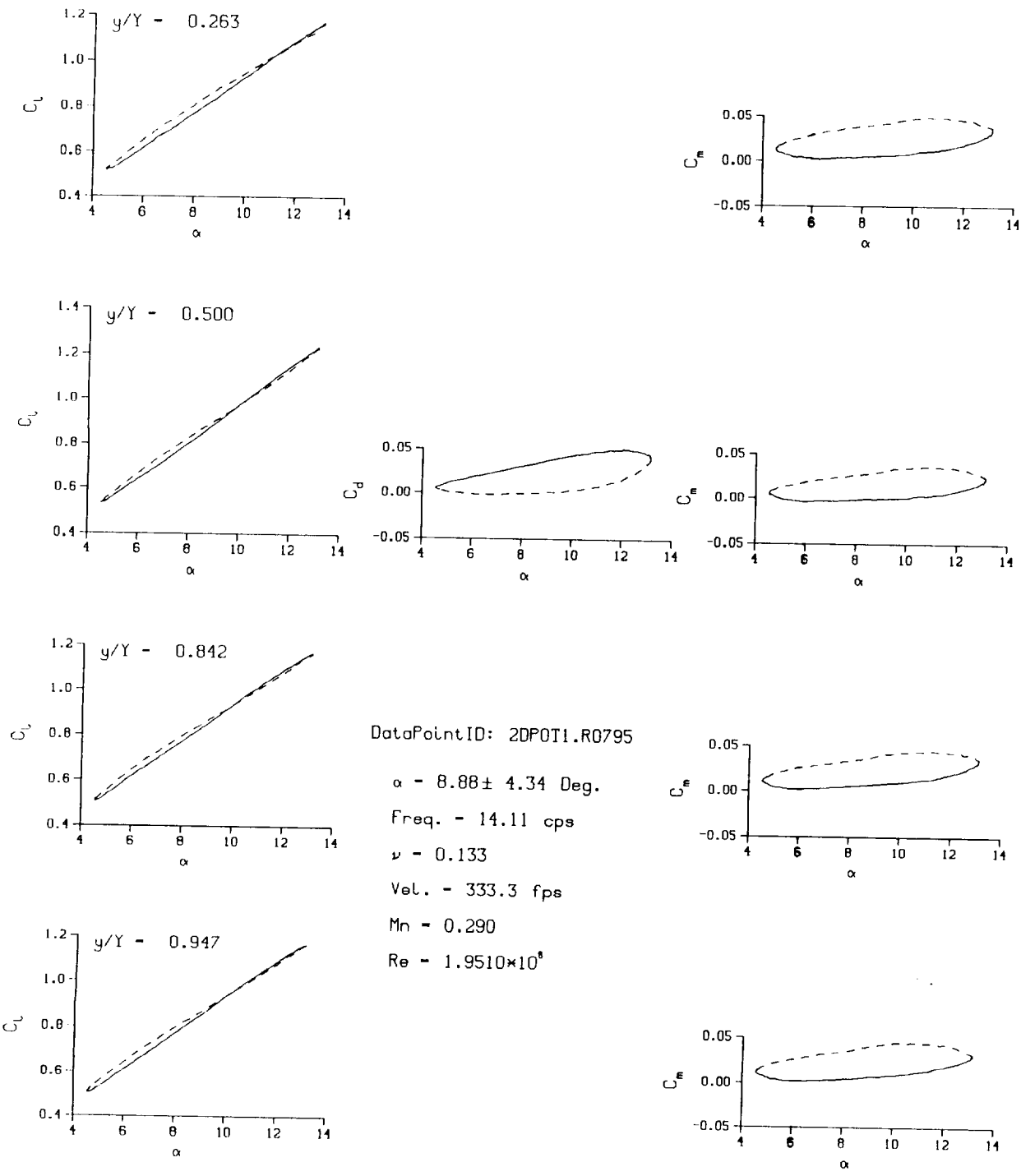

(c) v = 0.14

Figure 25. Concluded.

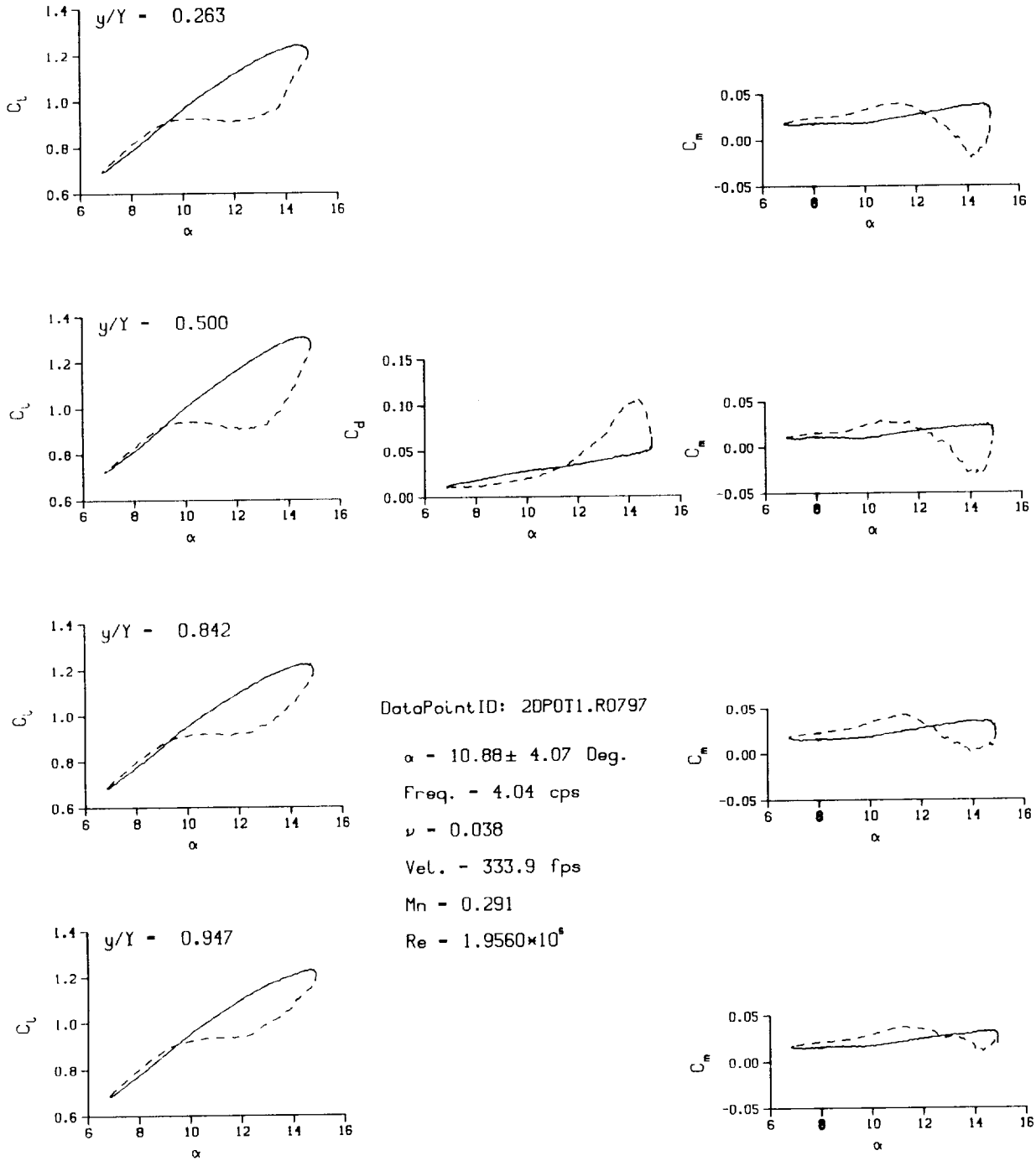

(a) v = 0.04

Figure 26. 2-D pitch oscillation data; BL-trip; α = 11 ± 4 deg.

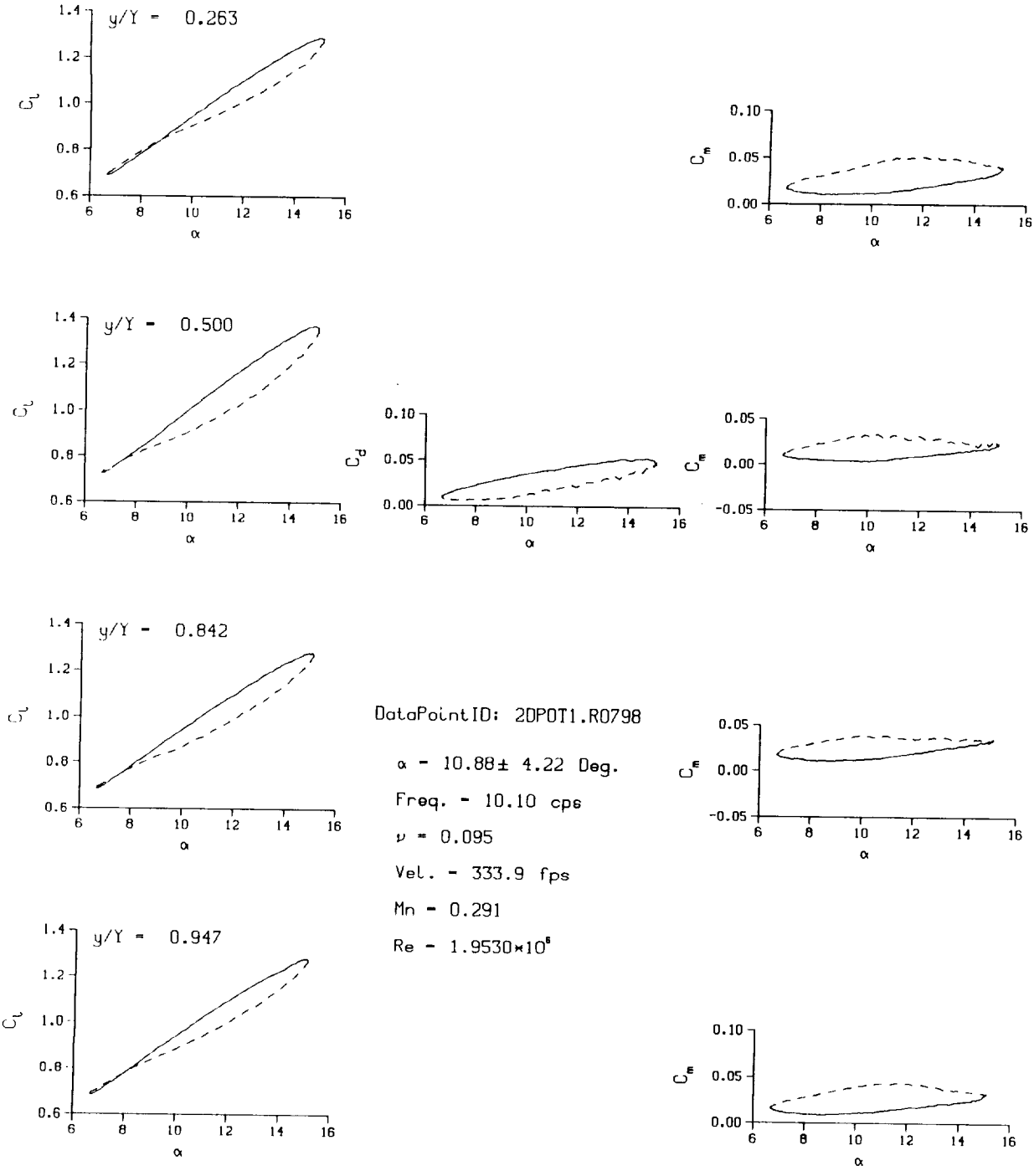

(b) v = 0.10

Figure 26. Continued.

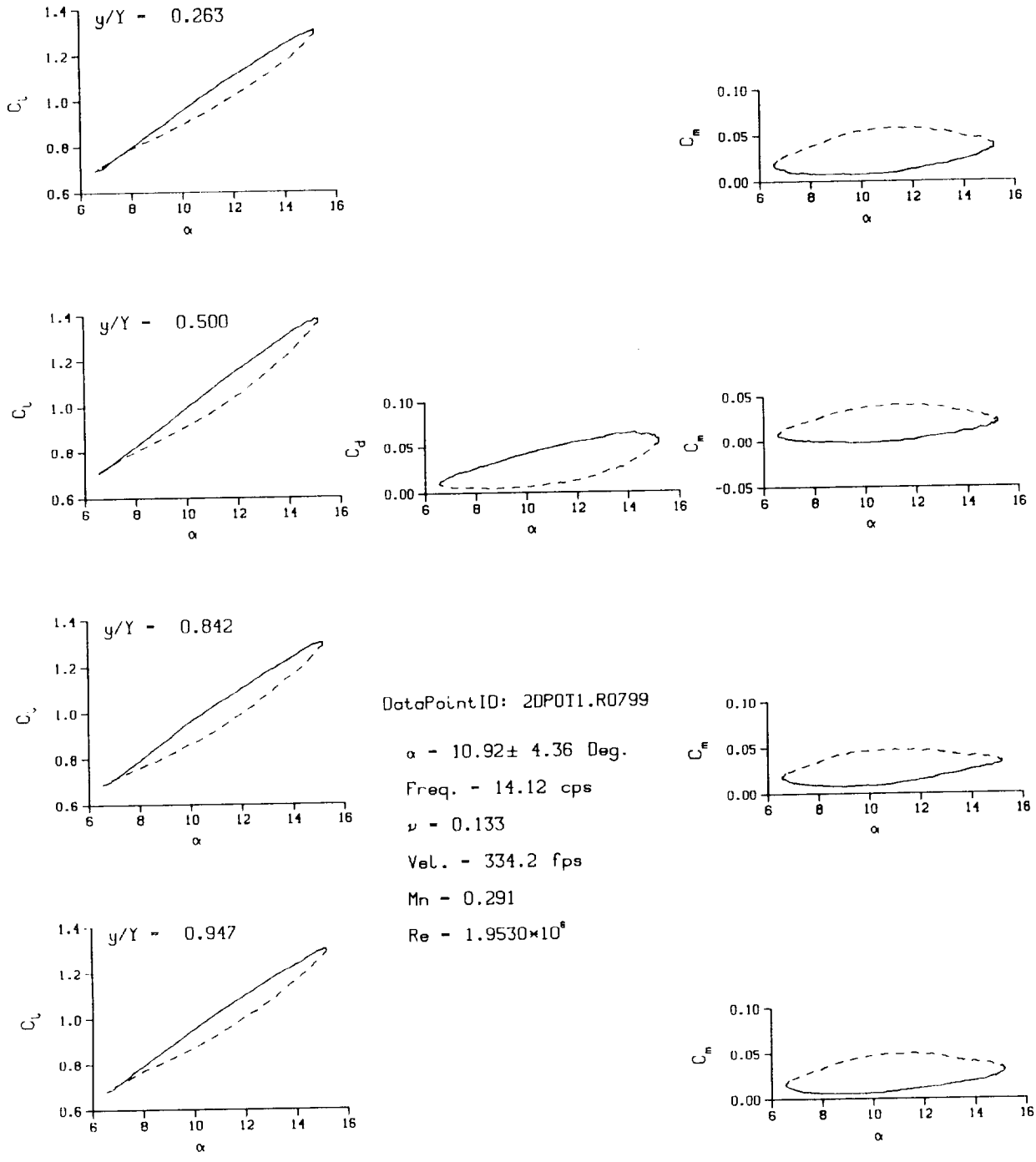

(c) v = 0.14

Figure 26. Concluded.

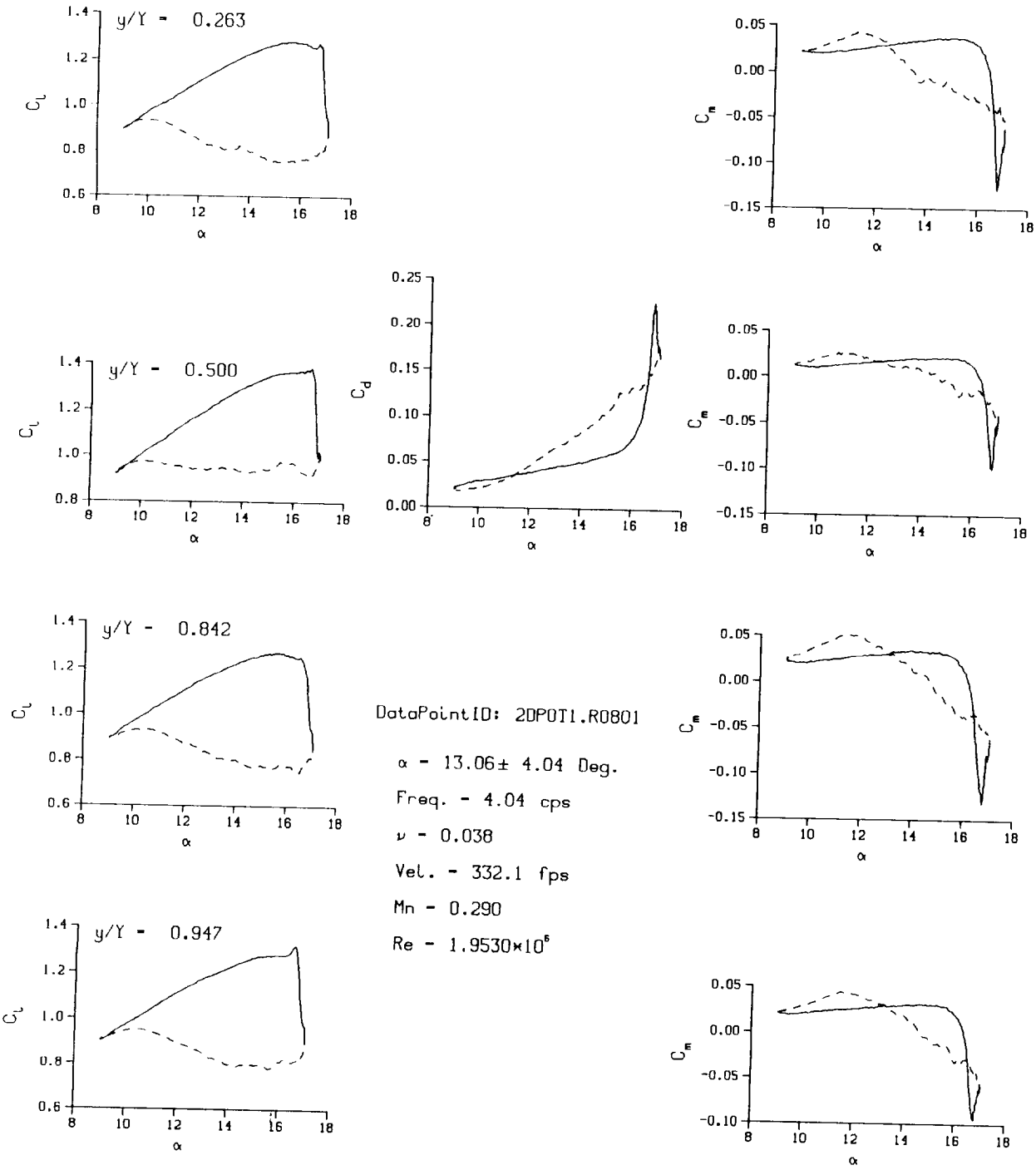

(a) v = 0.04

Figure 27. 2-D pitch oscillation data; BL-trip; α = 13 ± 4 deg.

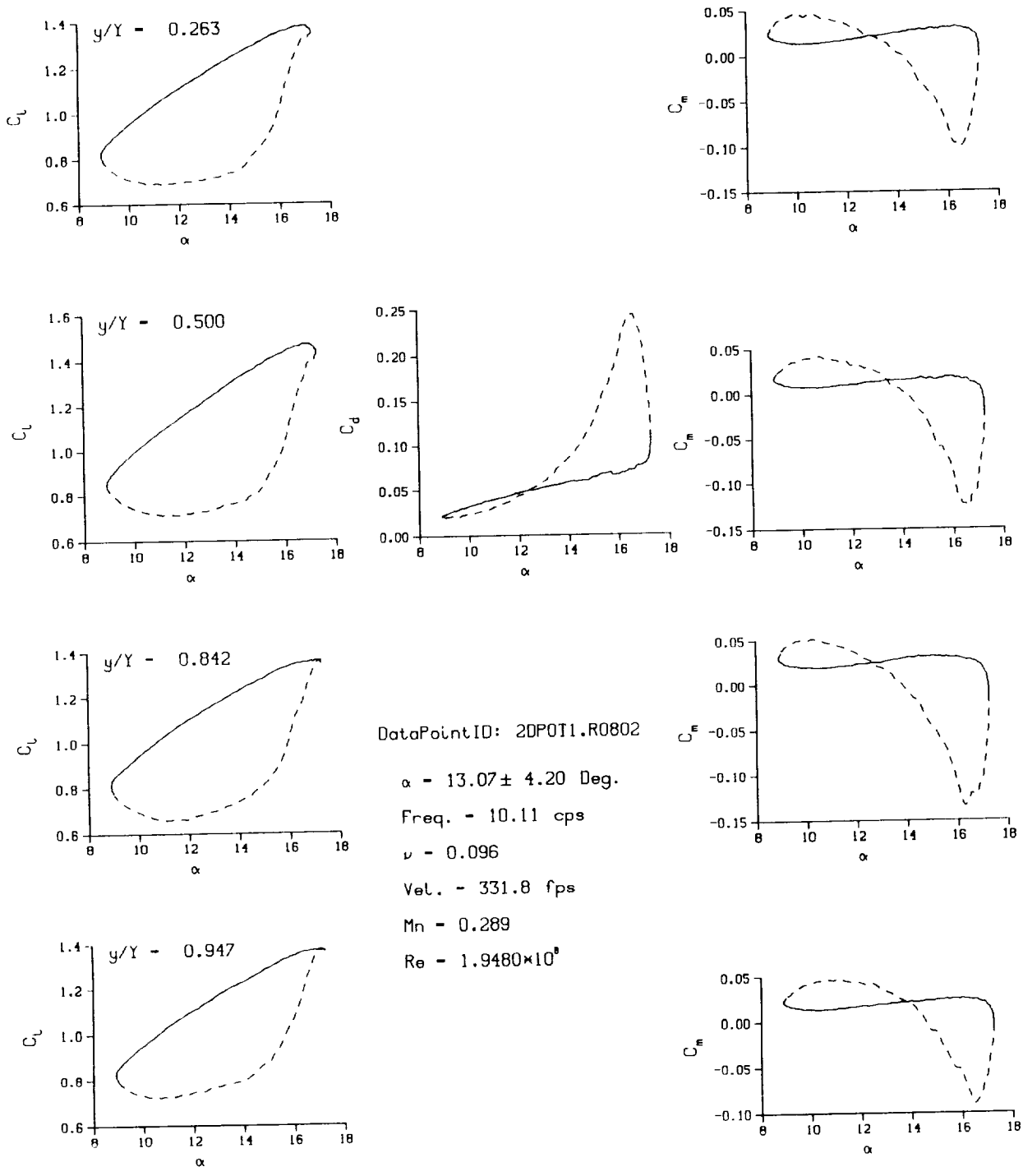

(b) v = 0.10

Figure 27. Continued.

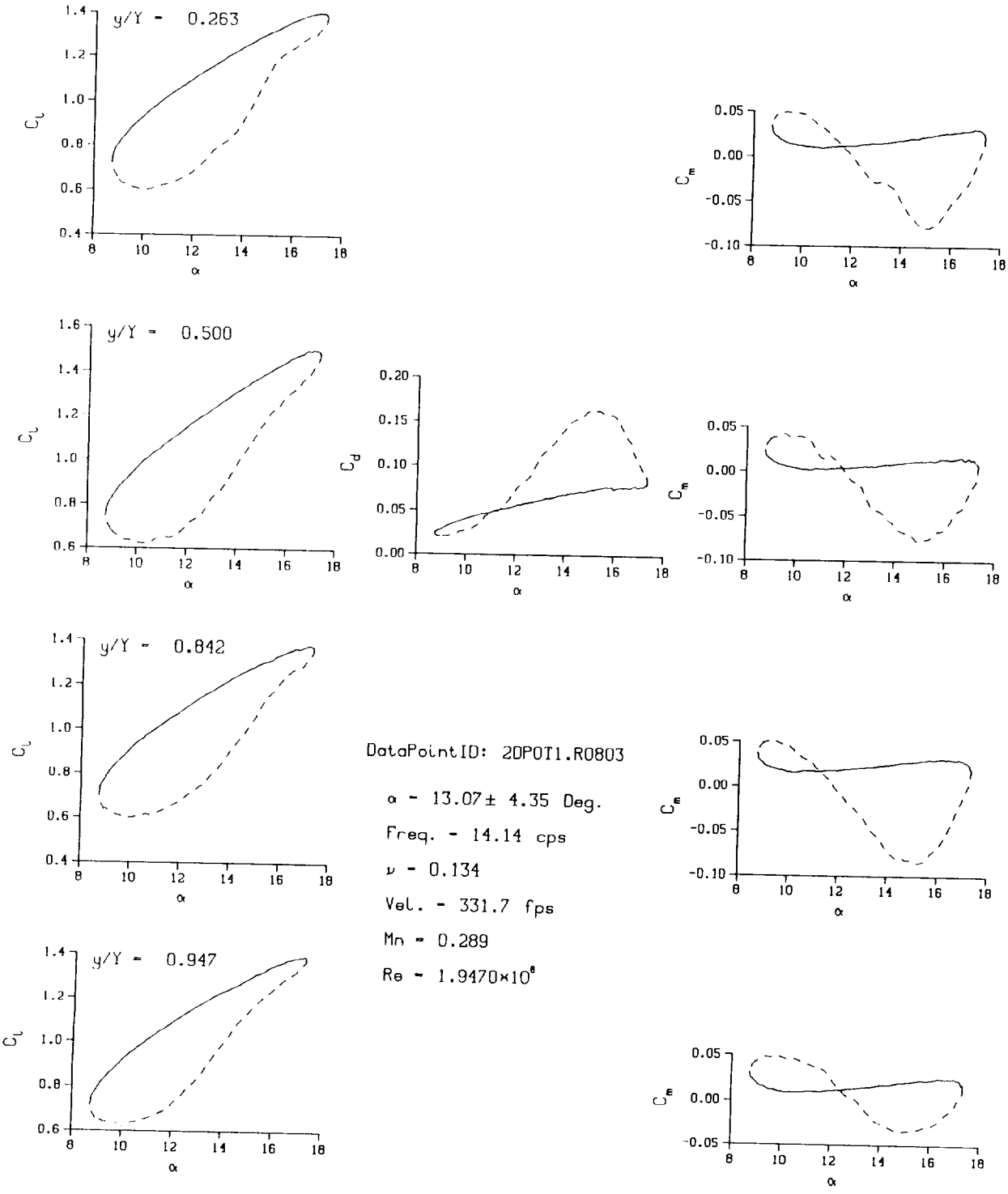

(c) ν = 0.14

Figure 27. Concluded.

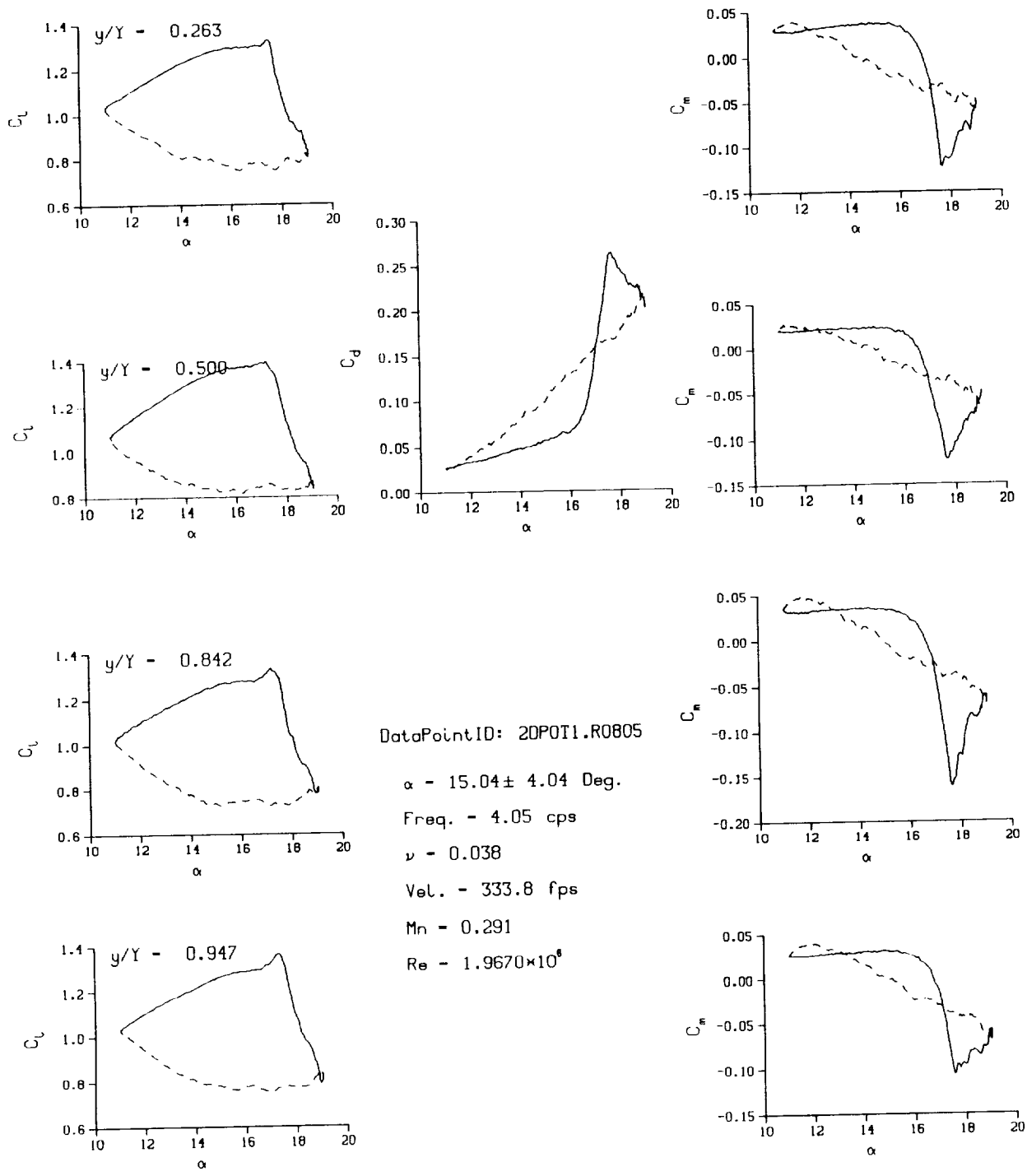

(a) ν = 0.04

Figure 28. 2-D pitch oscillation data; BL-trip; α = 15 ± 4 deg.

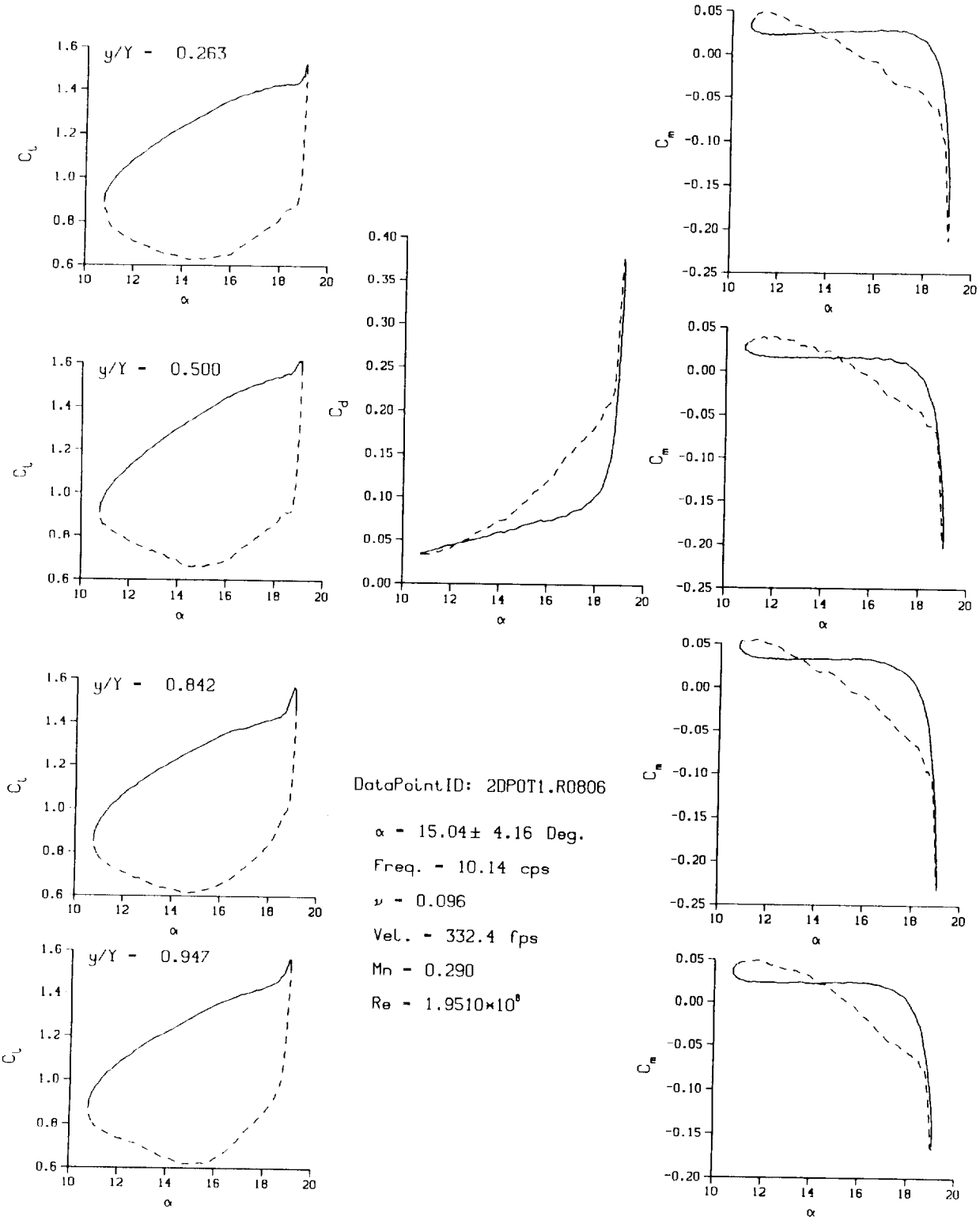

(b) v = 0.10

Figure 28. Continued.

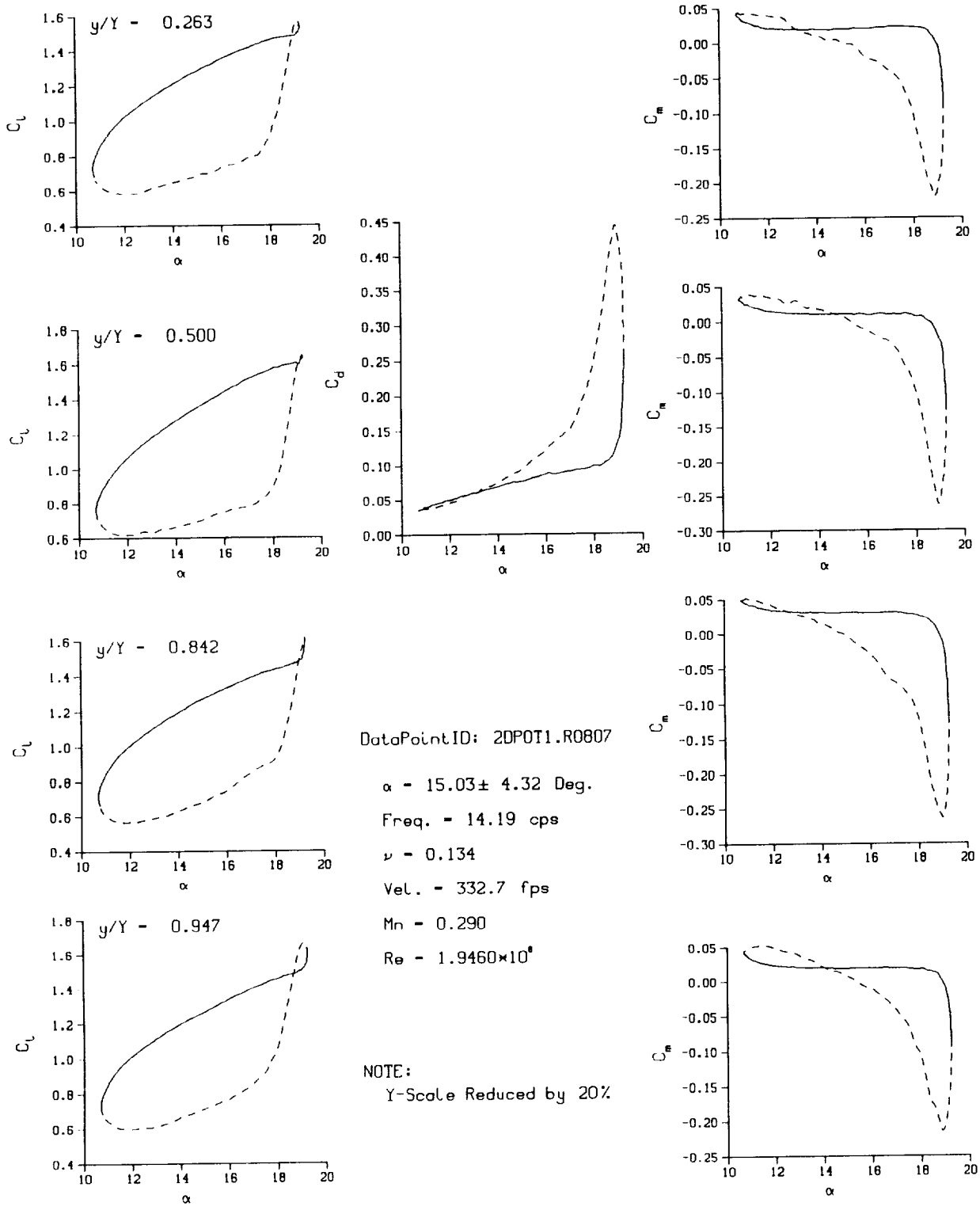

(c) v = 0.14

Figure 28. Concluded.

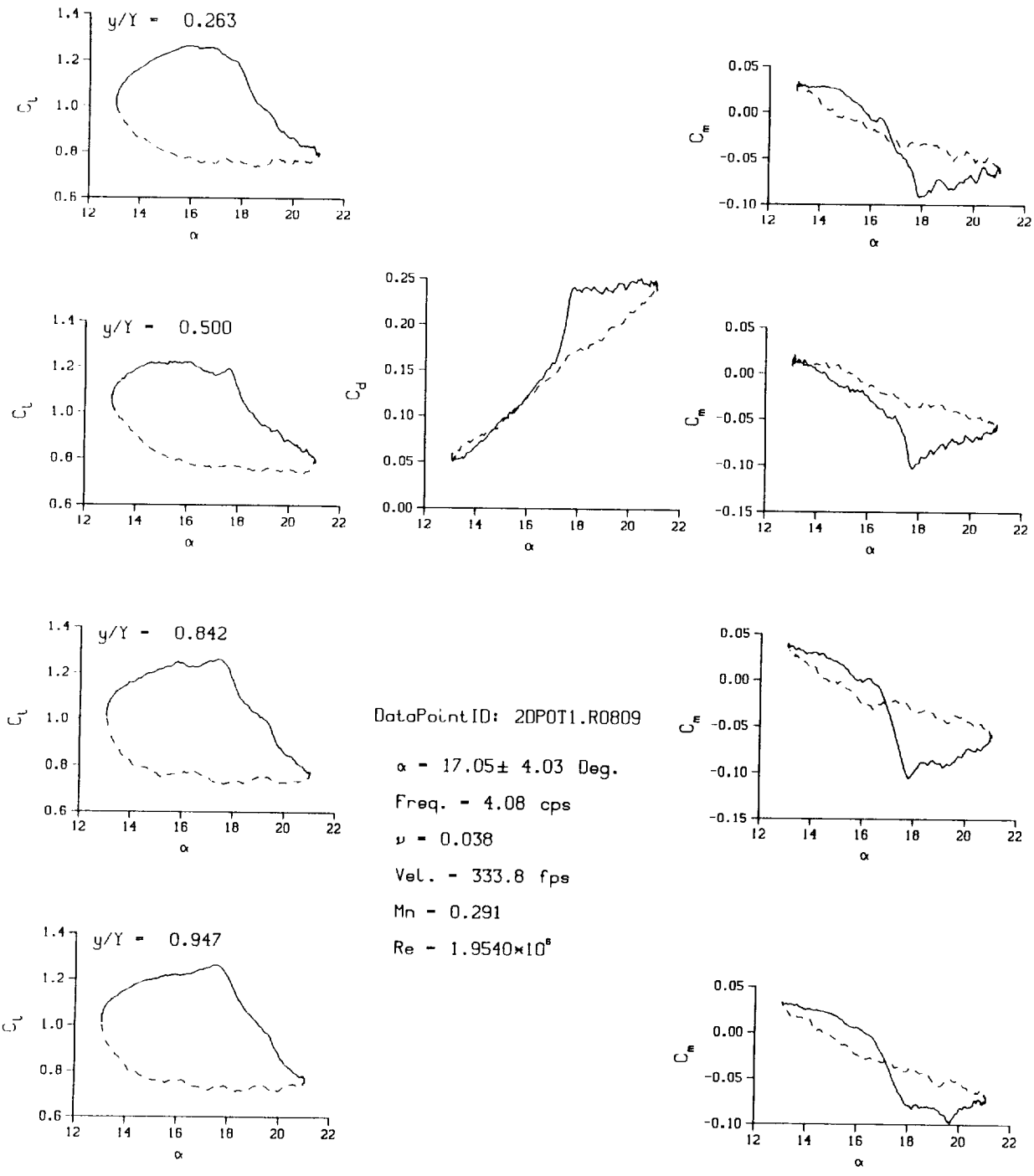

(a) v = 0.04

Figure 29. 2-D pitch oscillation data; BL-trip; α = 17 ± 4 deg.

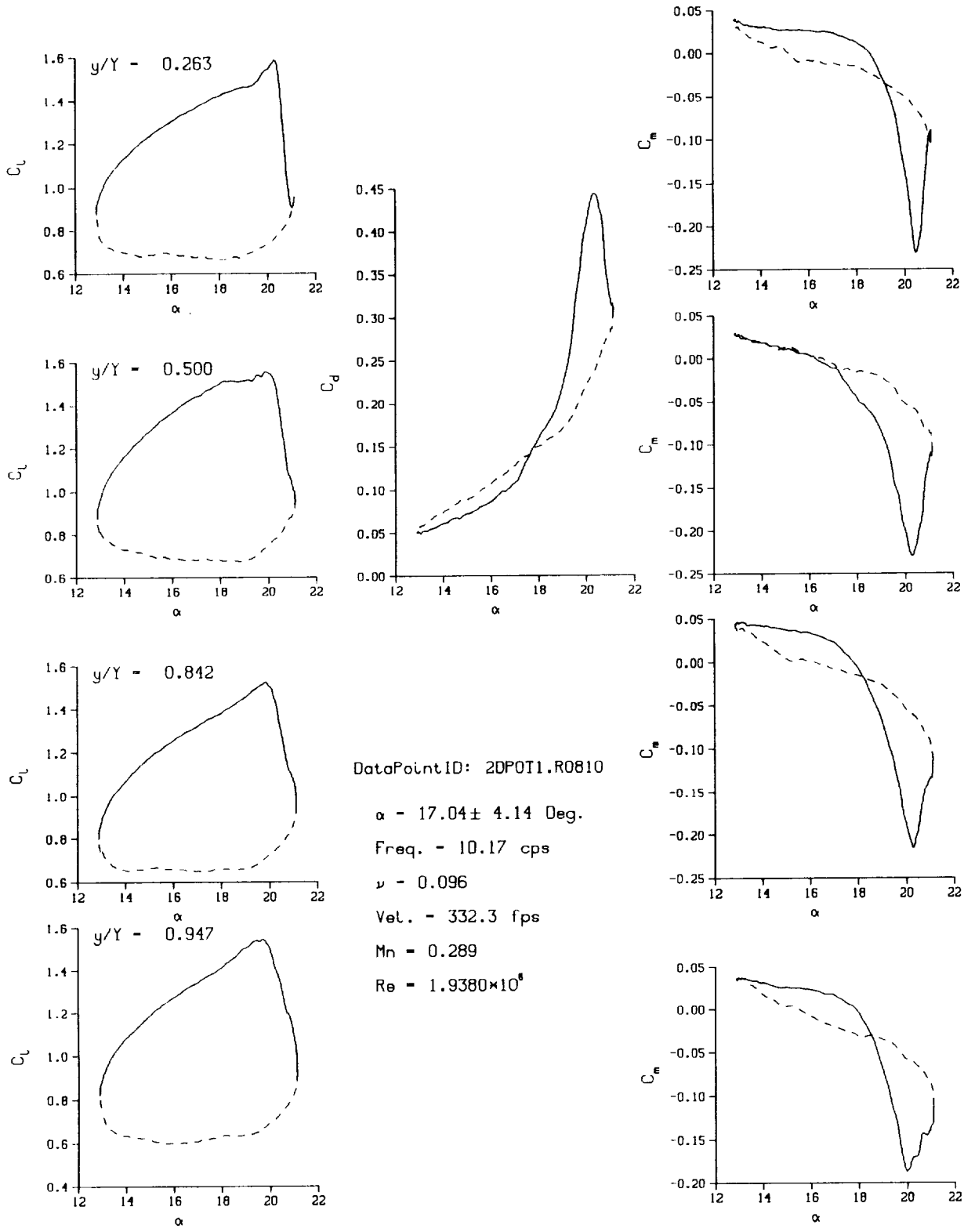

(b) v = 0.10

Figure 29. Continued.

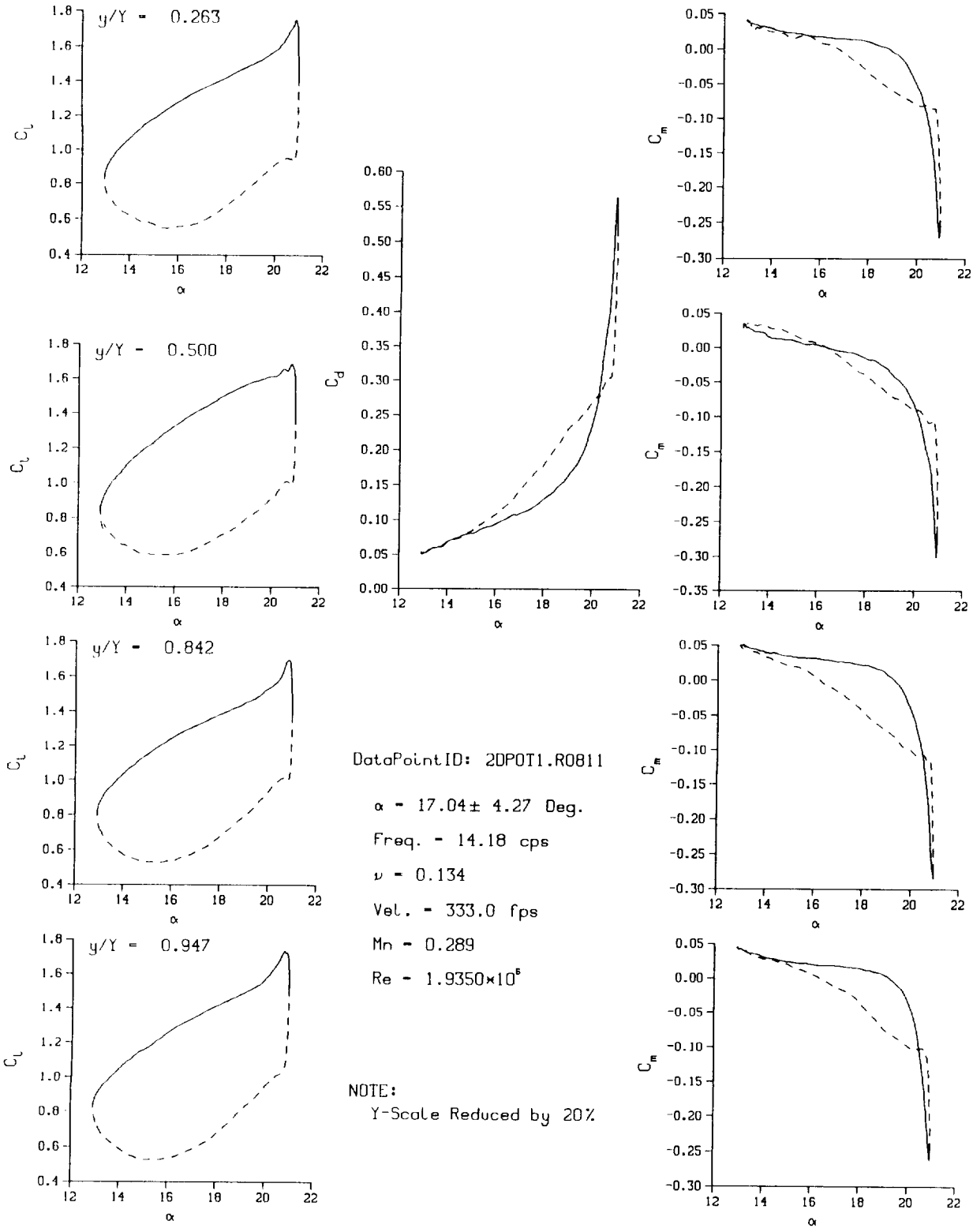

(c) v = 0.14

Figure 29. Concluded.

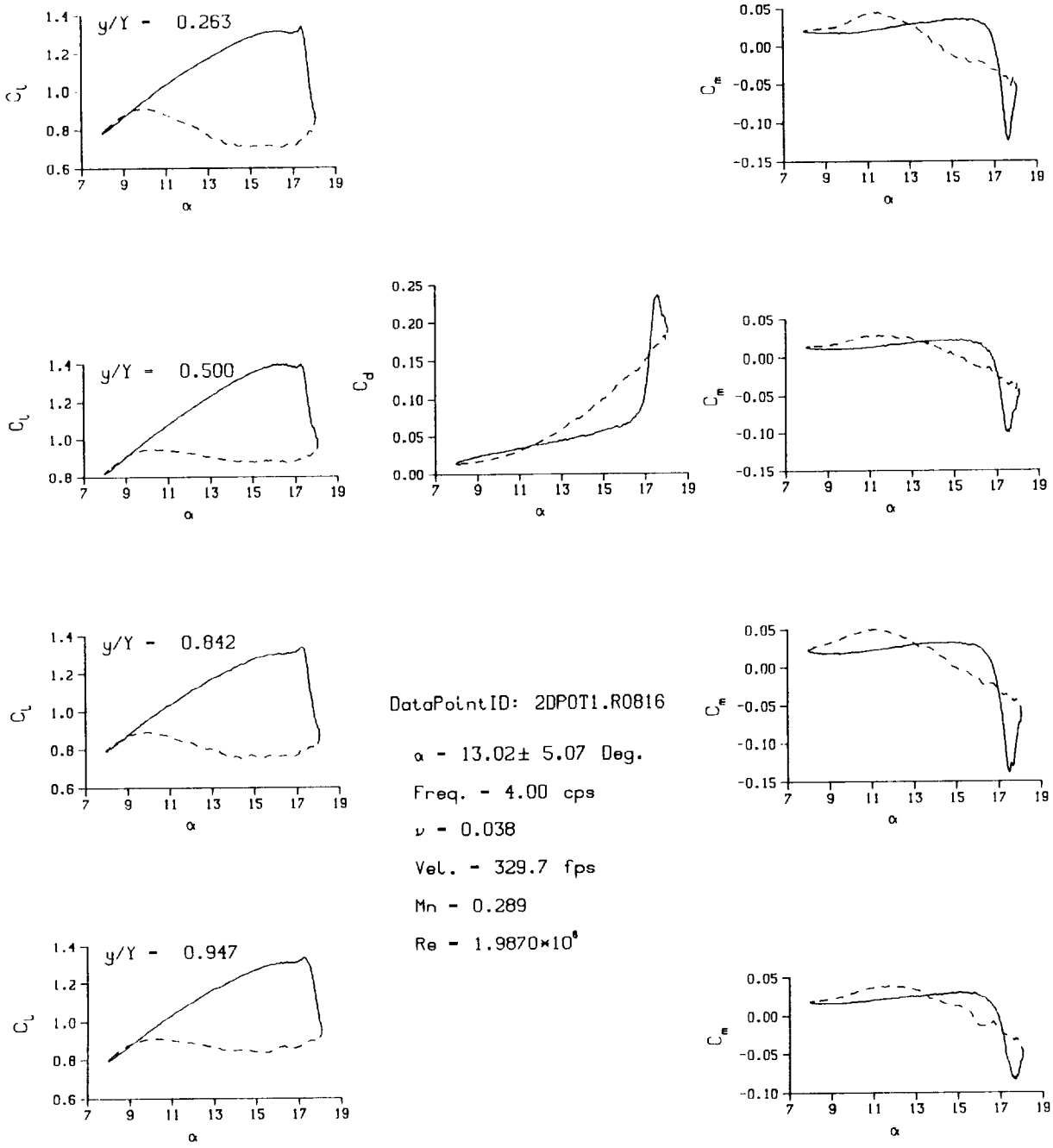

(a) v = 0.04

Figure 30. 2-D pitch oscillation data; BL-trip; α = 13 ± 5 deg.

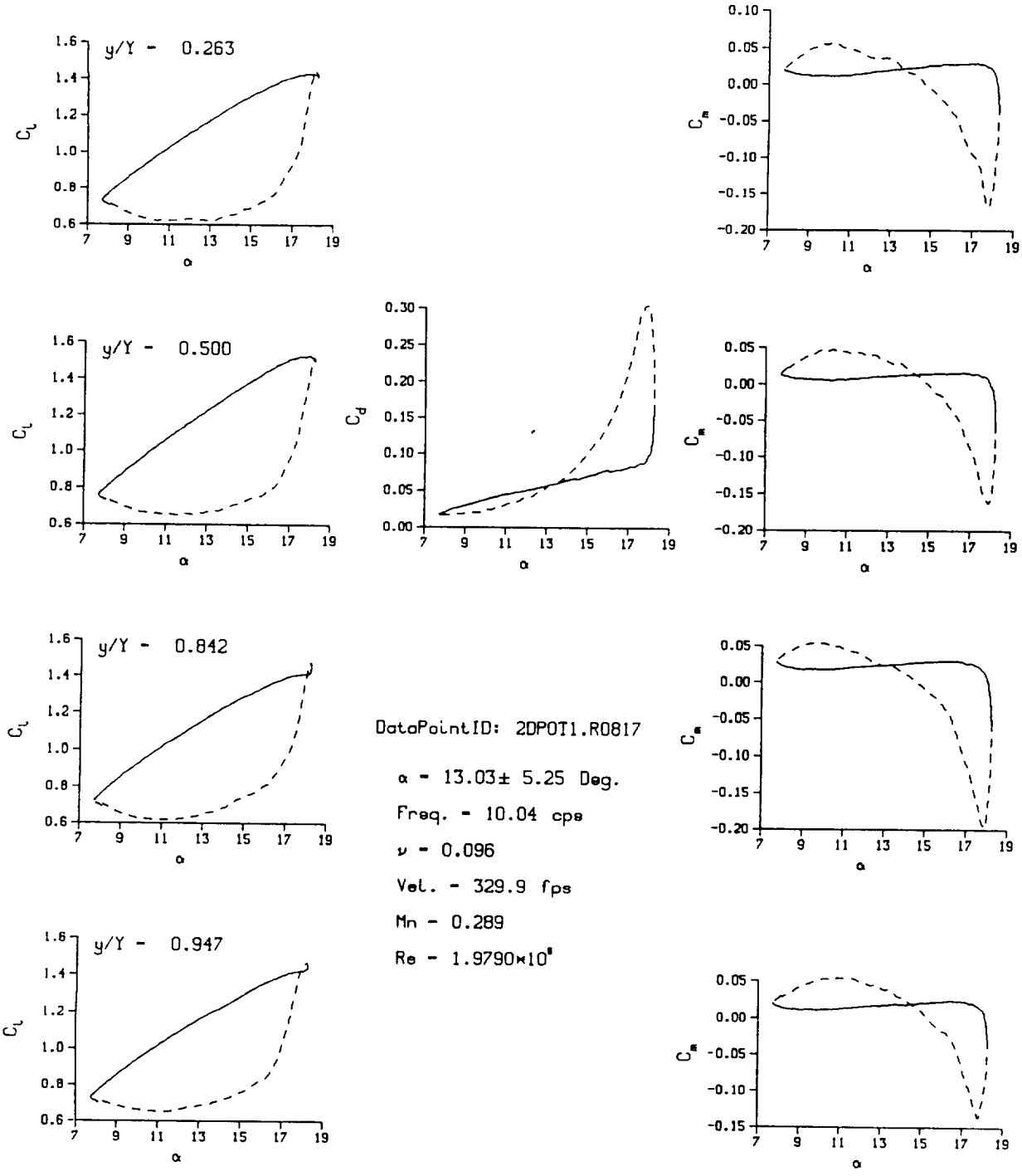

(b) v = 0.10

Figure 30. Concluded.

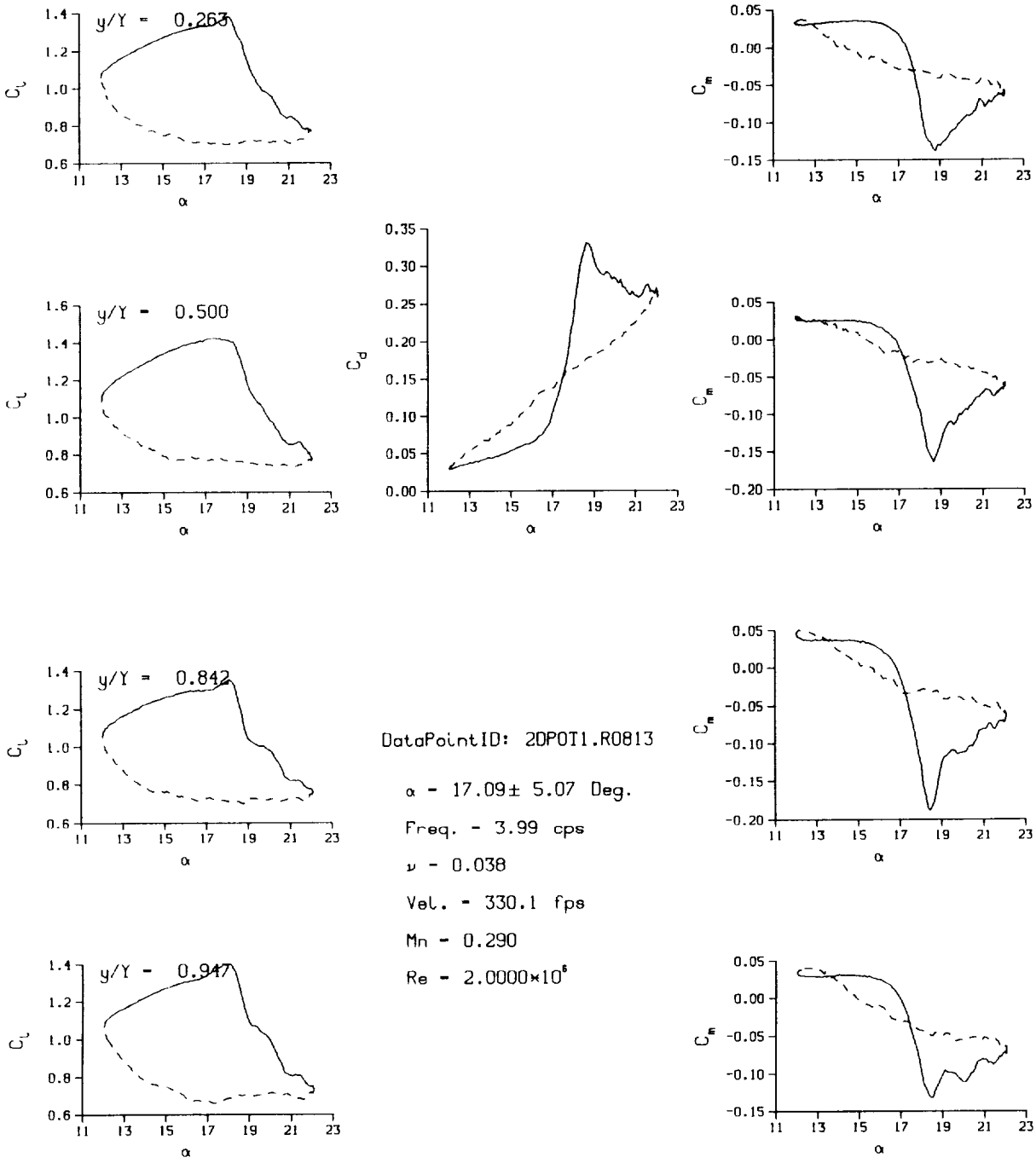

(a) v = 0.04

Figure 31. 2-D pitch oscillation data; BL-trip; α = 17± 5 deg.

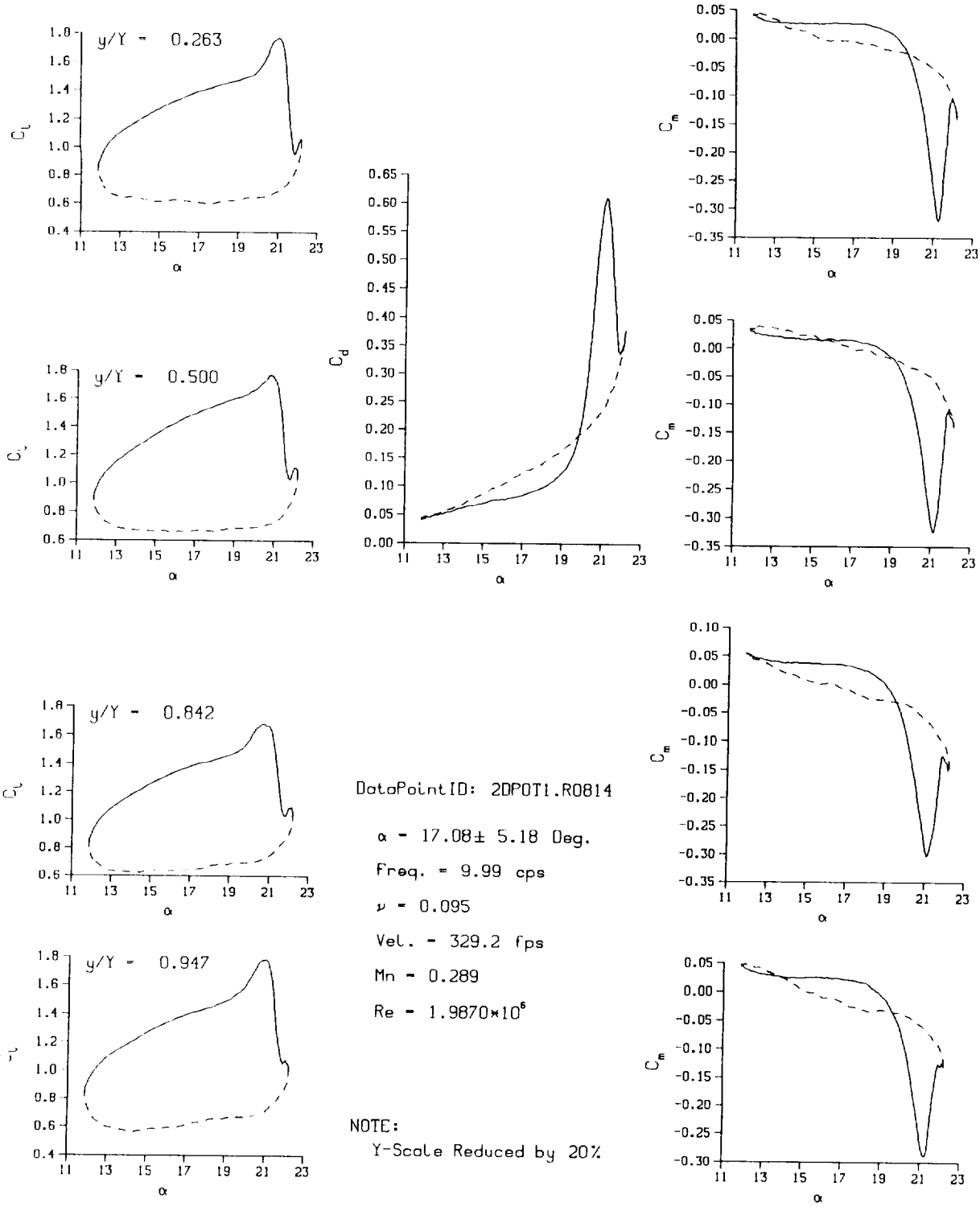

(b) v = 0.10

Figure 31. Concluded.

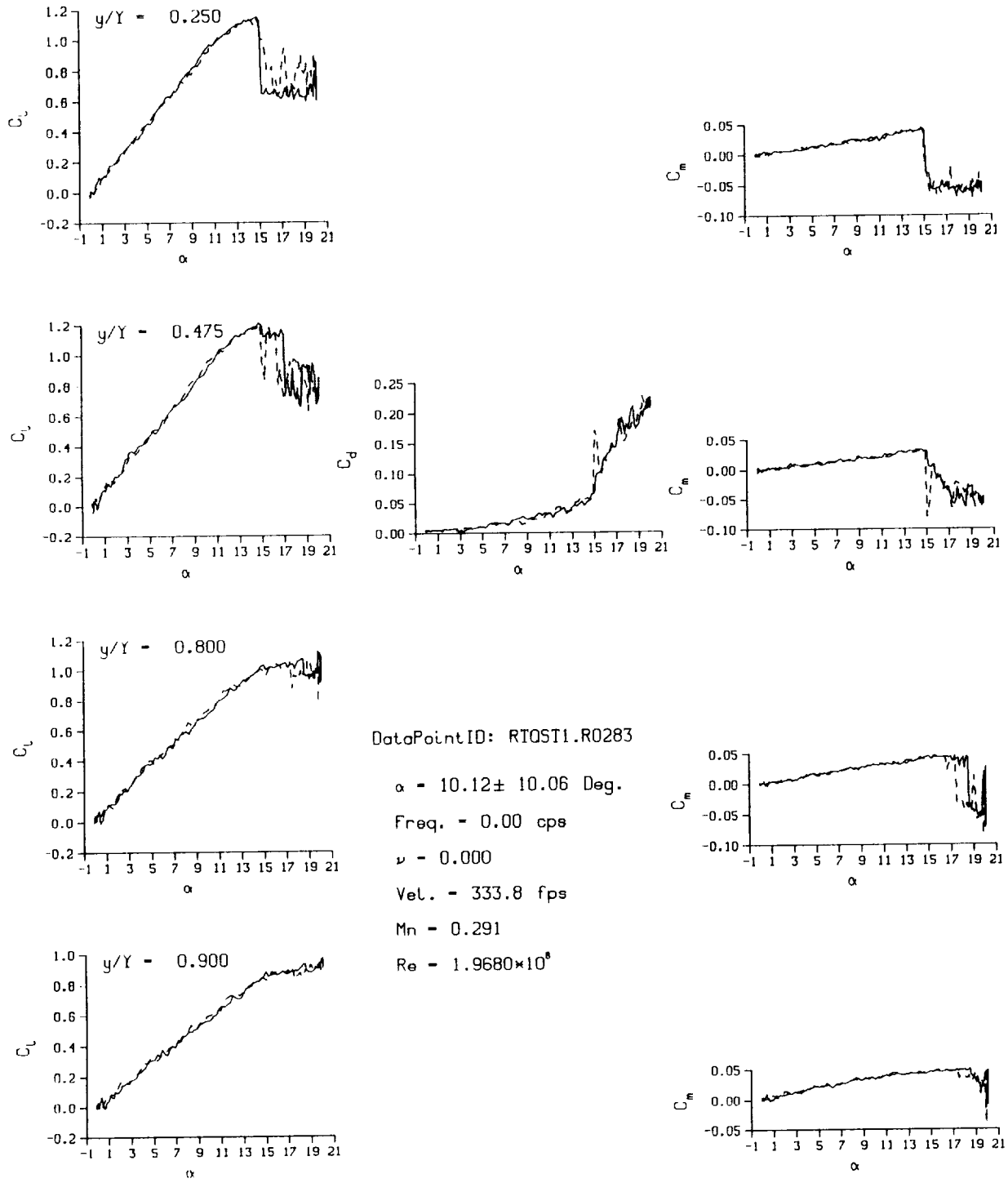

(a) Repeat no. 1

Figure 32. 3-D round tip quasi-steady data; BL-trip; $0 \leq \alpha \leq 20$ deg.

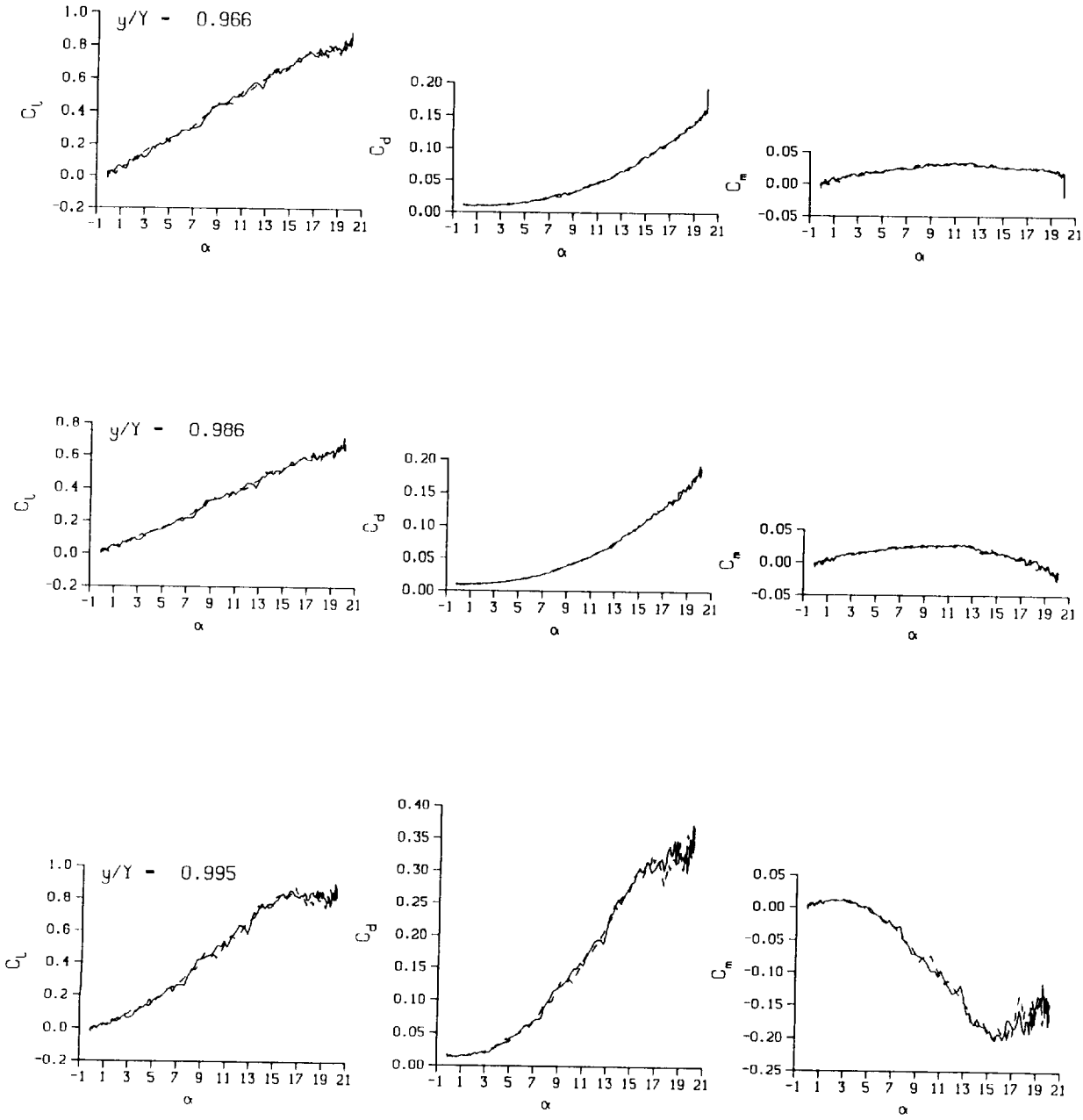

(a) Repeat no. 1. Concluded

Figure 32. Continued.

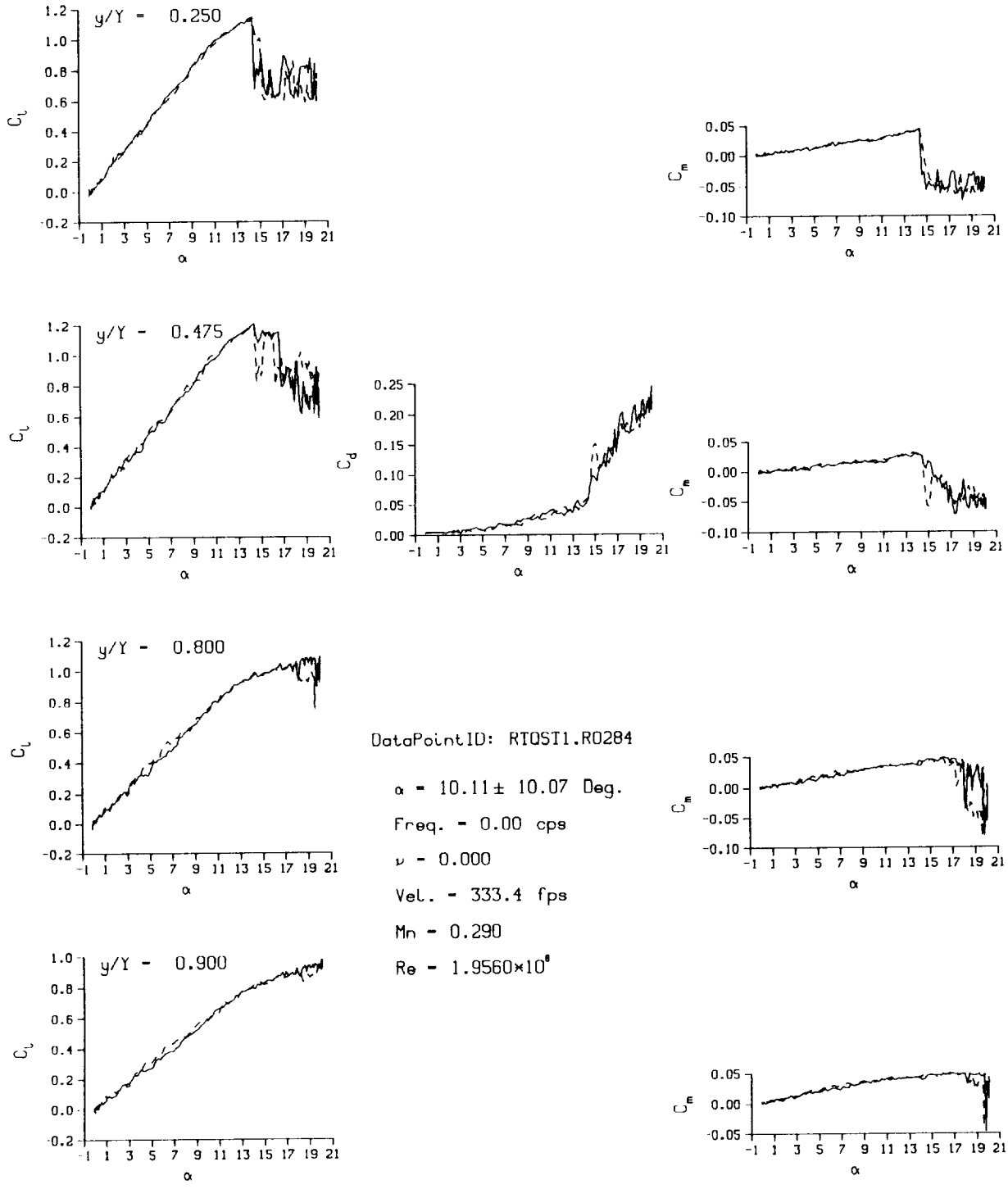

(b) Repeat no. 2

Figure 32. Continued.

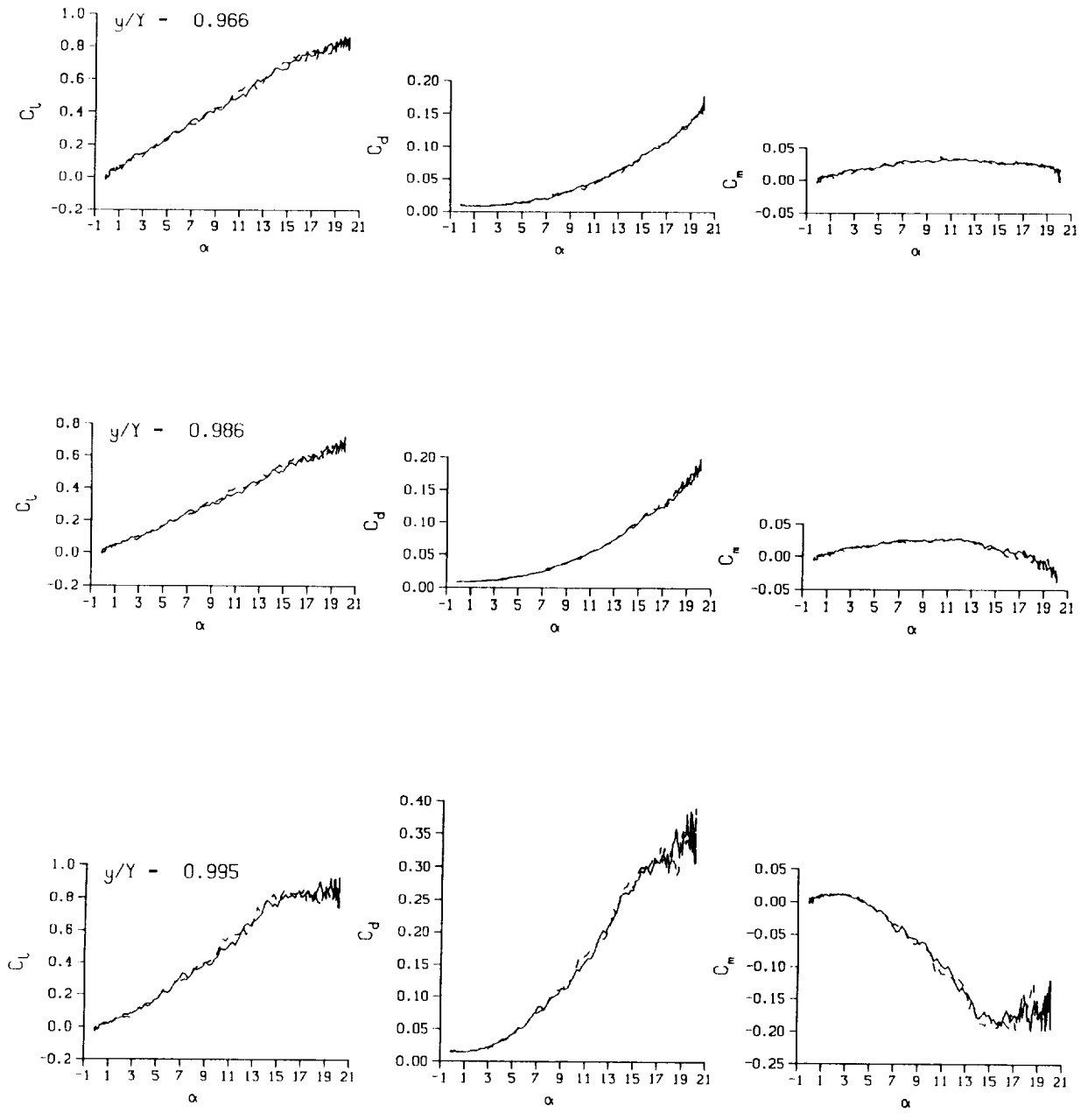

(b) Repeat no. 2. Concluded

Figure 32. Continued.

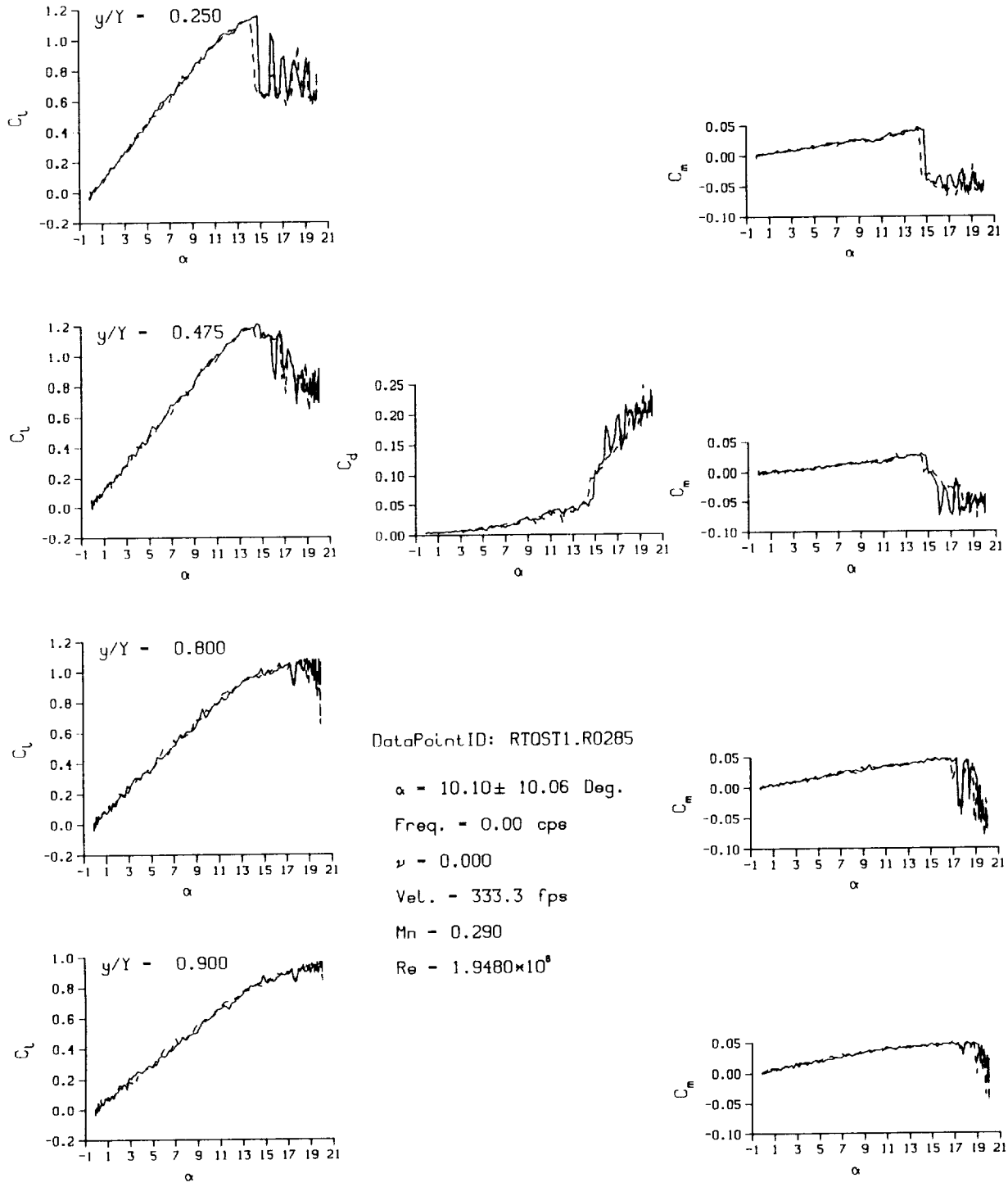

(c) Repeat no. 3

Figure 32. Continued.

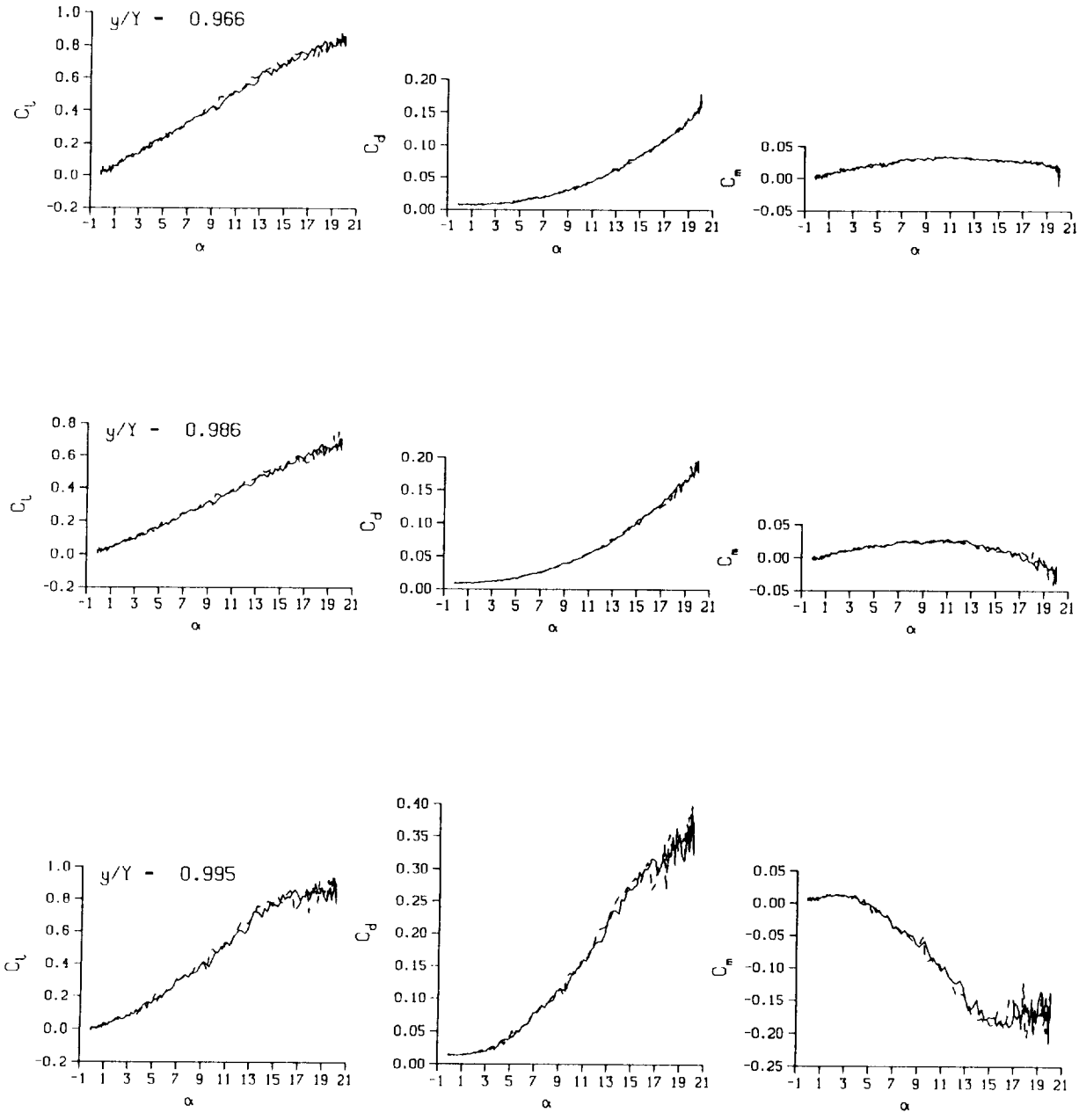

(c) Repeat no. 3. Concluded

Figure 32. Continued.

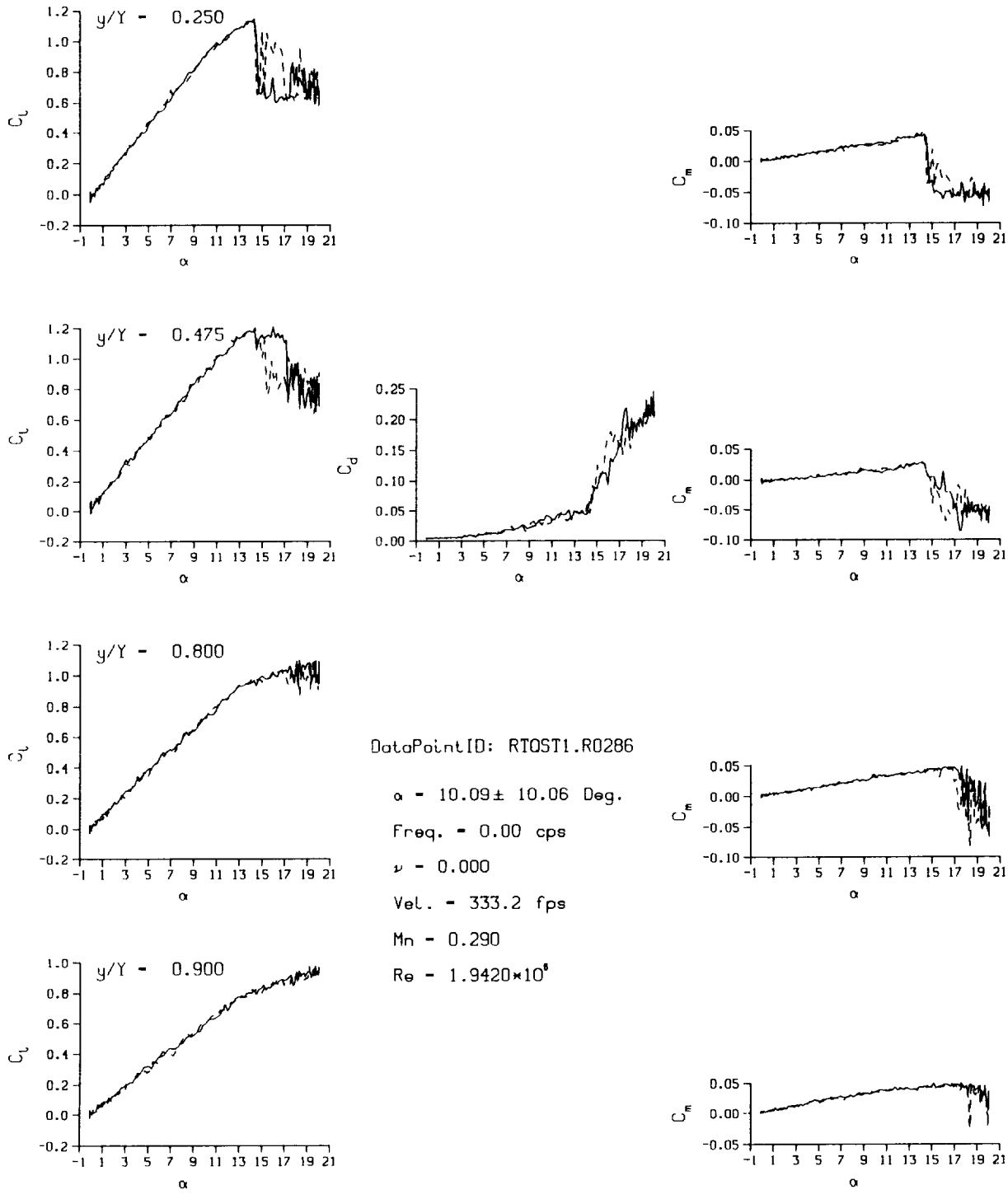

(d) Repeat no. 4

Figure 32. Continued.

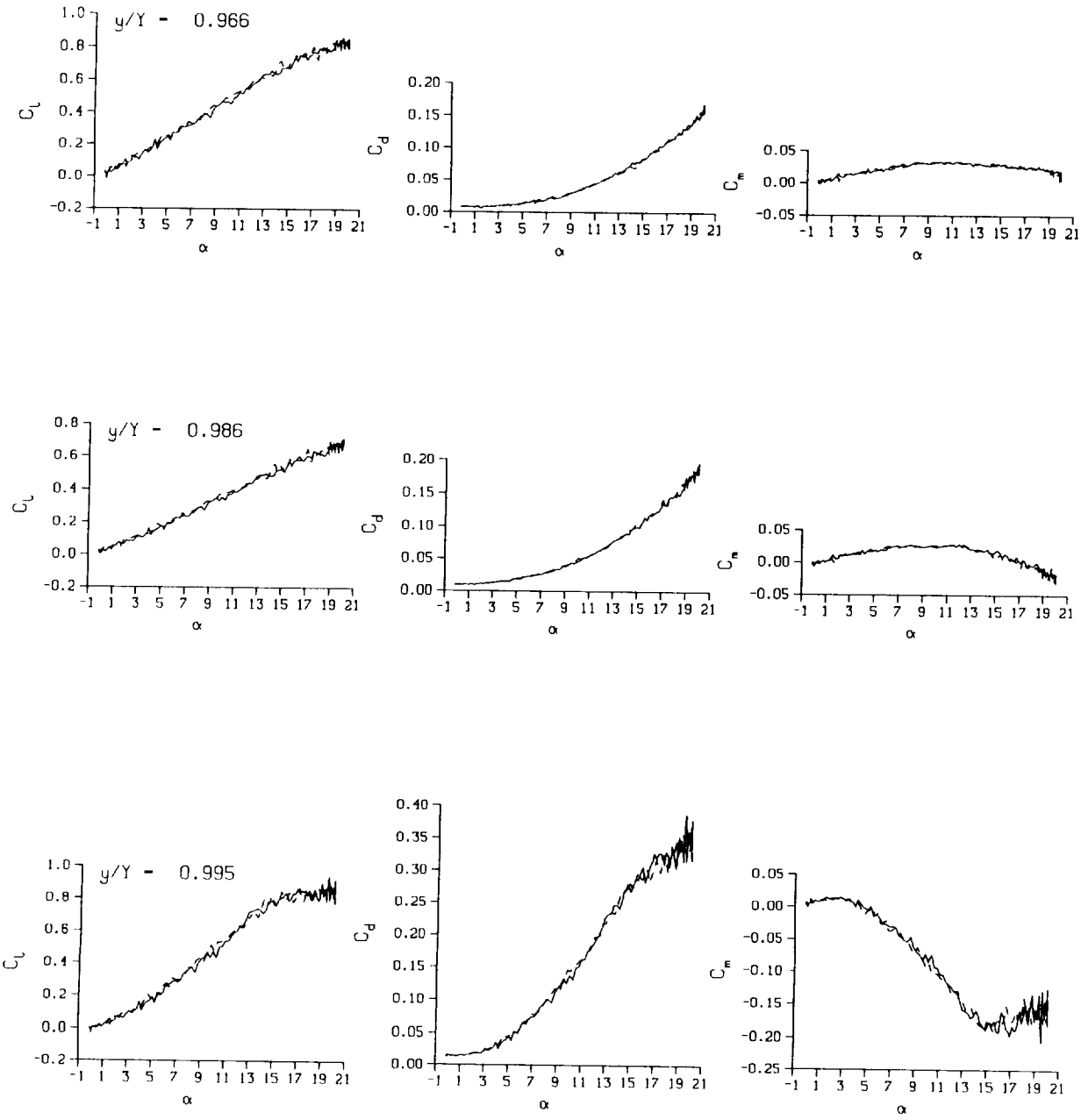

(d) Repeat no. 4. Concluded

Figure 32. Concluded.

C-2

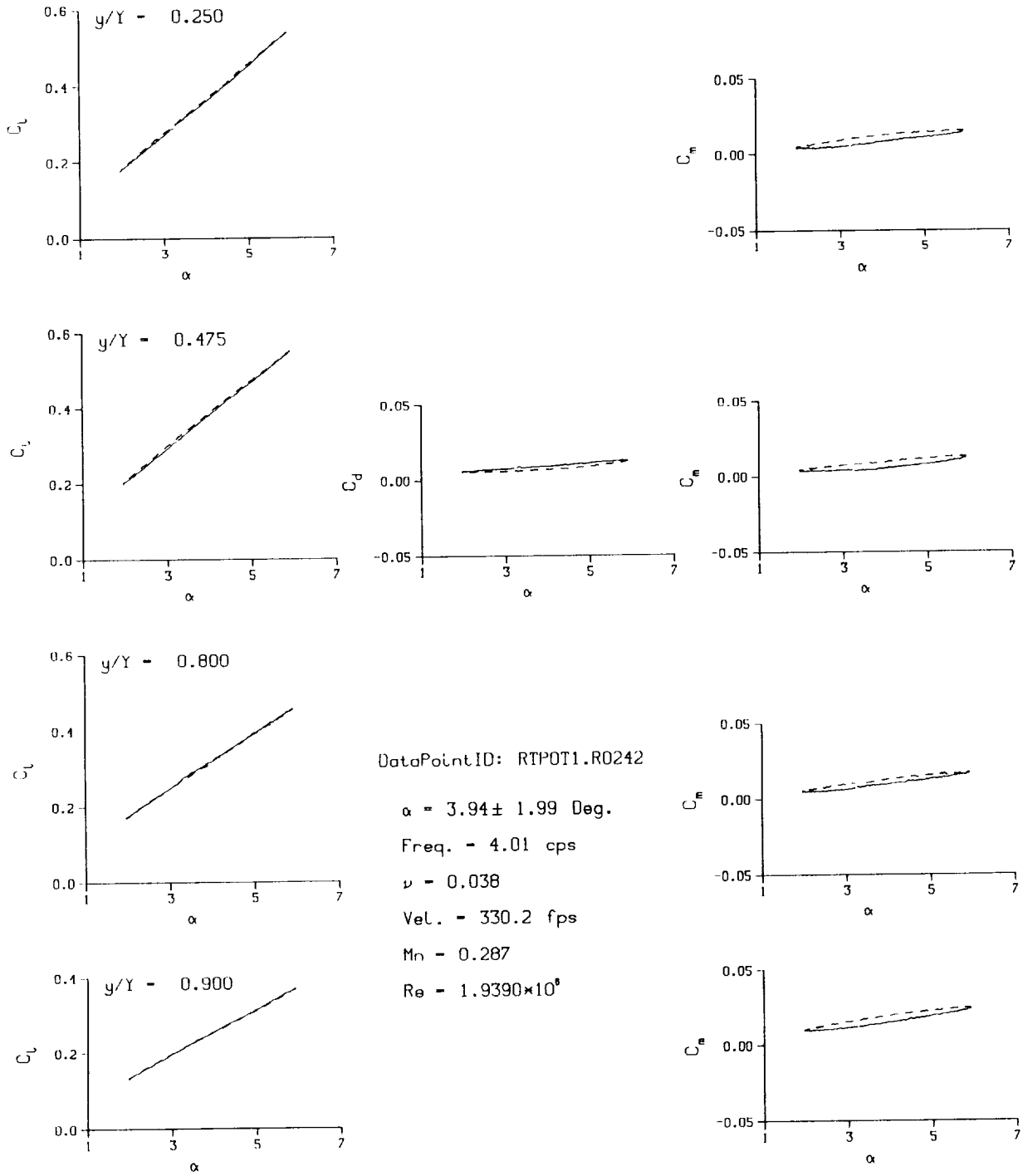

(a) v = 0.04

Figure 33. 3-D round tip pitch oscillation data; BL-trip; α = 4 ± 2 deg.

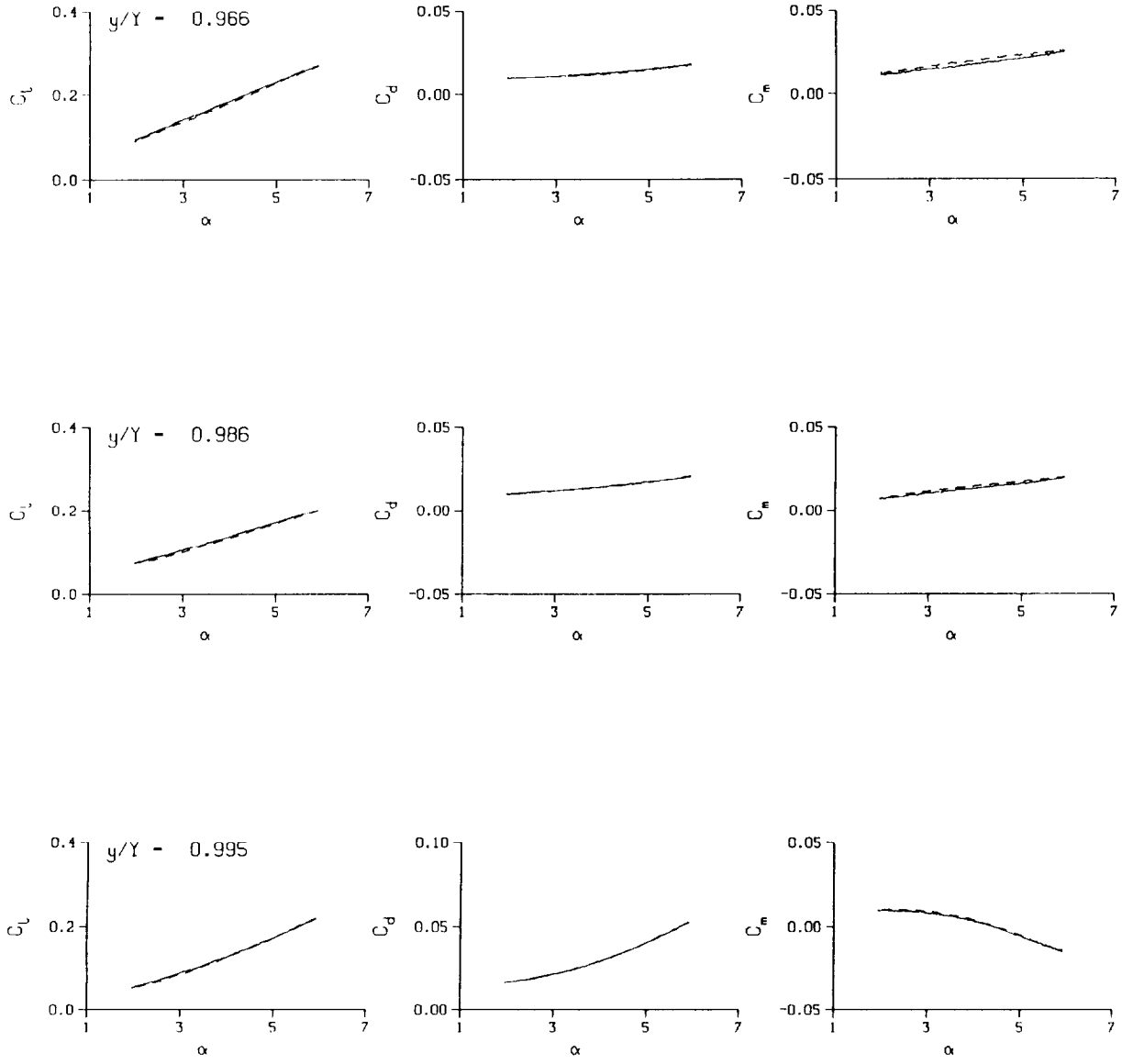

(a) v = 0.04. Concluded

Figure 33. Continued.

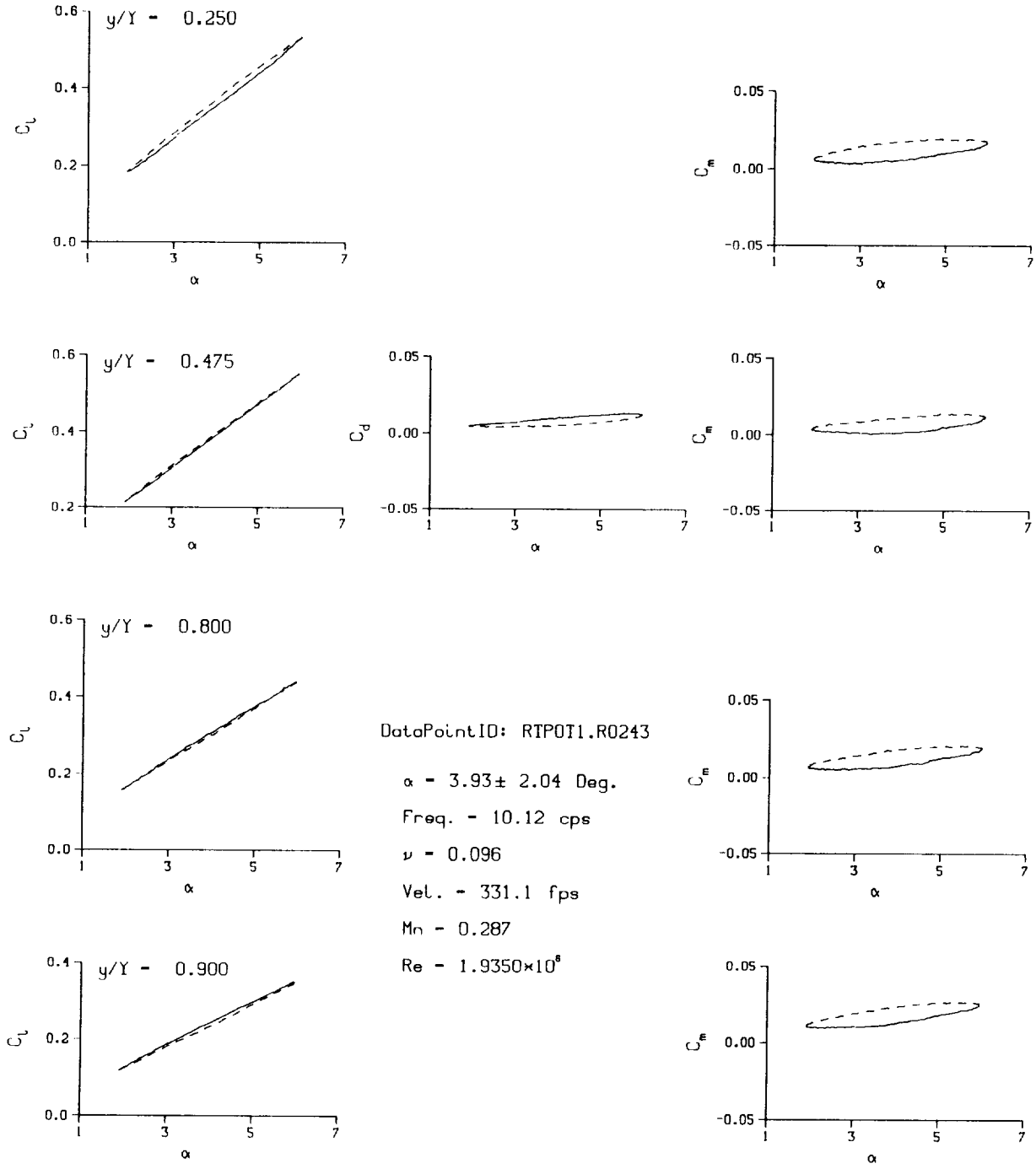

(b) v = 0.10

Figure 33. Continued.

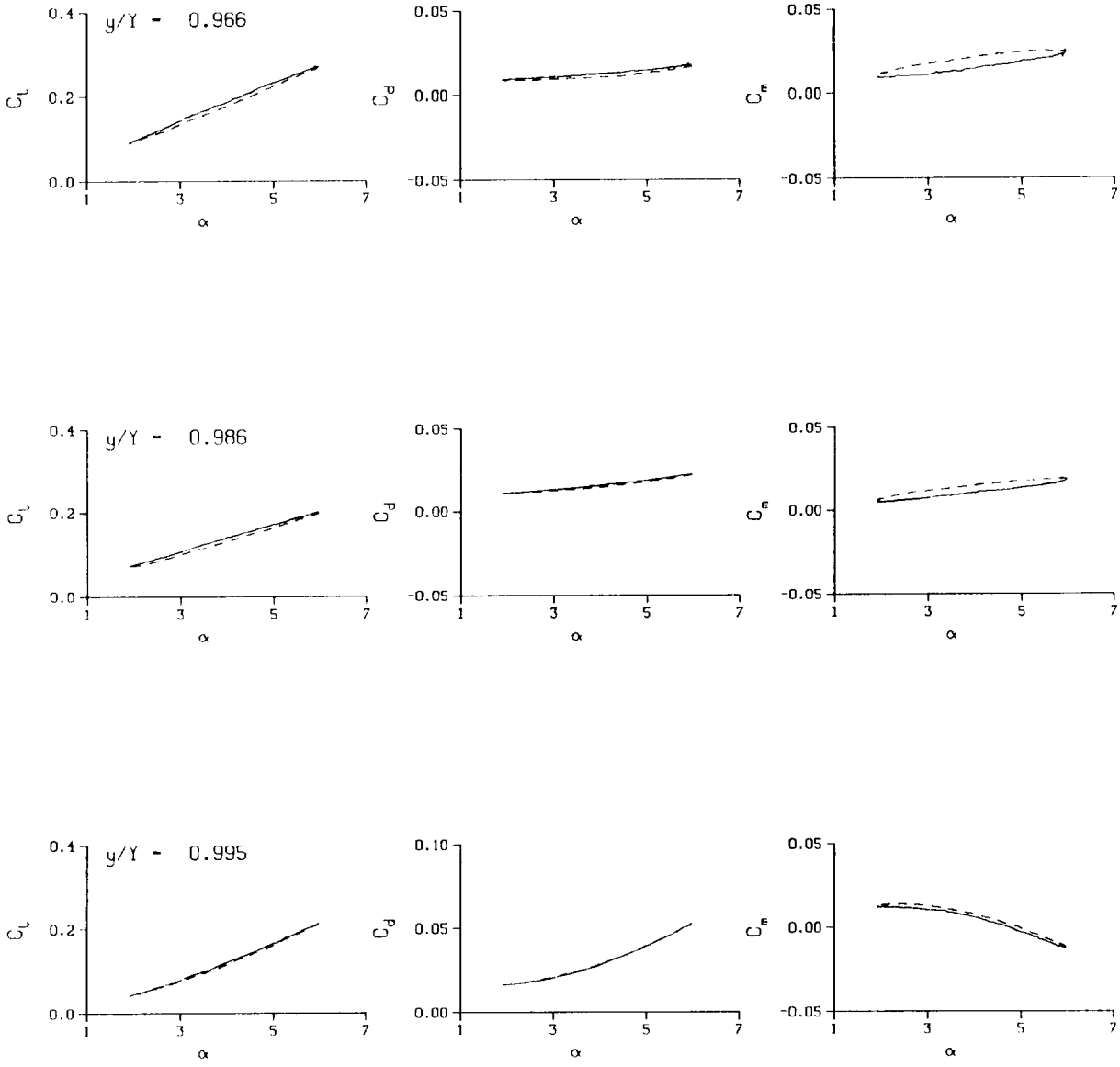

(b) v = 0.10. Concluded

Figure 33. Continued.

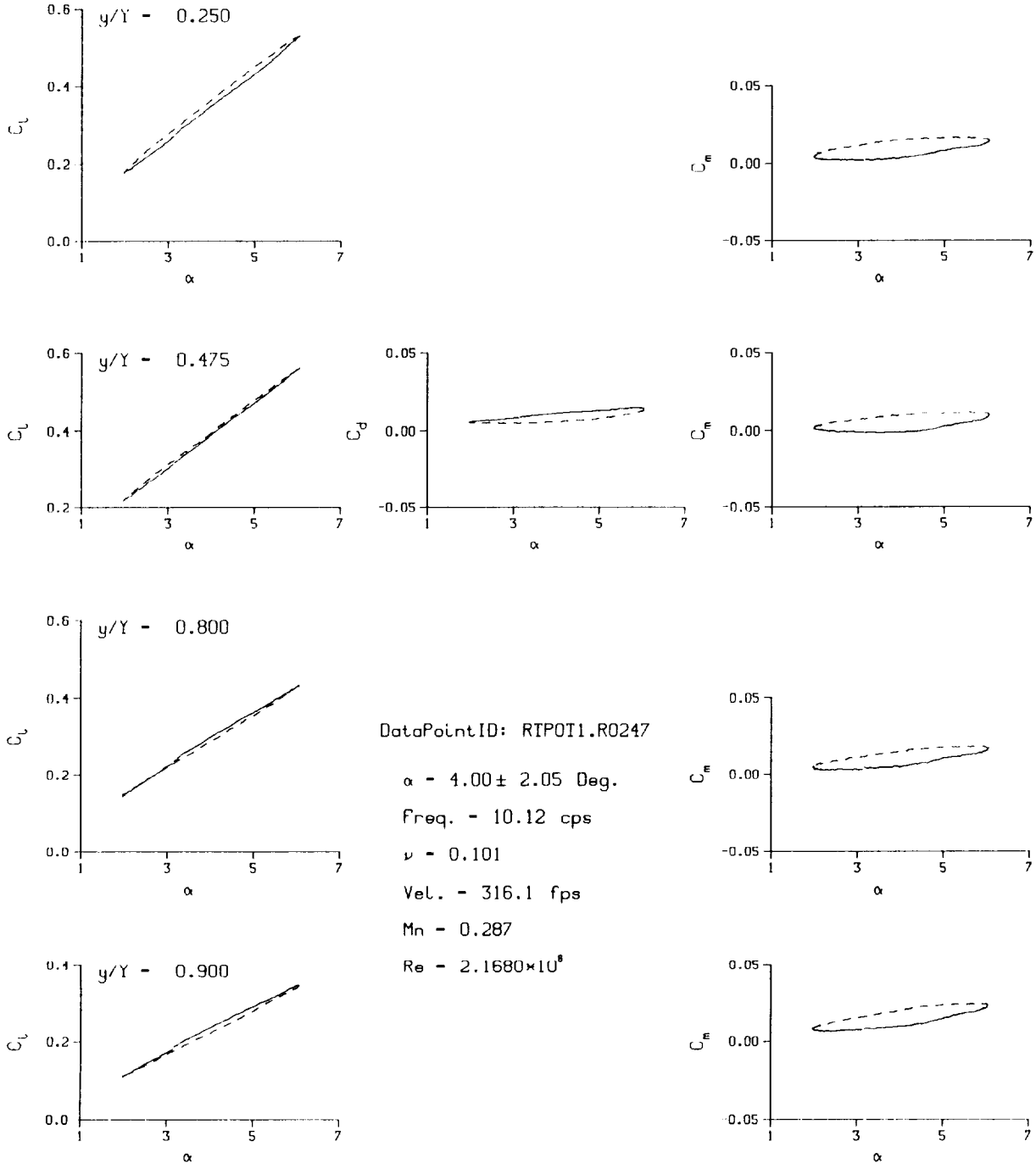

(b.1) ν = 0.10; repeat

Figure 33. Continued.

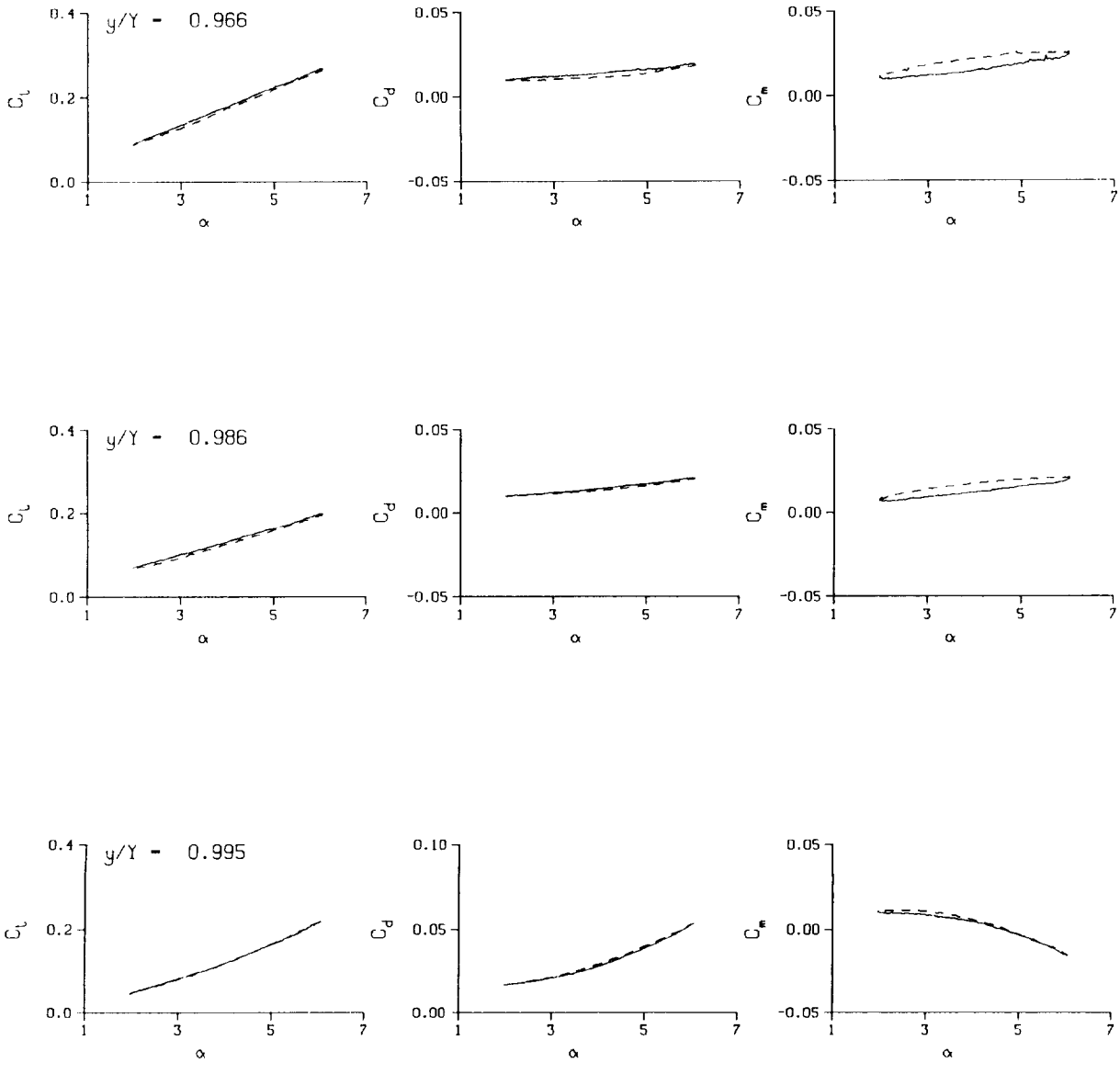

(b.1) v = 0.10; repeat. Concluded

Figure 33. Continued.

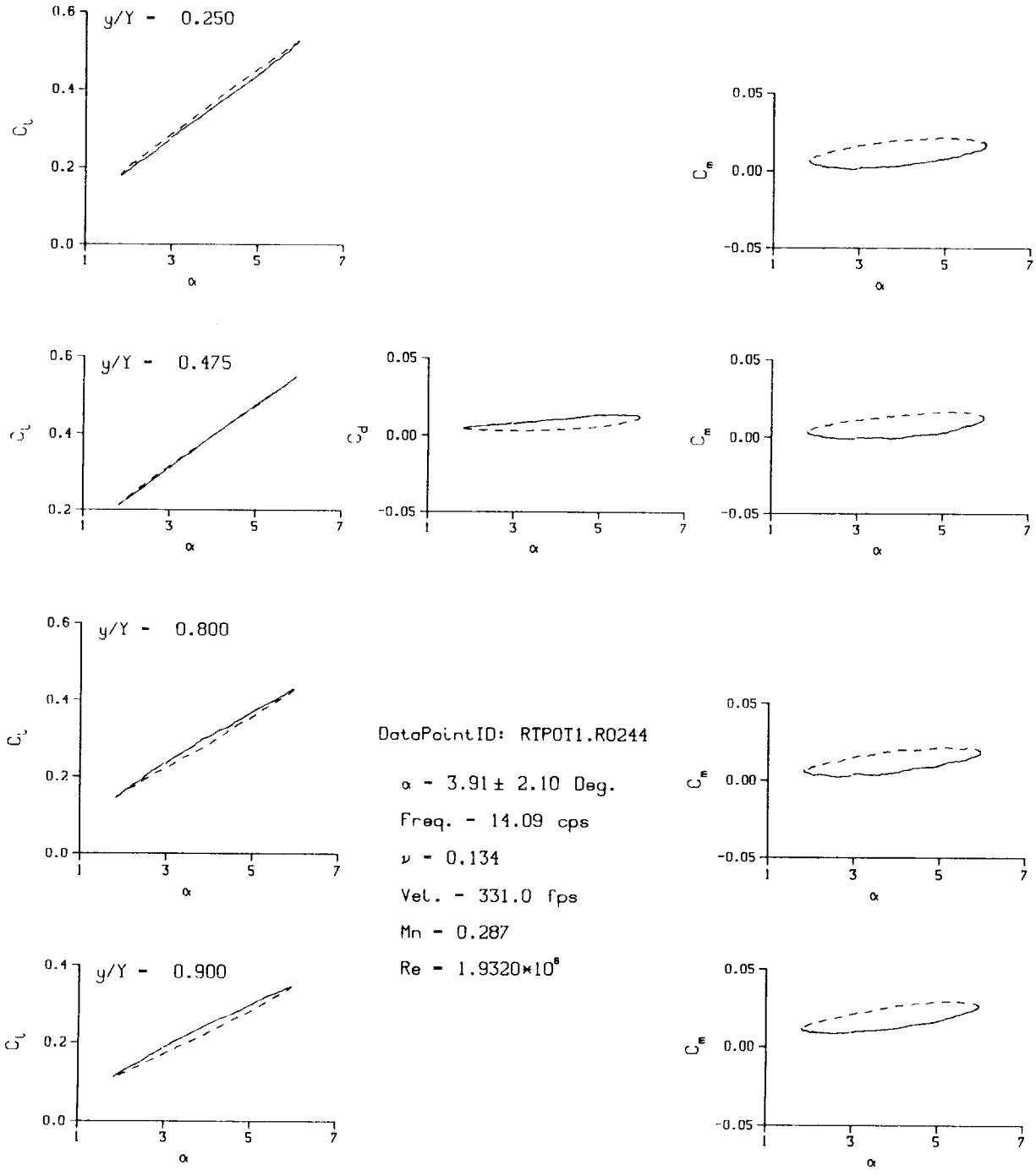

(c) v = 0.14

Figure 33. Continued.

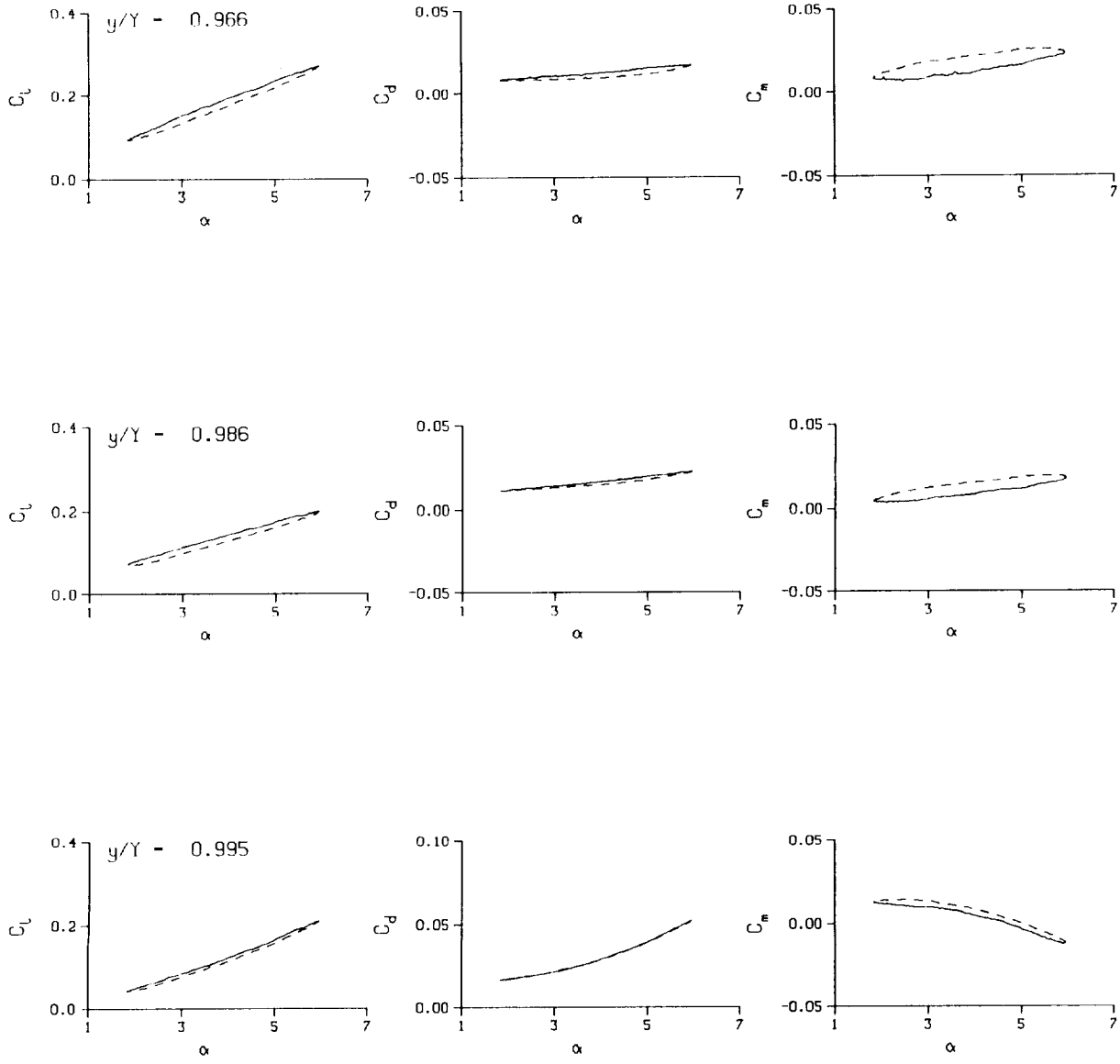

(c) v = 0.14. Concluded

Figure 33. Continued.

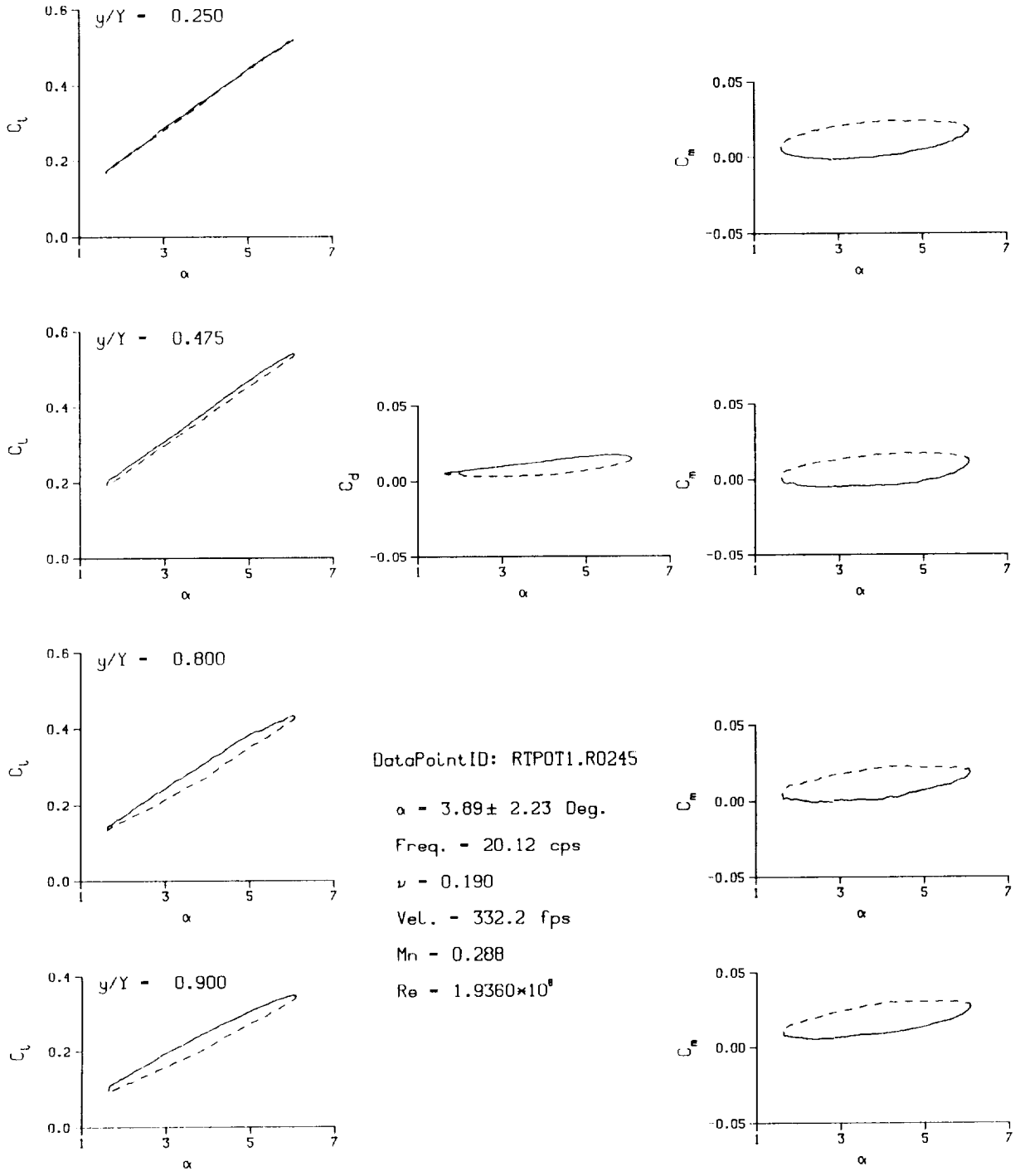

(d) v = 0.20

Figure 33. Continued.

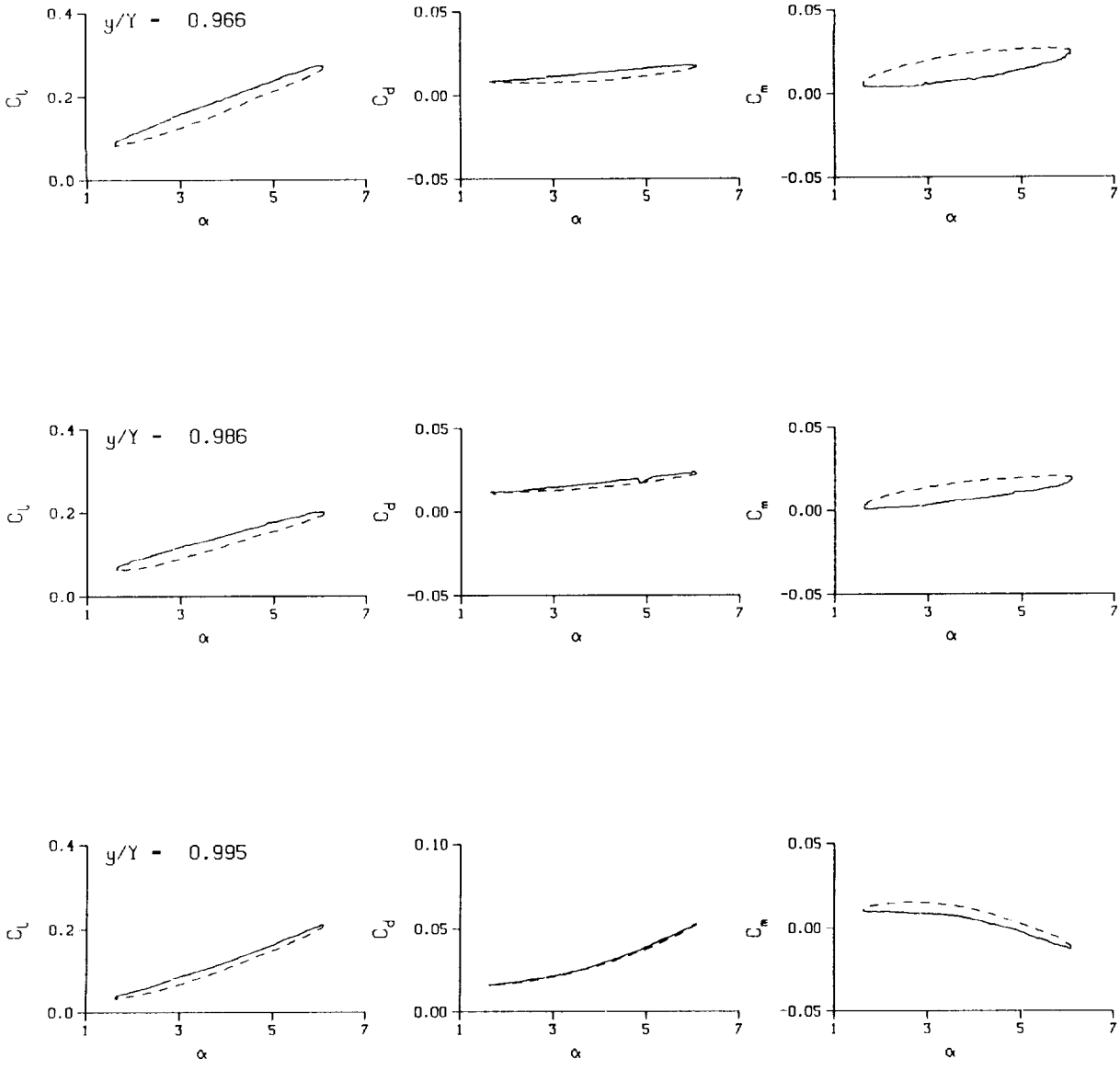

(d) v = 0.20. Concluded

Figure 33. Concluded.

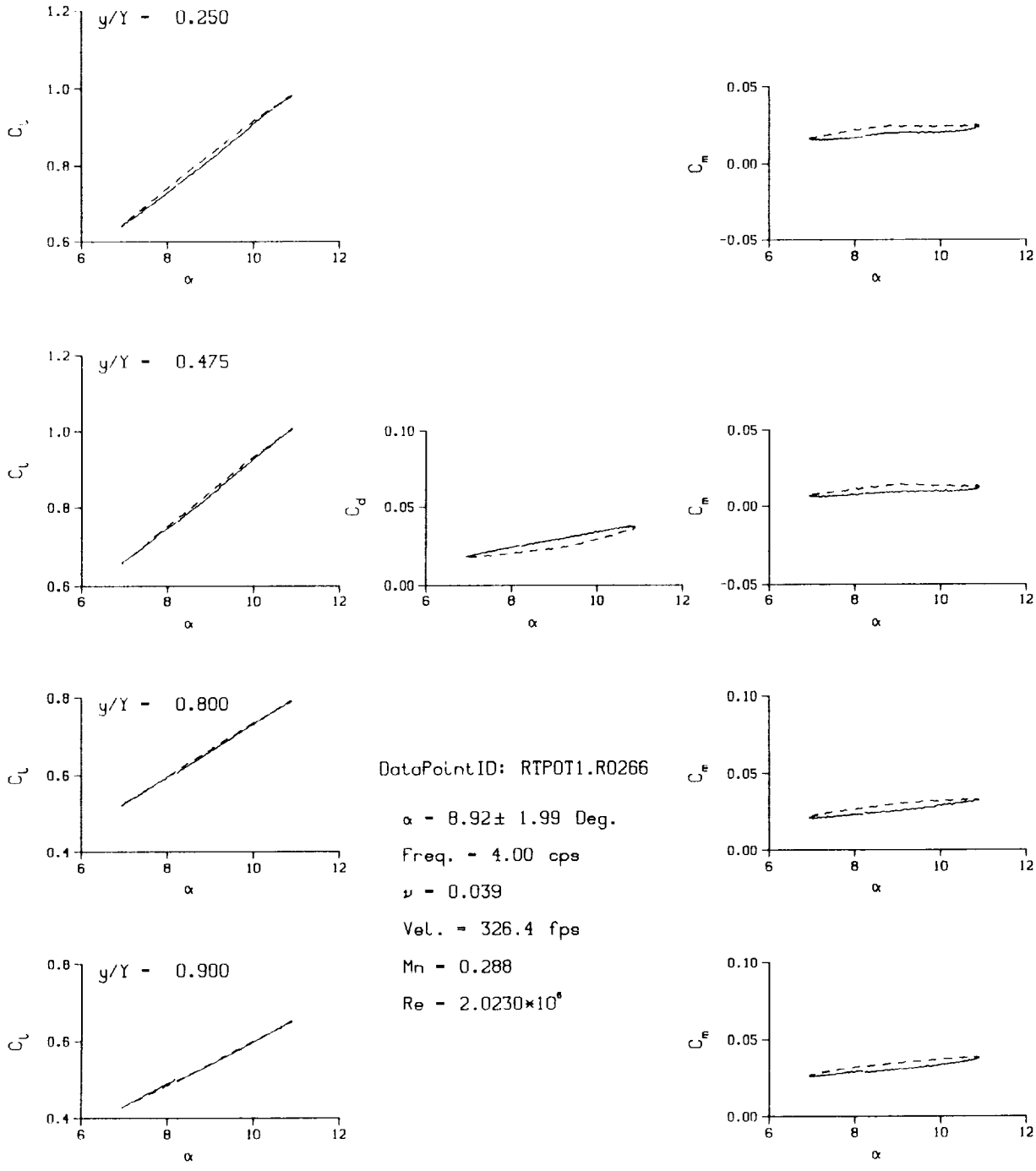

(a) ν = 0.04

Figure 34. 3-D round tip pitch oscillation data; BL-trip; α = 9 ± 2 deg.

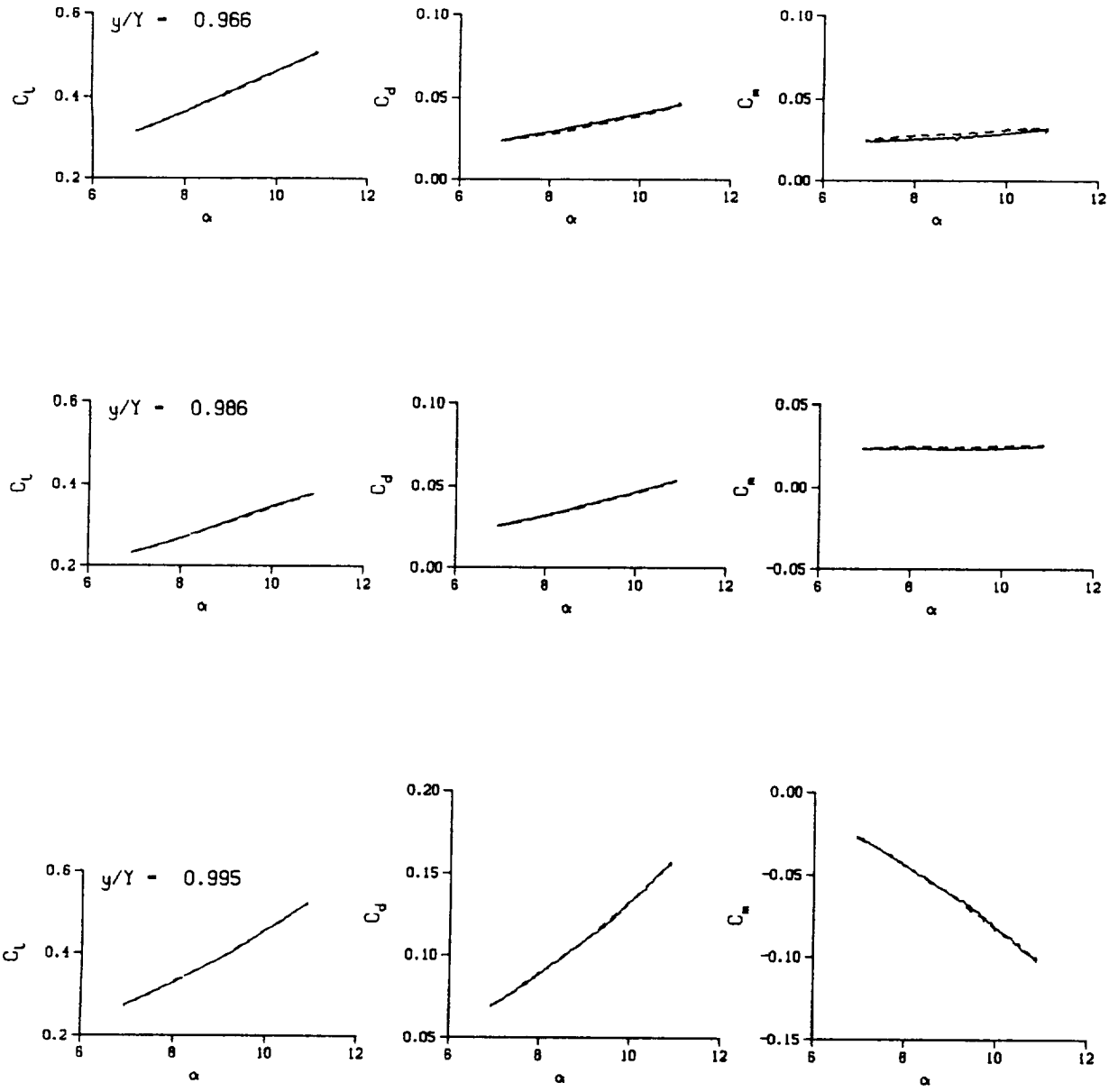

(a) v = 0.04. Concluded

Figure 34. Continued.

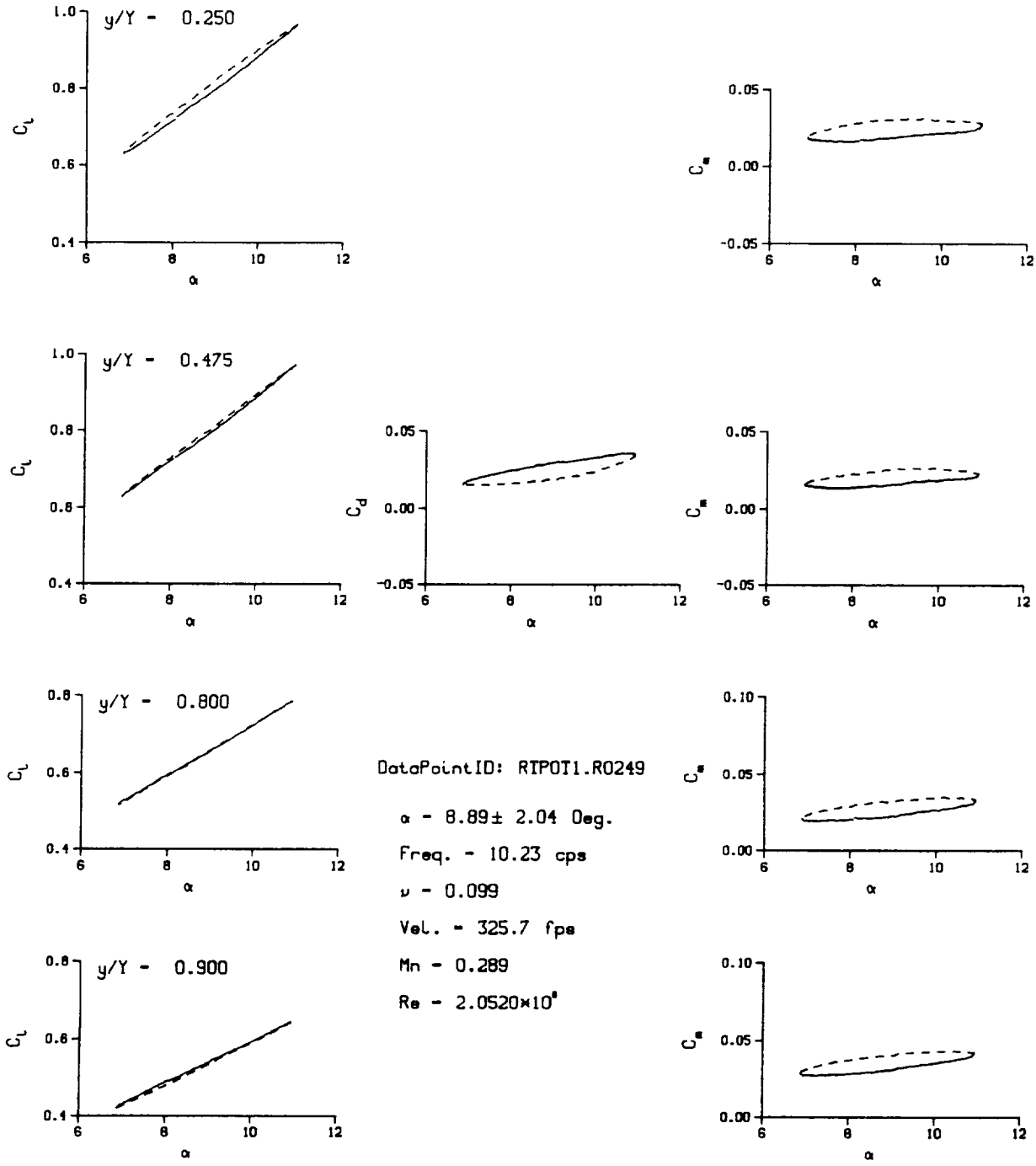

(b) ν = 0.10

Figure 34. Continued.

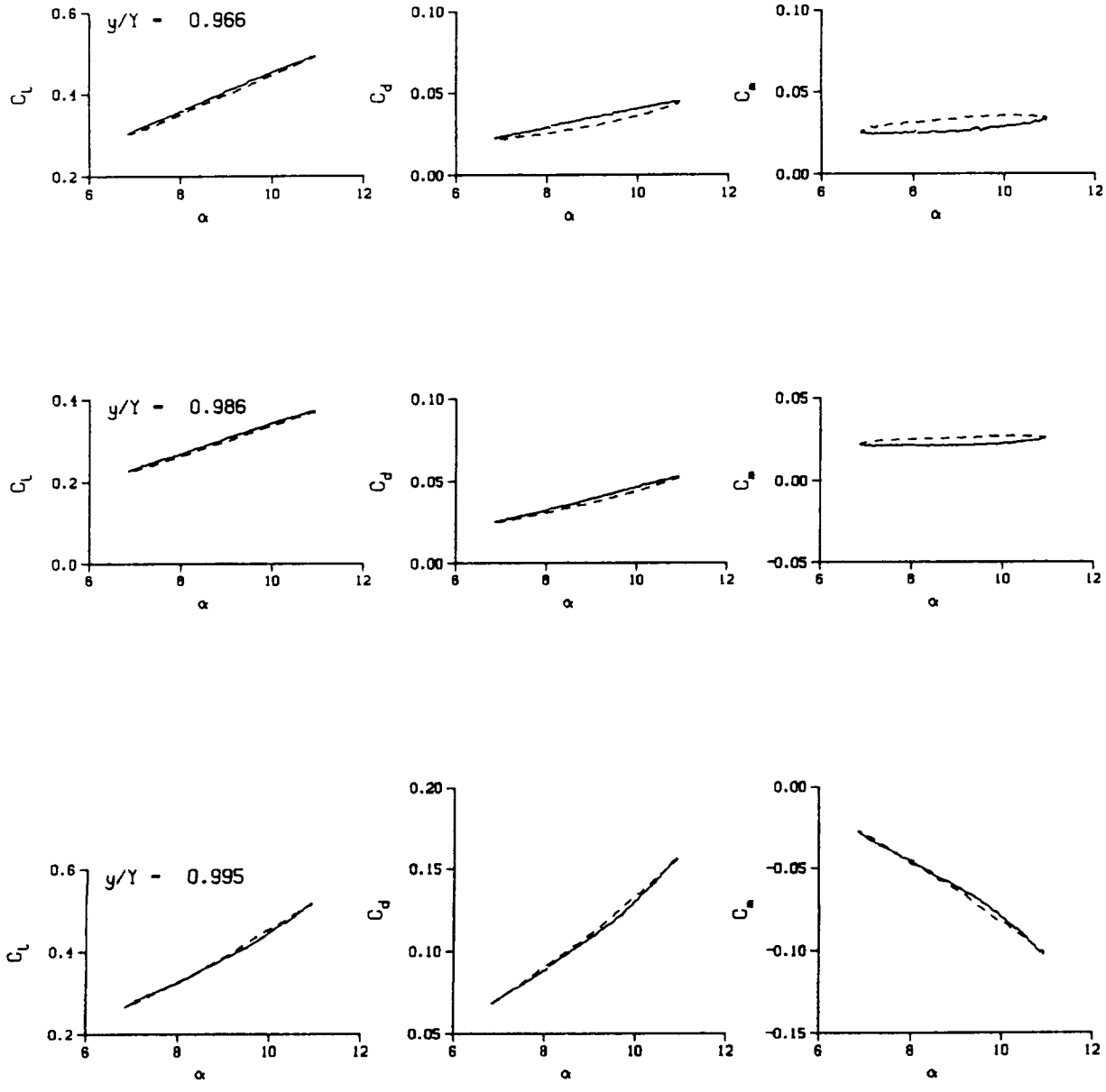

(b) v = 0.10. Concluded

Figure 34. Continued.

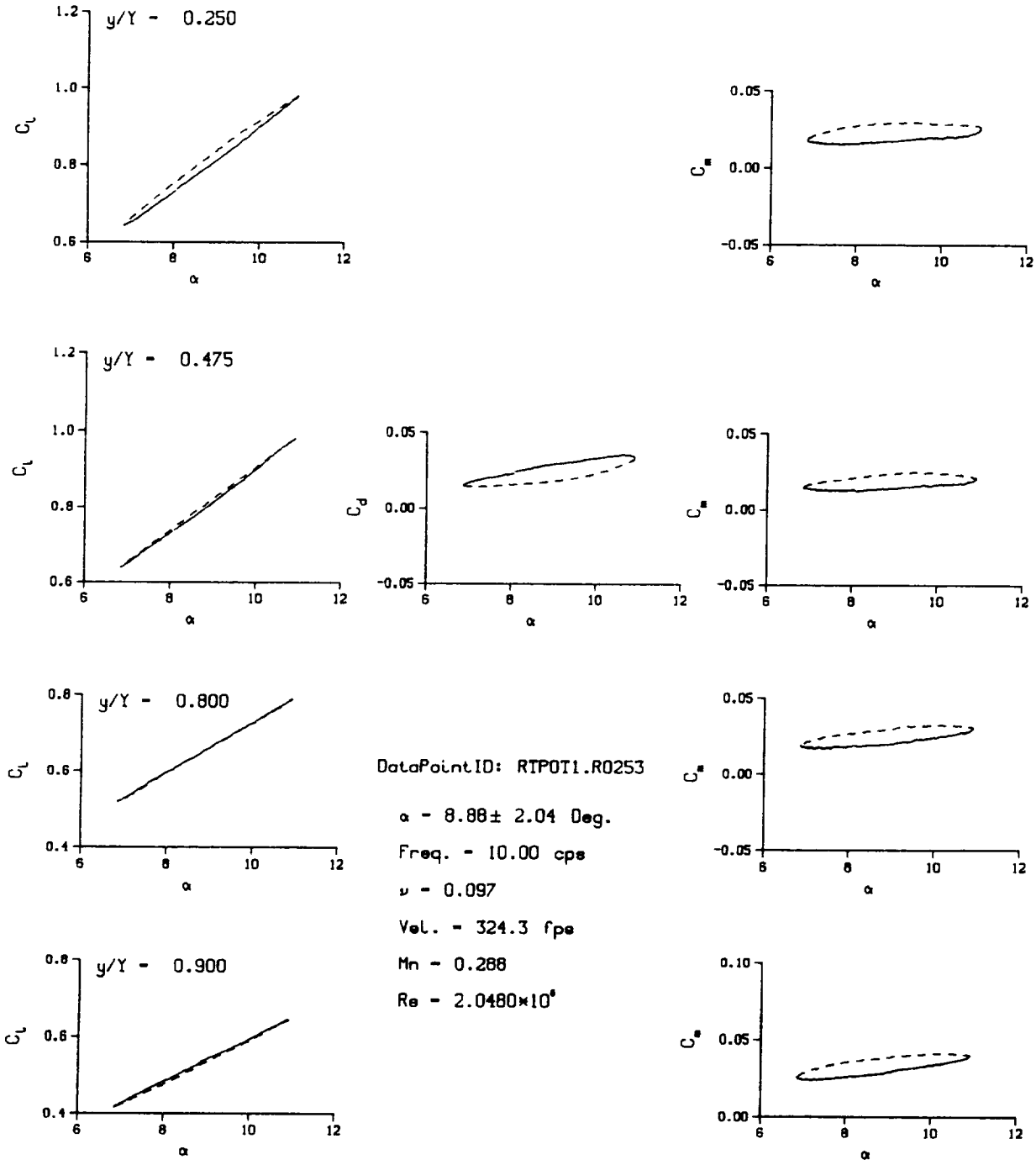

(b.1) ν = 0.10; repeat

Figure 34. Continued.

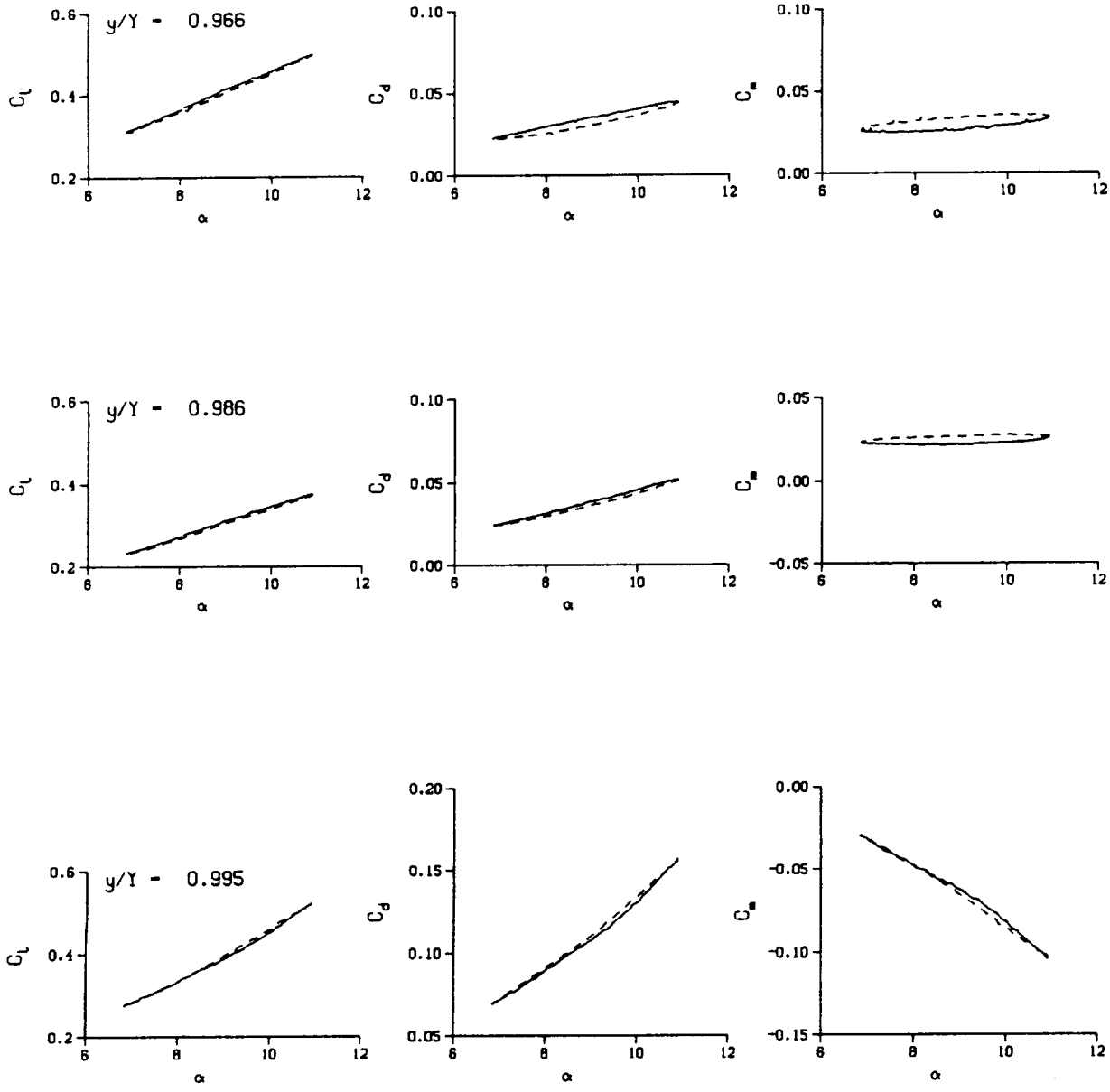

(b.1) v = 0.10; repeat. Concluded

Figure 34. Continued.

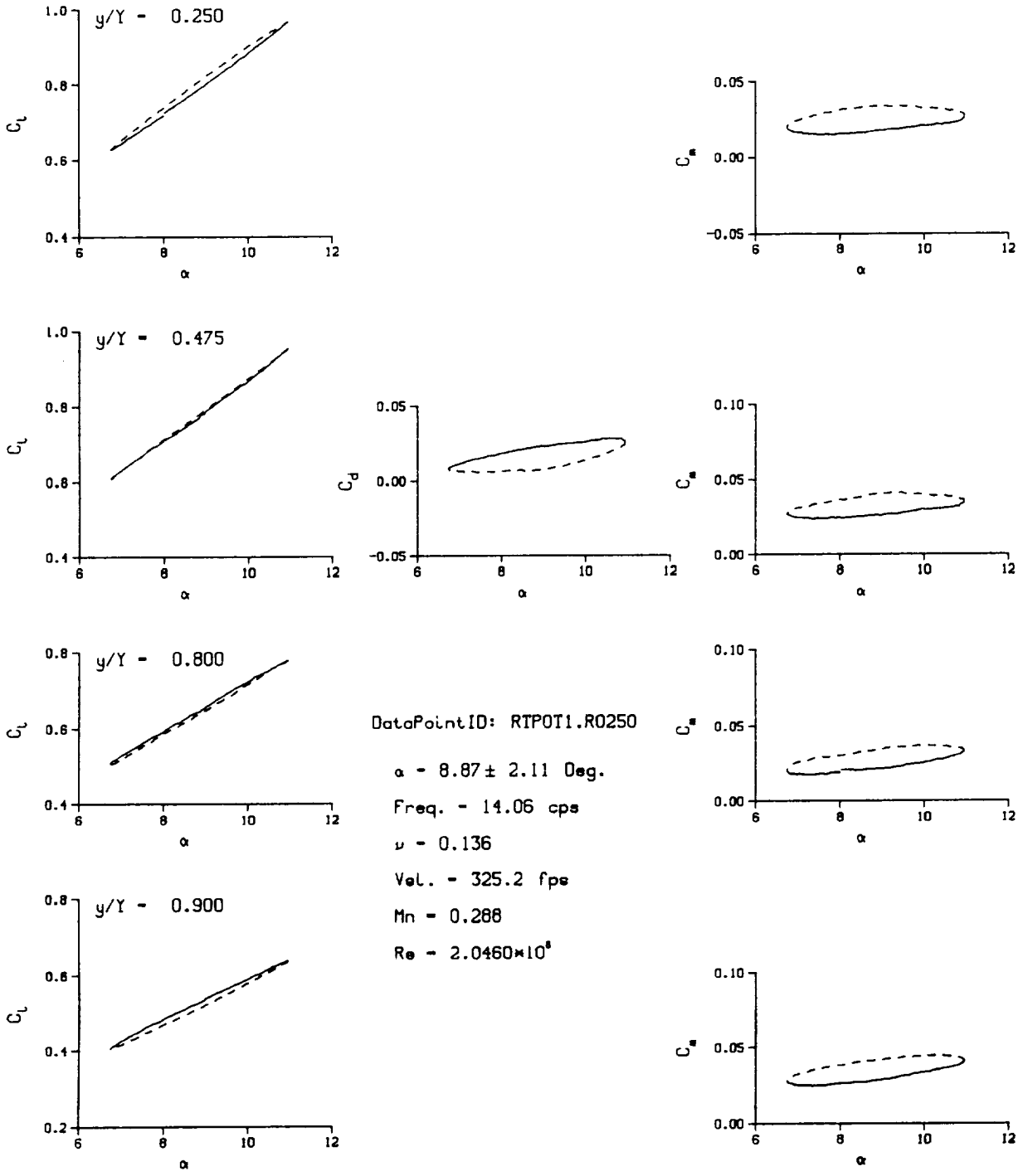

(c) v = 0.14

Figure 34. Continued.

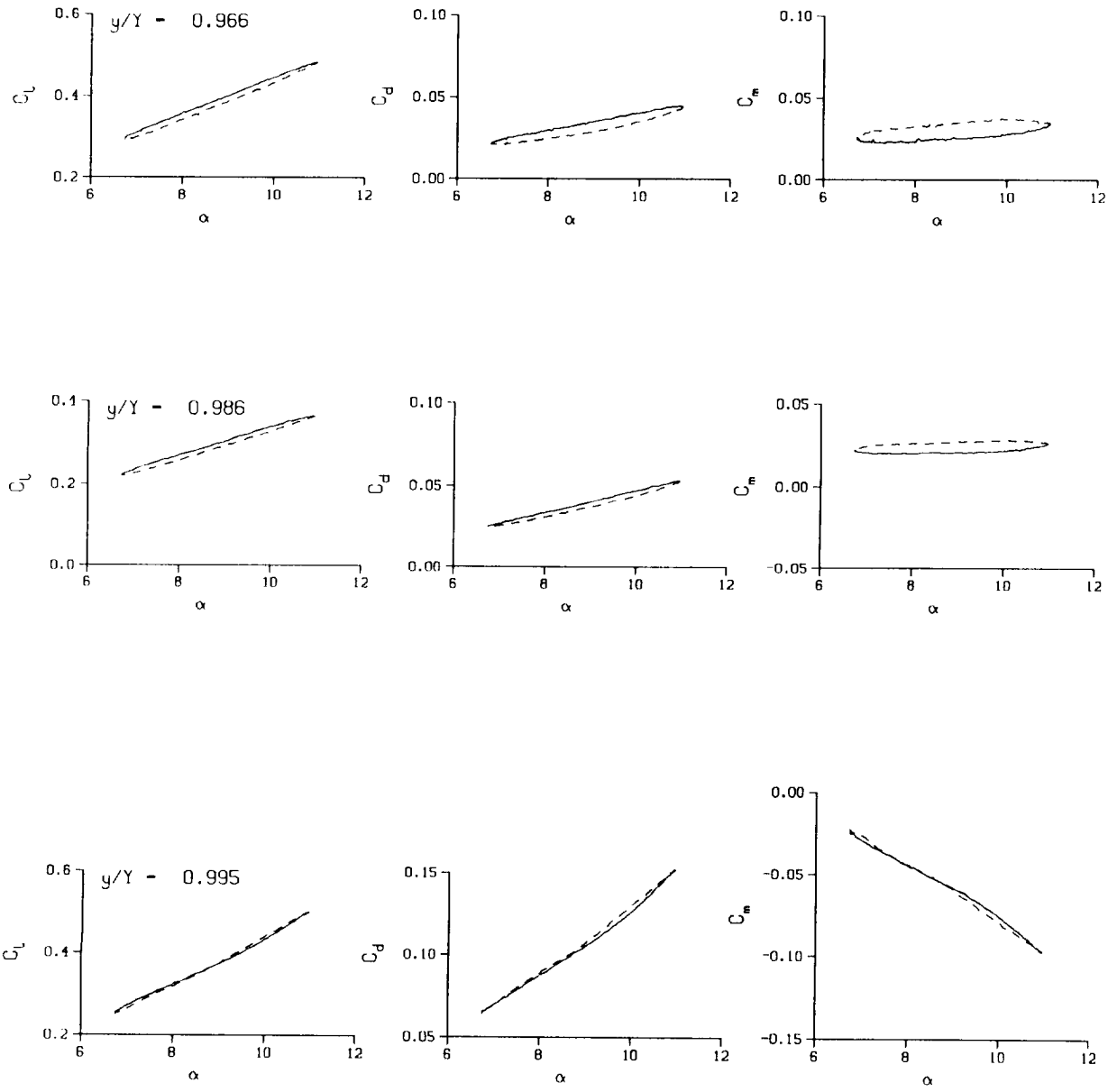

(c) v = 0.14. Concluded

Figure 34. Continued.

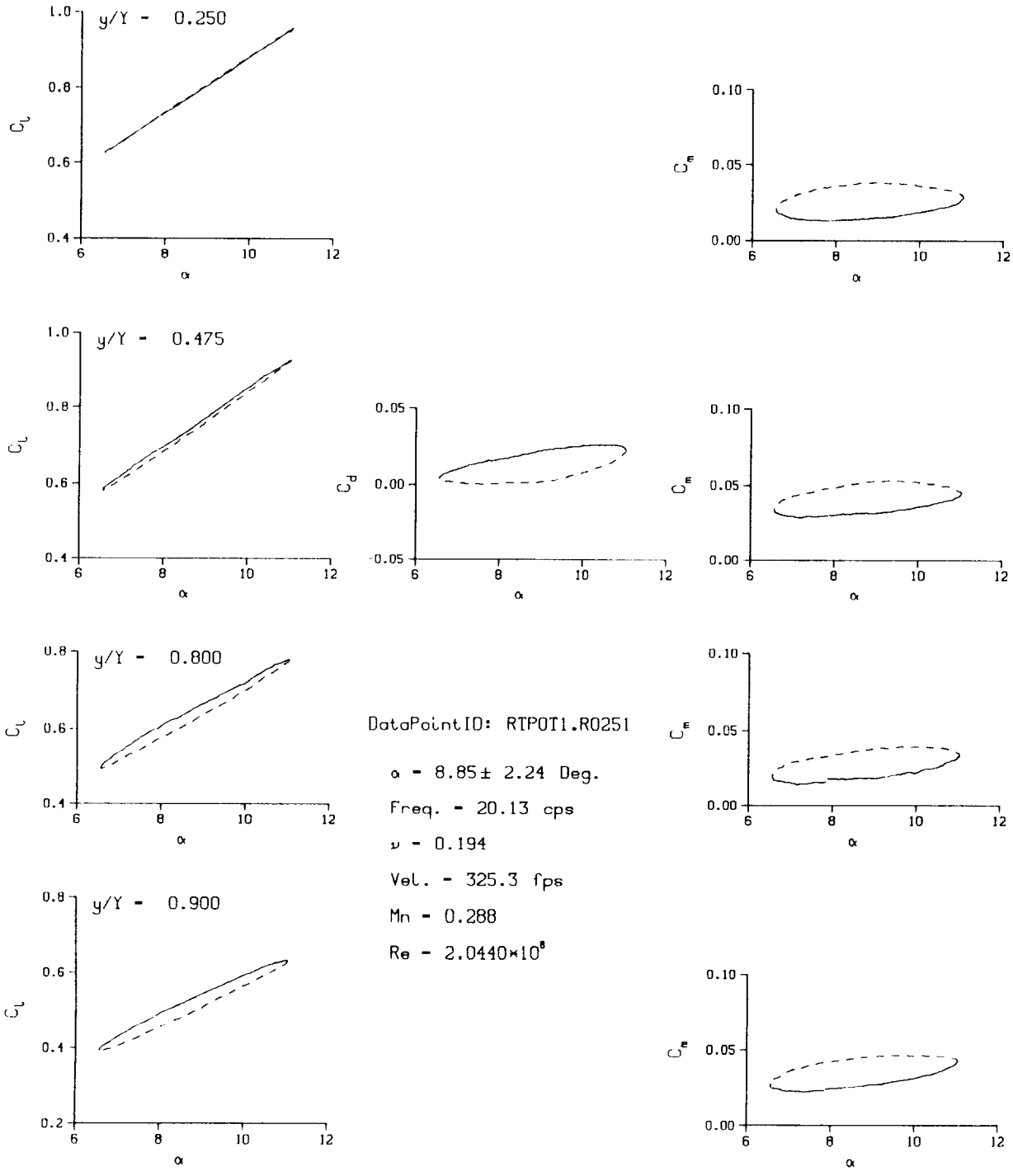

(d) v = 0.20

Figure 34. Continued.

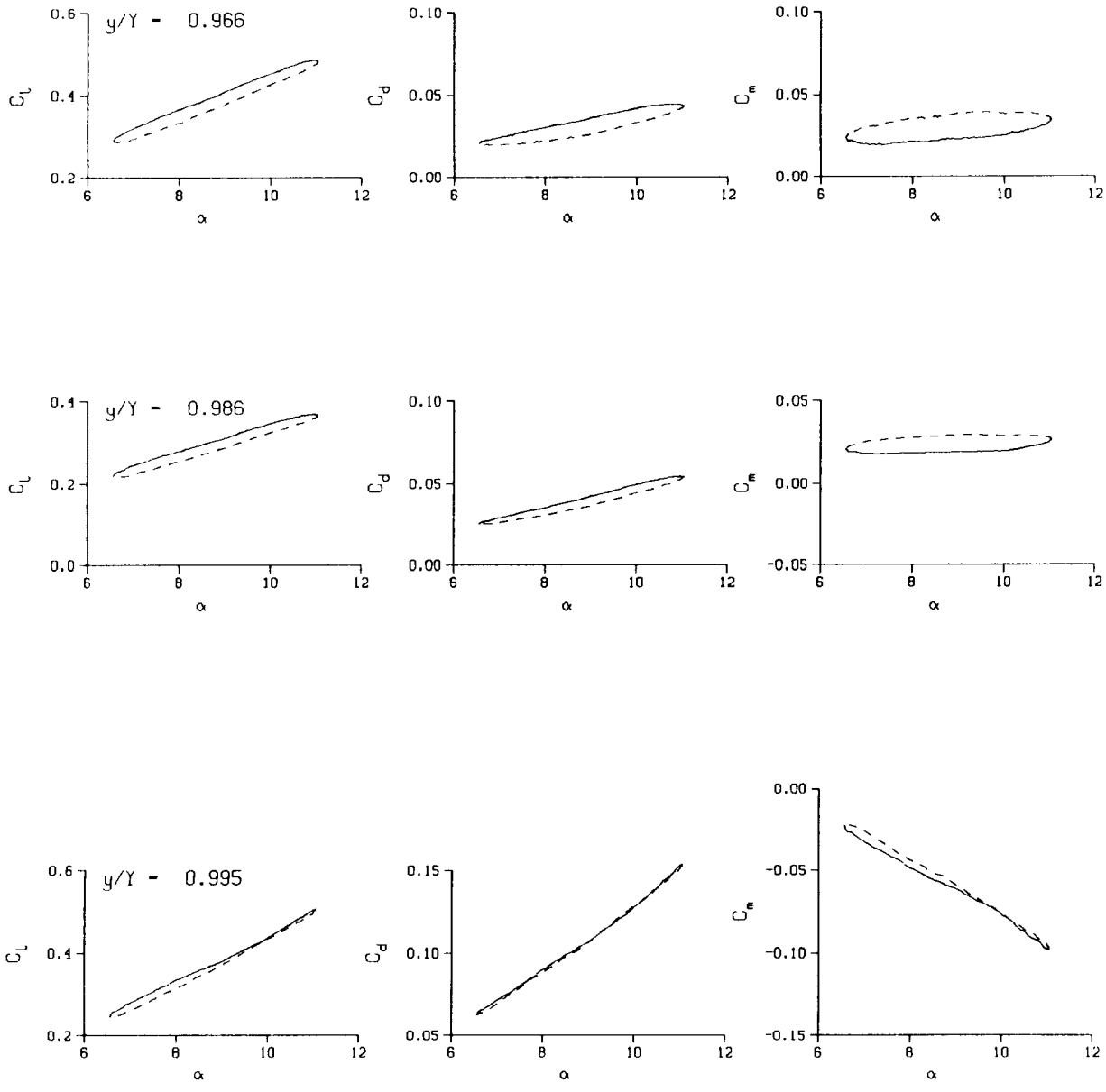

(d) v = 0.20. Concluded

Figure 34. Concluded.

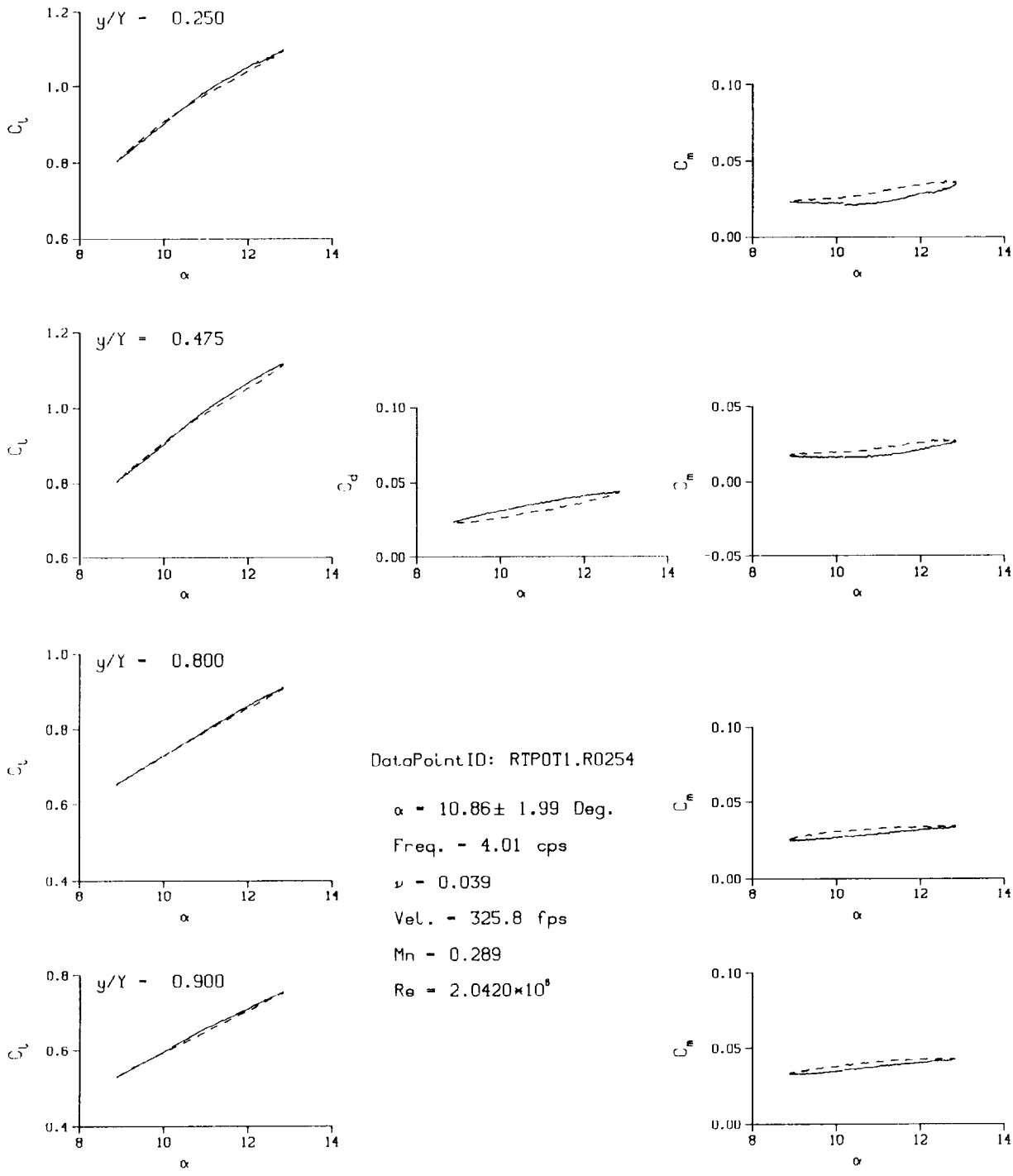

(a) ν = 0.04

Figure 35. 3-D round tip pitch oscillation data; BL-trip; α = 11 ± 2 deg.

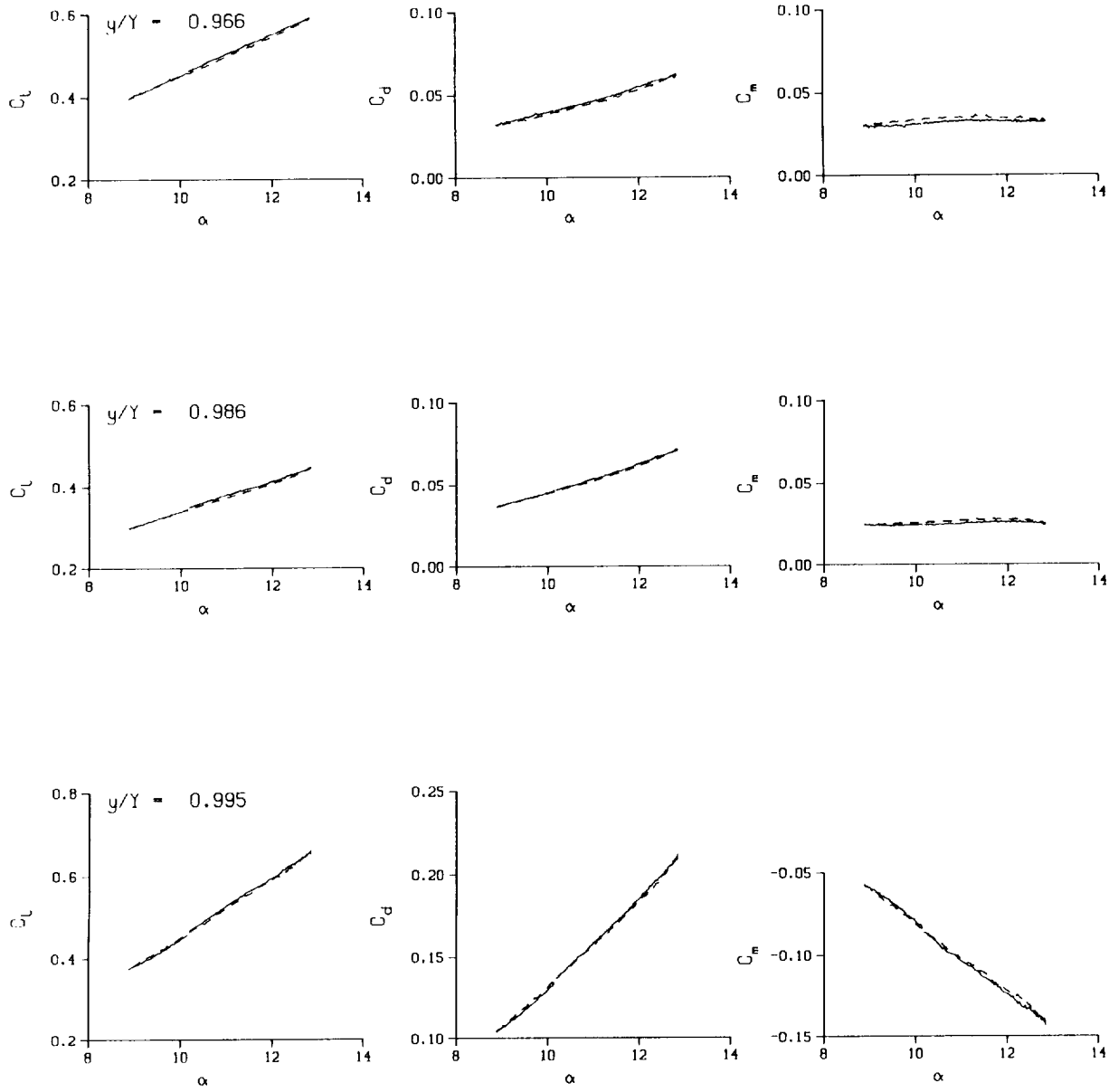

(a) v = 0.04. Concluded

Figure 35. Continued.

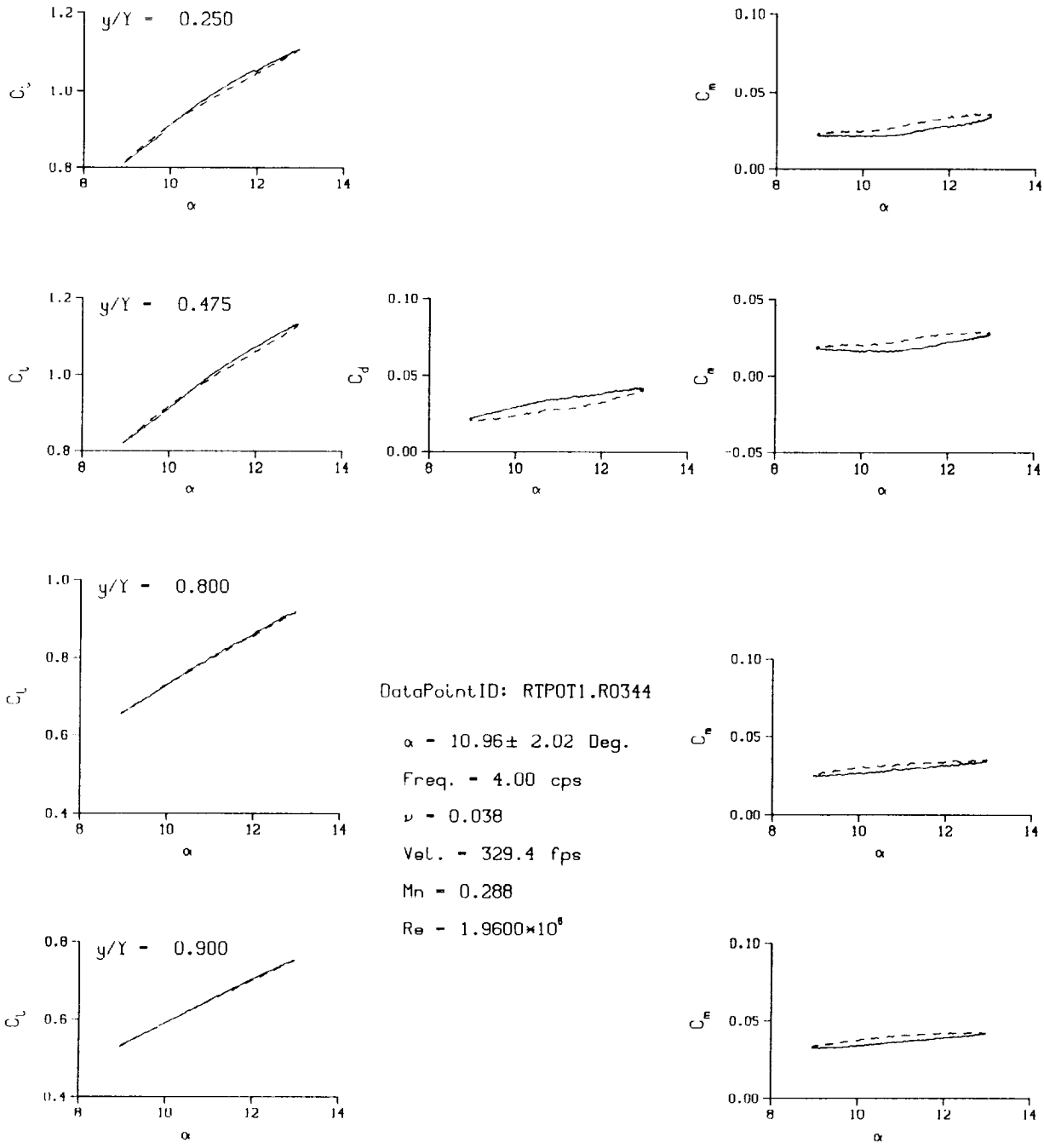

(a.1) v = 0.04; repeat

Figure 35. Continued.

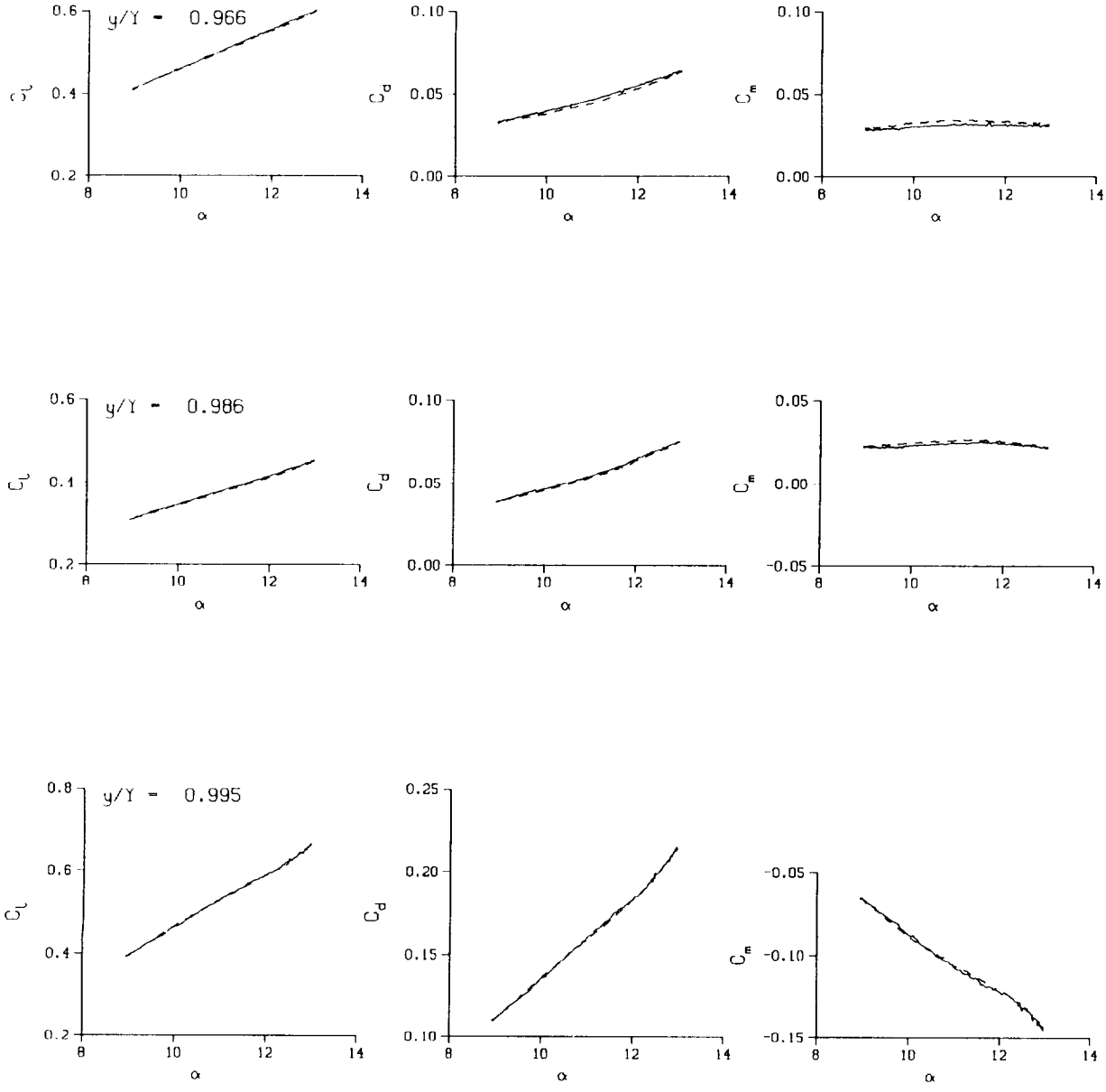

(a.1) v = 0.04; repeat. Concluded

Figure 35. Continued.

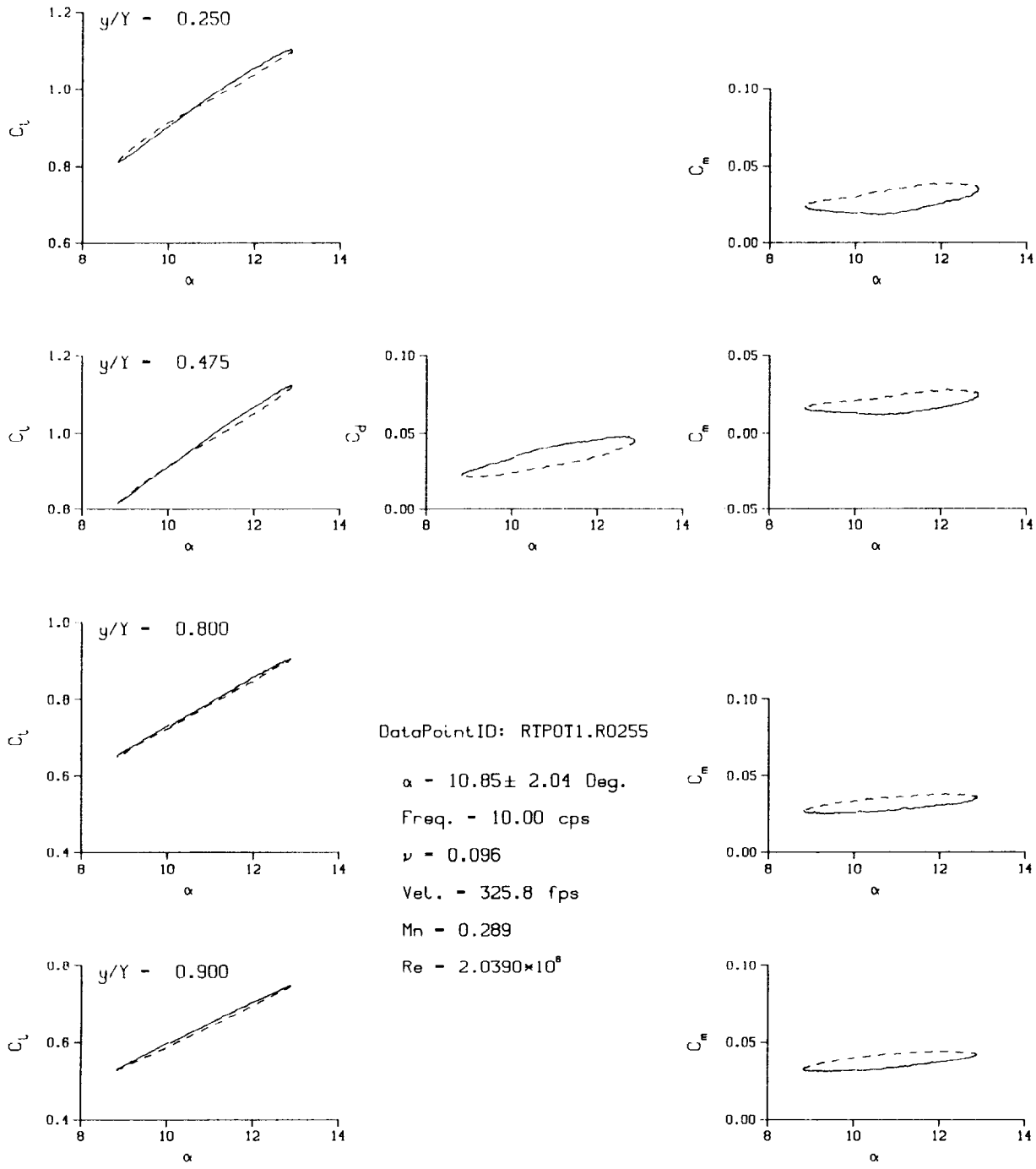

(b) v = 0.10

Figure 35. Continued.

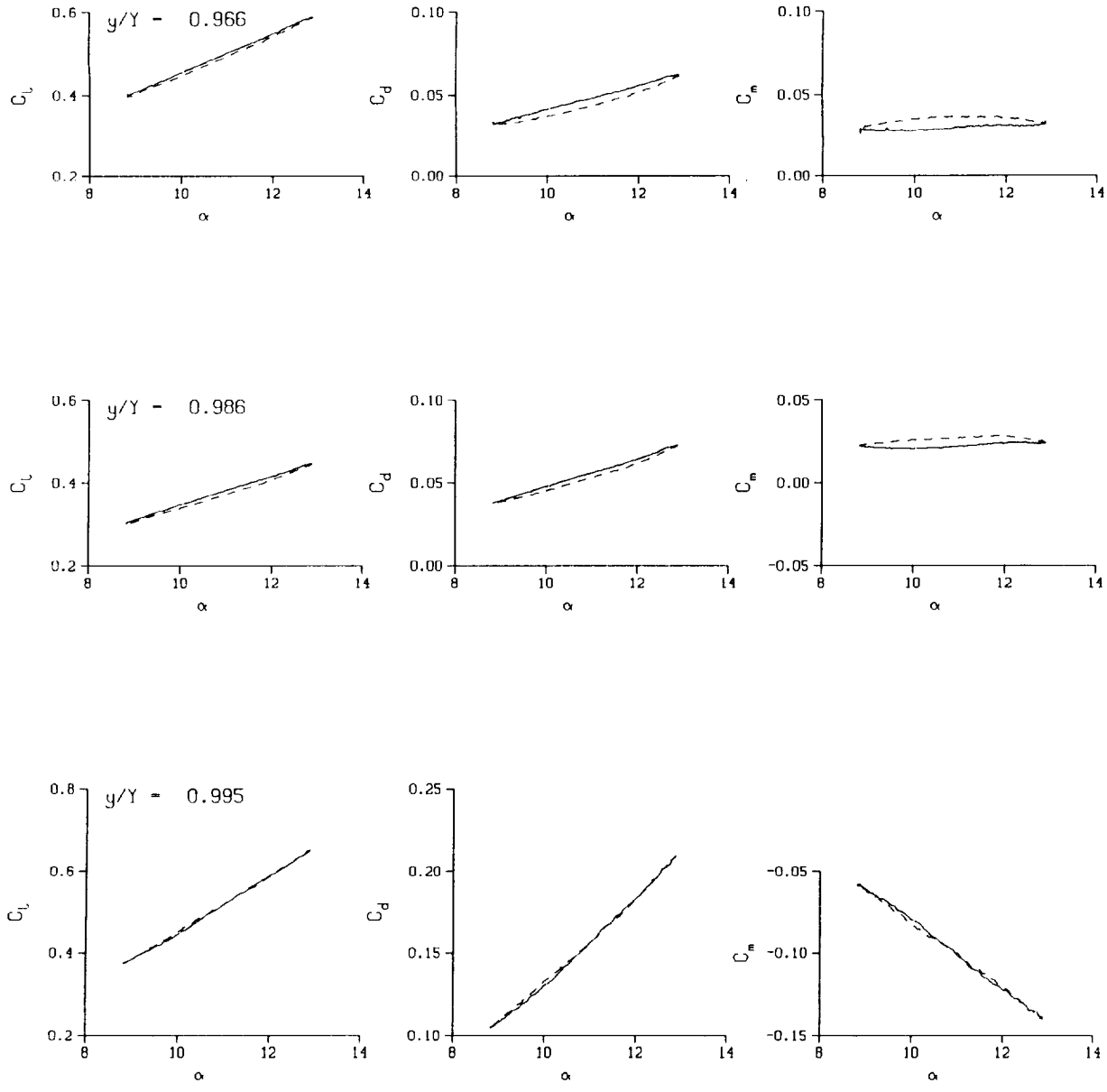

(b) v = 0.10. Concluded

Figure 35. Continued.

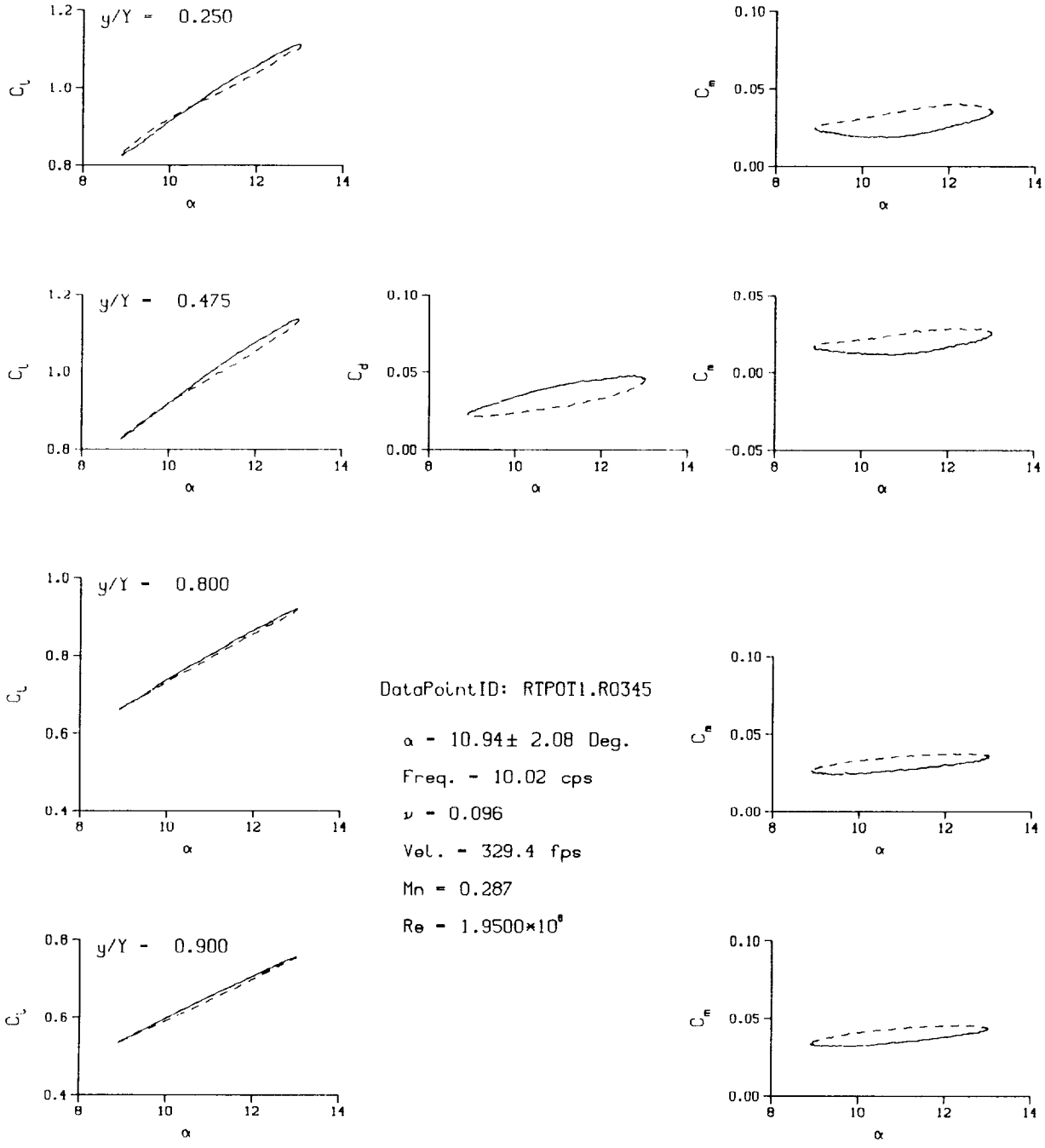

(b.1) ν = 0.10; repeat

Figure 35. Continued.

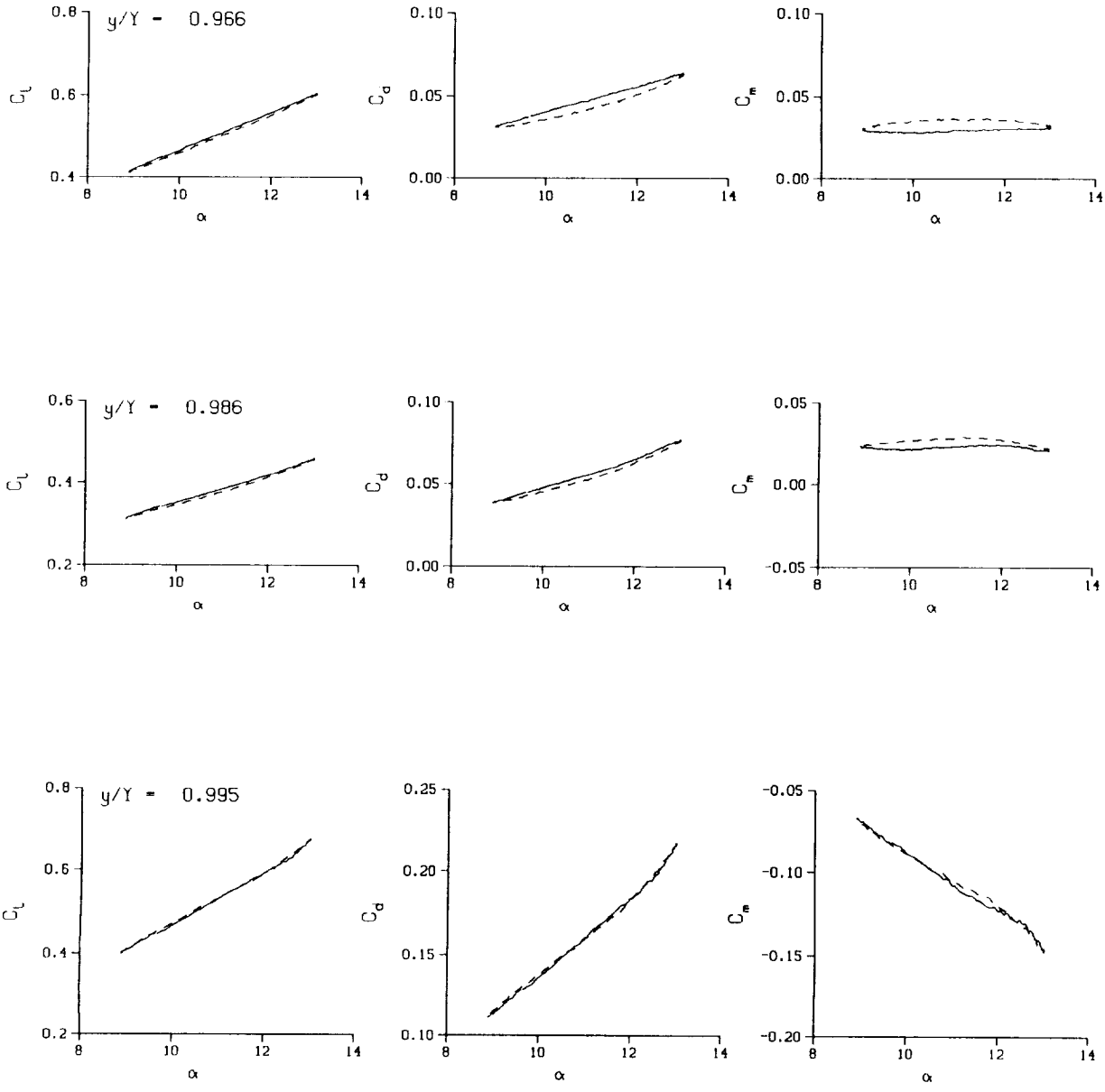

(b.1) v = 0.10; repeat. Concluded

Figure 35. Continued.

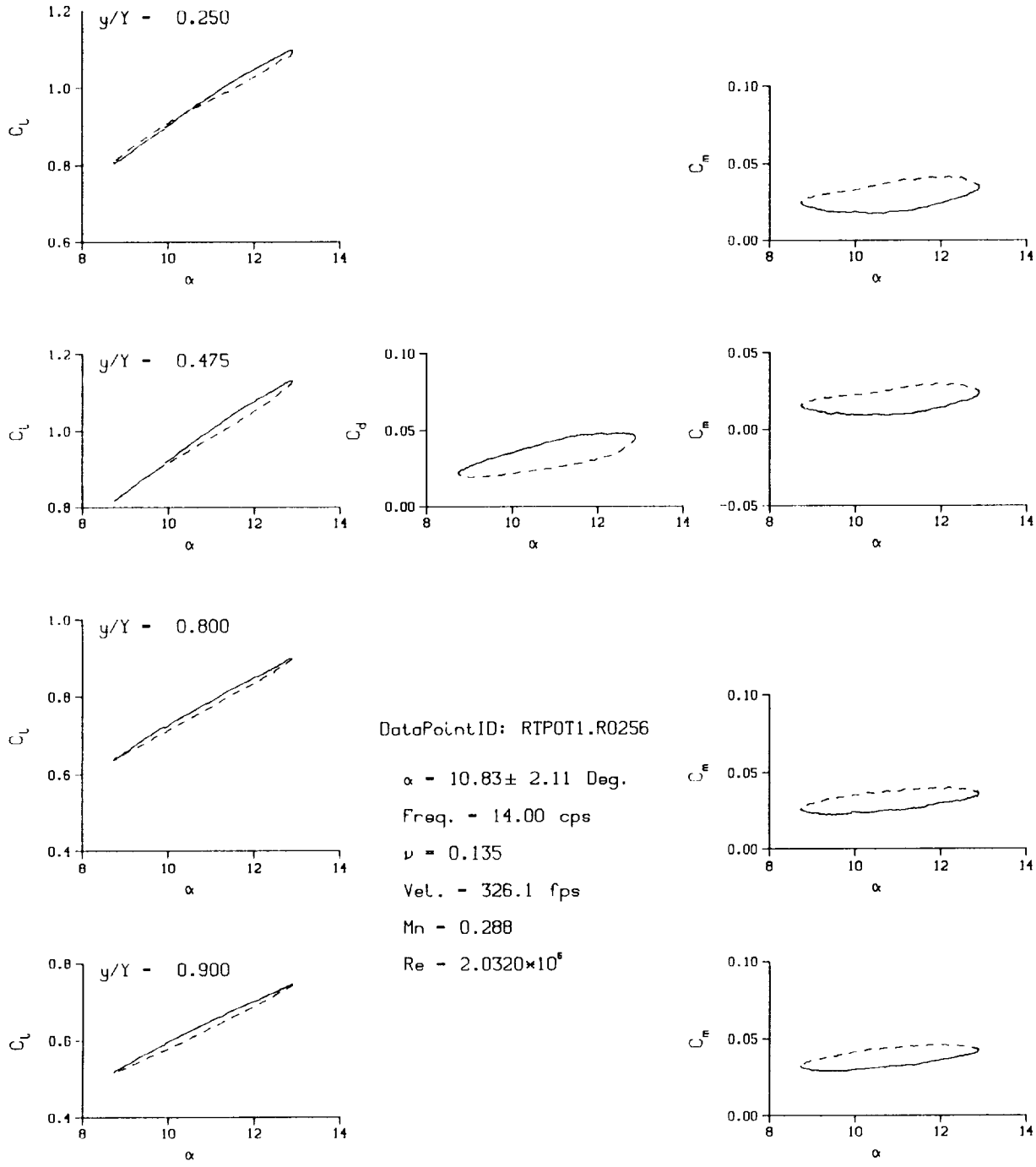

(c) v = 0.14

Figure 35. Continued.

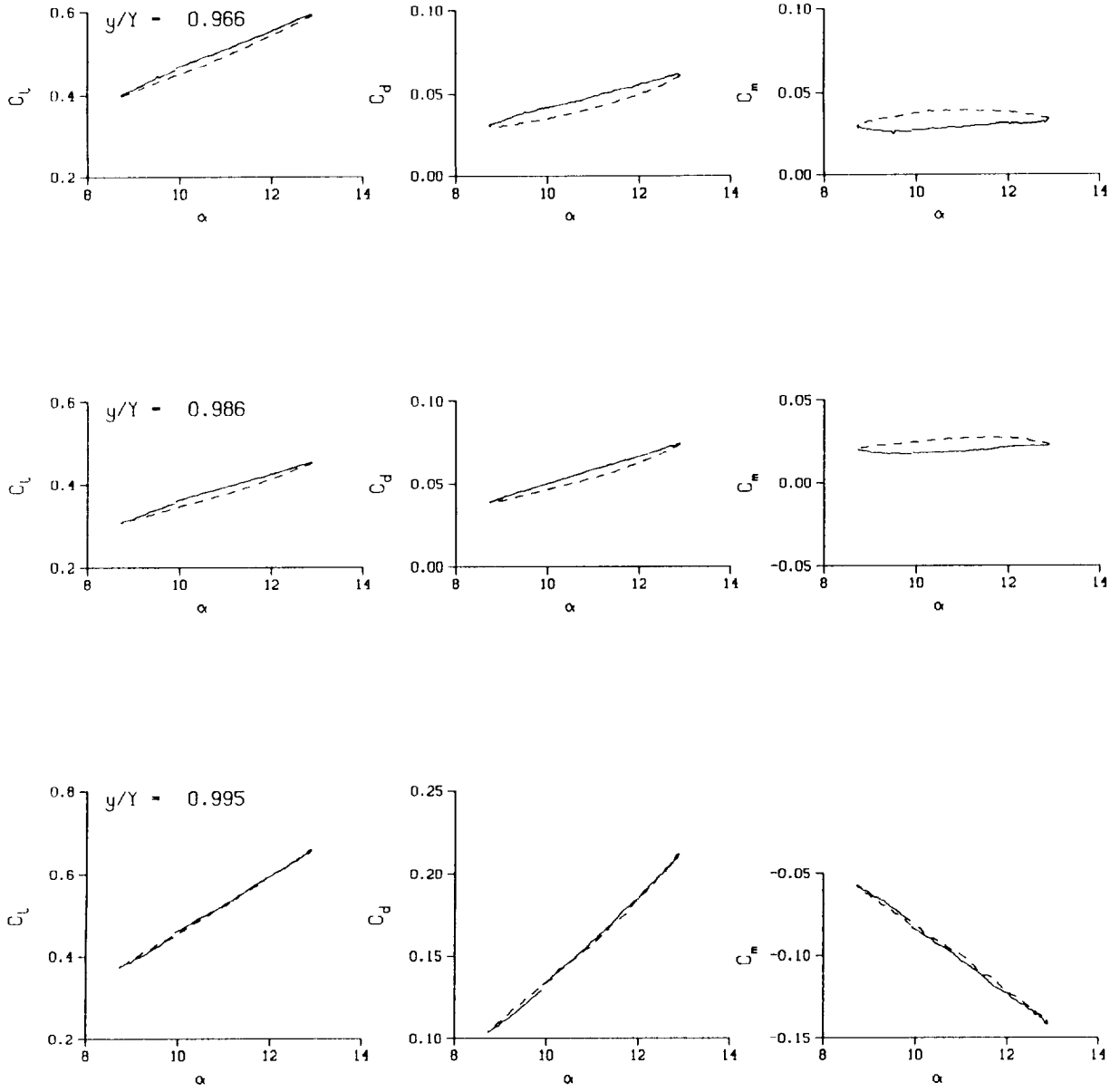

(c) v = 0.14. Concluded

Figure 35. Continued.

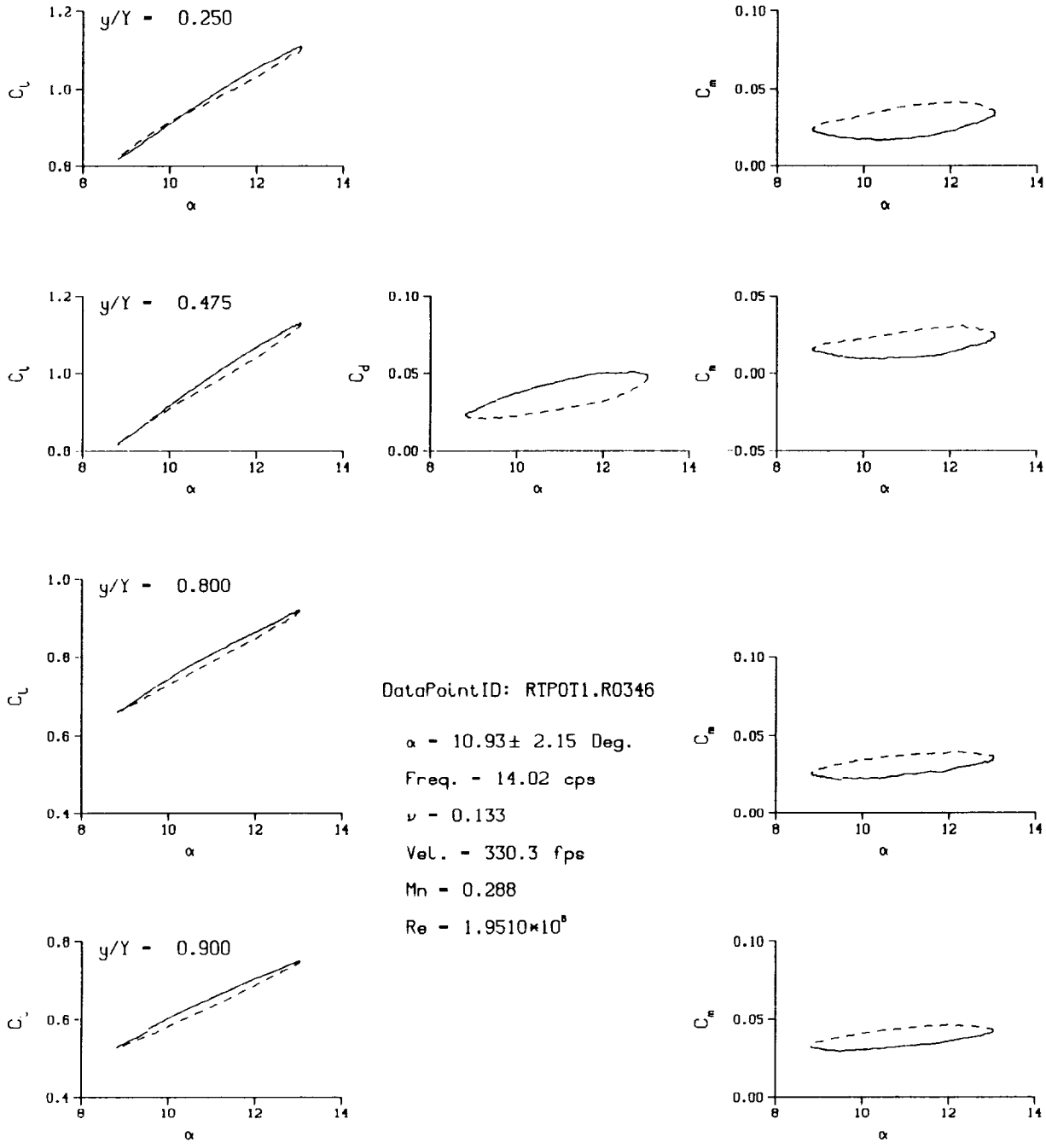

(c.1) v = 0.14; repeat

Figure 35. Continued.

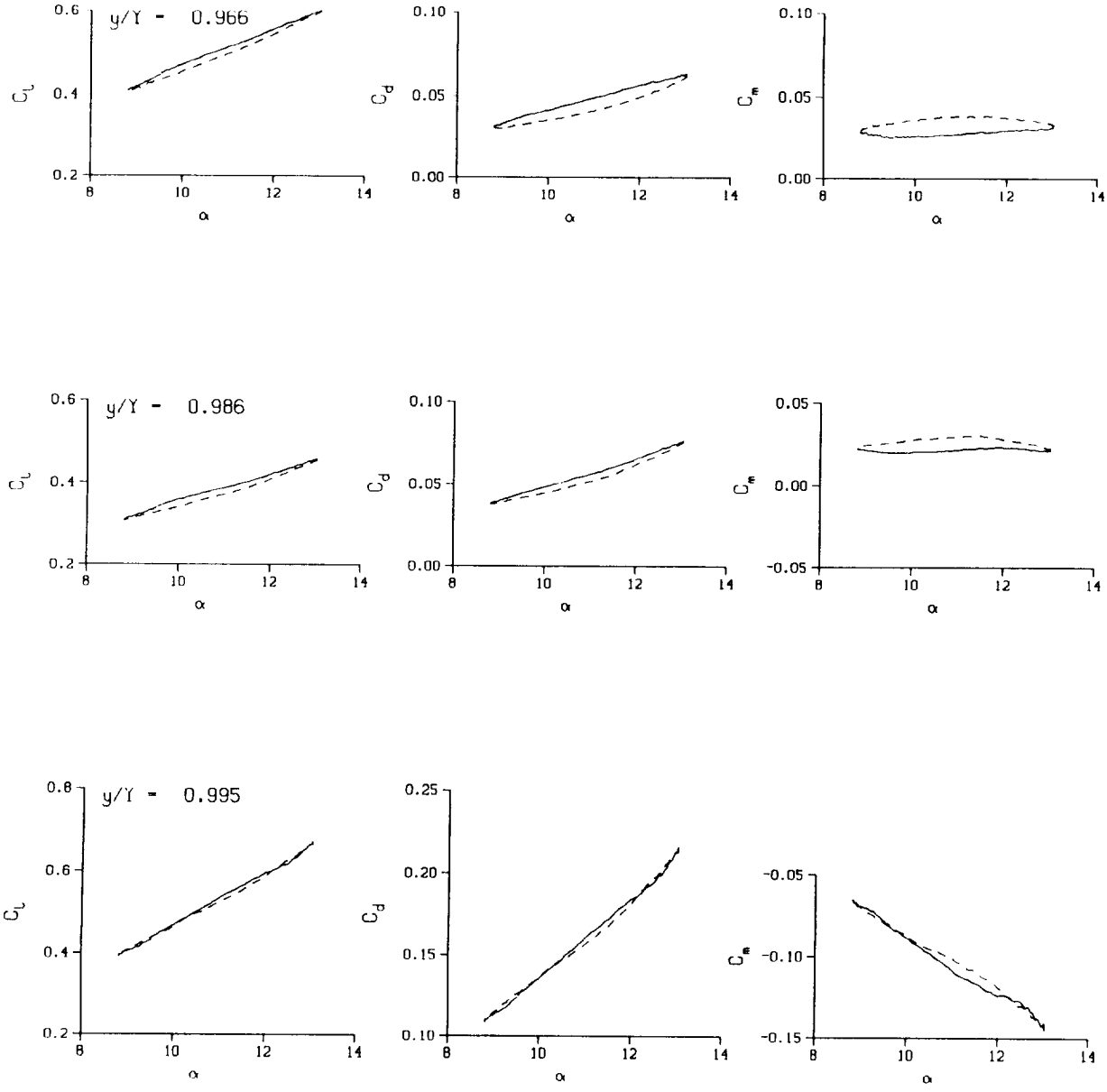

(c.1) v = 0.14; repeat. Concluded

Figure 35. Continued.

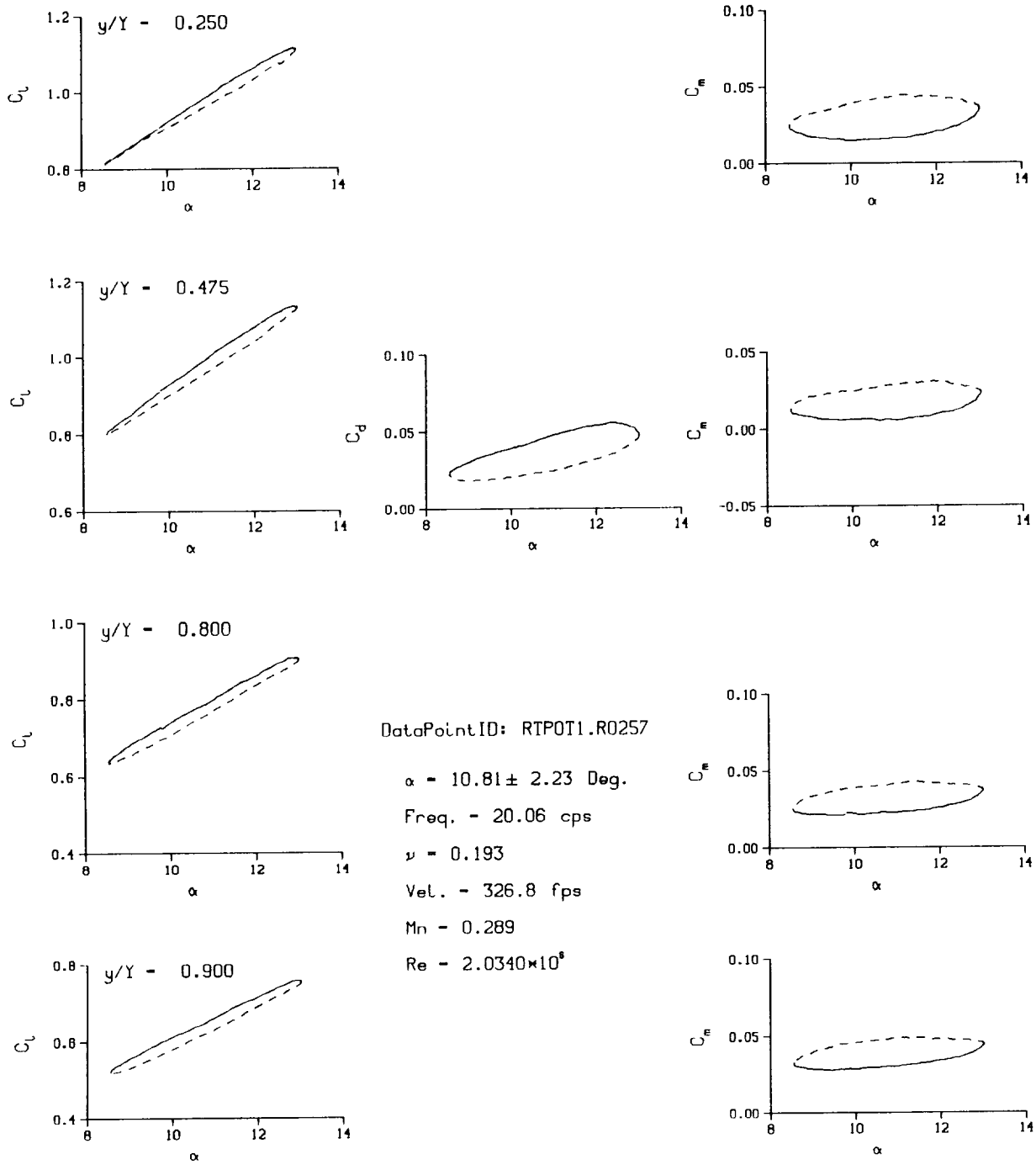

(d) ν = 0.20

Figure 35. Continued.

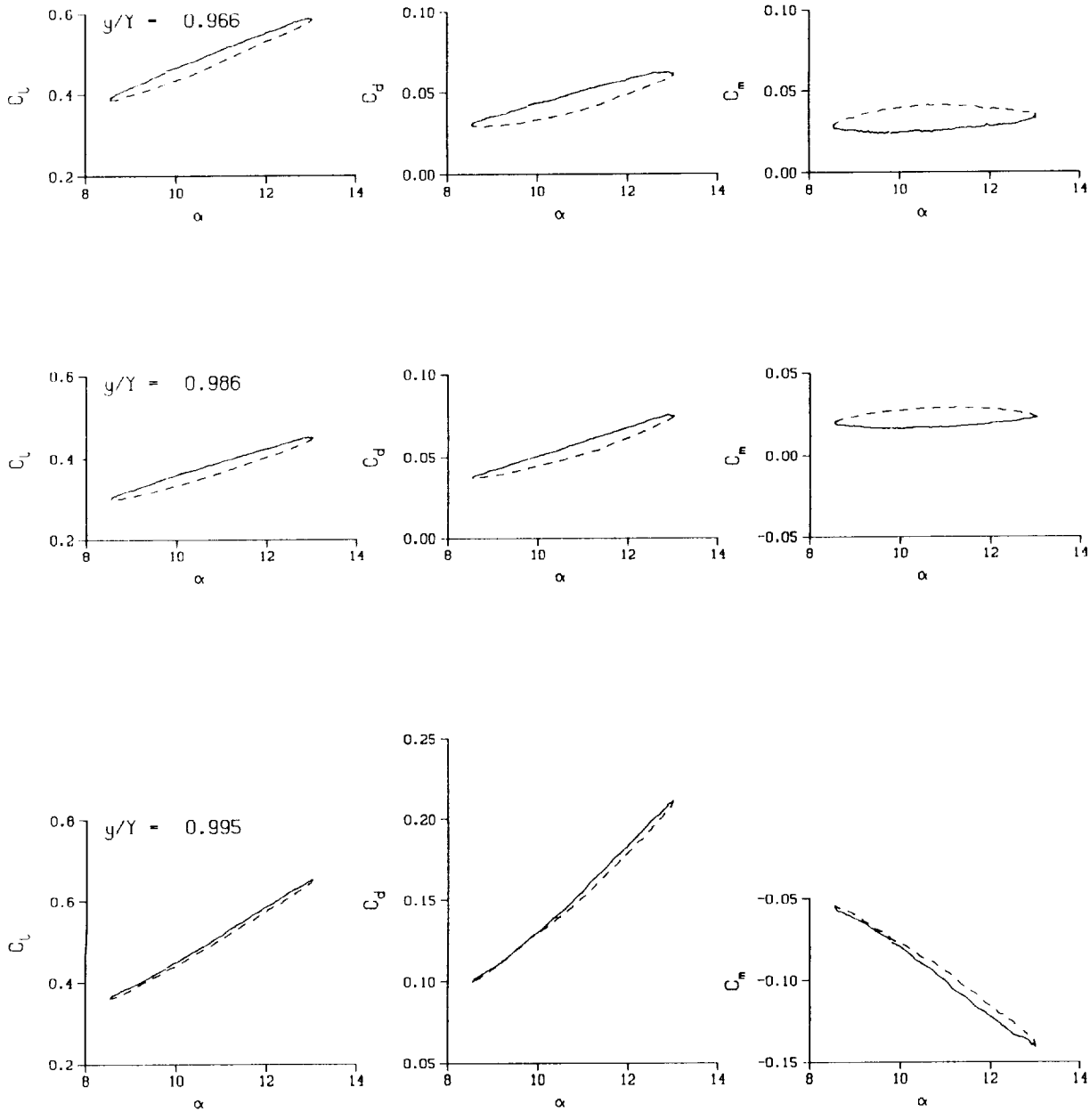

(d) v = 0.20. Concluded

Figure 35. Continued.

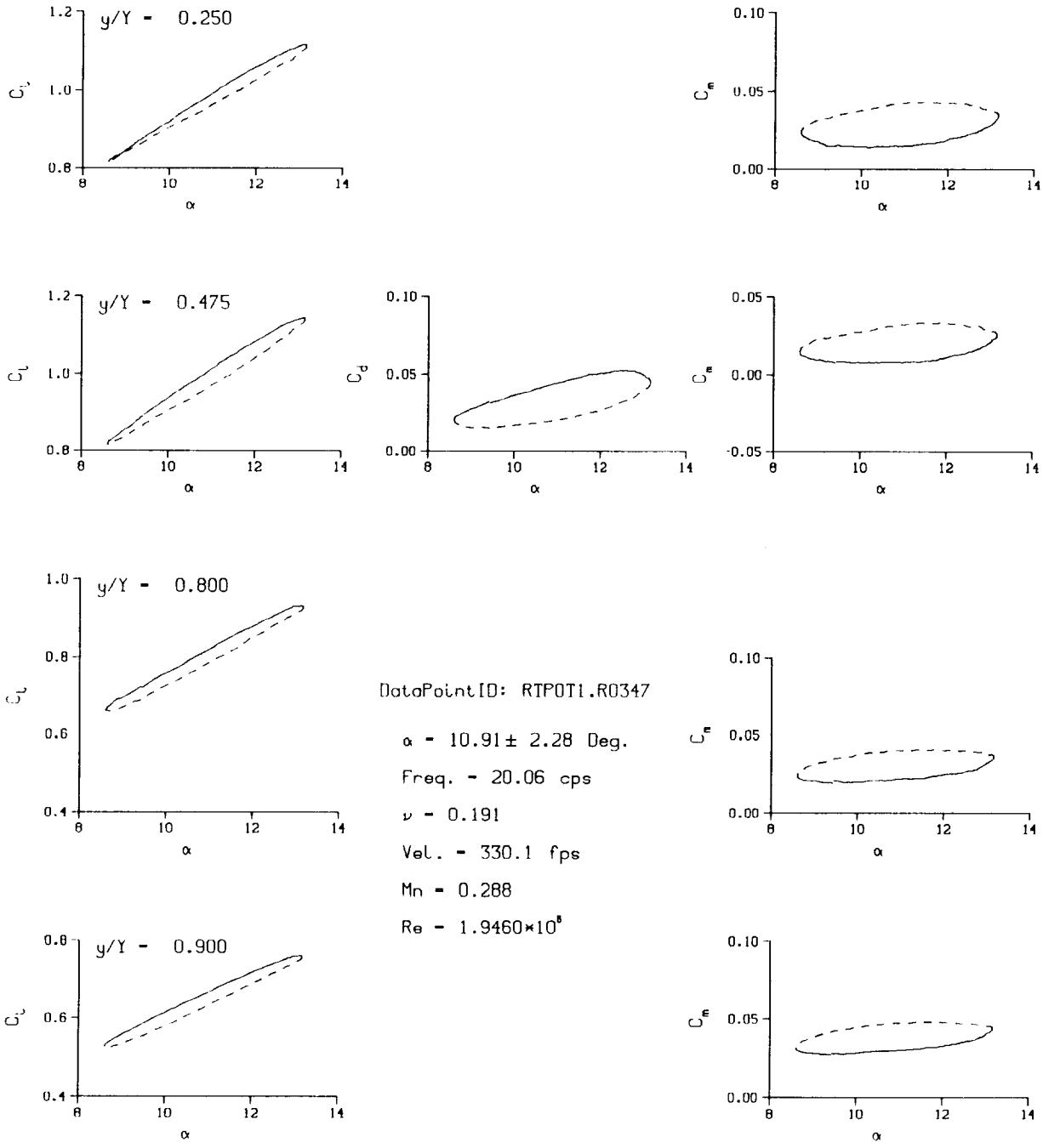

(d.1) v = 0.20; repeat

Figure 35. Continued.

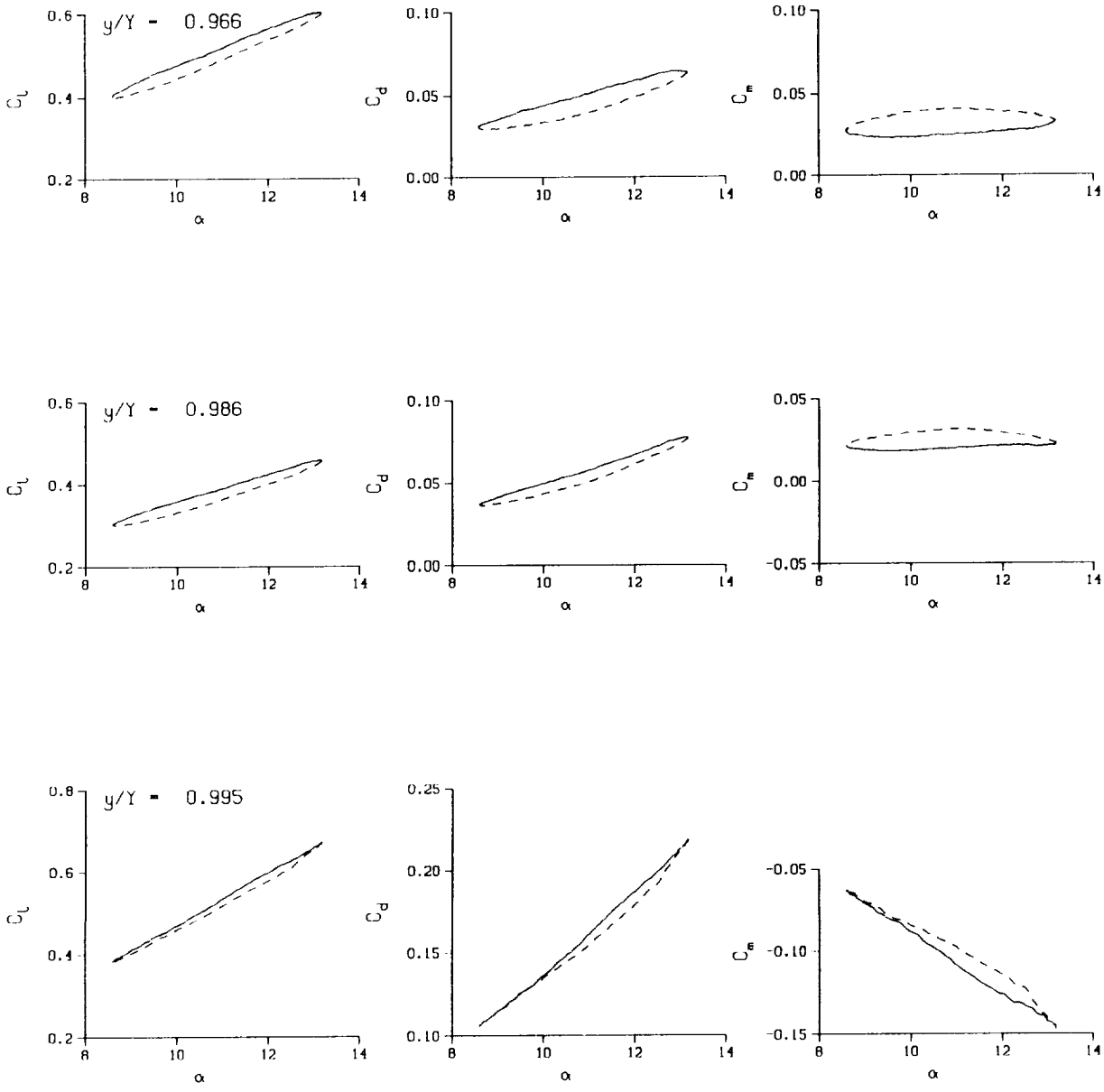

(d.1) v = 0.20; repeat. Concluded

Figure 35. Concluded.

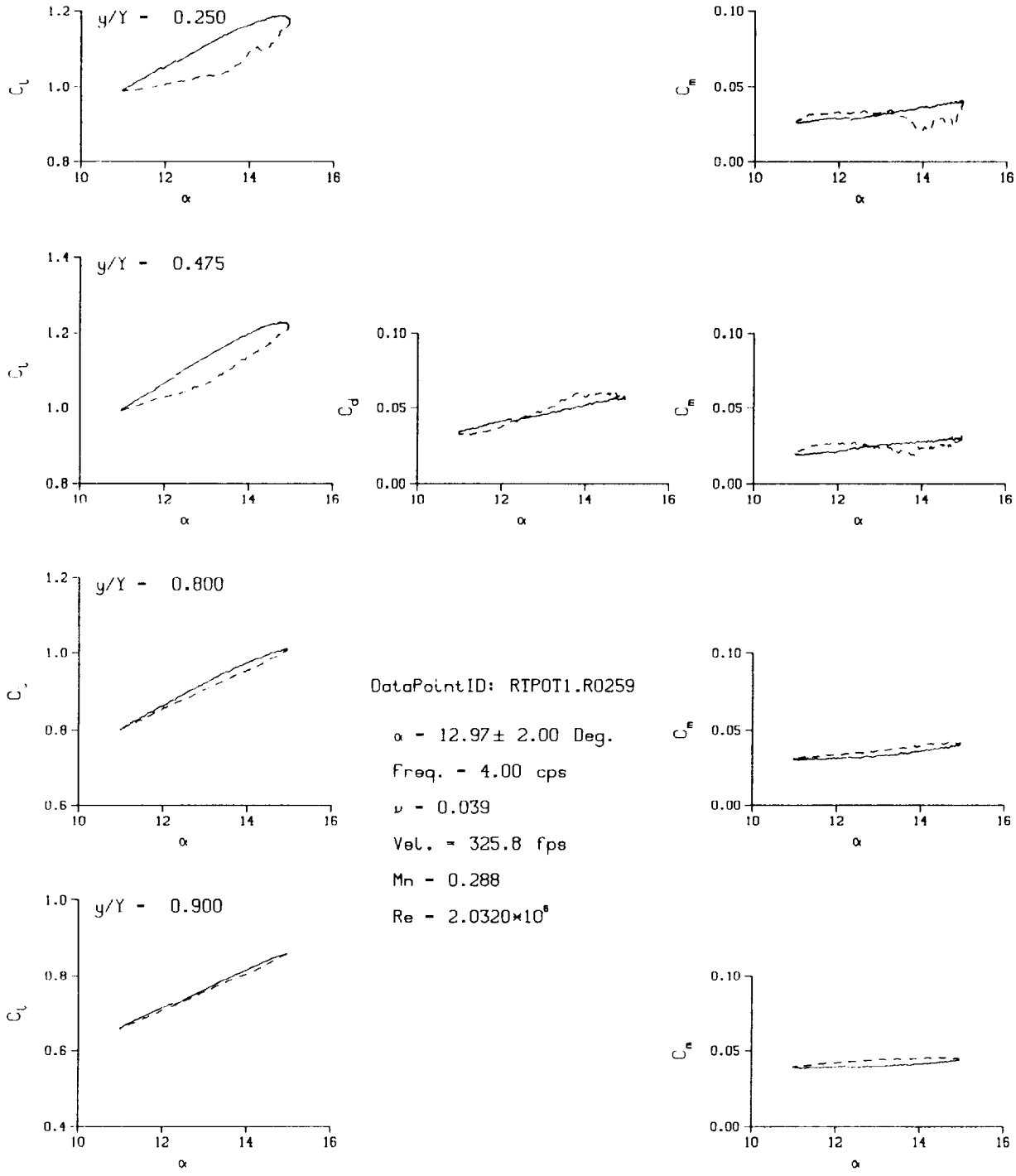

(a) v = 0.04

Figure 36. 3-D round tip pitch oscillation data; BL-trip; α = 13 ± 2 deg.

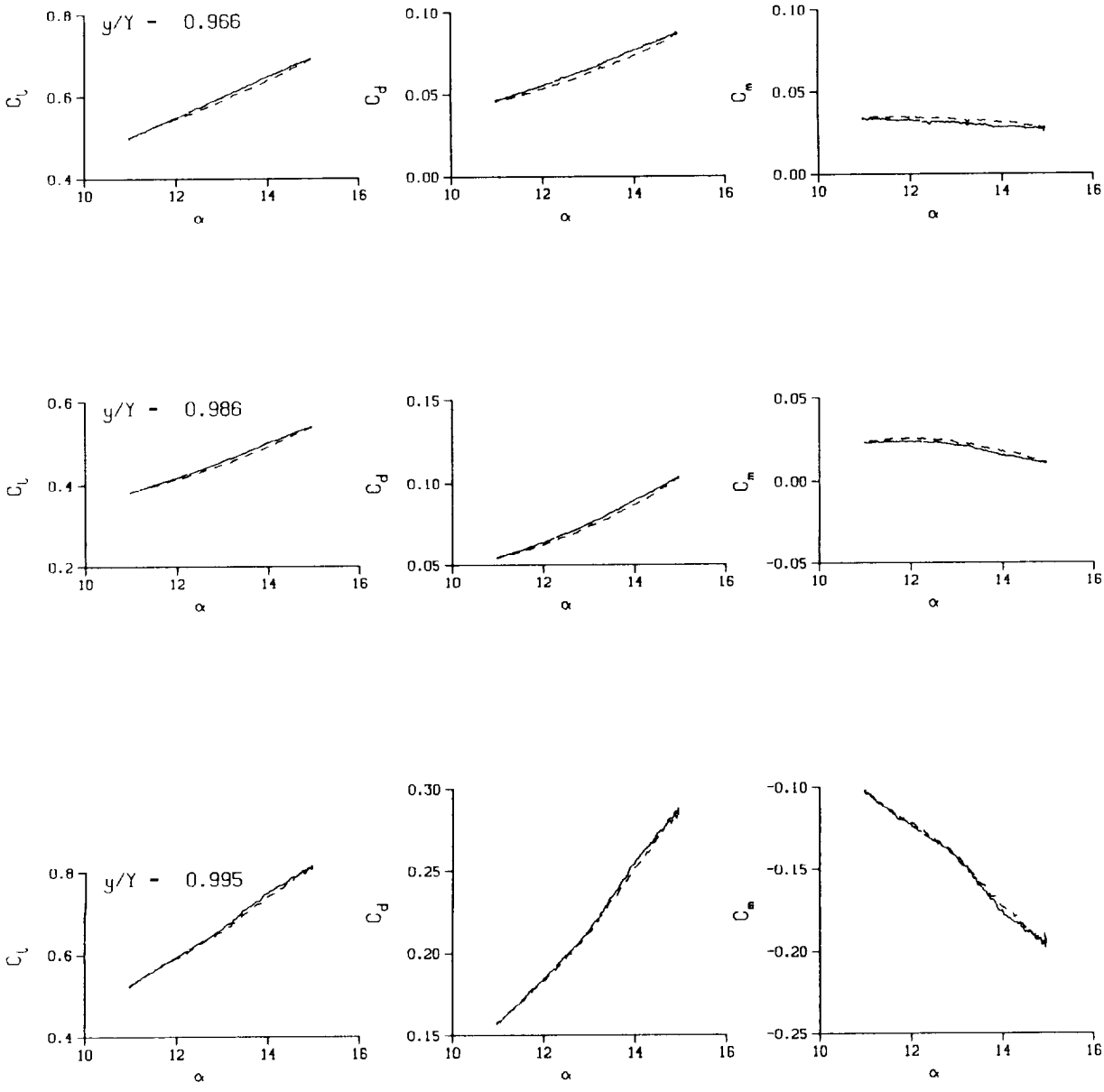

(a) v = 0.04. Concluded

Figure 36. Continued.

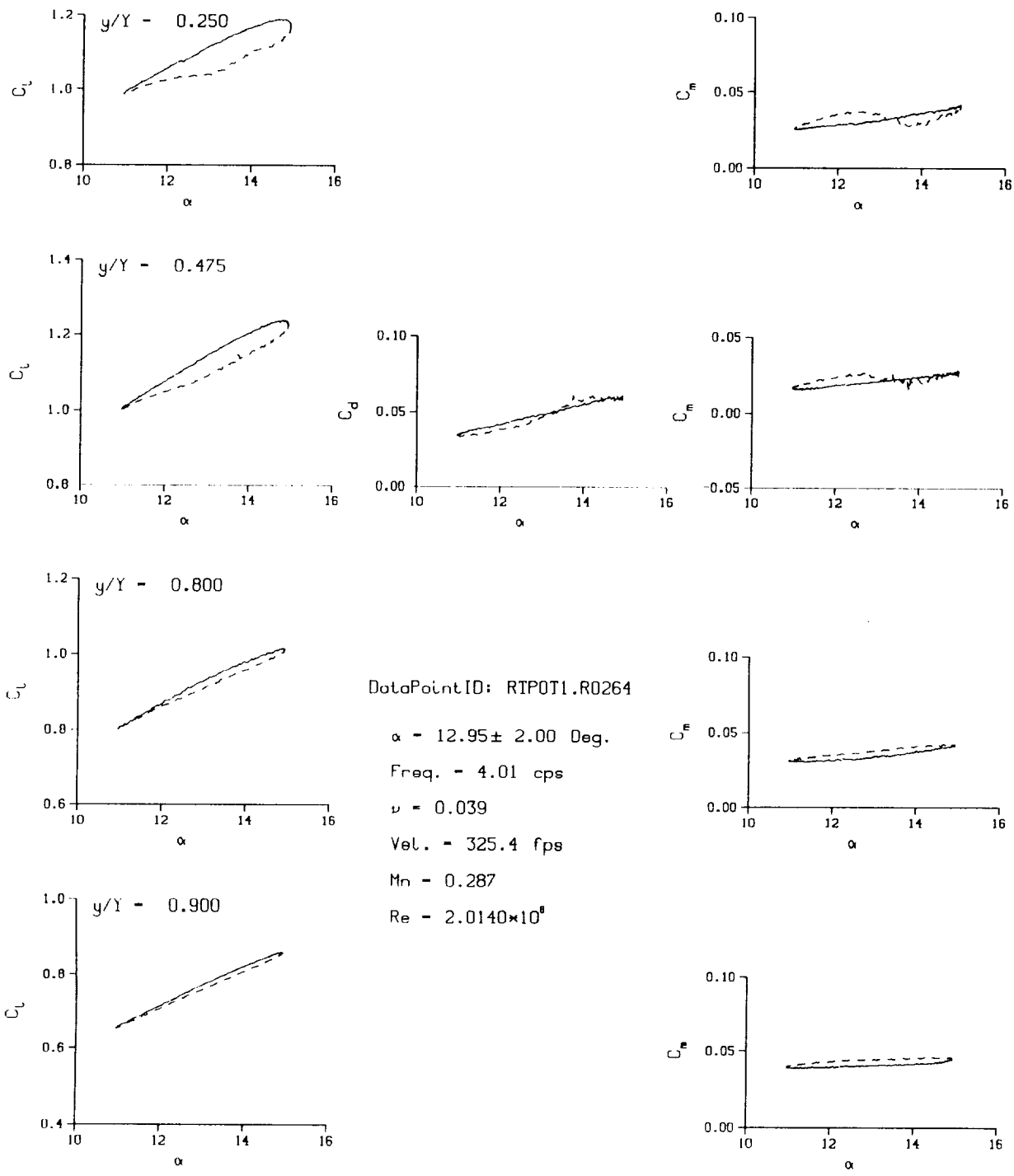

(a.1) v = 0.04; repeat

Figure 36. Continued.

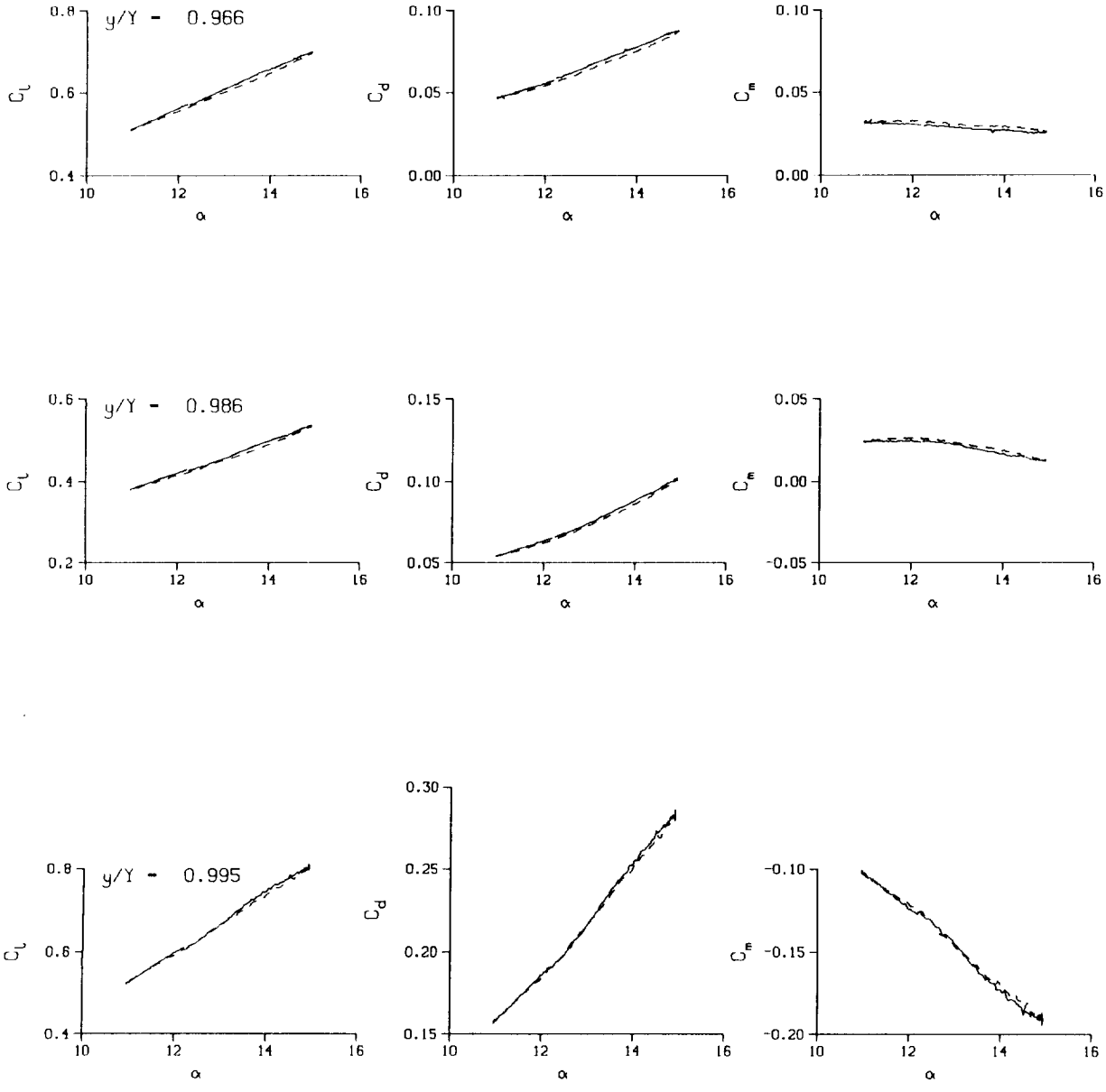

(a.1) v = 0.04; repeat. Concluded

Figure 36. Continued.

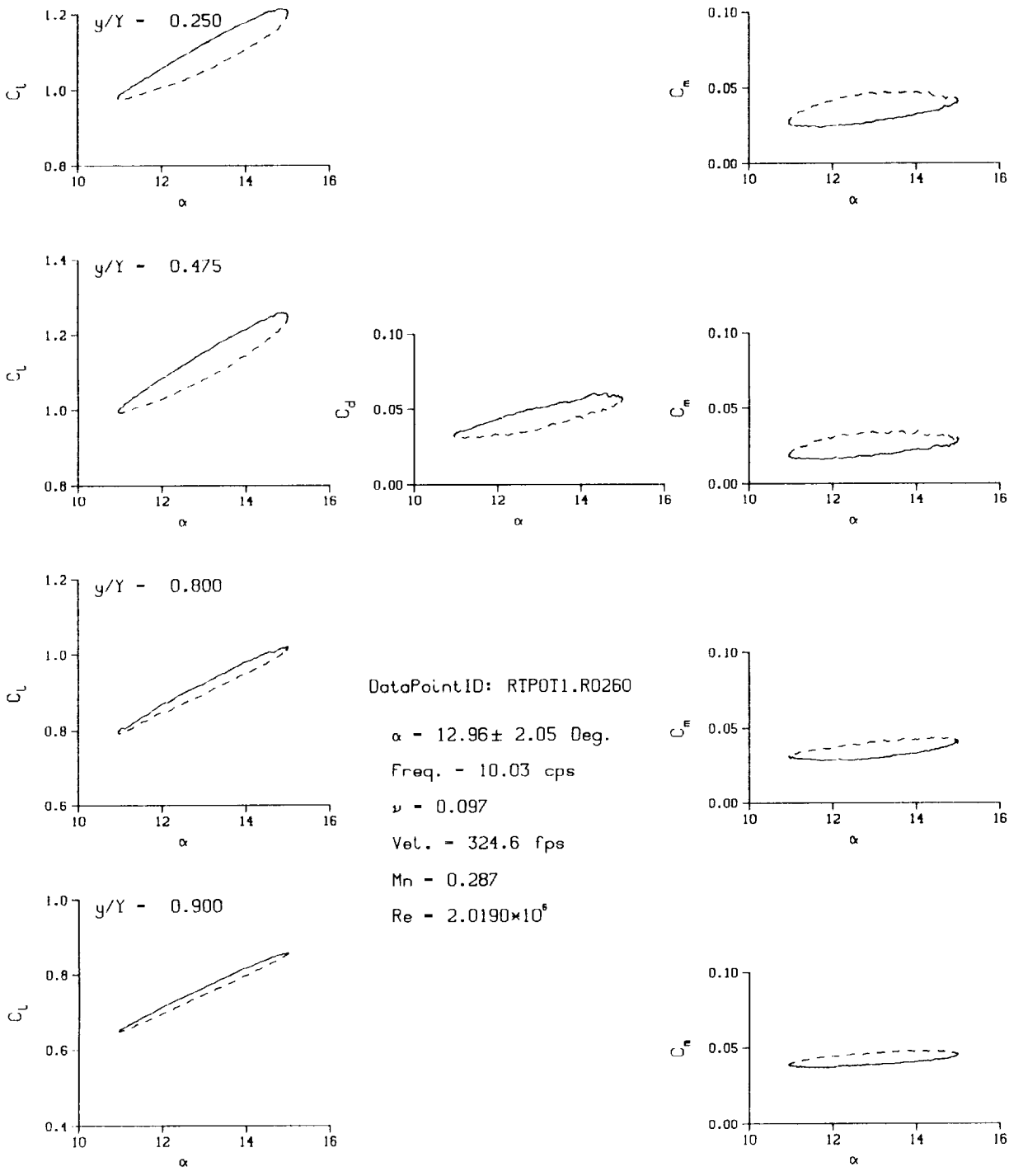

(b) v = 0.10

Figure 36. Continued.

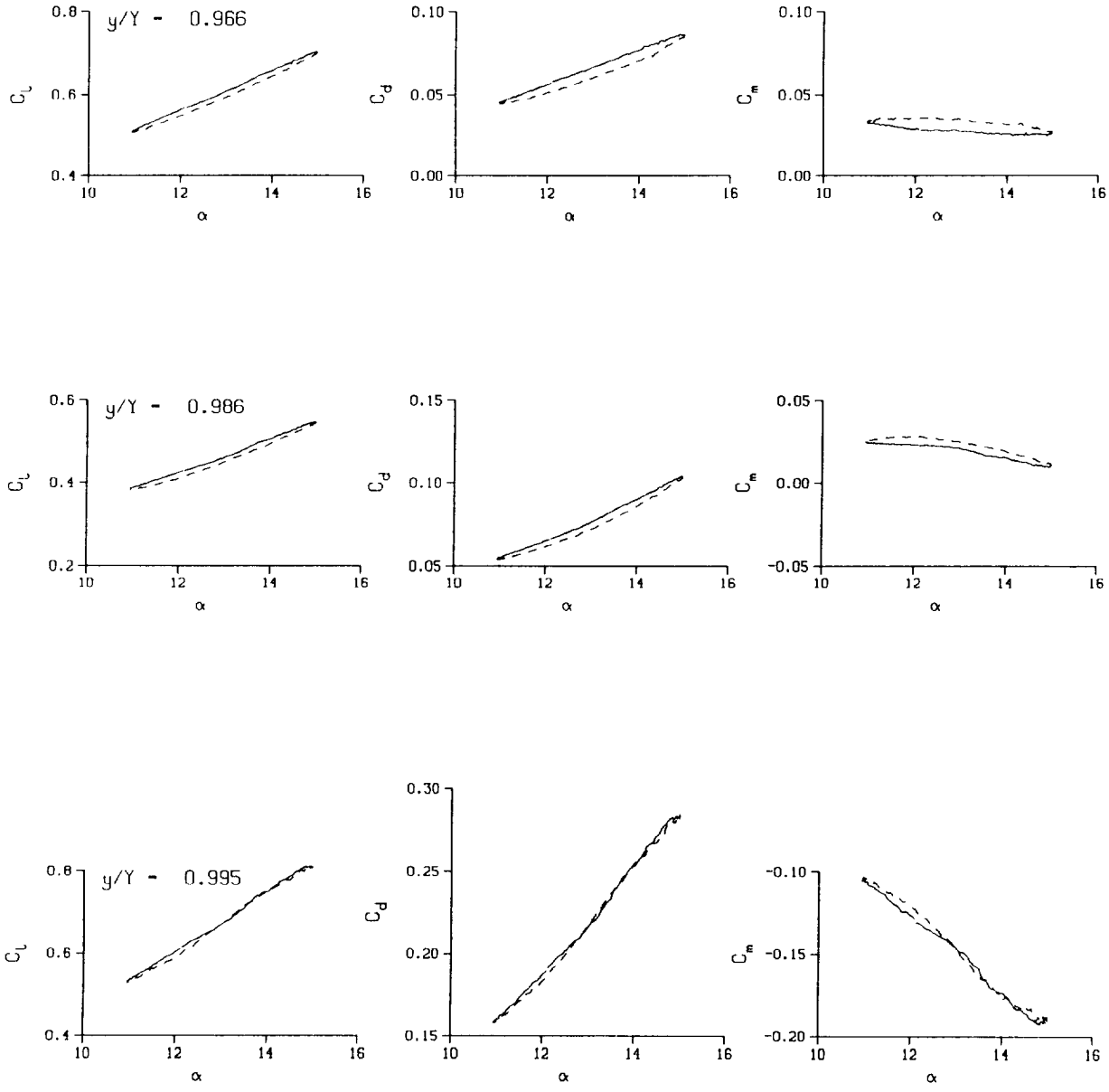

(b) v = 0.10. Concluded

Figure 36. Continued.

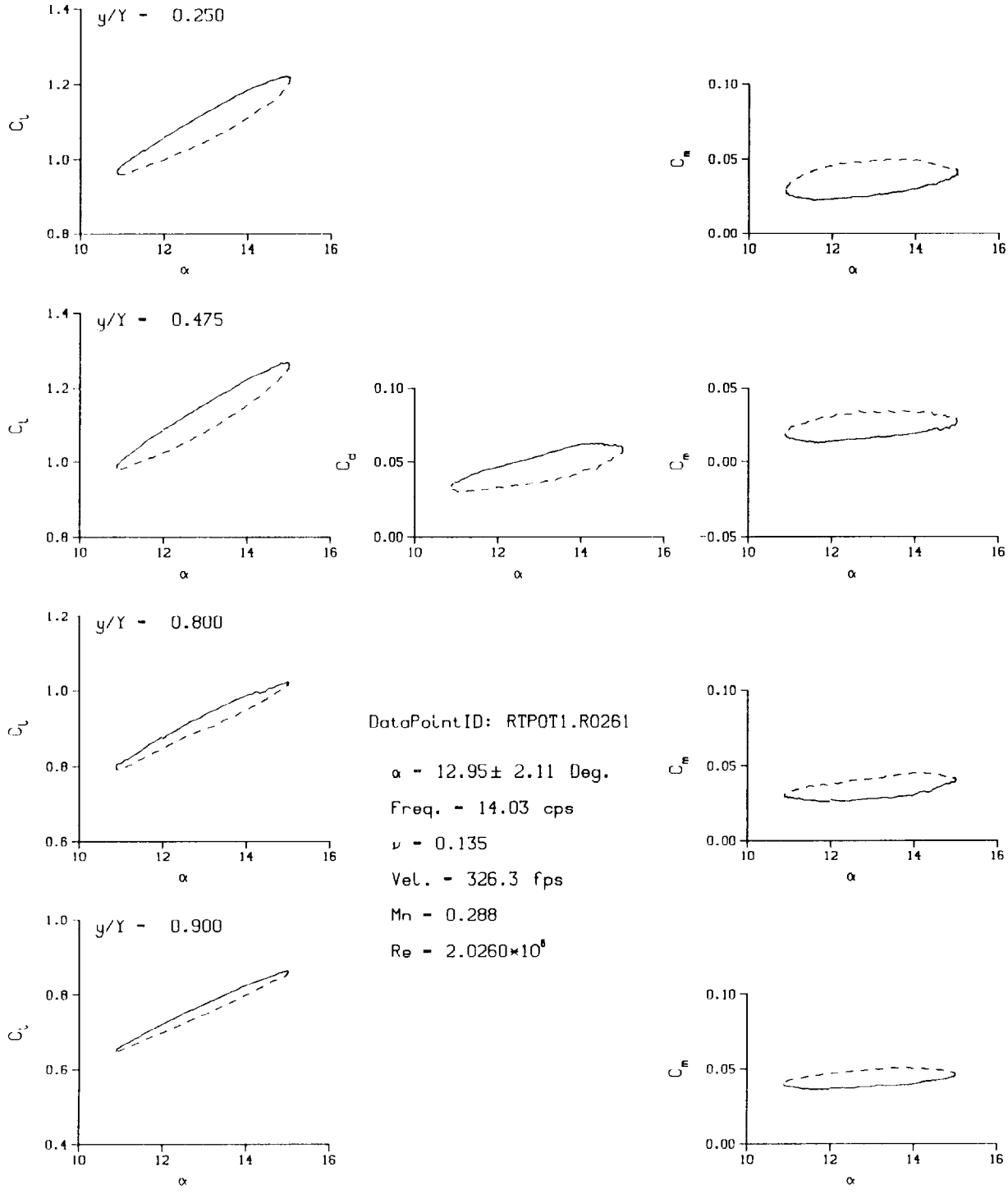

(c) v = 0.14

Figure 36. Continued.

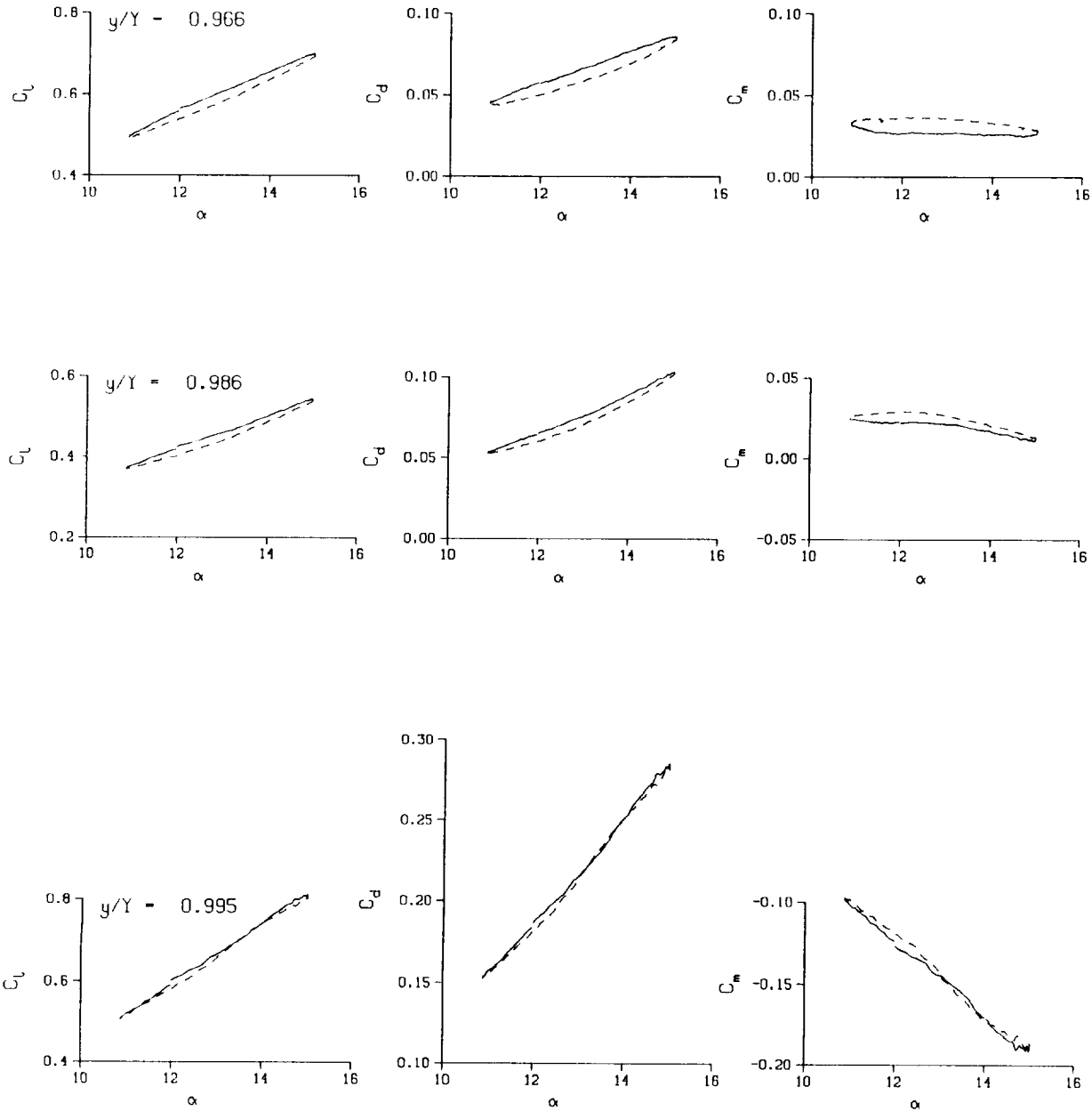

(c) v = 0.14. Concluded

Figure 36. Continued.

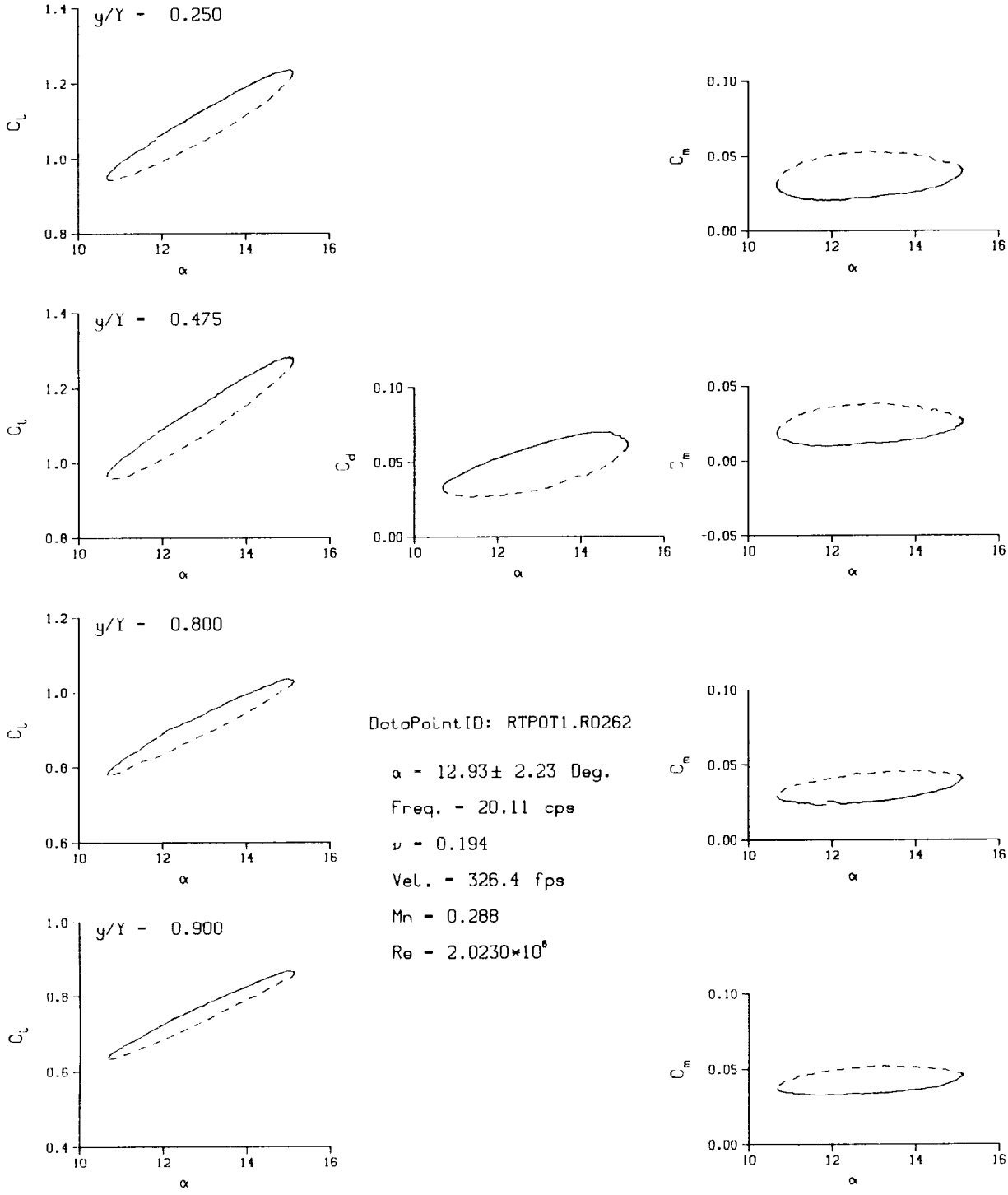

(d) v = 0.20

Figure 36. Continued.

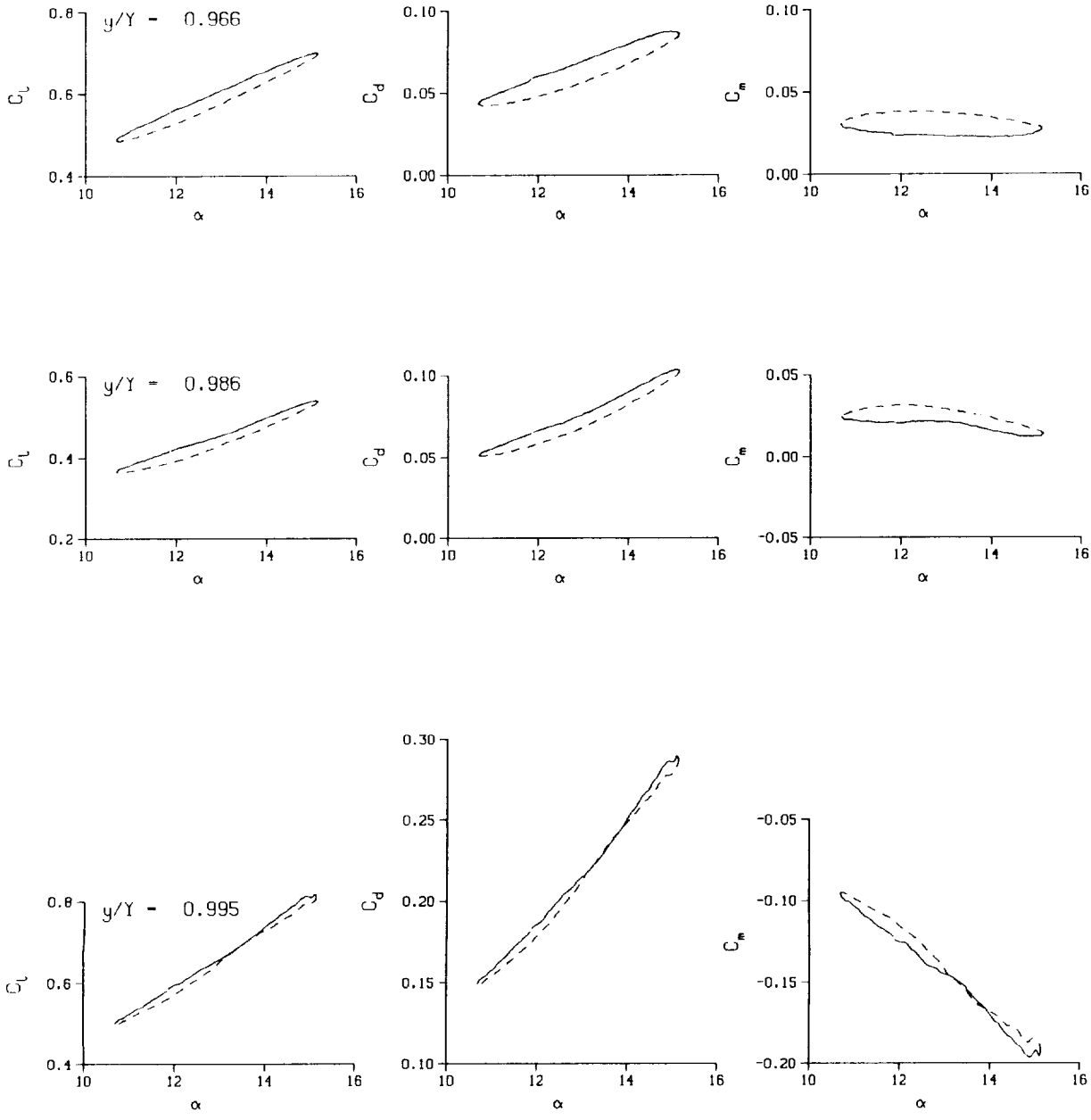

(d) v = 0.20. Concluded

Figure 36. Concluded.

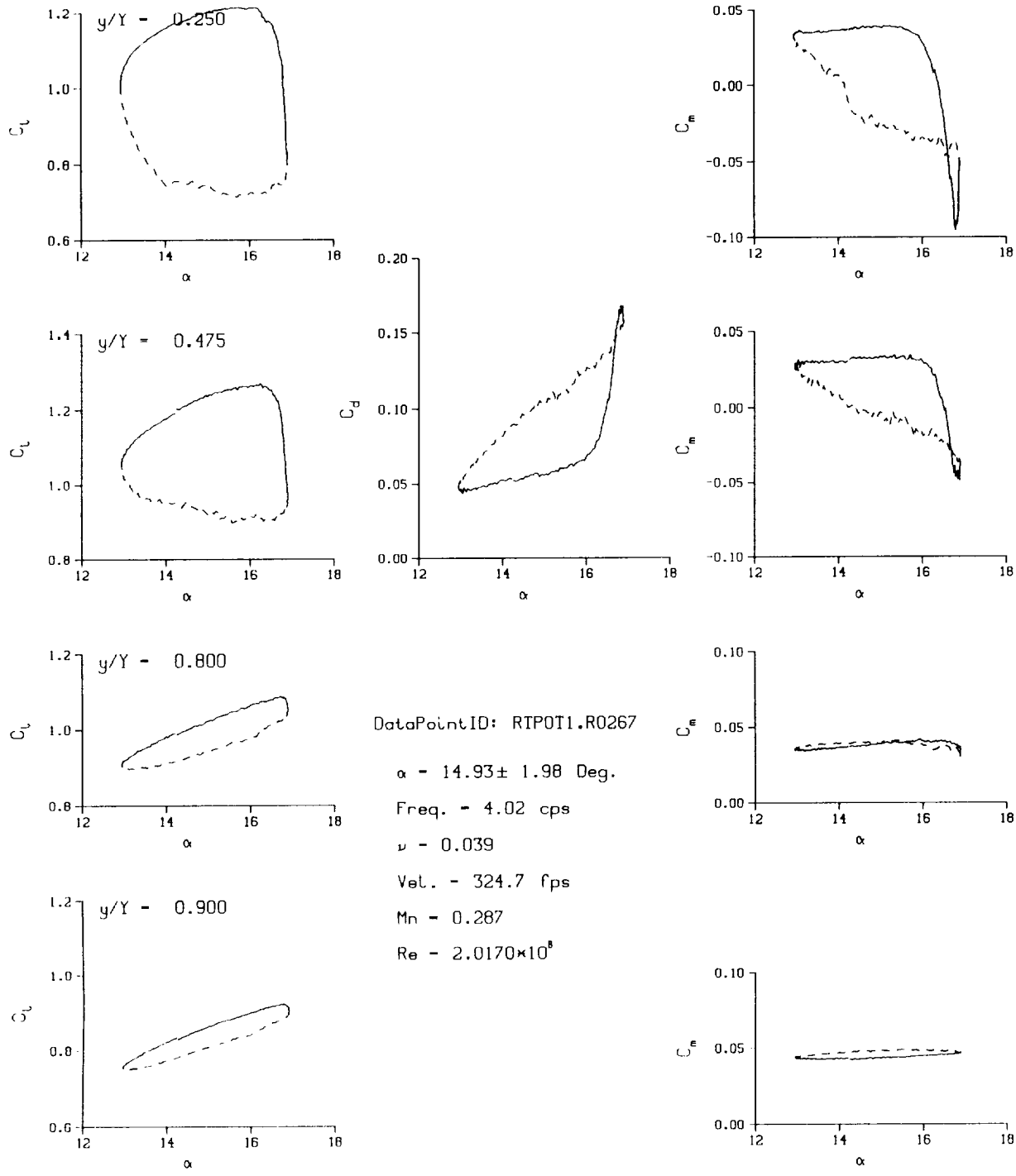

(a) ν = 0.04

Figure 37. 3-D round tip pitch oscillation data; BL-trip; α = 15 ± 2 deg.

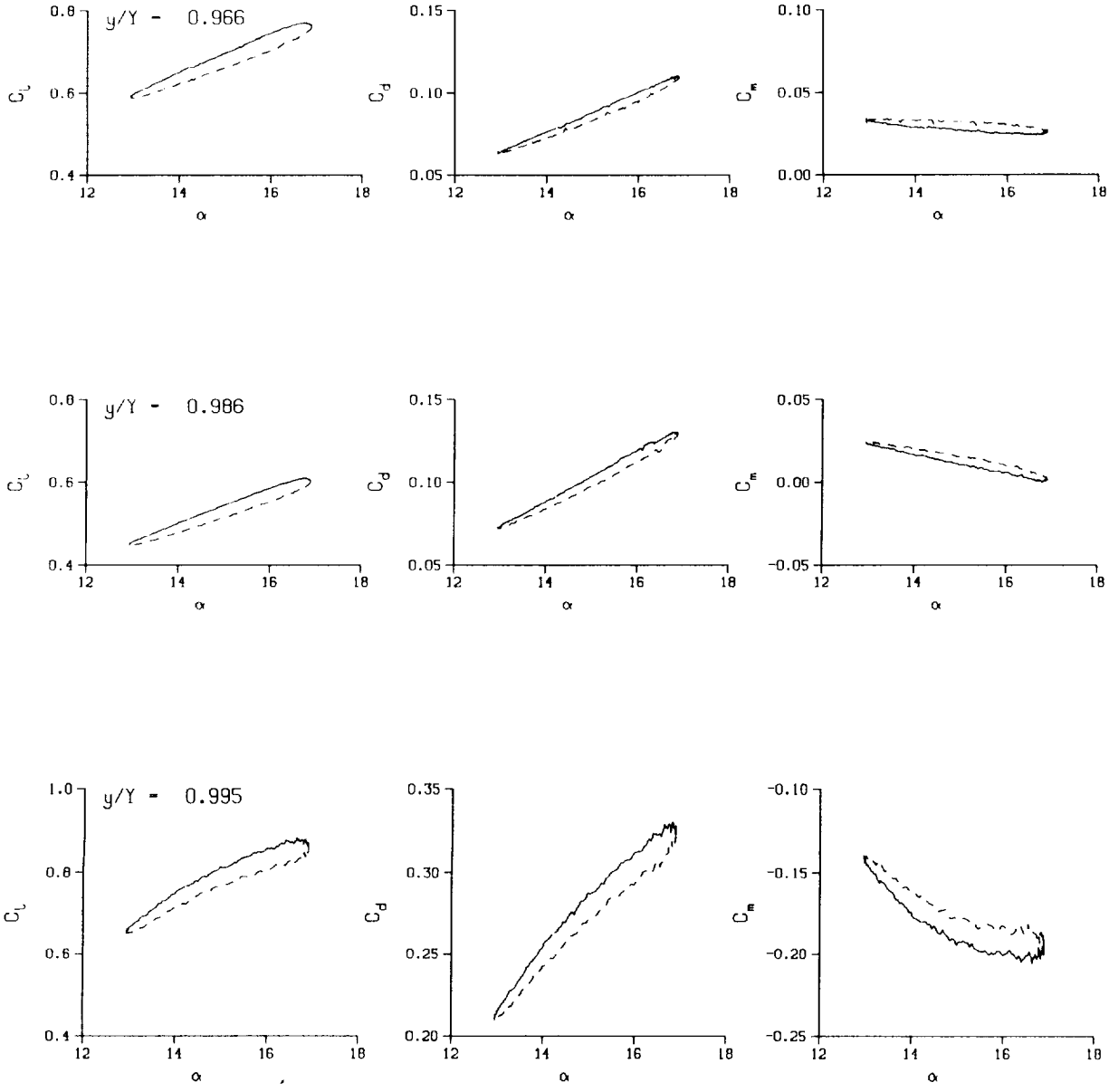

(a) v = 0.04. Concluded

Figure 37. Continued.

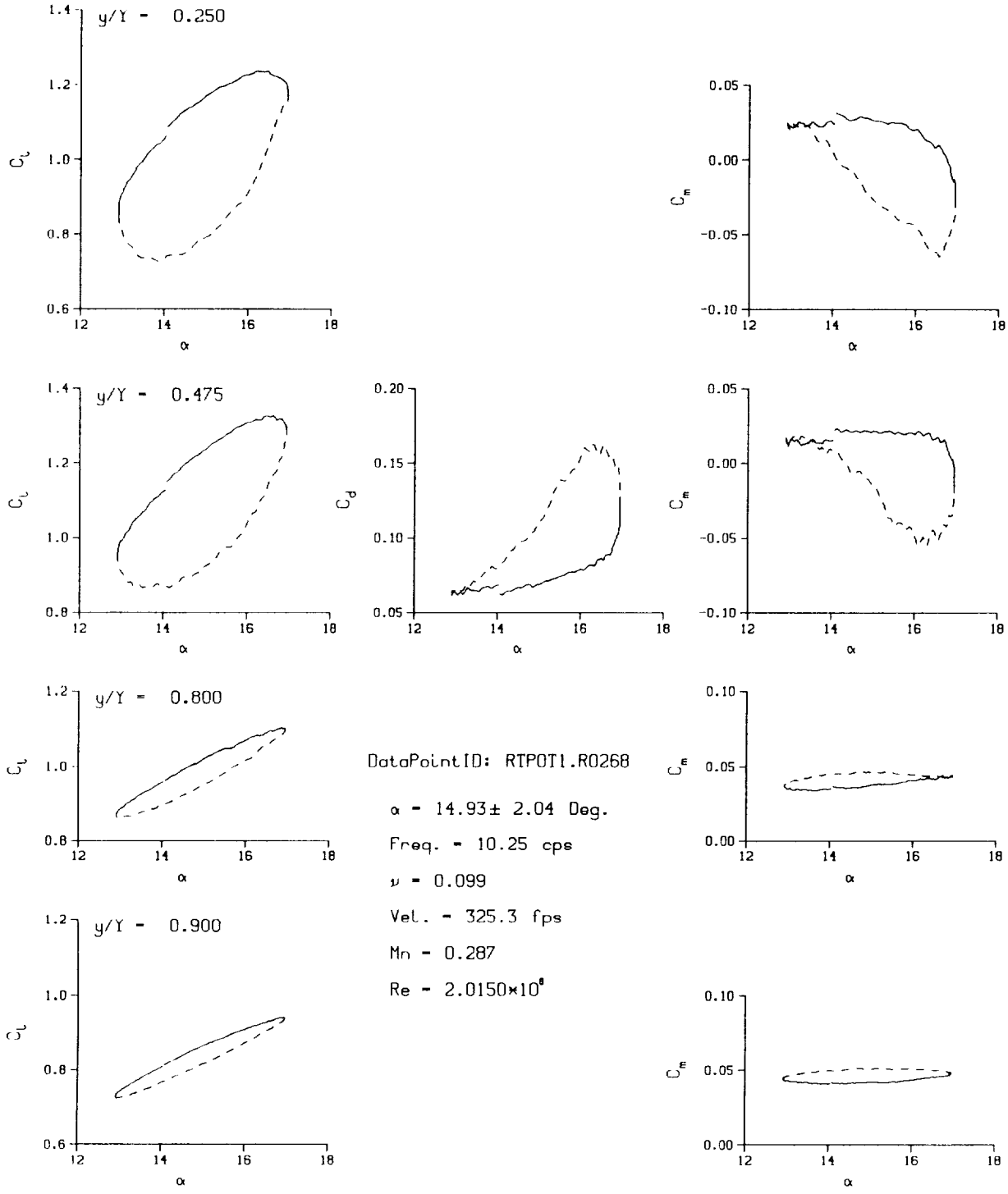

(b) ν = 0.10

Figure 37. Continued.

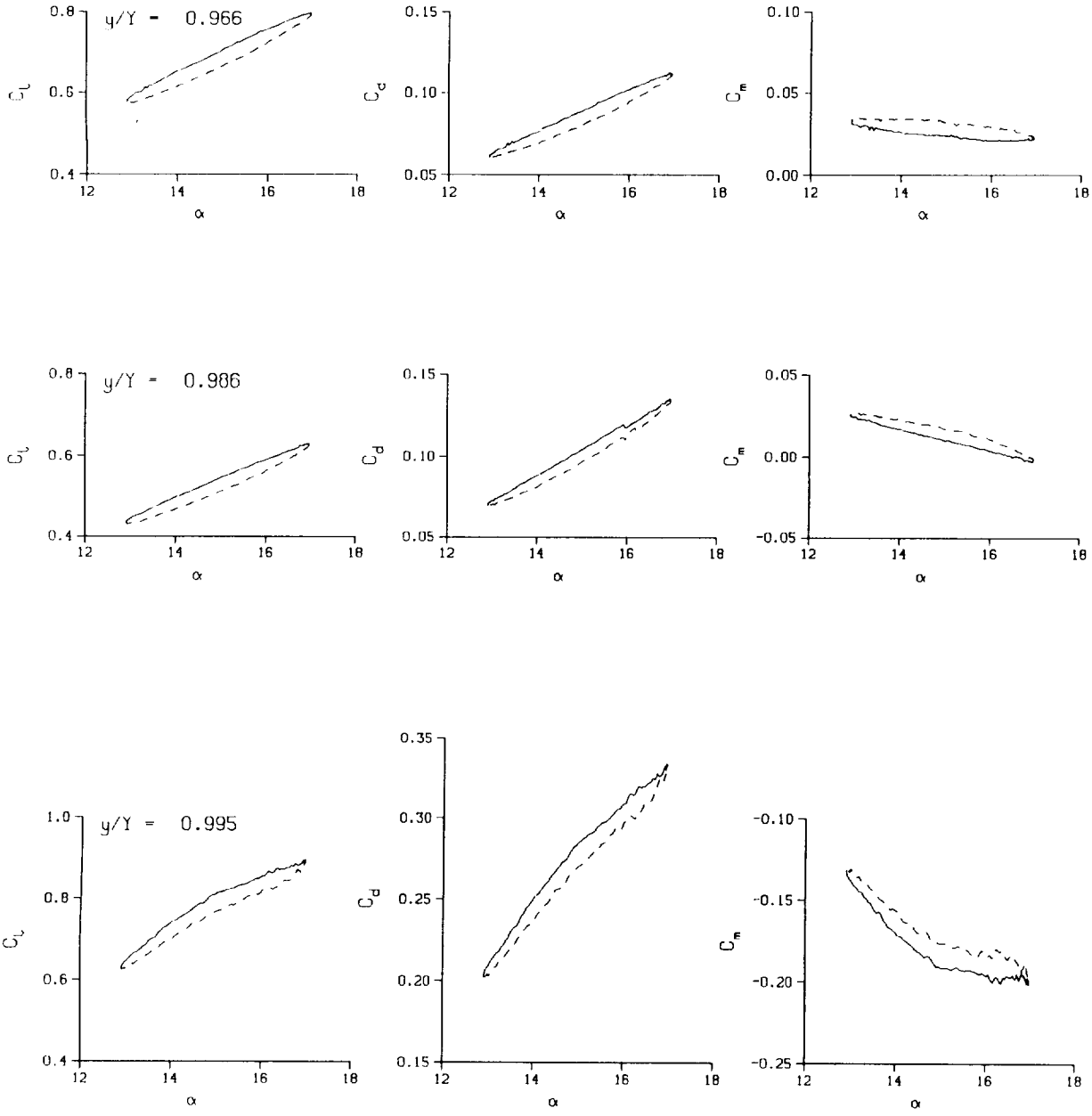

(b) v = 0.10. Concluded

Figure 37. Continued.

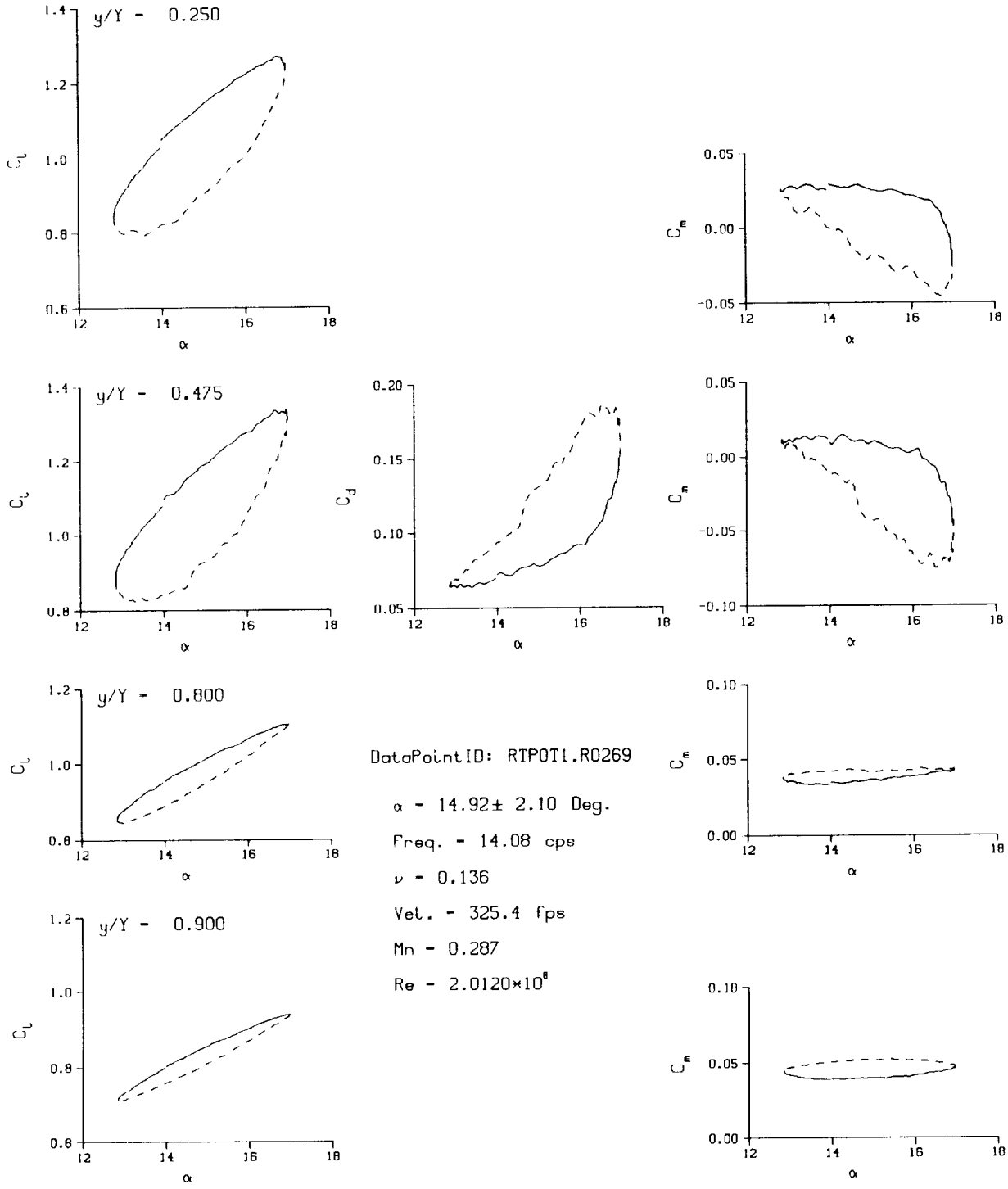

(c) v = 0.14

Figure 37. Continued.

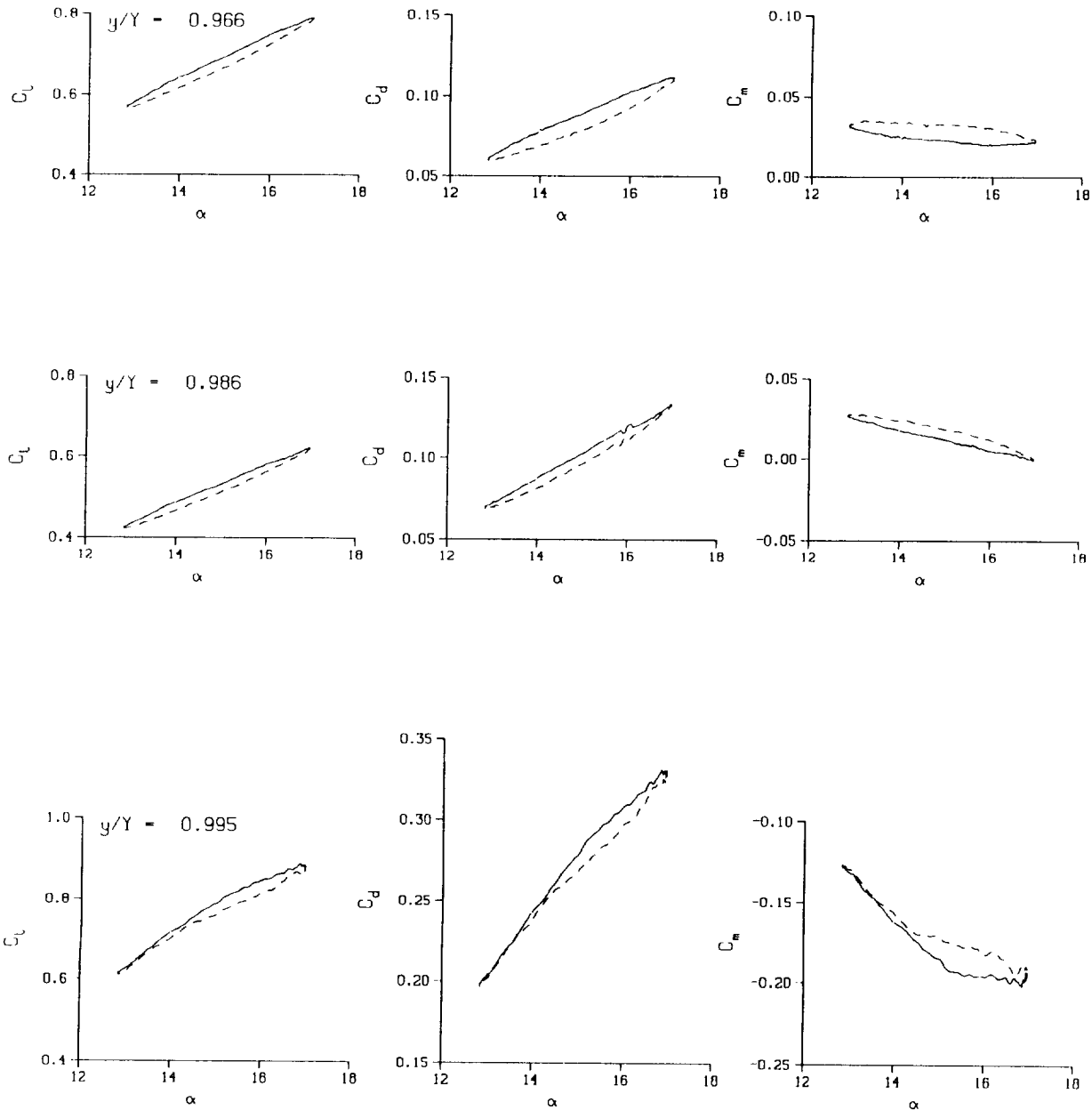

(c) v = 0.14. Concluded

Figure 37. Continued.

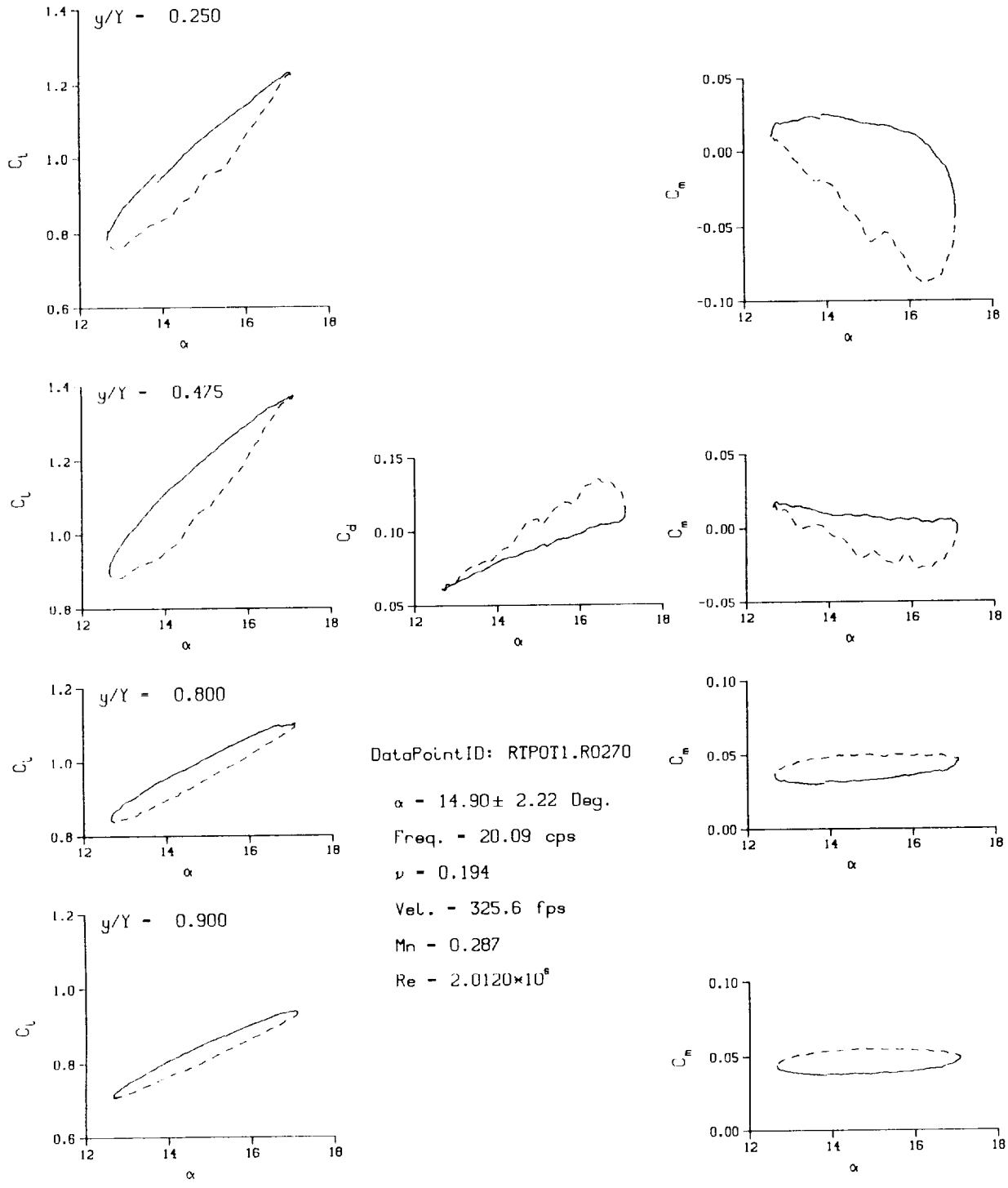

(d) v = 0.20

Figure 37. Continued.

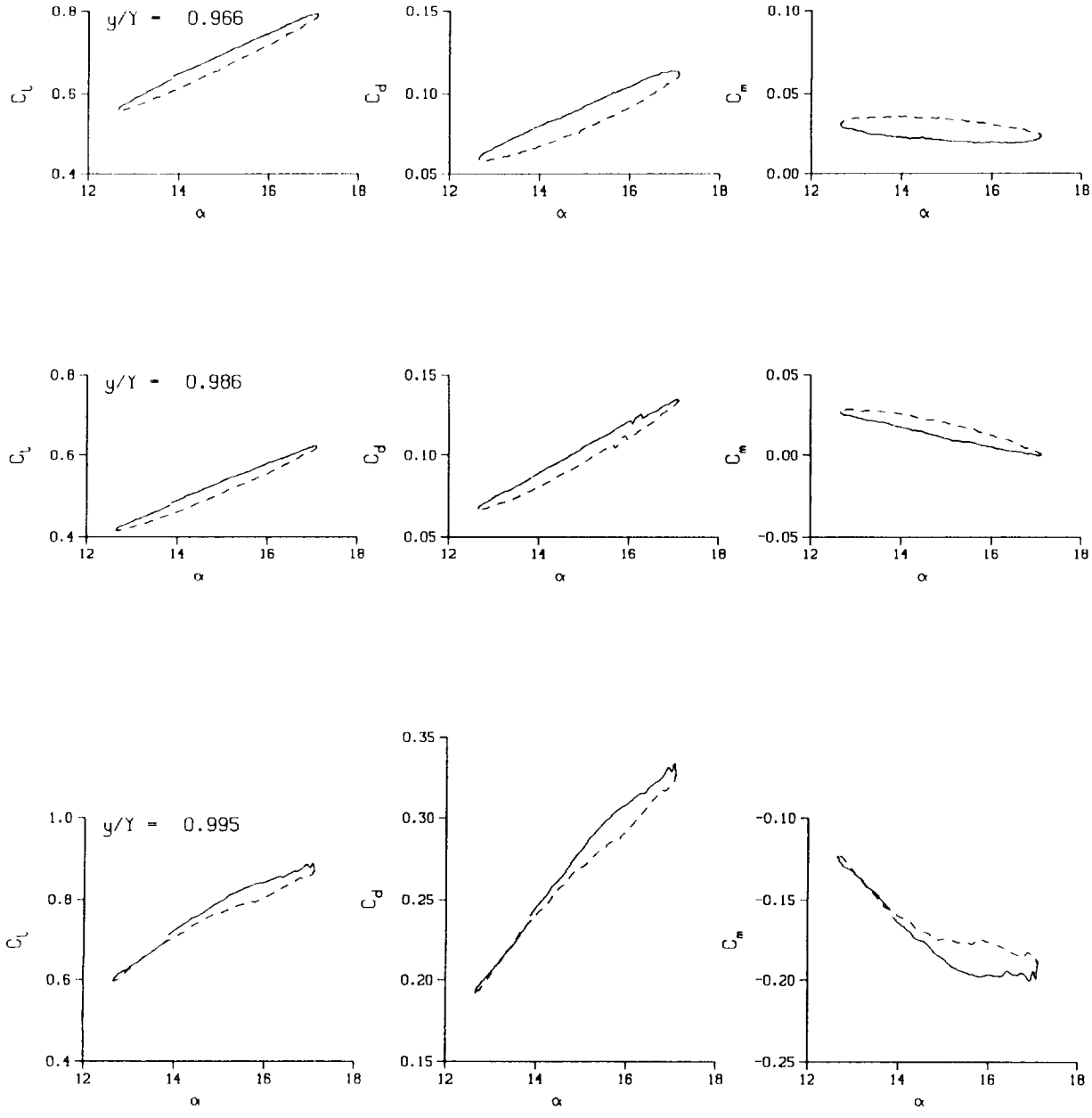

(d) v = 0.20. Concluded

Figure 37. Concluded.

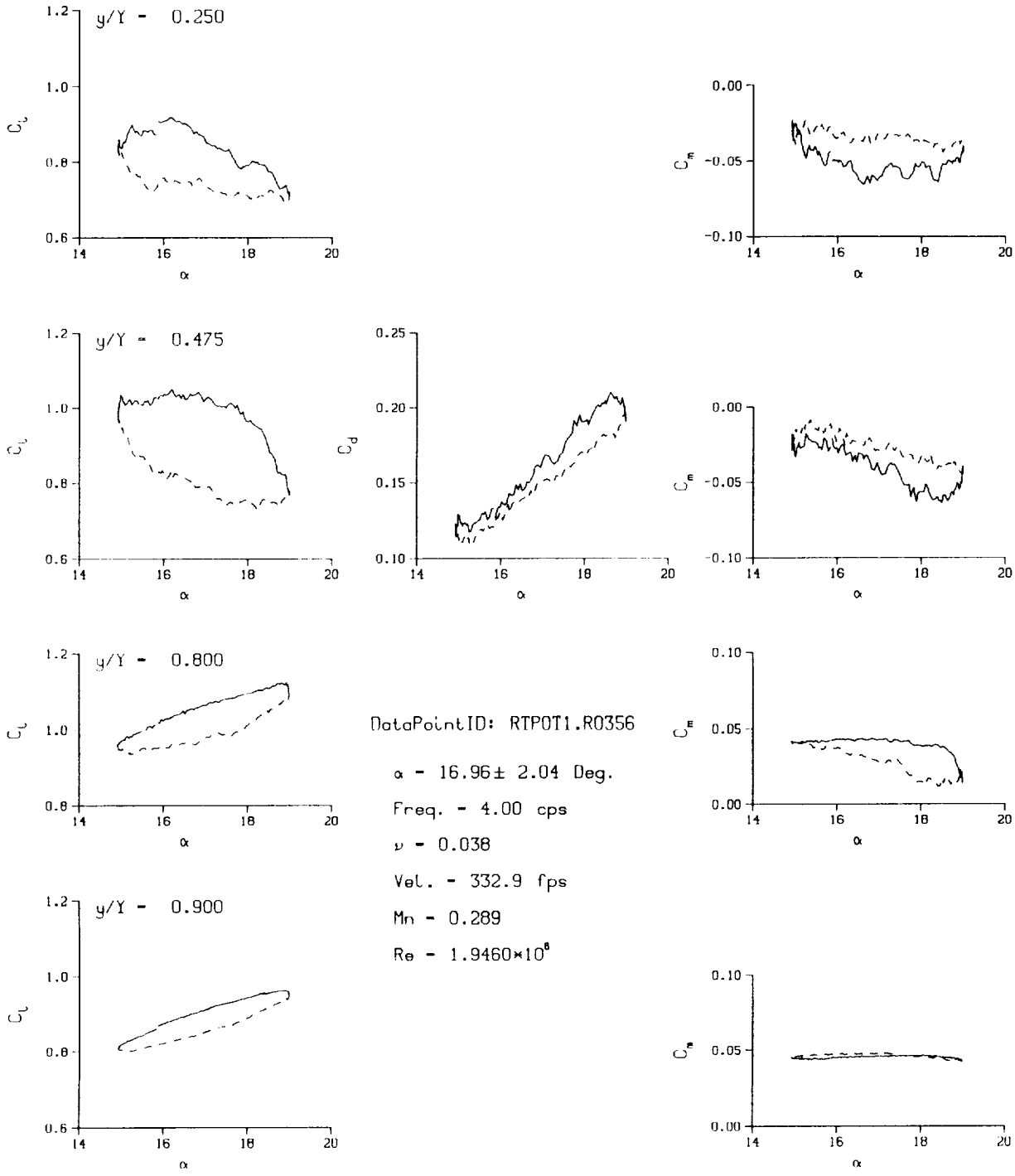

(a) ν = 0.04

Figure 38. 3-D round tip pitch oscillation data; BL-trip; α = 17 ± 2 deg.

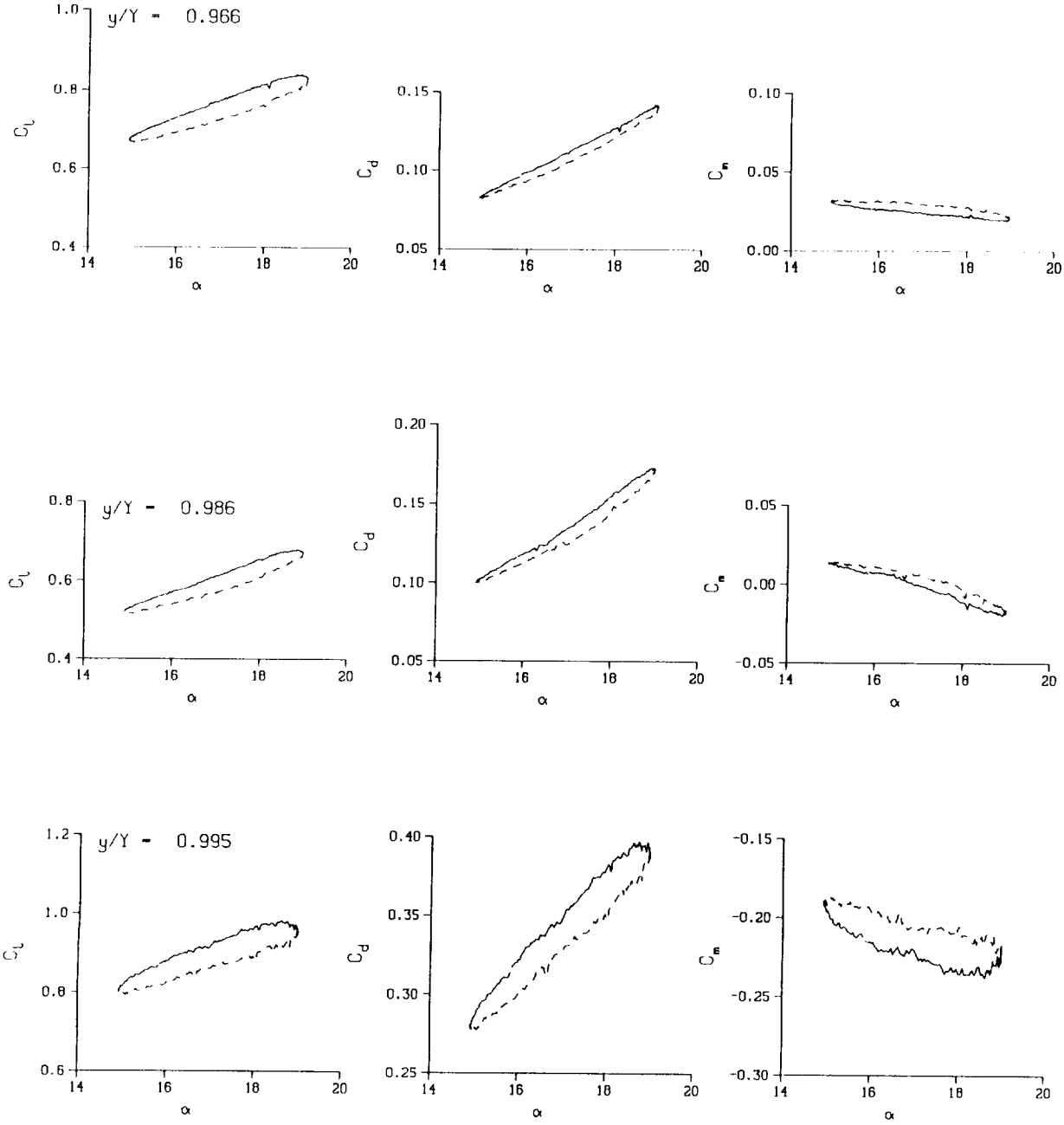

(a) v = 0.04. Concluded

Figure 38. Continued.

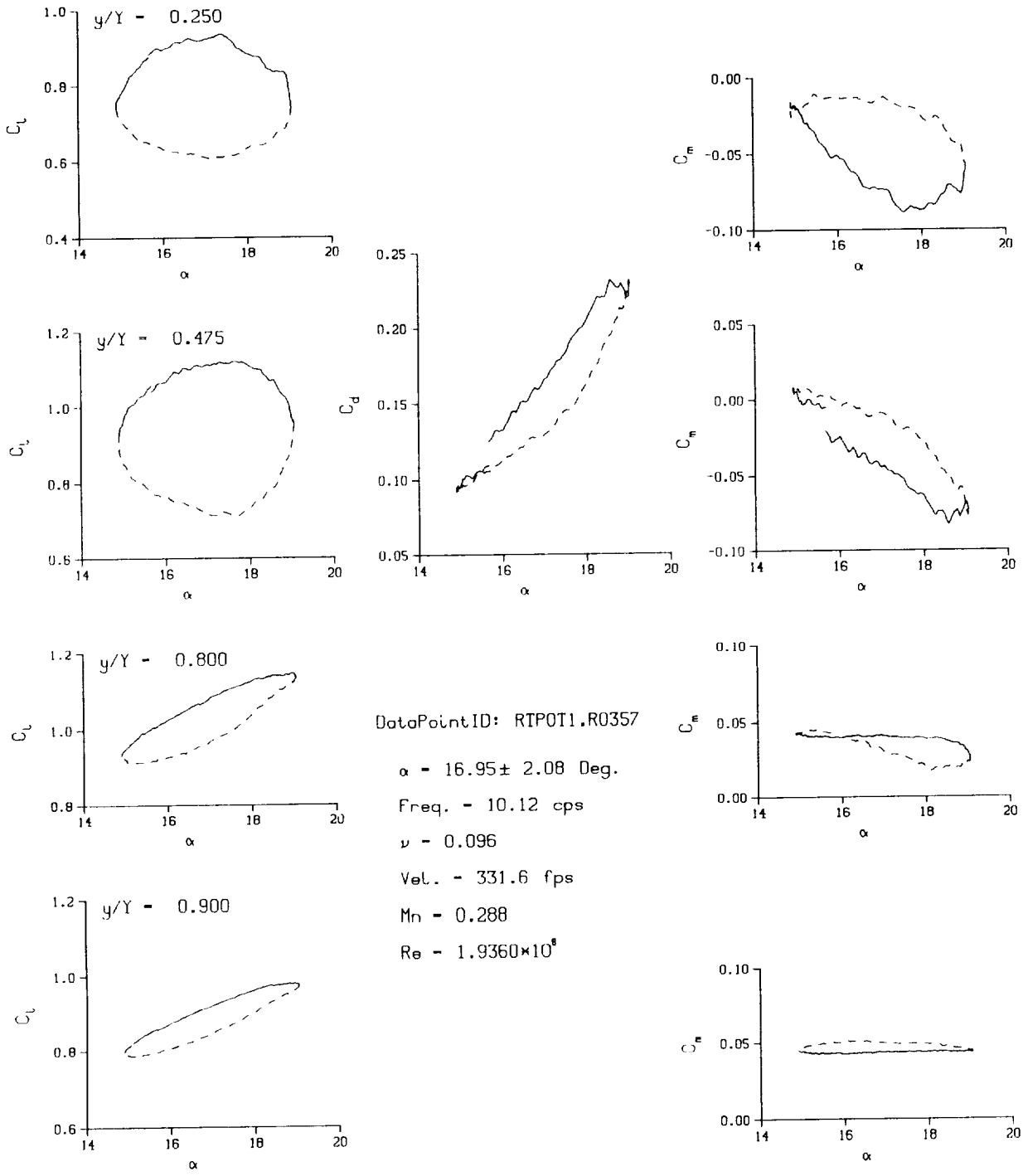

(b) v = 0.10

Figure 38. Continued.

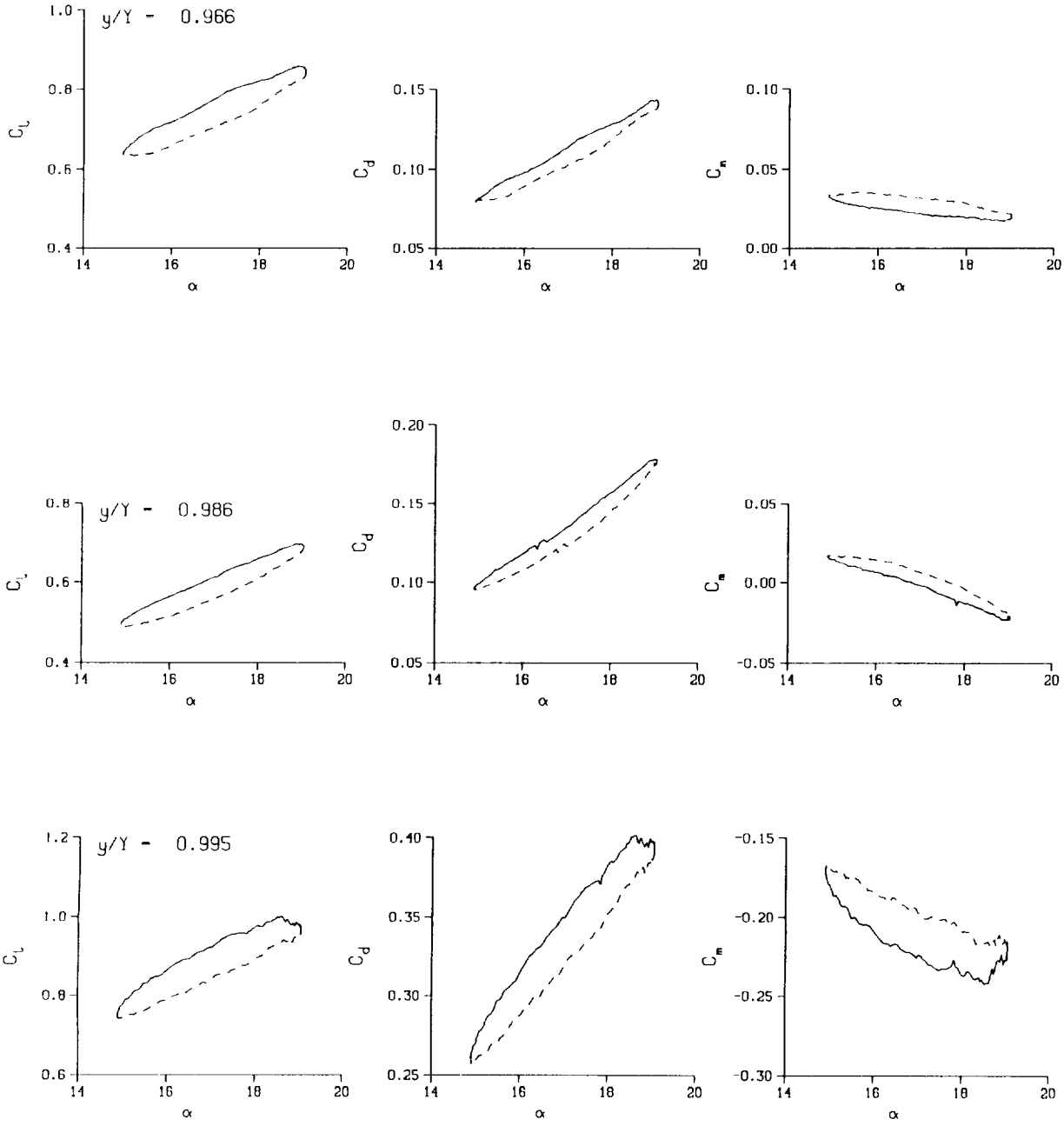

(b) v = 0.10. Concluded

Figure 38. Continued.

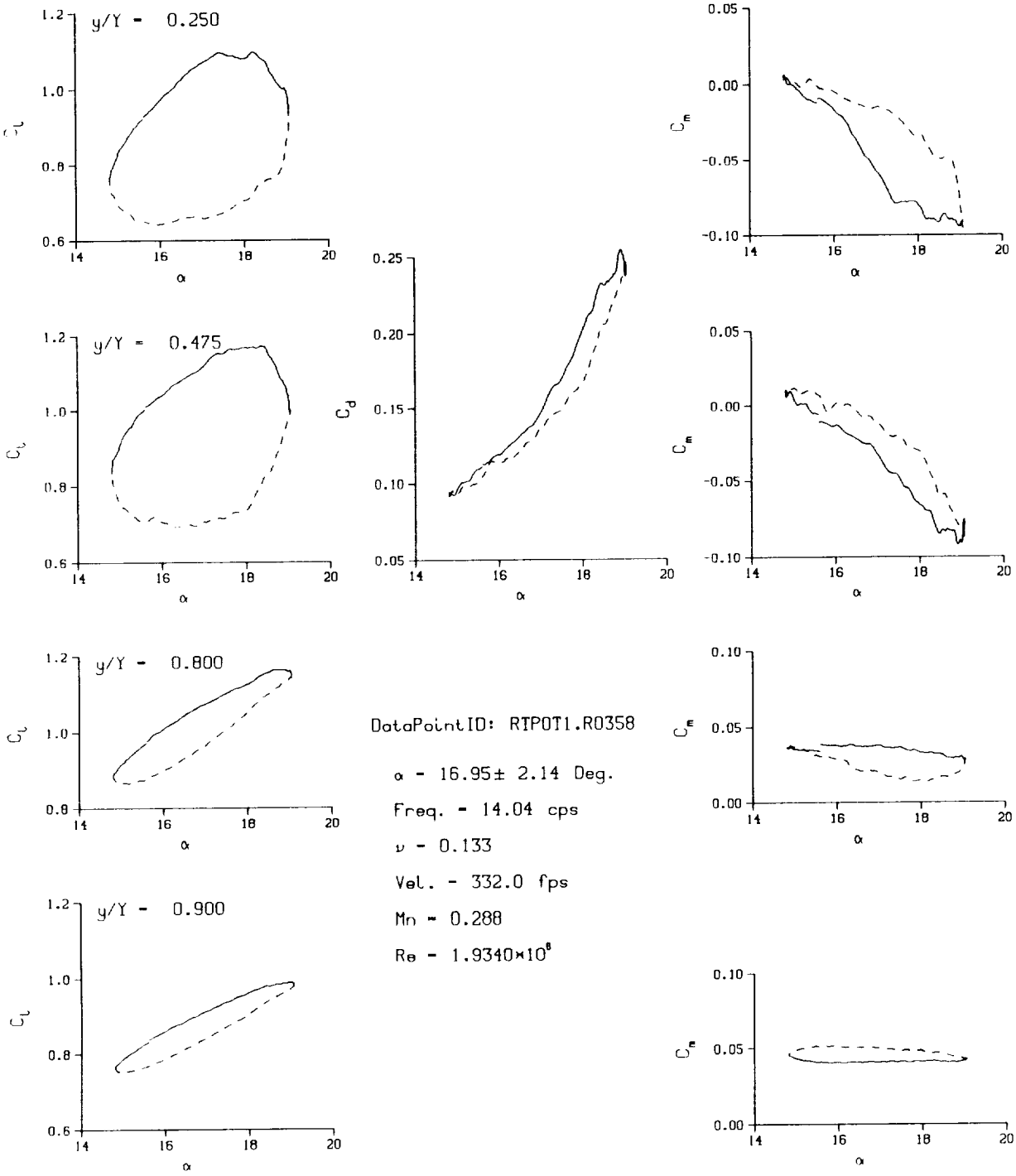

(c) v = 0.14

Figure 38. Continued.

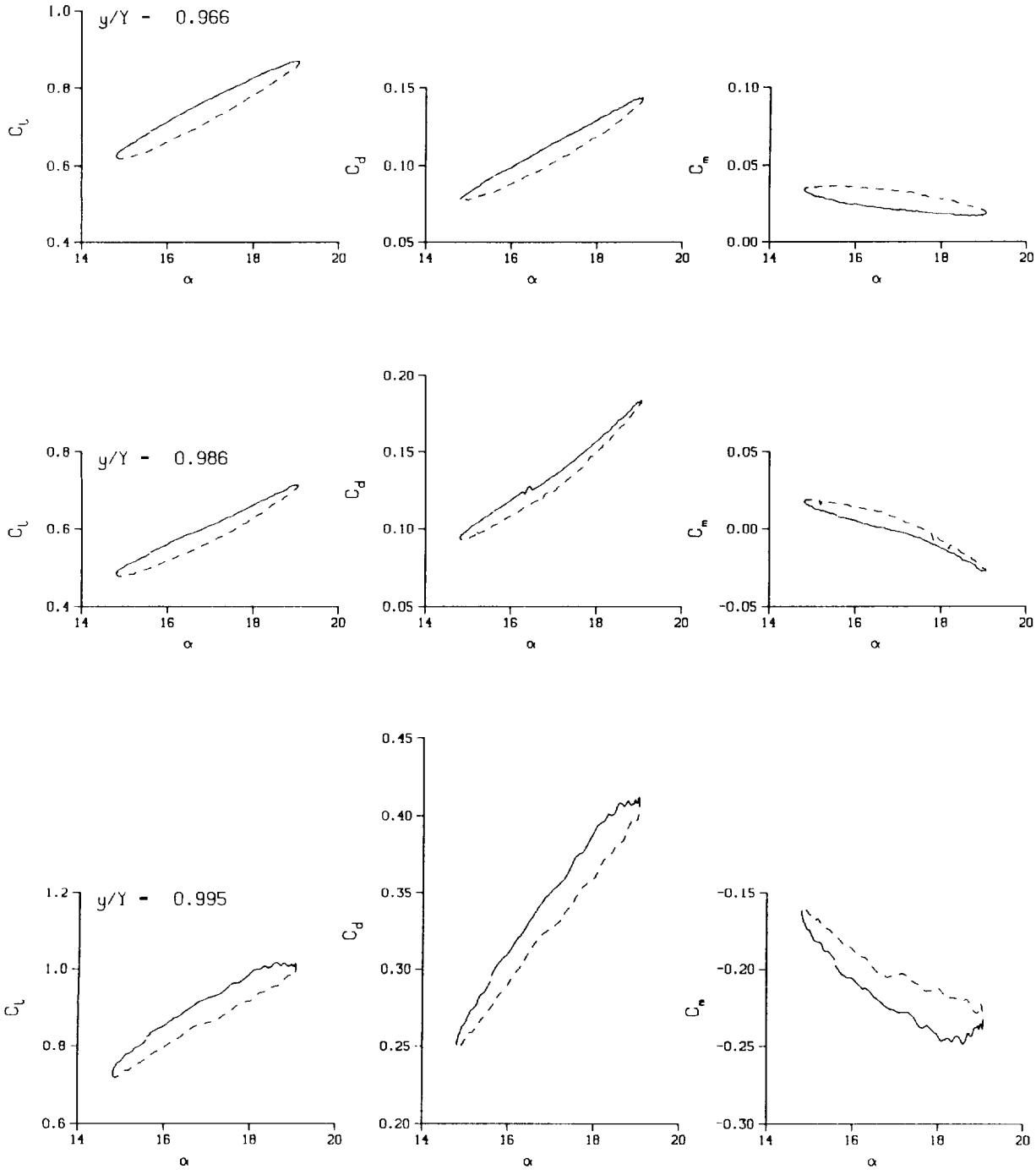

(c) v = 0.14. Concluded

Figure 38. Continued.

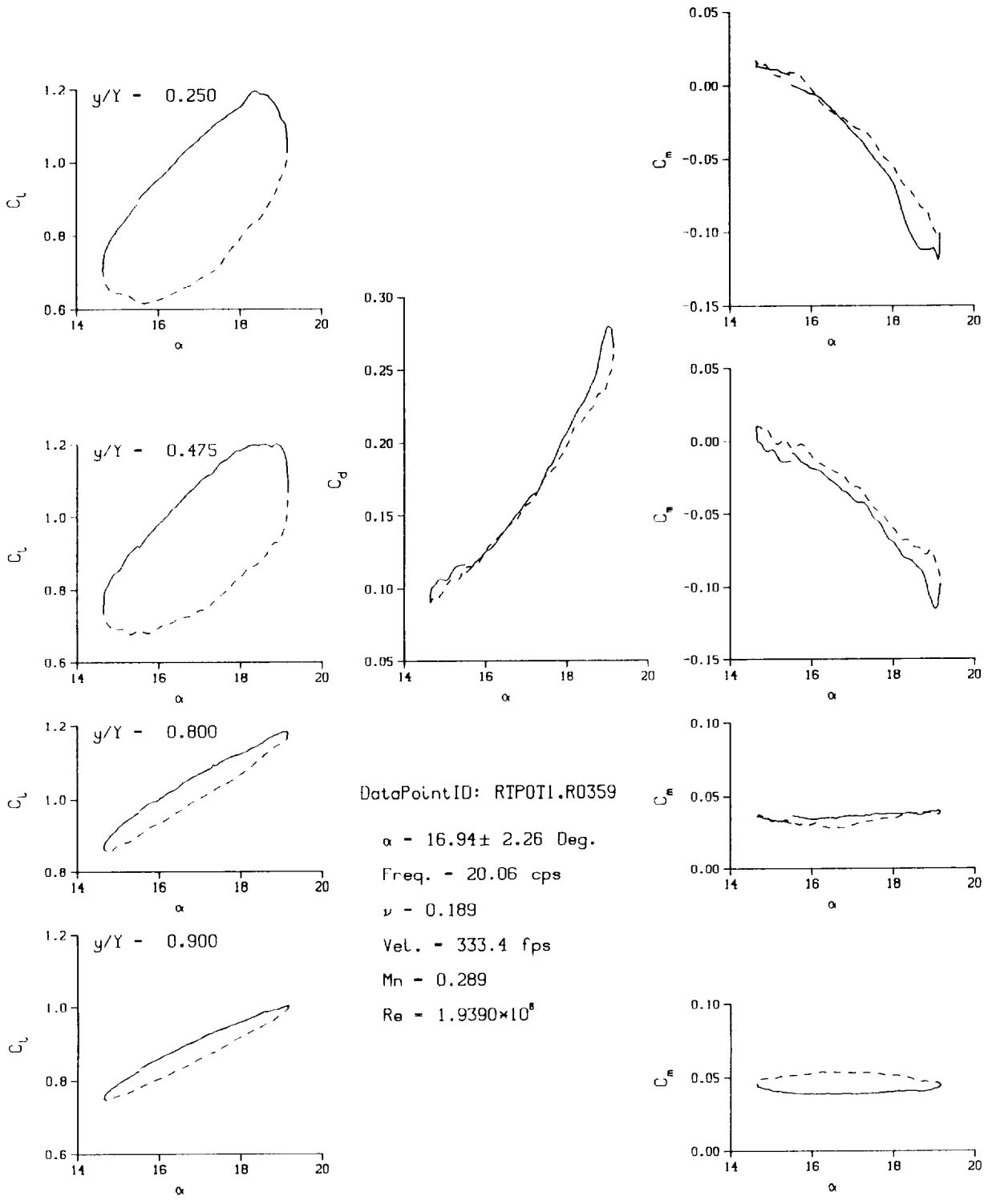

(d) v = 0.20

Figure 38. Continued.

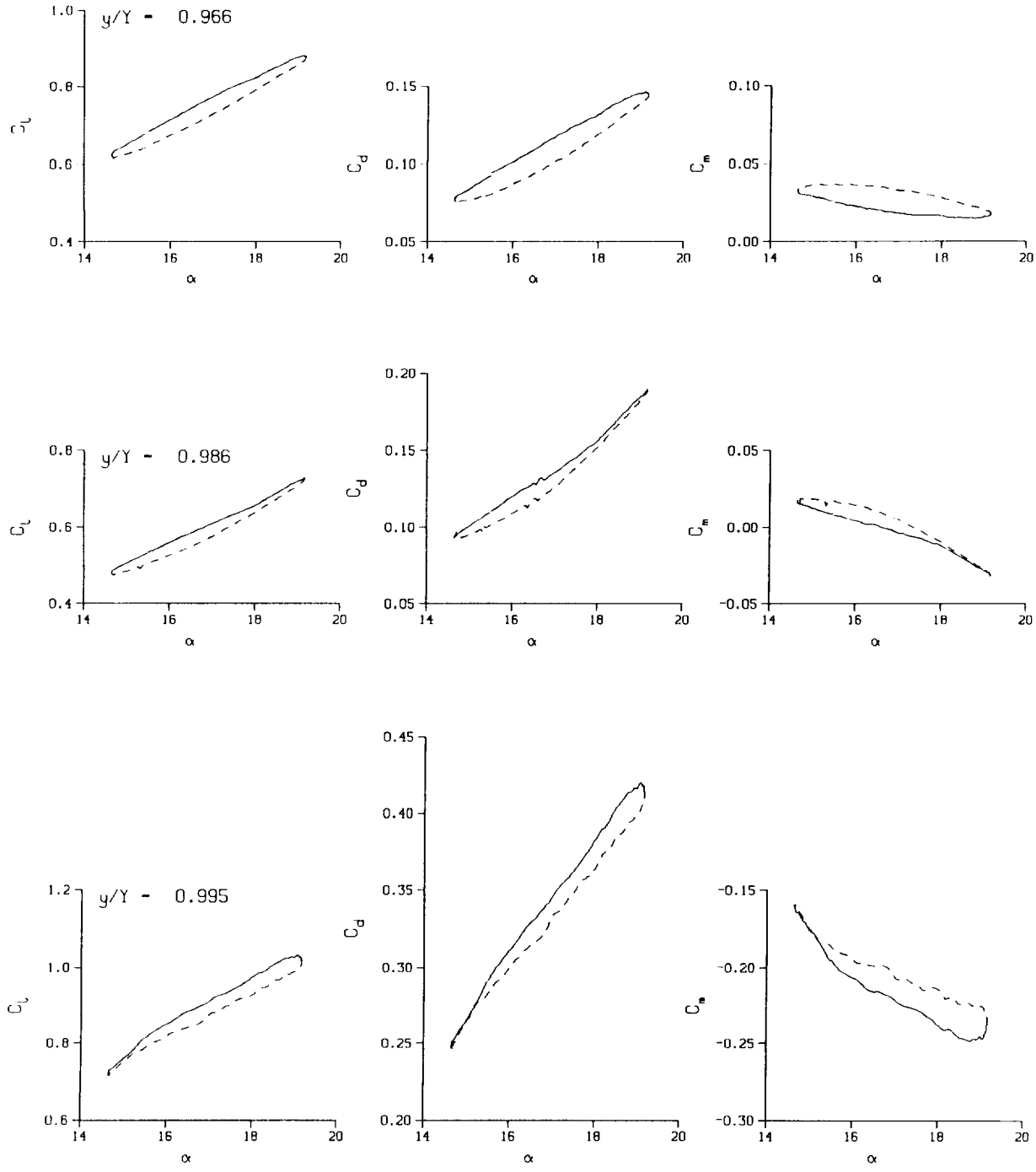

(d) v = 0.20. Concluded

Figure 38. Concluded.

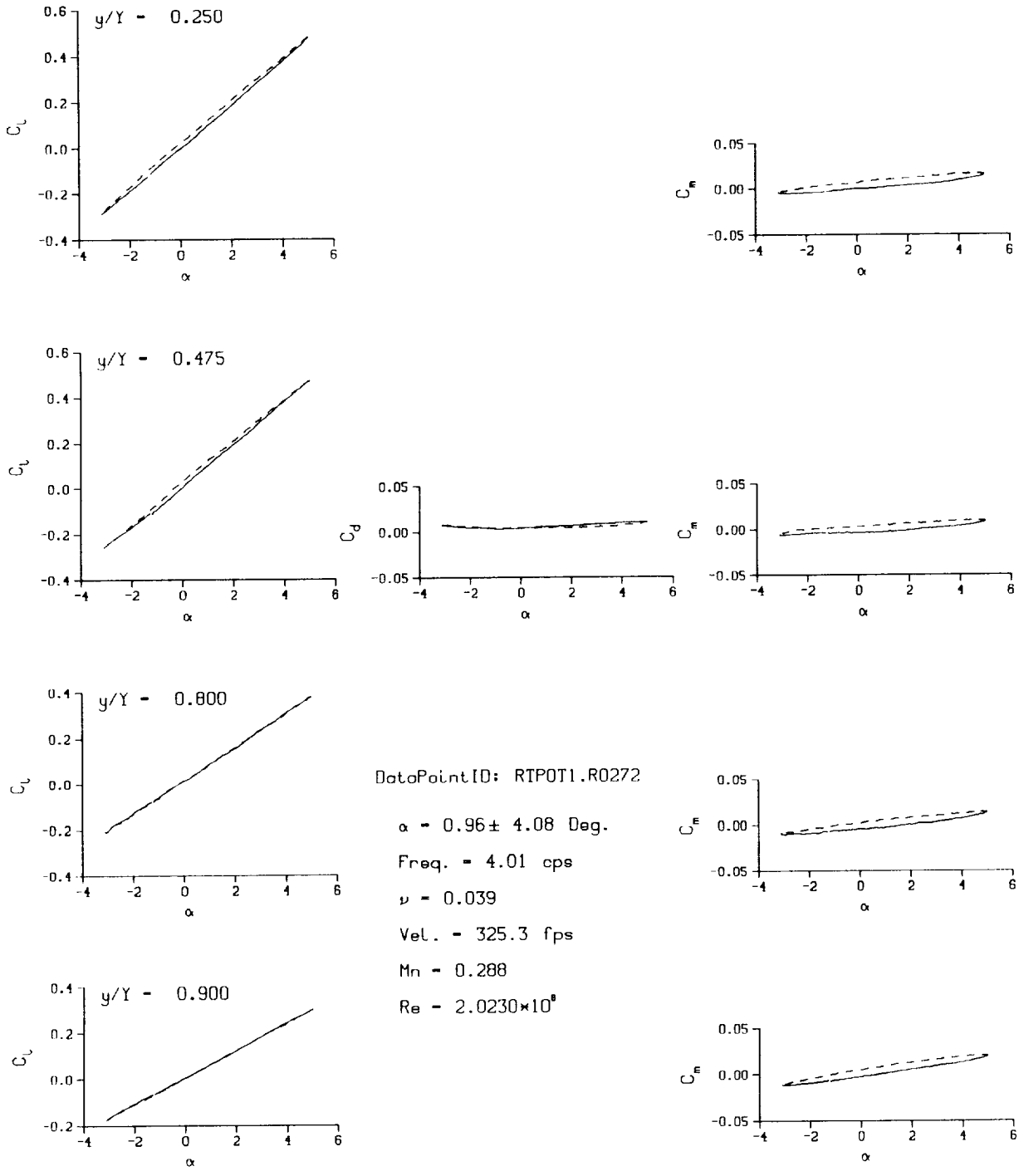

(a) v = 0.04

Figure 39. 3-D round tip pitch oscillation data; BL-trip; α = 1 ± 4 deg.

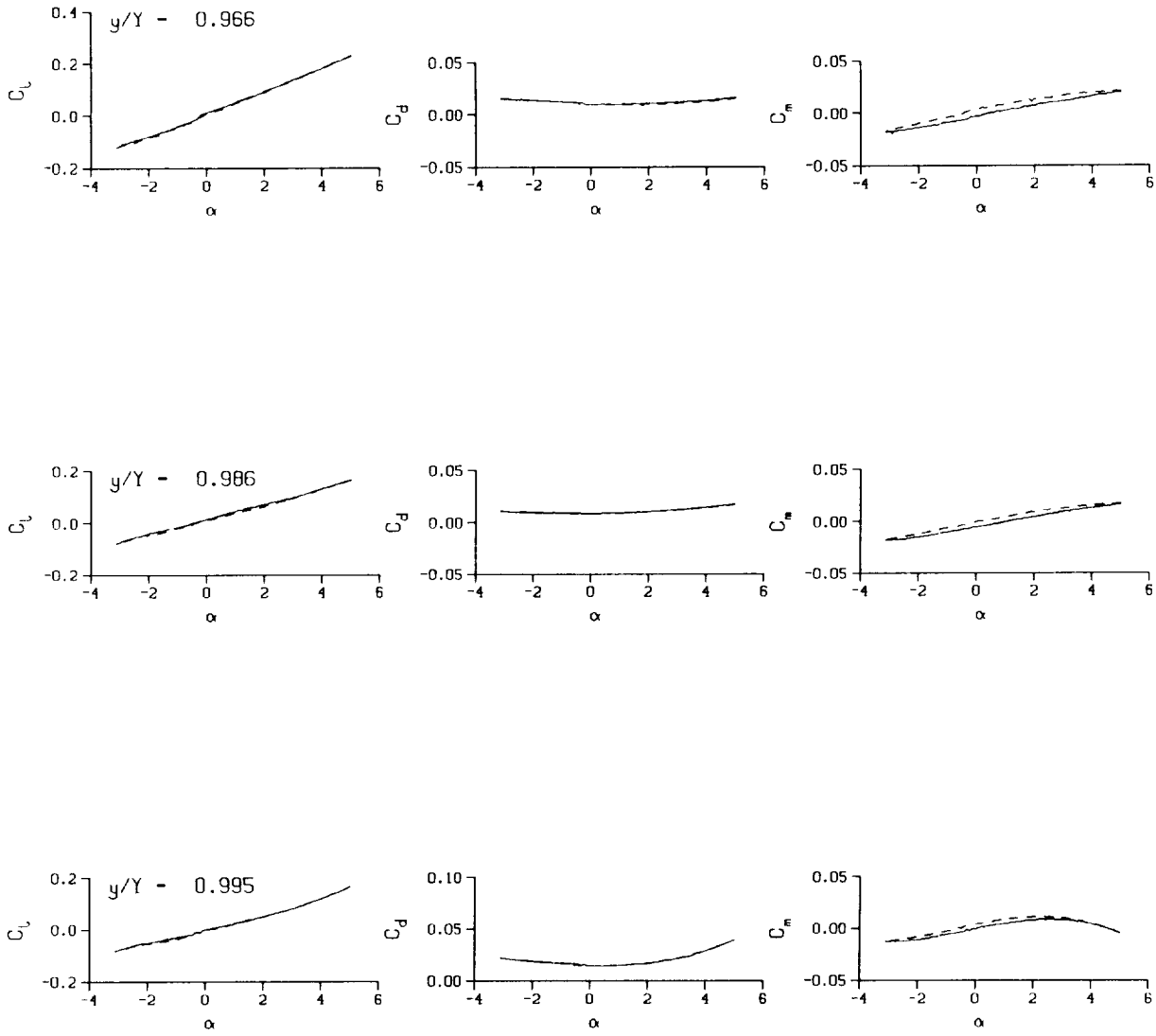

(a) v = 0.04. Concluded

Figure 39. Continued.

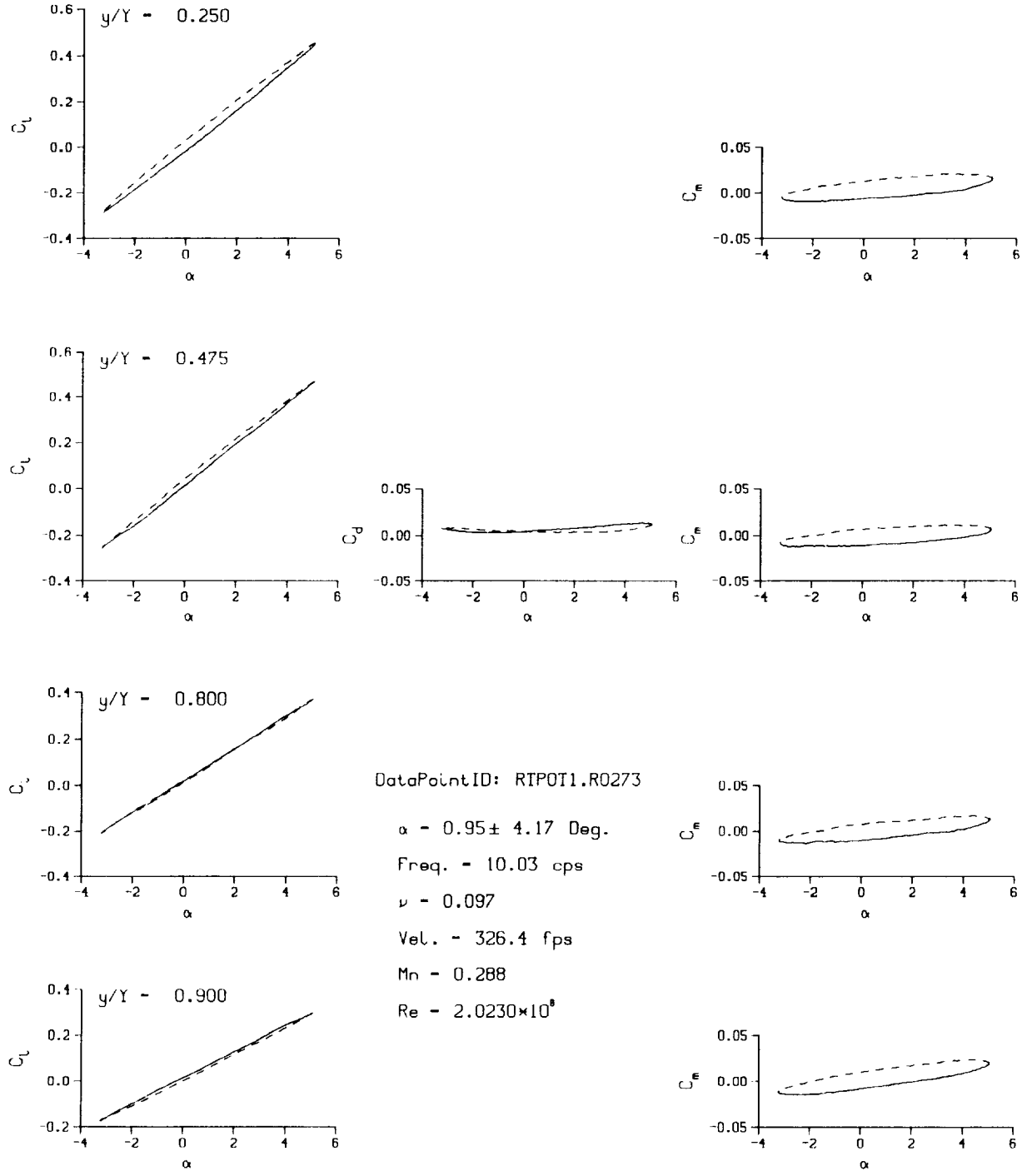

(b) v = 0.10

Figure 39. Continued.

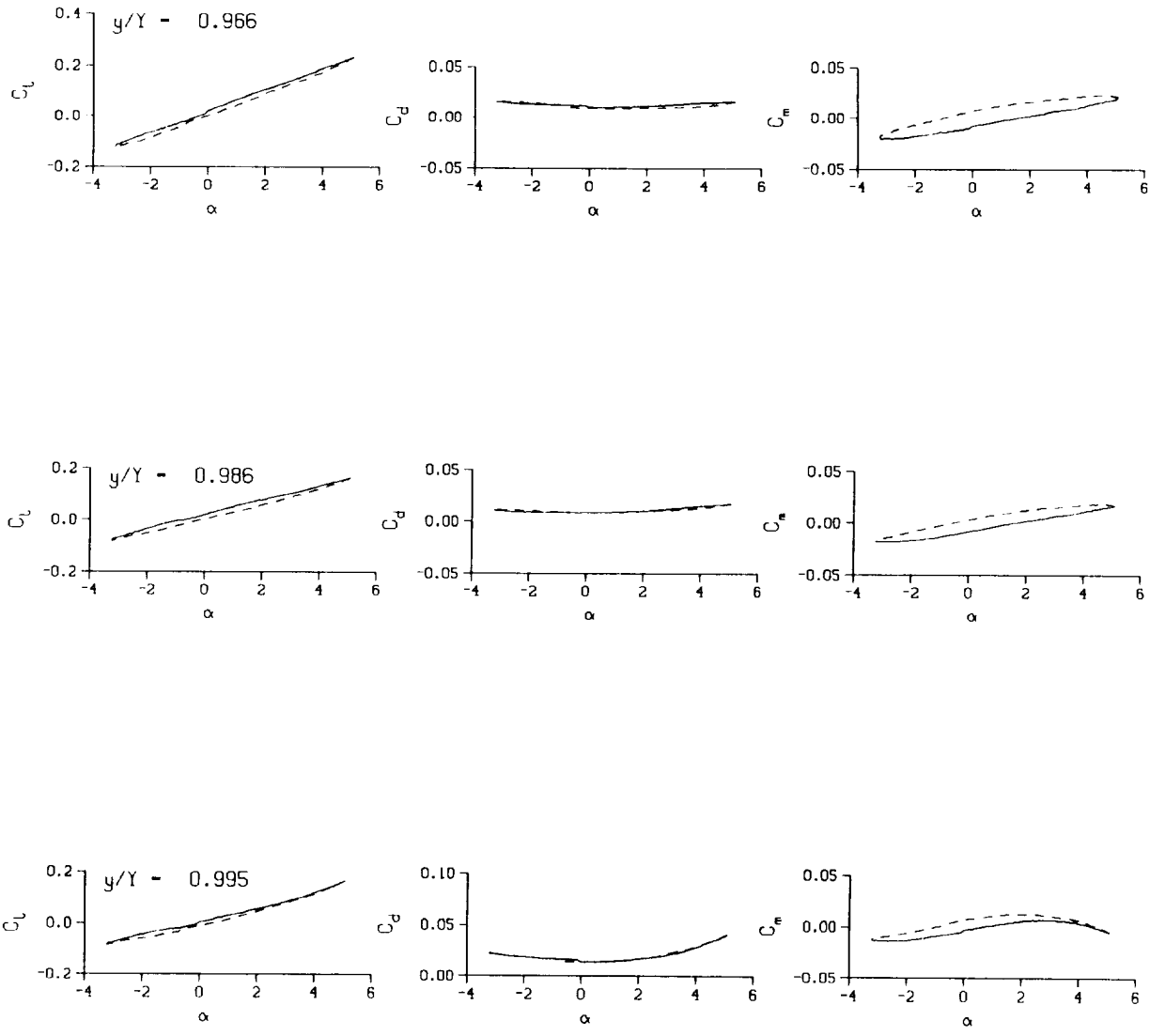

(b) v = 0.10. Concluded

Figure 39. Continued.

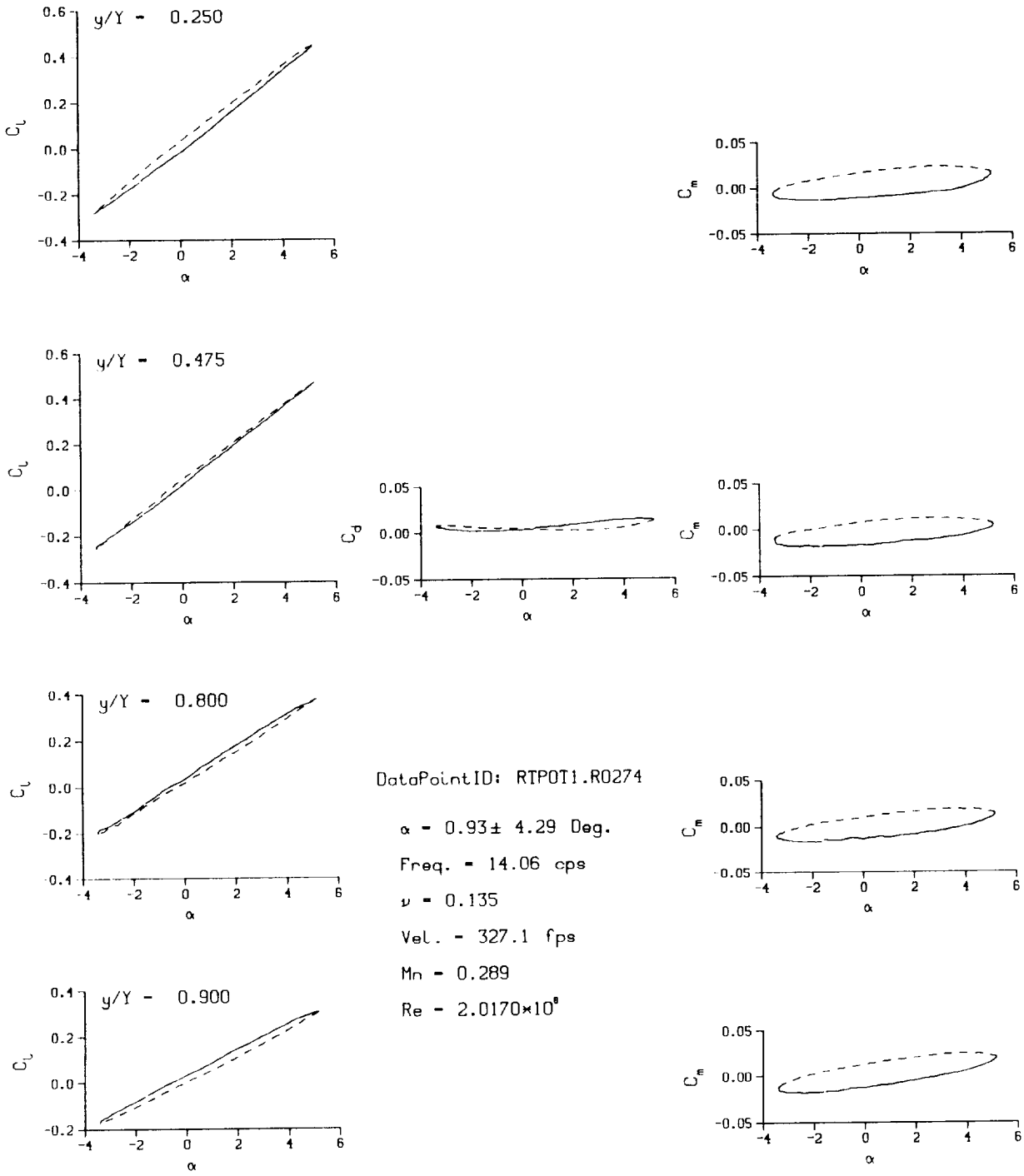

(c) v = 0.14

Figure 39. Continued.

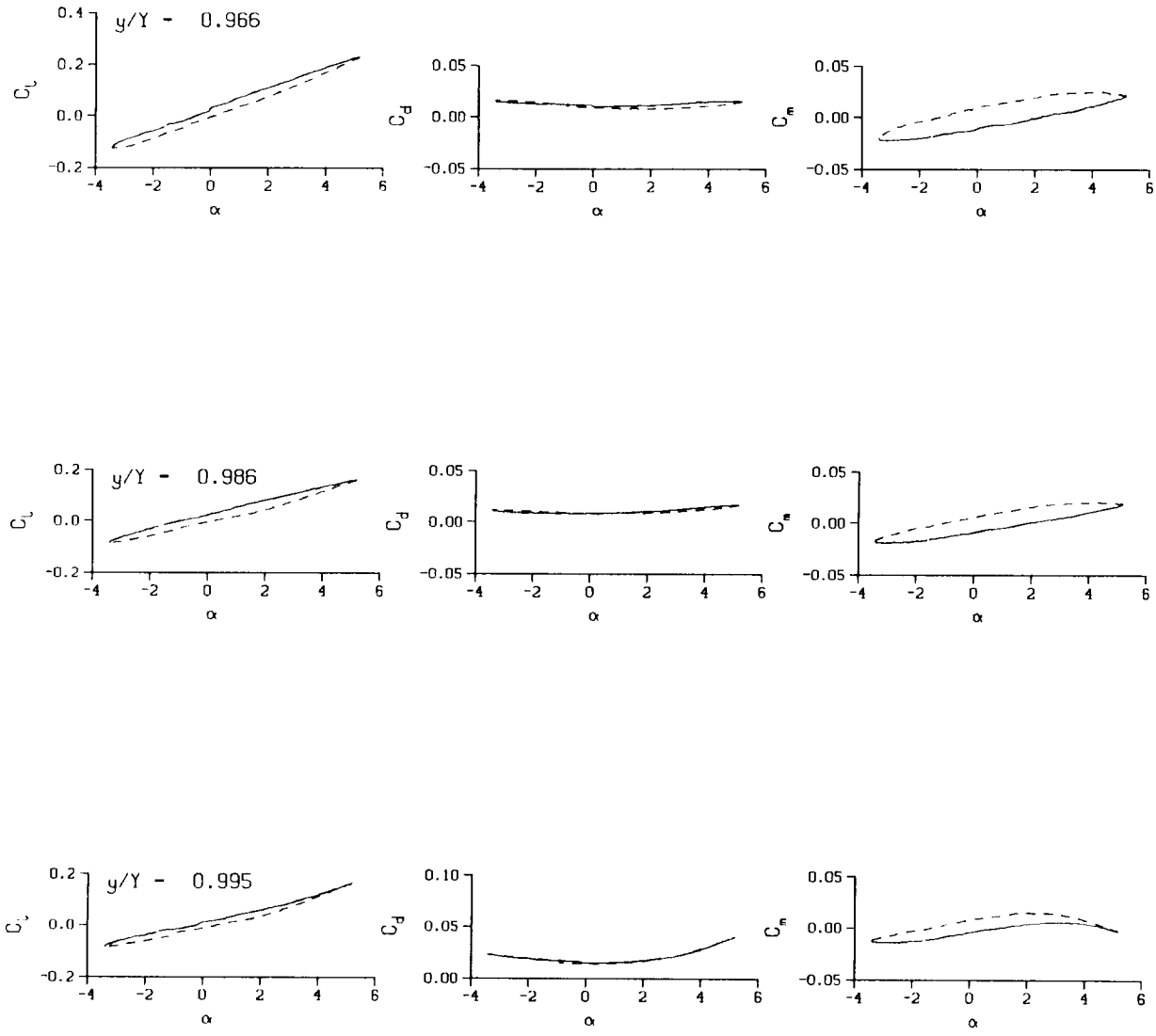

(c) v = 0.14. Concluded

Figure 39. Concluded.

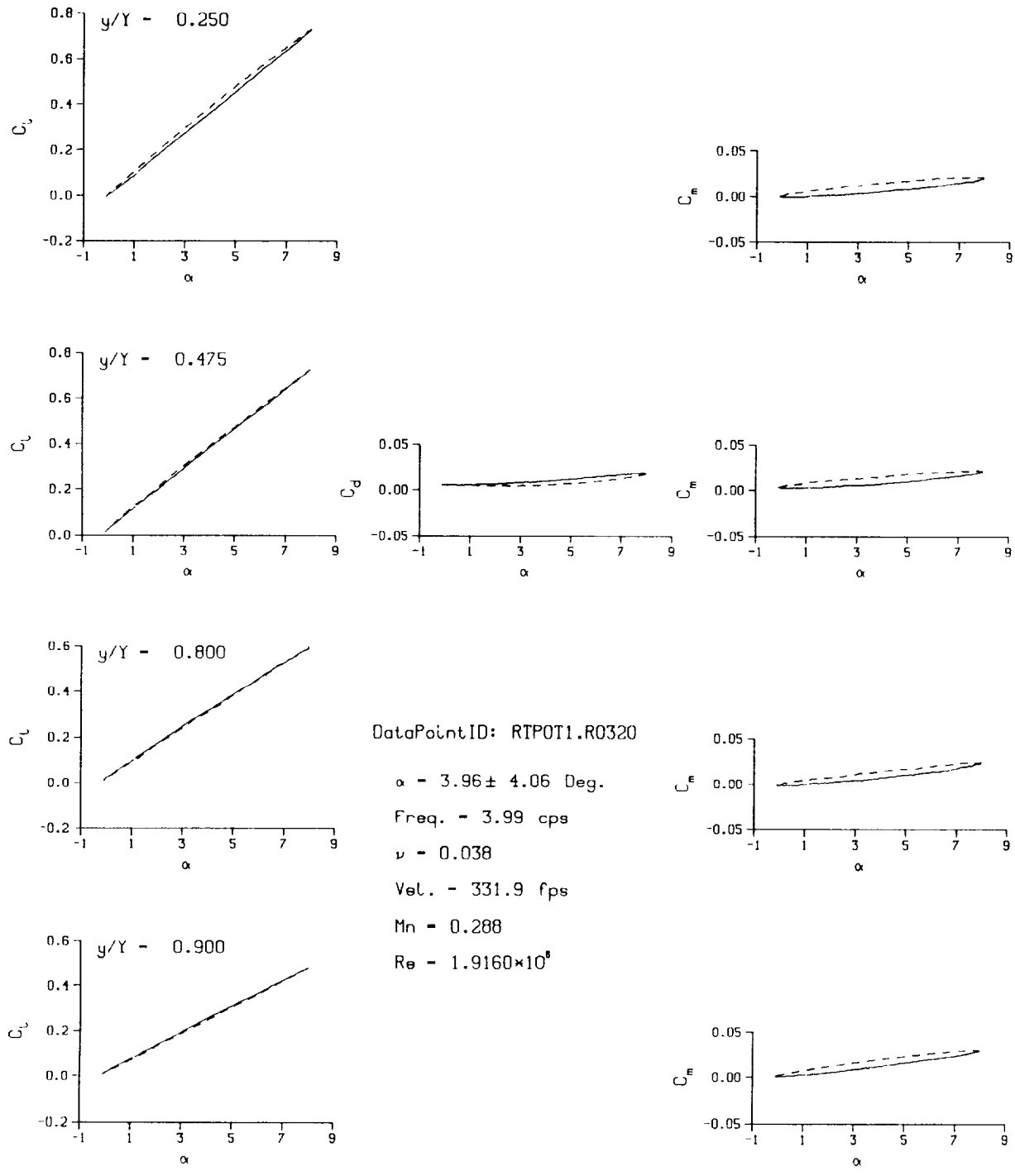

(a) ν = 0.04

Figure 40. 3-D round tip pitch oscillation data; BL-trip; α = 4 ± 4 deg.

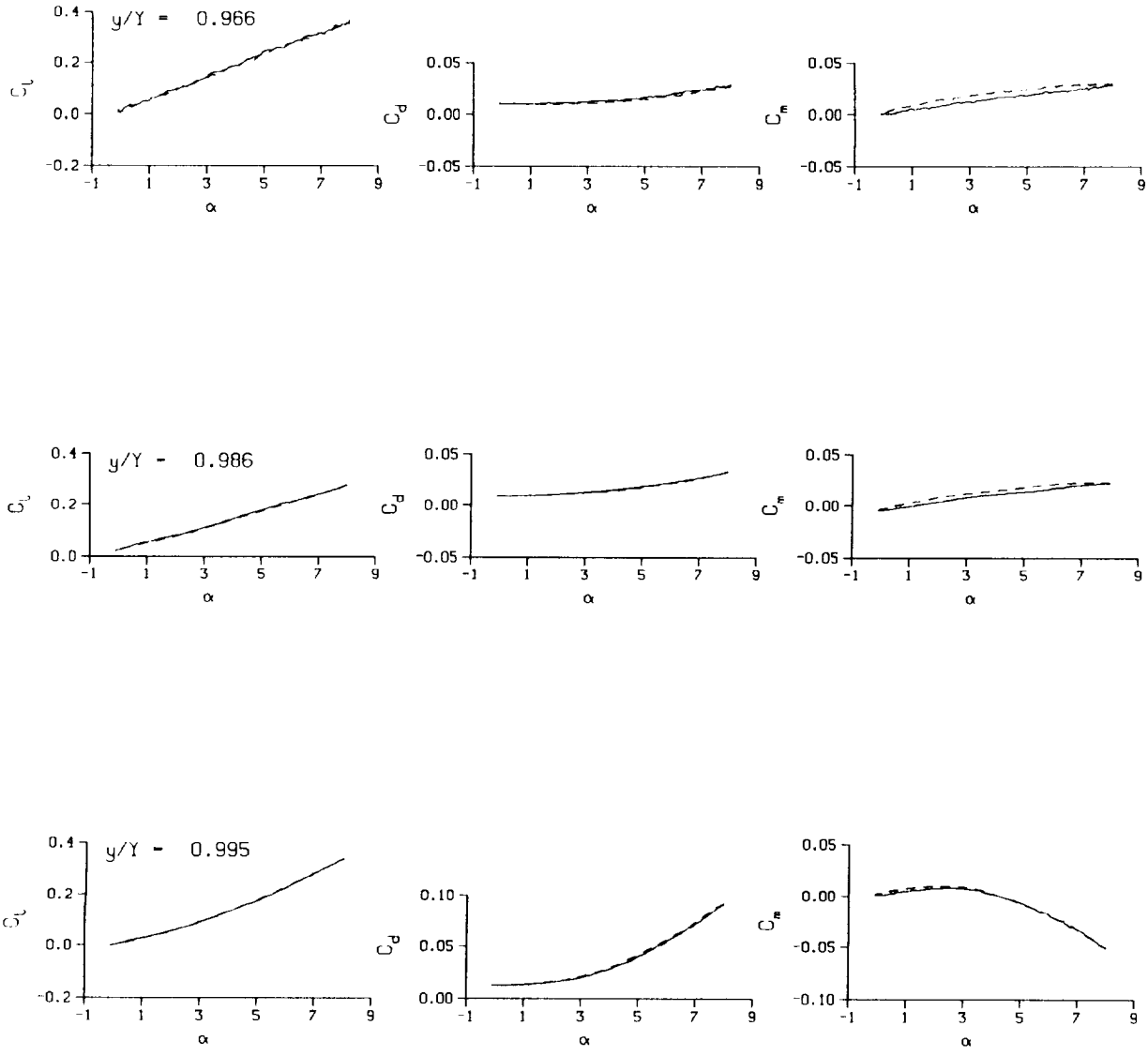

(a) v = 0.04. Concluded

Figure 40. Continued.

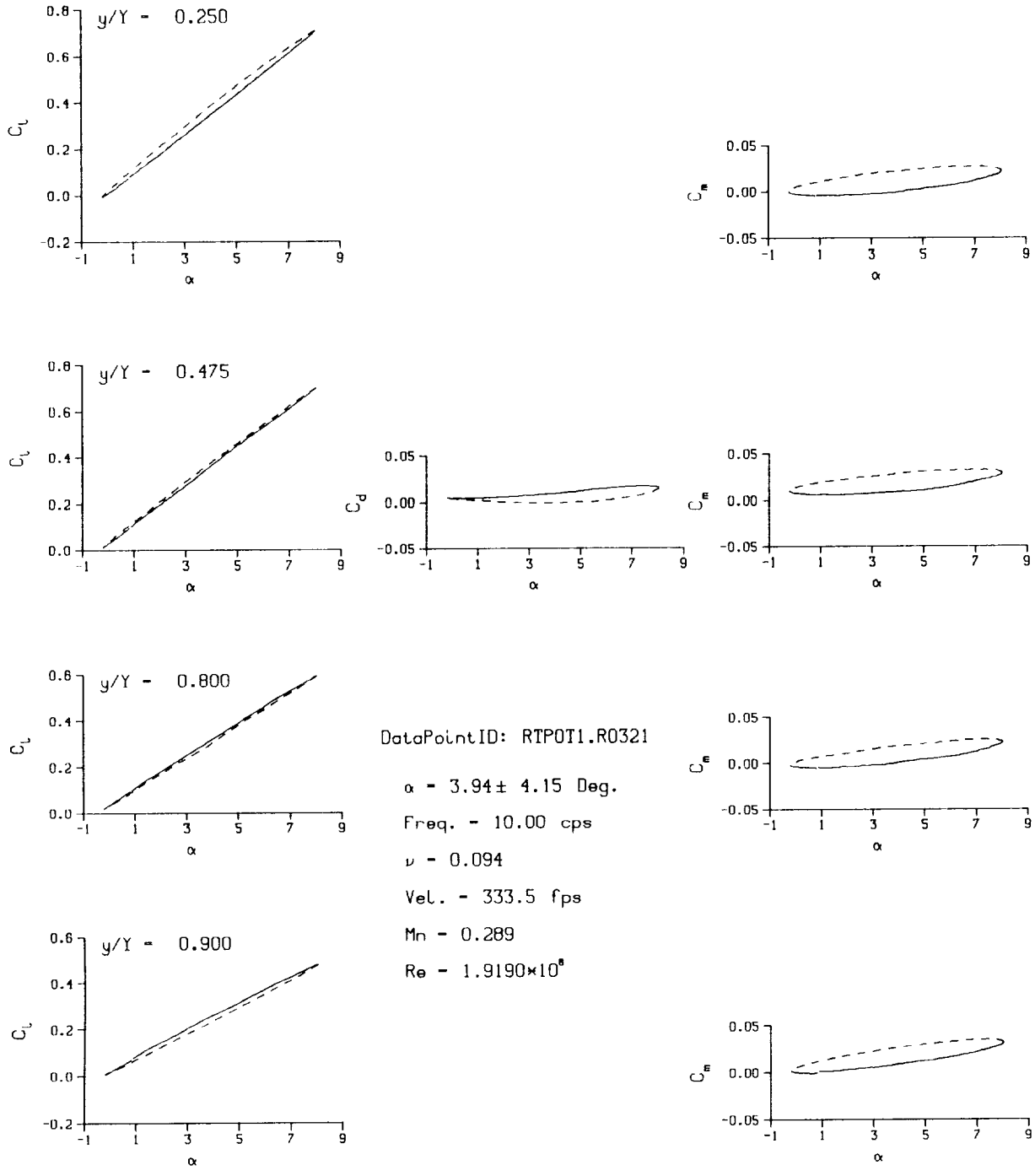

(b) v = 0.10

Figure 40. Continued.

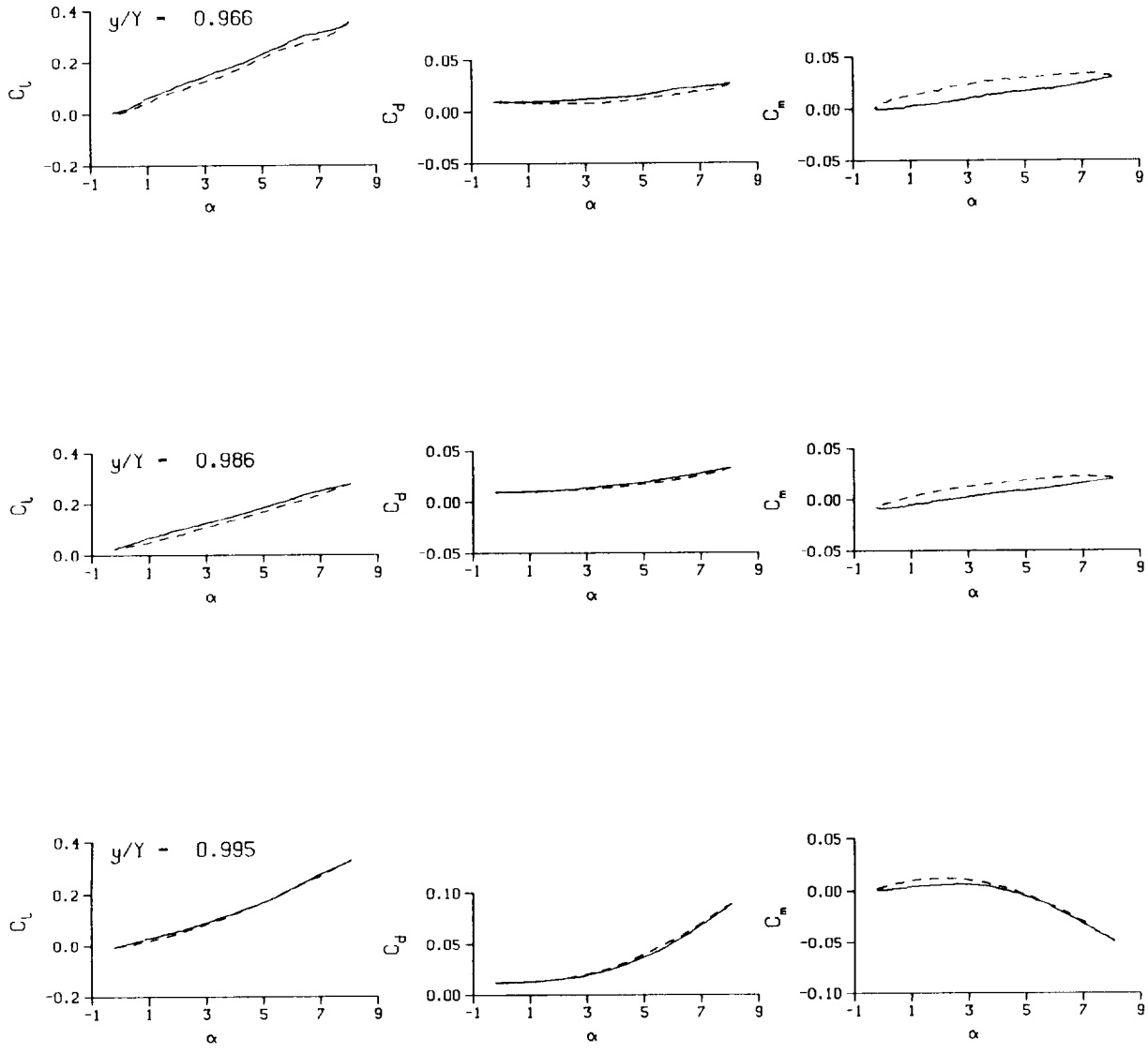

(b) v = 0.10. Concluded

Figure 40. Continued.

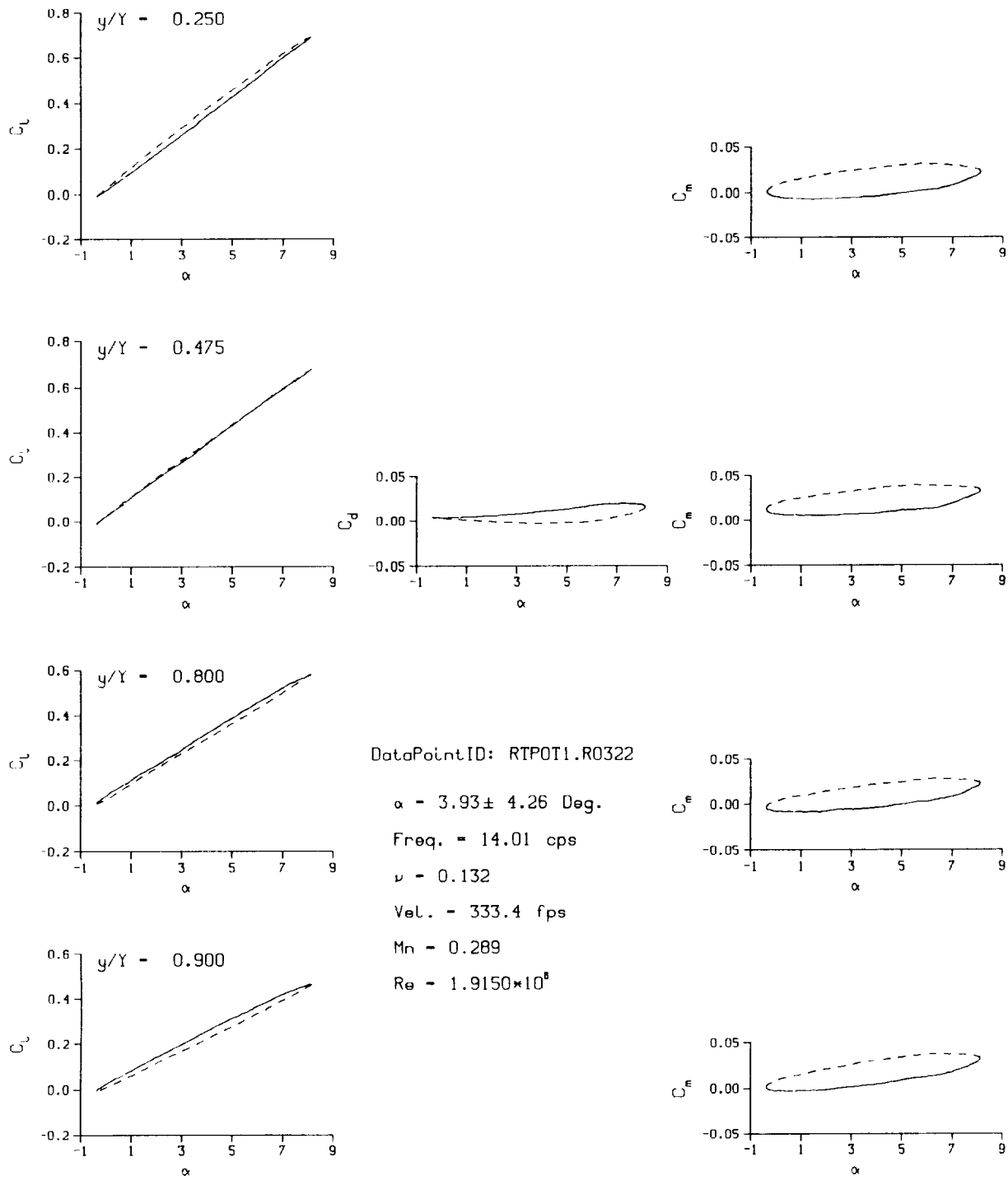

(c) v = 0.14

Figure 40. Continued.

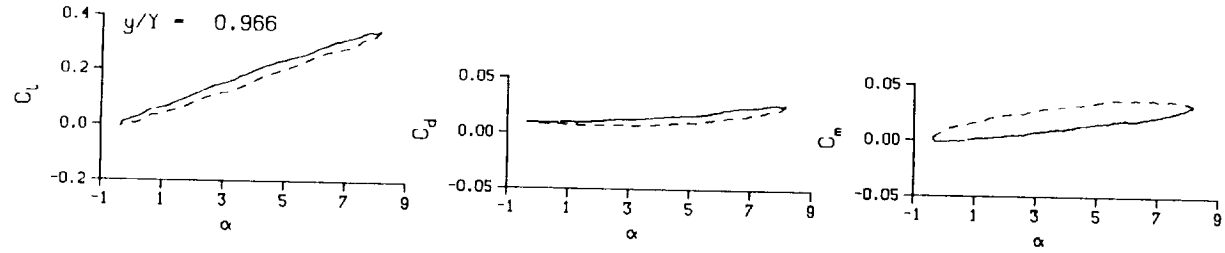

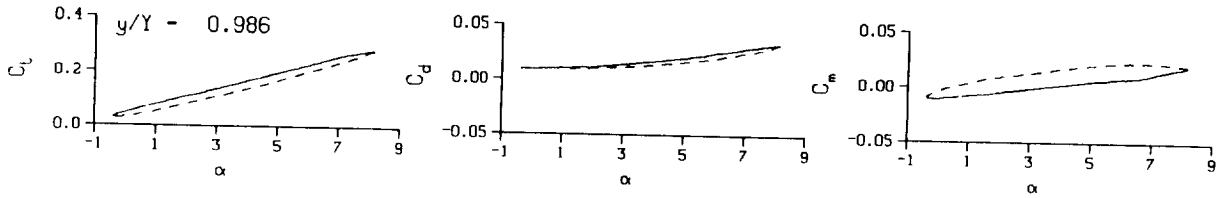

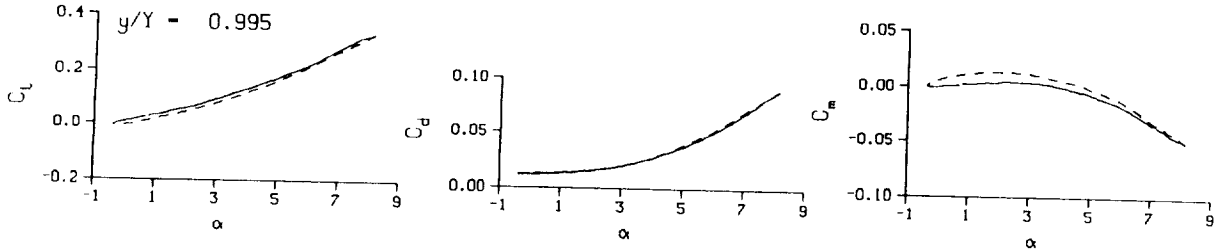

(c) v = 0.14. Concluded

Figure 40. Concluded.

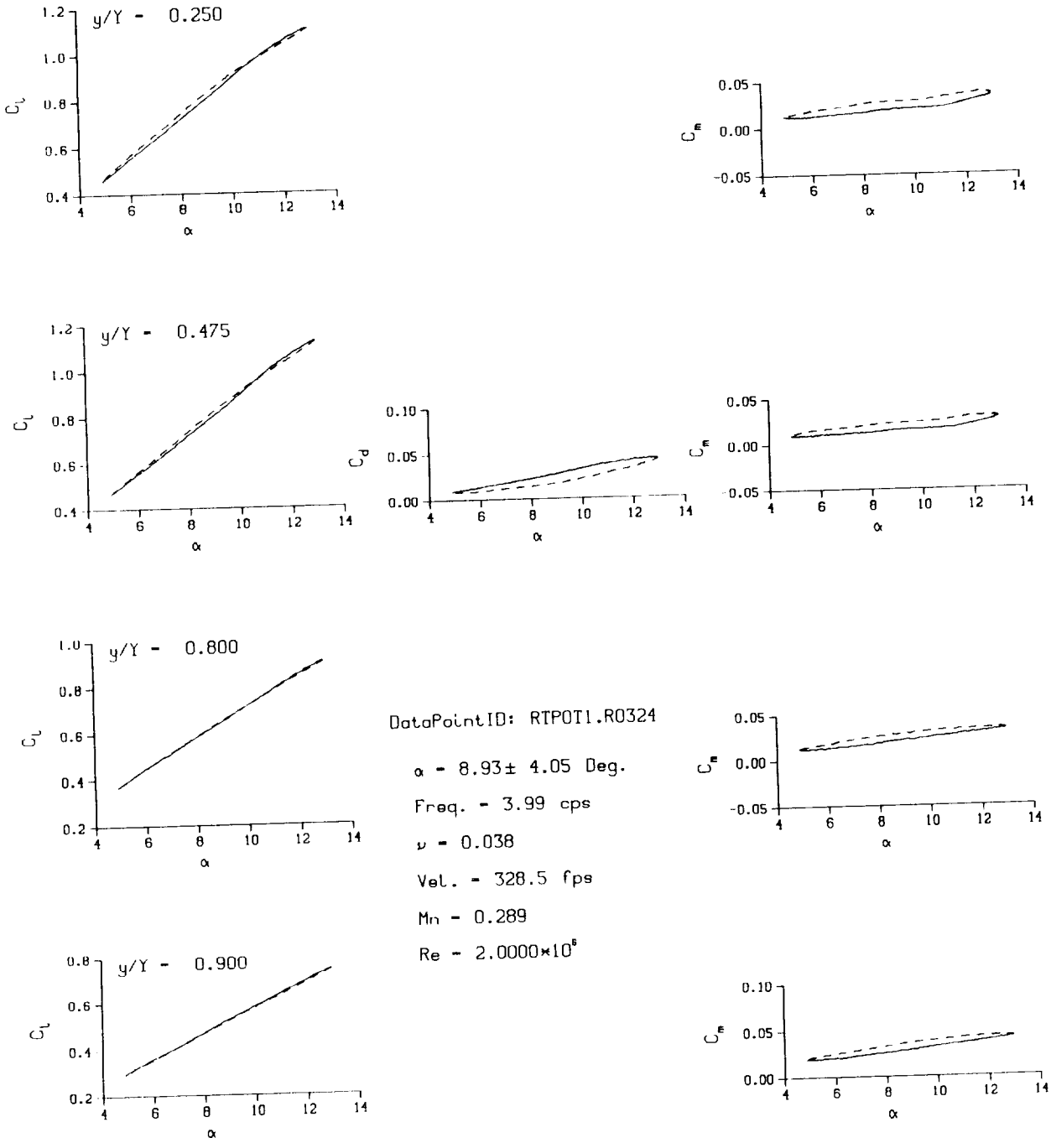

(a) ν = 0.04

Figure 41. 3-D round tip pitch oscillation data; BL-trip; α = 9 ± 4 deg.

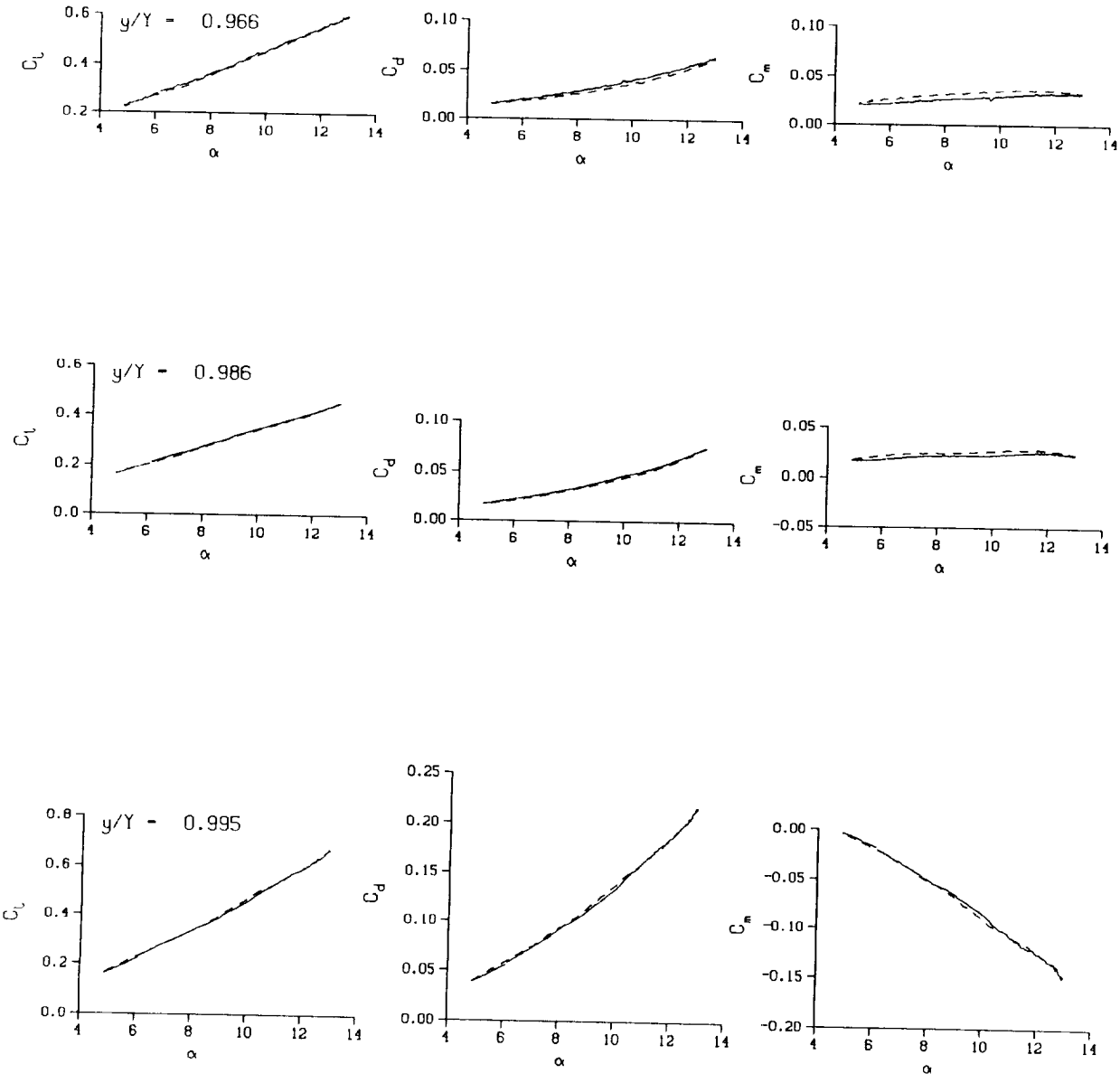

(a) v = 0.04. Concluded

Figure 41. Continued.

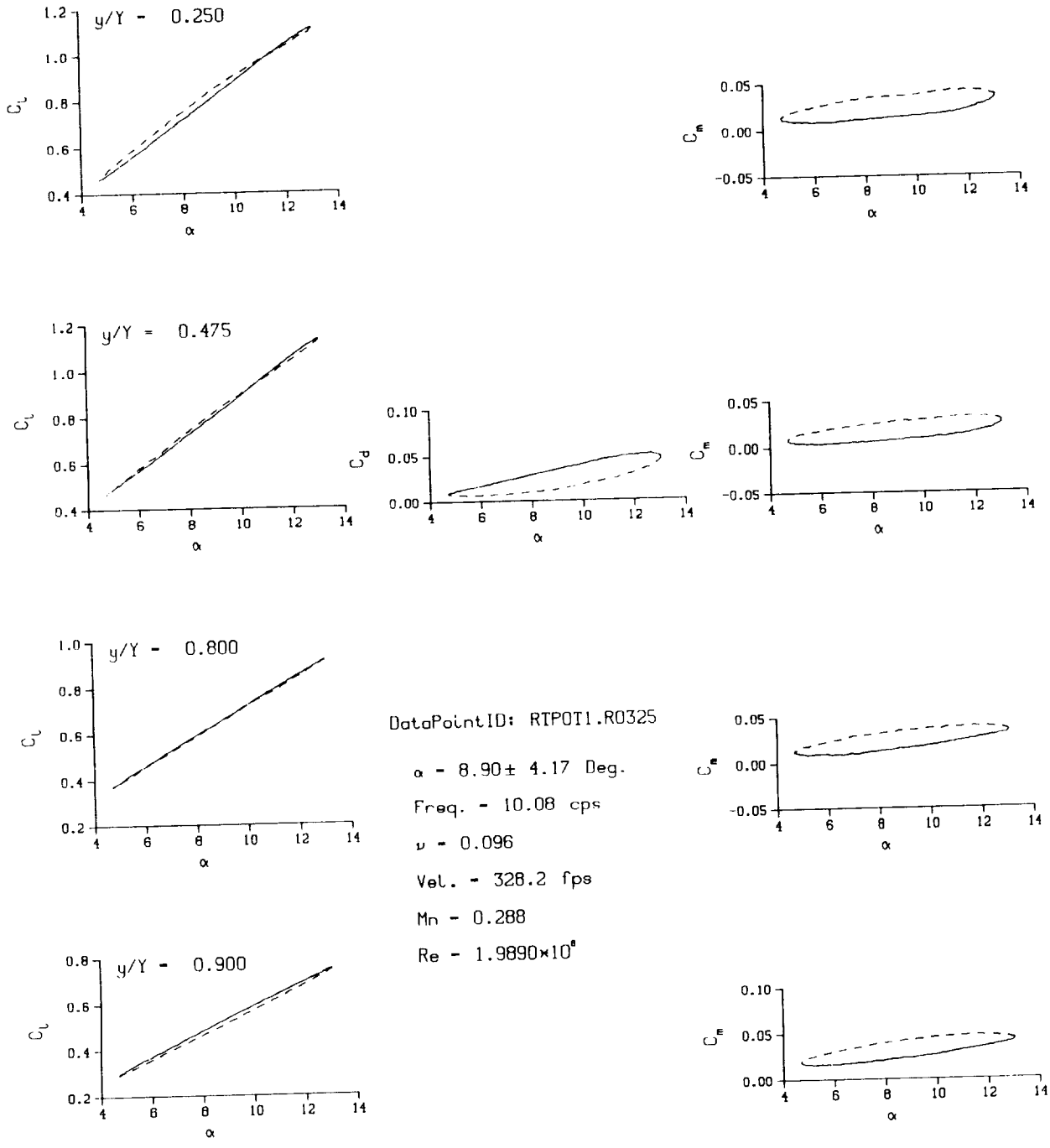

(b) v = 0.10

Figure 41. Continued.

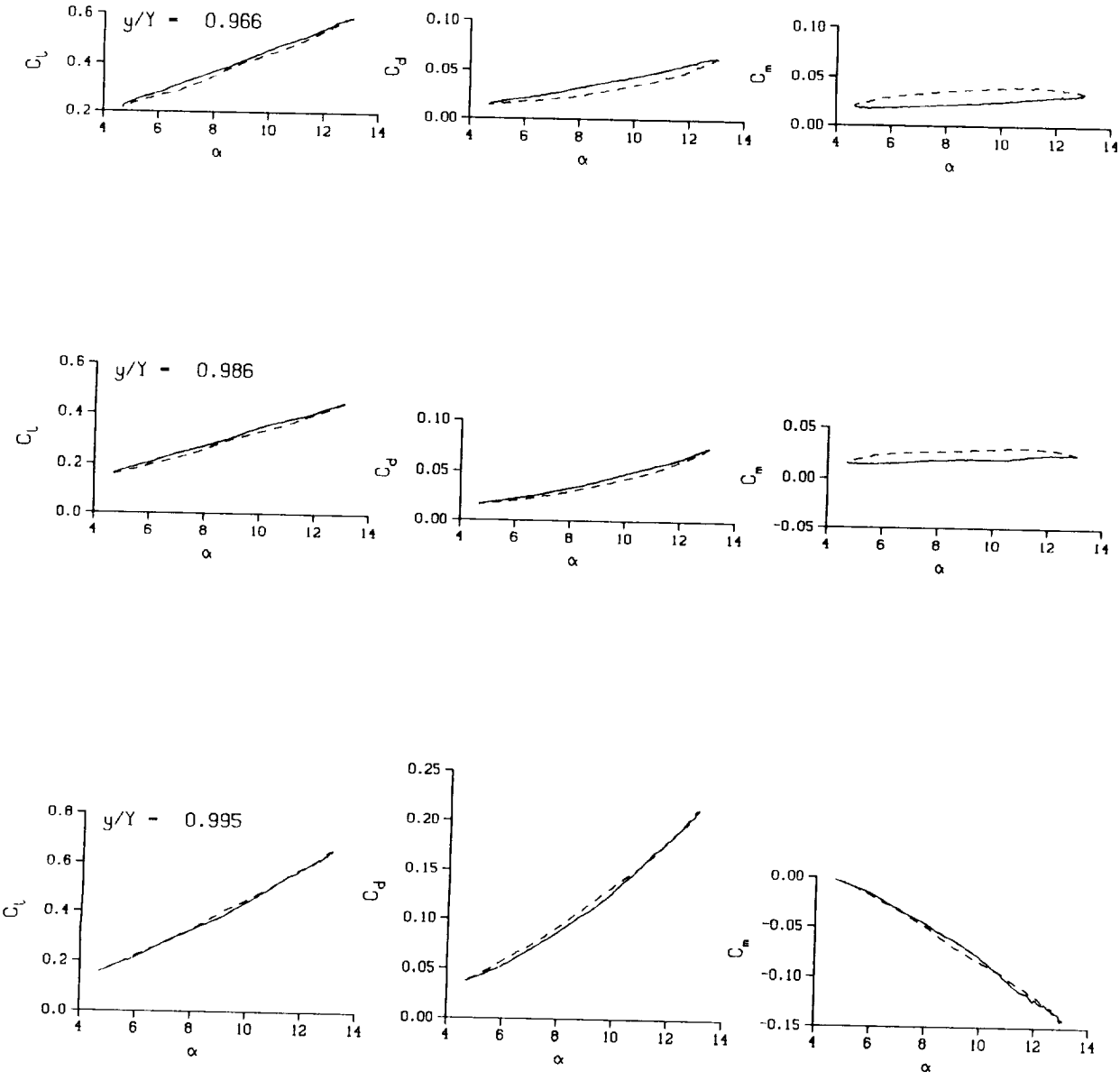

(b) v = 0.10. Concluded

Figure 41. Continued.

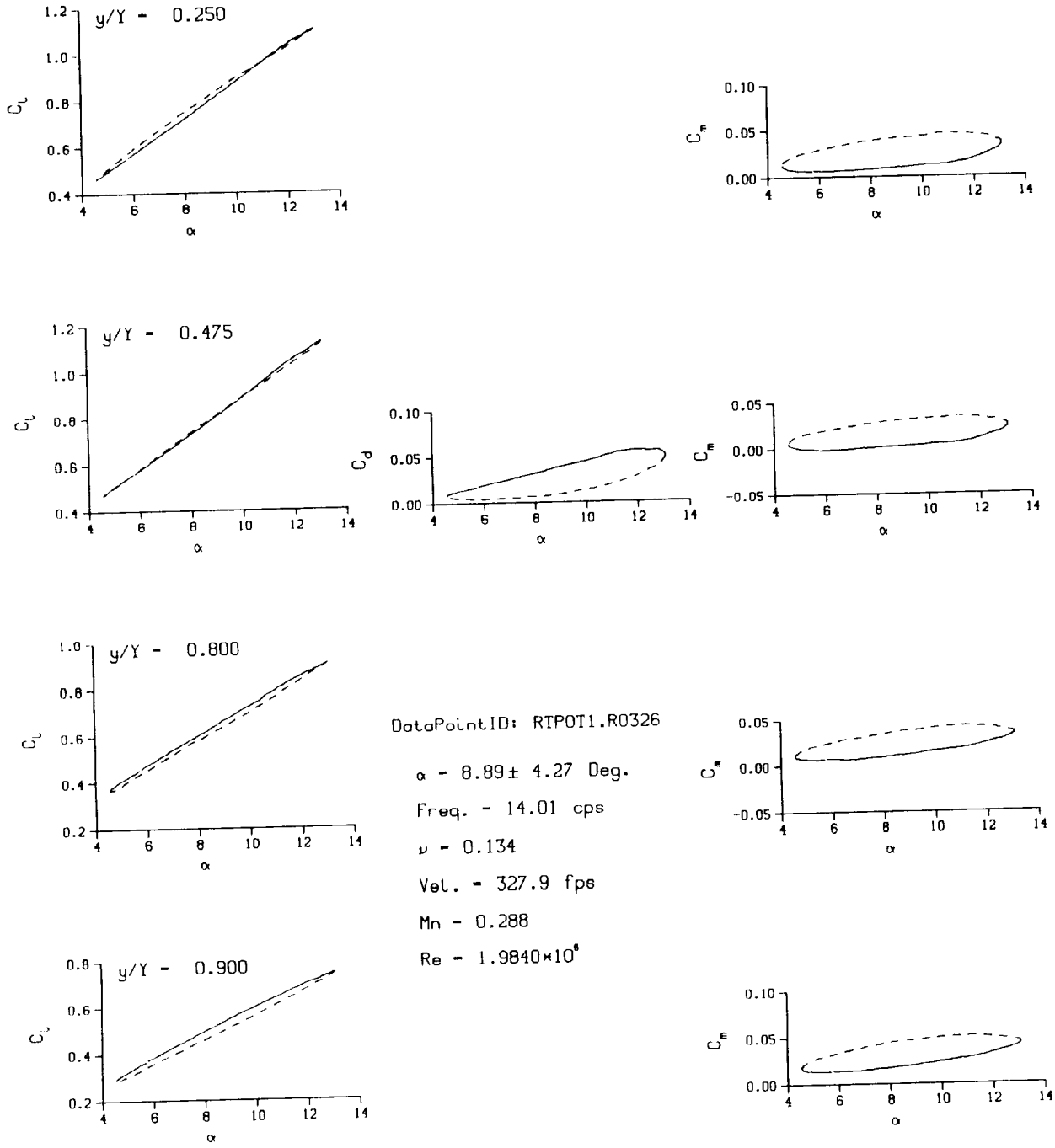

(c) v = 0.14

Figure 41. Continued.

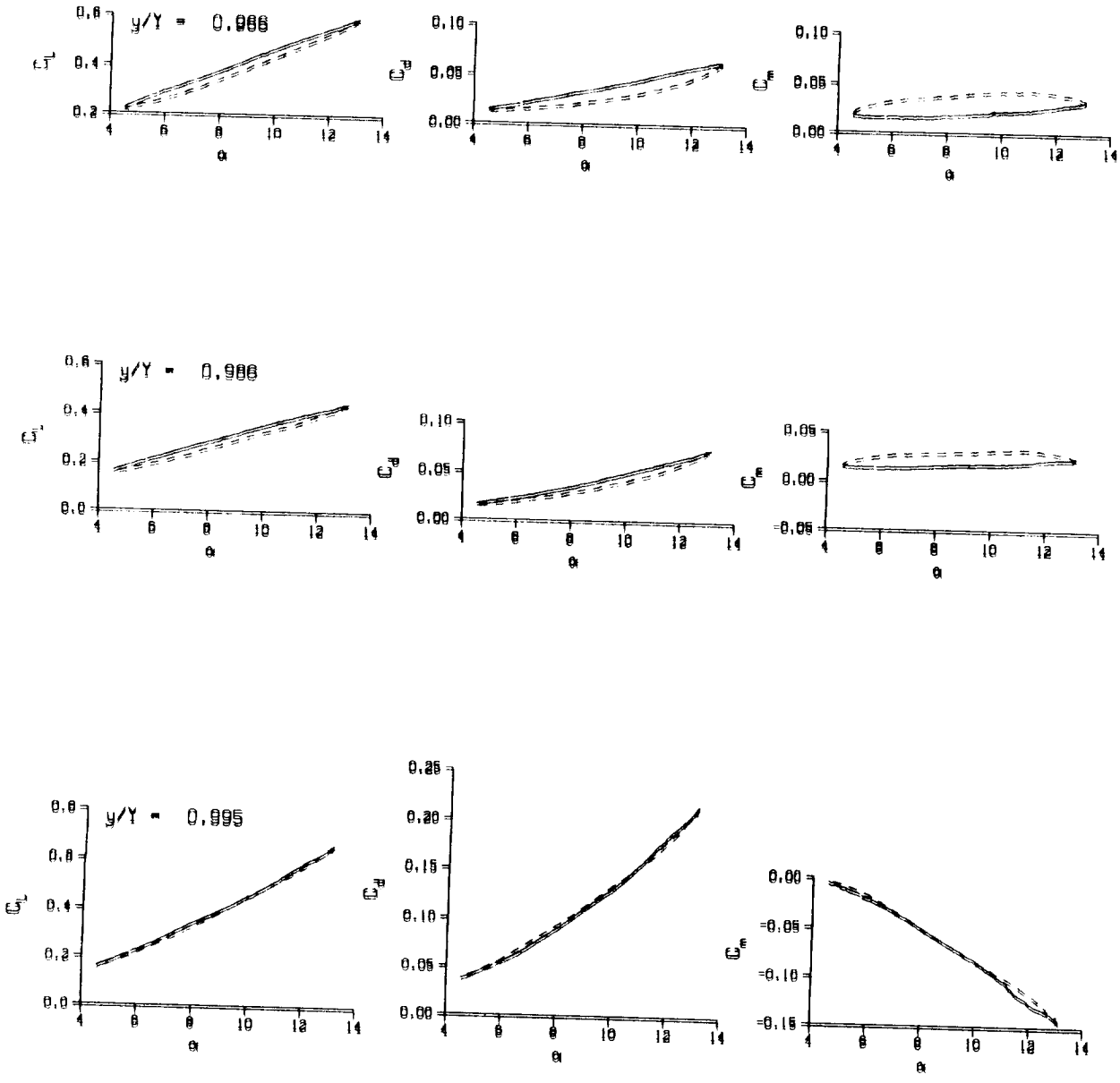

(c) v = 0.14. Concluded

Figure 41. Concluded.

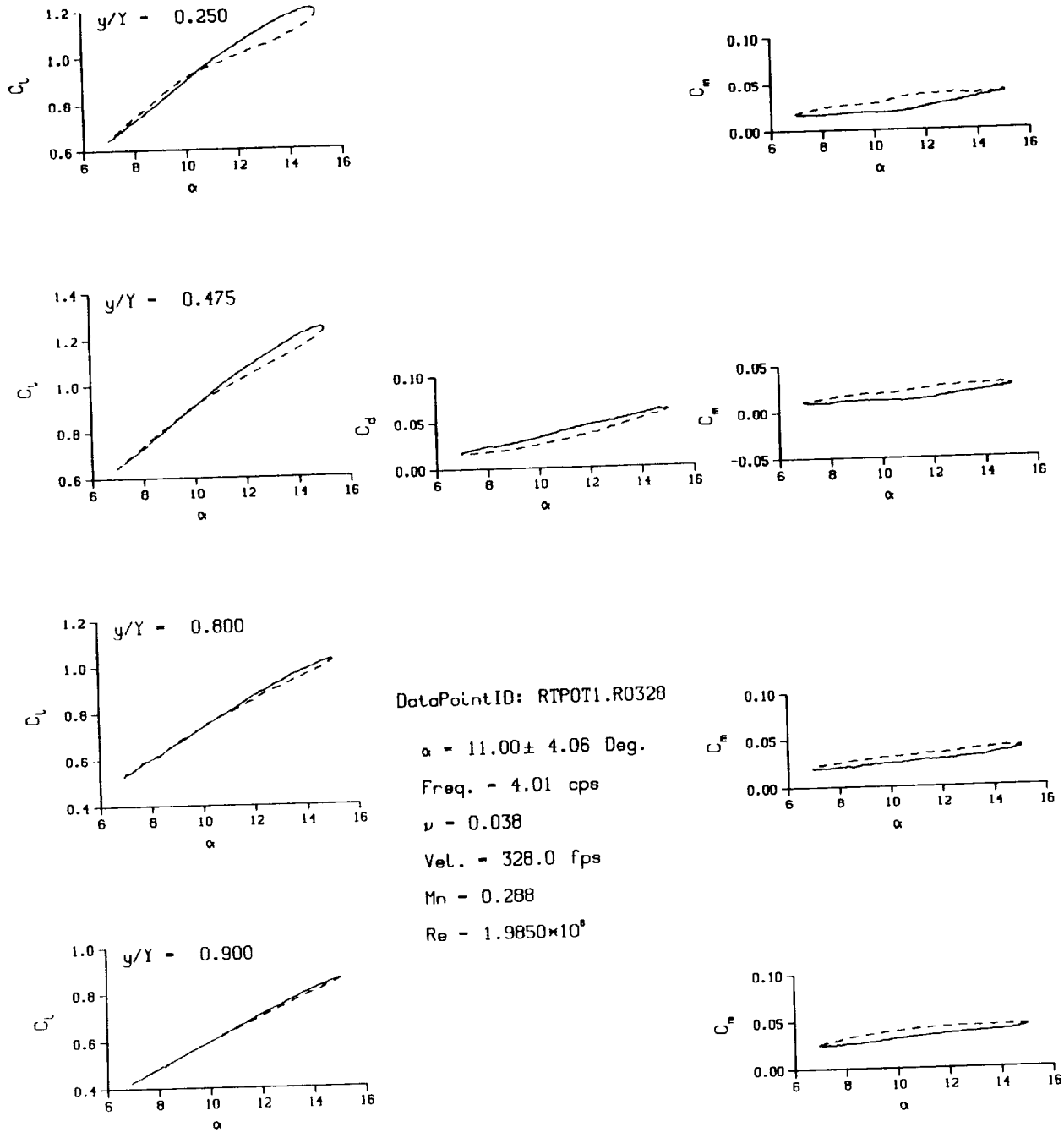

(a) ν = 0.04

Figure 42. 3-D round tip pitch oscillation data; BL-trip; α = 11 ± 4 deg.

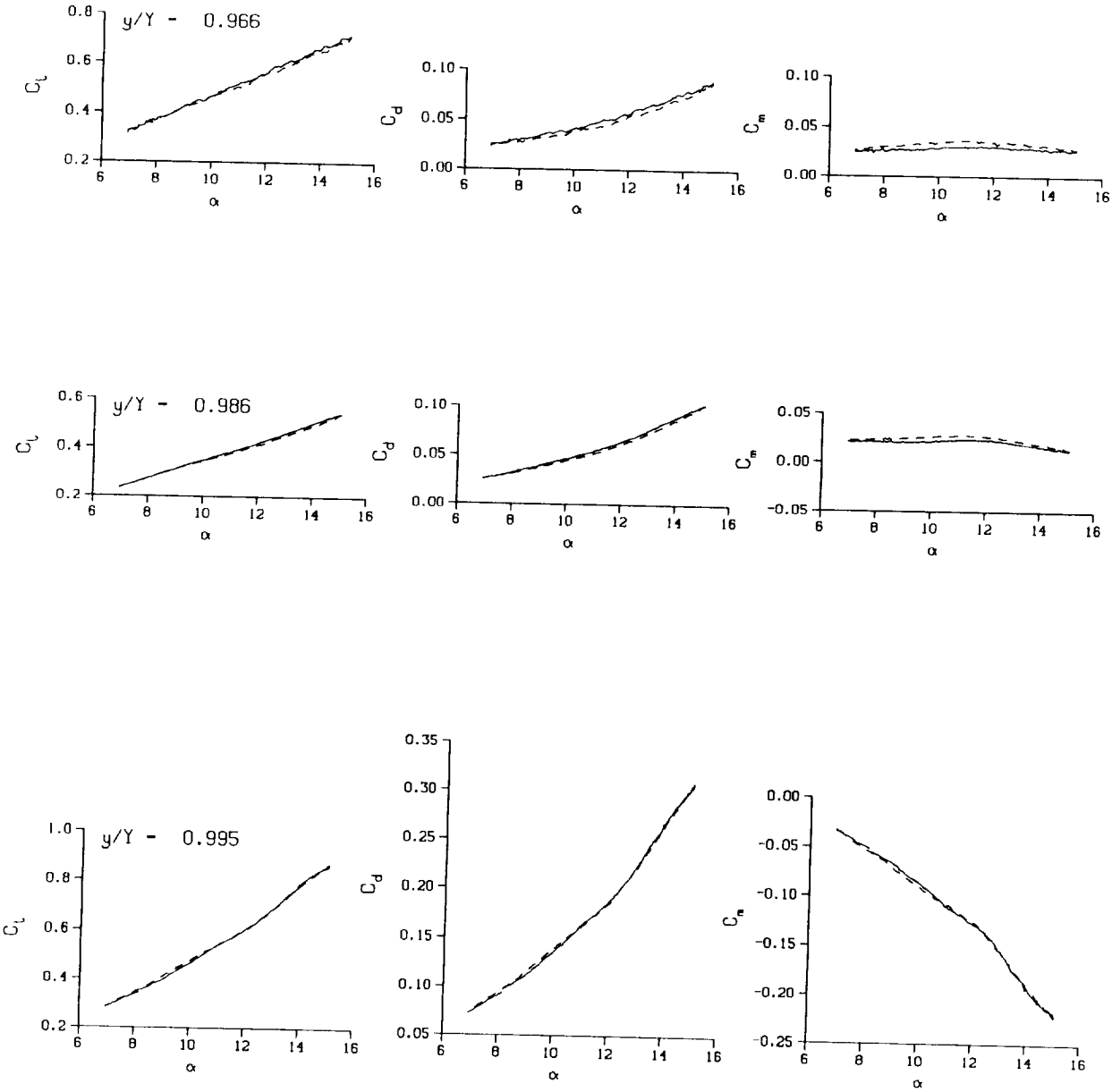

(a) v = 0.04. Concluded

Figure 42. Continued.

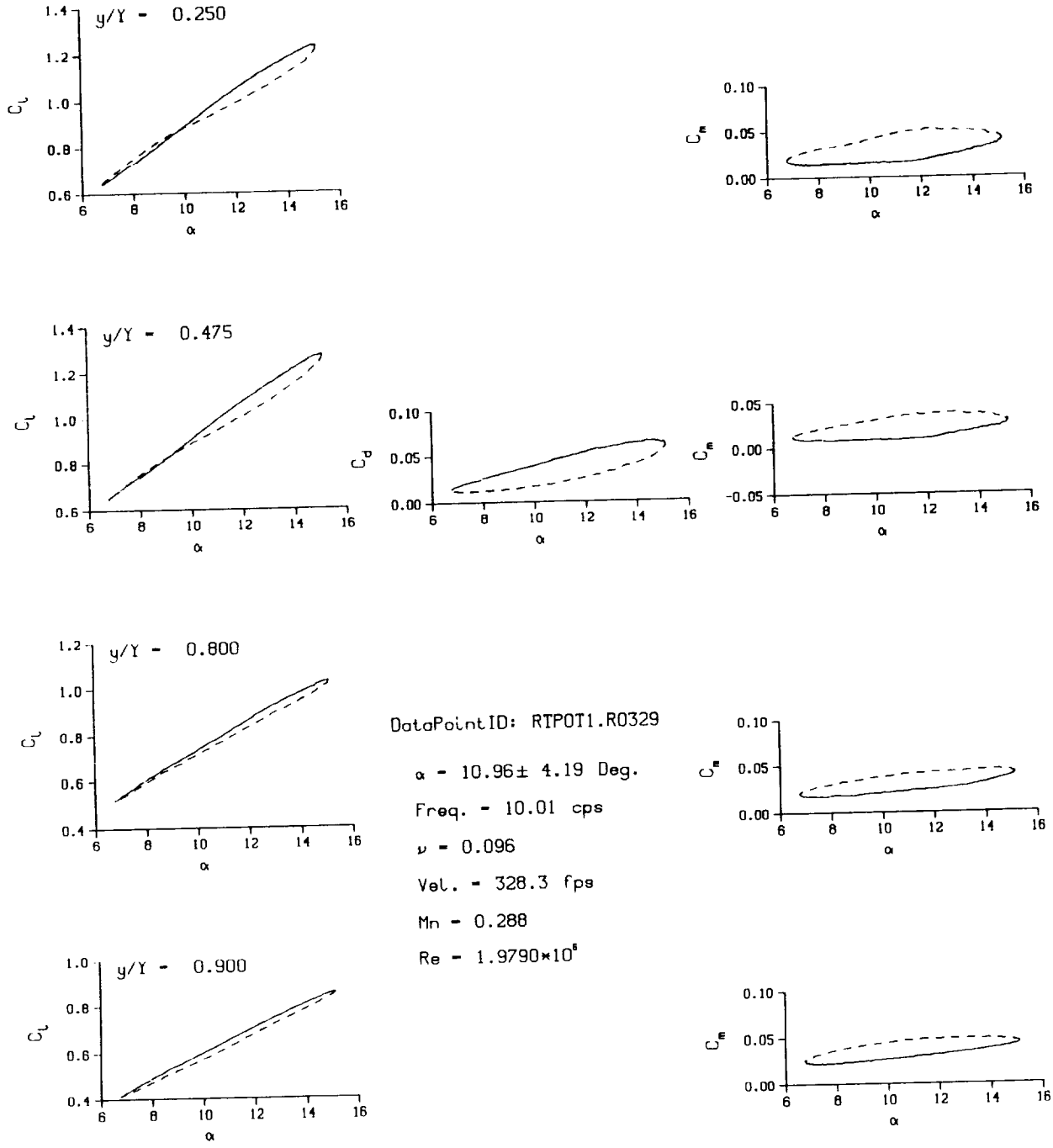

(b) v = 0.10

Figure 42. Continued.

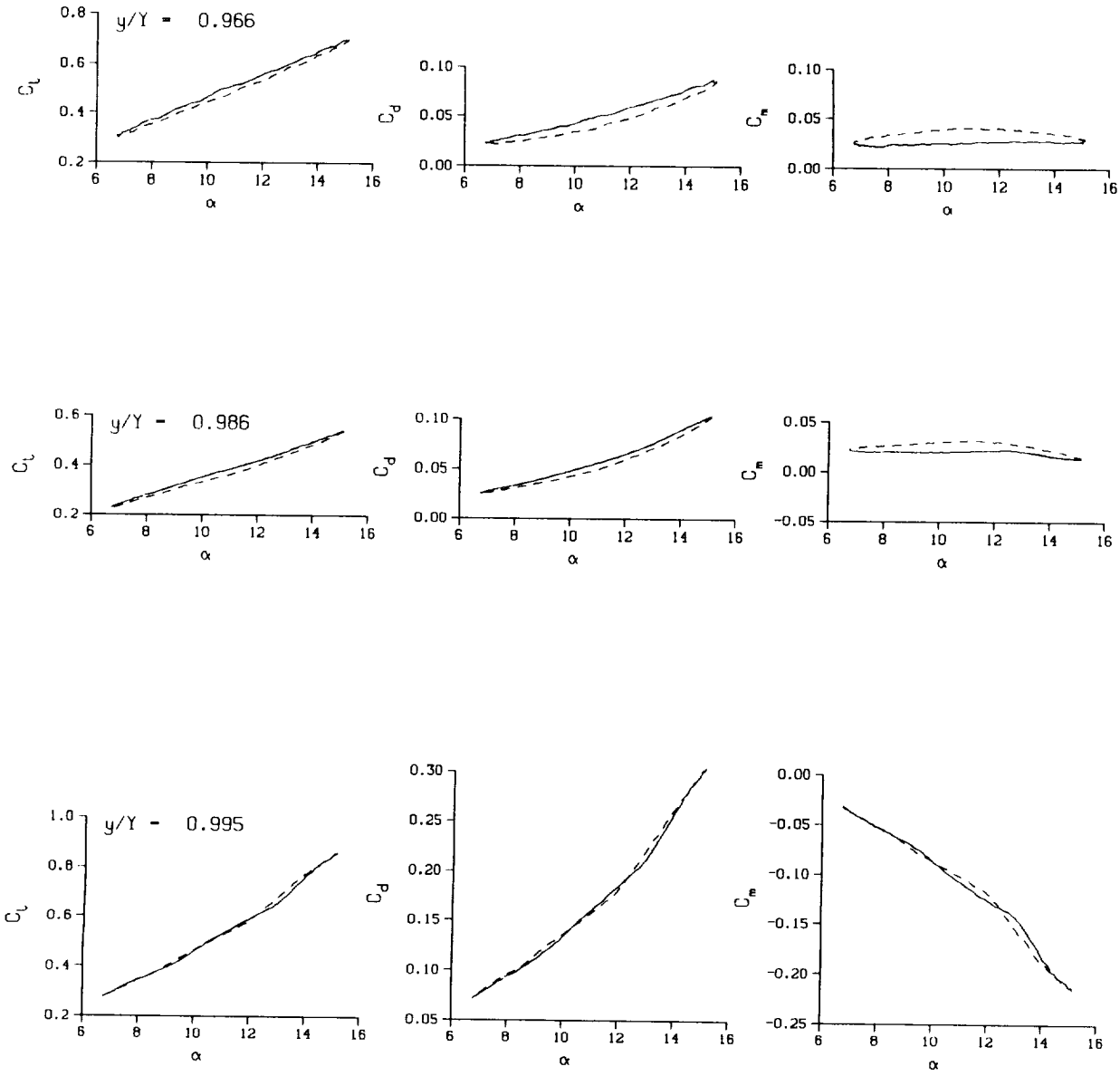

(b) v = 0.10. Concluded

Figure 42. Continued.

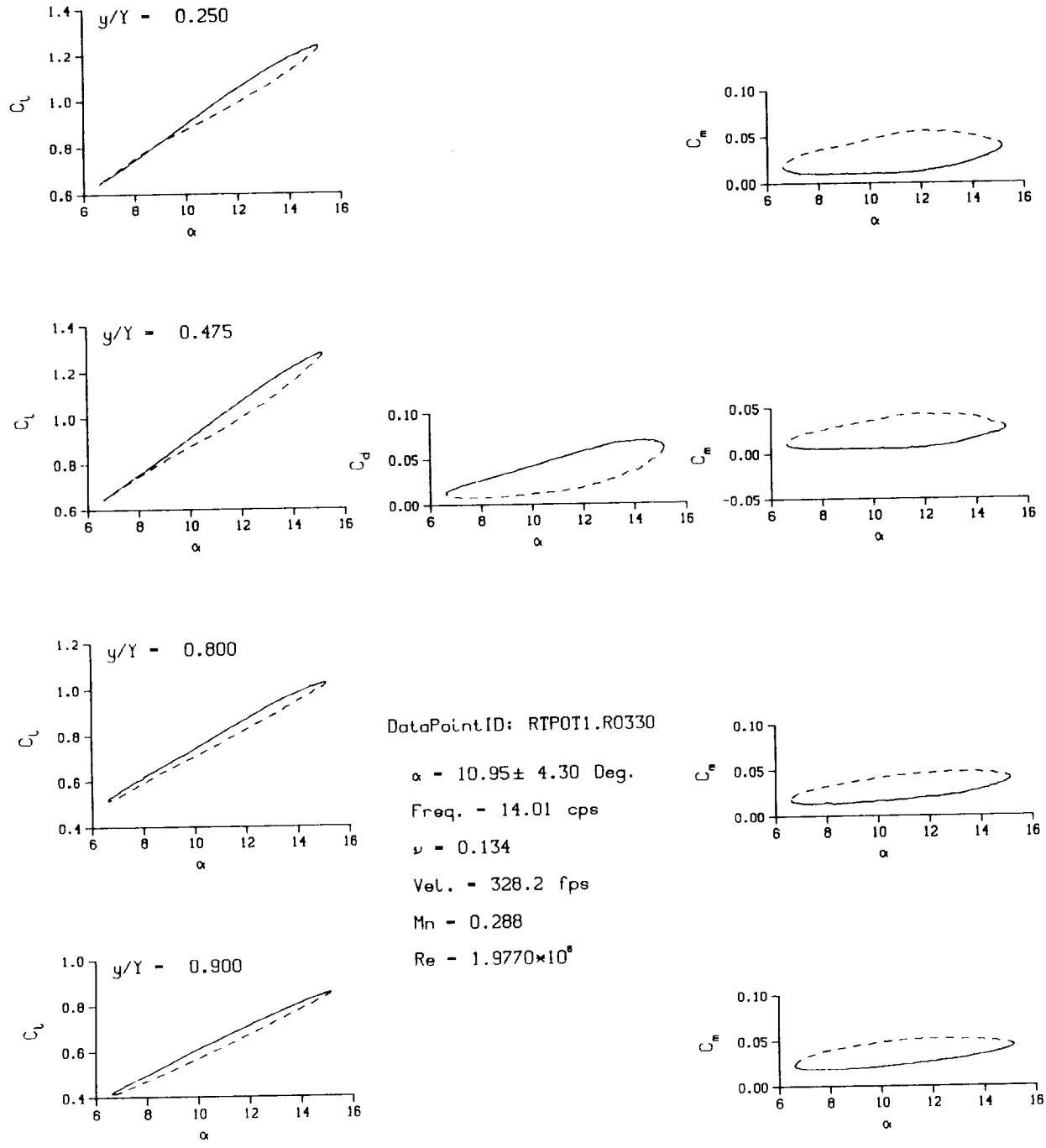

(c) v = 0.14

Figure 42. Continued.

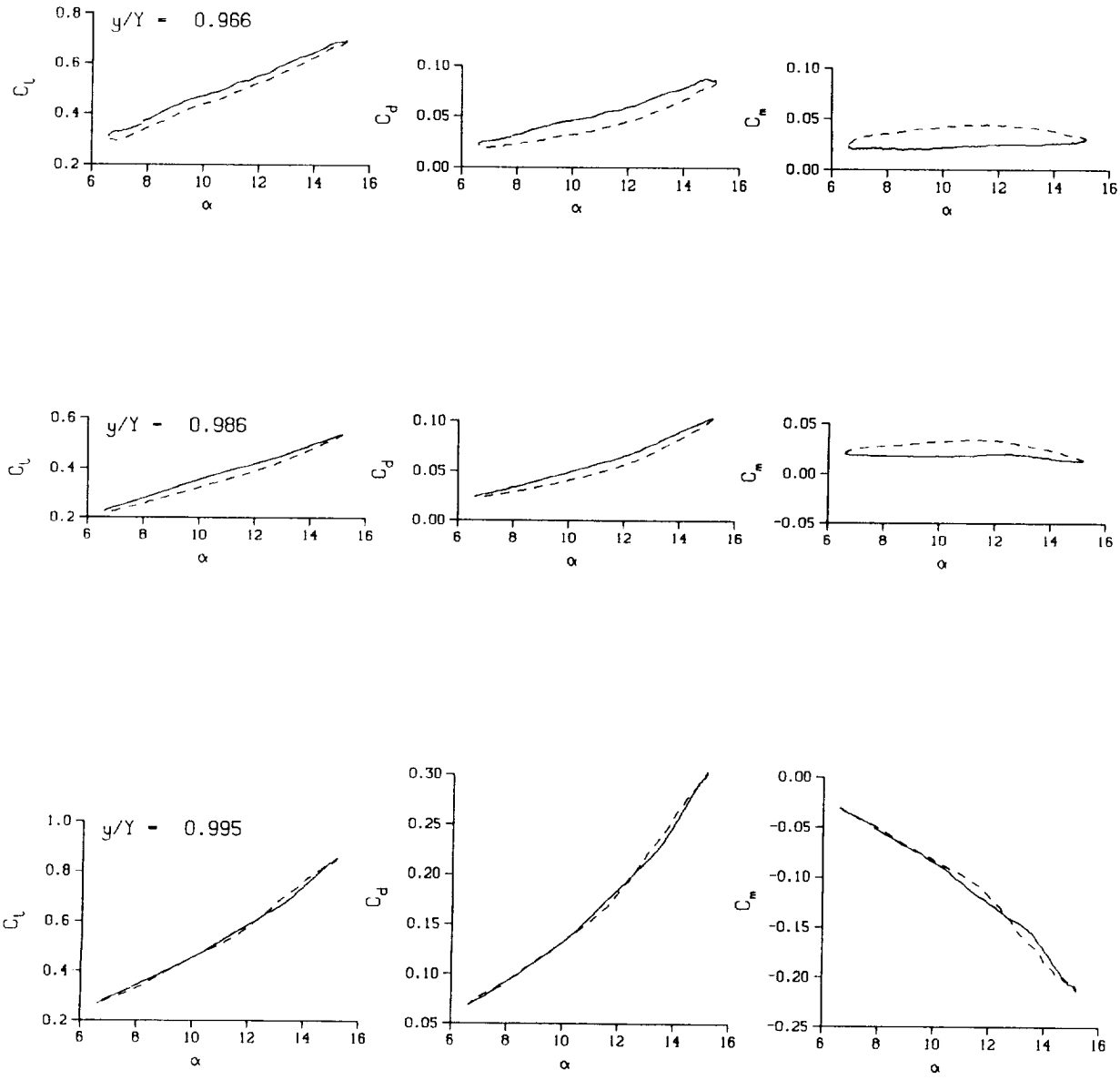

(c) v = 0.14. Concluded

Figure 42. Concluded.

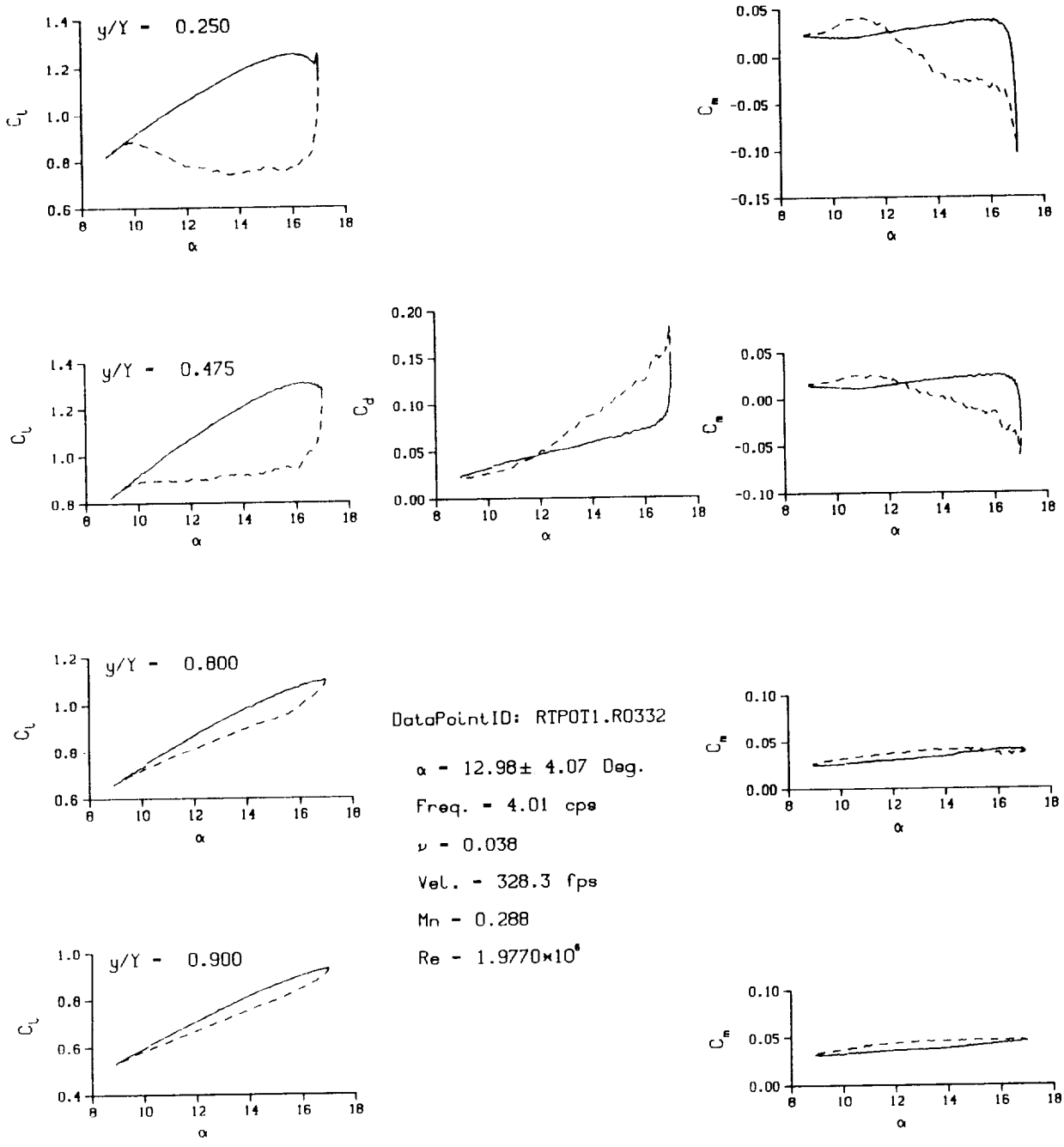

(a) v = 0.04

Figure 43. 3-D round tip pitch oscillation data; BL-trip; α = 13 ± 4 deg.

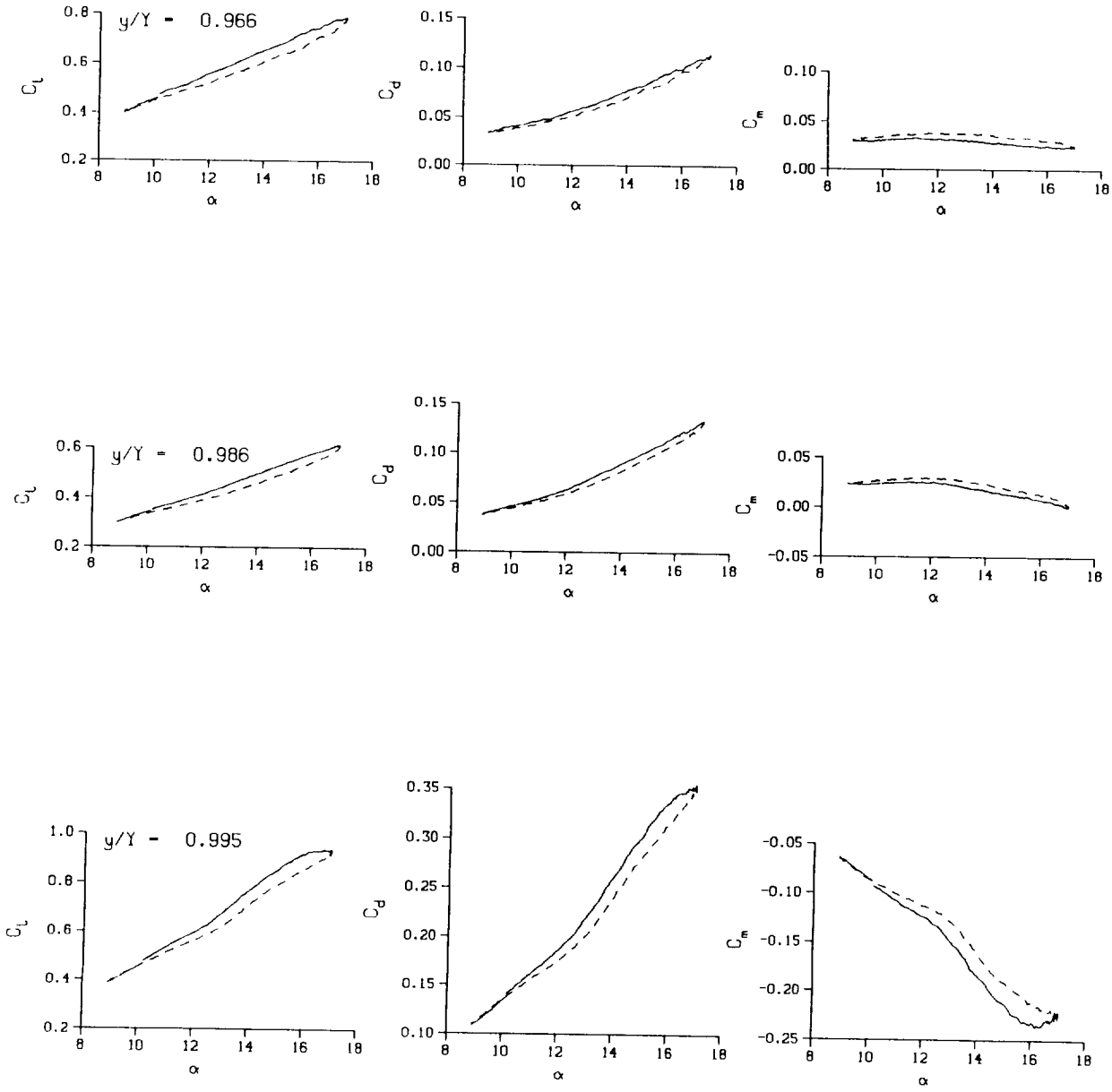

(a) v = 0.04. Concluded

Figure 43. Continued.

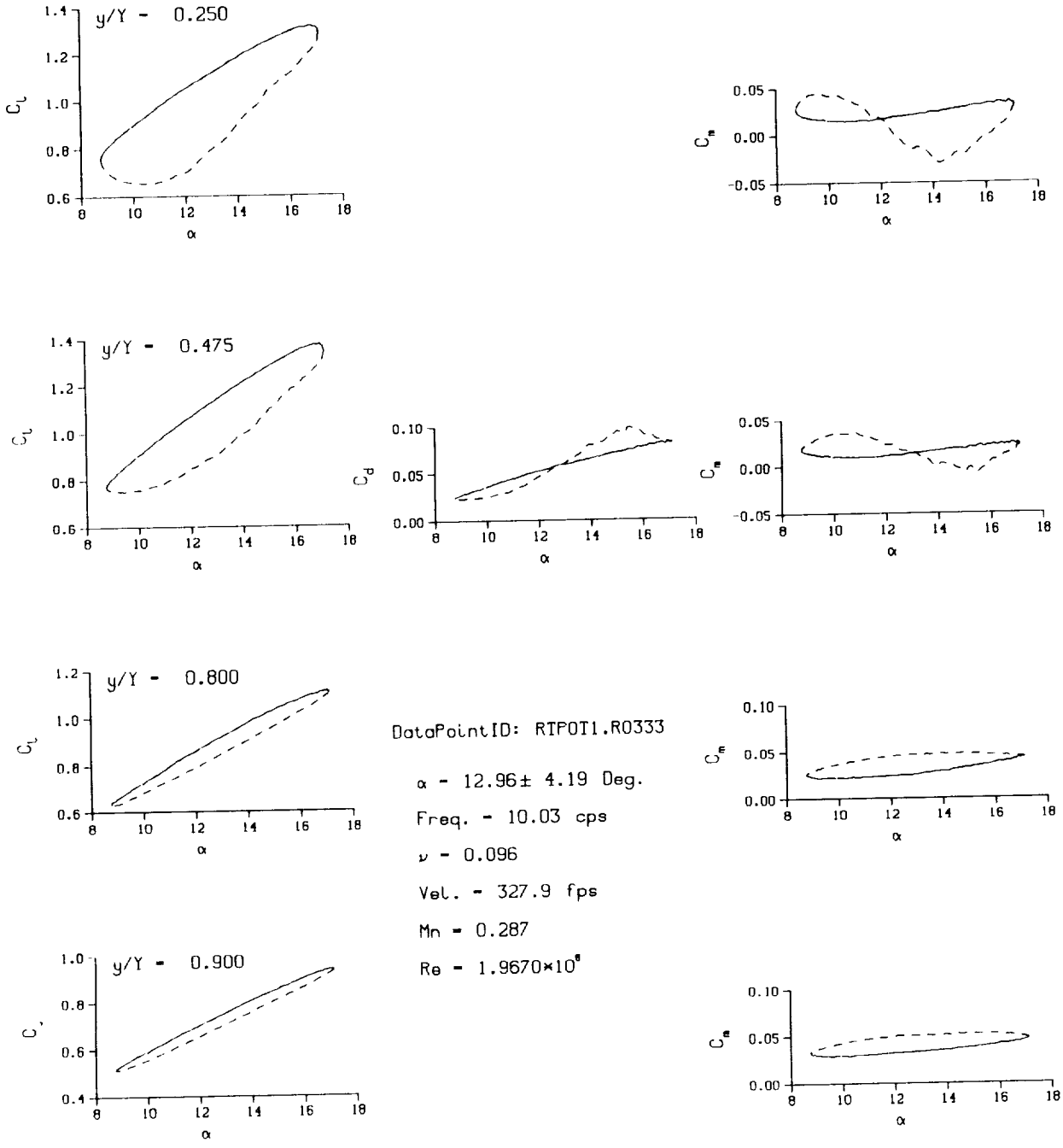

(b) ν = 0.10

Figure 43. Continued.

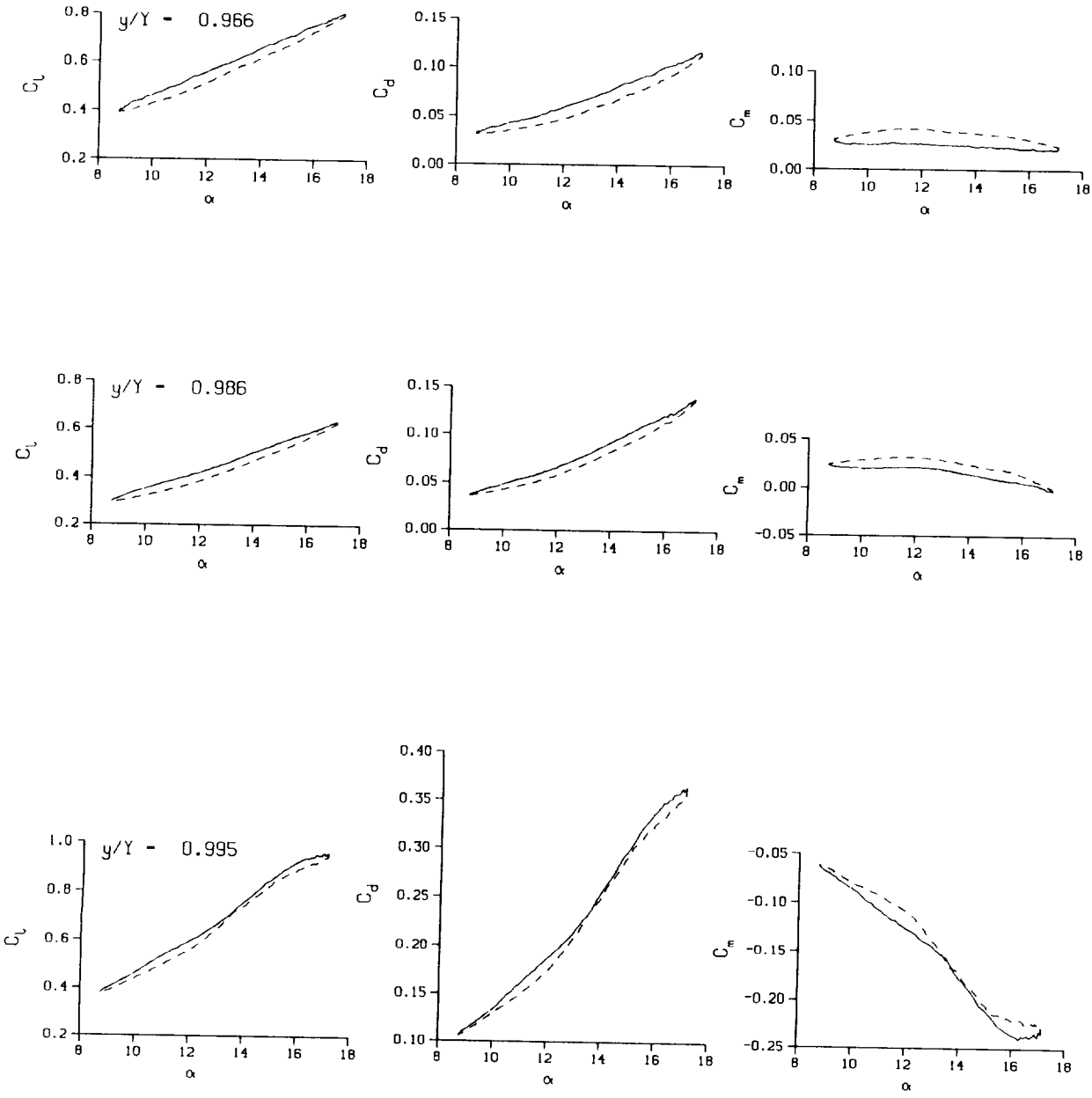

(b) v = 0.10. Concluded

Figure 43. Continued.

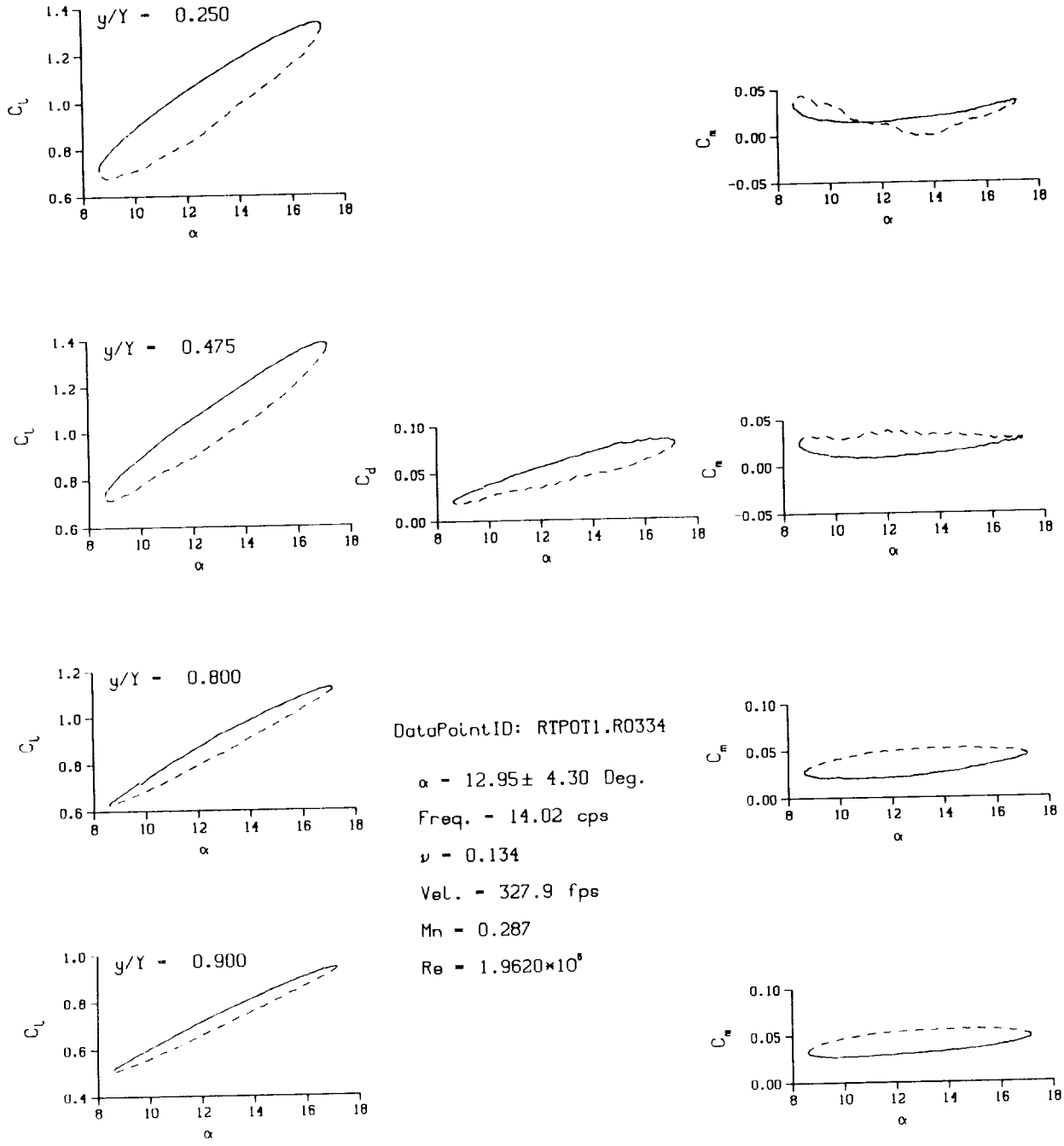

(c) v = 0.14

Figure 43. Continued.

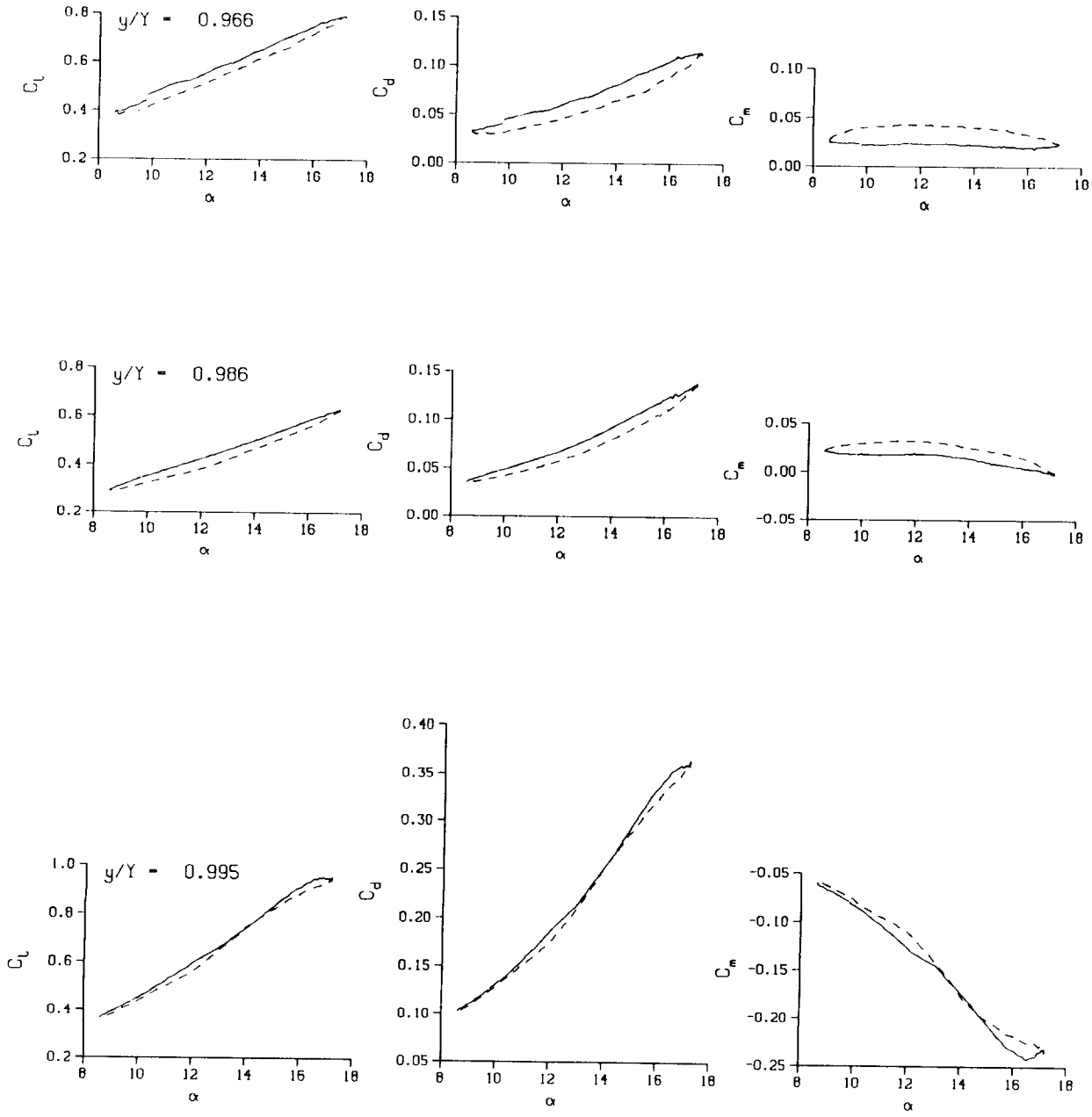

(c) v = 0.14. Concluded

Figure 43. Concluded.

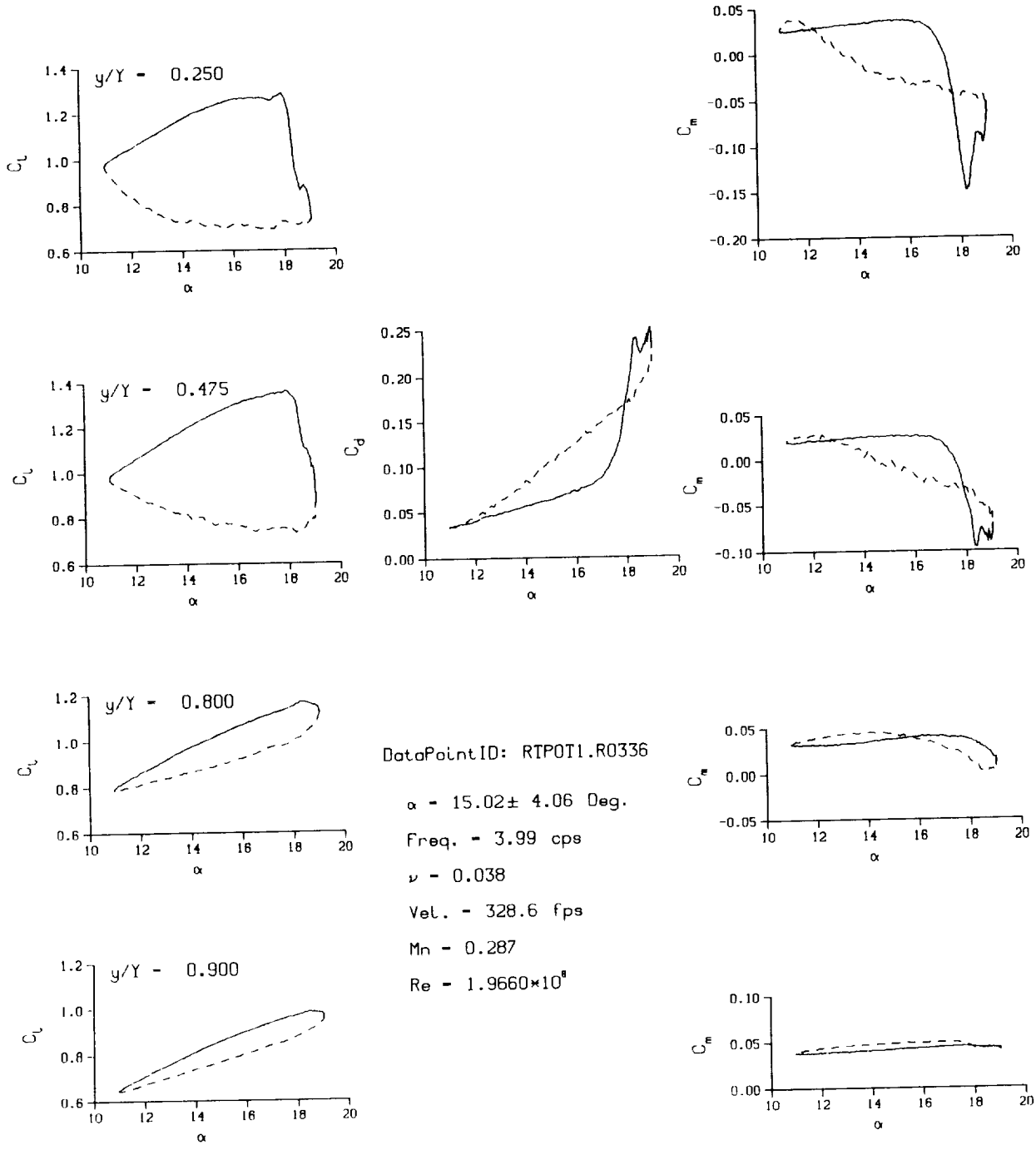

(a) ν = 0.04

Figure 44. 3-D round tip pitch oscillation data; BL-trip; α = 15 ± 4 deg.

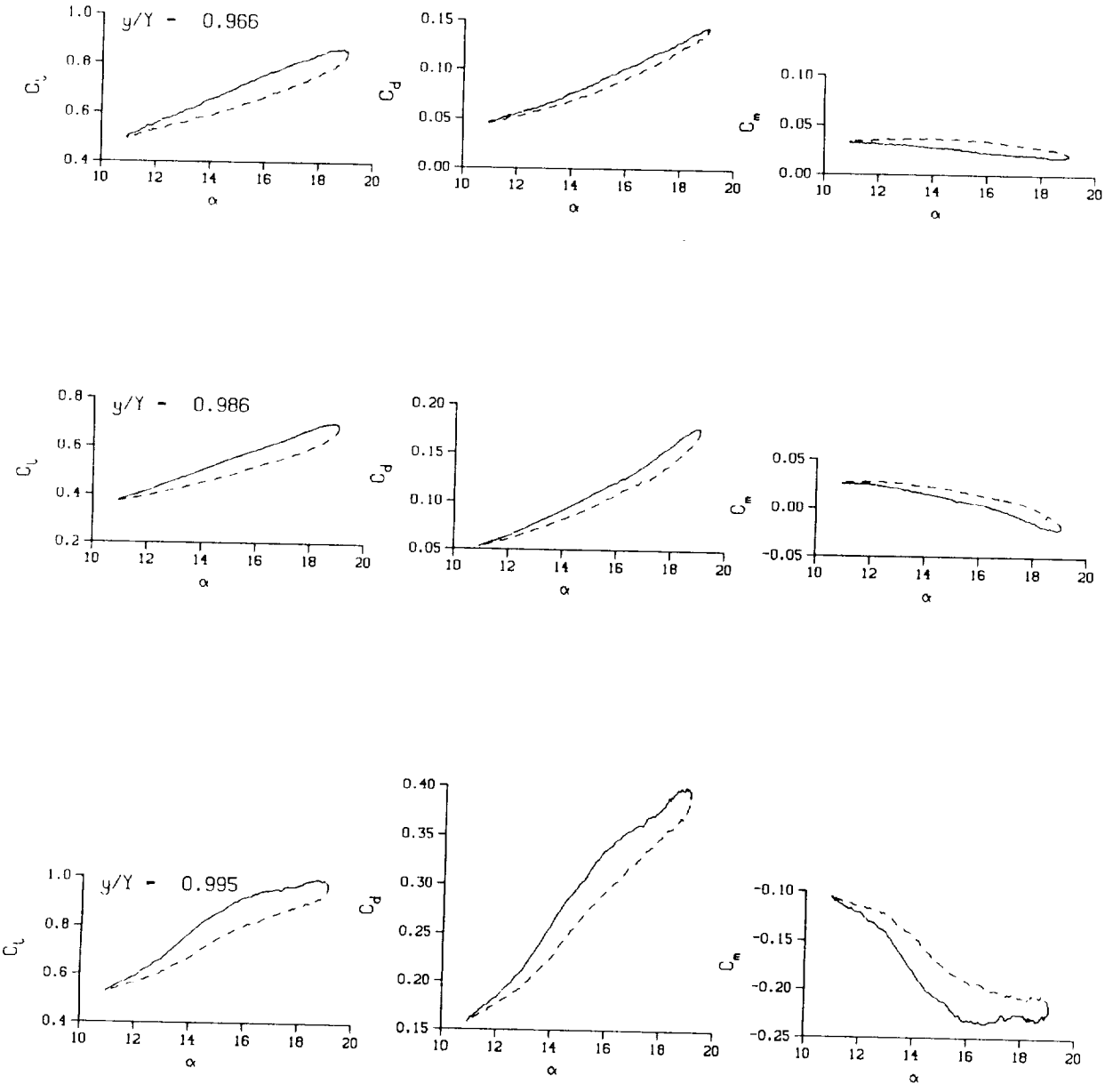

(a) v = 0.04. Concluded

Figure 44. Continued.

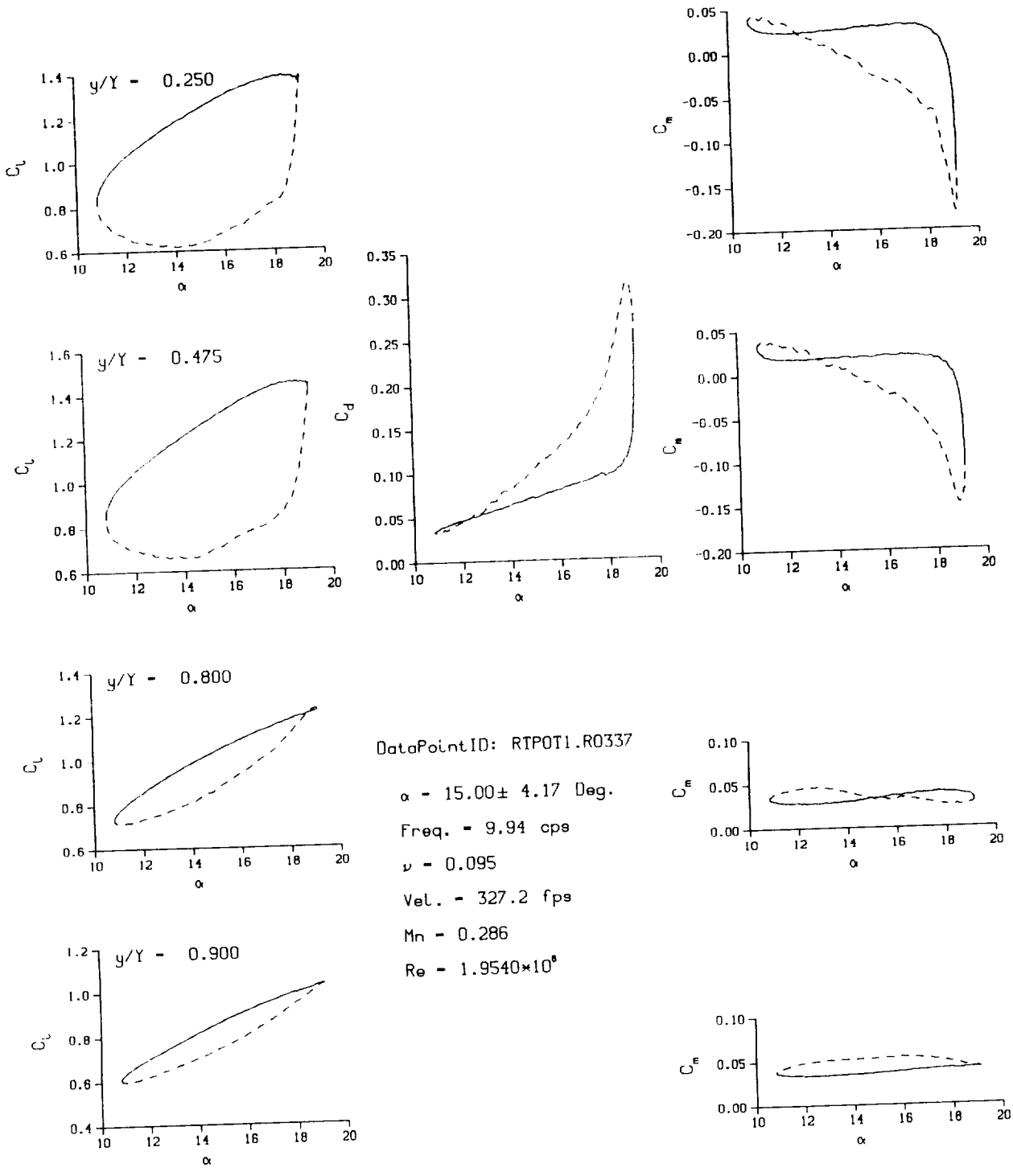

(b) ν = 0.10

Figure 44. Continued.

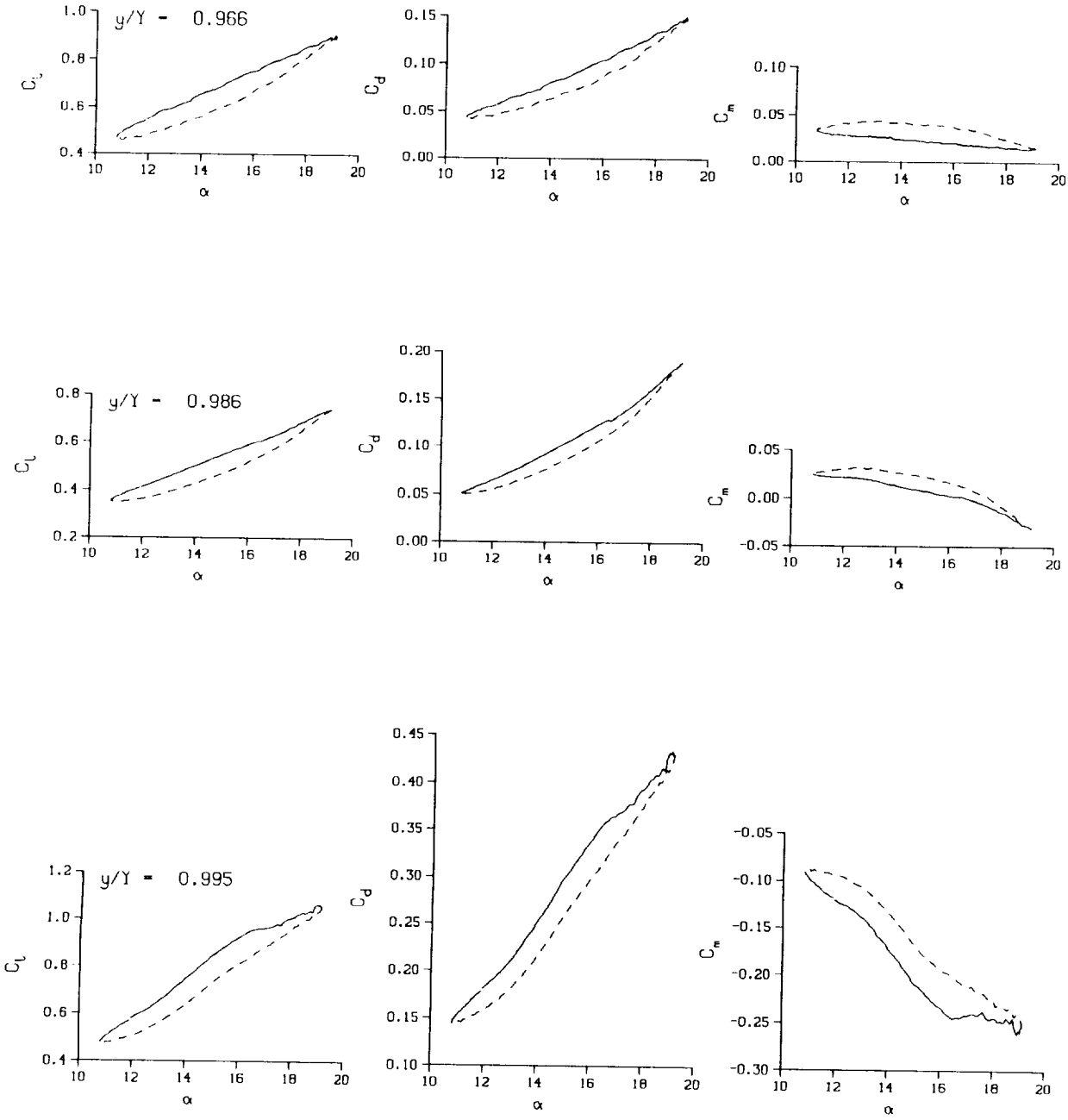

(b) v = 0.10. Concluded

Figure 44. Continued.

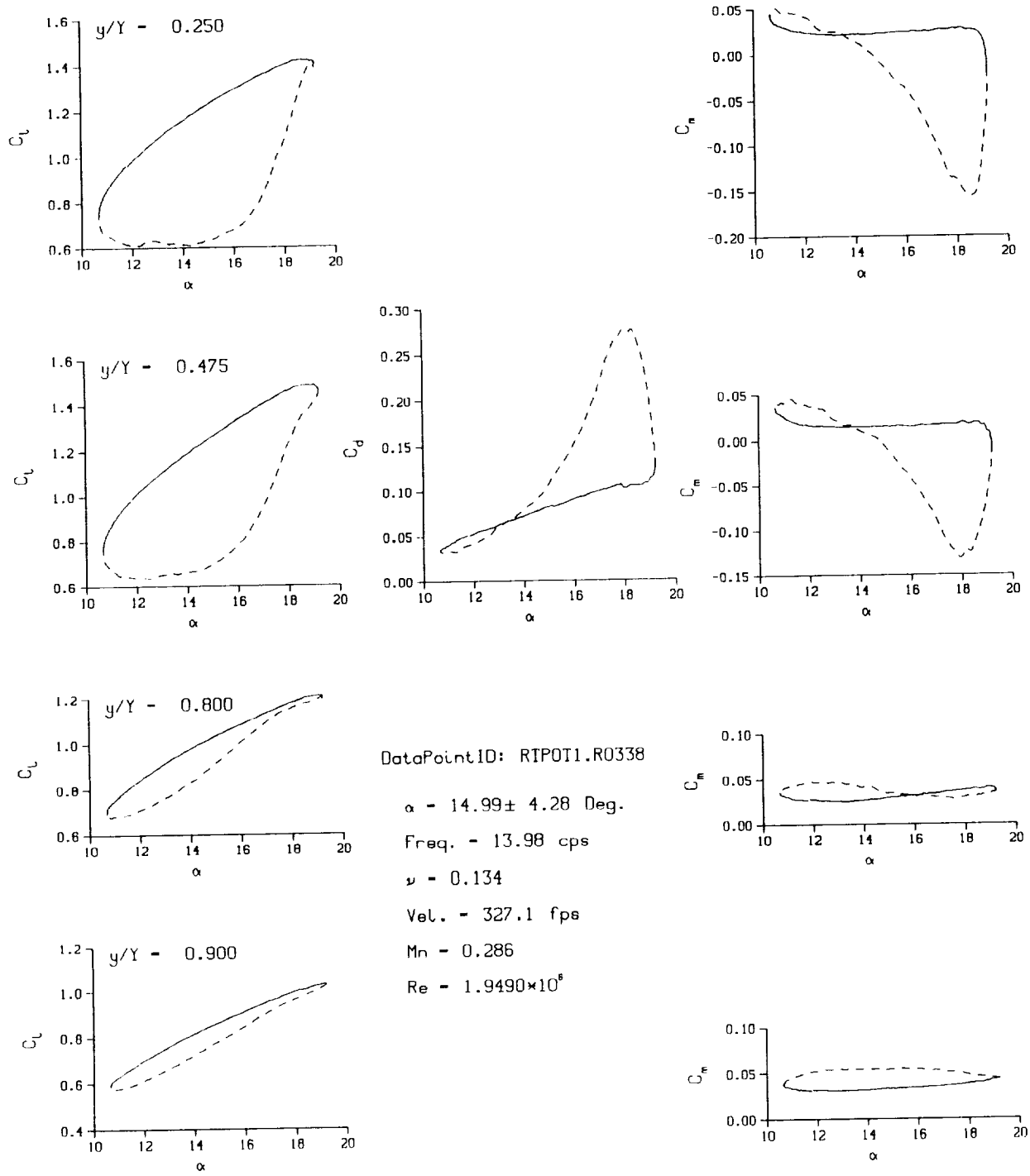

(c) v = 0.14

Figure 44. Continued.

C-3

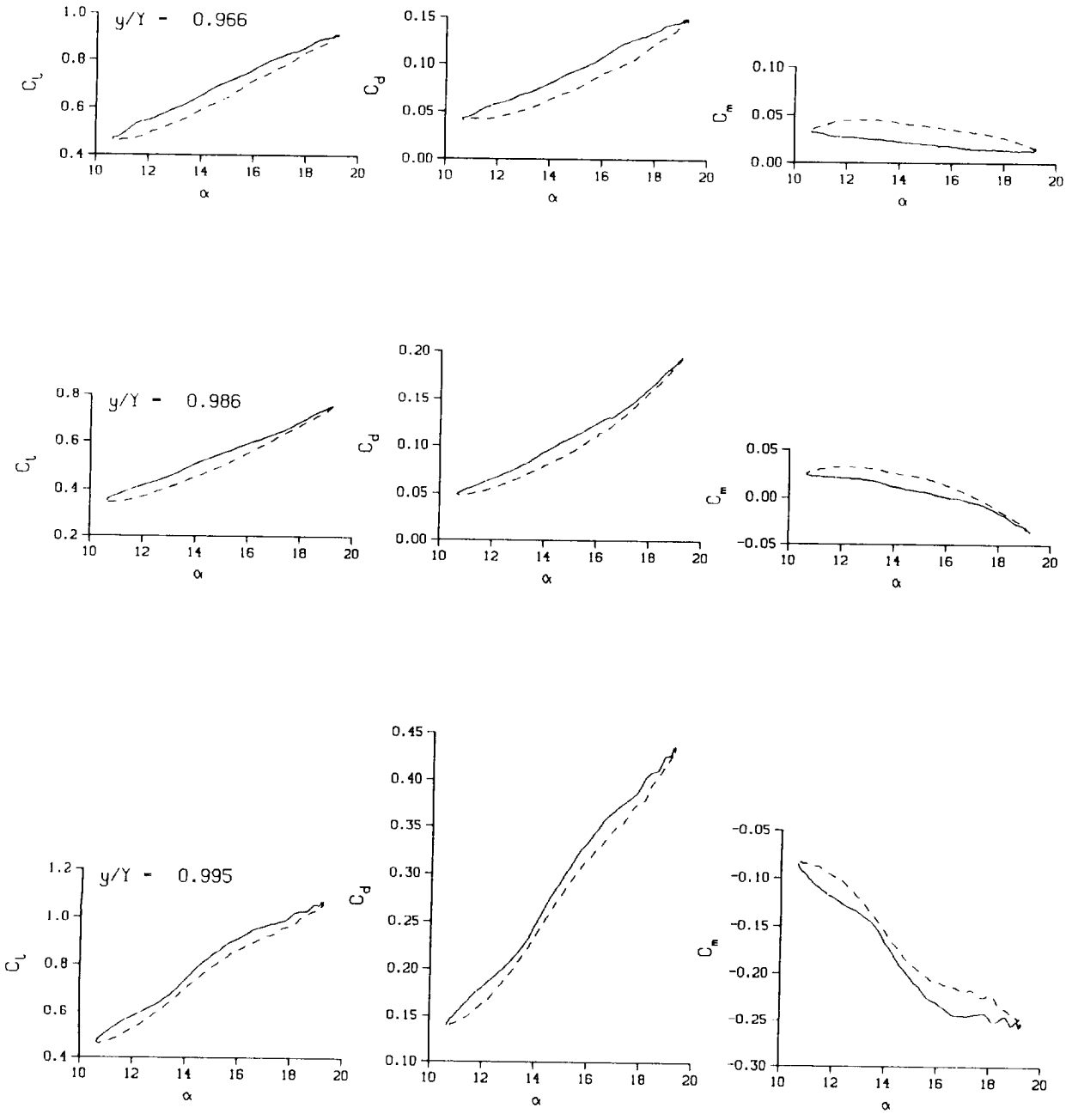

(c) v = 0.14. Concluded

Figure 44. Concluded.

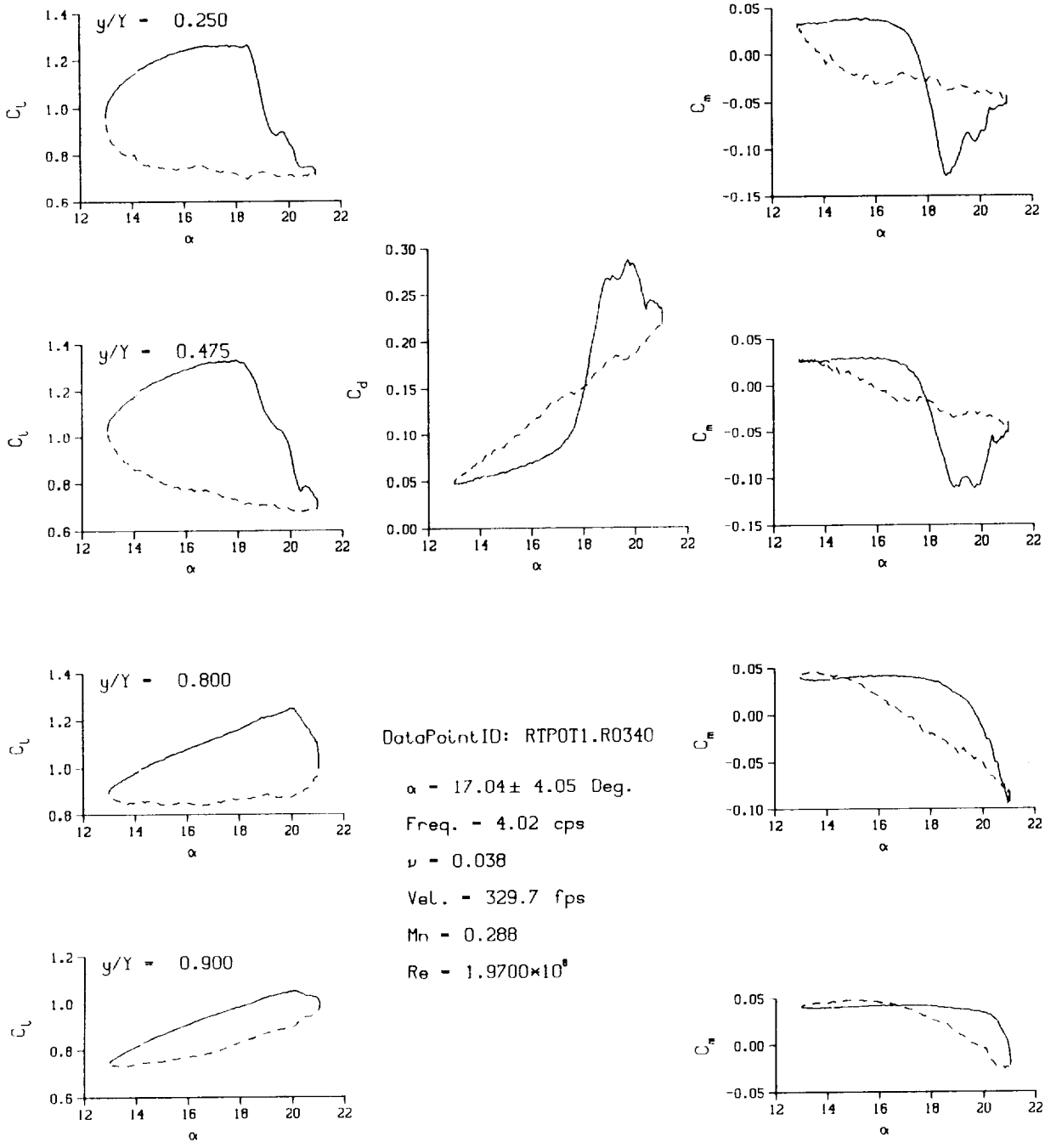

(a) v = 0.04

Figure 45. 3-D round tip pitch oscillation data; BL-trip; α = 17 ± 4 deg.

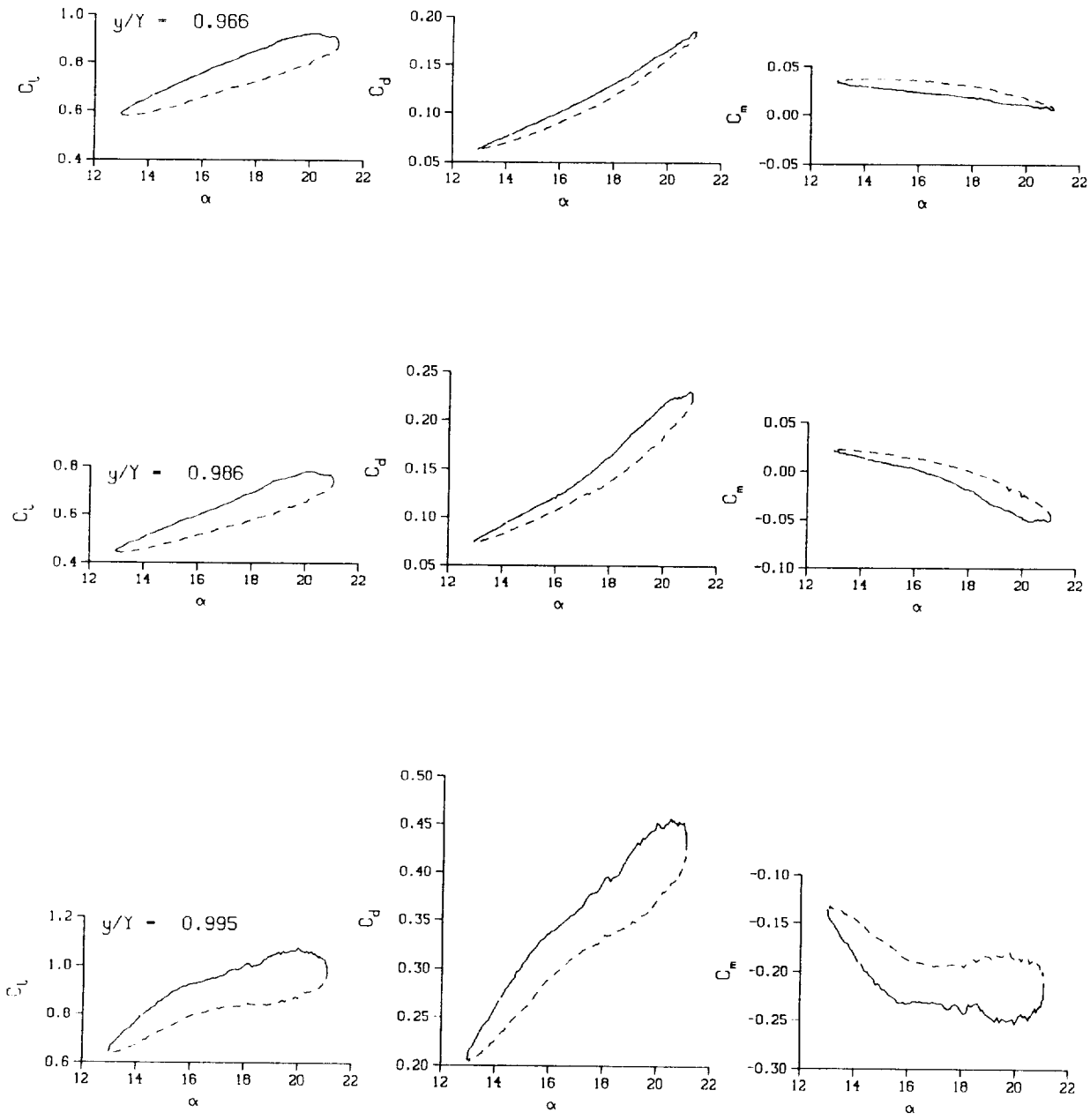

(a) v = 0.04. Concluded

Figure 45. Continued.

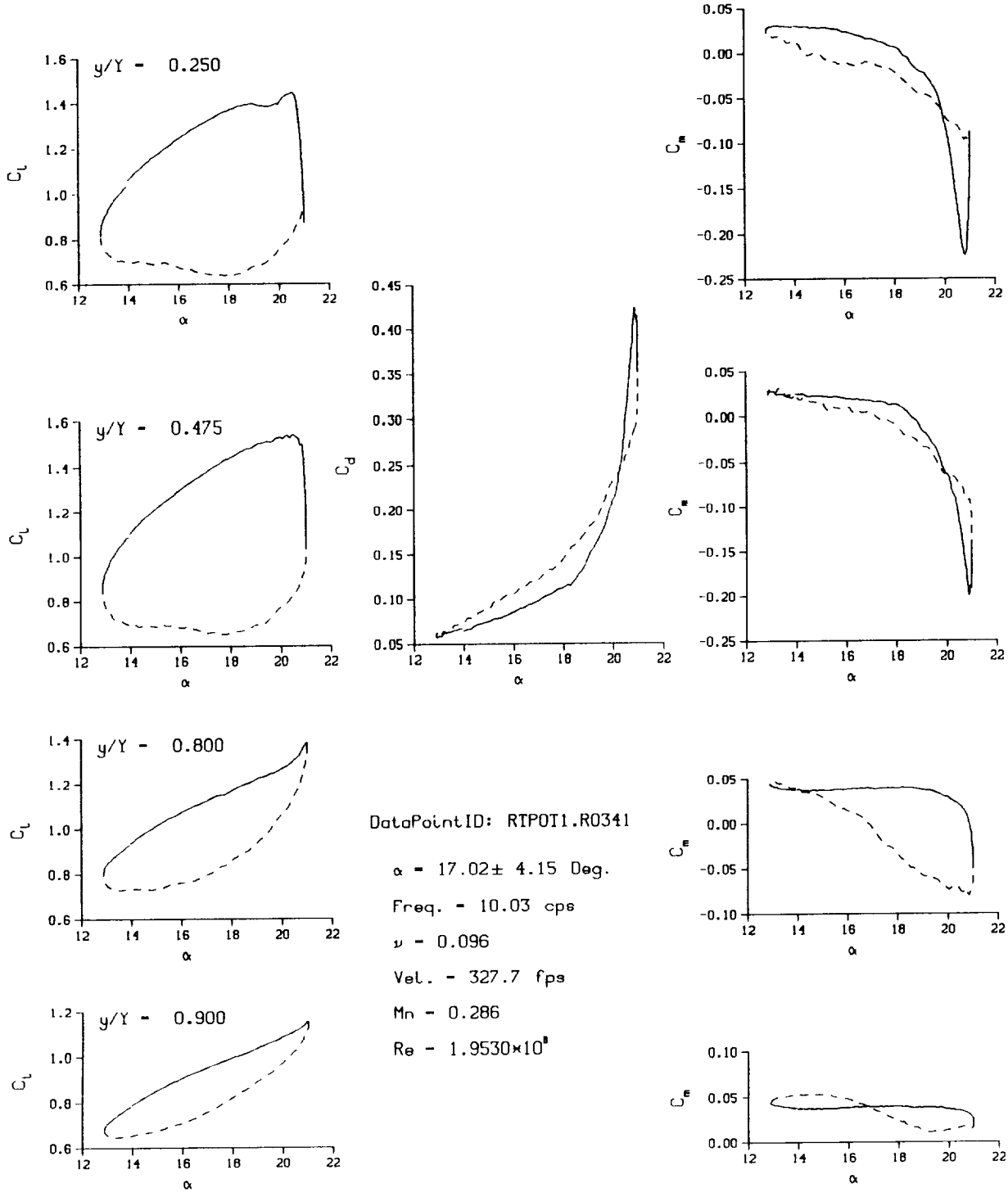

(b) v = 0.10

Figure 45. Continued.

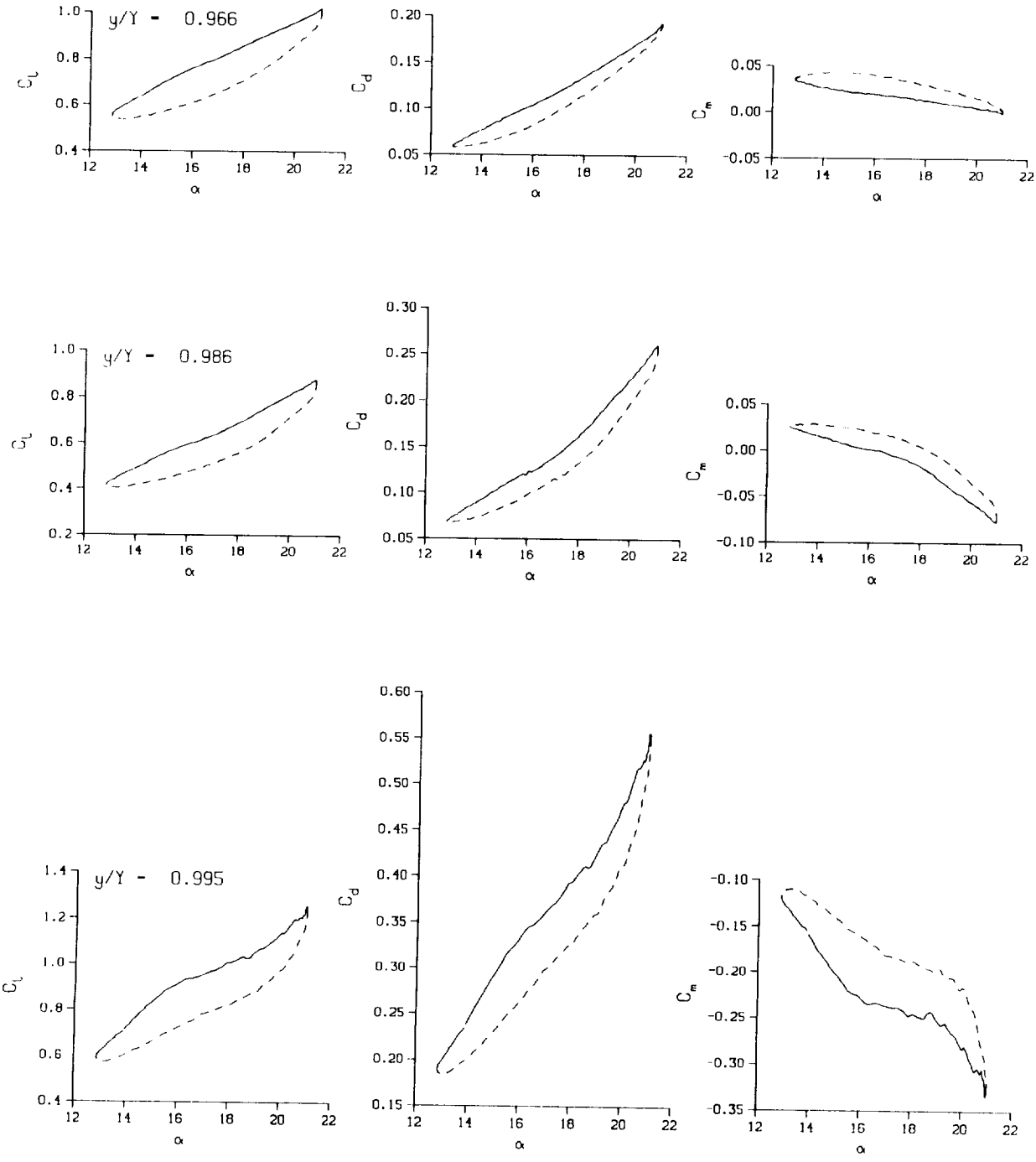

(b) v = 0.10. Concluded

Figure 45. Continued.

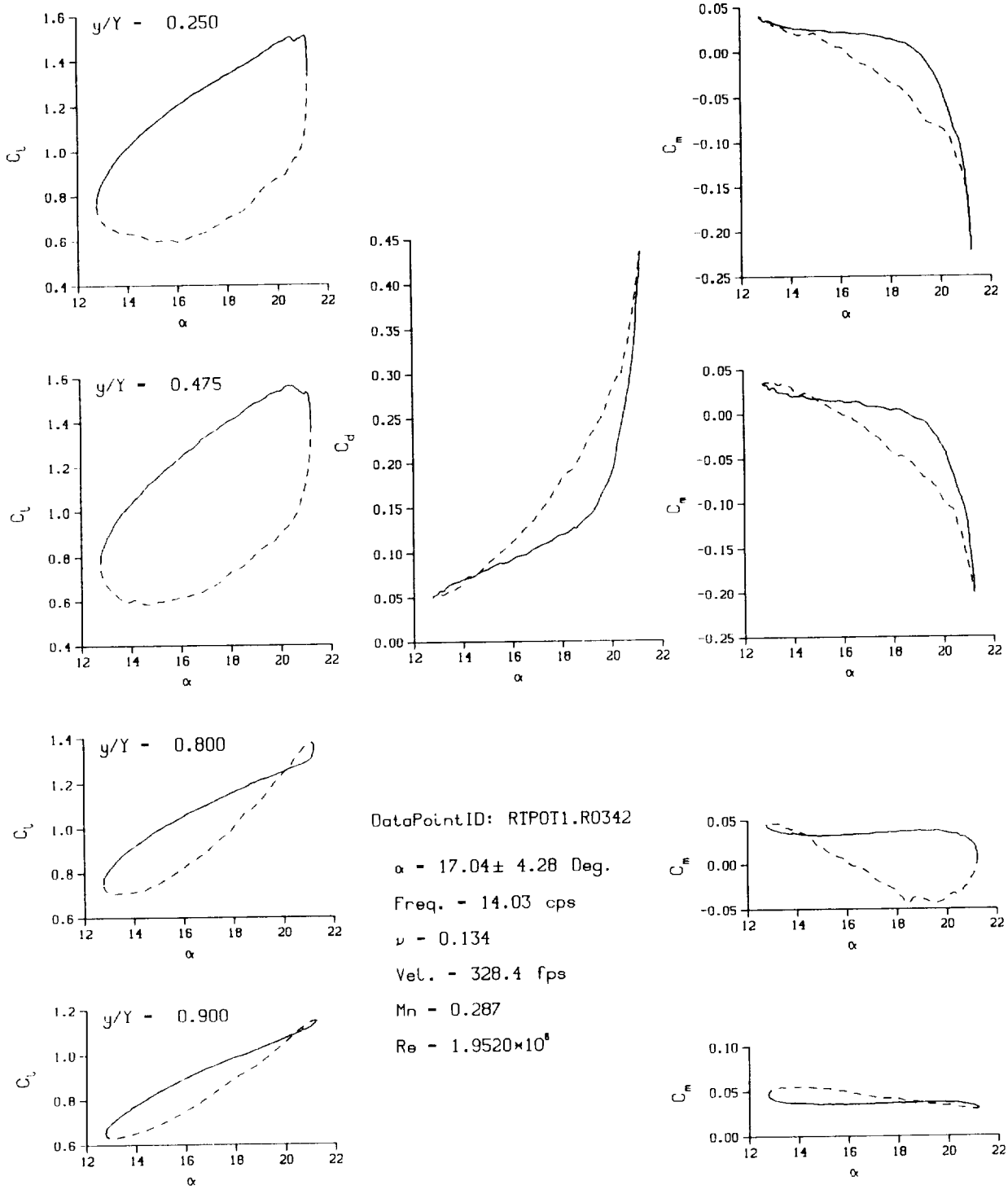

(c) $\nu = 0.14$

Figure 45. Continued.

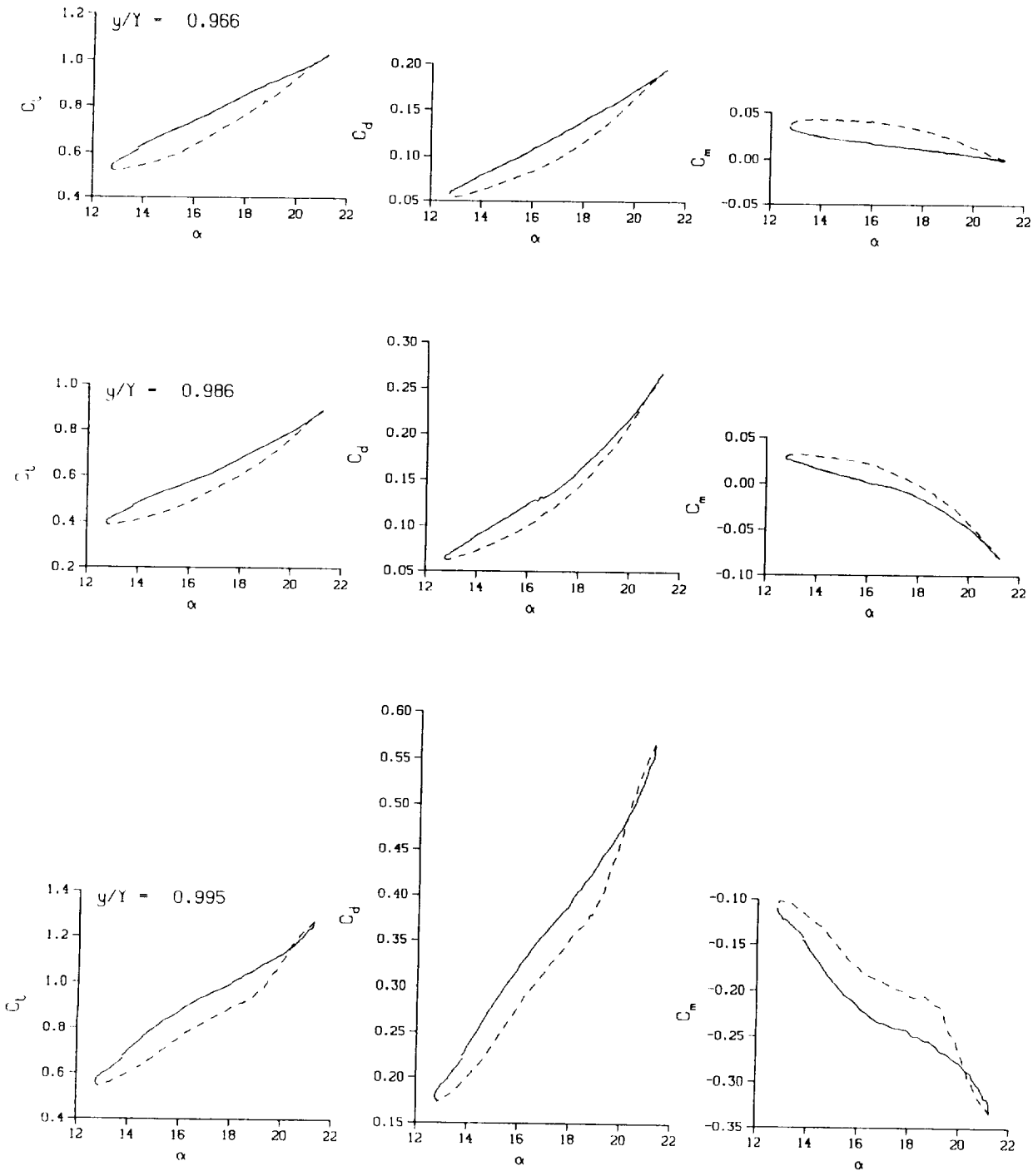

(c) v = 0.14. Concluded

Figure 45. Concluded.

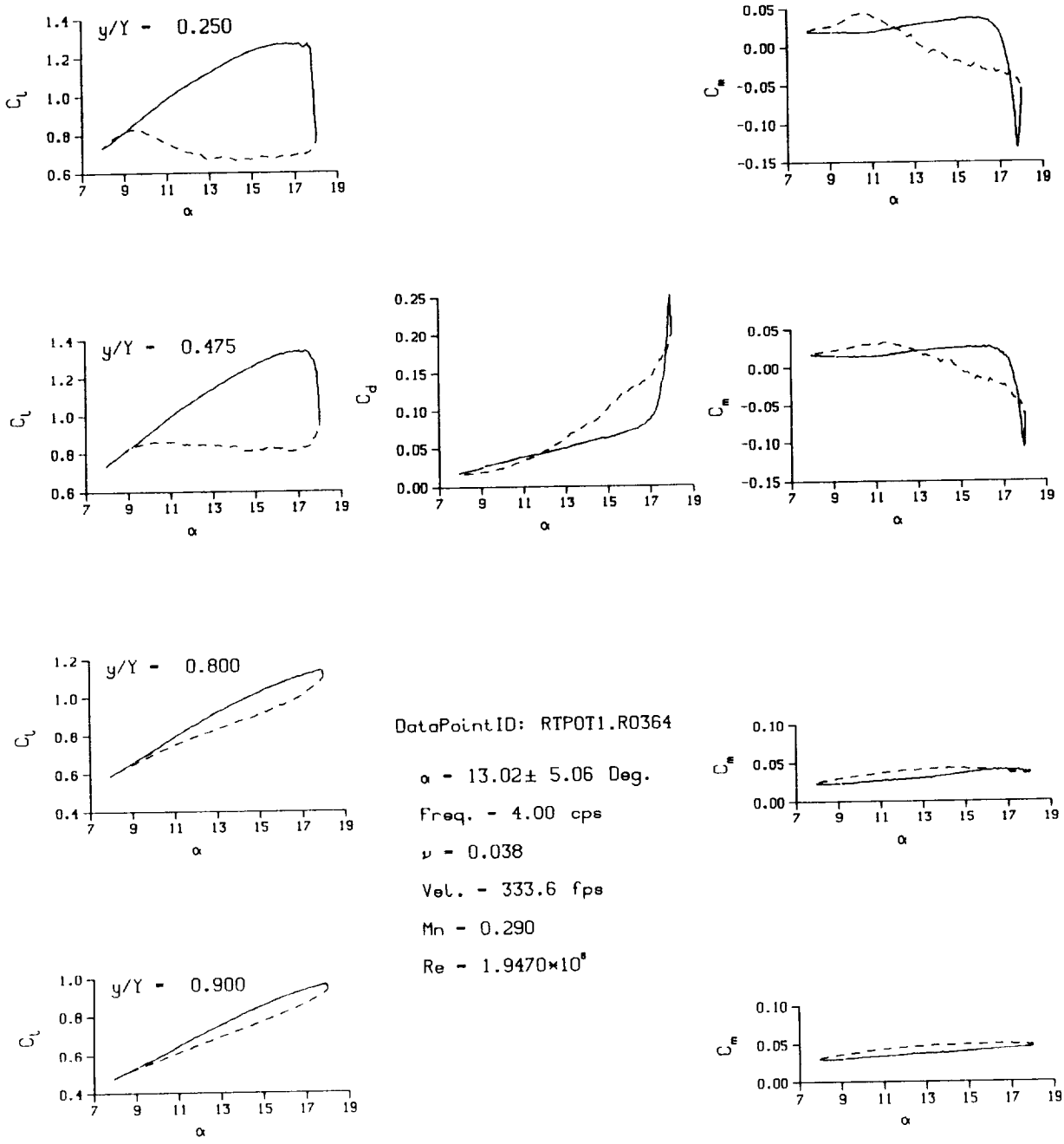

(a) ν = 0.04

Figure 46. 3-D round tip pitch oscillation data; BL-trip; α = 13 ± 5 deg.

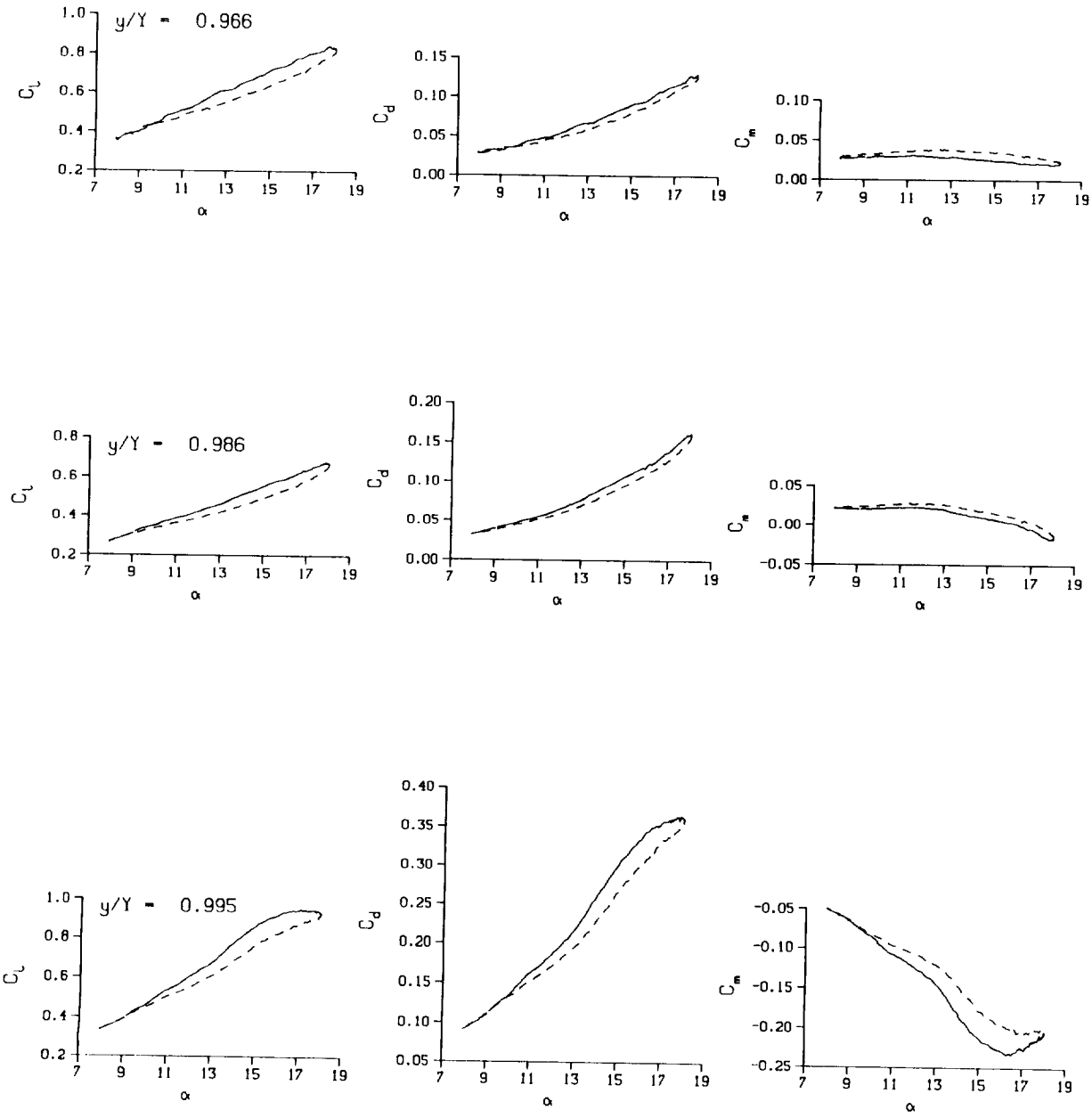

(a) v = 0.04. Concluded

Figure 46. Continued.

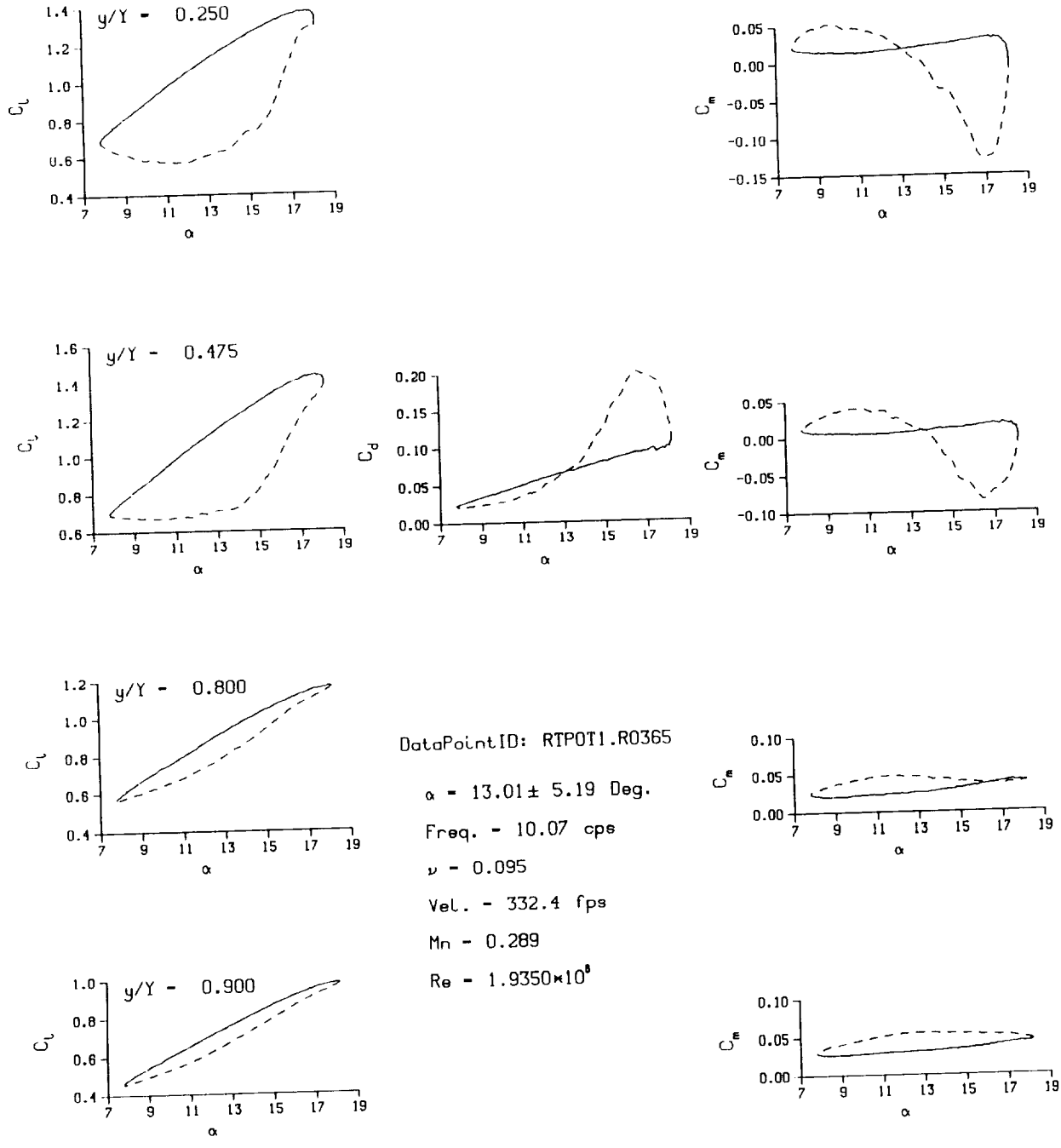

(b) v = 0.10

Figure 46. Continued.

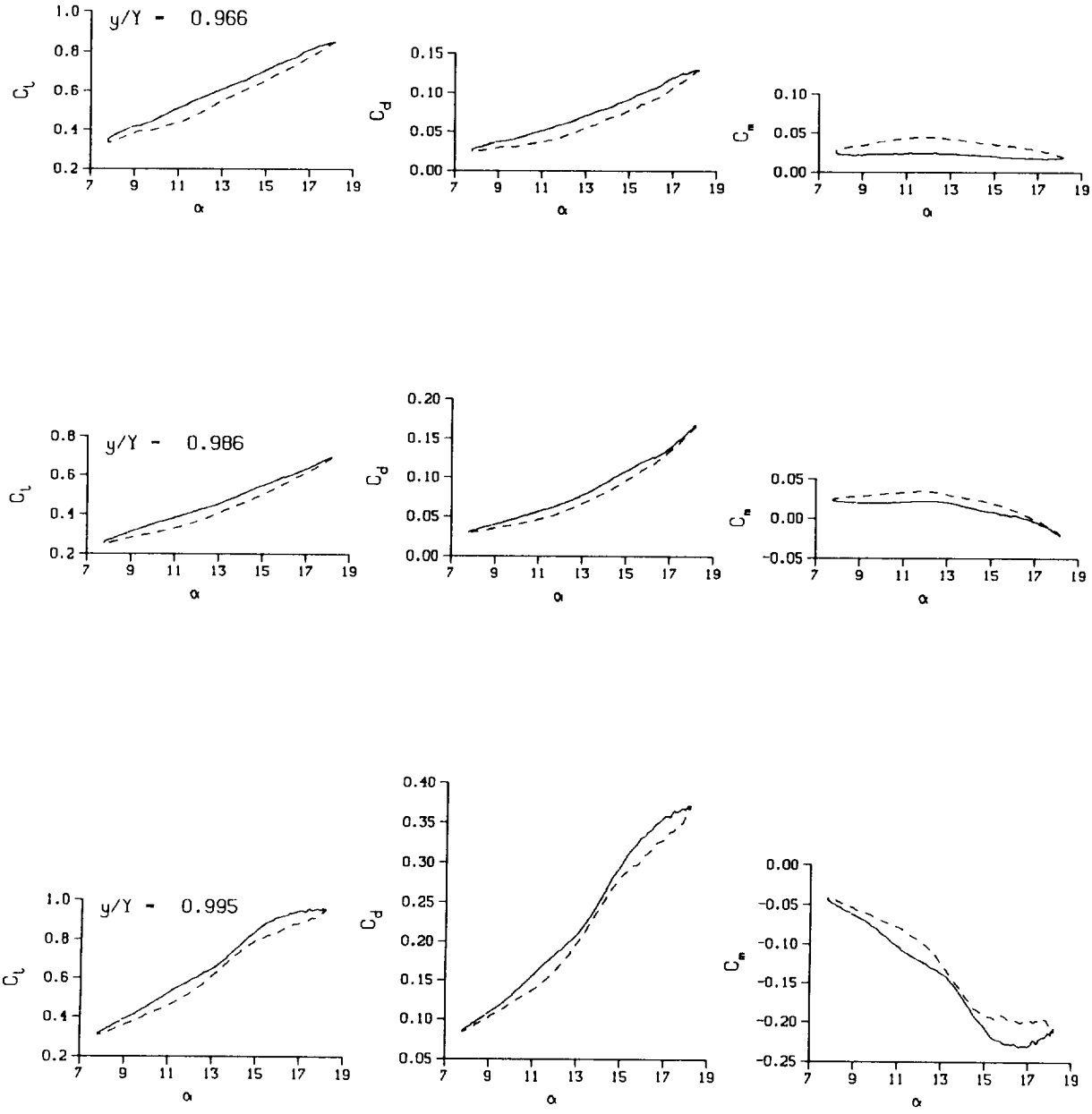

(b) v = 0.10. Concluded

Figure 46. Concluded.

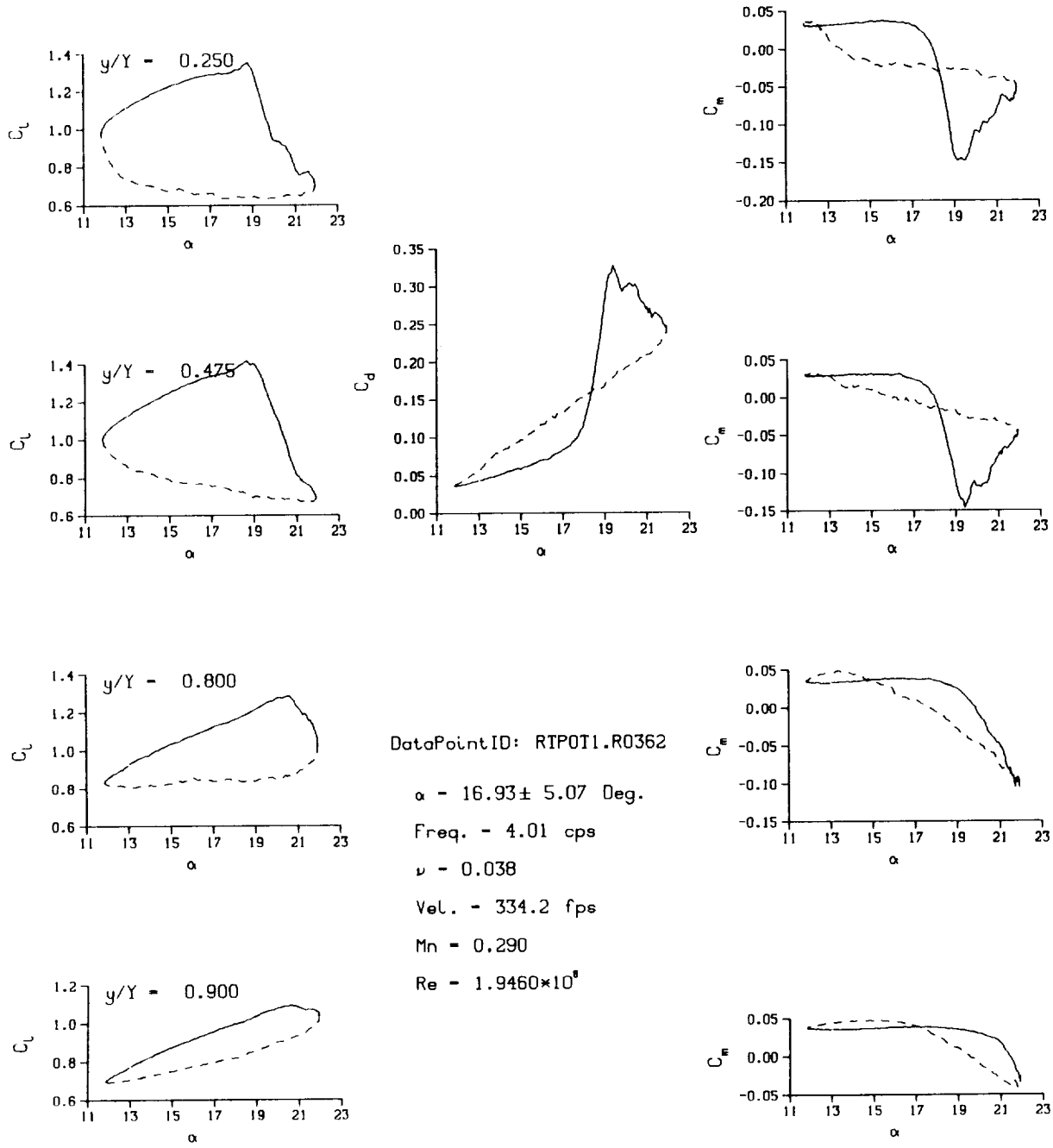

(a) v = 0.04

Figure 47. 3-D round tip pitch oscillation data; BL-trip; α = 17 ± 5 deg.

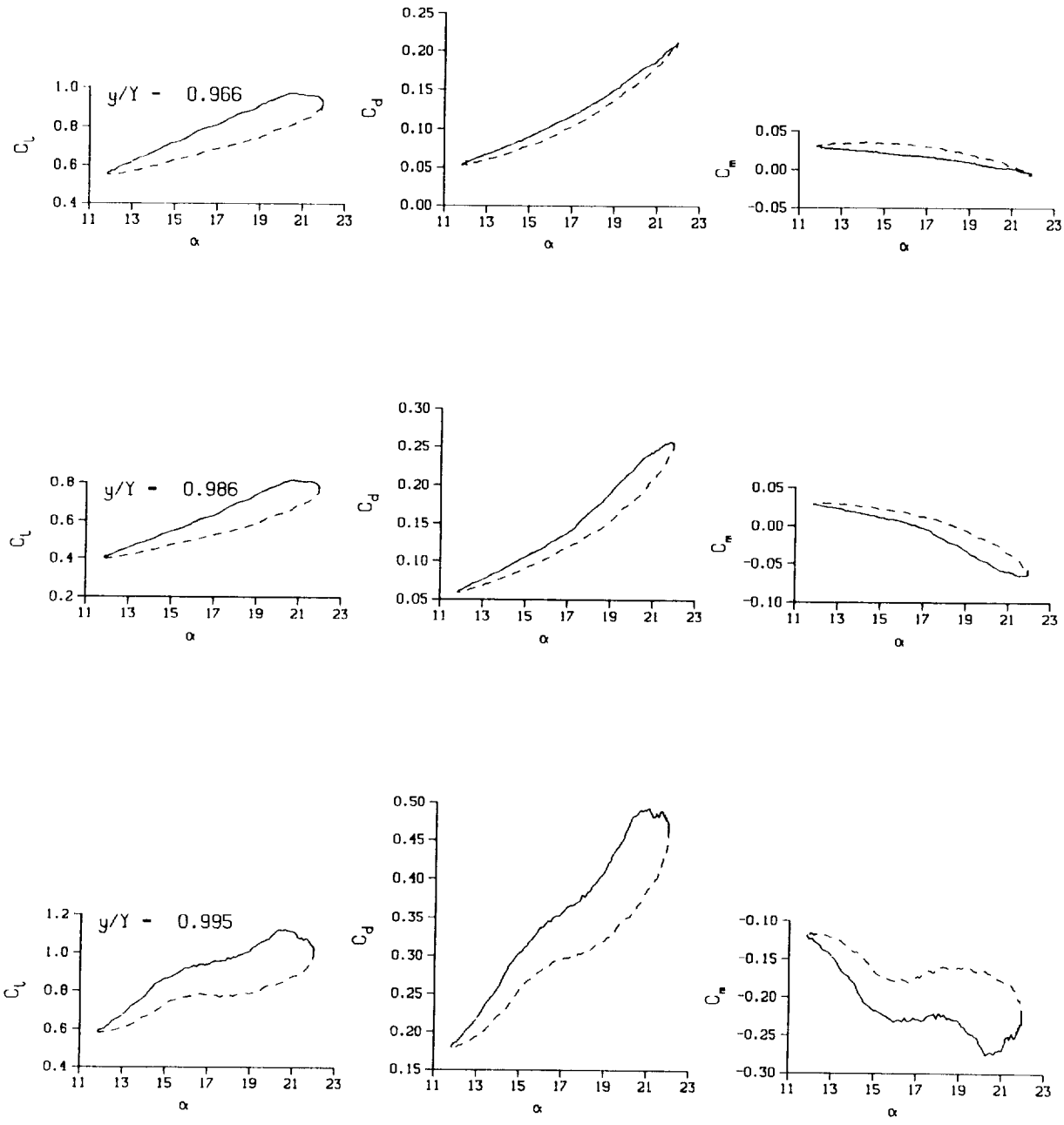

(a) v = 0.04. Concluded

Figure 47. Continued.

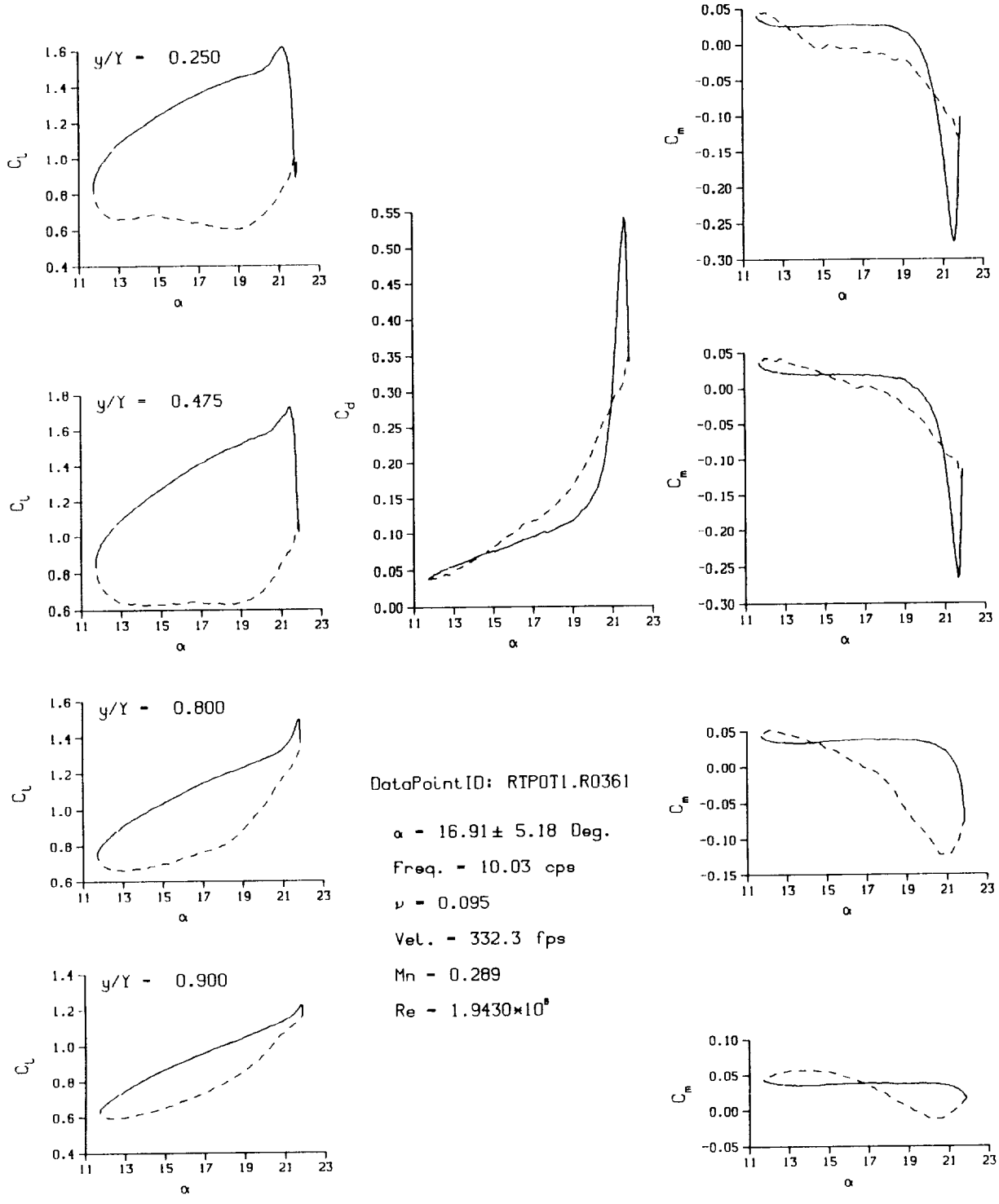

(b) v = 0.10

Figure 47. Continued.

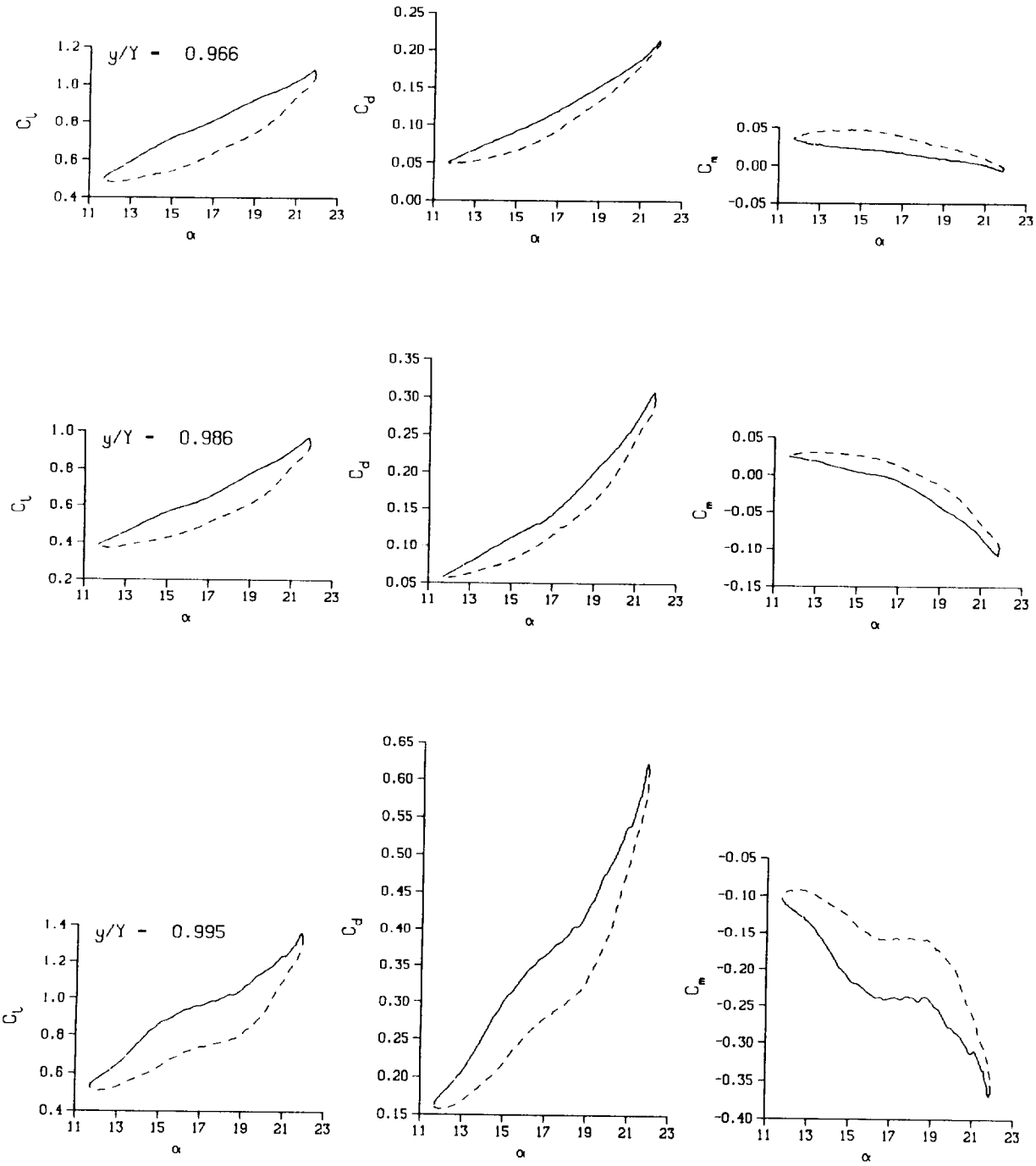

(b) v = 0.10. Concluded

Figure 47. Concluded.

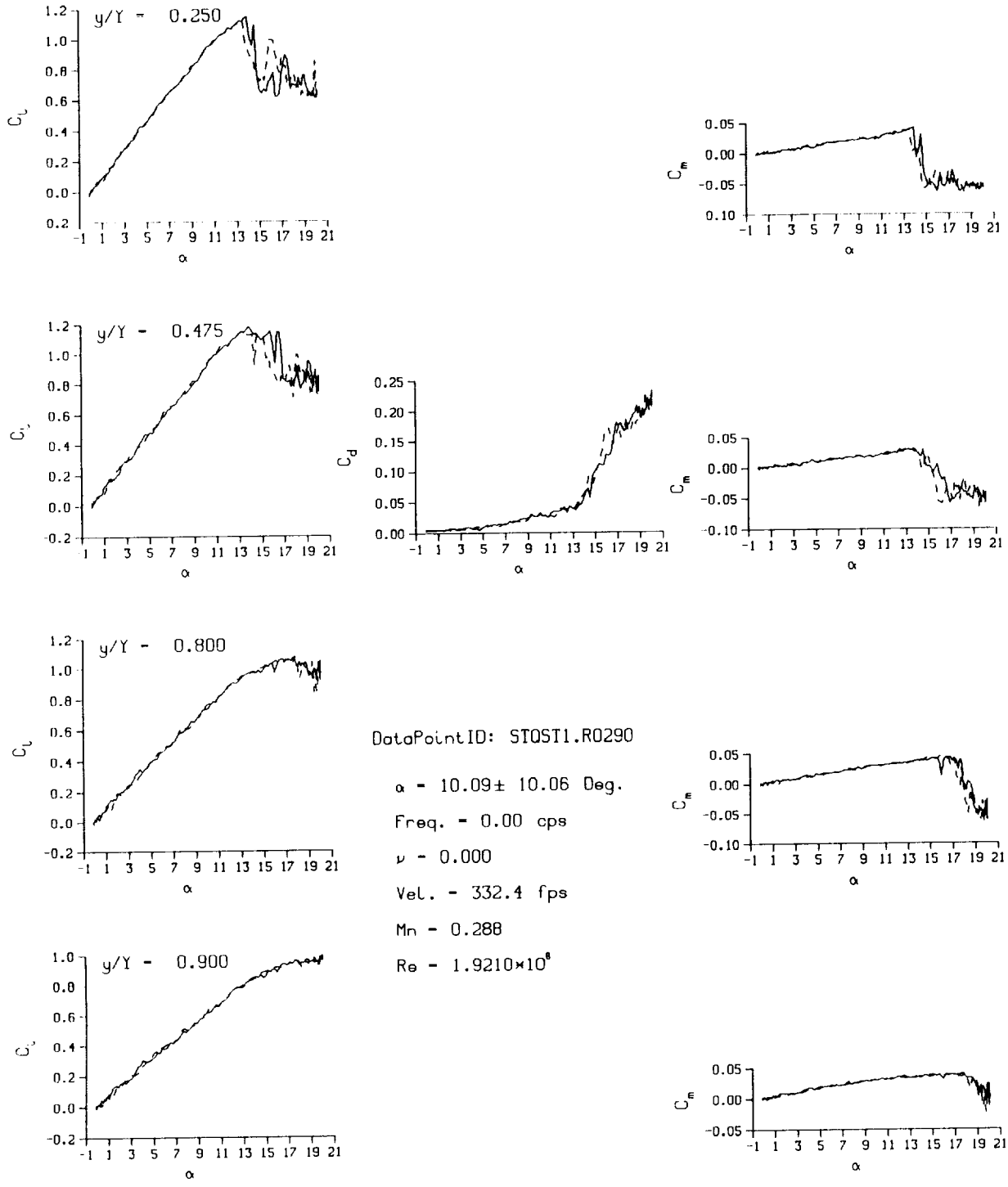

(a) Repeat no. 1

Figure 48. 3-D square tip quasi-steady data; BL-trip; $0 \leq \alpha \leq 20$ deg.

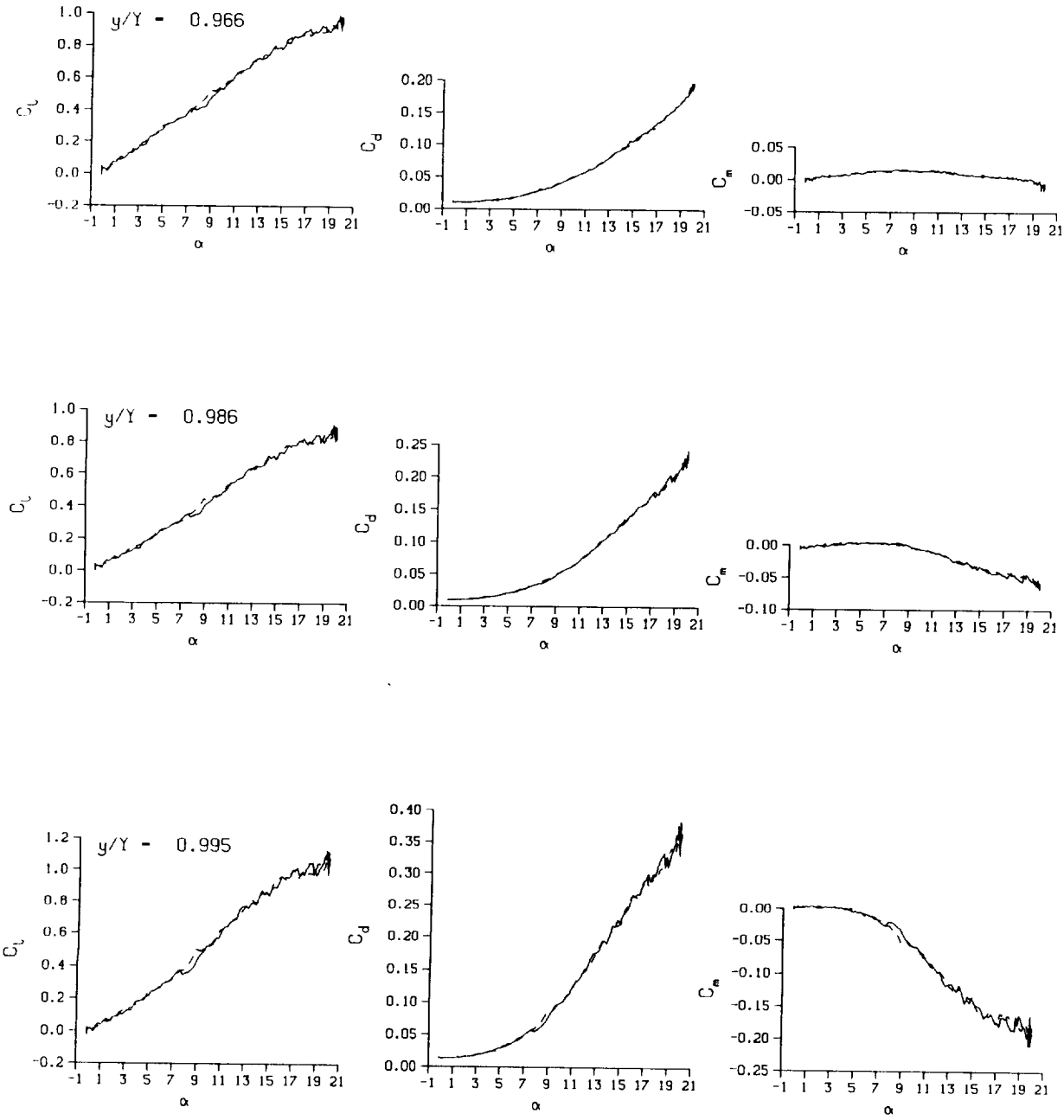

(a) Repeat no. 1. Concluded

Figure 48. Continued.

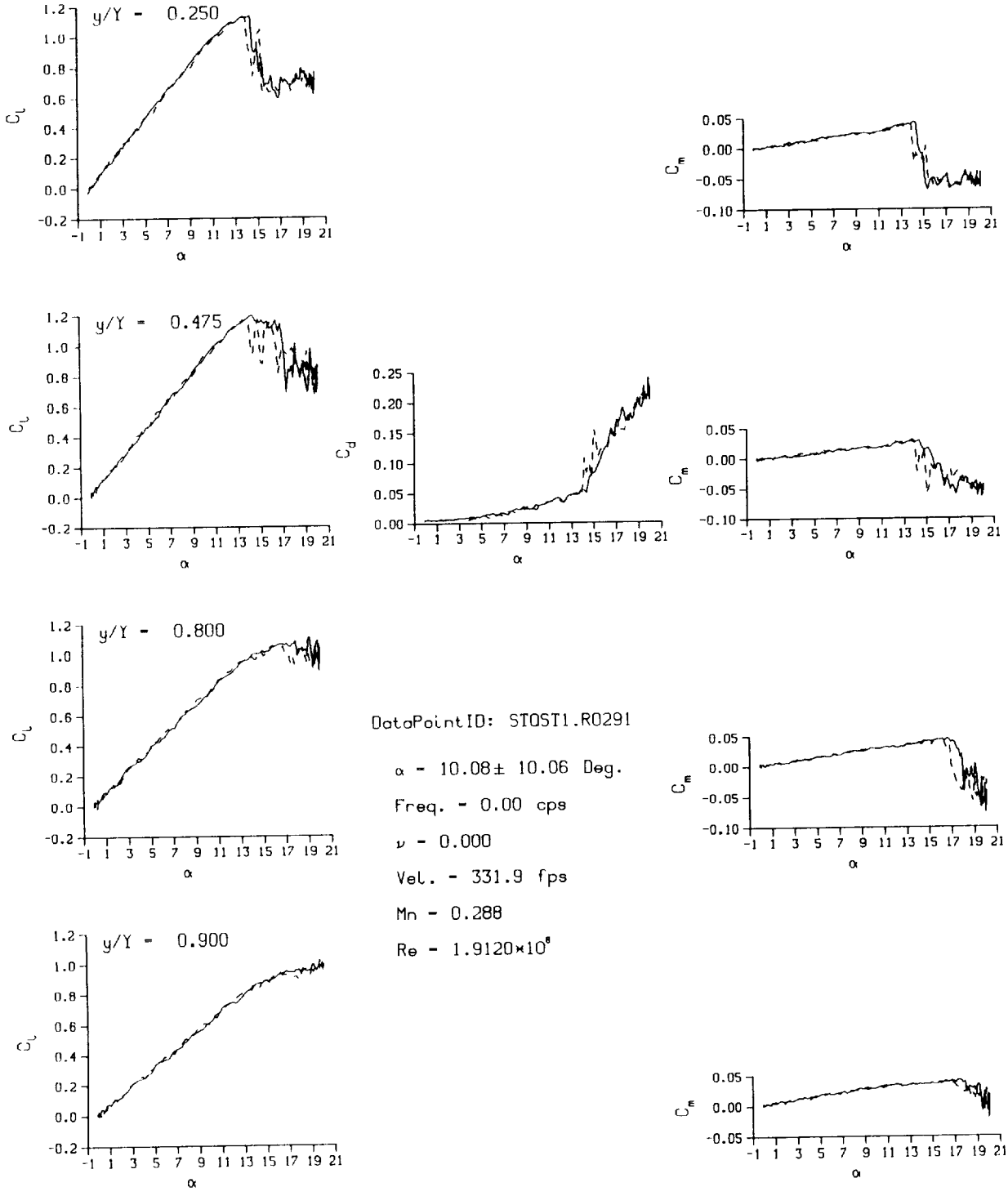

(b) Repeat no. 2

Figure 48. Continued.

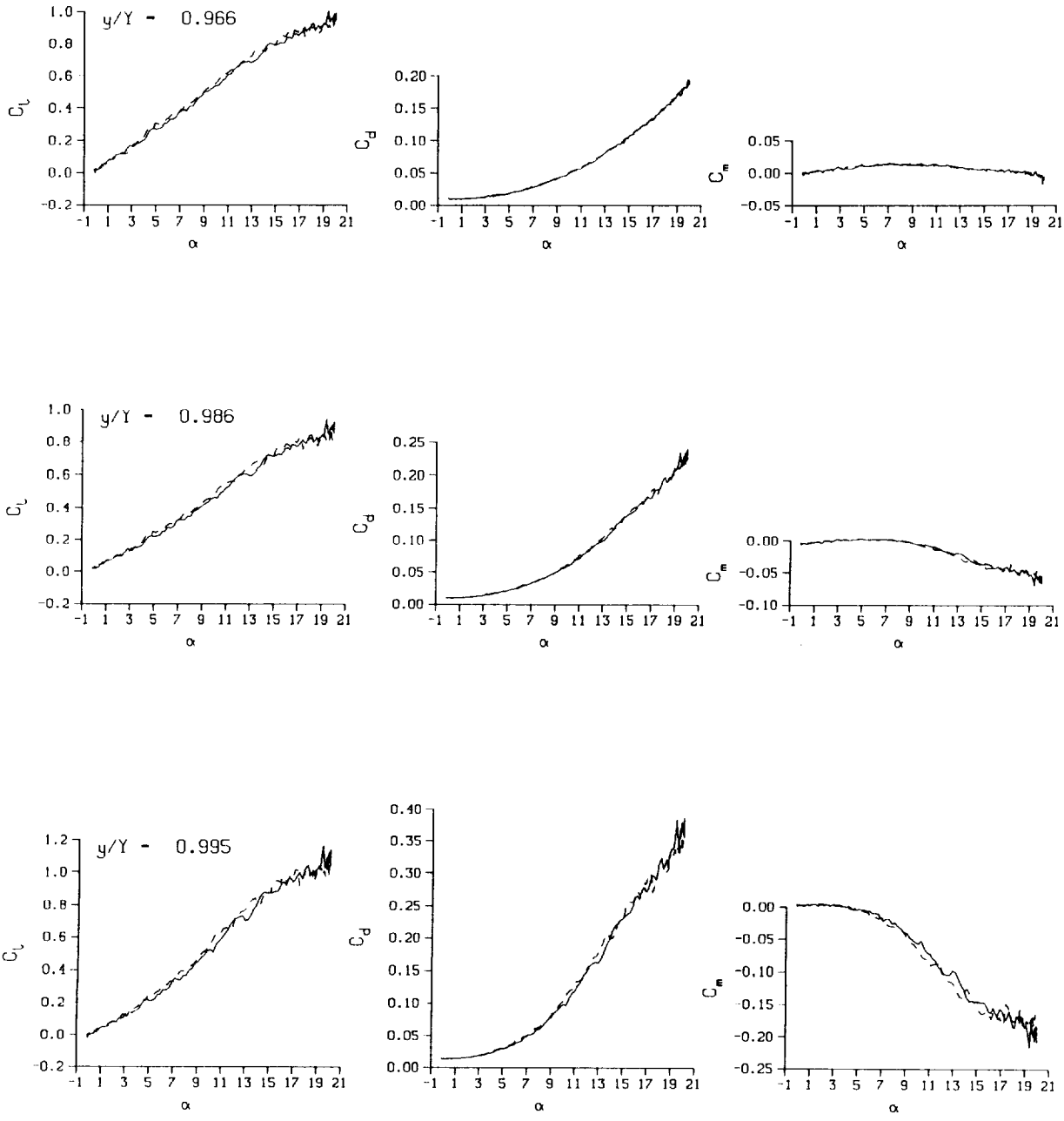

(b) Repeat no. 2. Concluded

Figure 48. Concluded.

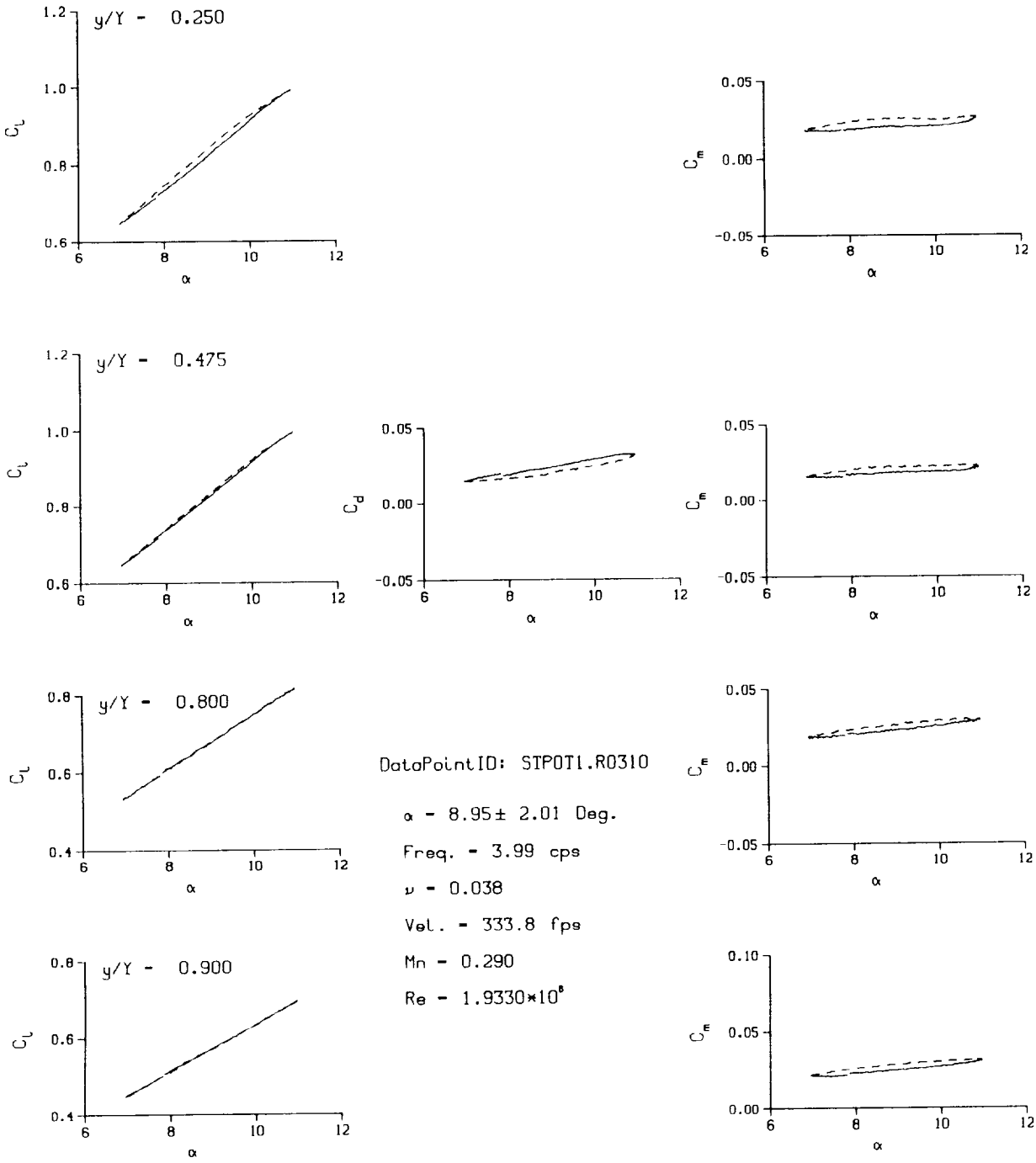

(a) ν = 0.04

Figure 49. 3-D square tip pitch oscillation data; BL-trip; α = 9 ± 2 deg.

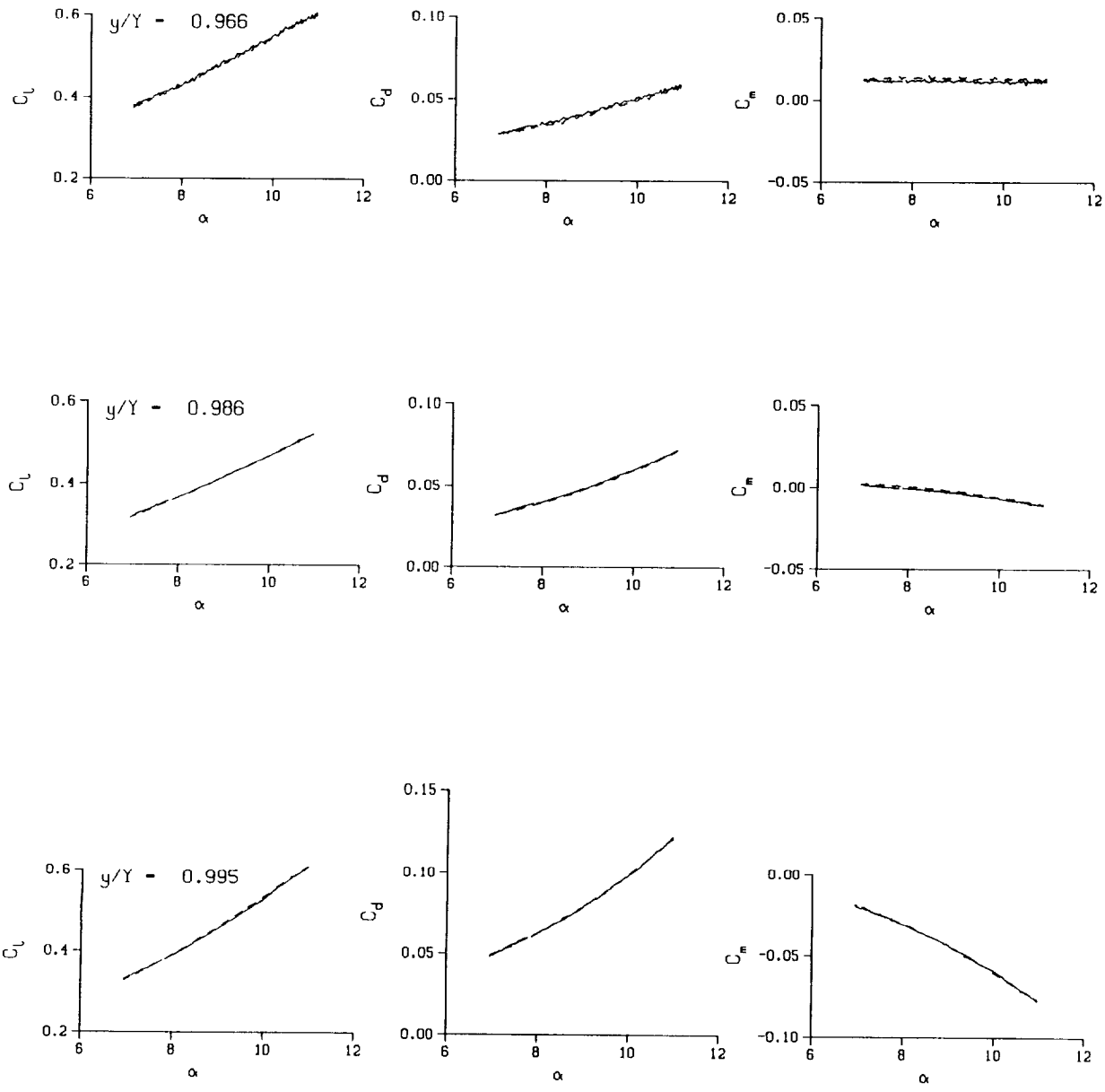

(a) v = 0.04. Concluded

Figure 49. Continued.

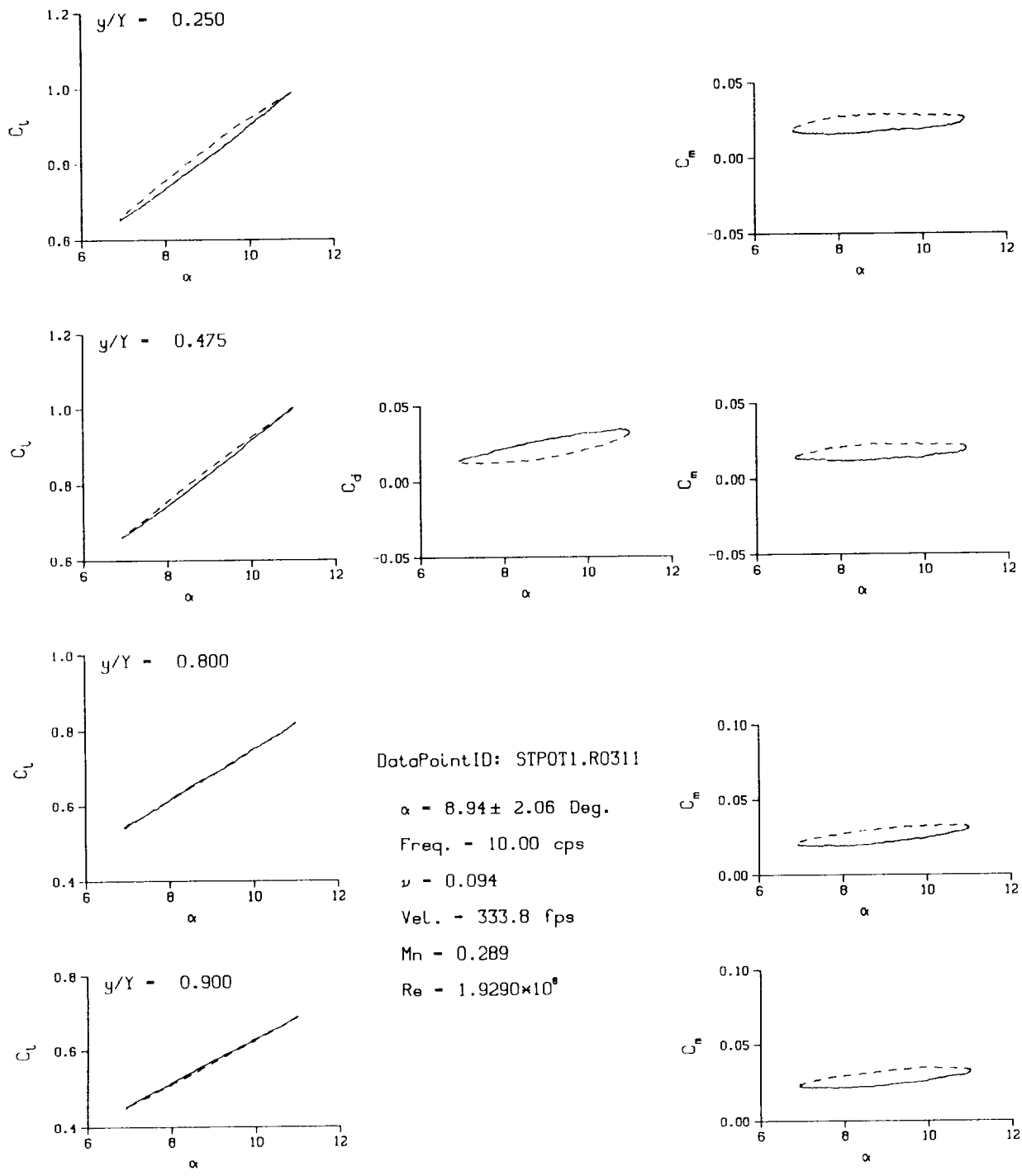

(b) ν = 0.10

Figure 49. Continued.

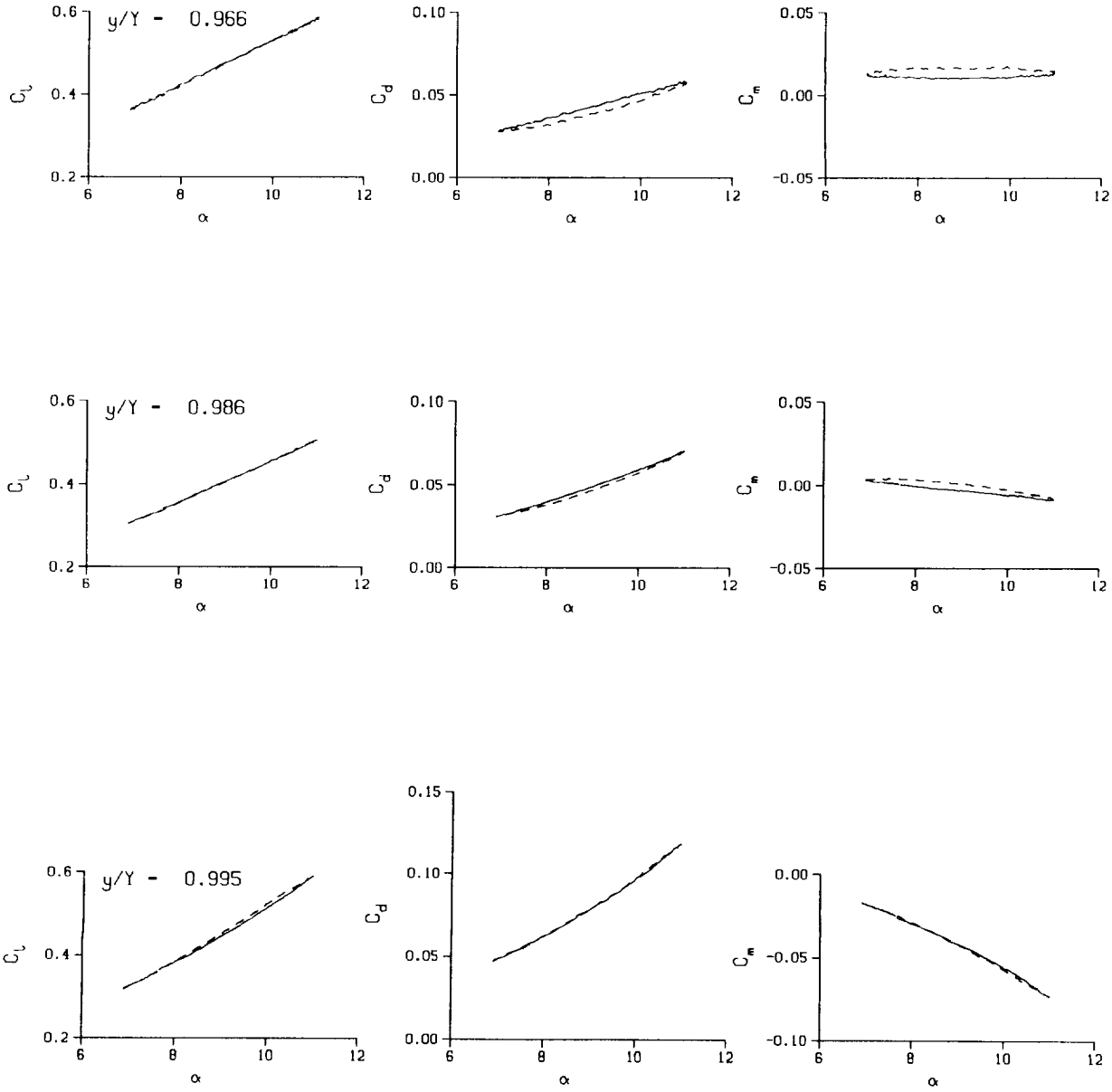

(b) v = 0.10. Concluded

Figure 49. Continued.

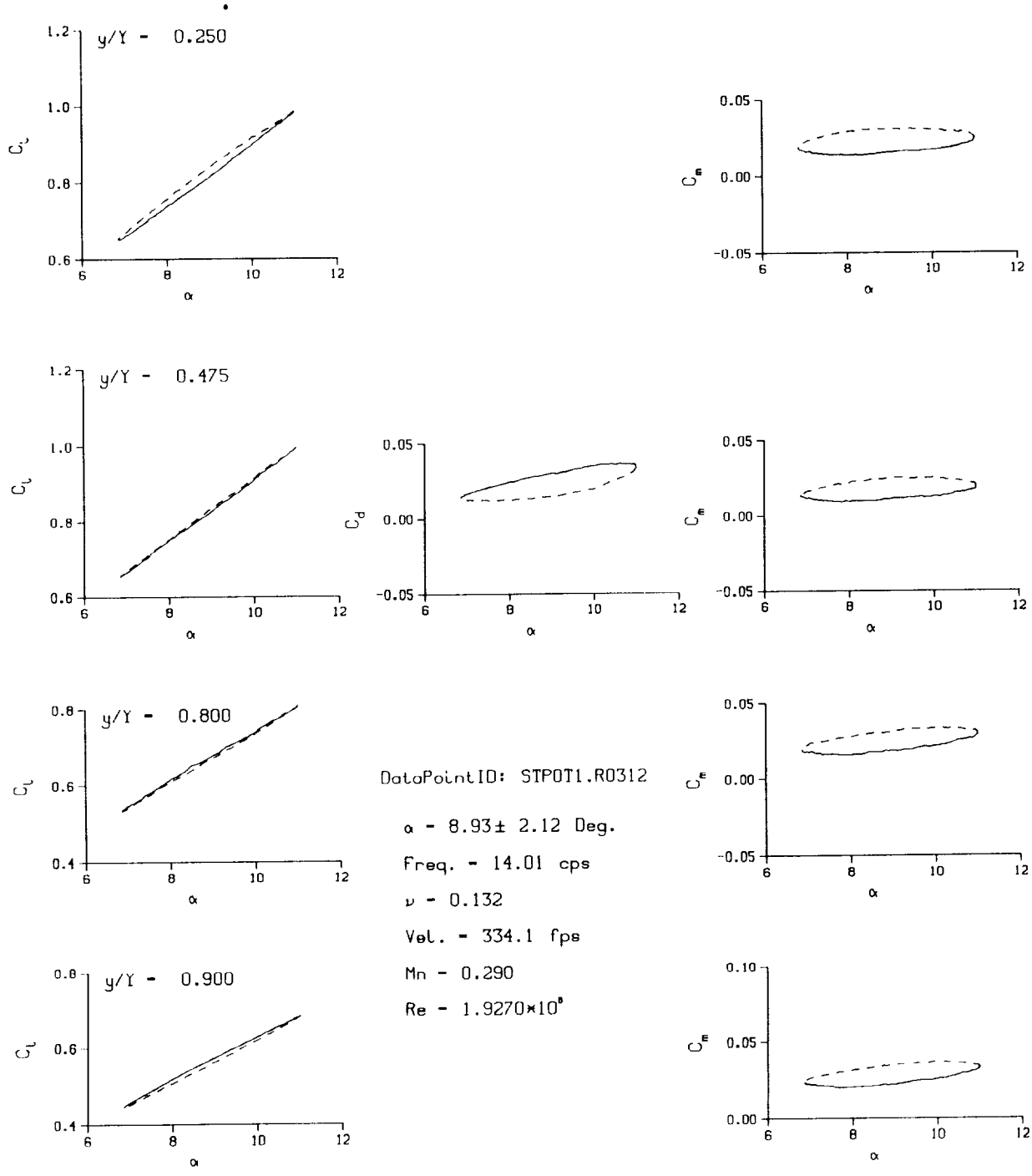

(c) v = 0.14

Figure 49. Continued.

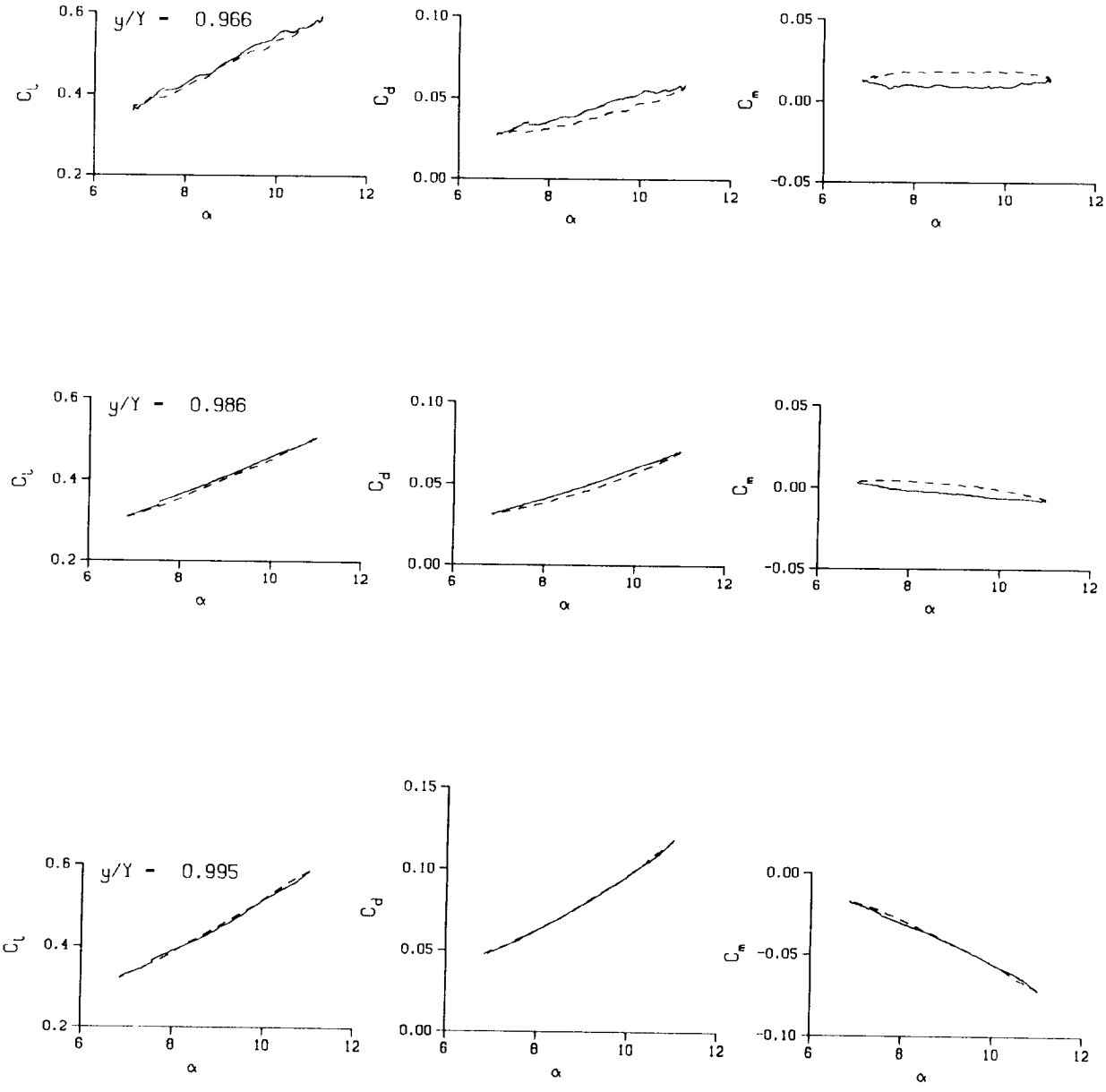

(c) v = 0.14. Concluded

Figure 49. Continued.

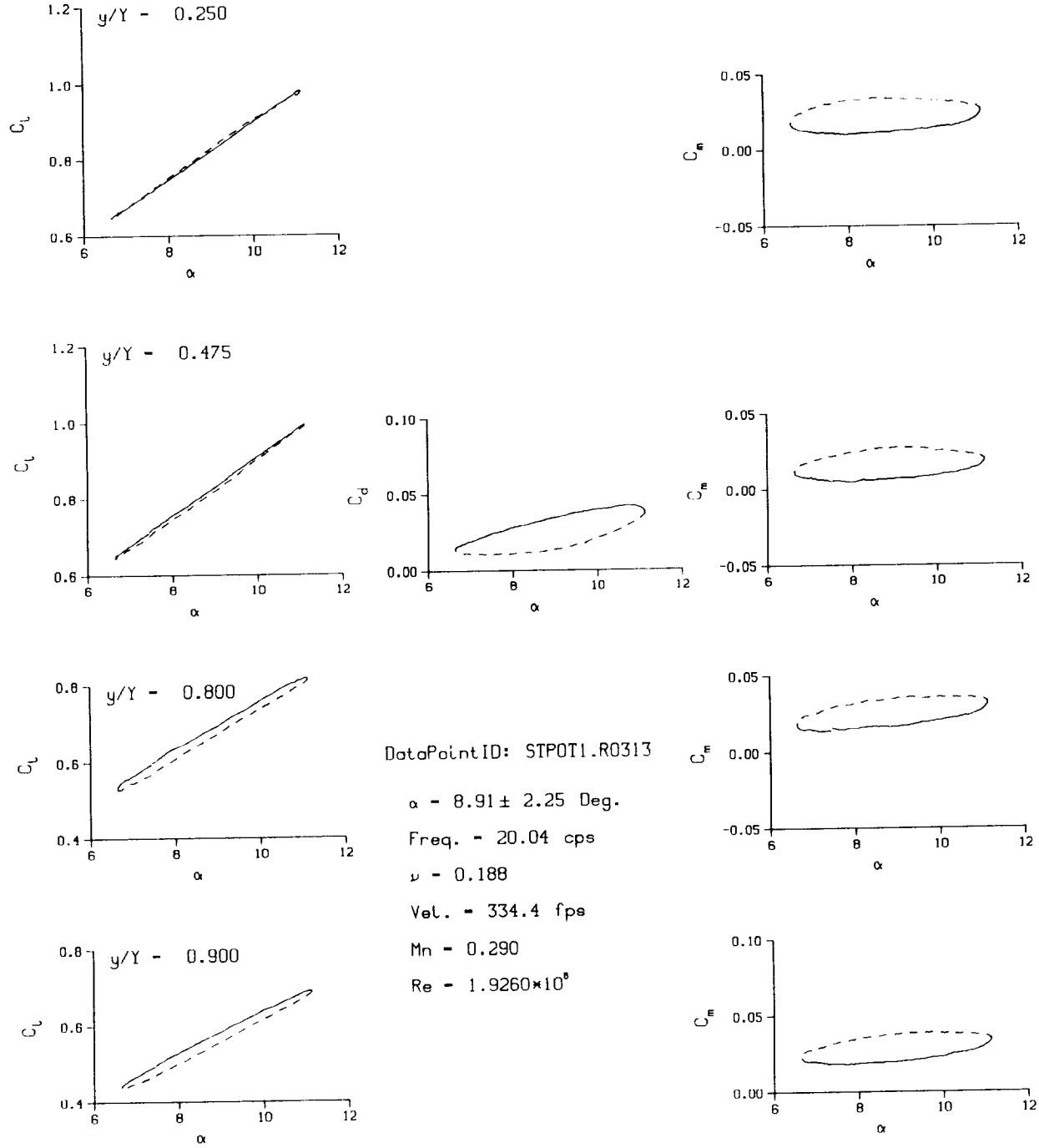

(d) ν = 0.20

Figure 49. Continued.

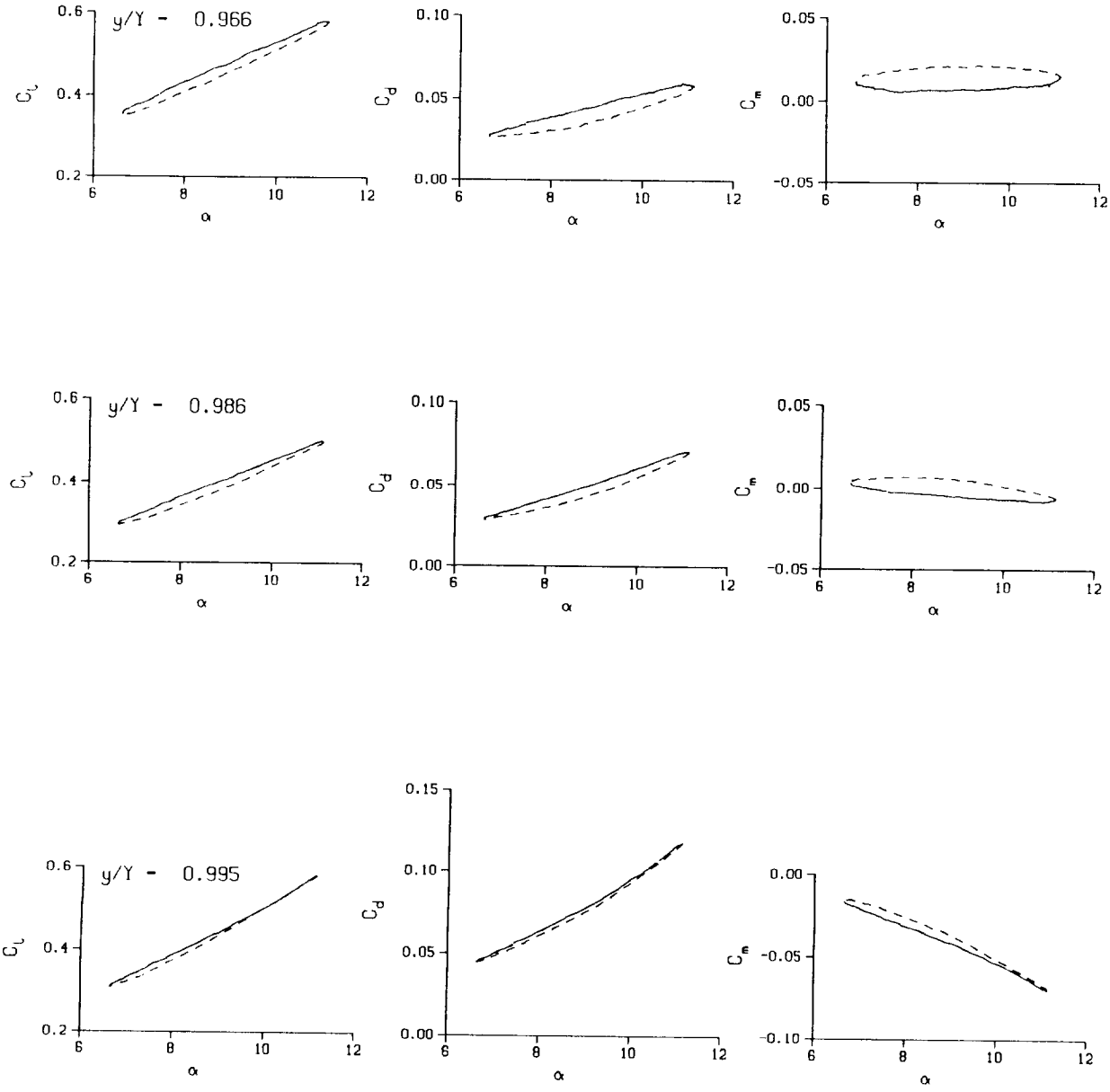

(d) v = 0.20. Concluded

Figure 49. Concluded.

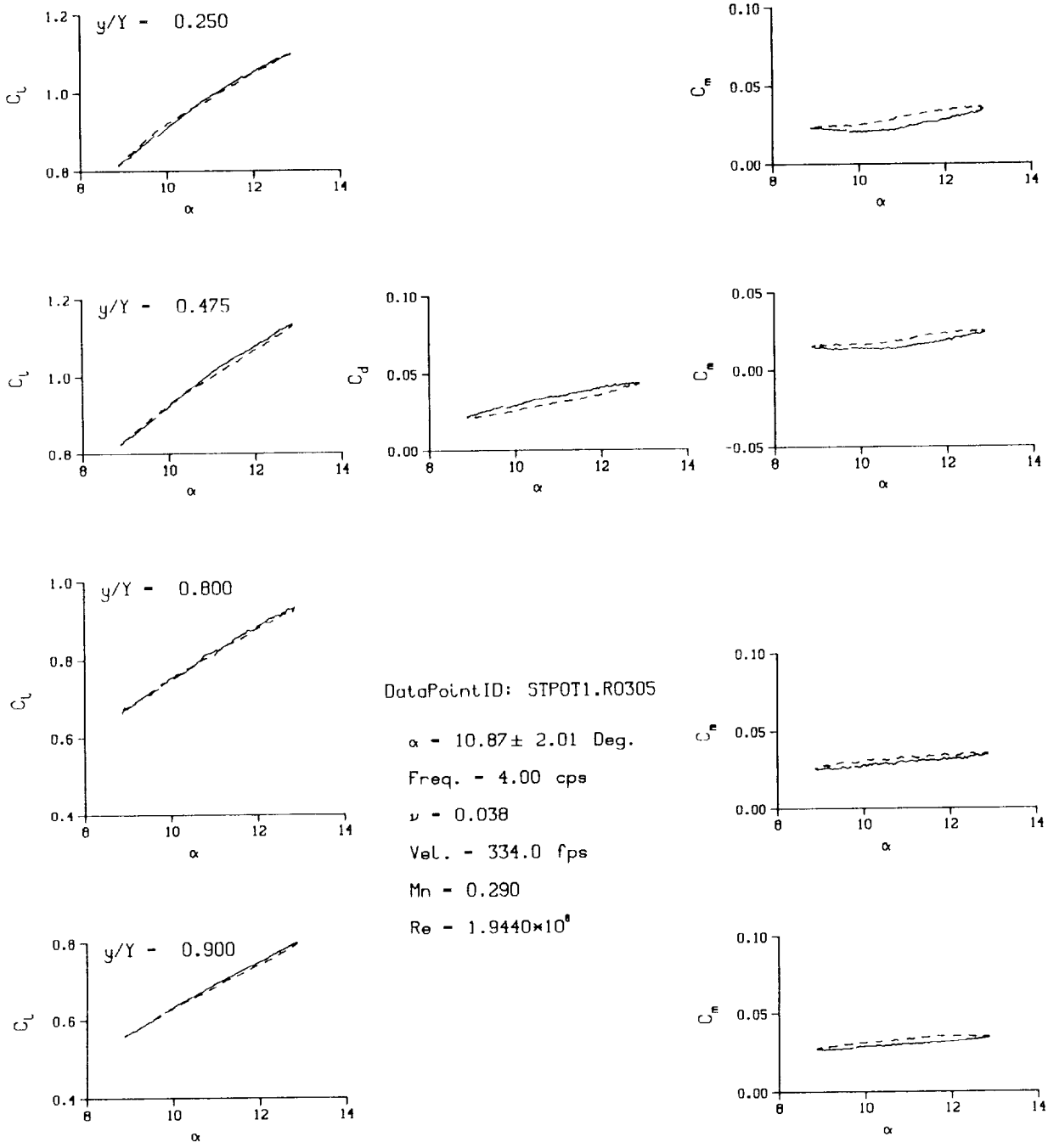

(a) v = 0.04

Figure 50. 3-D square tip pitch oscillation data; BL-trip; α = 11 ± 2 deg.

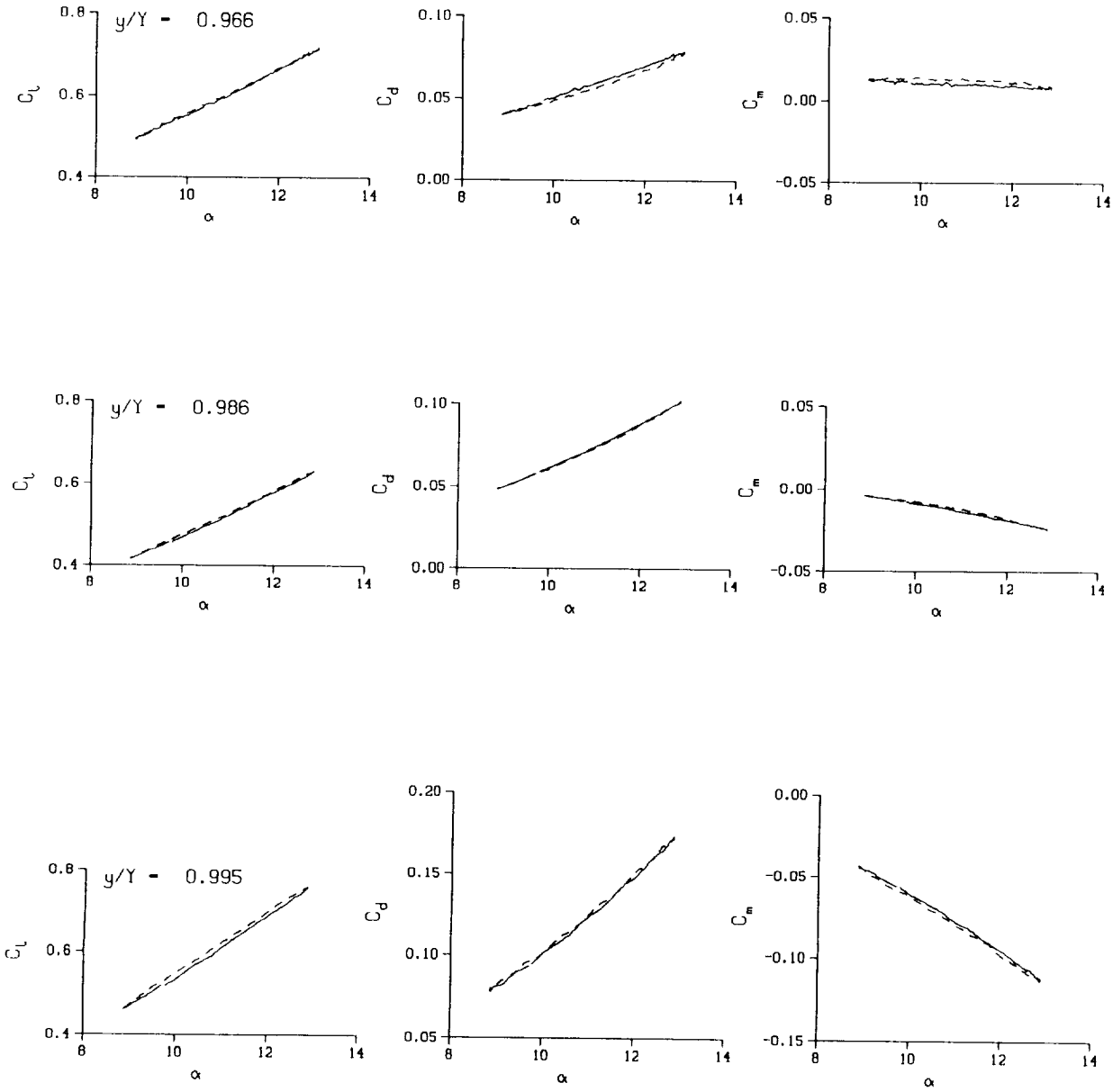

(a) v = 0.04. Concluded

Figure 50. Continued.

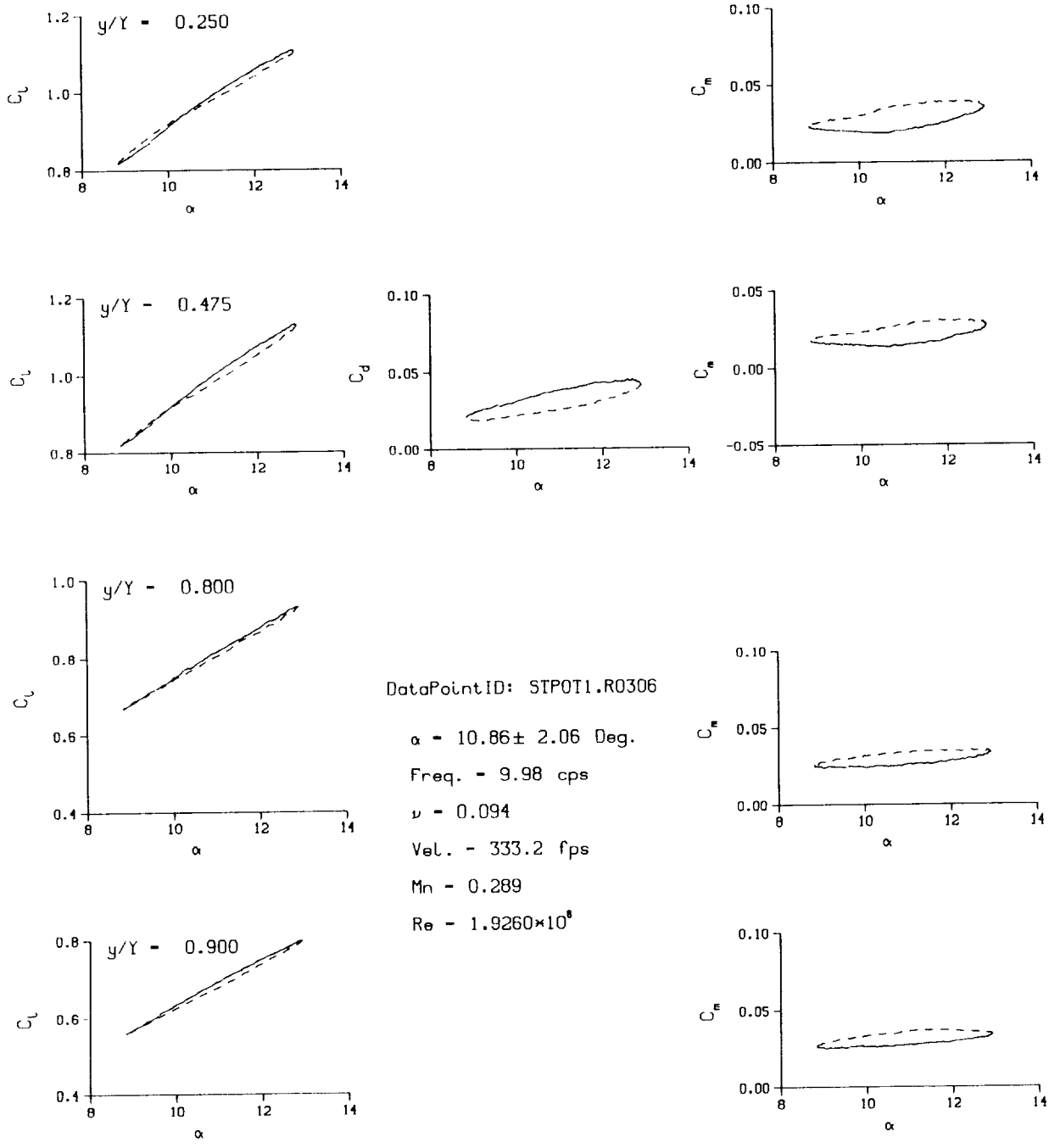

(b) v = 0.10

Figure 50. Continued.

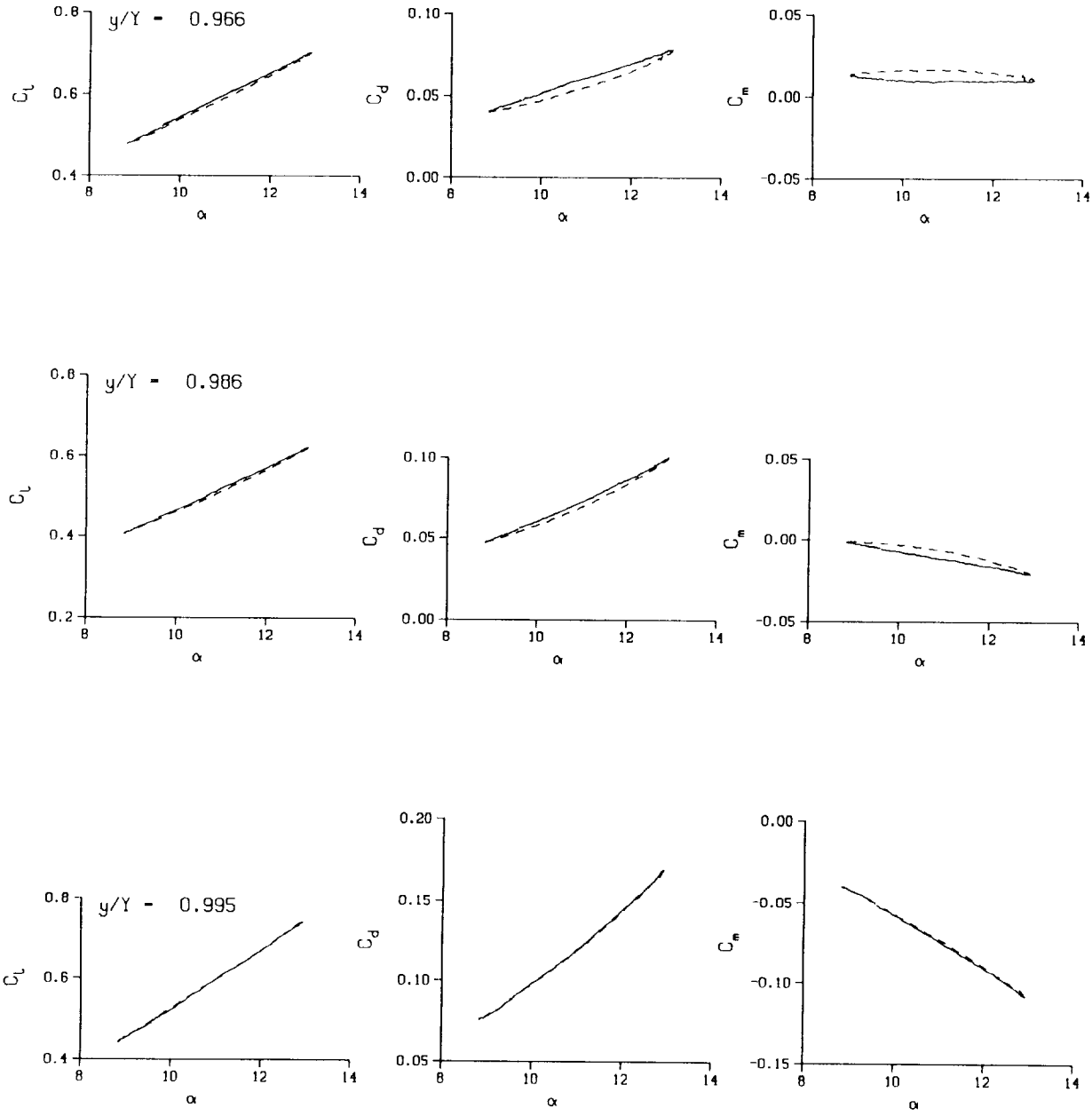

(b) v = 0.10. Concluded

Figure 50. Continued.

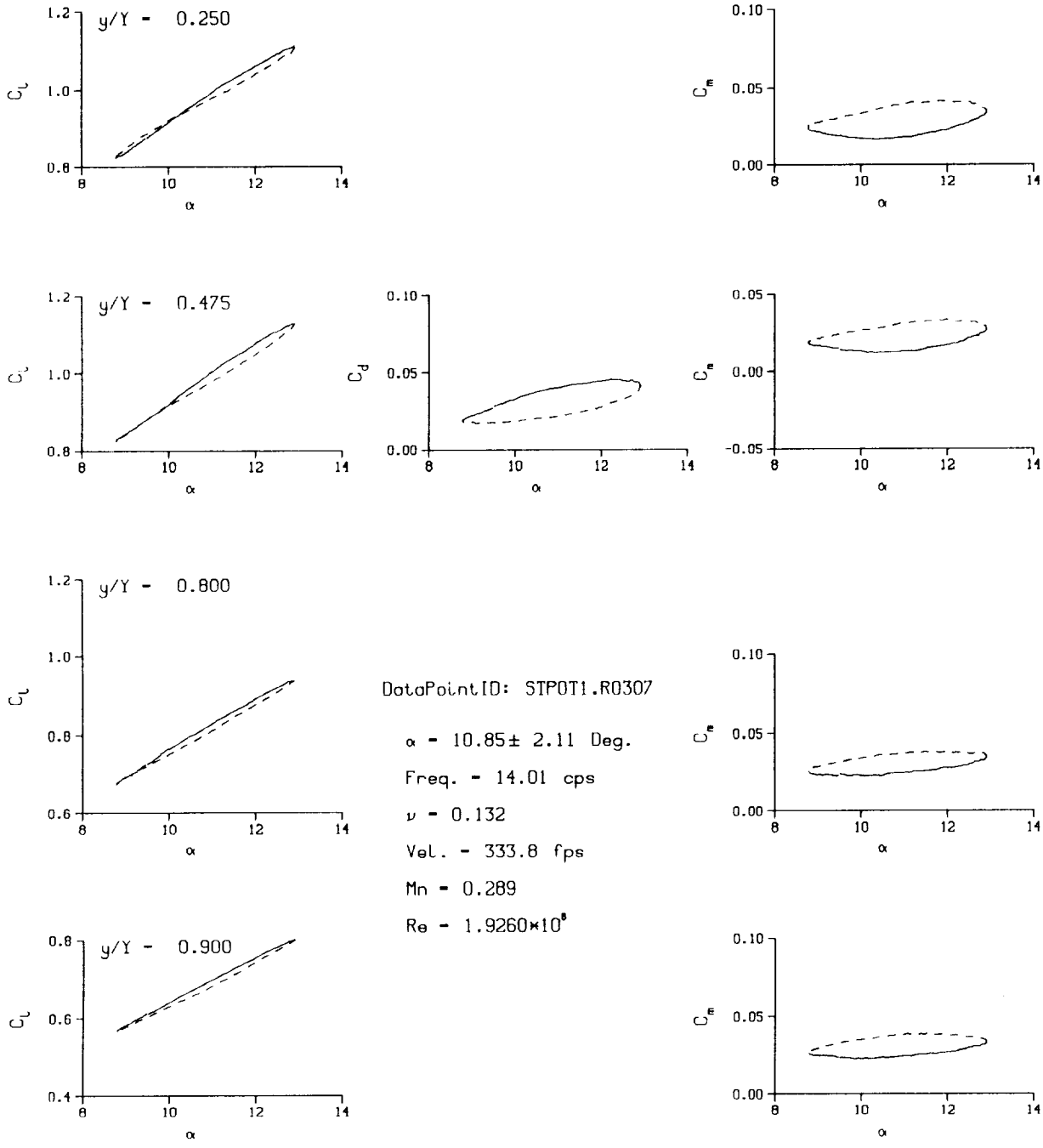

(c) ν = 0.14

Figure 50. Continued.

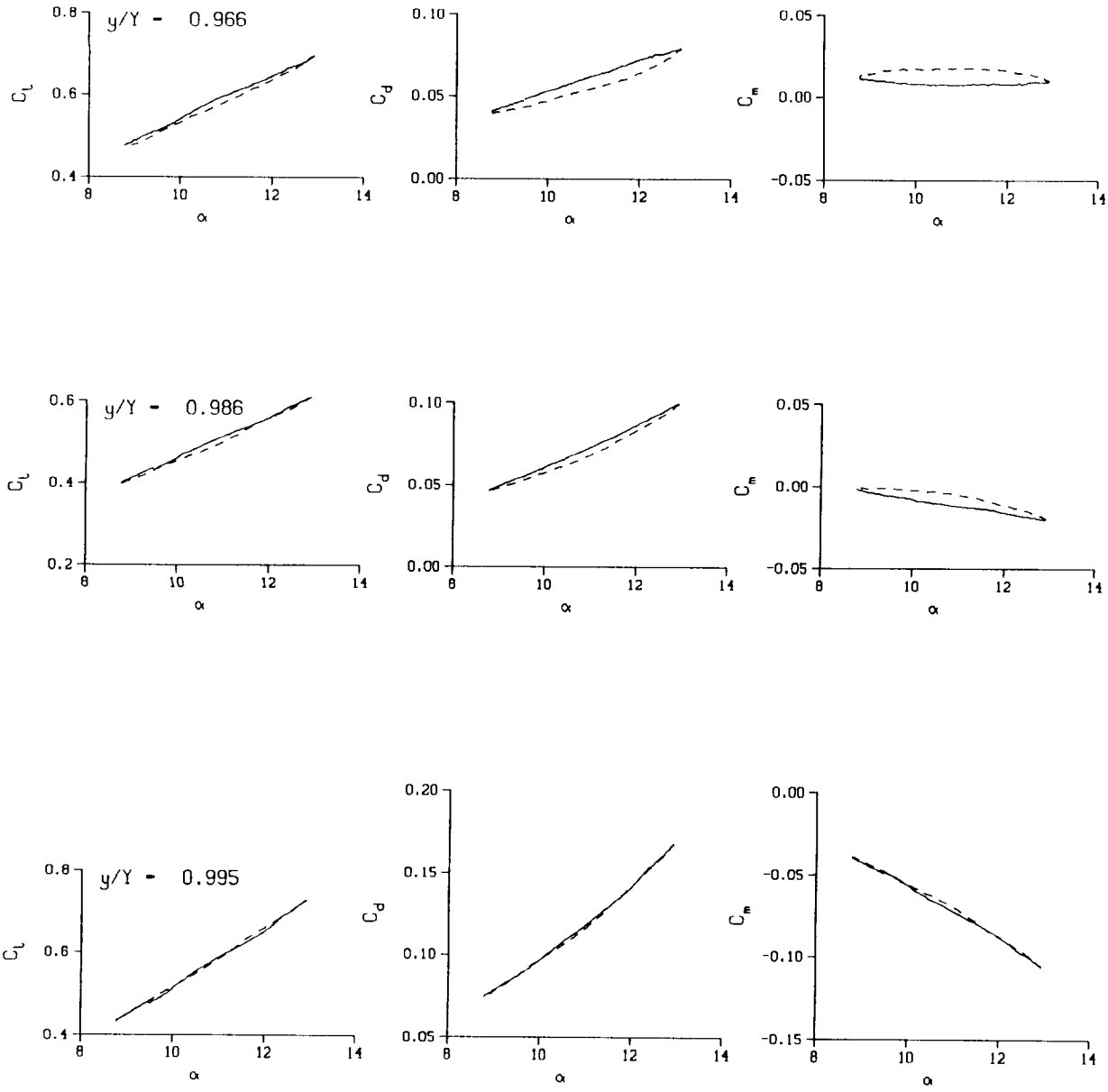

(c) v = 0.14. Concluded

Figure 50. Continued.

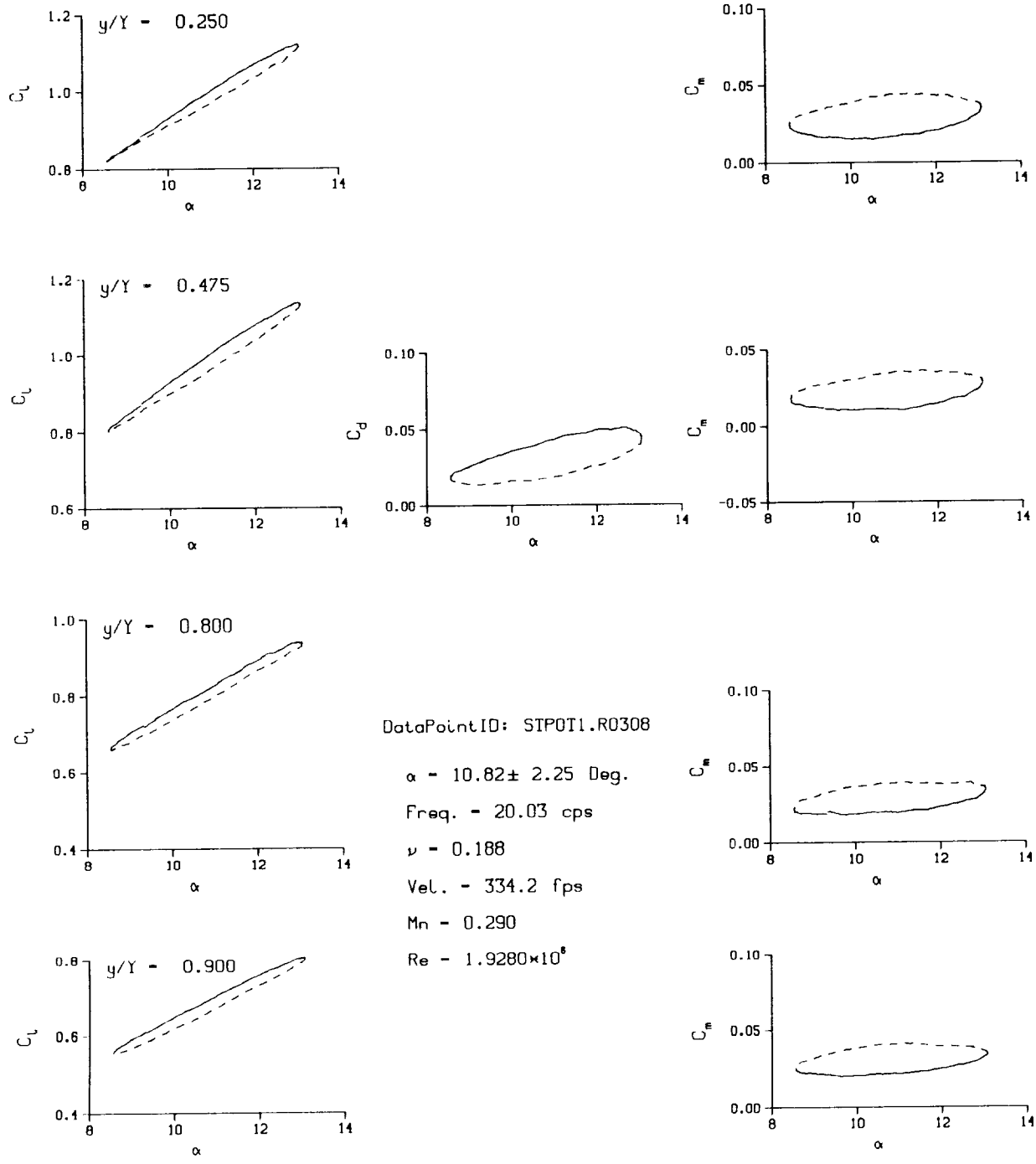

(d) v = 0.20

Figure 50. Continued.

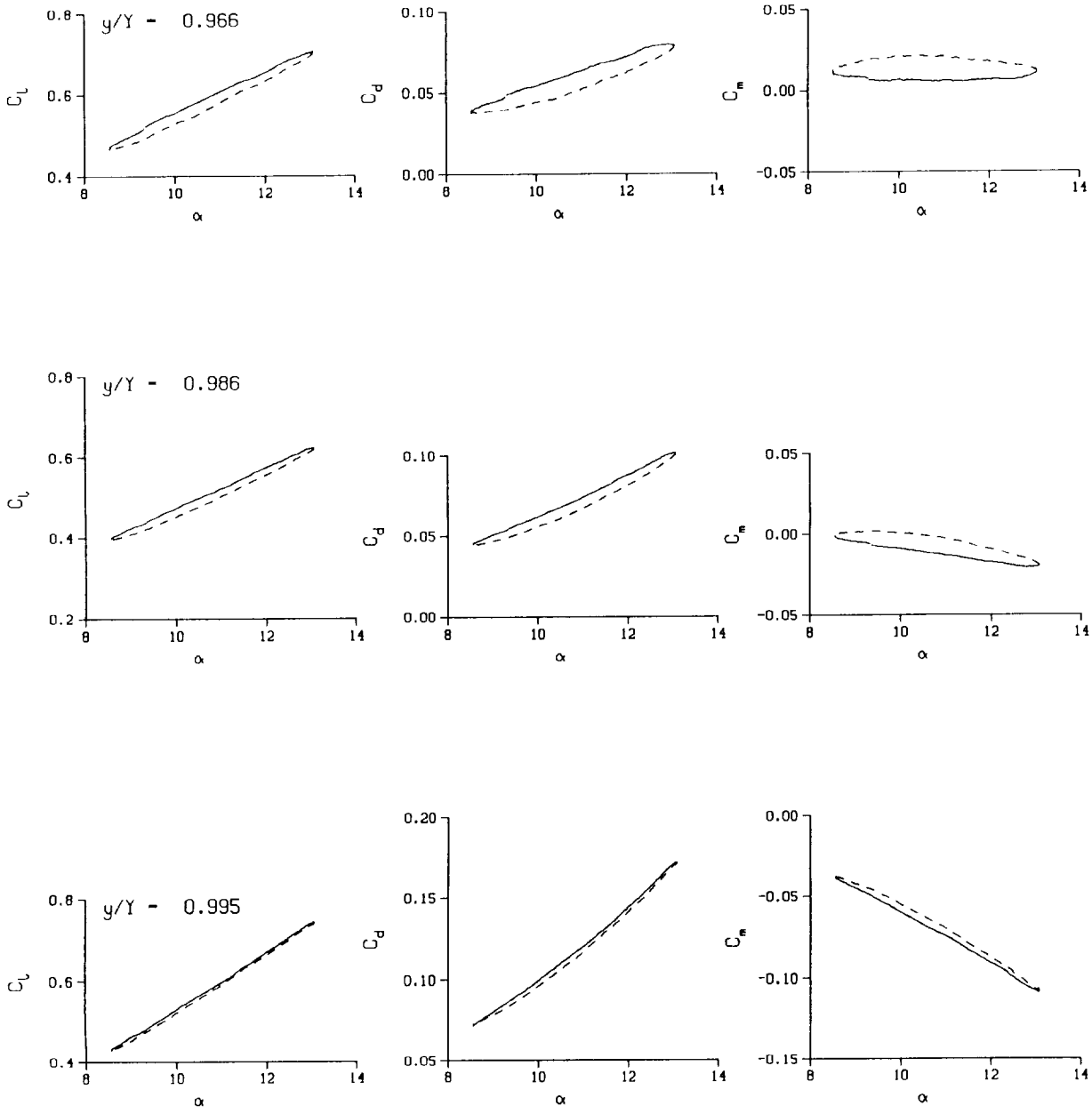

(d) v = 0.20. Concluded

Figure 50. Concluded.

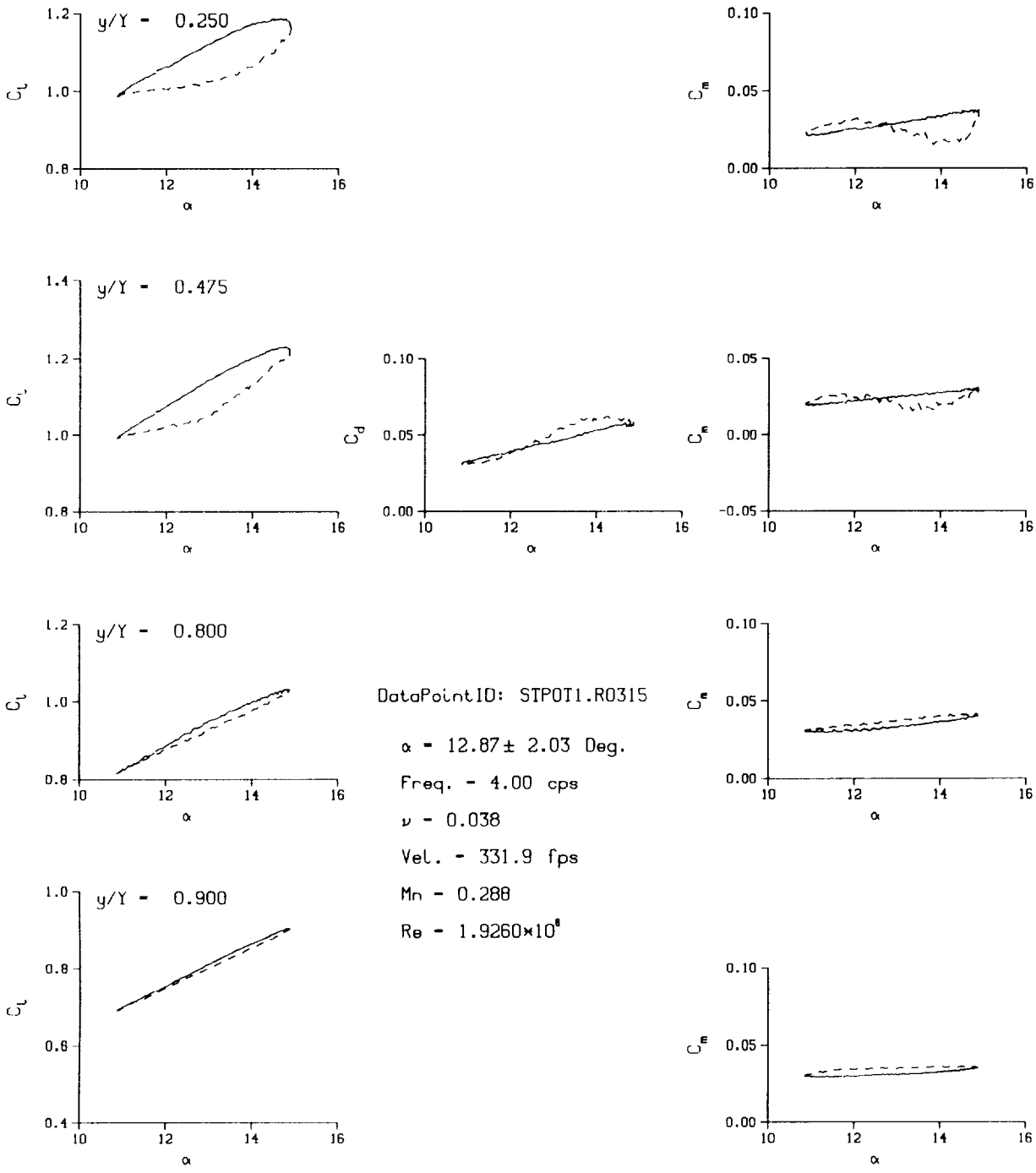

(a) ν = 0.04

Figure 51. 3-D square tip pitch oscillation data; BL-trip; α = 13 ± 2 deg.

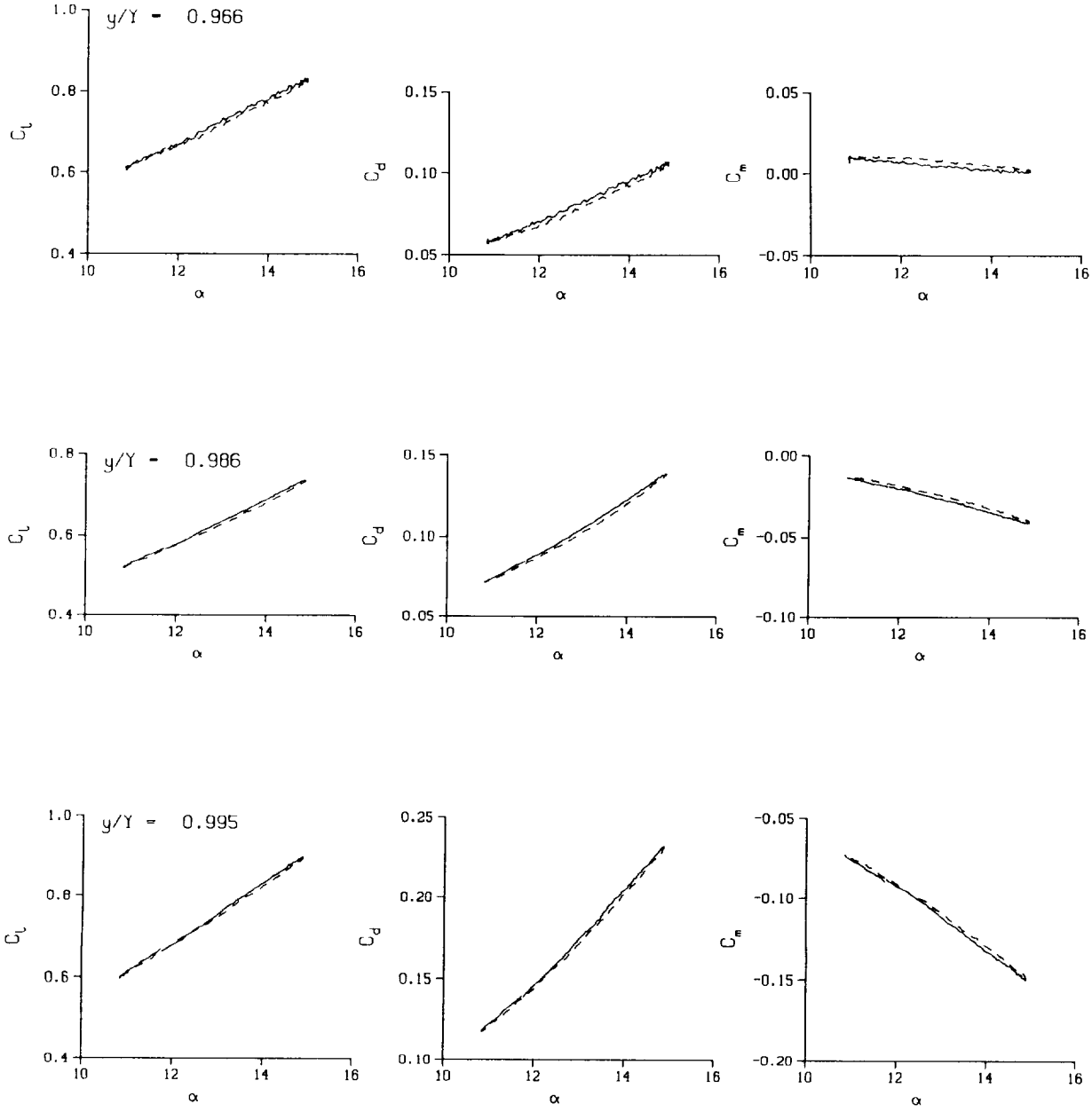

(a) v = 0.04. Concluded

Figure 51. Continued.

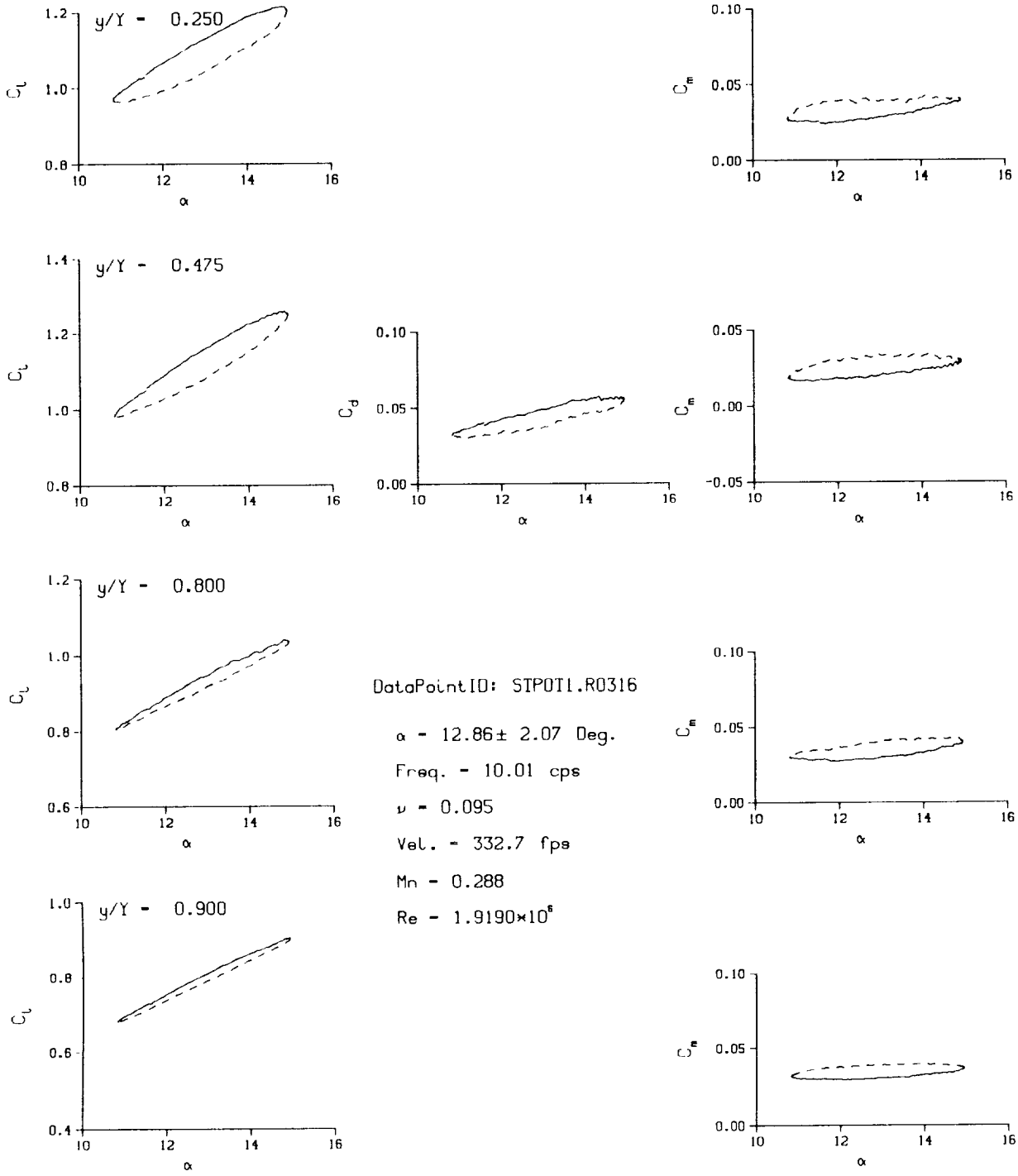

(b) v = 0.10

Figure 51. Continued.

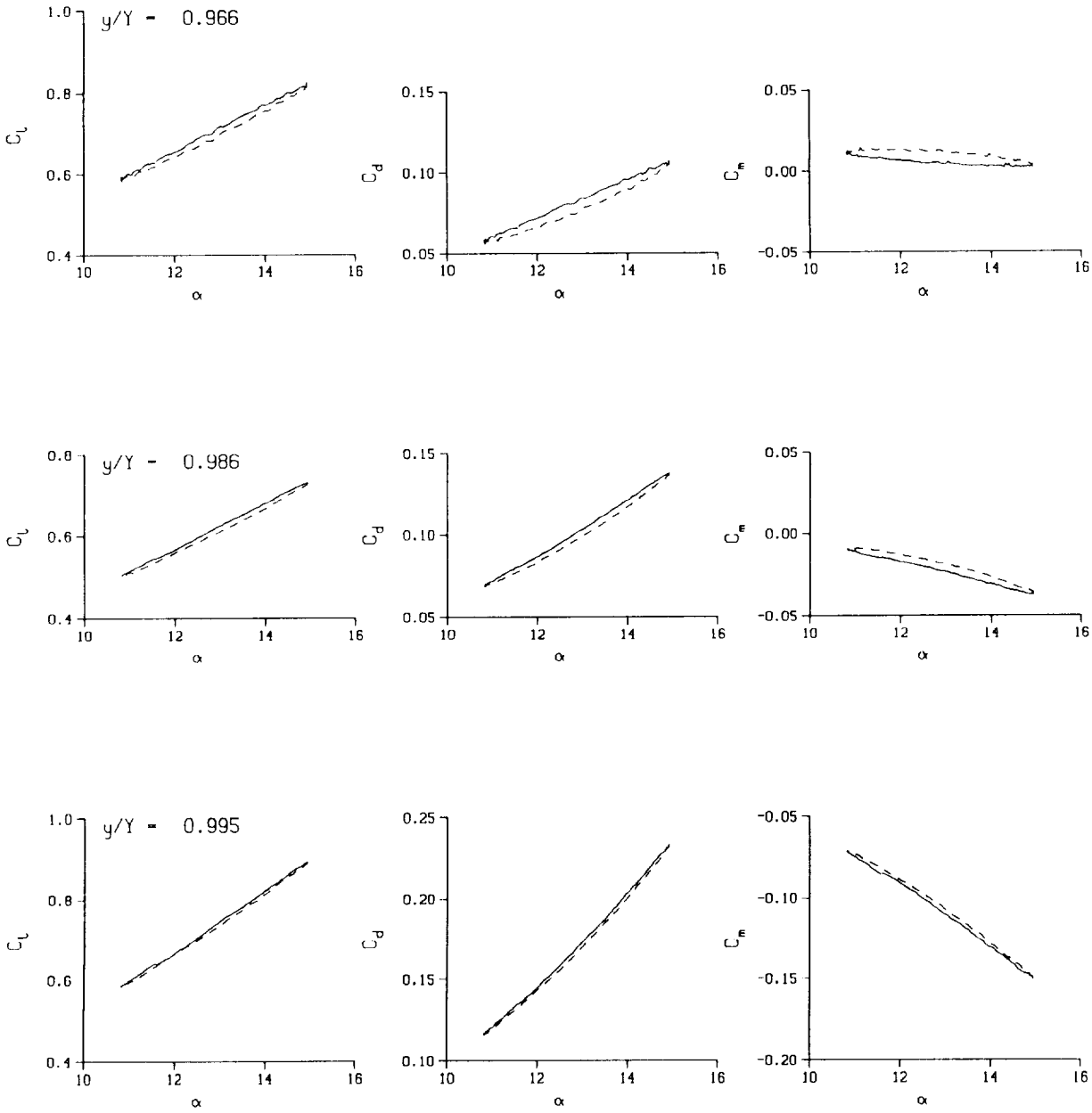

(b) v = 0.10. Concluded

Figure 51. Continued.

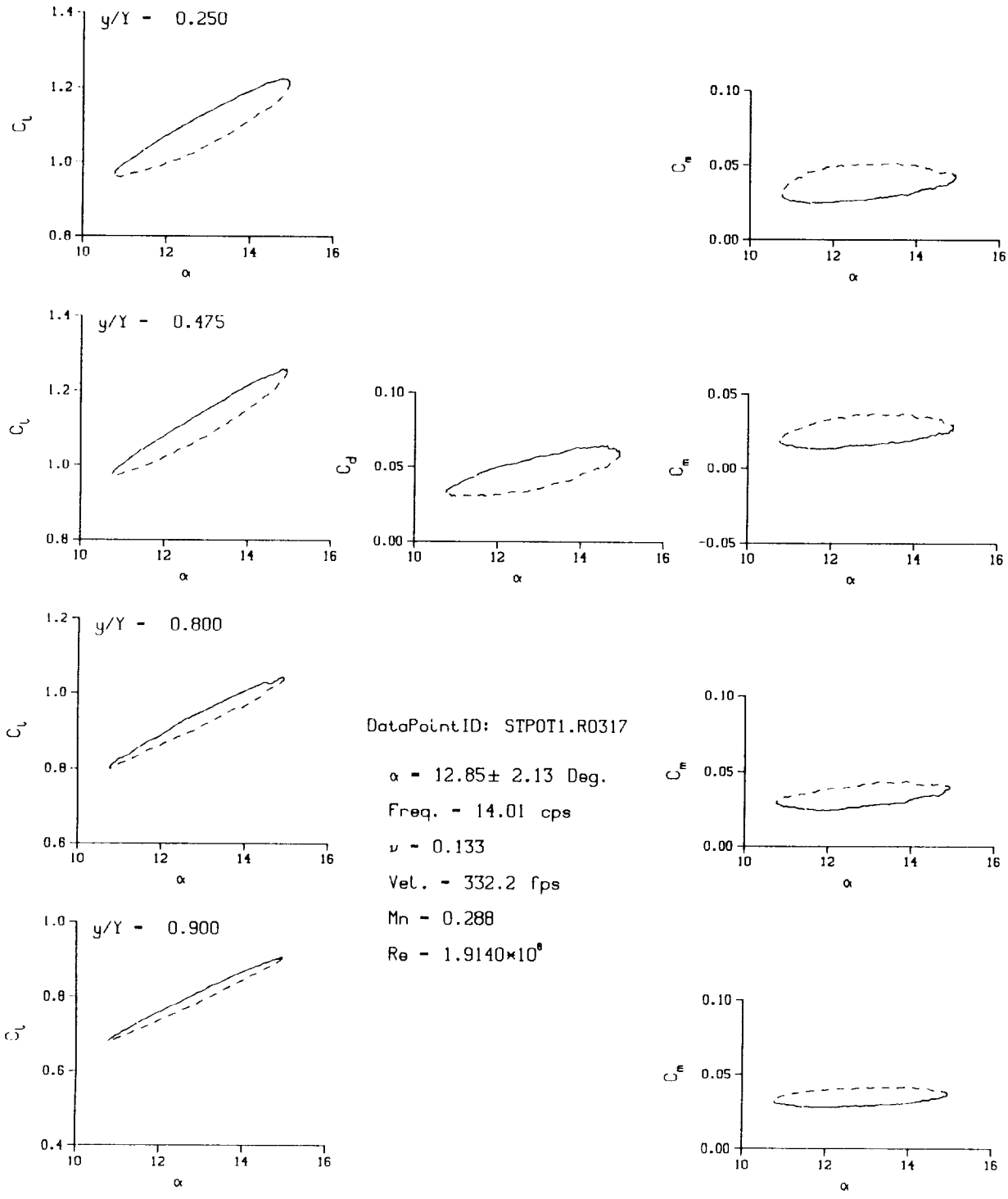

(c) v = 0.14

Figure 51. Continued.

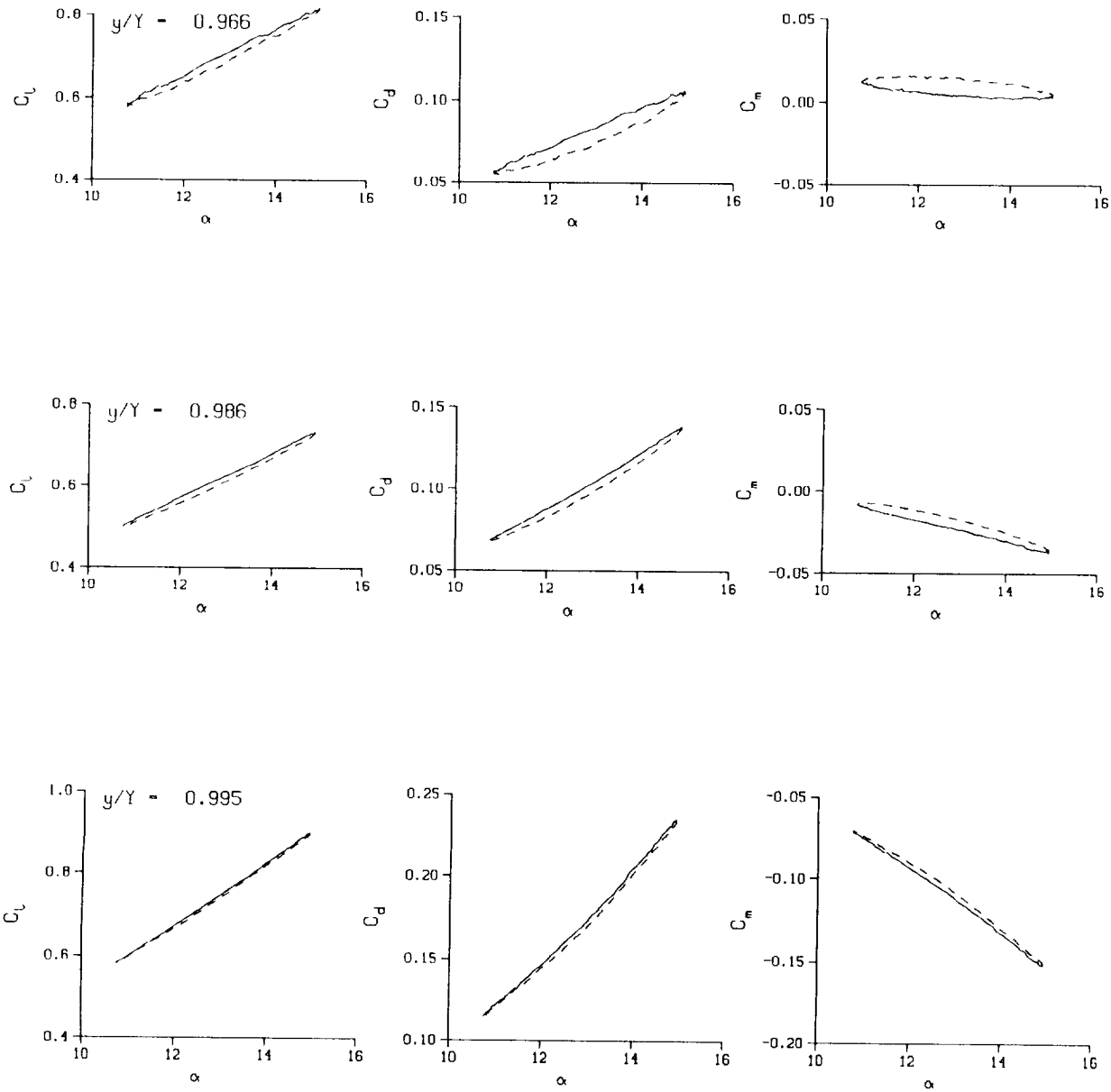

(c) v = 0.14. Concluded

Figure 51. Continued.

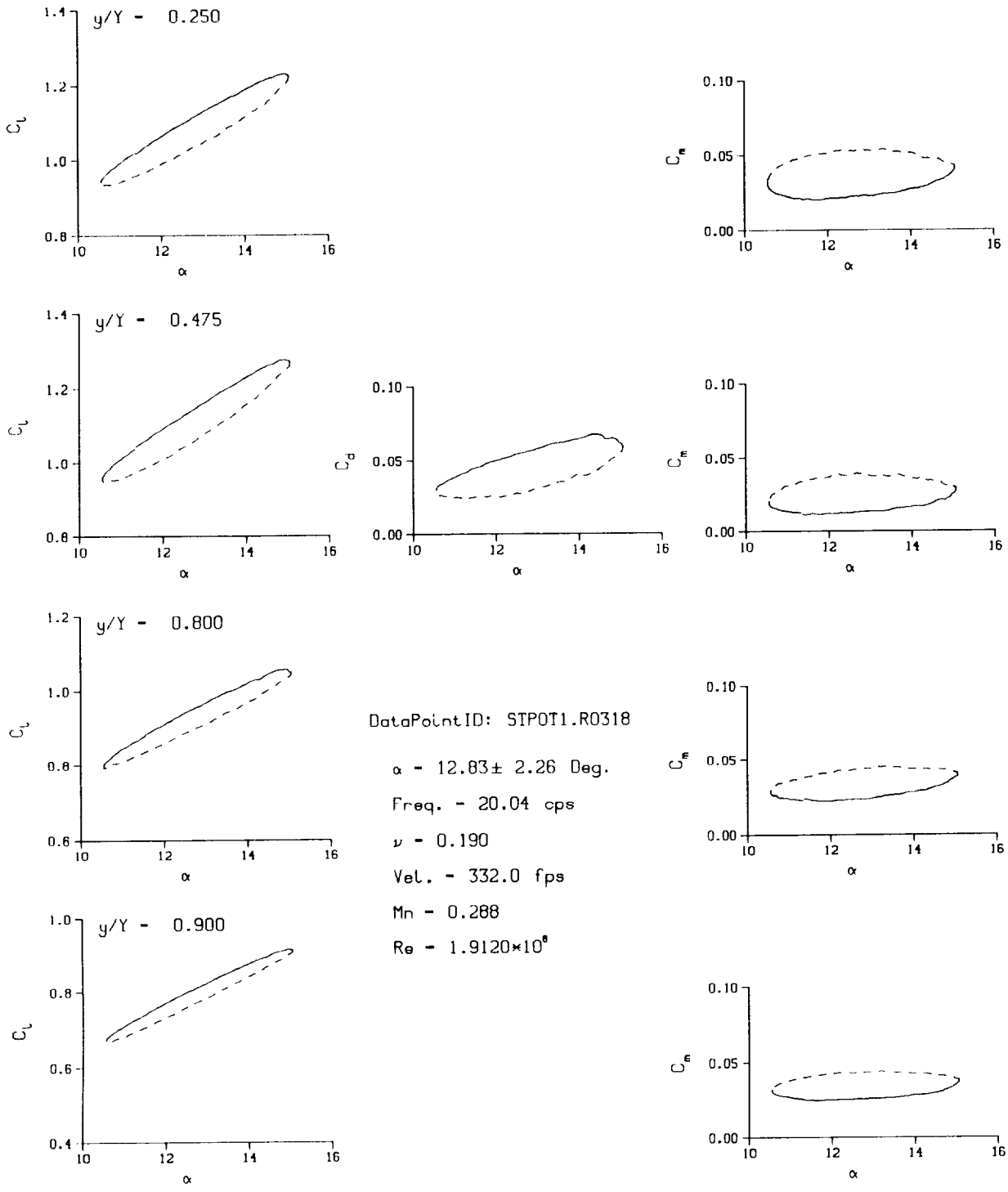

(d) v = 0.20

Figure 51. Continued.

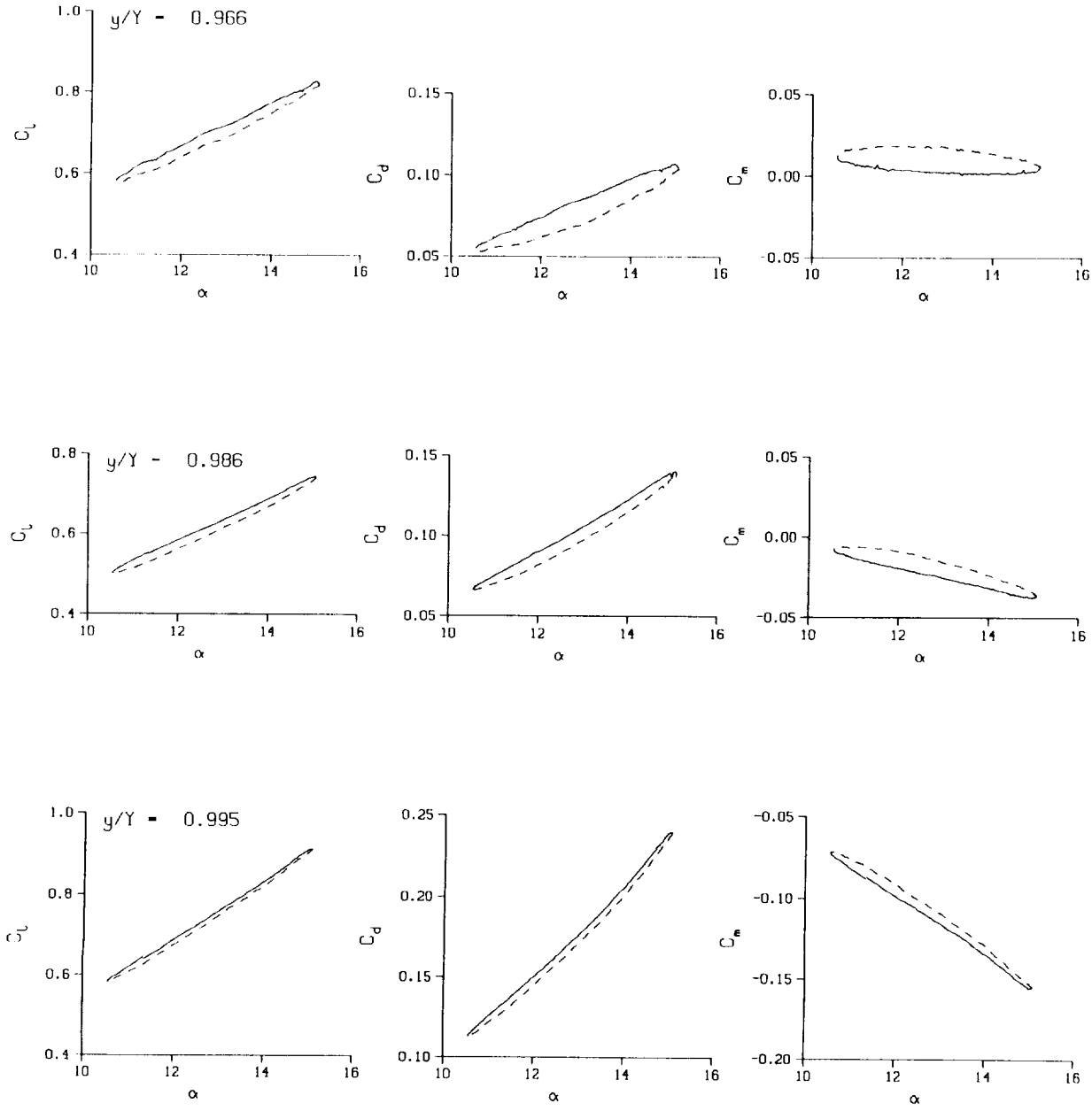

(d) v = 0.20. Concluded

Figure 51. Concluded.

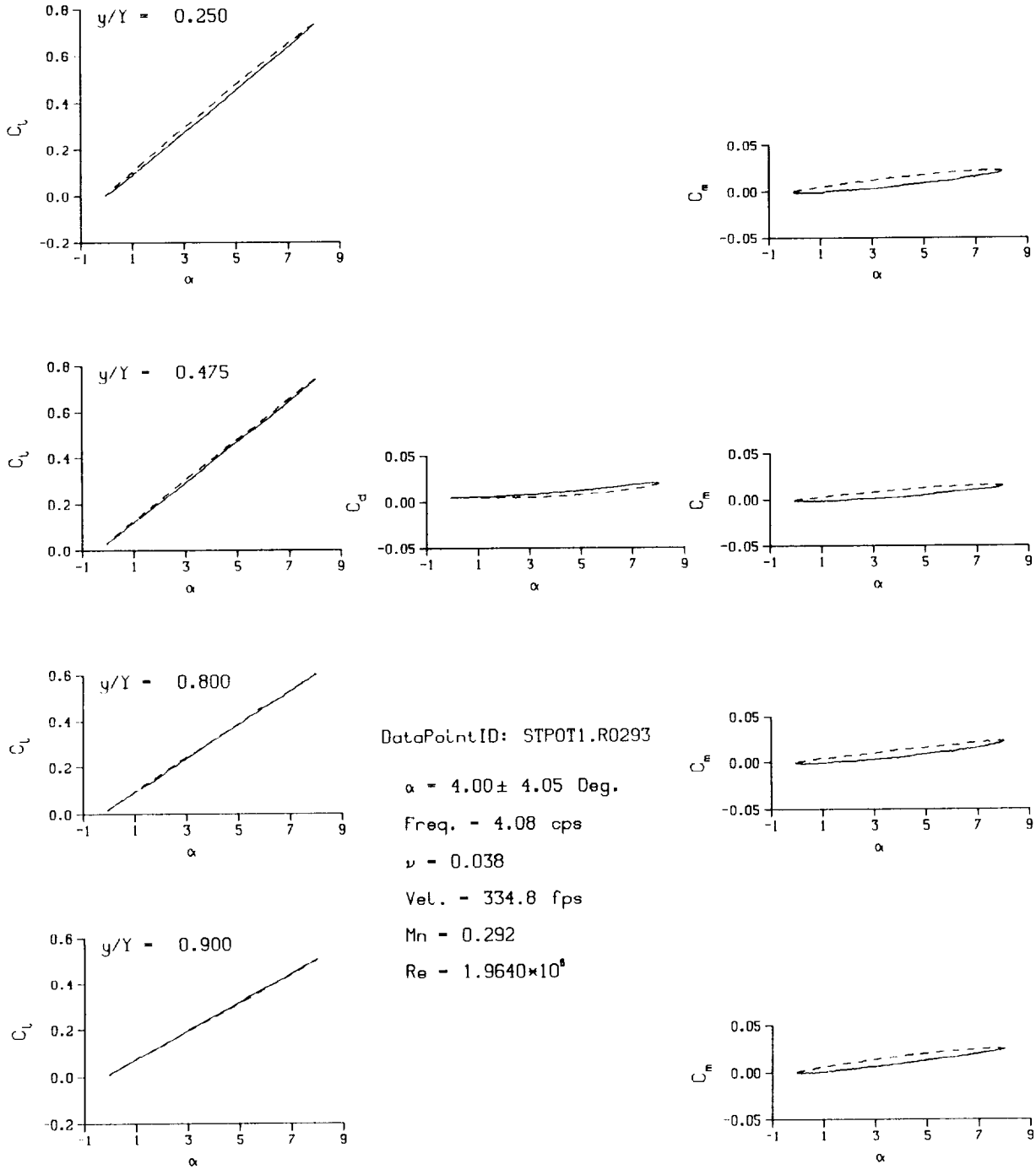

(a) v = 0.04

Figure 52. 3-D square tip pitch oscillation data; BL-trip; α = 4 ± 4 deg.

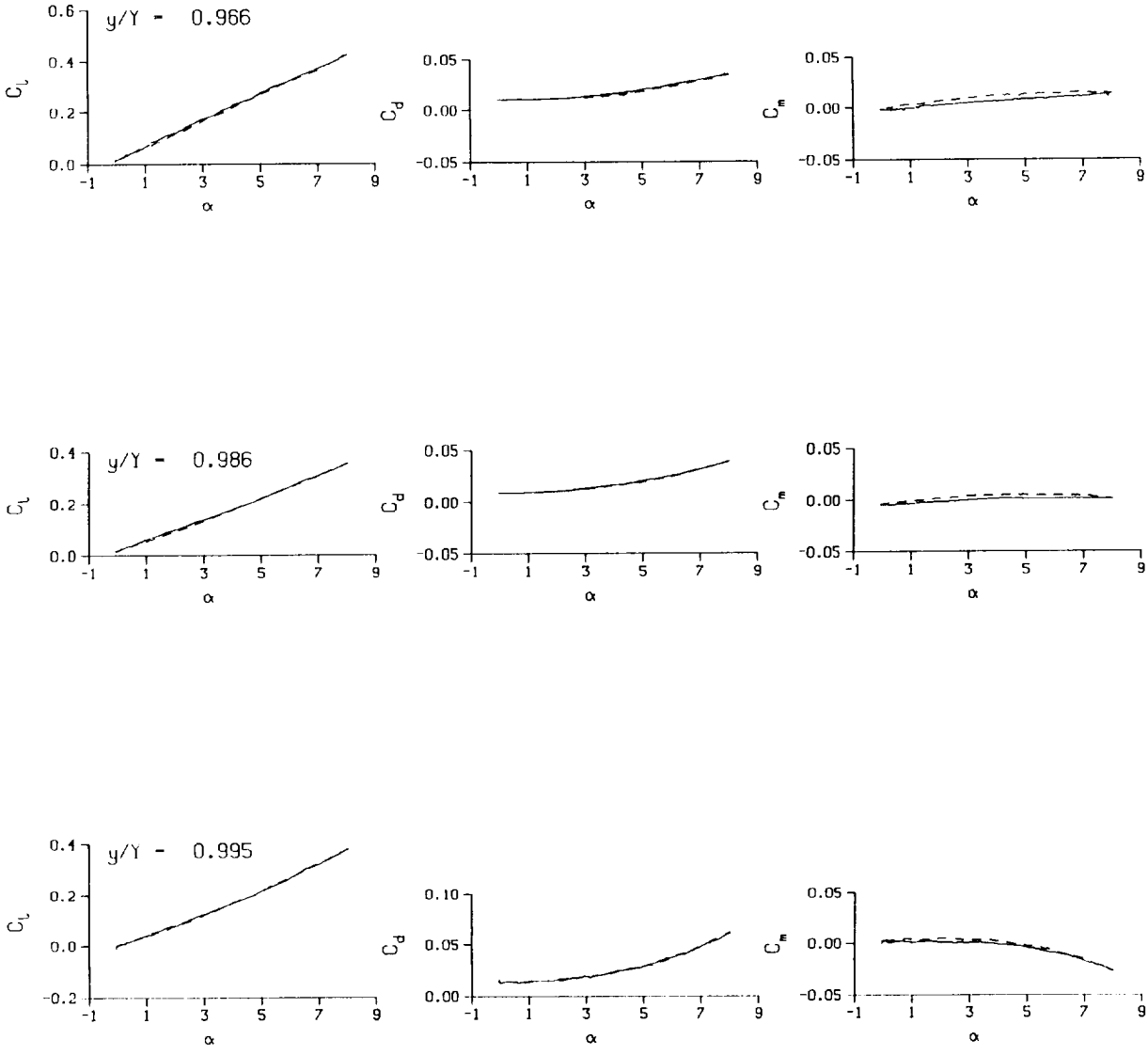

(a) v = 0.04. Concluded

Figure 52. Continued.

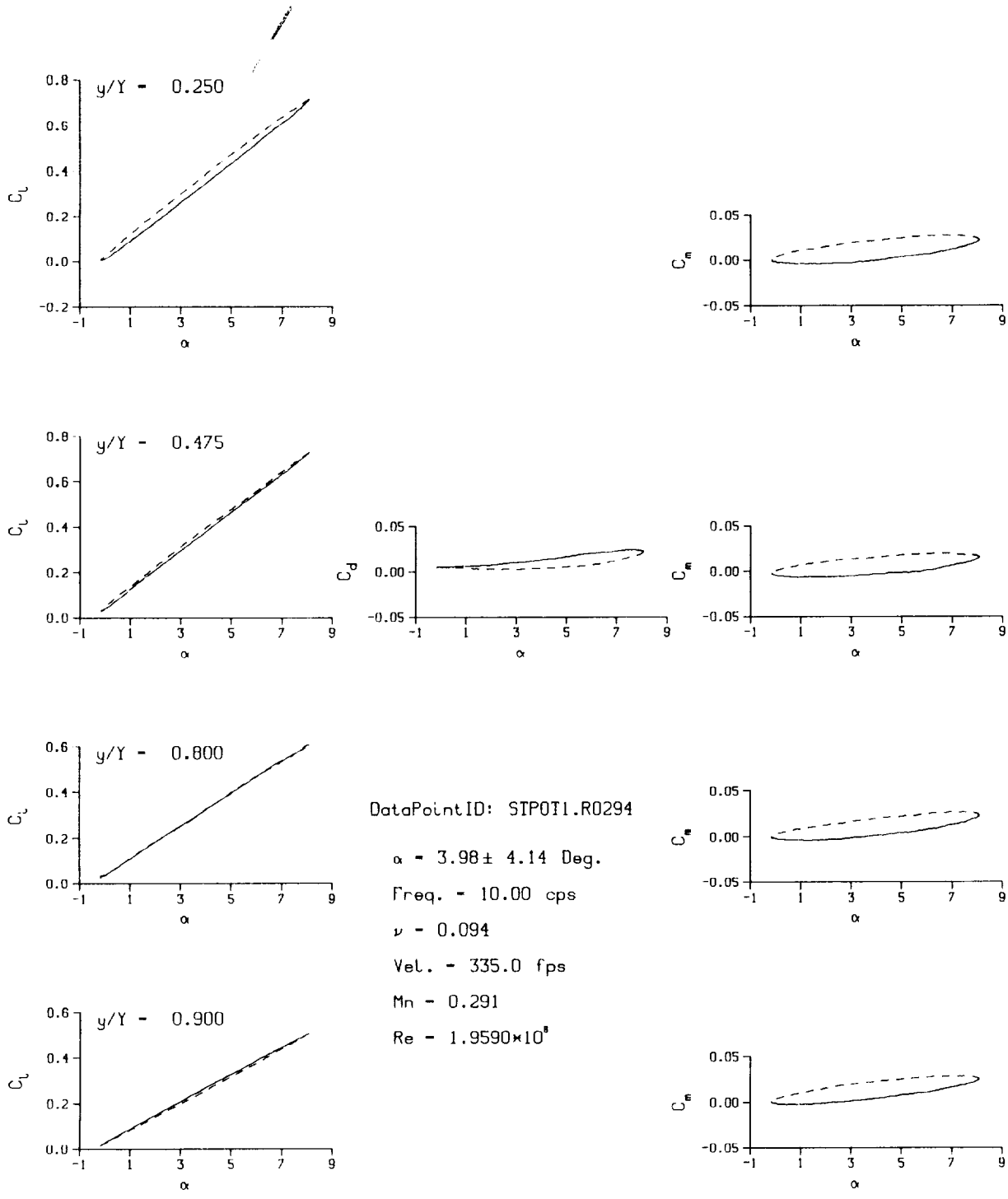

(b) v = 0.10

Figure 52. Continued.

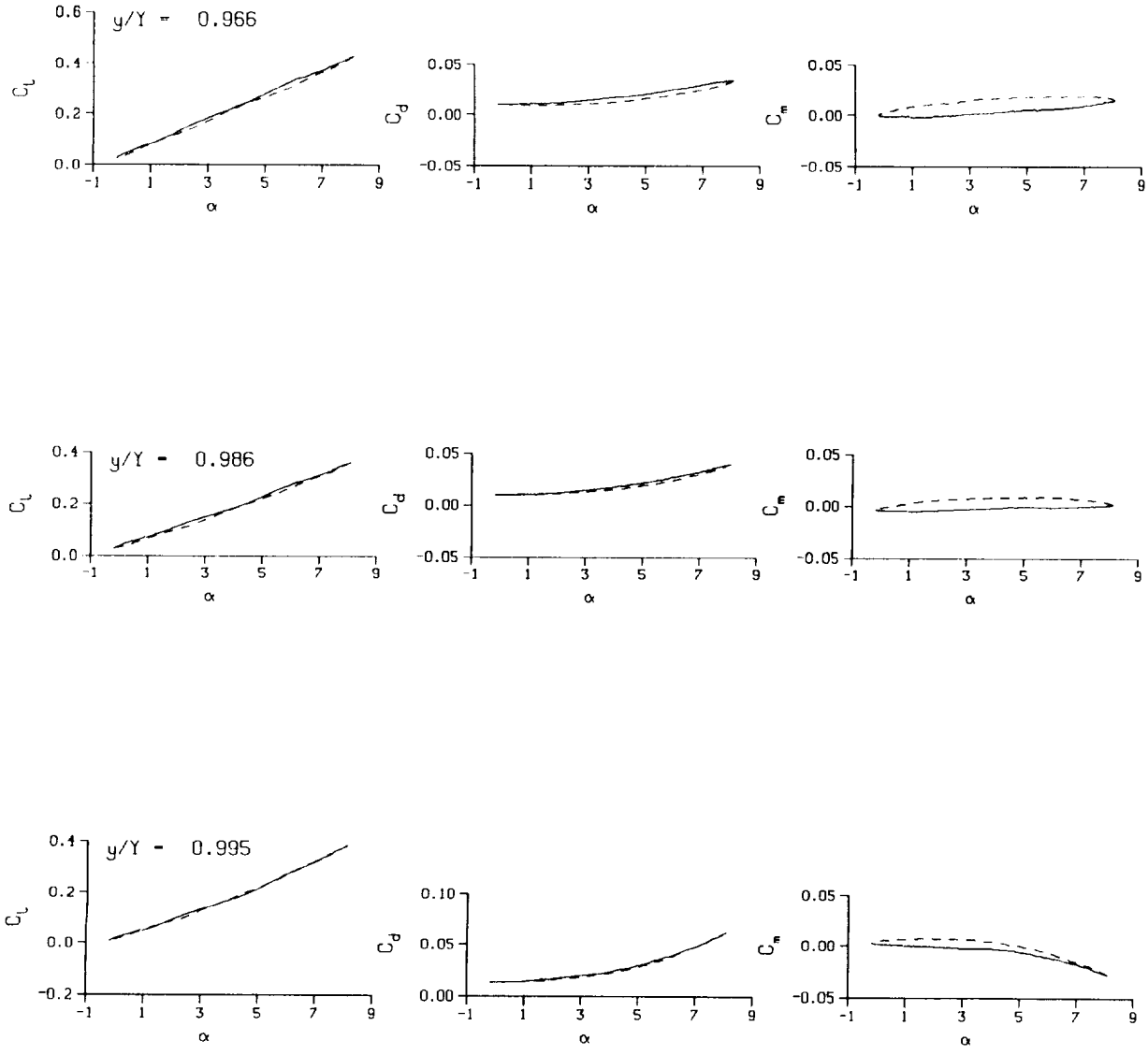

(b) v = 0.10. Concluded

Figure 52. Continued.

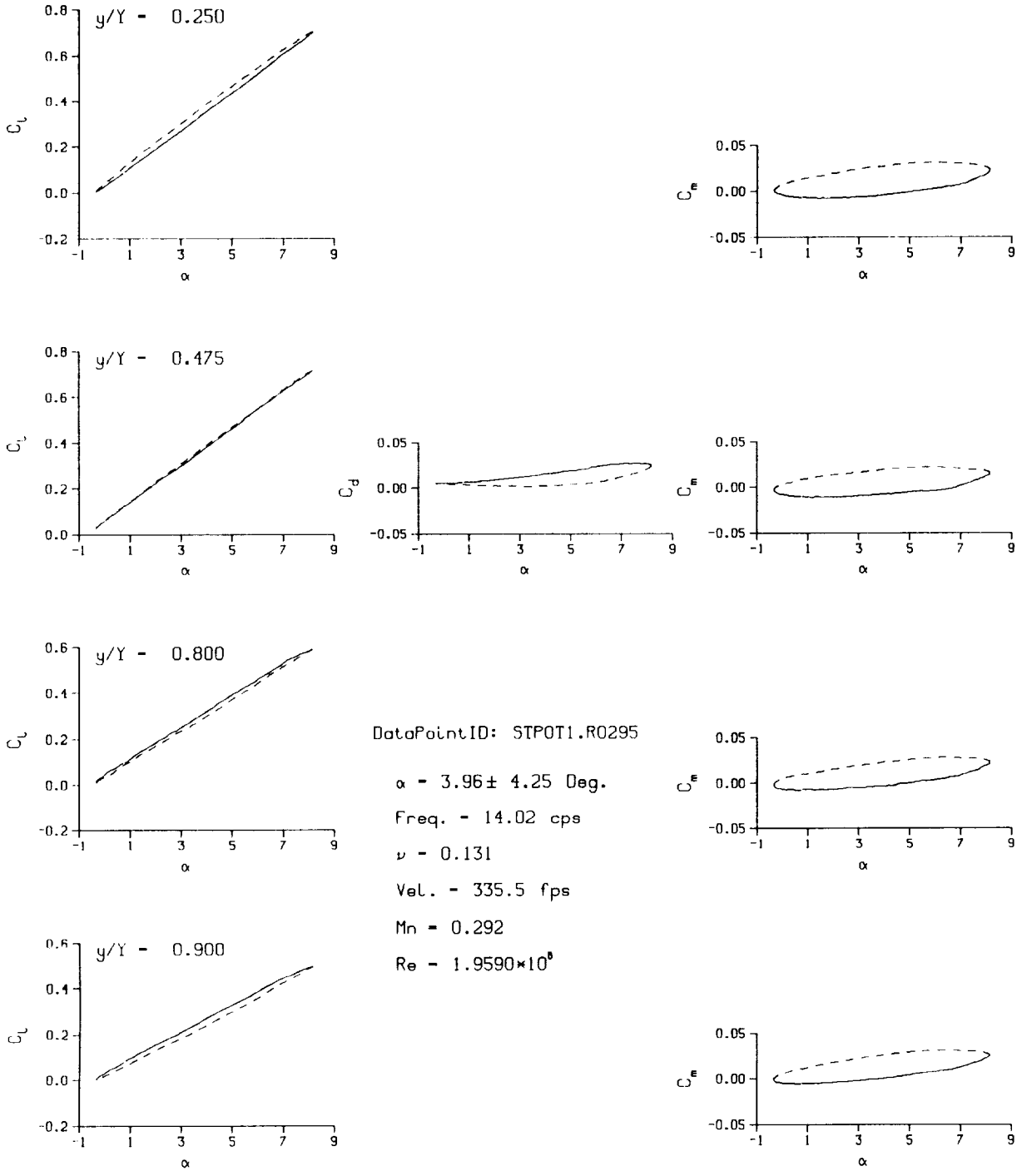

(c) ν = 0.14

Figure 52. Continued.

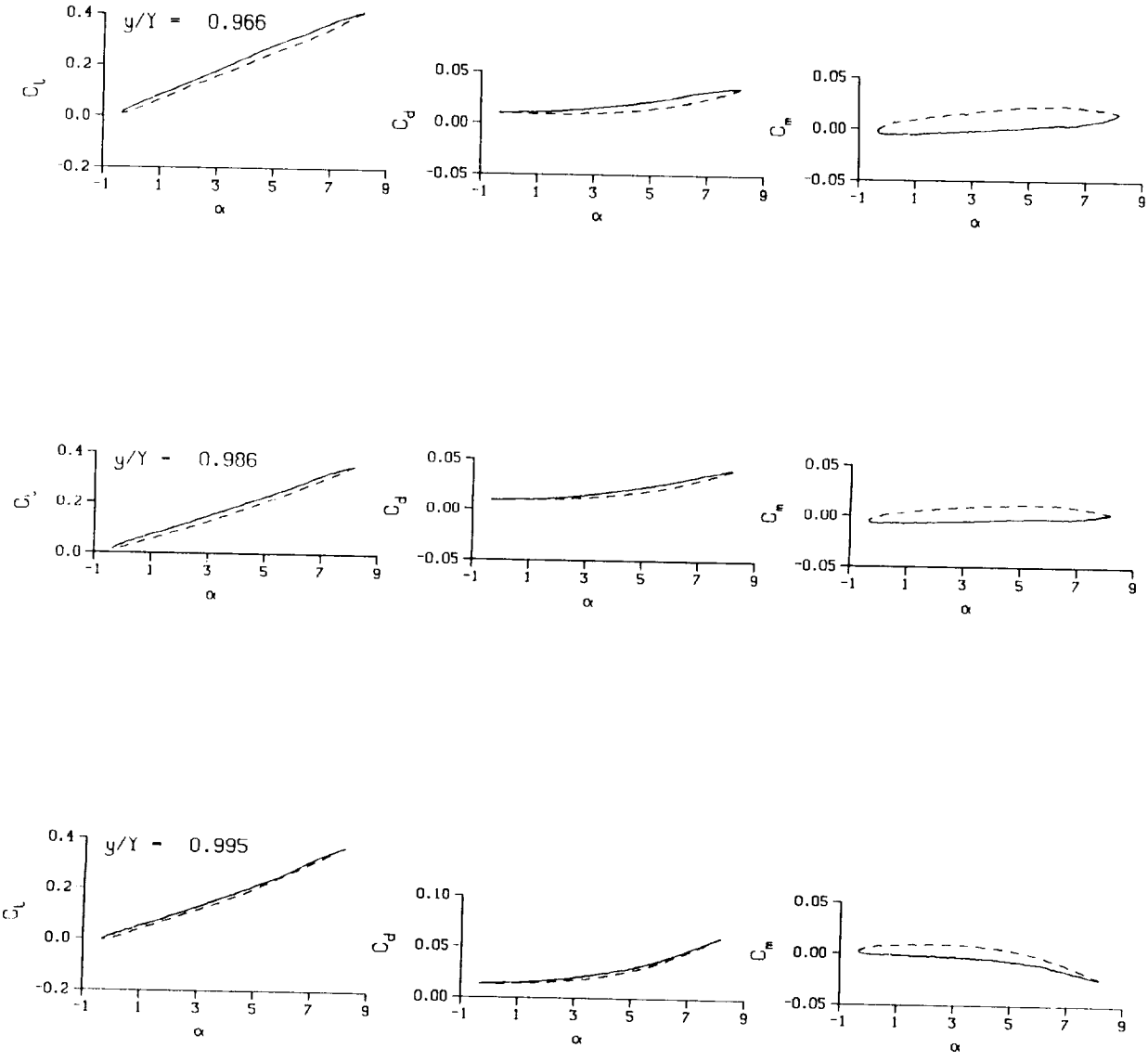

(c) v = 0.14. Concluded

Figure 52. Concluded.

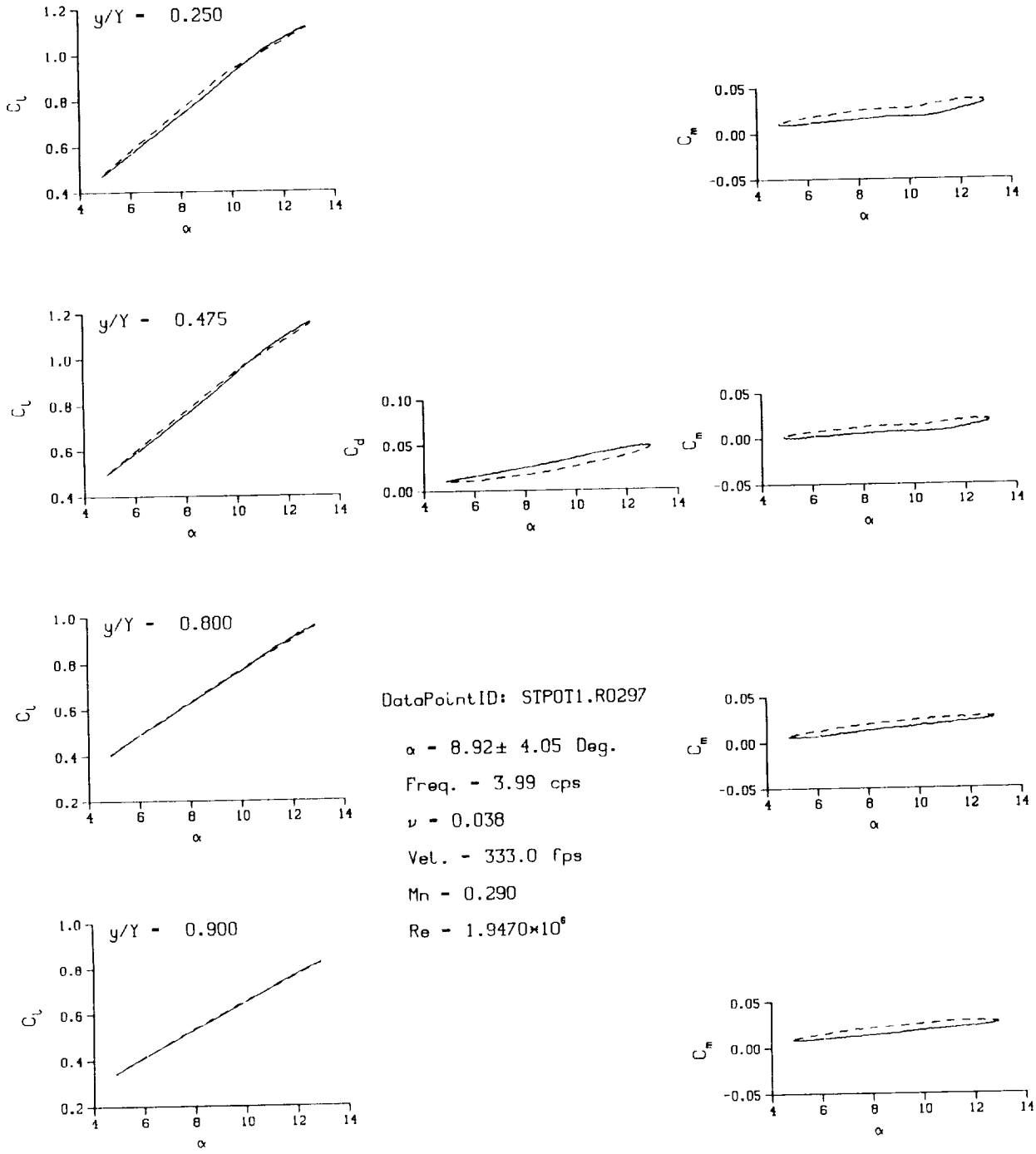

(a) ν = 0.04

Figure 53. 3-D square tip pitch oscillation data; BL-trip; α = 9 ± 4 deg.

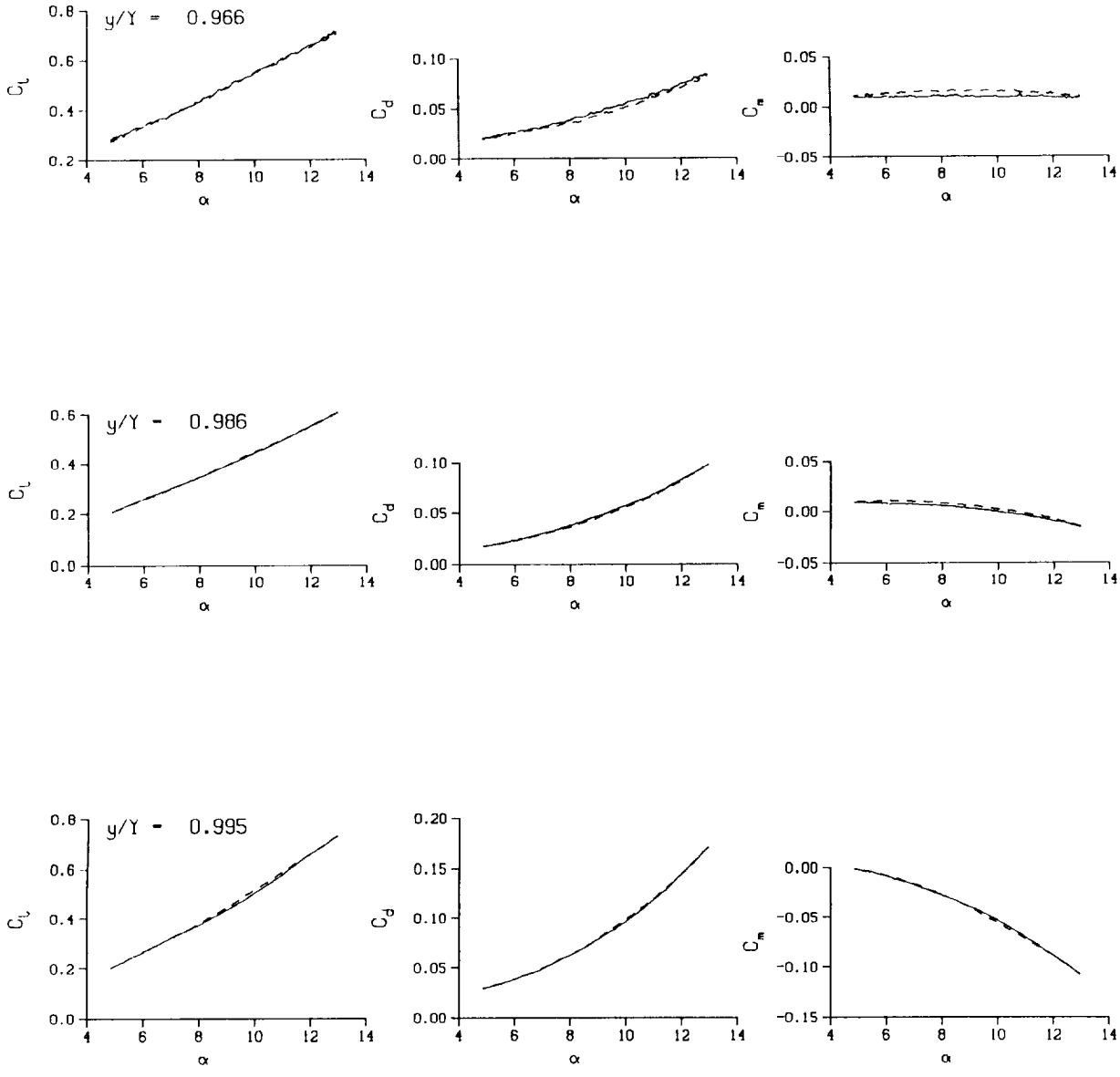

(a) v = 0.04. Concluded

Figure 53. Continued.

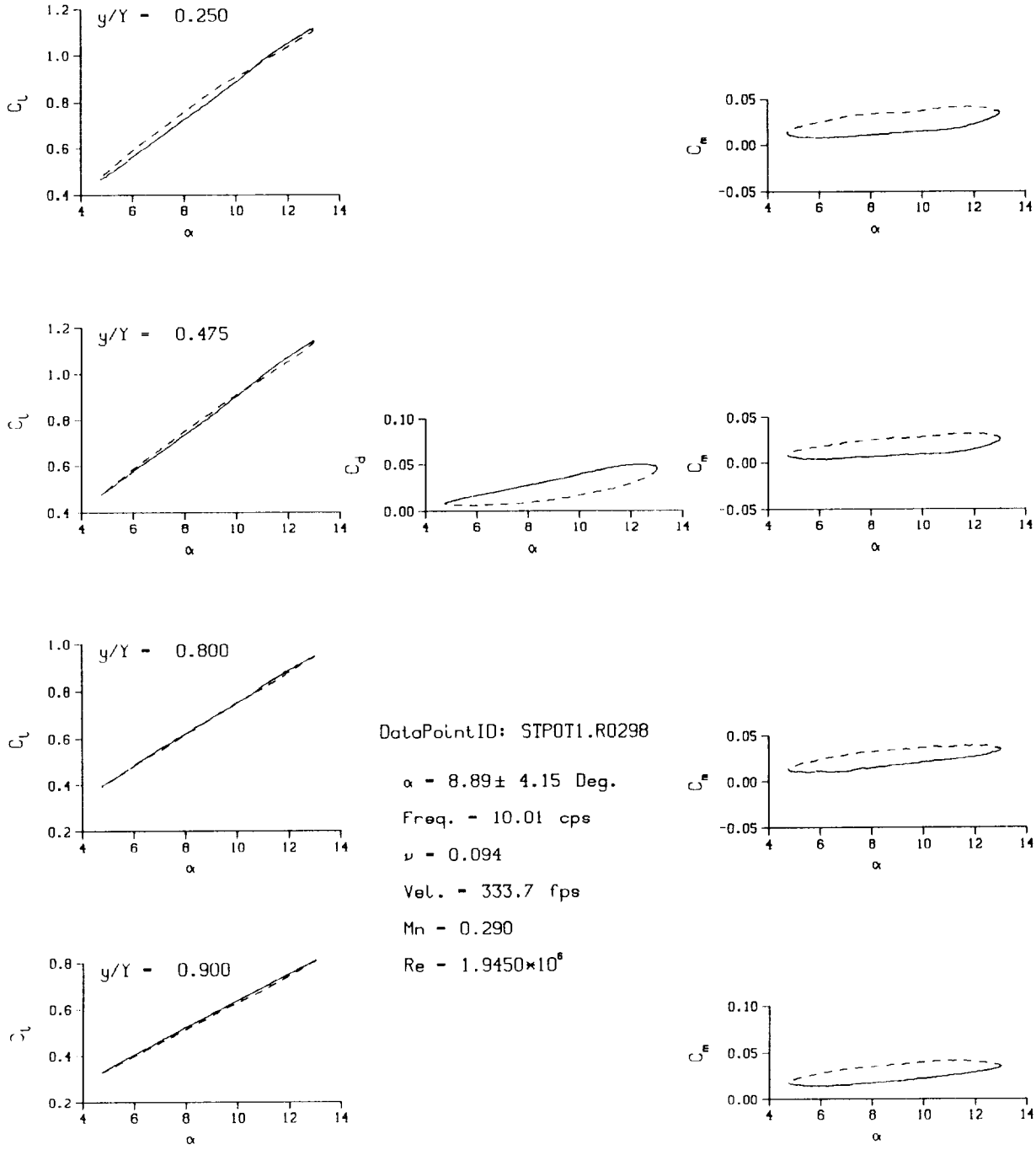

(b) v = 0.10

Figure 53. Continued.

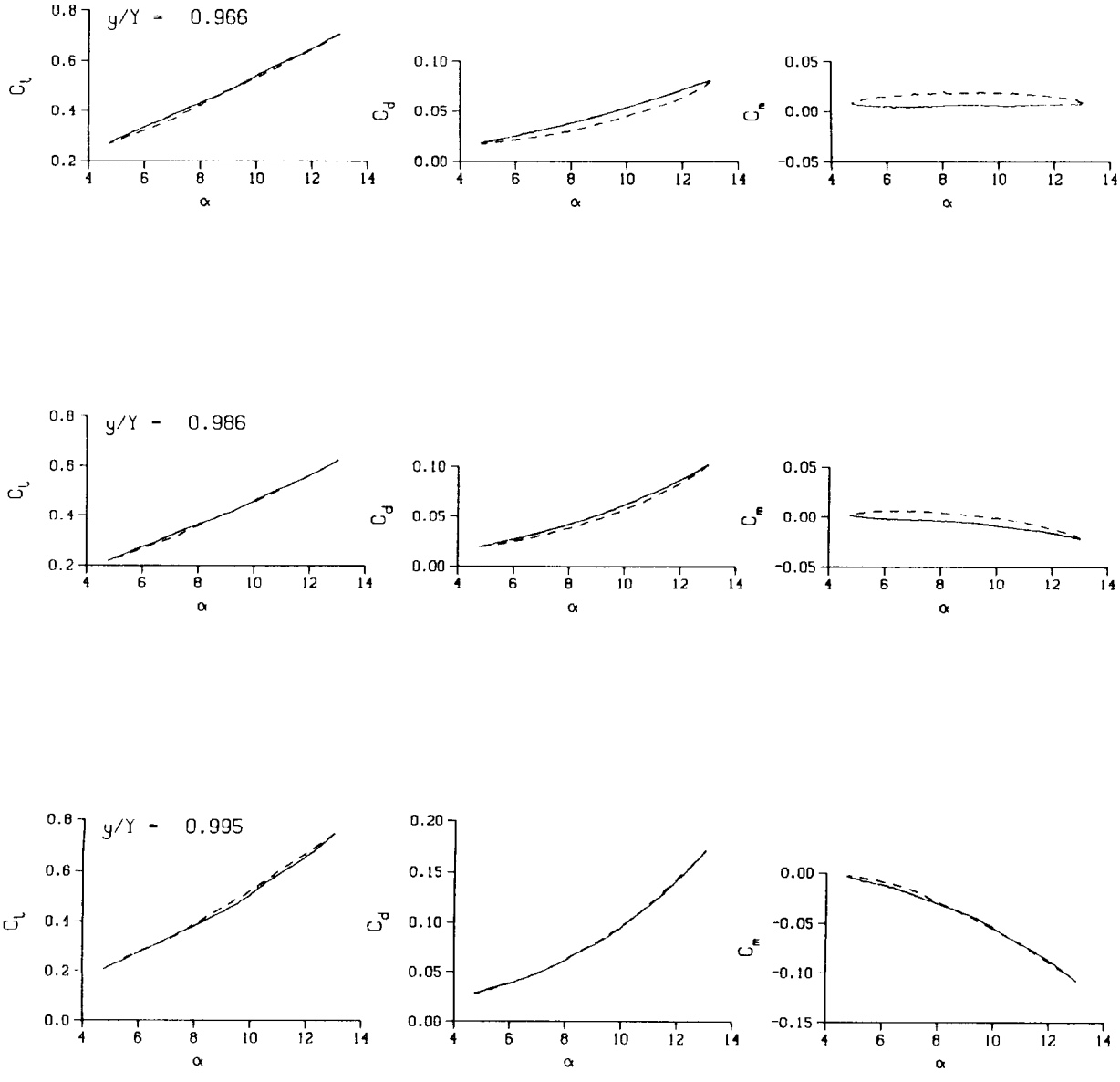

(b) v = 0.10. Concluded

Figure 53. Continued.

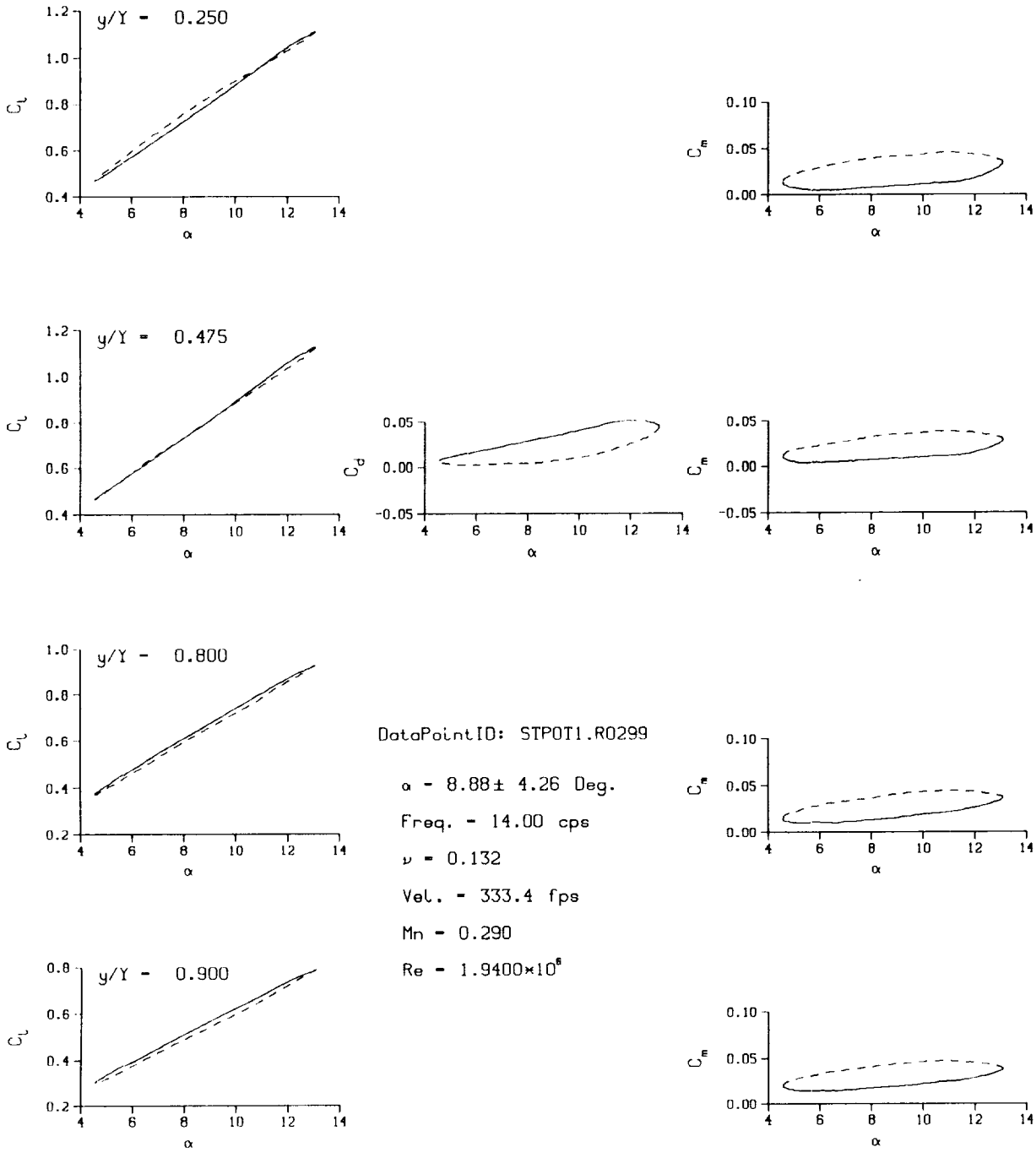

(c) v = 0.14

Figure 53. Continued.

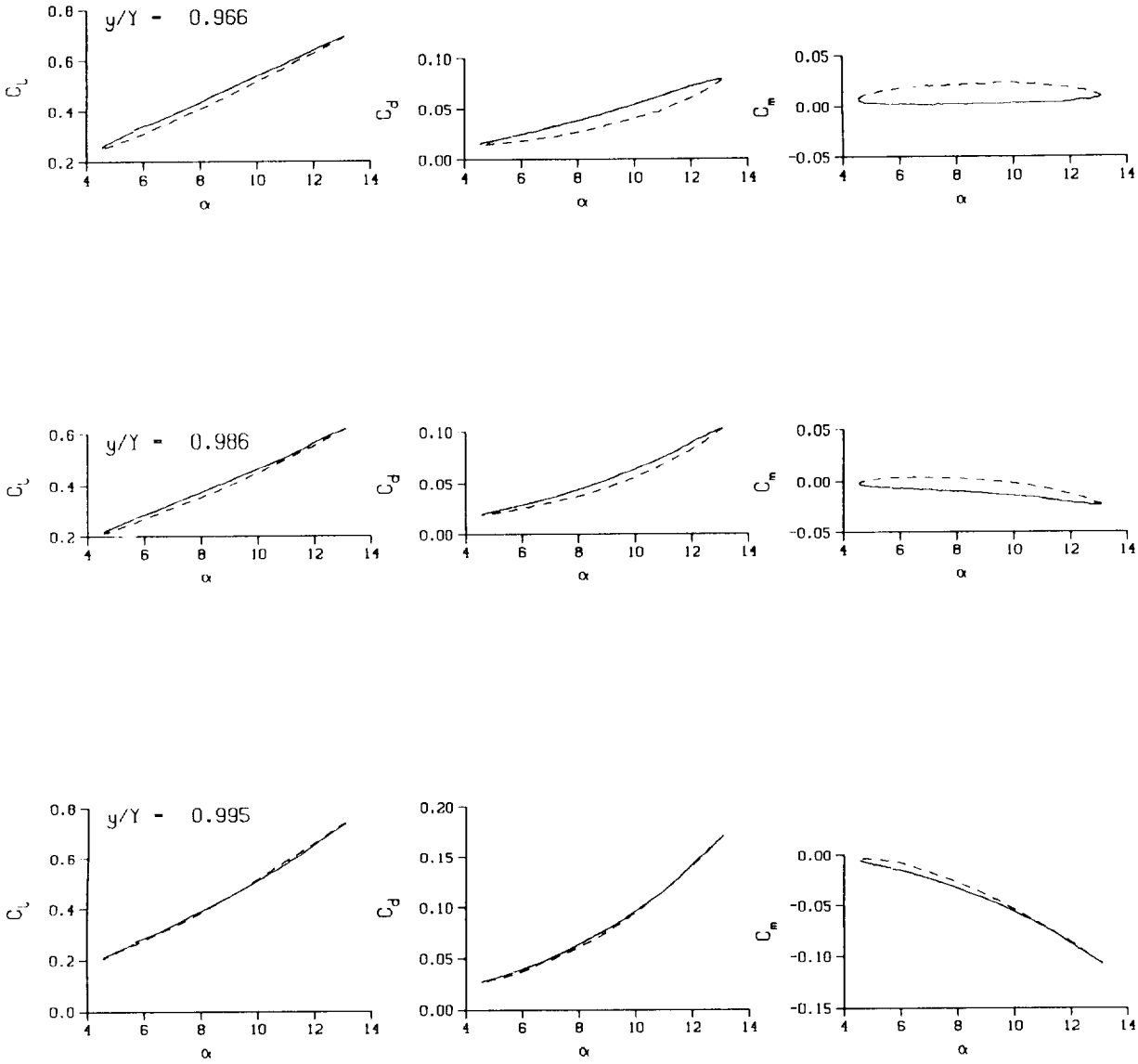

(c) v = 0.14. Concluded

Figure 53. Concluded.

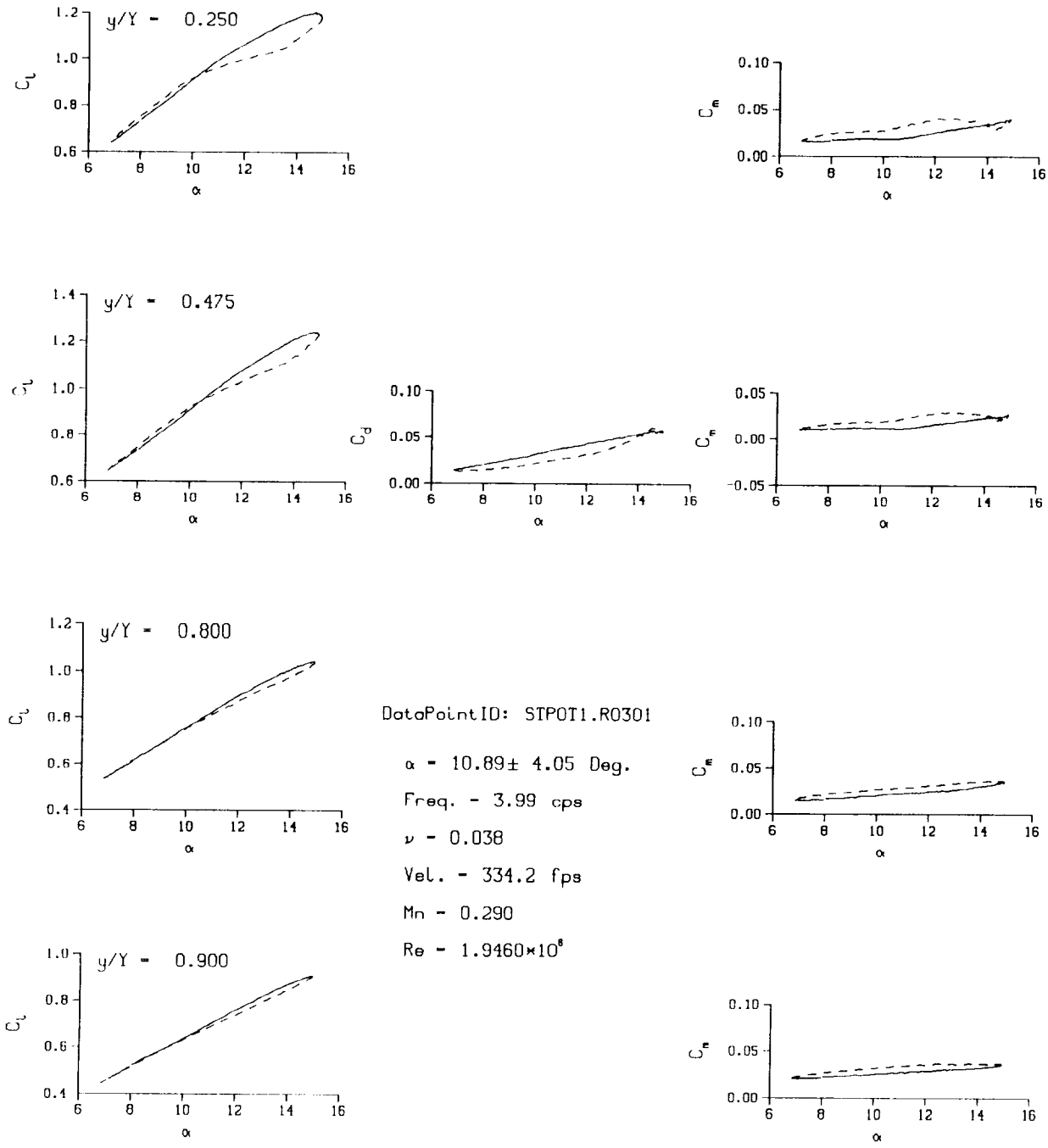

(a) v = 0.04

Figure 54. 3-D square tip pitch oscillation data; BL-trip; α = 11 ± 4 deg.

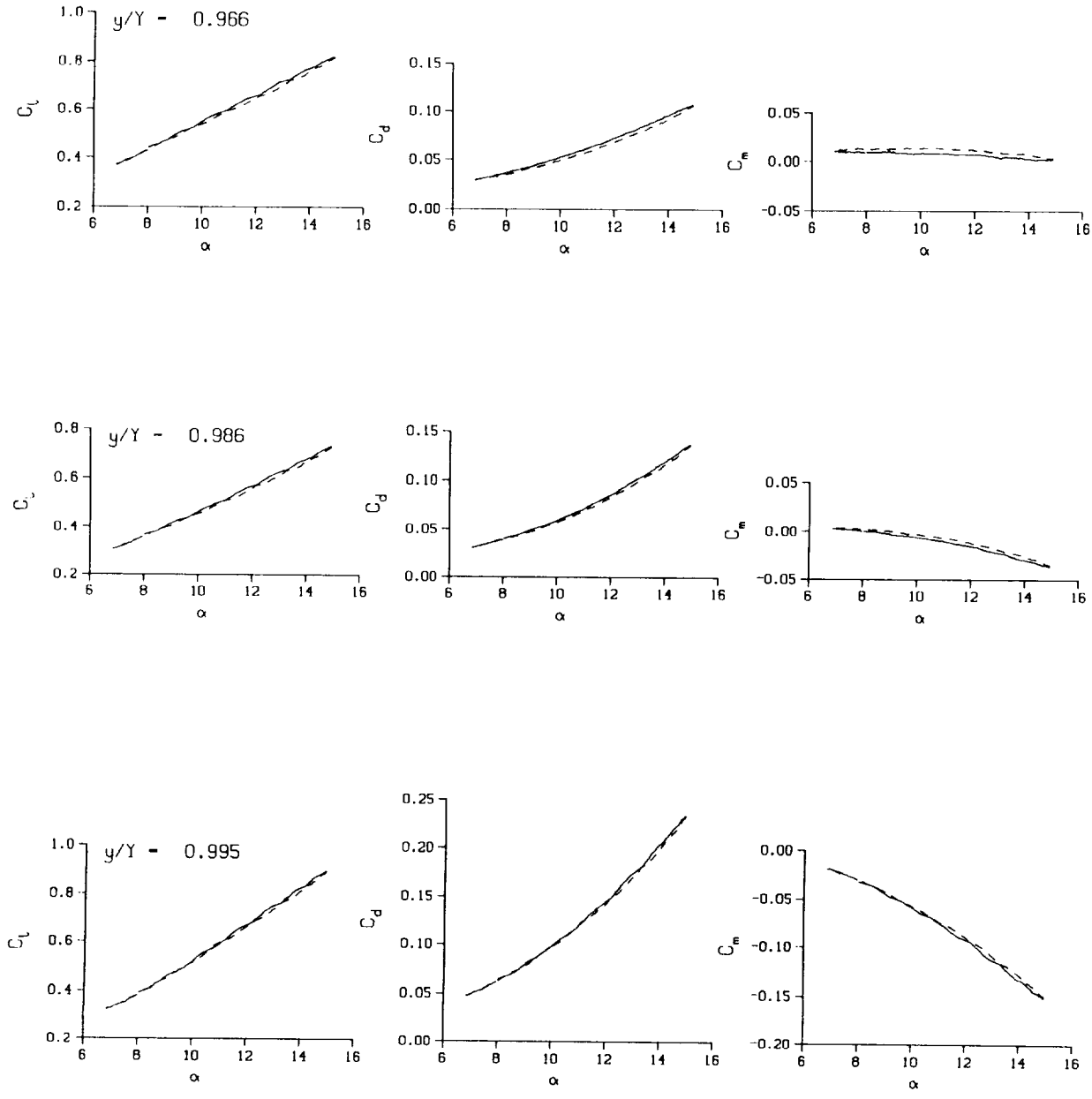

(a) v = 0.04. Concluded

Figure 54. Continued.

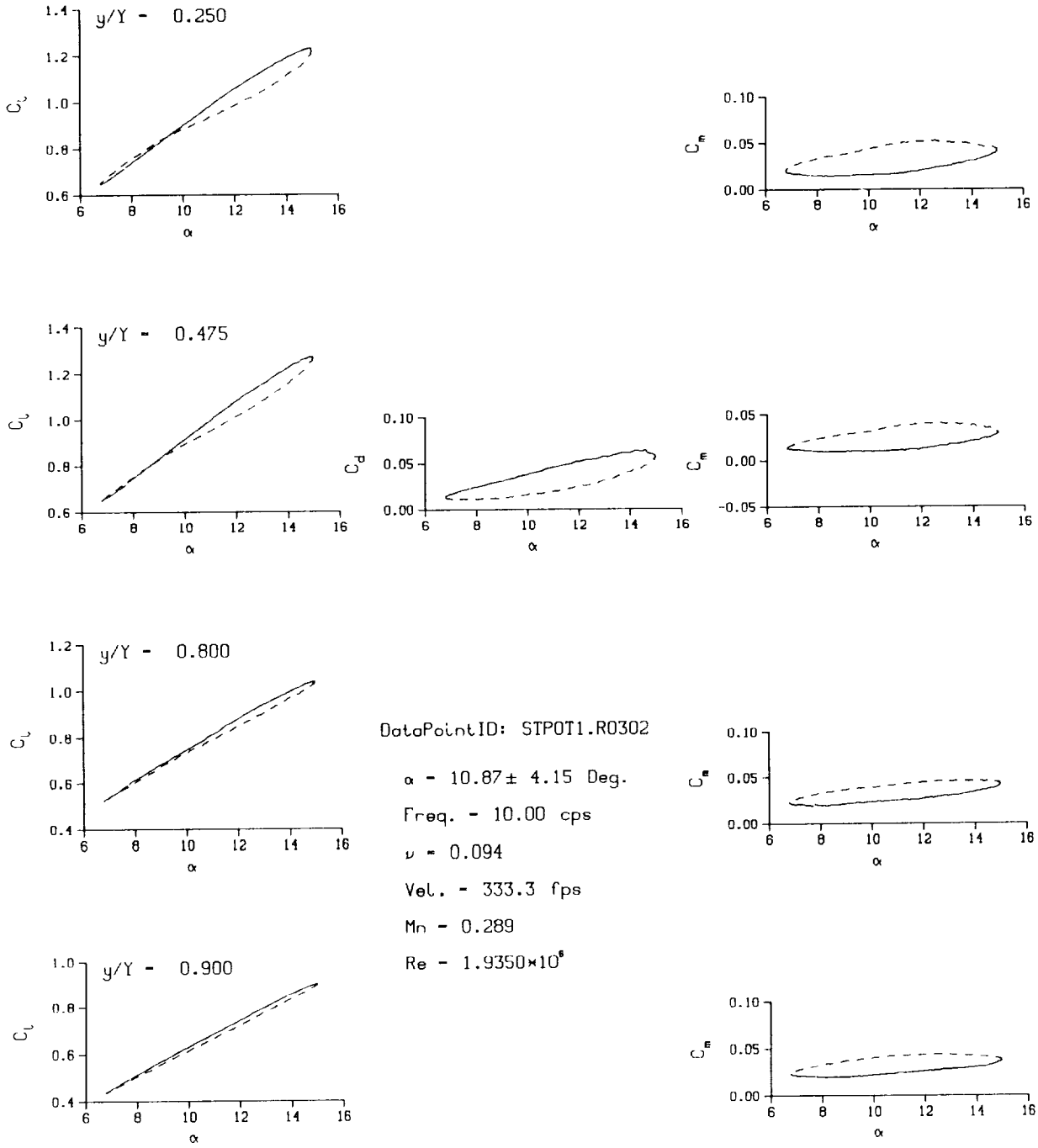

(b) v = 0.10

Figure 54. Continued.

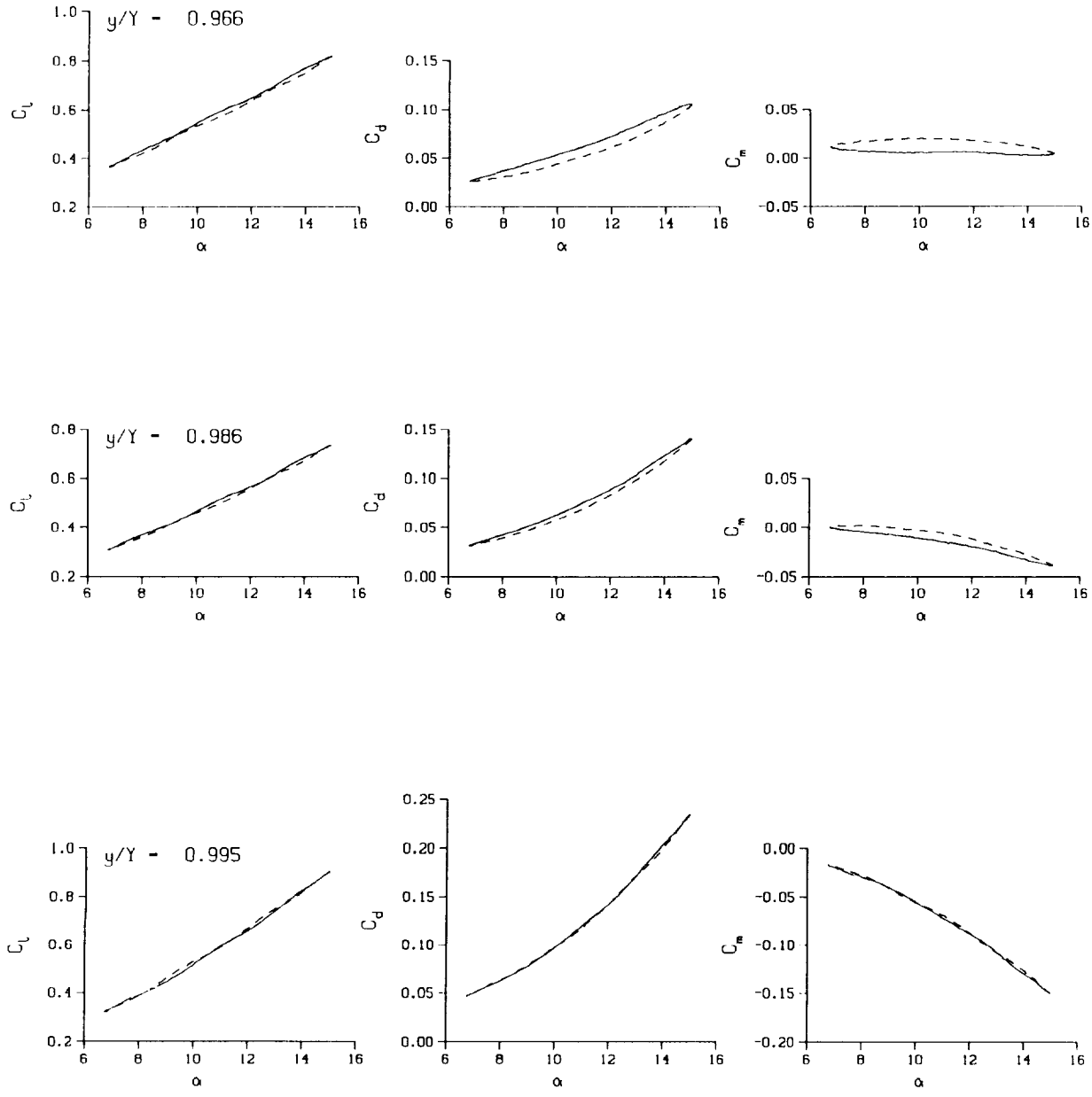

(b) v = 0.10. Concluded

Figure 54. Continued.

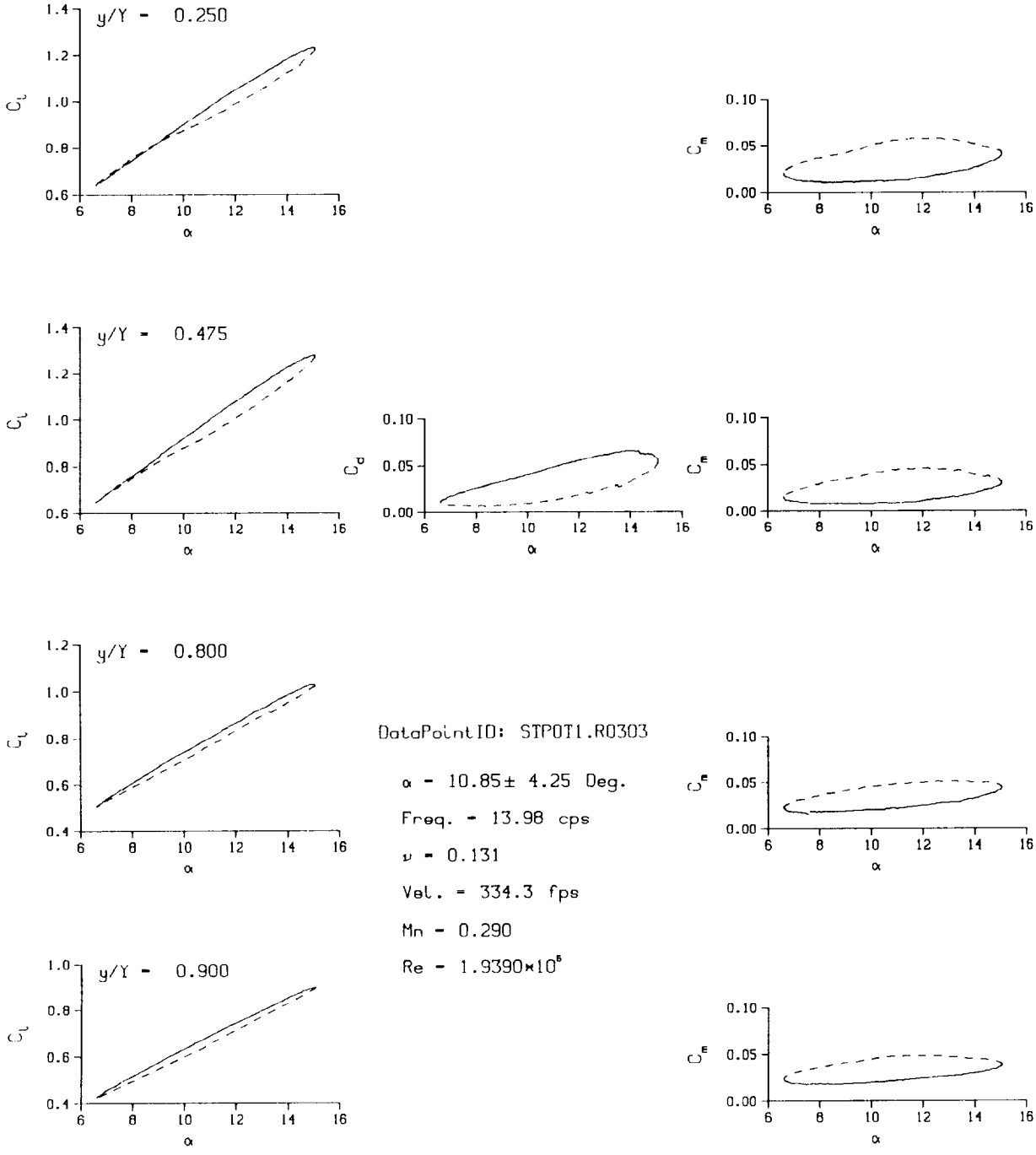

(c) ν = 0.14

Figure 54. Continued.

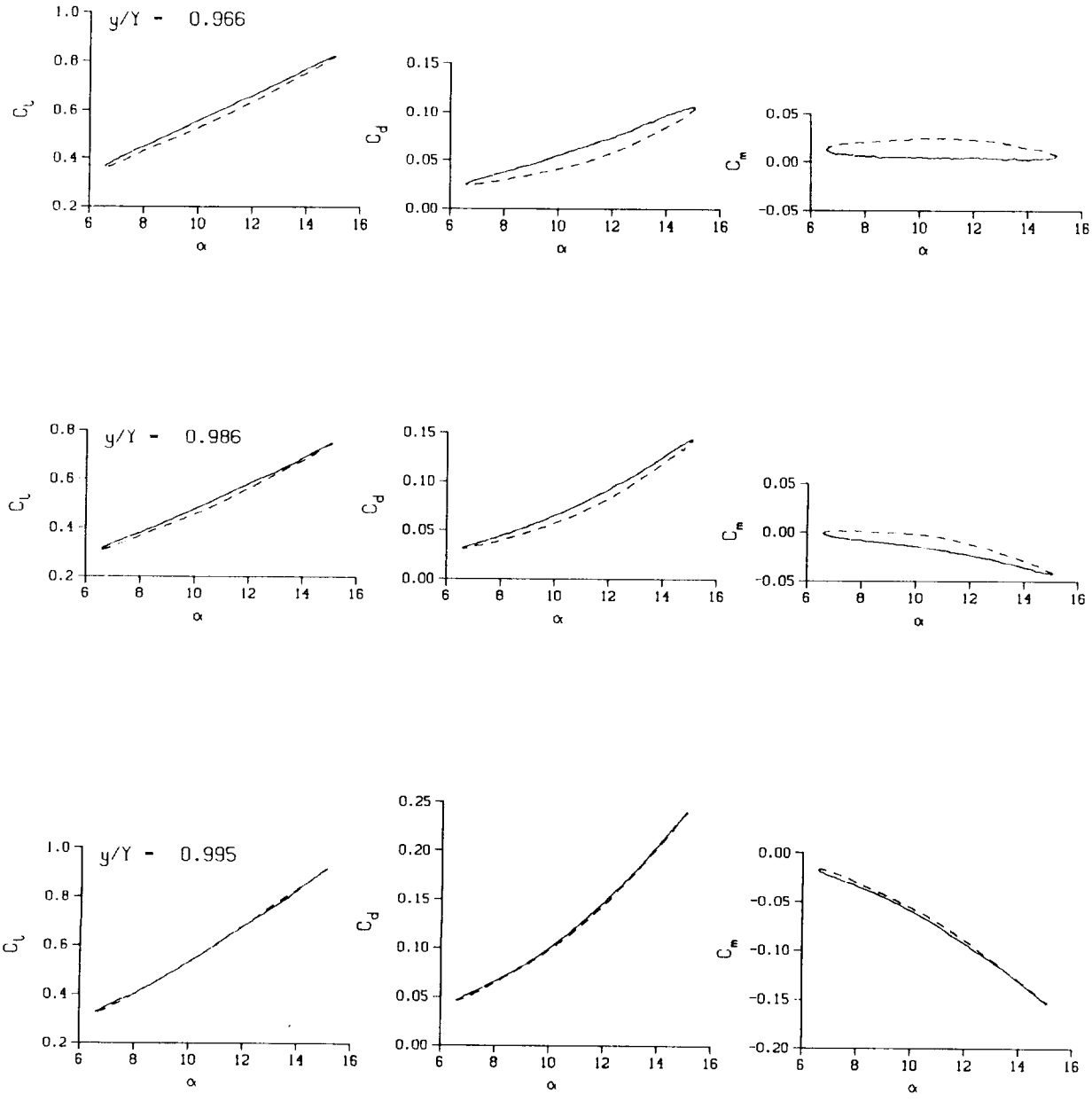

(c) v = 0.14. Concluded

Figure 54. Concluded.

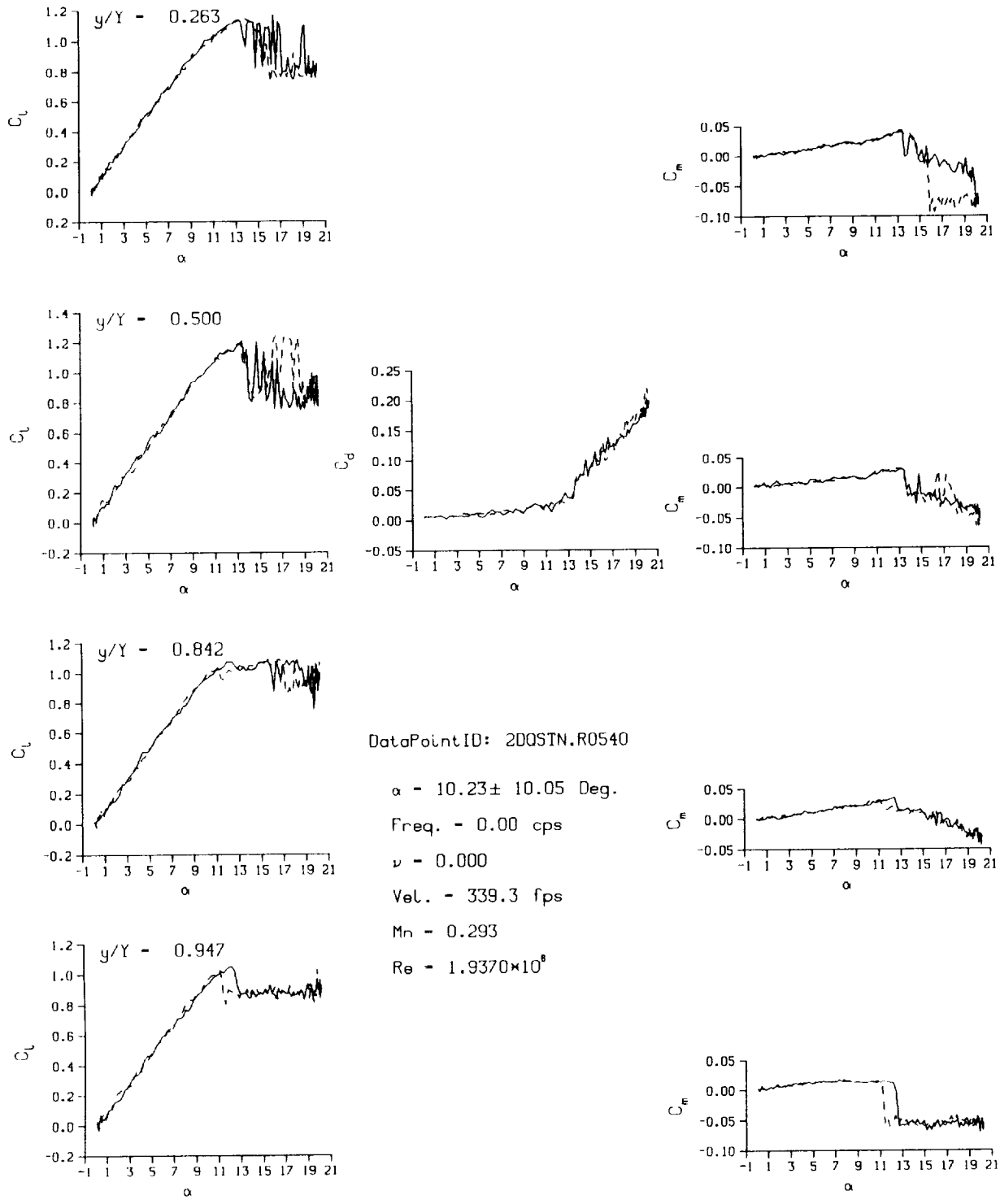

(a) Repeat no. 1

Figure 55. 2-D quasi-steady data; no BL-trip; 0 ≤ α ≤ 20 deg.

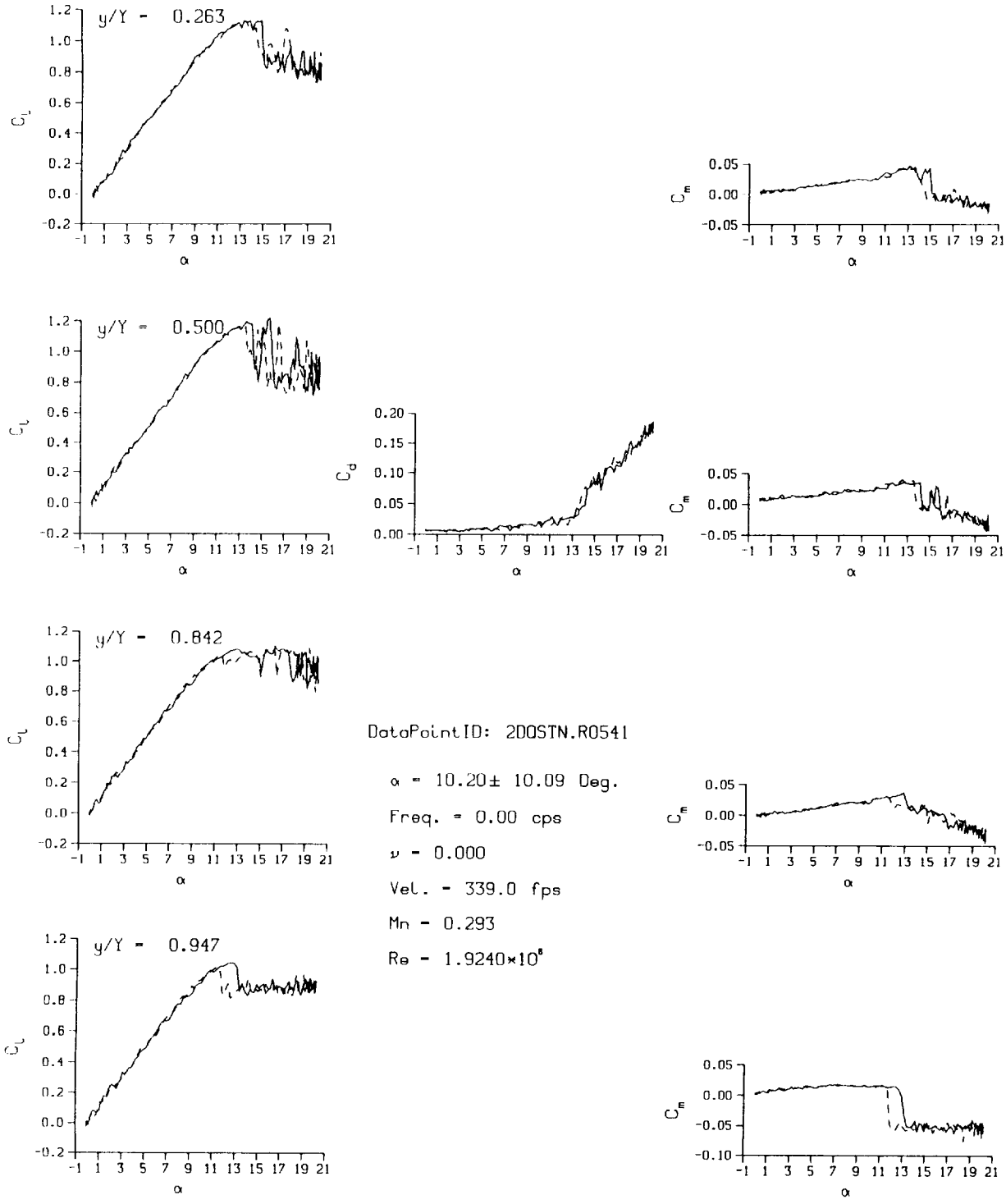

(b) Repeat no. 2

Figure 55. Continued.

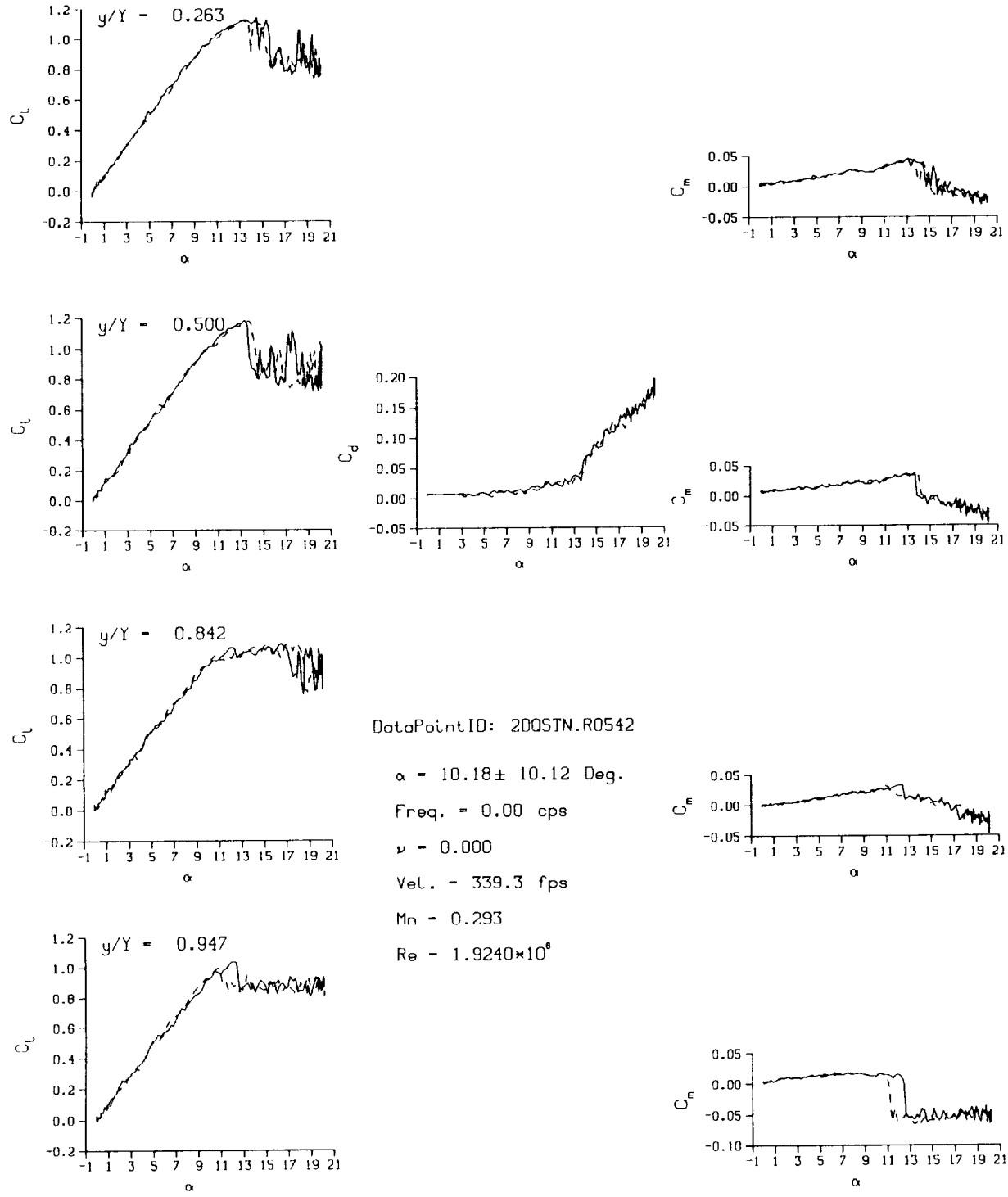

(c) Repeat no. 3

Figure 55. Continued.

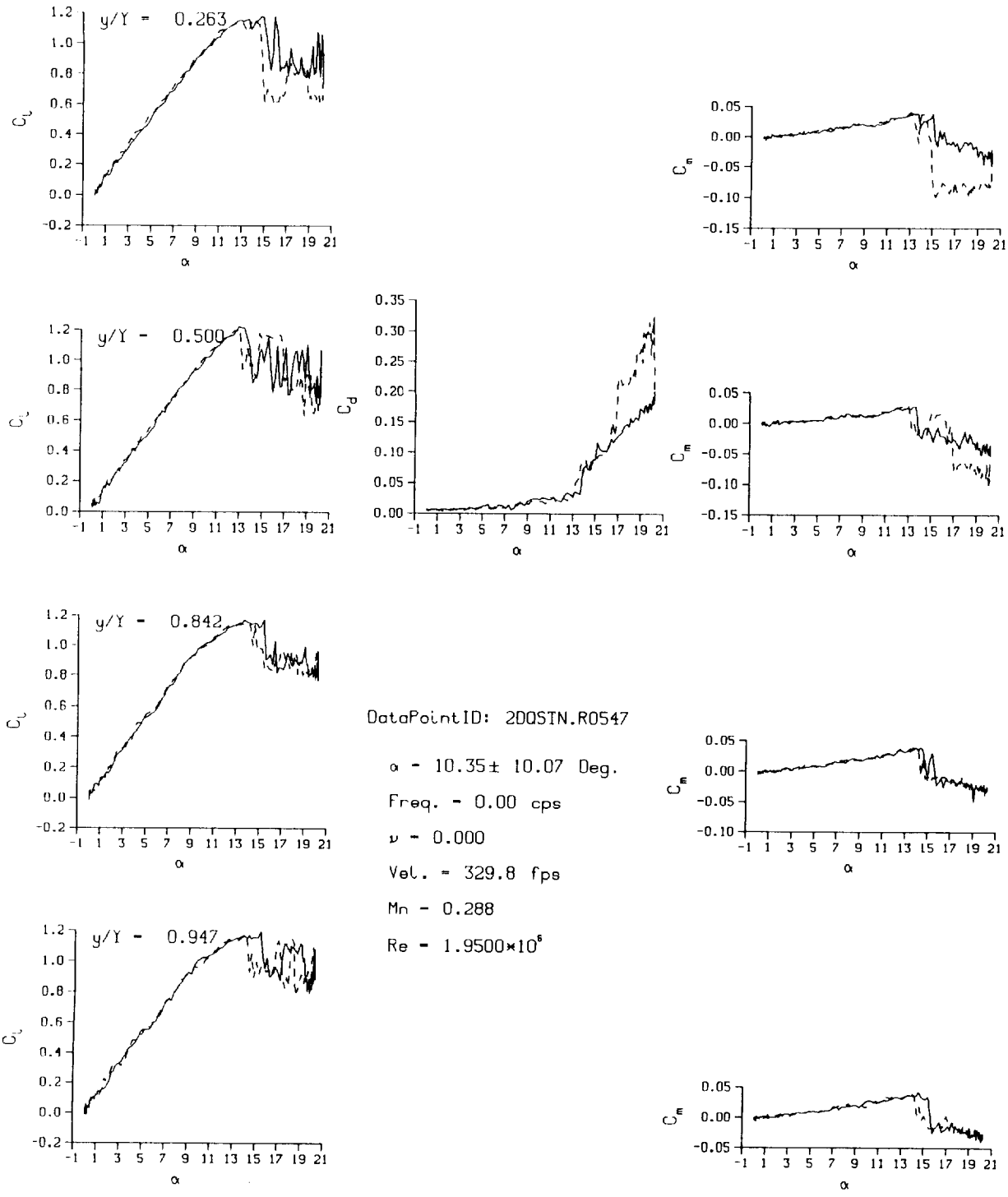

(d) Repeat no. 4

Figure 55. Continued.

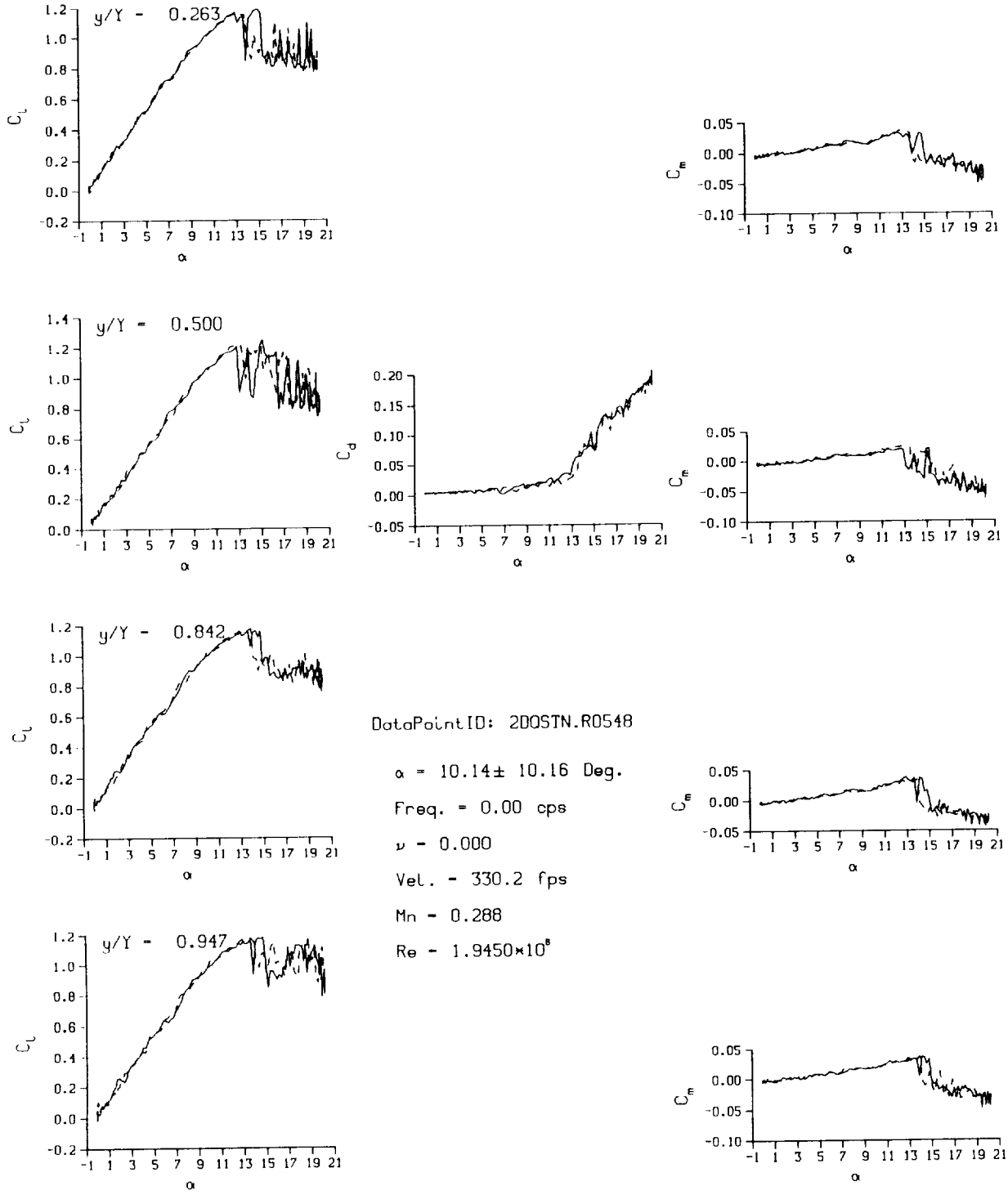

(e) Repeat no. 5

Figure 55. Continued.

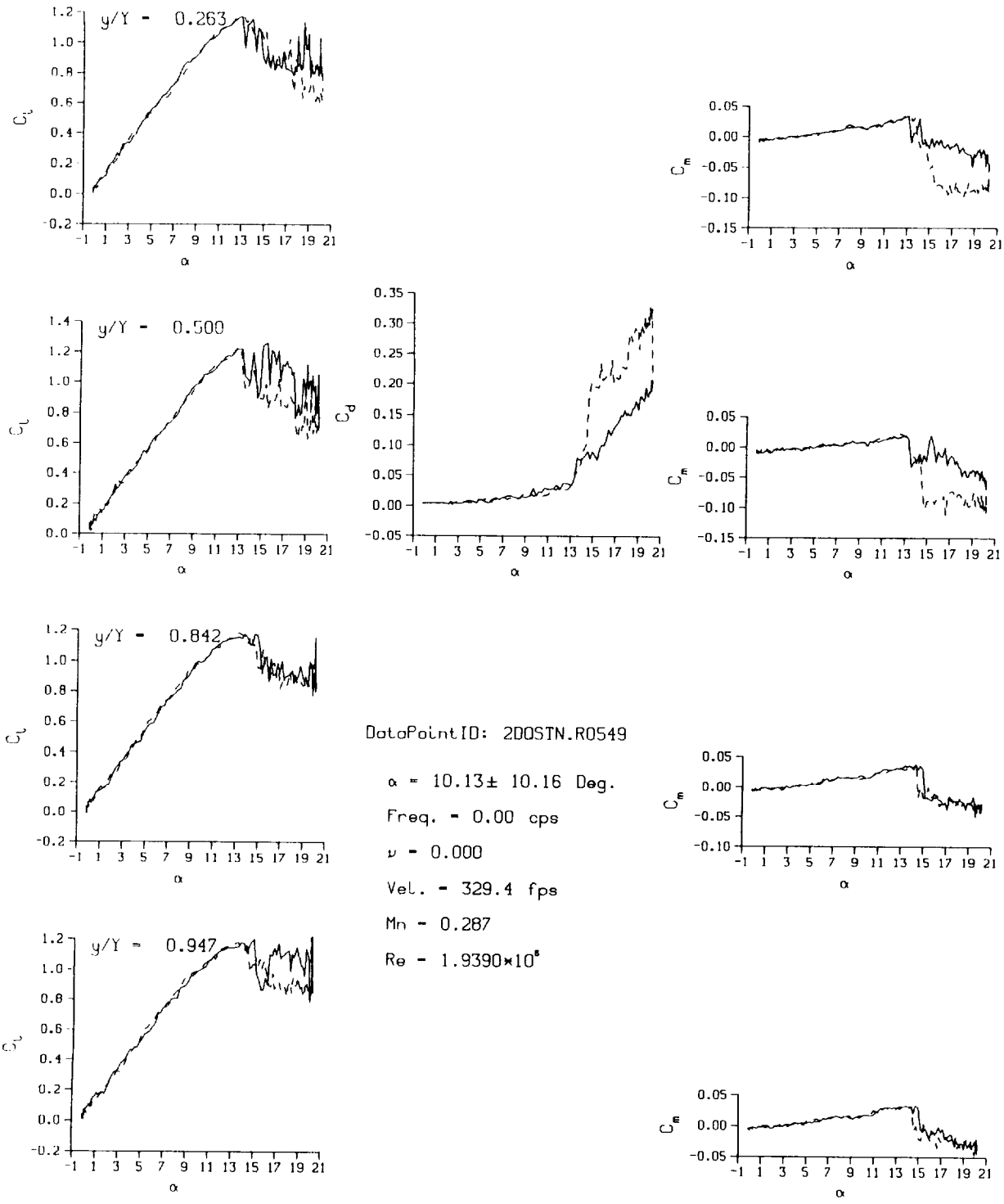

(f) Repeat no. 6

Figure 55. Concluded.

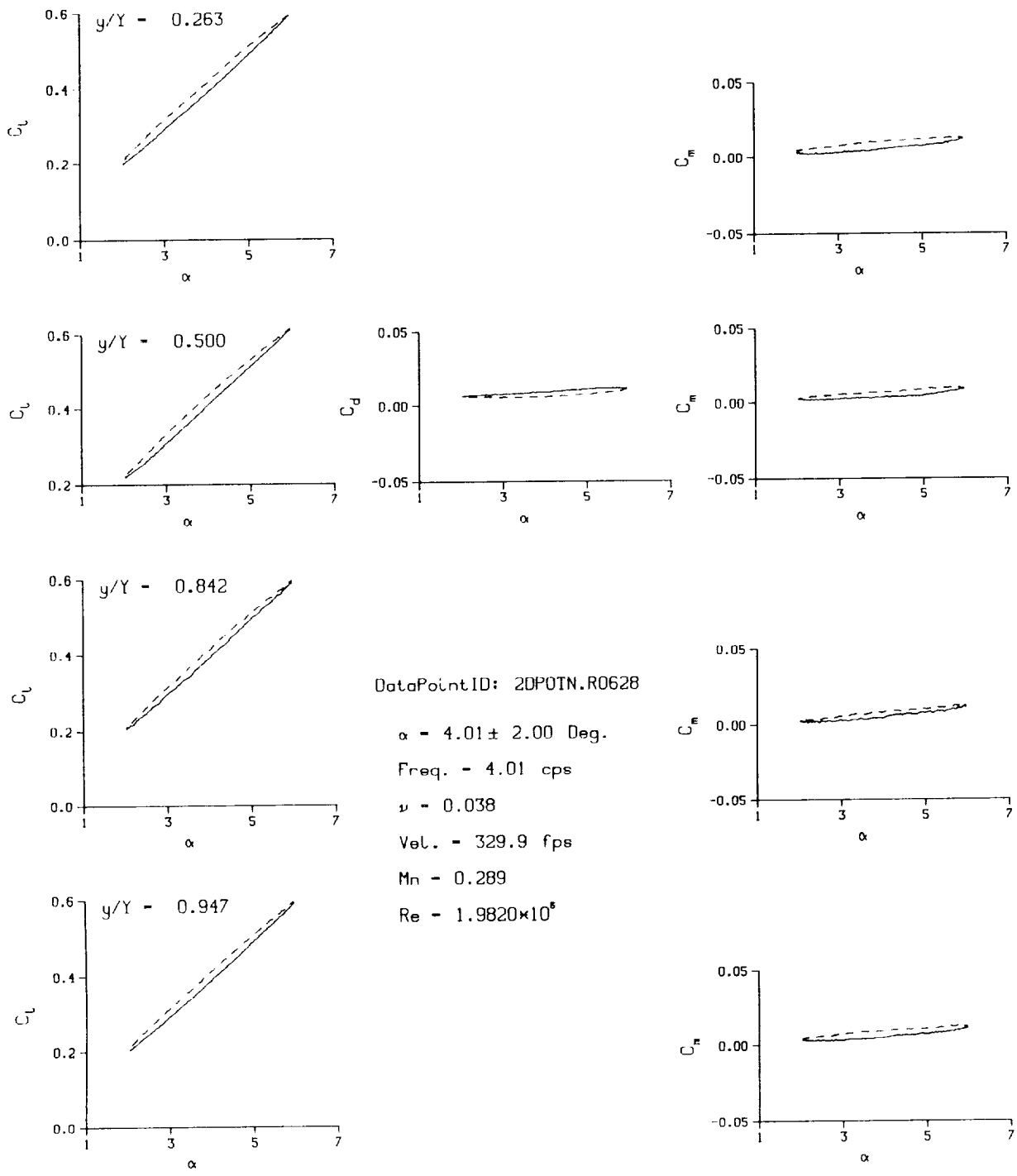

(a) v = 0.04

Figure 56. 2-D pitch oscillation data; no BL-trip; α = 4 ± 2 deg.

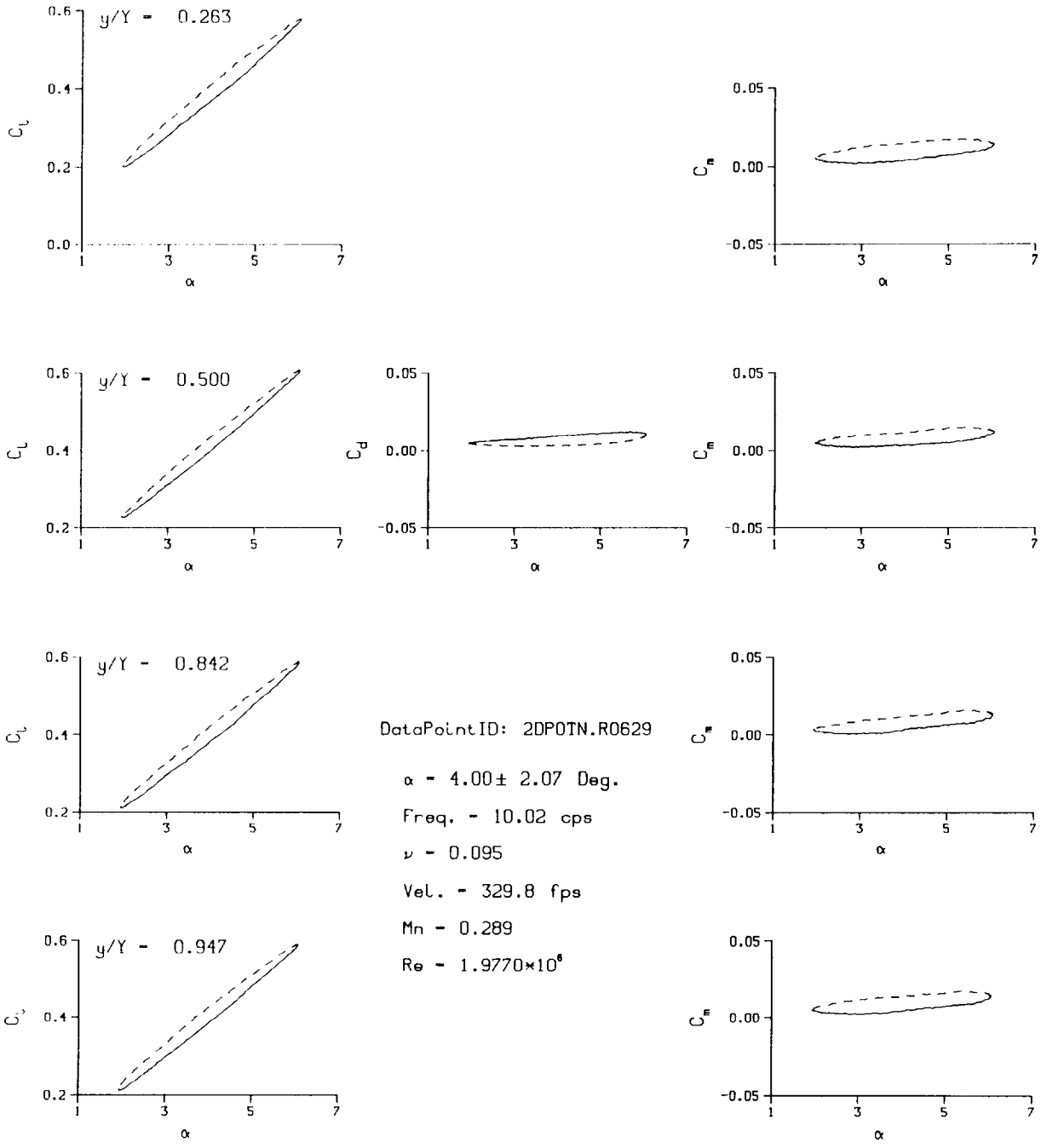

(b) ν = 0.10

Figure 56. Continued.

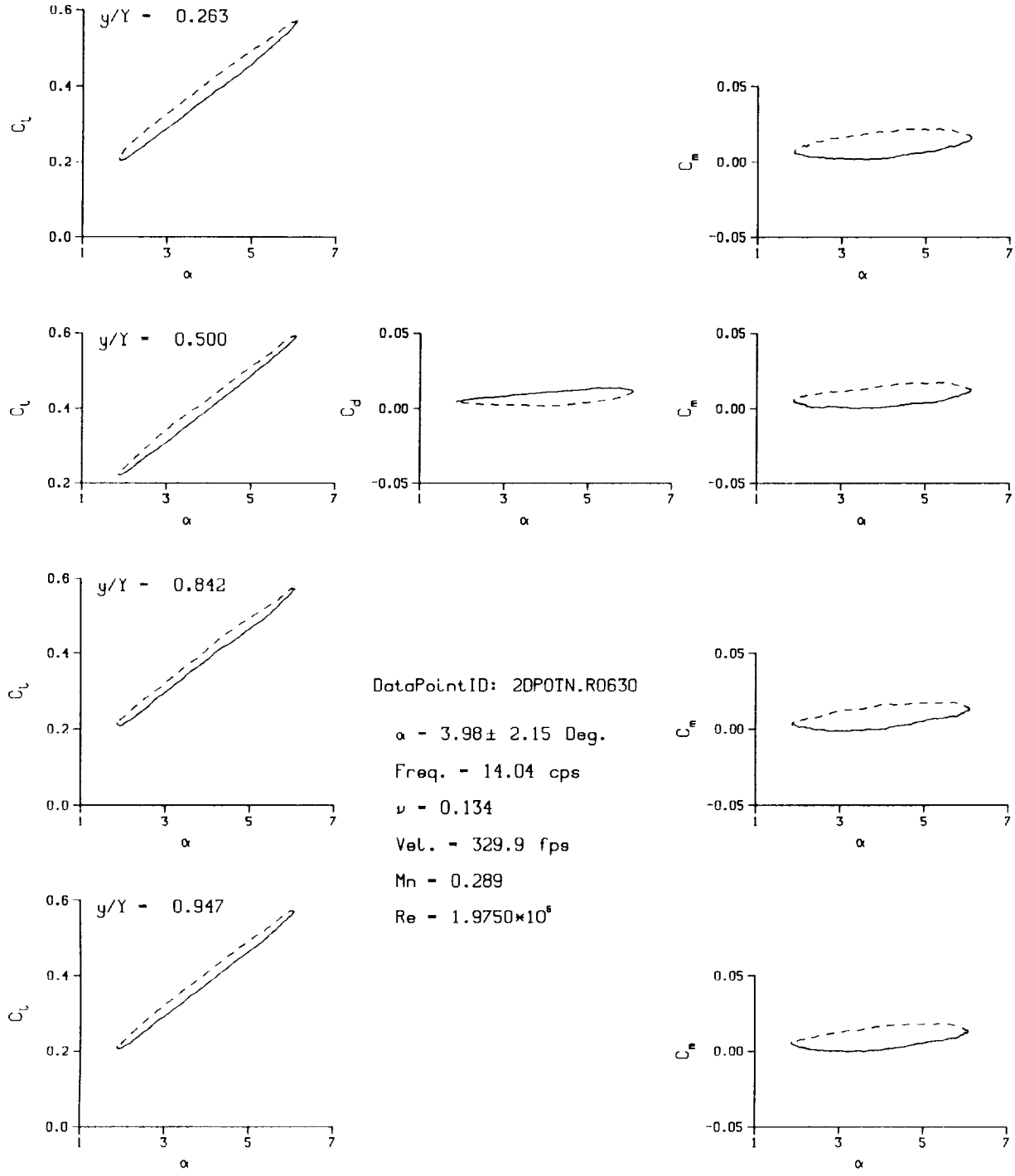

(c) v = 0.14

Figure 56. Continued.

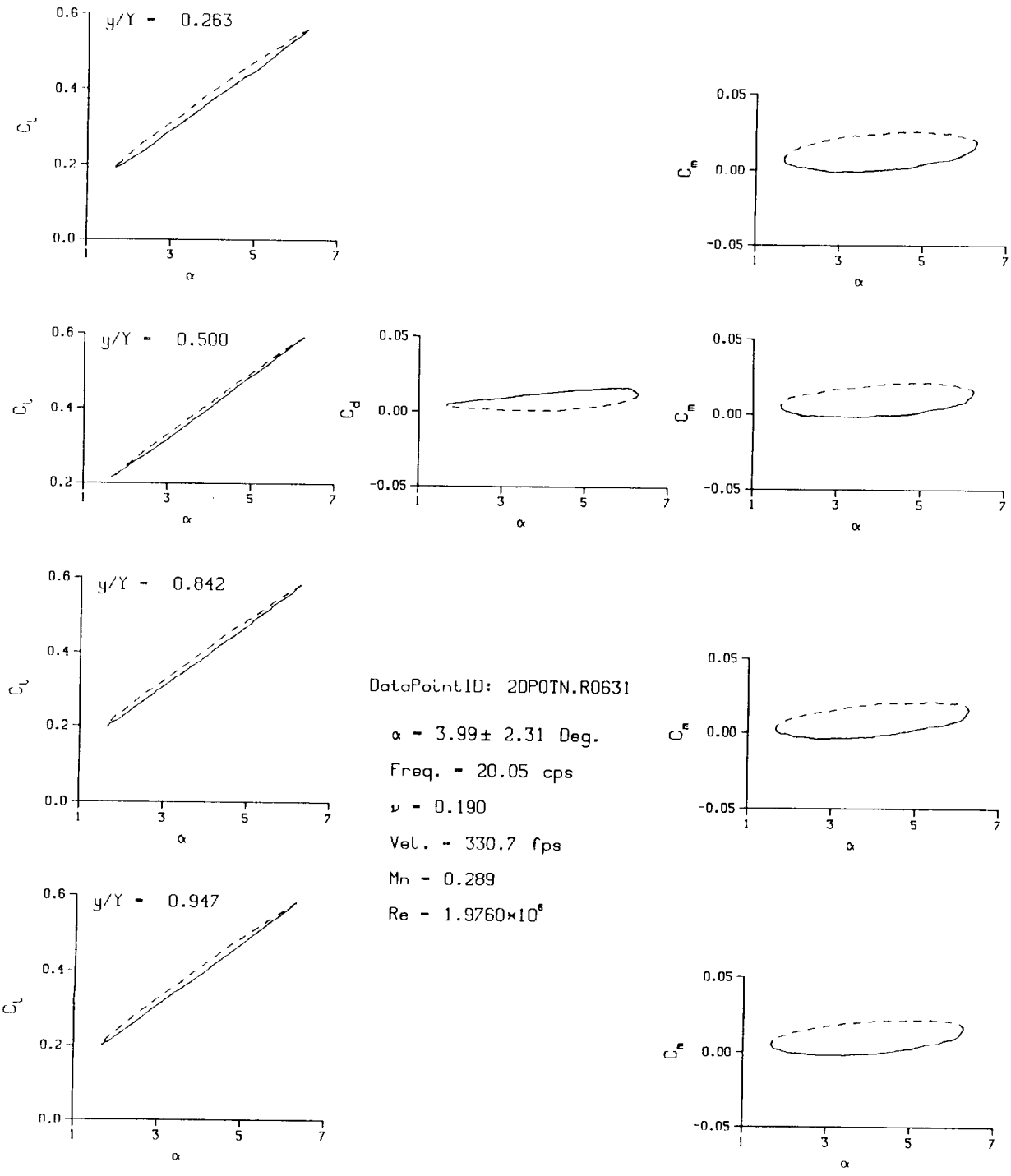

(d) v = 0.20

Figure 56. Concluded.

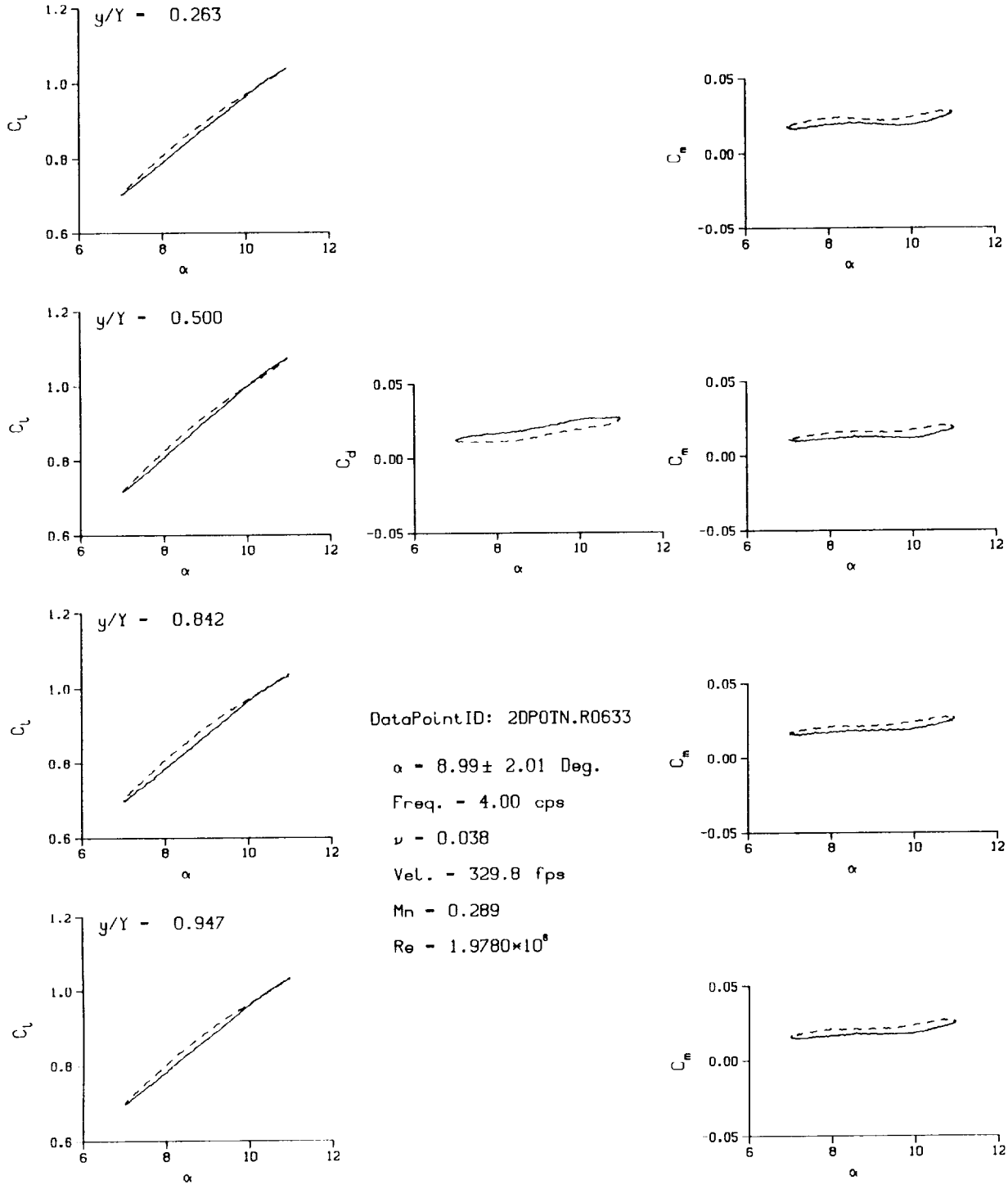

(a) ν = 0.04

Figure 57. 2-D pitch oscillation data; no BL-trip; α = 9 ± 2 deg.

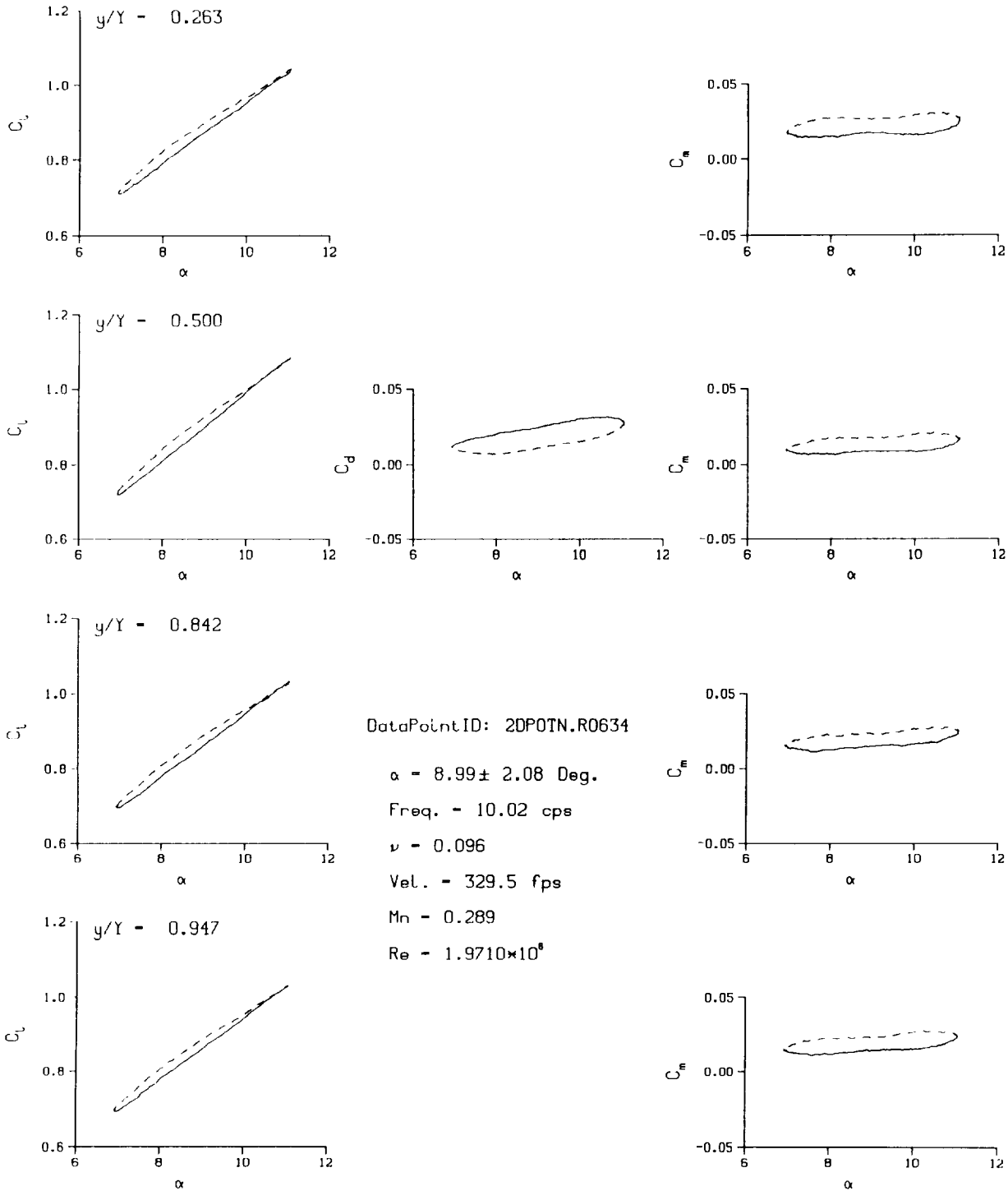

(b) ν = 0.10

Figure 57. Continued.

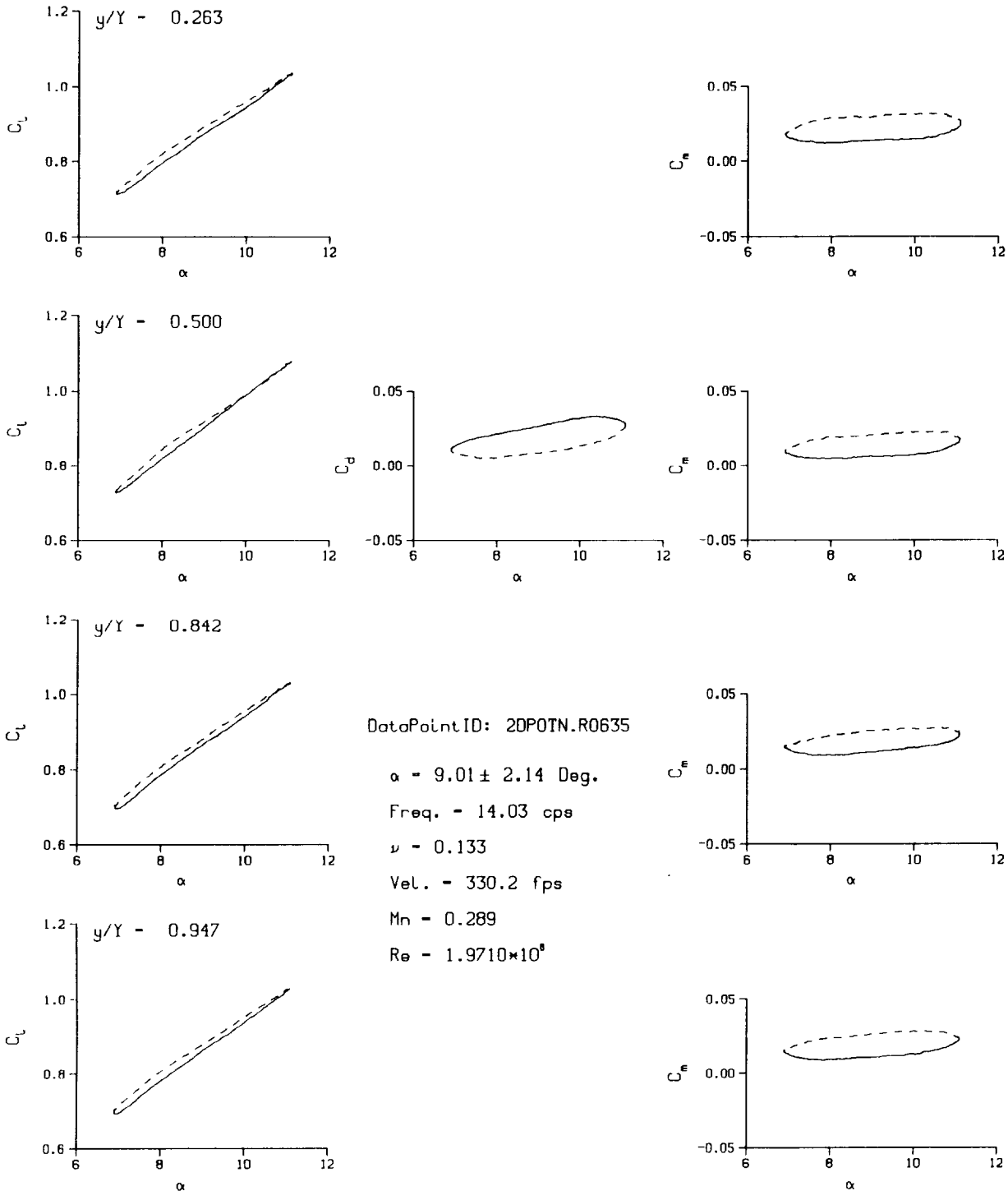

(c) v = 0.14

Figure 57. Continued.

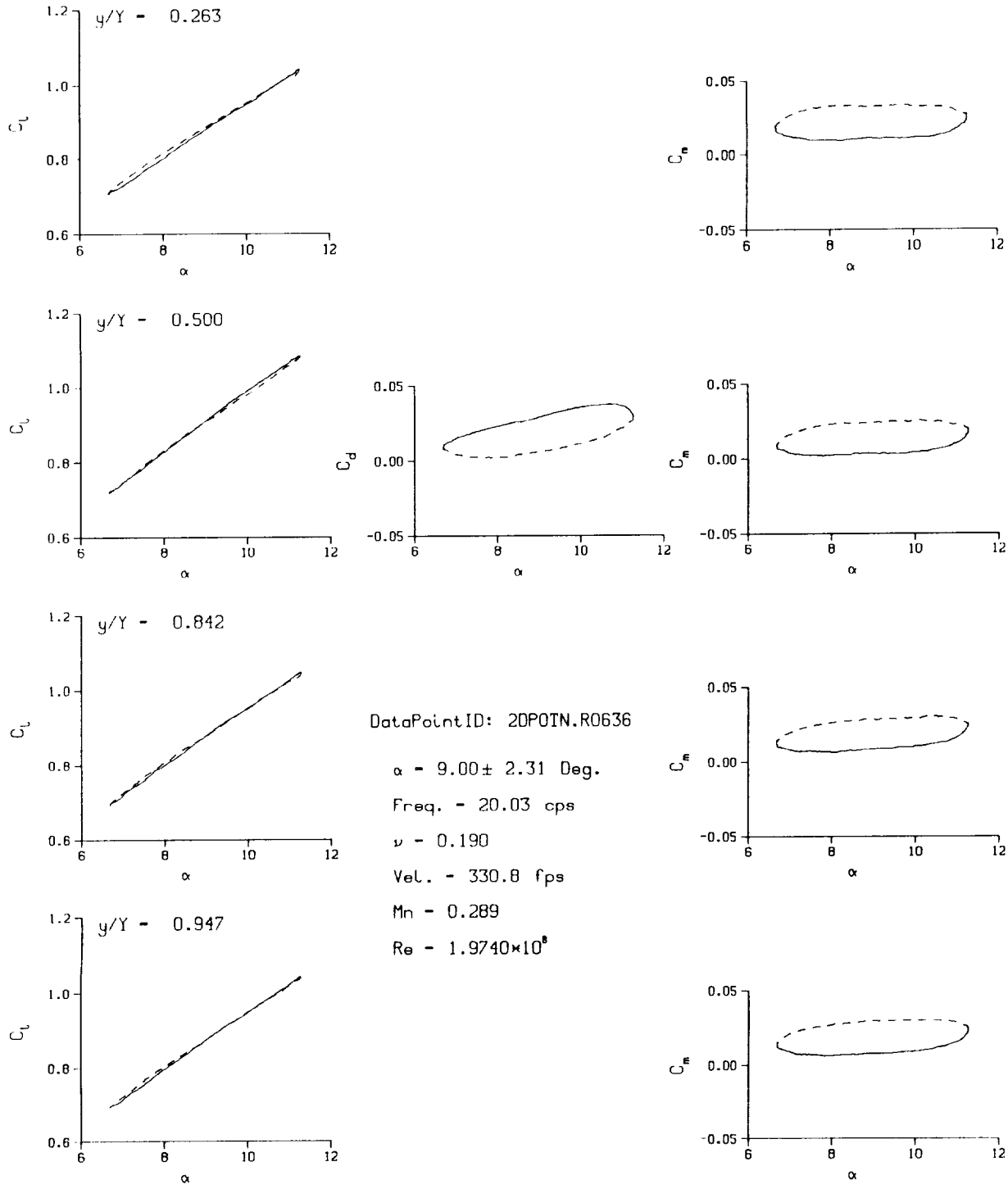

(d) ν = 0.20

Figure 57. Concluded.

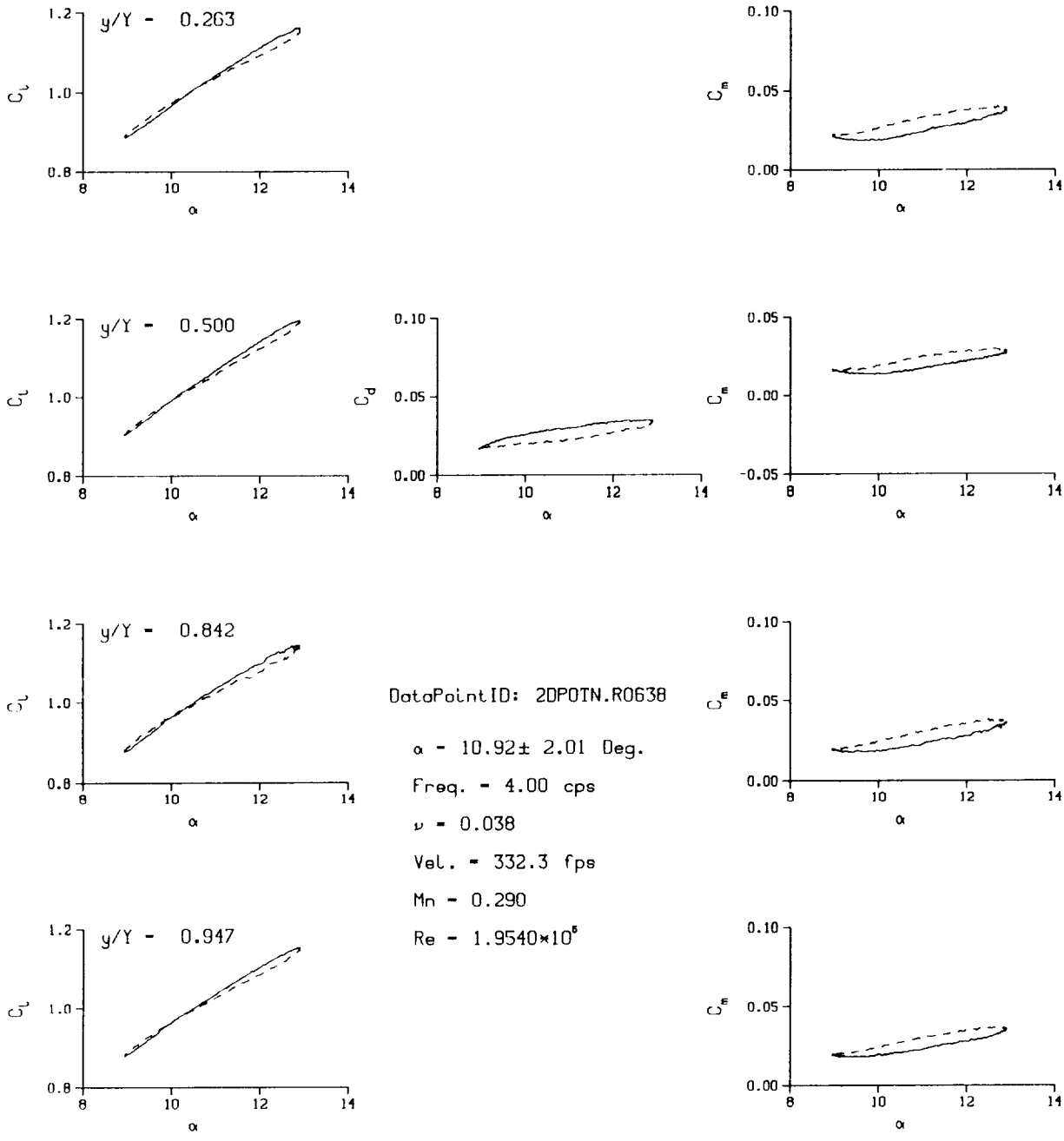

(a) v = 0.04

Figure 58. 2-D pitch oscillation data; no BL-trip; α = 11 ± 2 deg.

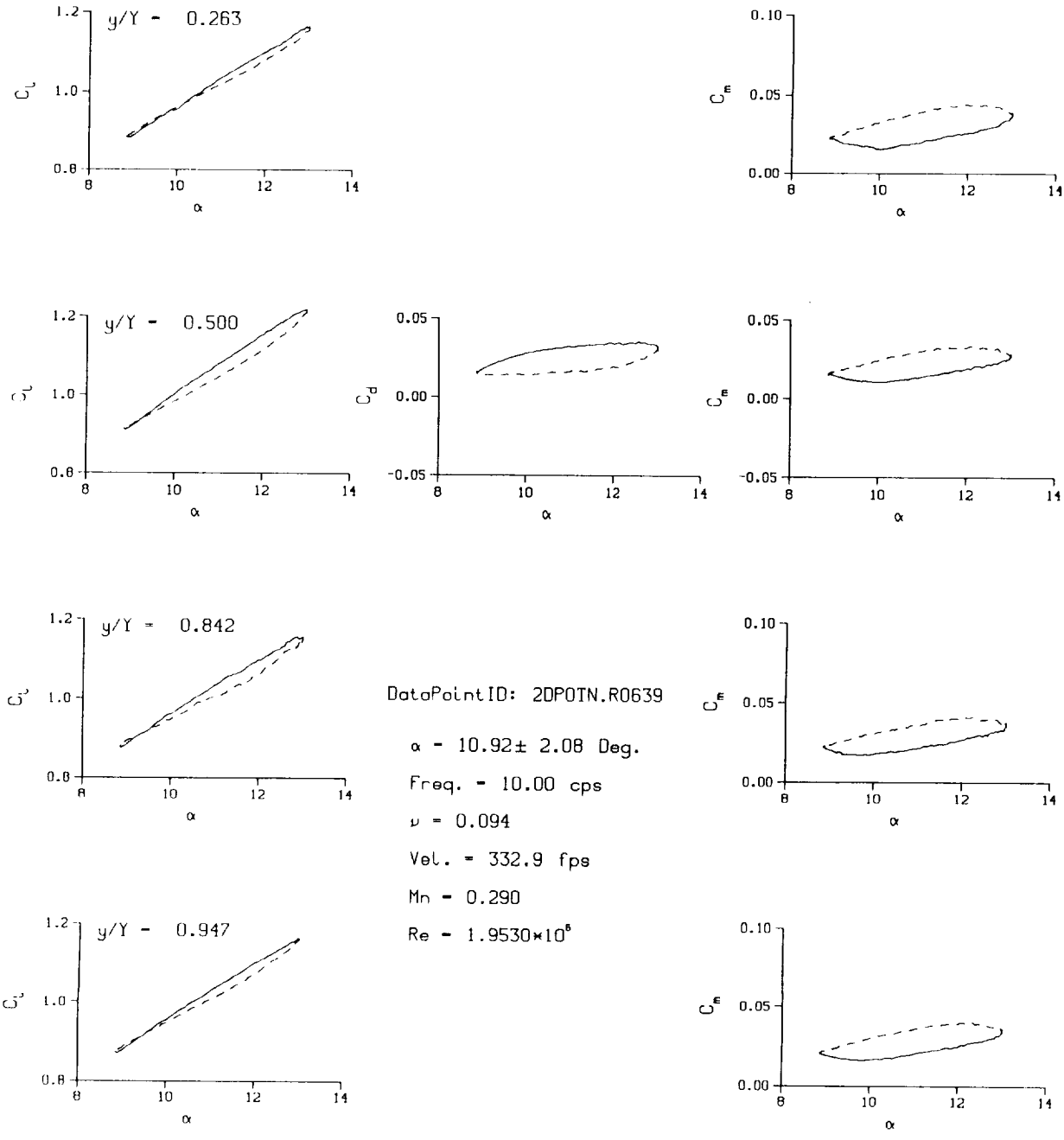

(b) v = 0.10

Figure 58. Continued.

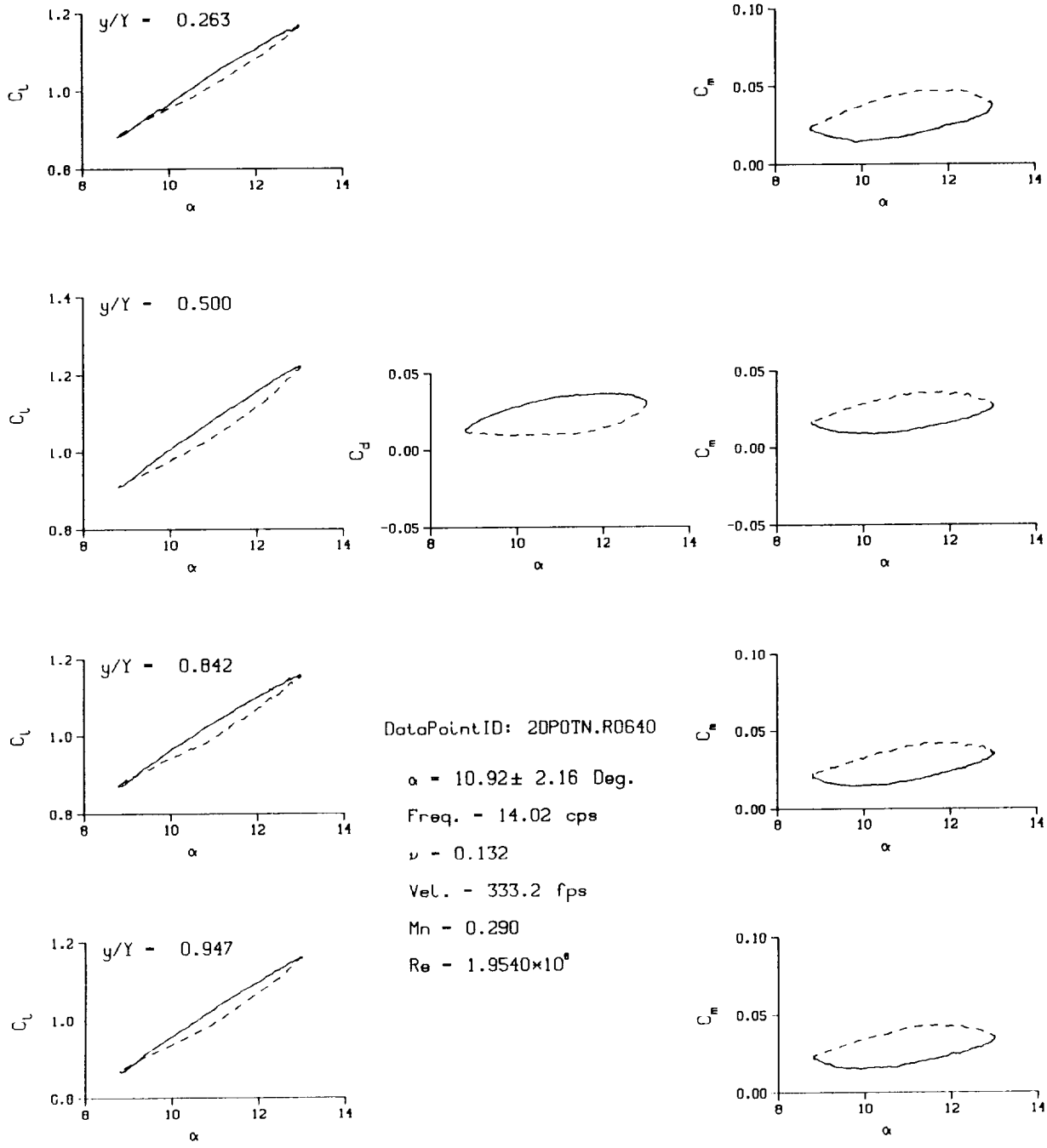

(c) v = 0.14

Figure 58. Continued.

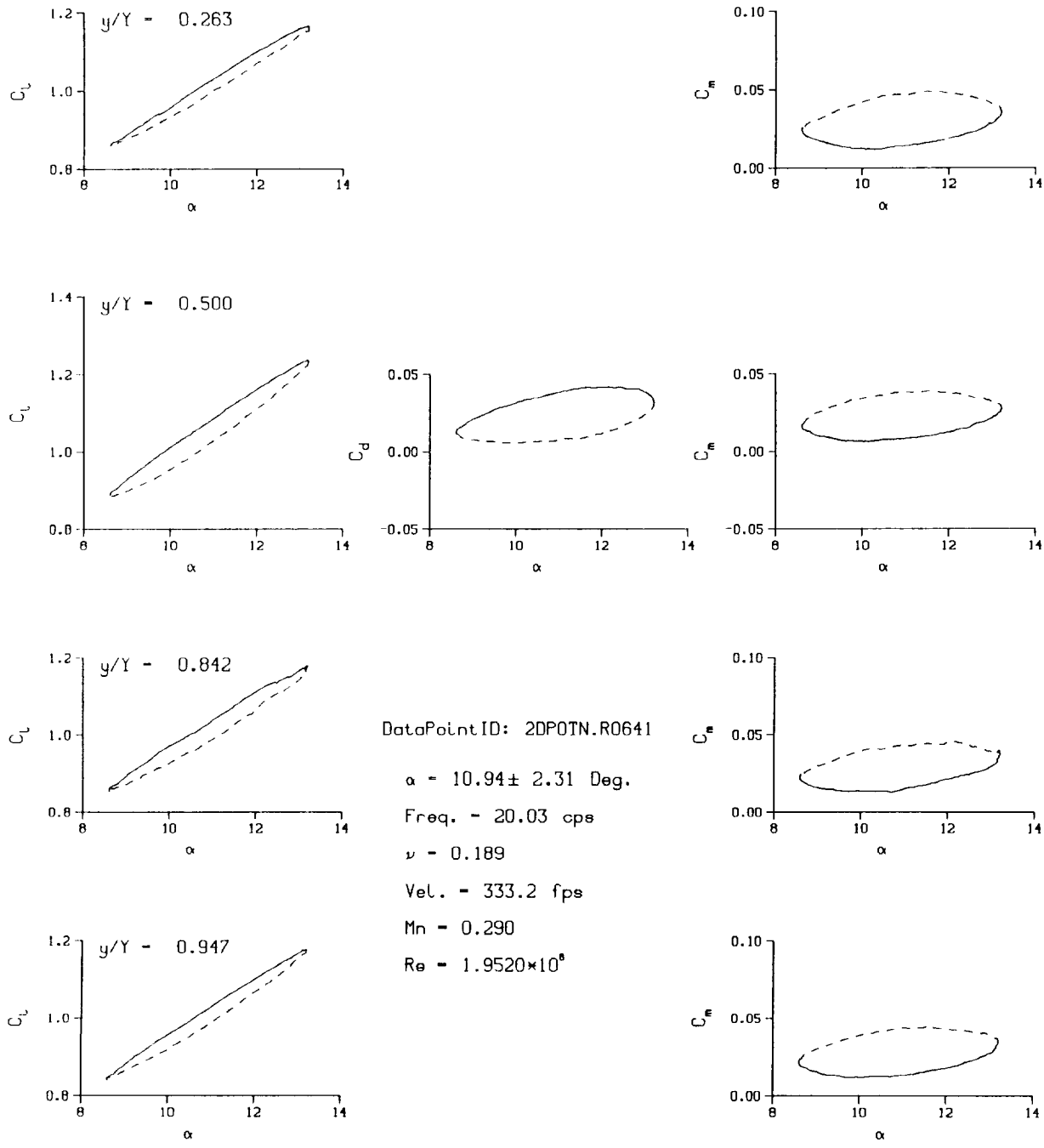

(d) ν = 0.20

Figure 58. Concluded.

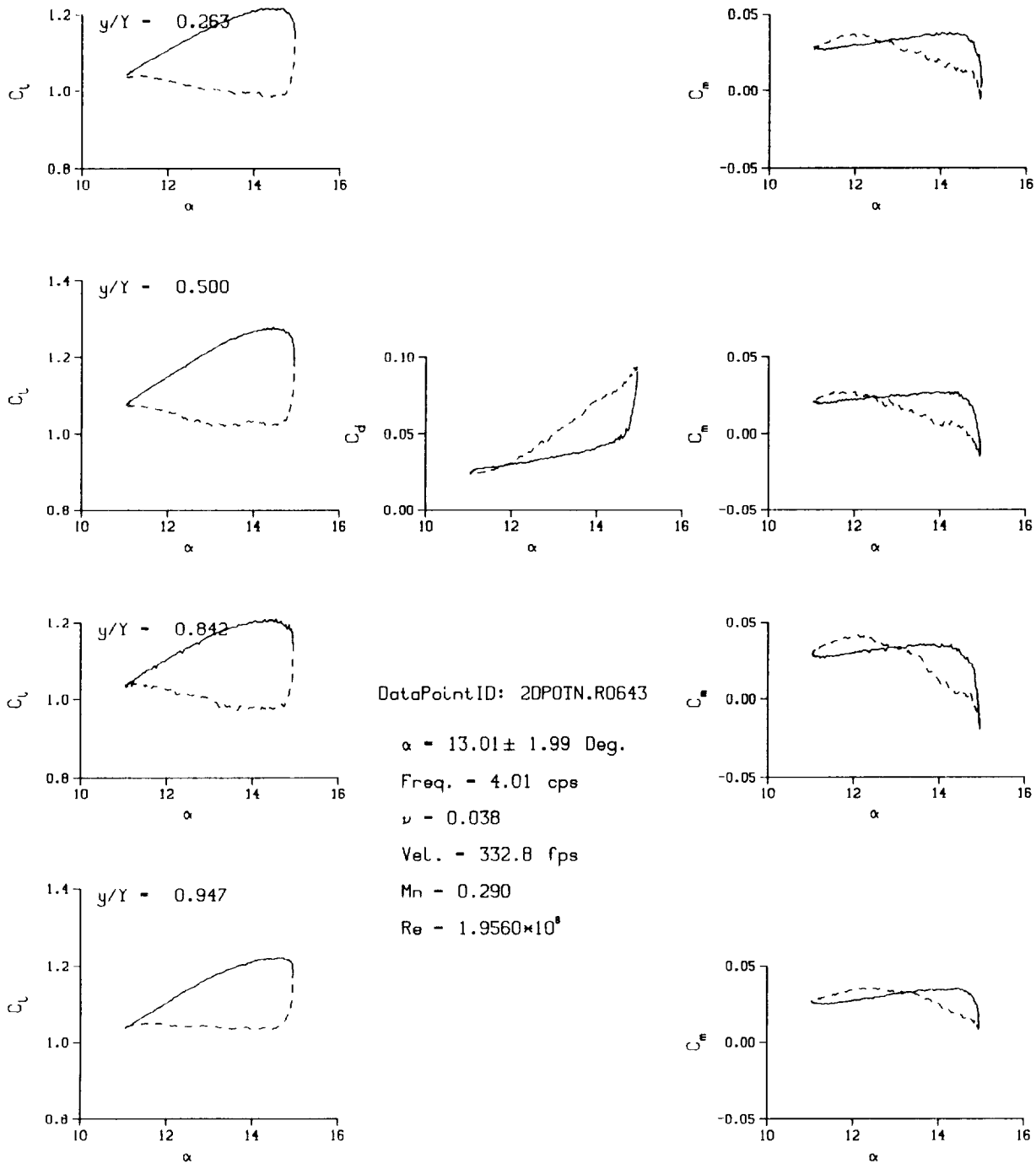

(a) v = 0.04

Figure 59. 2-D pitch oscillation data; no BL-trip; α = 13 ± 2 deg.

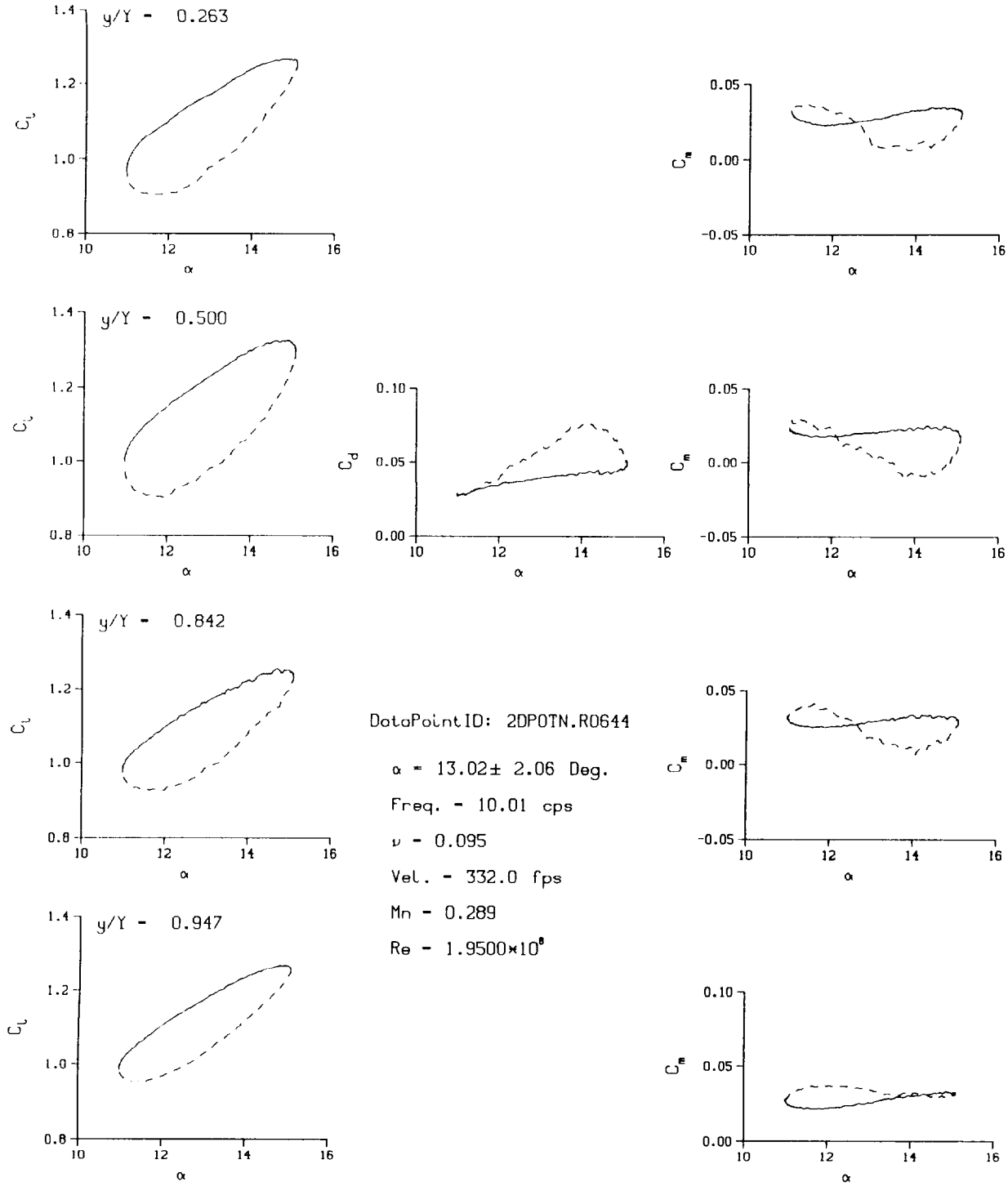

(b) v = 0.10

Figure 59. Continued.

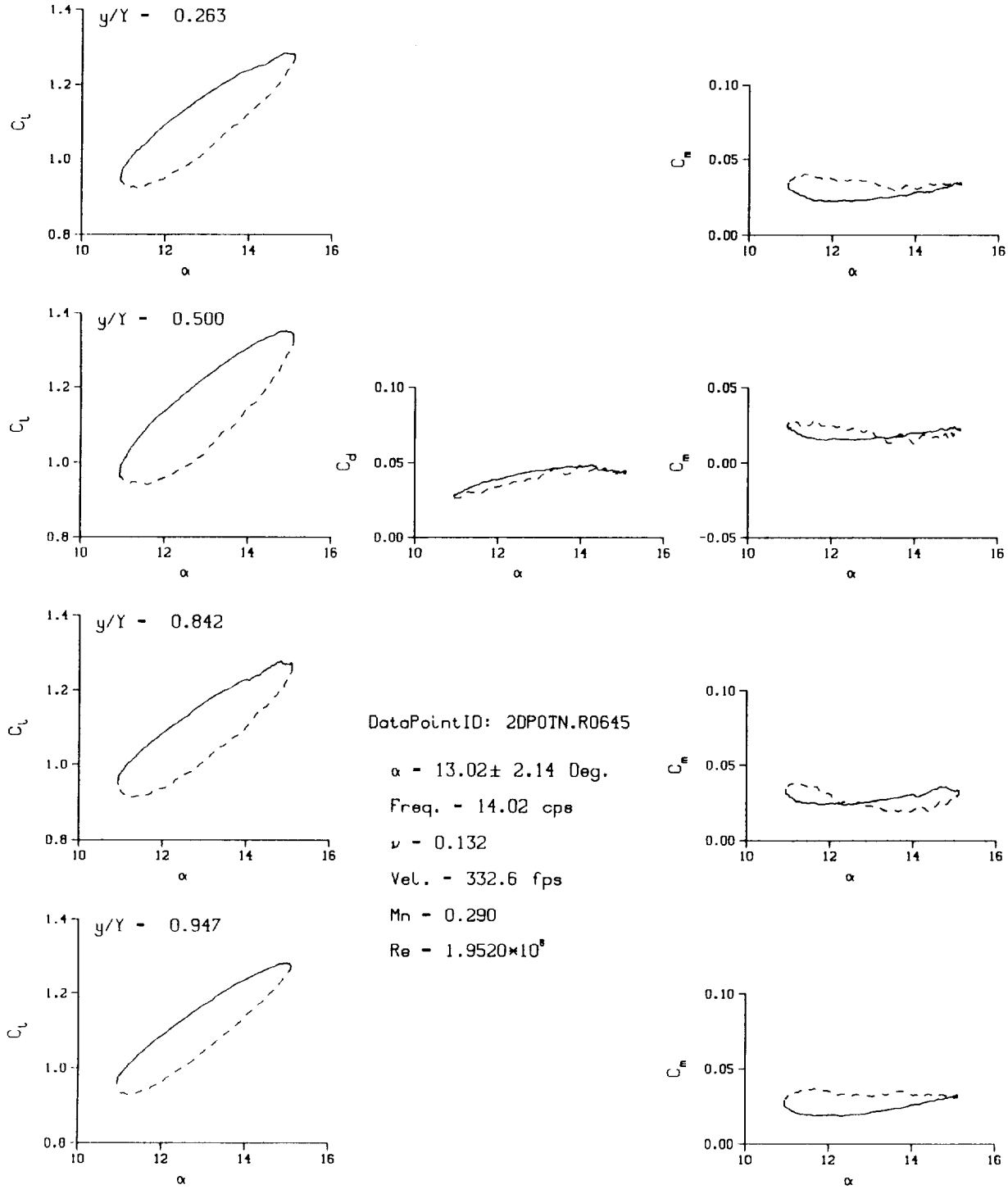

(c) v = 0.14

Figure 59. Continued.

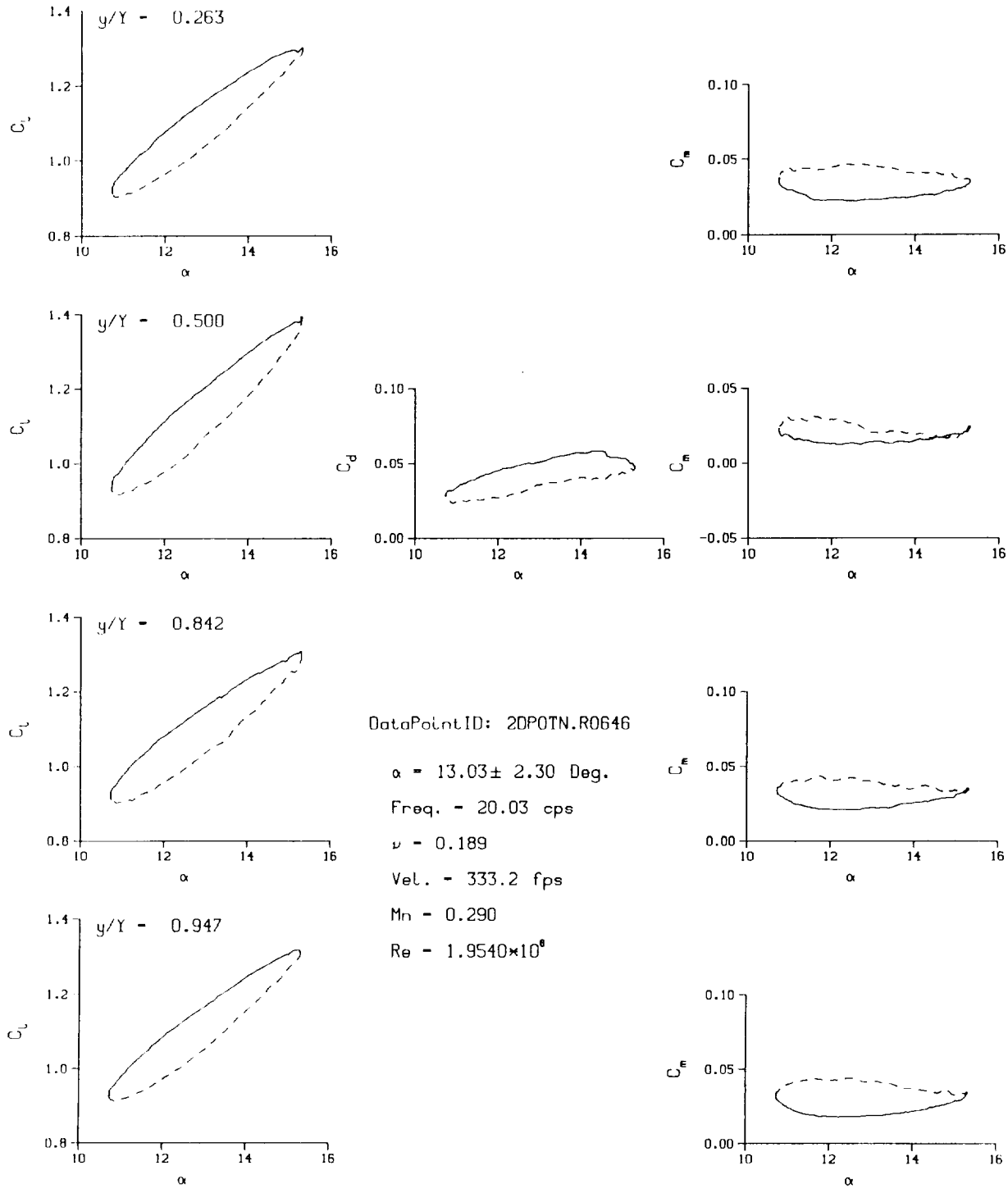

(d) v = 0.20

Figure 59. Concluded.

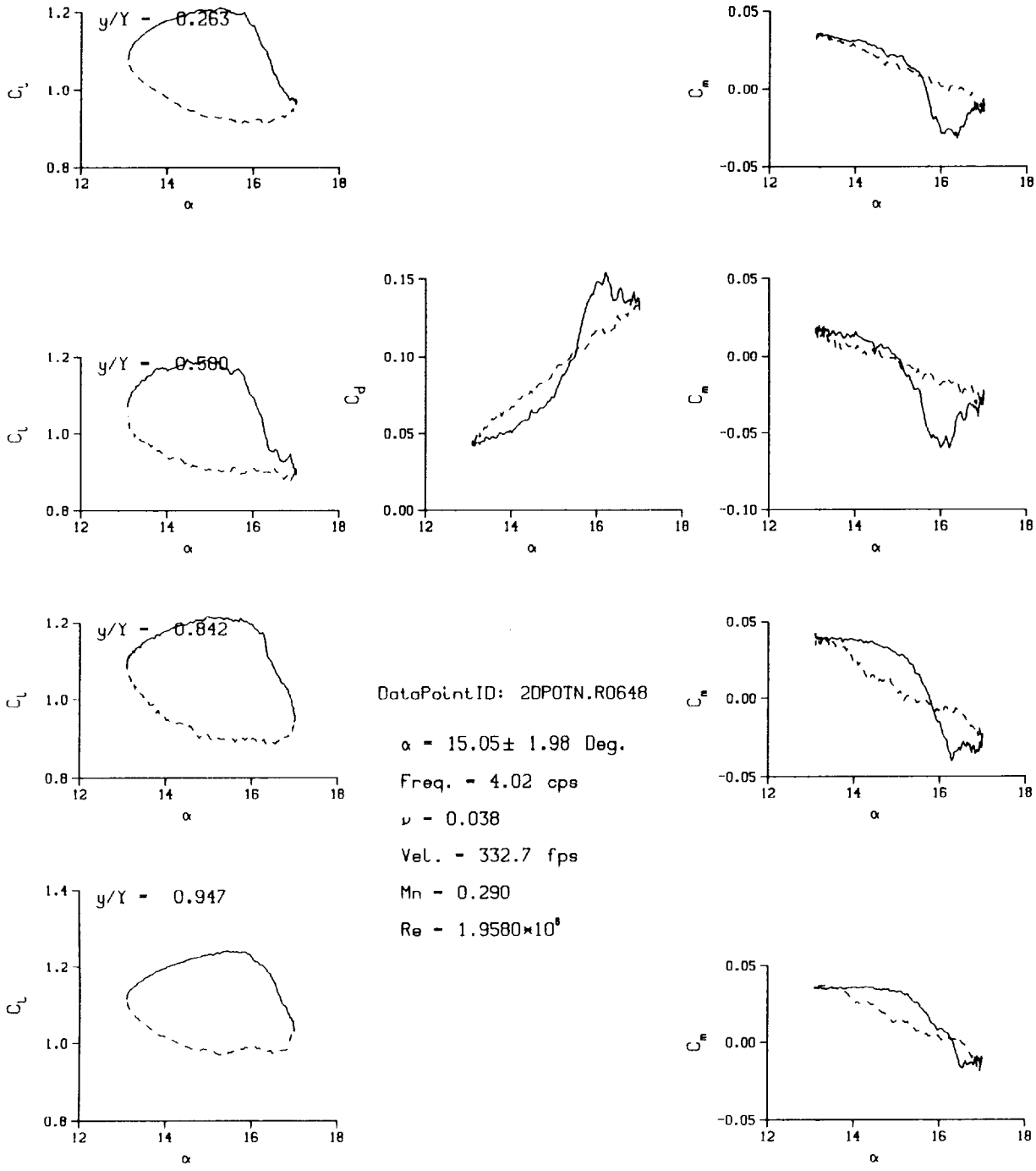

(a) v = 0.04

Figure 60. 2-D pitch oscillation data; no BL-trip; α = 15 ± 2 deg.

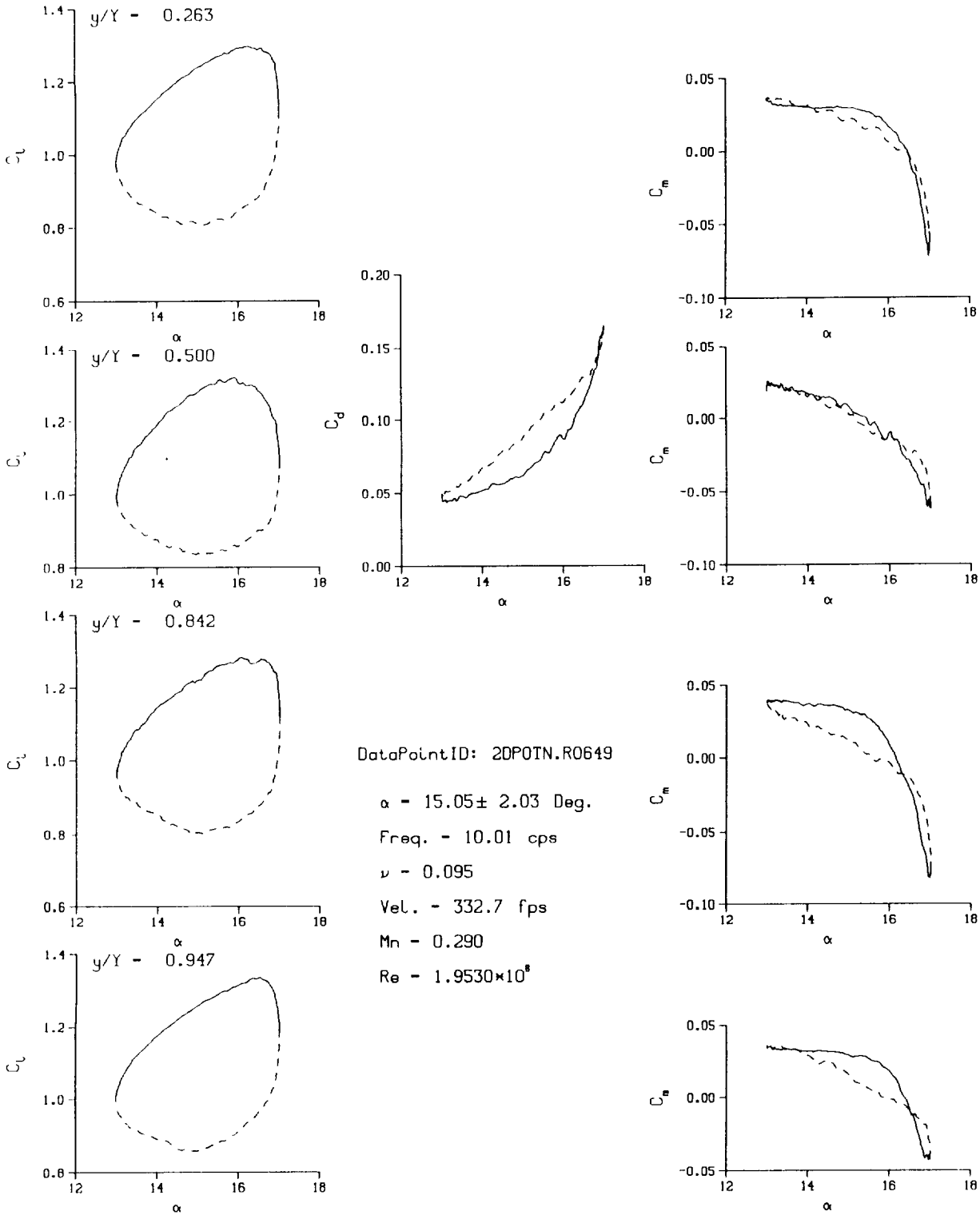

(b) v = 0.10

Figure 60. Continued.

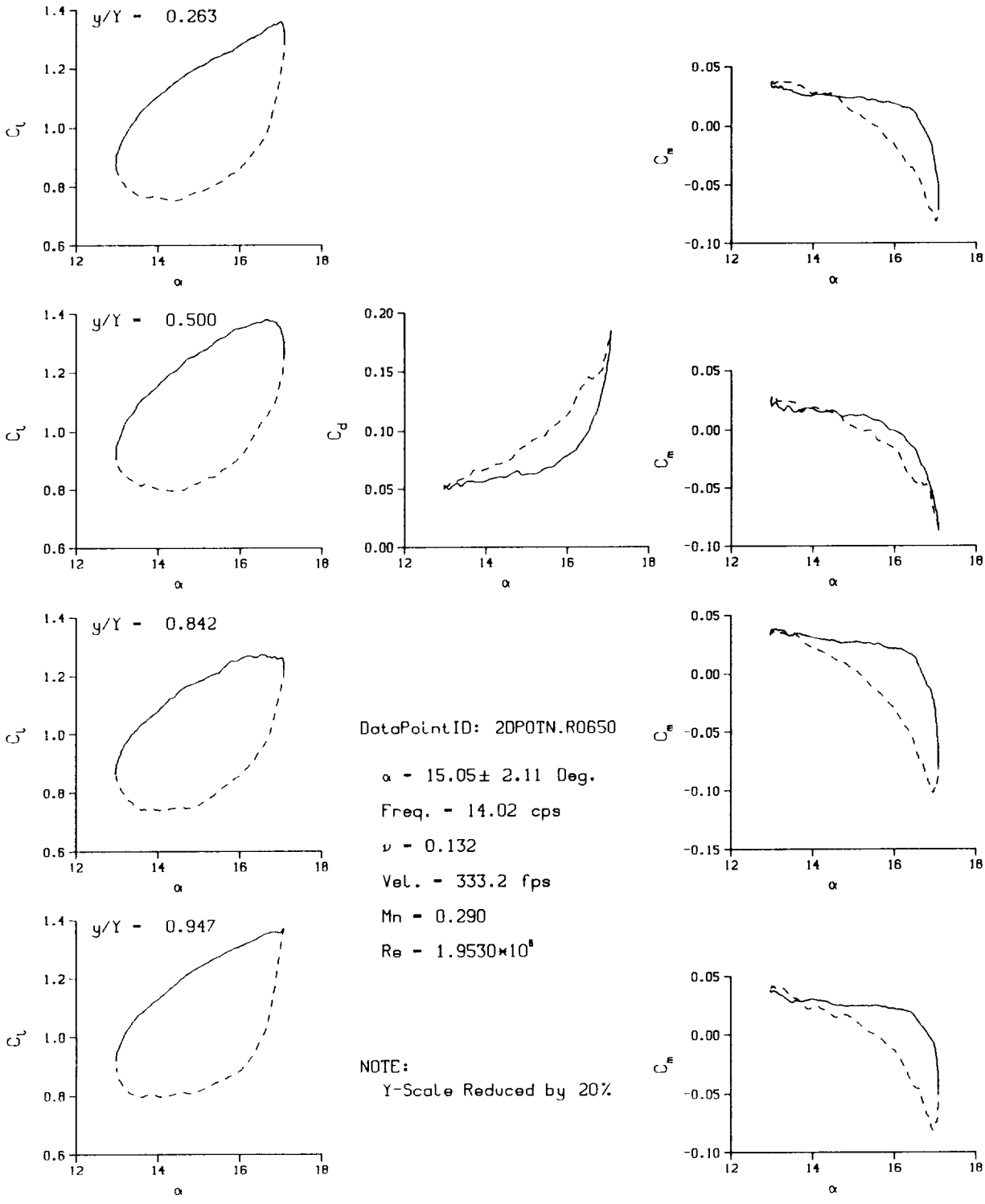

(c) v = 0.14

Figure 60. Continued.

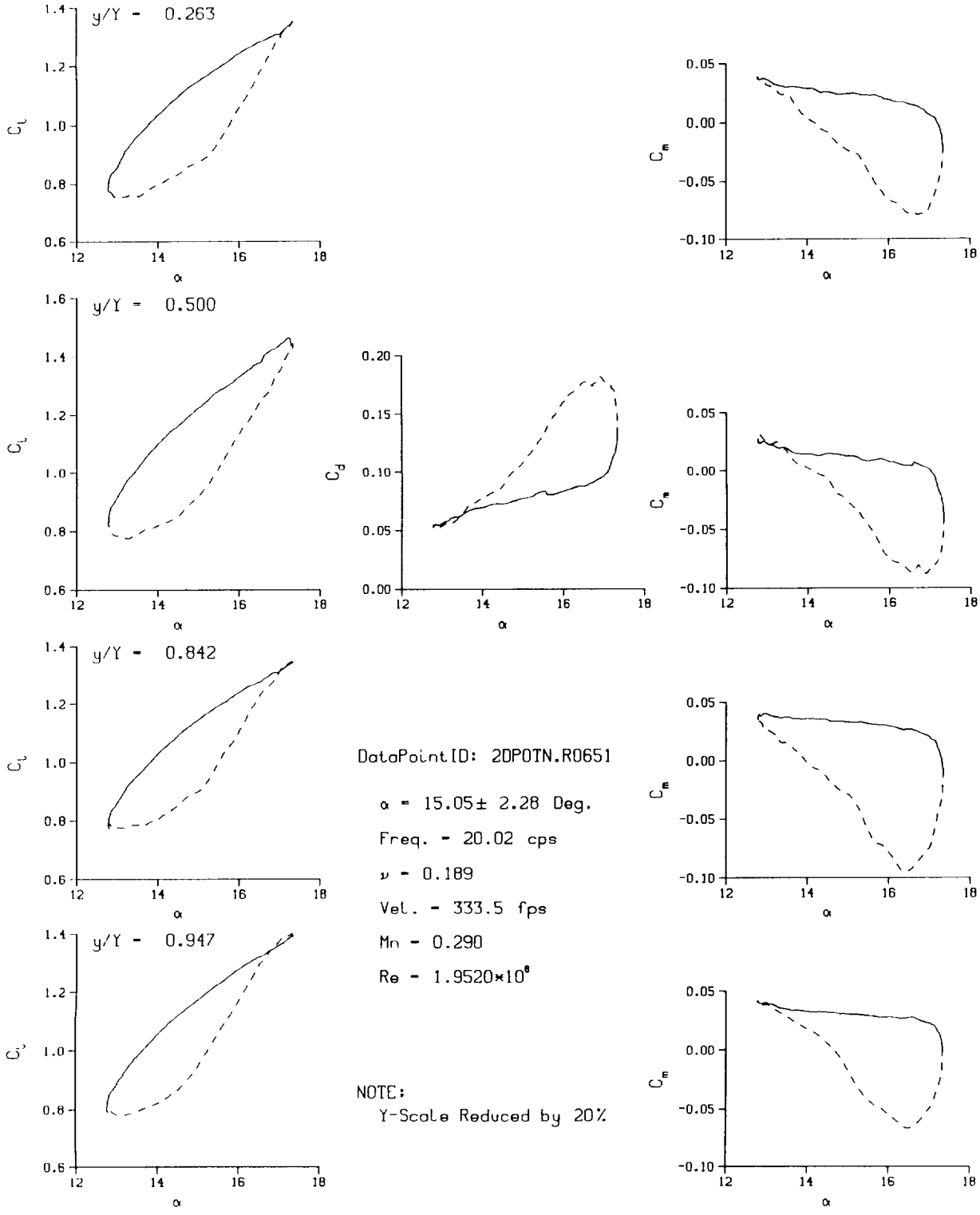

(d) v = 0.20

Figure 60. Concluded.

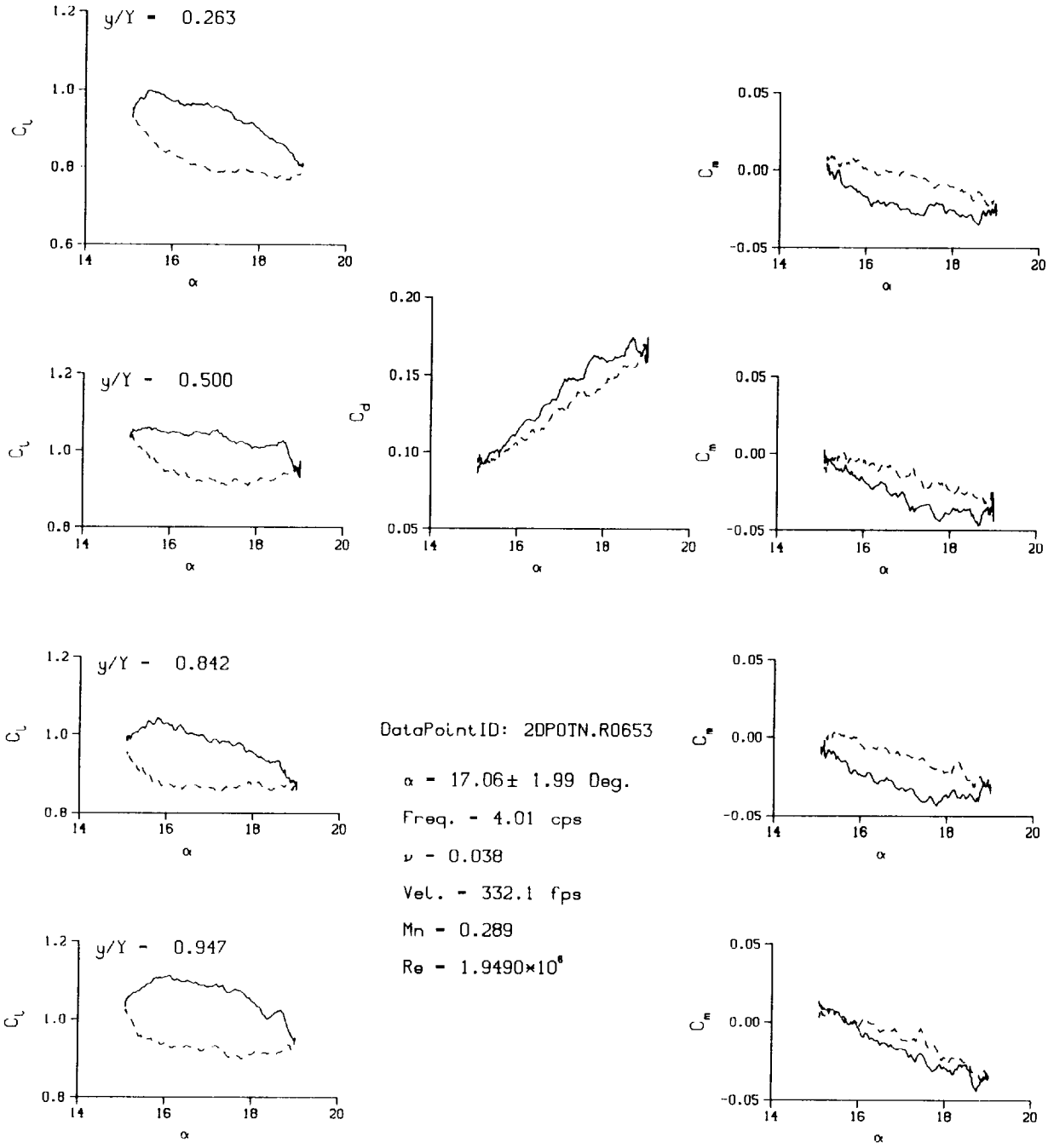

(a) ν = 0.04

Figure 61. 2-D pitch oscillation data; no BL-trip; α = 17 ± 2 deg.

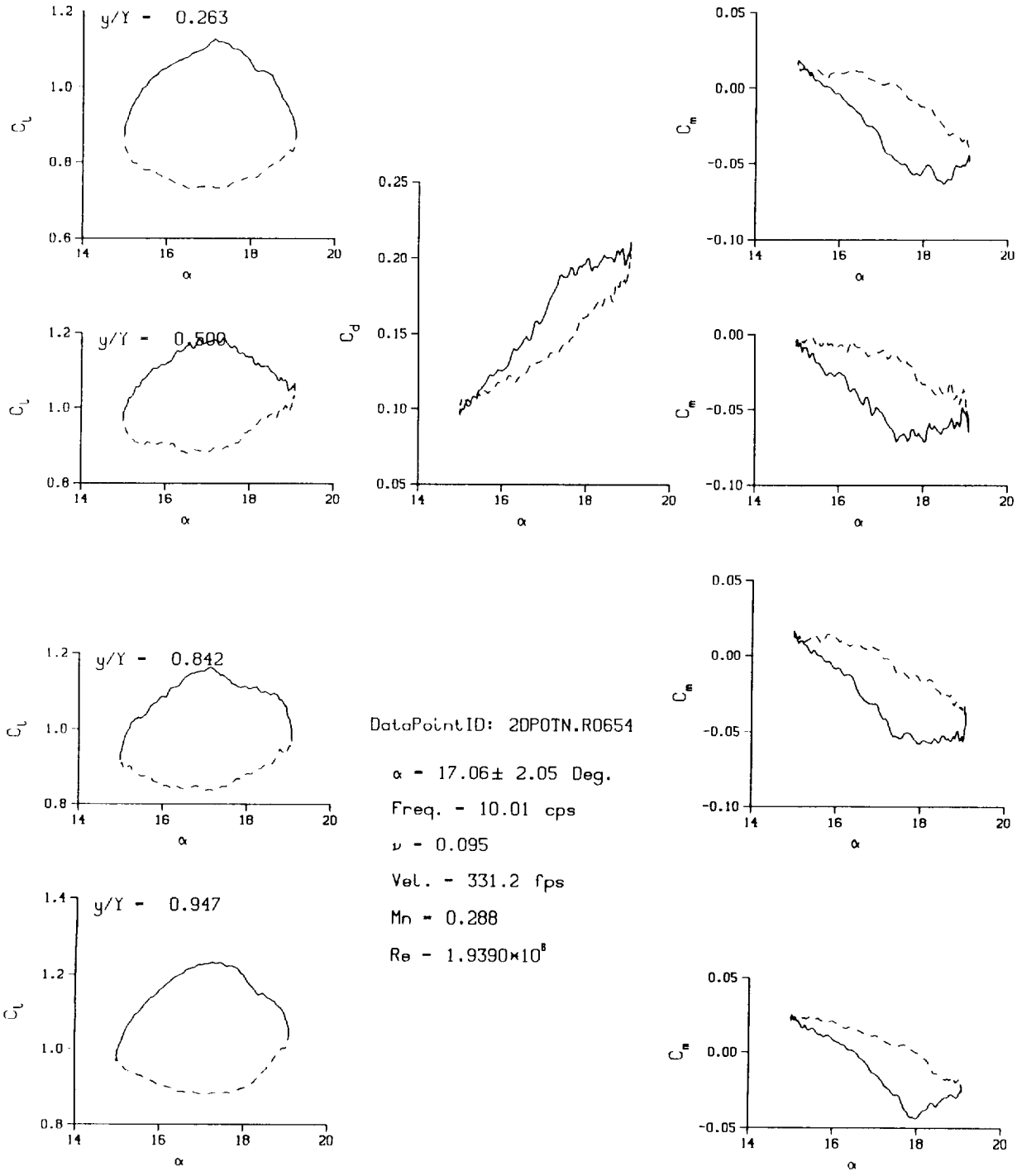

(b) v = 0.10

Figure 61. Continued.

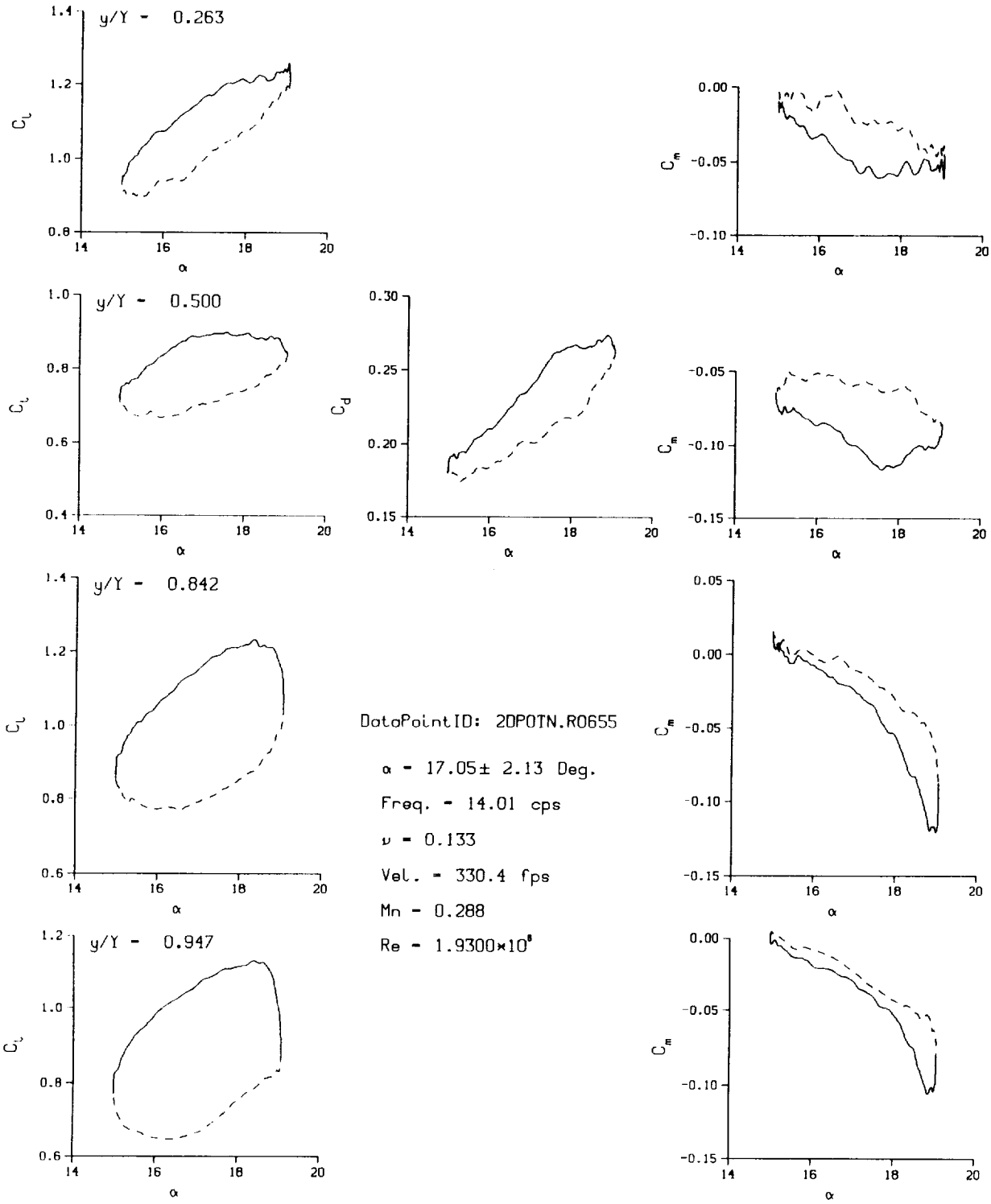

(c) v = 0.14

Figure 61. Continued.

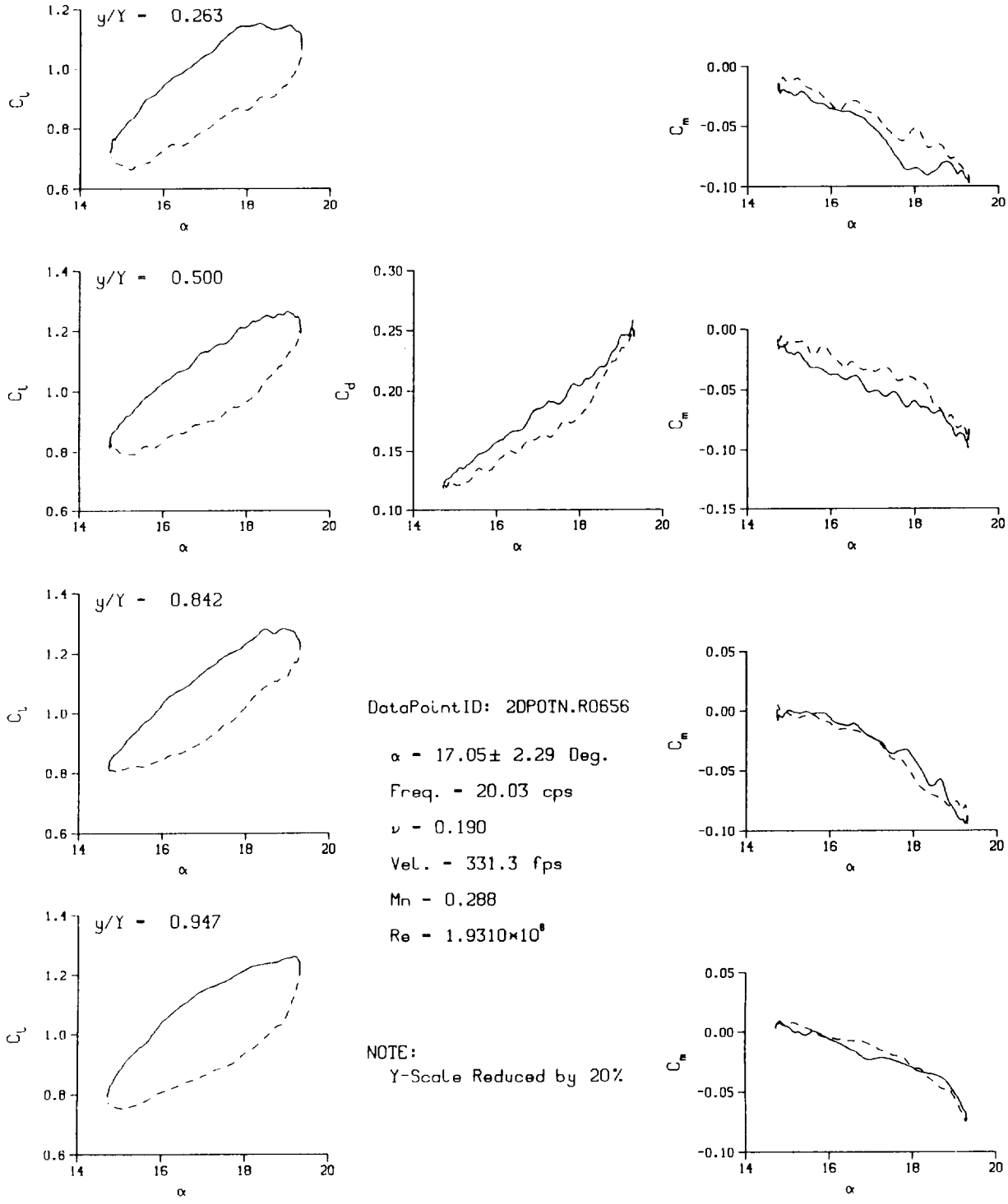

(d) v = 0.20

Figure 61. Concluded.

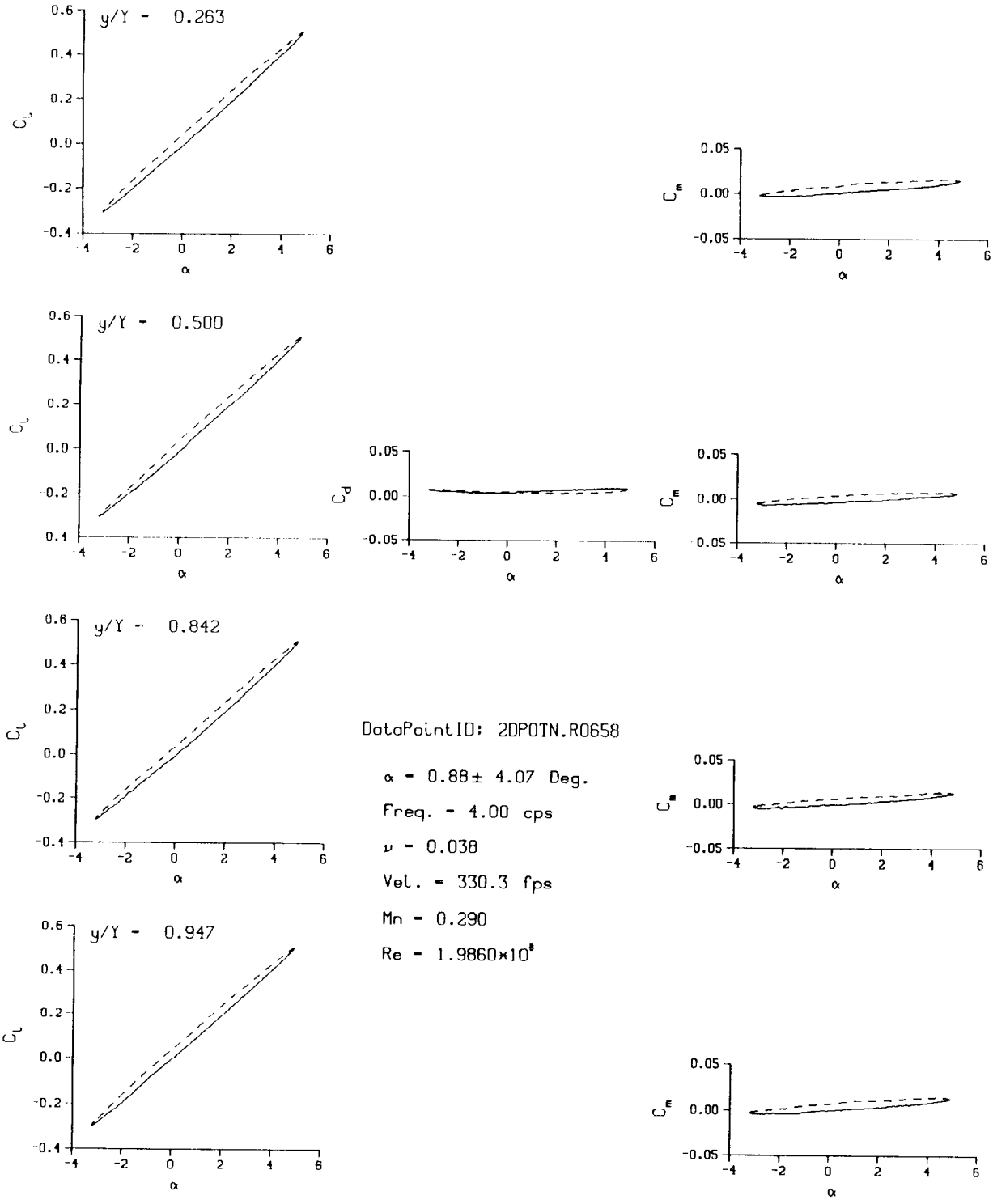

(a) v = 0.04

Figure 62. 2-D pitch oscillation data; no BL-trip; α = 1 ± 4 deg.

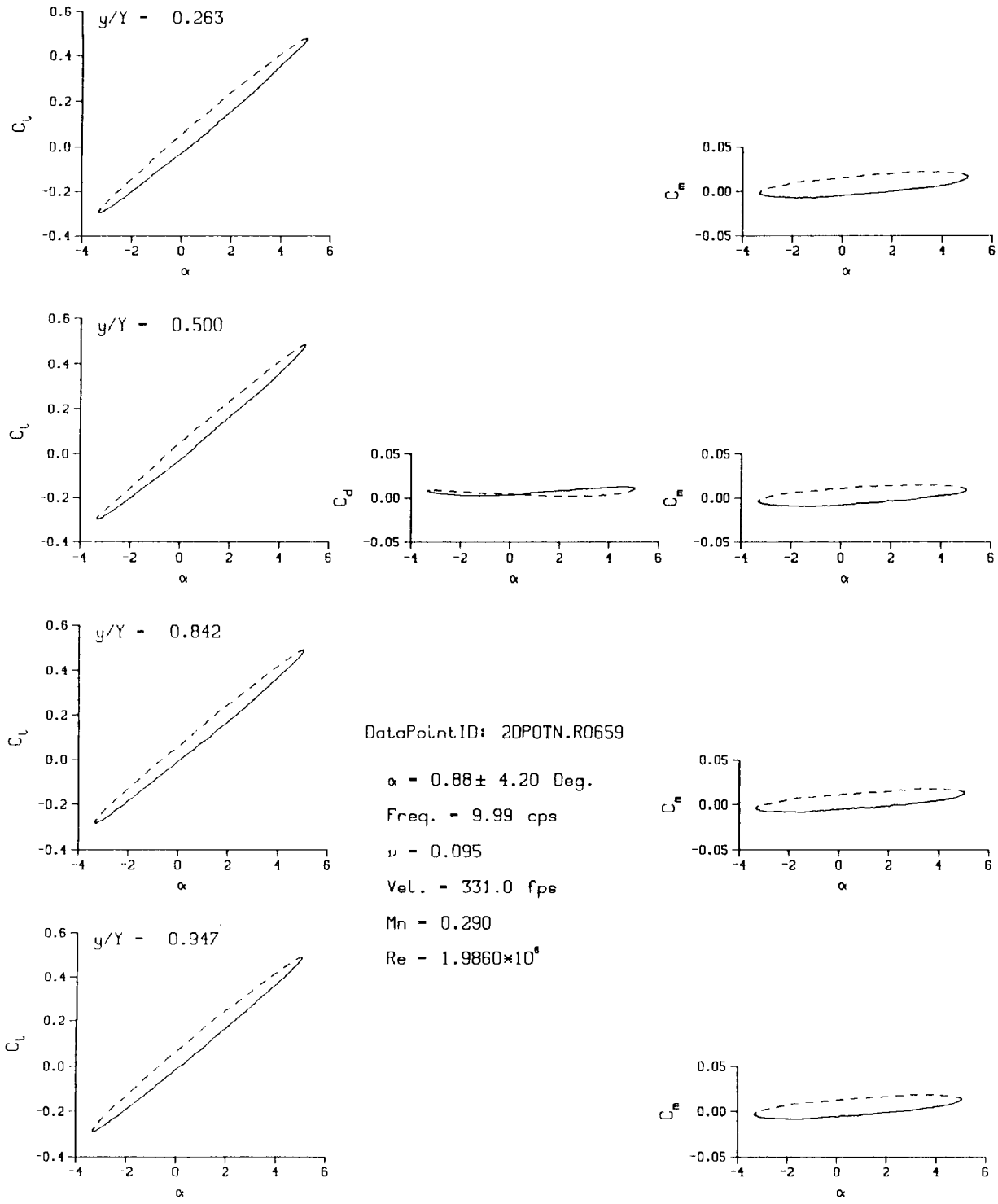

(b) ν = 0.10

Figure 62. Continued.

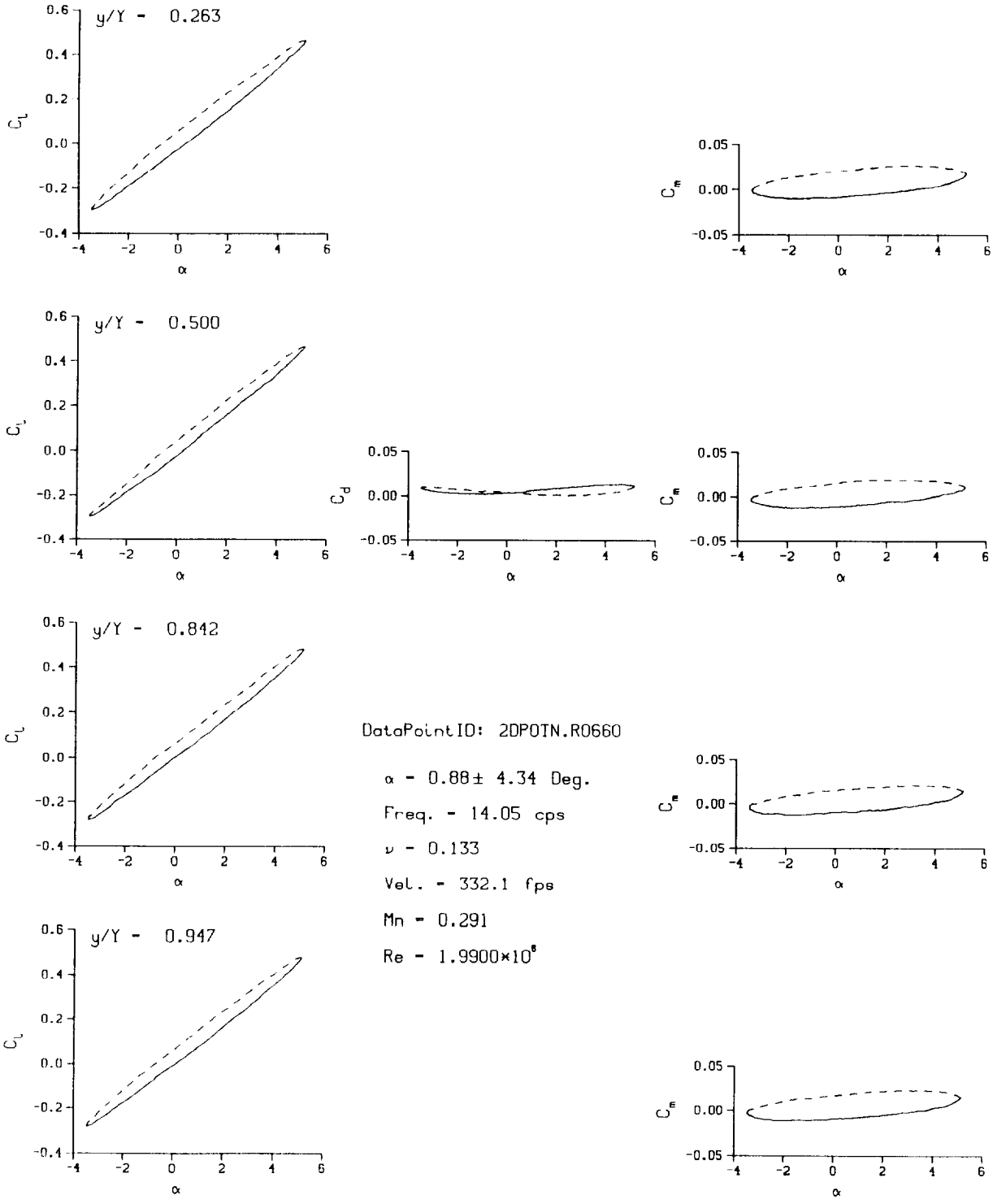

(c) v = 0.14

Figure 62. Concluded.

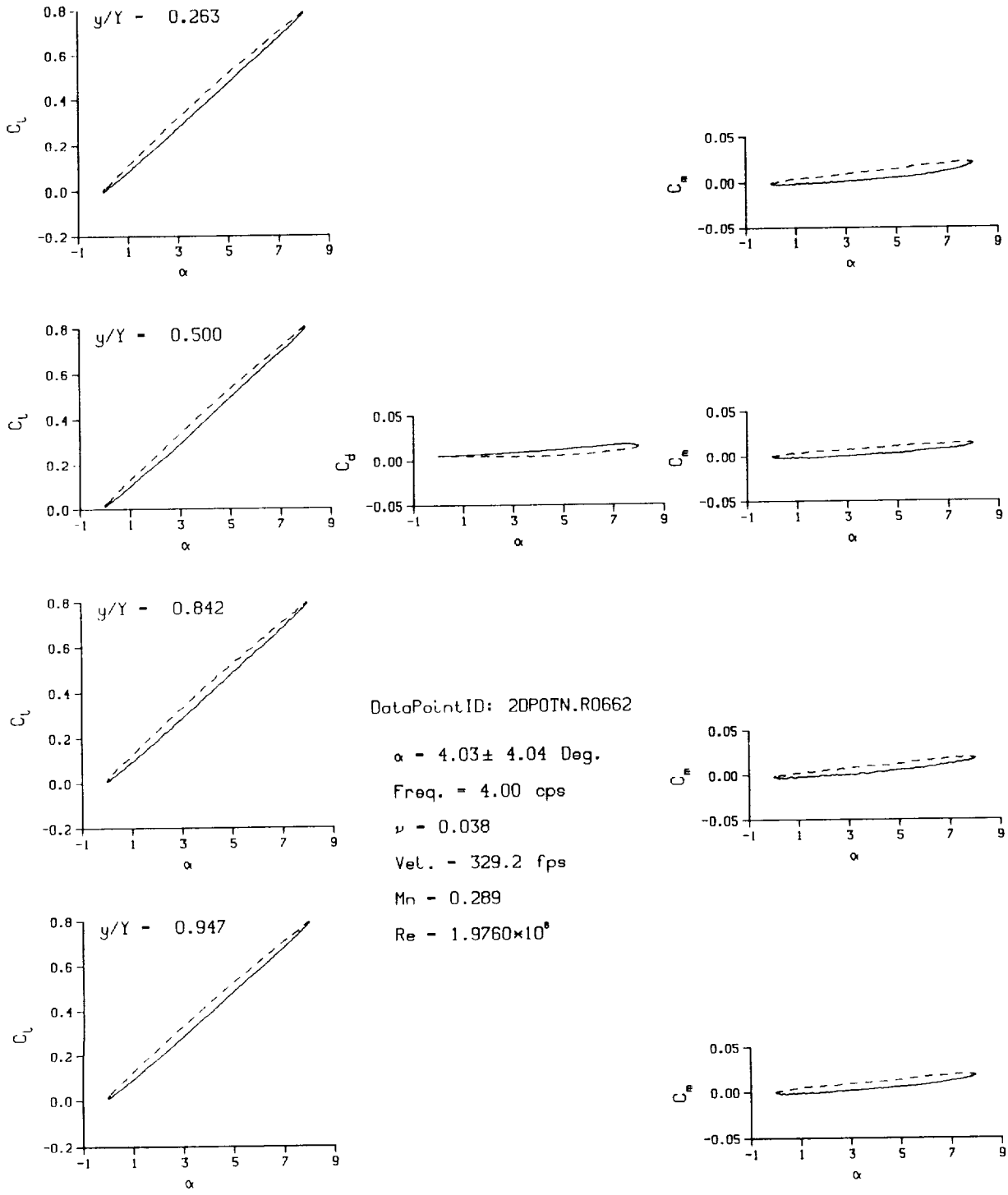

(a) v = 0.04

Figure 63. 2-D pitch oscillation data; no BL-trip; α = 4 ± 4 deg.

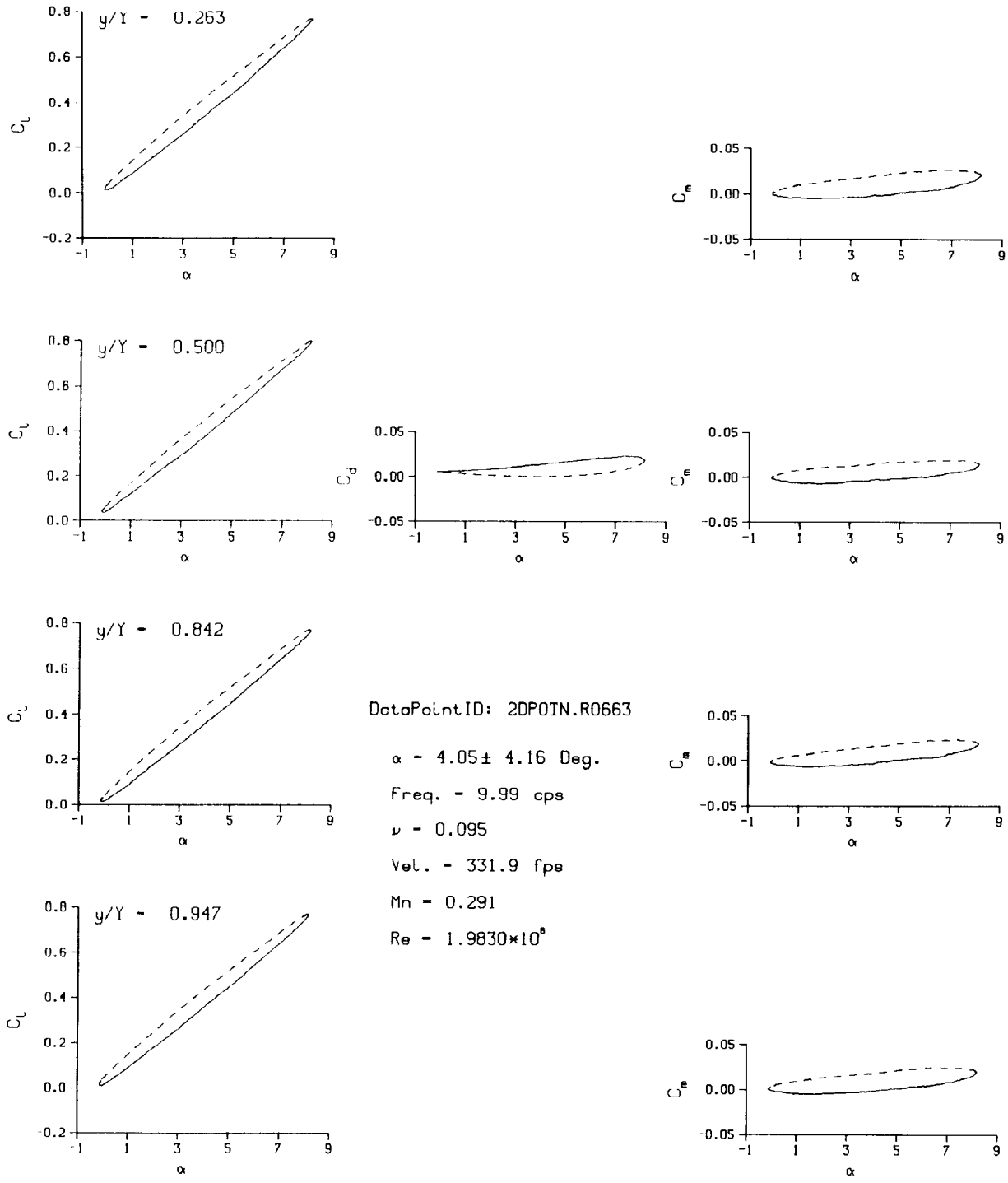

(b) ν = 0.10

Figure 63. Continued.

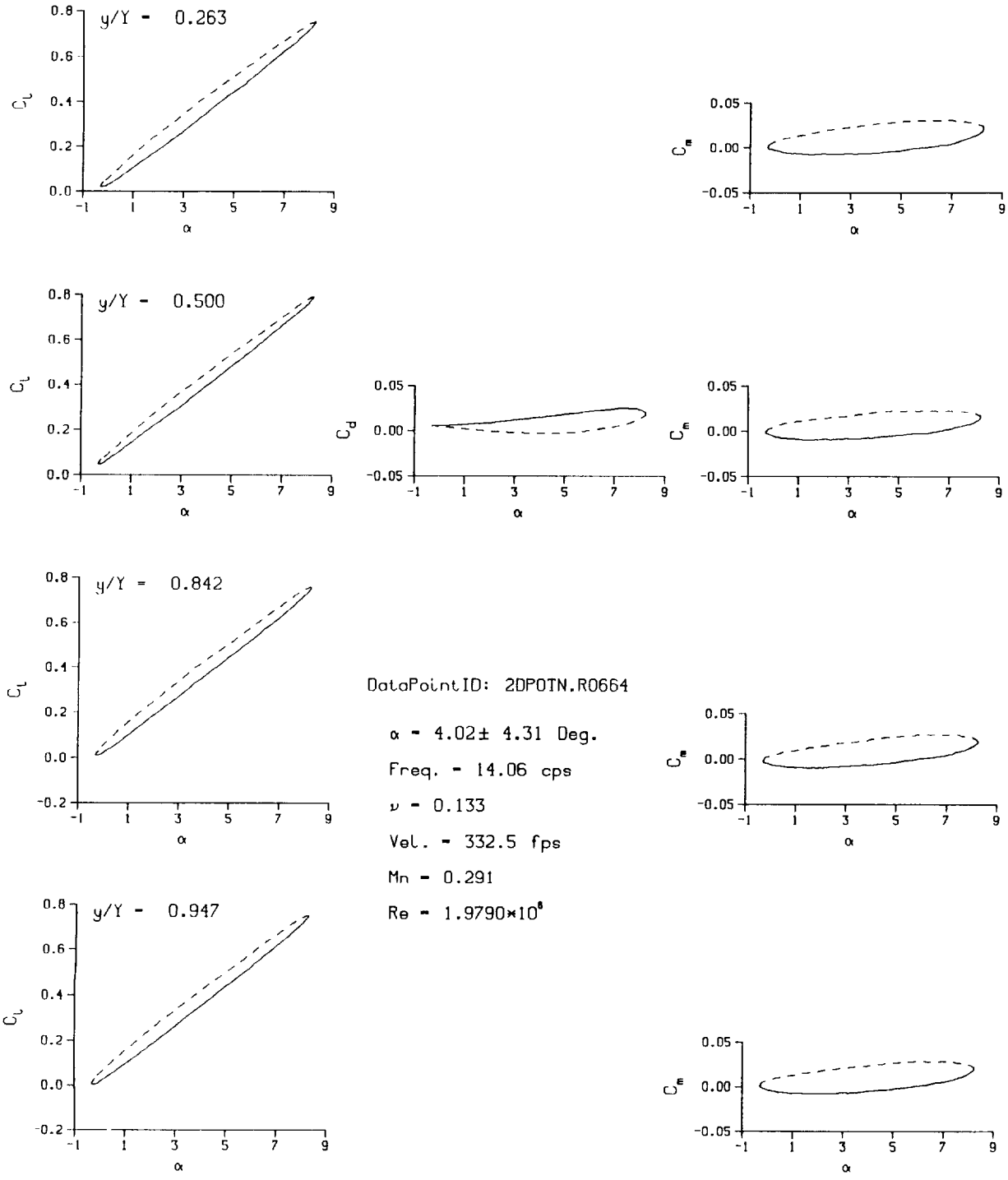

(c) v = 0.14

Figure 63. Concluded.

C-4.

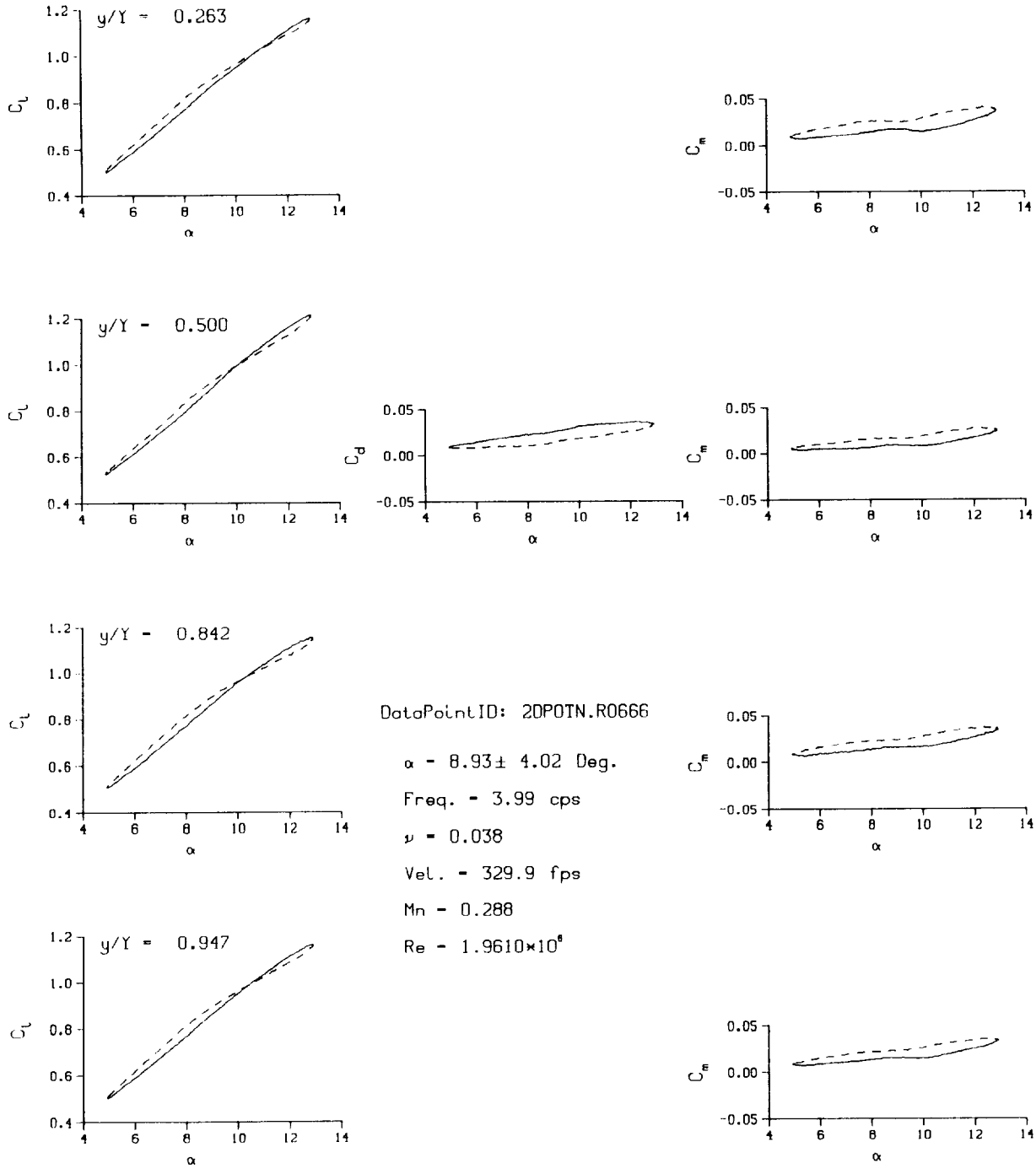

(a) v = 0.04

Figure 64. 2-D pitch oscillation data; no BL-trip; α = 9 ± 4 deg.

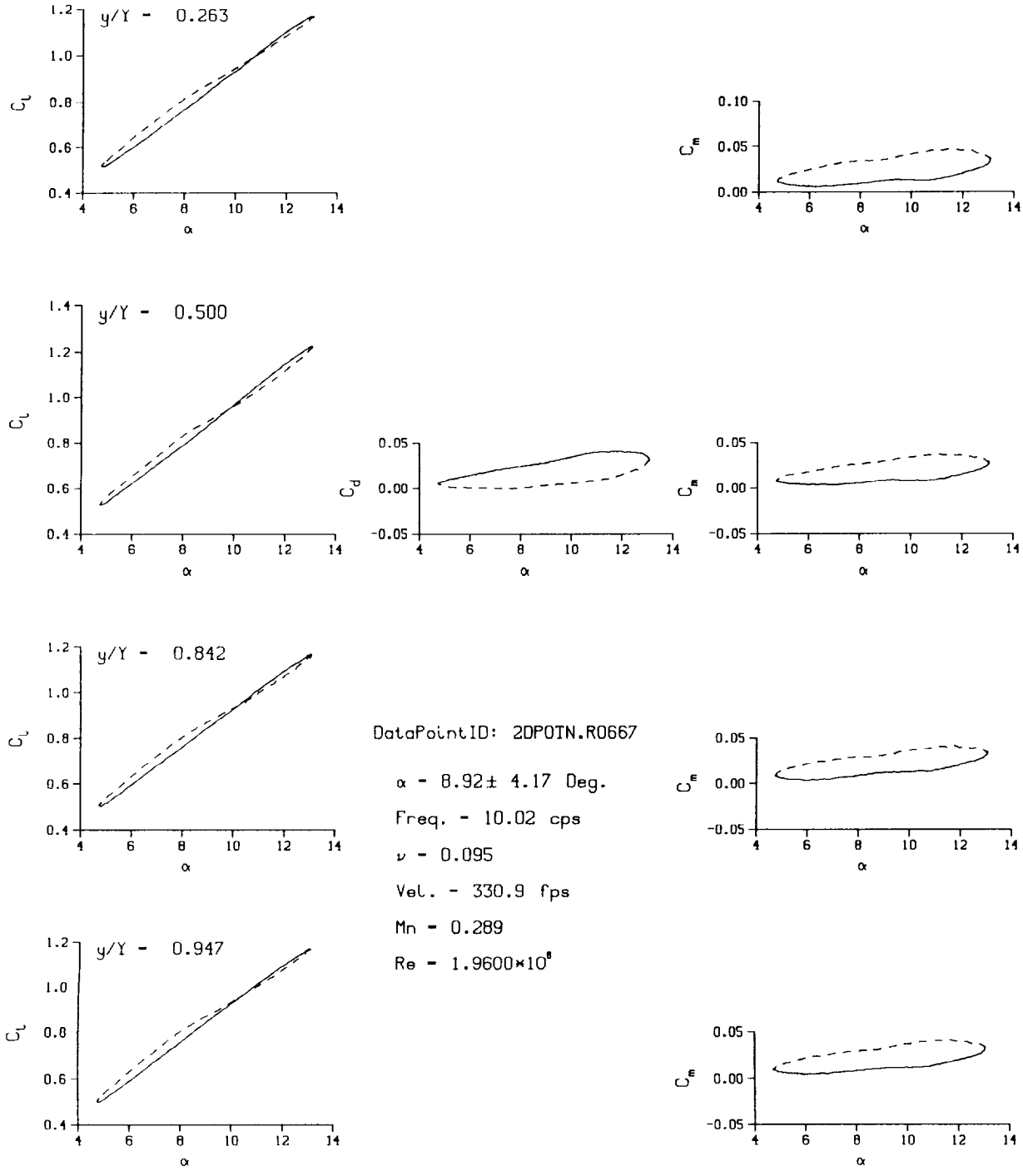

(b) v = 0.10

Figure 64. Continued.

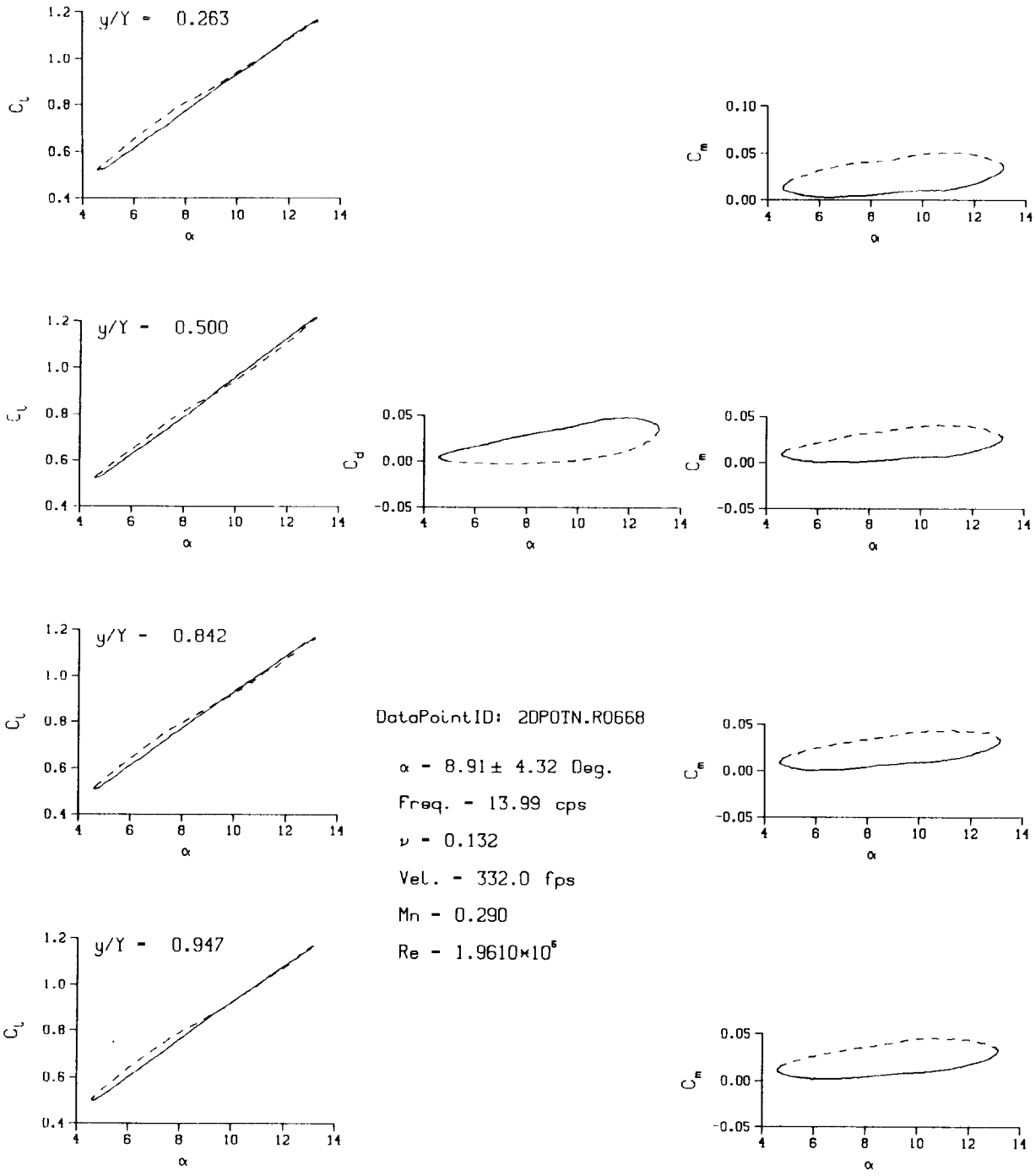

(c) ν = 0.14

Figure 64. Concluded.

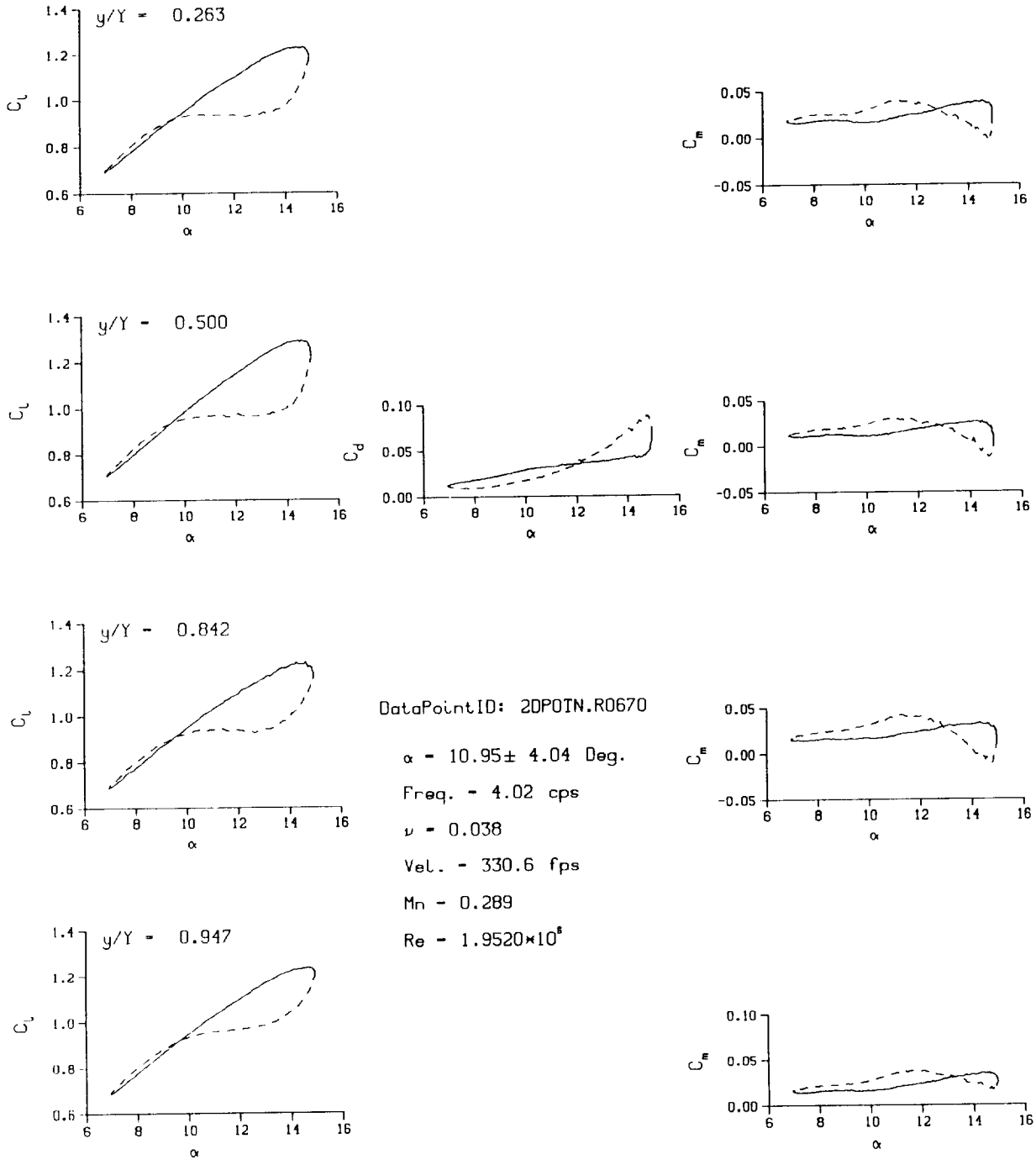

(a) ν = 0.04

Figure 65. 2-D pitch oscillation data; no BL-trip; α = 11 ± 4 deg.

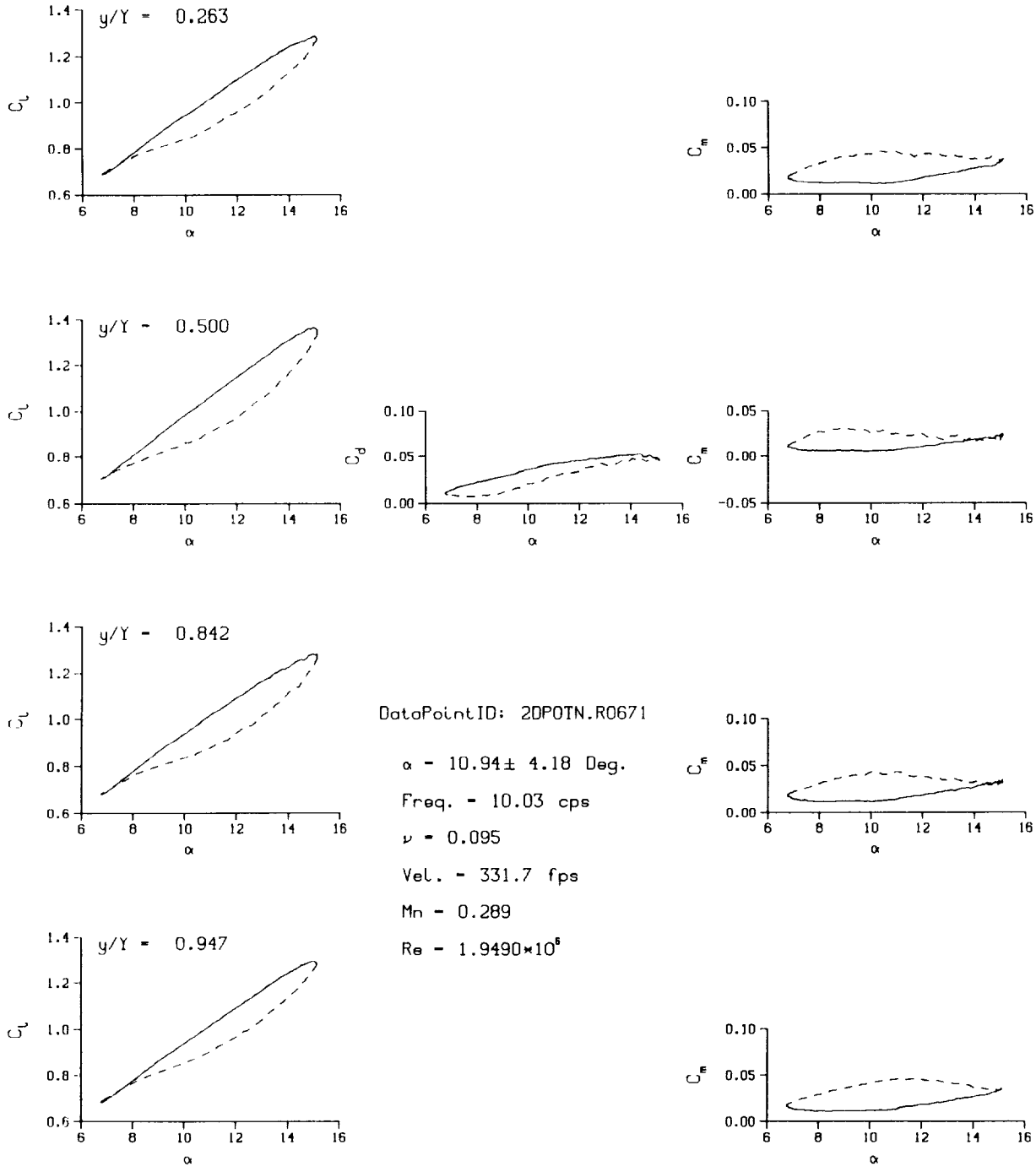

(b) ν = 0.10

Figure 65. Continued.

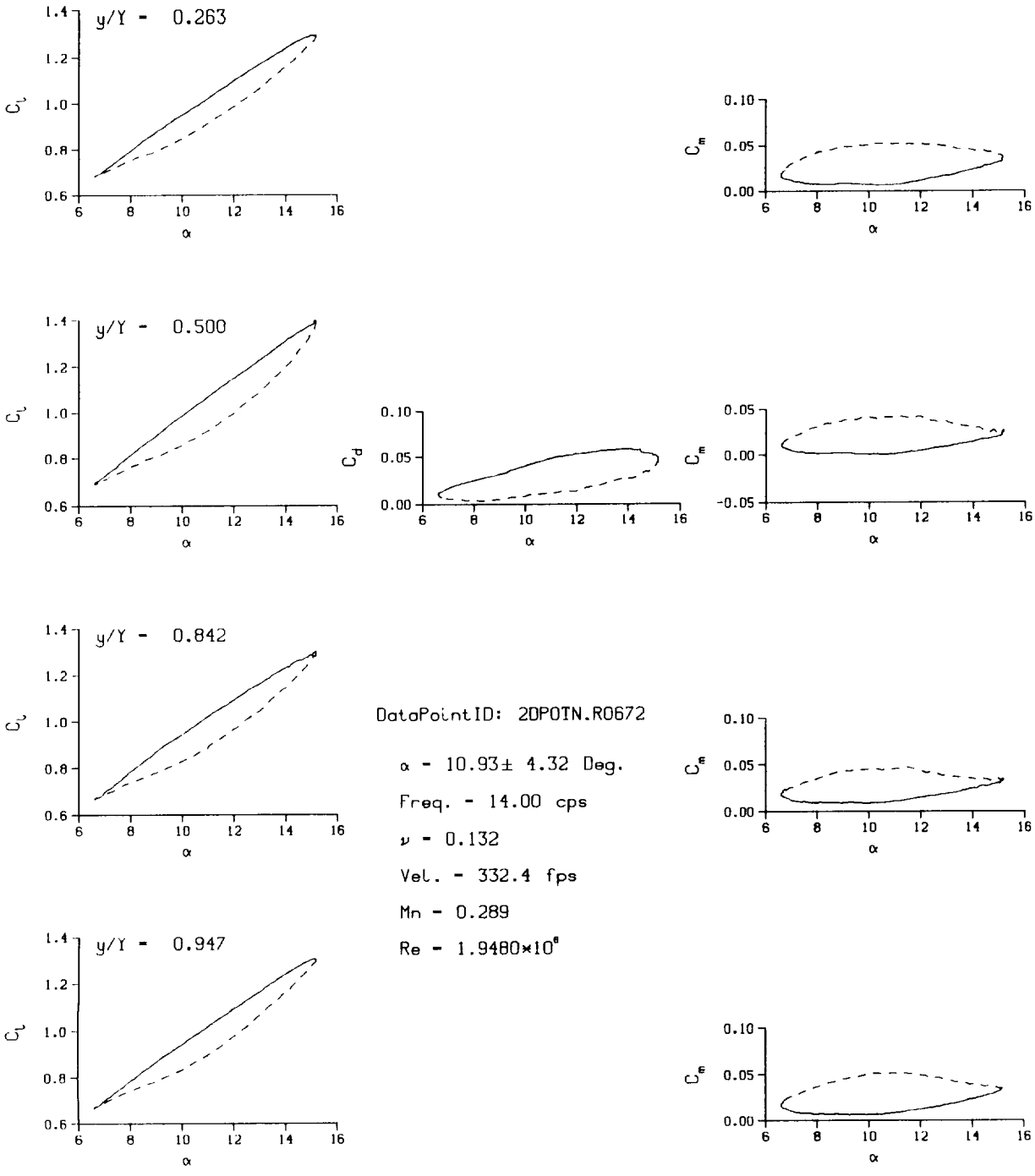

(c) v = 0.14

Figure 65. Concluded.

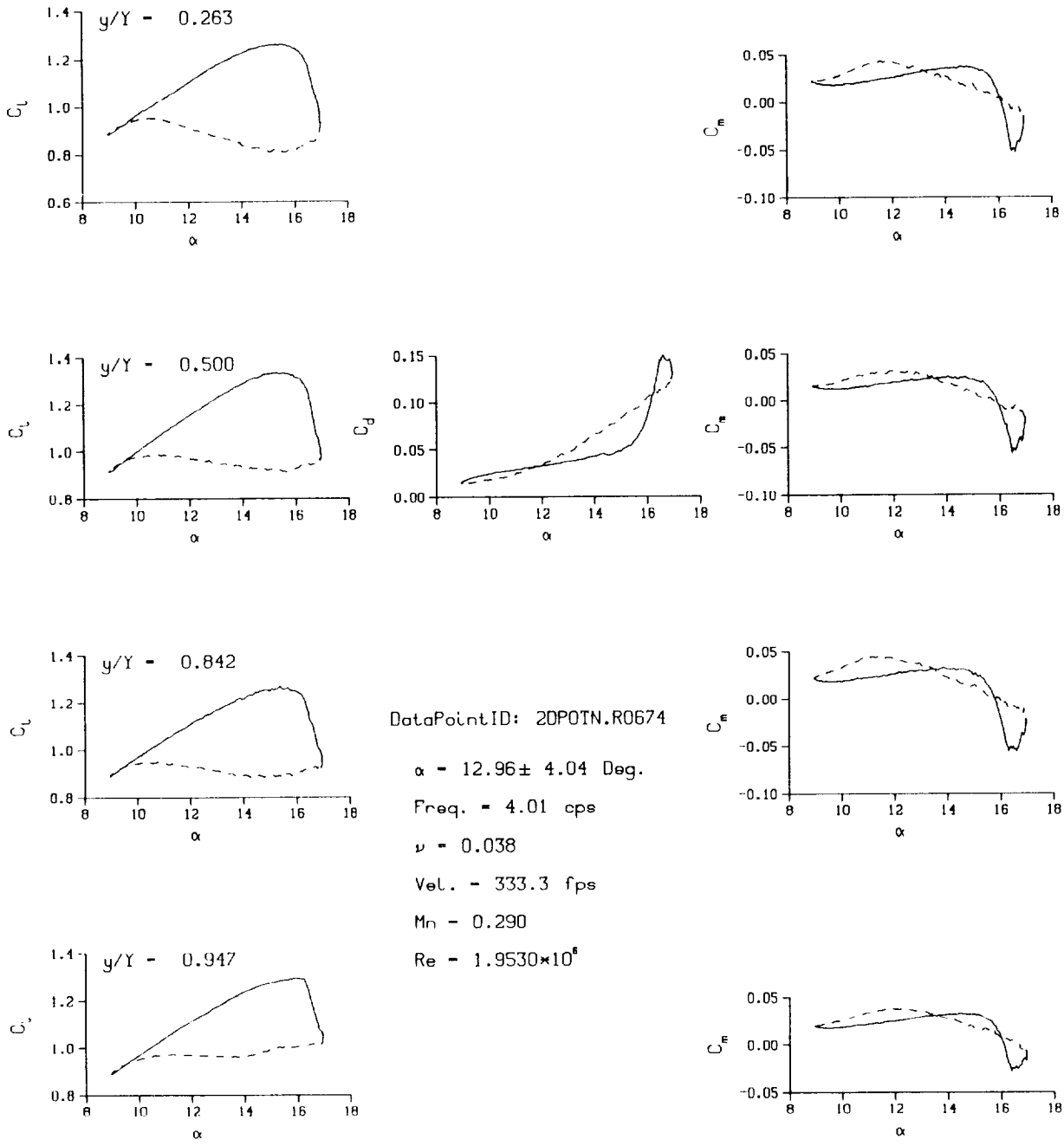

(a) ν = 0.04

Figure 66. 2-D pitch oscillation data; no BL-trip; α = 13 ± 4 deg.

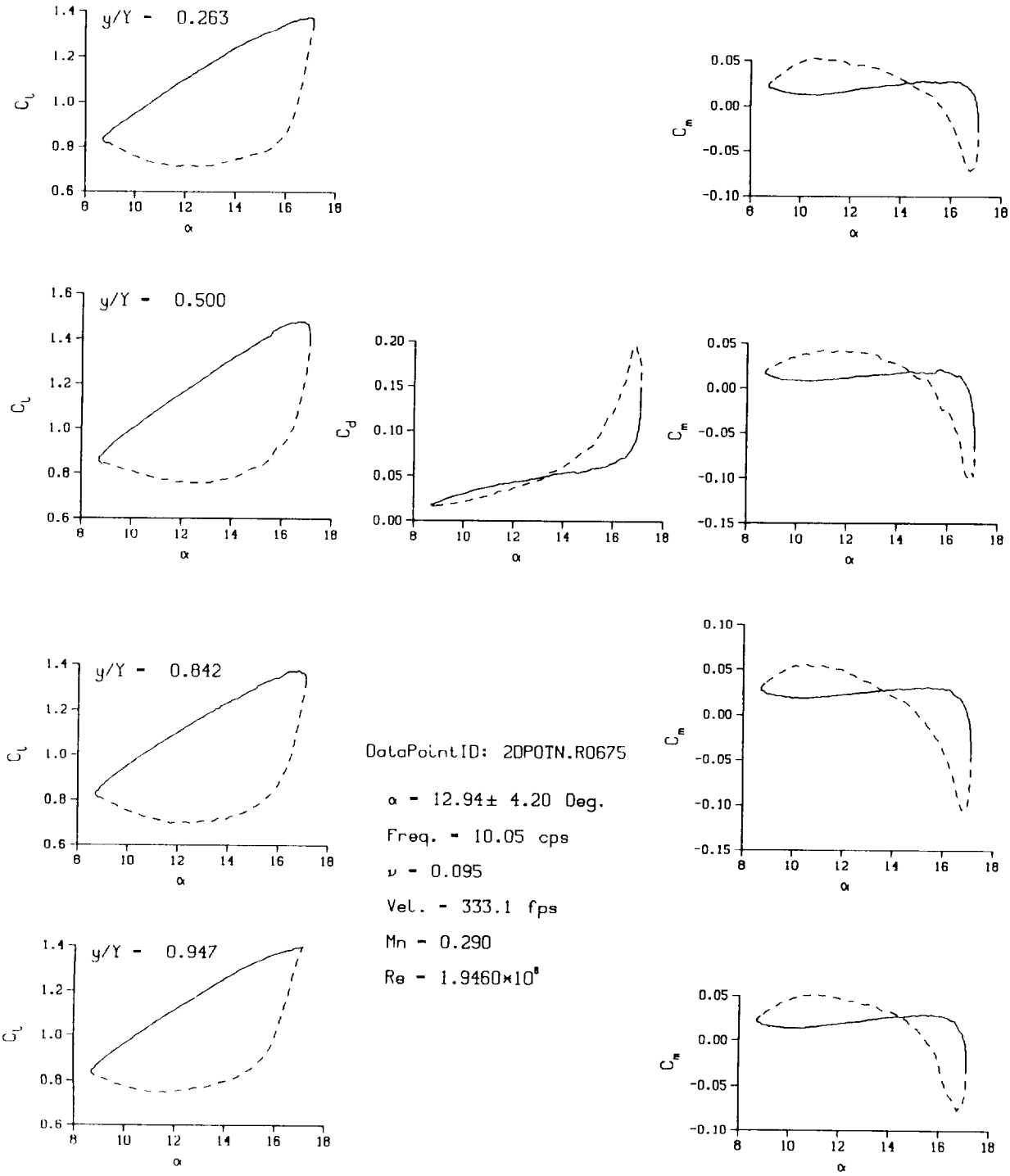

(b) v = 0.10

Figure 66. Continued.

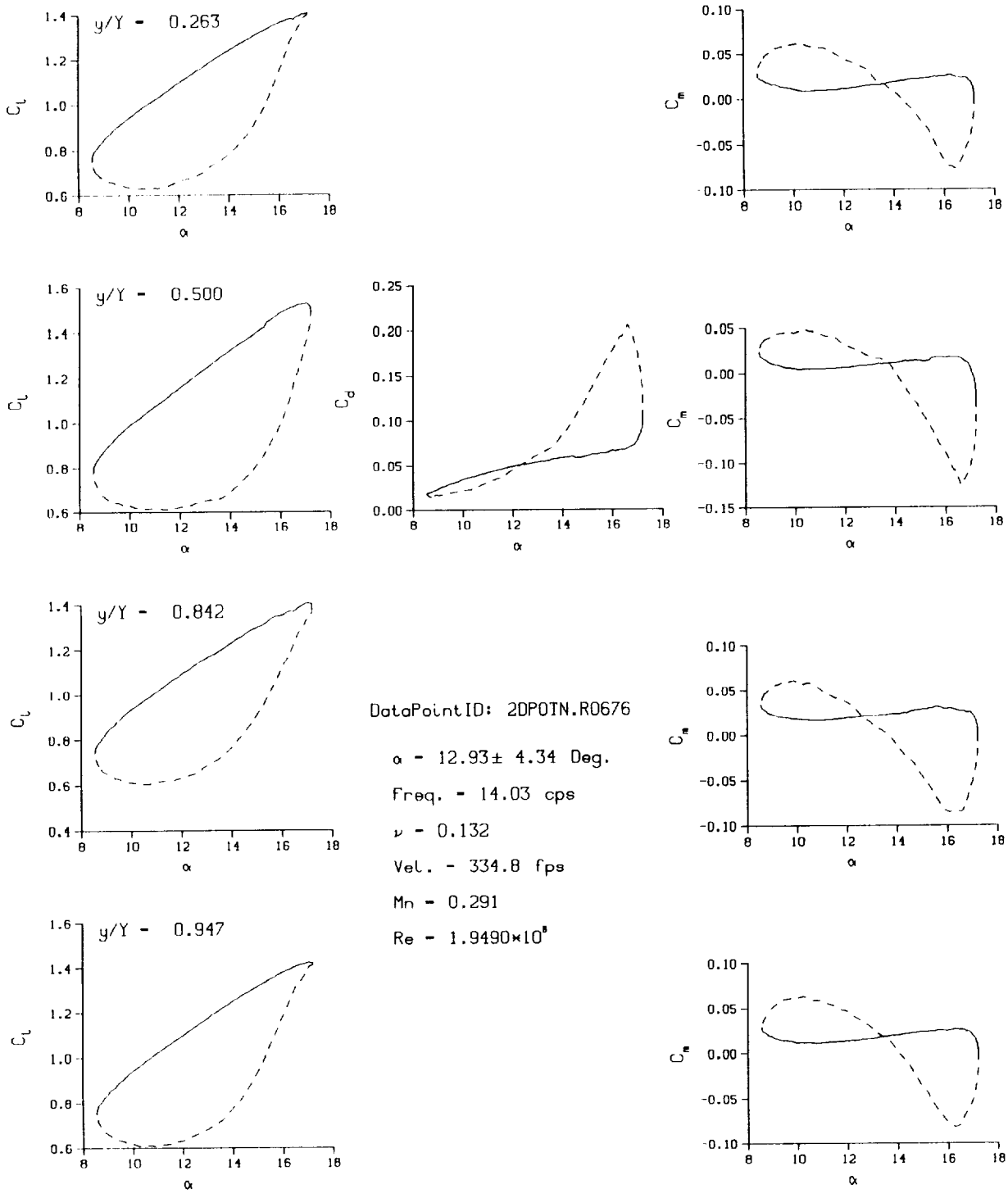

(c) v = 0.14

Figure 66. Concluded.

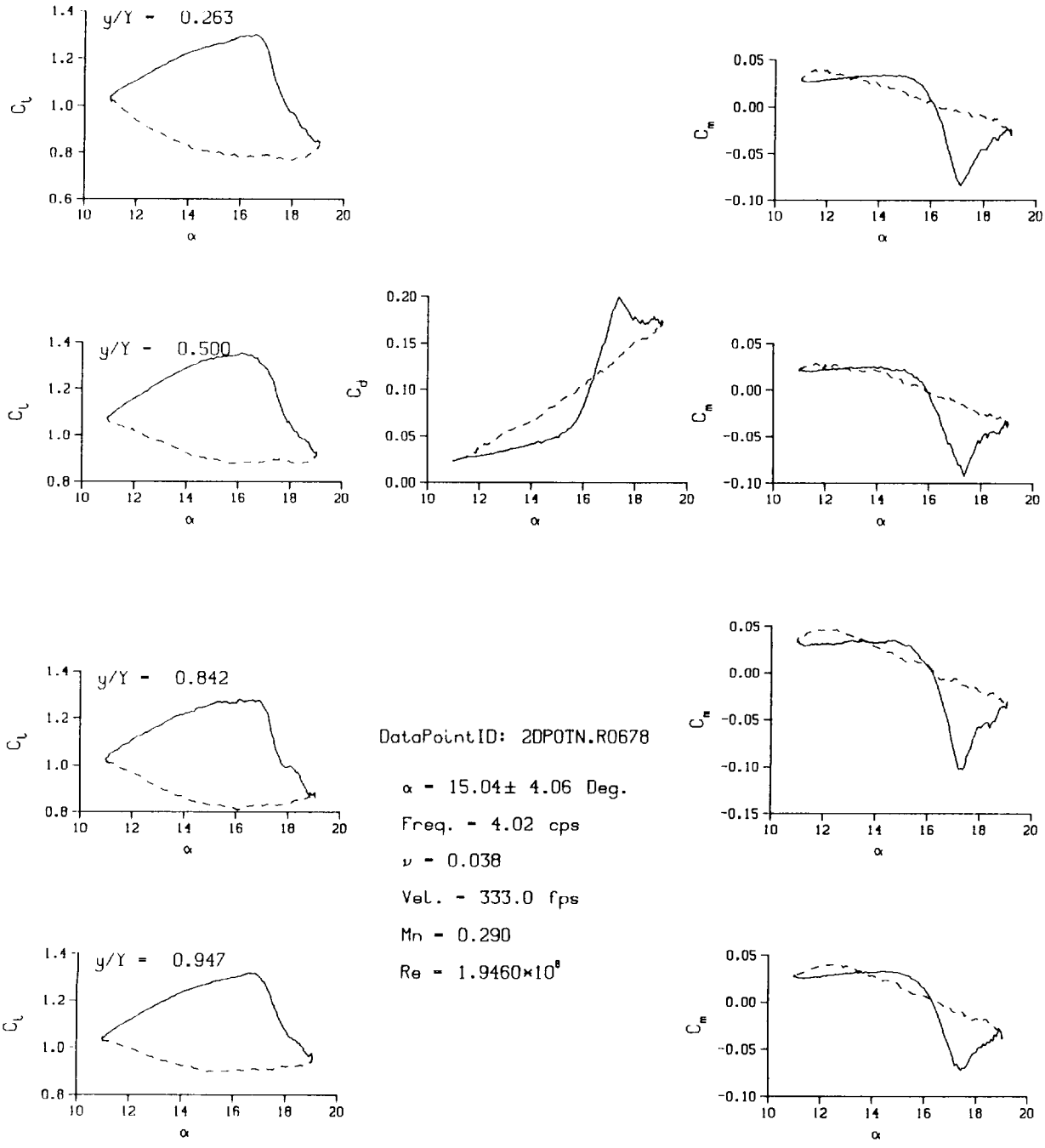

(a) ν = 0.04

Figure 67. 2-D pitch oscillation data; no BL-trip; α = 15 ± 4 deg.

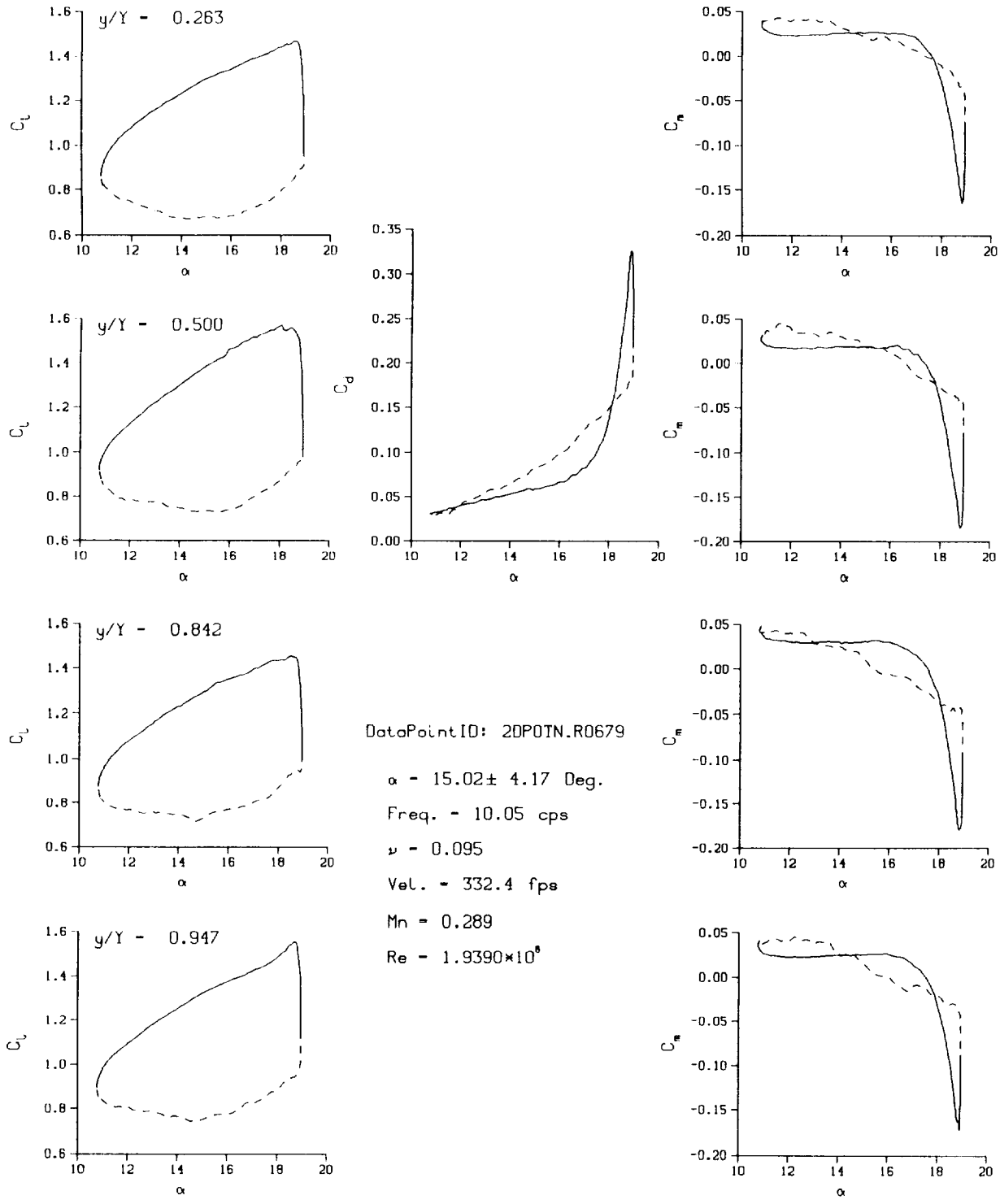

(b) v = 0.10

Figure 67. Continued.

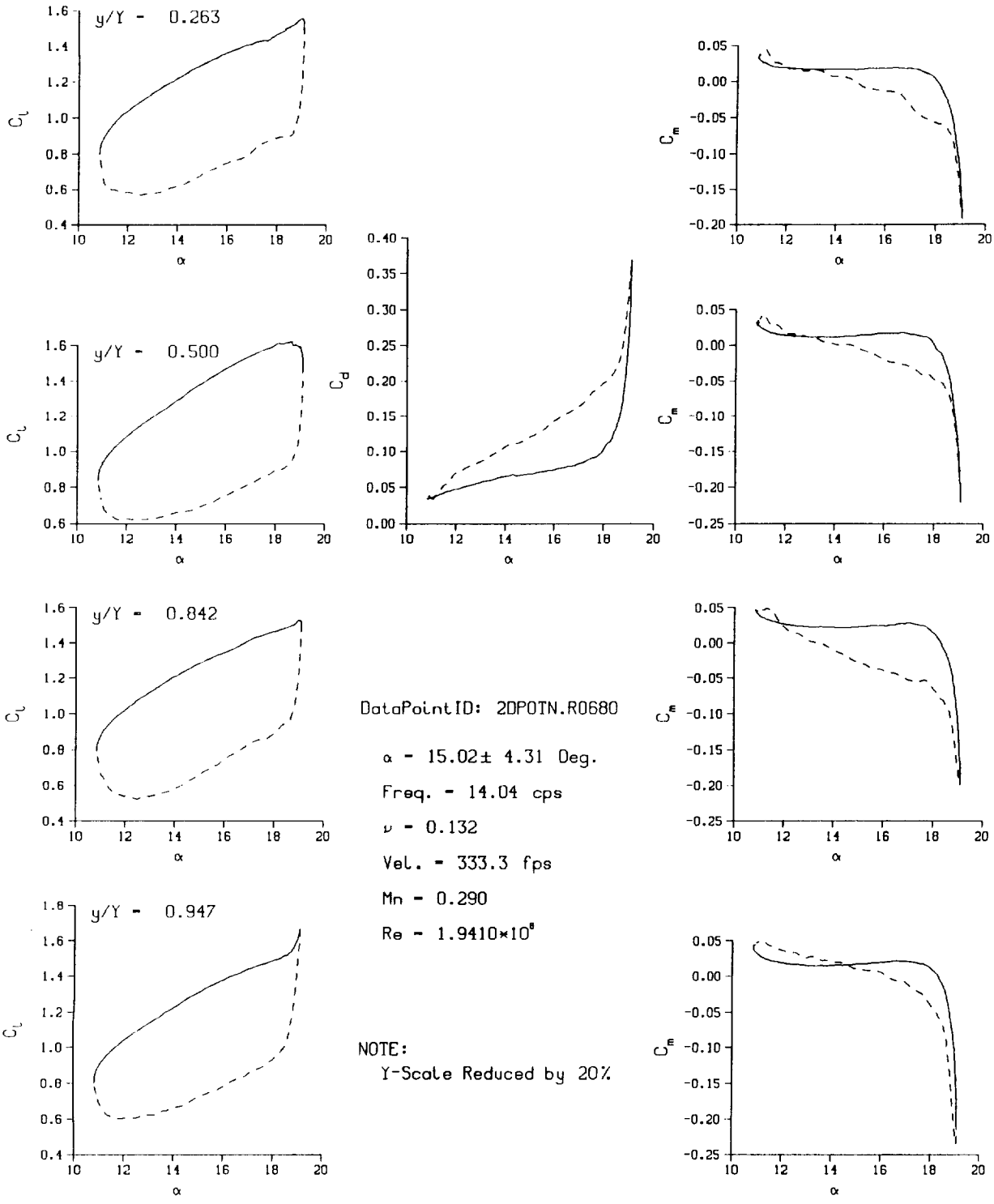

(c) v = 0.14

Figure 67. Concluded.

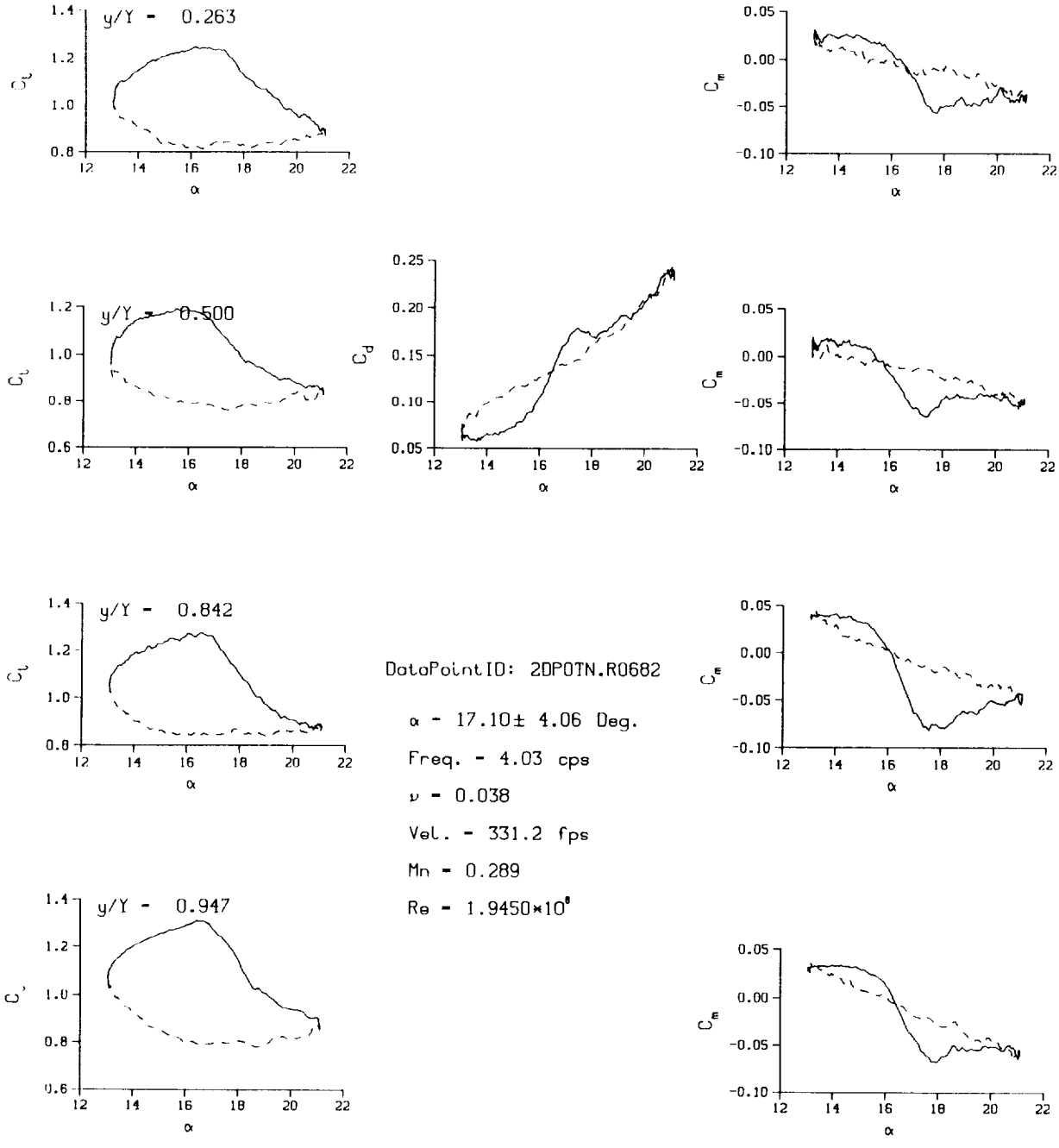

(a) v = 0.04

Figure 68. 2-D pitch oscillation data; no BL-trip; α = 17 ± 4 deg.

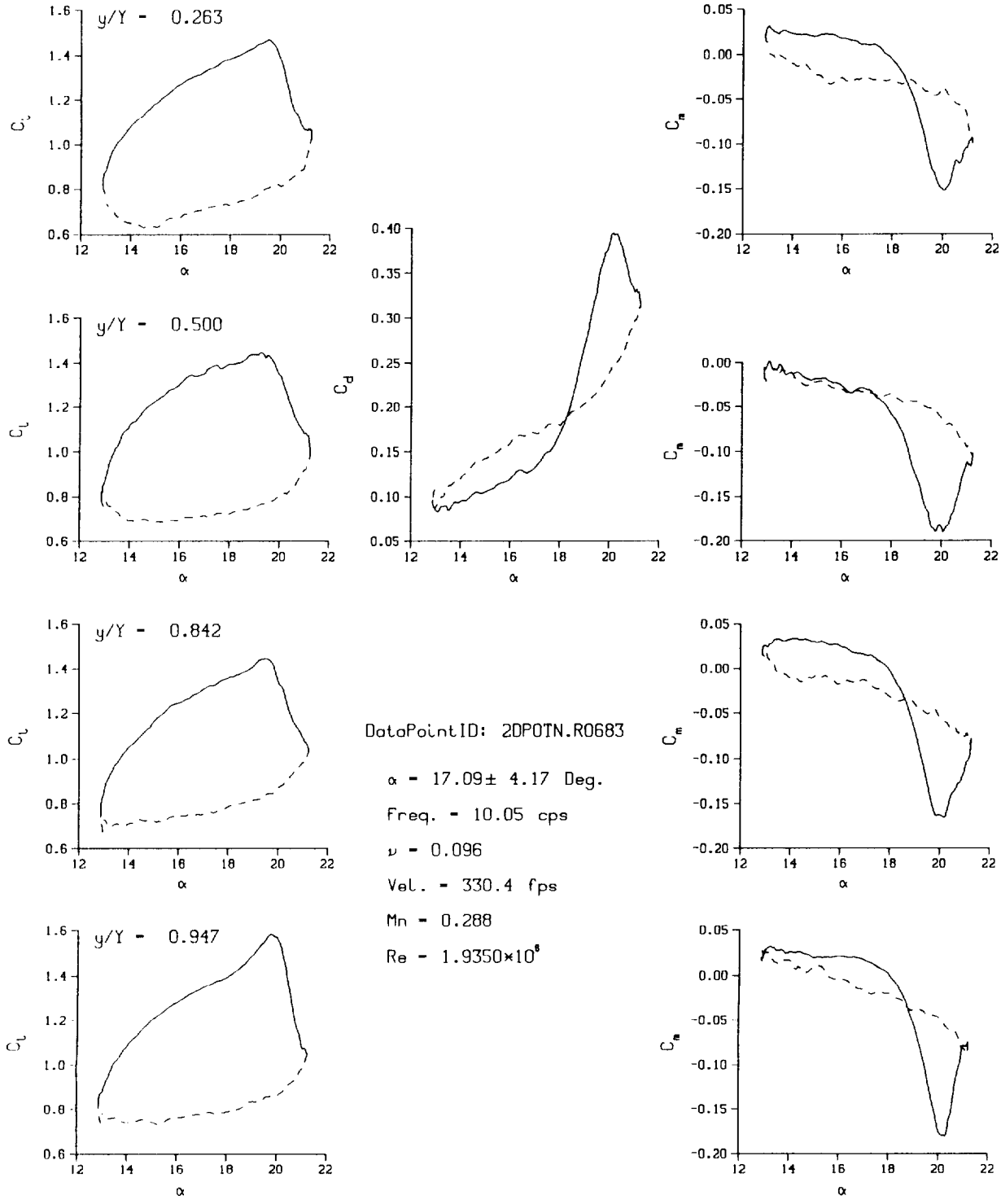

(b) v = 0.10

Figure 68. Continued.

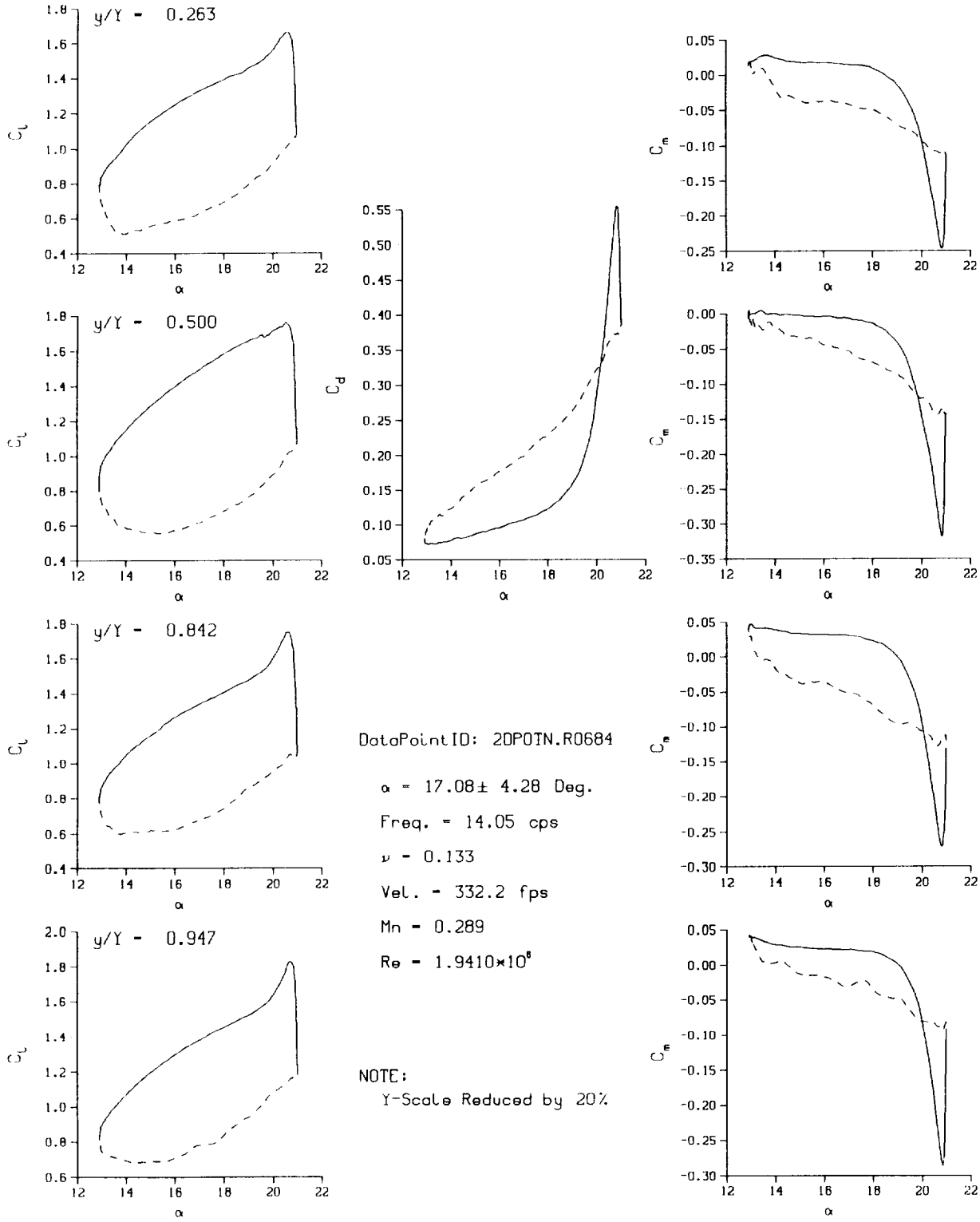

(c) ν = 0.14

Figure 68. Concluded.

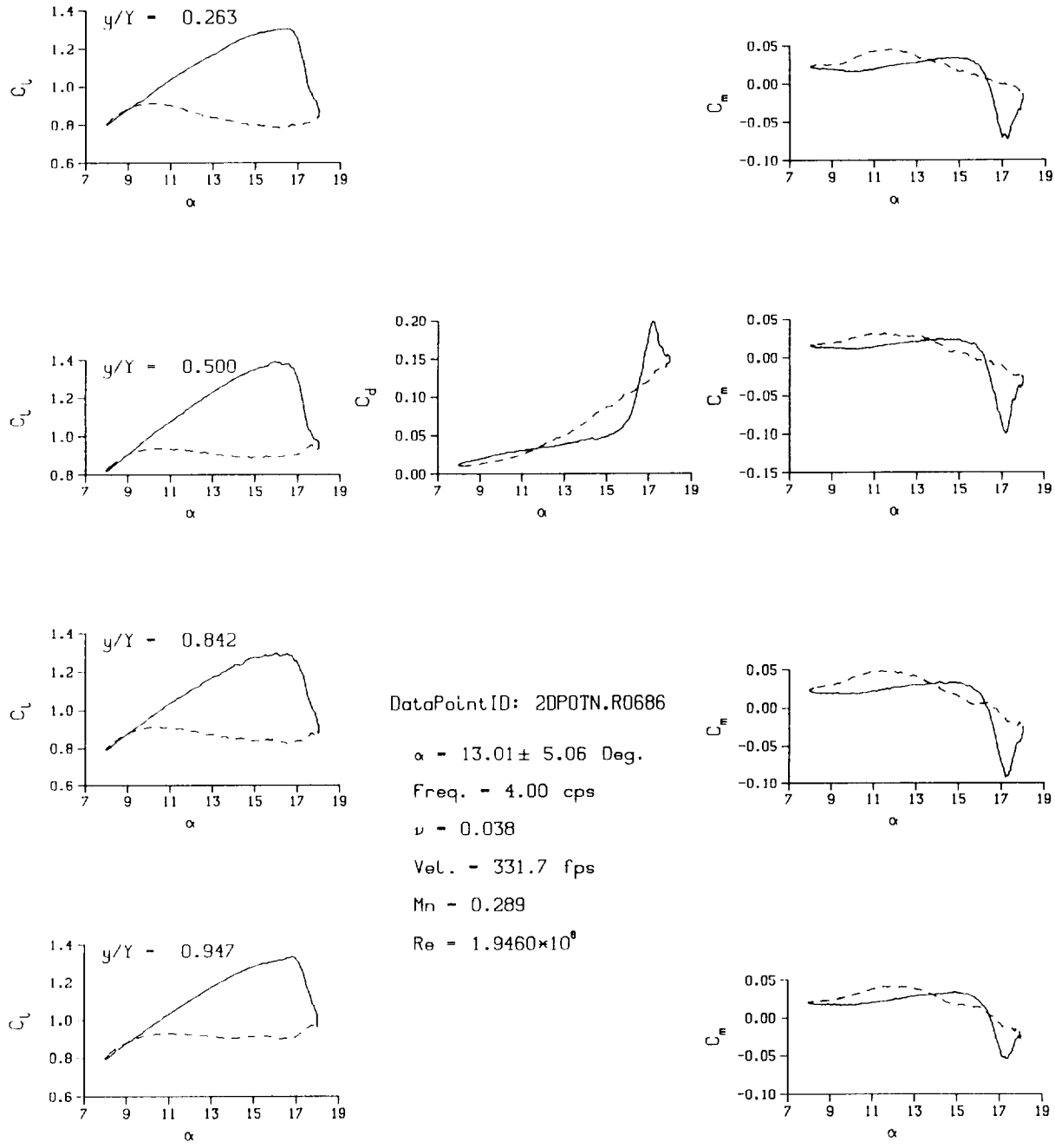

(a) v = 0.04

Figure 69. 2-D pitch oscillation data; no BL-trip; α = 13 ± 5 deg.

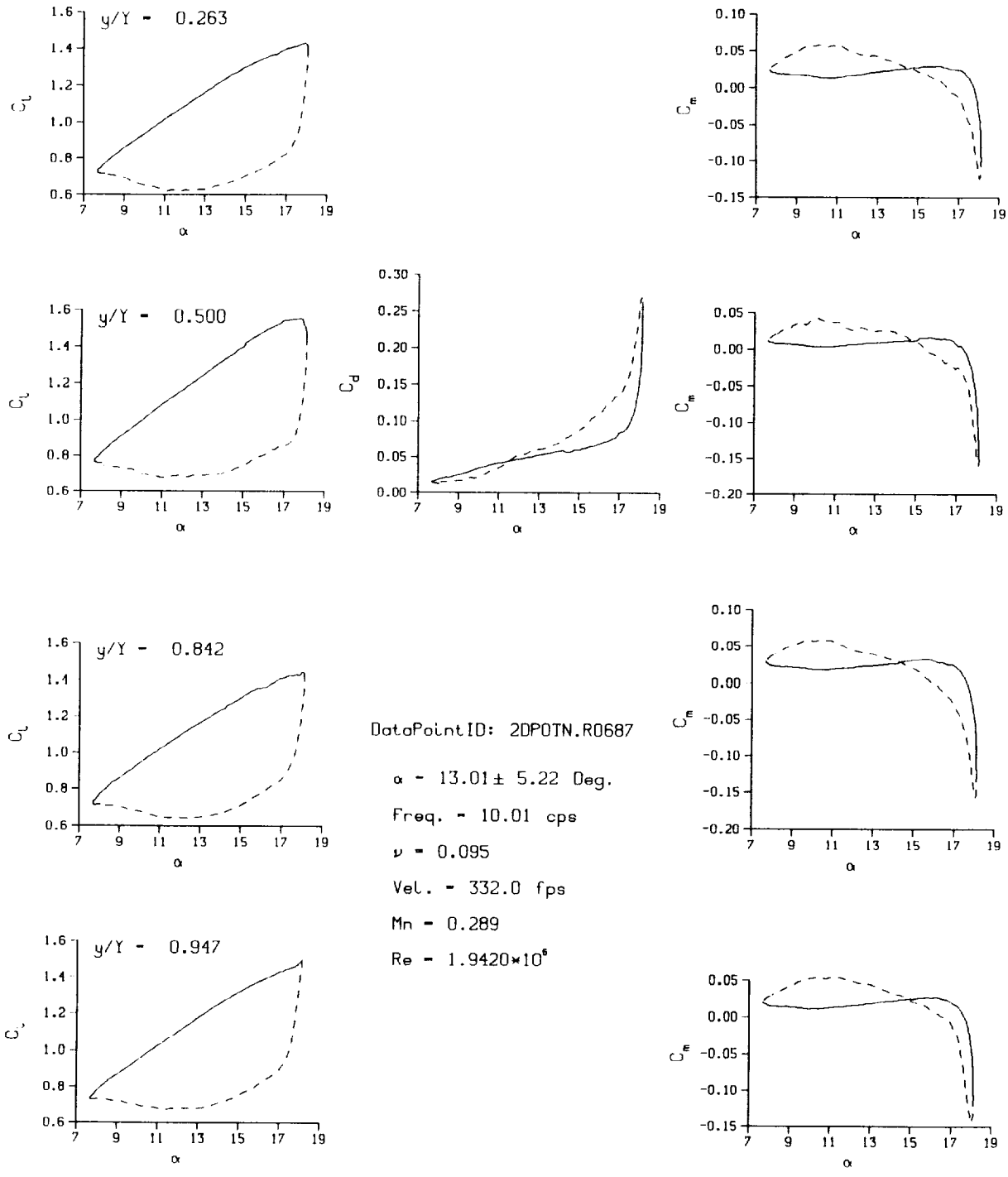

(b) ν = 0.10

Figure 69. Concluded.

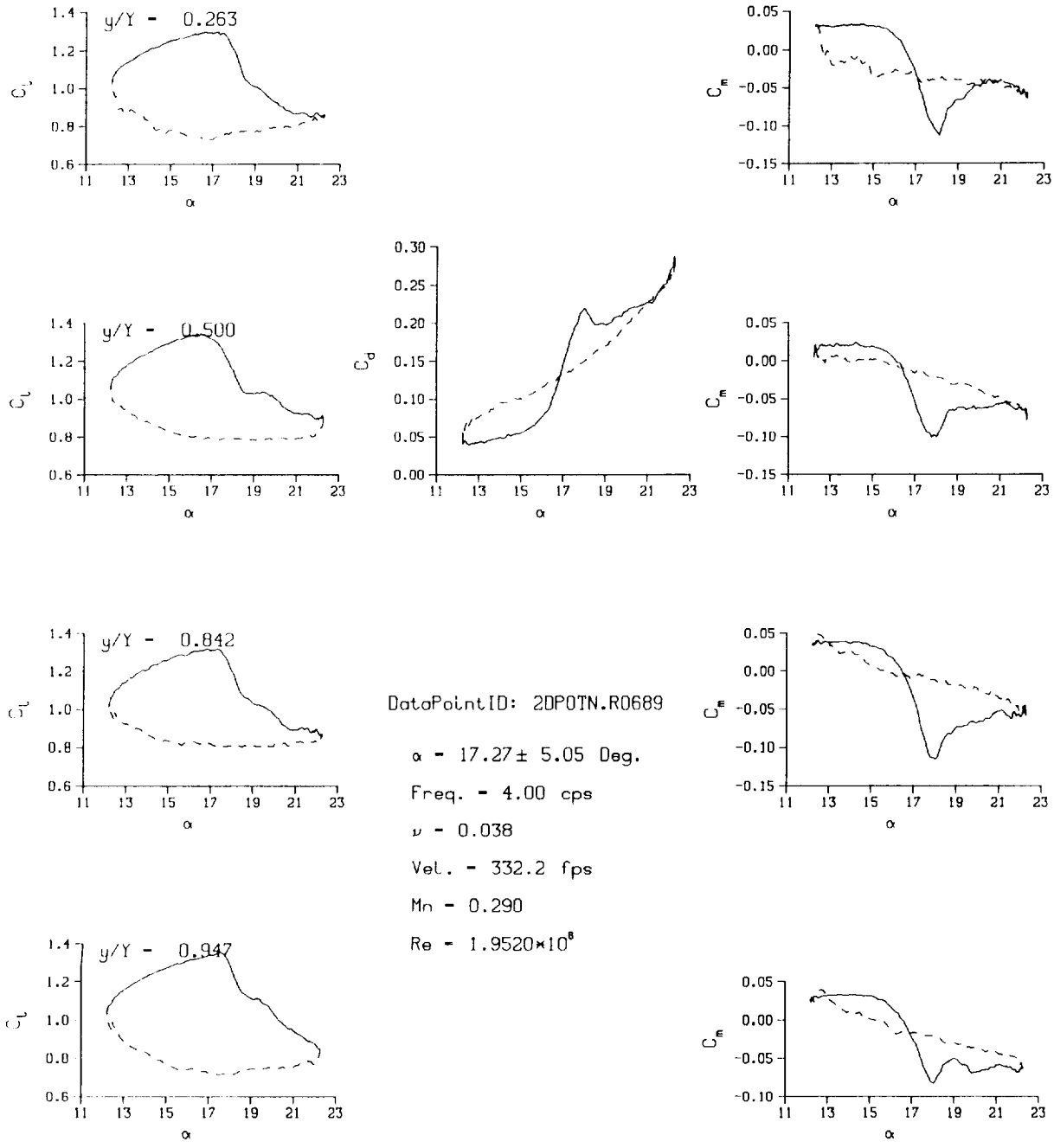

(a) ν = 0.04

Figure 70. 2-D pitch oscillation data; no BL-trip; α = 17 ± 5 deg.

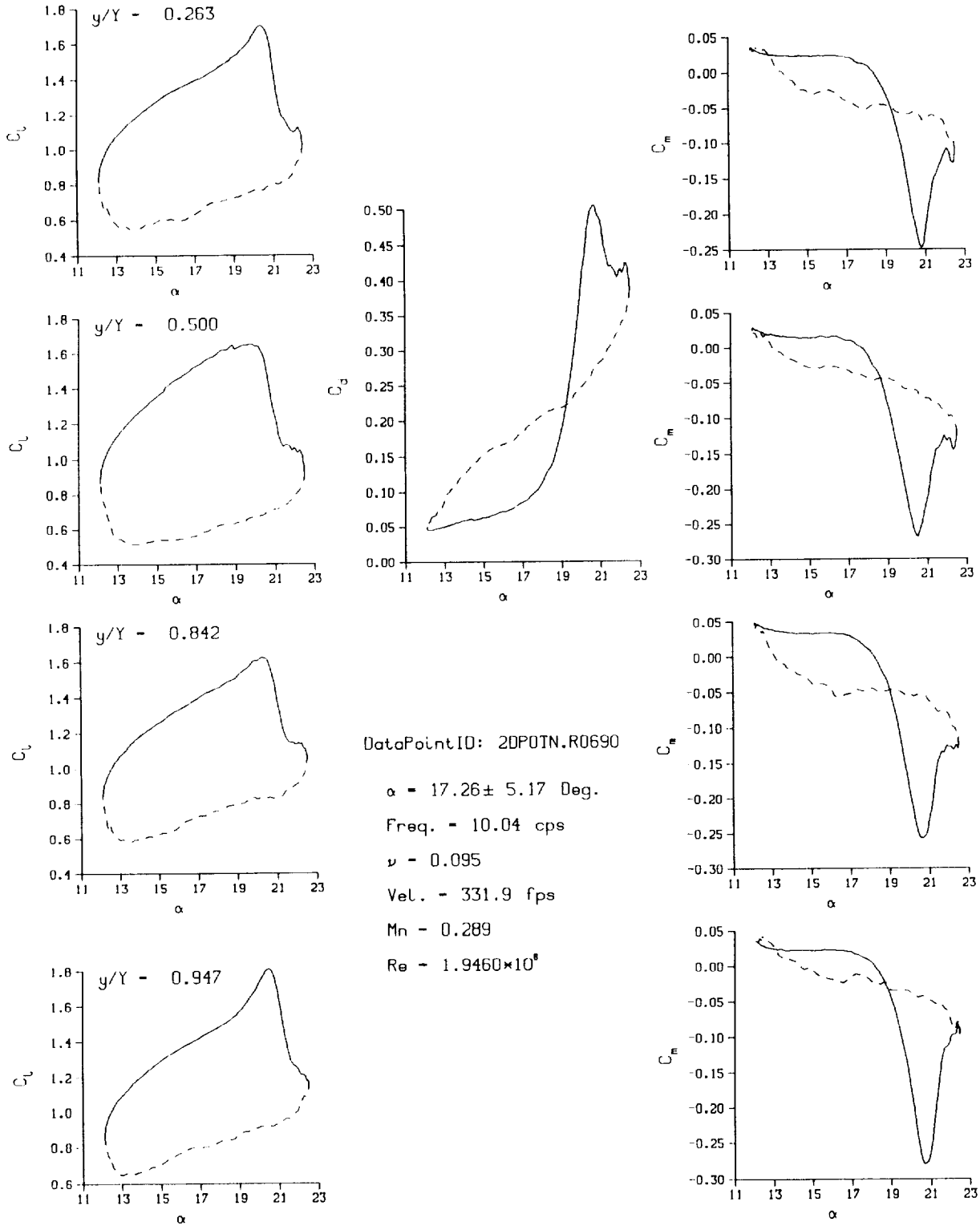

(b) ν = 0.10

Figure 70. Concluded.

The next figure series begins on page 304.

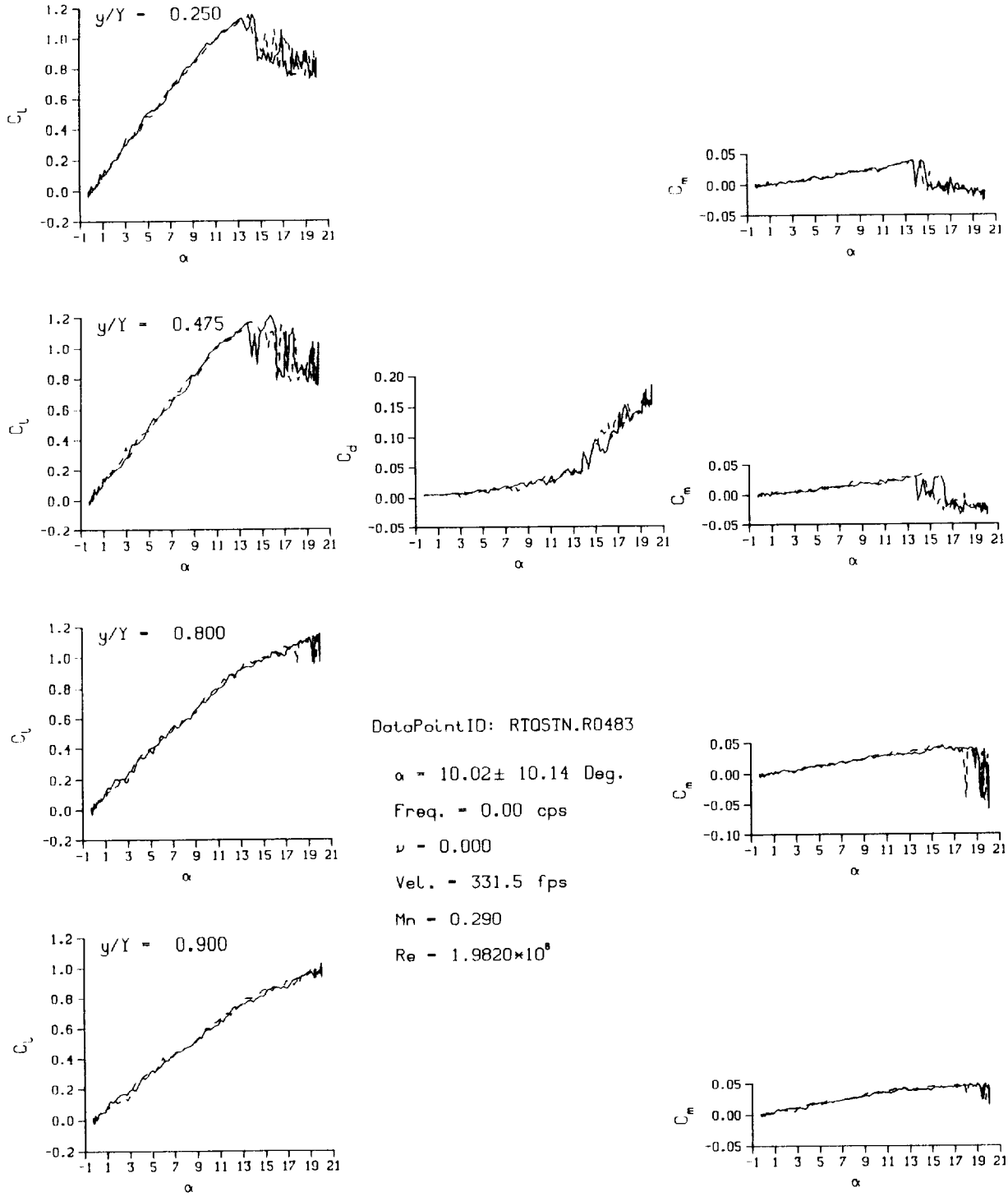

(a) Repeat no. 1

Figure 71. 3-D round tip quasi-steady data; no BL-trip; $0 \leq \alpha \leq 20$ deg.

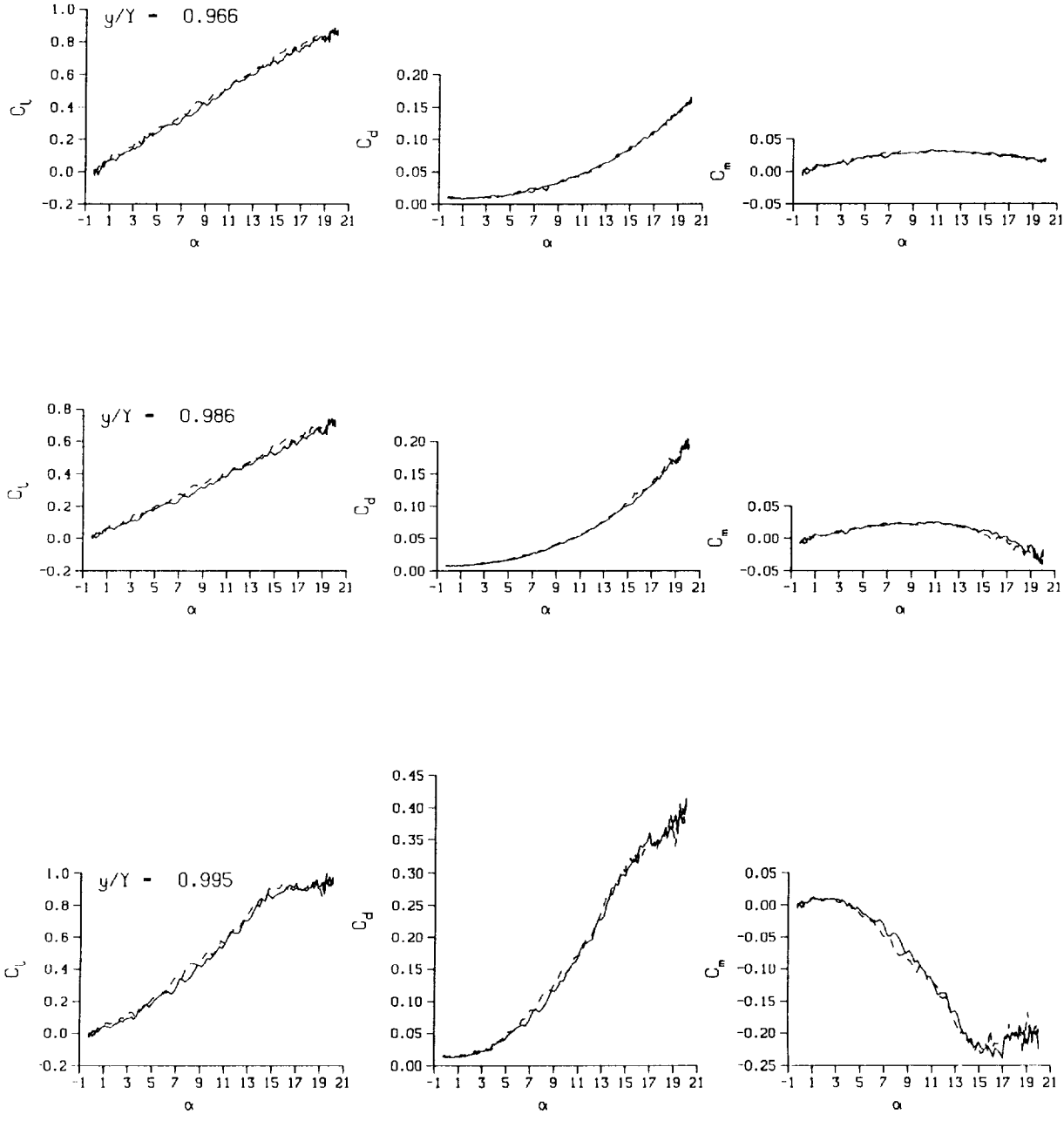

(a) Repeat no. 1. Concluded

Figure 71. Continued.

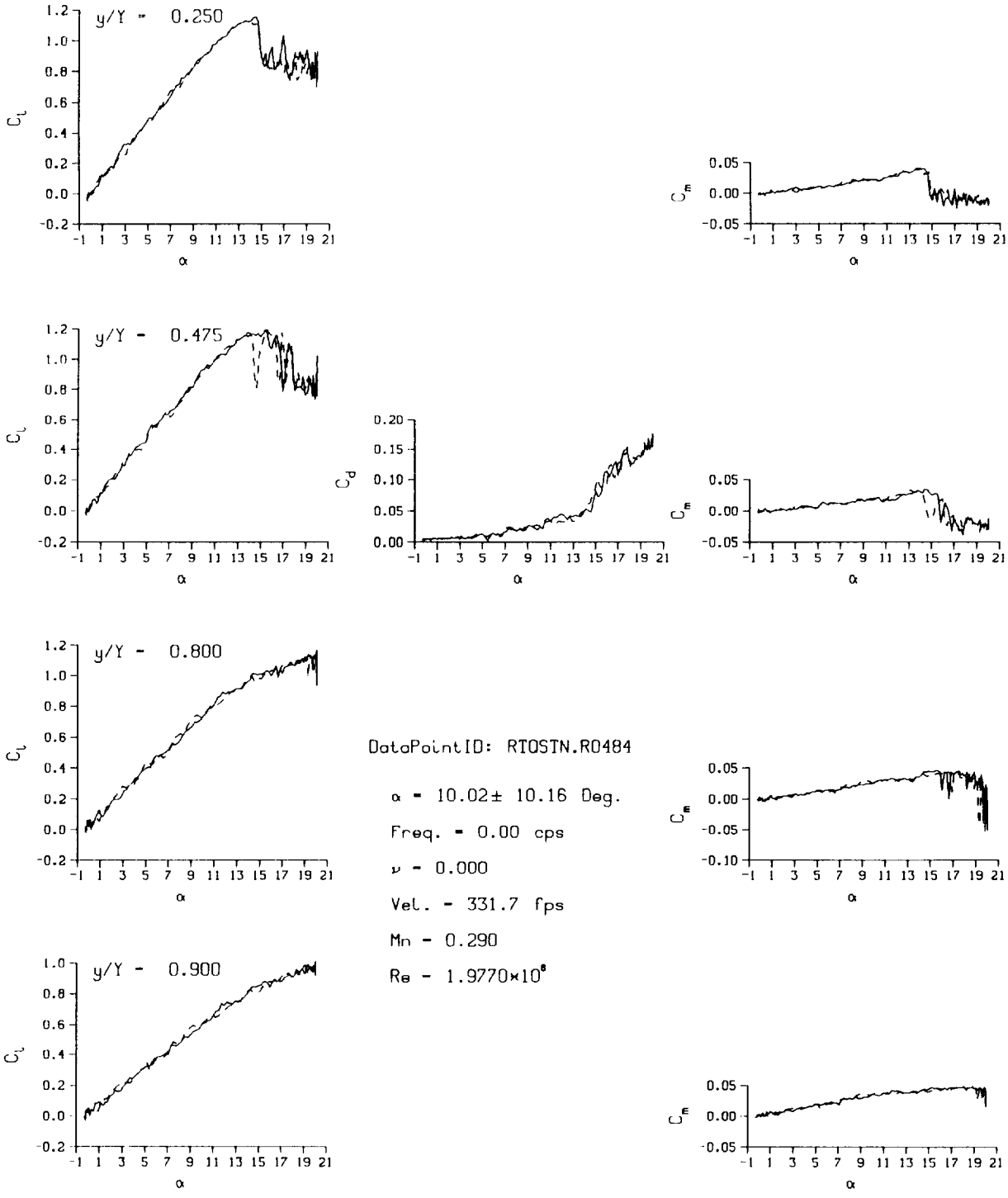

(b) Repeat no. 2

Figure 71. Continued.

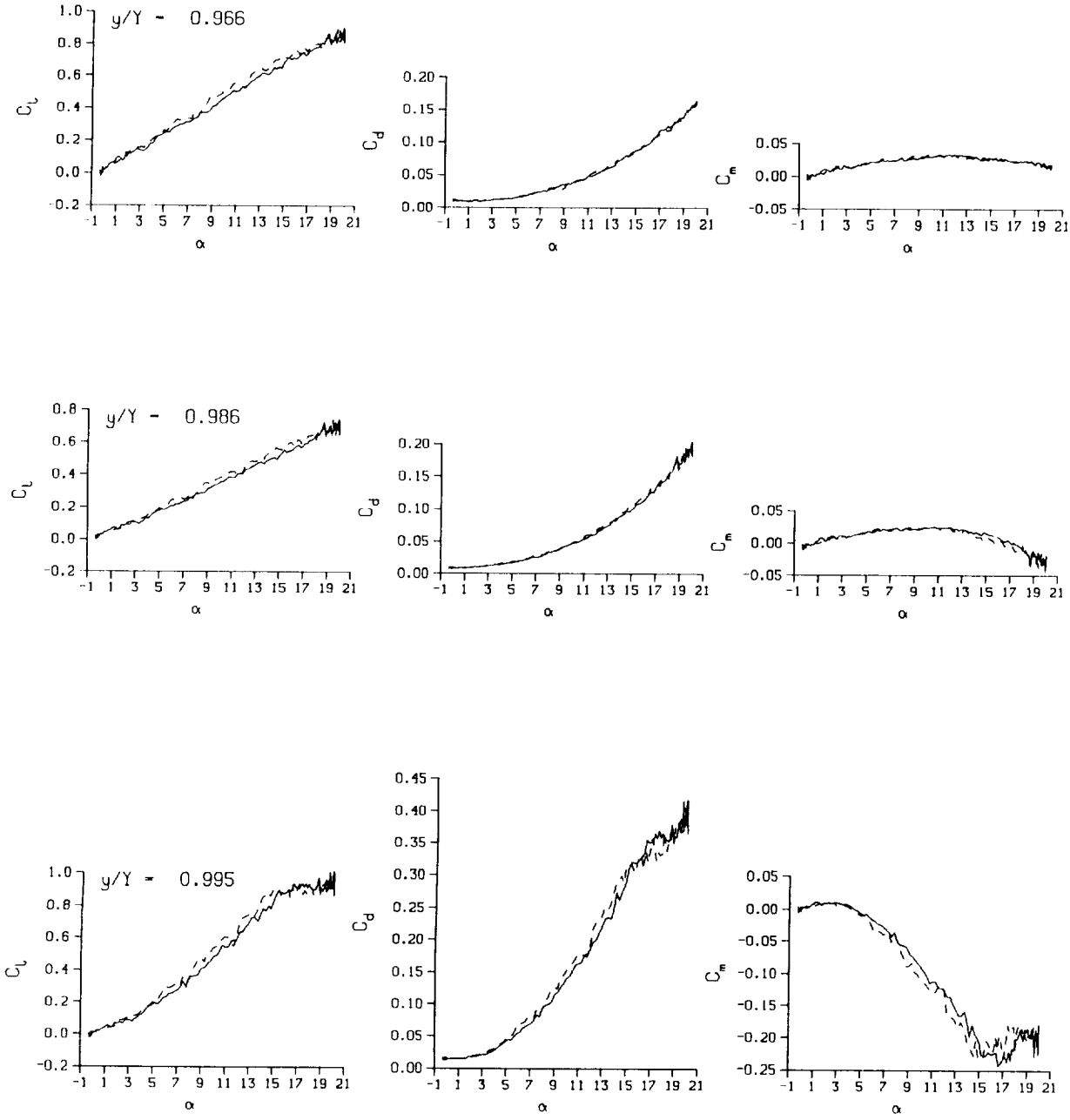

(b) Repeat no. 2. Concluded

Figure 71. Continued.

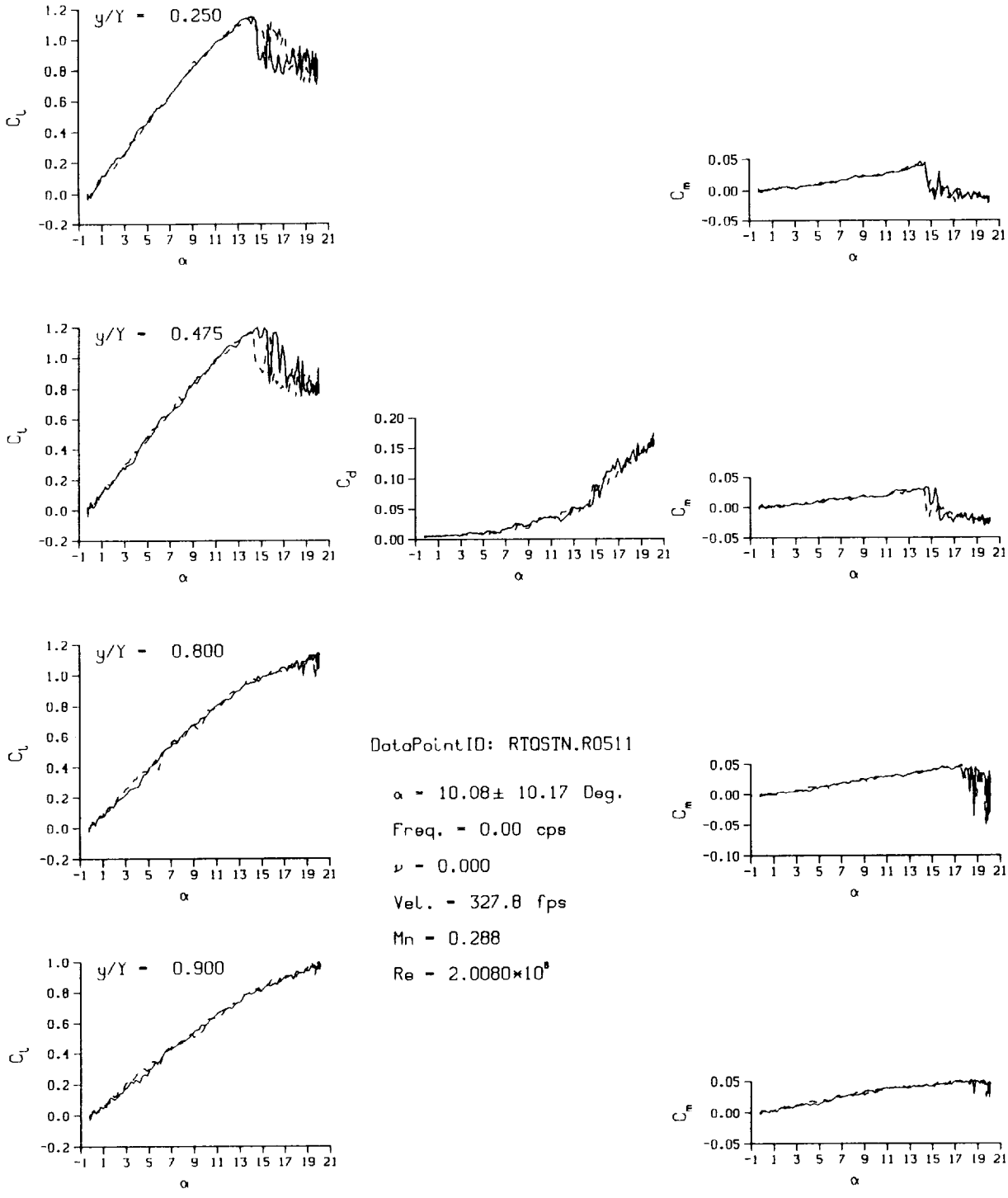

(c) Repeat no. 3

Figure 71. Continued.

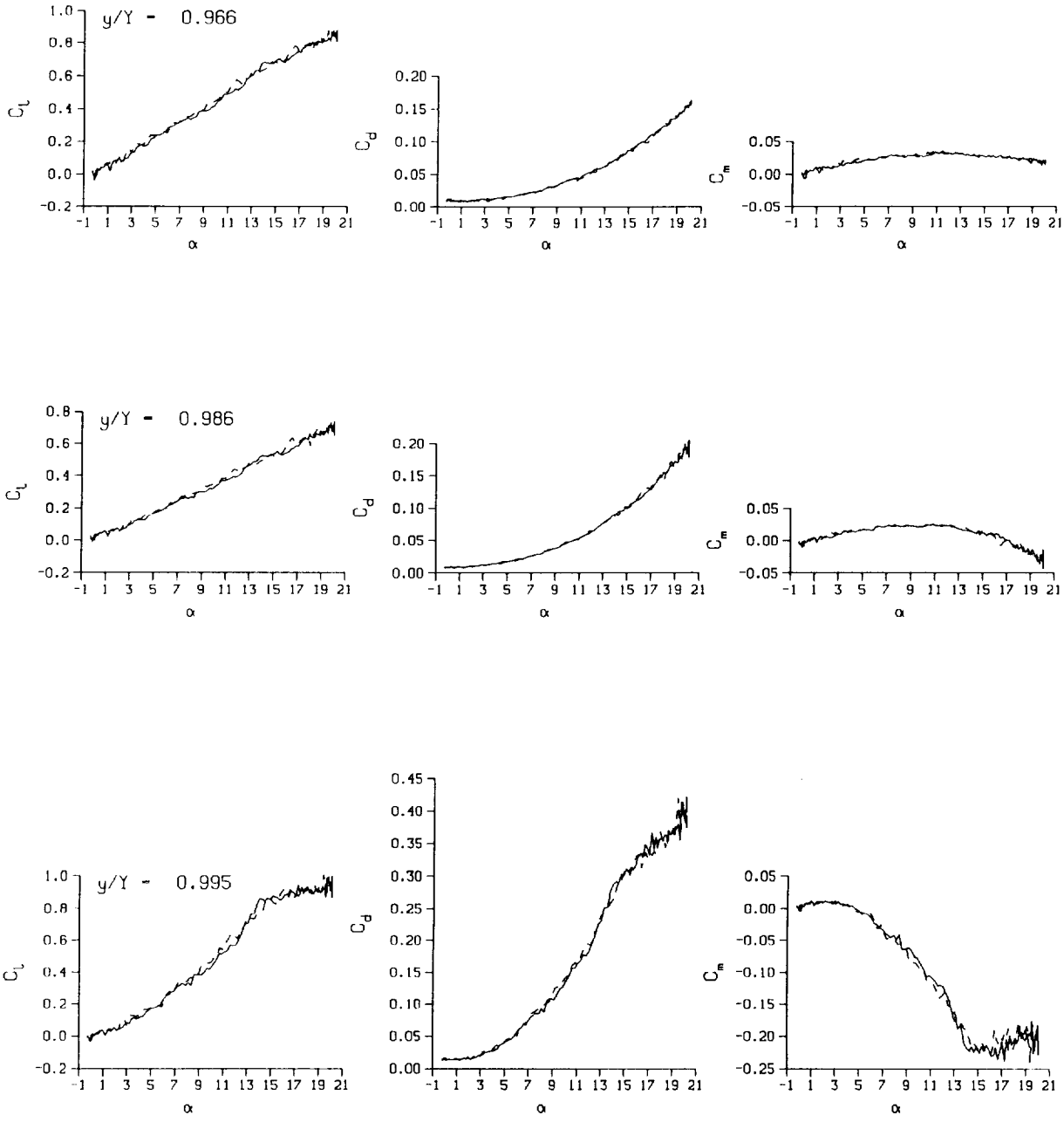

(c) Repeat no. 3. Concluded

Figure 71. Concluded.

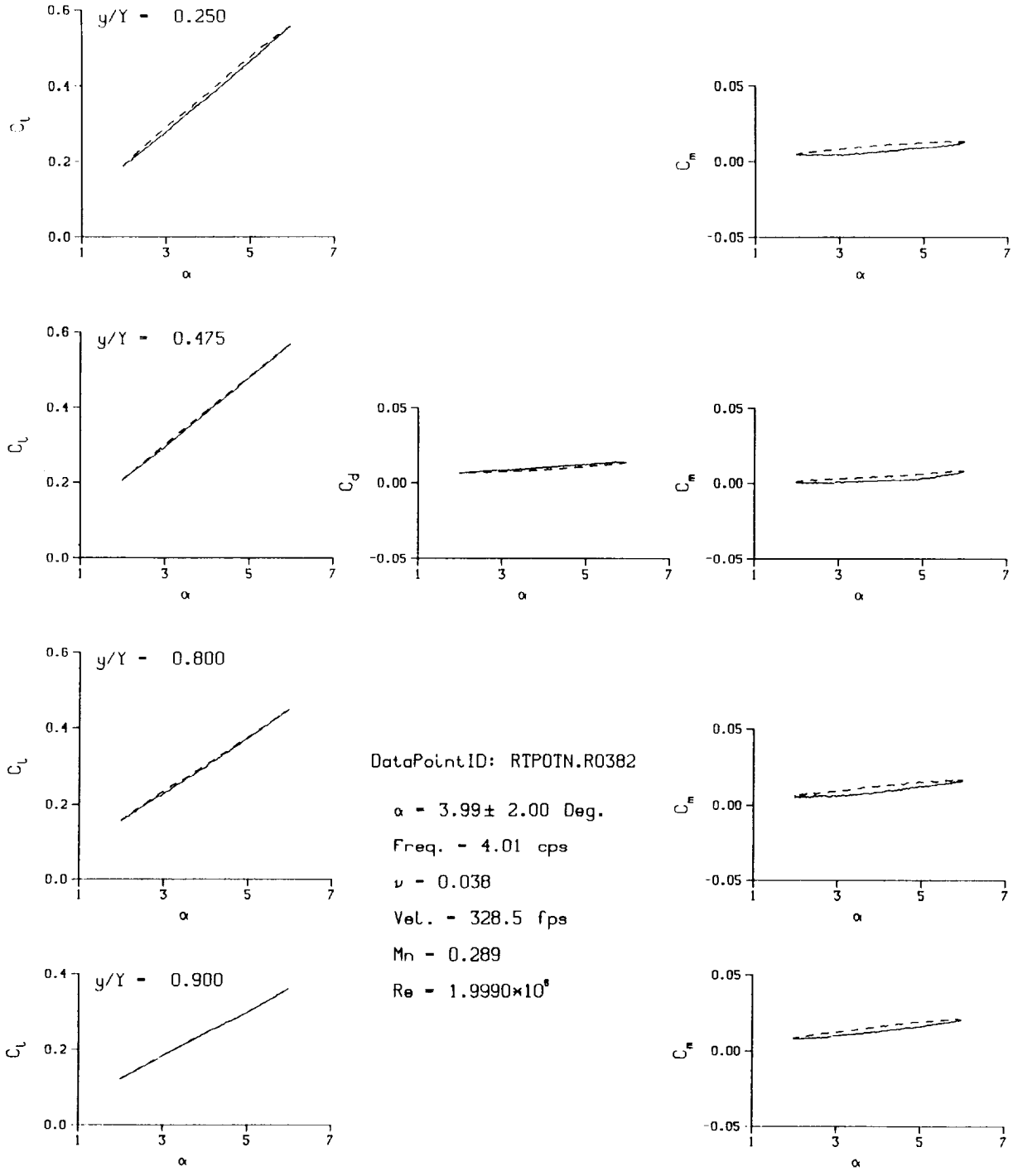

(a) ν = 0.04

Figure 72. 3-D round tip pitch oscillation data; no BL-trip; α = 4 ± 2 deg.

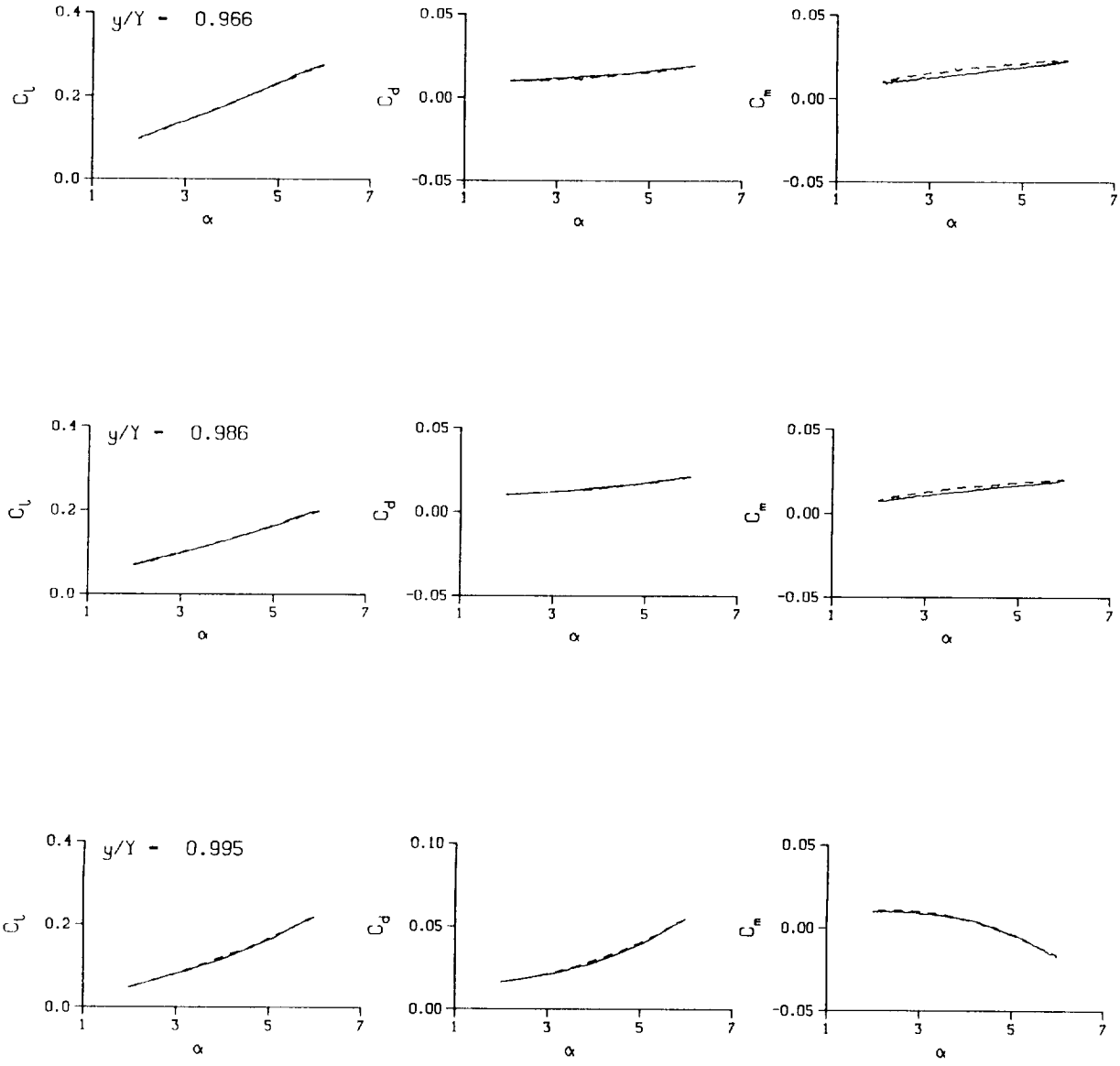

(a) v = 0.04. Concluded

Figure 72. Continued.

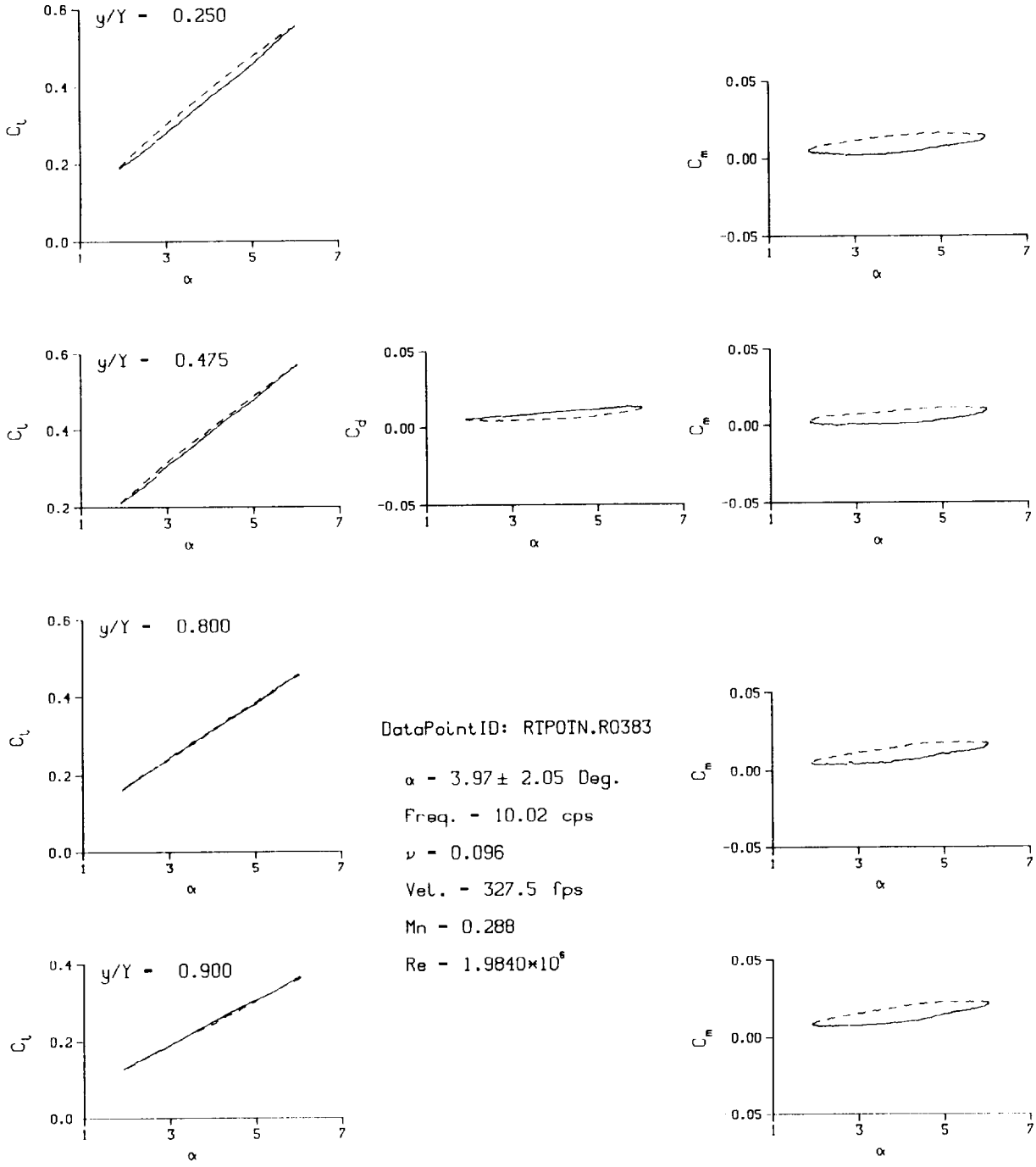

(b) v = 0.10

Figure 72. Continued.

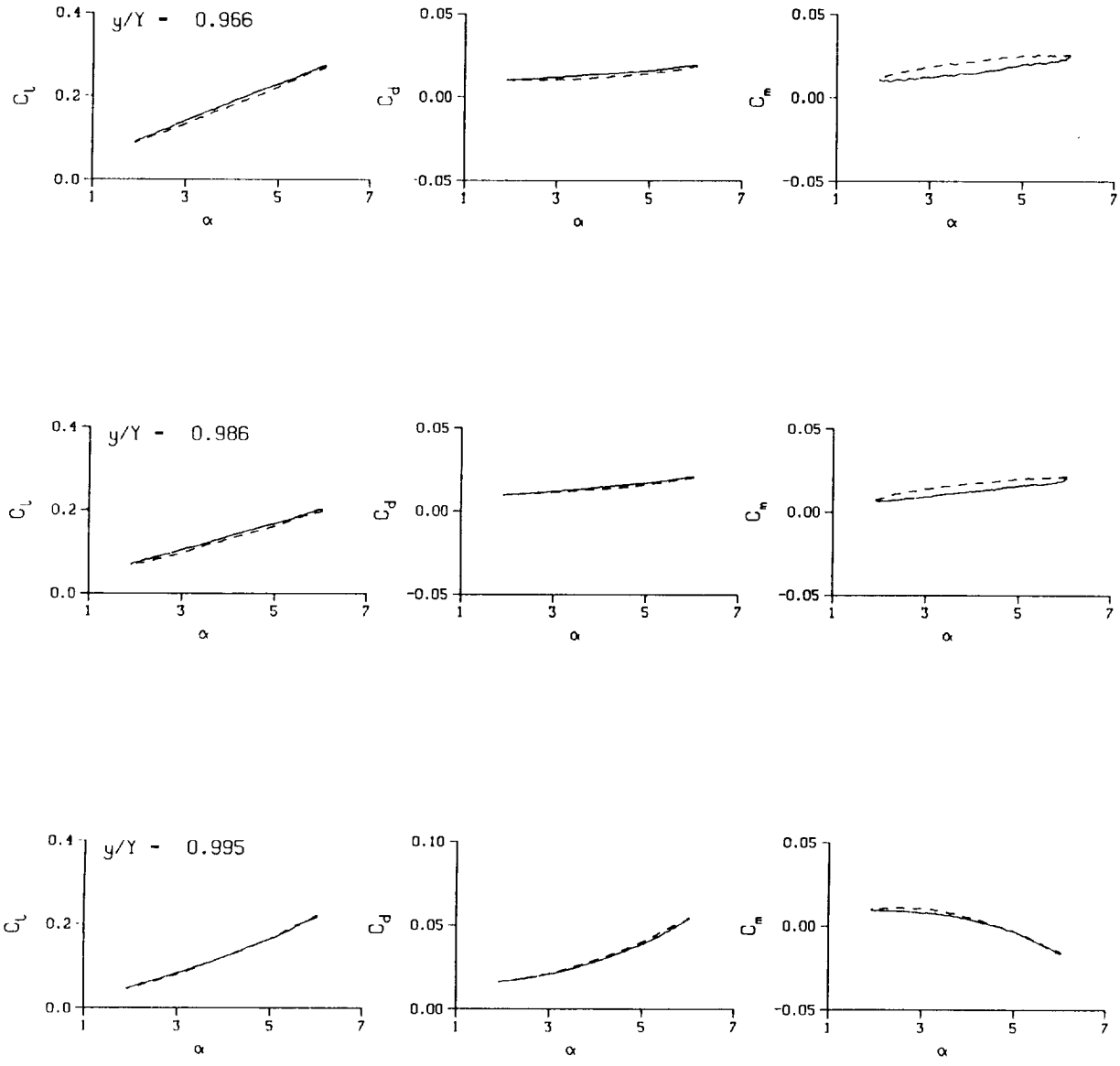

(b) v = 0.10. Concluded

Figure 72. Continued.

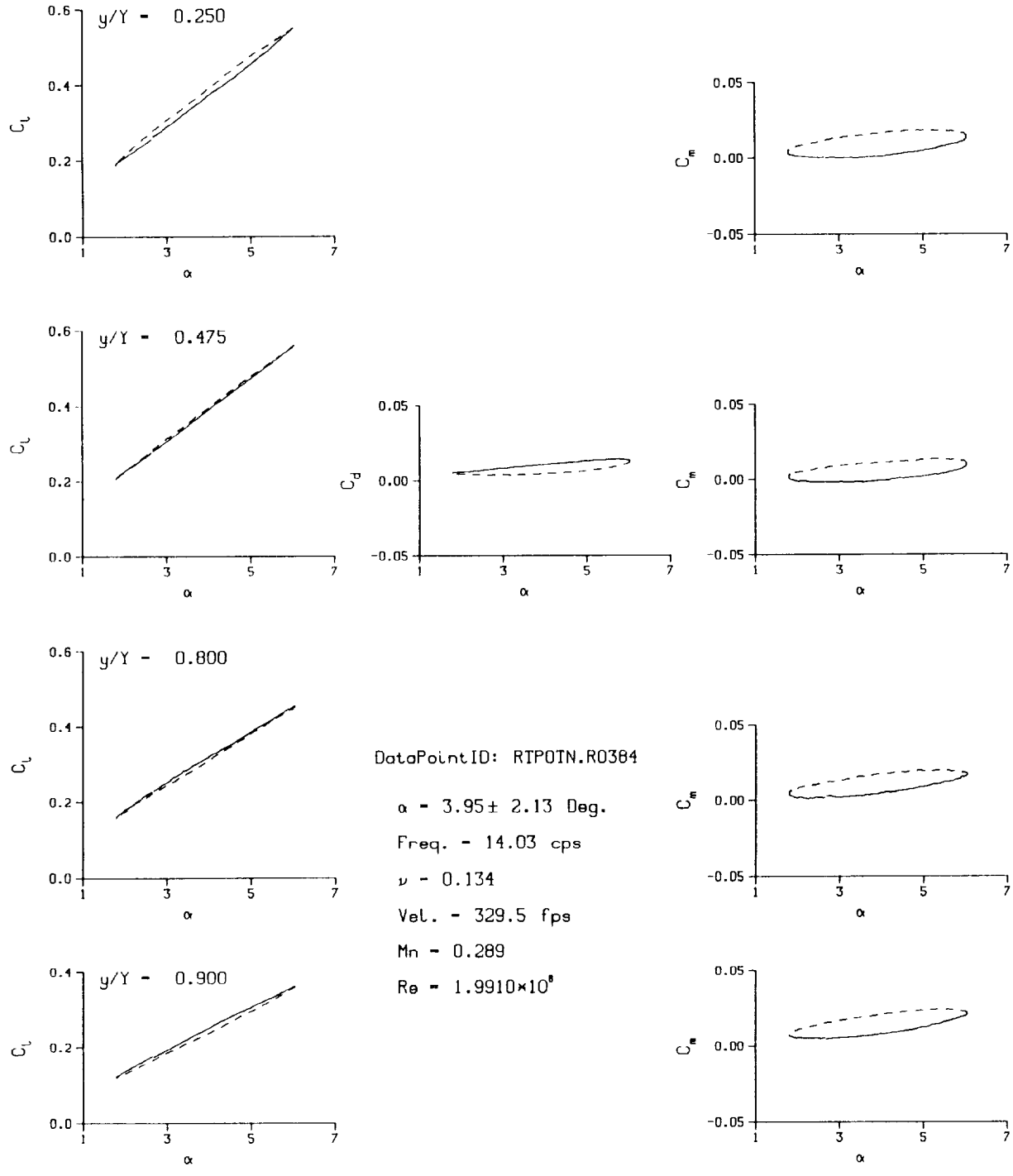

(c) v = 0.14

Figure 72. Continued.

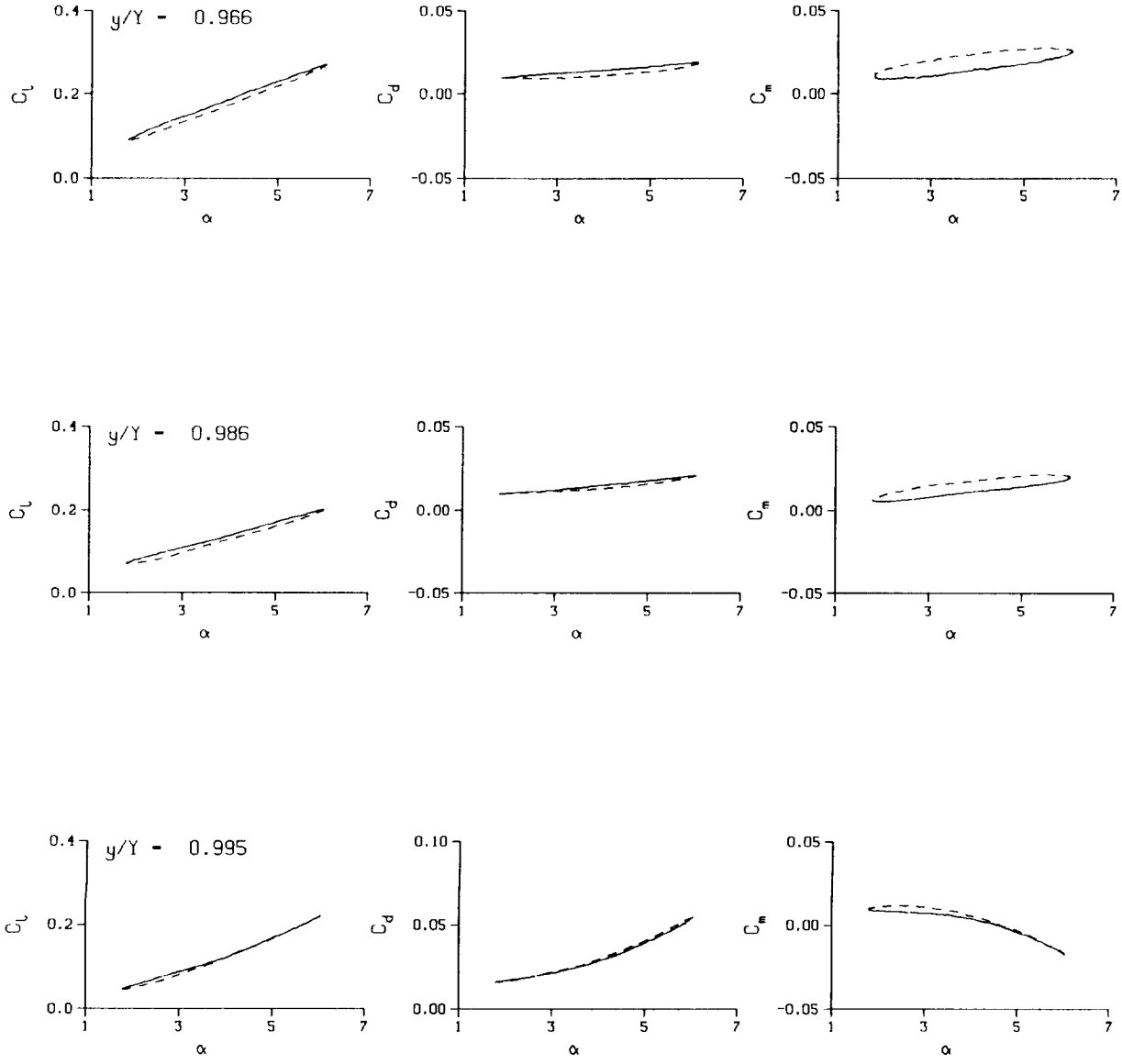

(c) v = 0.14. Concluded

Figure 72. Continued.

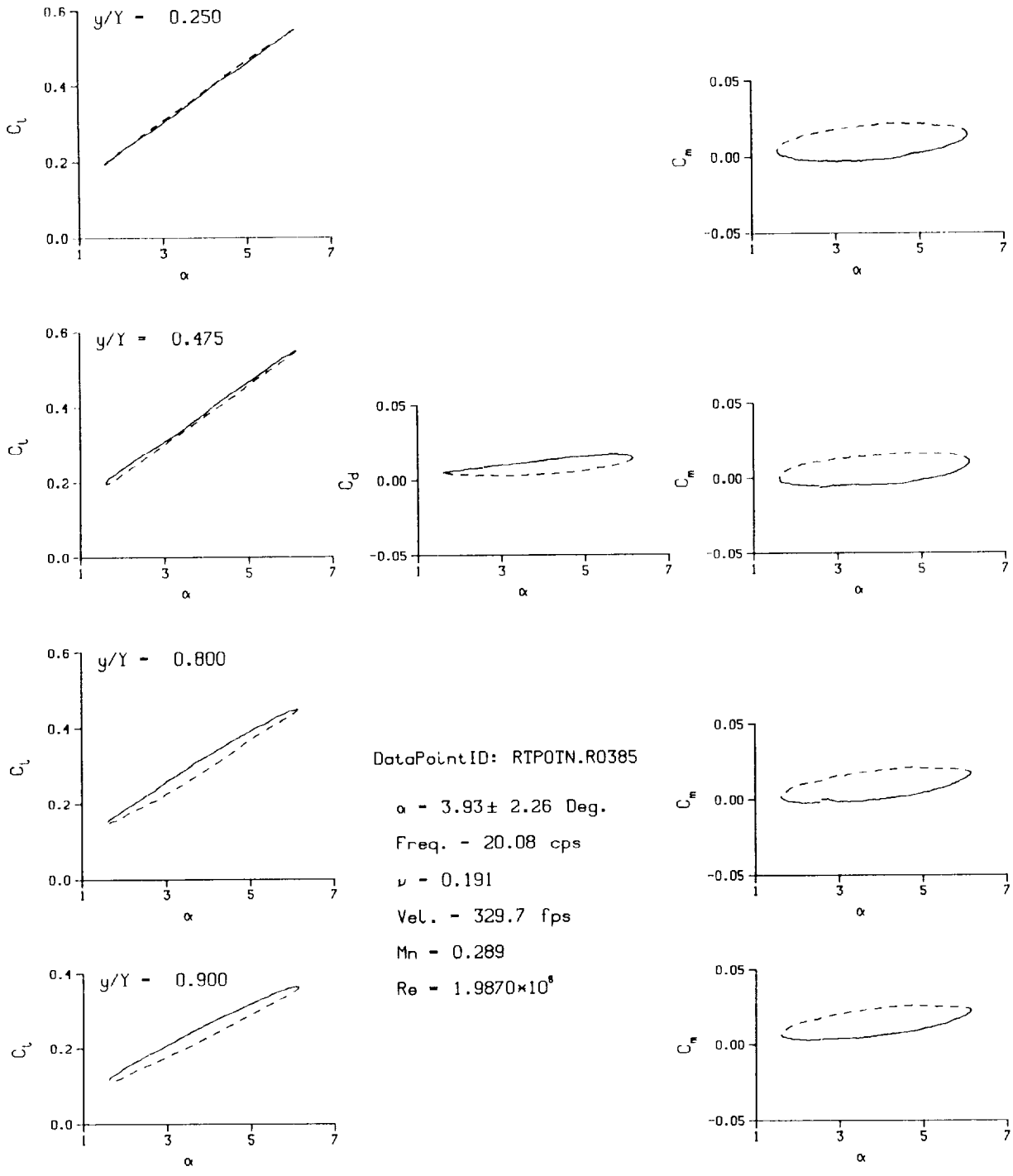

(d) ν = 0.20

Figure 72. Continued.

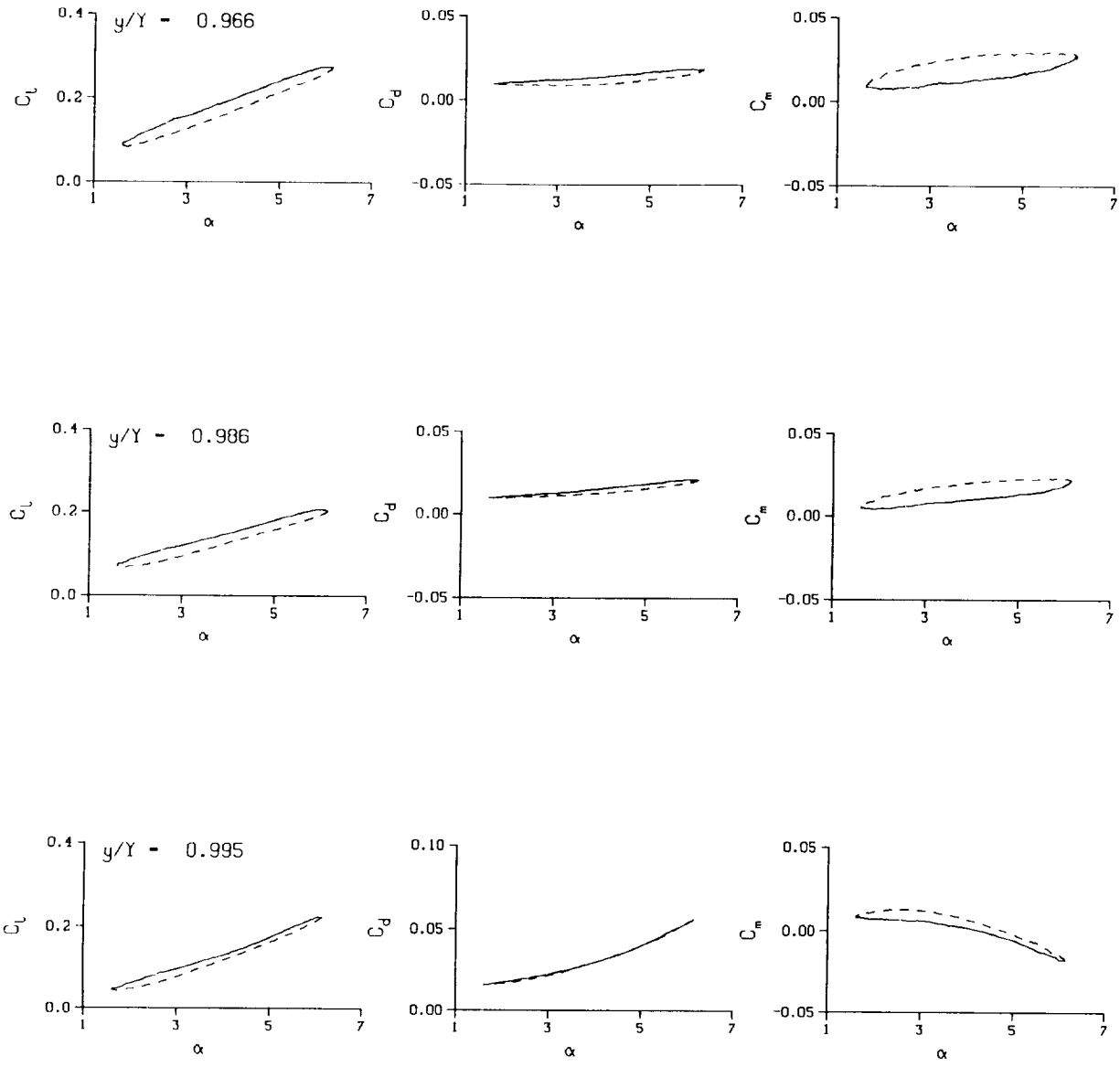

(d) v = 0.20. Concluded

Figure 72. Concluded.

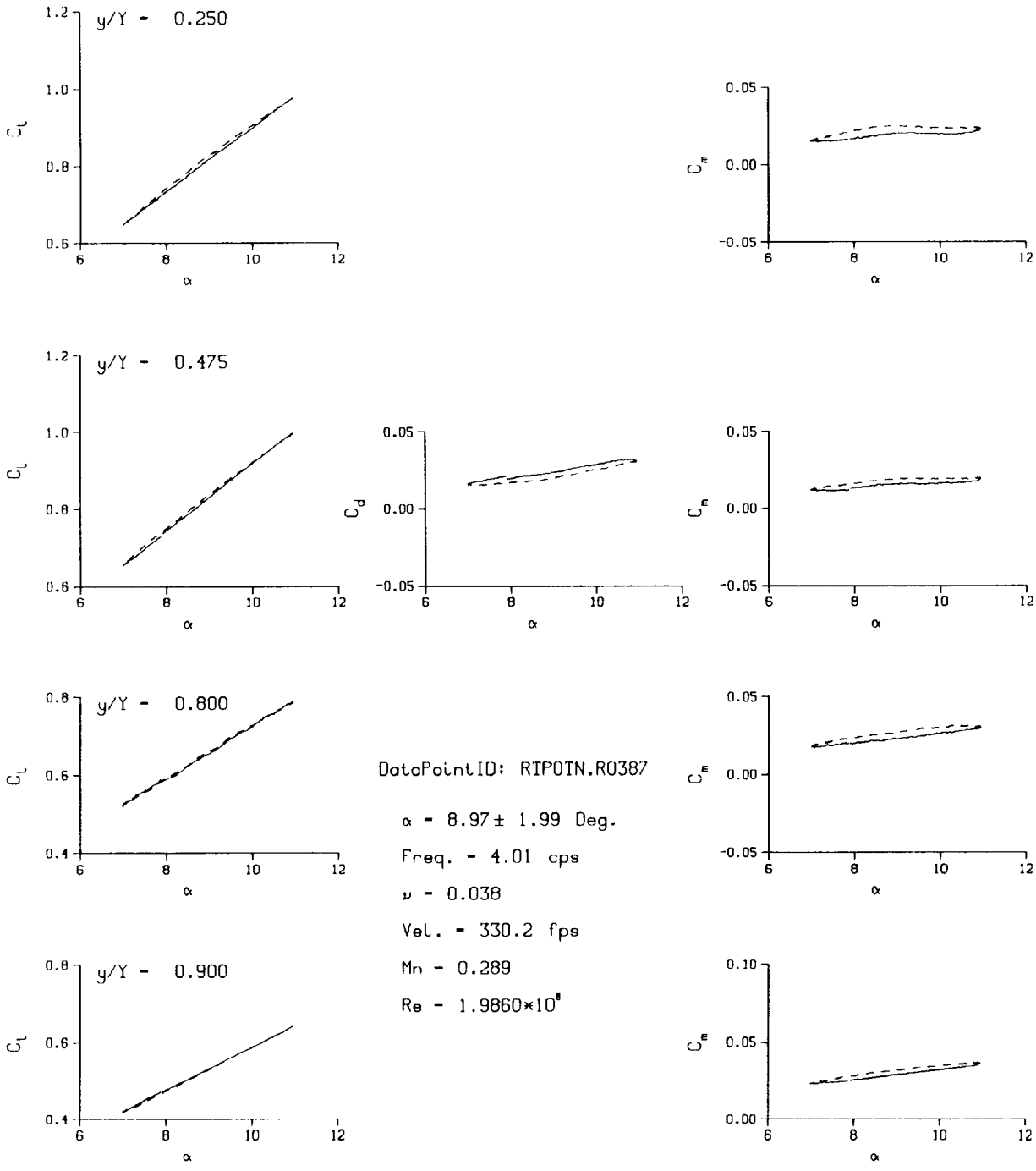

(a) v = 0.04

Figure 73. 3-D round tip pitch oscillation data; no BL-trip; α = 9 ± 2 deg.

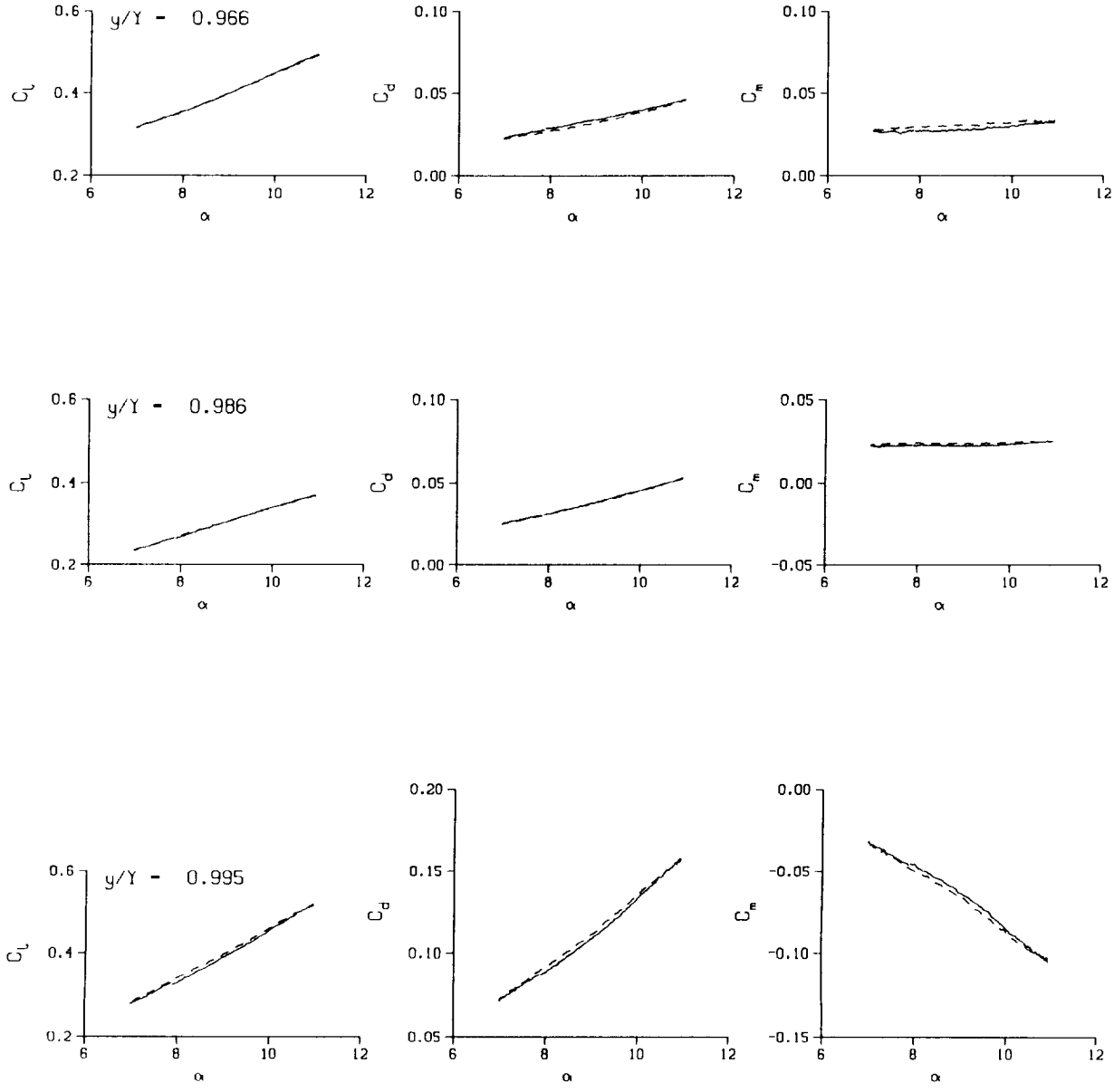

(a) v = 0.04. Concluded

Figure 73. Continued.

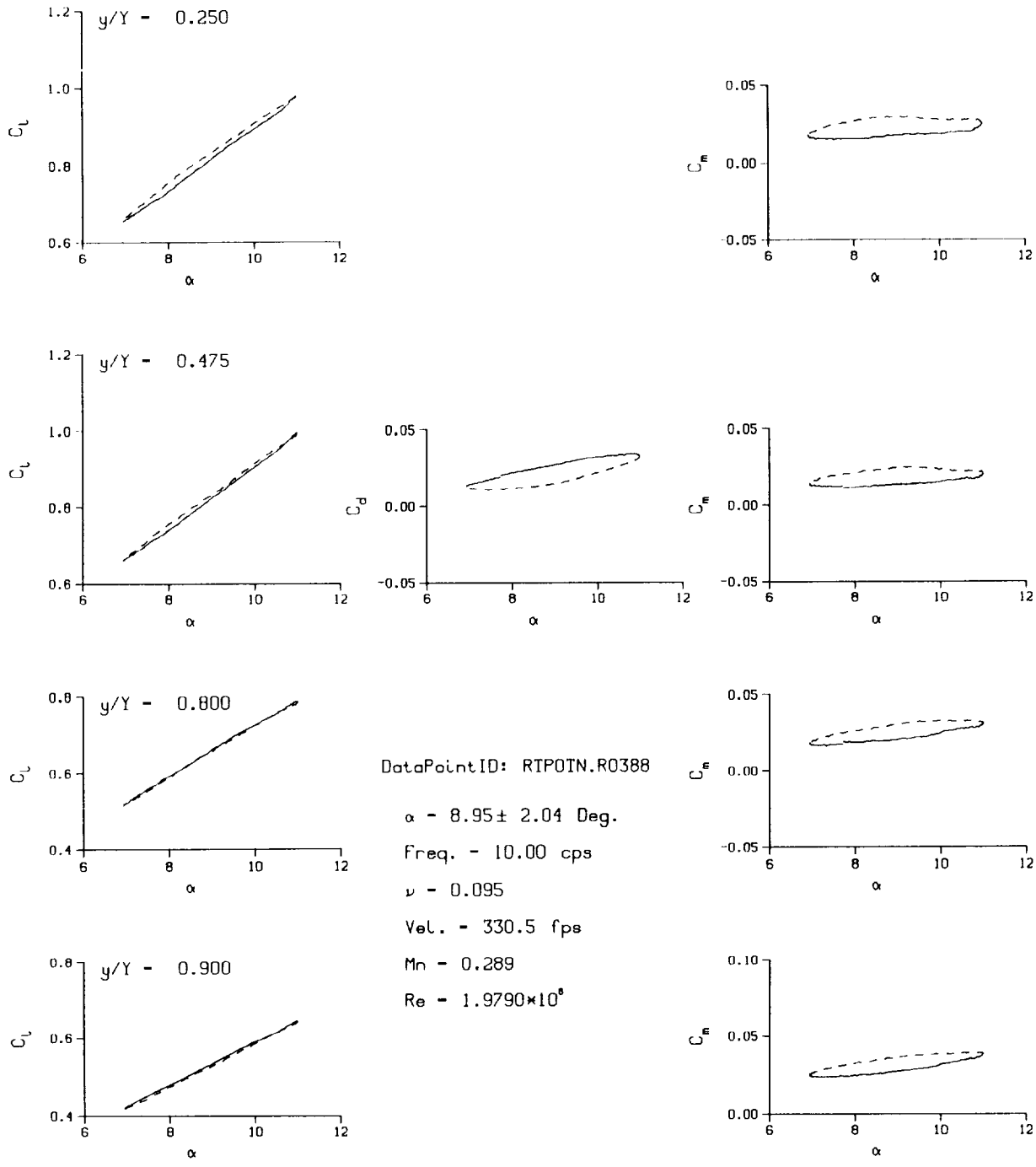

(b) ν = 0.10

Figure 73. Continued.

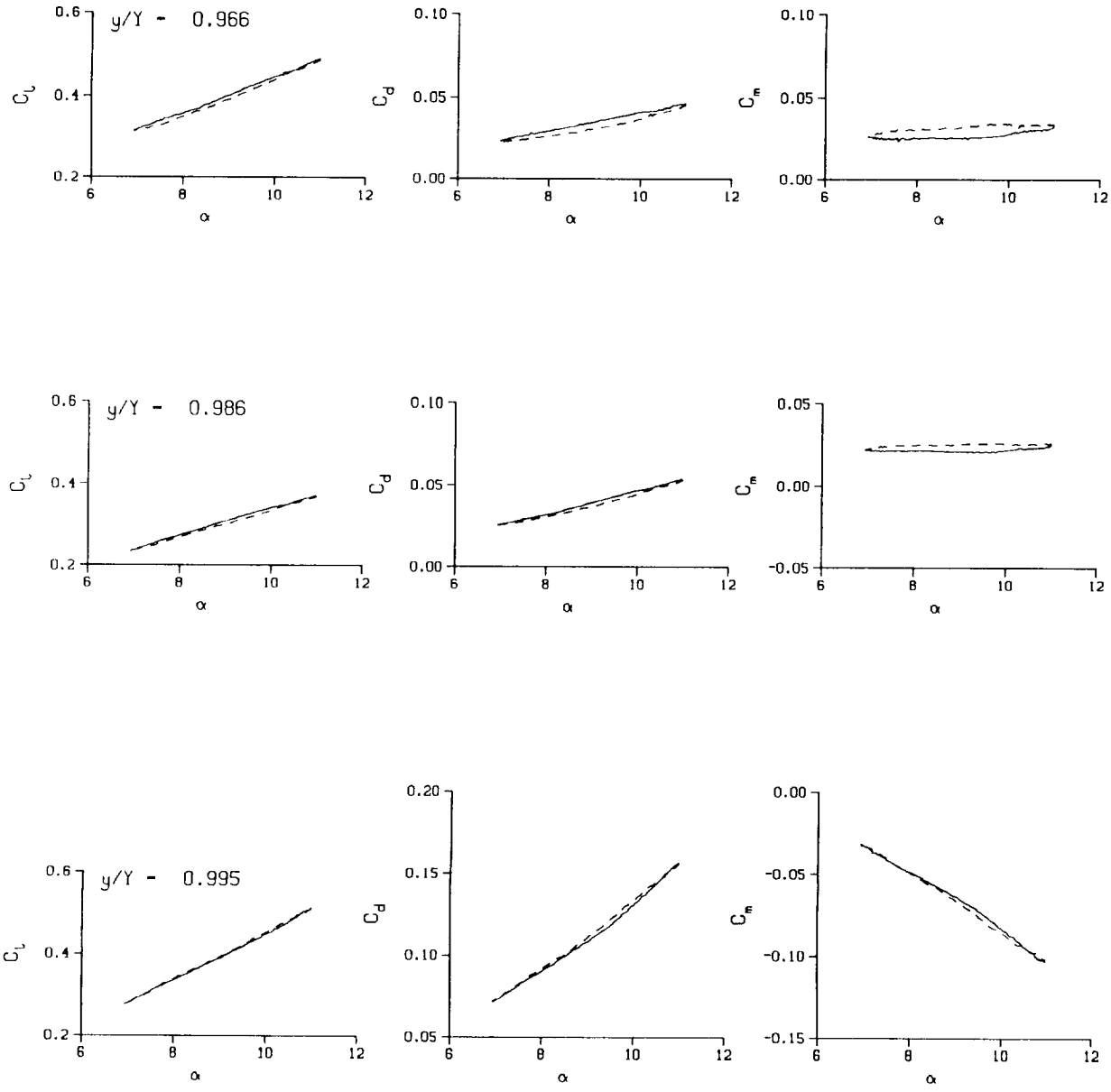

(b) v = 0.10. Concluded

Figure 73. Continued.

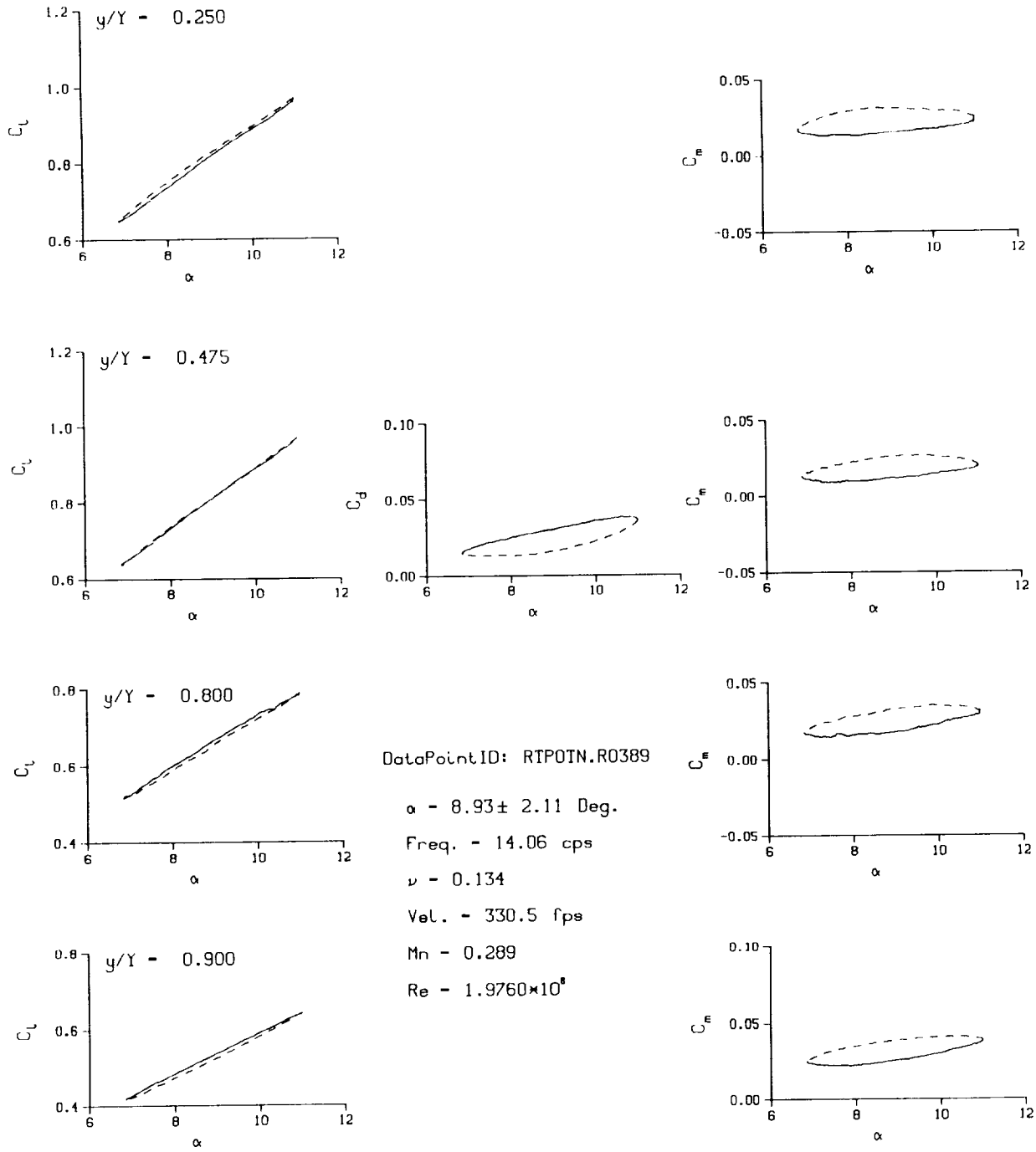

(c) v = 0.14

Figure 73. Continued.

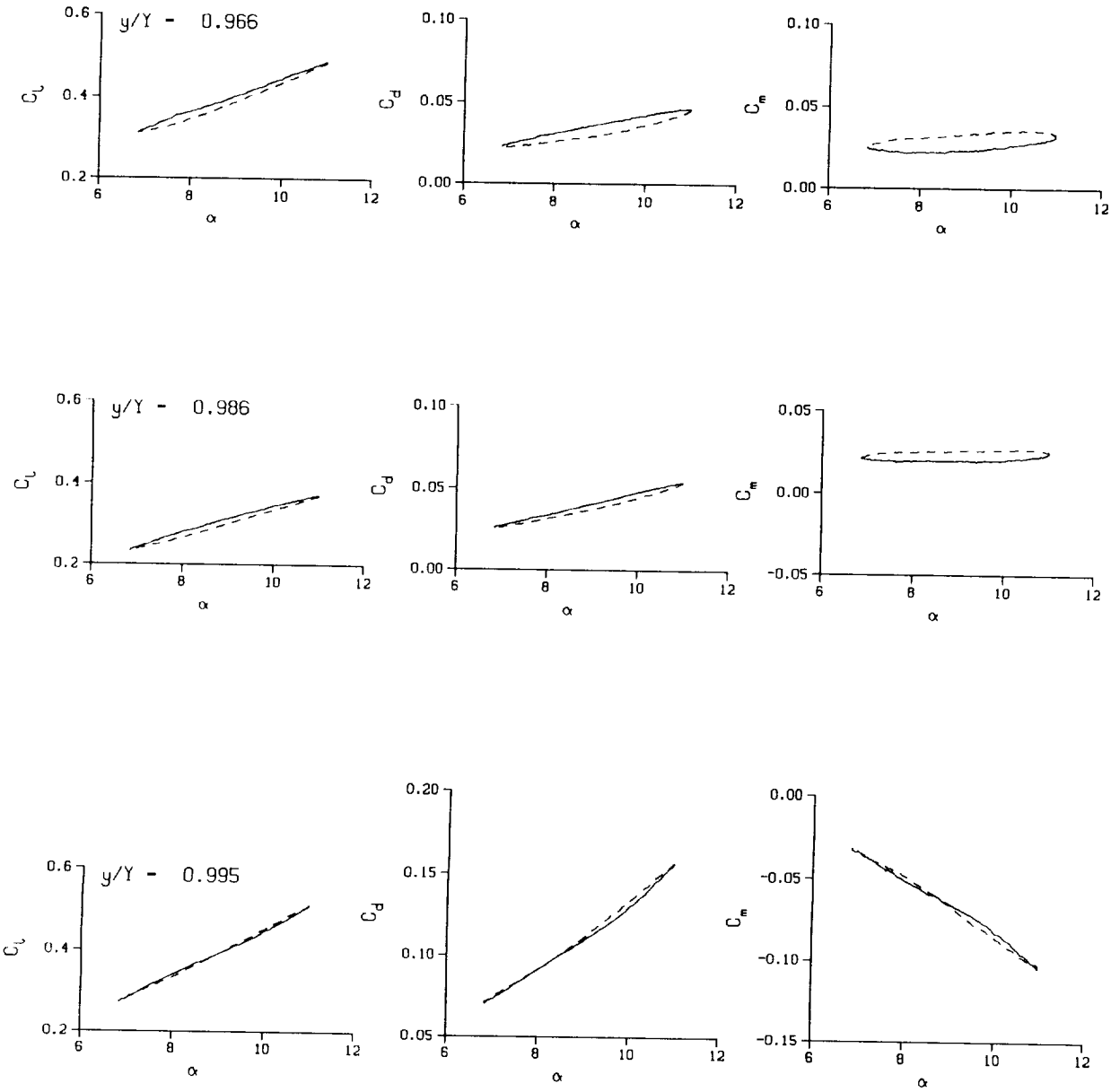

(c) v = 0.14. Concluded

Figure 73. Continued.

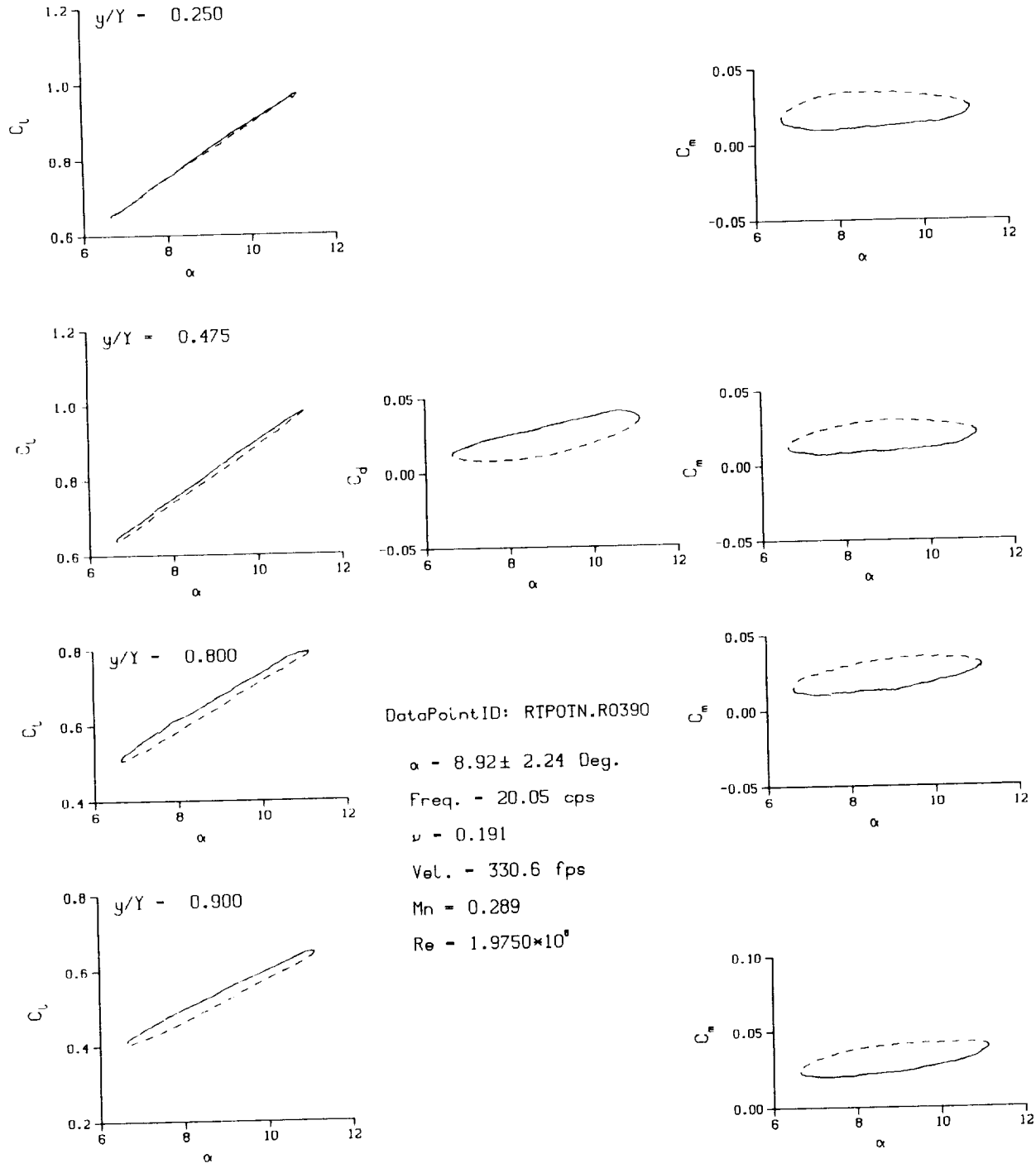

(d) v = 0.20

Figure 73. Continued.

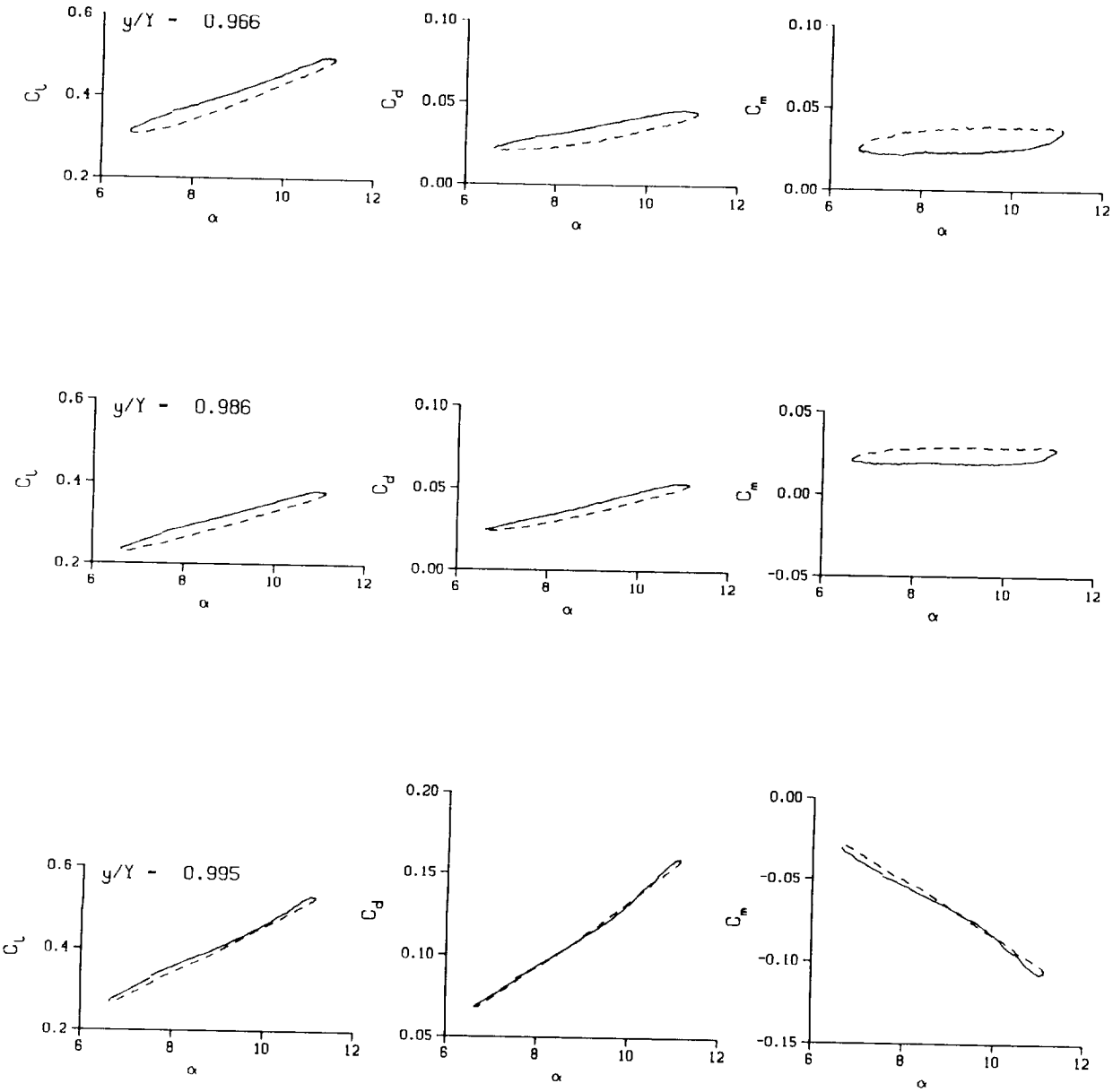

(d) v = 0.20. Concluded

Figure 73. Concluded.

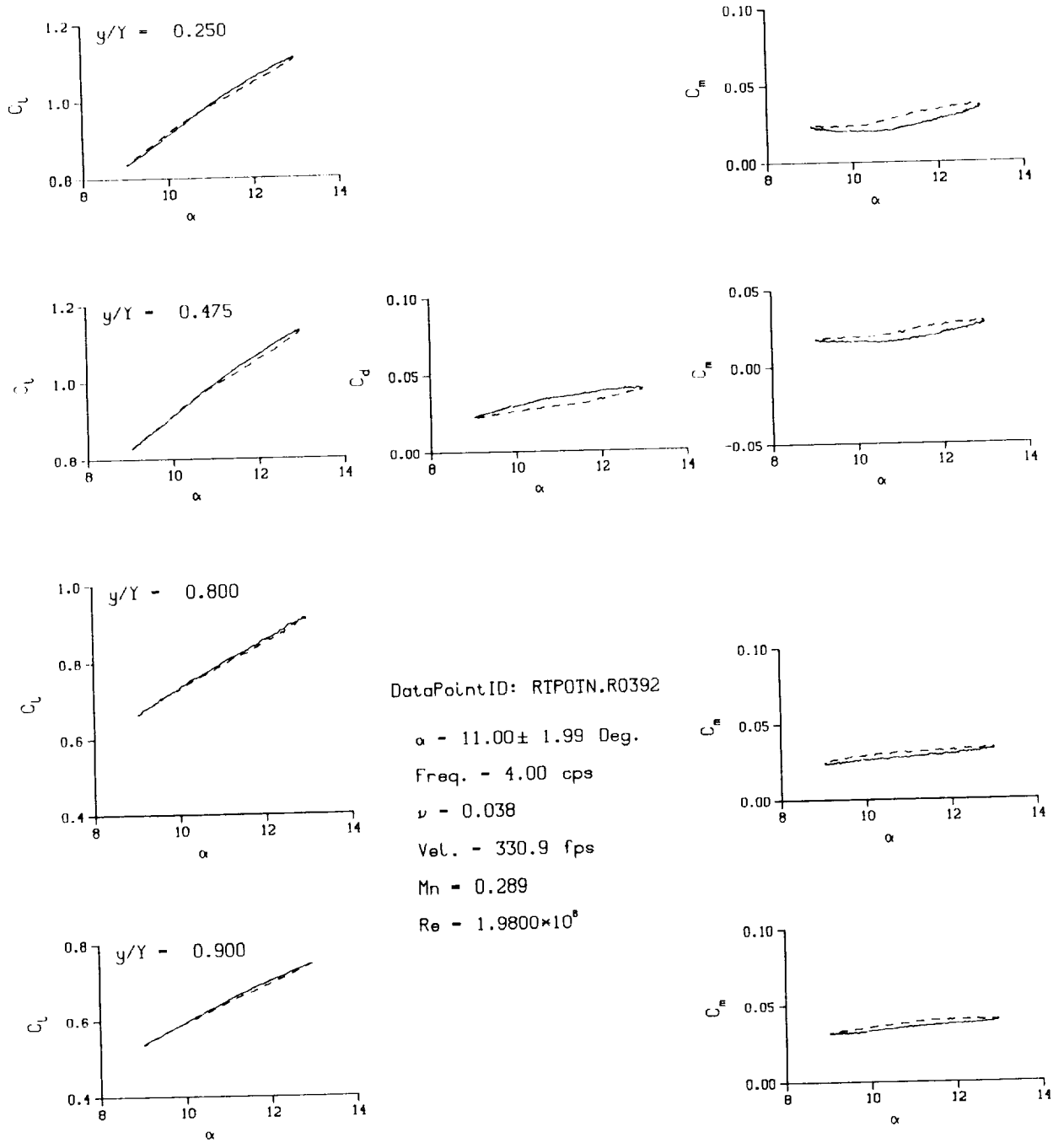

(a) v = 0.04

Figure 74. 3-D round tip pitch oscillation data; no BL-trip; α = 11 ± 2 deg.

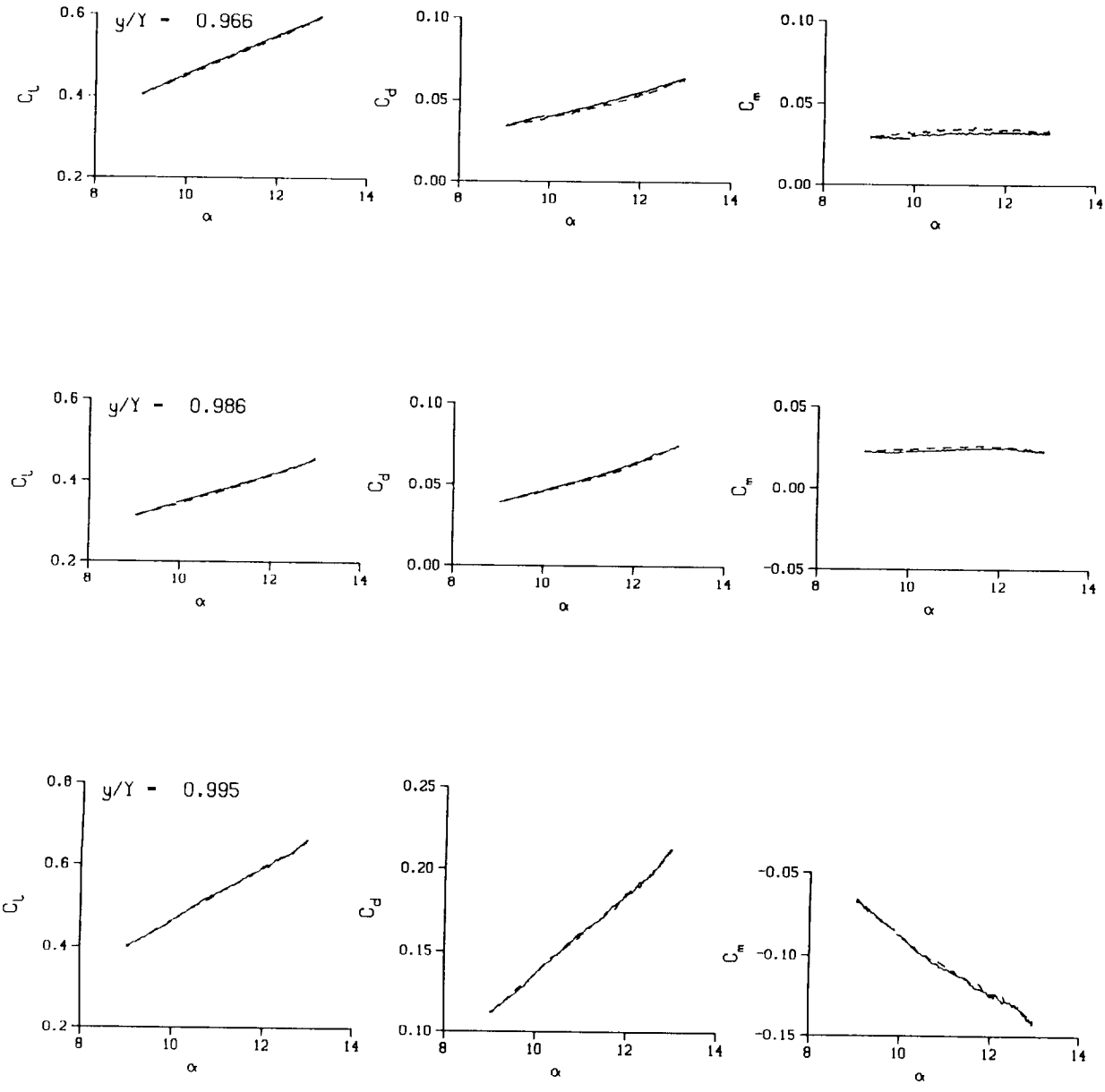

(a) v = 0.04. Concluded

Figure 74. Continued.

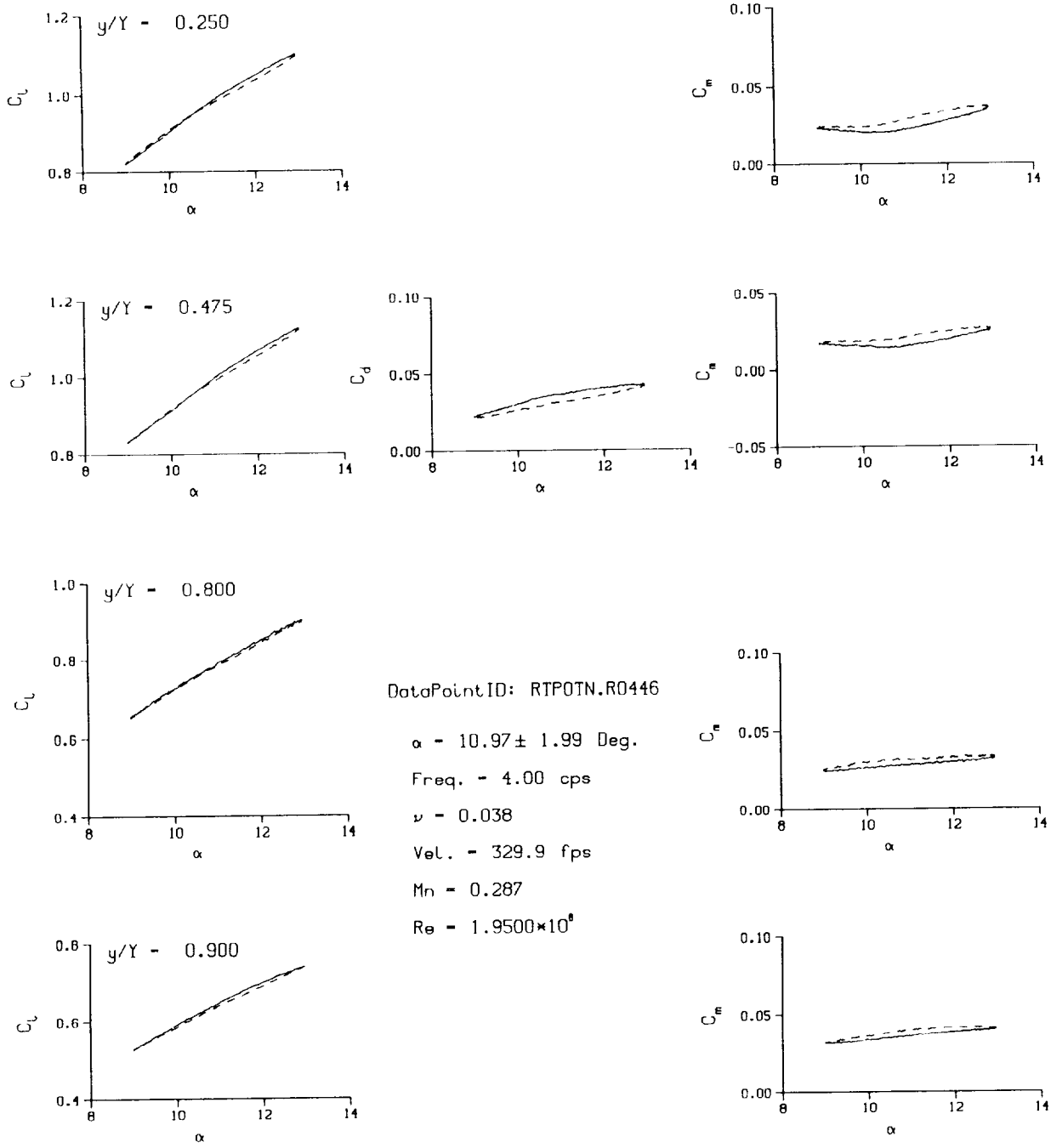

(a.1) ν = 0.04; repeat

Figure 74. Continued.

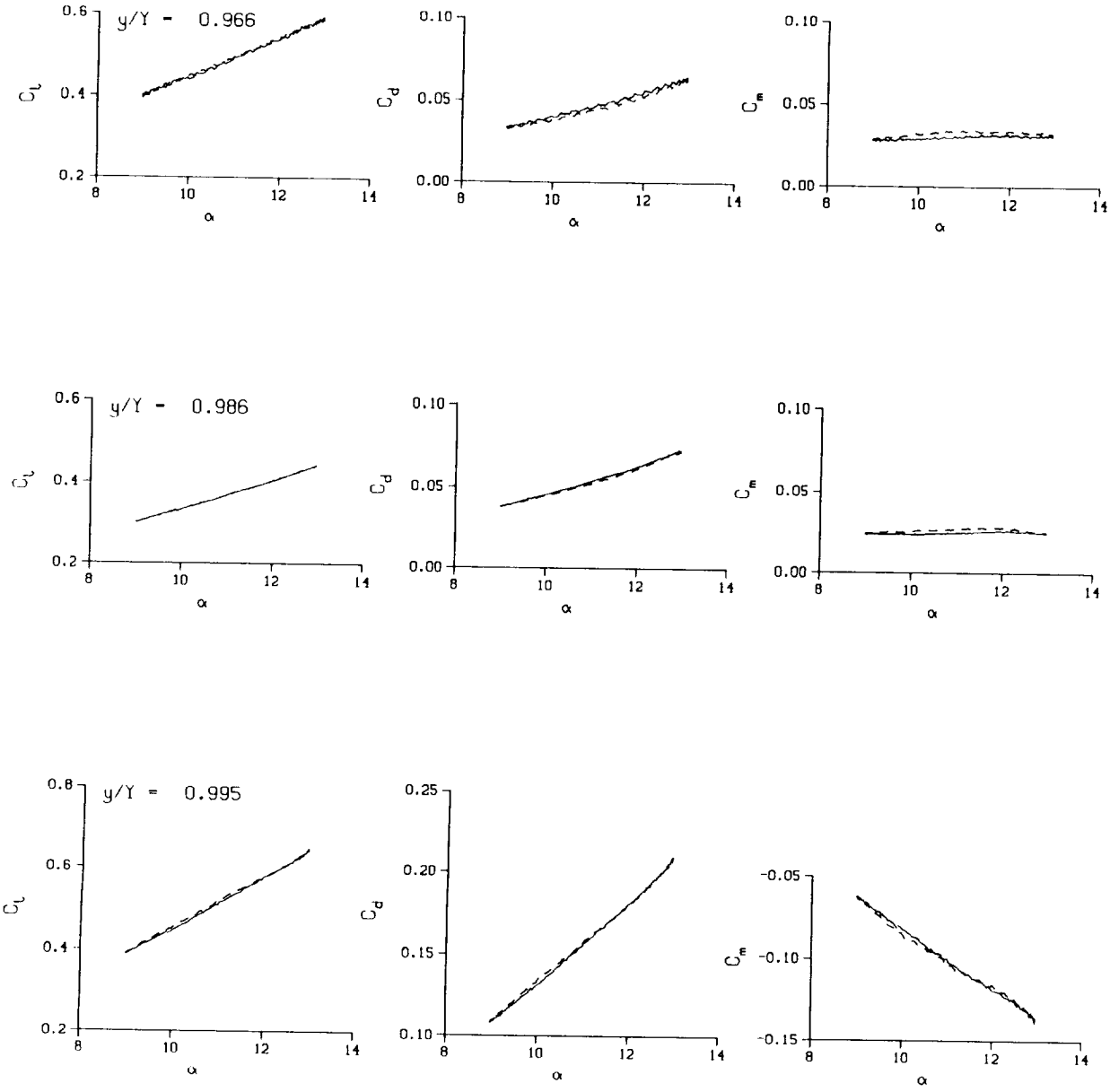

(a.1) v = 0.04; repeat. Concluded

Figure 74. Continued.

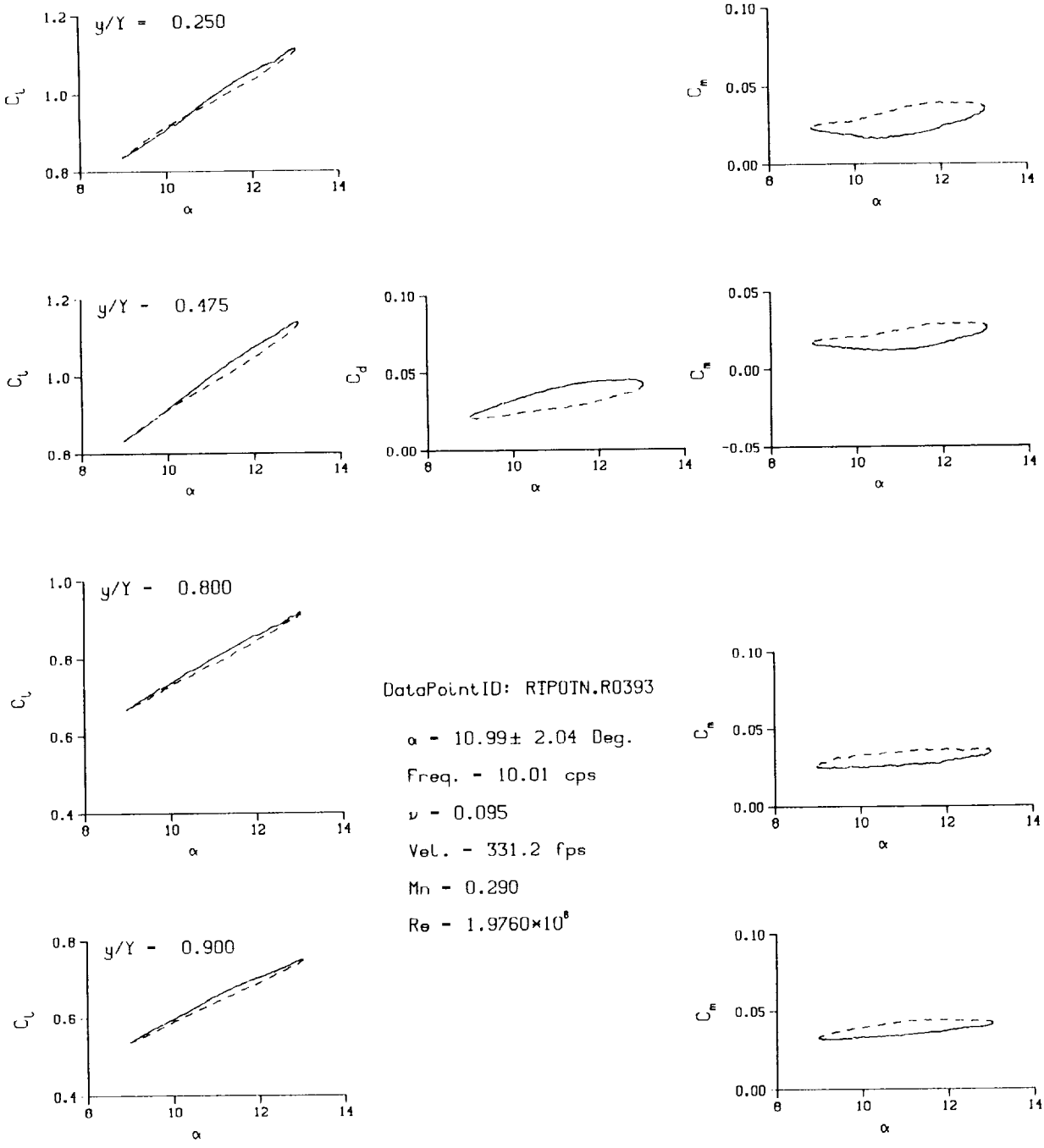

(b) v = 0.10

Figure 74. Continued.

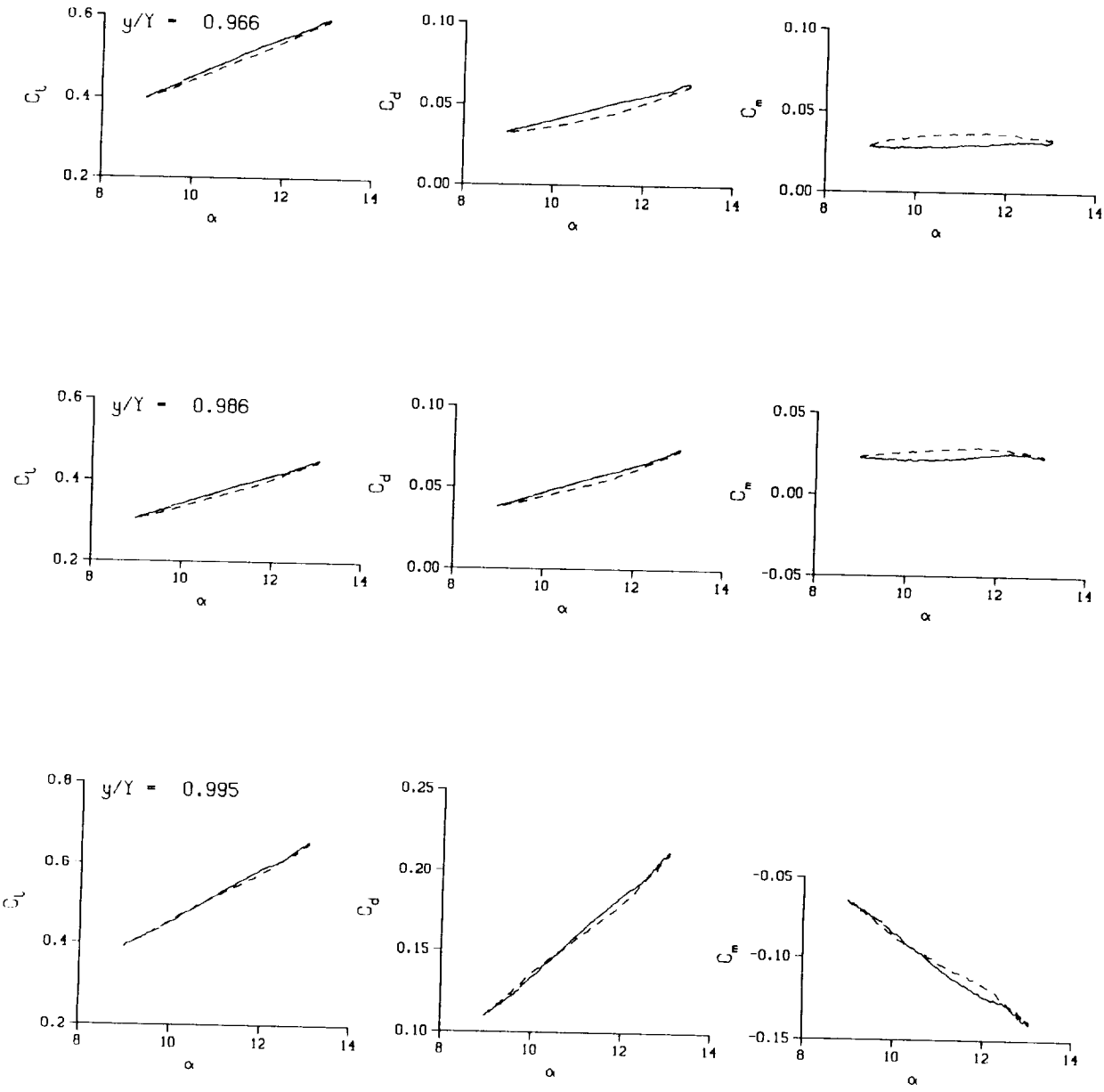

(b) v = 0.10. Concluded

Figure 74. Continued.

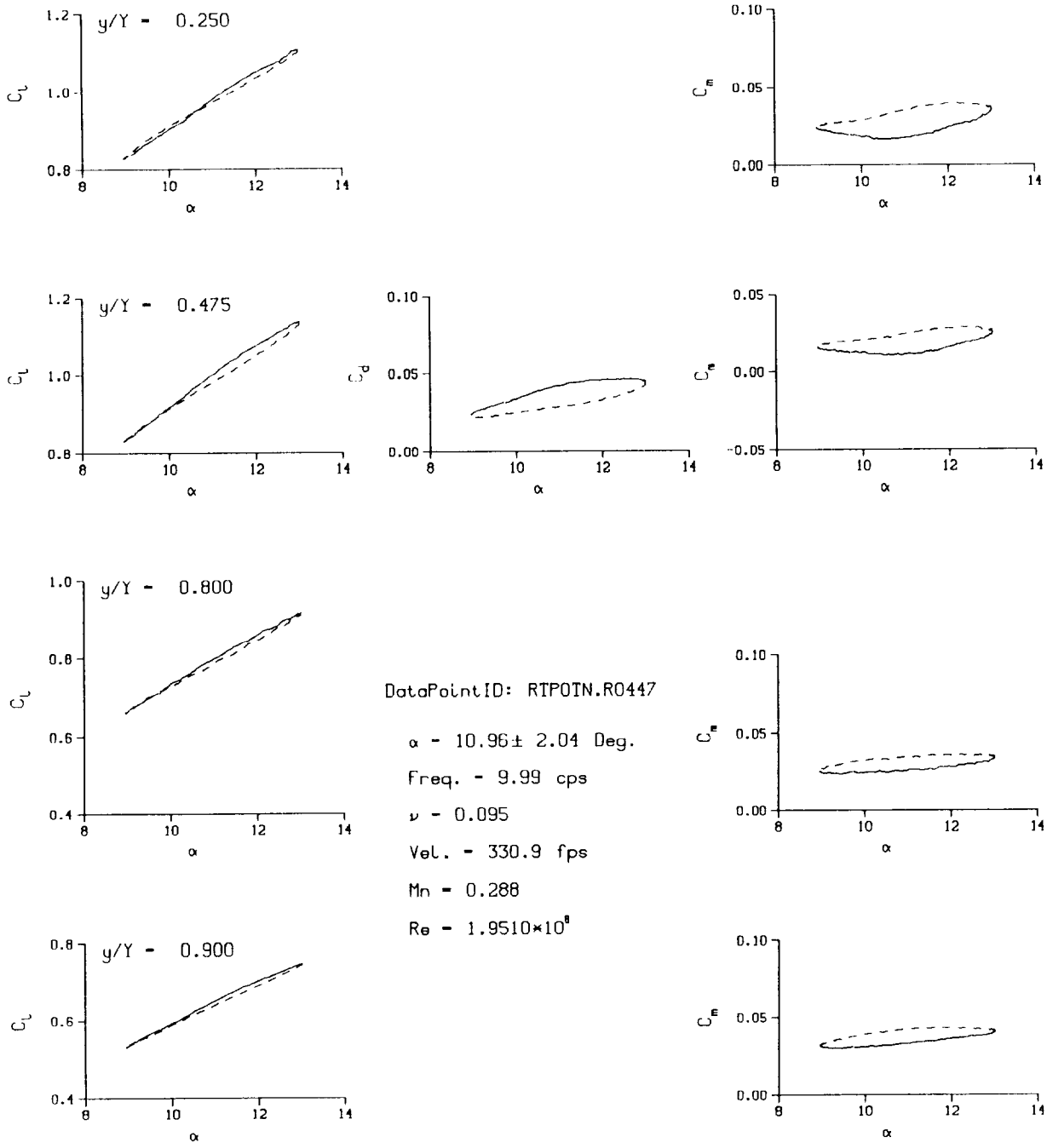

(b.1) v = 0.10; repeat

Figure 74. Continued.

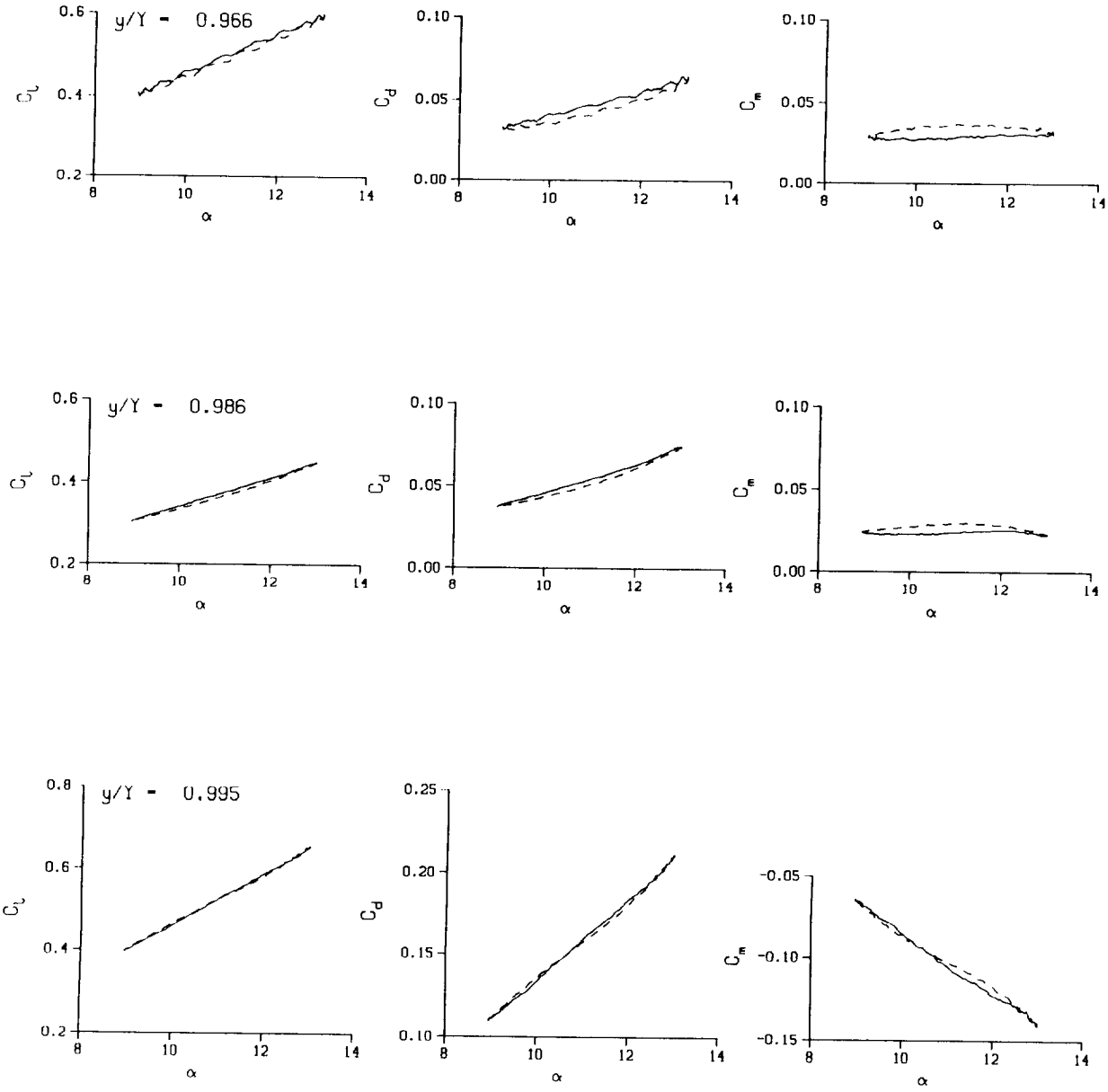

(b.1) v = 0.10; repeat. Concluded

Figure 74. Continued.

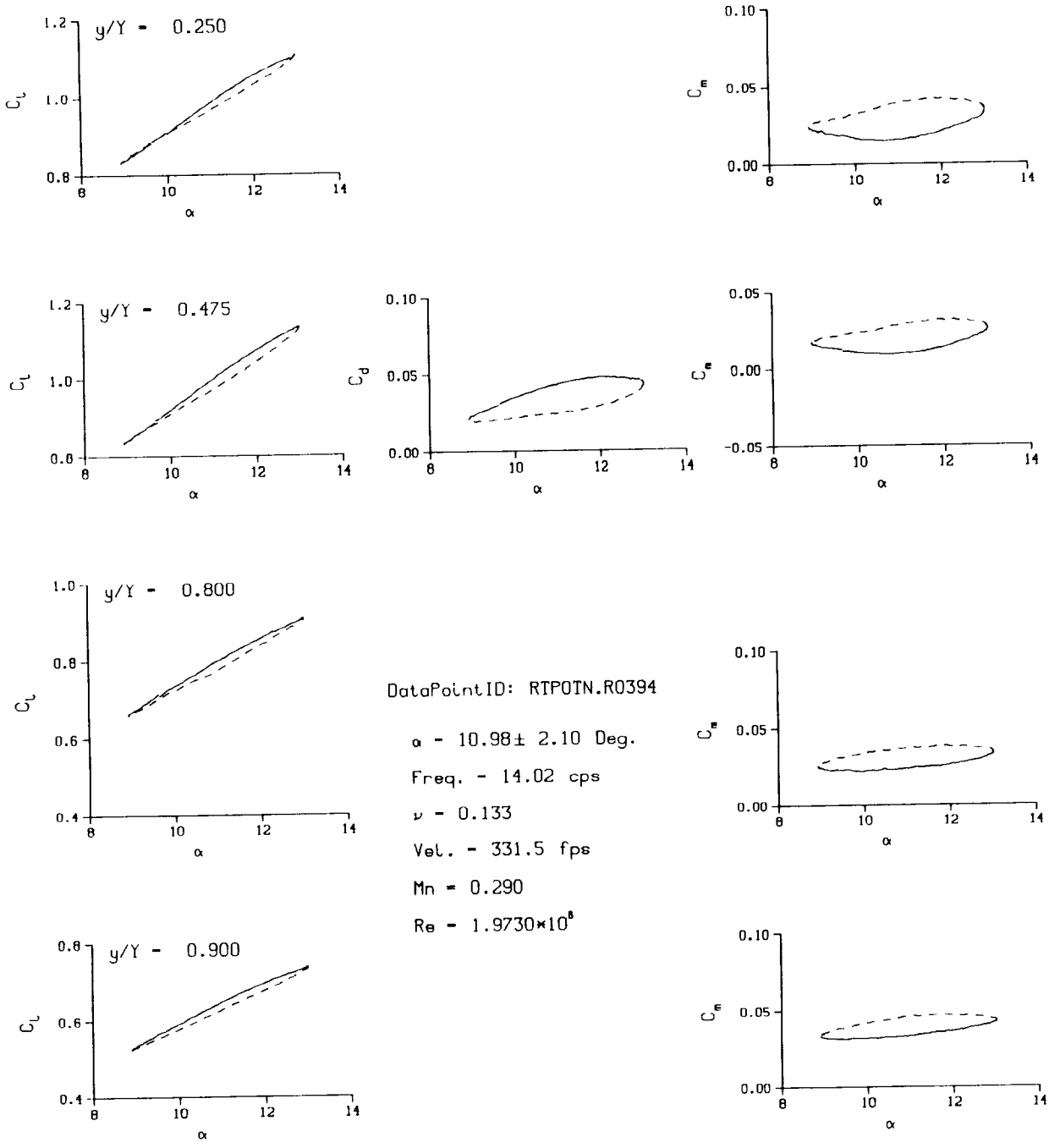

(c) v = 0.14

Figure 74. Continued.

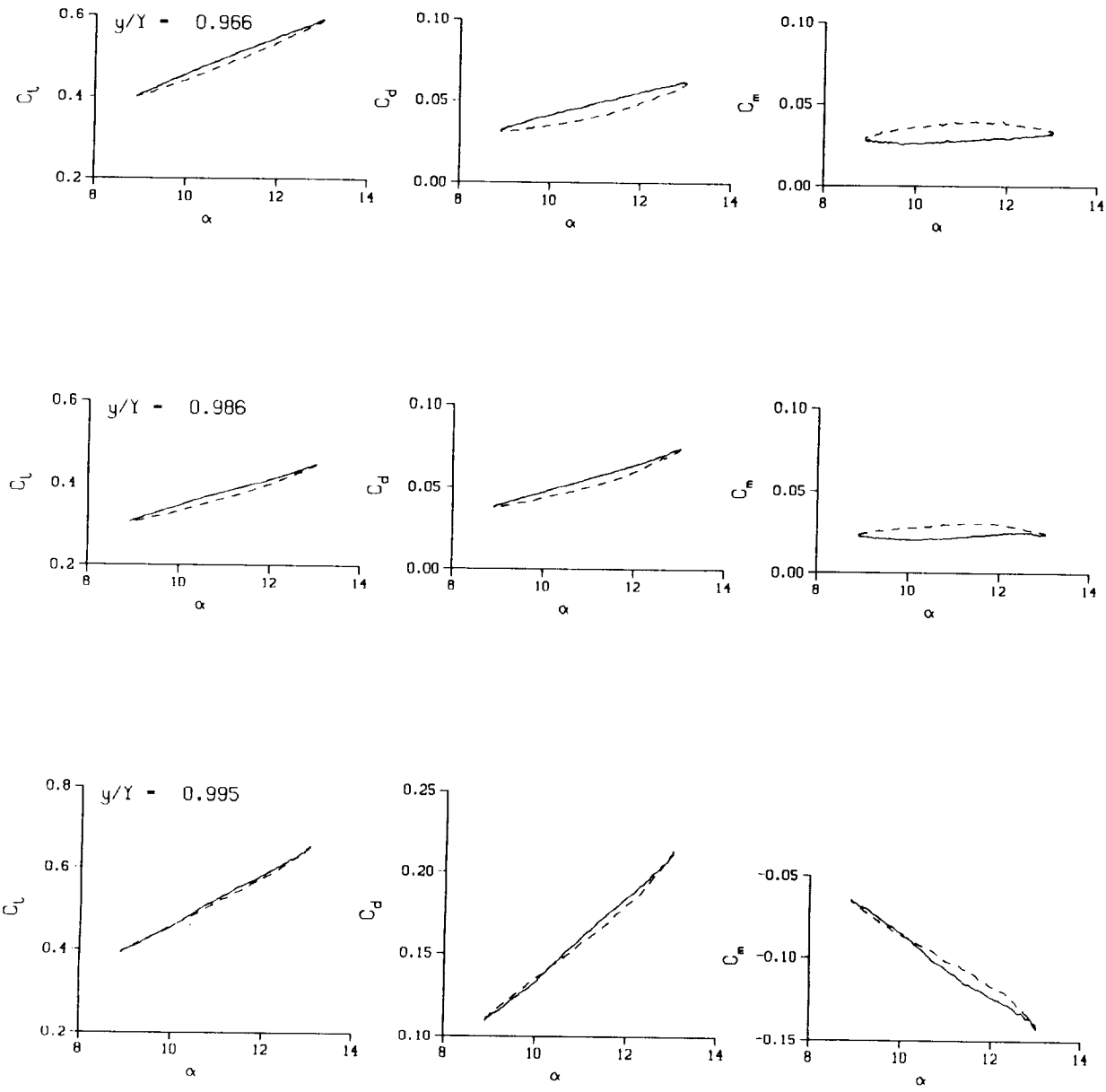

(c) v = 0.14. Concluded

Figure 74. Continued.

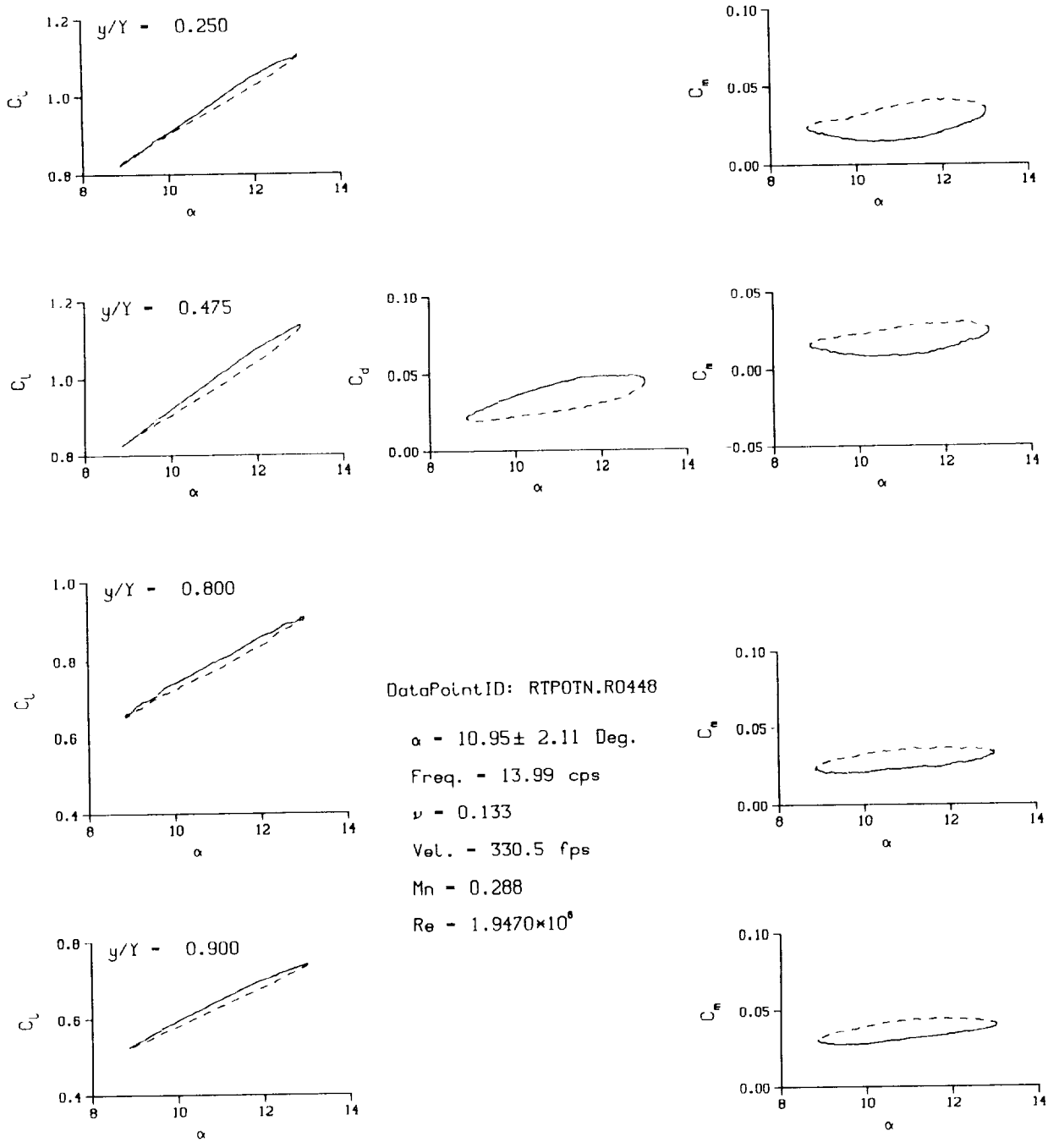

(c.1) ν = 0.14; repeat

Figure 74. Continued.

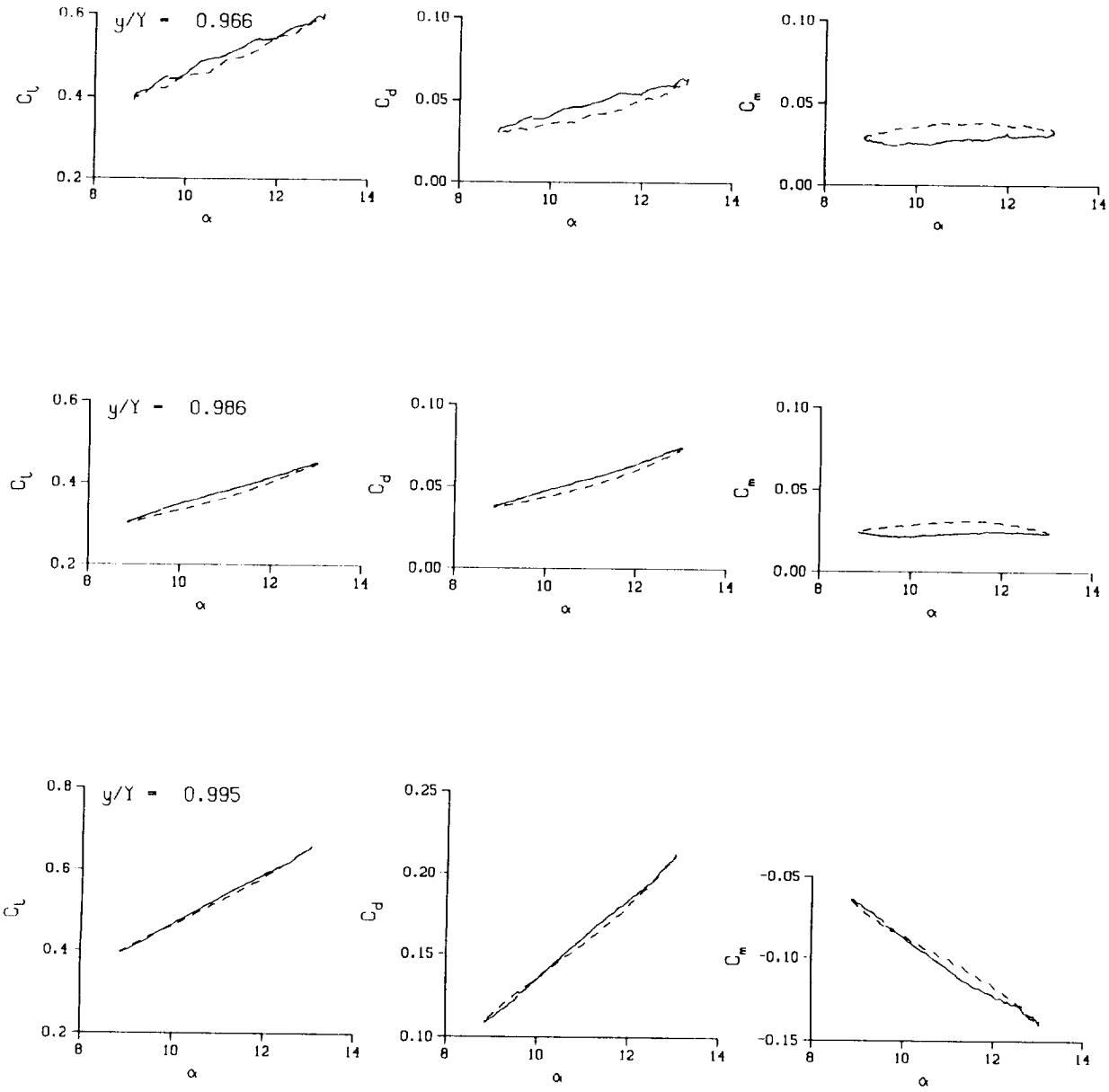

(c.1) v = 0.14; repeat. Concluded

Figure 74. Continued.

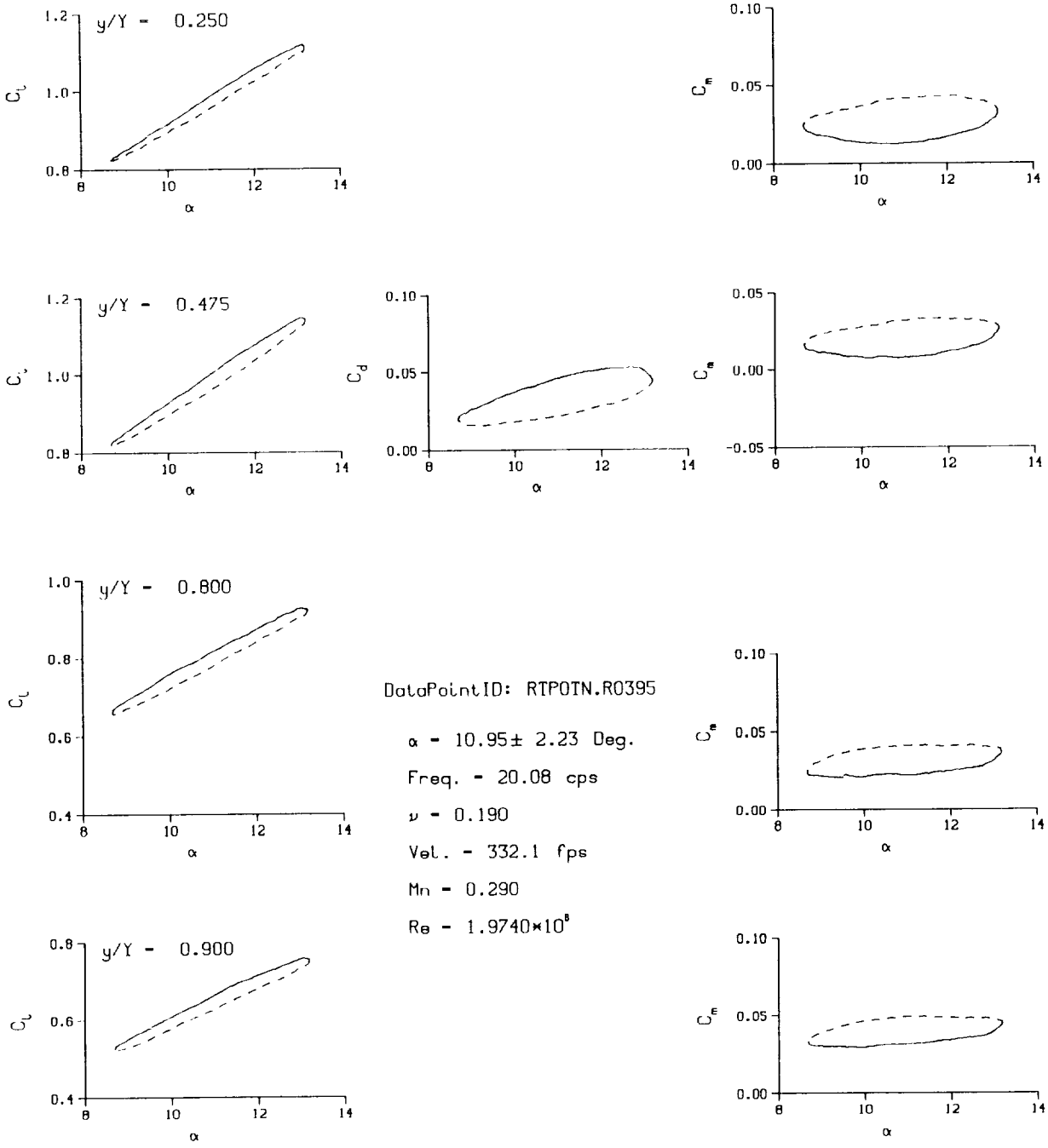

(d) ν = 0.20

Figure 74. Continued.

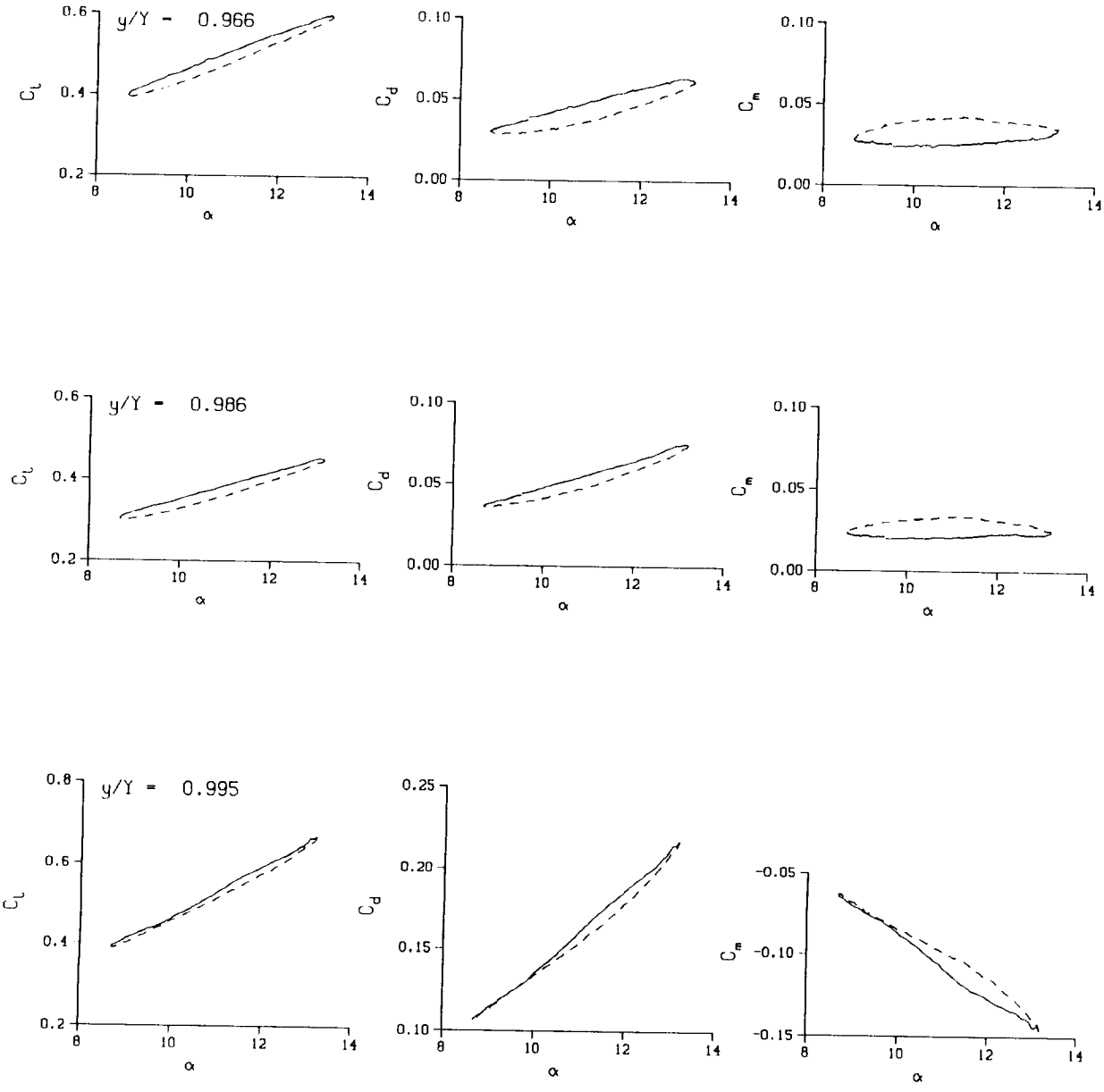

(d) v = 0.20. Concluded

Figure 74. Concluded.

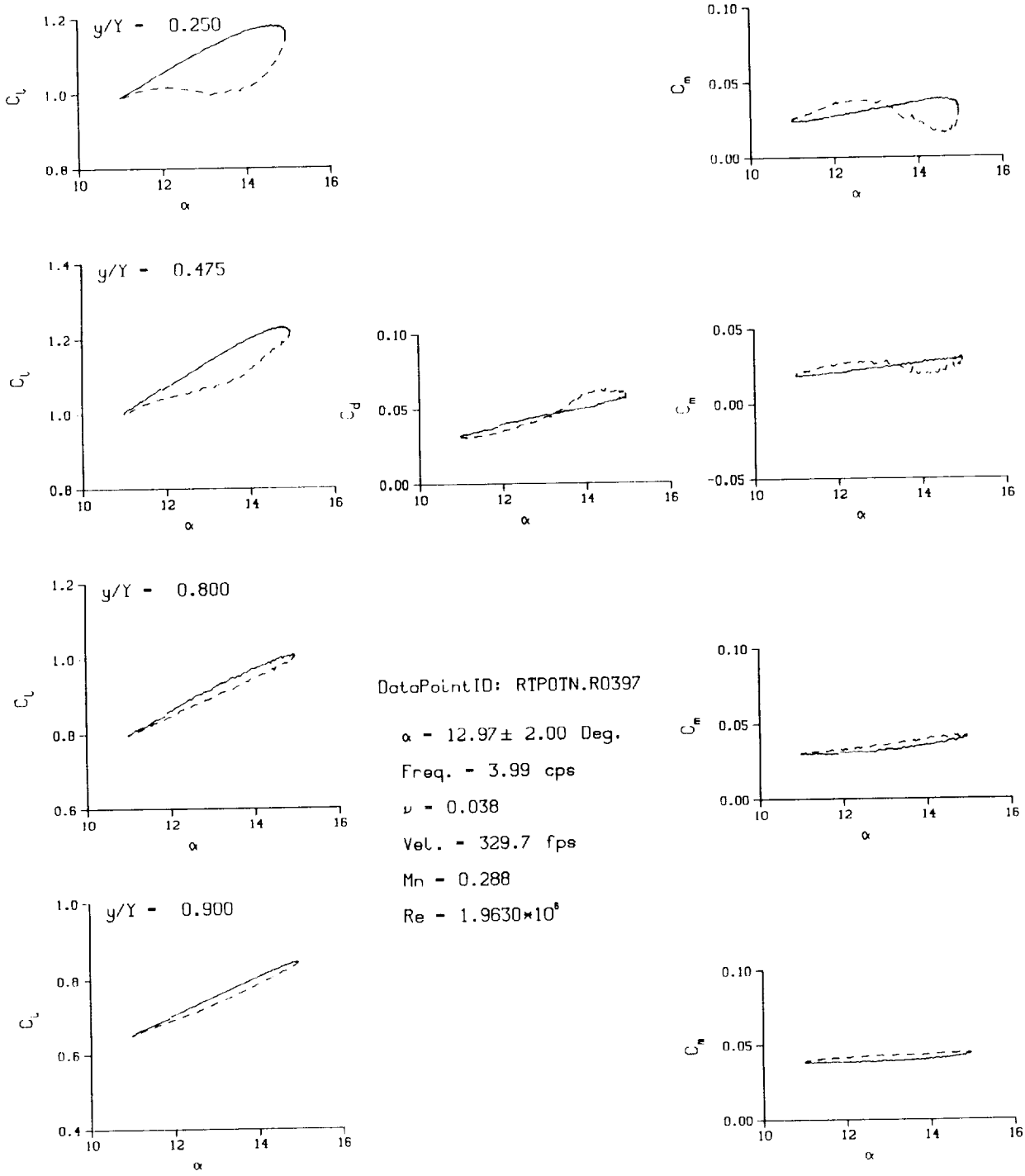

(a) ν = 0.04

Figure 75. 3-D round tip pitch oscillation data; no BL-trip; α = 13 ± 2 deg.

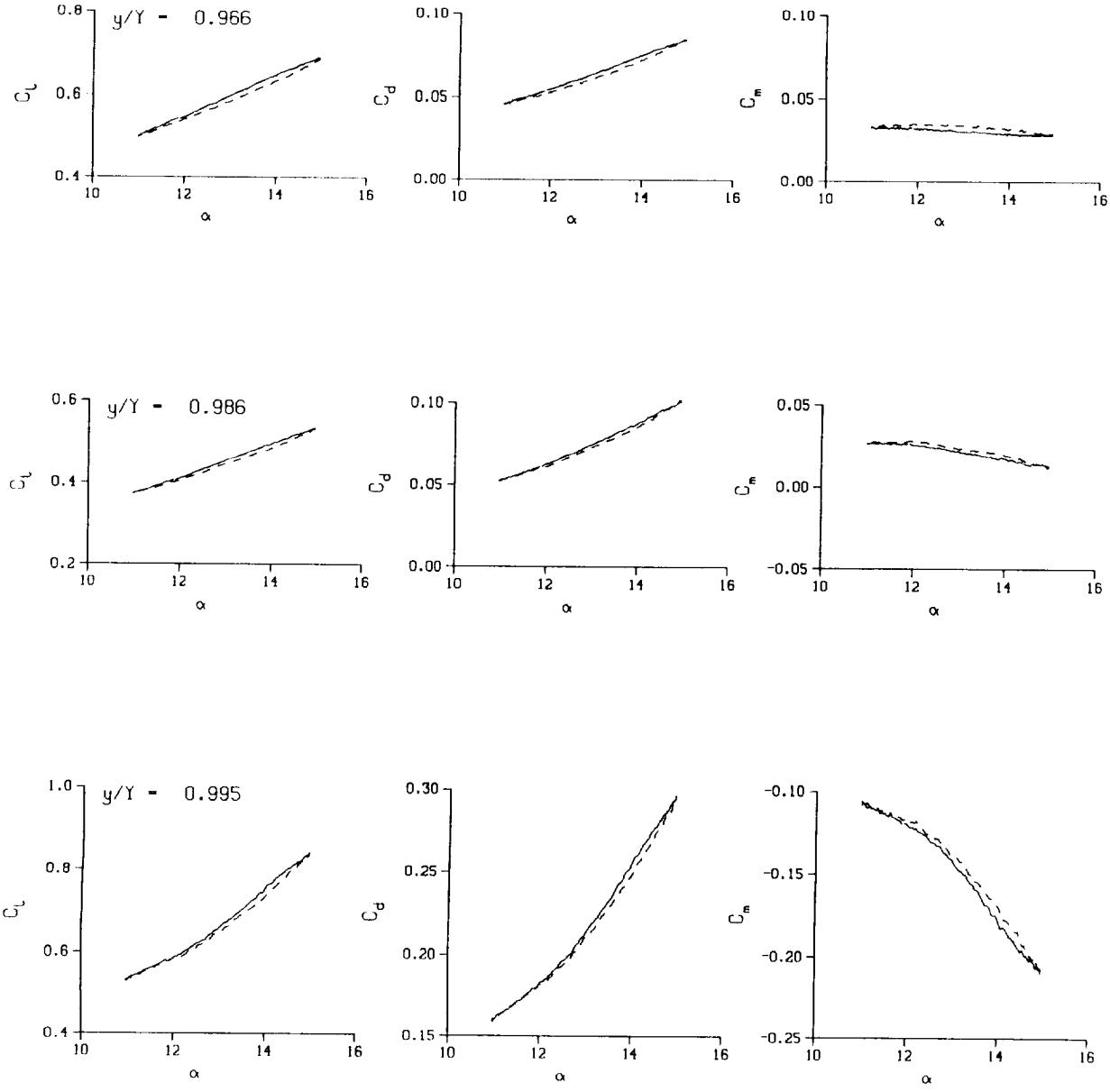

(a) v = 0.04. Concluded

Figure 75. Continued.

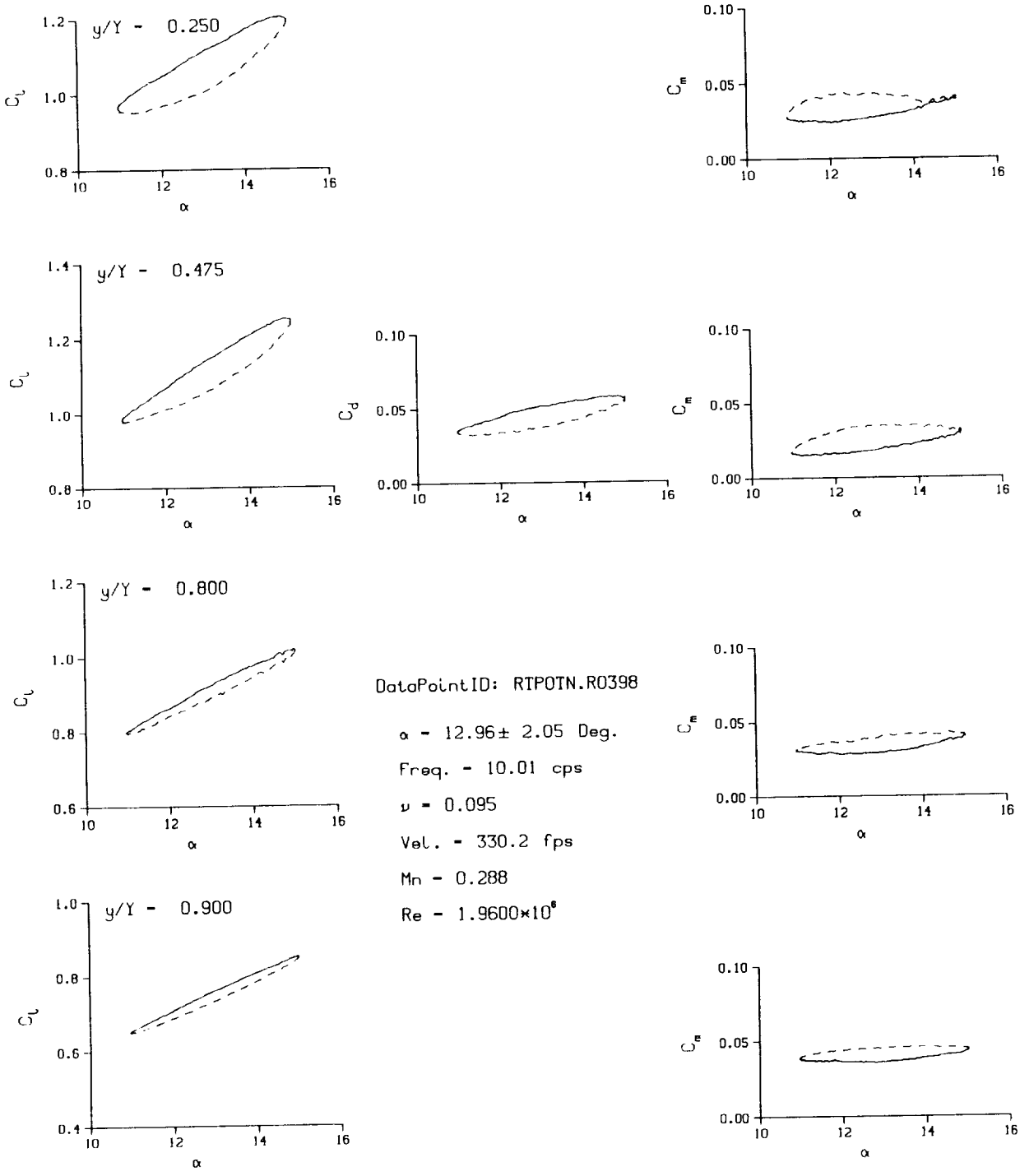

(b) v = 0.10

Figure 75. Continued.

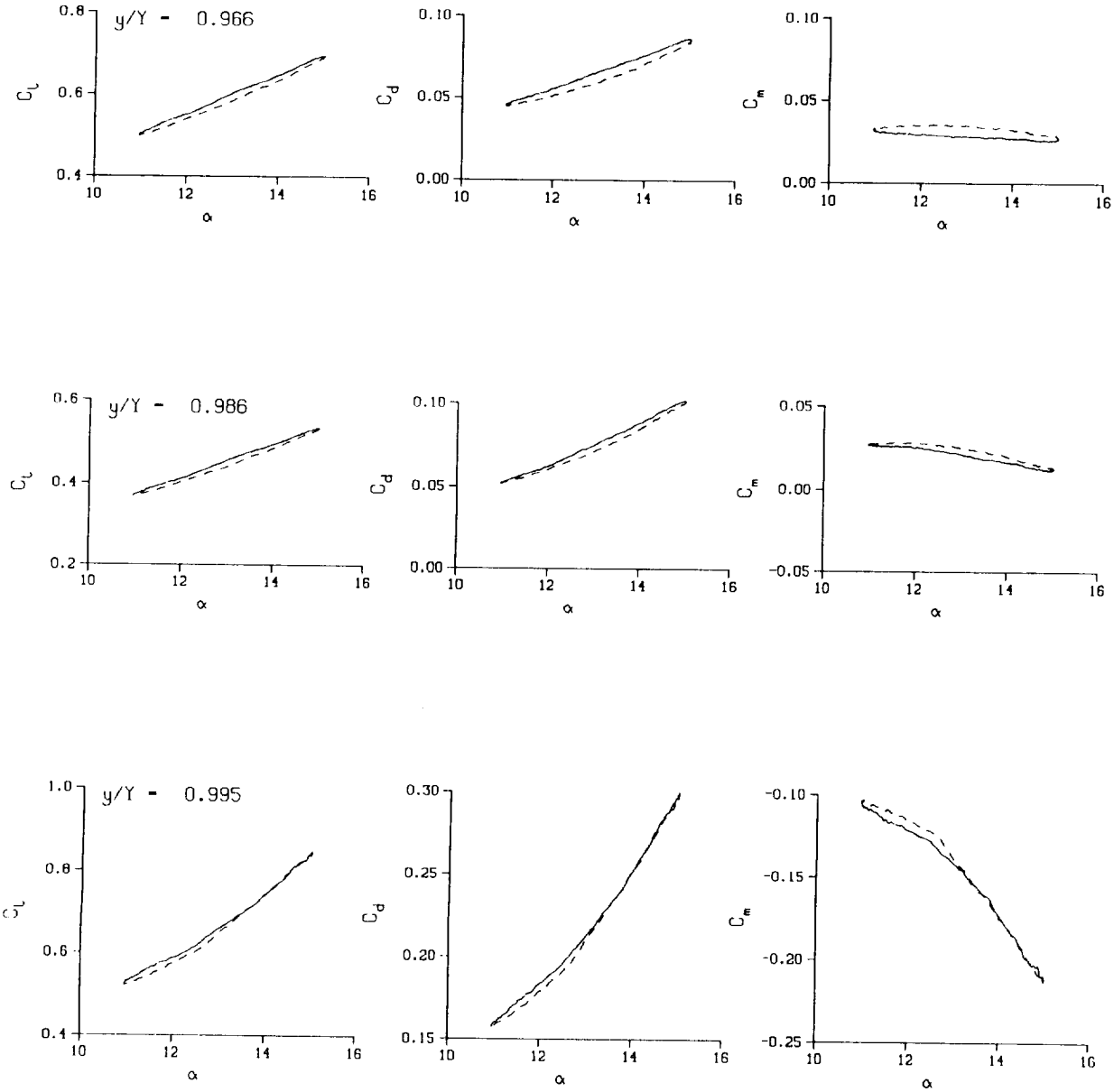

(b) v = 0.10. Concluded

Figure 75. Continued.

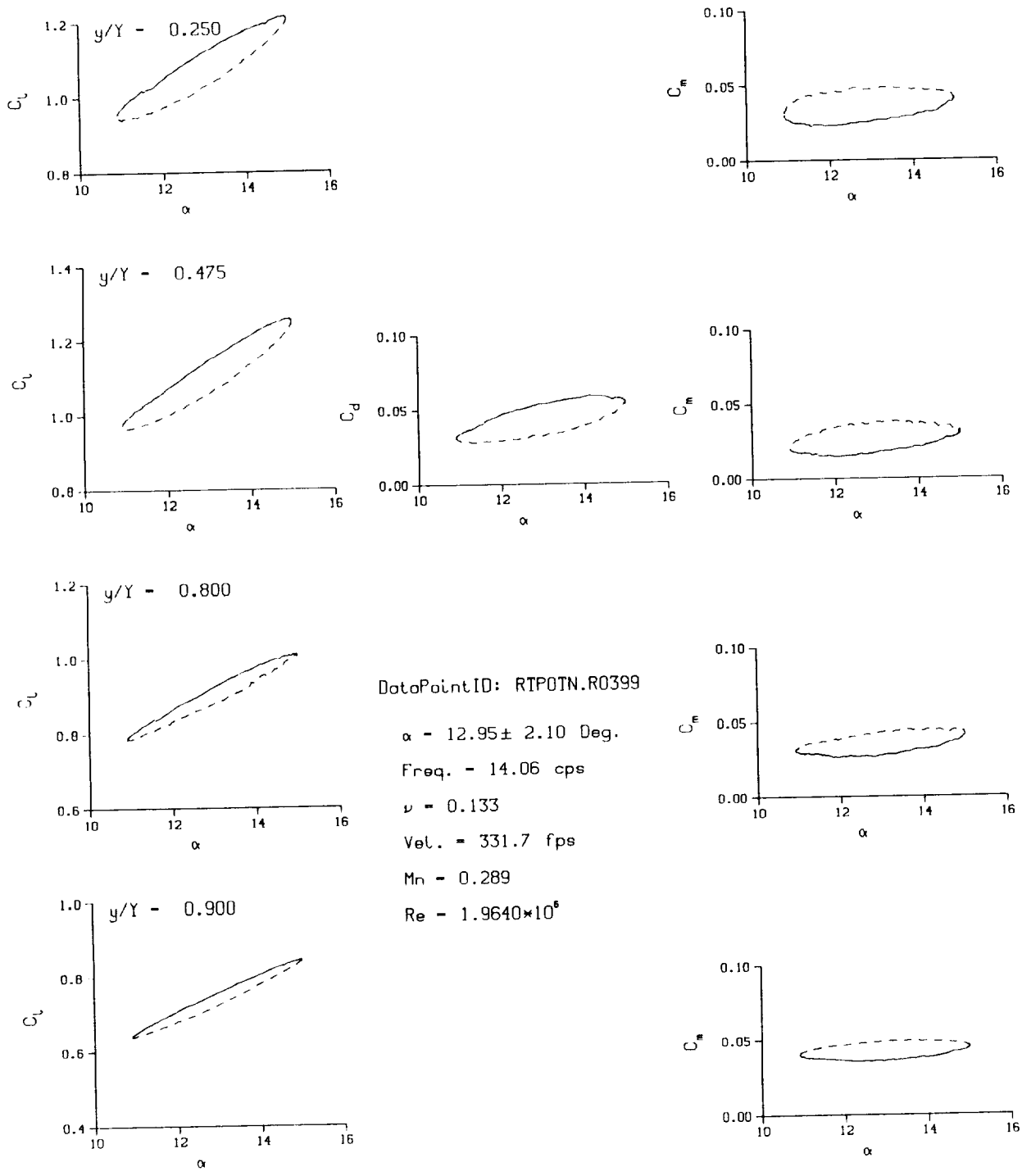

(c) v = 0.14

Figure 75. Continued.

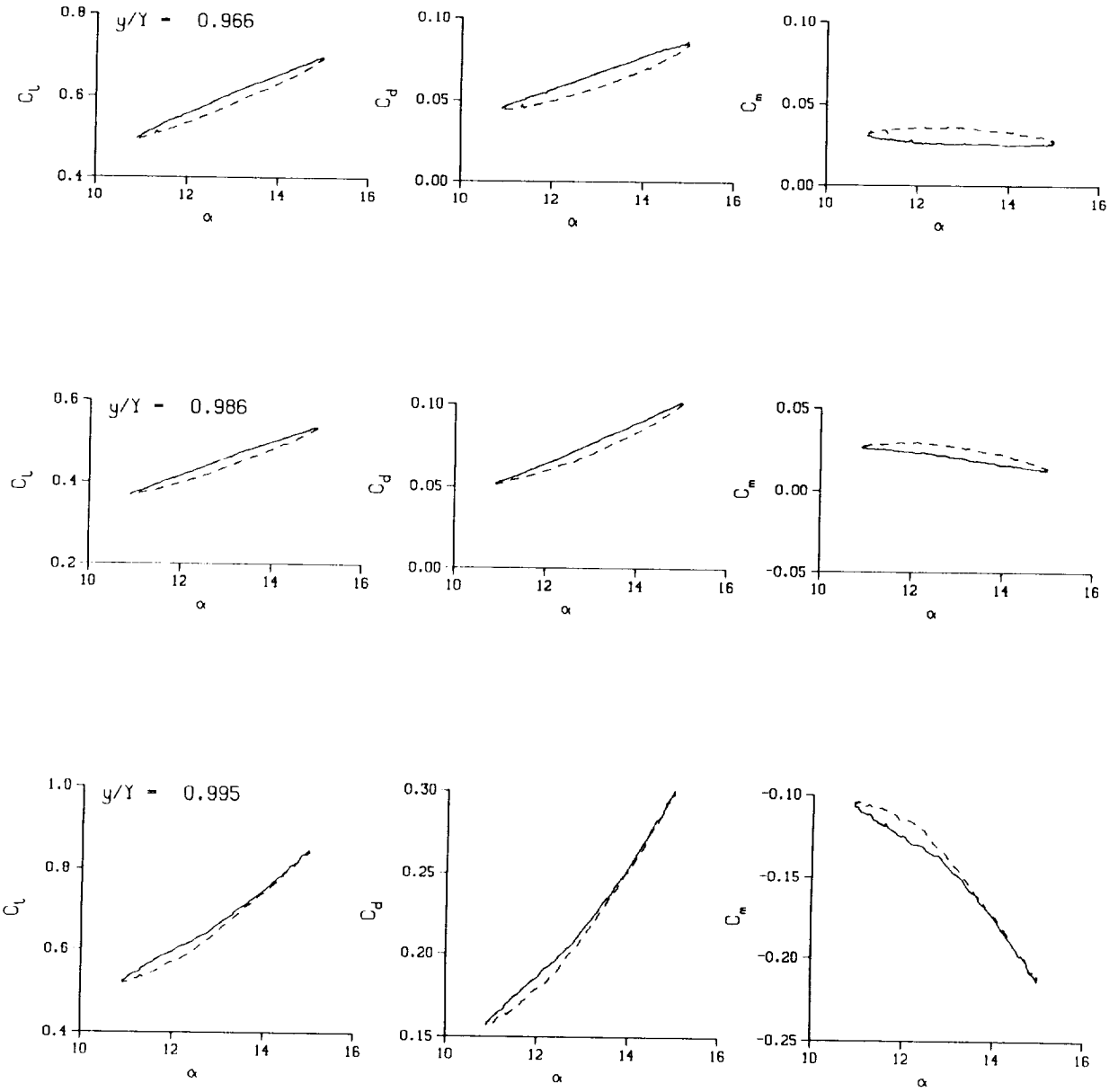

(c) v = 0.14. Concluded

Figure 75. Continued.

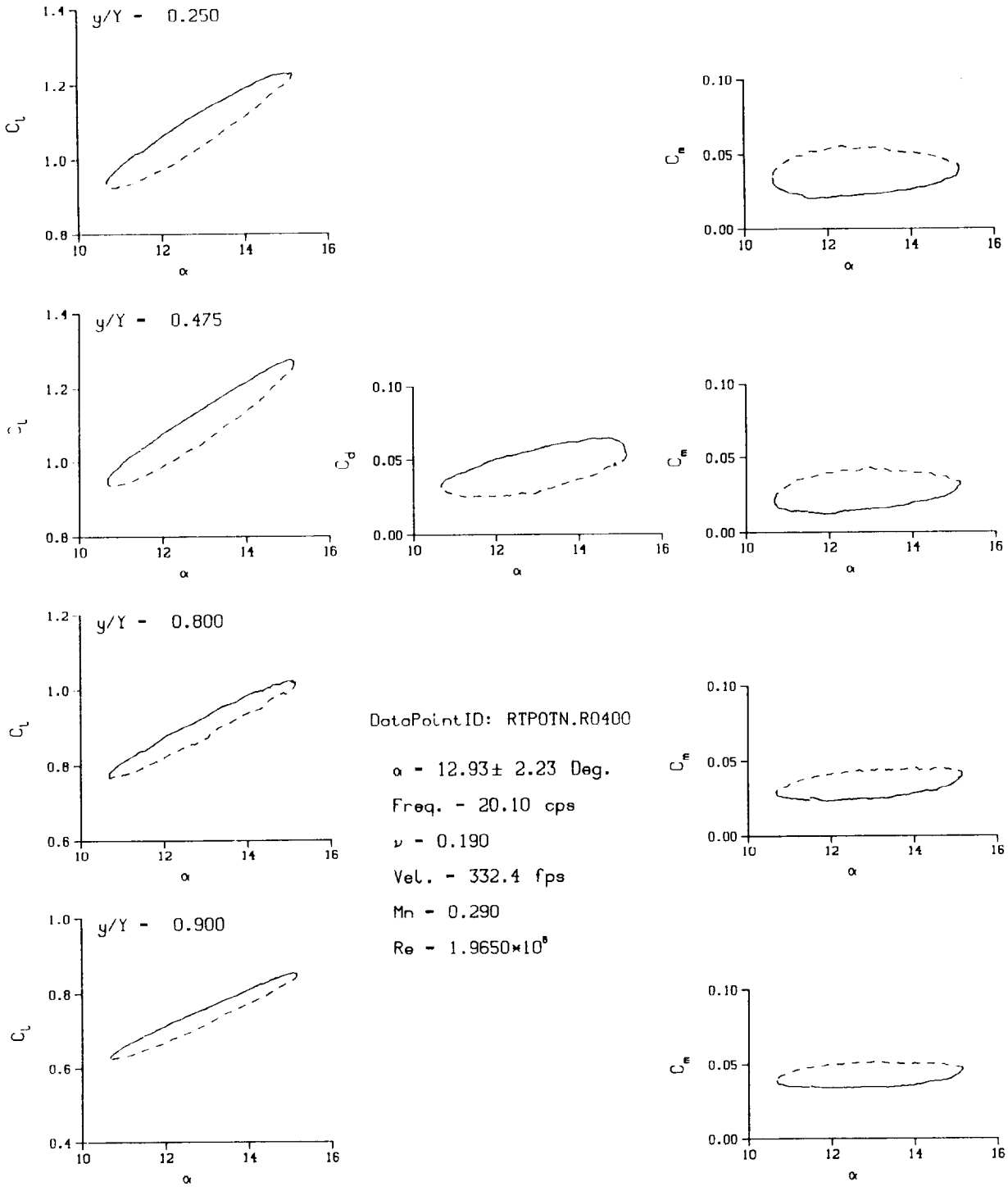

(d) v = 0.20

Figure 75. Continued.

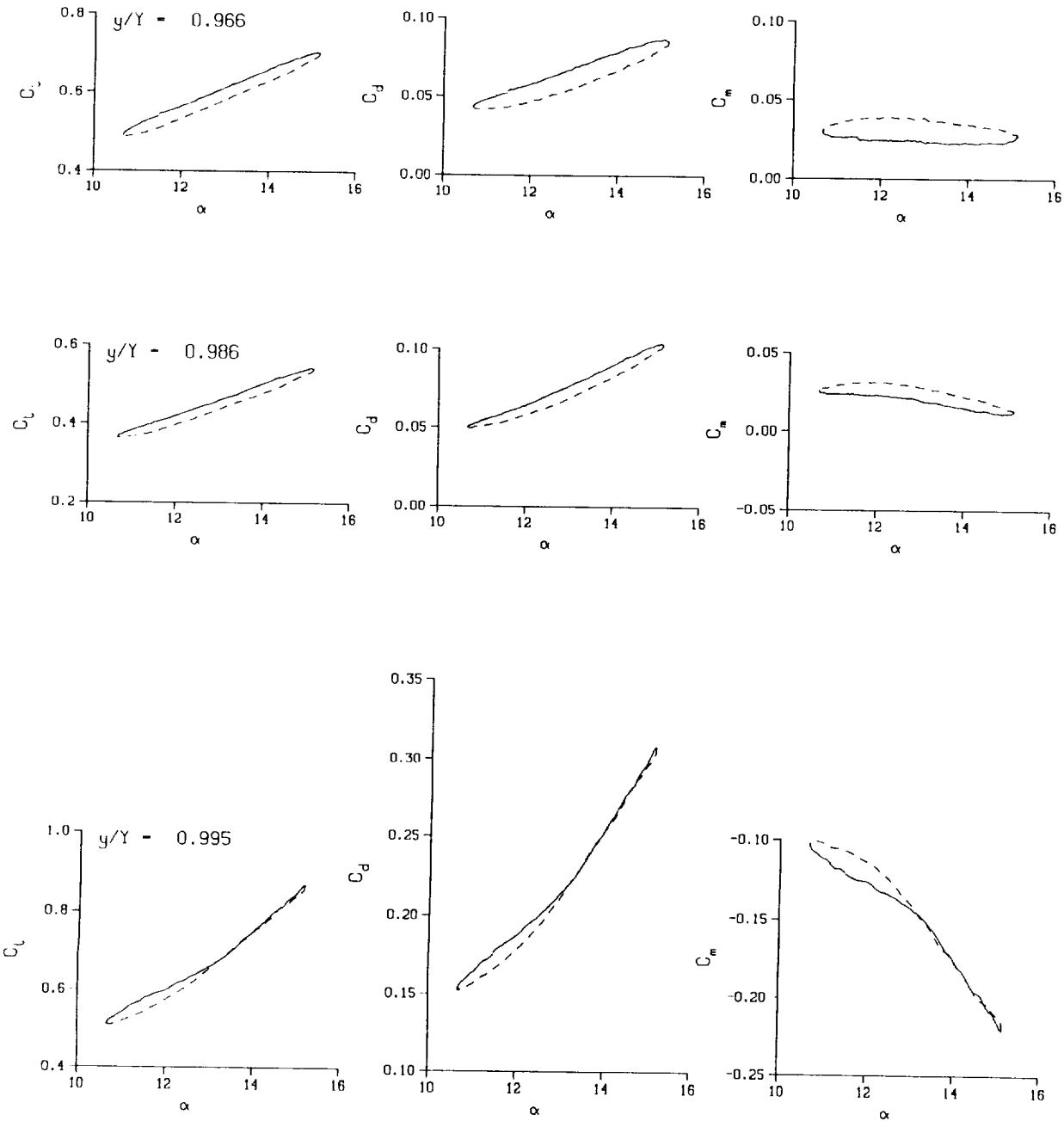

(d) v = 0.20. Concluded

Figure 75. Concluded.

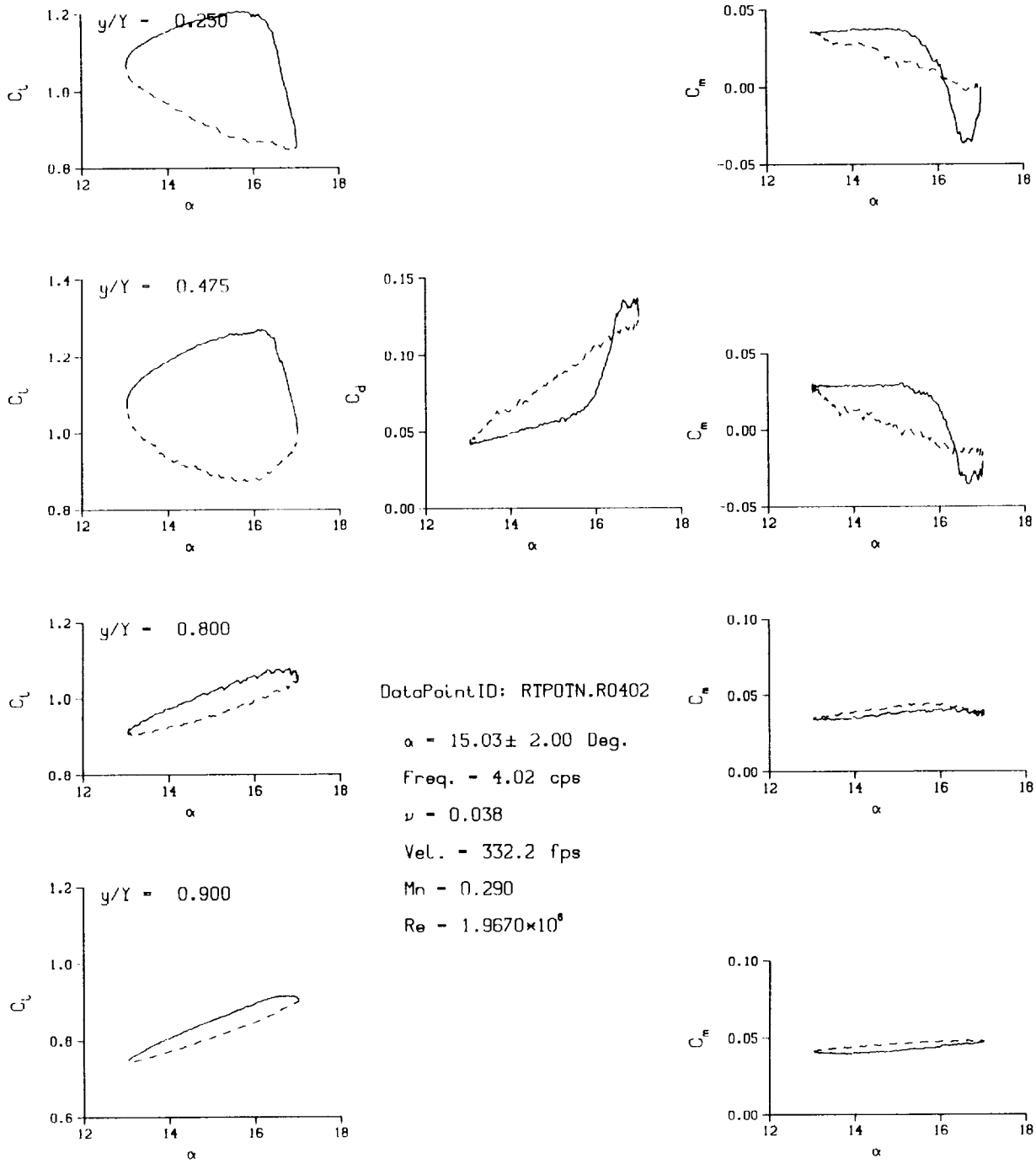

(a) ν = 0.04

Figure 76. 3-D round tip pitch oscillation data; no BL-trip; α = 15 ± 2 deg.

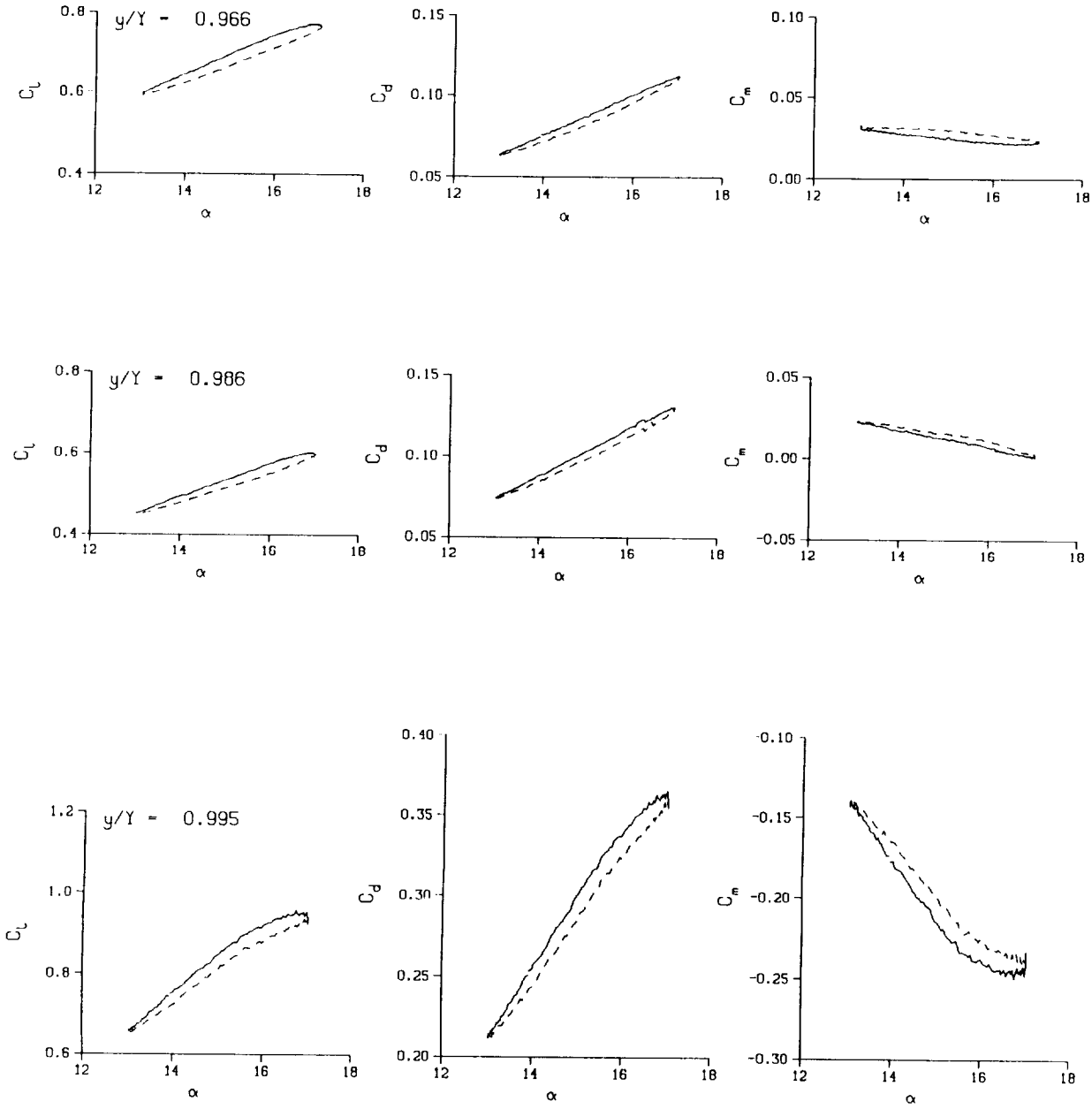

(a) v = 0.04. Concluded

Figure 76. Continued.

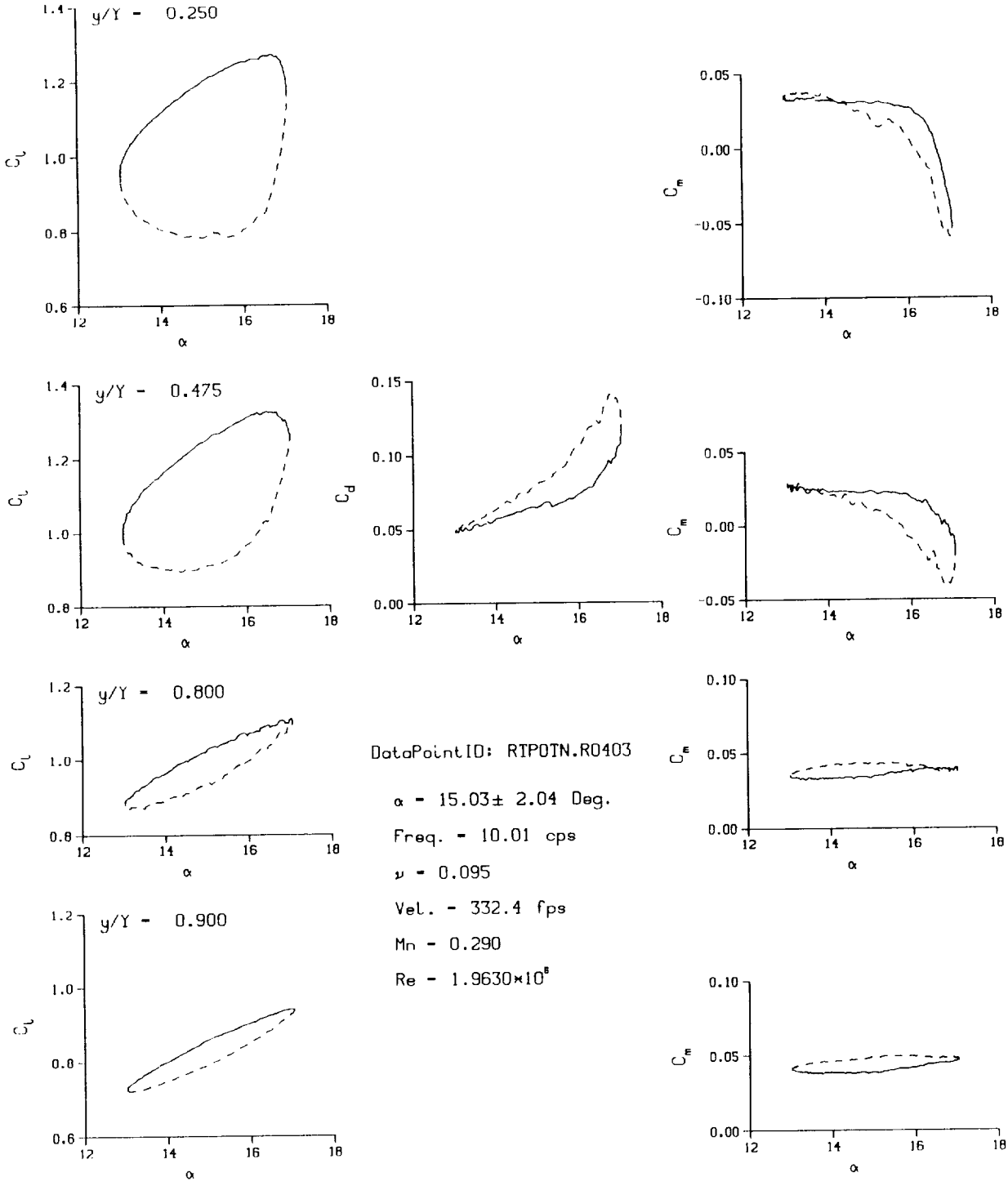

(b) v = 0.10

Figure 76. Continued.

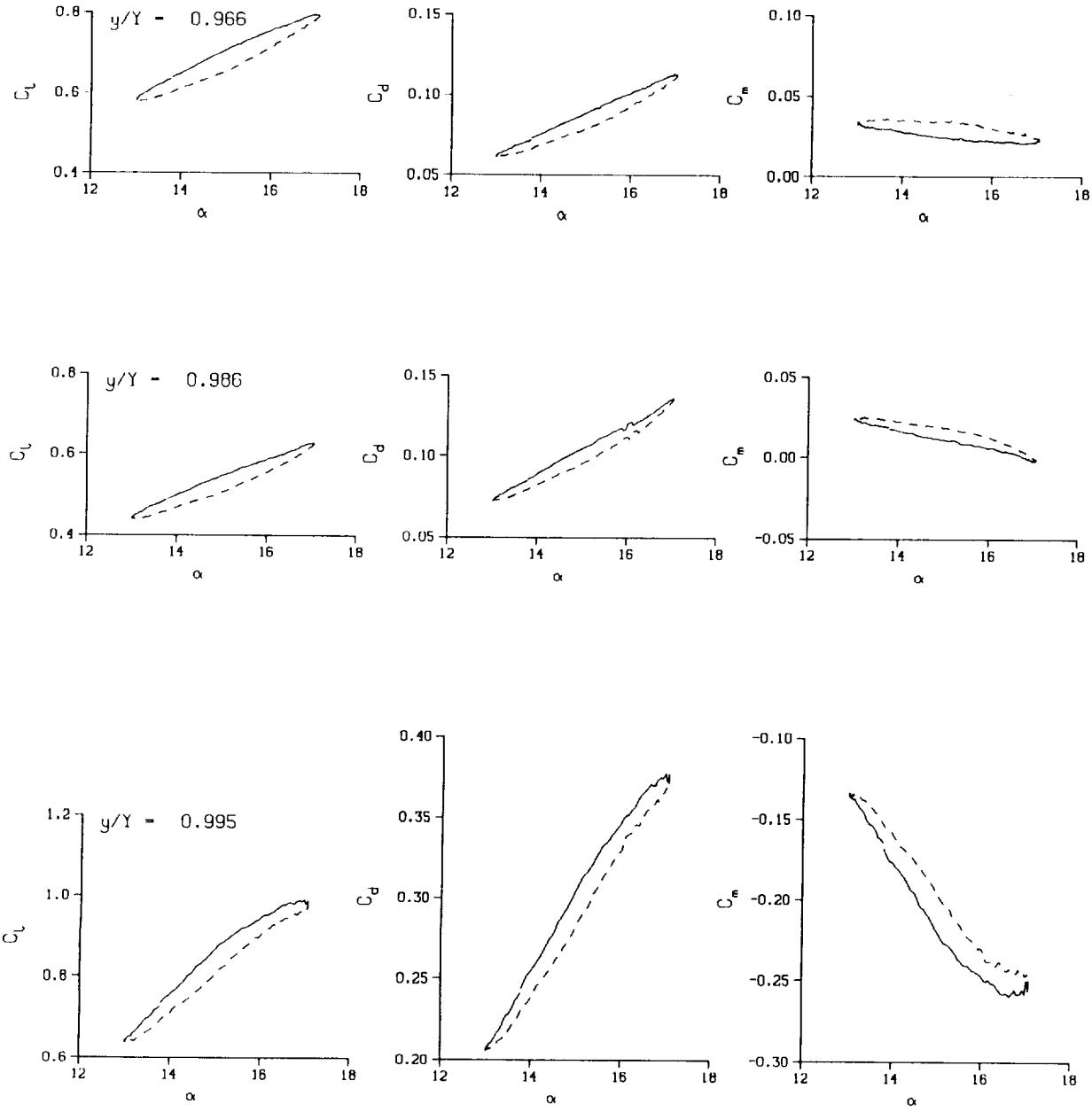

(b) v = 0.10. Concluded

Figure 76. Continued.

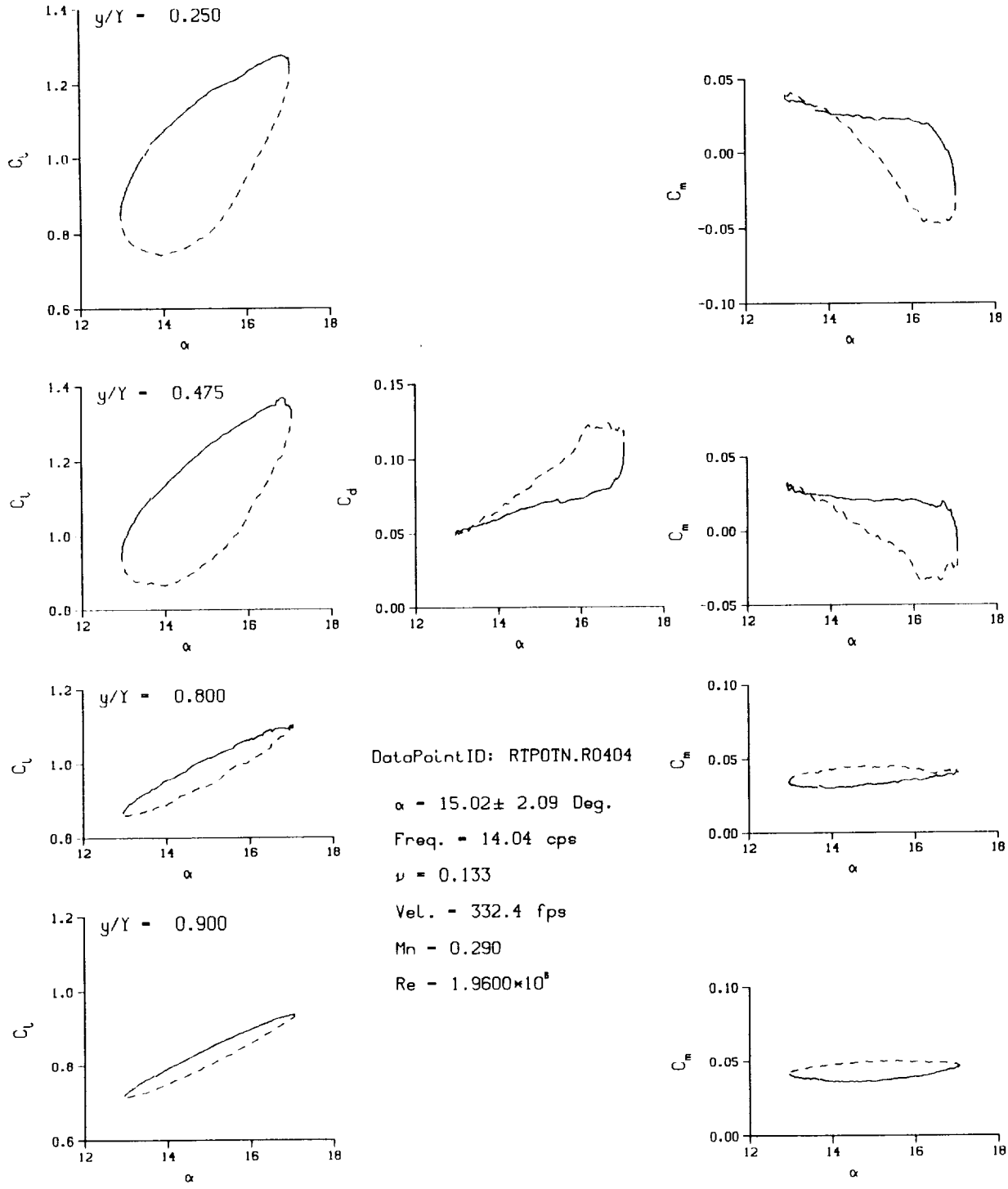

(c) v = 0.14

Figure 76. Continued.

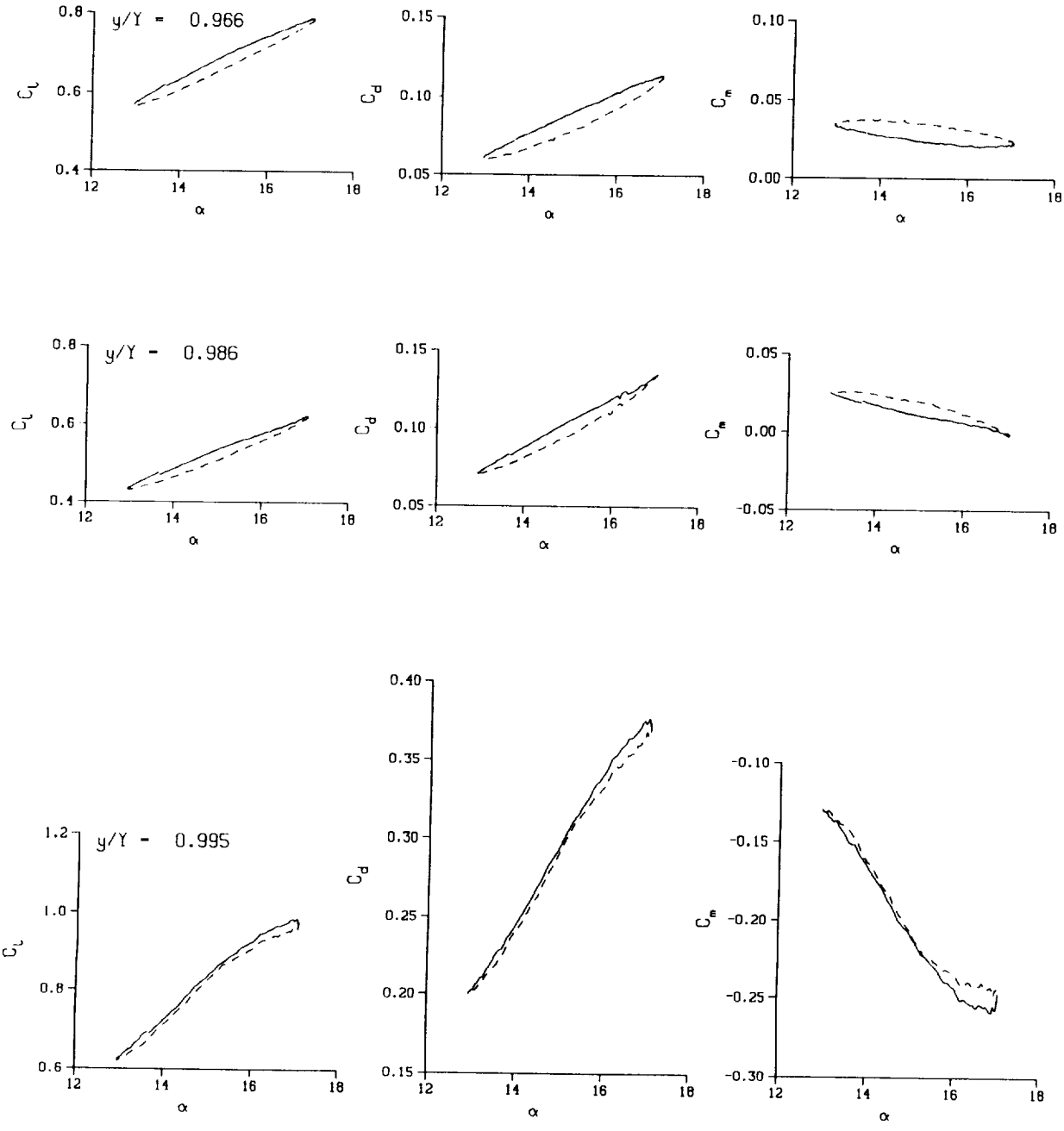

(c) v = 0.14. Concluded

Figure 76. Continued.

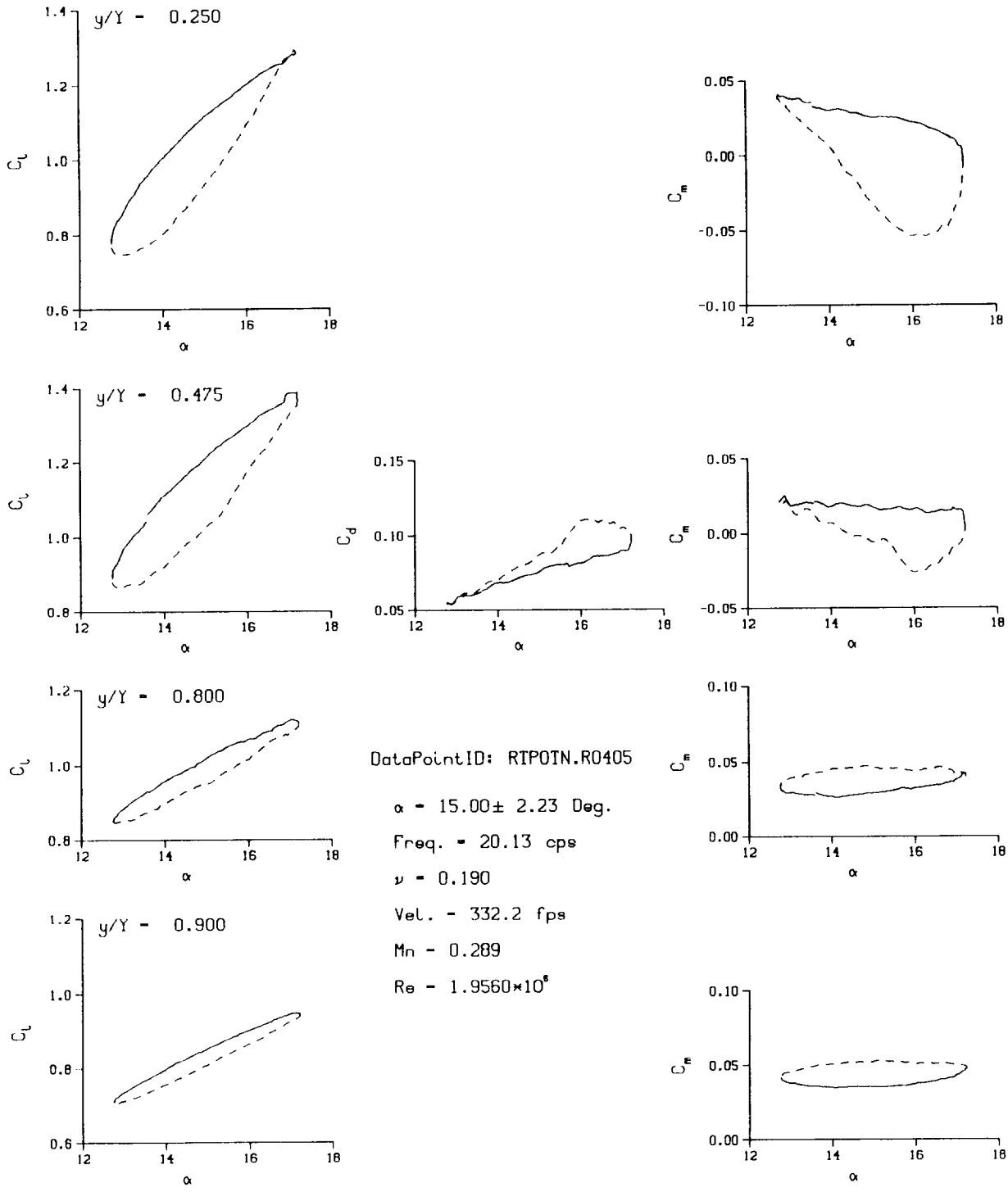

(d) v = 0.20

Figure 76. Continued.

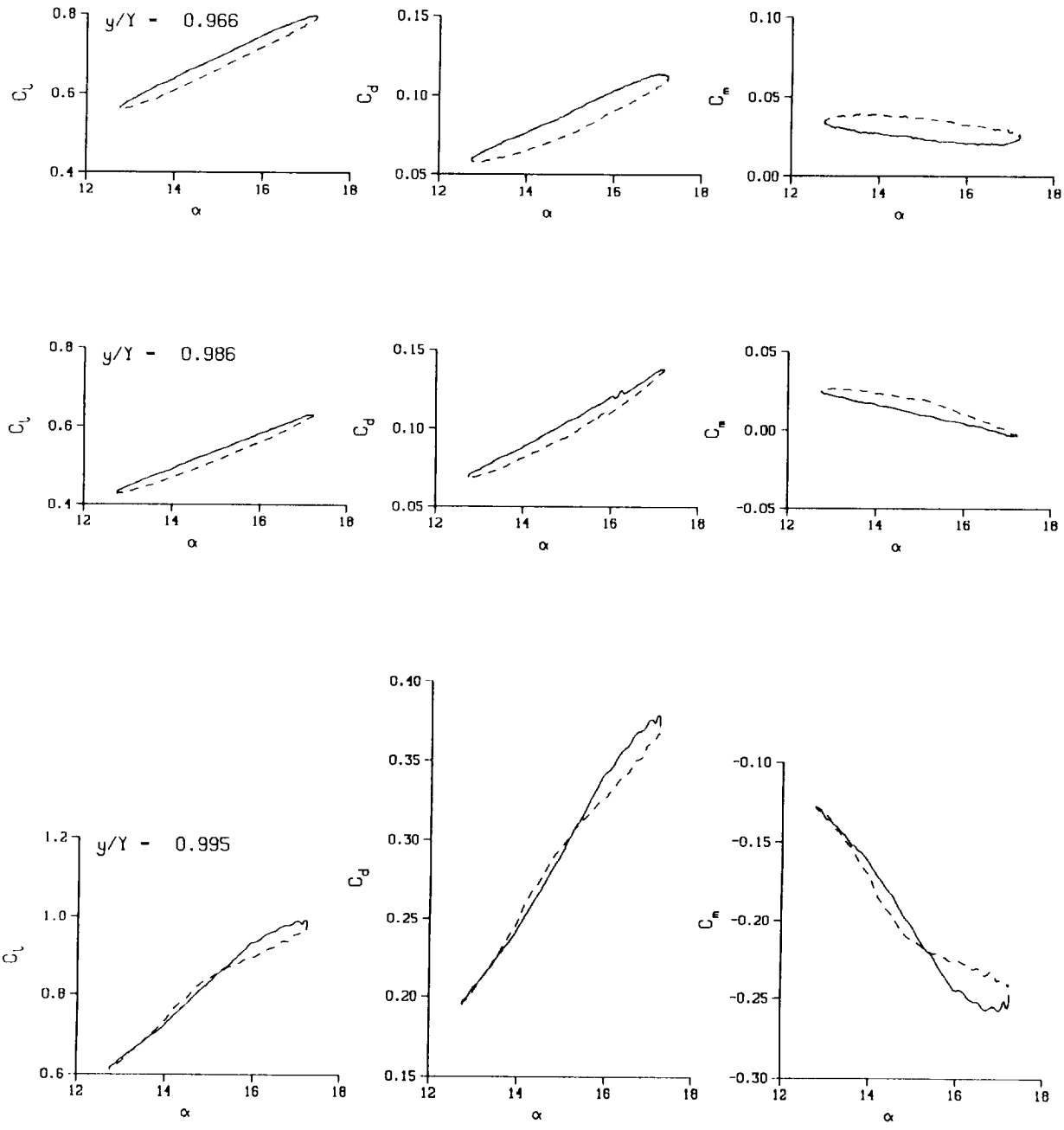

(d) v = 0.20. Concluded

Figure 76. Concluded.

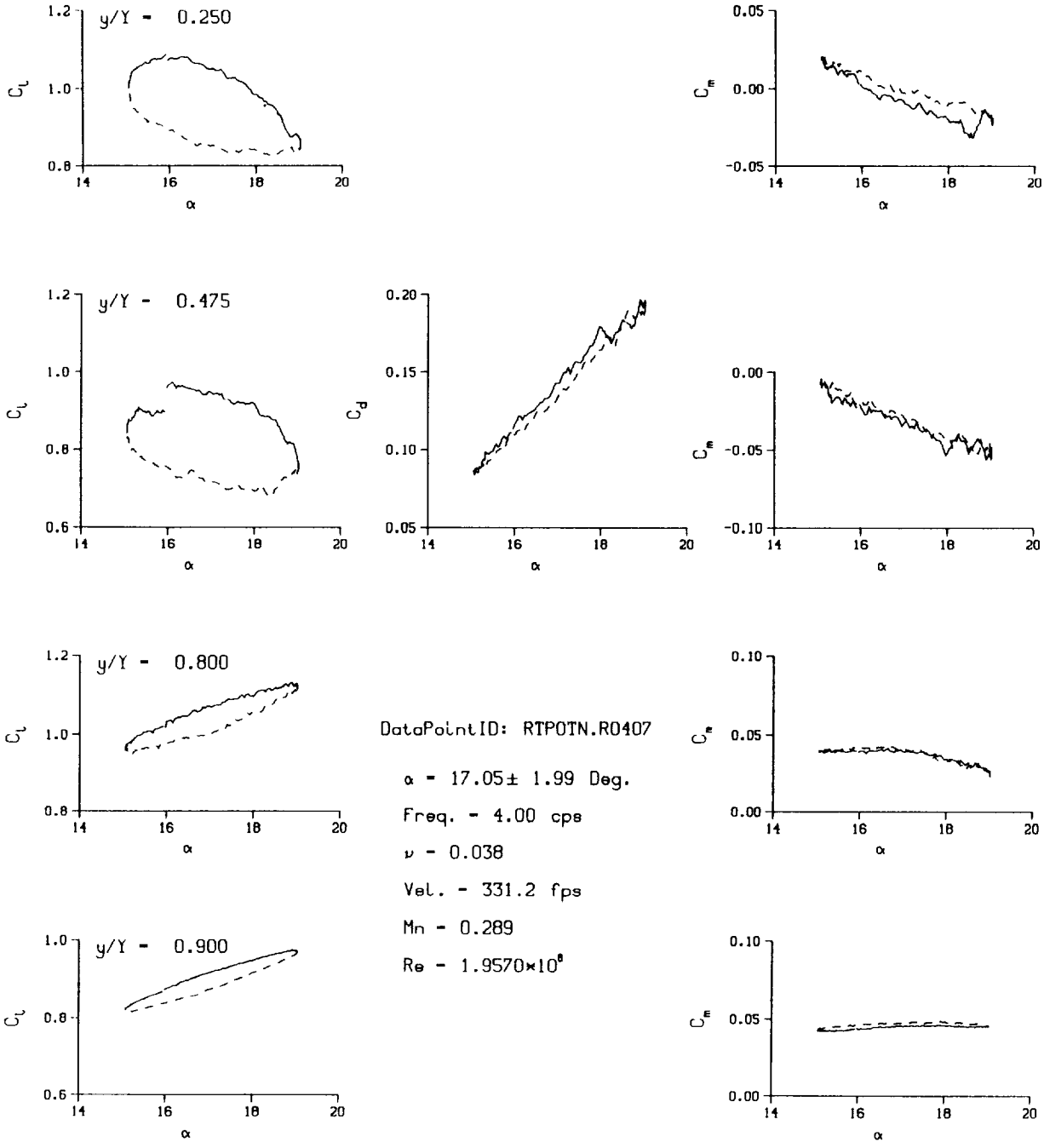

(a) v = 0.04

Figure 77. 3-D round tip pitch oscillation data; no BL-trip; α = 17 ± 2 deg.

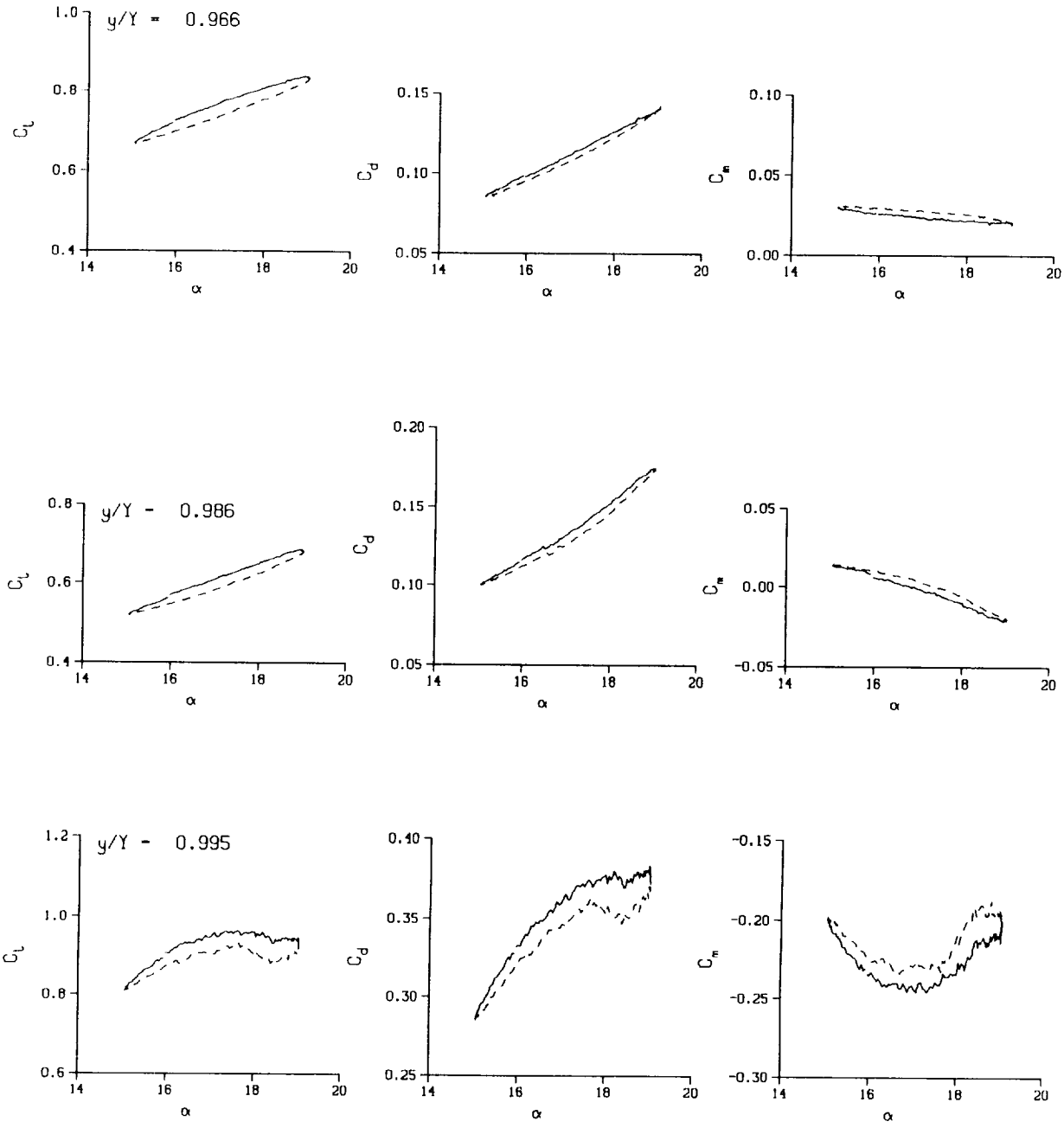

(a) v = 0.04. Concluded

Figure 77. Continued.

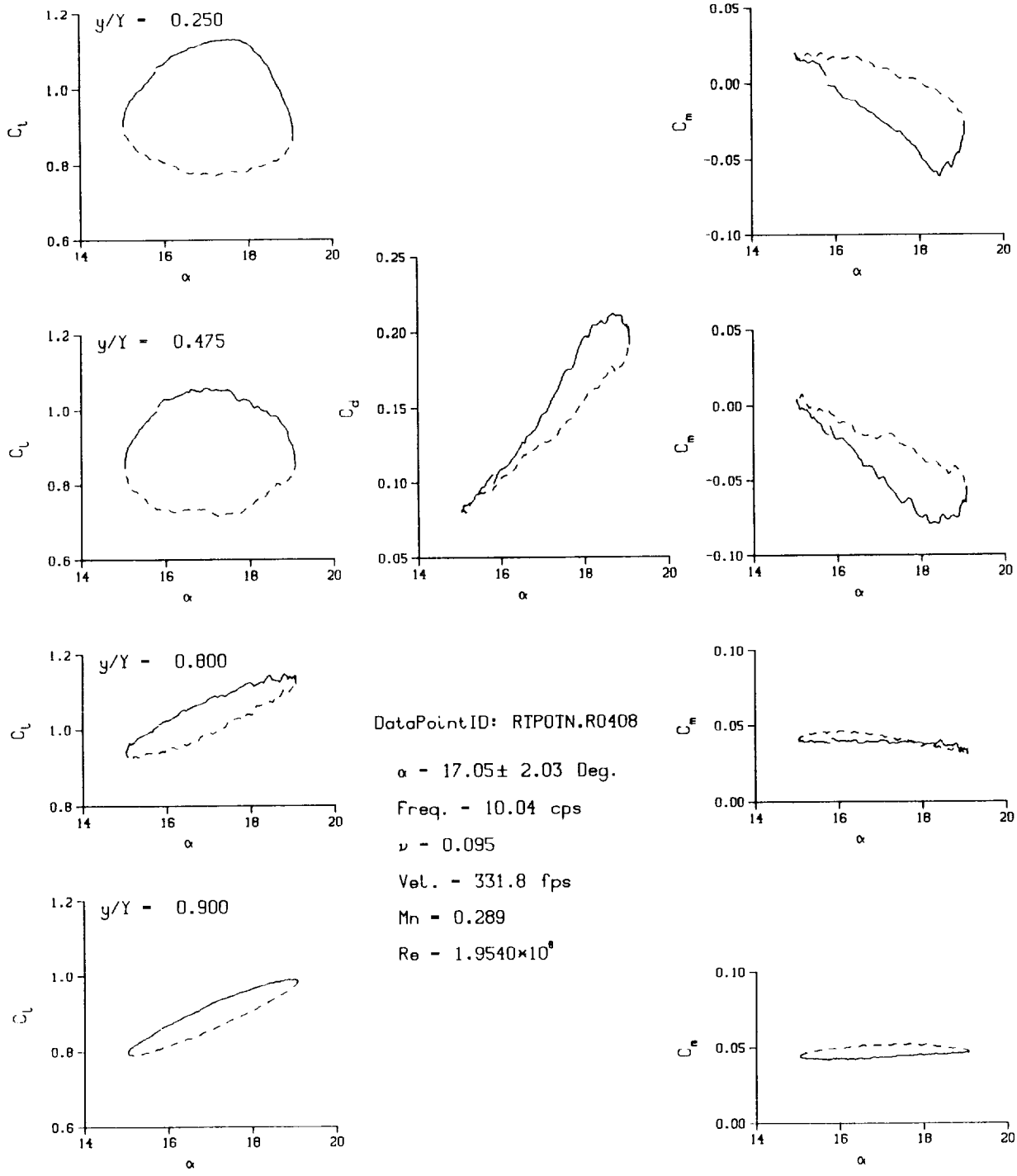

(b) v = 0.10

Figure 77. Continued.

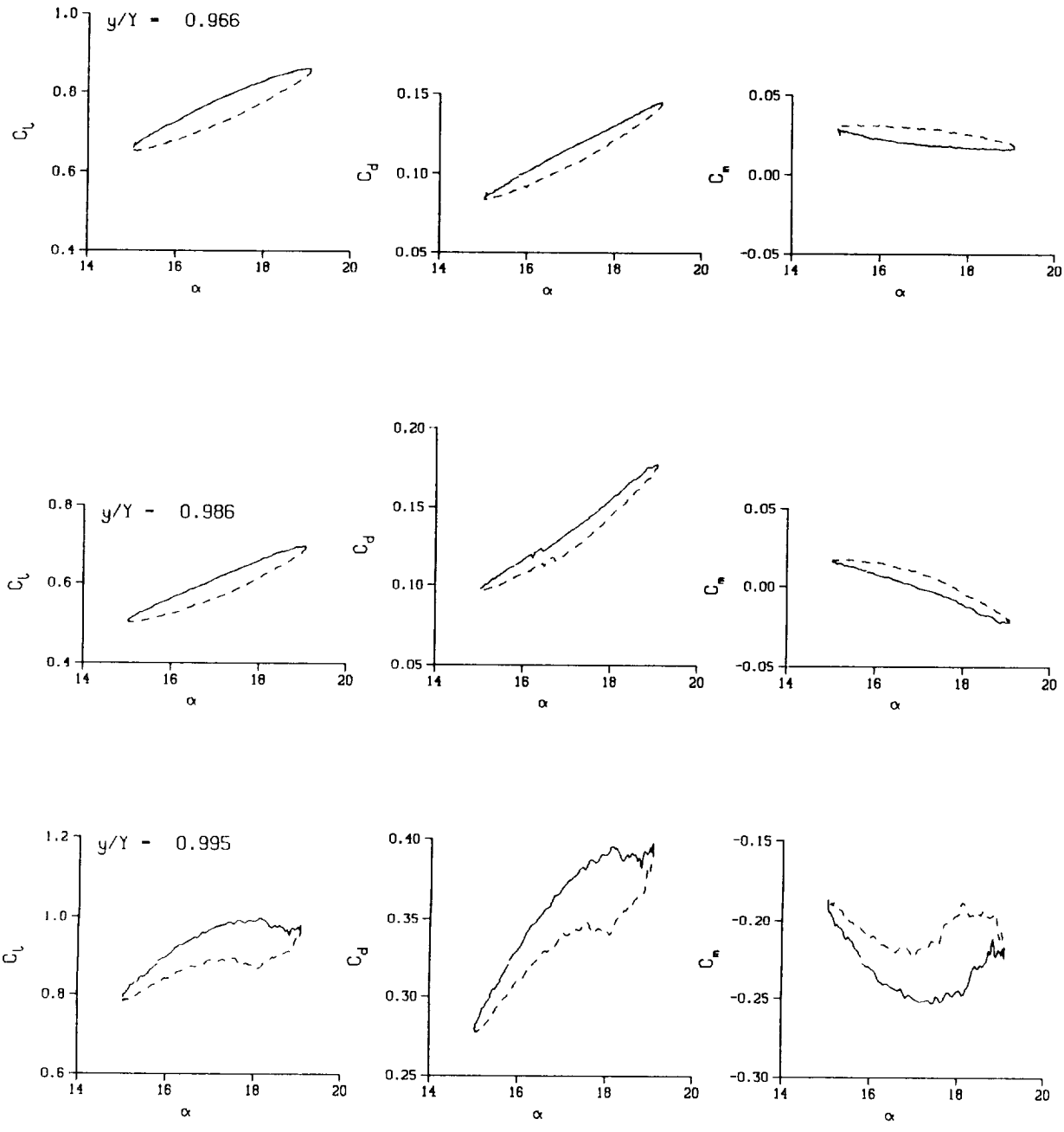

(b) v = 0.10. Concluded

Figure 77. Continued.

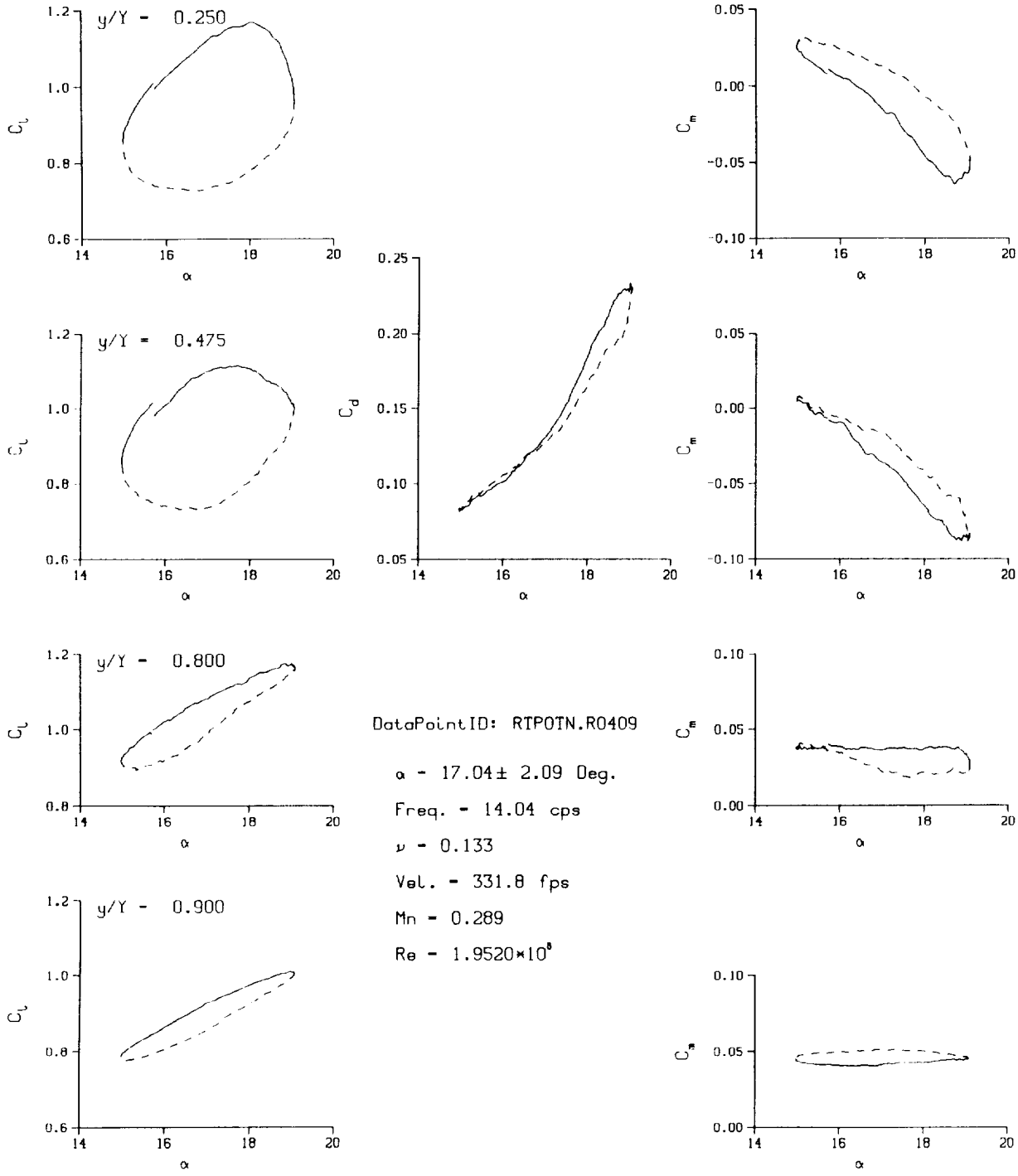

(c) v = 0.14

Figure 77. Continued.

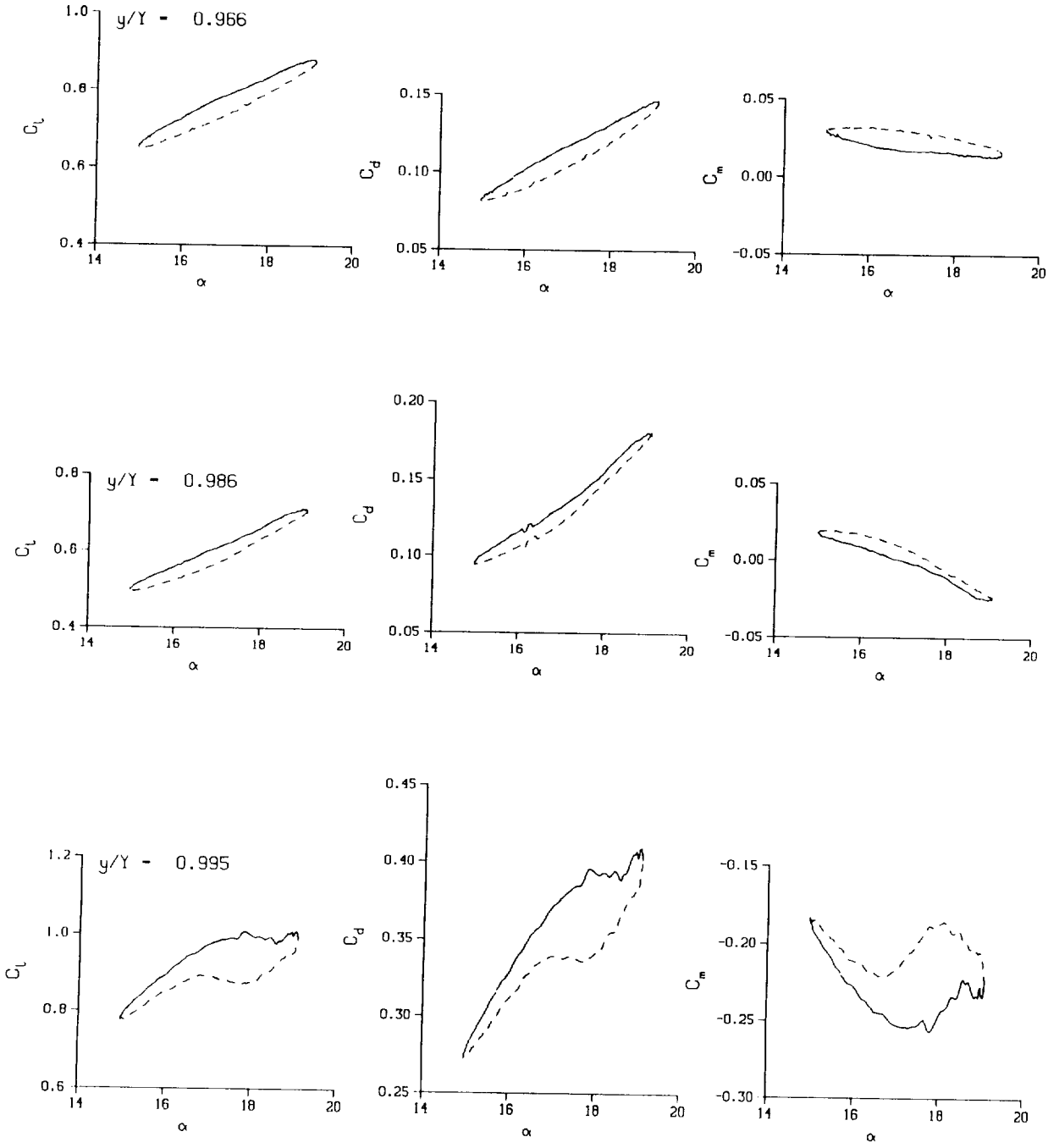

(c) v = 0.14. Concluded

Figure 77. Continued.

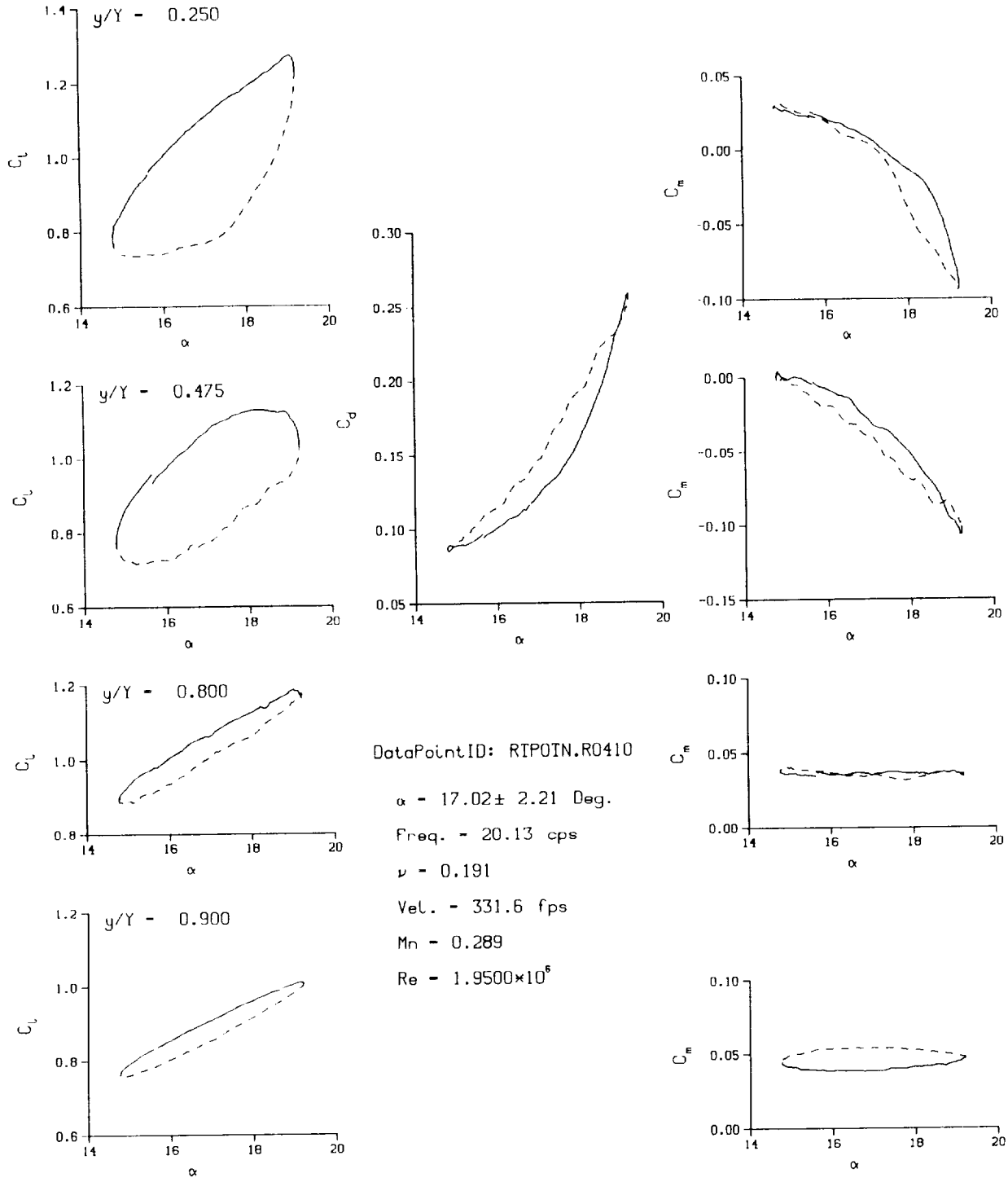

(d) ν = 0.20

Figure 77. Continued.

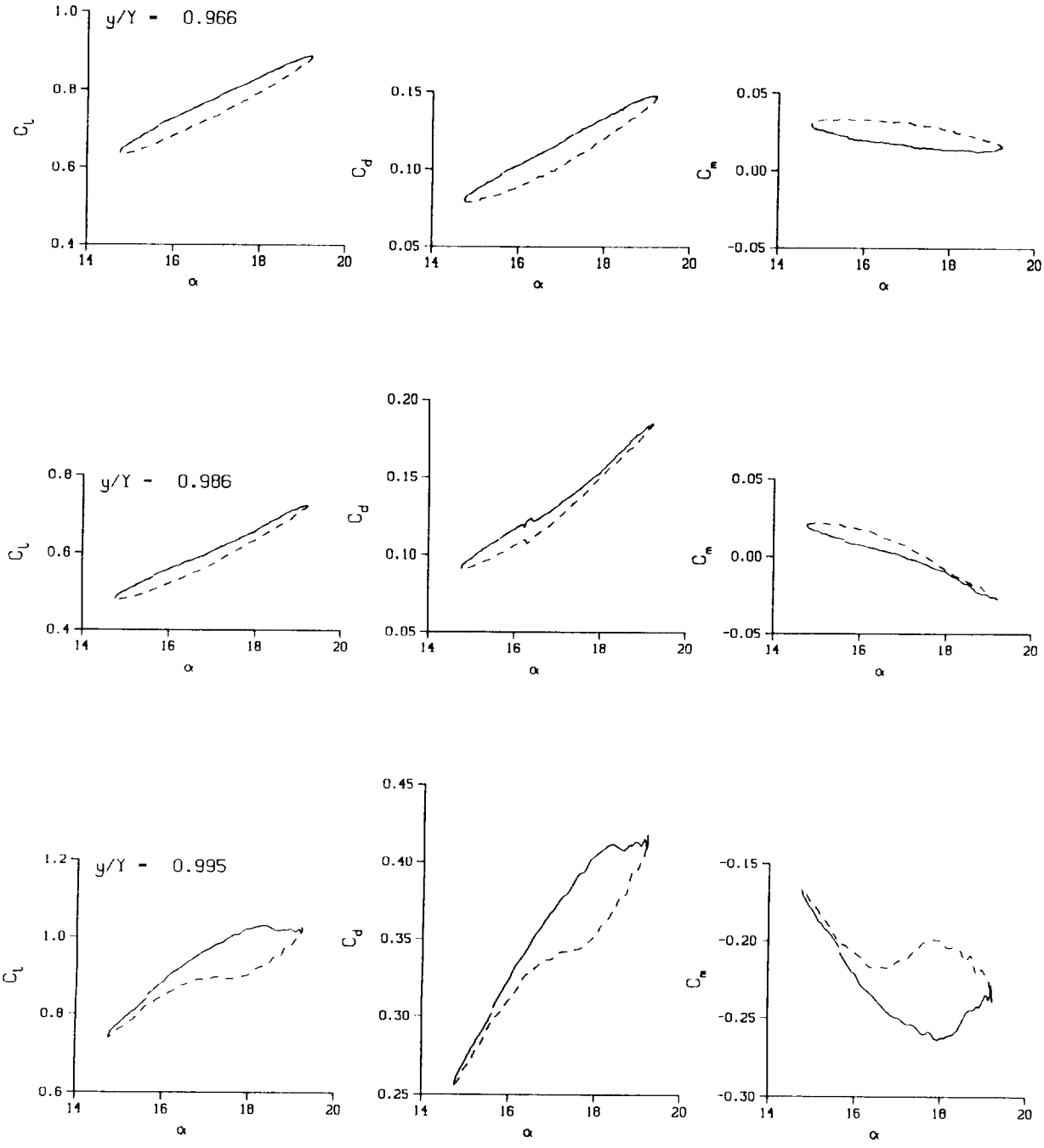

(d) v = 0.20. Concluded

Figure 77. Concluded.

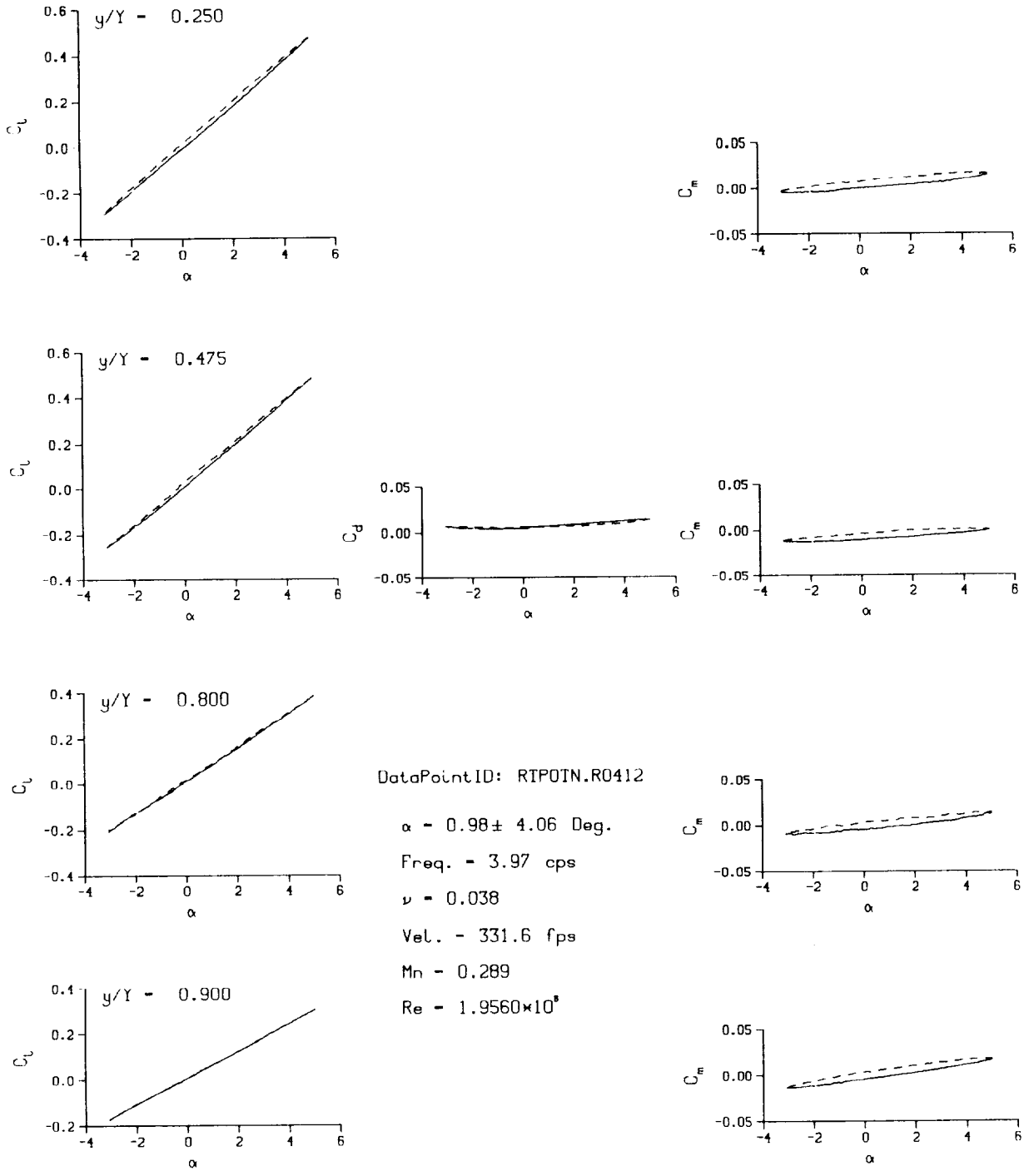

(a) ν = 0.04

Figure 78. 3-D round tip pitch oscillation data; no BL-trip; α = 1 ± 4 deg.

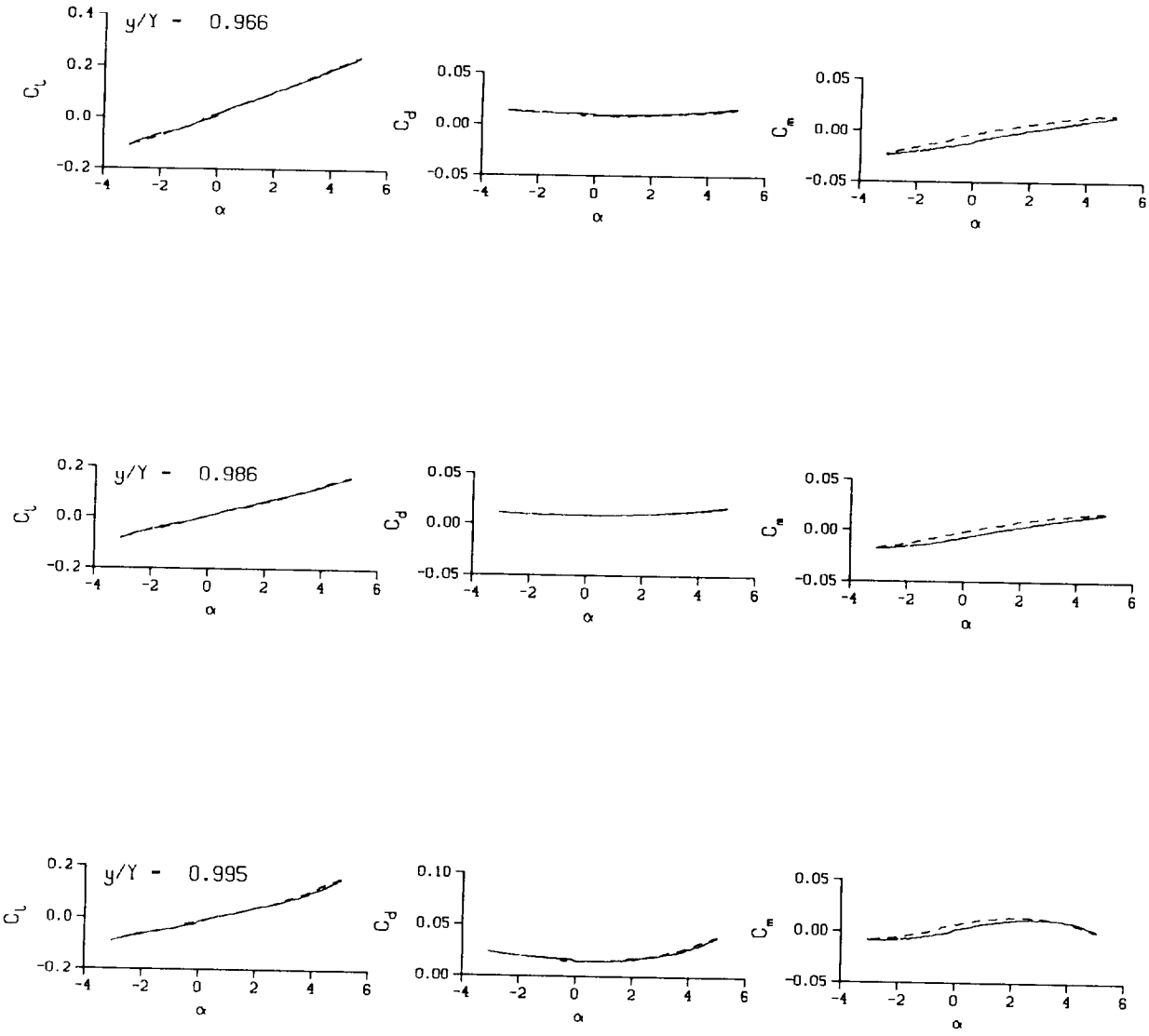

(a) v = 0.04. Concluded

Figure 78. Continued.

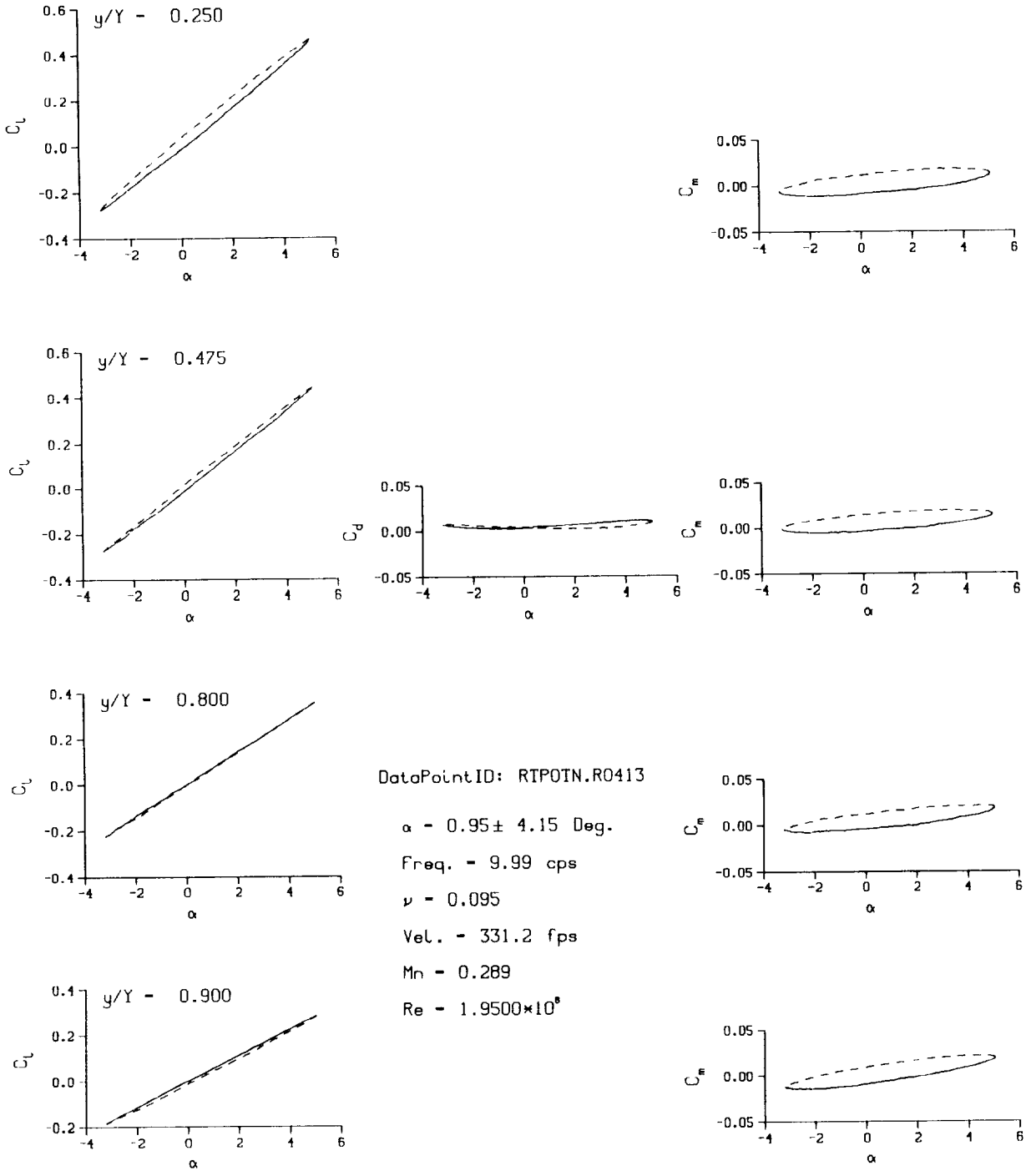

(b) ν = 0.10

Figure 78. Continued.

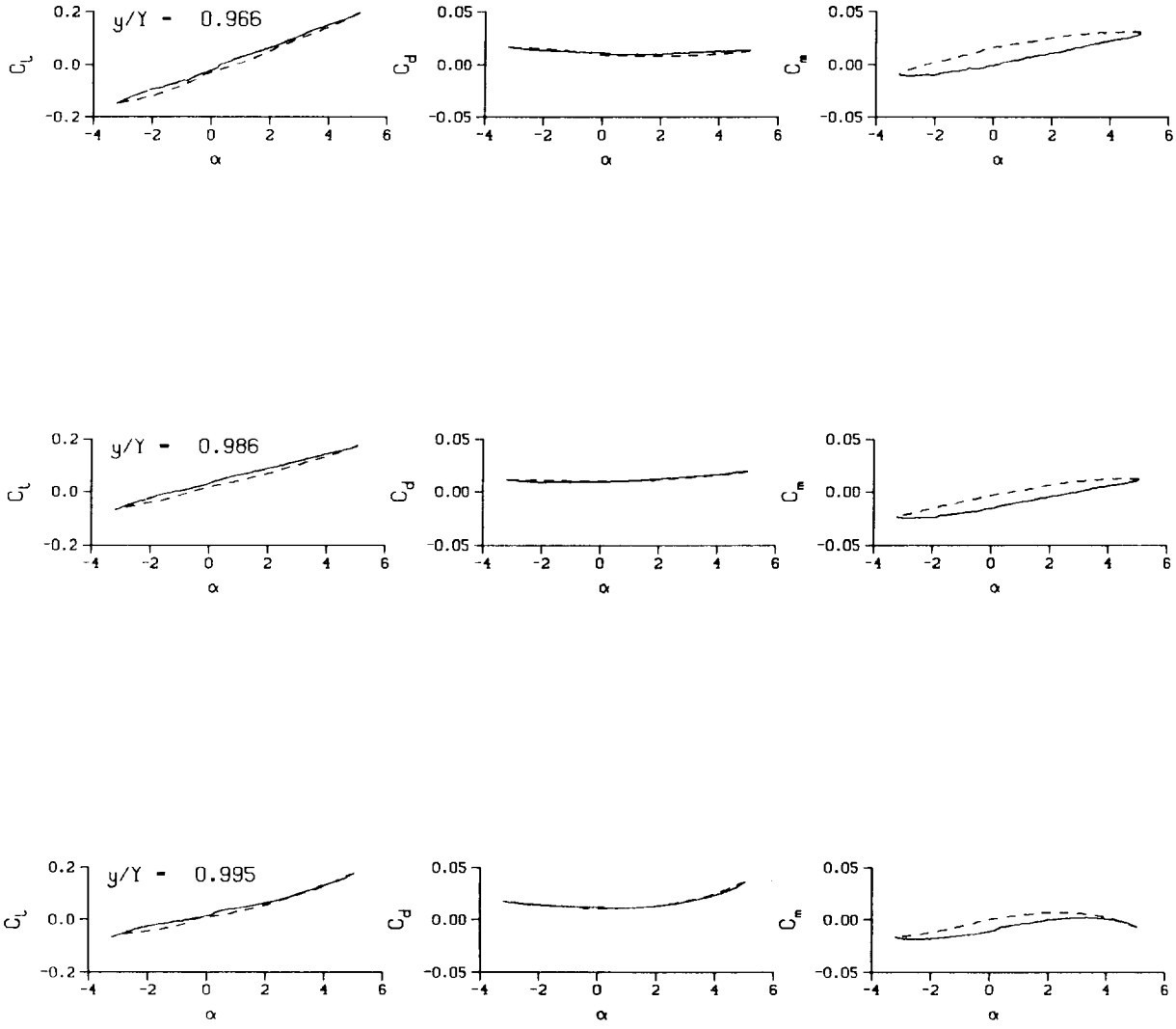

(b) v = 0.10. Concluded

Figure 78. Continued.

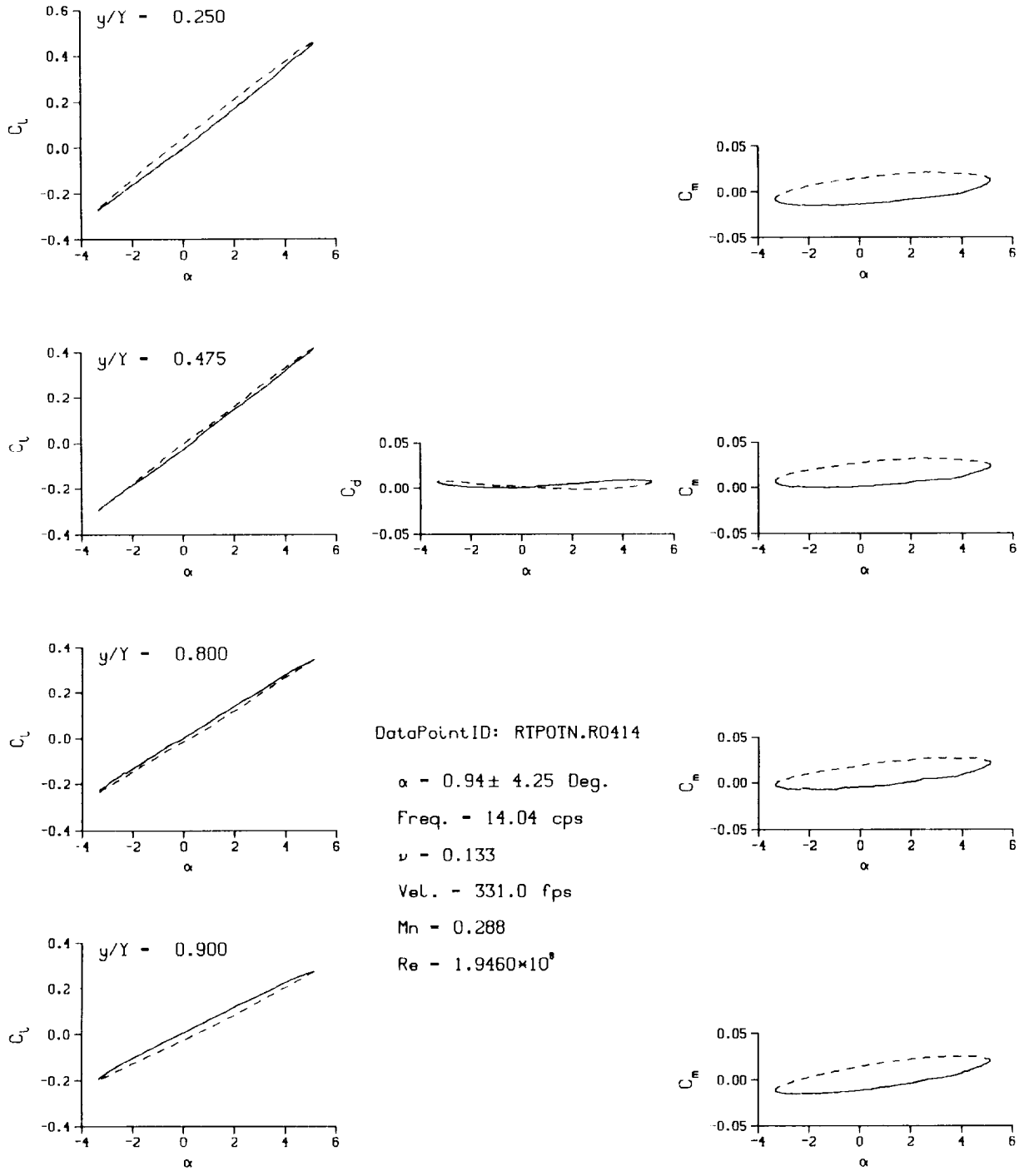

(c) ν = 0.14

Figure 78. Continued.

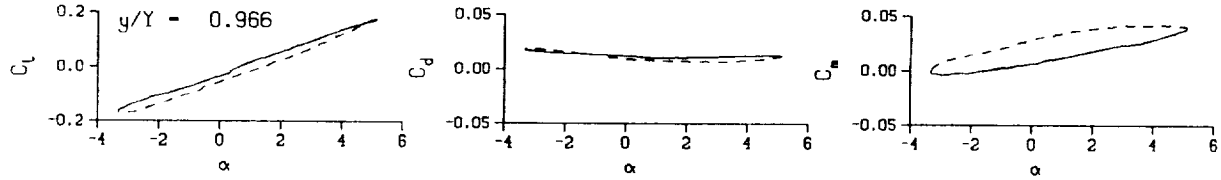

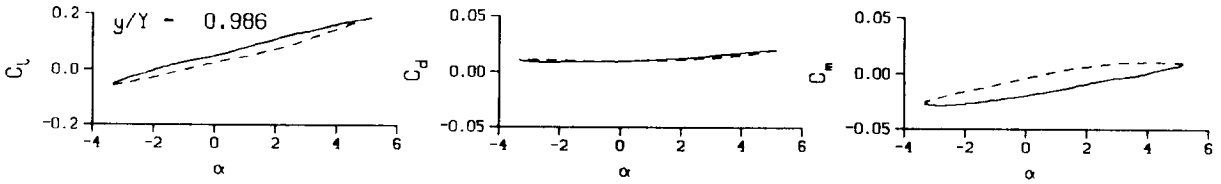

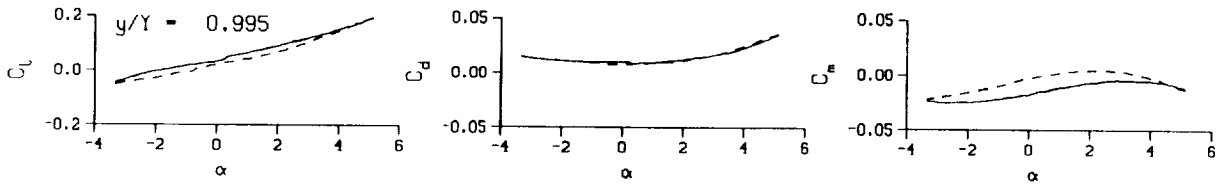

(c) v = 0.14. Concluded

Figure 78. Concluded.

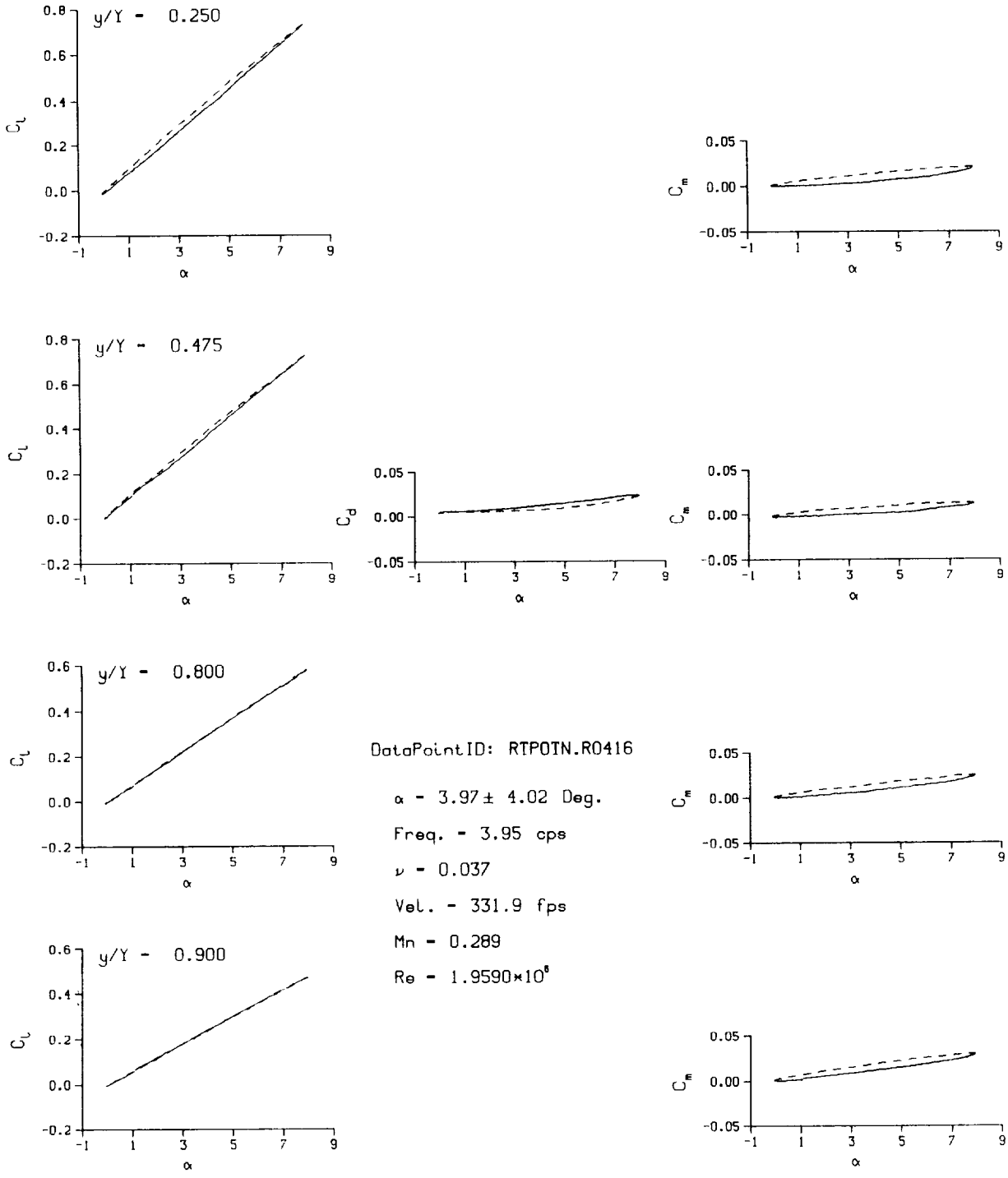

(a) ν = 0.04

Figure 79. 3-D round tip pitch oscillation data; no BL-trip; α = 4 ± 4 deg.

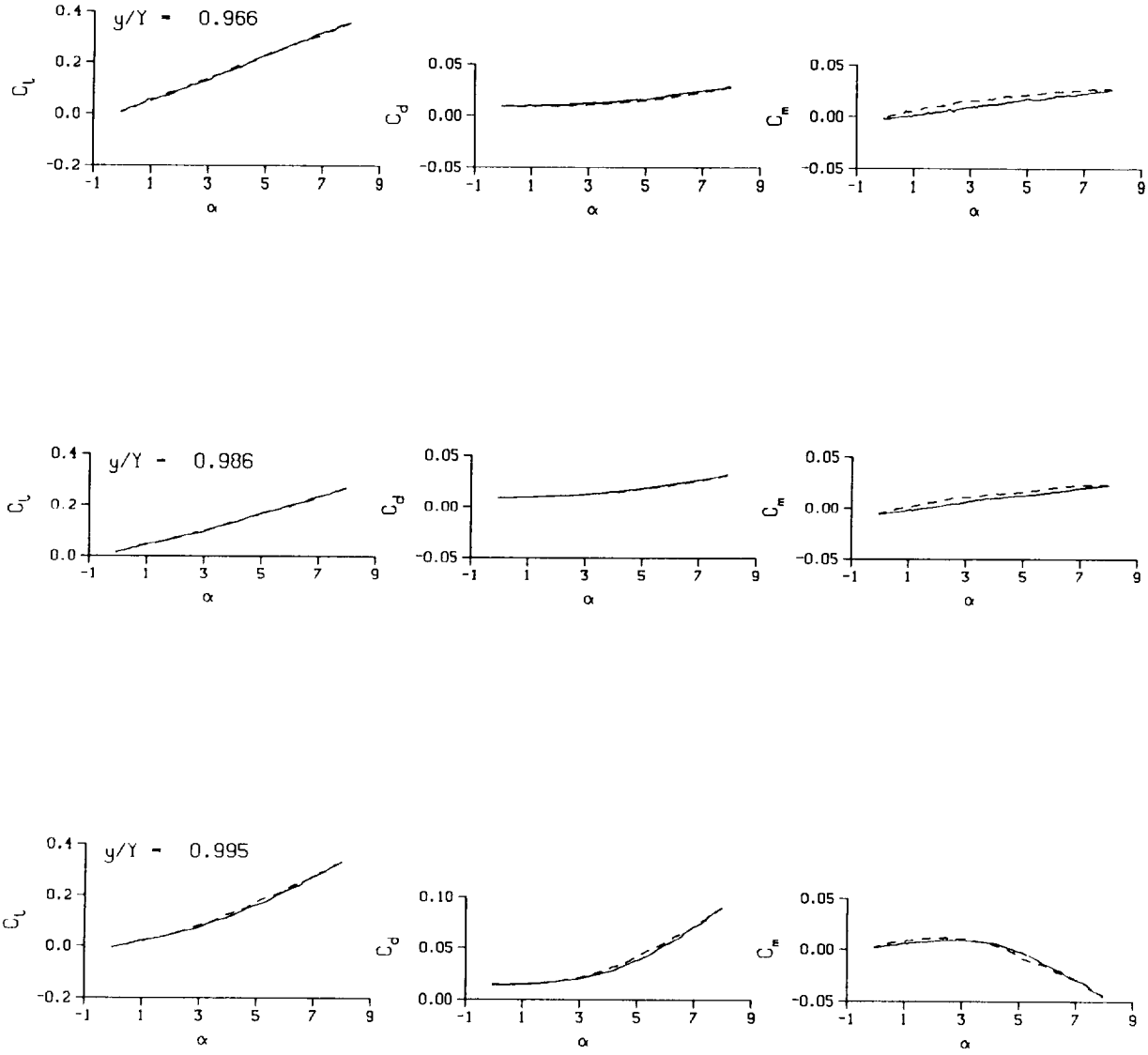

(a) v = 0.04. Concluded

Figure 79. Continued.

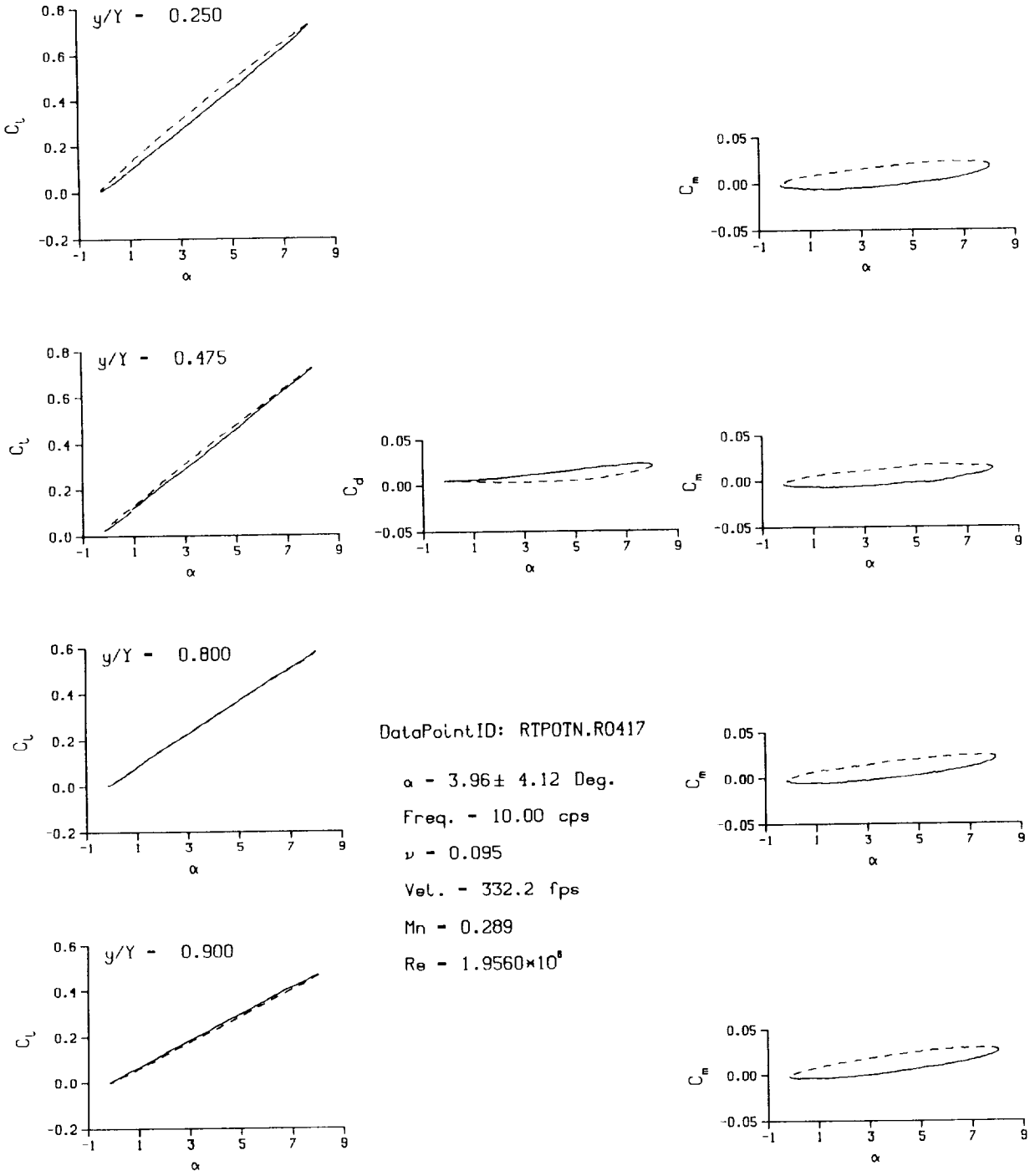

(b) v = 0.10

Figure 79. Continued.

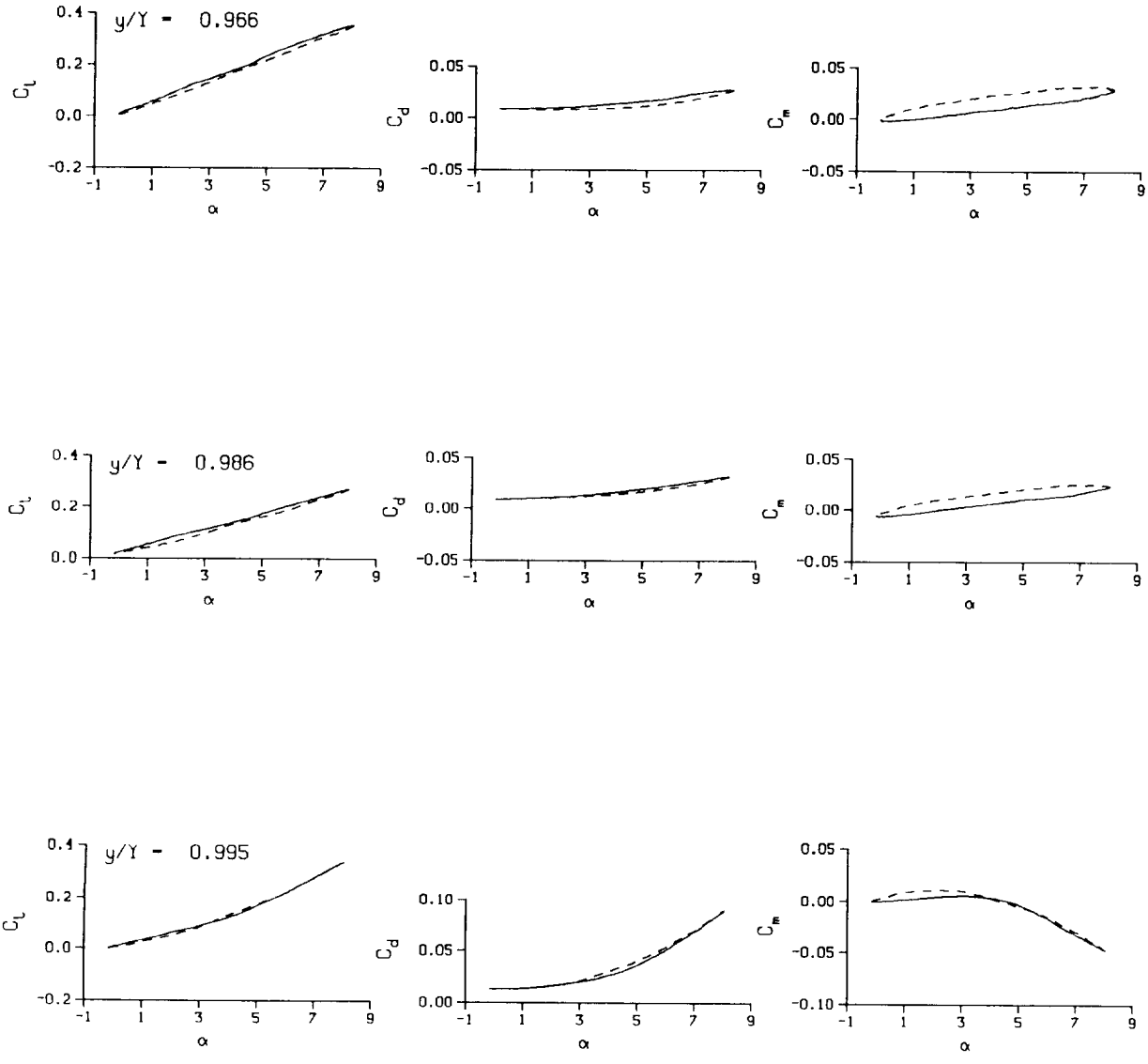

(b) v = 0.10. Concluded

Figure 79. Continued.

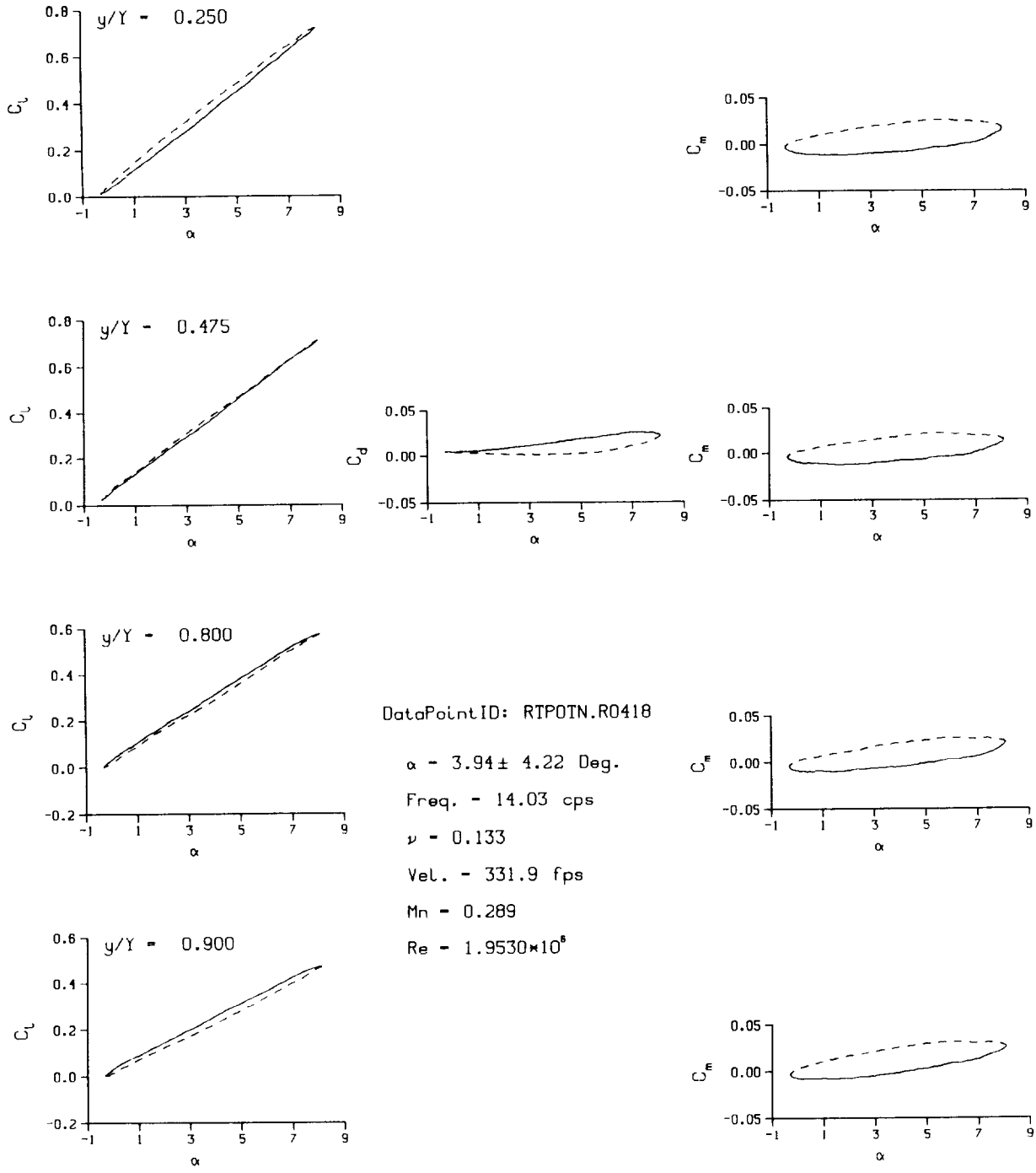

(c) ν = 0.14

Figure 79. Continued.

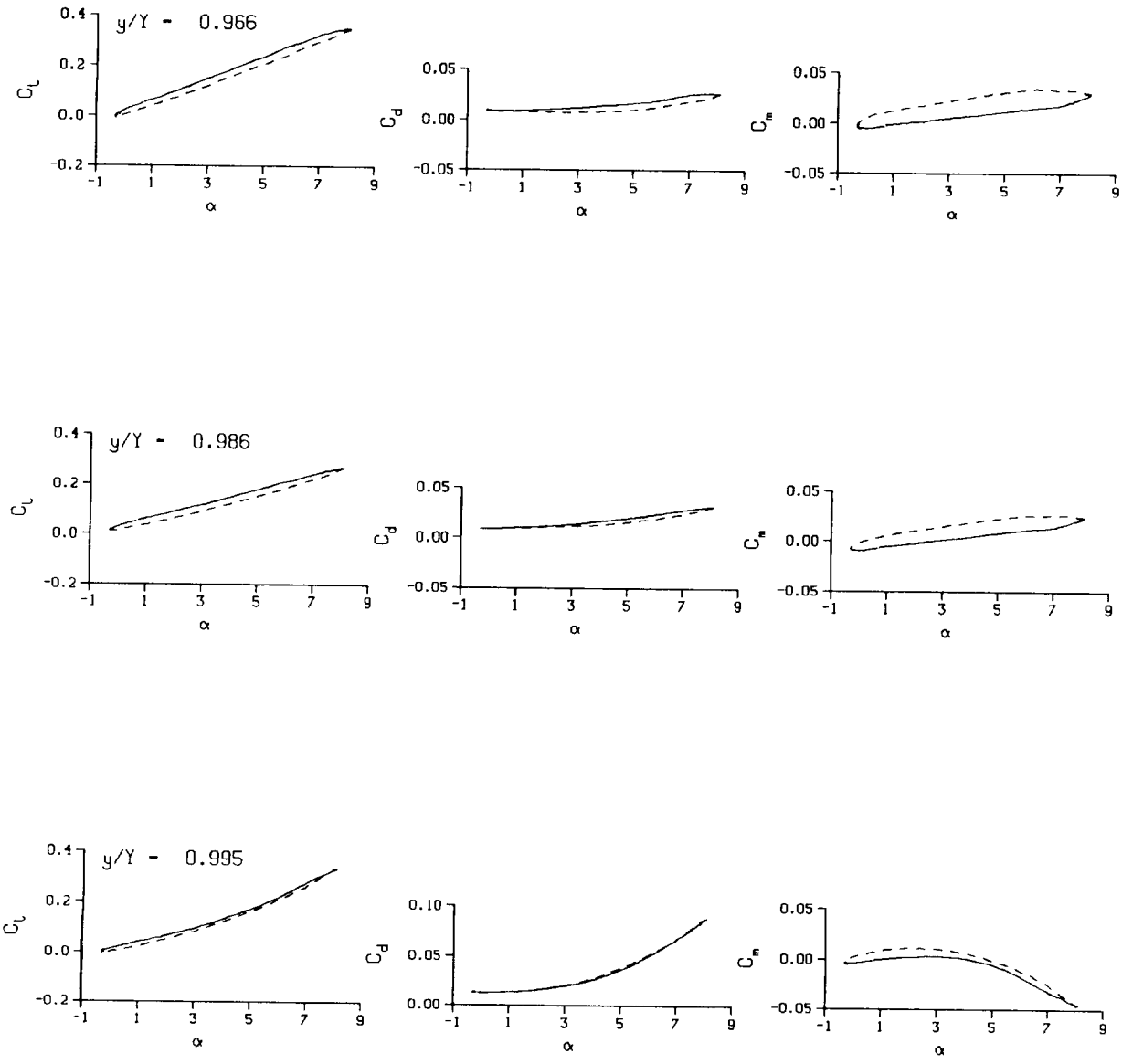

(c) v = 0.14. Concluded

Figure 79. Concluded.

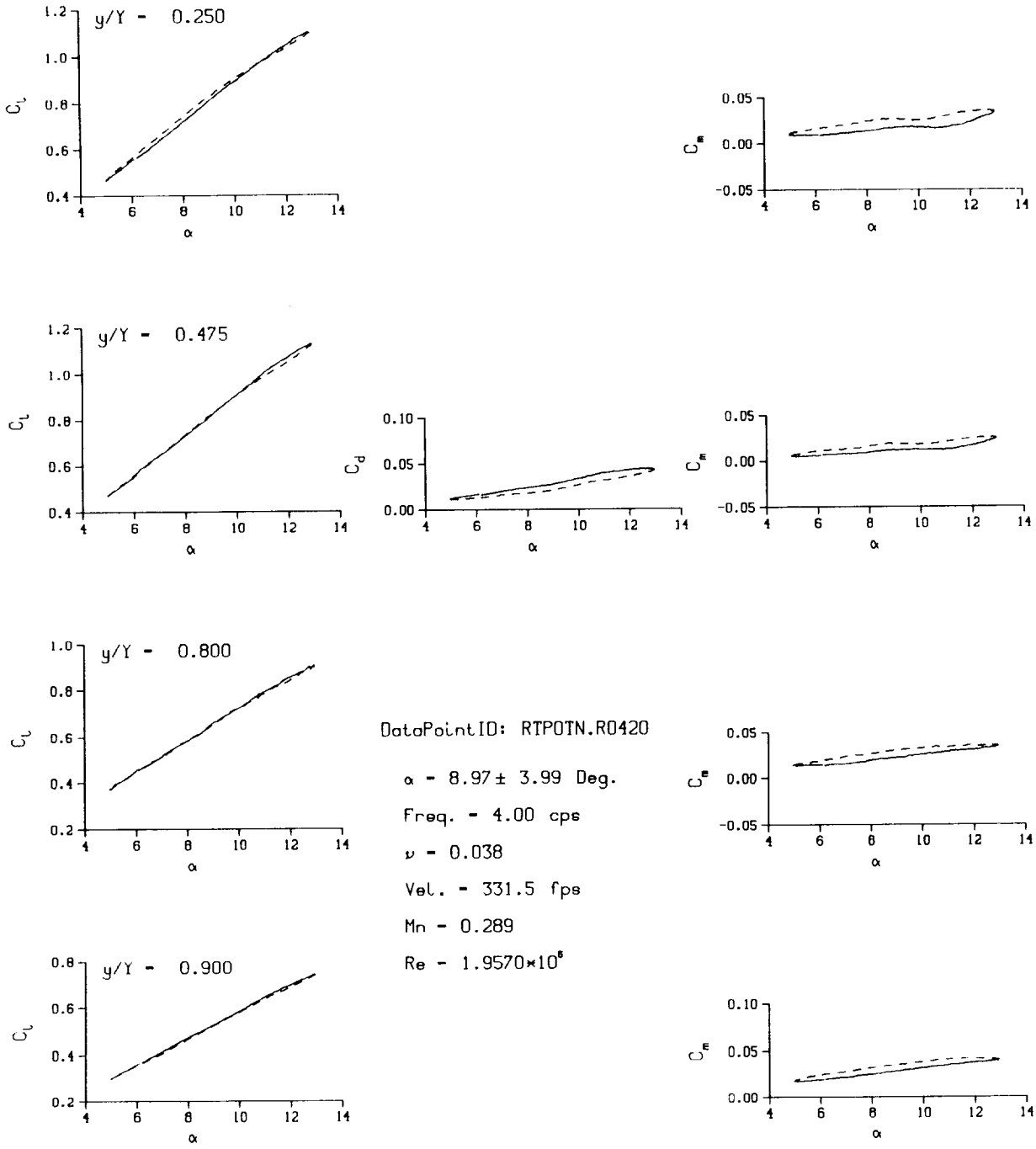

(a) ν = 0.04

Figure 80. 3-D round tip pitch oscillation data; no BL-trip; α = 9 ± 4 deg.

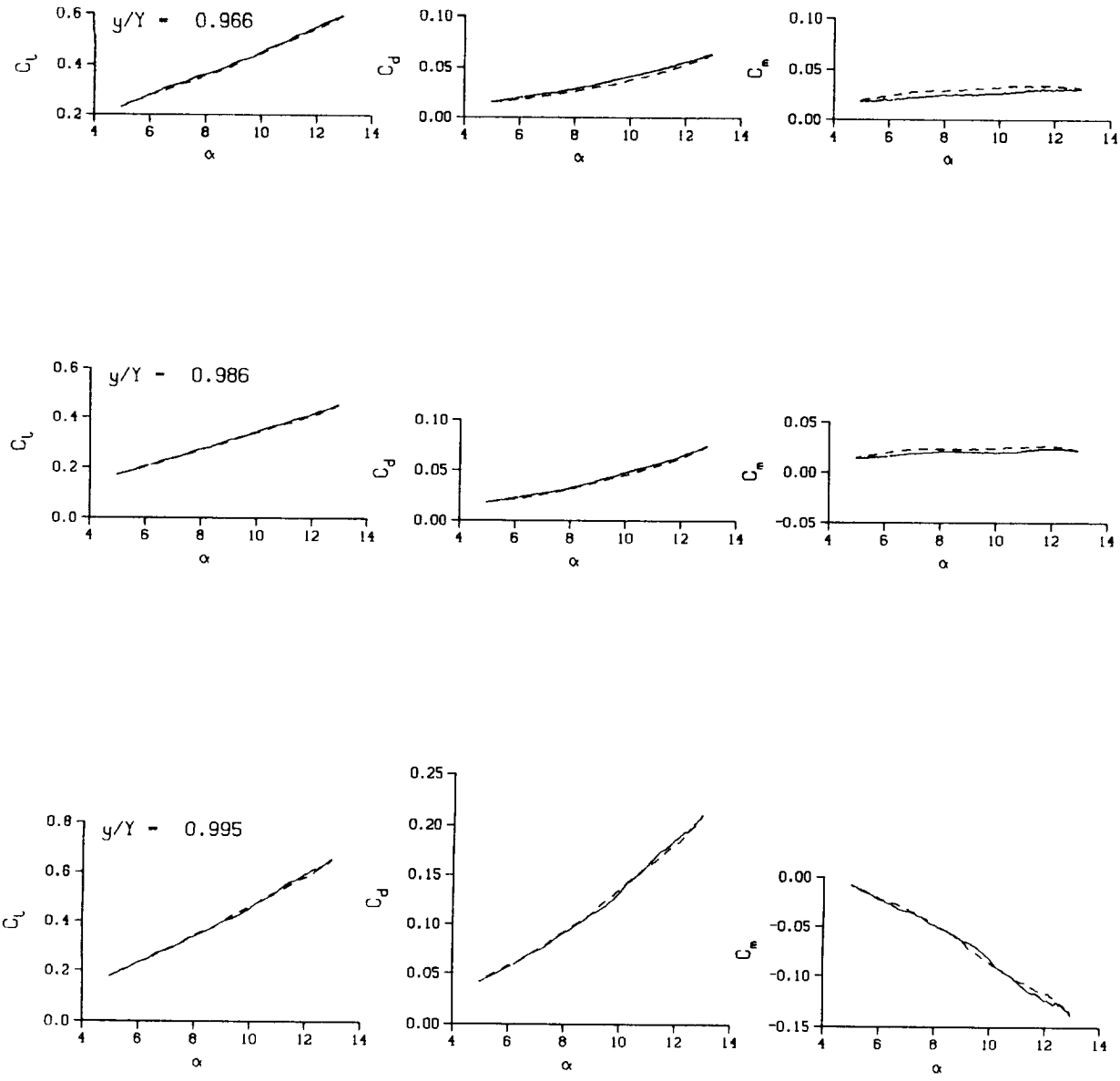

(a) v = 0.04. Concluded

Figure 80. Continued.

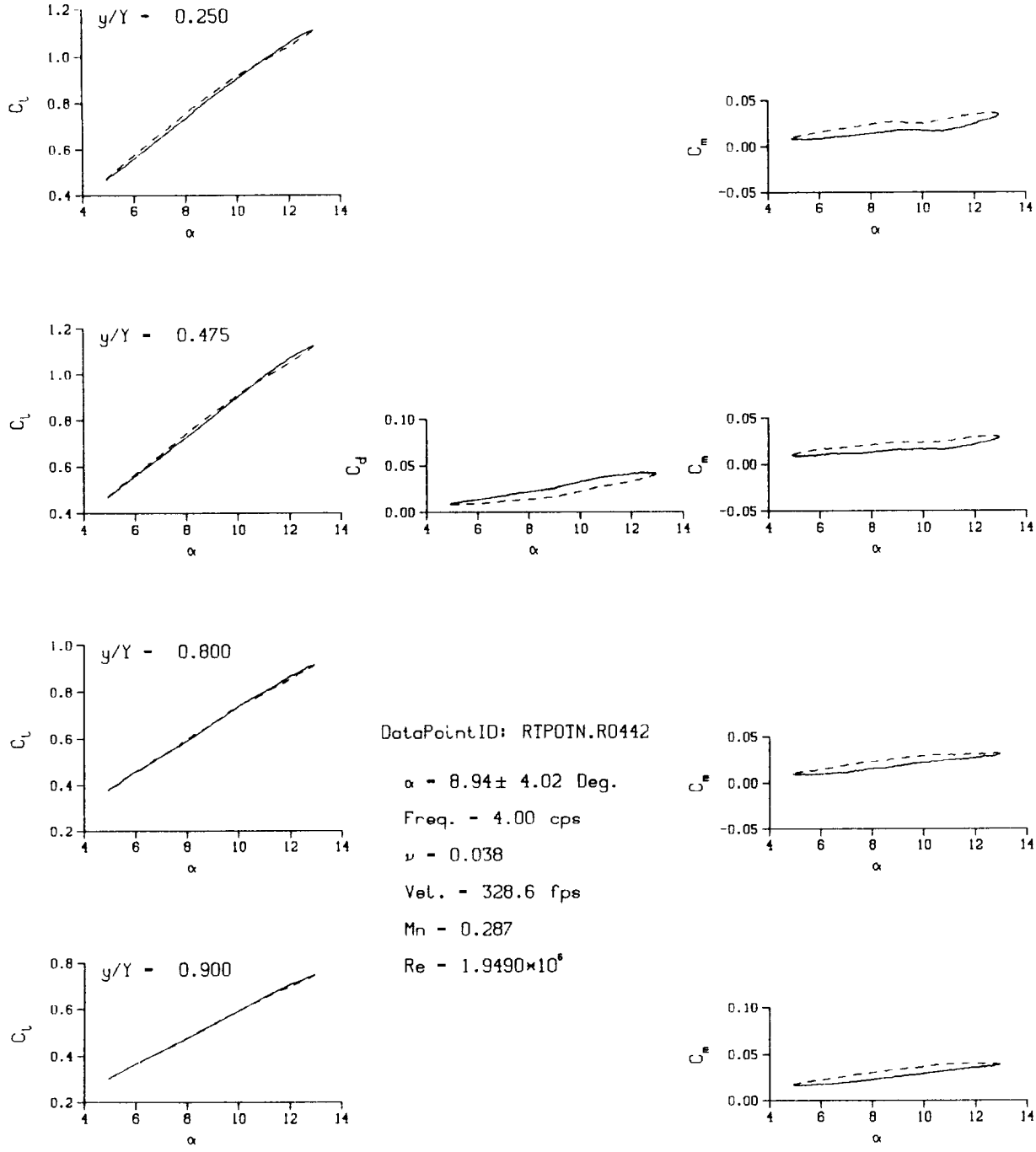

(a.1) v = 0.04; repeat

Figure 80. Continued.

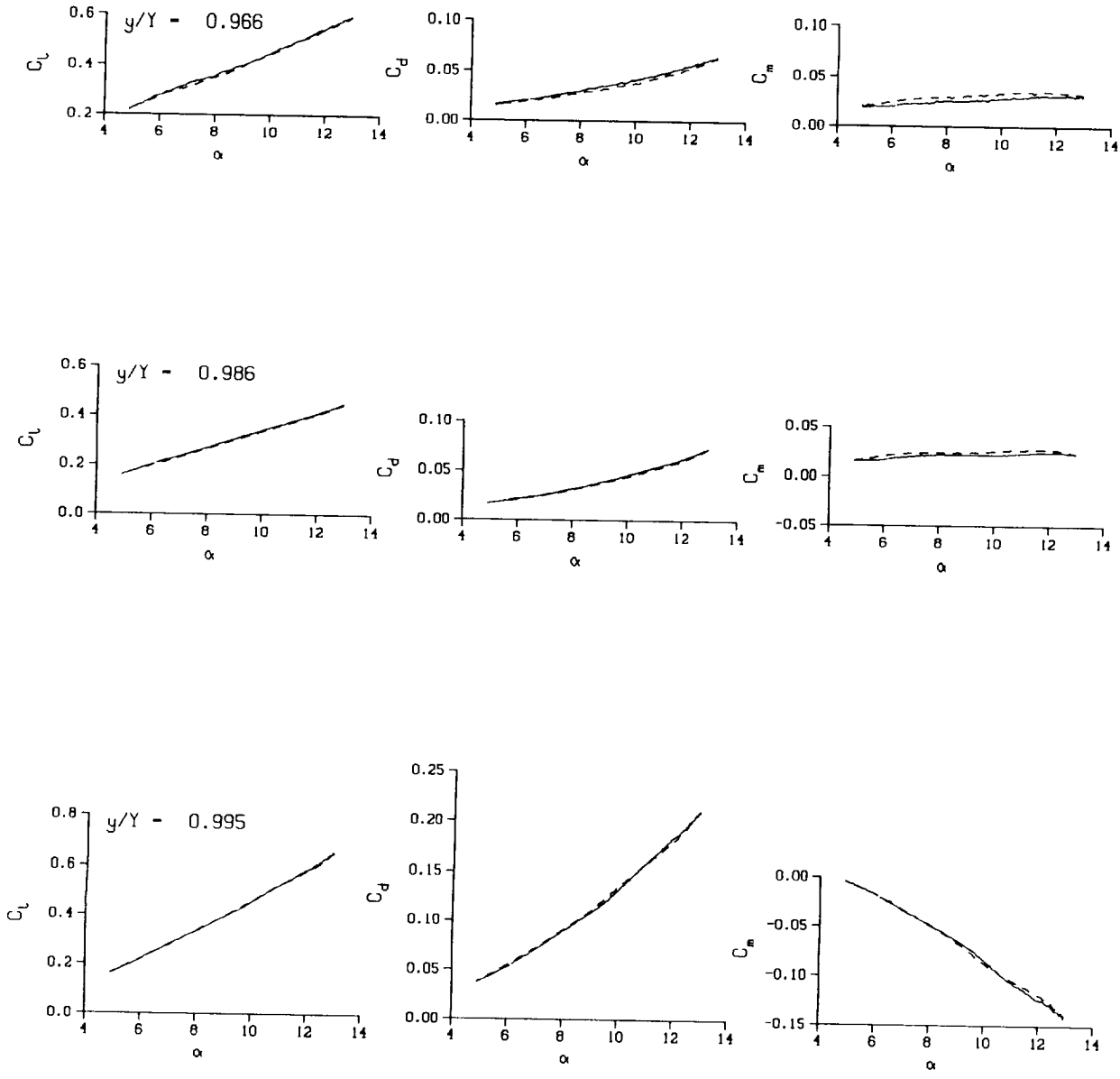

(a.1) v = 0.04; repeat. Concluded

Figure 80. Continued.

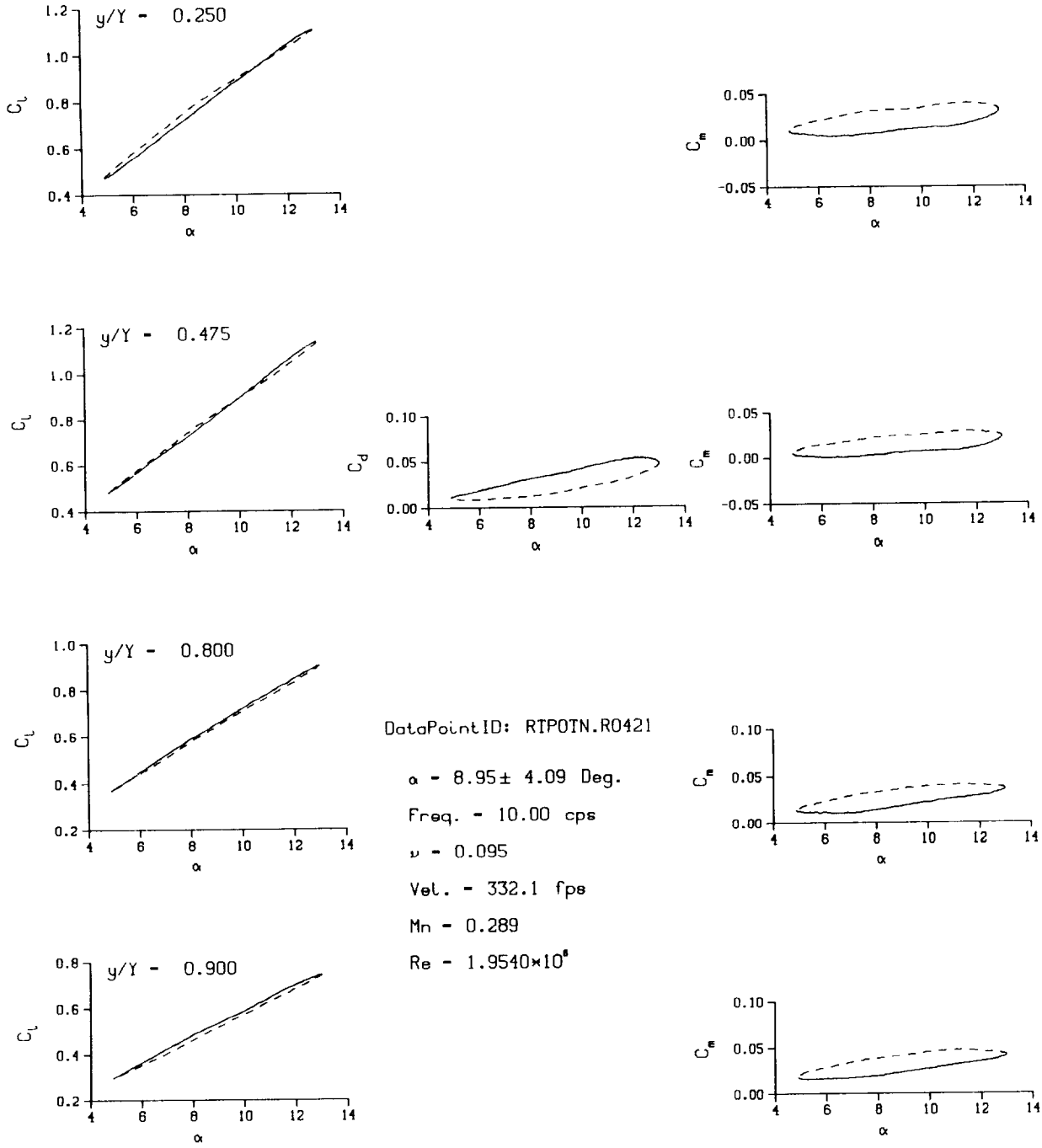

(b) v = 0.10

Figure 80. Continued.

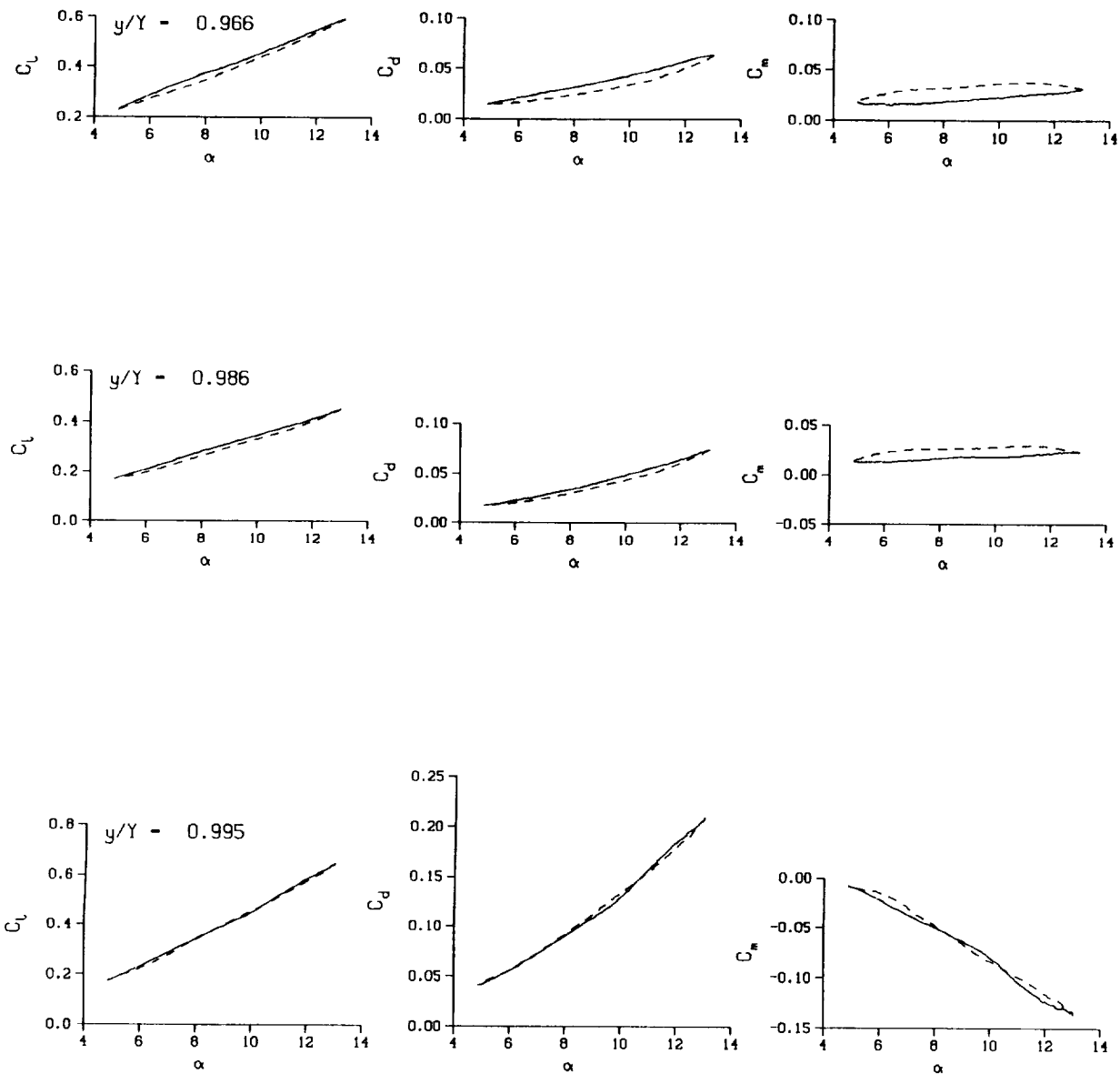

(b) v = 0.10. Concluded

Figure 80. Continued.

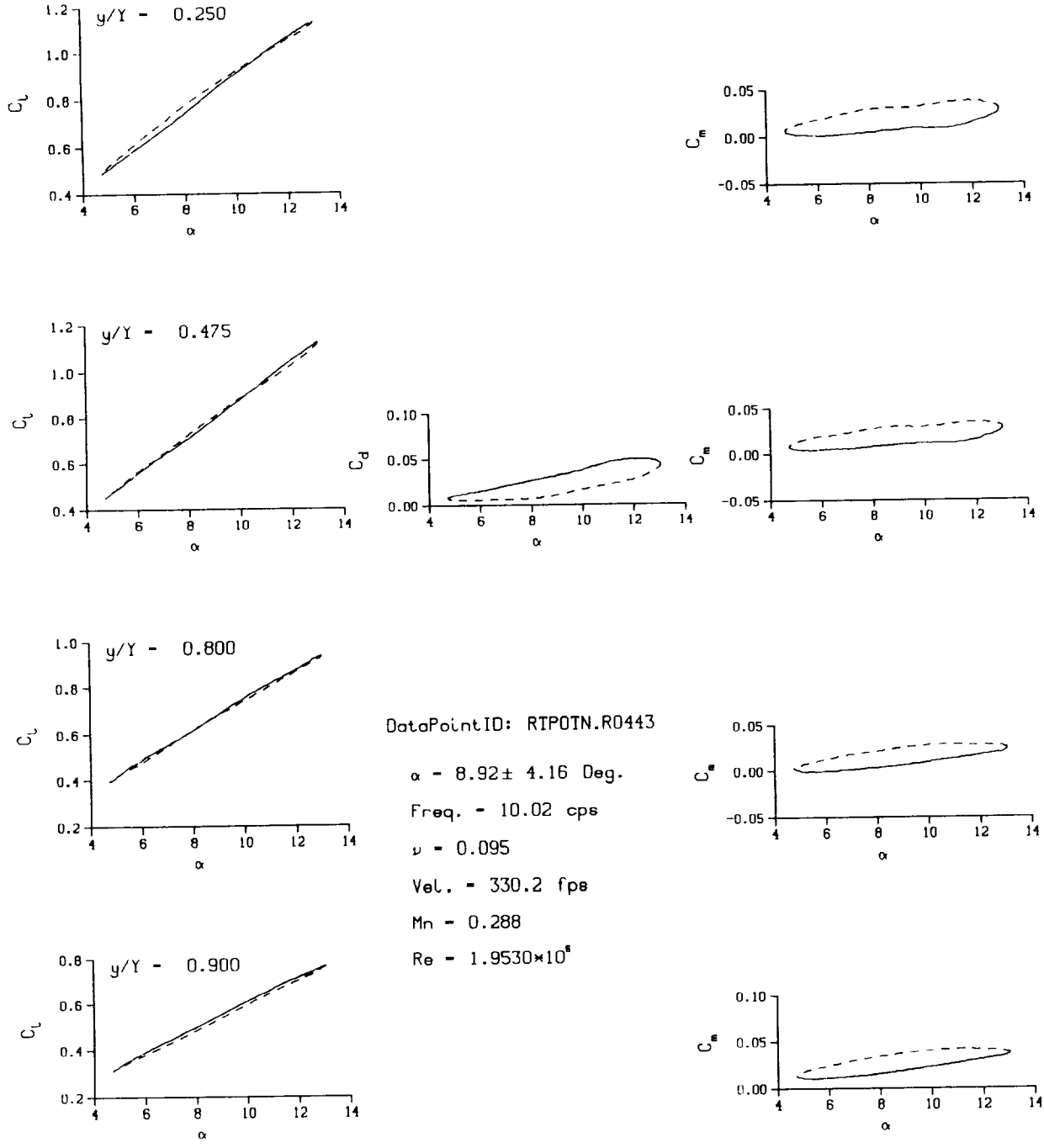

(b.1) v = 0.10; repeat

Figure 80. Continued.

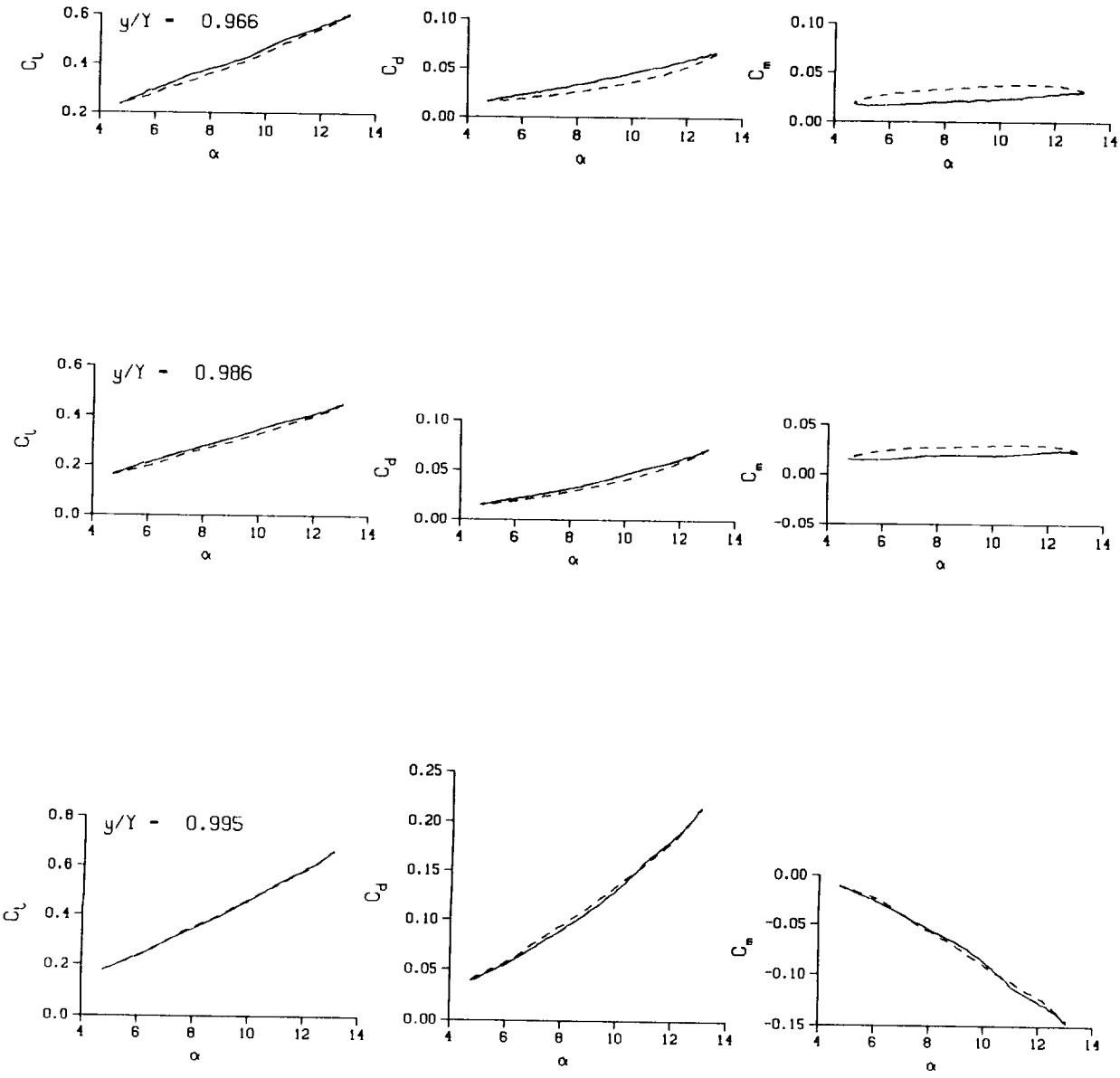

(b.1) v = 0.10; repeat. Concluded

Figure 80. Continued.

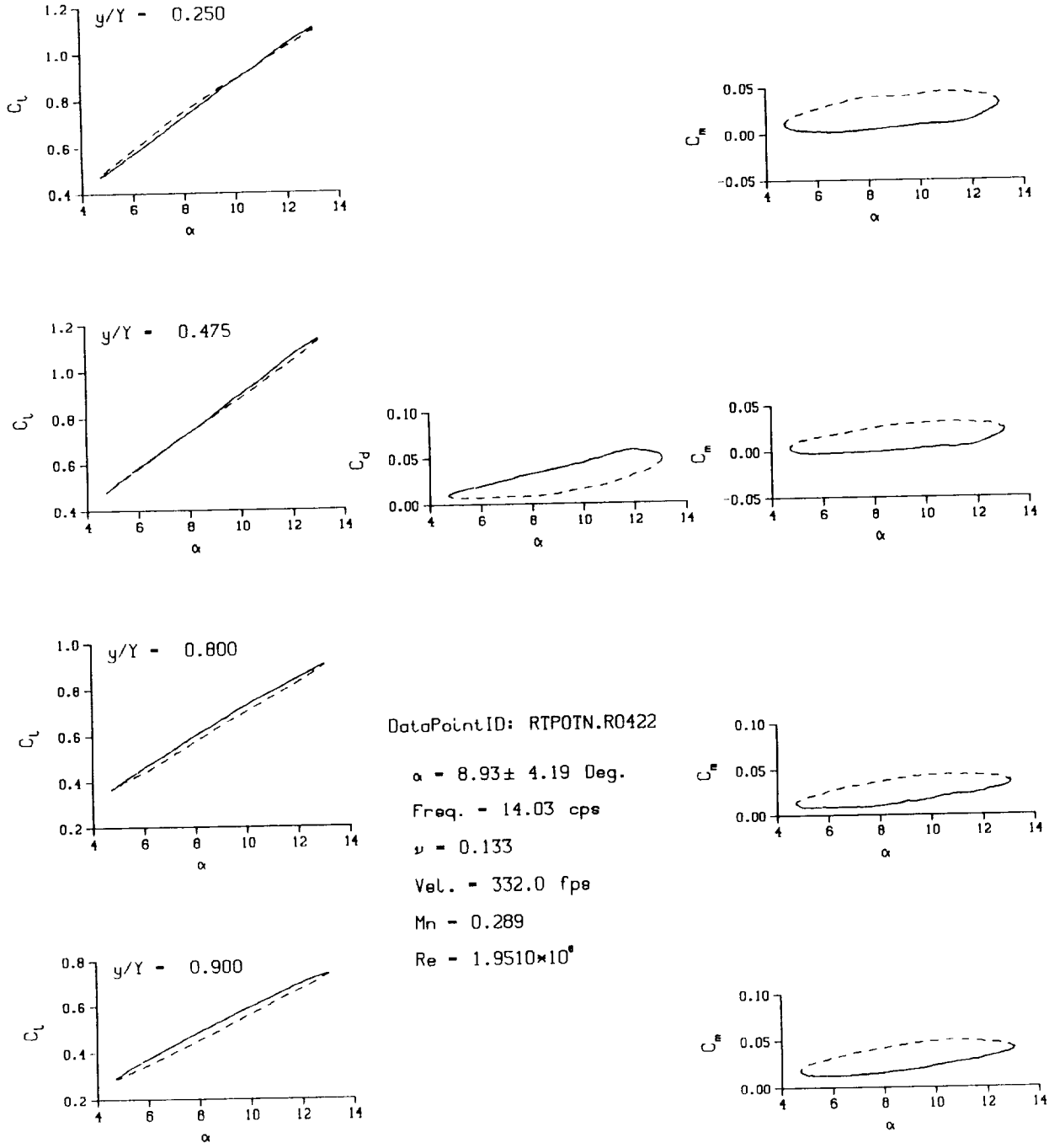

(c) v = 0.14

Figure 80. Continued.

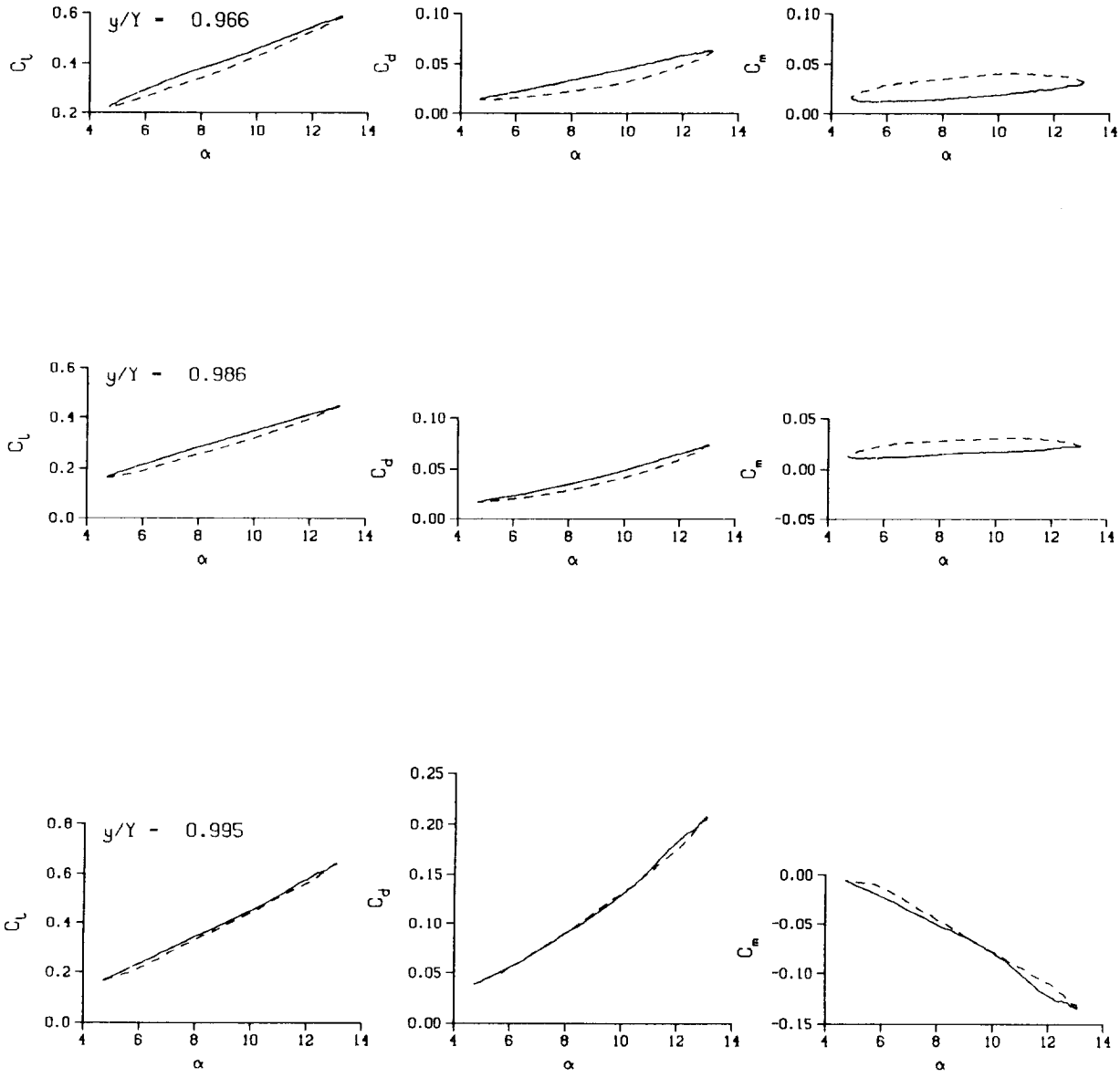

(c) v = 0.14. Concluded

Figure 80. Continued.

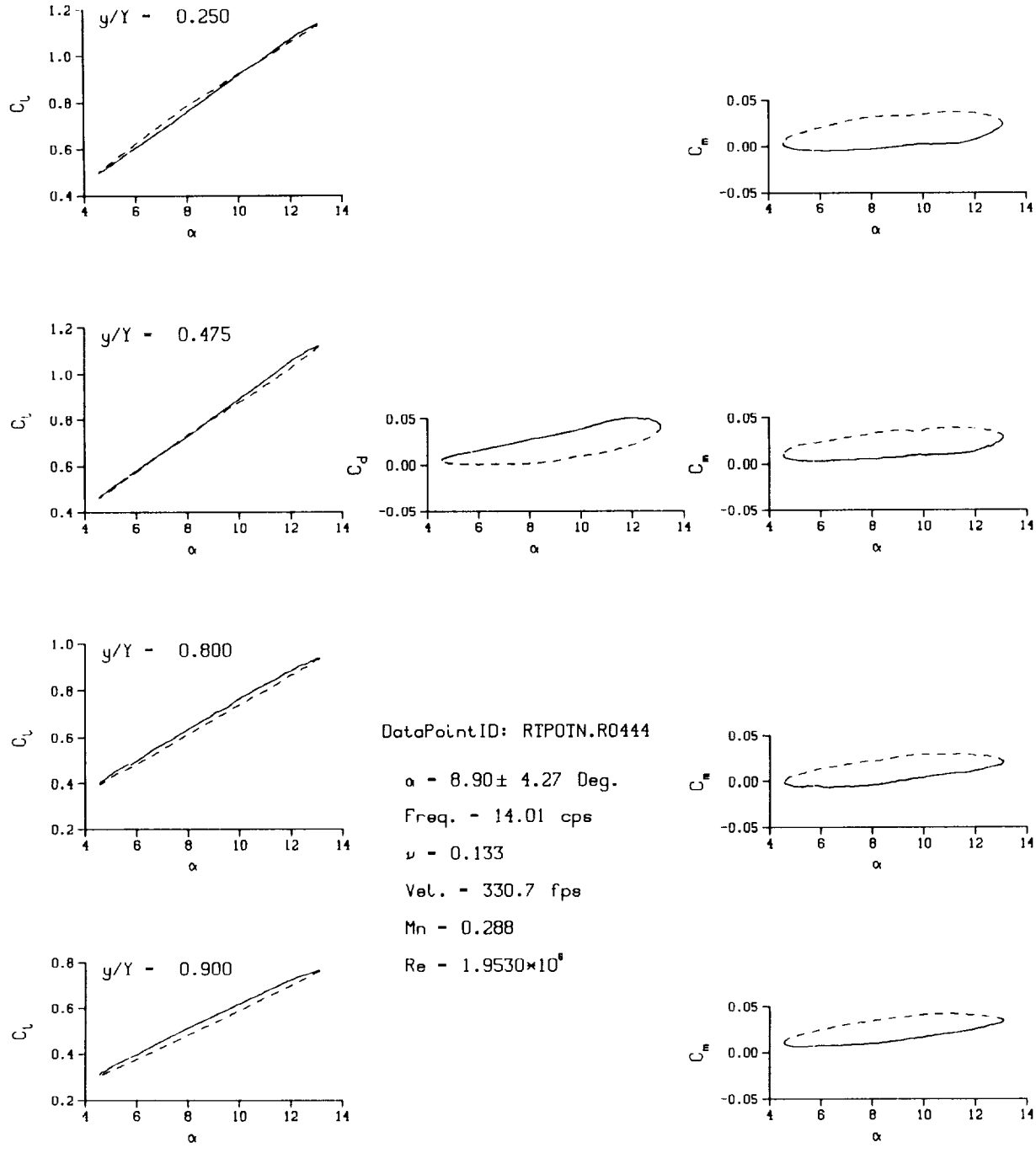

(c.1) v = 0.14; repeat

Figure 80. Continued.

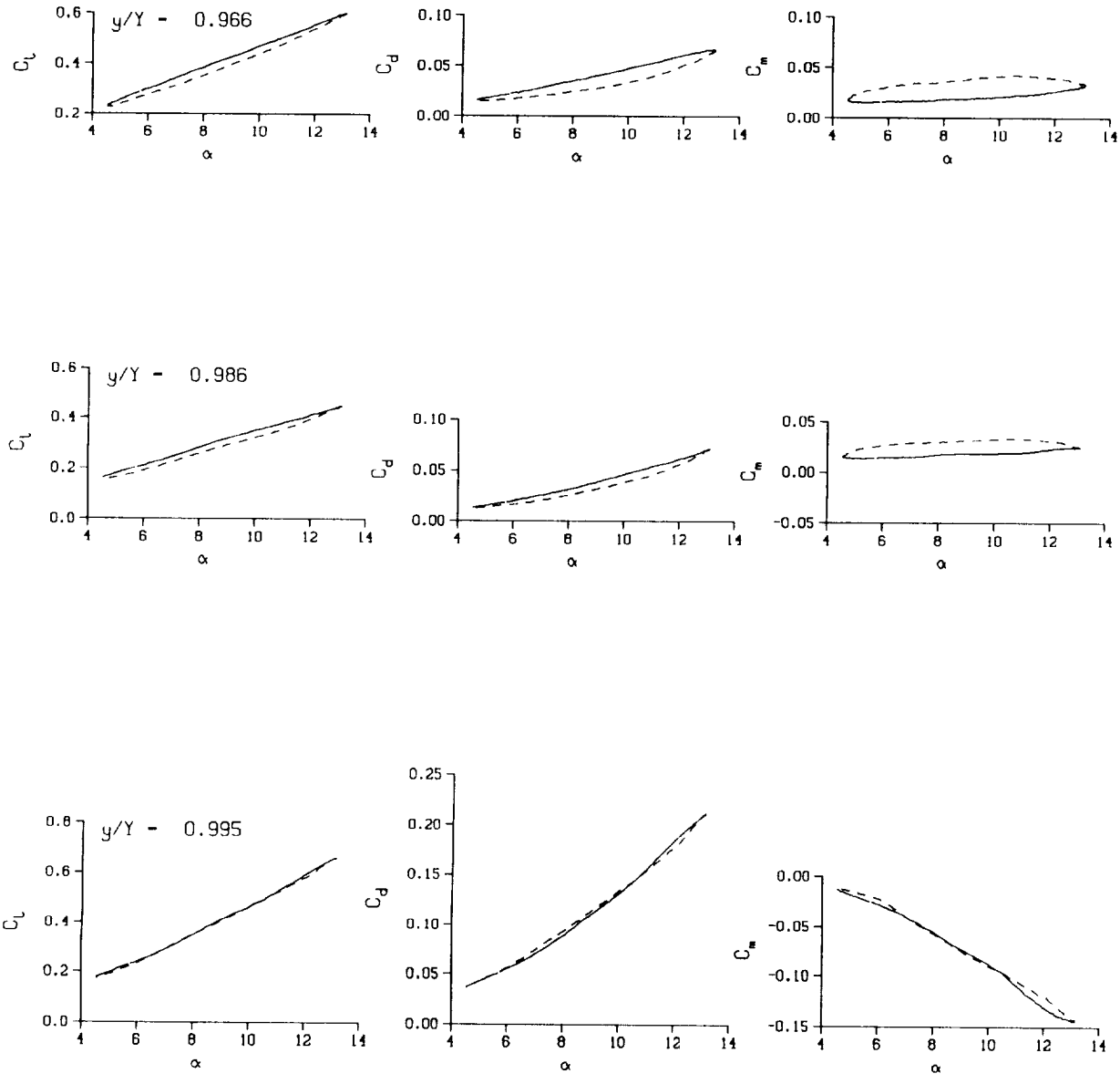

(c.1) v = 0.14; repeat. Concluded

Figure 80. Concluded.

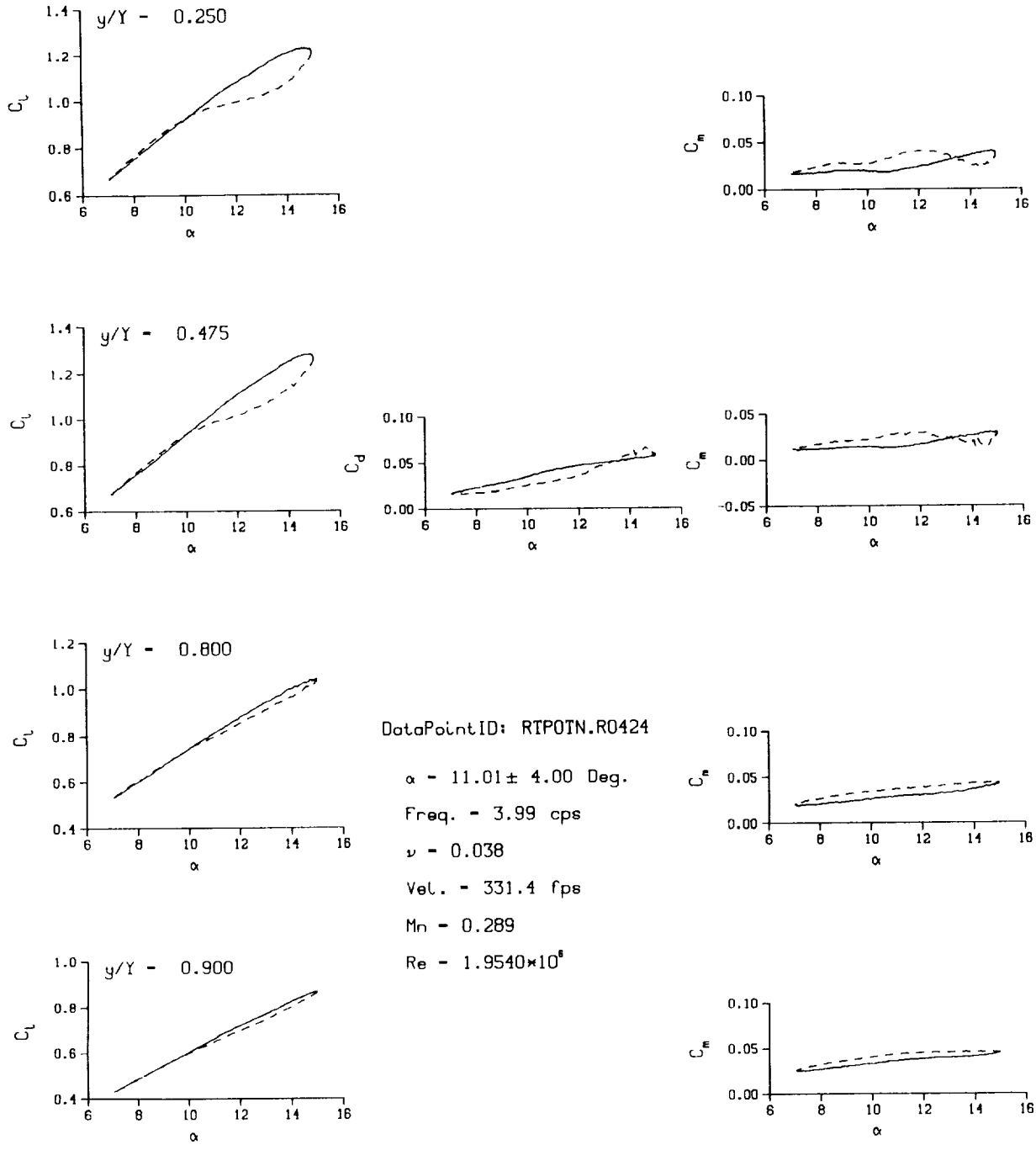

(a) v = 0.04

Figure 81. 3-D round tip pitch oscillation data; no BL-trip; α = 11 ± 4 deg.

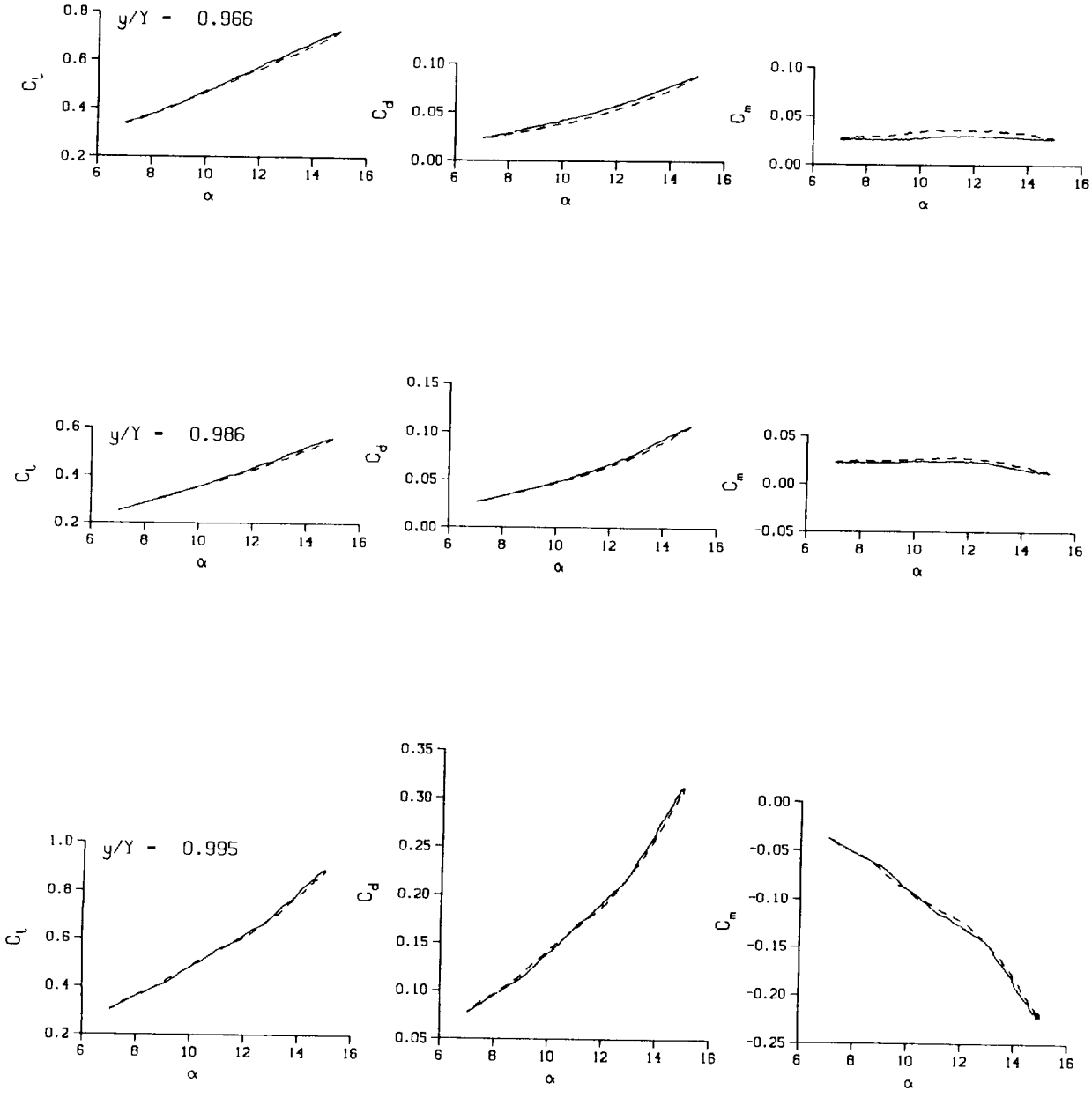

(a) v = 0.04. Concluded

Figure 81. Continued.

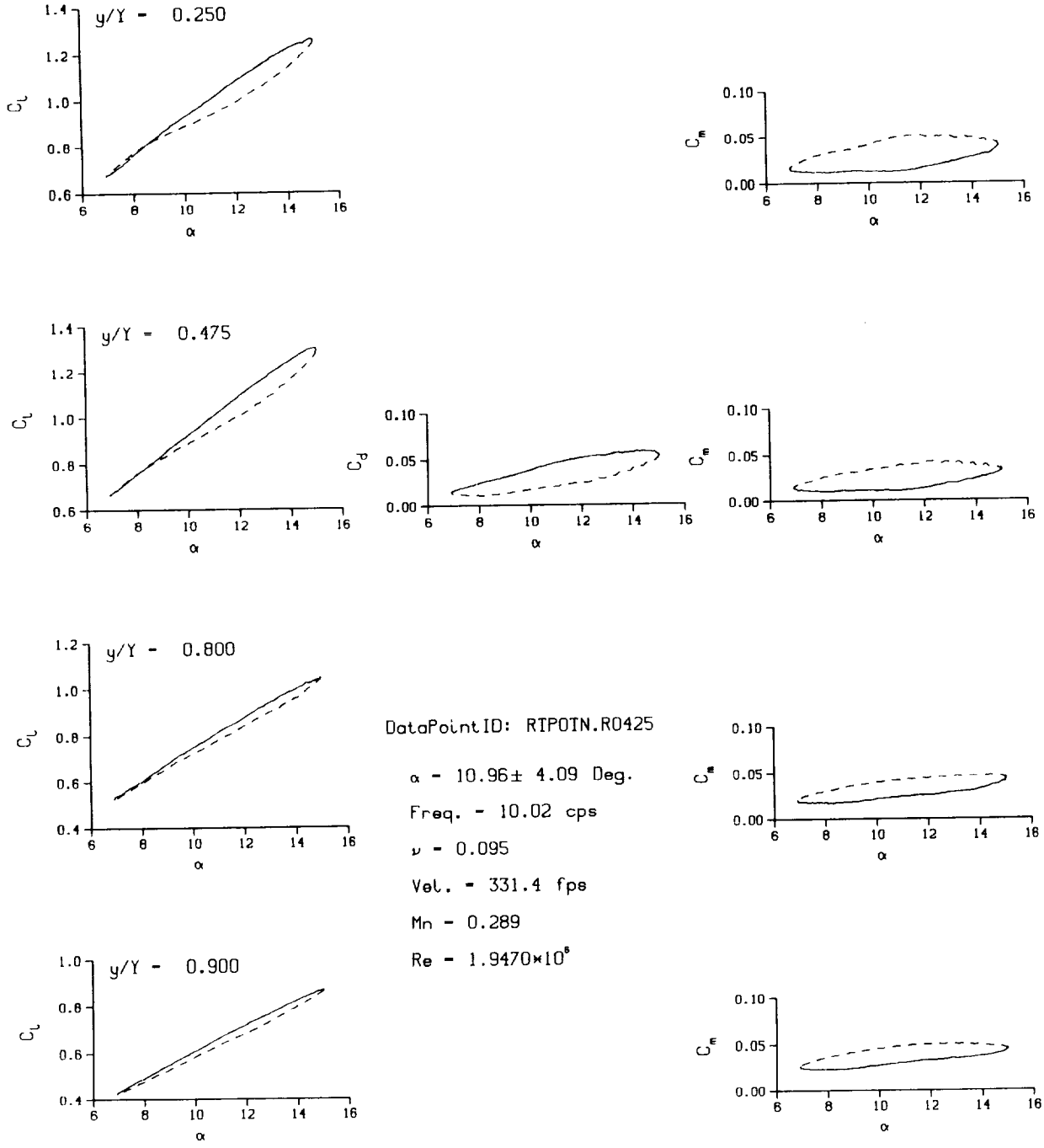

(b) v = 0.10

Figure 81. Continued.

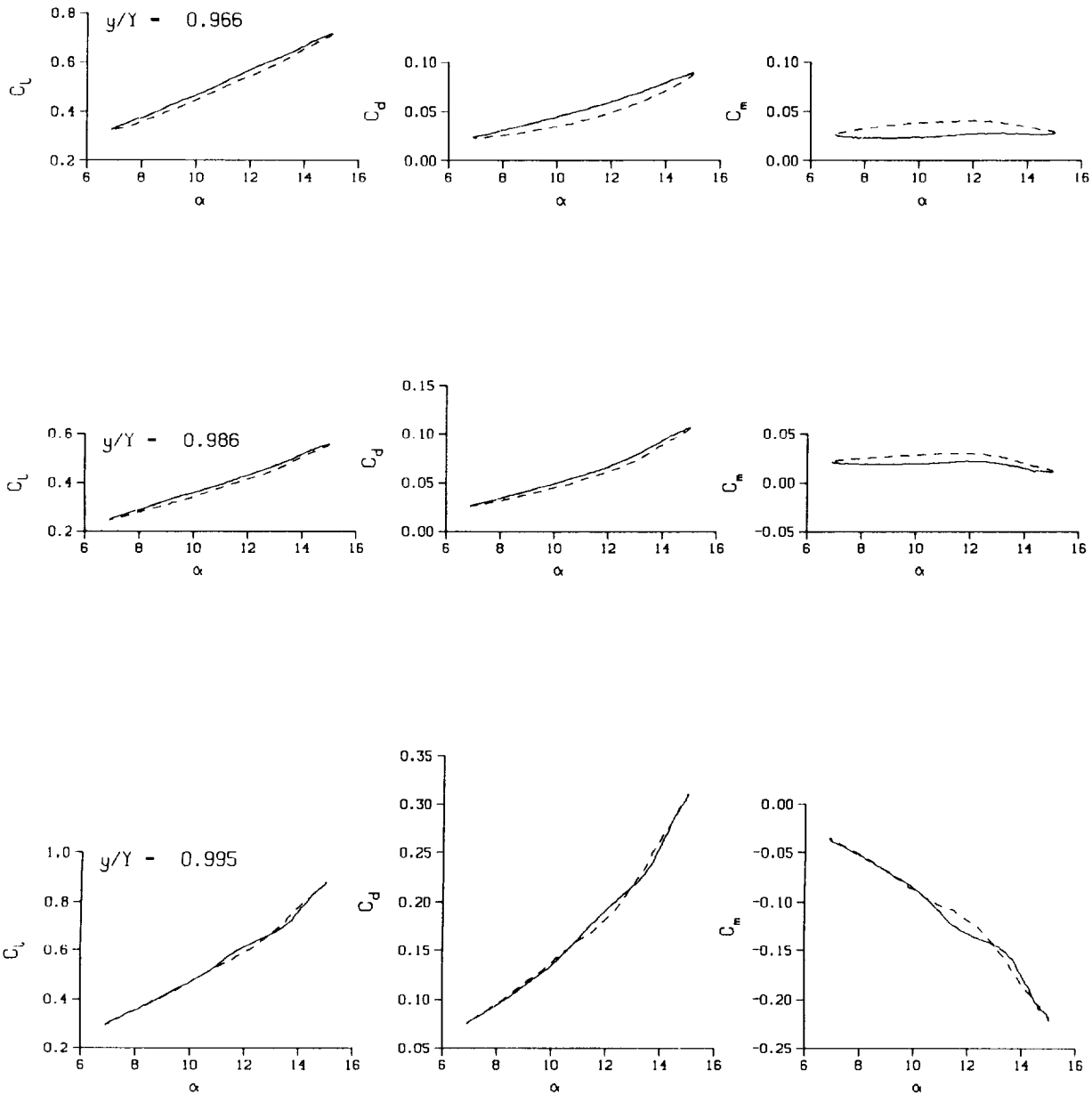

(b) v = 0.10. Concluded

Figure 81. Continued.

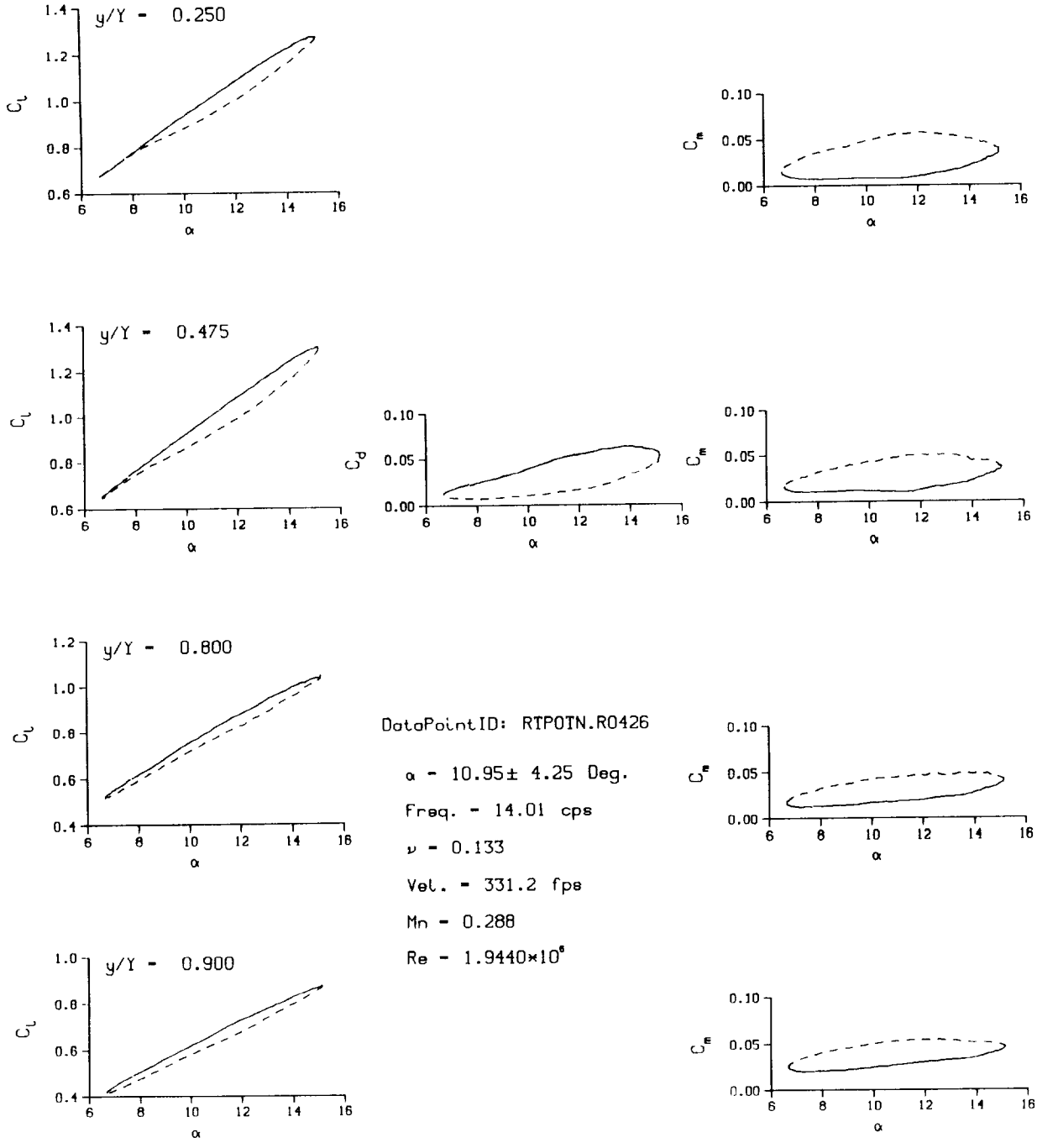

(c) ν = 0.14

Figure 81. Continued.

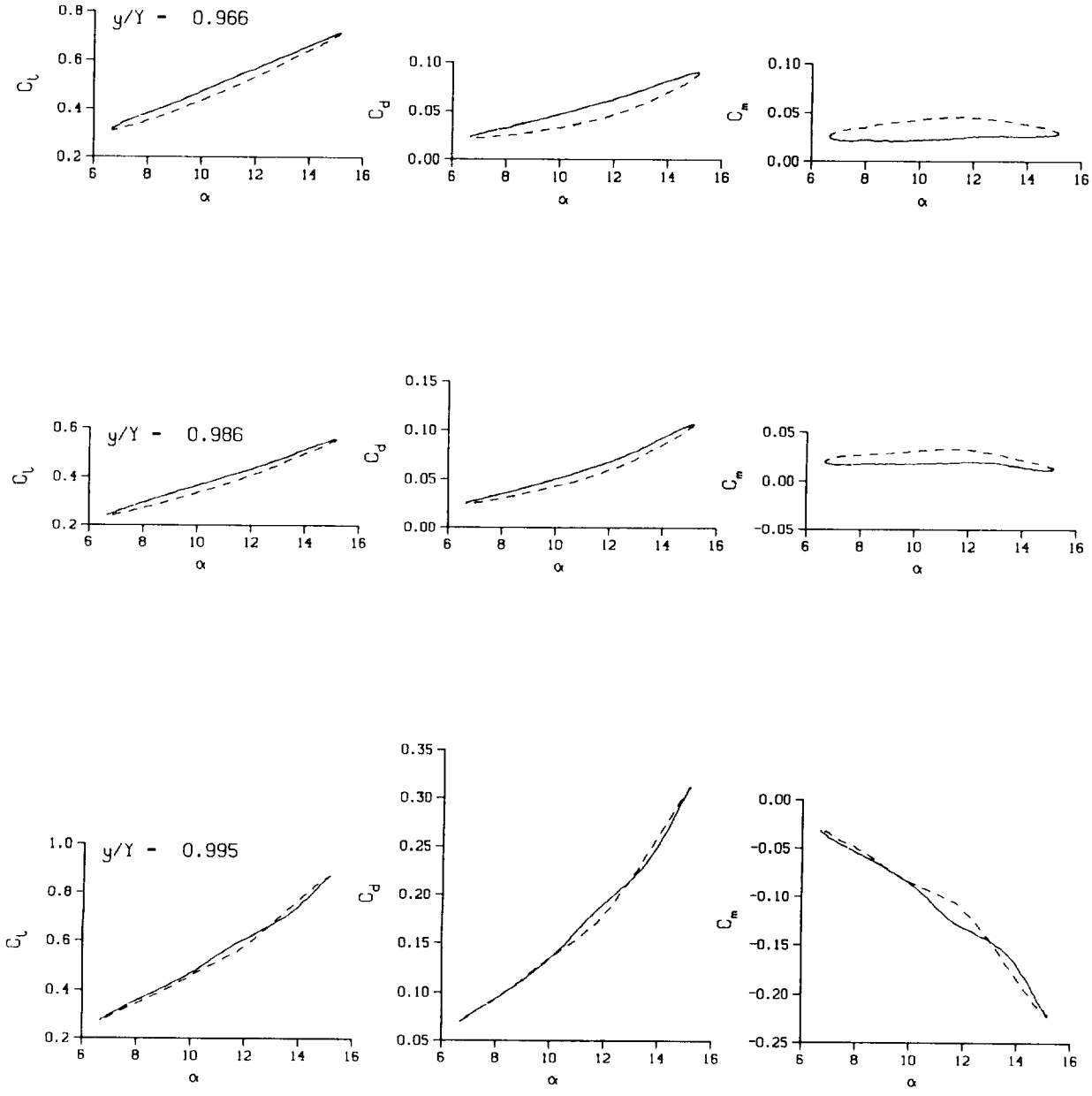

(c) v = 0.14. Concluded

Figure 81. Concluded.

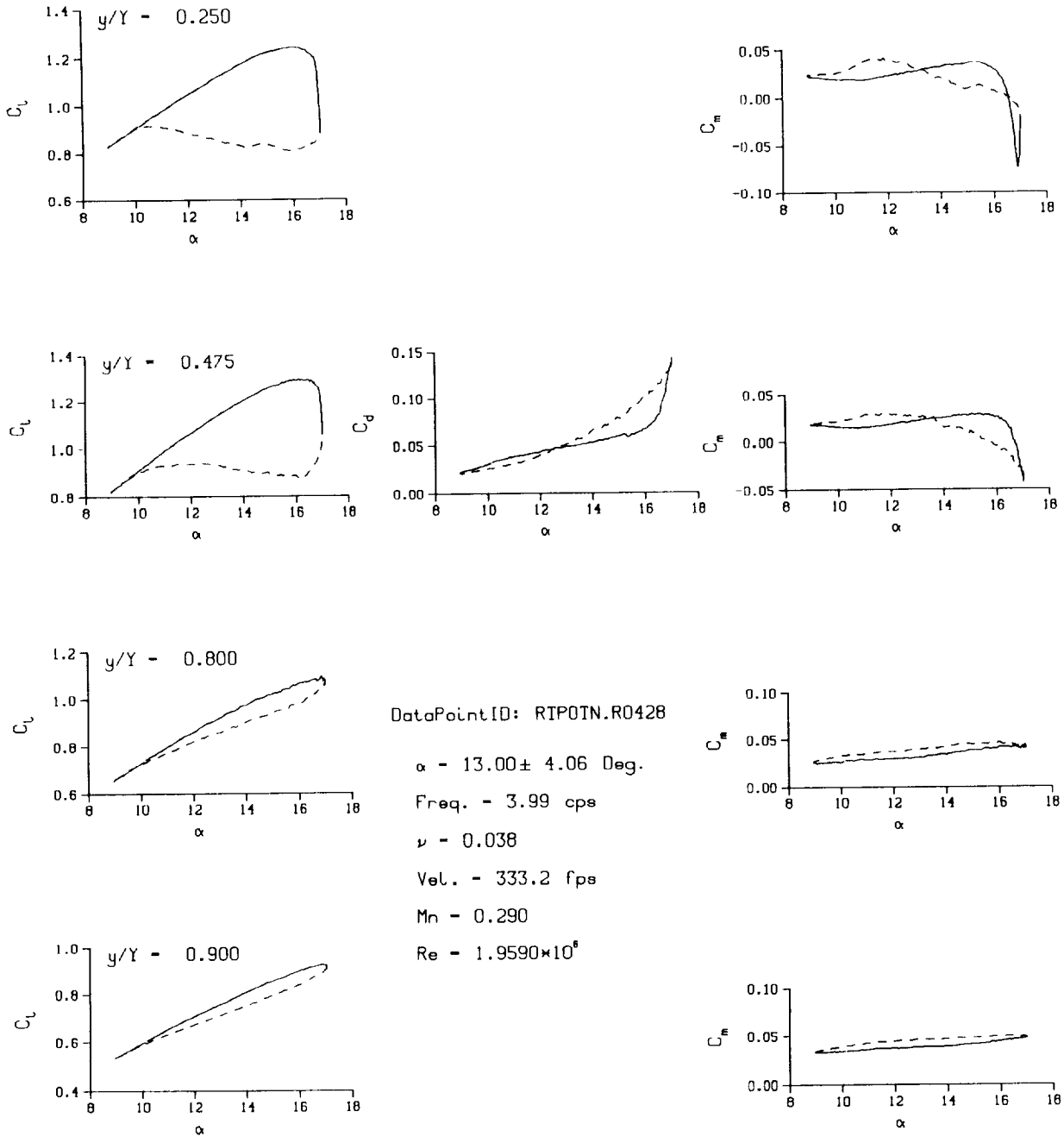

(a) ν = 0.04

Figure 82. 3-D round tip pitch oscillation data; no BL-trip; α = 13 ± 4 deg.

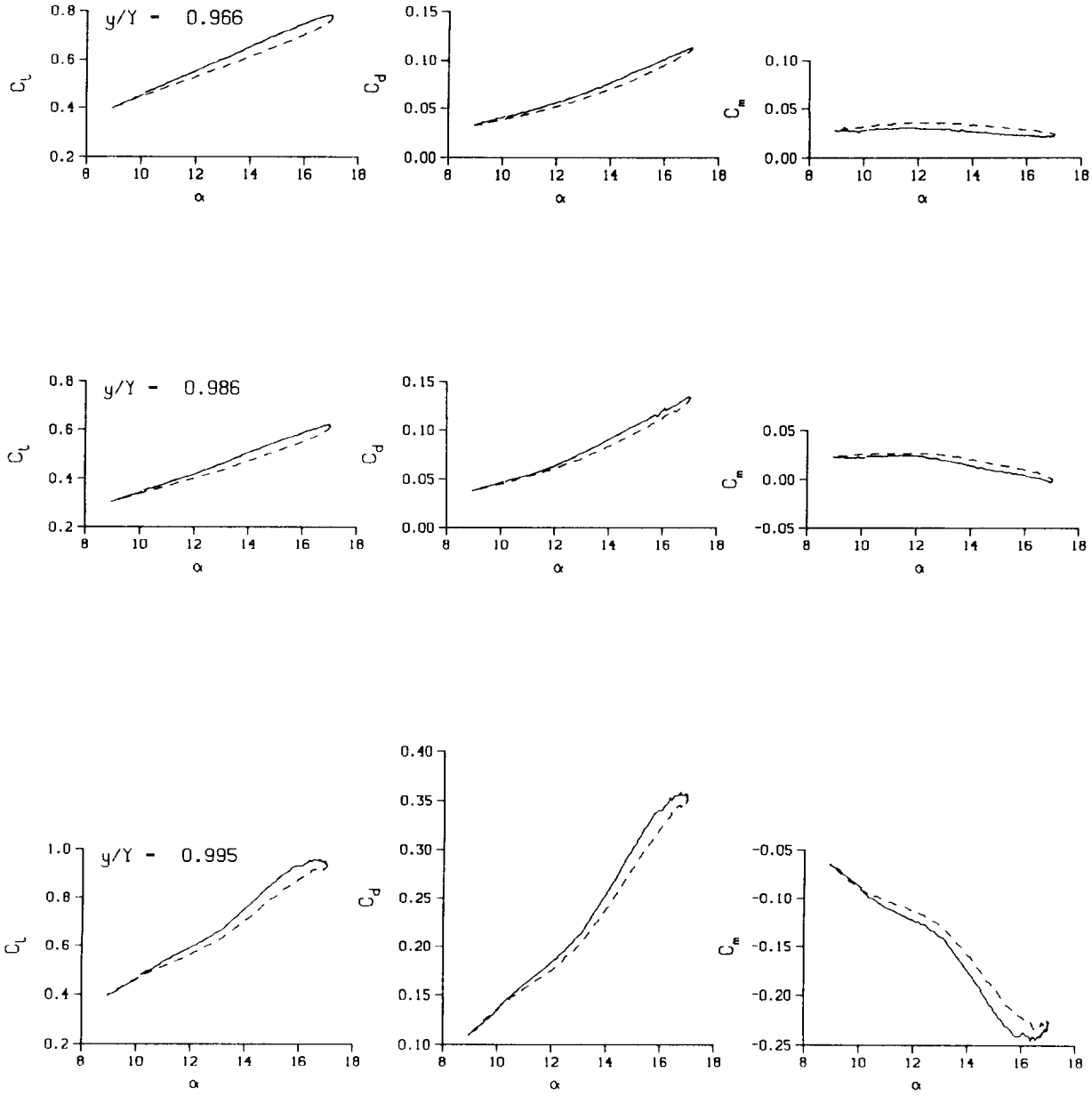

(a) v = 0.04. Concluded

Figure 82. Continued.

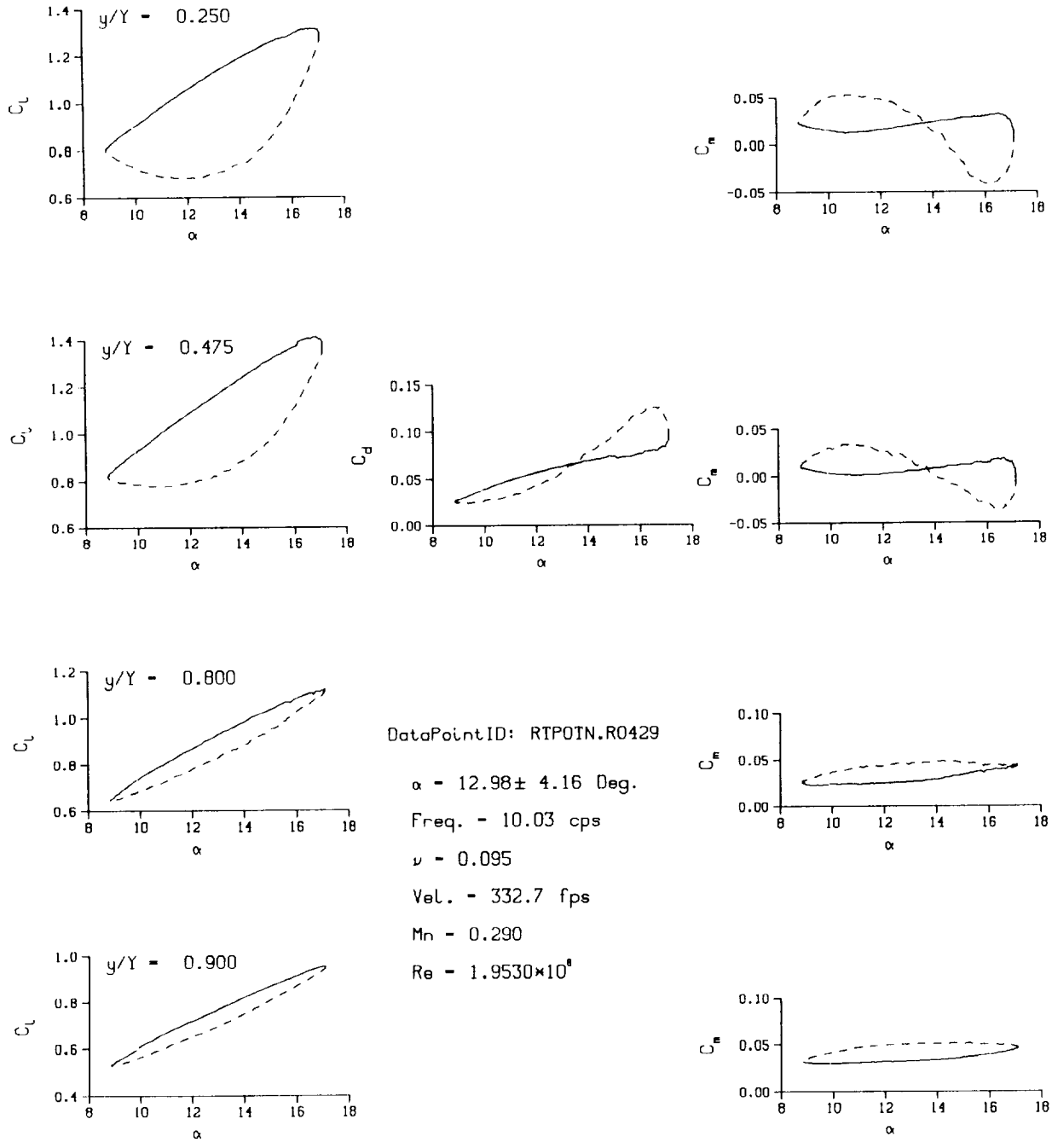

(b) v = 0.10

Figure 82. Continued.

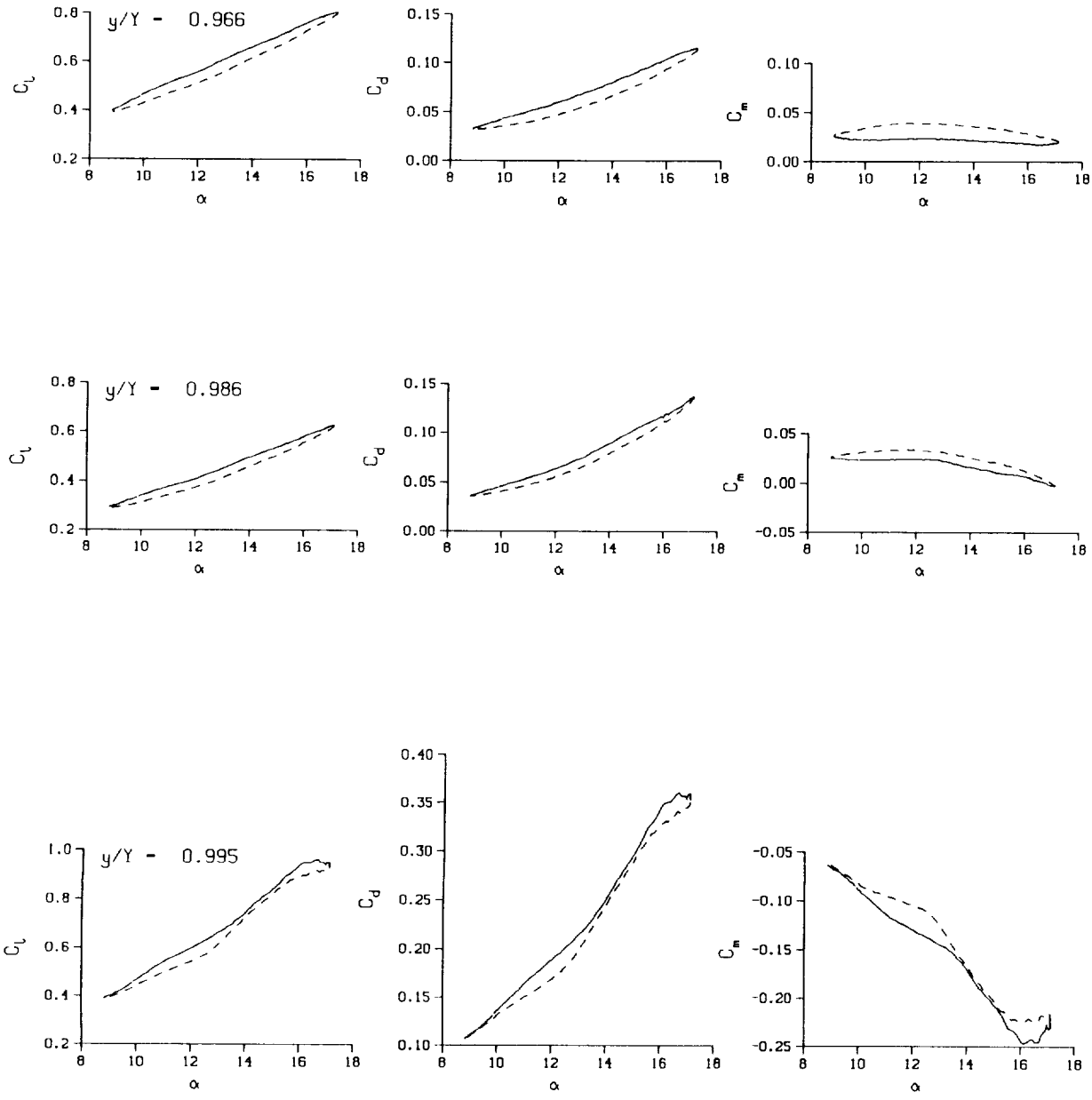

(b) v = 0.10. Concluded

Figure 82. Continued.

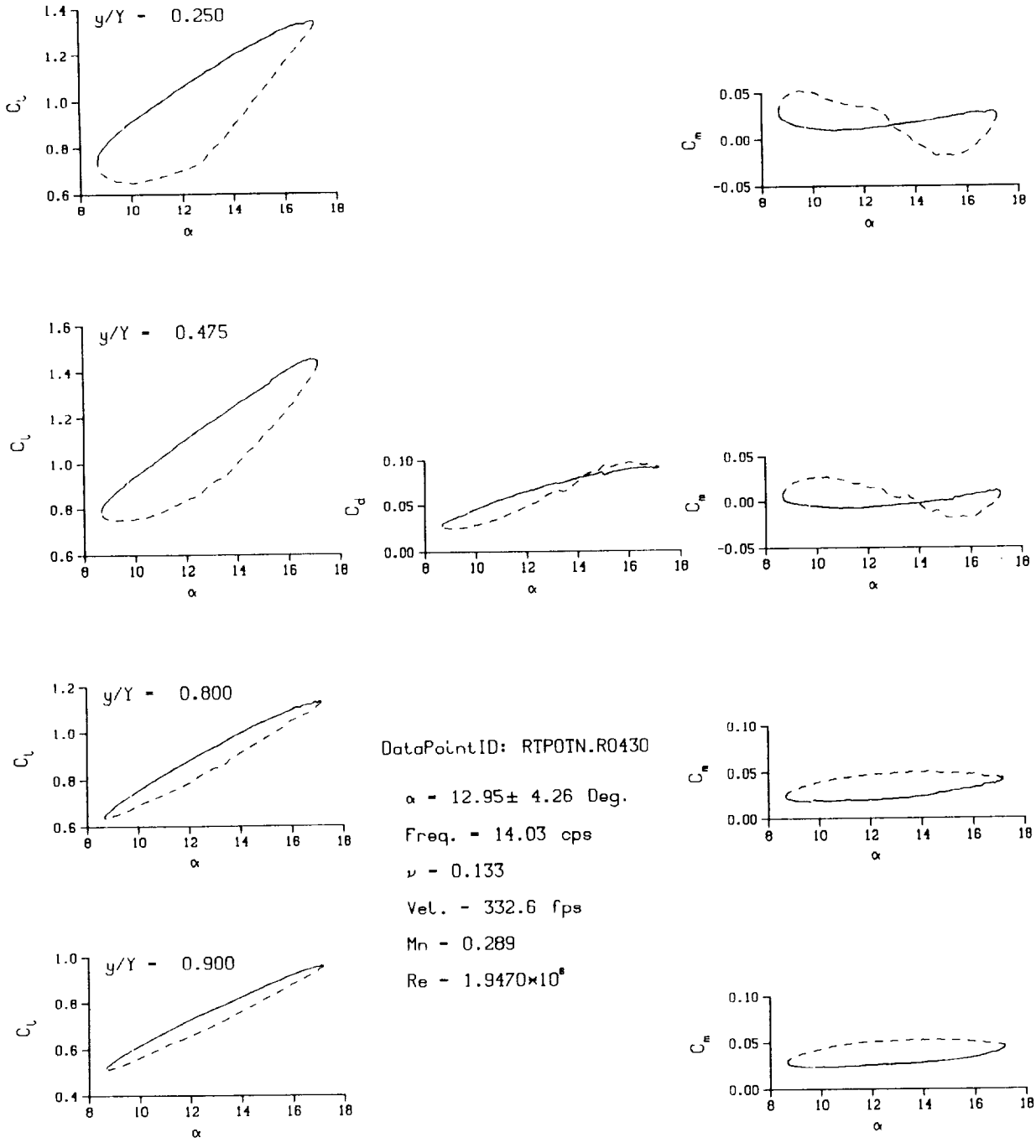

(c) v = 0.14

Figure 82. Continued.

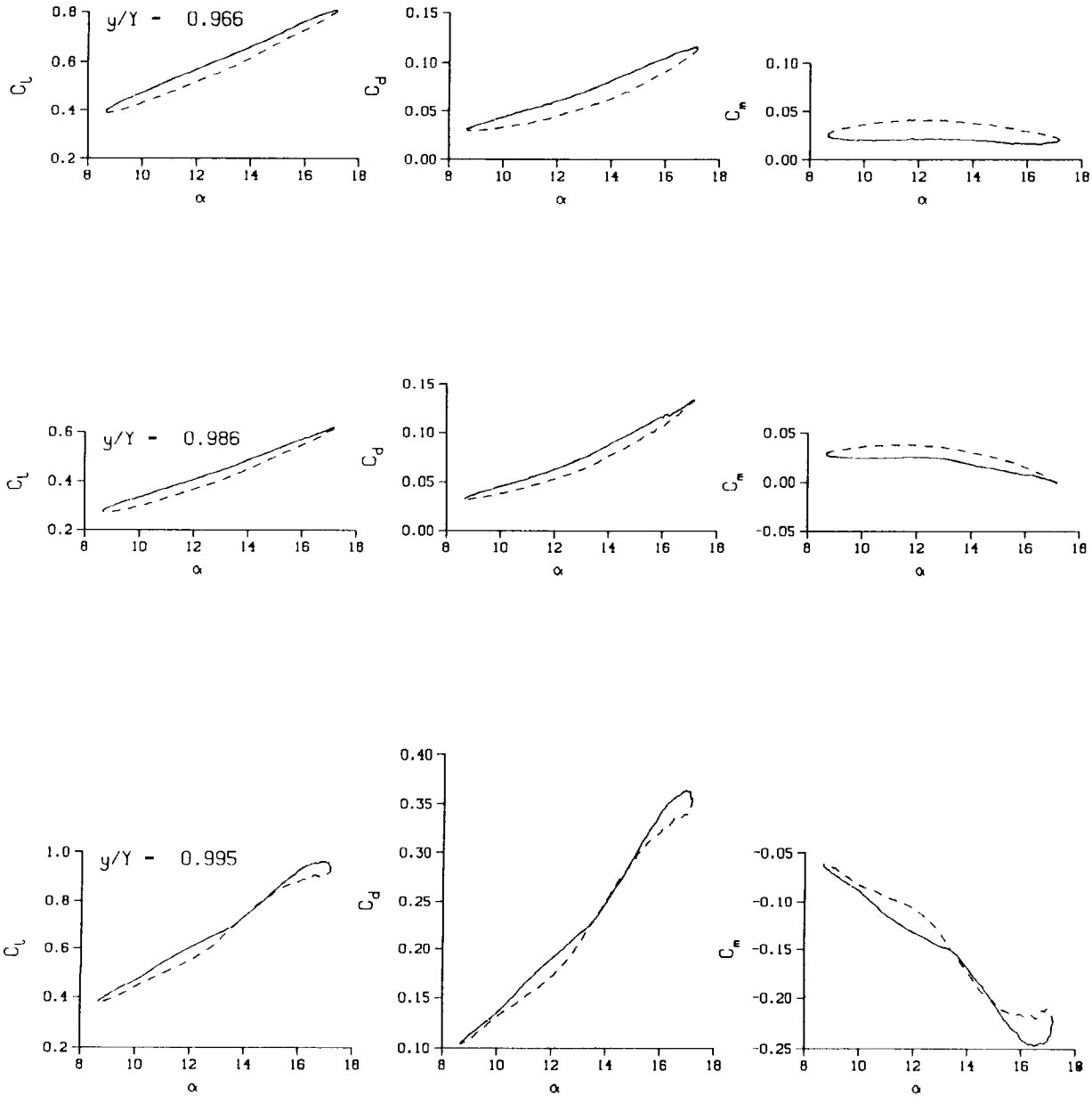

(c) v = 0.14. Concluded

Figure 82. Concluded.

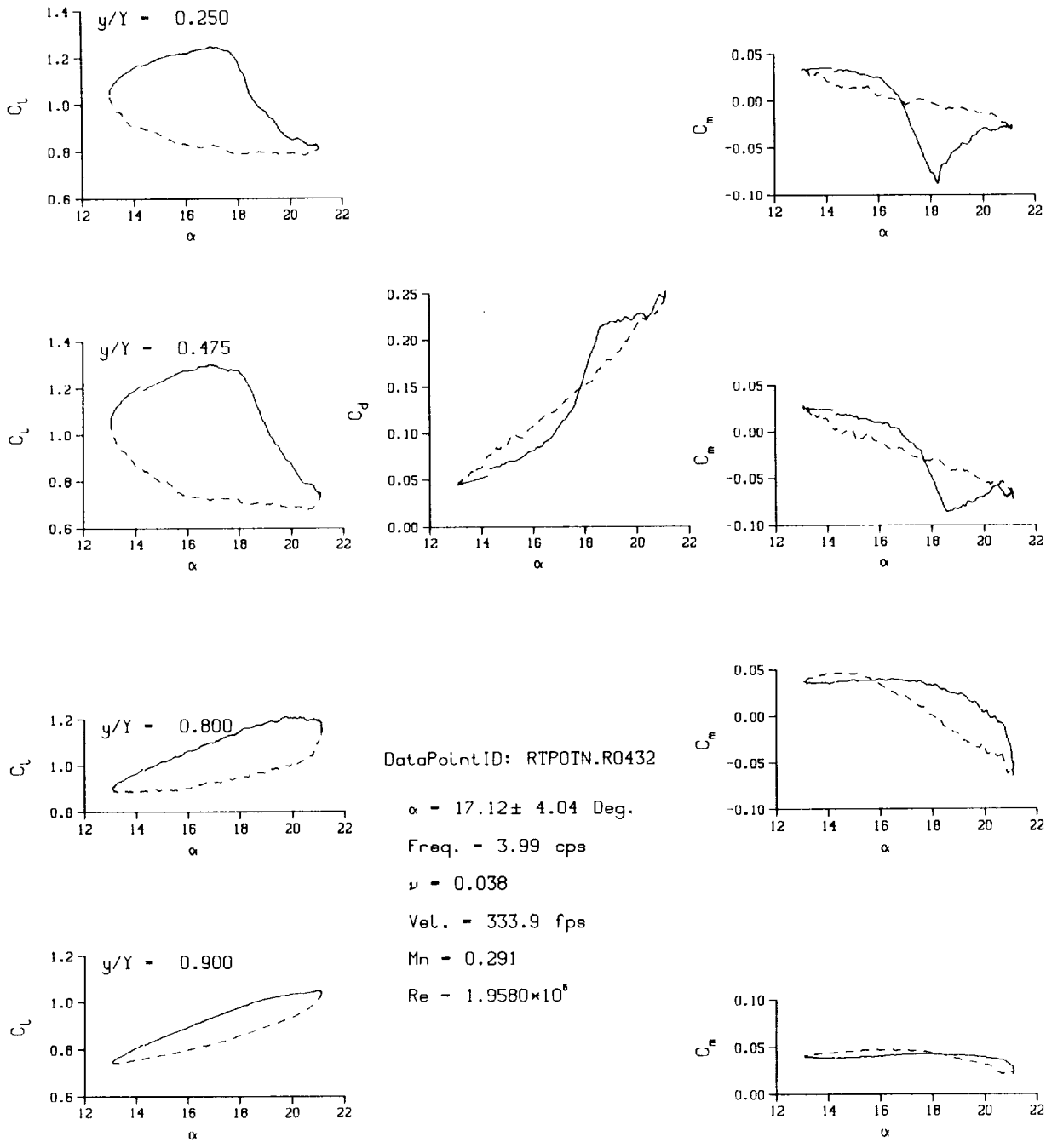

(a) ν = 0.04

Figure 83. 3-D round tip pitch oscillation data; no BL-trip; α = 17 ± 4 deg.

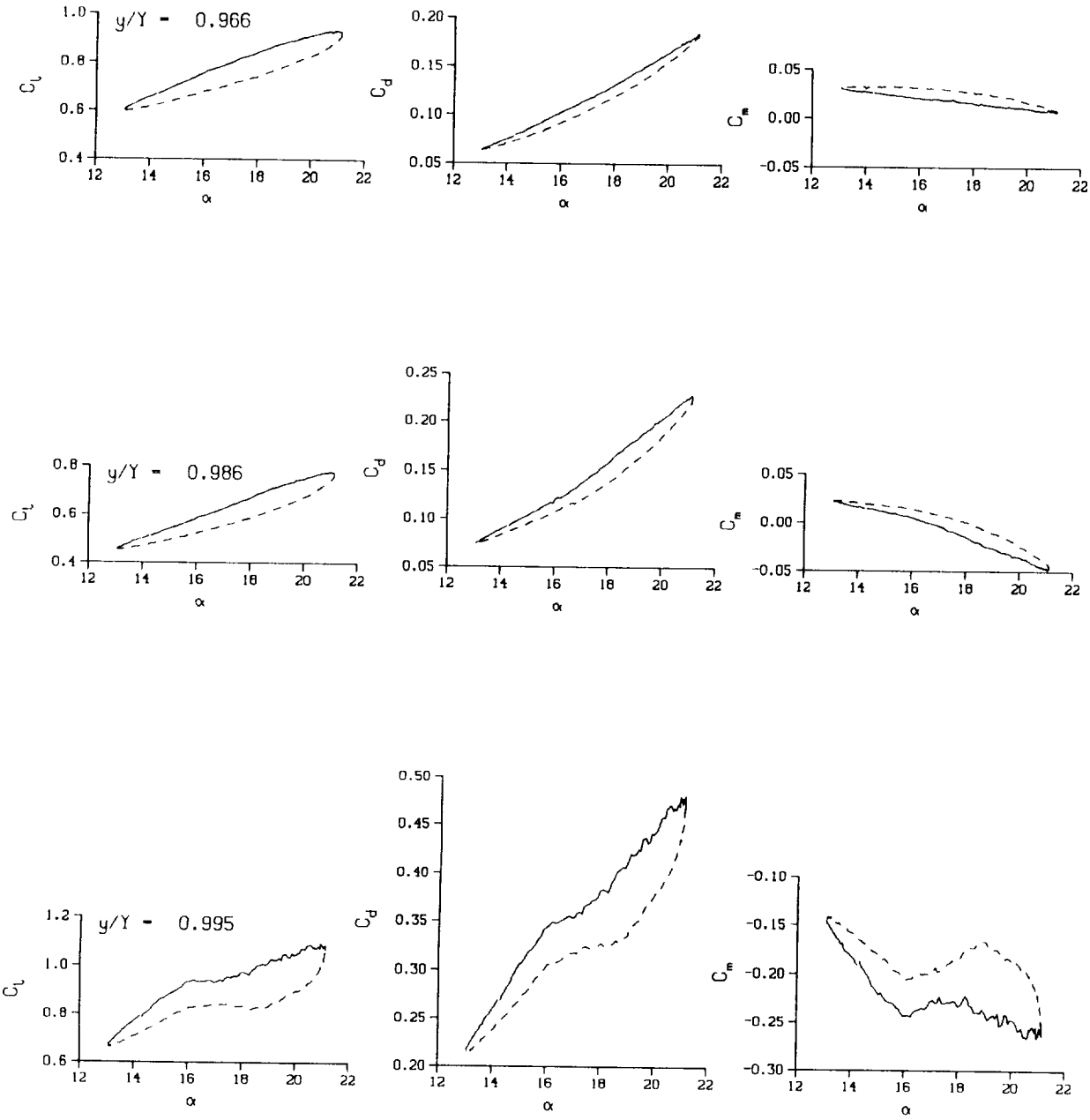

(a) v = 0.04. Concluded

Figure 83. Continued.

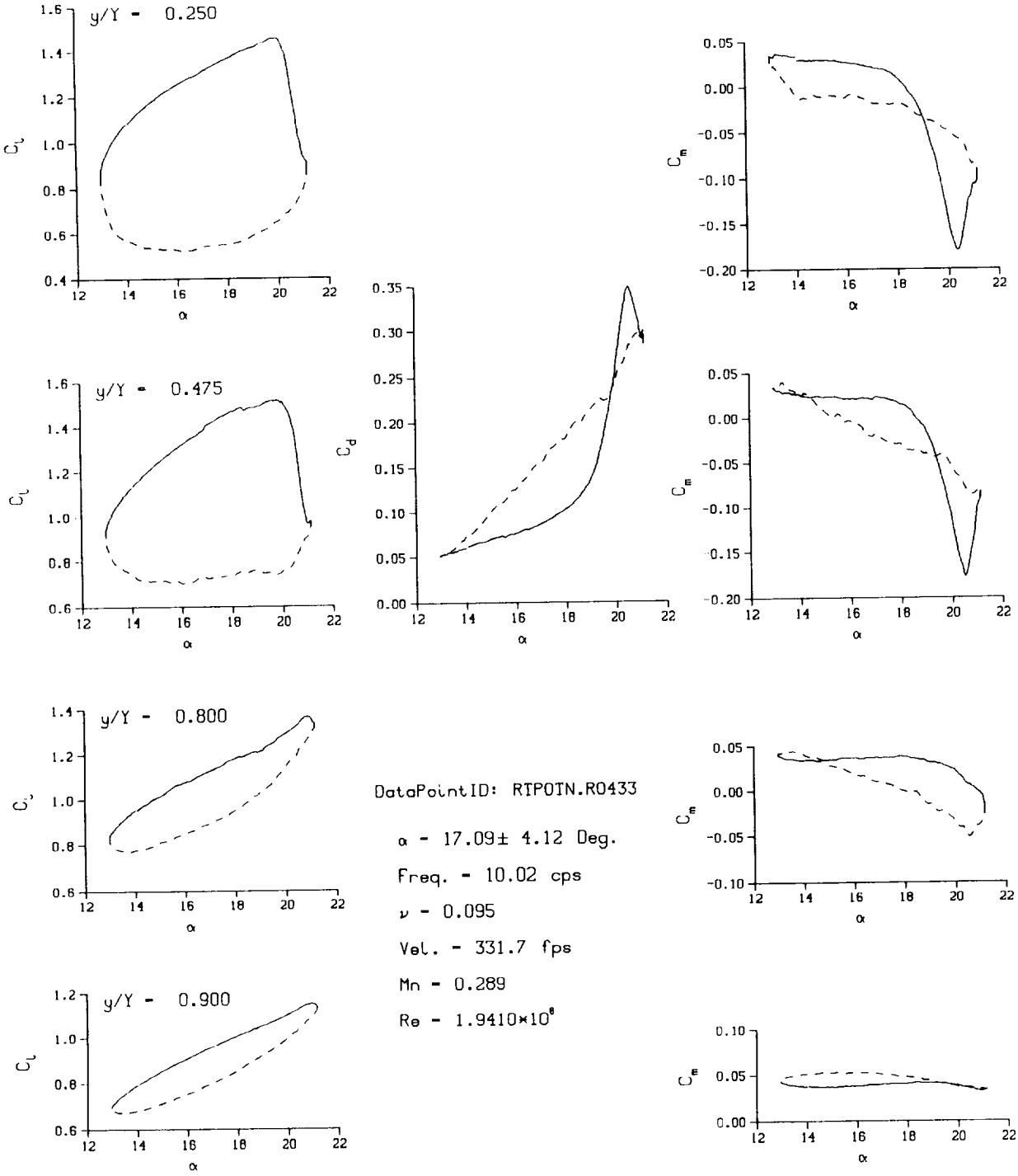

(b) v = 0.10

Figure 83. Continued.

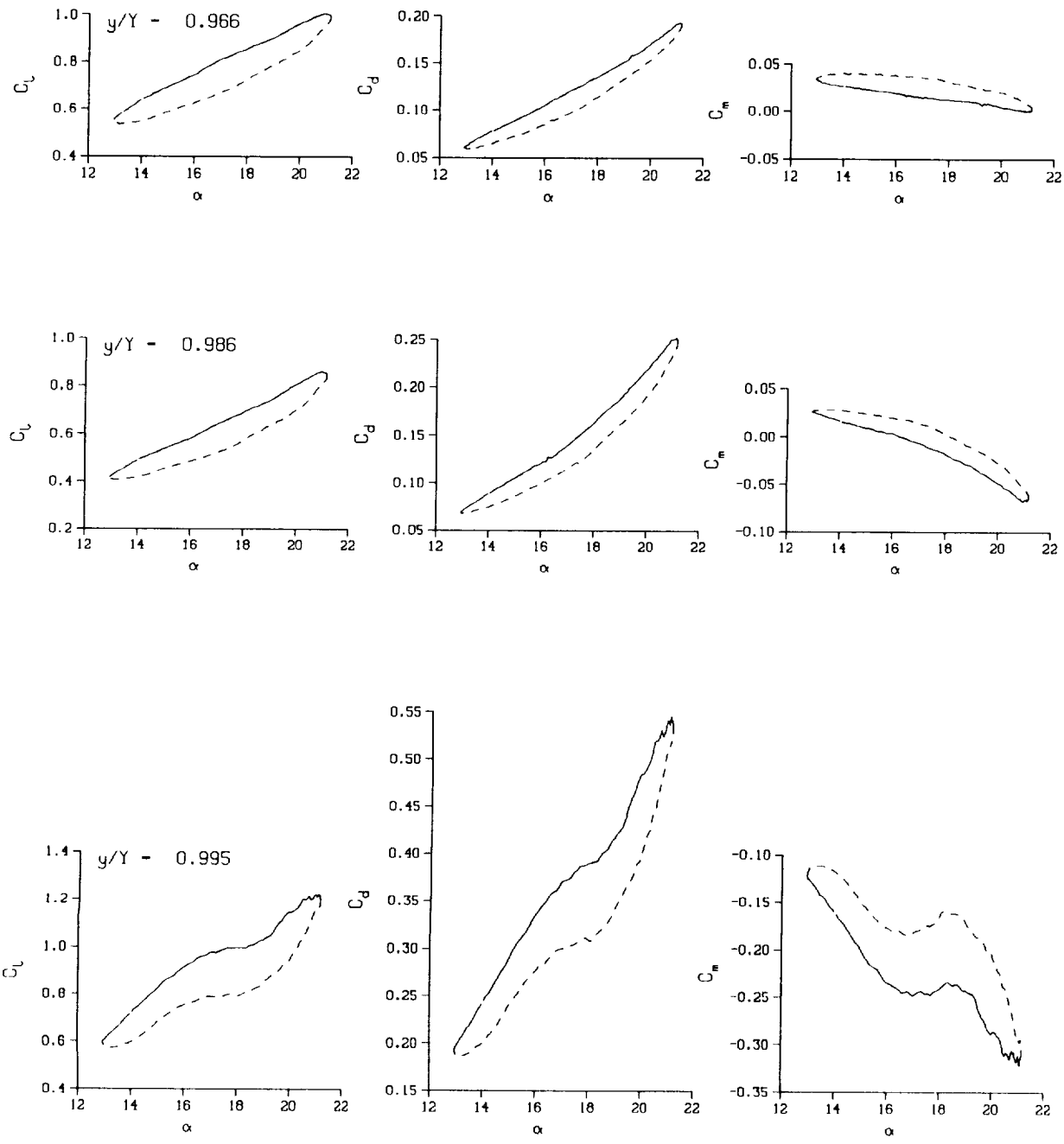

(b) v = 0.10. Concluded

Figure 83. Continued.

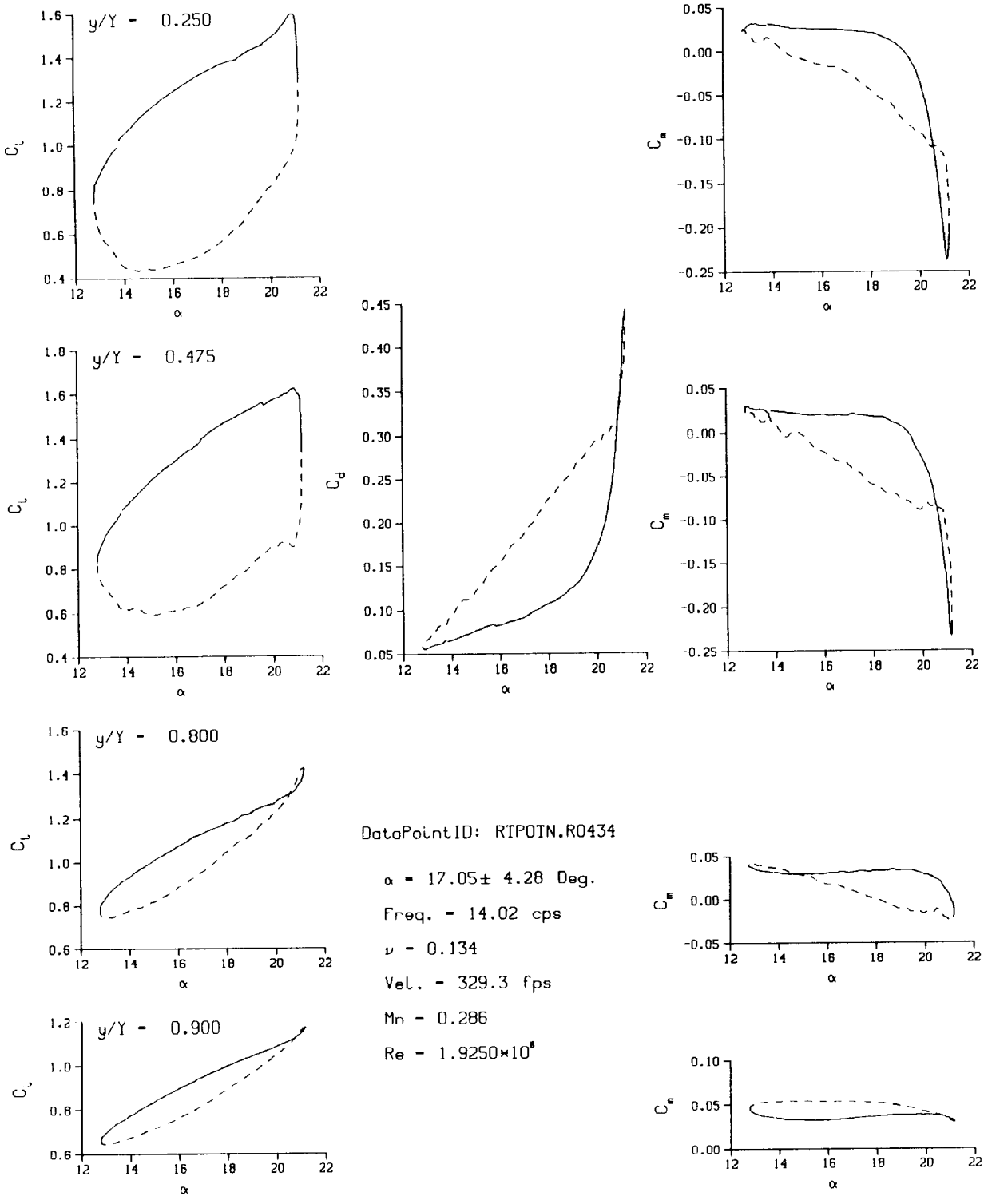

(c) ν = 0.14

Figure 83. Continued.

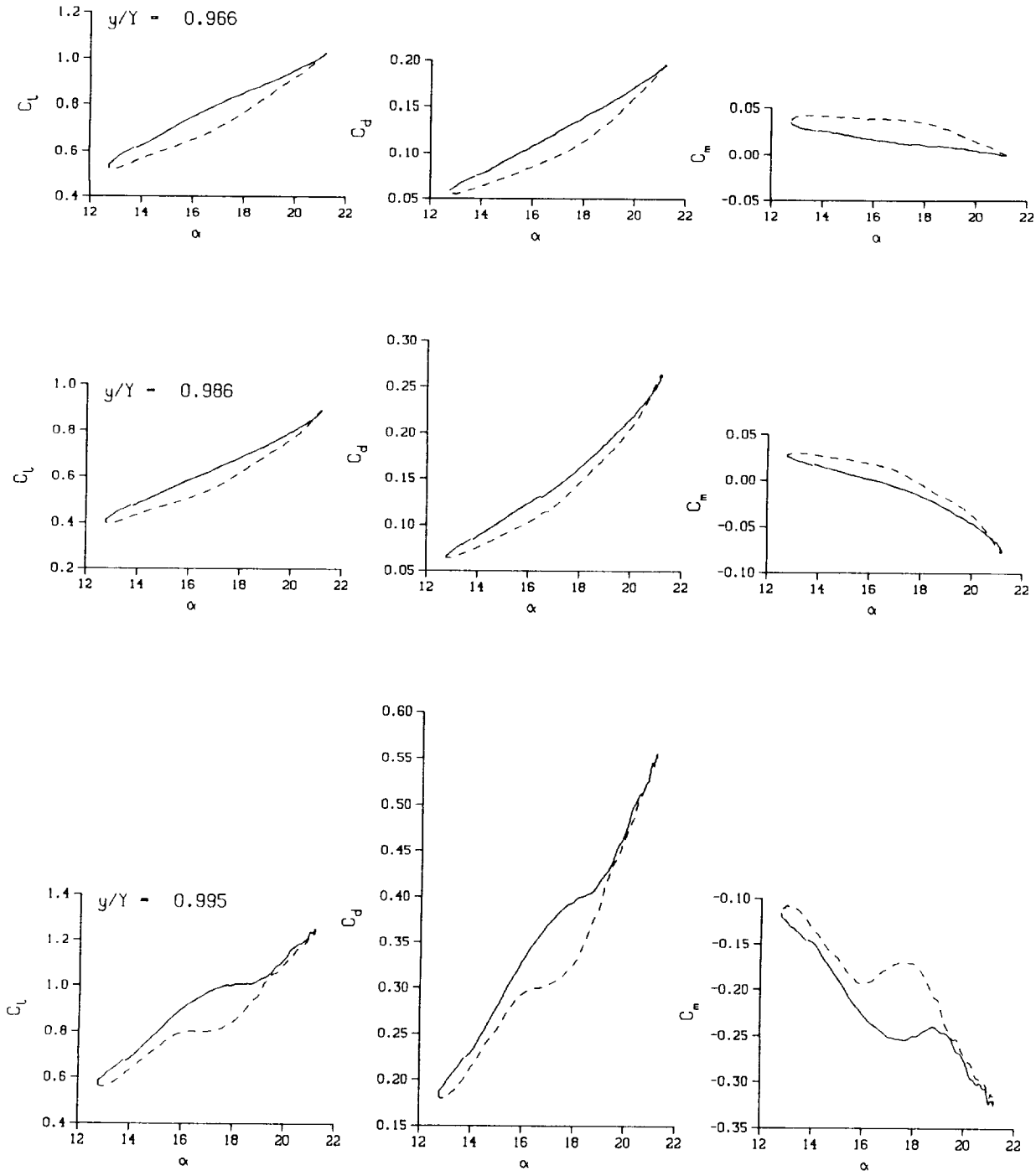

(c) v = 0.14. Concluded

Figure 83. Concluded.

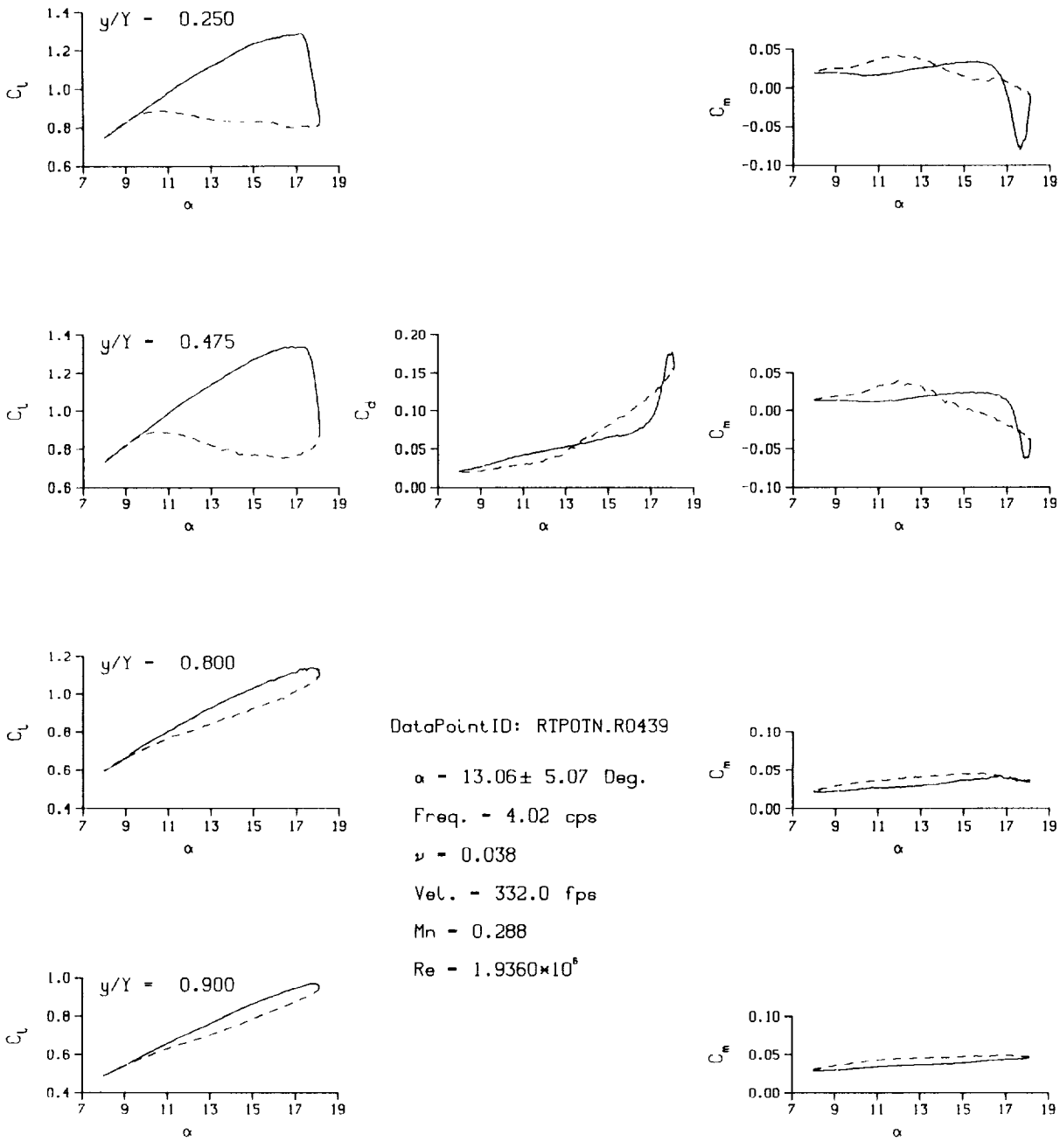

(a) v = 0.04

Figure 84. 3-D round tip pitch oscillation data; no BL-trip; α = 13 ± 5 deg.

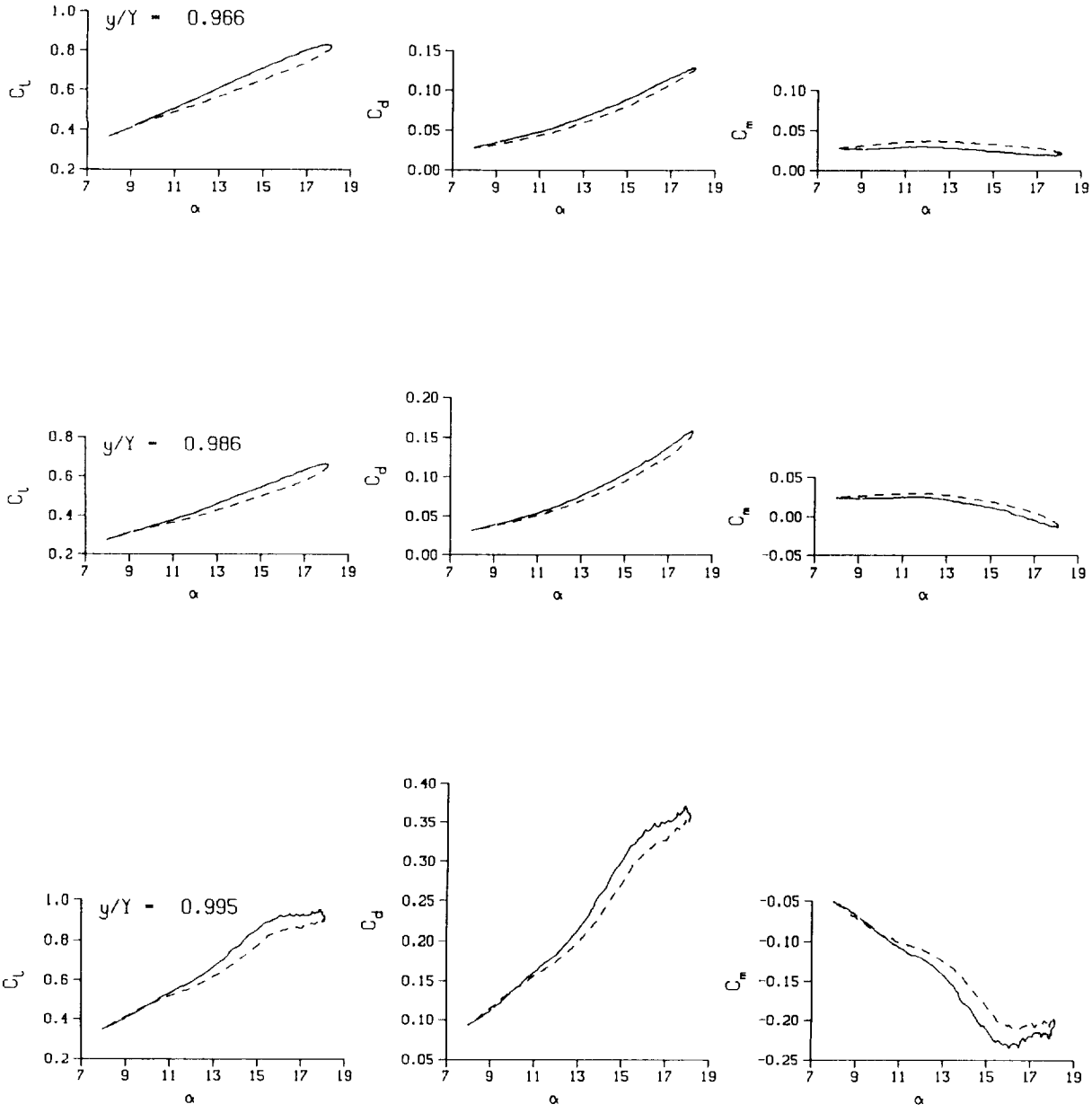

(a) v = 0.04. Concluded

Figure 84. Continued.

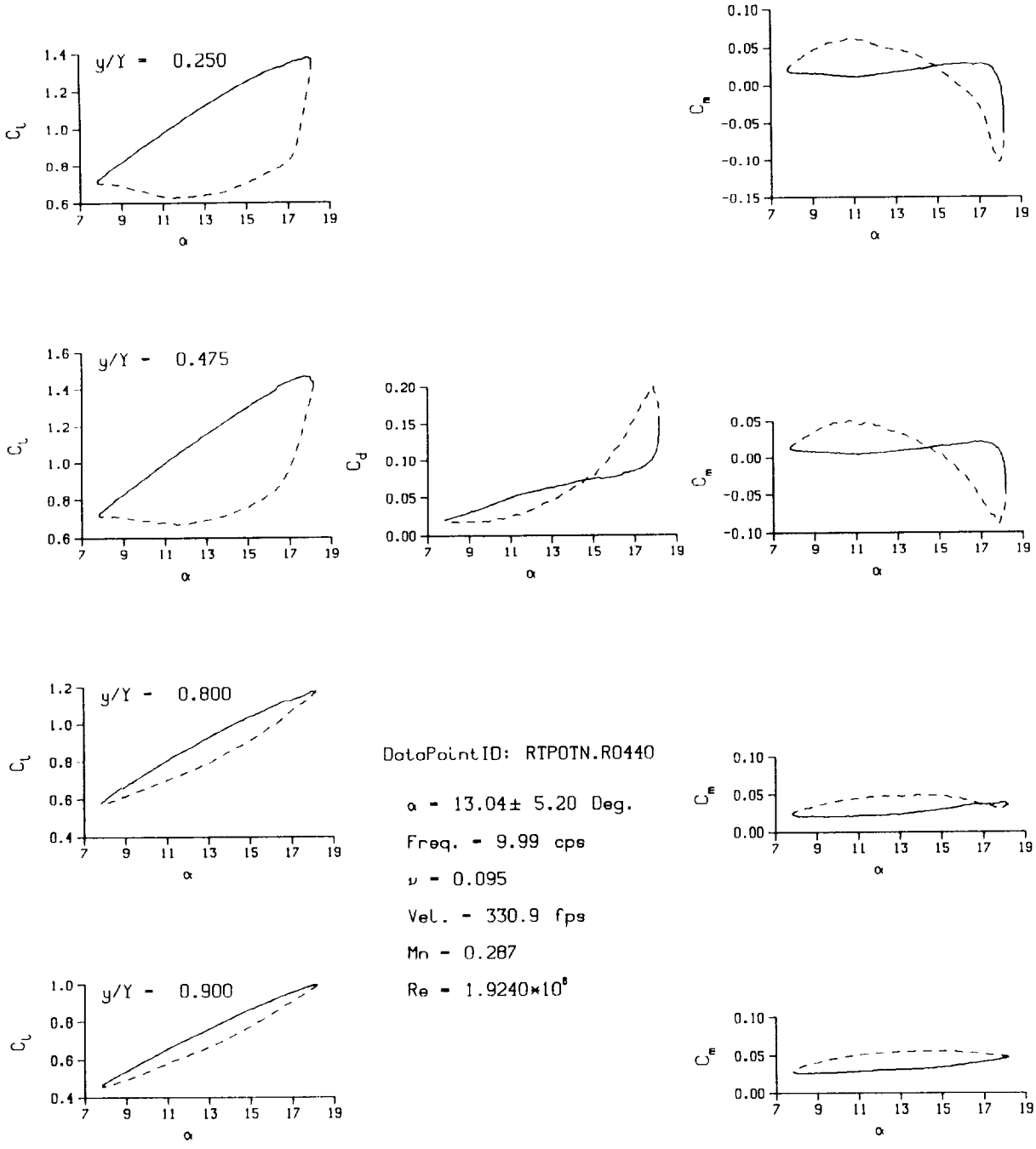

(b) v = 0.10

Figure 84. Continued.

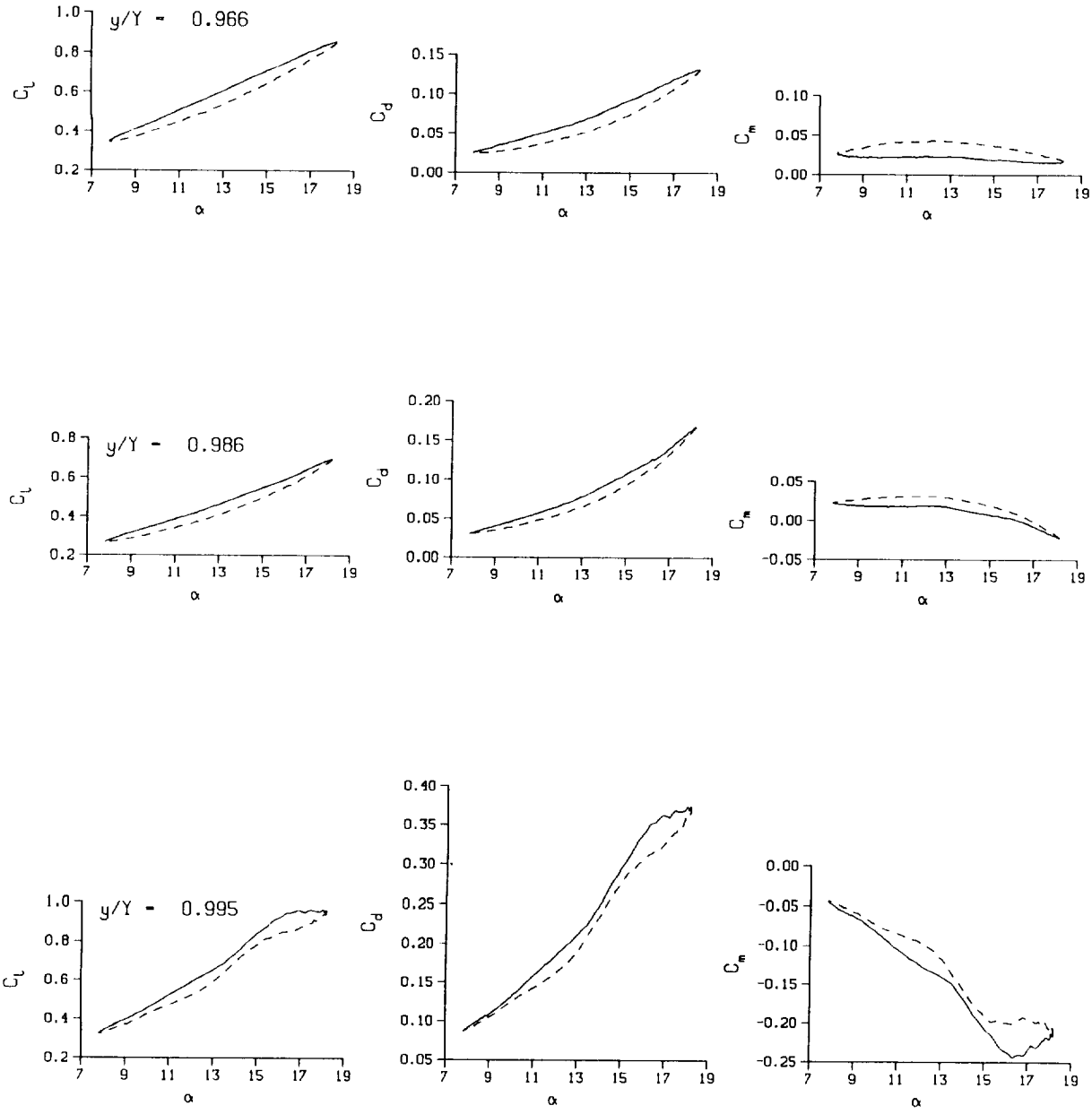

(b) v = 0.10. Concluded

Figure 84. Concluded.

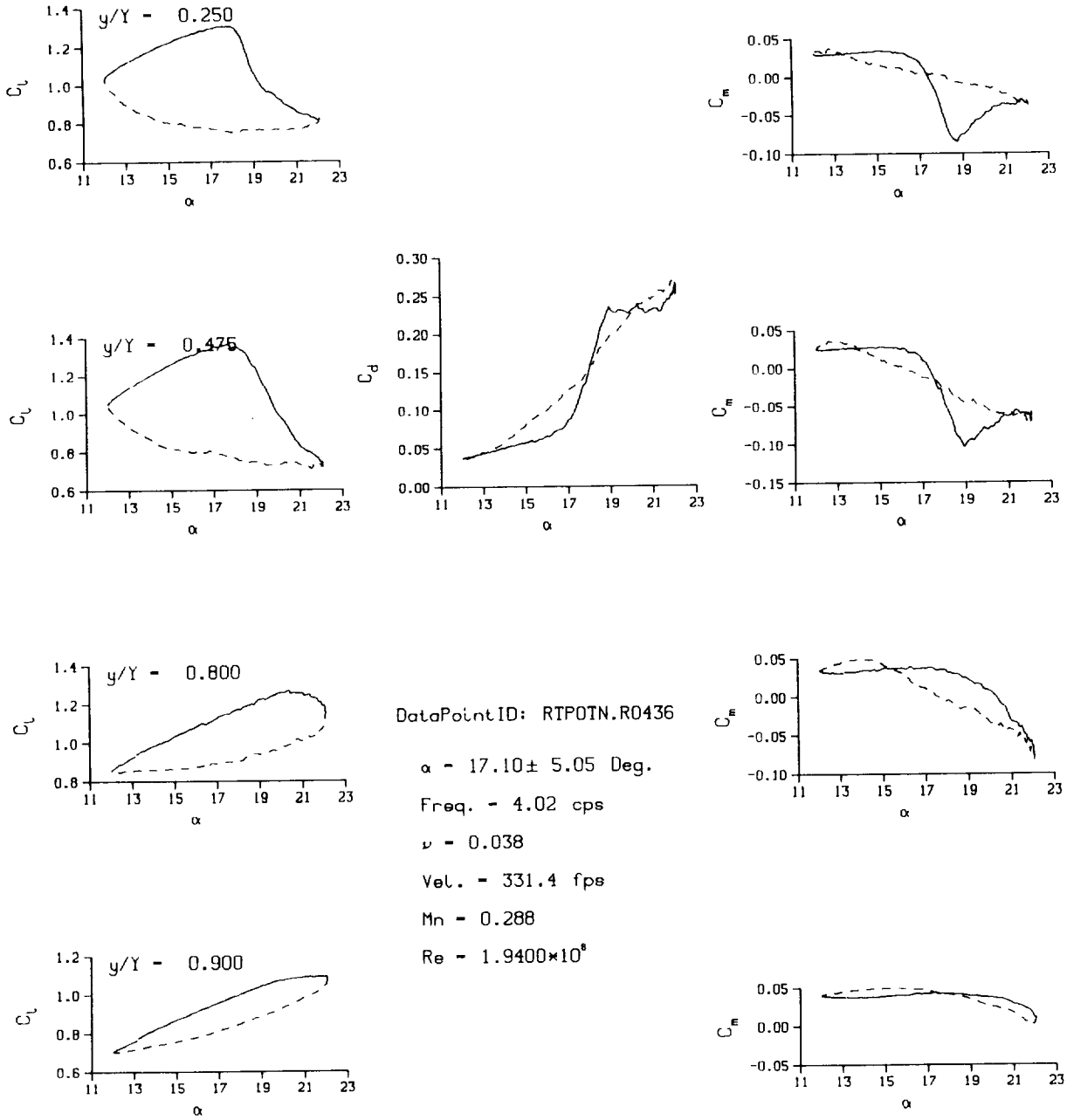

(a) ν = 0.04

Figure 85. 3-D round tip pitch oscillation data; no BL-trip; α = 17 ± 5 deg.

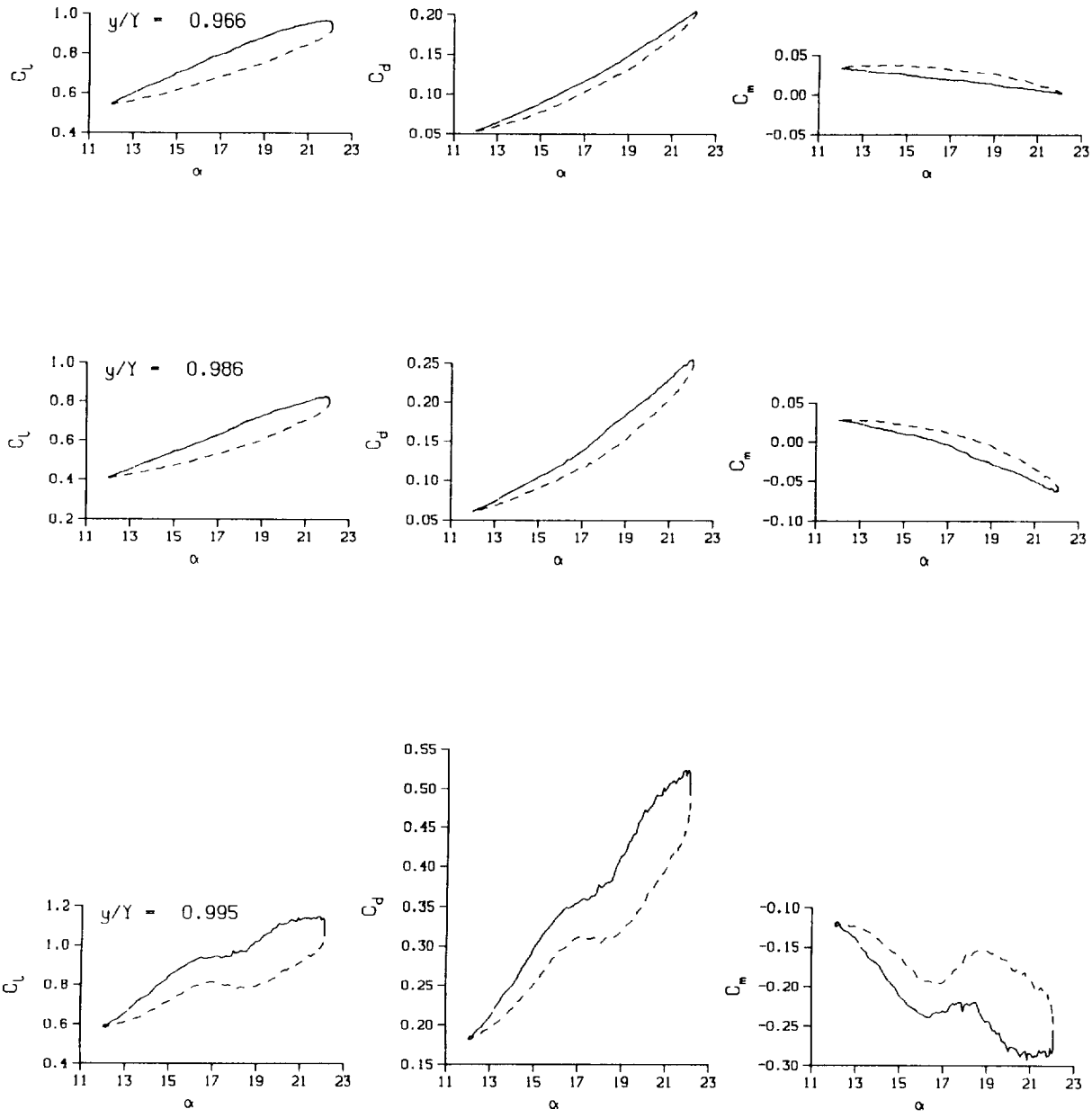

(a) v = 0.04. Concluded

Figure 85. Continued.

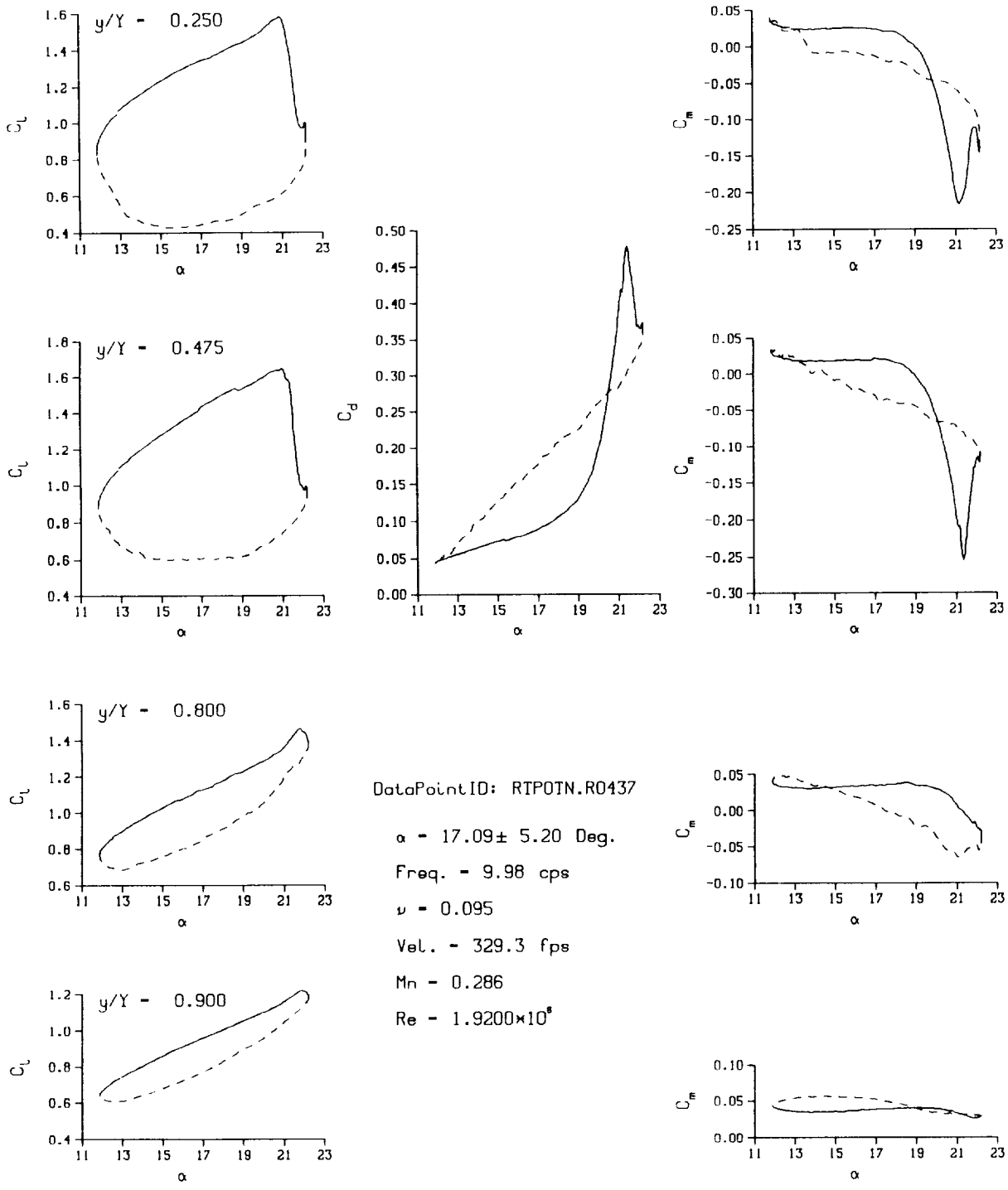

(b) v = 0.10

Figure 85. Continued.

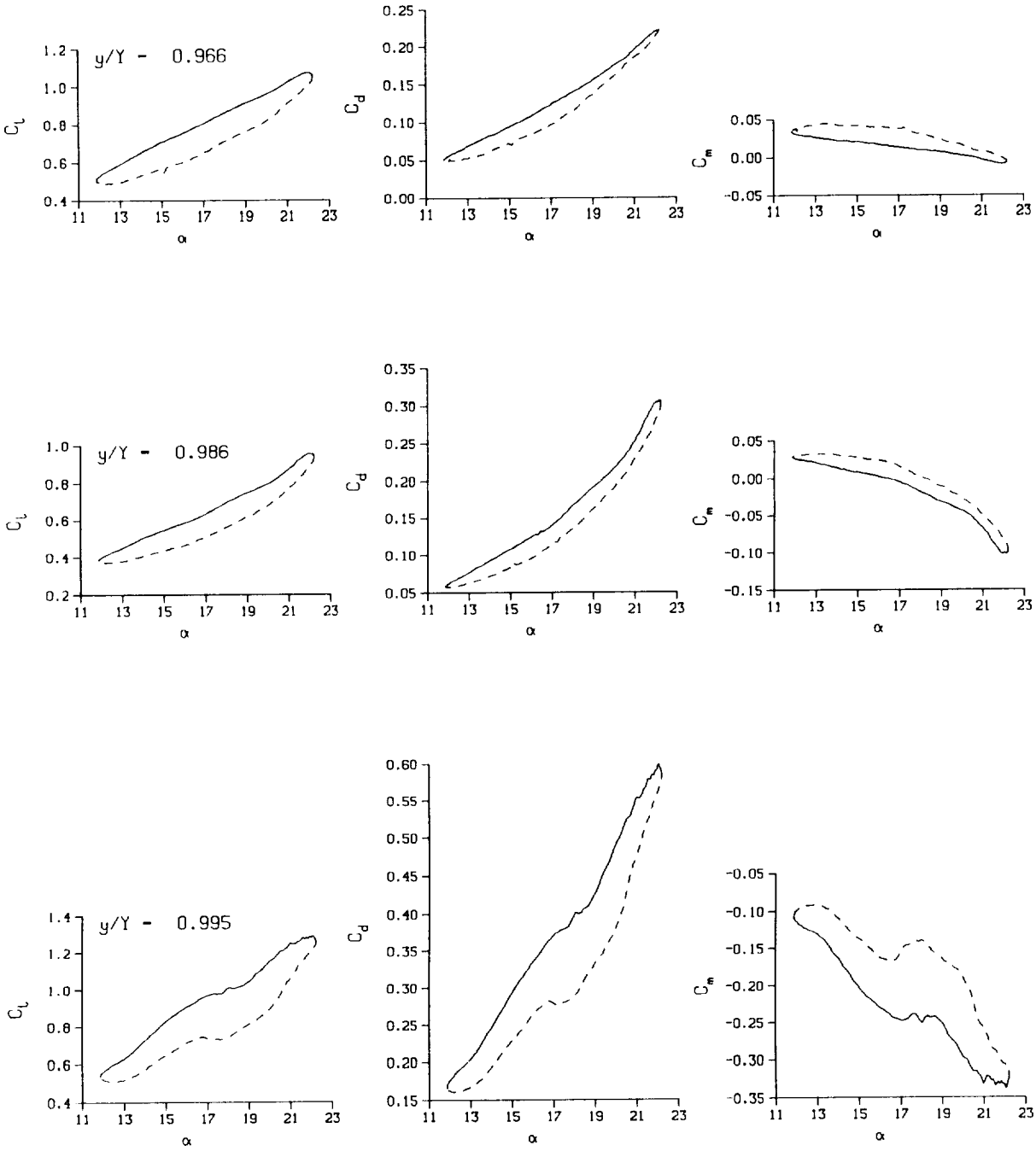

(b) v = 0.10. Concluded

Figure 85. Concluded.

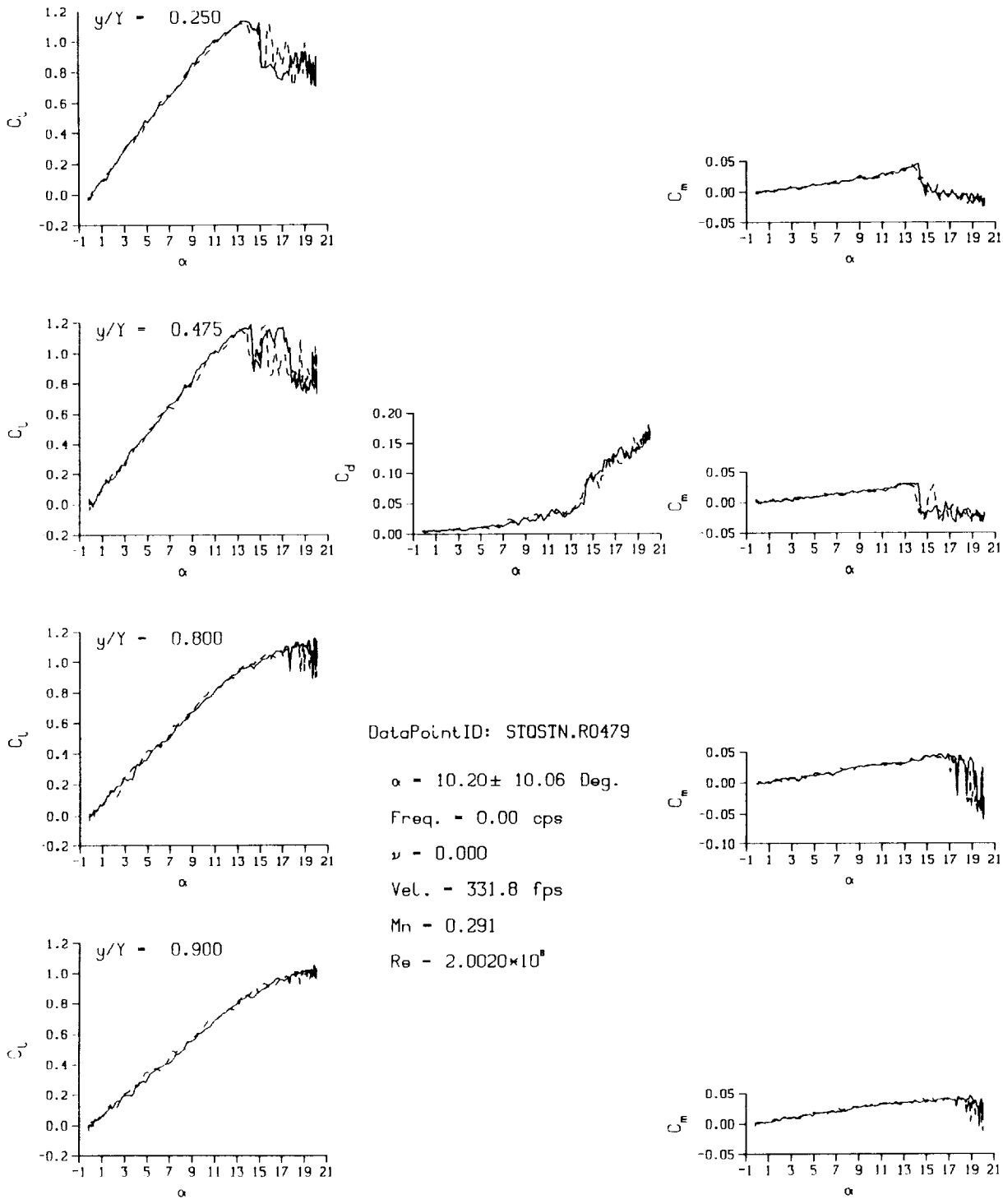

(a) Repeat no. 1

Figure 86. 3-D square tip quasi-steady data; no BL-trip; $0 \leq \alpha \leq 20$ deg.

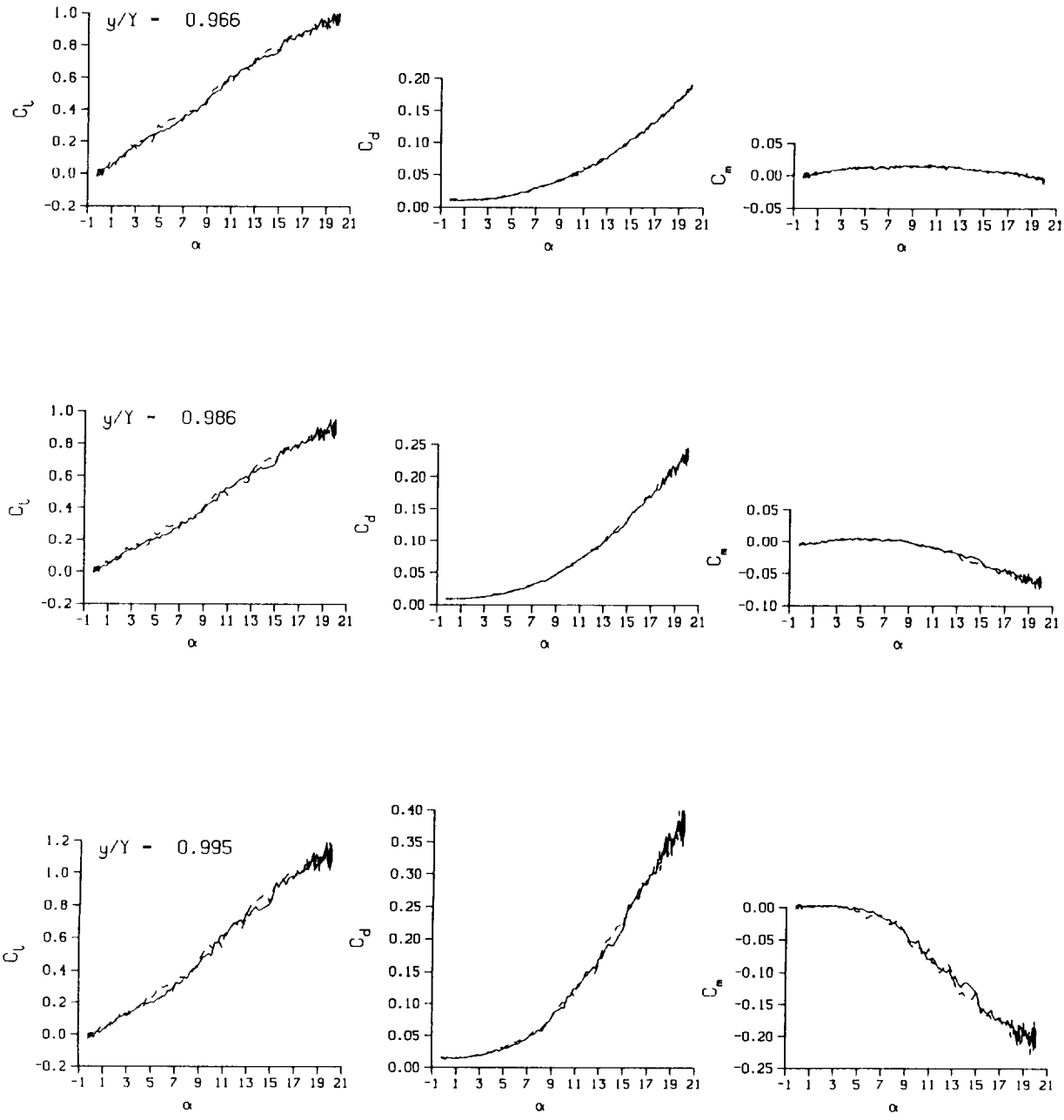

(a) Repeat no. 1. Concluded

Figure 86. Continued.

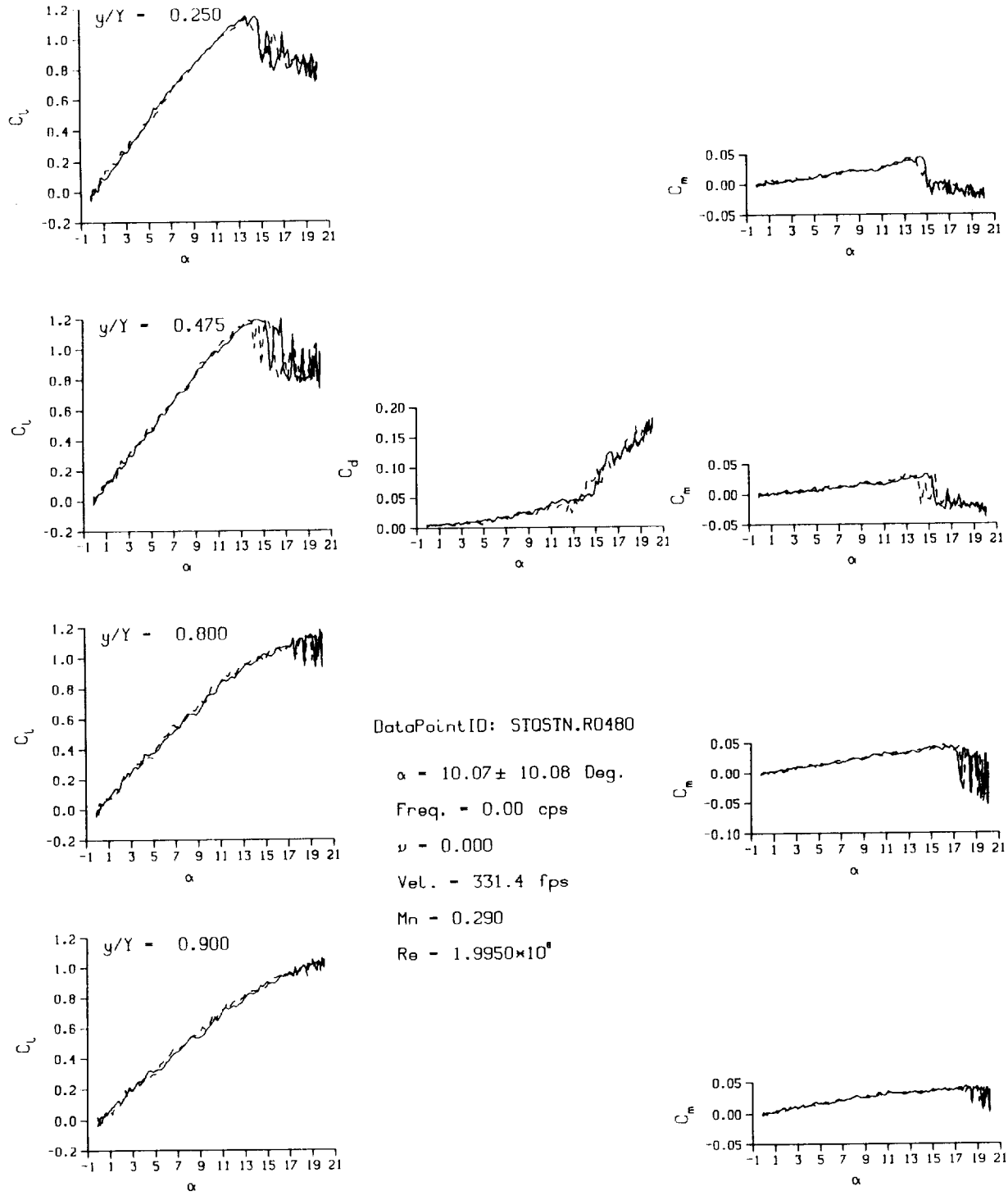

(b) Repeat no. 2

Figure 86. Continued.

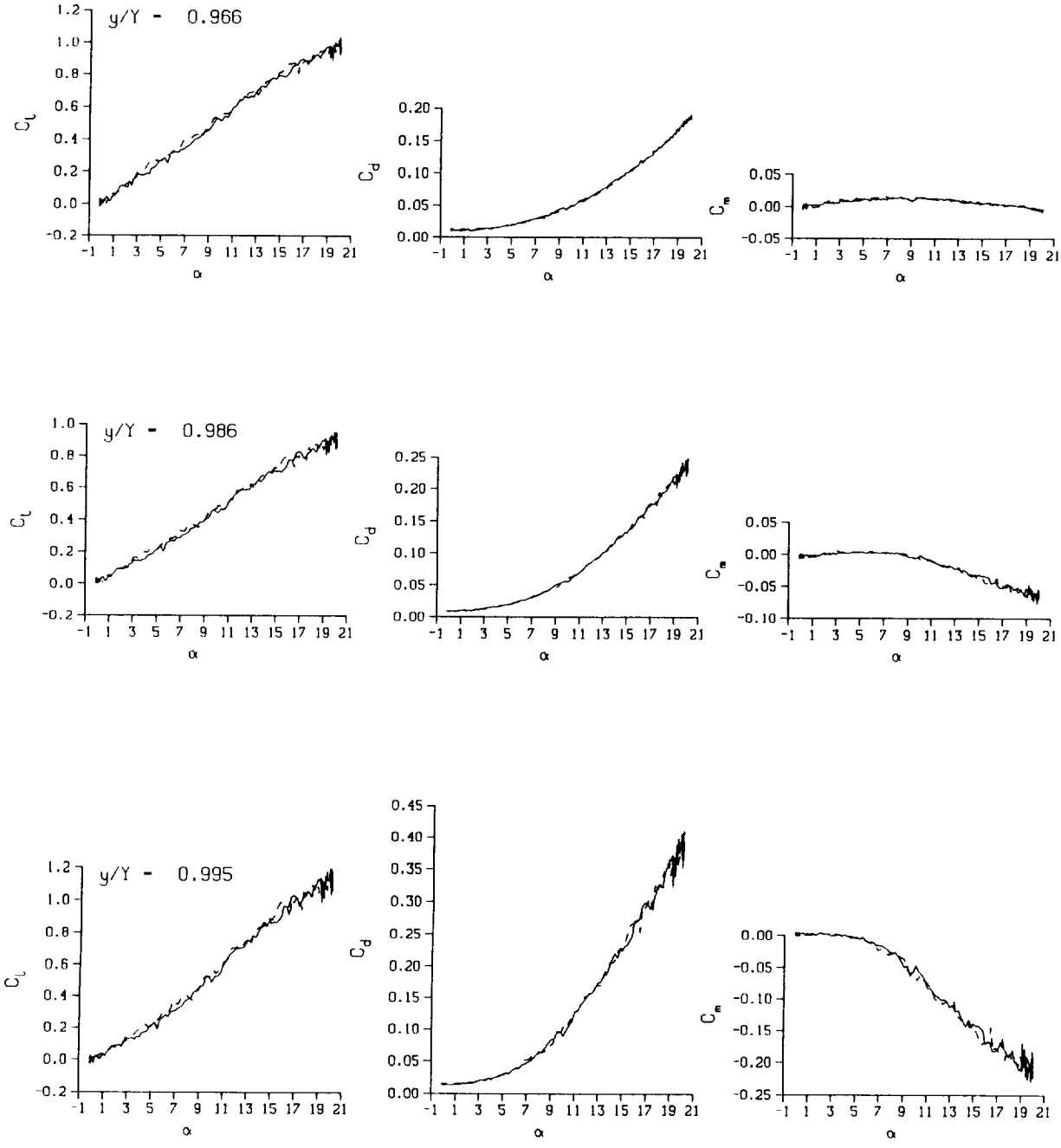

(b) Repeat no. 2. Concluded

Figure 86. Continued.

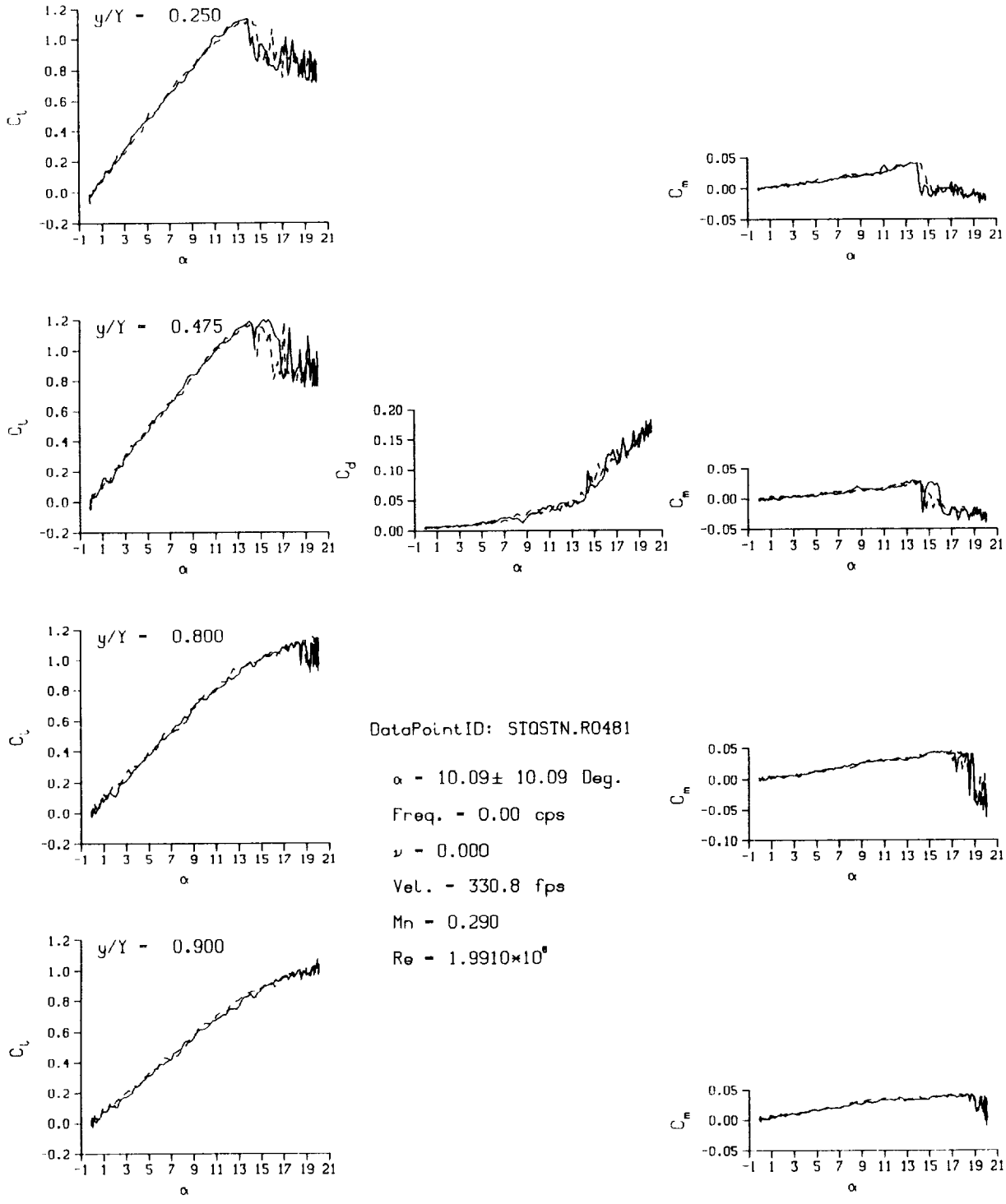

(c) Repeat no. 3

Figure 86. Continued.

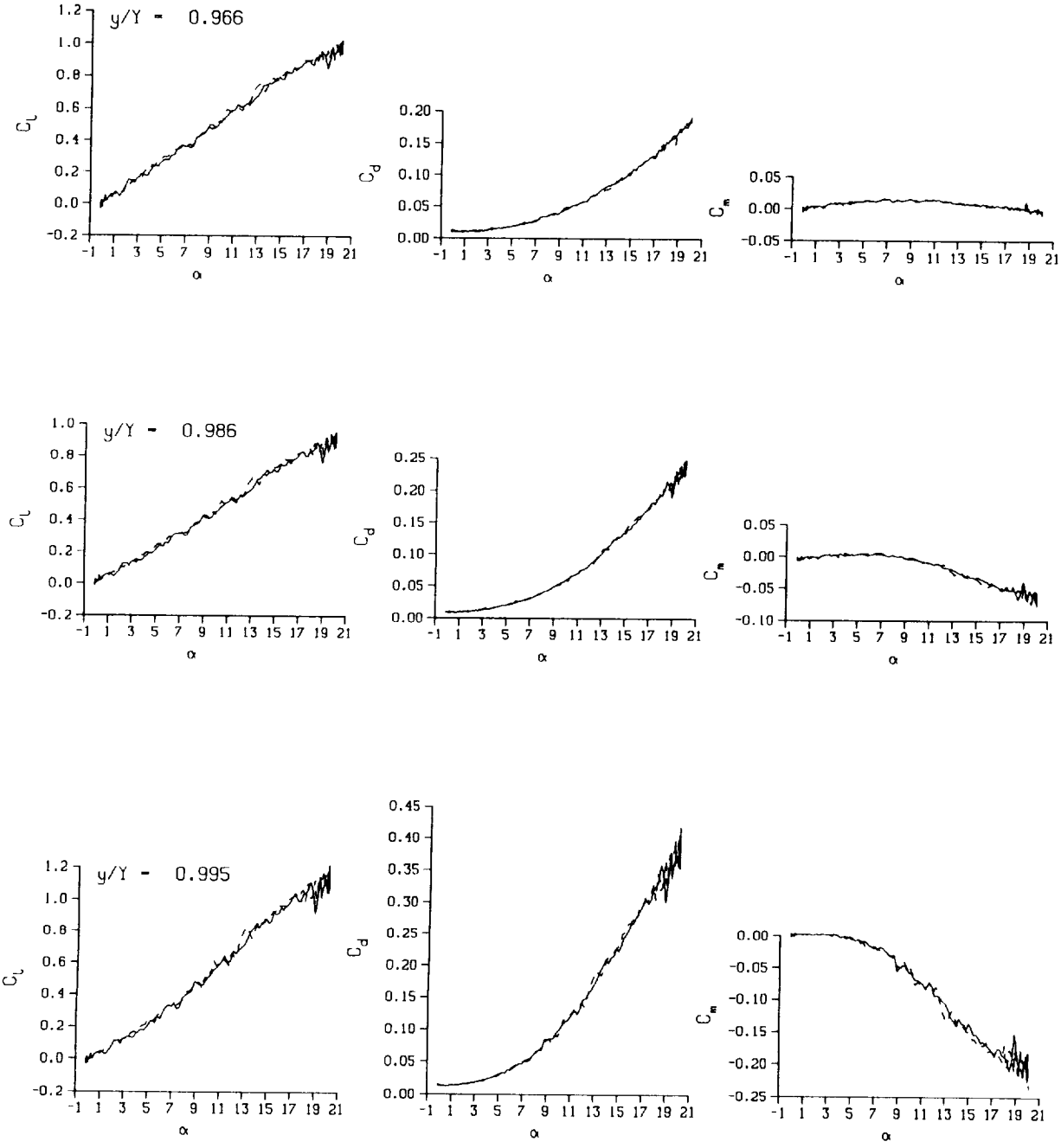

(c) Repeat no. 3. Concluded

Figure 86. Concluded.

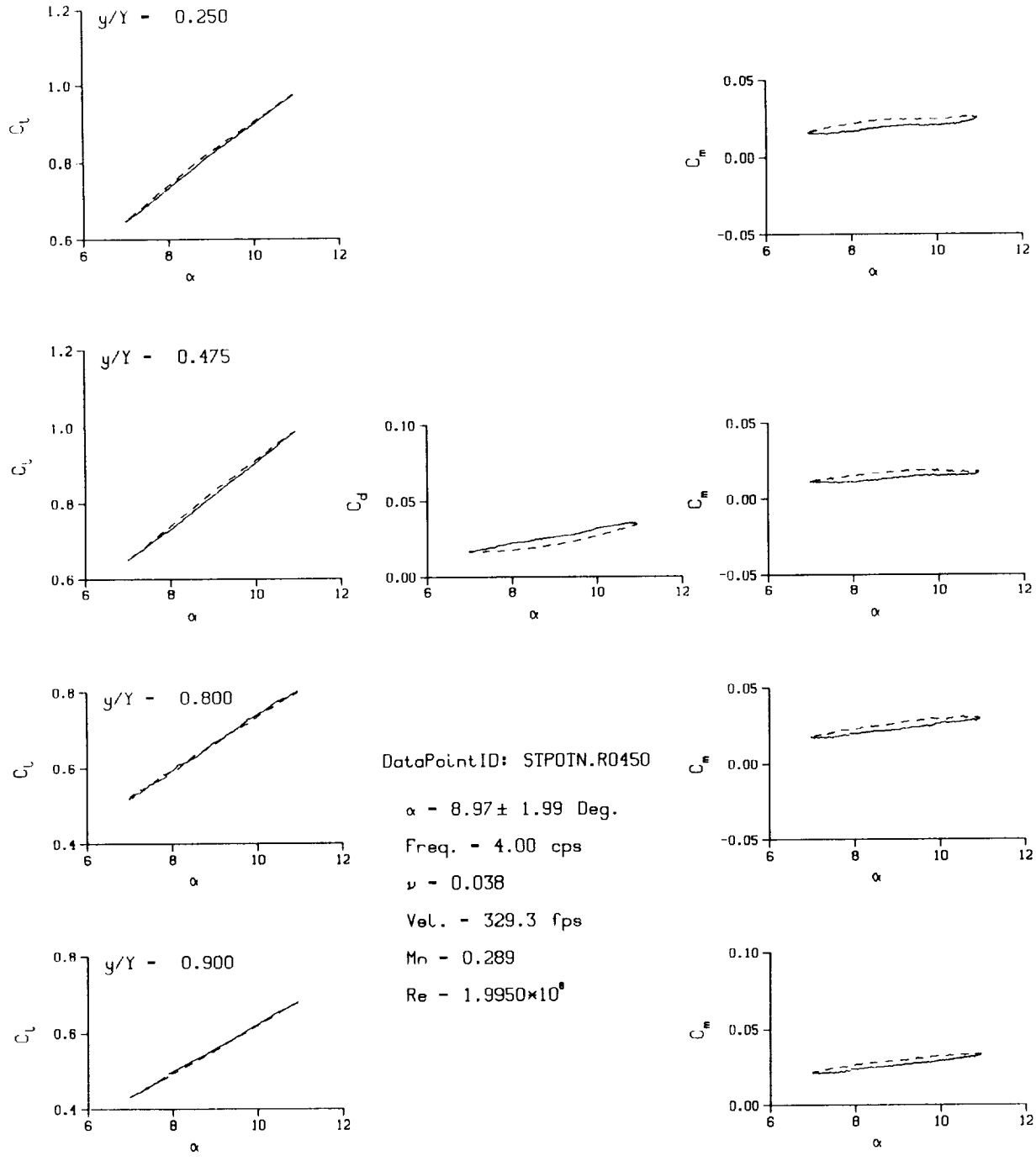

(a) ν = 0.04

Figure 87. 3-D square tip pitch oscillation data; no BL-trip; α = 9 ± 2 deg.

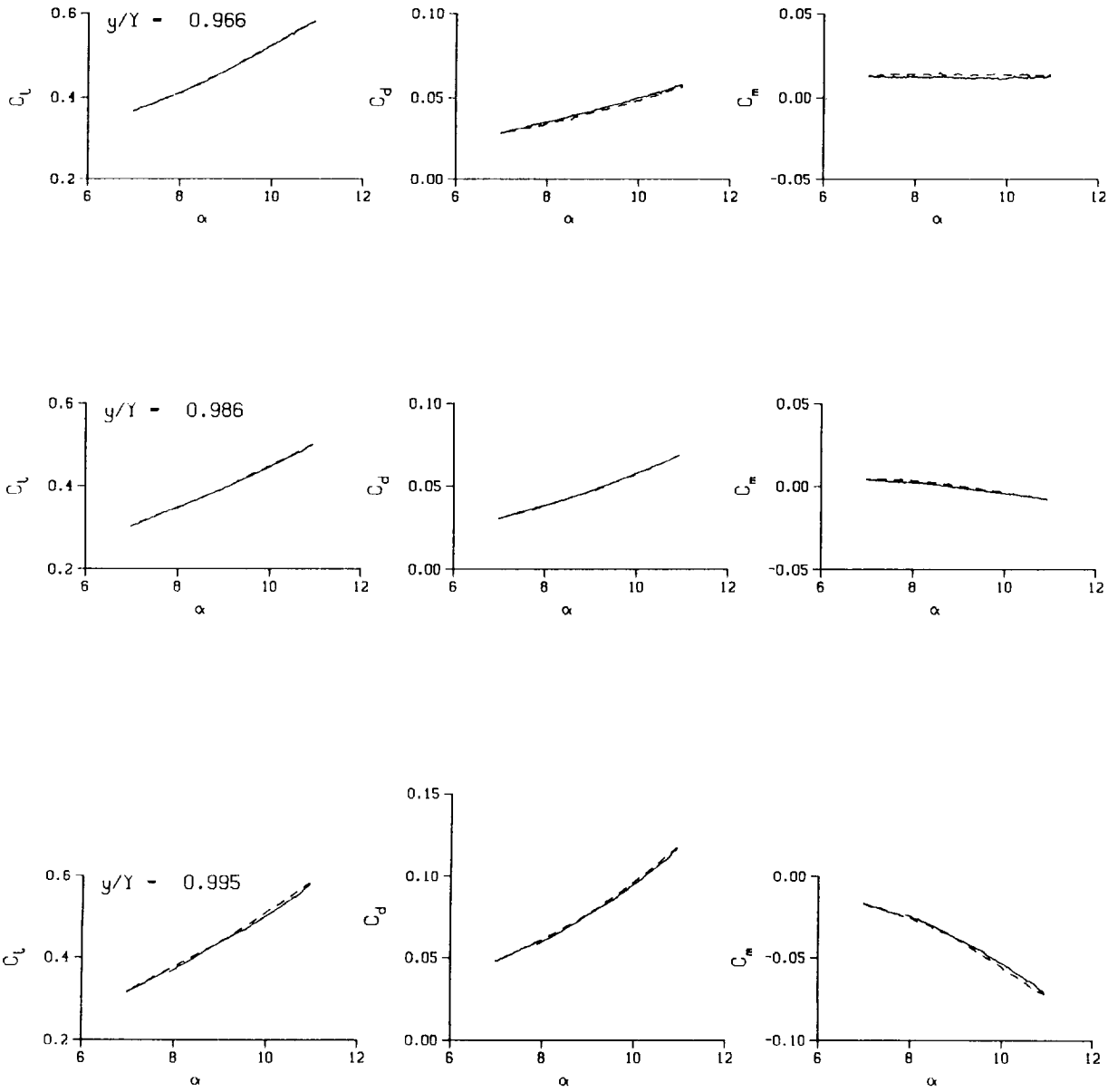

(a) v = 0.04. Concluded

Figure 87. Continued.

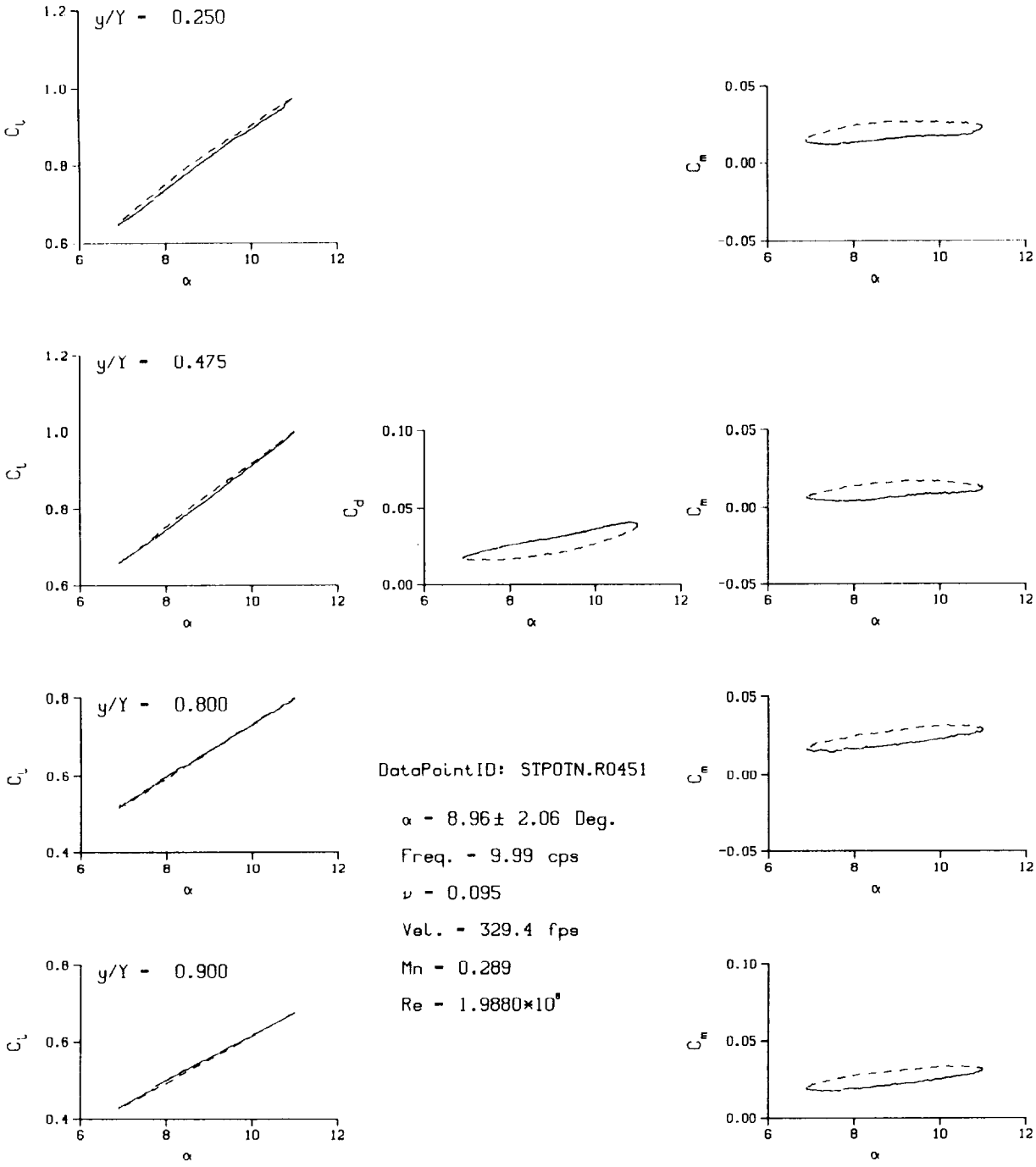

(b) v = 0.10

Figure 87. Continued.

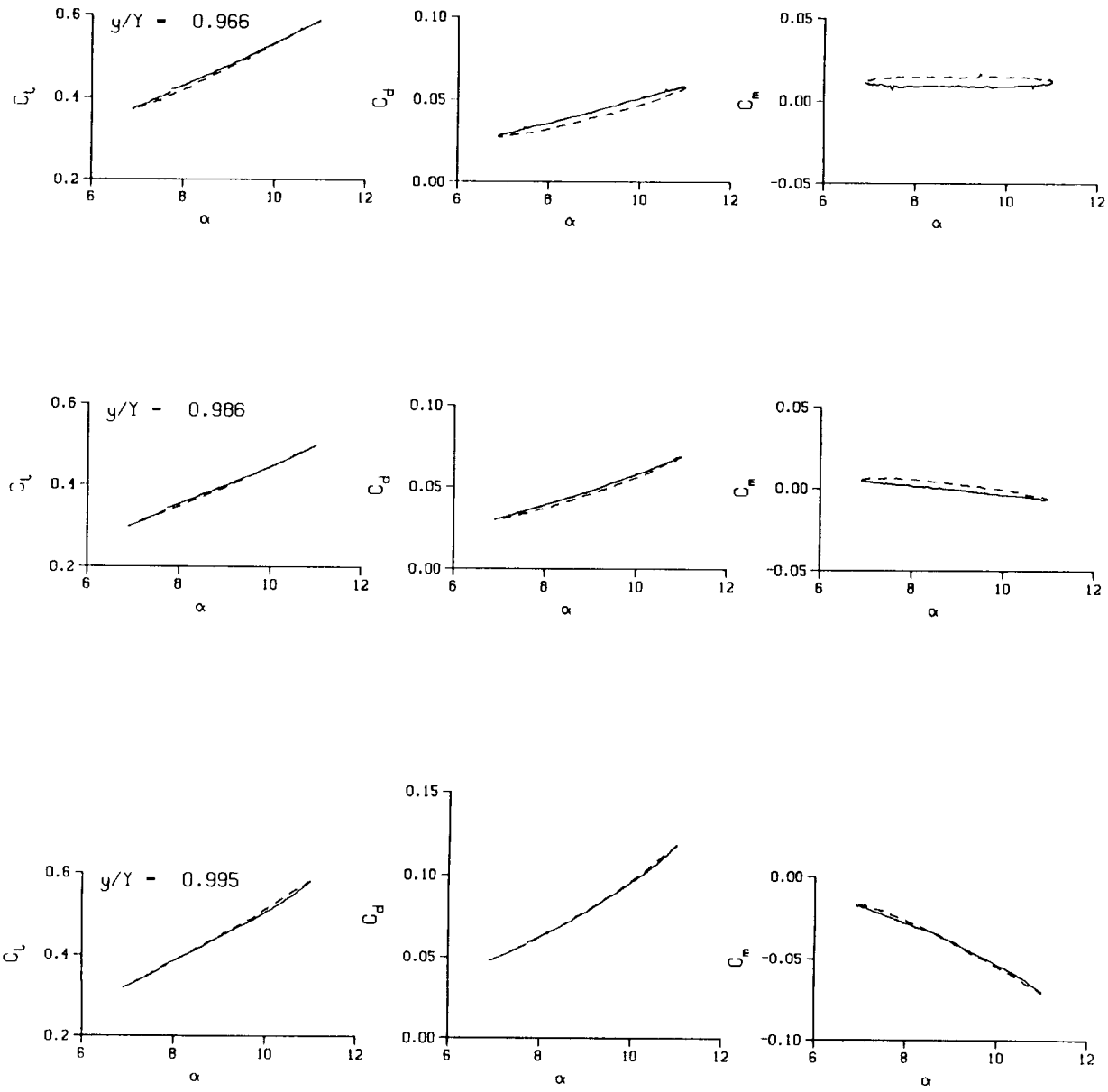

(b) v = 0.10. Concluded

Figure 87. Continued.

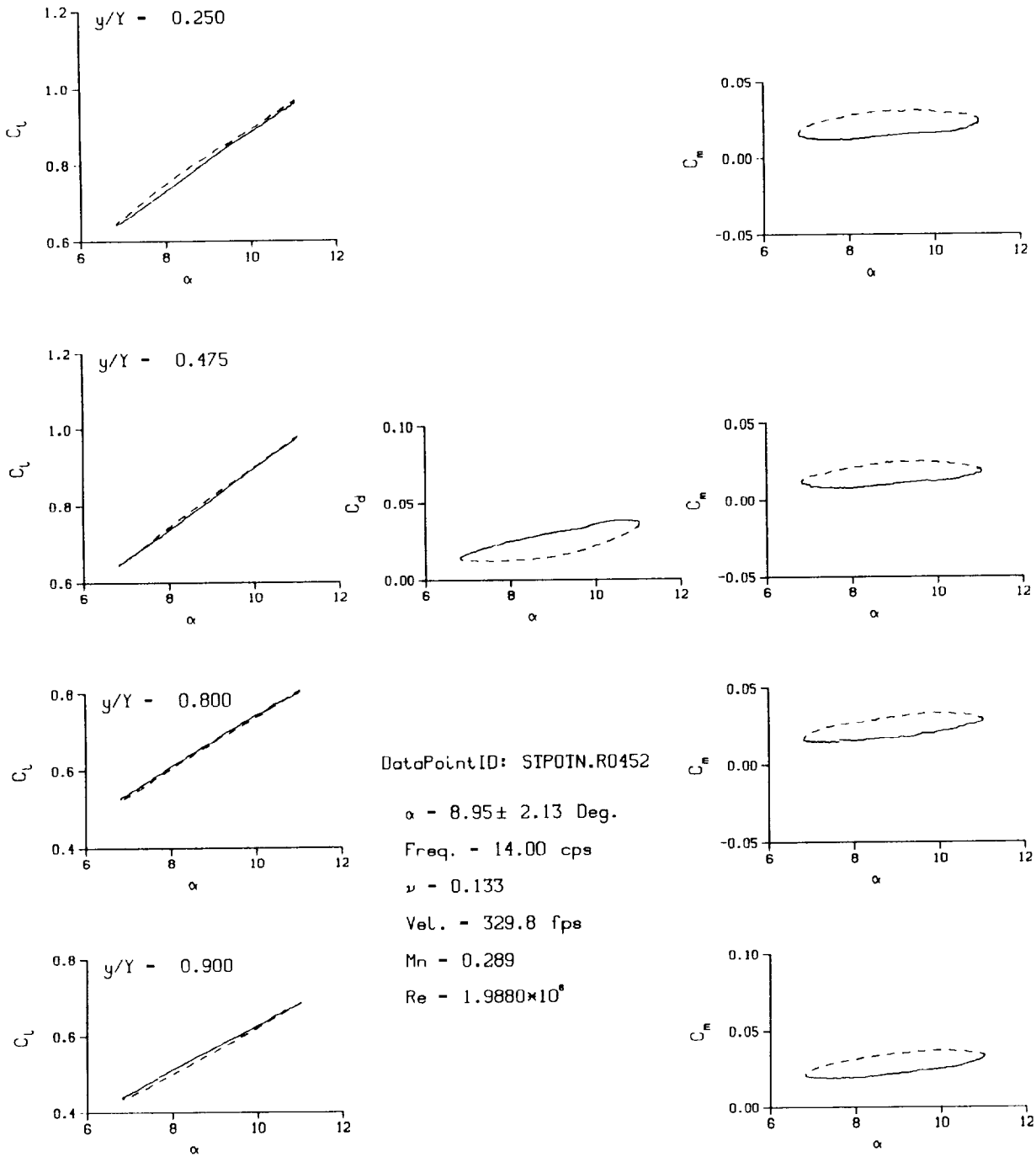

(c) v = 0.14

Figure 87. Continued.

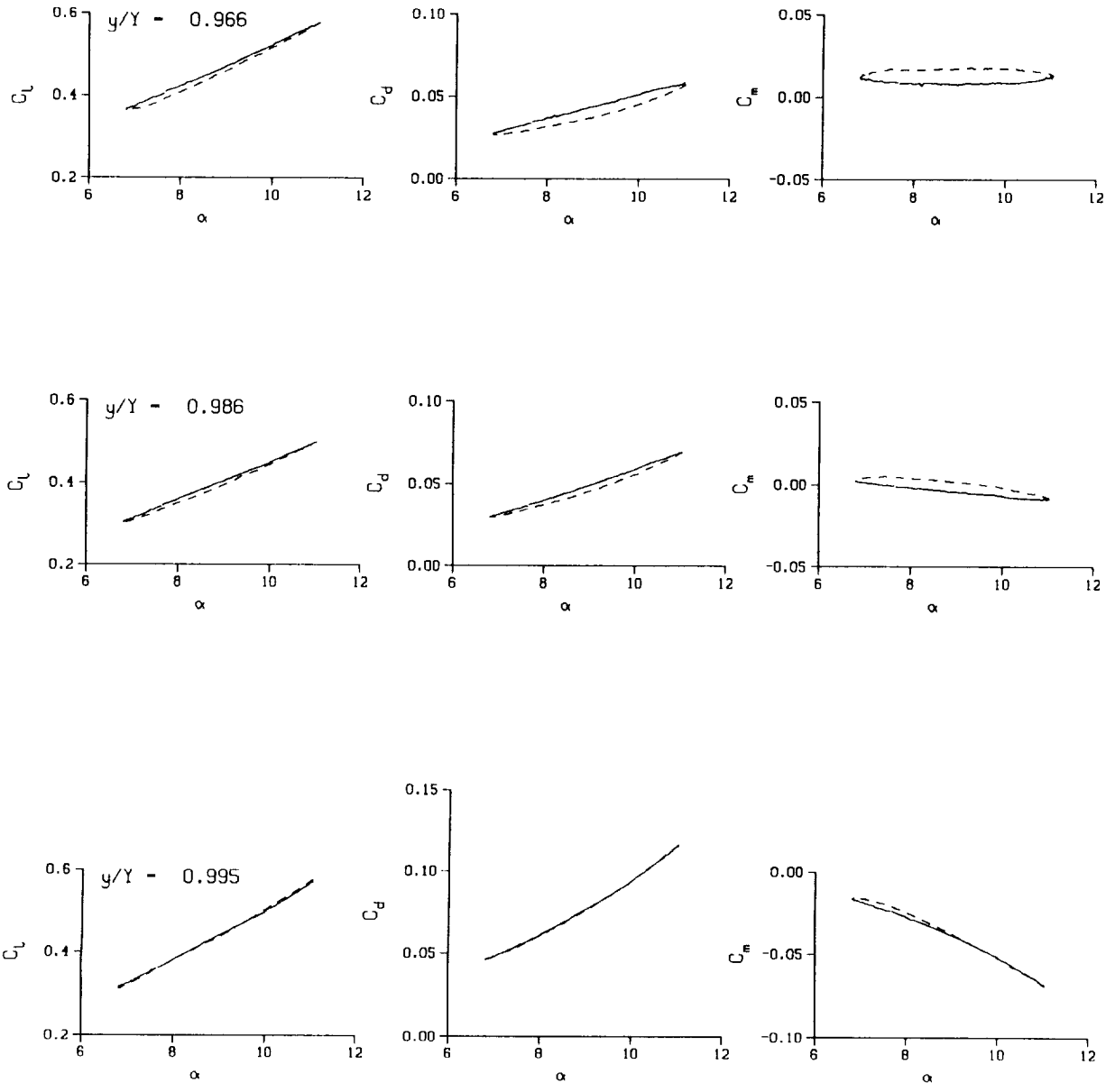

(c) v = 0.14. Concluded

Figure 87. Continued.

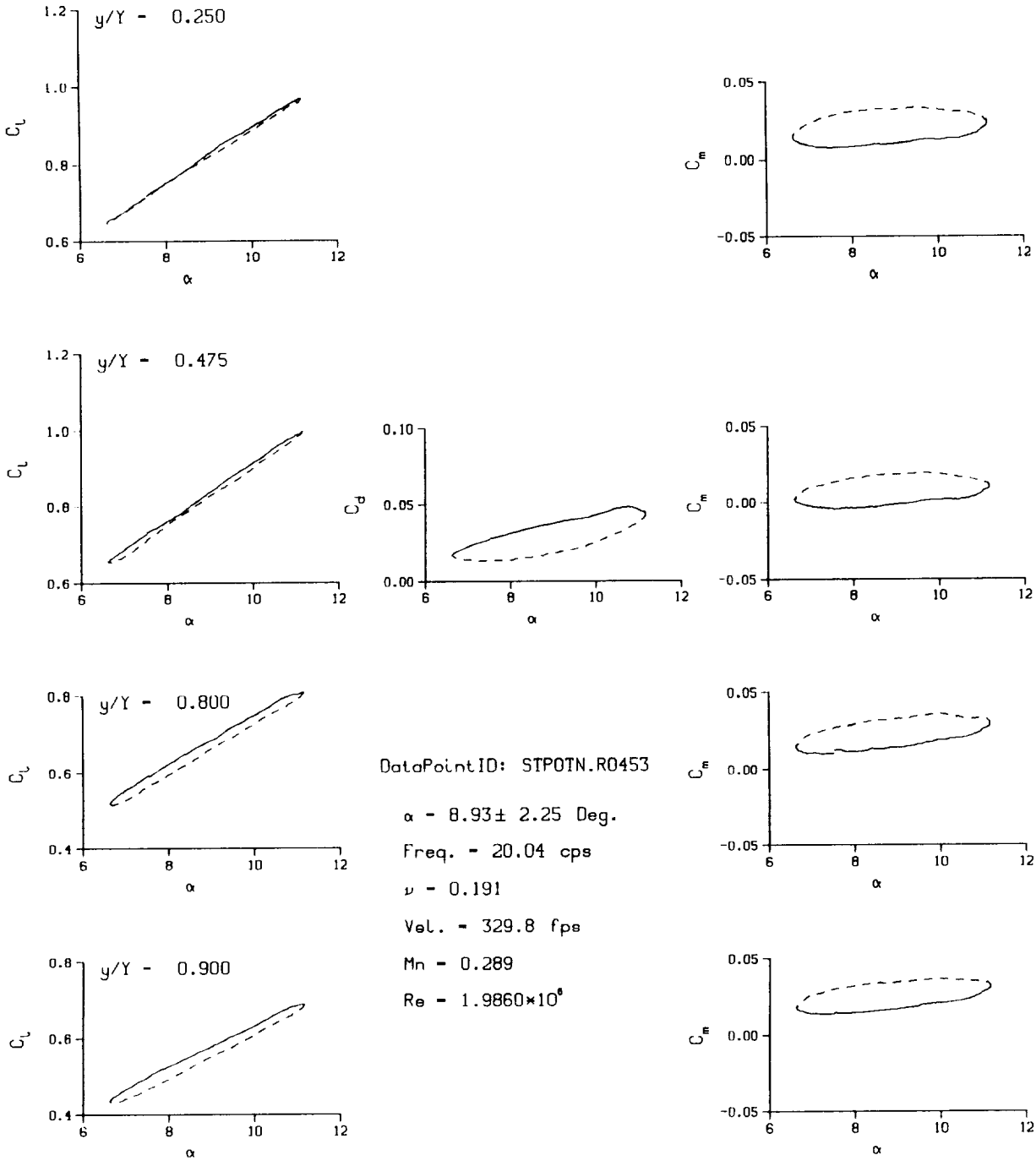

(d) v = 0.20

Figure 87. Continued.

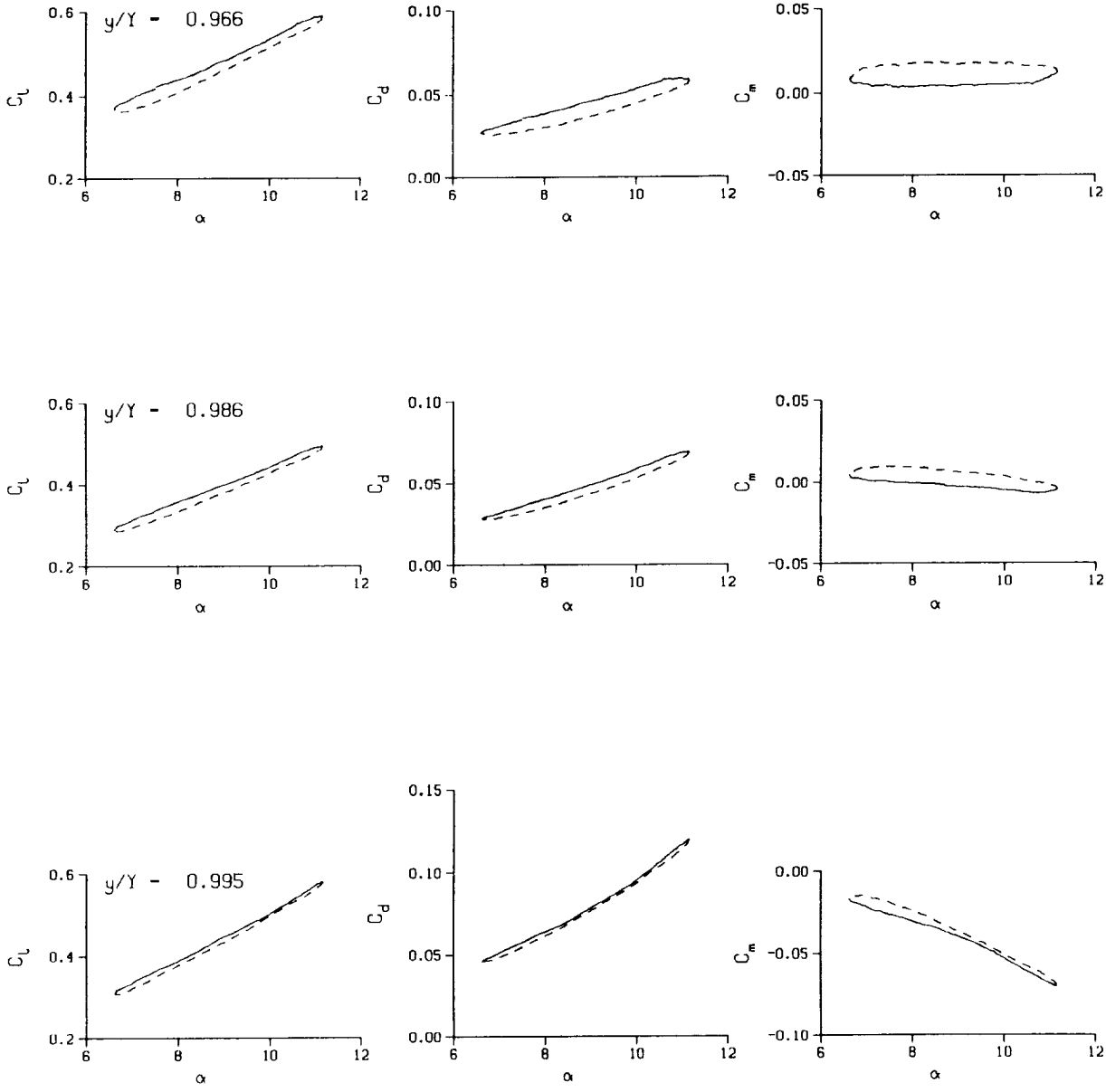

(d) v = 0.20. Concluded

Figure 87. Concluded.

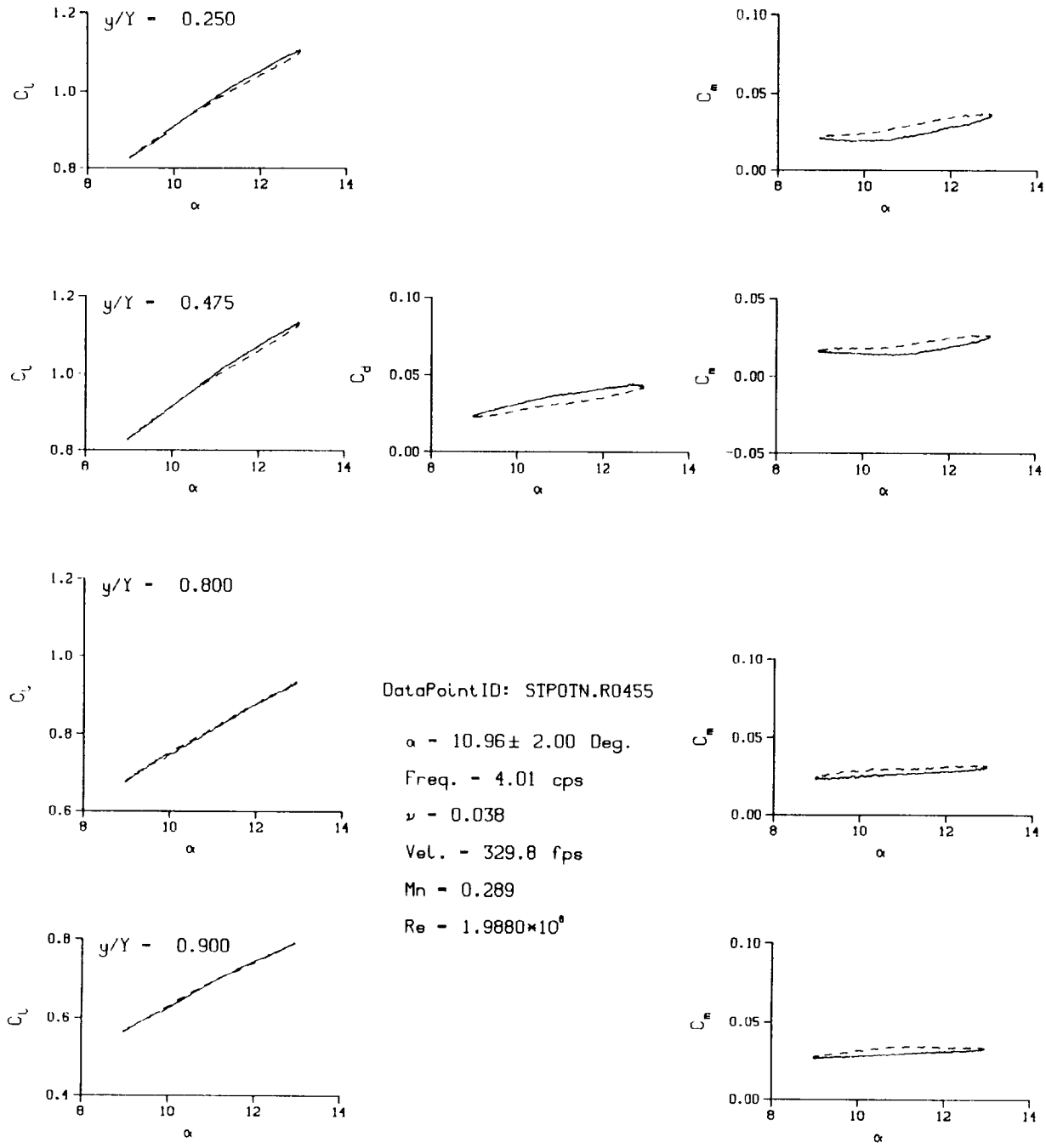

(a) v = 0.04

Figure 88. 3-D Square tip pitch oscillation data; no BL-trip; α = 11 ± 2 deg.

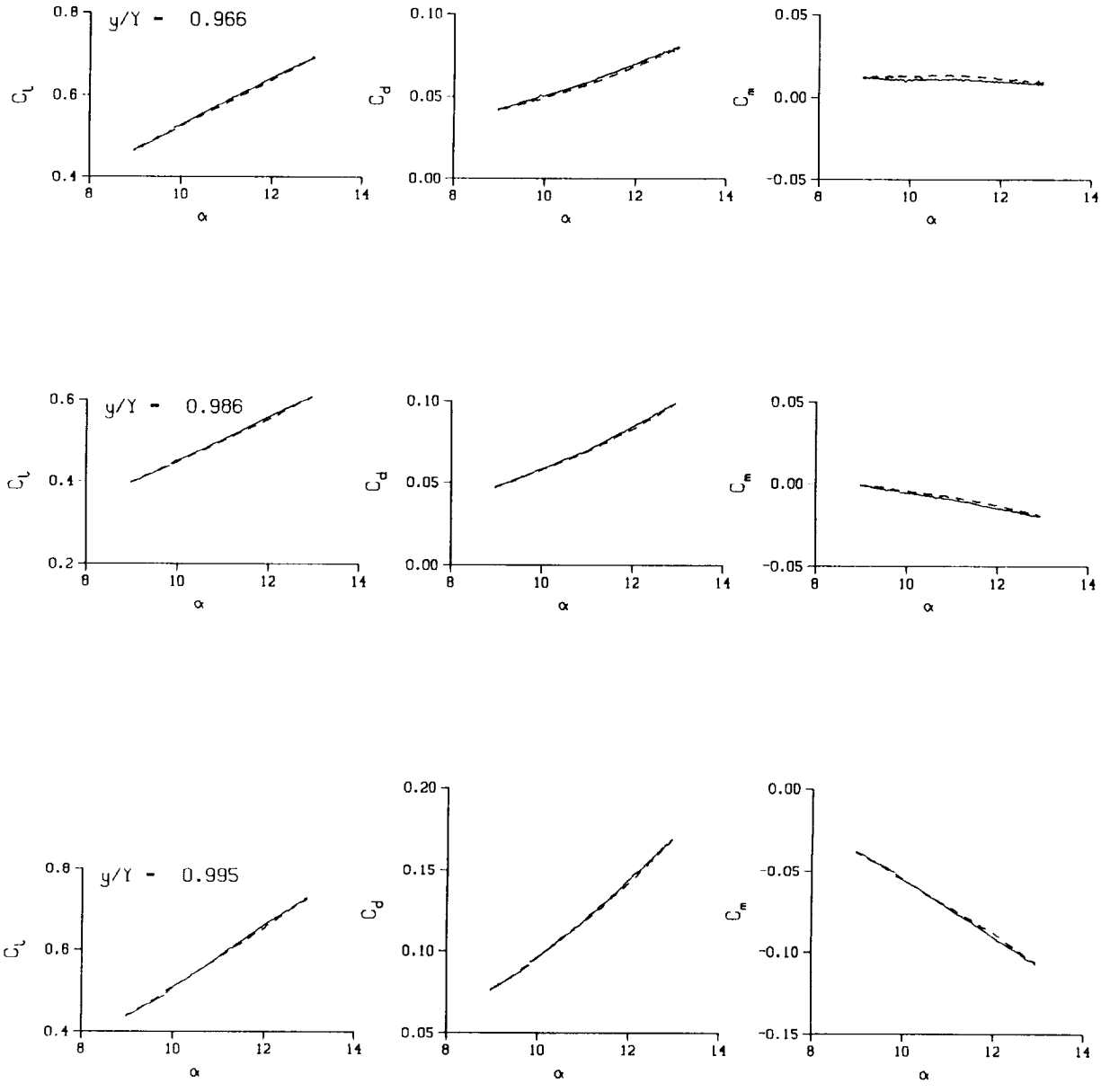

(a) v = 0.04. Concluded

Figure 88. Continued.

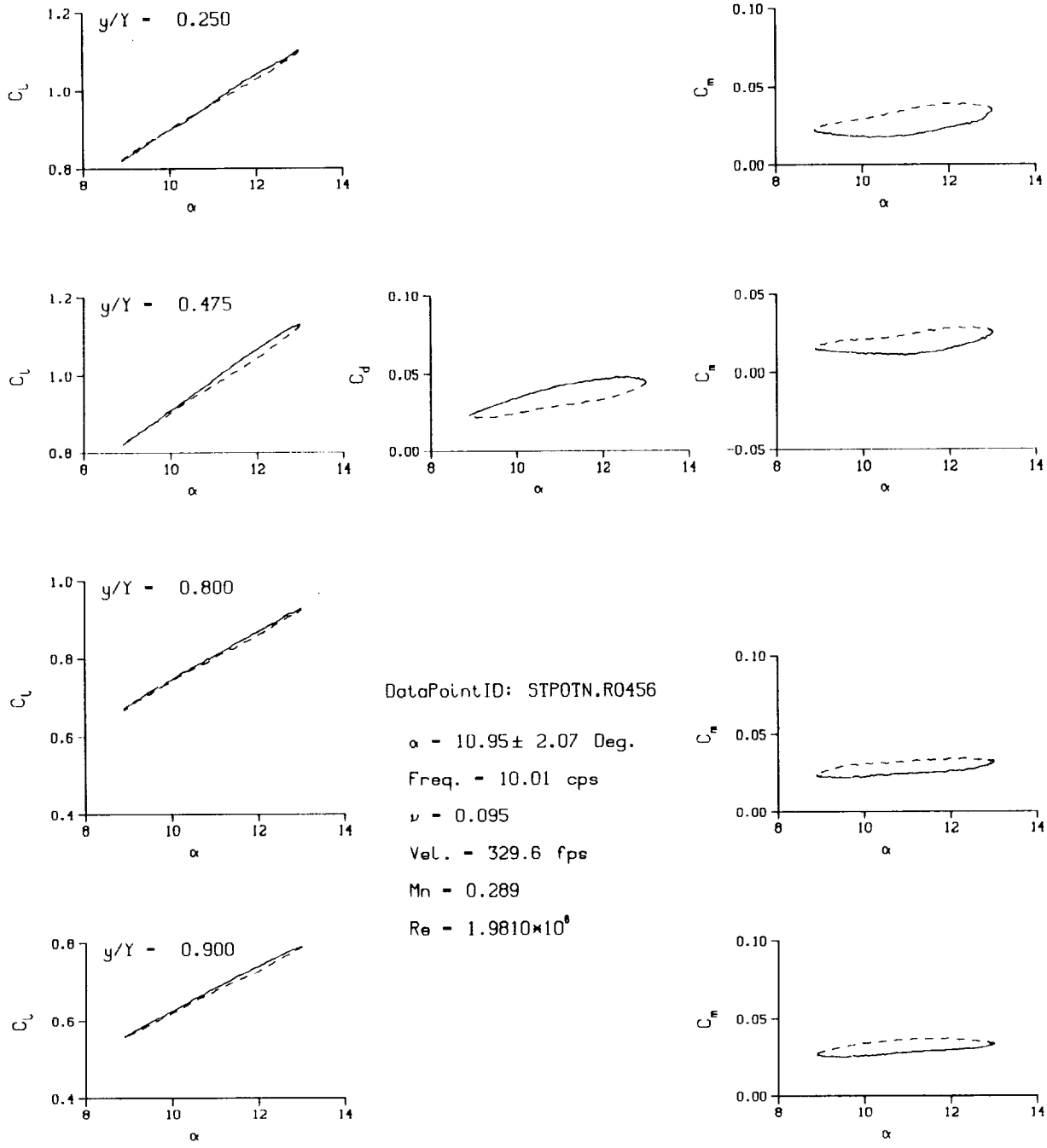

(b) v = 0.10

Figure 88. Continued.

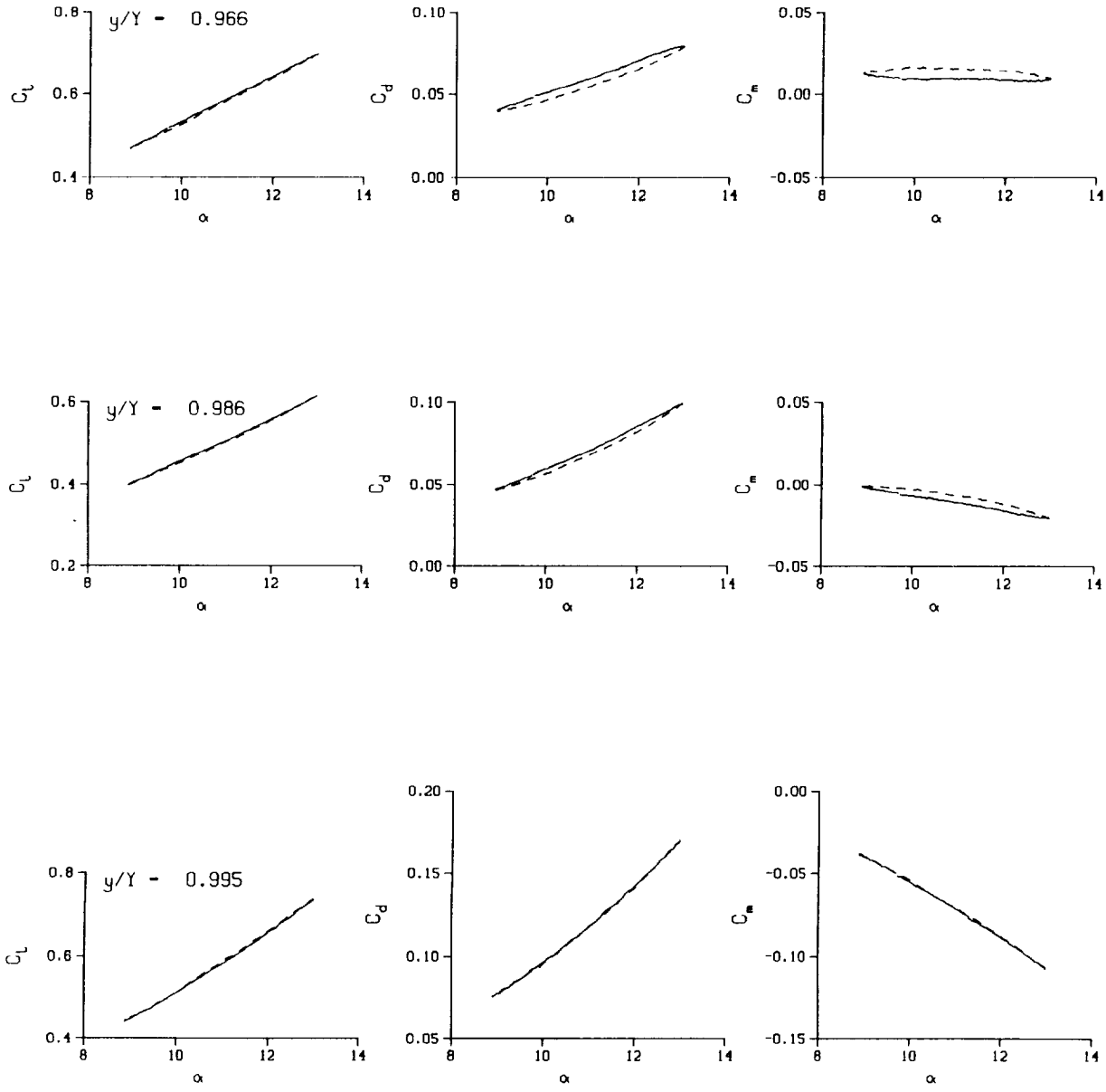

(b) v = 0.10. Concluded

Figure 88. Continued.

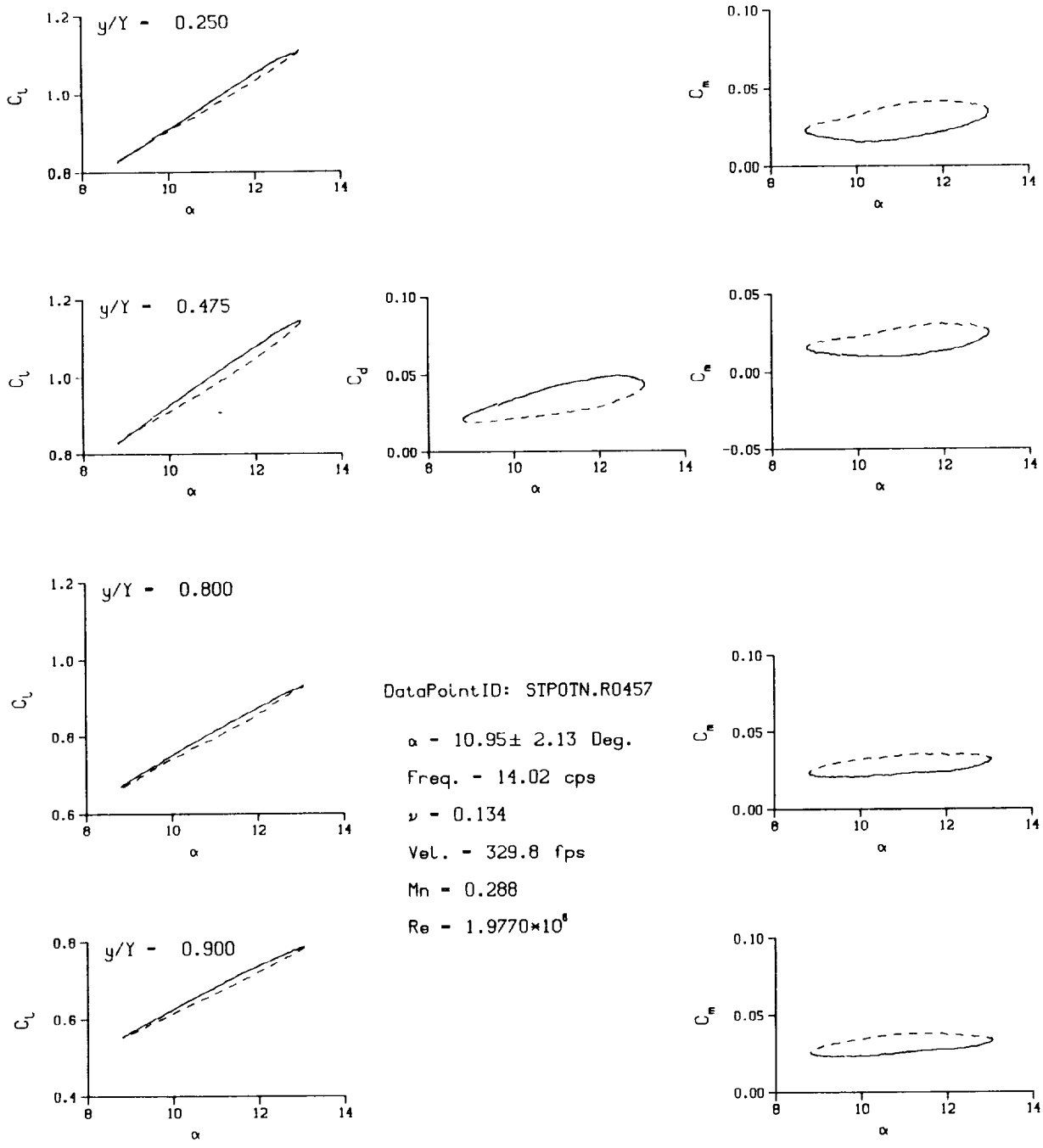

(c) v = 0.14

Figure 88. Continued.

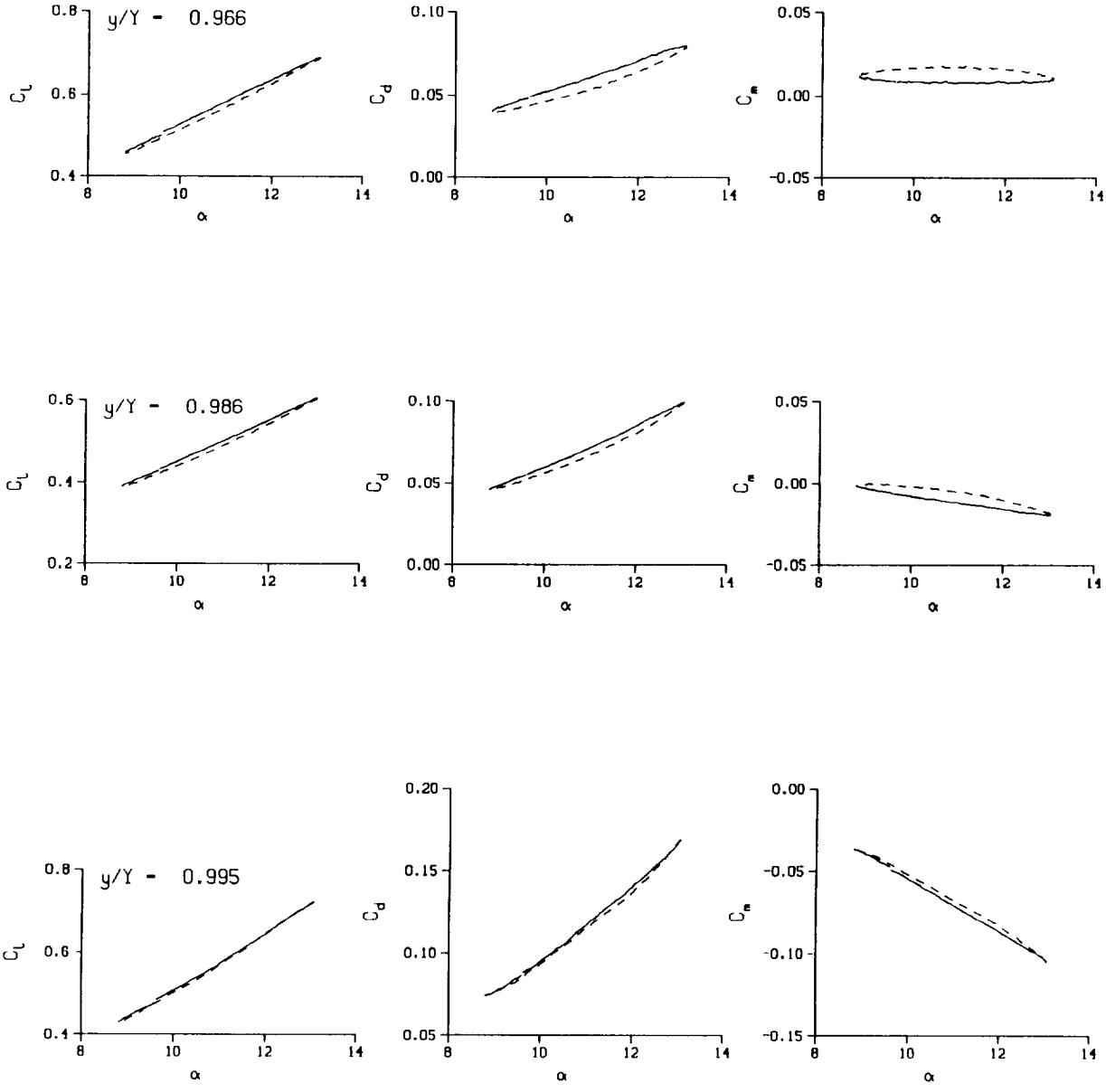

(c) v = 0.14. Concluded

Figure 88. Continued.

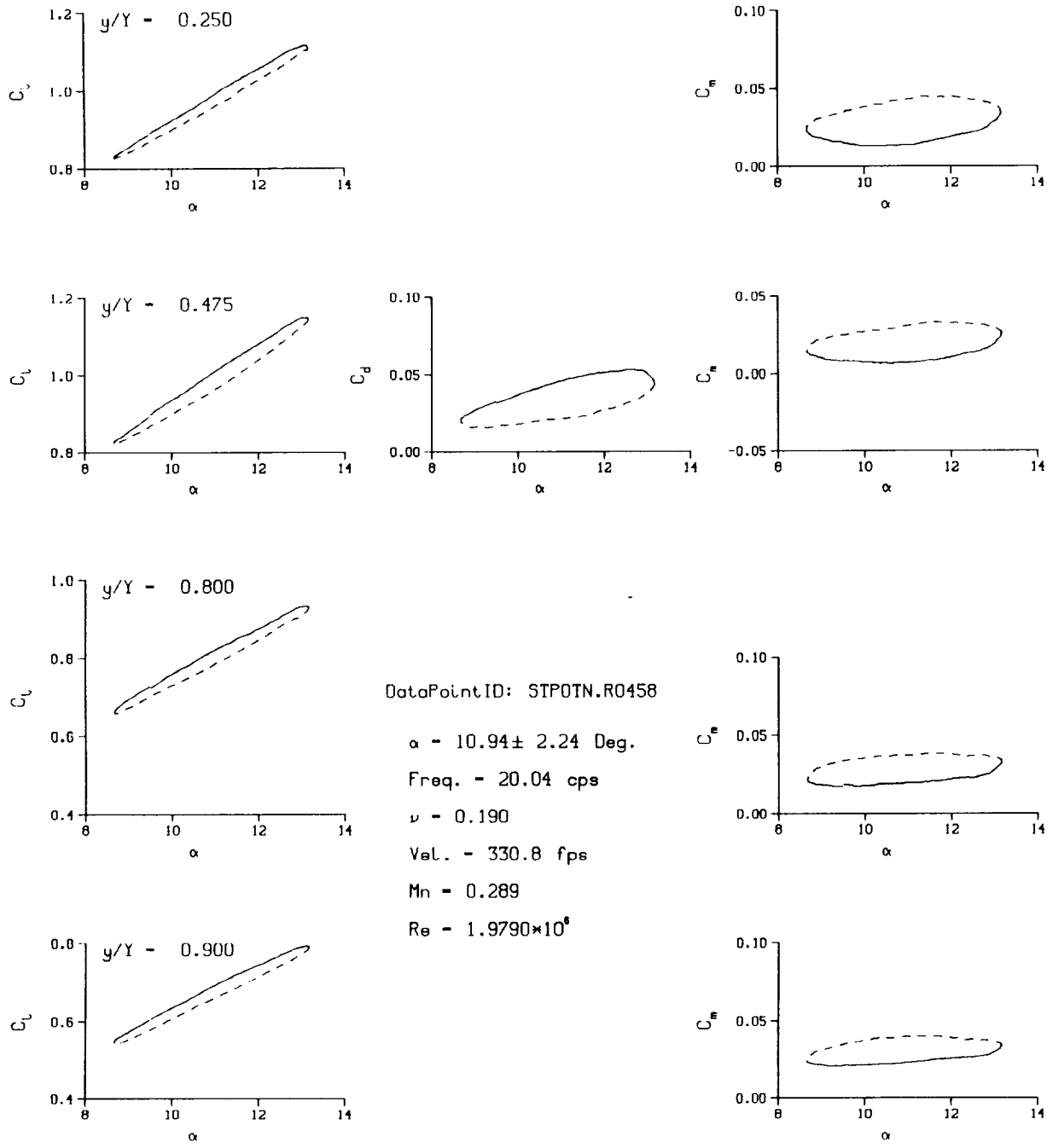

(d) v = 0.20

Figure 88. Continued.

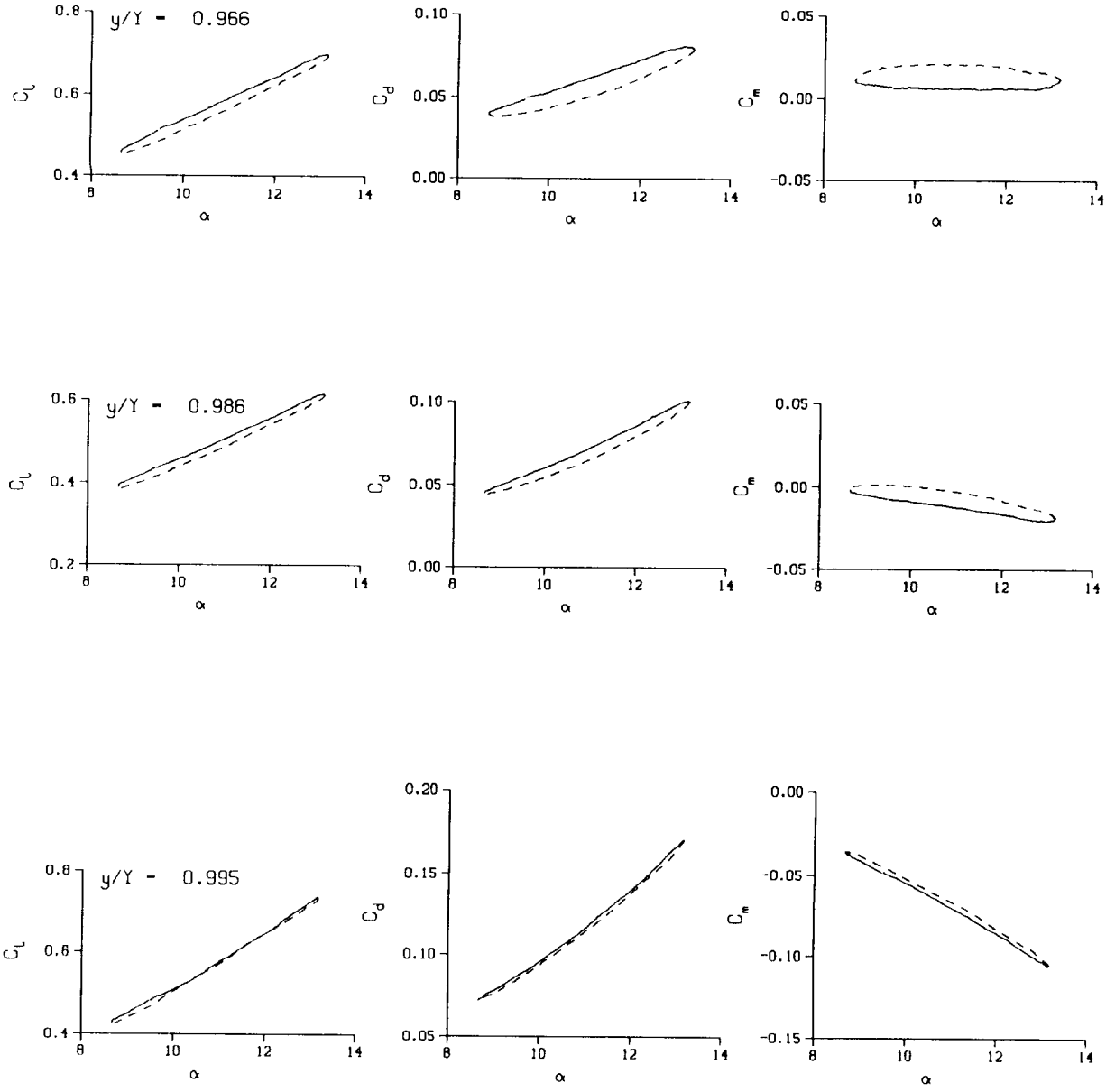

(d) v = 0.20. Concluded

Figure 88. Concluded.

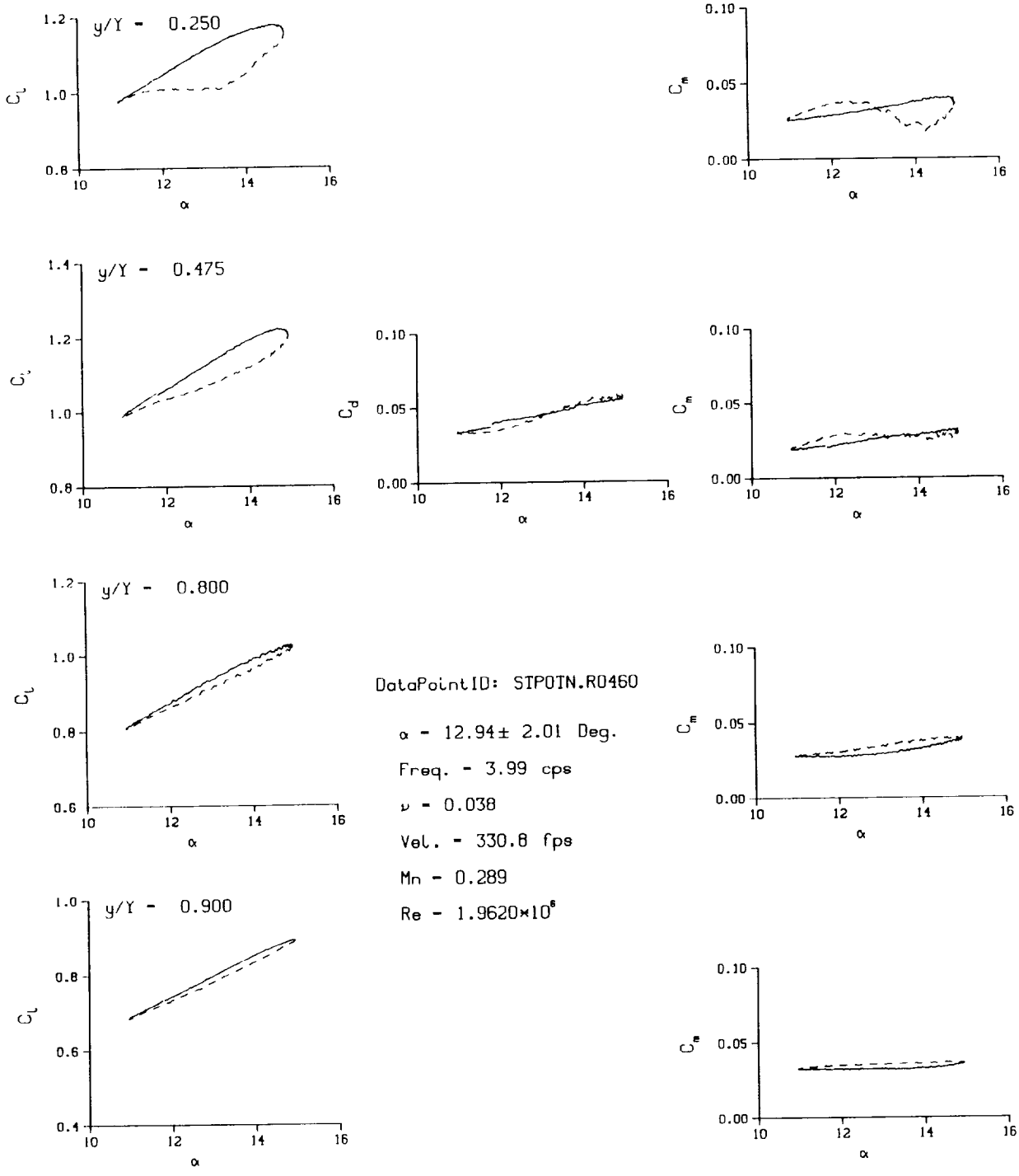

(a) ν = 0.04

Figure 89. 3-D square tip pitch oscillation data; no BL-trip; α = 13 ± 2 deg.

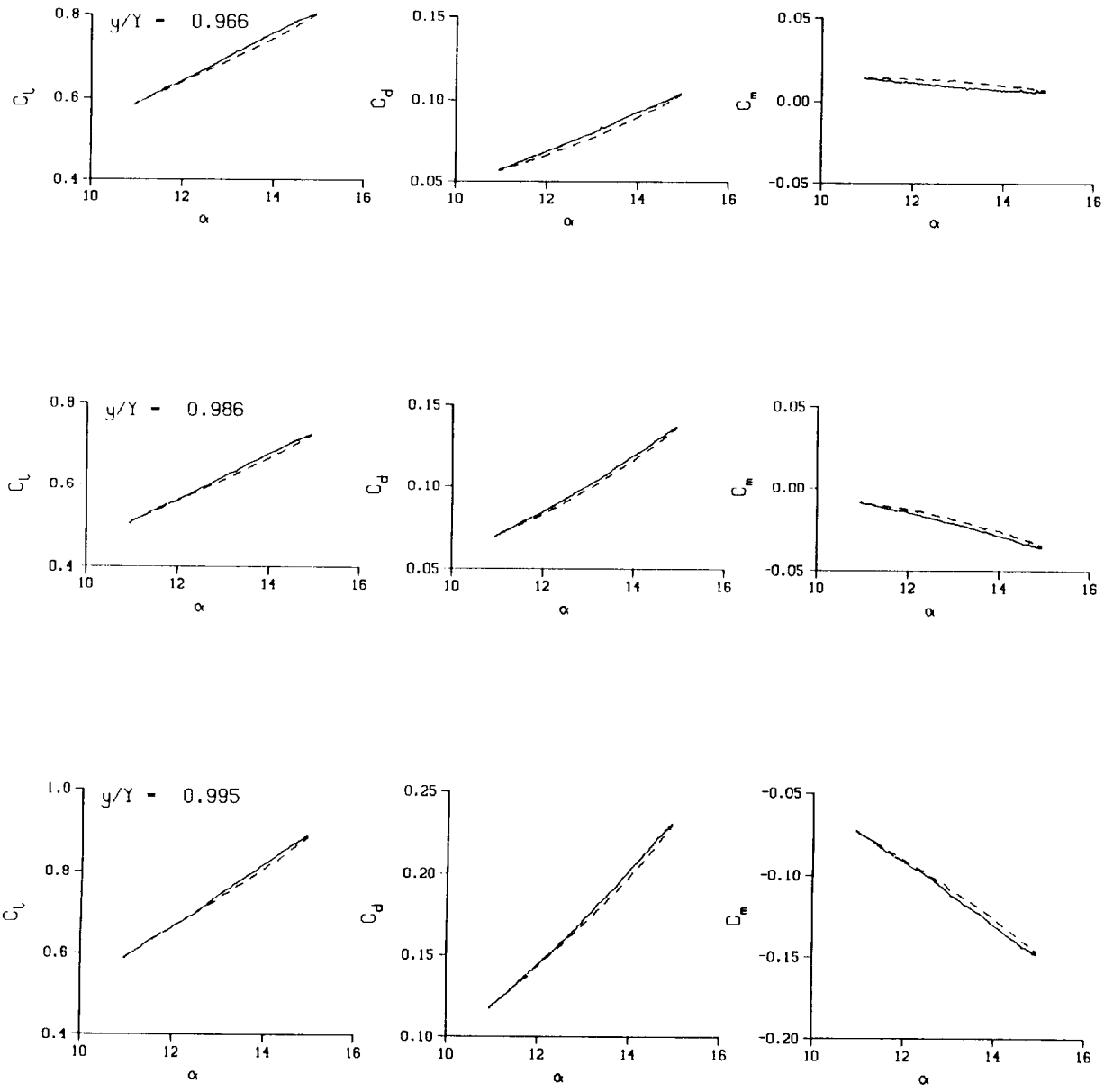

(a) v = 0.04. Concluded

Figure 89. Continued.

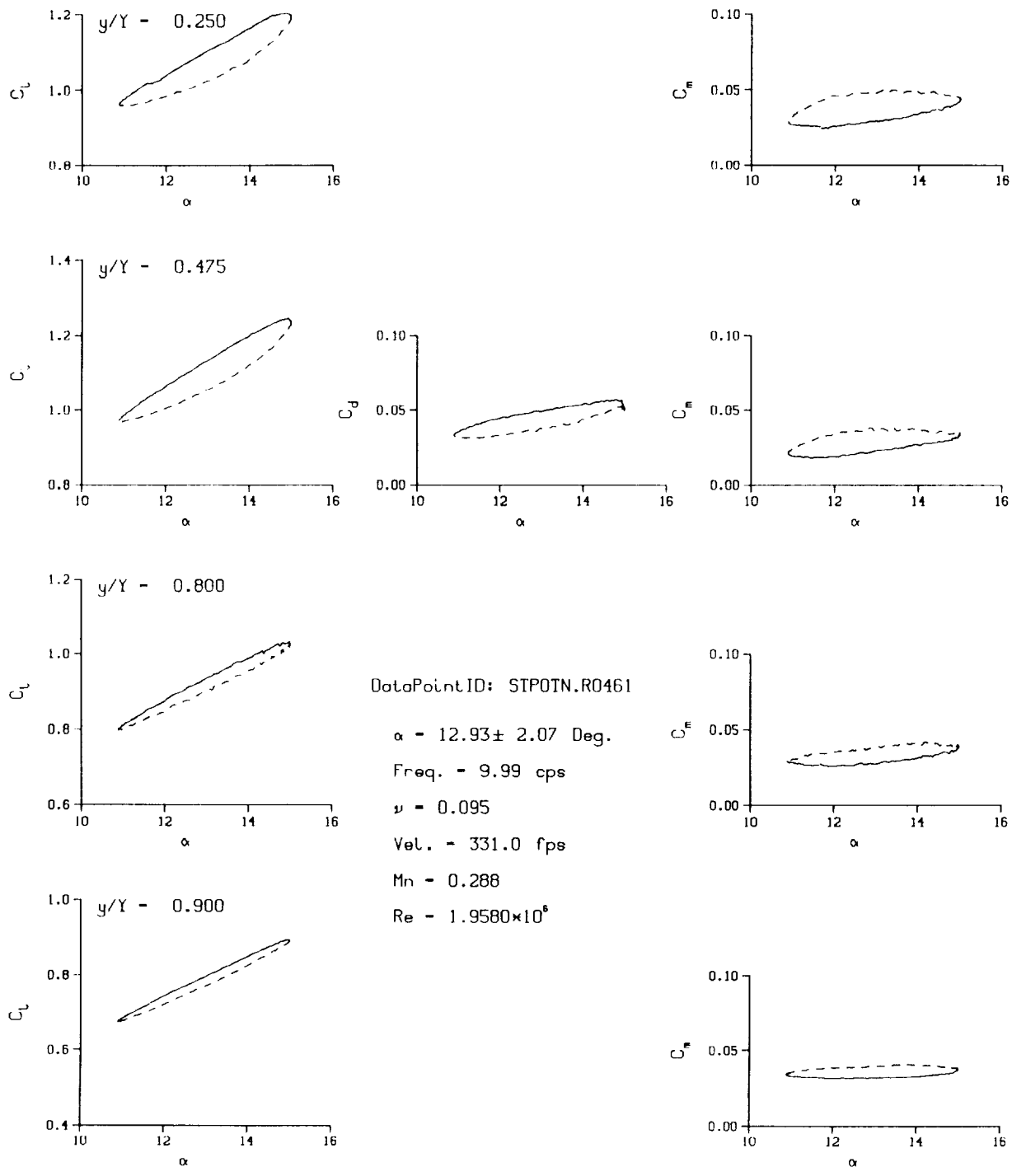

(b) v = 0.10

Figure 89. Continued.

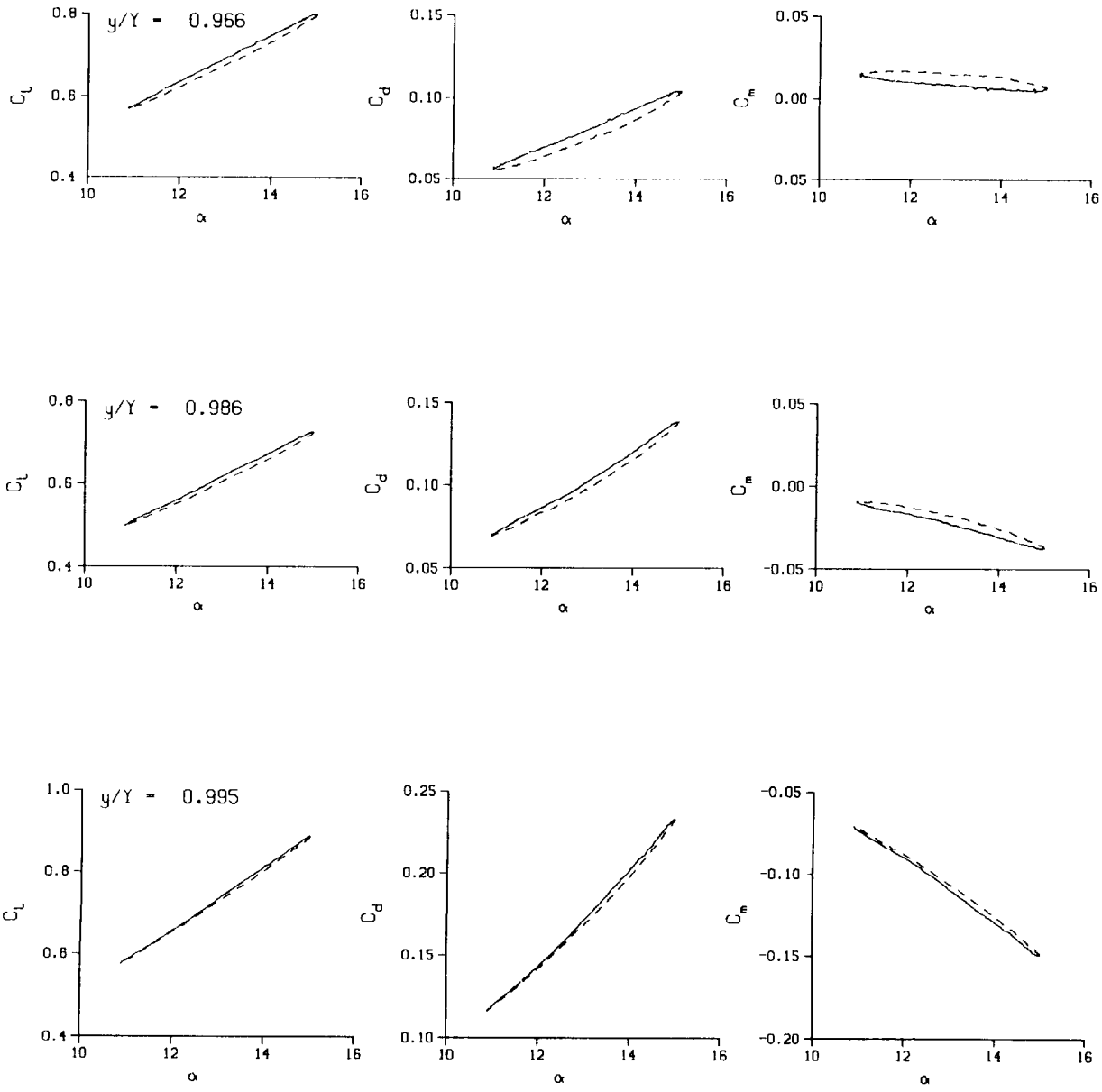

(b) v = 0.10. Concluded

Figure 89. Continued.

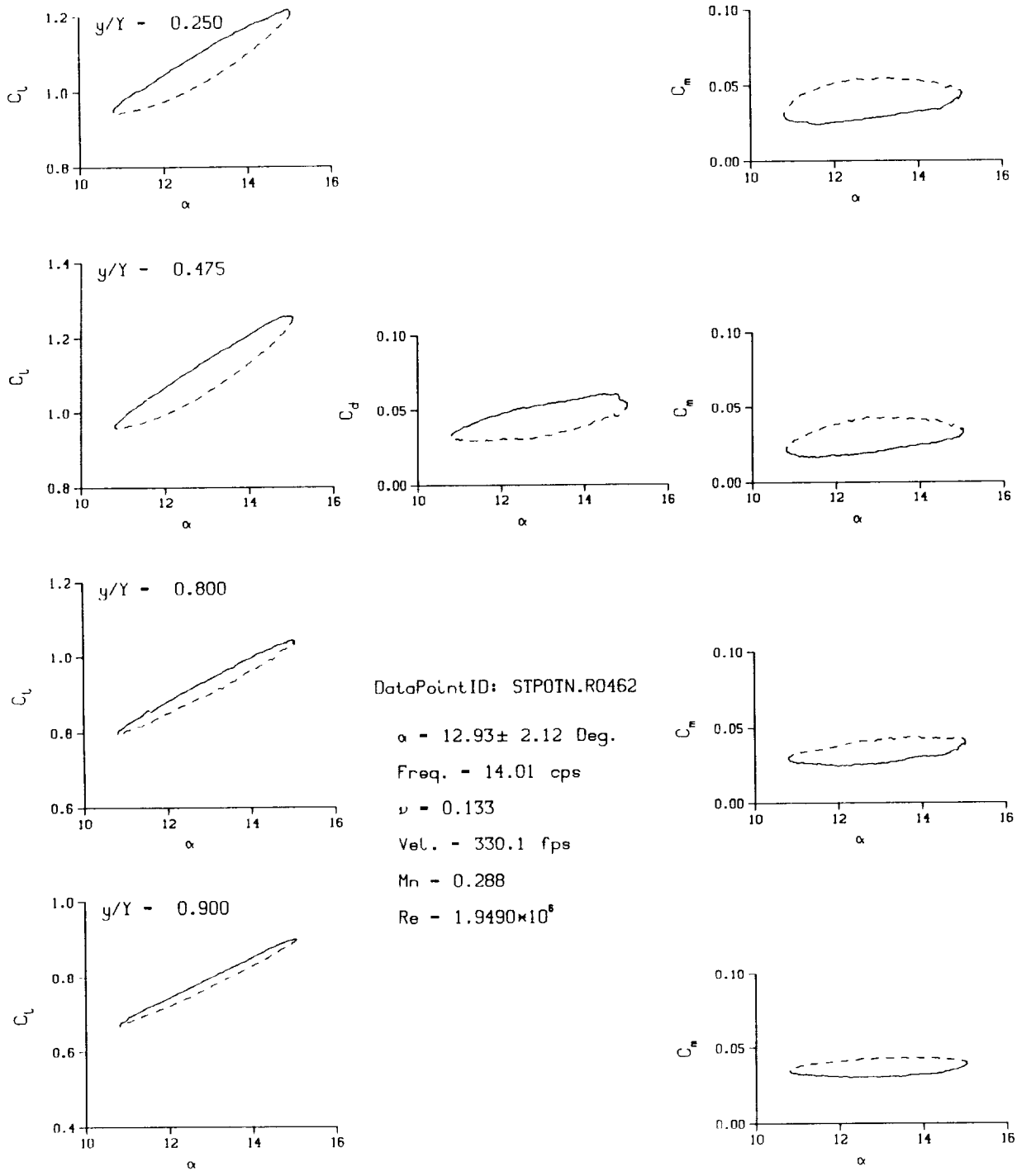

(c) v = 0.14

Figure 89. Continued.

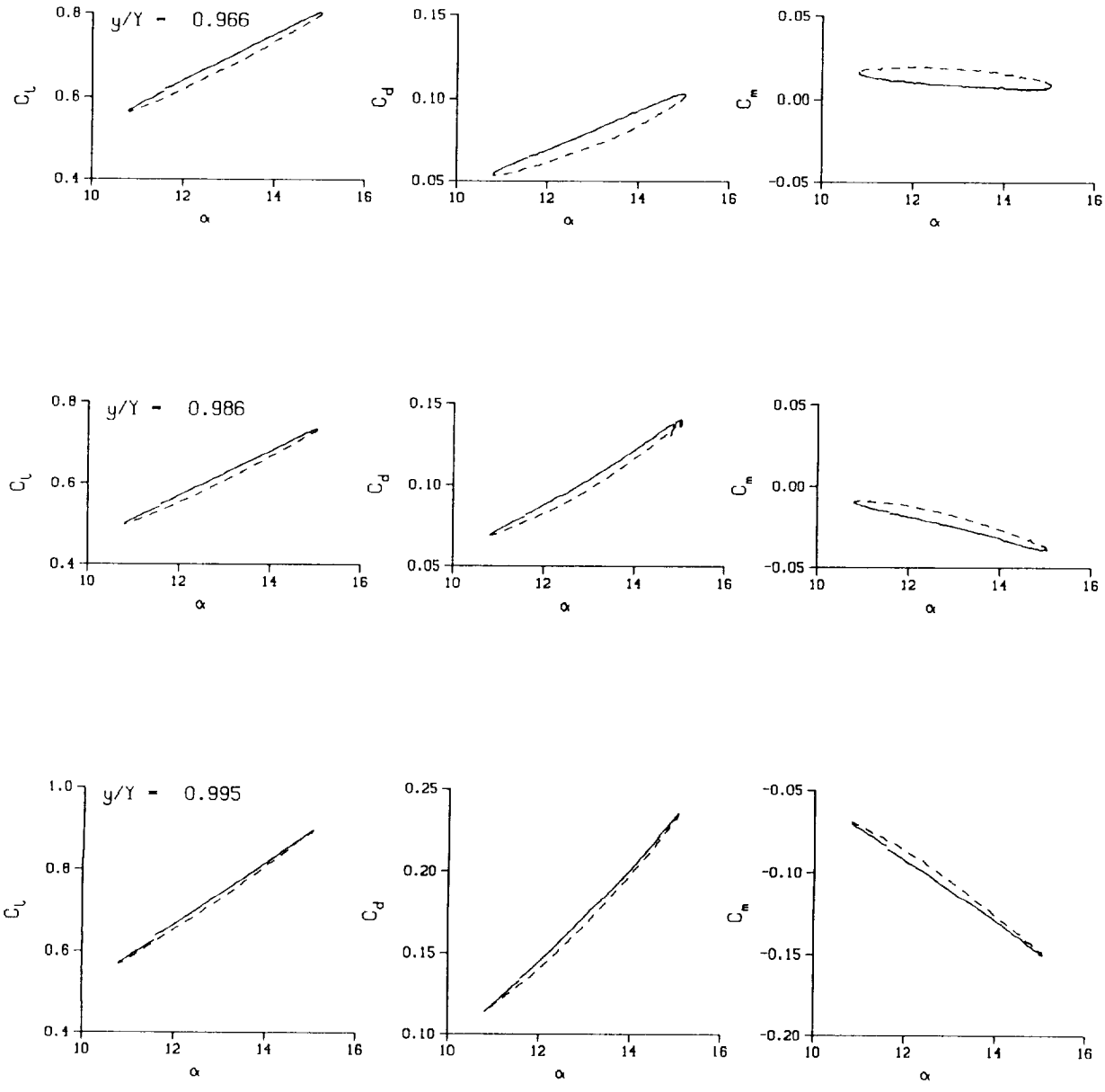

(c) v = 0.14. Concluded

Figure 89. Continued.

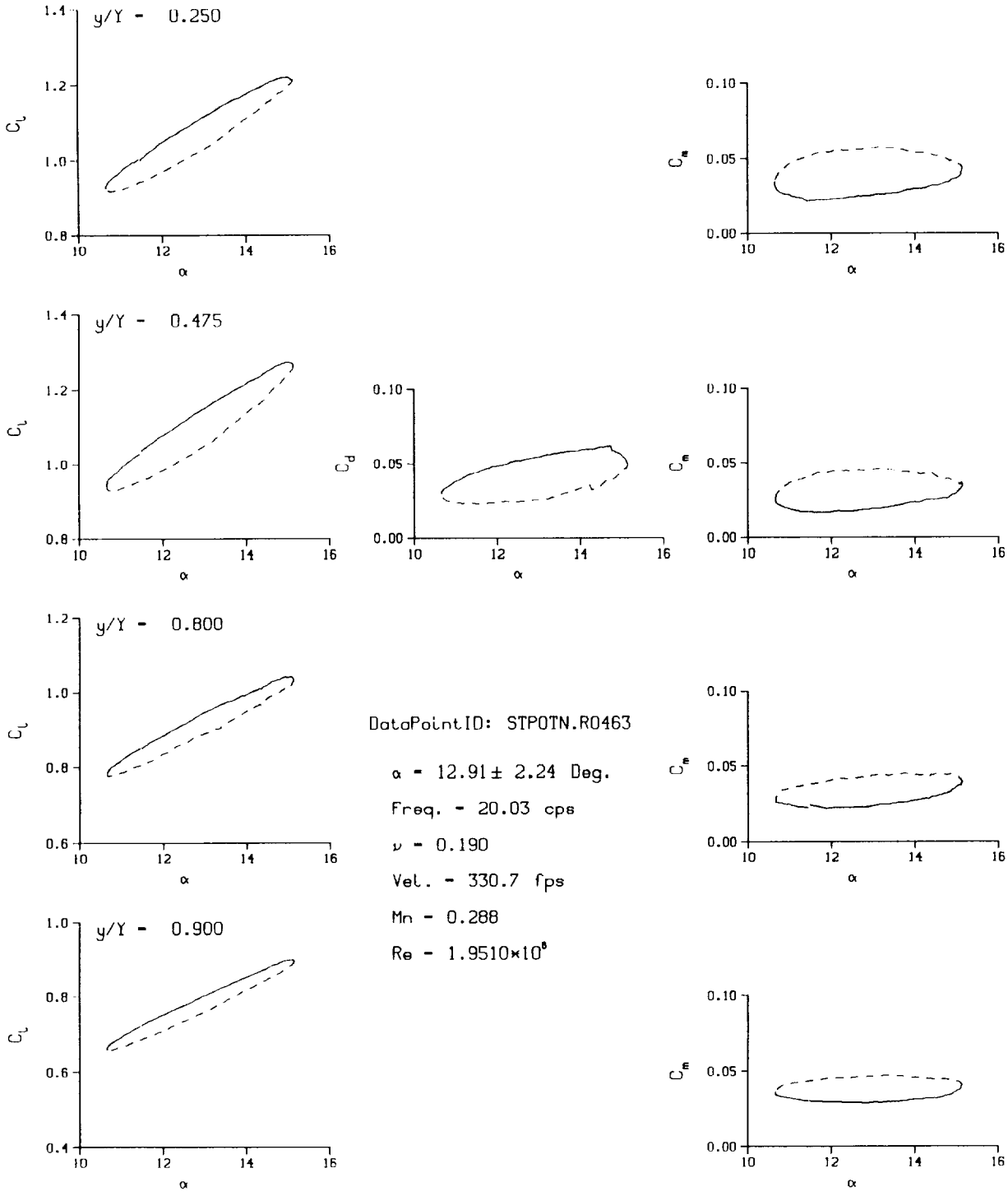

(d) v = 0.20

Figure 89. Continued.

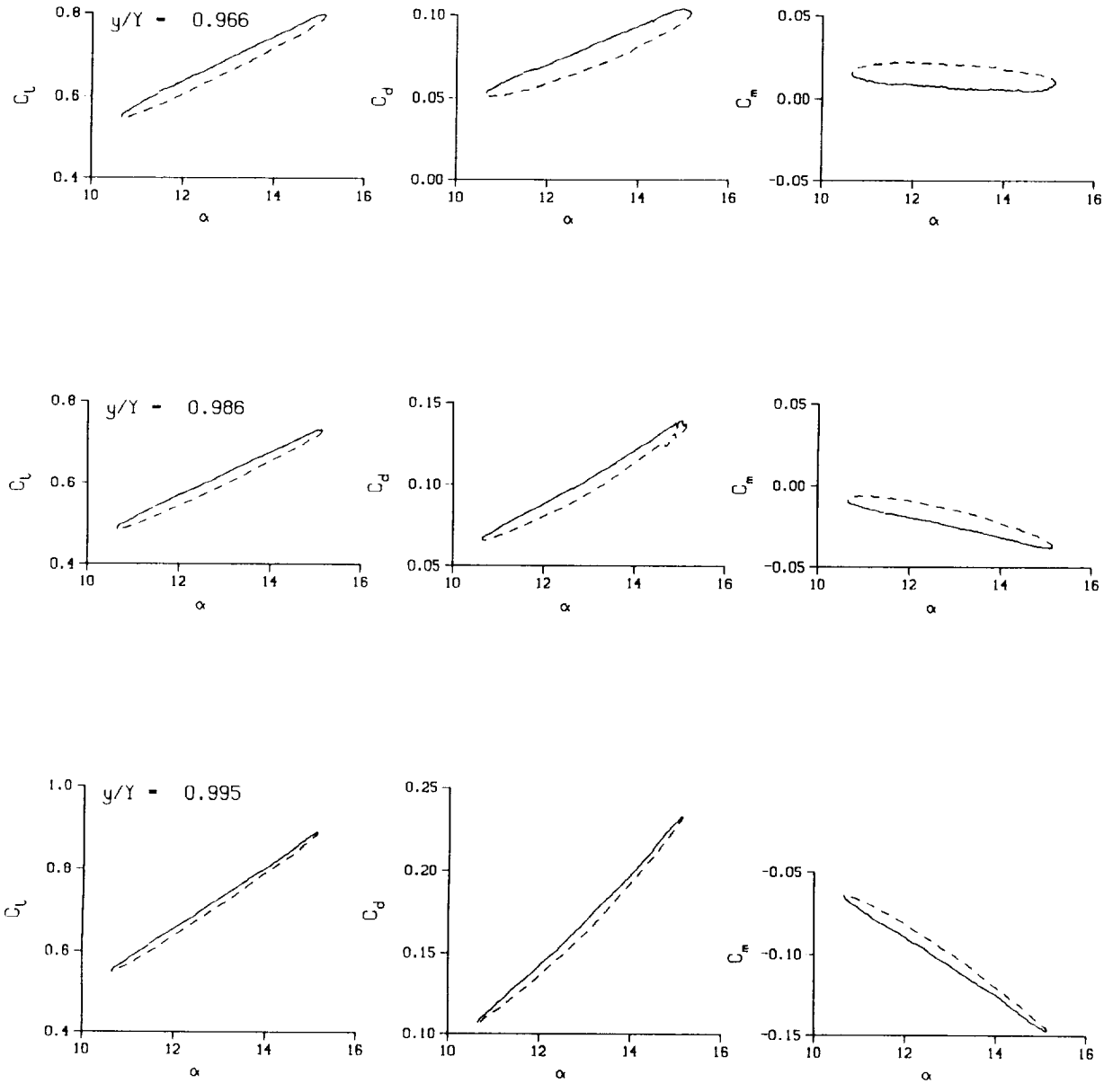

(d) v = 0.20. Concluded

Figure 89. Concluded.

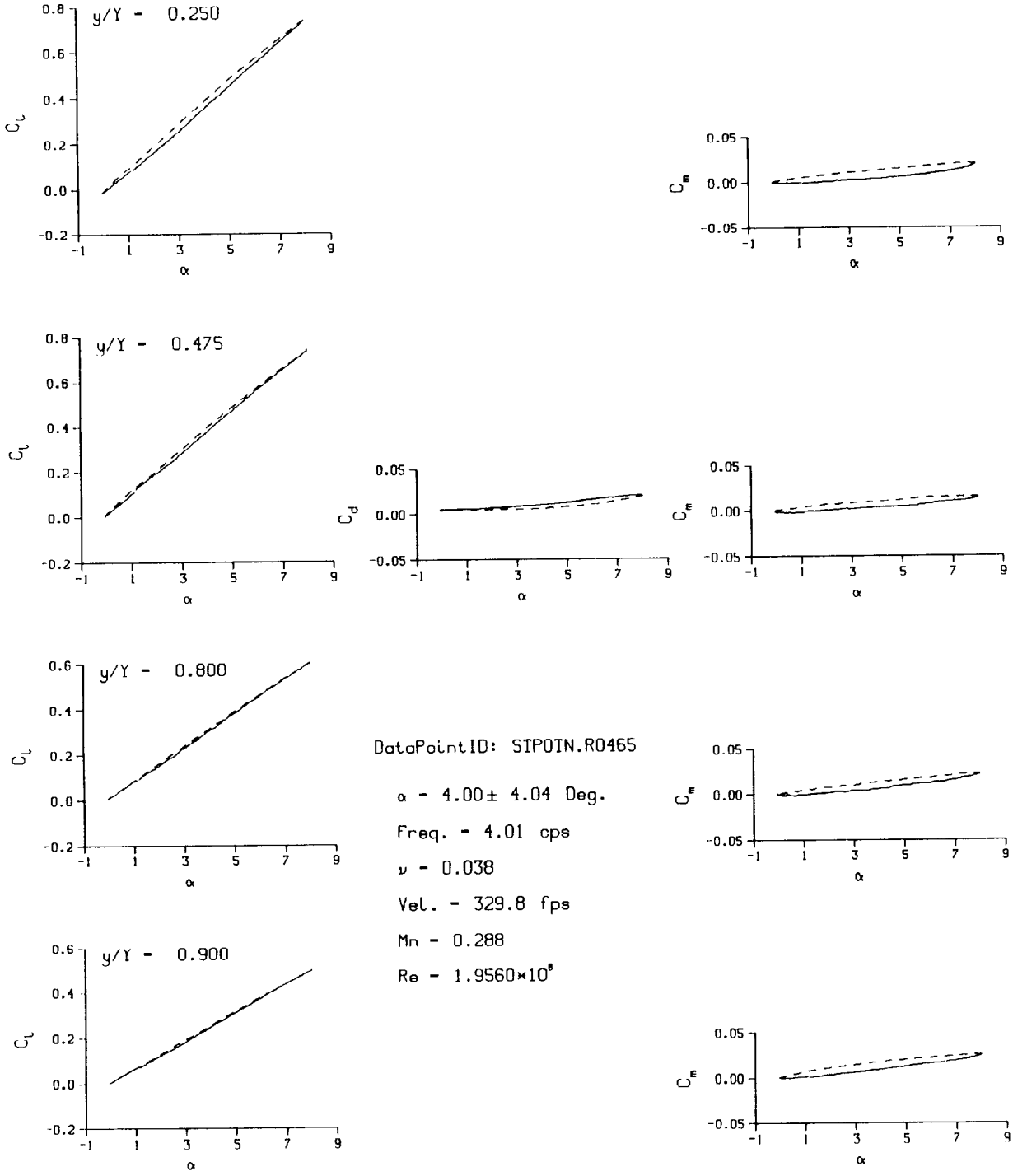

(a) ν = 0.04

Figure 90. 3-D square tip pitch oscillation data; no BL-trip; α = 4 ± 4 deg.

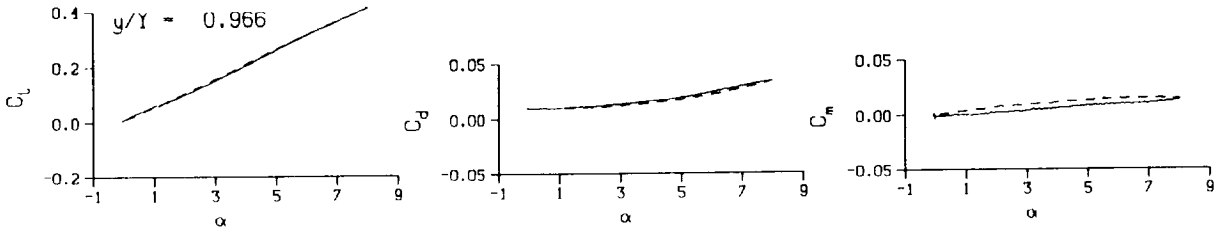

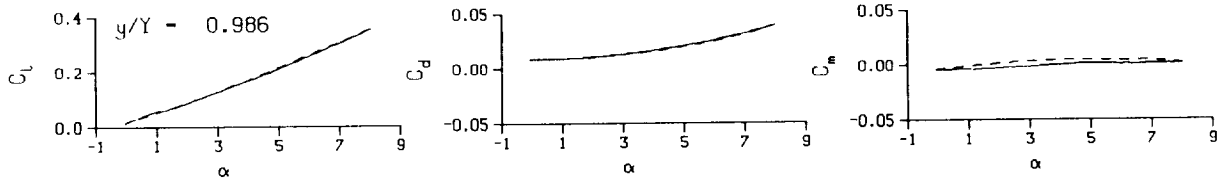

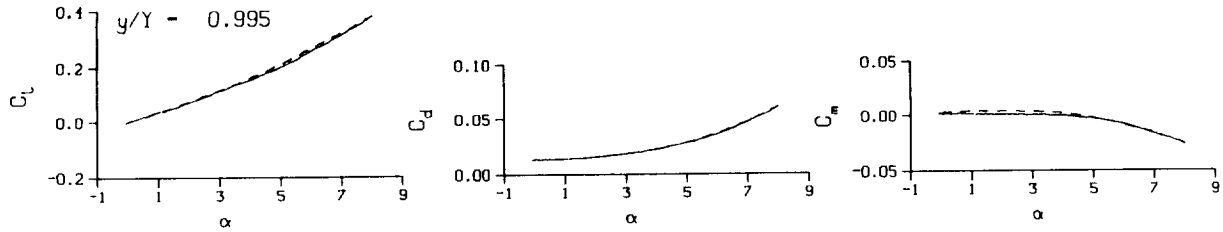

(a) v = 0.04. Concluded

Figure 90. Continued.

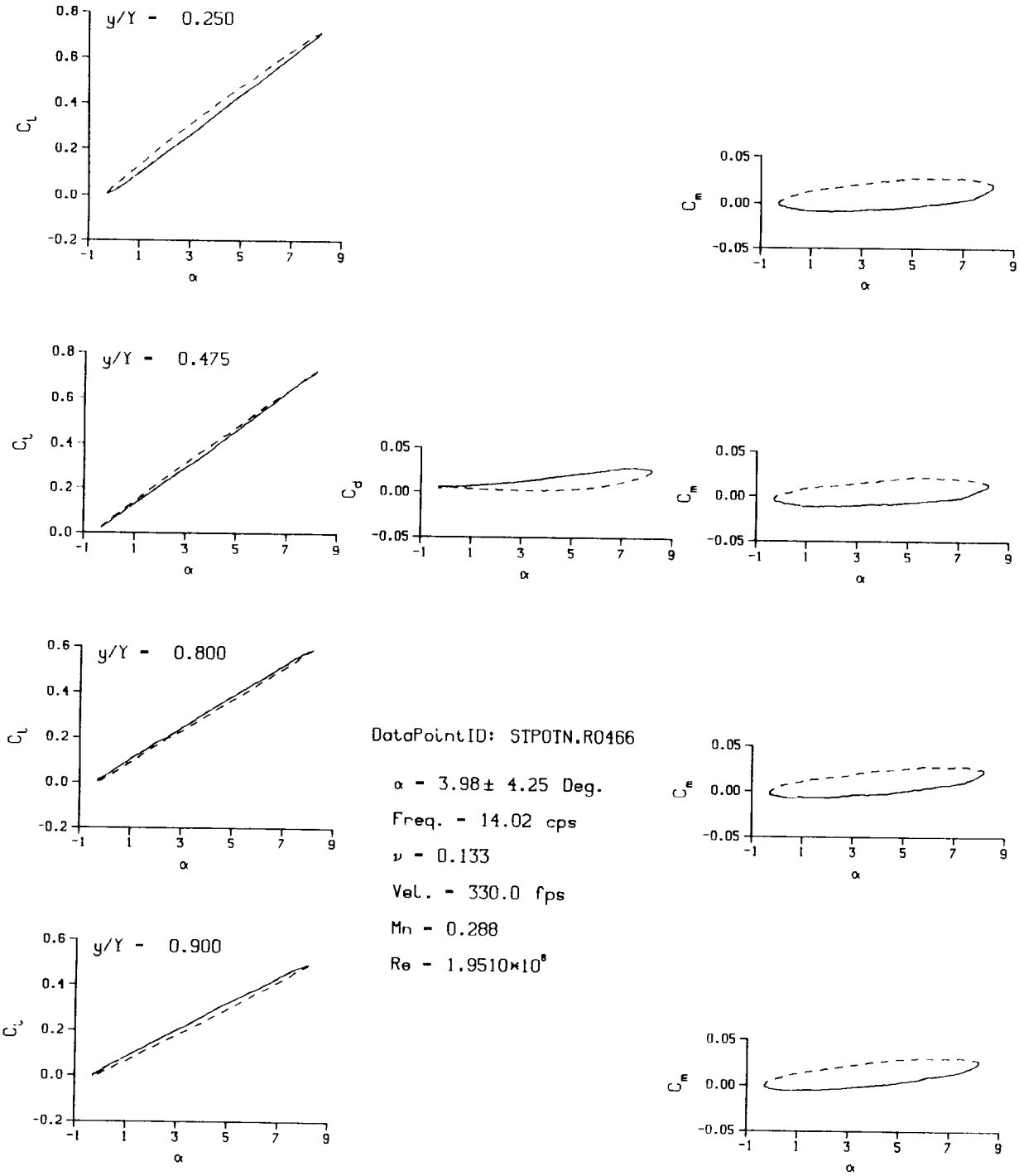

(b) v = 0.10

Figure 90. Continued.

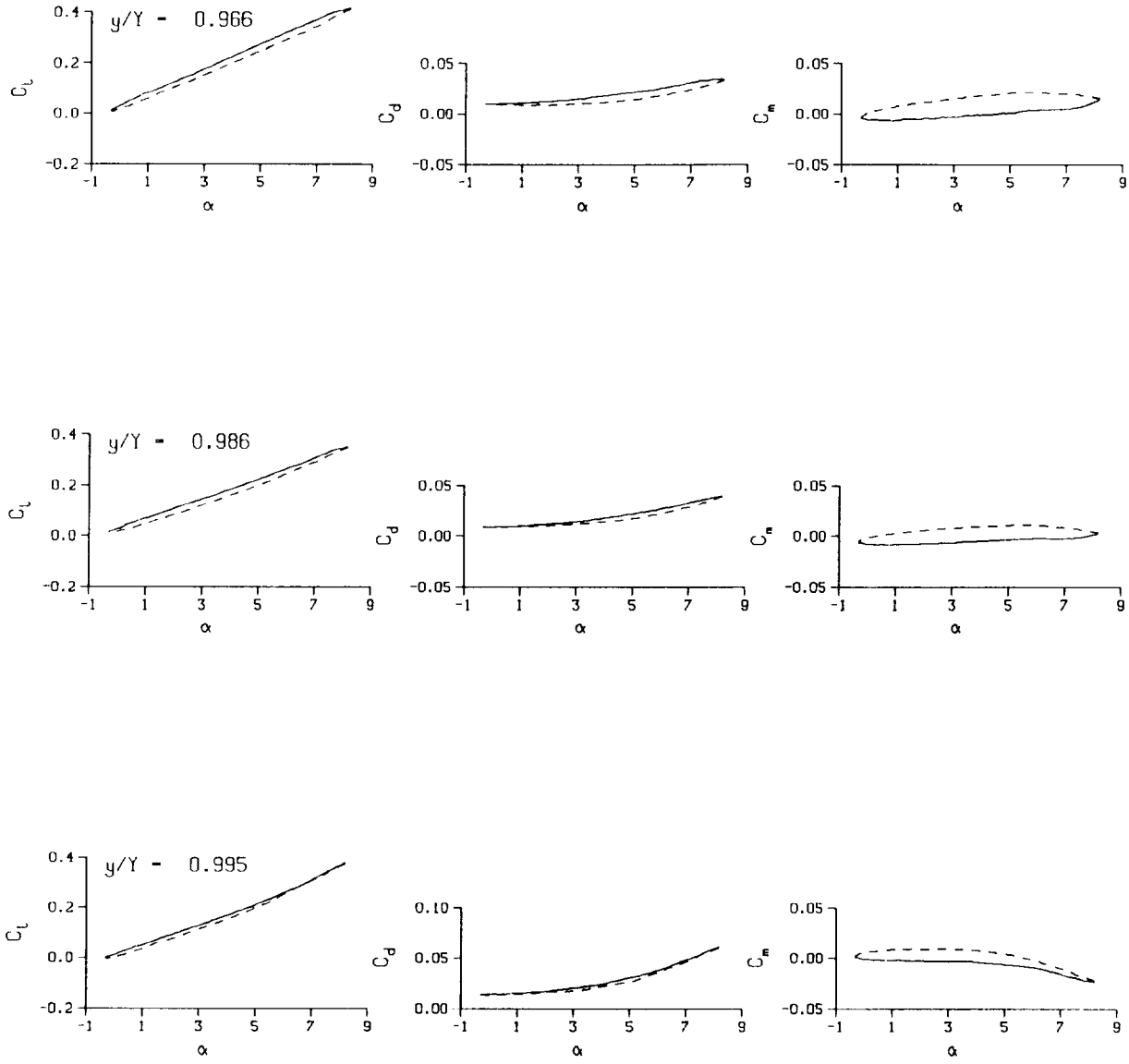

(b) v = 0.10. Concluded

Figure 90. Continued.

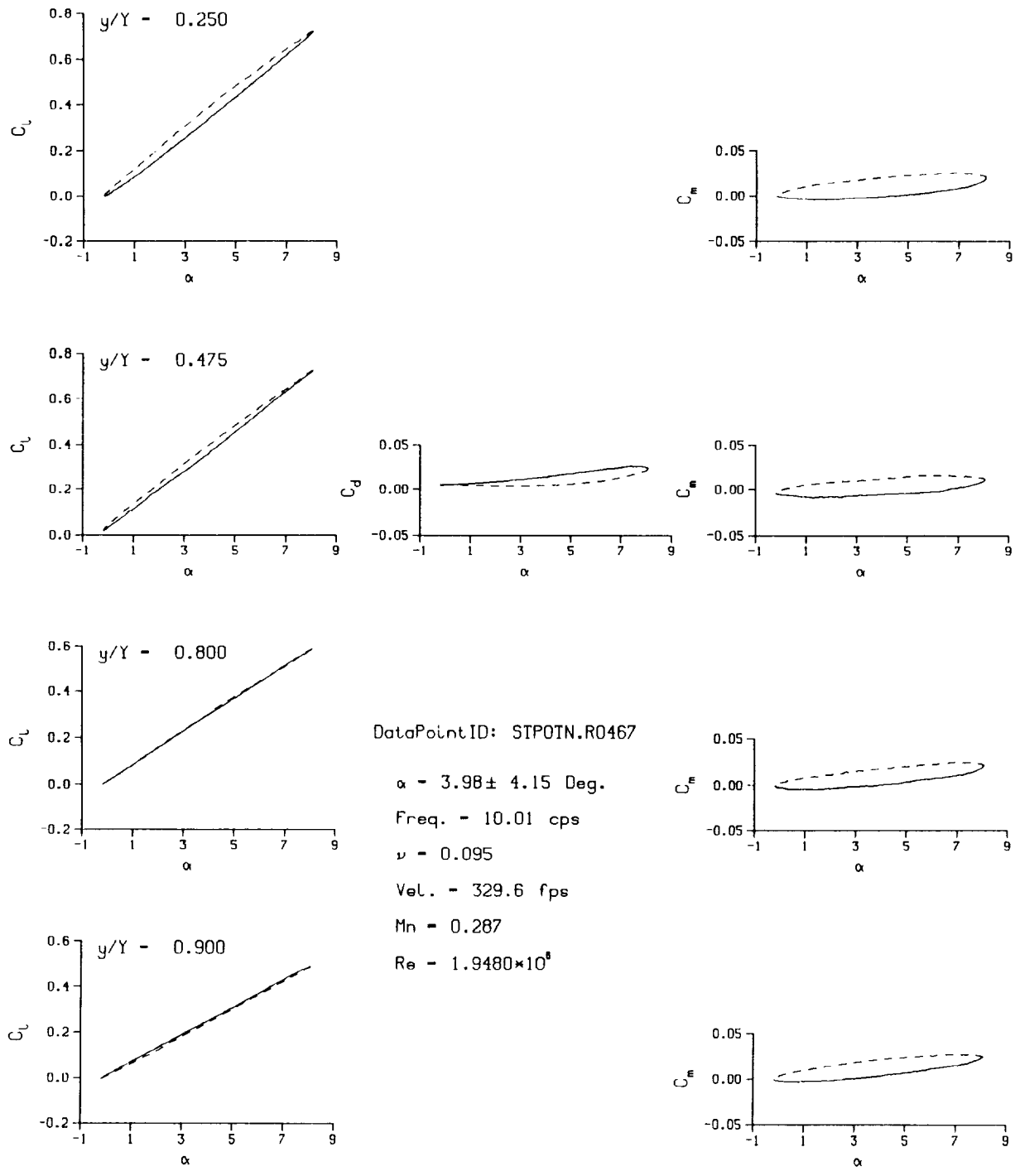

(c) v = 0.14

Figure 90. Continued.

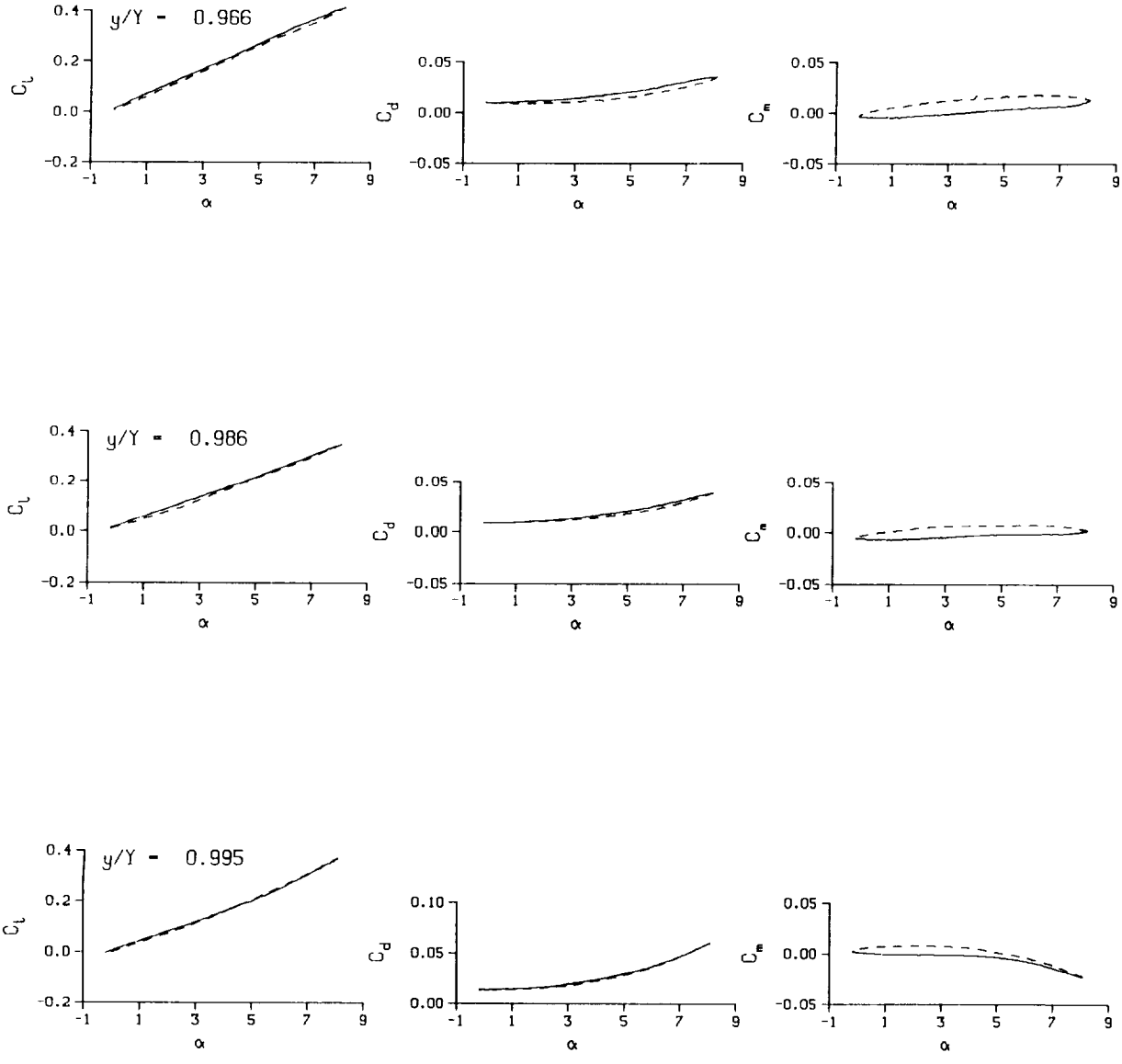

(c) v = 0.14. Concluded

Figure 90. Concluded.

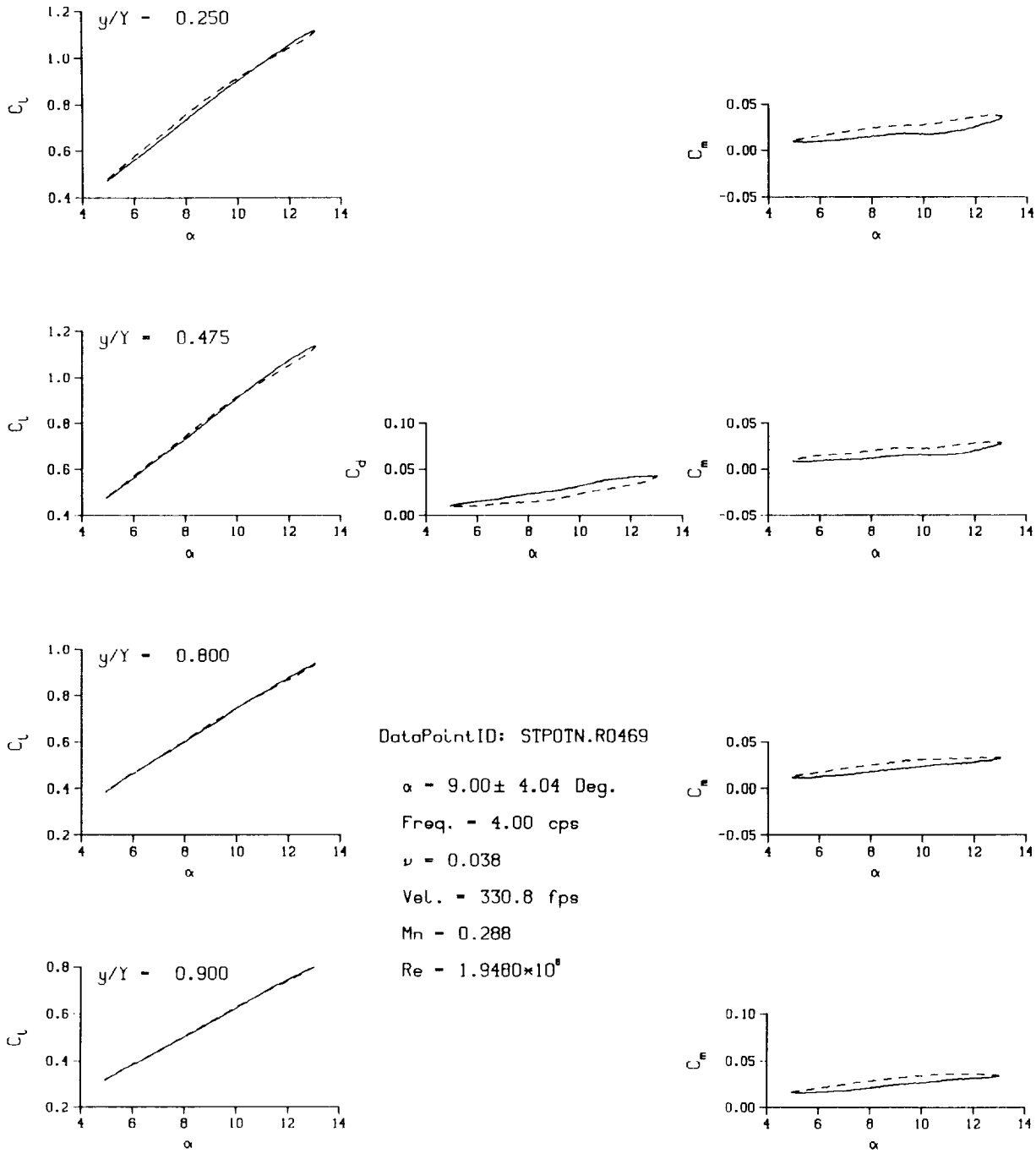

(a) ν = 0.04

Figure 91. 3-D square tip pitch oscillation data; no BL-trip; α = 9 ± 4 deg.

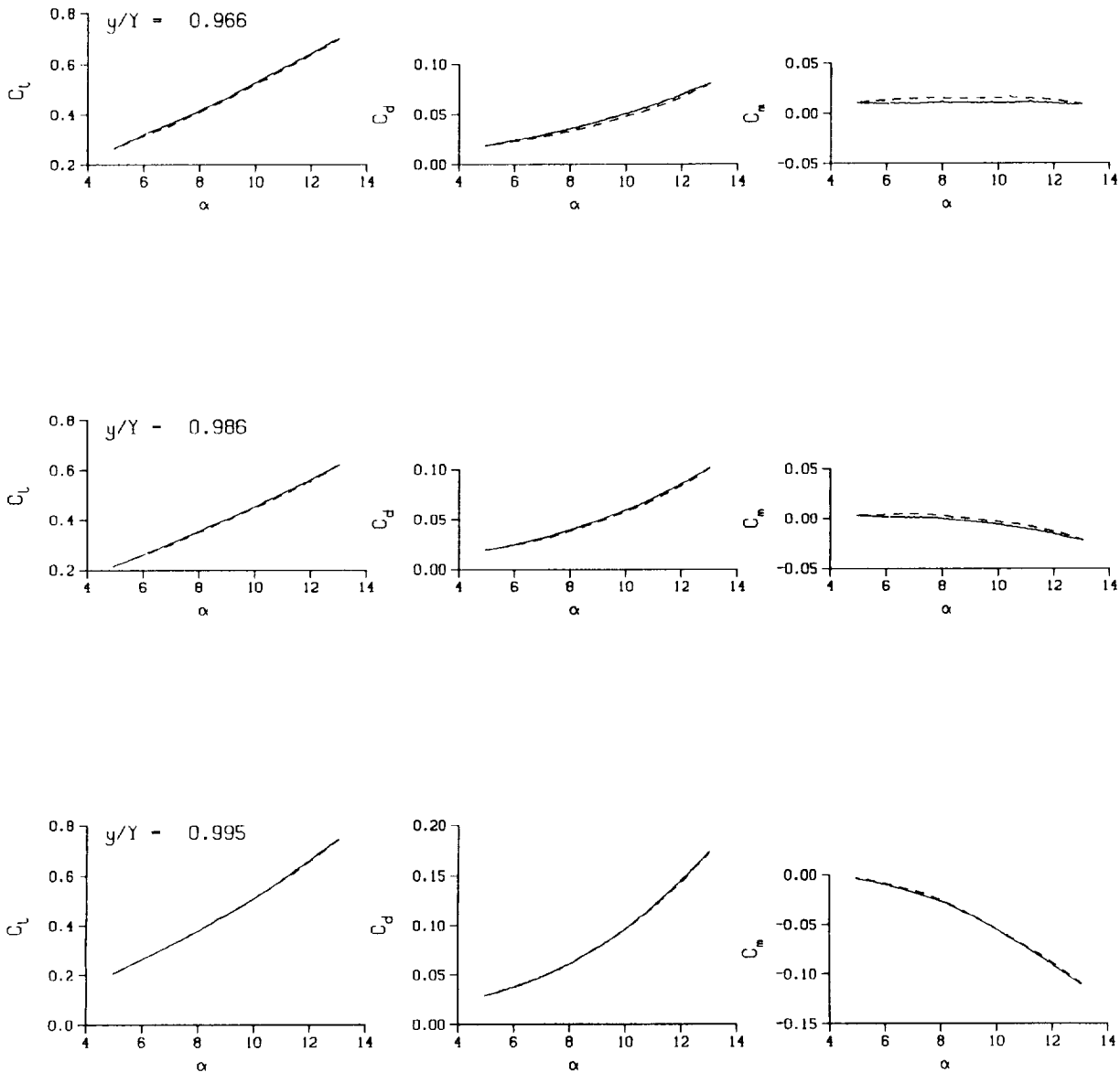

(a) v = 0.04. Concluded

Figure 91. Continued.

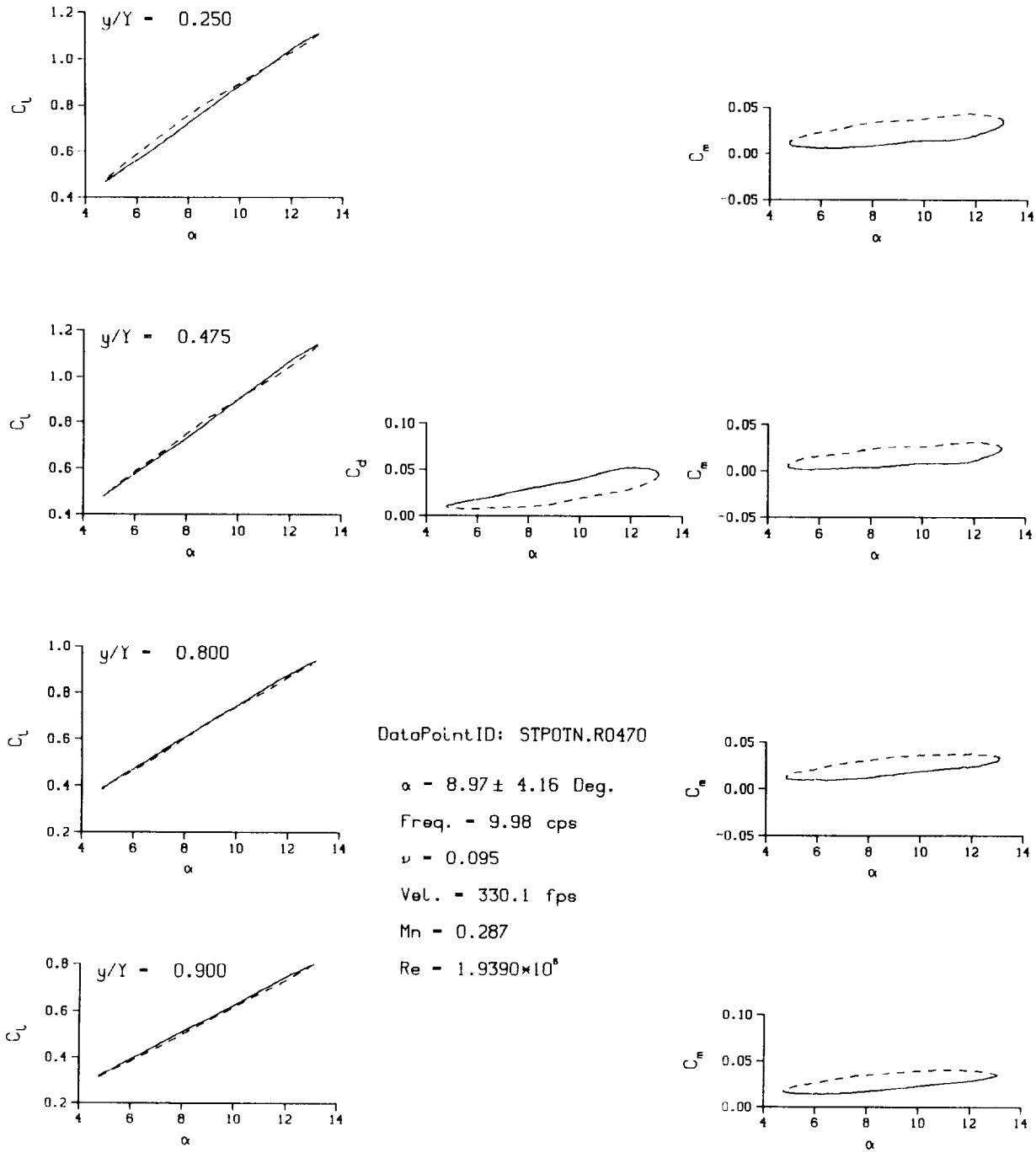

(b) v = 0.10

Figure 91. Continued.

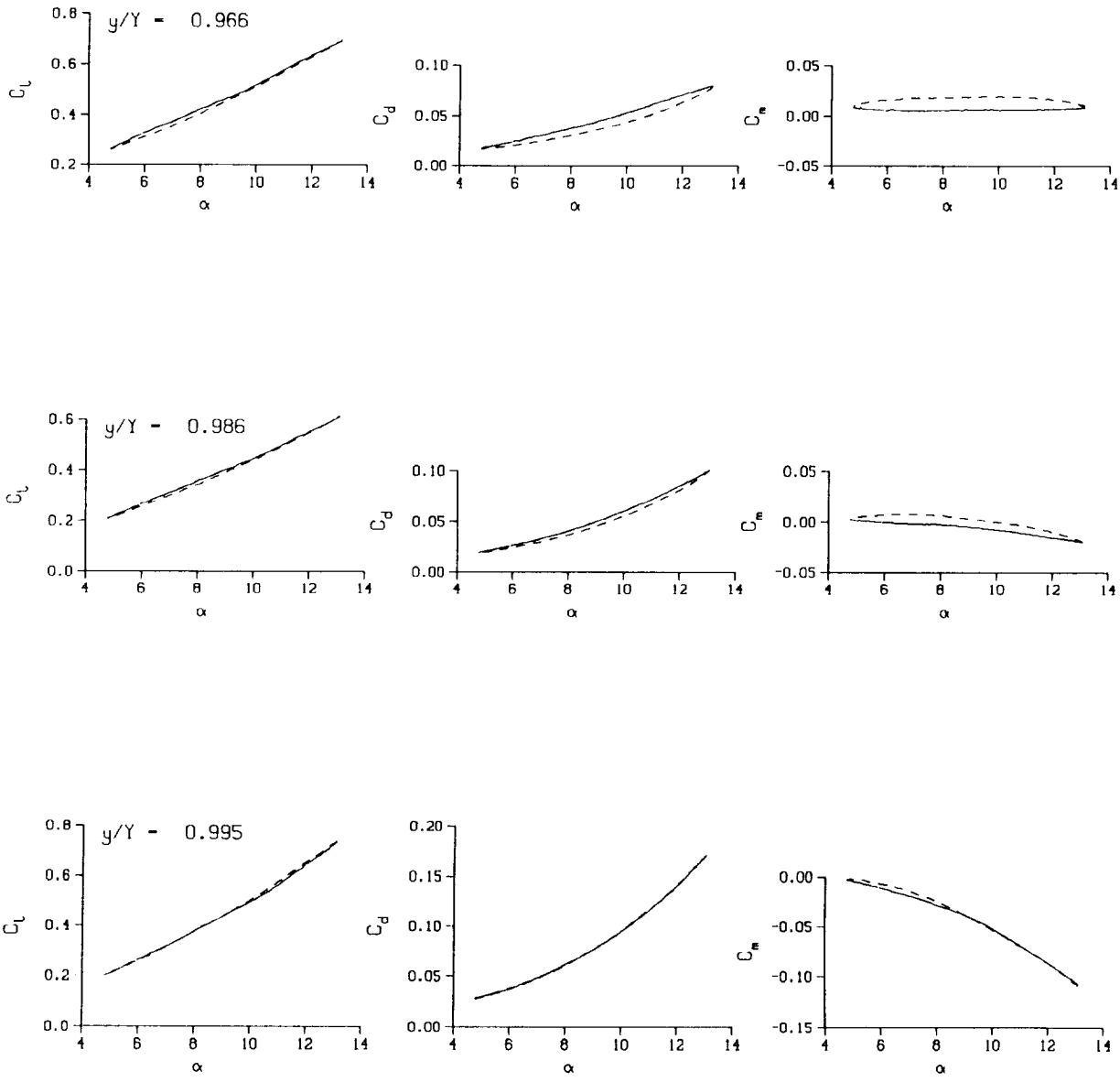

(b) v = 0.10. Concluded

Figure 91. Continued.

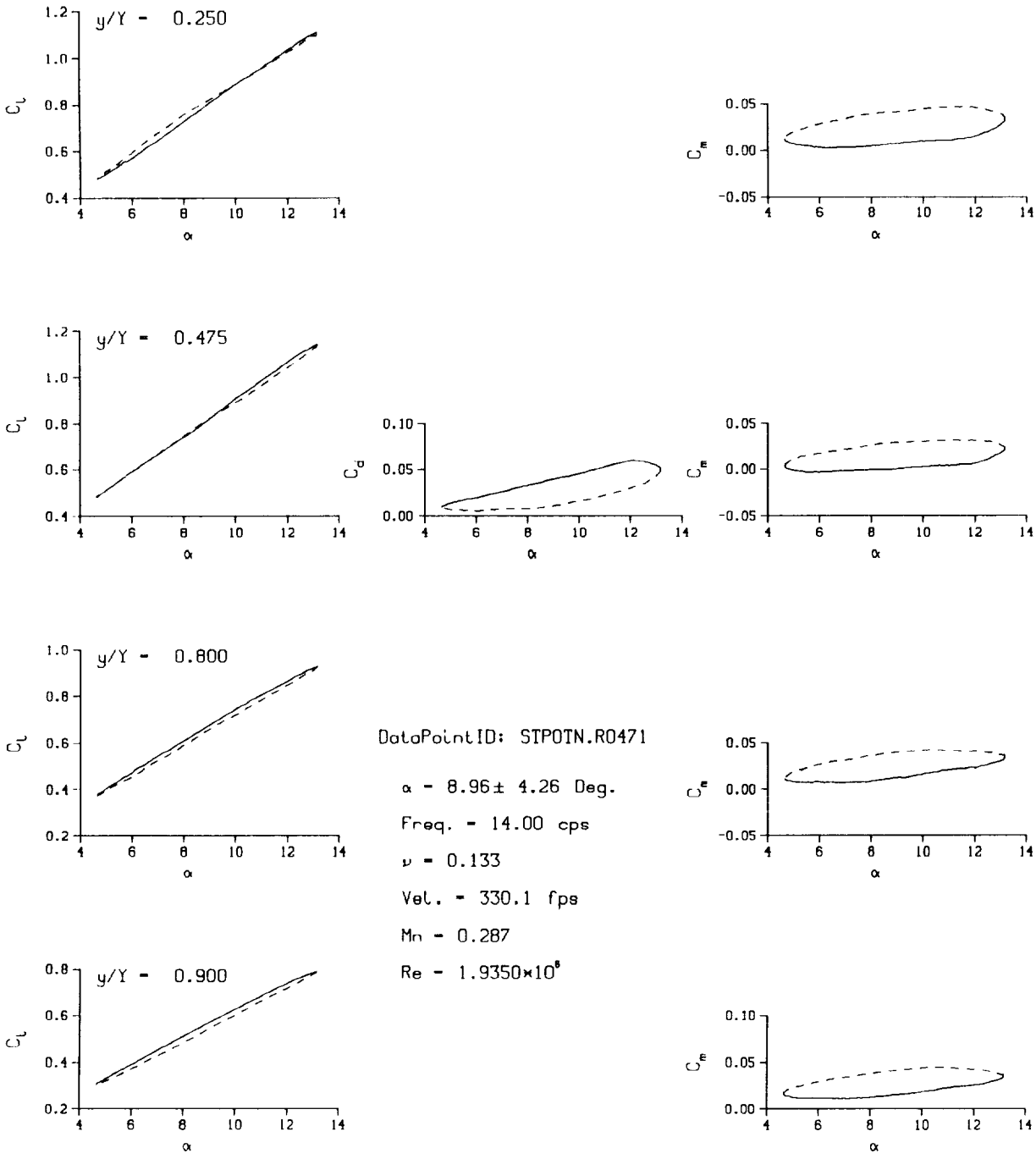

(c) ν = 0.14

Figure 91. Continued.

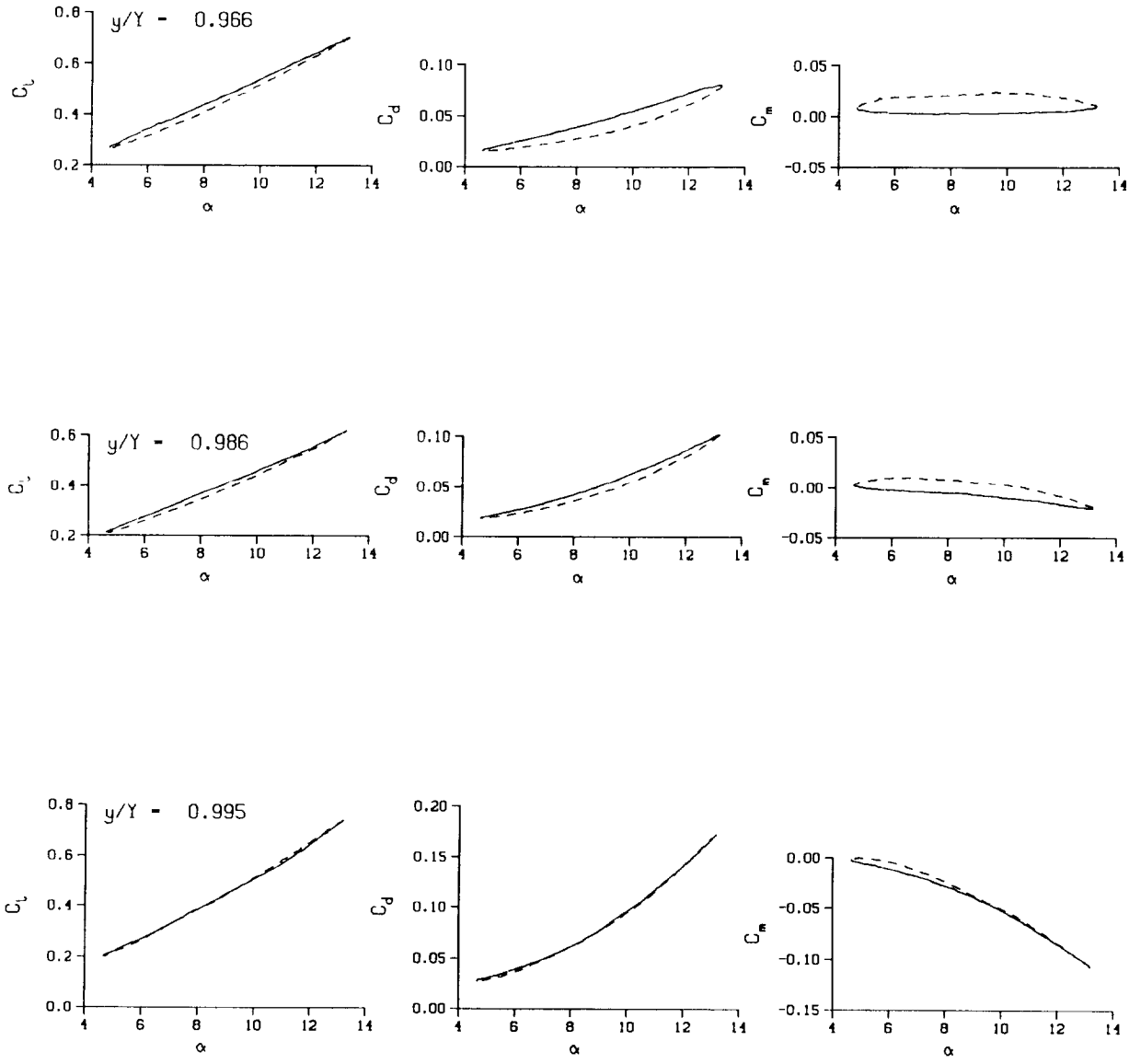

(c) v = 0.14. Concluded

Figure 91. Concluded.

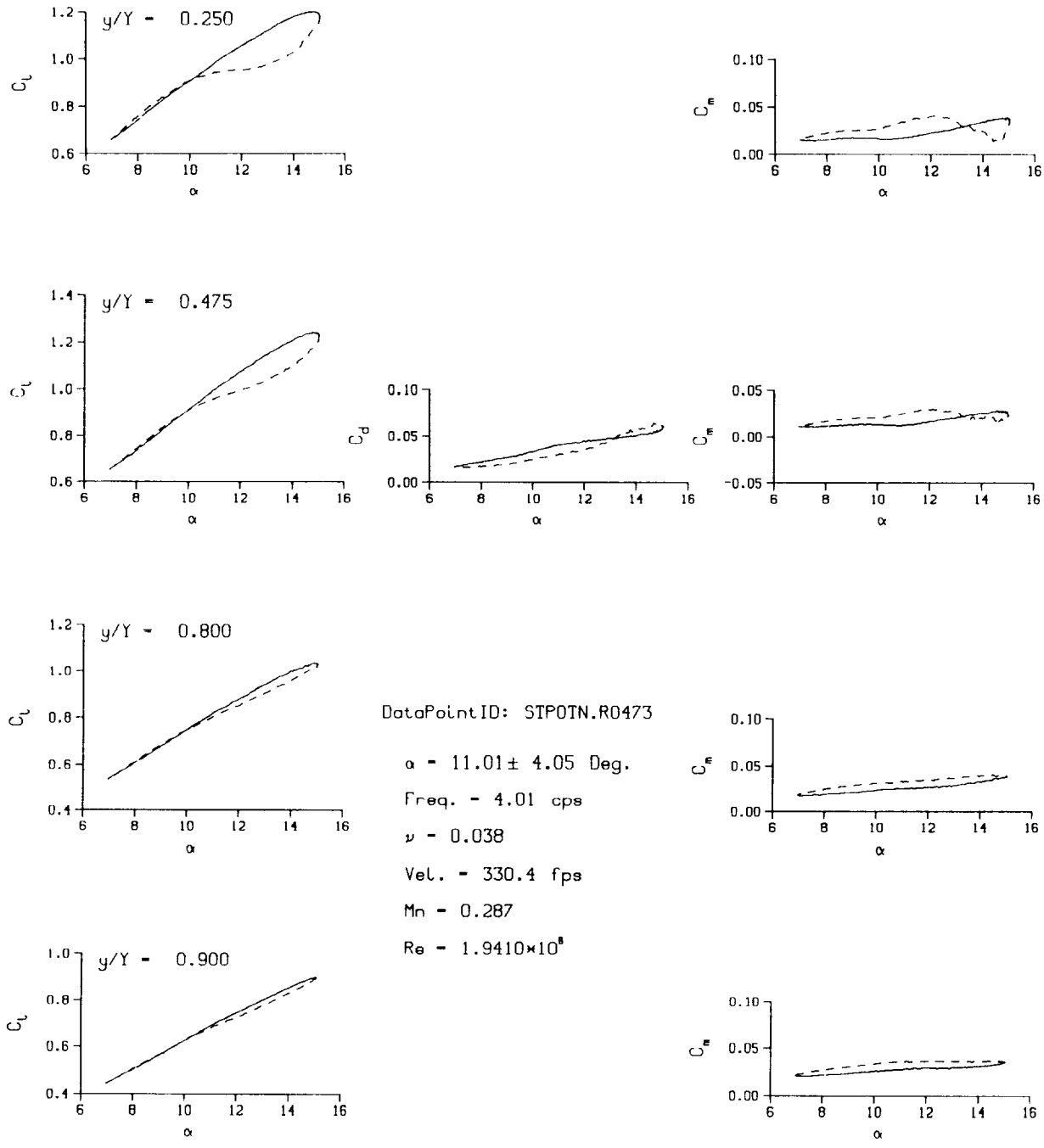

(a) ν = 0.04

Figure 92. 3-D square tip pitch oscillation data; no BL-trip; α = 11 ± 4 deg.

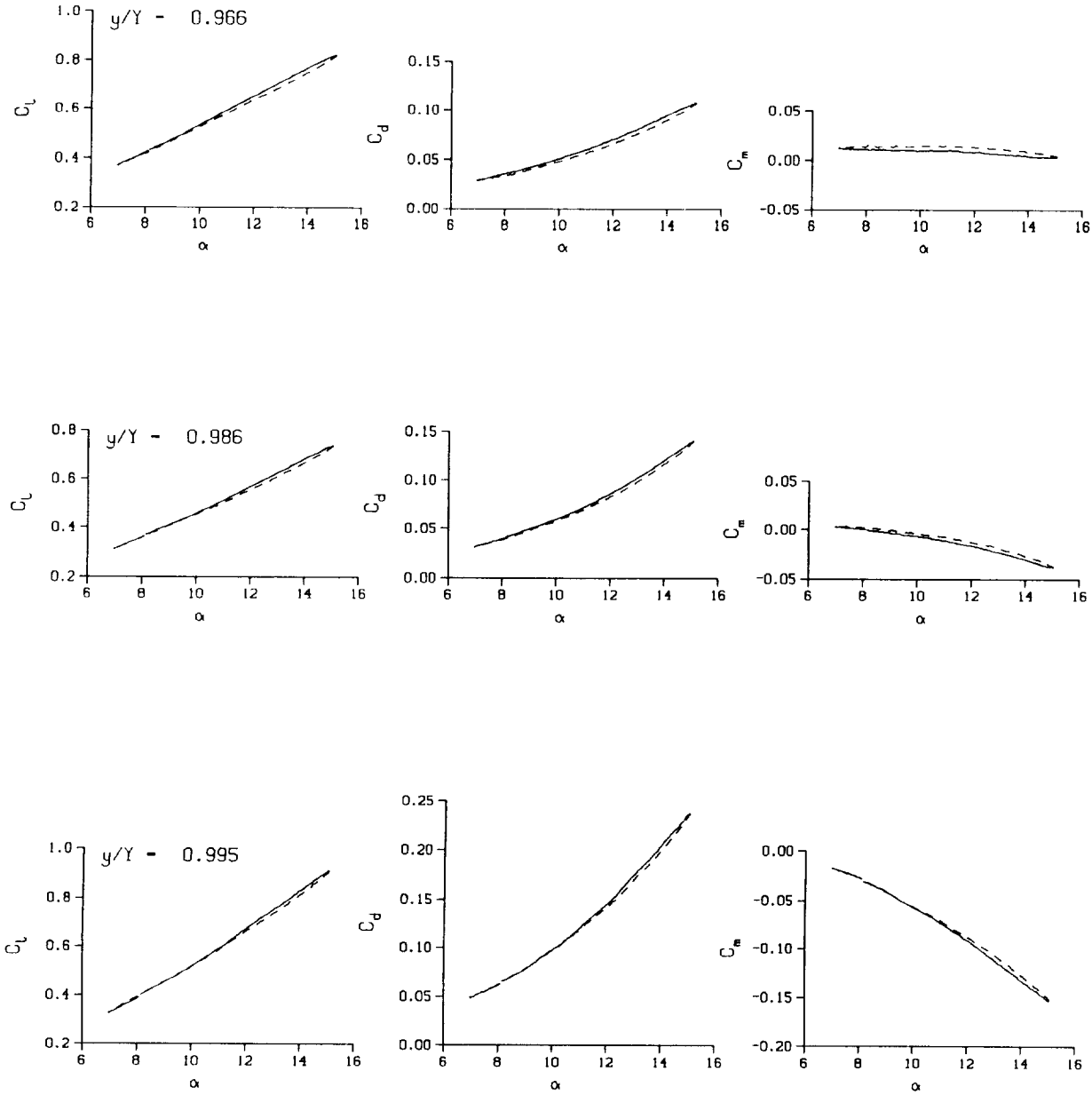

(a) v = 0.04. Concluded

Figure 92. Continued.

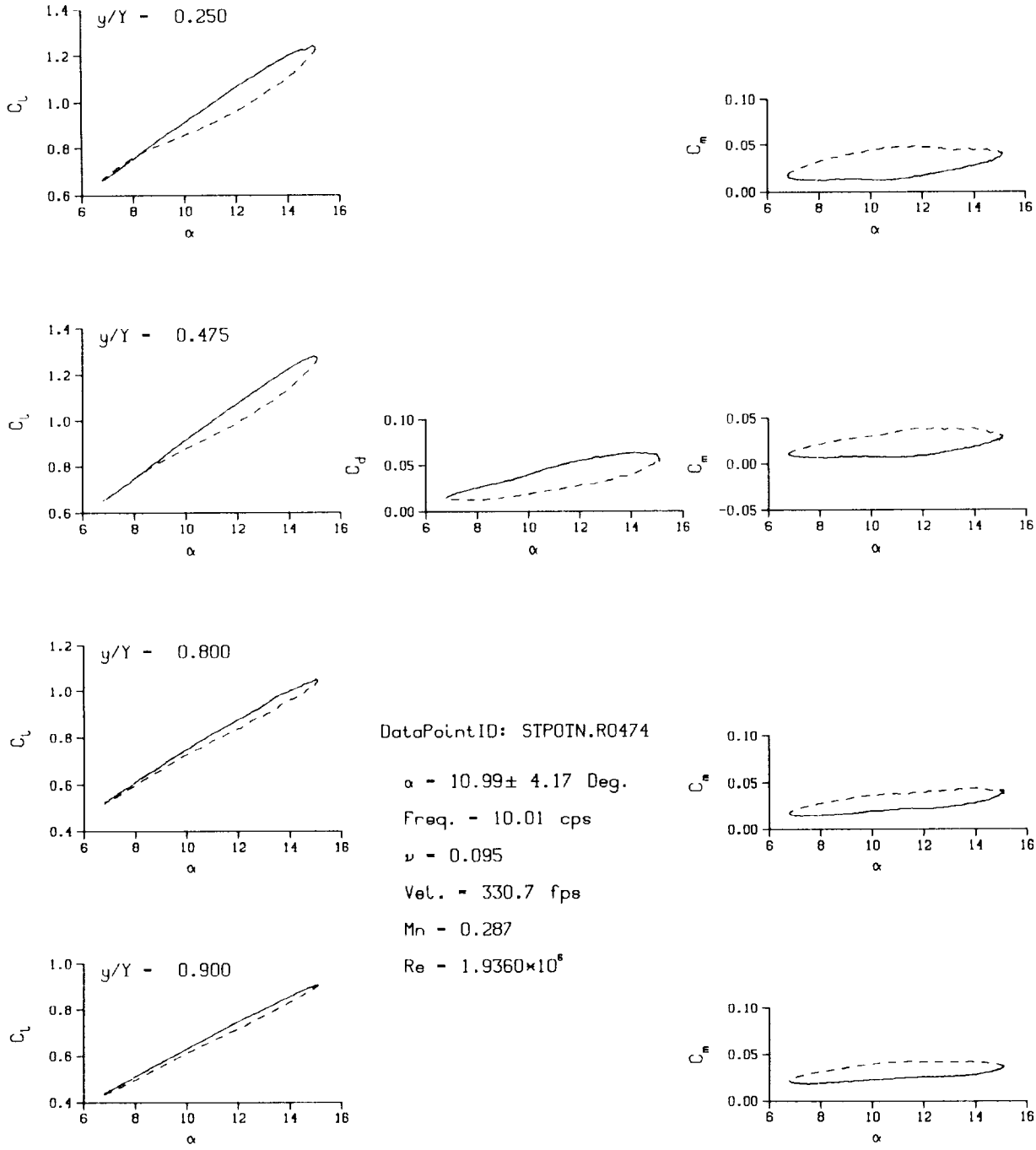

(b) v = 0.10

Figure 92. Continued.

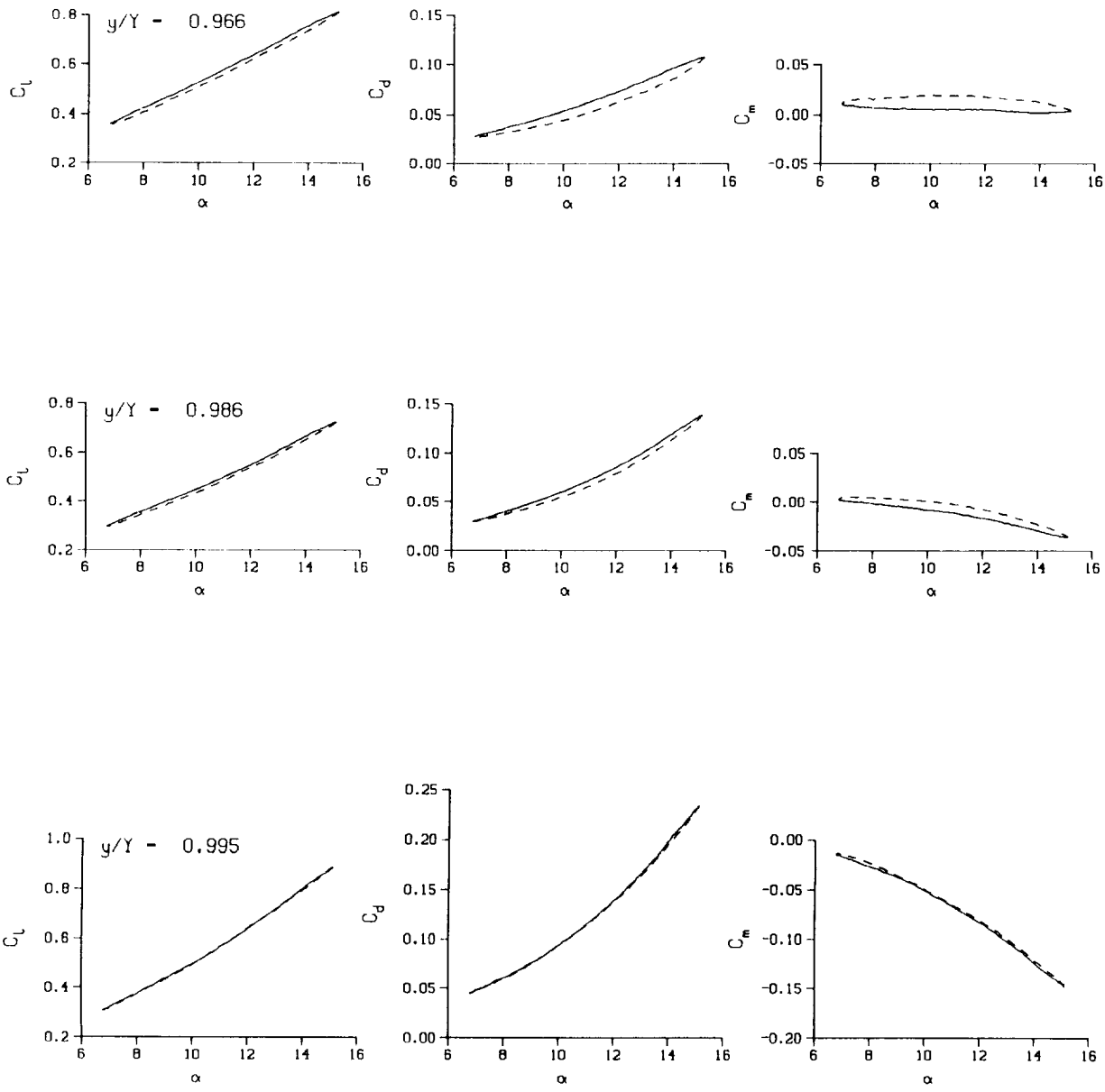

(b) v = 0.10. Concluded

Figure 92. Continued.

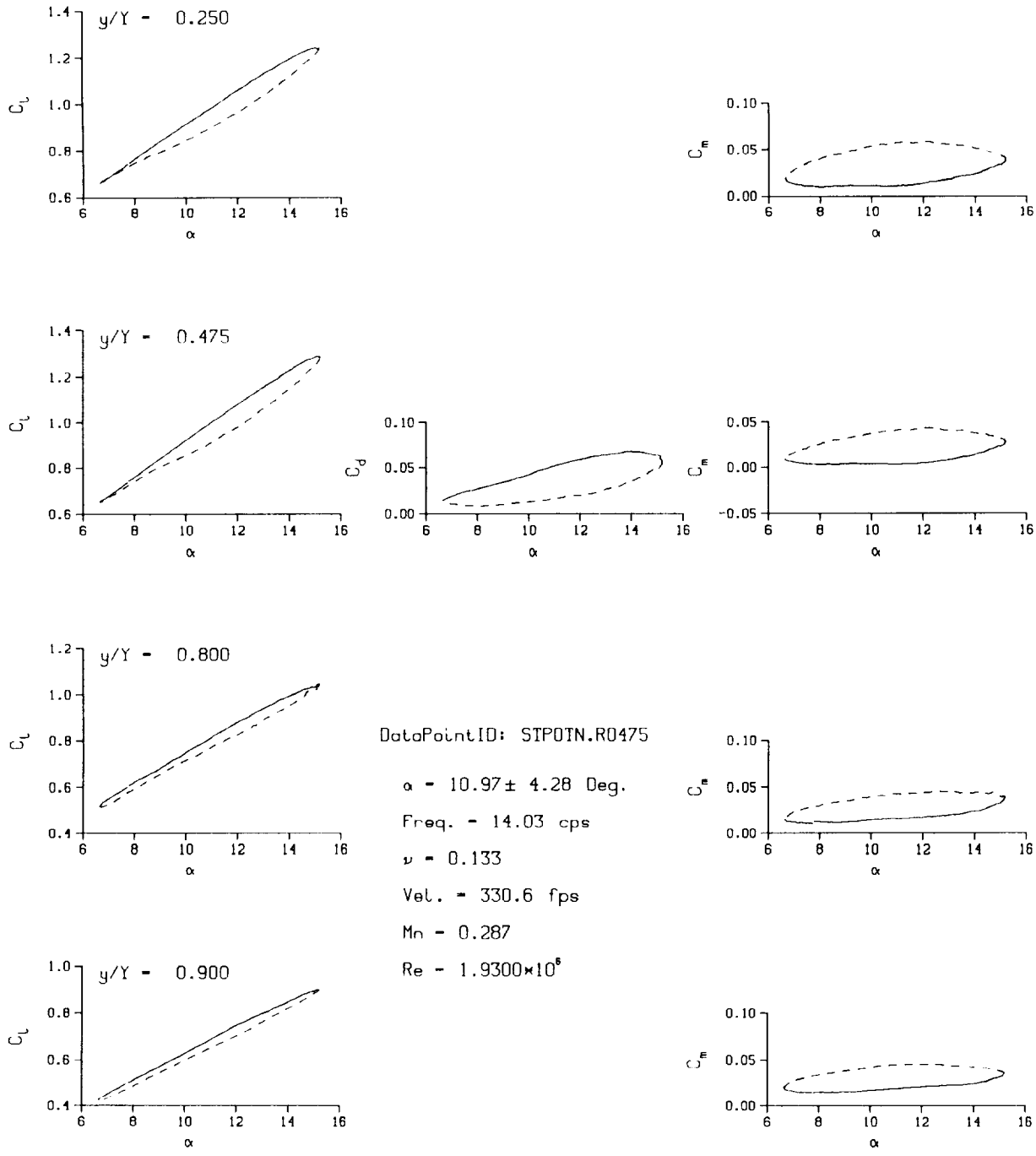

(c) ν = 0.14

Figure 92. Continued.

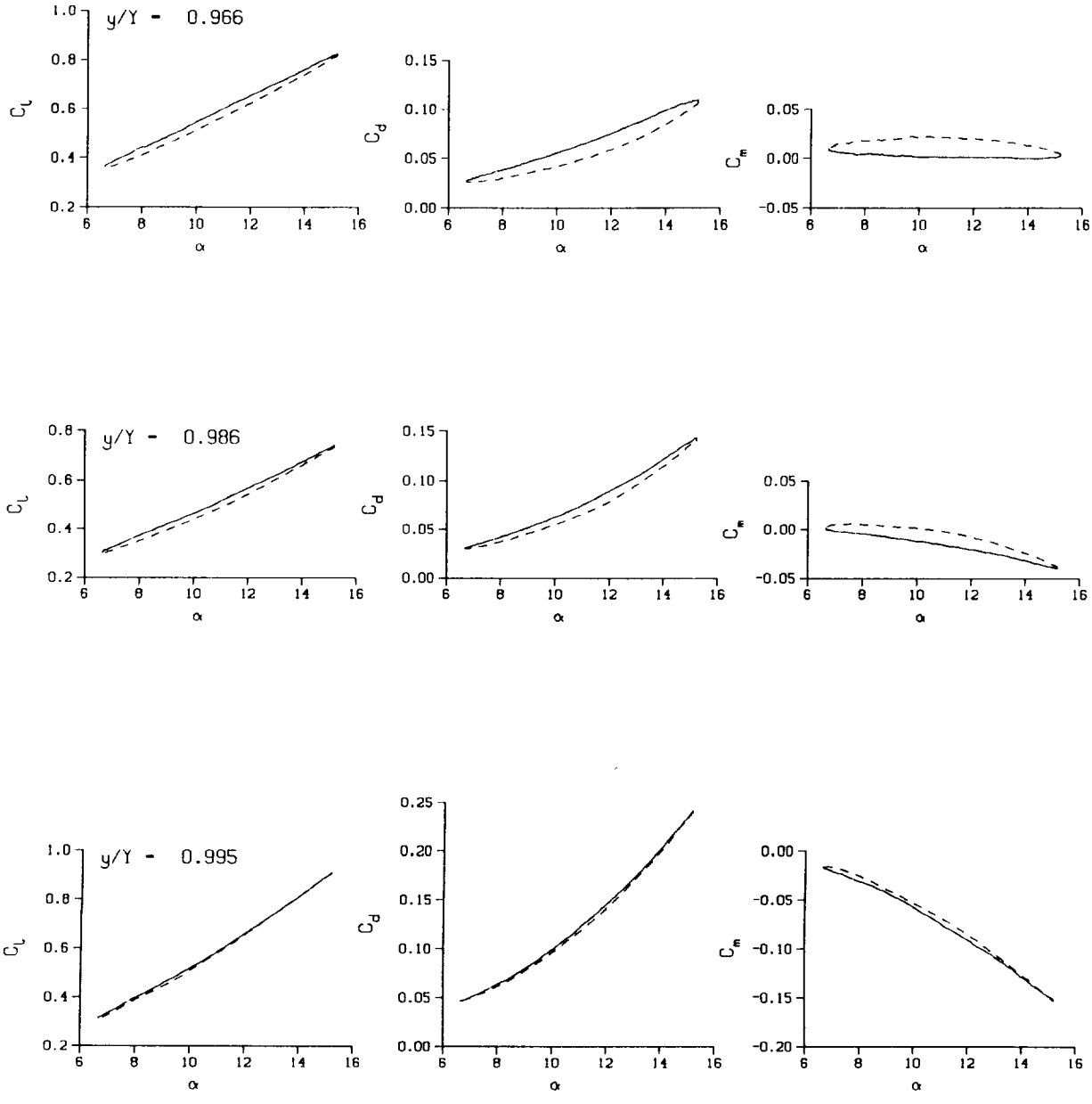

(c) v = 0.14. Concluded

Figure 92. Concluded.

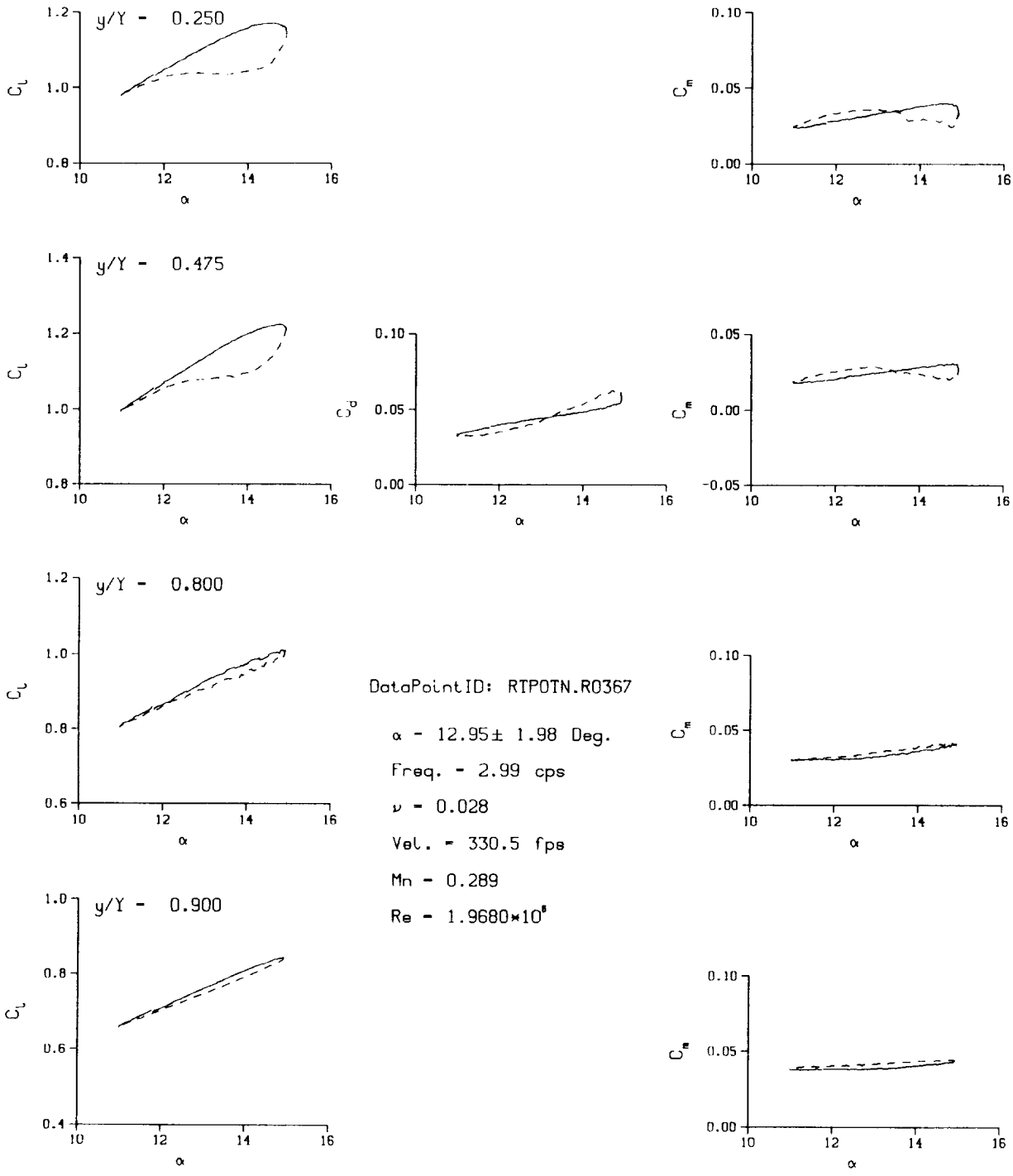

(a) ν = 0.028

Figure 93. Frequency sweep; no BL-trip; q = 117 psf.

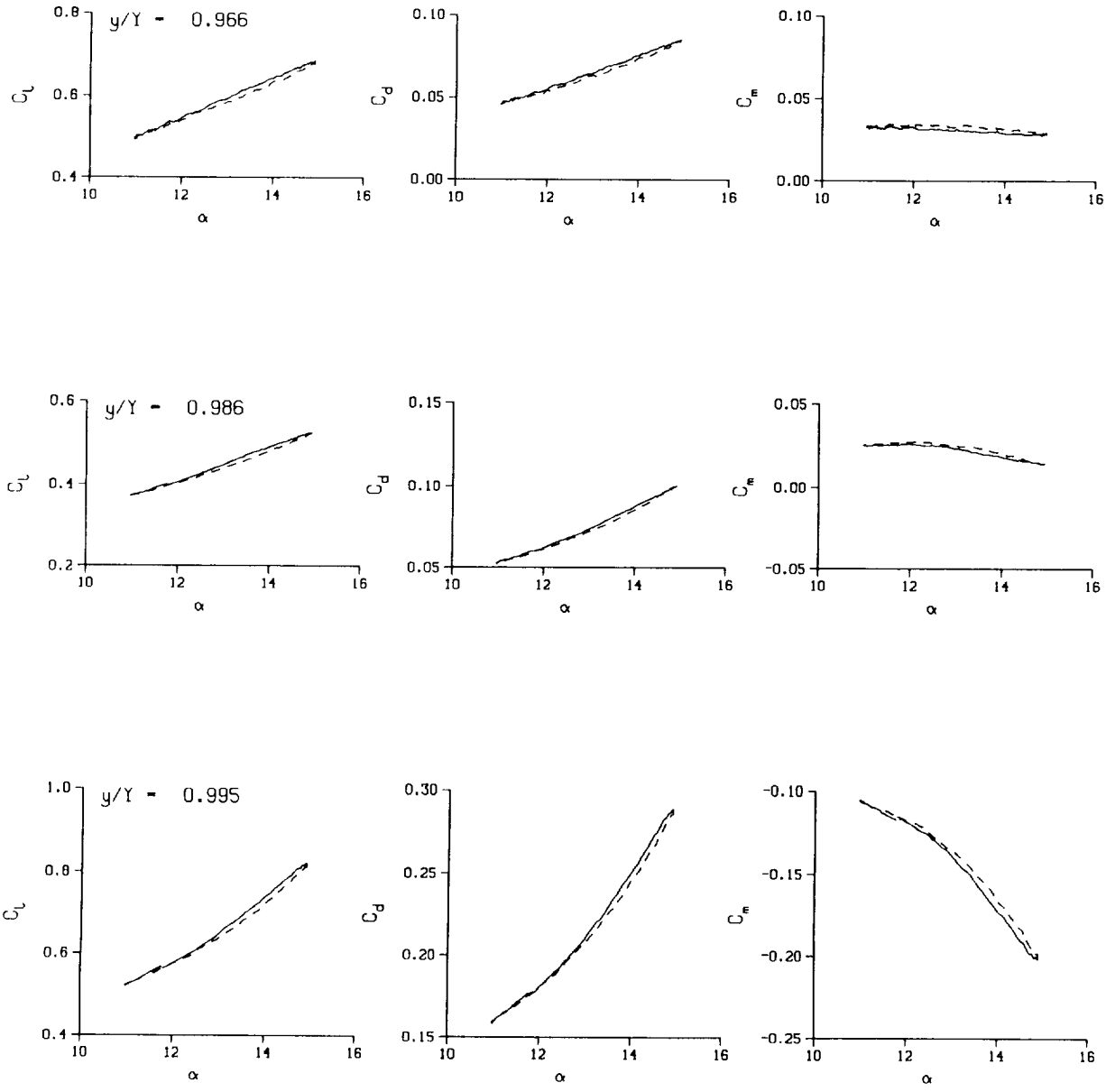

(a) v = 0.028. Concluded

Figure 93. Continued.

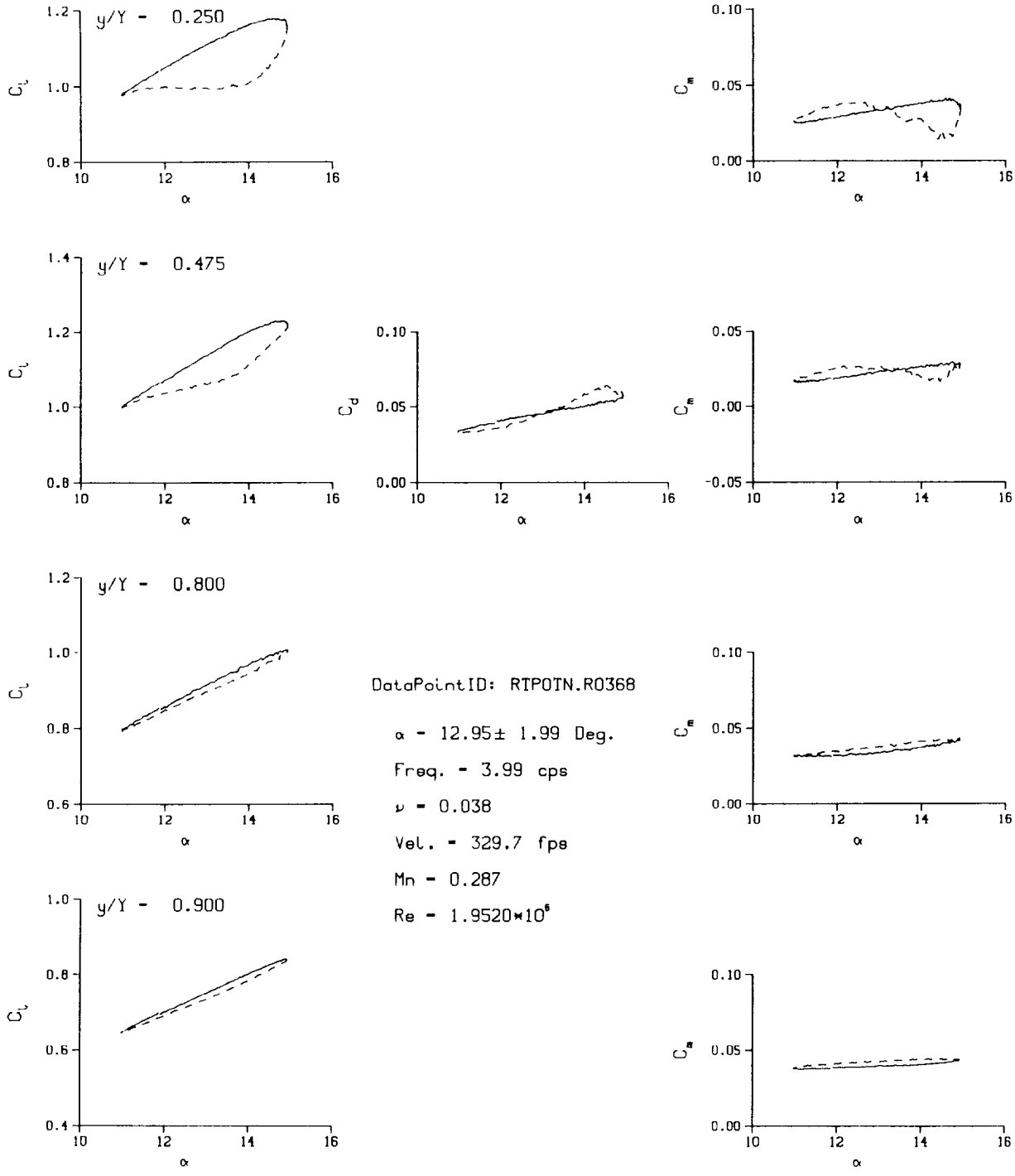

(b) ν = 0.038

Figure 93. Continued.

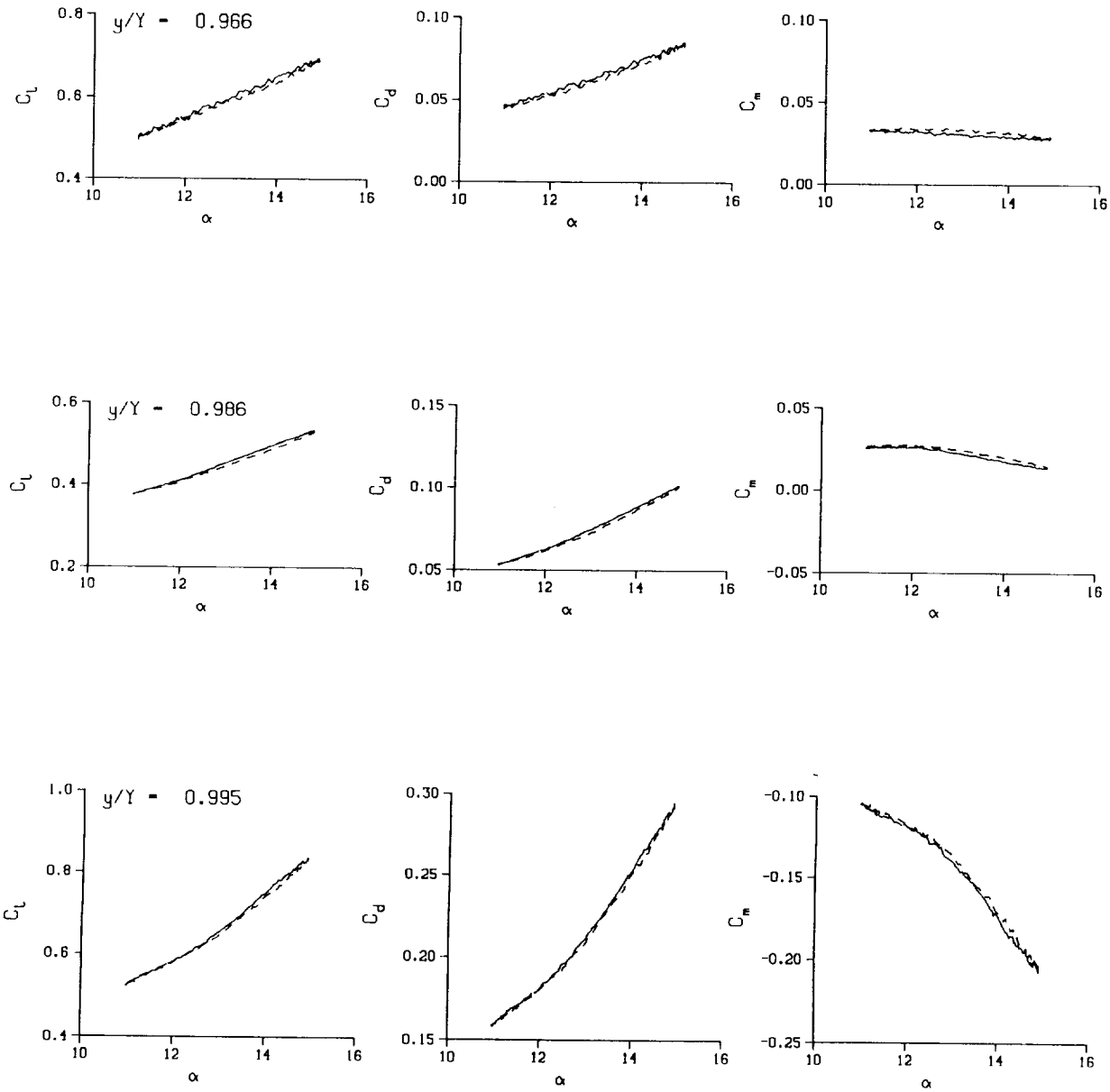

(b) v = 0.038. Concluded

Figure 93. Continued.

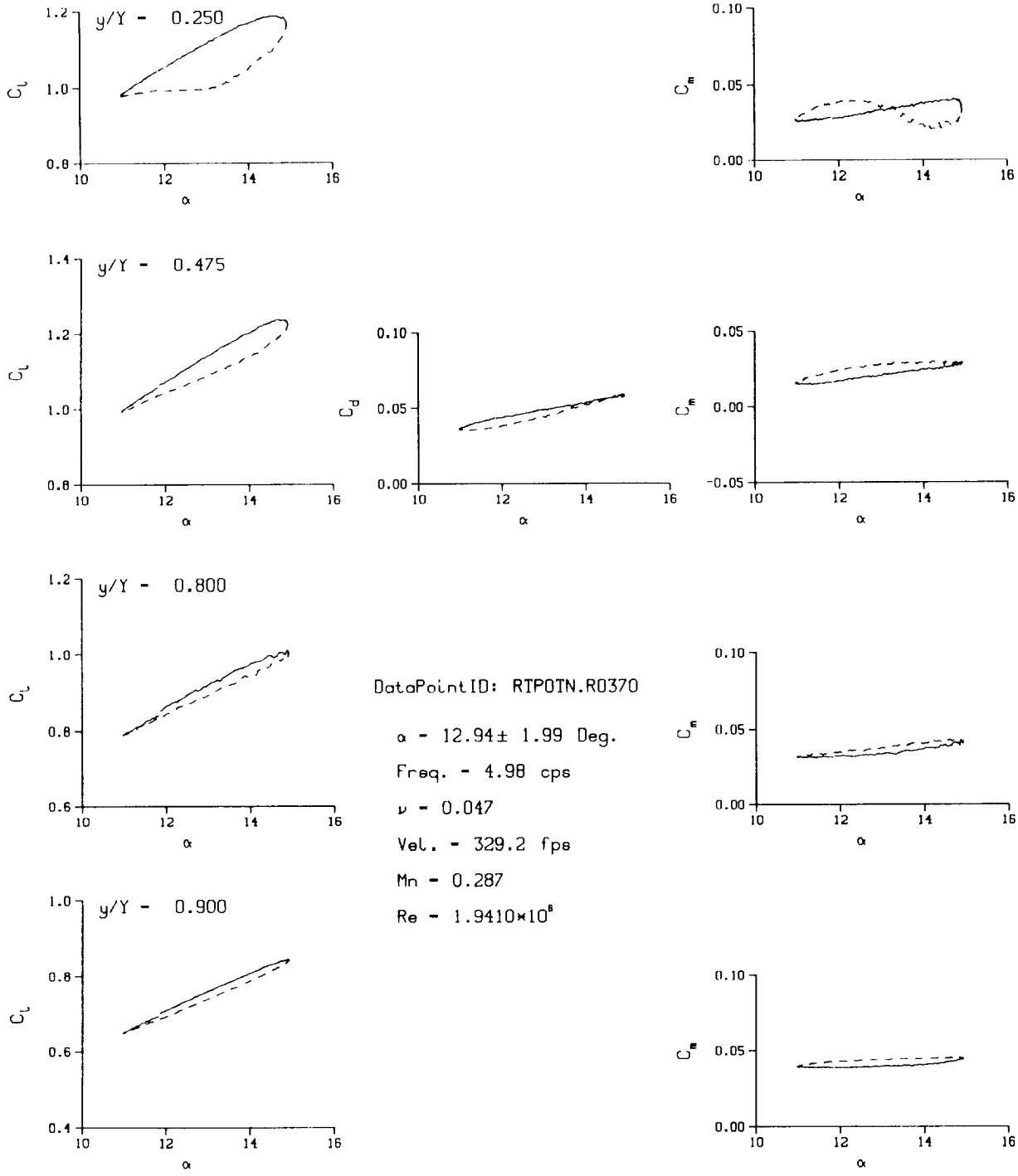

(c) ν = 0.047

Figure 93. Continued.

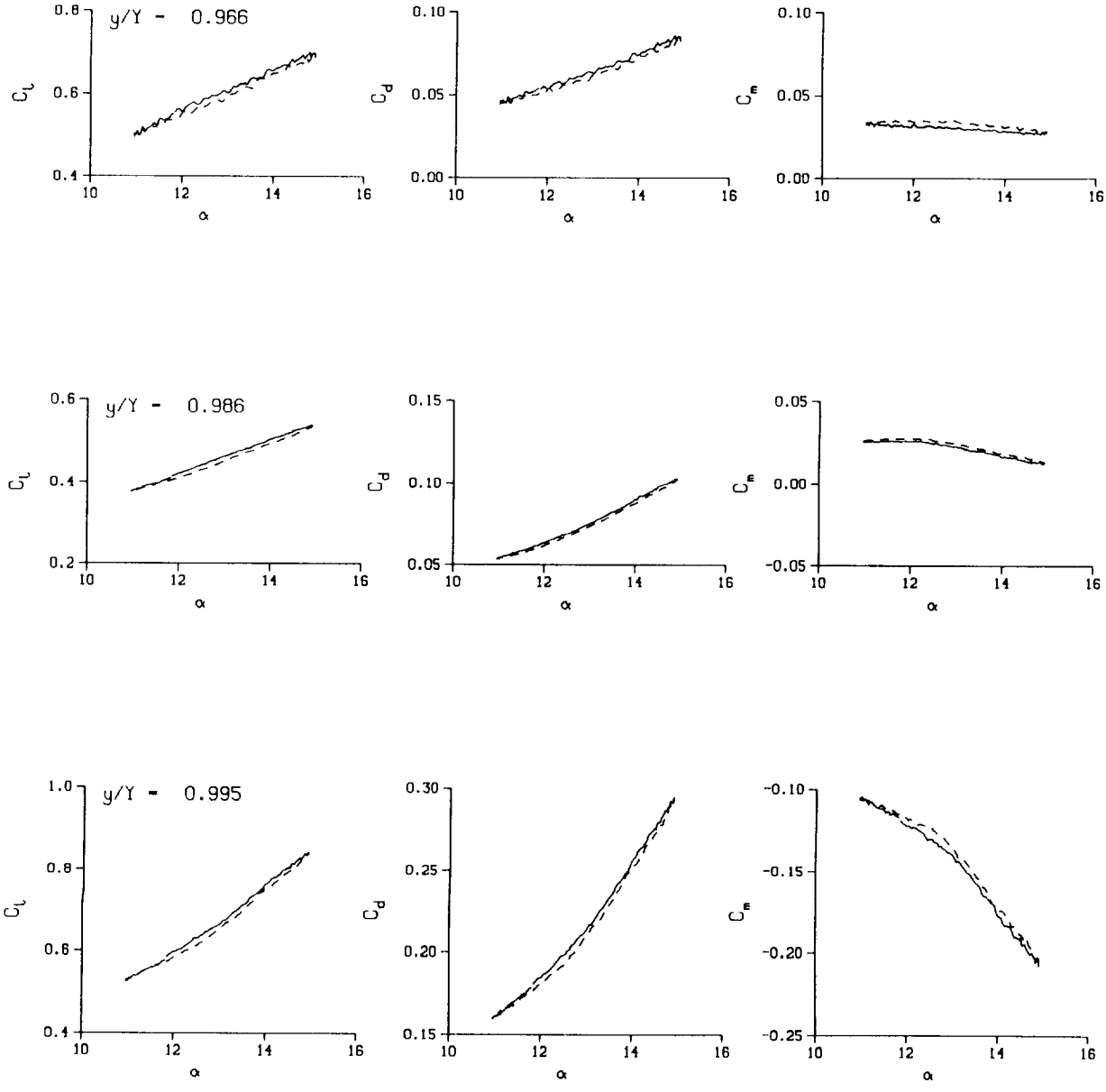

(c) v = 0.047. Concluded

Figure 93. Continued.

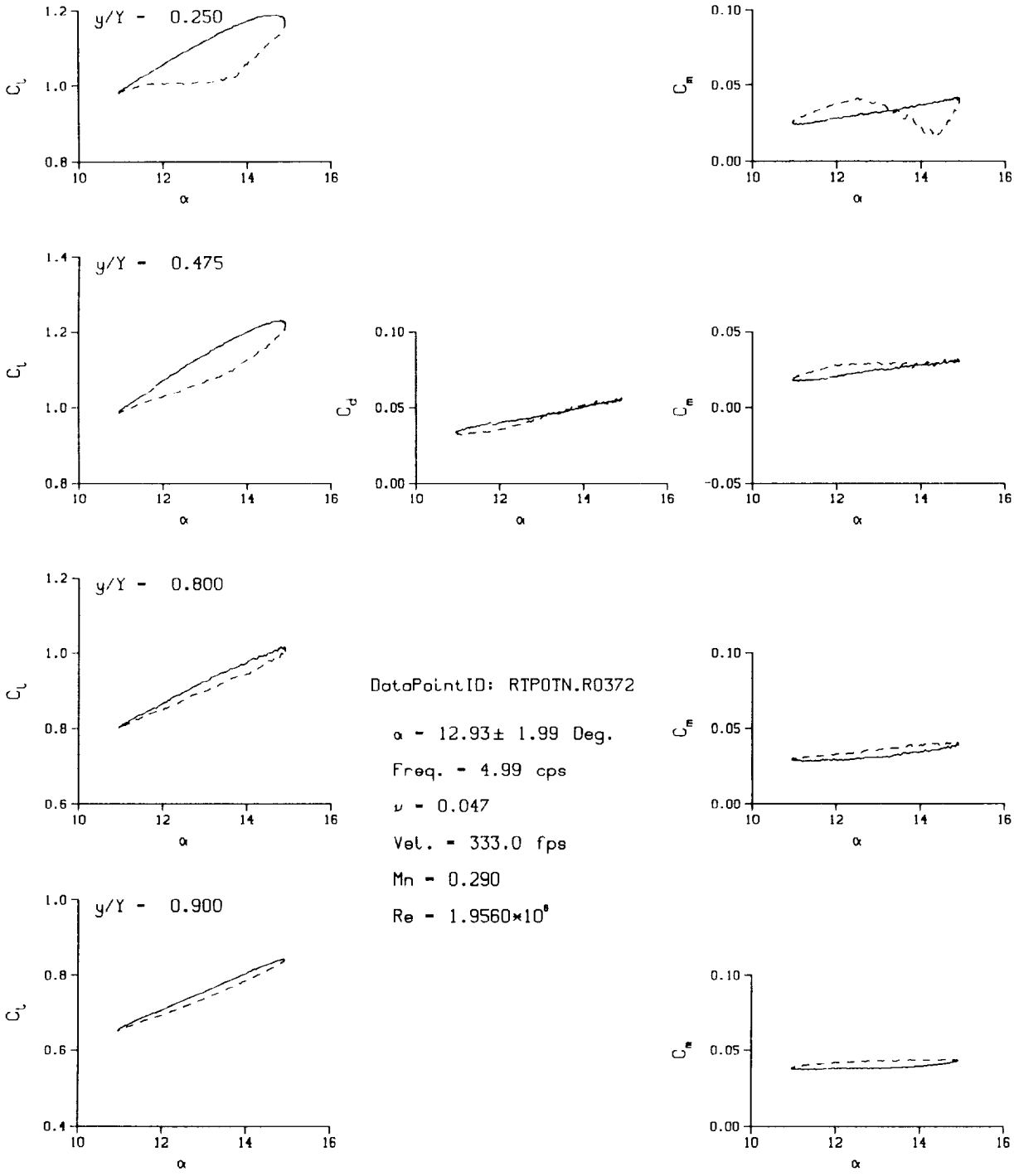

(c.1) v = 0.047; repeat

Figure 93. Continued.

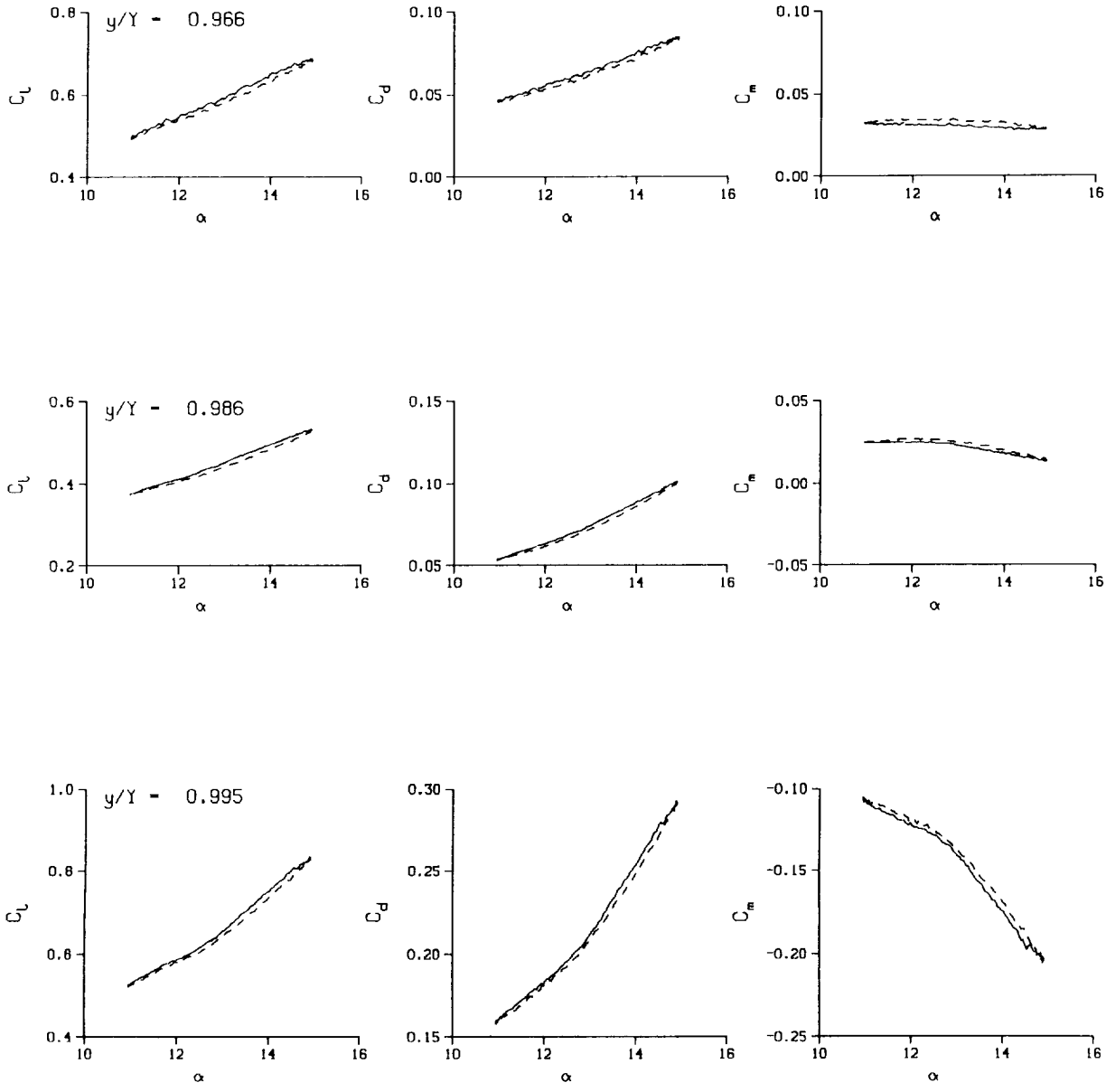

(c.1) v = 0.047; repeat. Concluded

Figure 93. Continued.

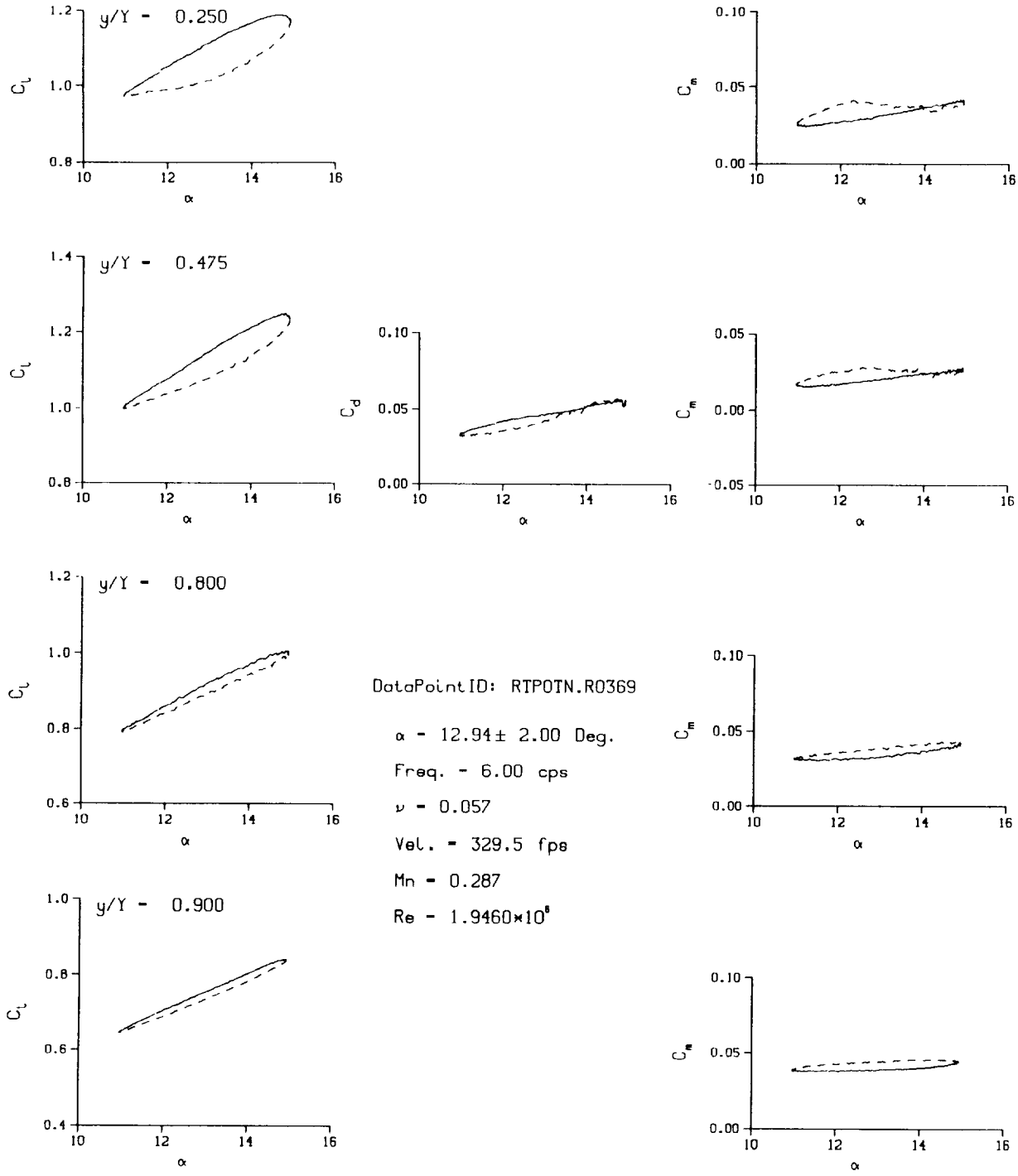

(d) ν = 0.057

Figure 93. Continued.

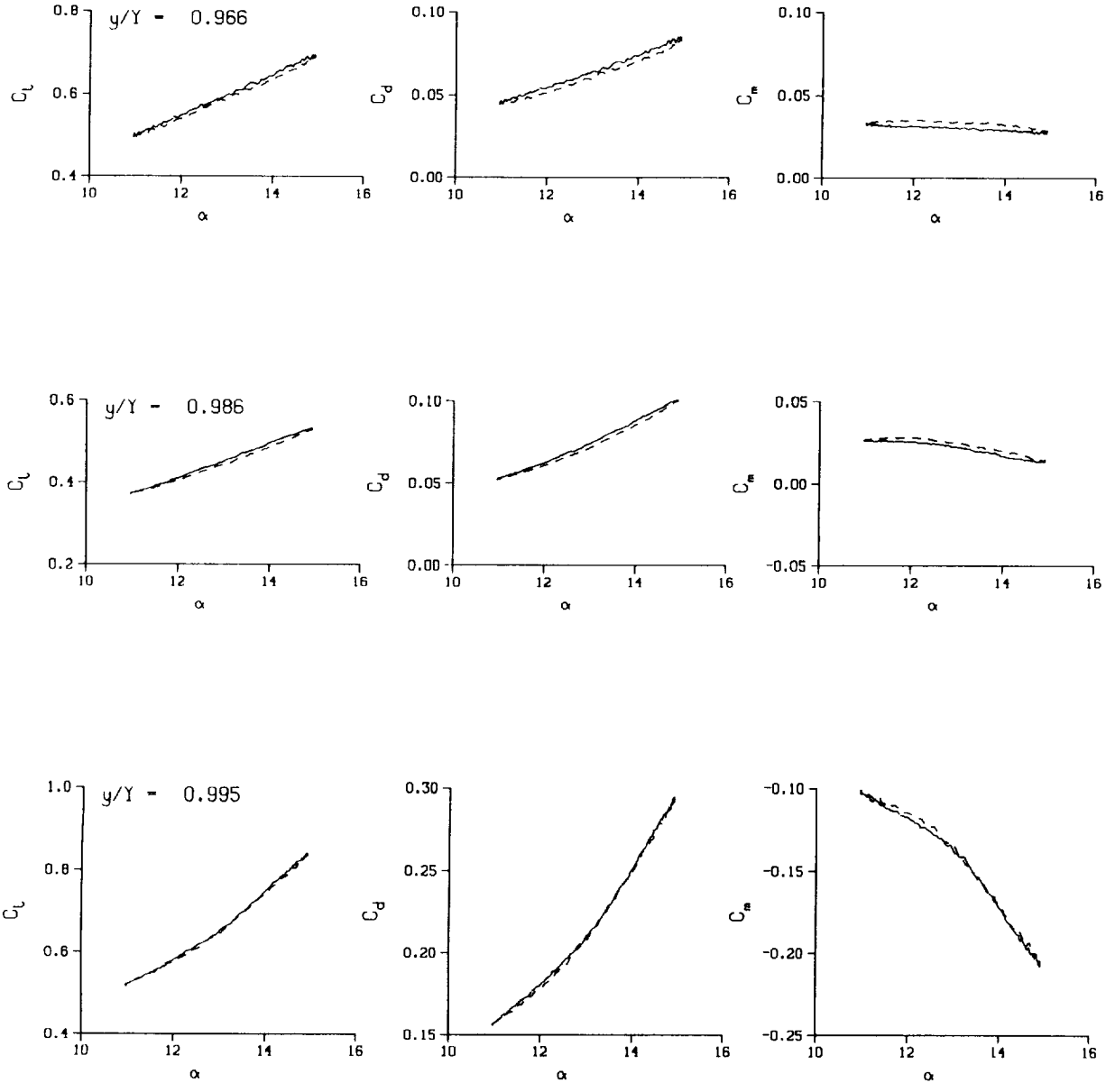

(d) v = 0.057. Concluded

Figure 93. Continued.

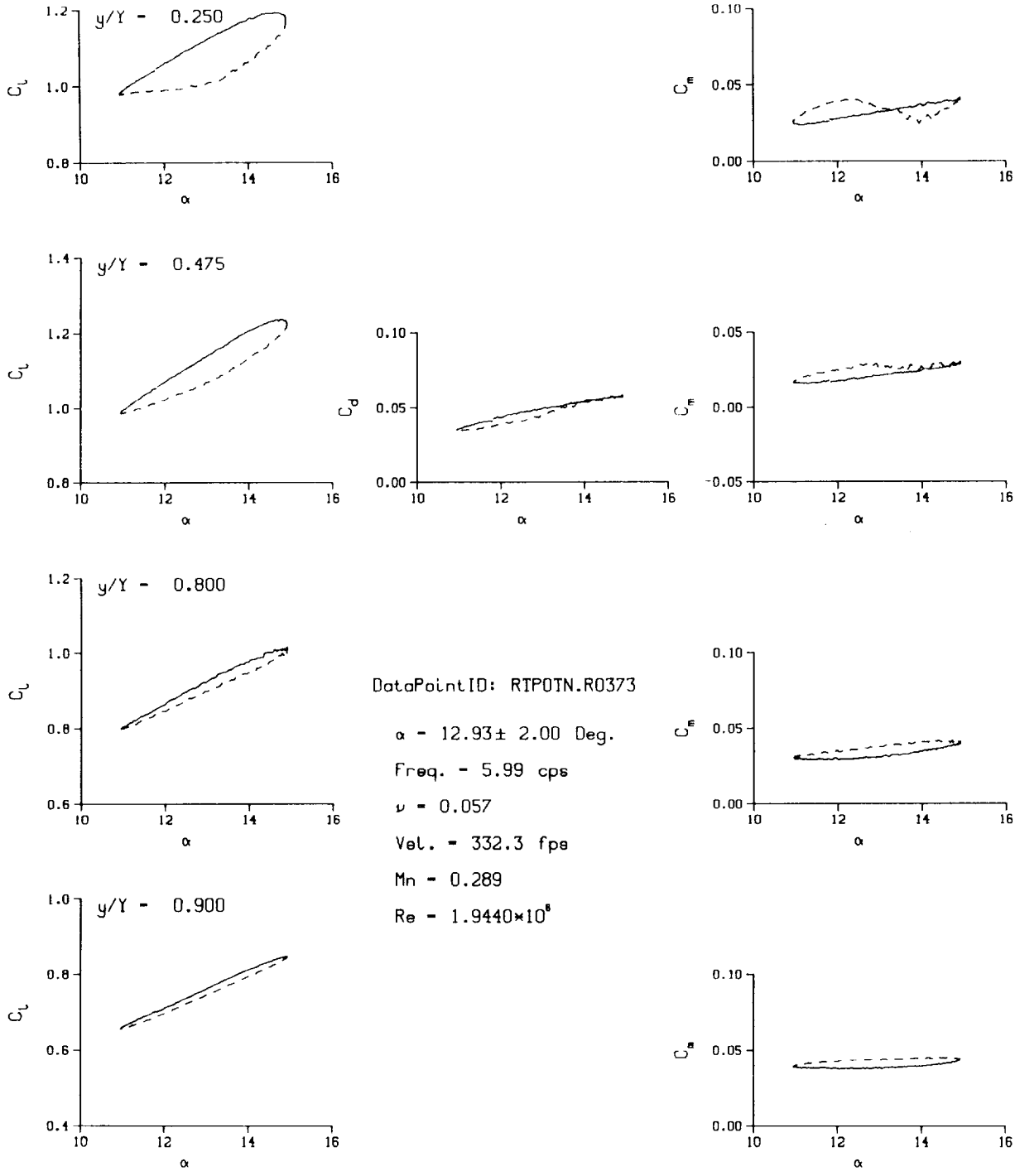

(d.1) v = 0.057; repeat

Figure 93. Continued.

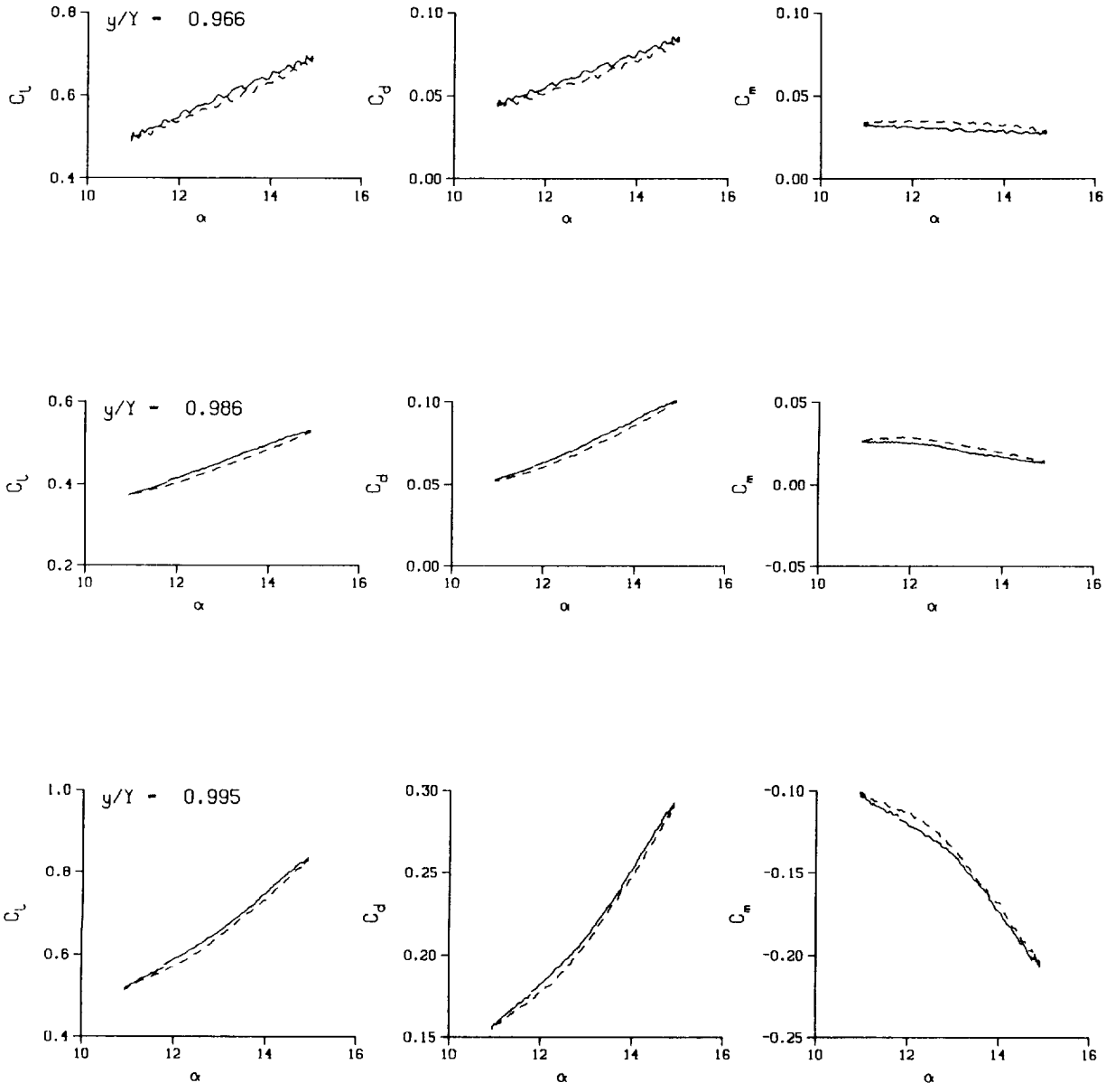

(d.1) v = 0.057; repeat. Concluded

Figure 93. Continued.

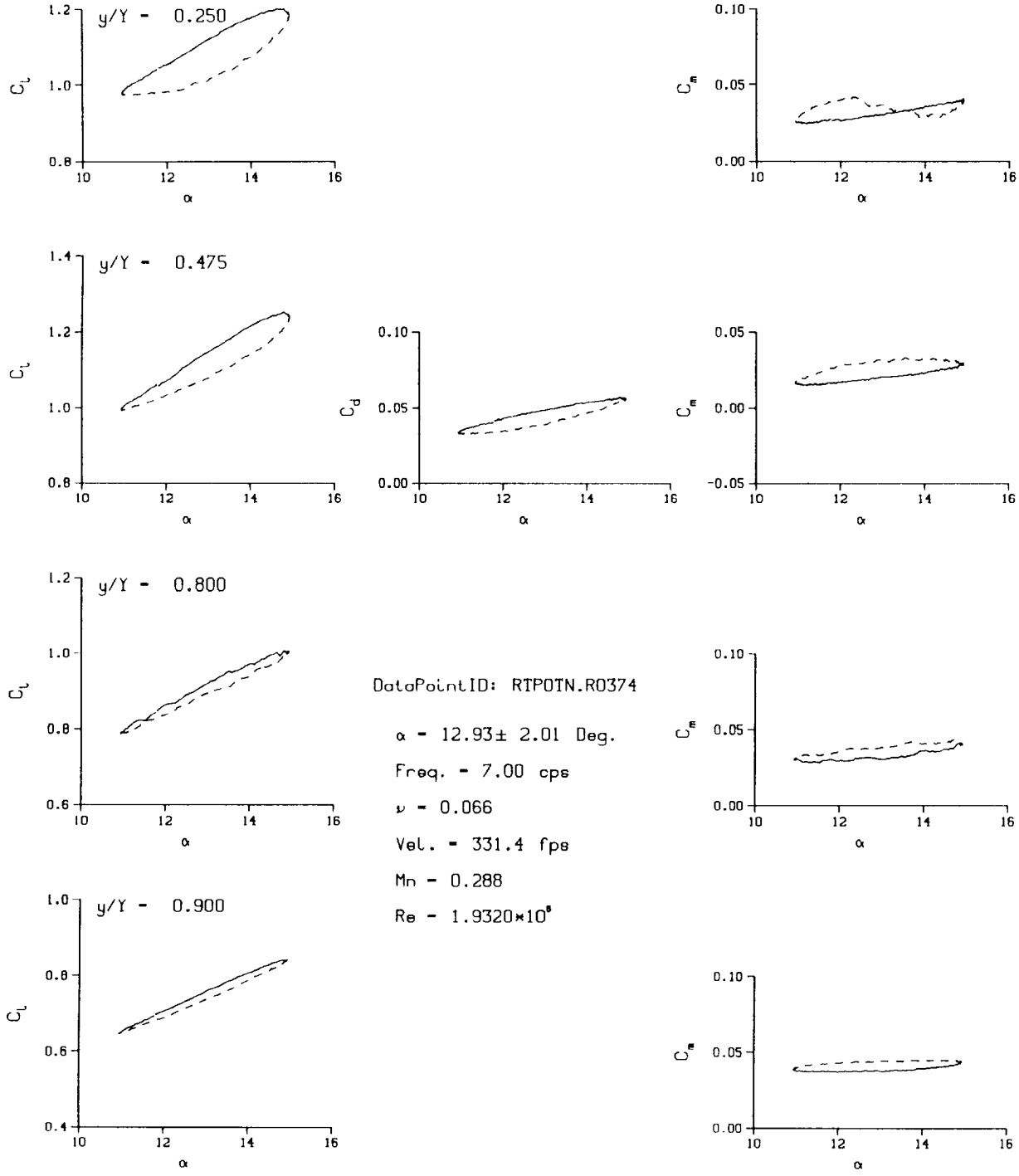

(e) v = 0.066

Figure 93. Continued.

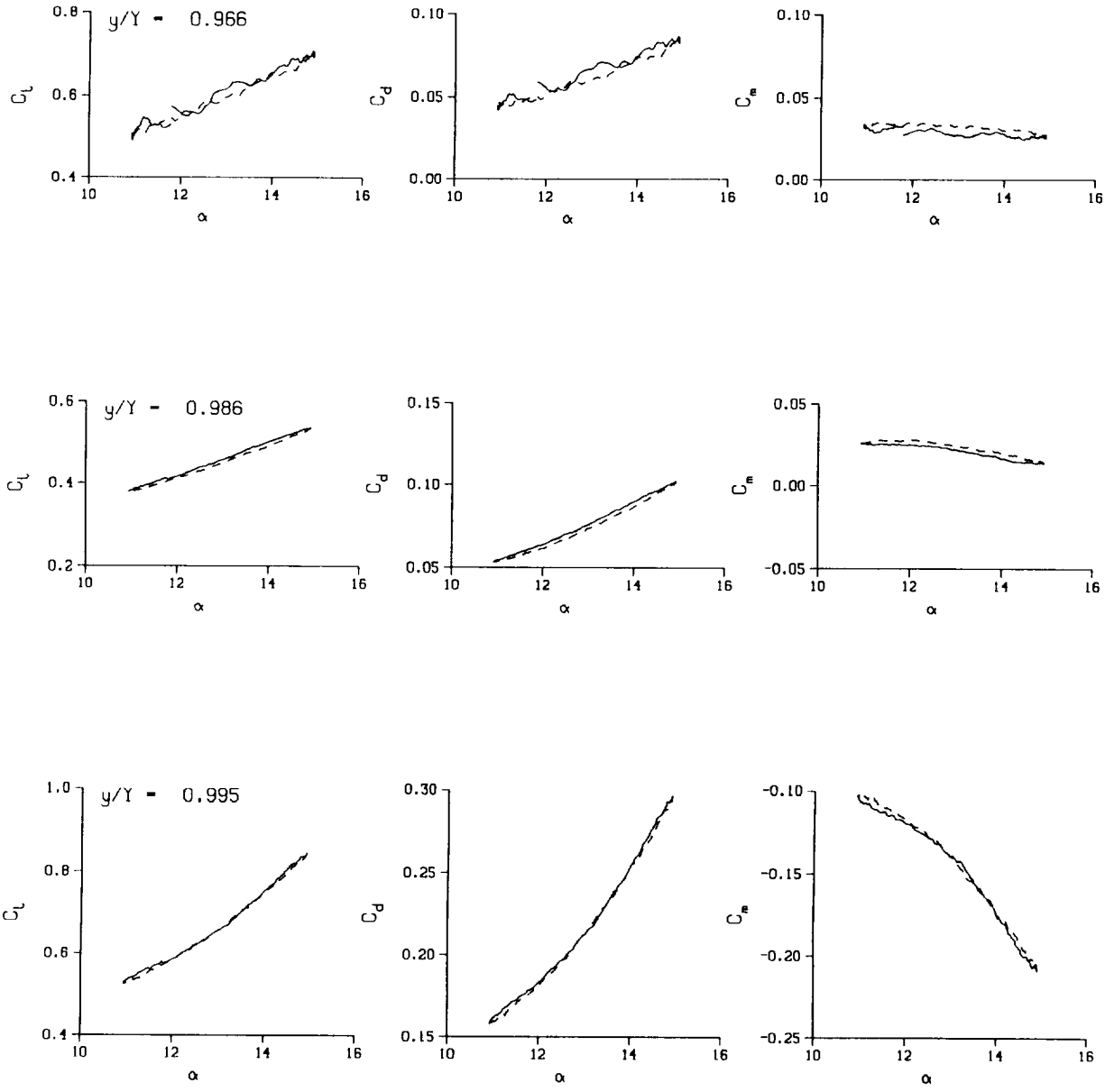

(e) v = 0.066. Concluded

Figure 93. Continued.

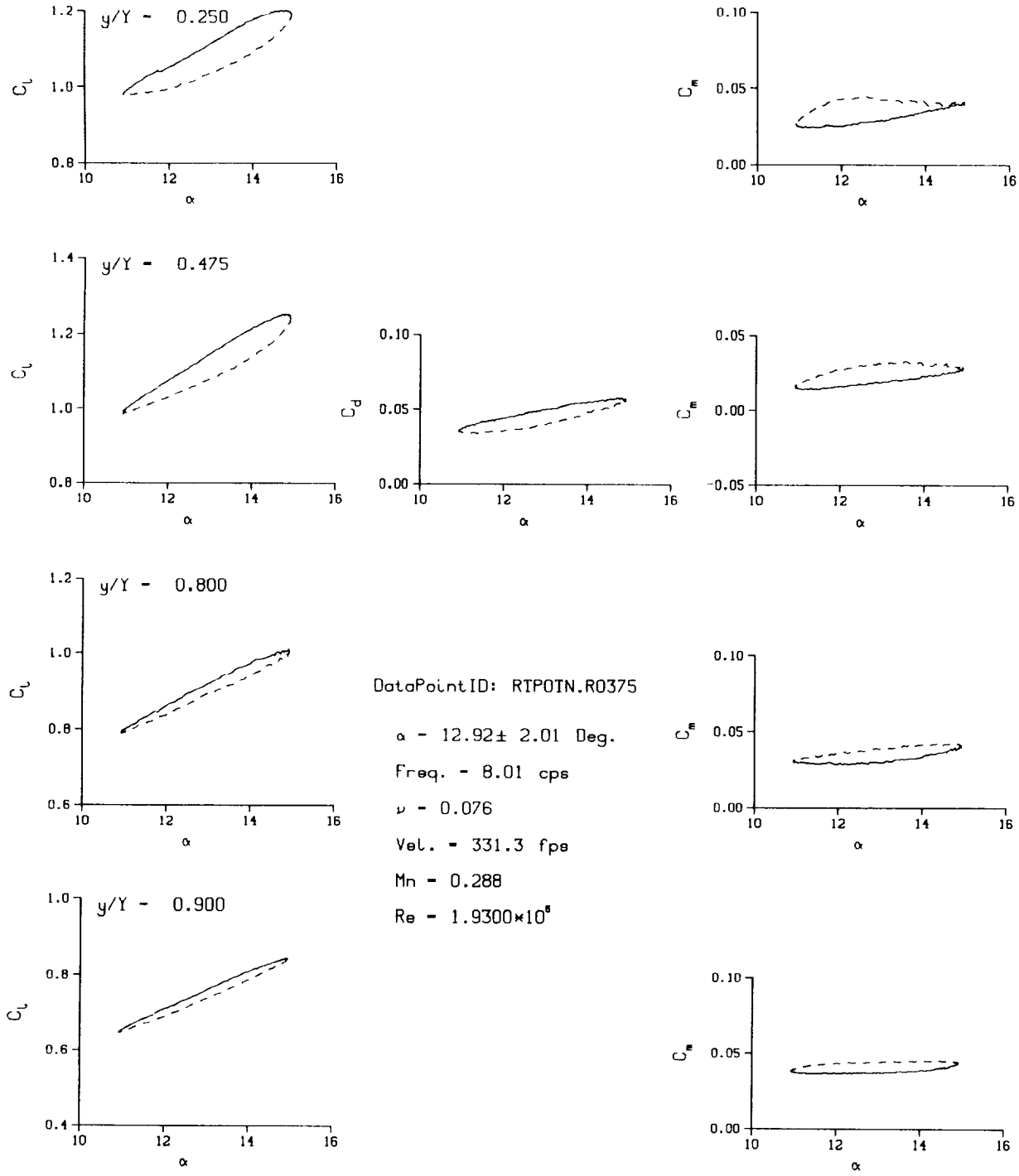

(f) v = 0.076

Figure 93. Continued.

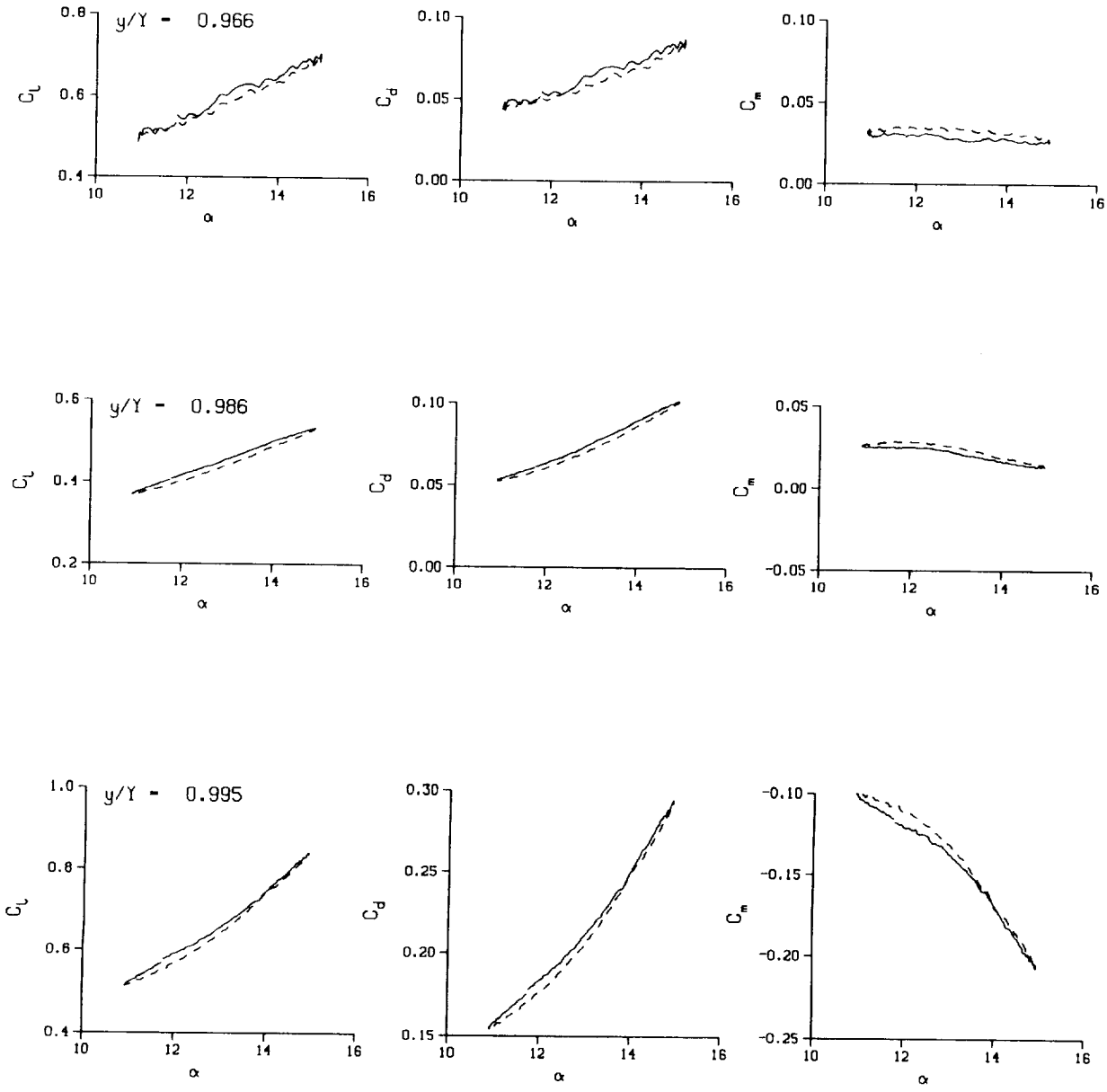

(f) v = 0.076. Concluded

Figure 93. Concluded

C-6

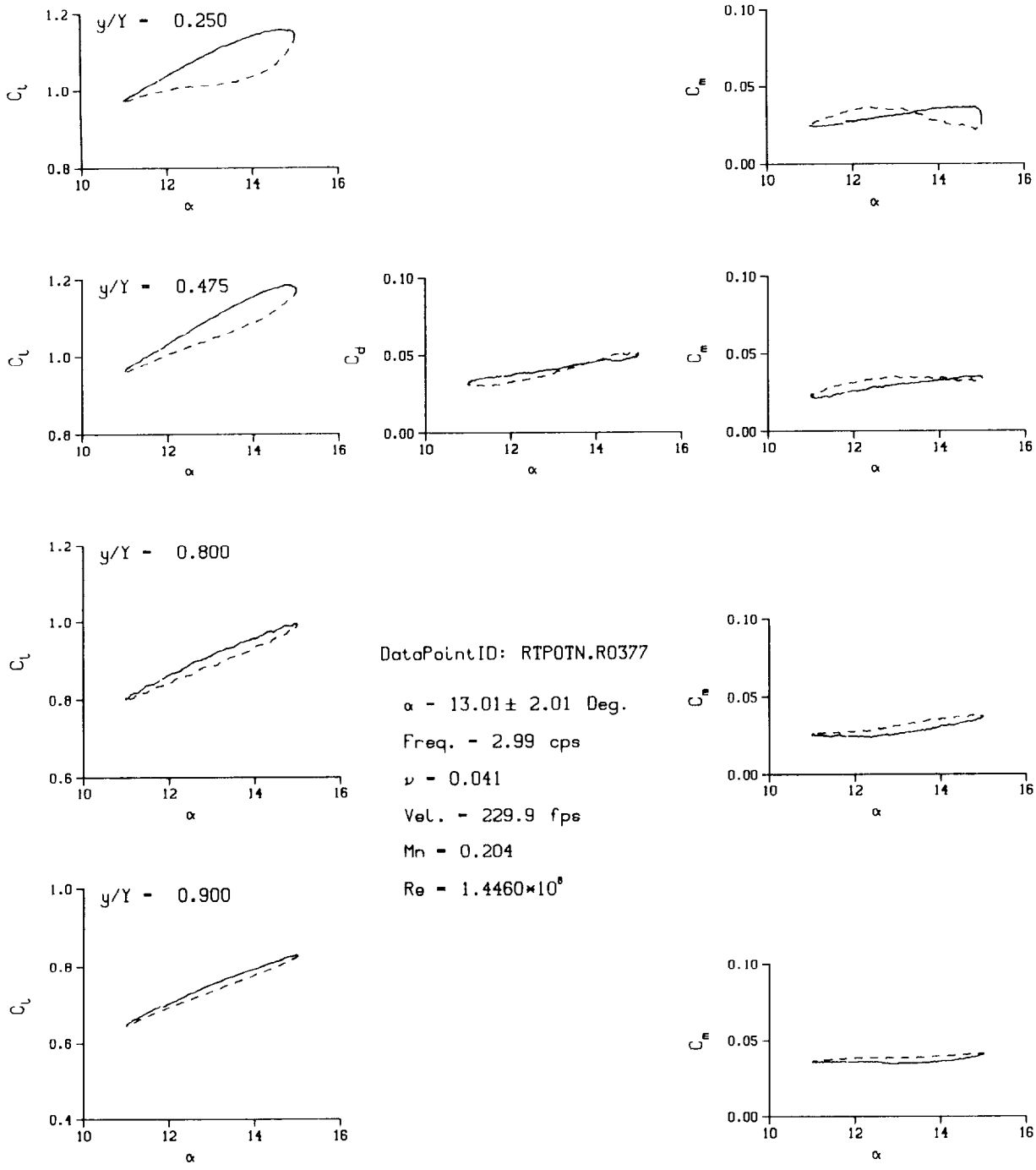

(a) ν = 0.041

Figure 94. Frequency sweep; no BL-trip; q = 60 psf.

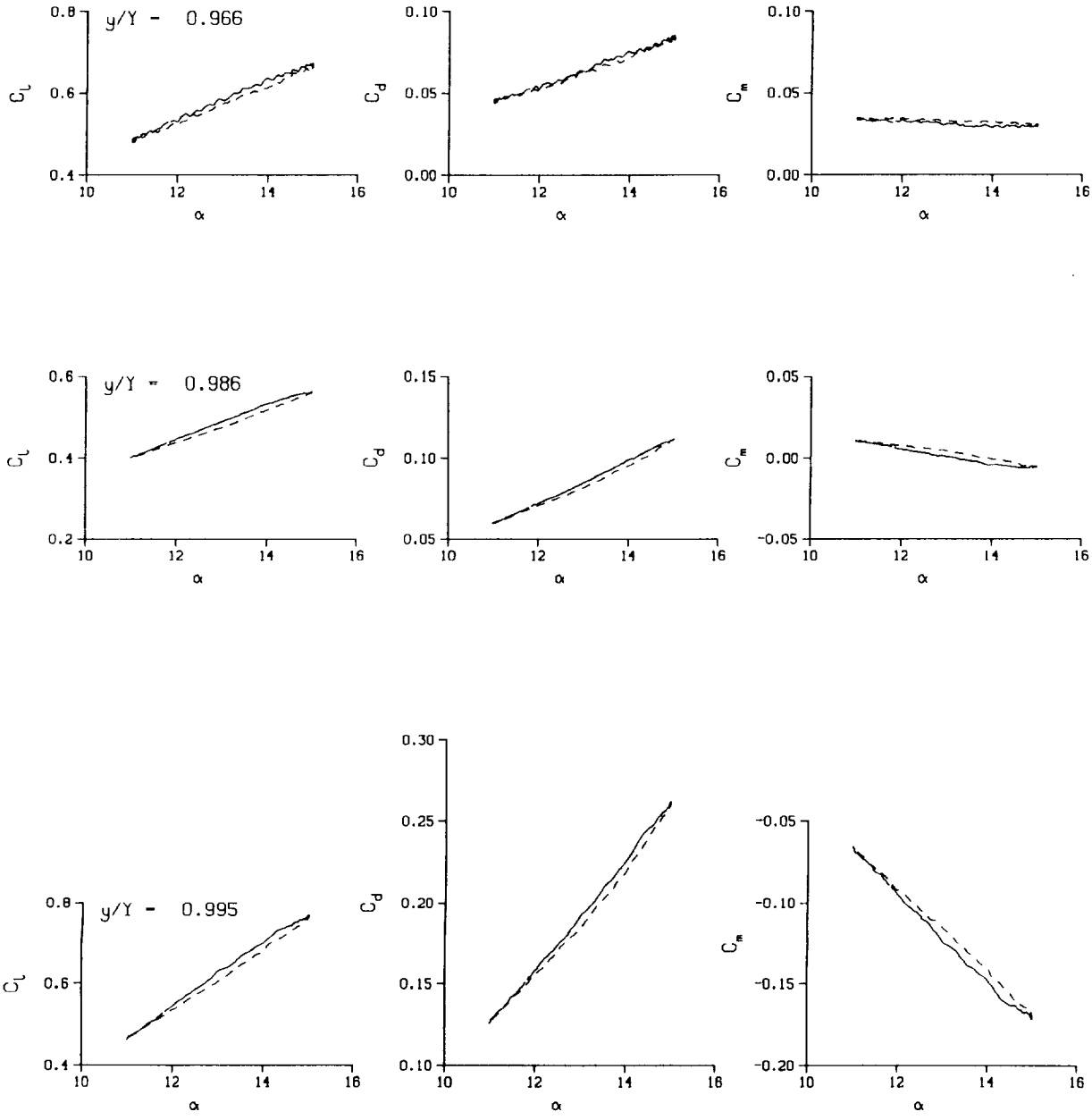

(a) v = 0.041. Concluded

Figure 94. Continued.

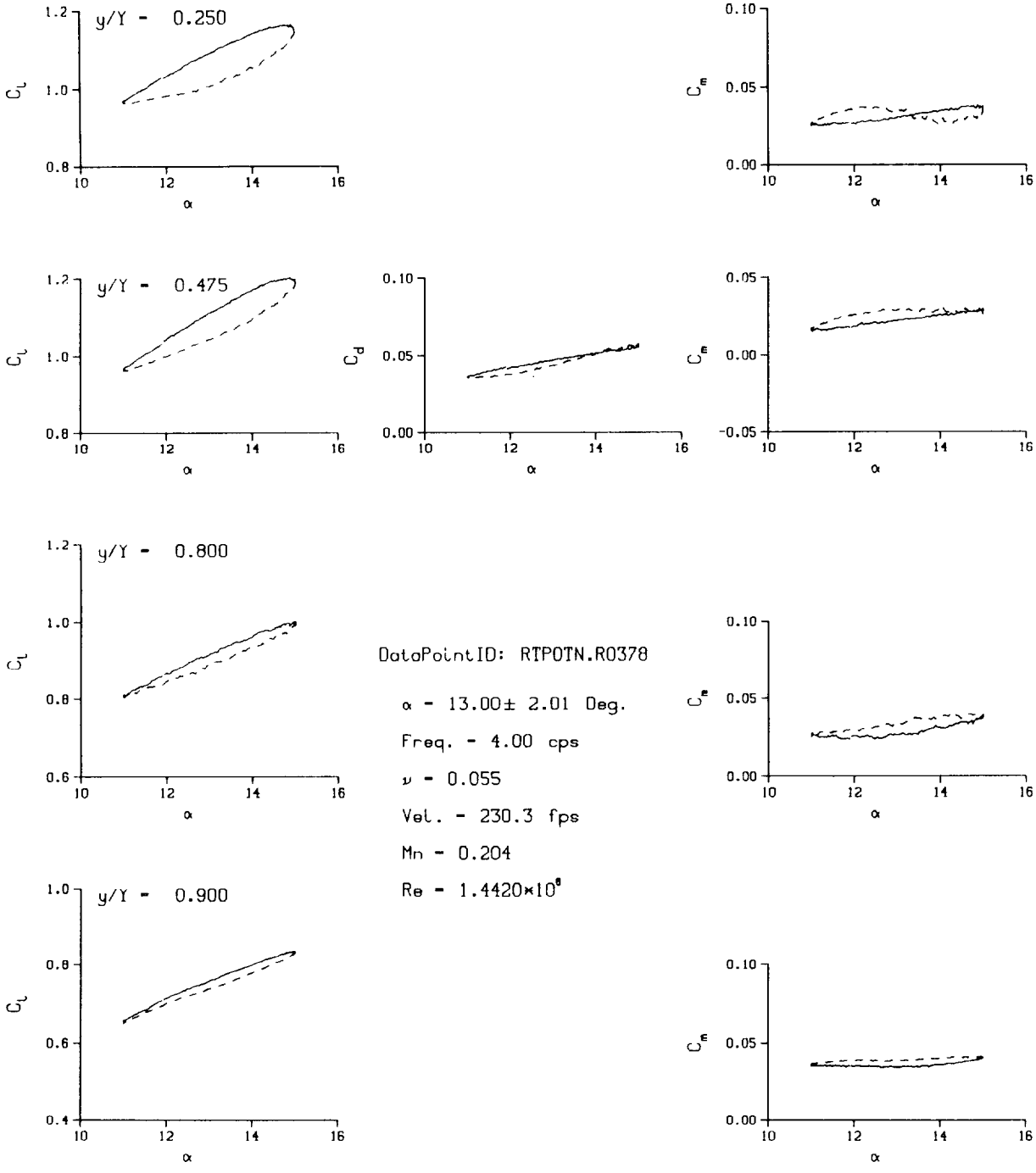

(b) v = 0.055

Figure 94. Continued.

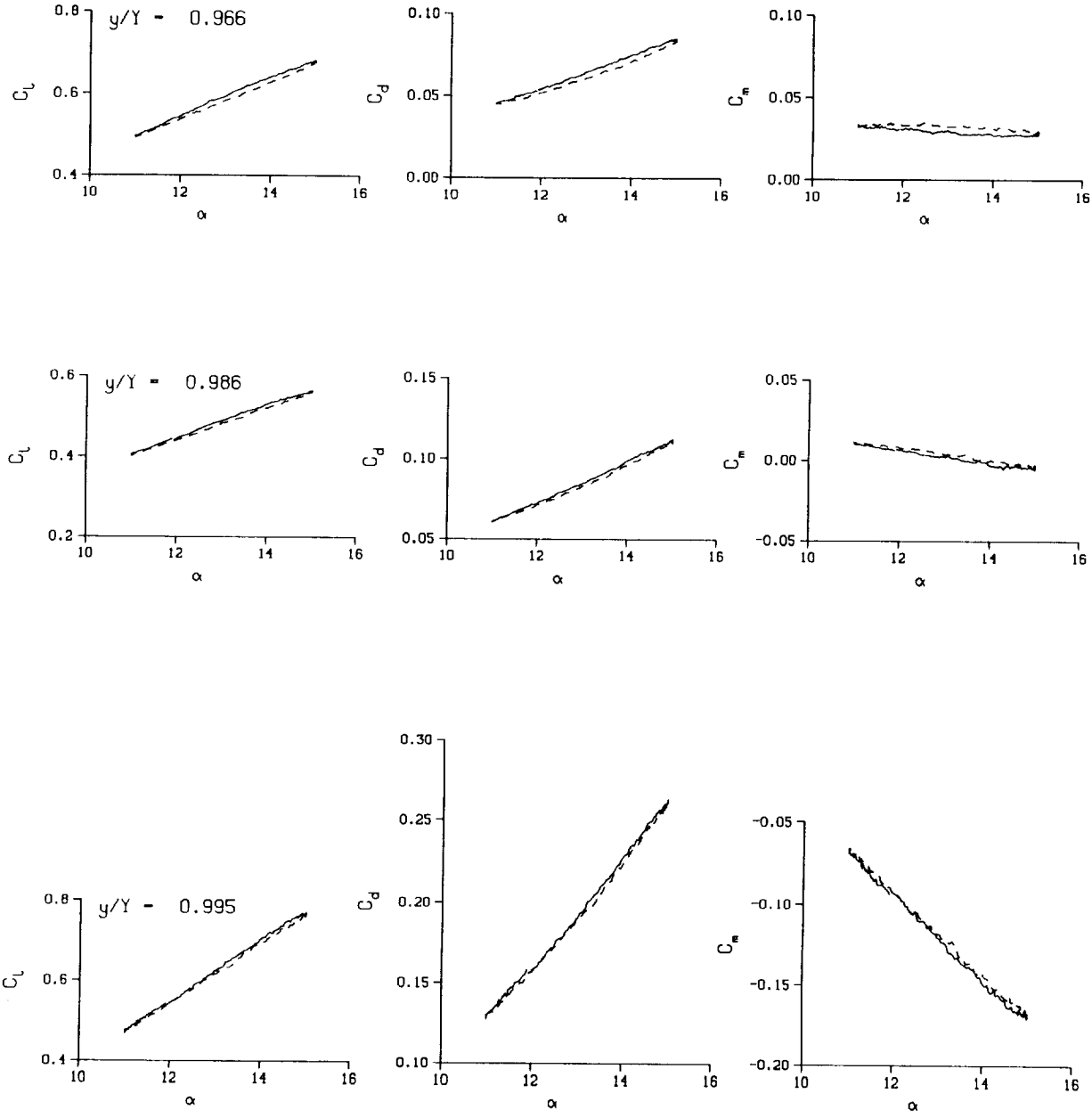

(b) v = 0.055. Concluded

Figure 94. Continued.

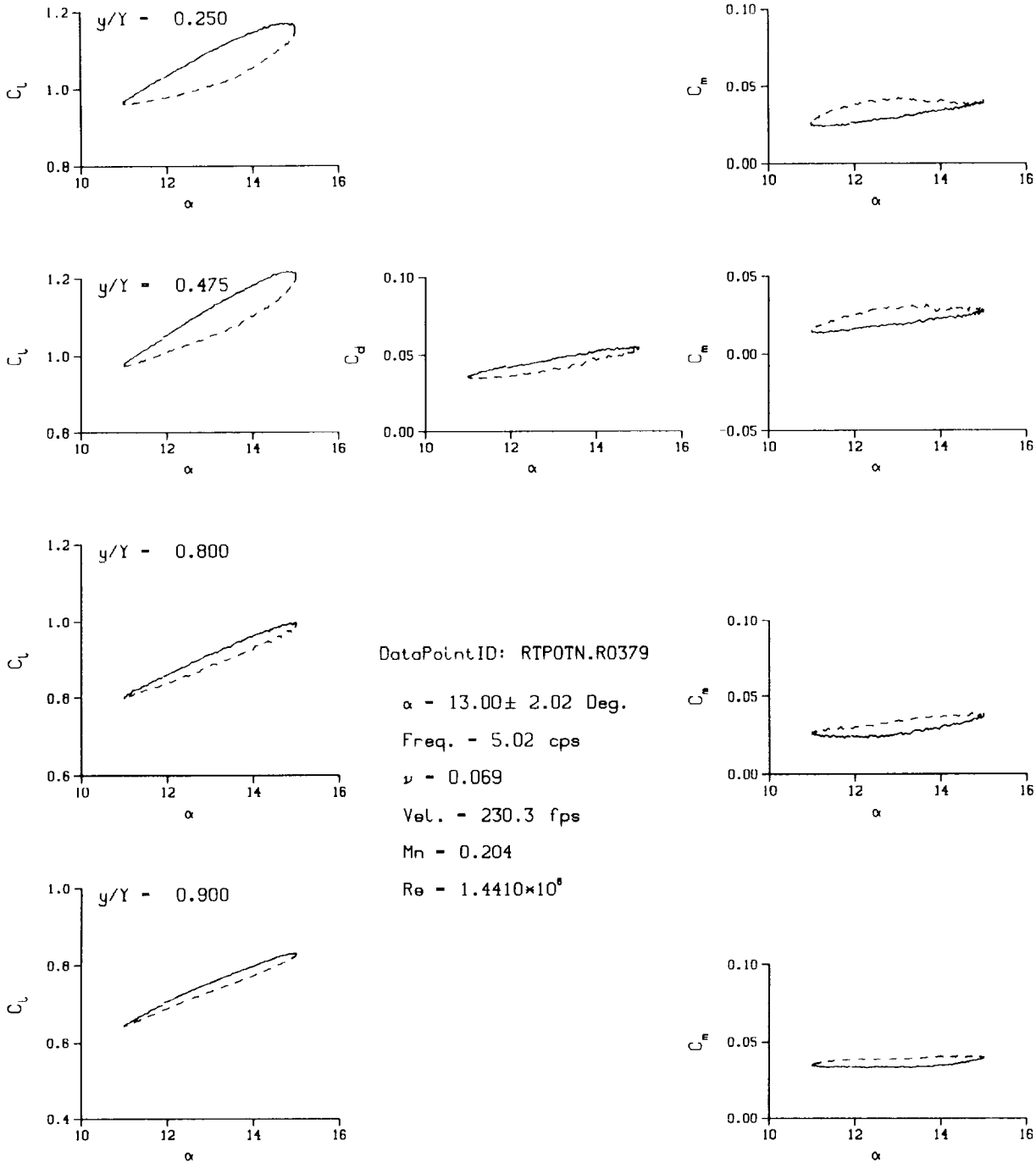

(c) ν = 0.069

Figure 94. Continued.

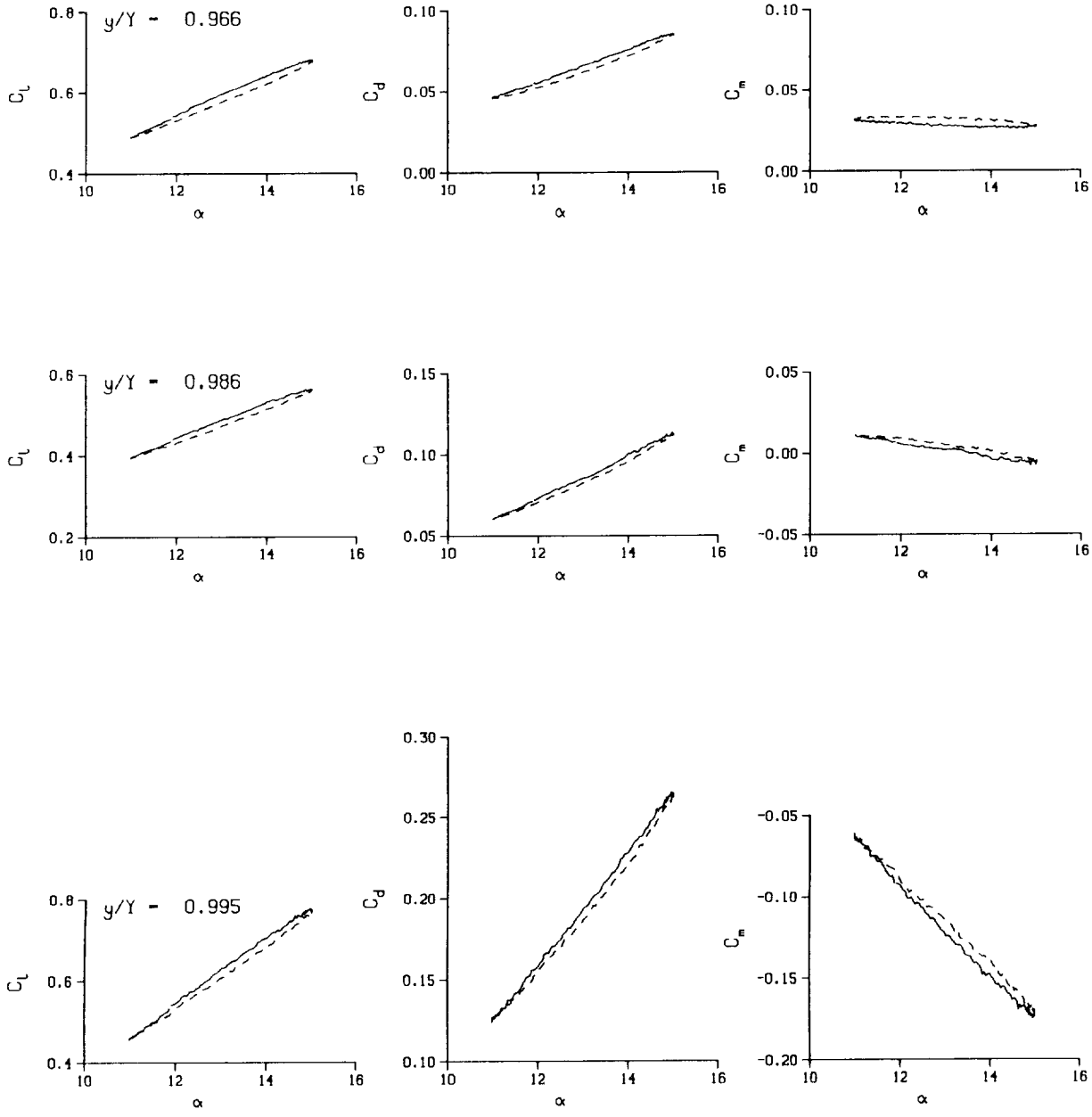

(c) v = 0.069. Concluded

Figure 94. Continued.

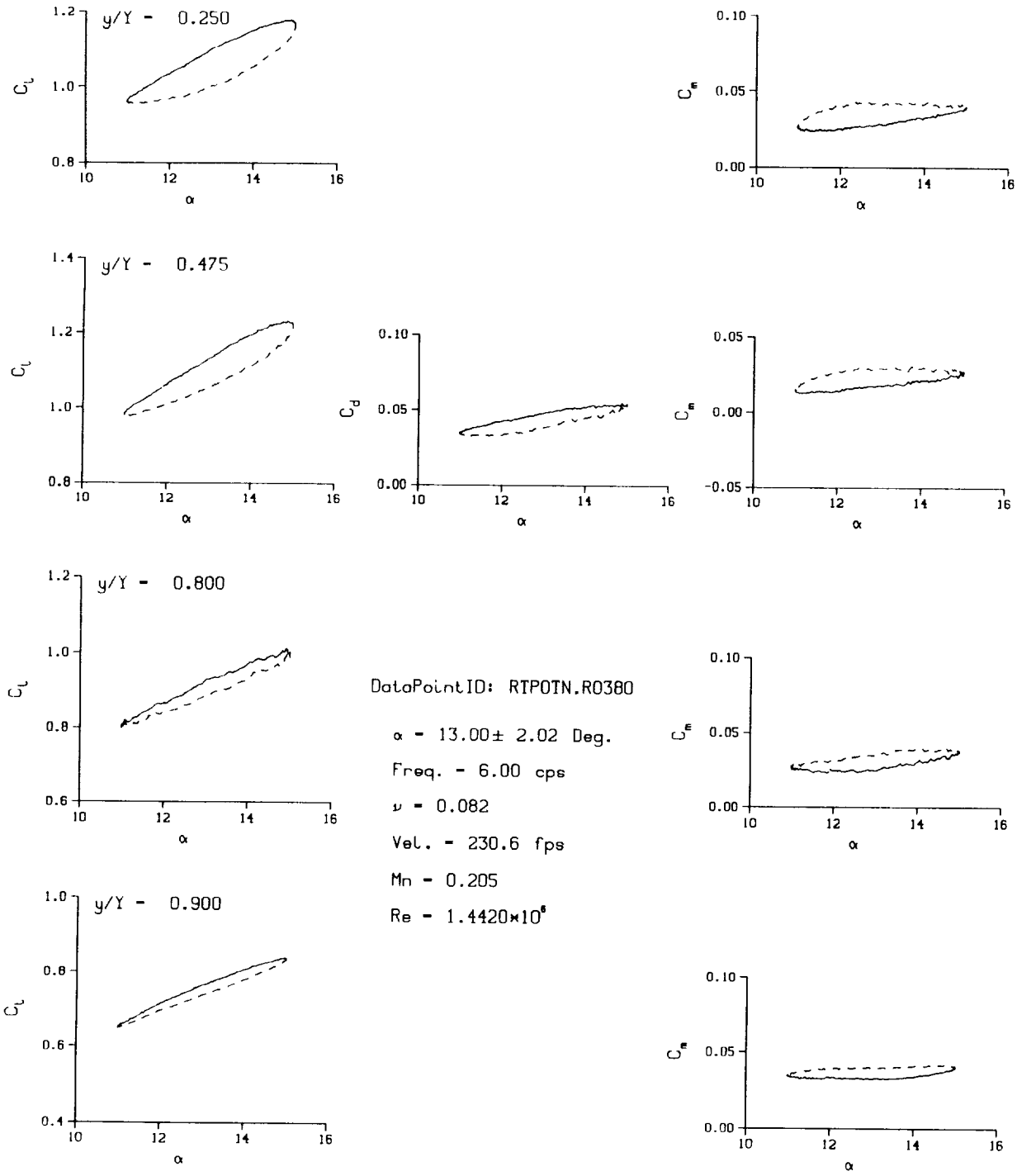

(d) ν = 0.082

Figure 94. Continued.

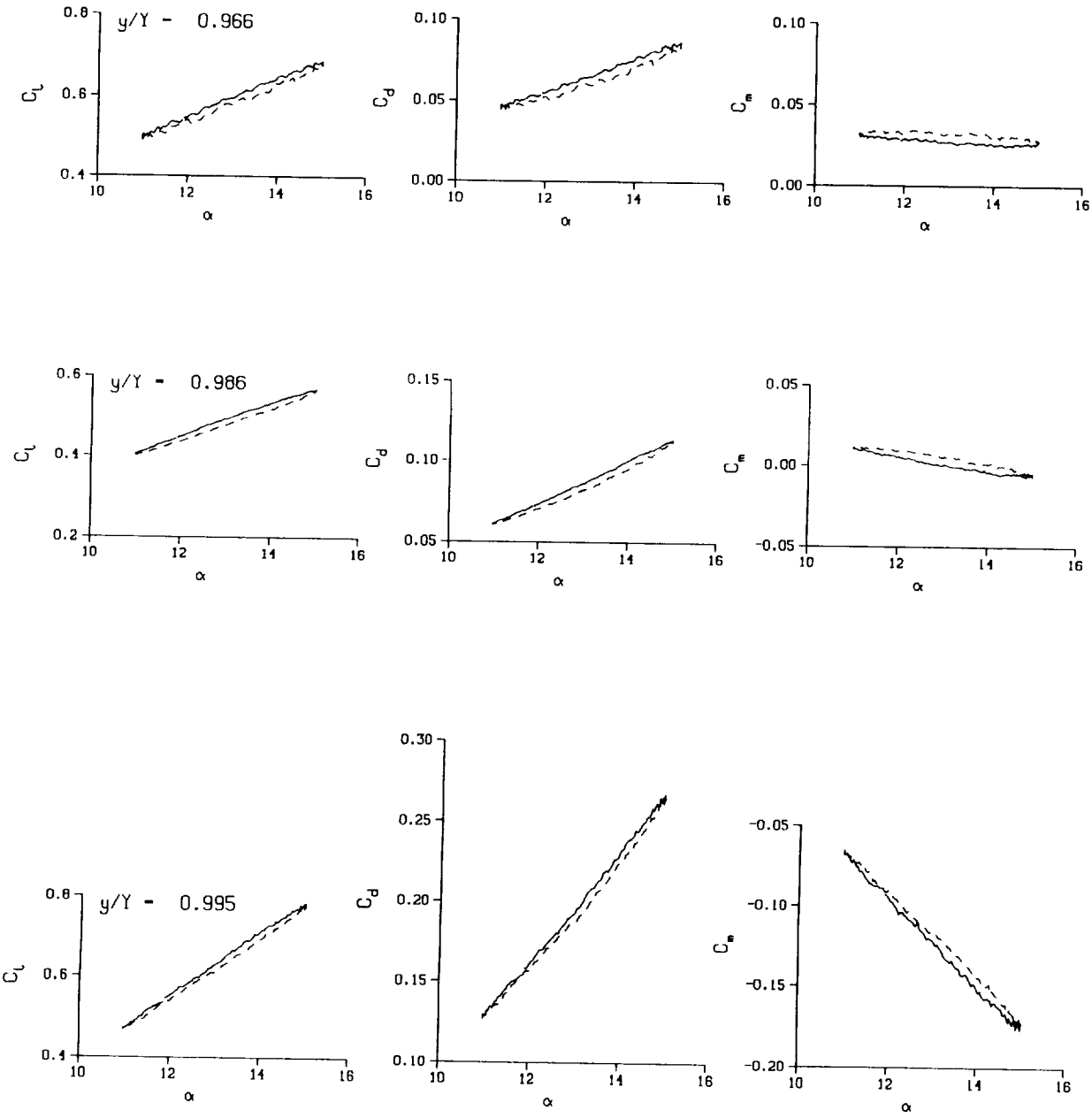

(d) v = 0.082. Concluded

Figure 94. Concluded.

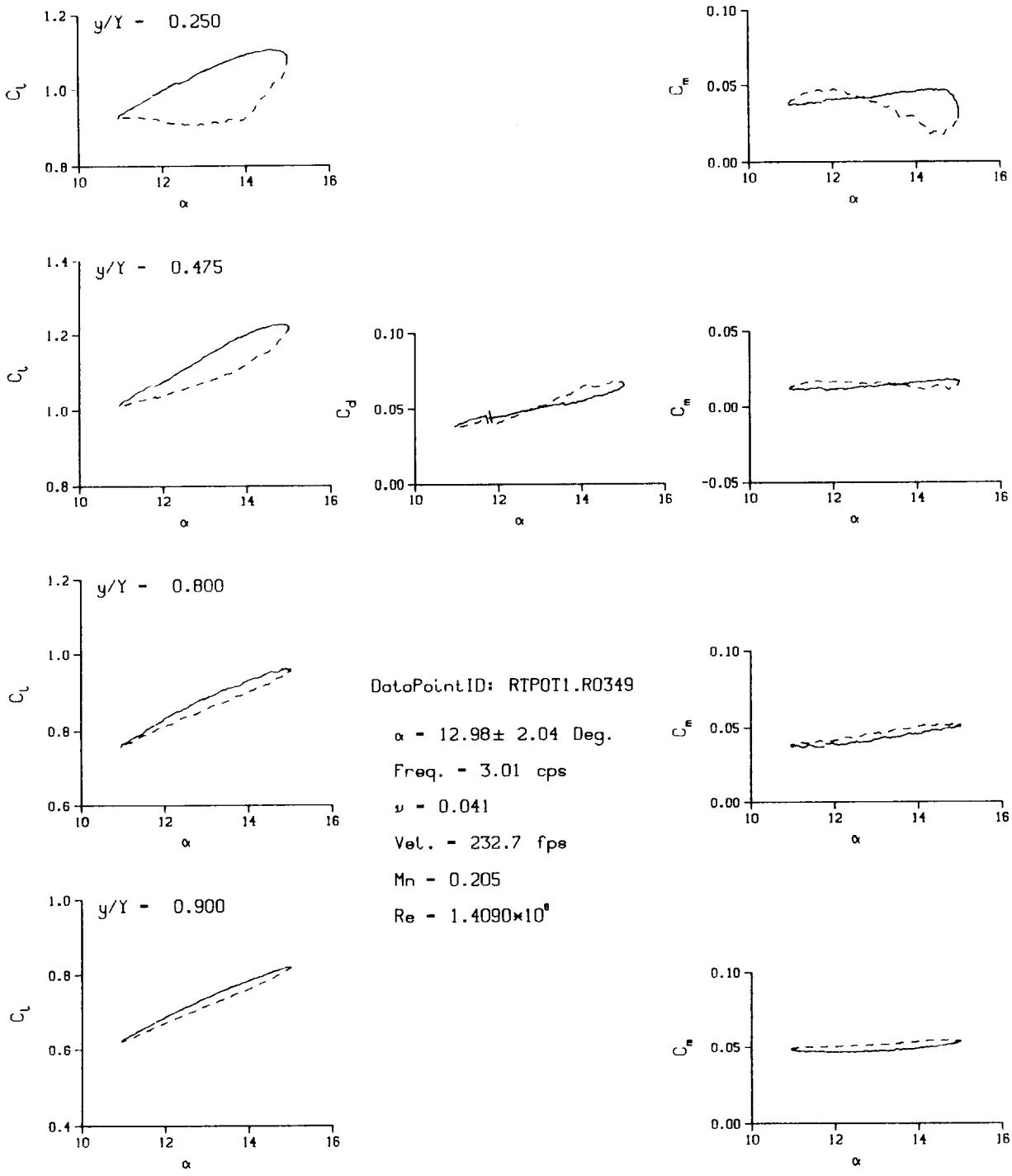

(a) v = 0.041

Figure 95. Frequency sweep; with BL-trip; q = 60 psf.

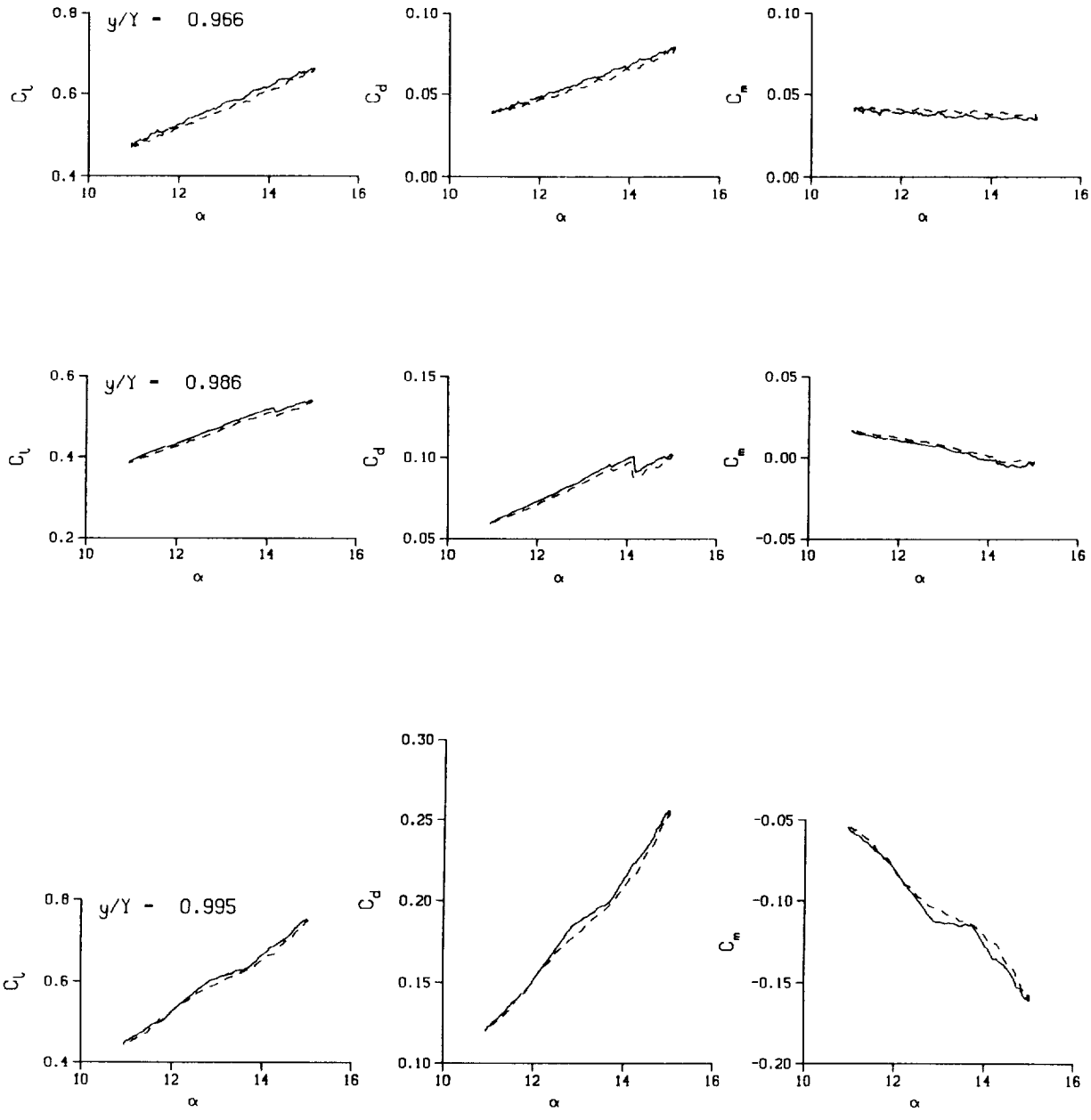

(a) v = 0.041. Concluded

Figure 95. Continued.

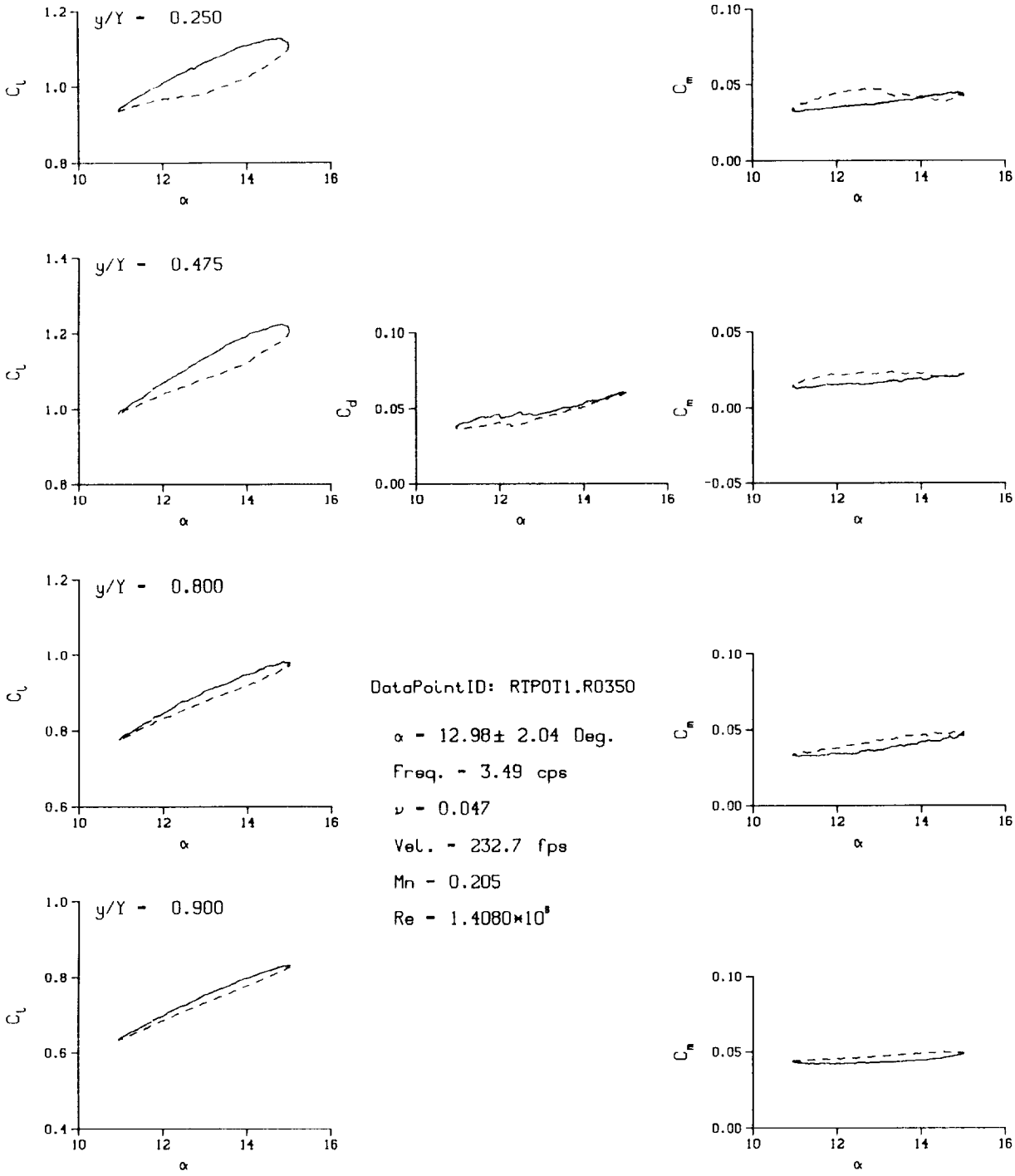

(b) ν = 0.047

Figure 95. Continued.

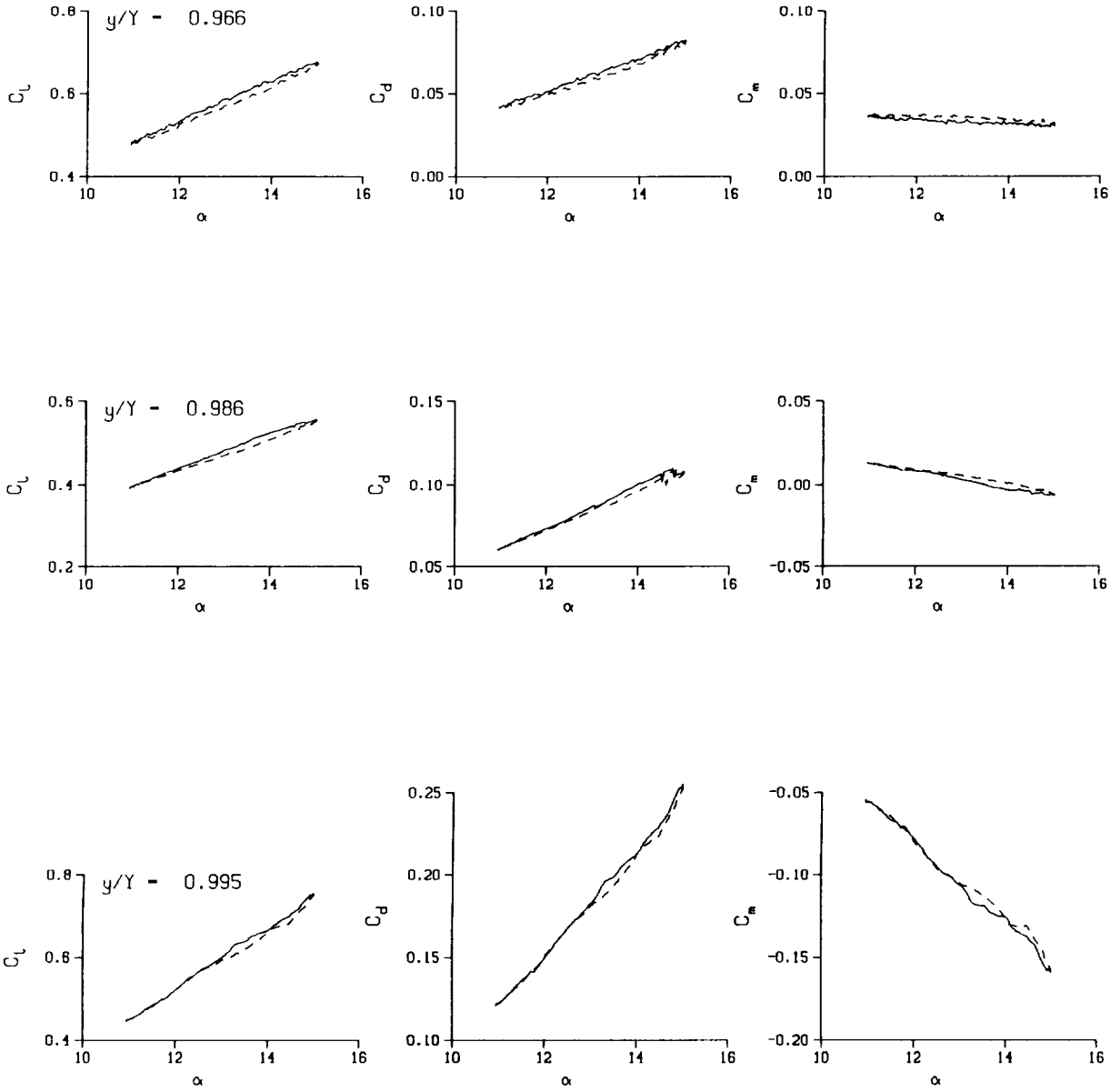

(b) v = 0.047. Concluded

Figure 95. Continued.

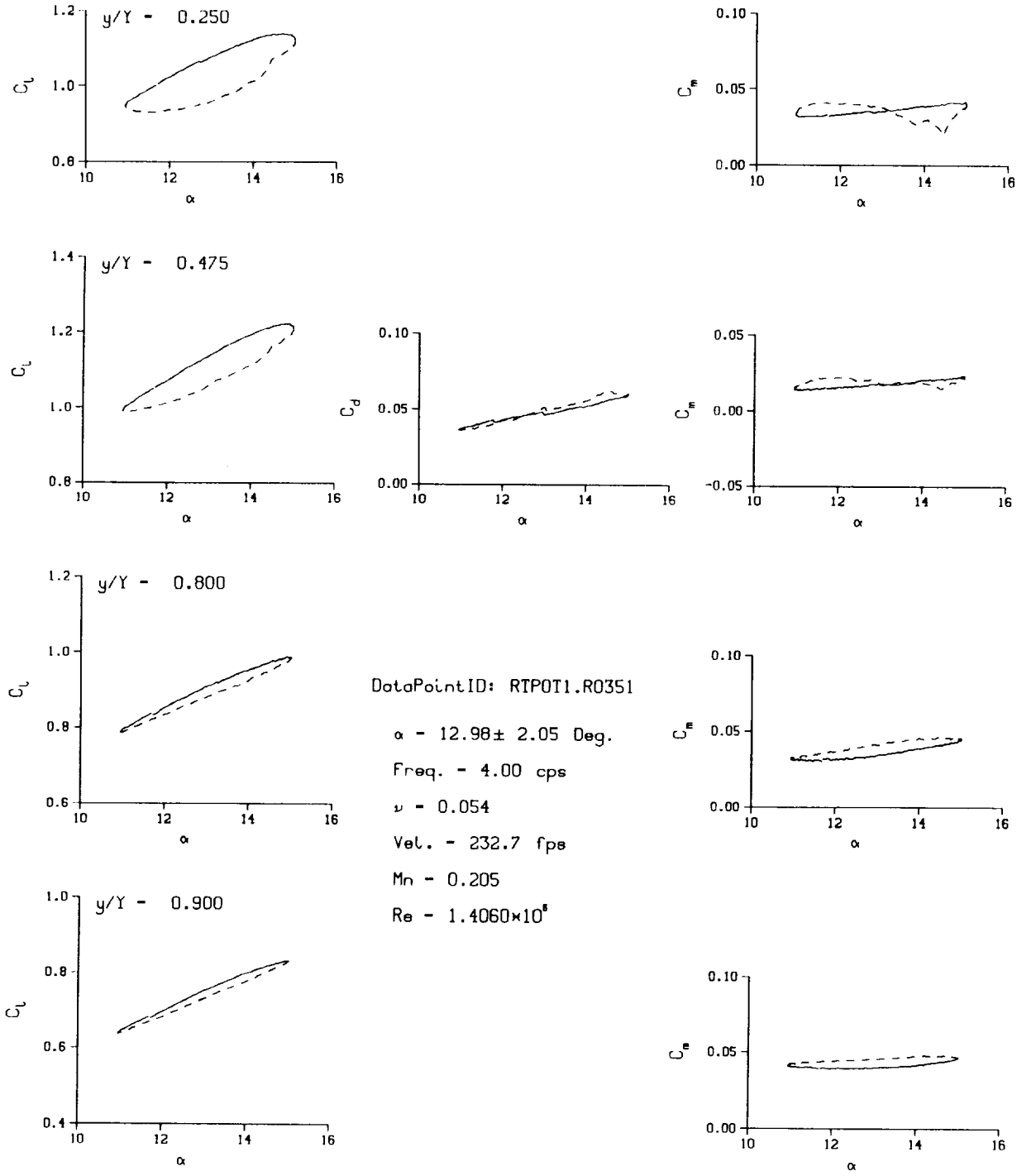

(c) ν = 0.054

Figure 95. Continued.

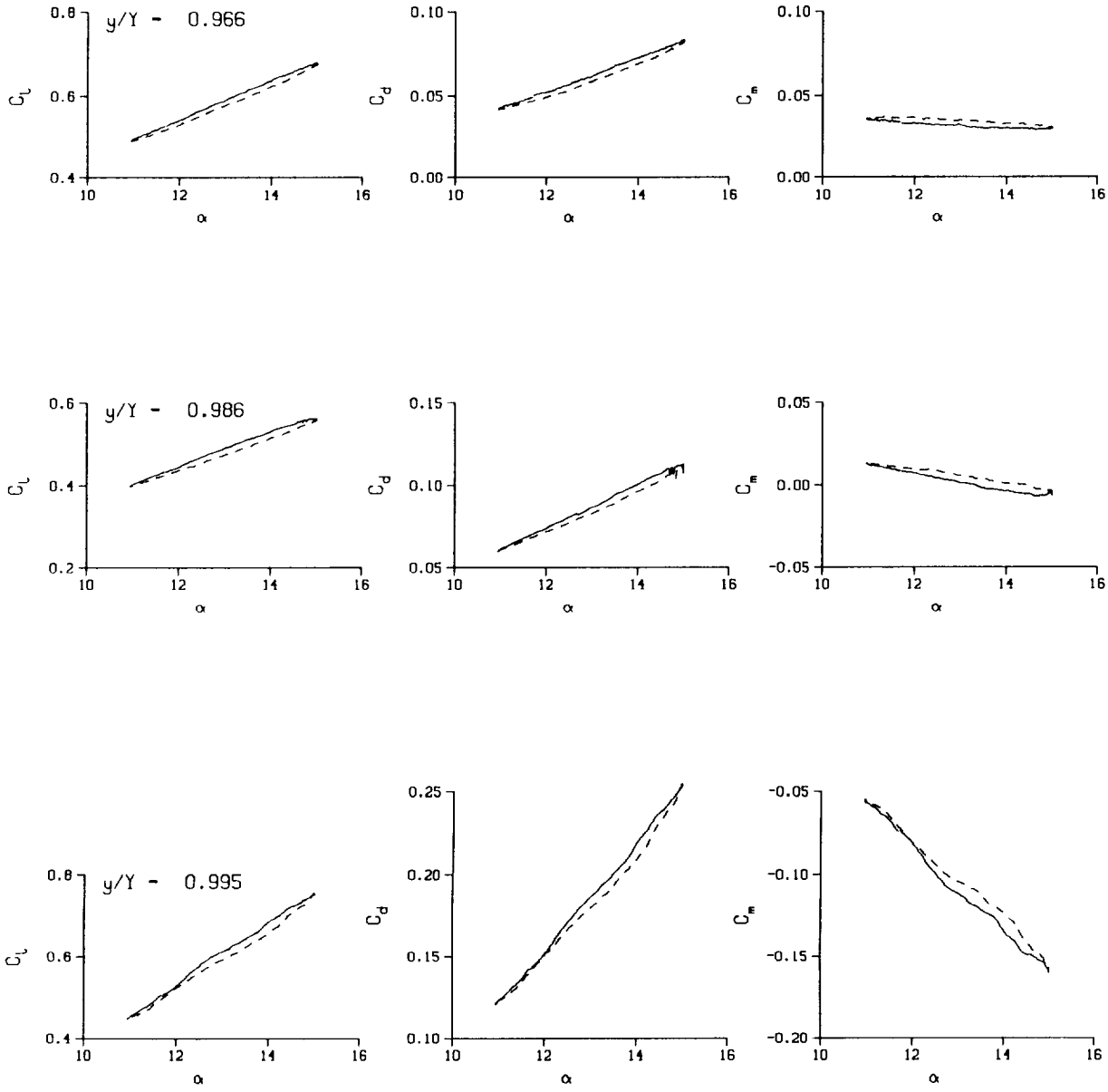

(c) v = 0.054. Concluded

Figure 95. Continued.

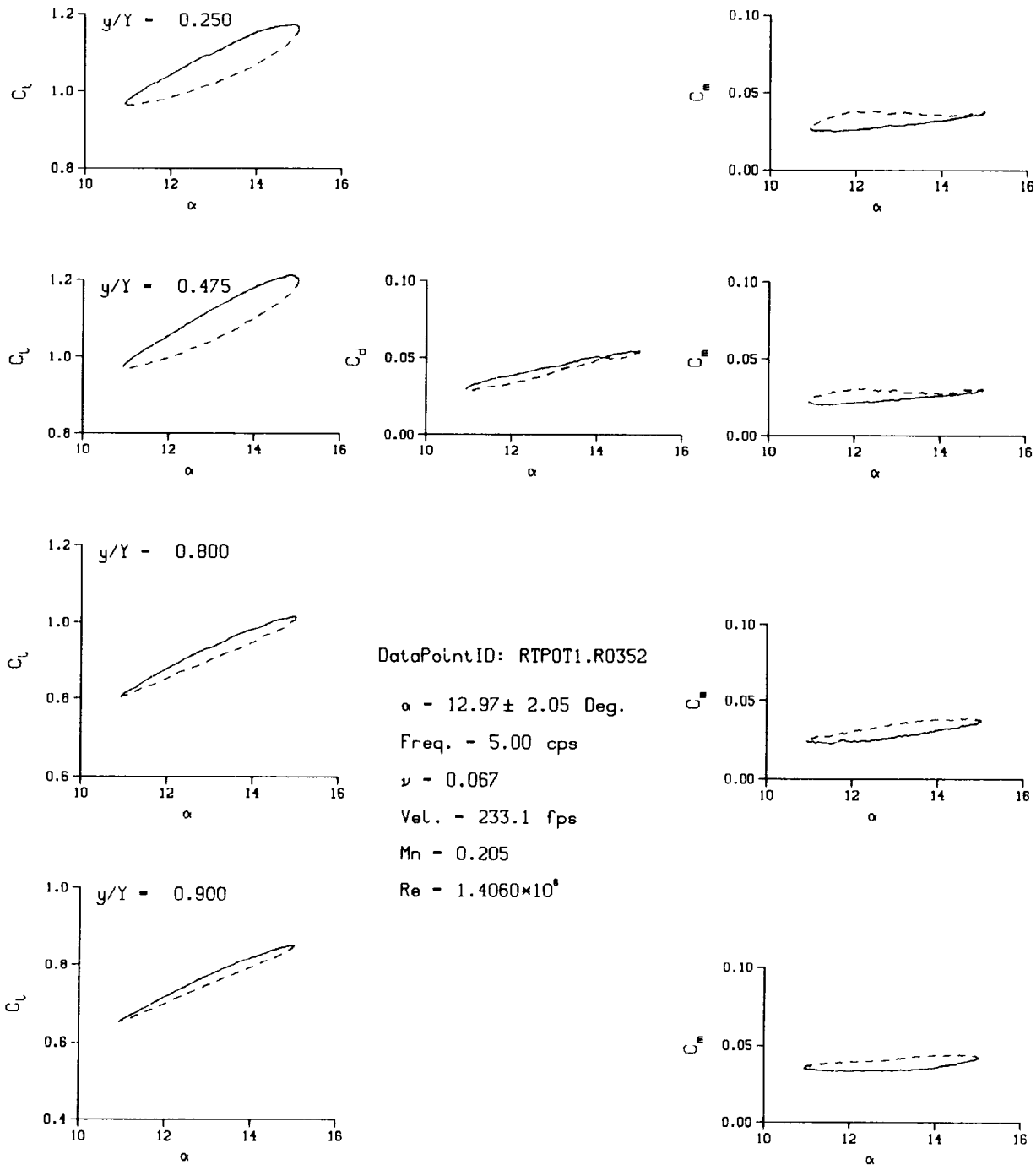

(d) ν = 0.067

Figure 95. Continued.

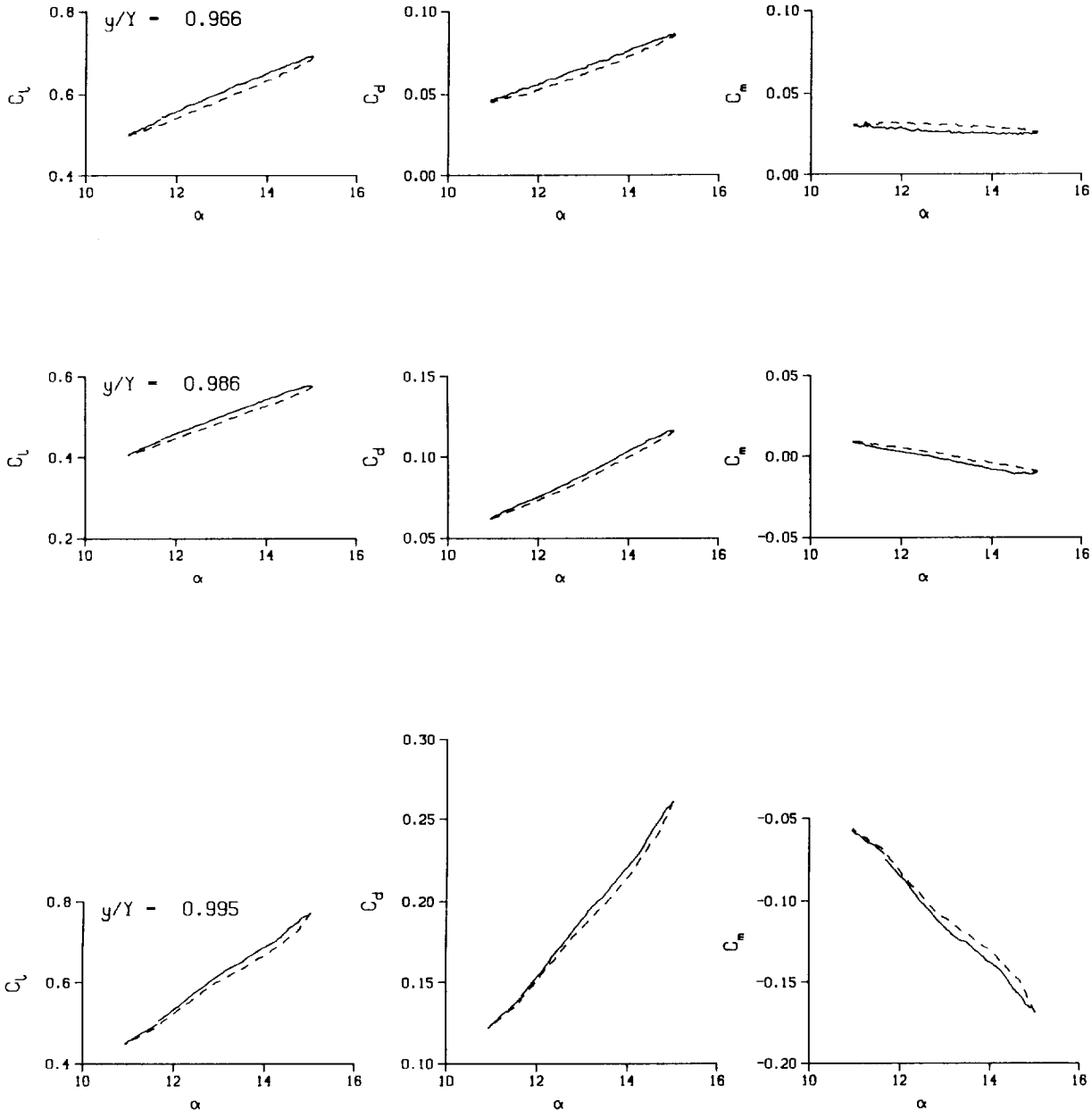

(d) v = 0.067. Concluded

Figure 95. Continued.

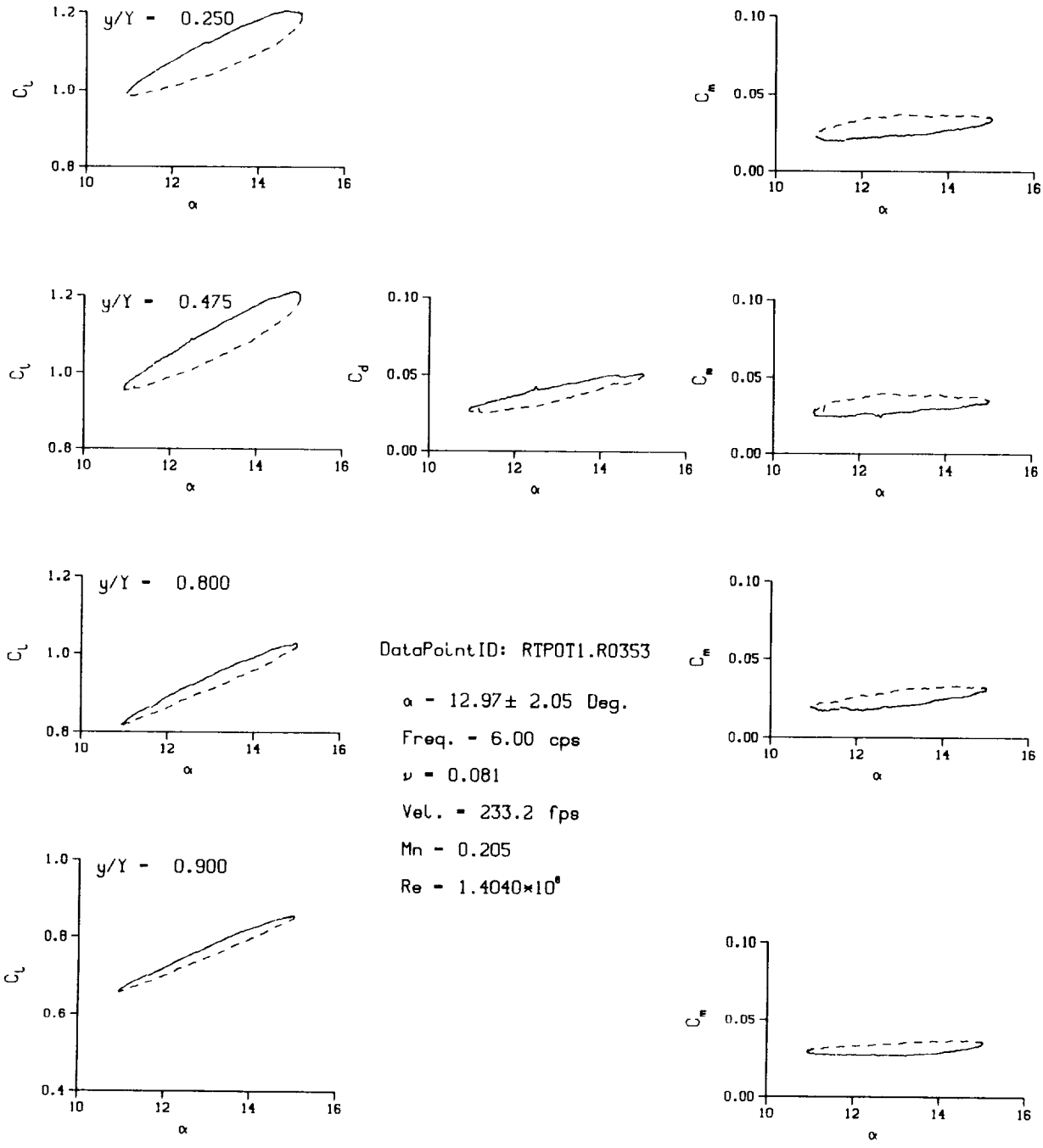

(e) ν = 0.081

Figure 95. Continued.

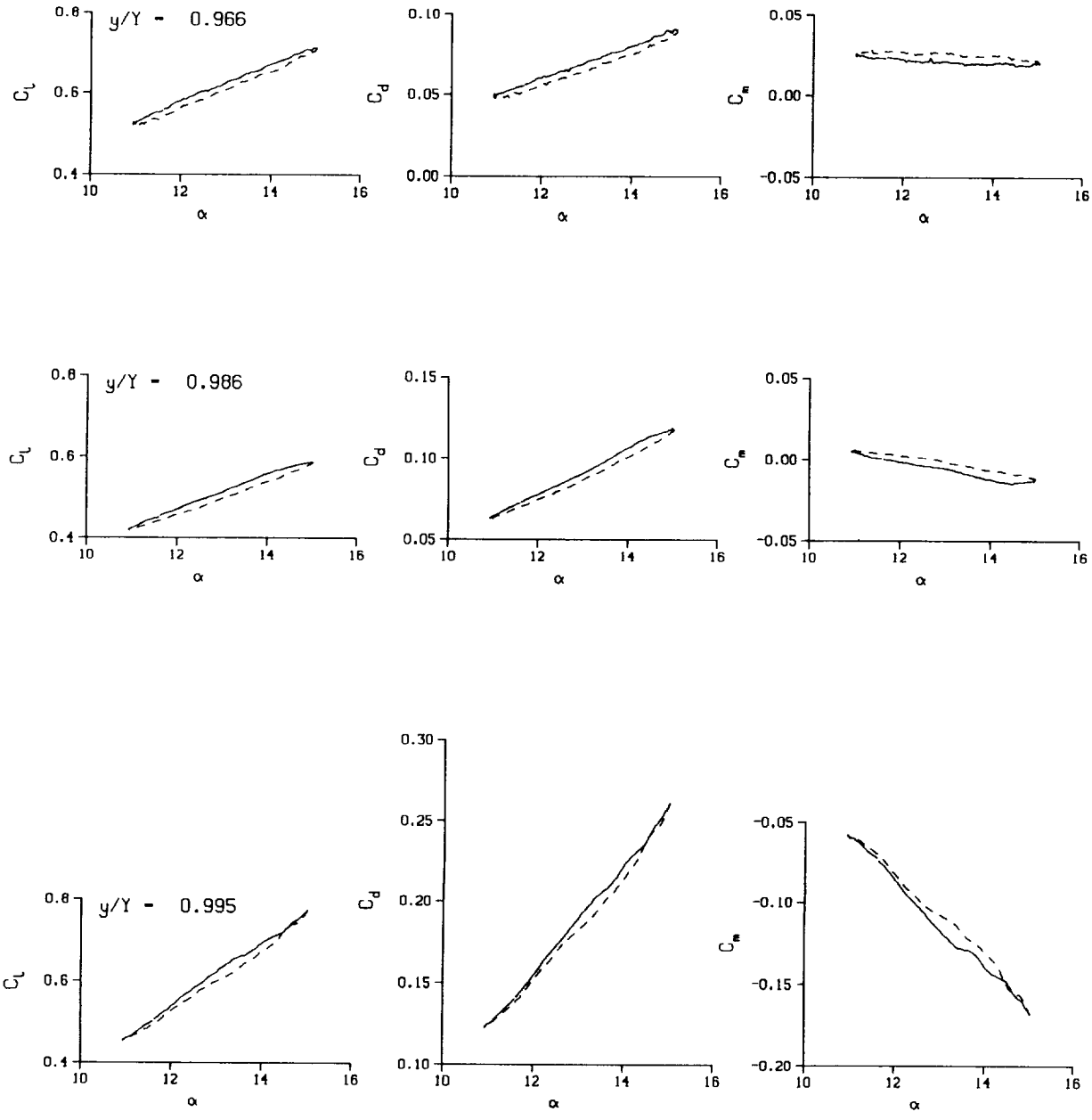

(e) v = 0.081. Concluded

Figure 95. Continued.

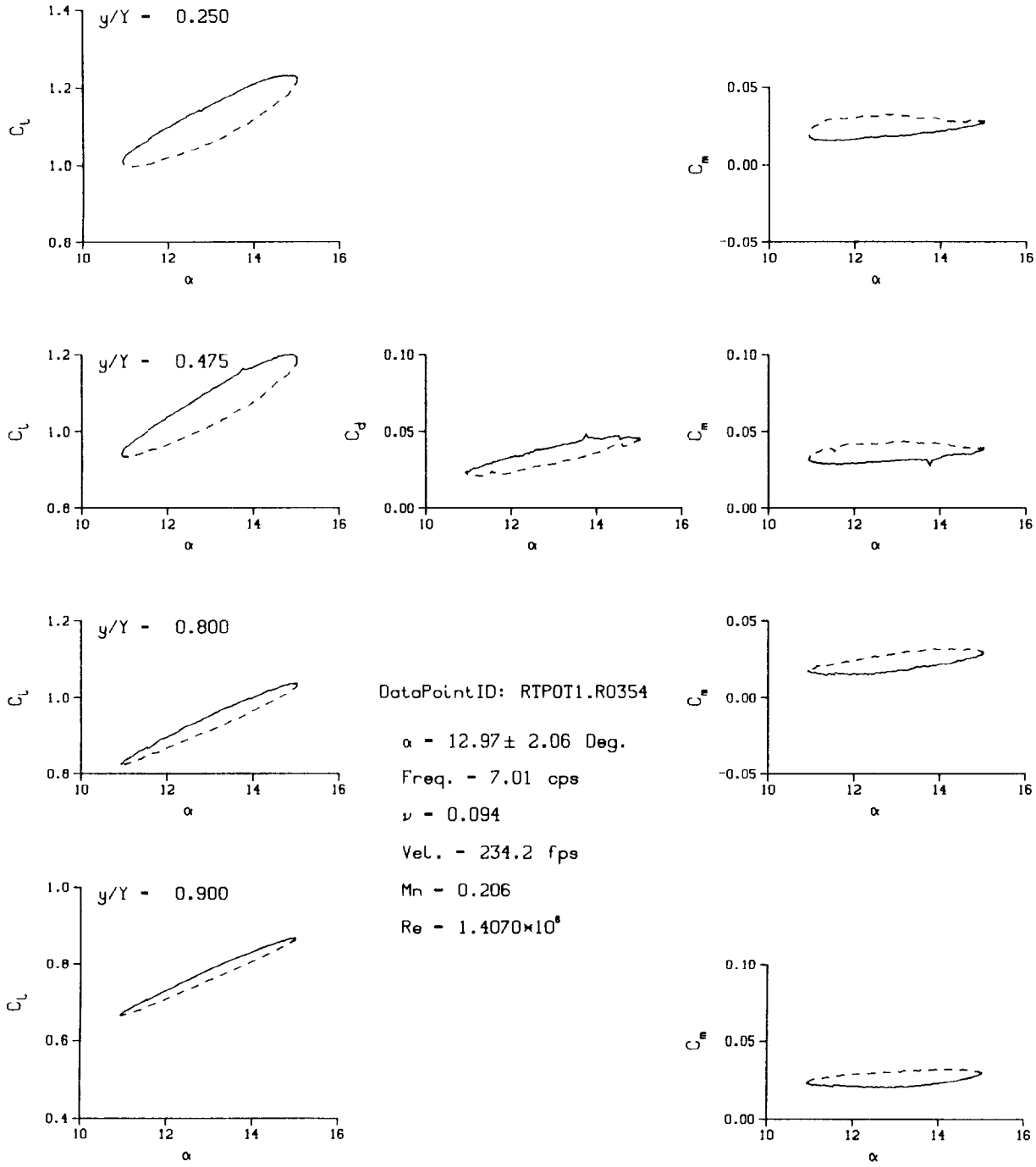

(f) ν = 0.094

Figure 95. Continued.

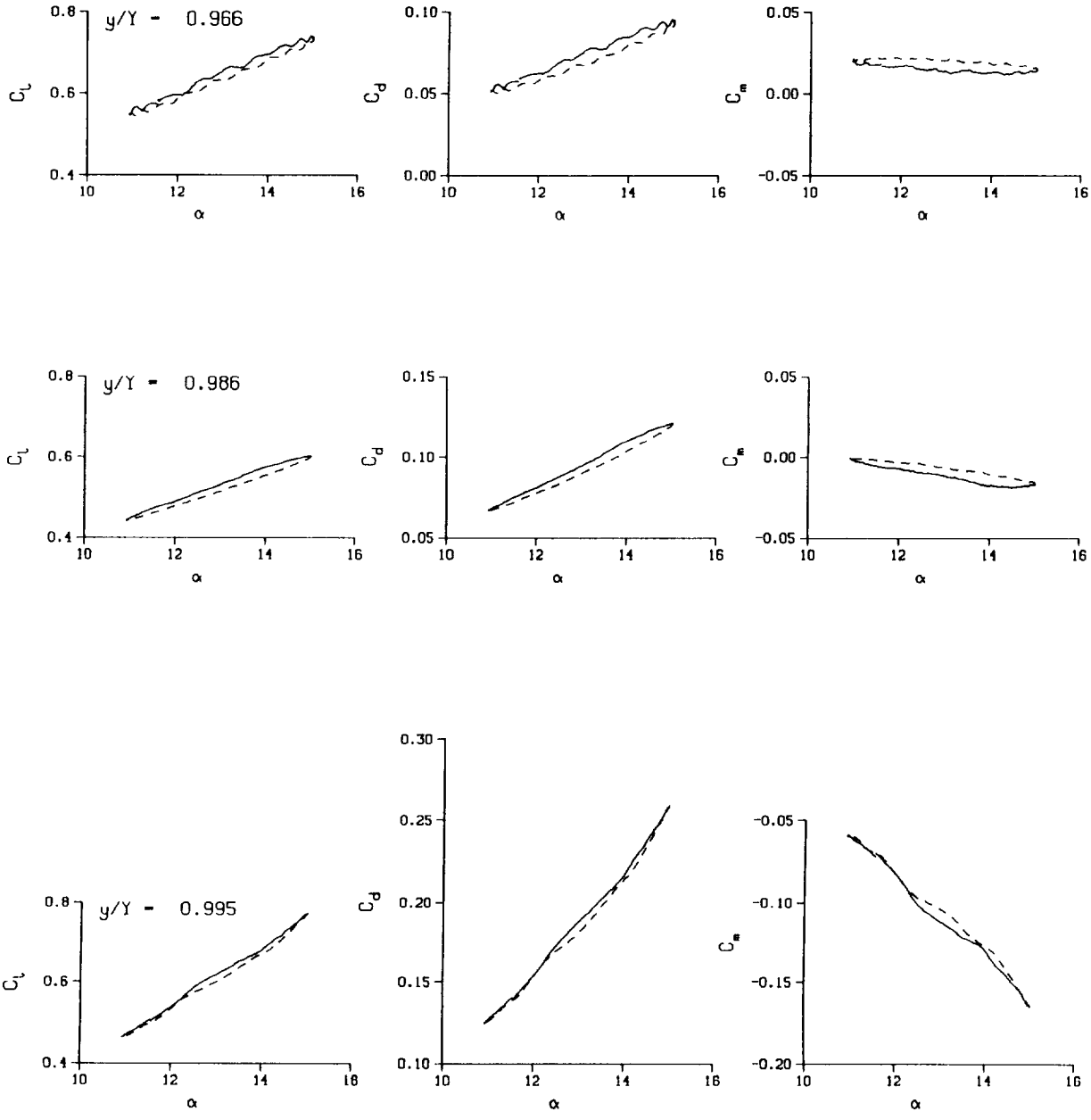

(f) v = 0.094. Concluded

Figure 95. Concluded.

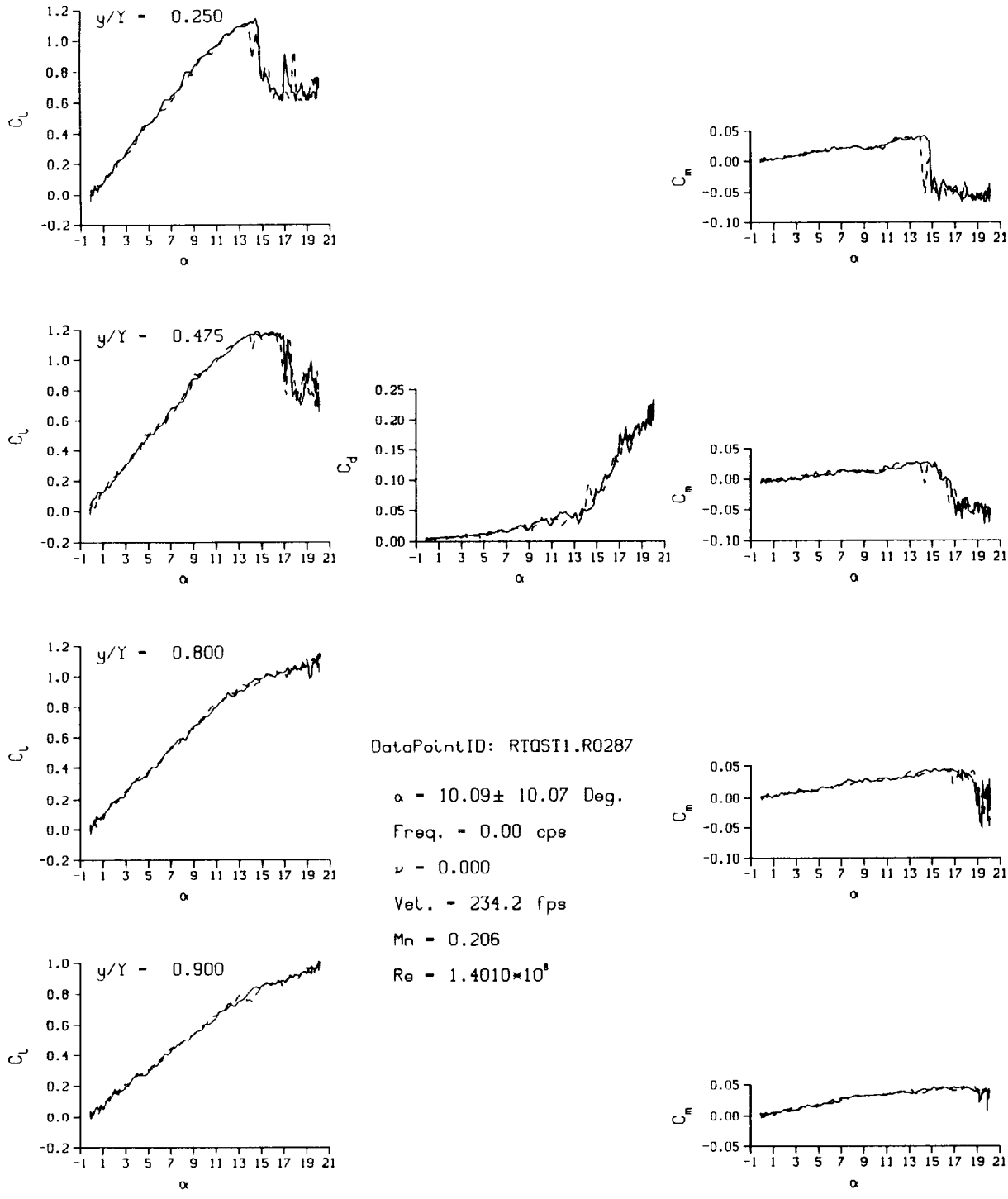

(a) Repeat no. 1

Figure 96. 3-D round tip quasi-steady data; with BL-trip; q = 60.

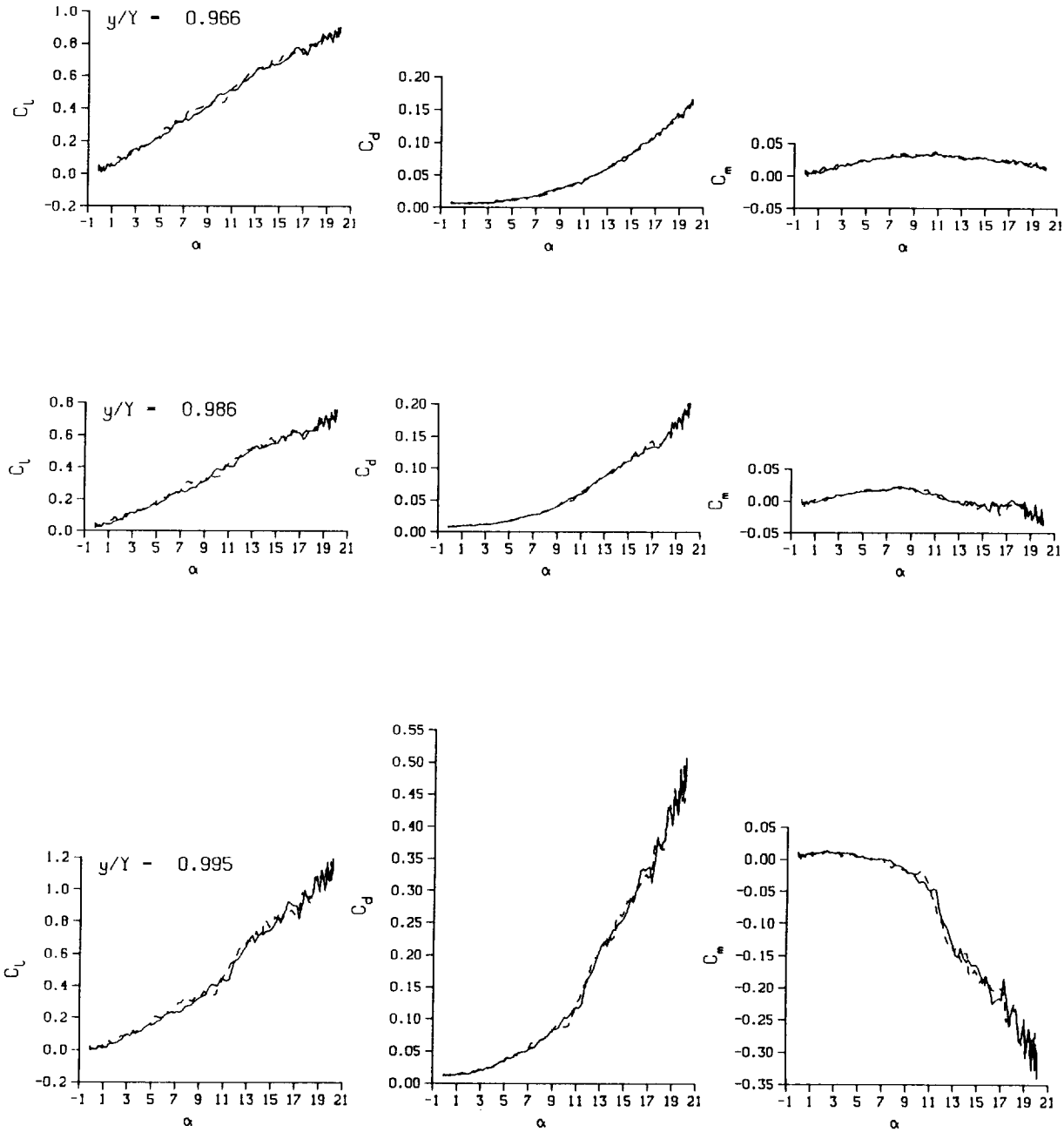

(a) Repeat no. 1. Concluded

Figure 96. Continued.

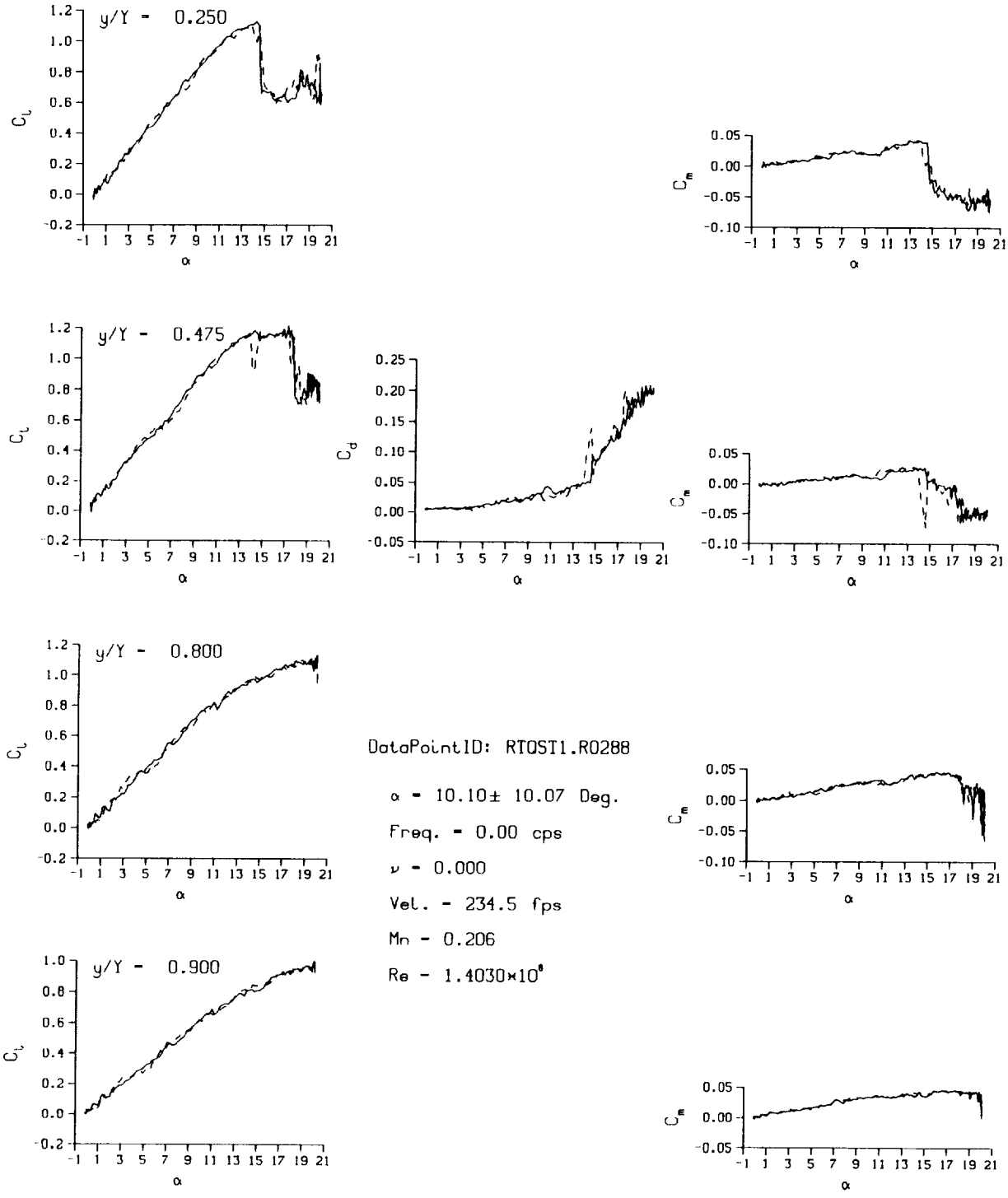

(b) Repeat no. 2

Figure 96. Continued.

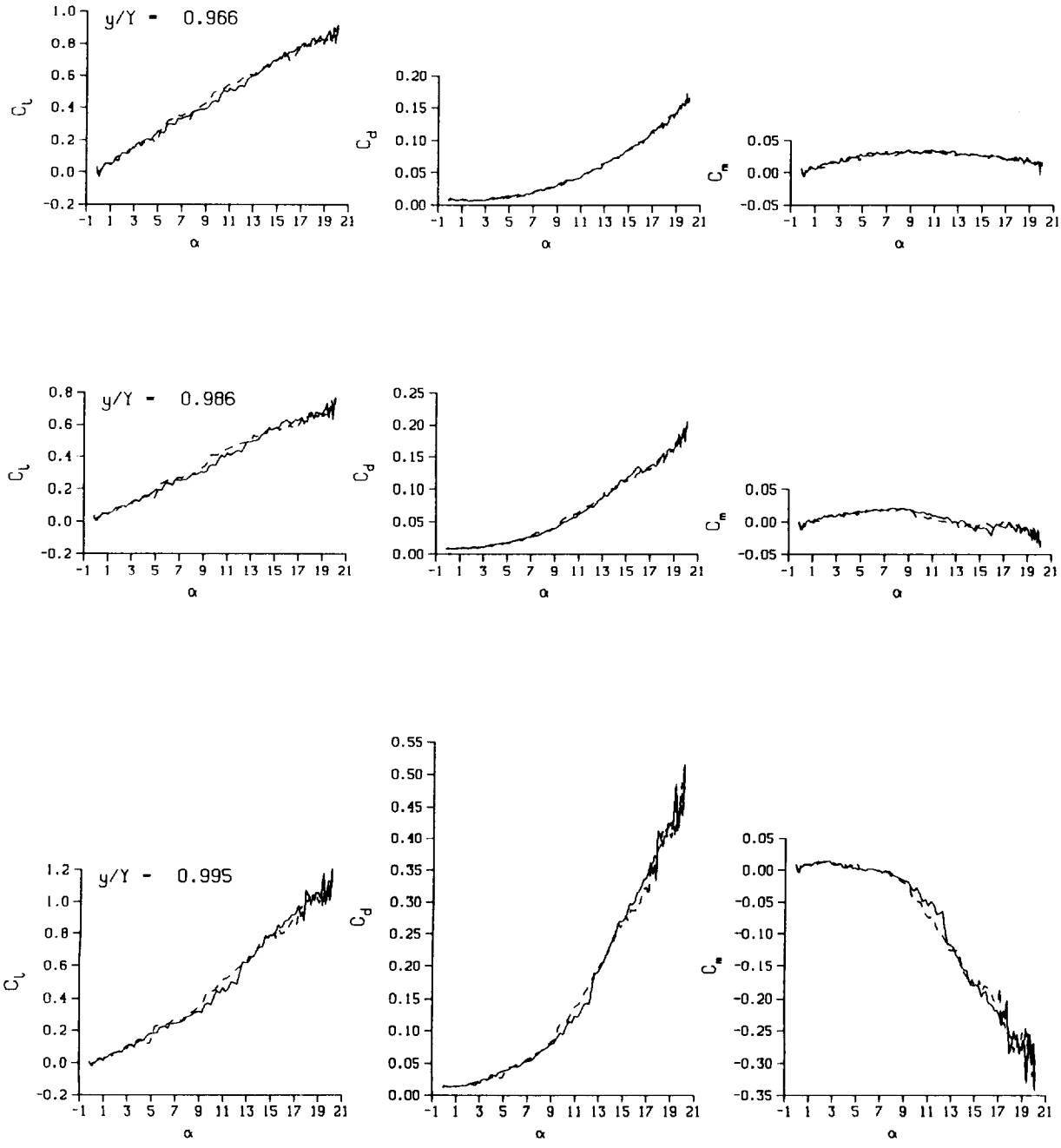

(b) Repeat no. 2. Concluded

Figure 96. Concluded.

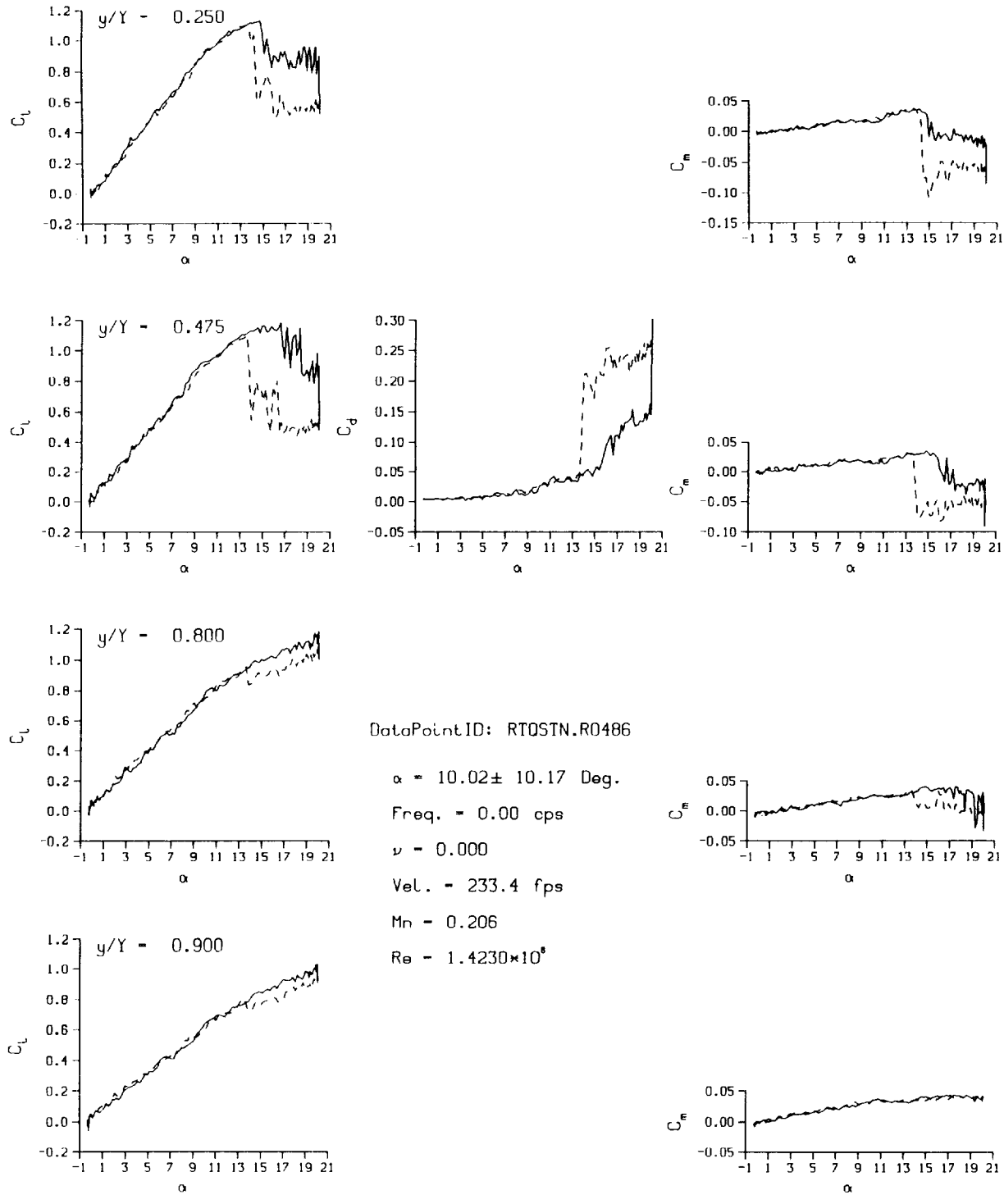

(a) Repeat no. 1

Figure 97. 3-D round tip quasi-steady data; no BL-trip; q = 60.

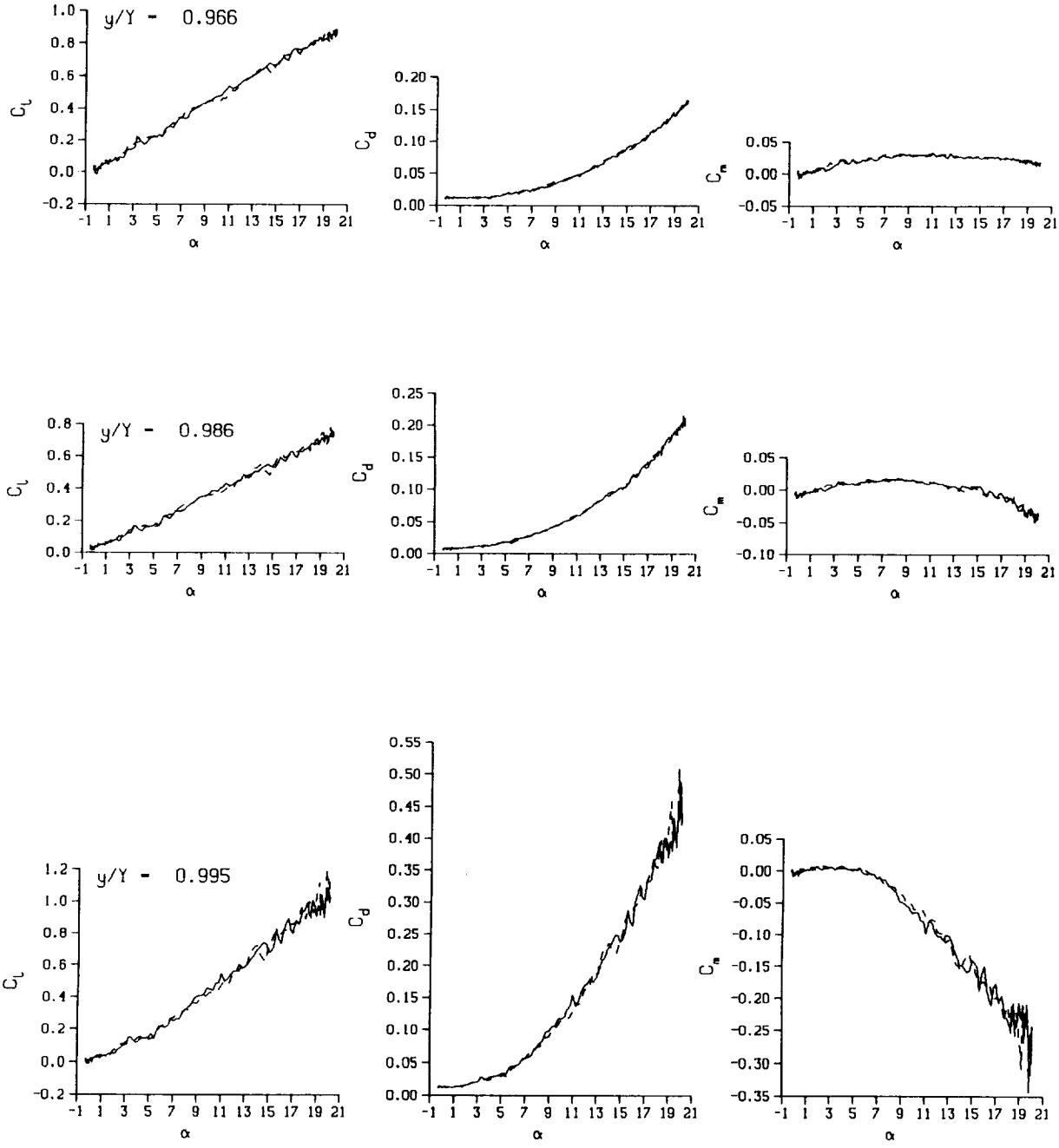

(a) Repeat no. 1. Concluded

Figure 97. Continued.

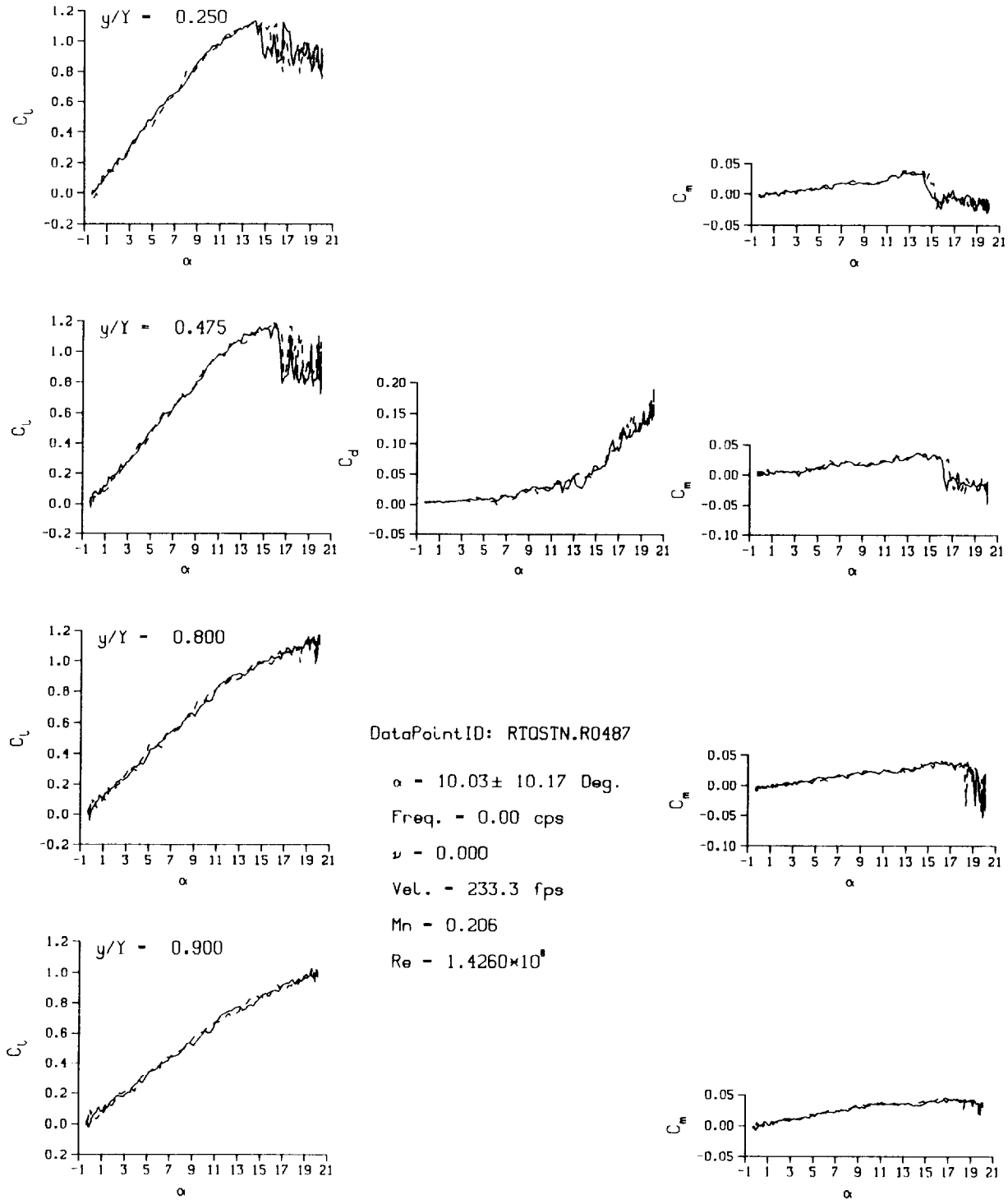

(b) Repeat no. 2

Figure 97. Continued.

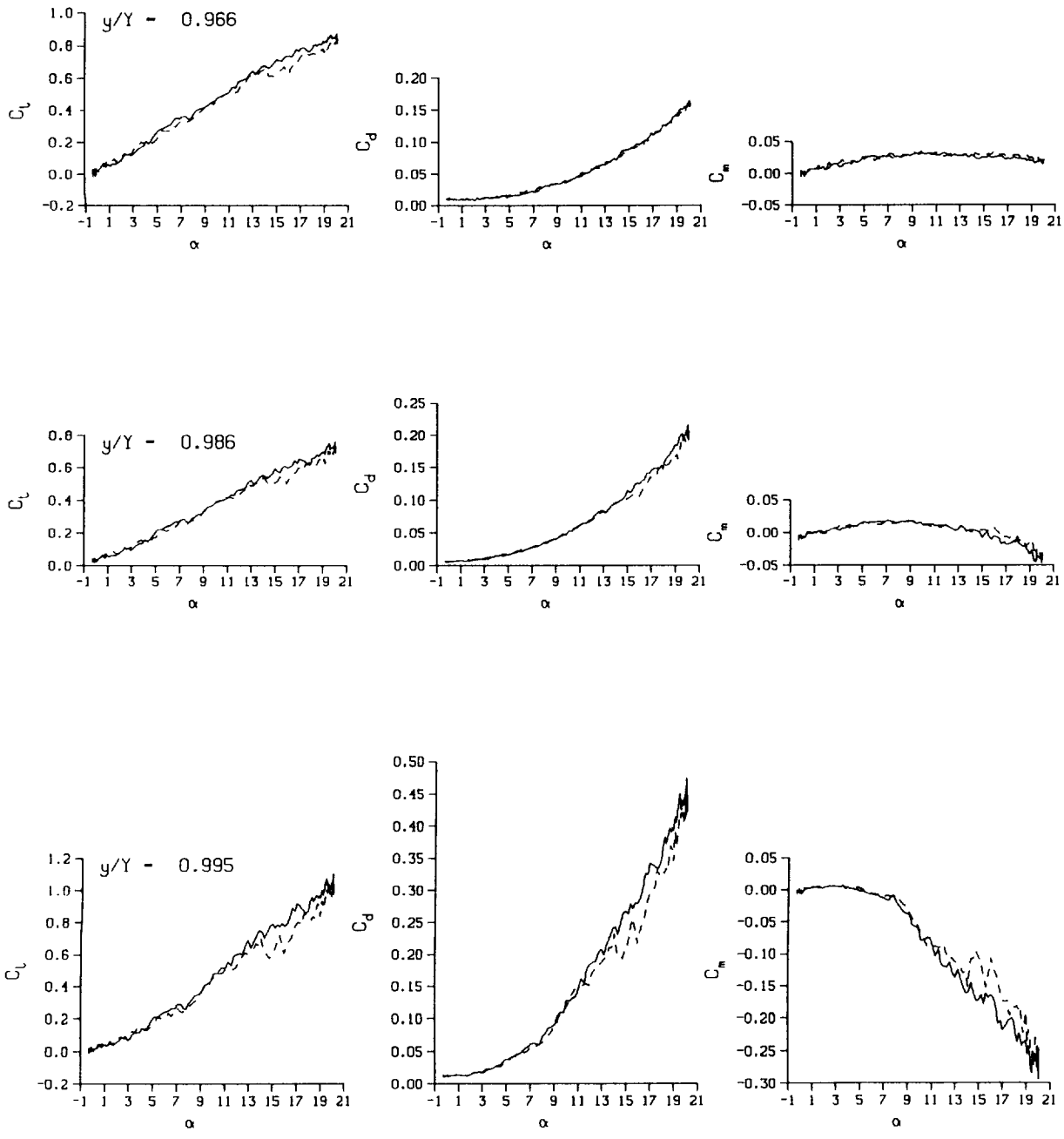

(b) Repeat no. 2. Concluded

Figure 97. Continued.

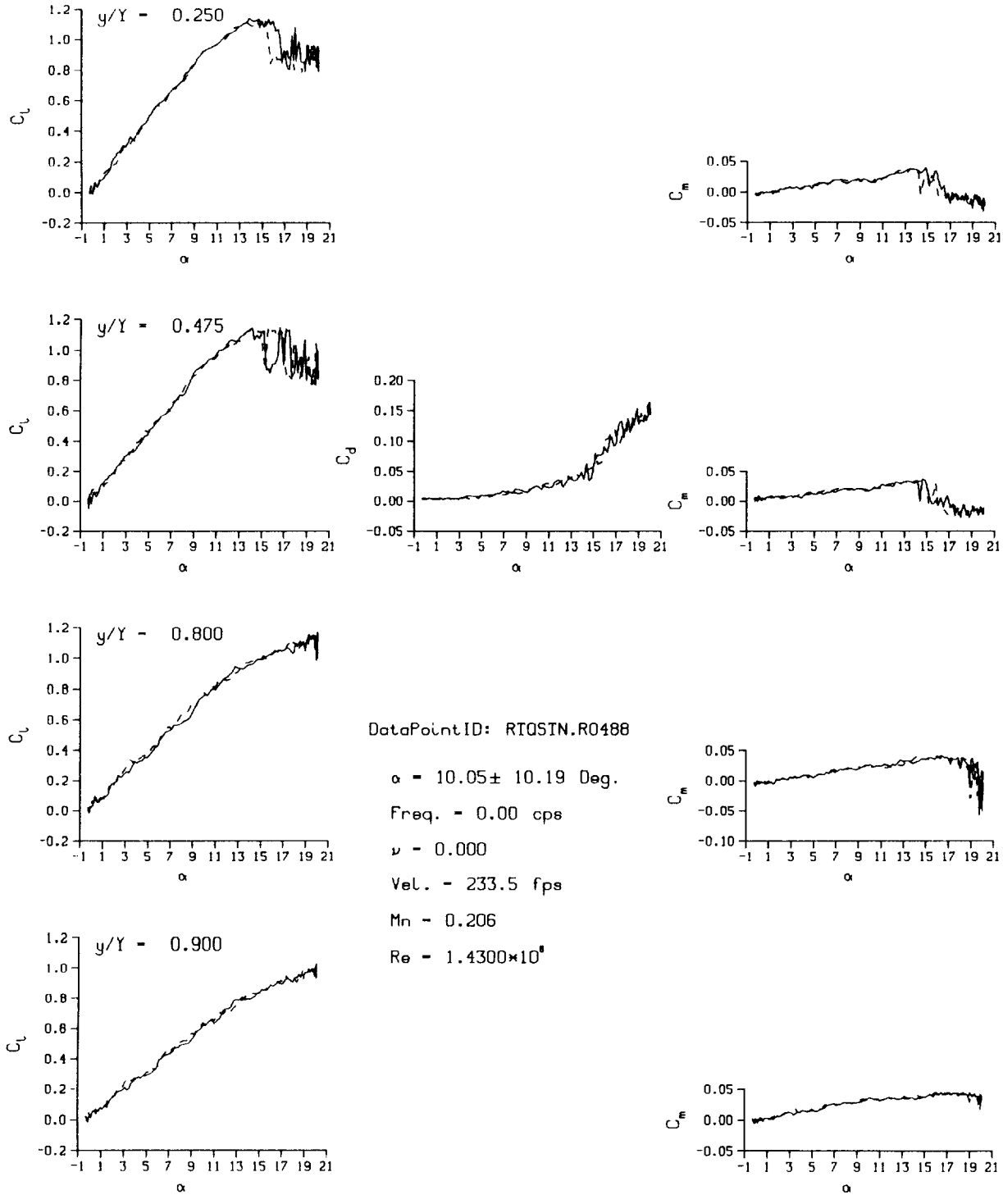

(c) Repeat no. 3

Figure 97. Continued.

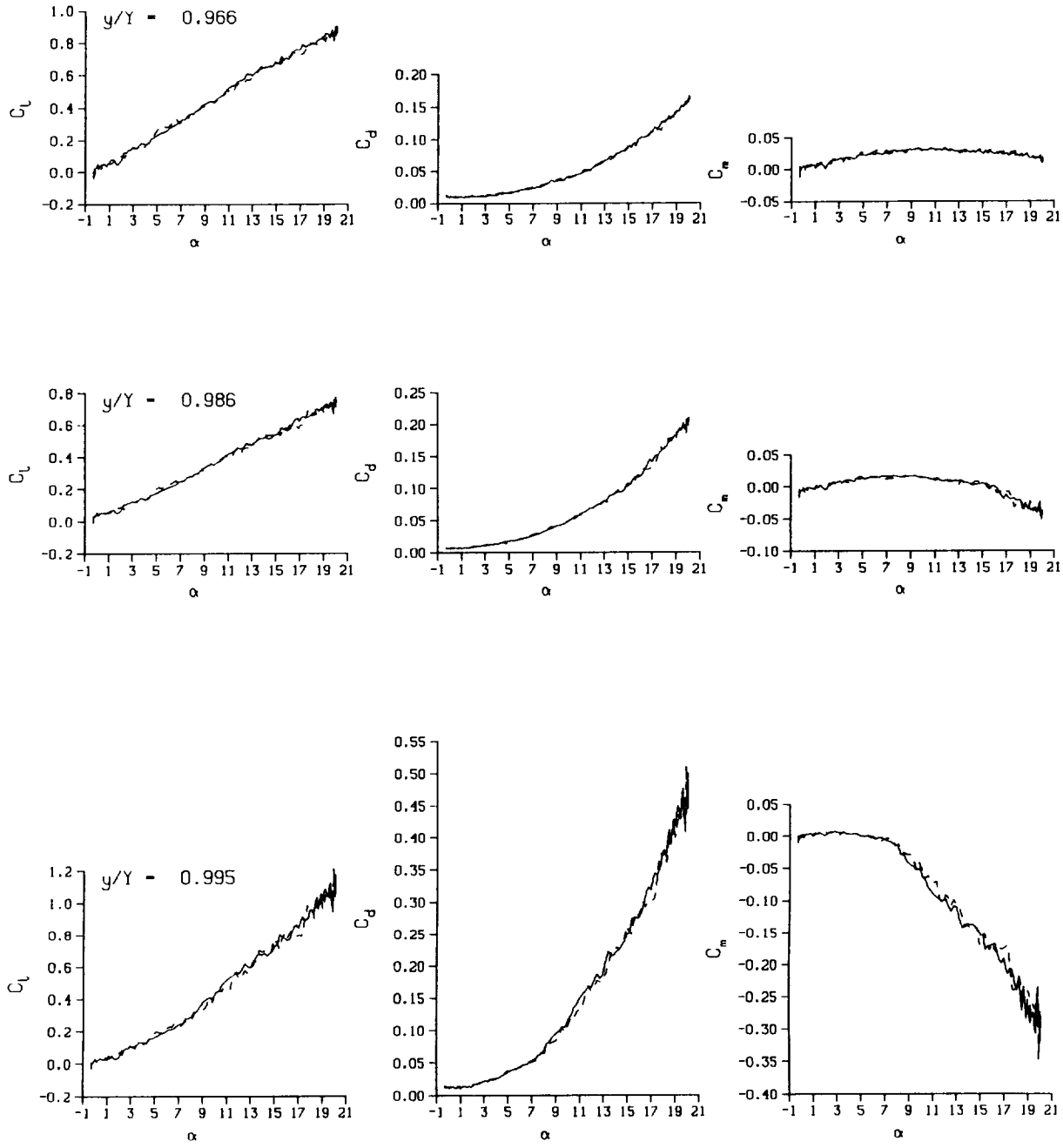

(c) Repeat no. 3. Concluded

Figure 97. Continued.

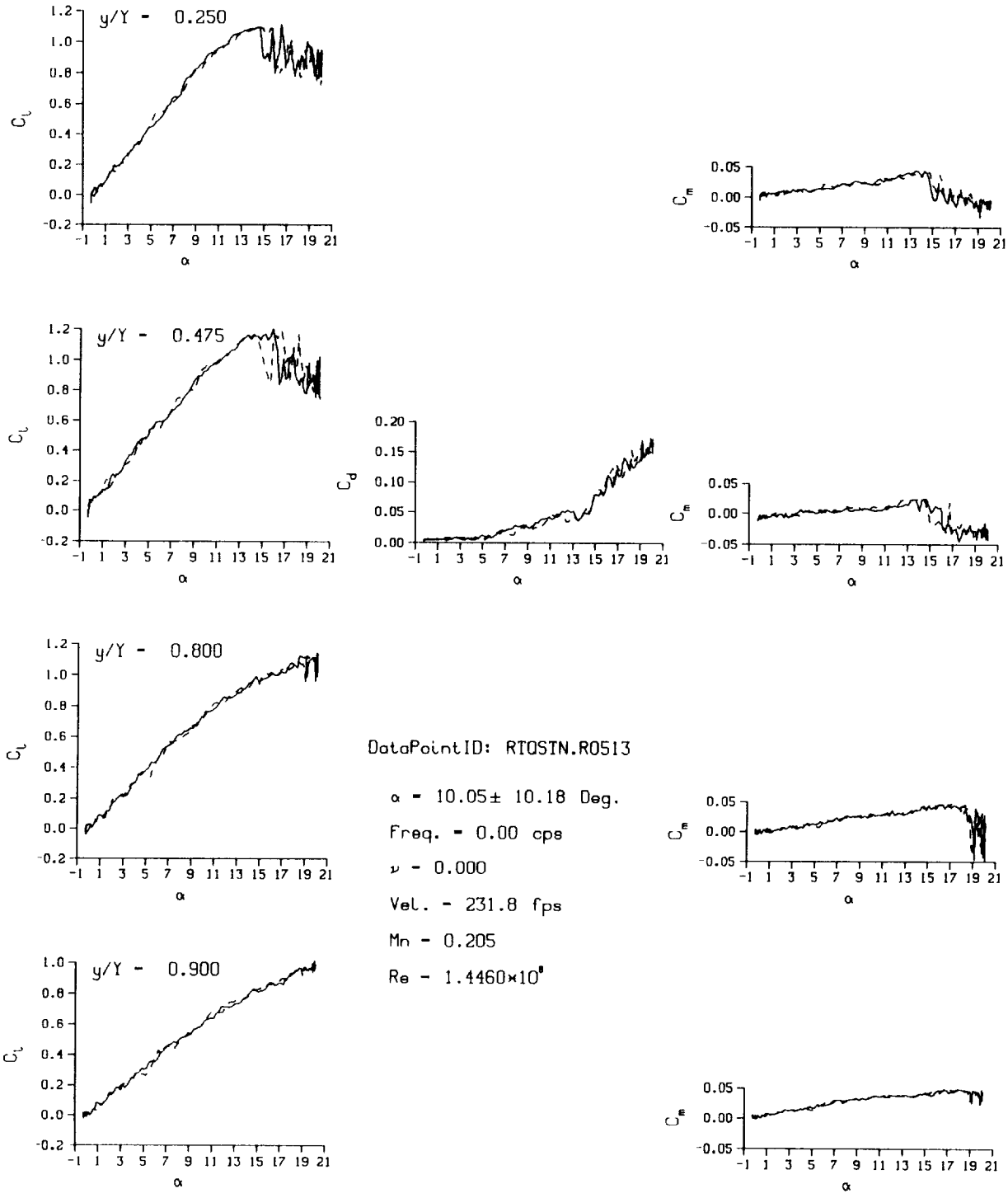

(d) Repeat no. 4

Figure 97. Continued.

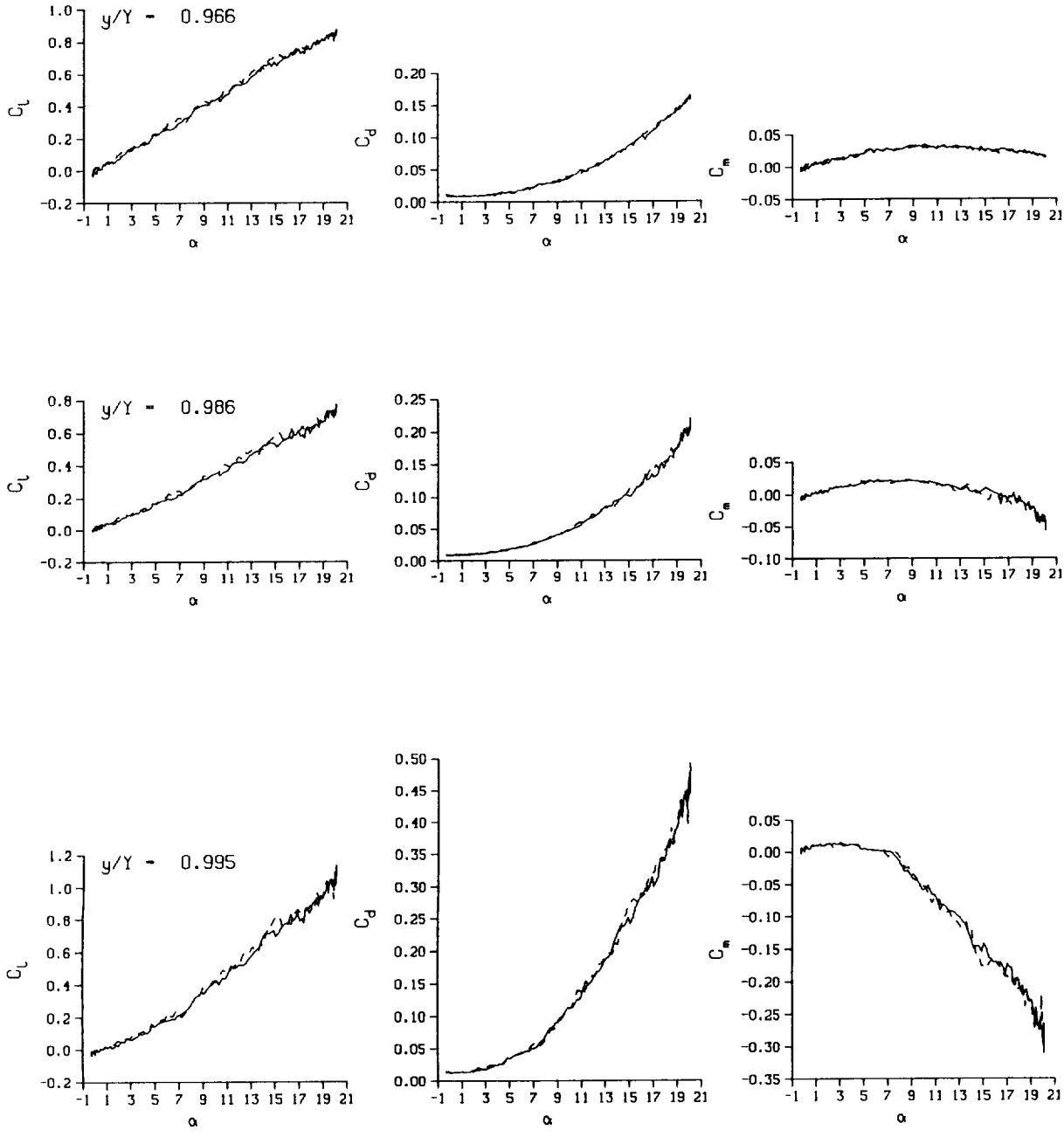

(d) Repeat no. 4. Concluded

Figure 97. Continued.

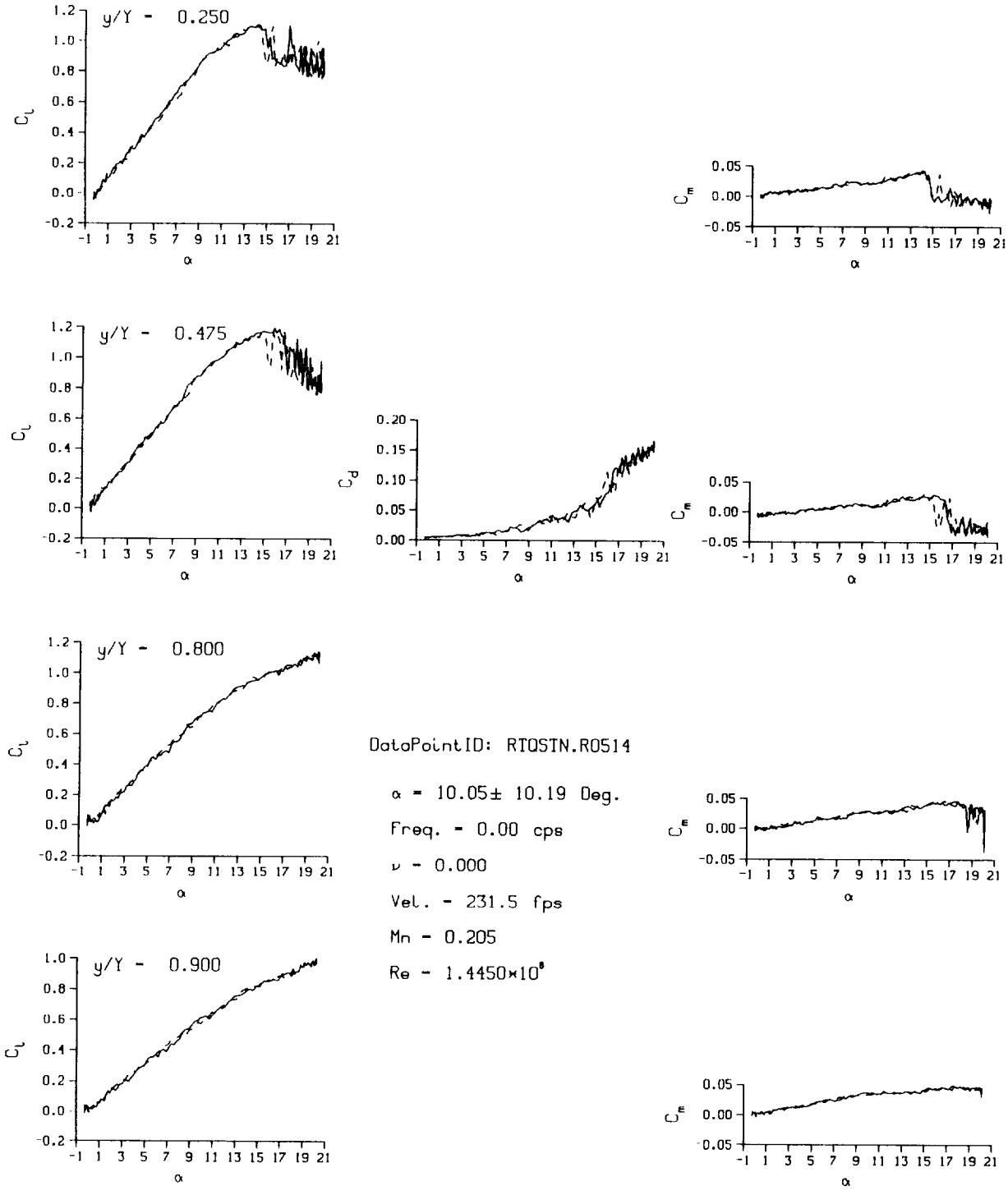

(e) Repeat no. 5

Figure 97. Continued.

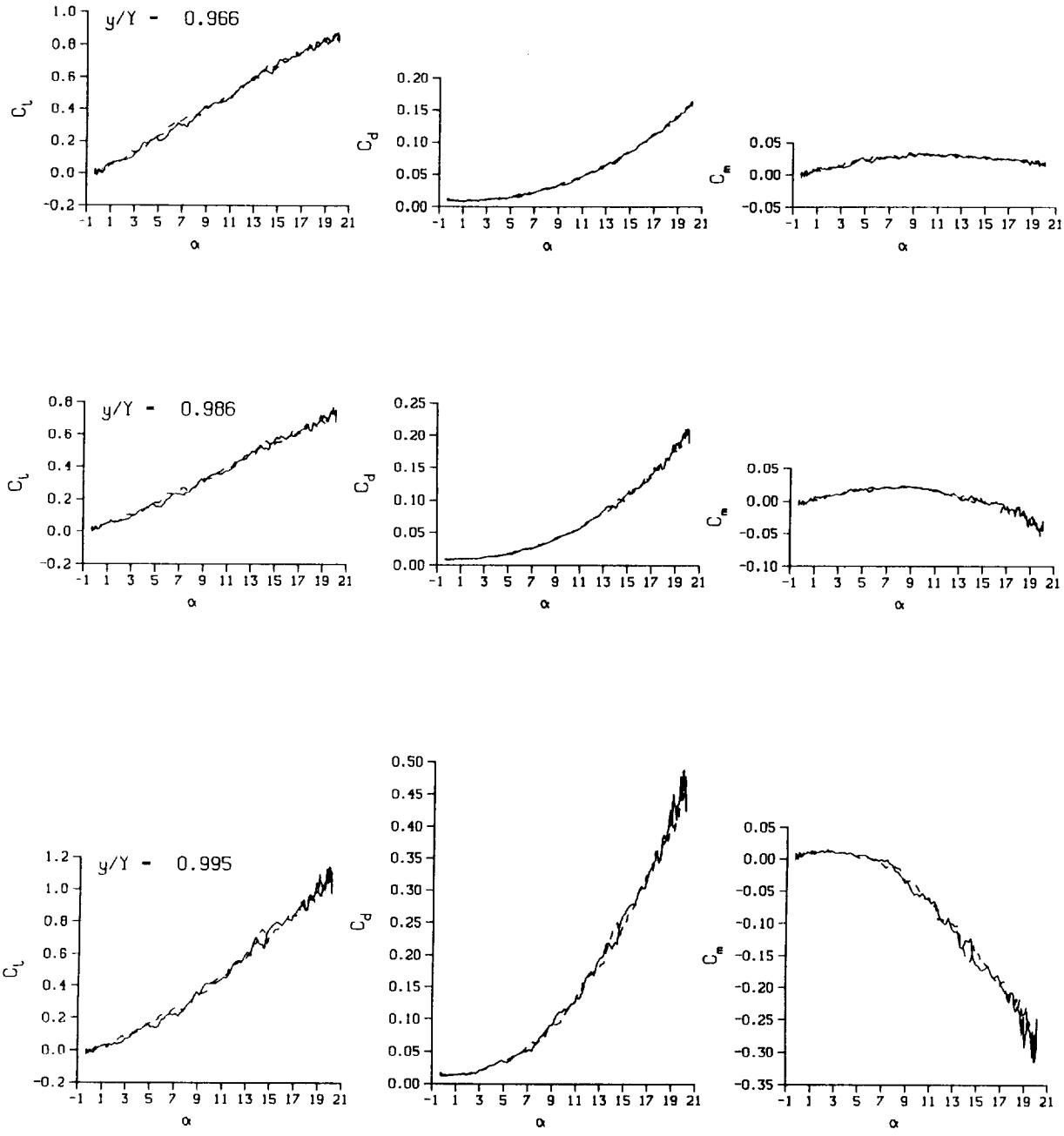

(e) Repeat no. 5. Concluded

Figure 97. Concluded.

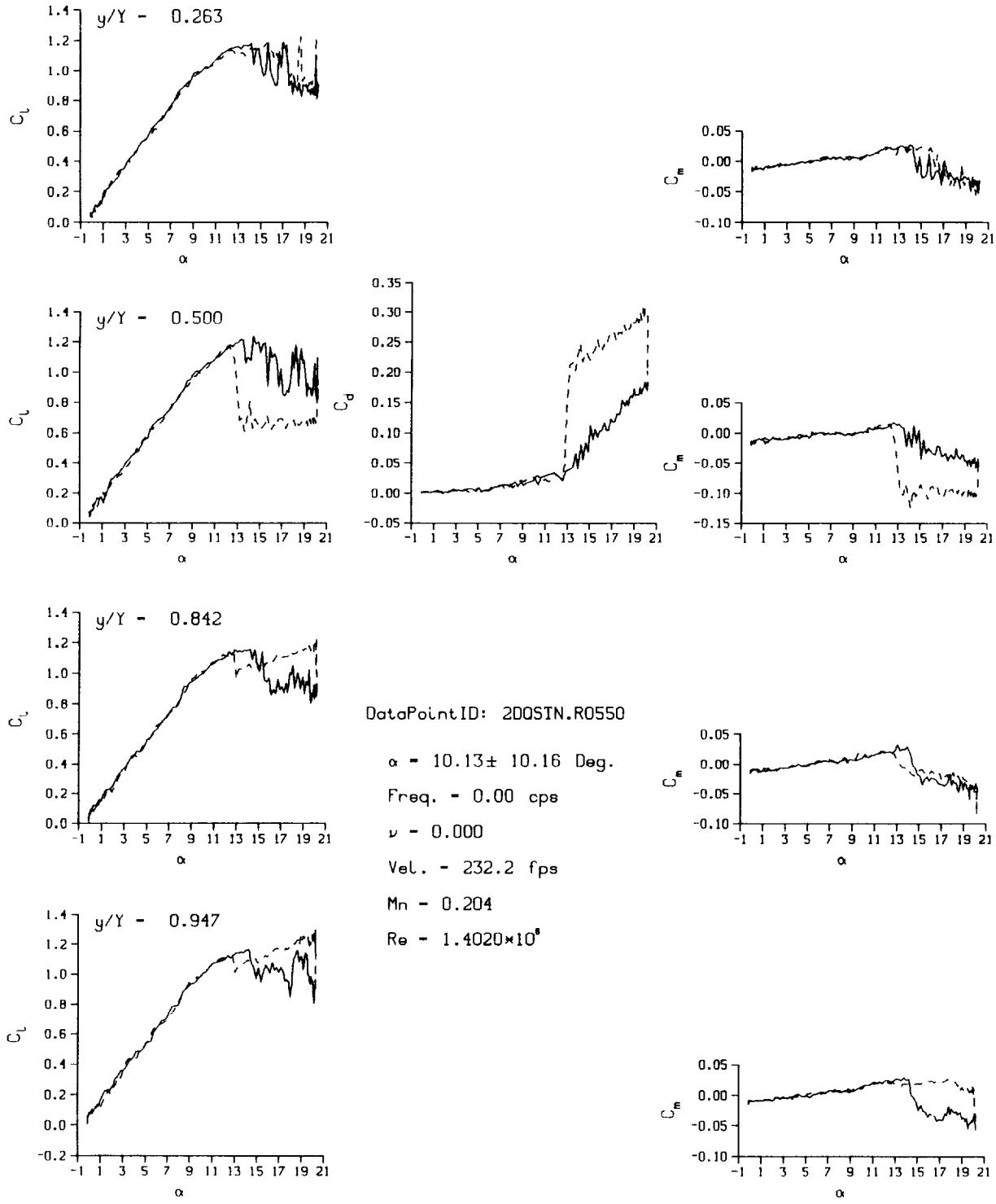

(a) Repeat no. 1

Figure 98. 2-D quasi-steady data; no BL-trip; q = 60.

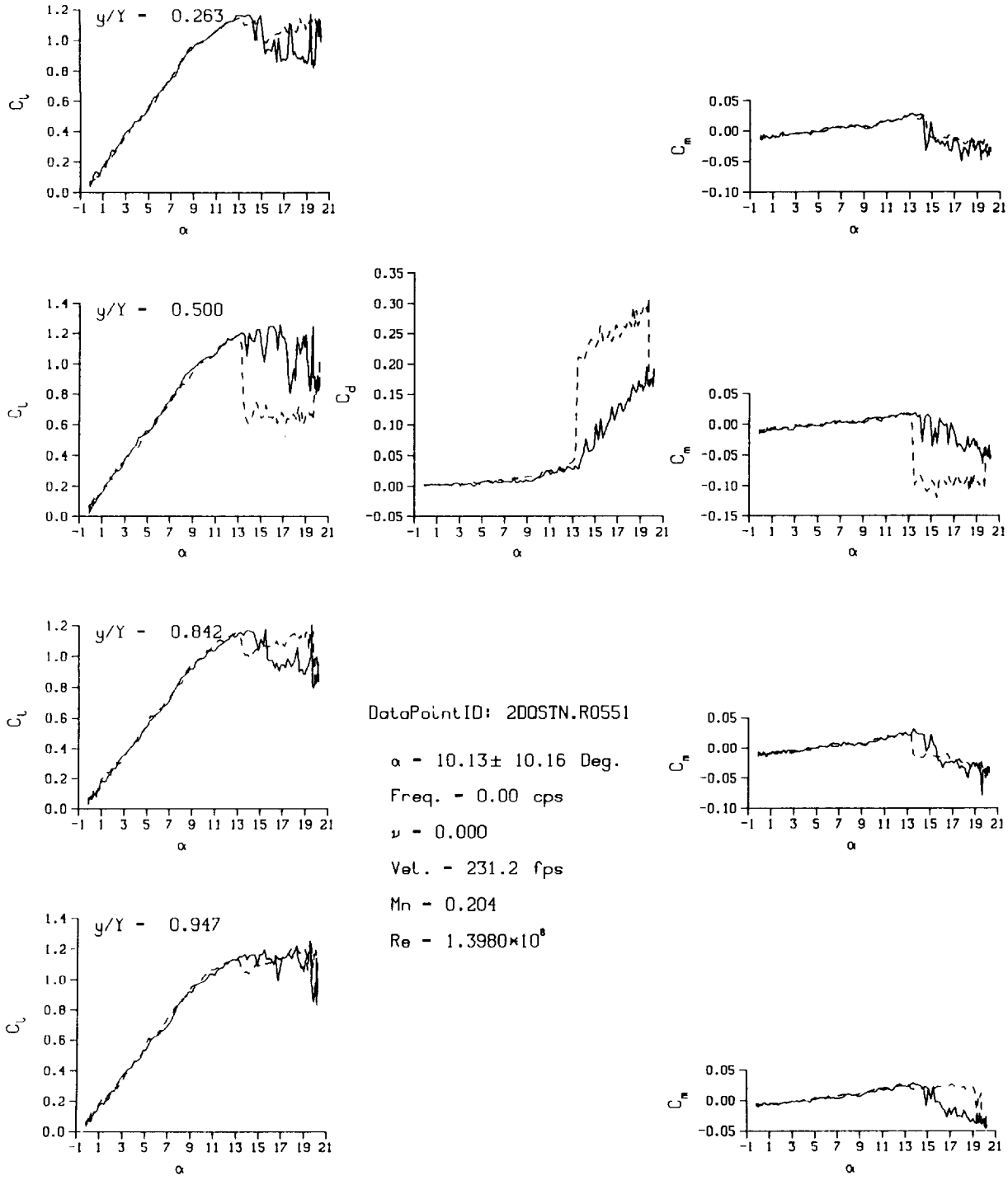

(b) Repeat no. 2

Figure 98. Continued.

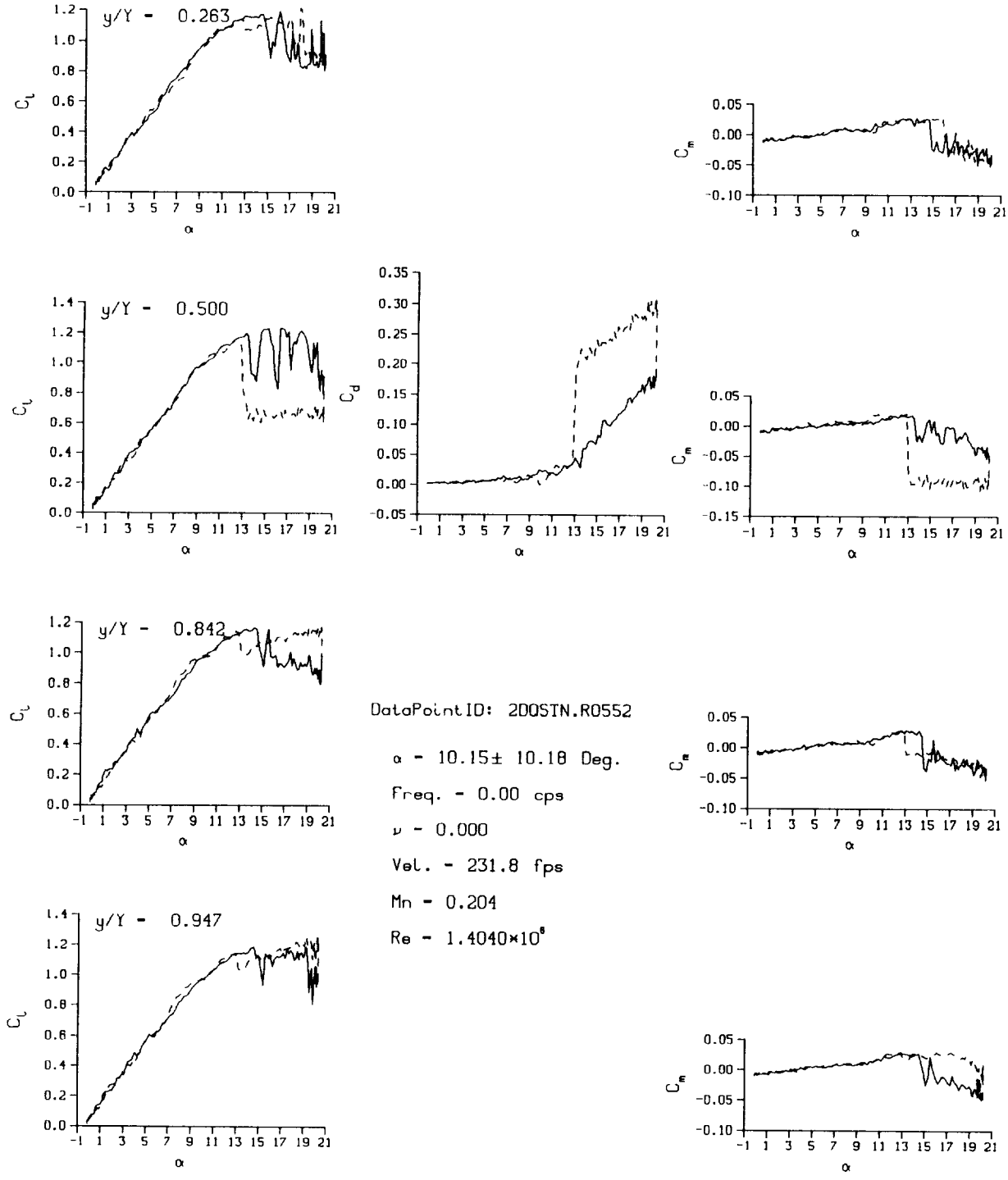

(c) Repeat no. 3

Figure 98. Continued.

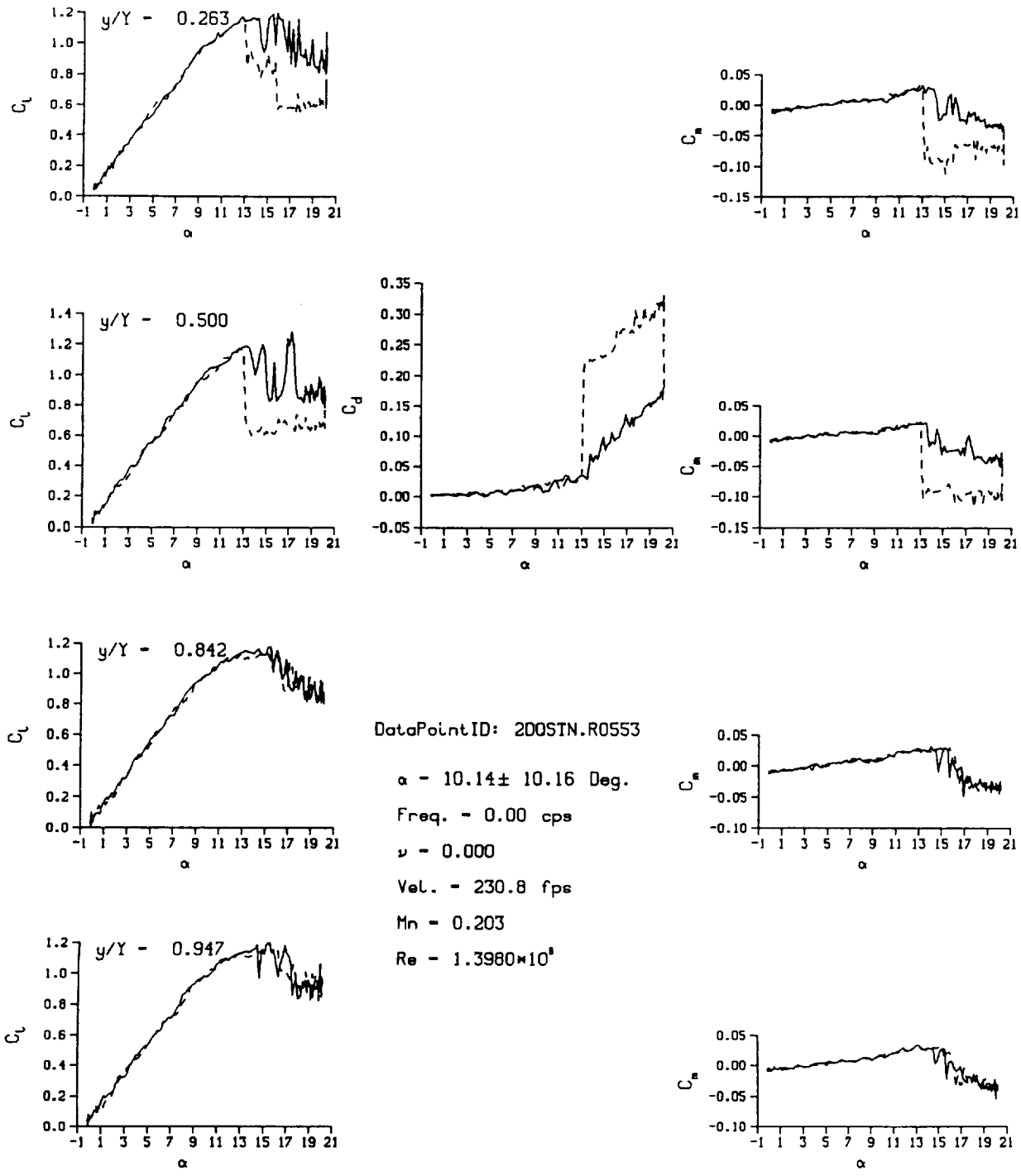

(d) Repeat no. 4

Figure 98. Concluded.

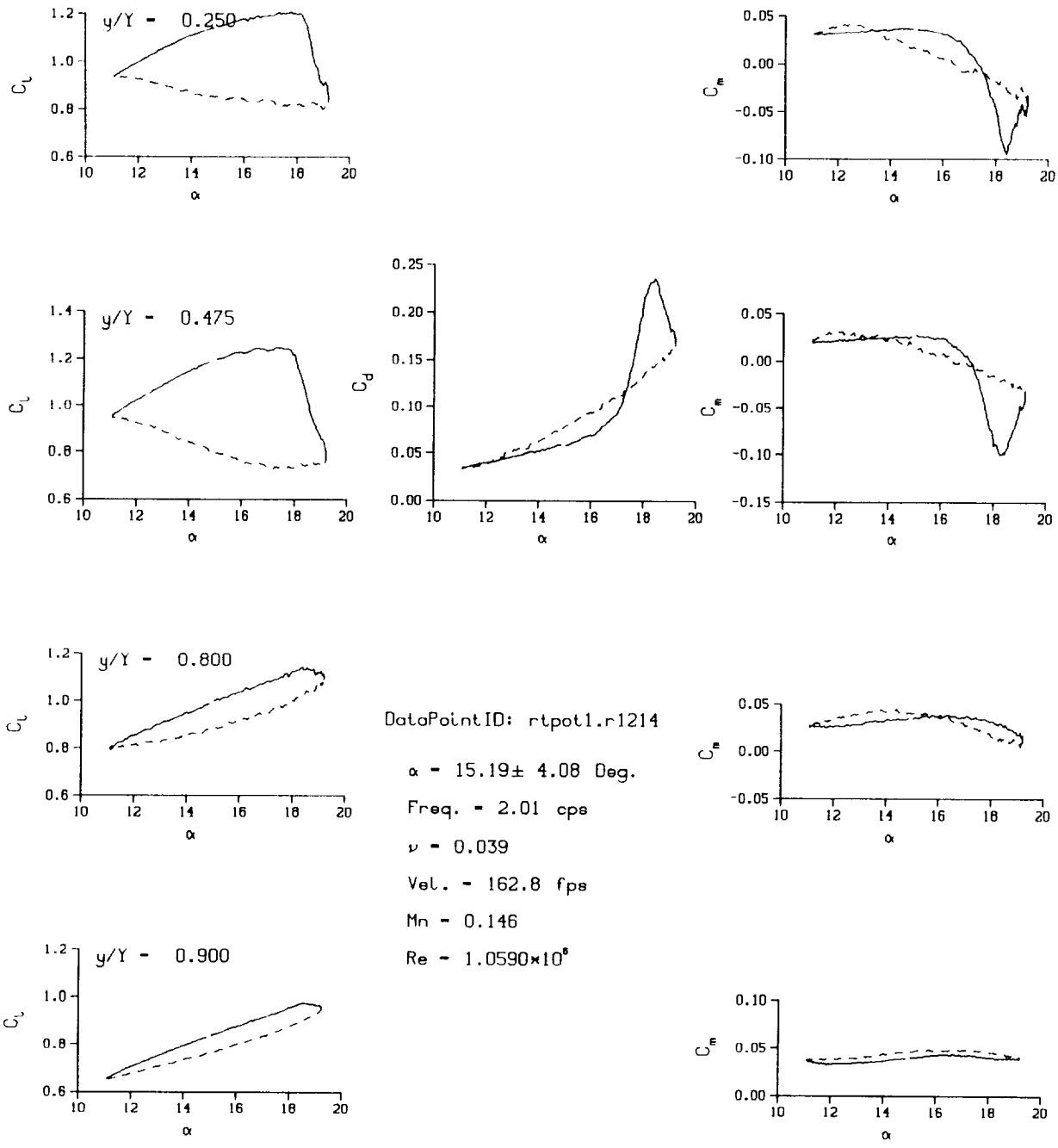

(a) ν = 0.039

Figure 99. 3-D round tip pitch oscillation data for surface flow visualization at q = 30; BL-trip; α = 15 ± 4 deg.

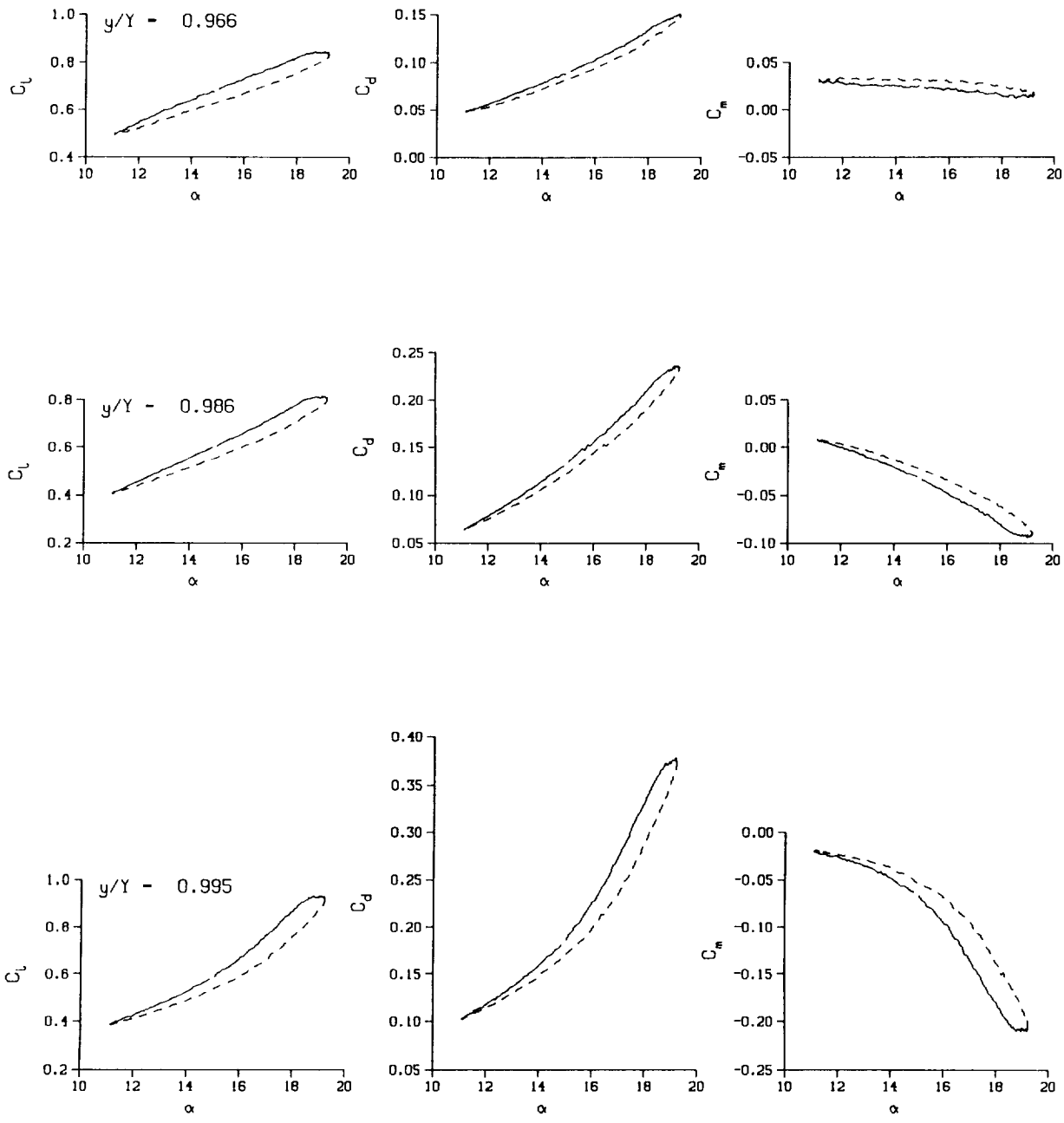

(a) v = 0.039. Concluded

Figure 99. Continued.

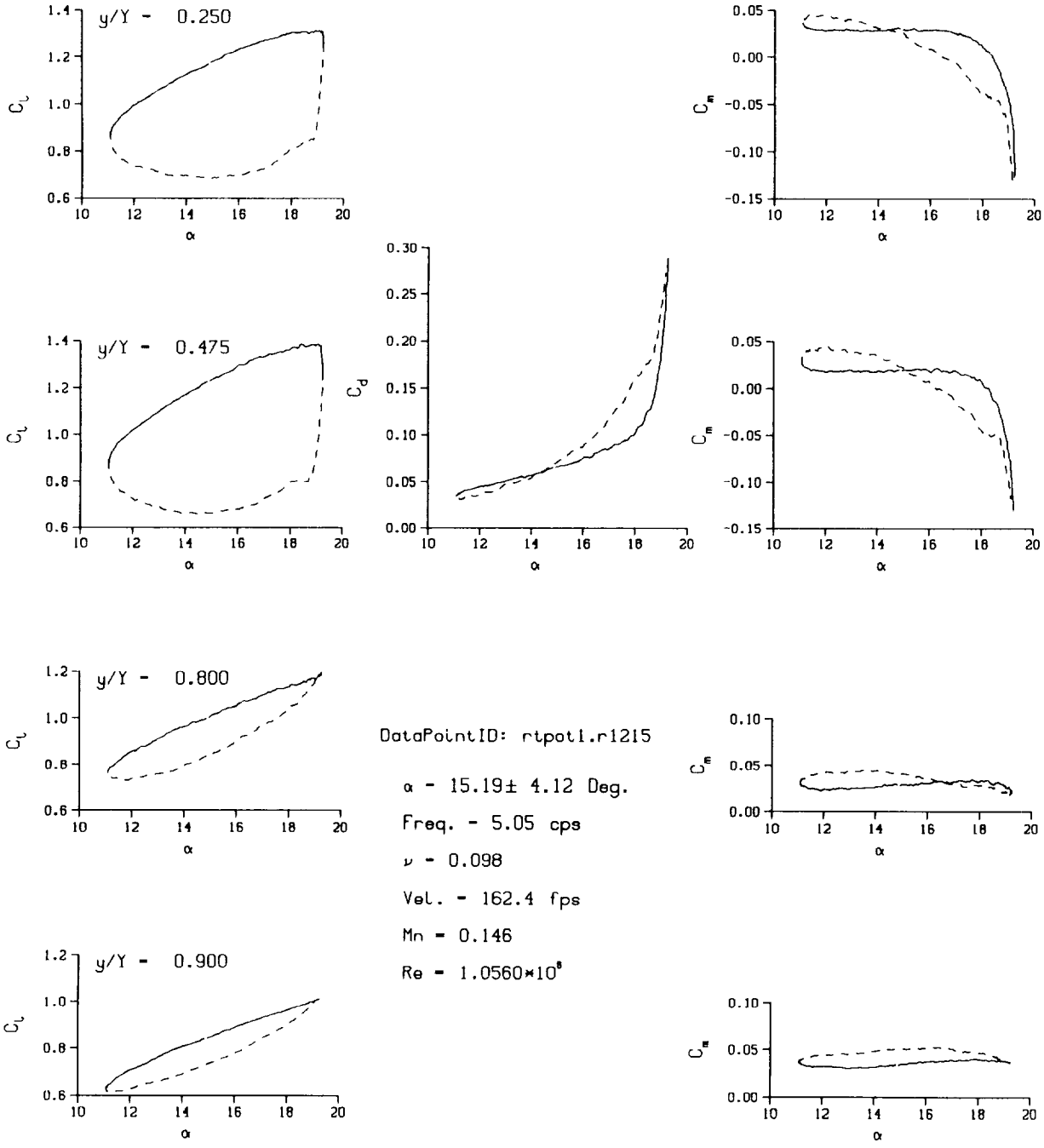

(b) v = 0.098

Figure 99. Continued.

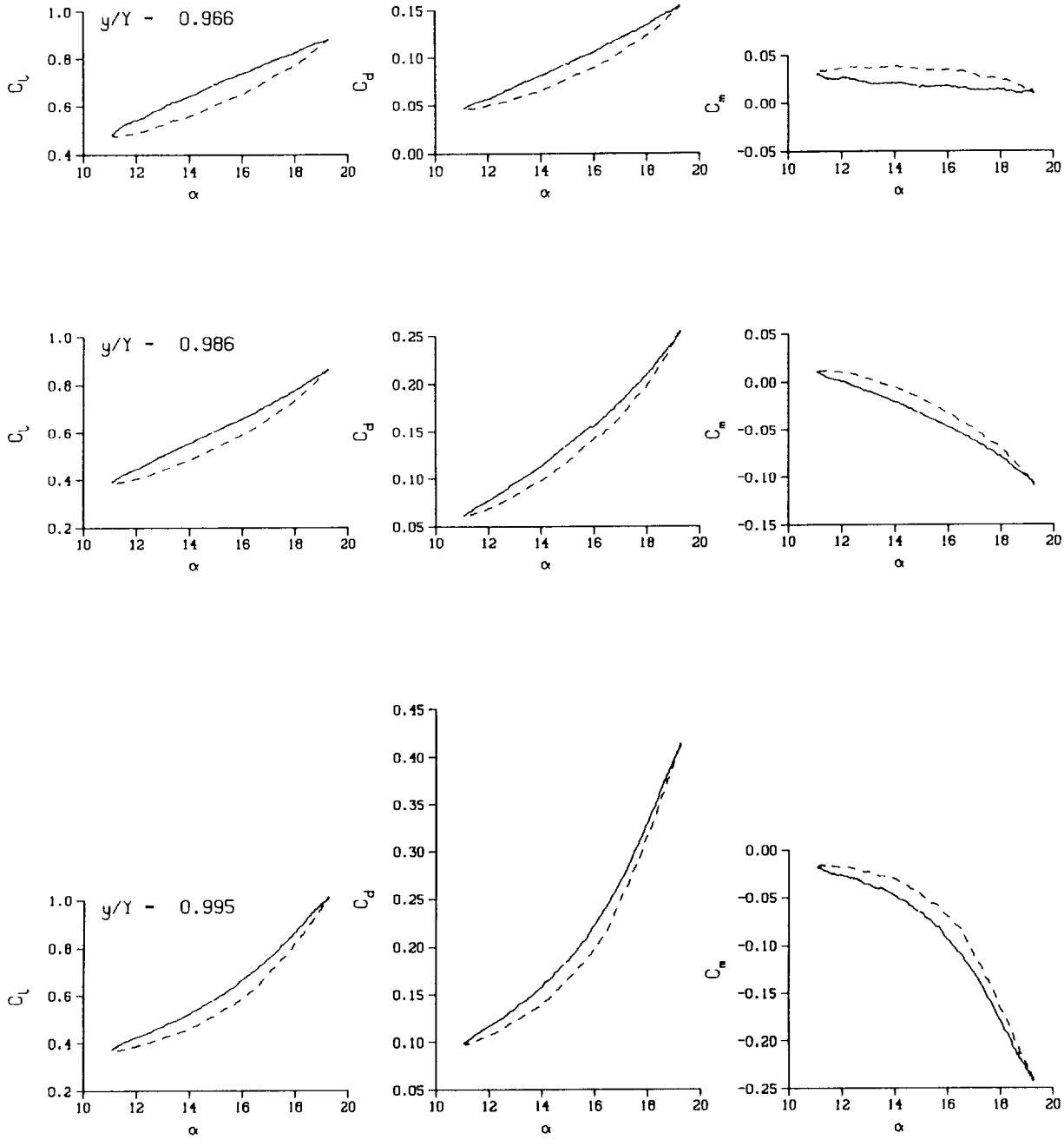

(b) v = 0.098. Concluded

Figure 99. Continued.

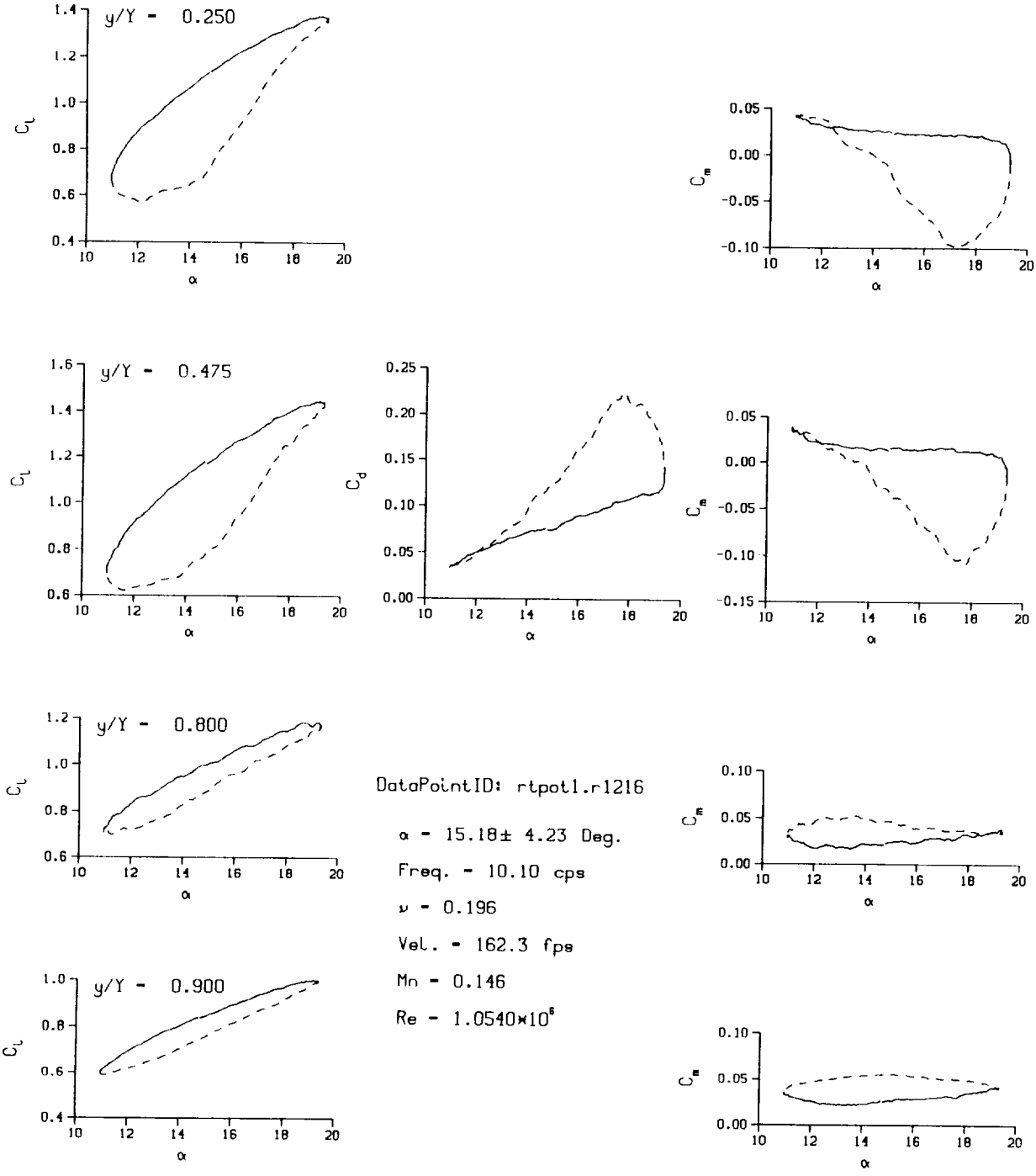

(c) ν = 0.196

Figure 99. Continued.

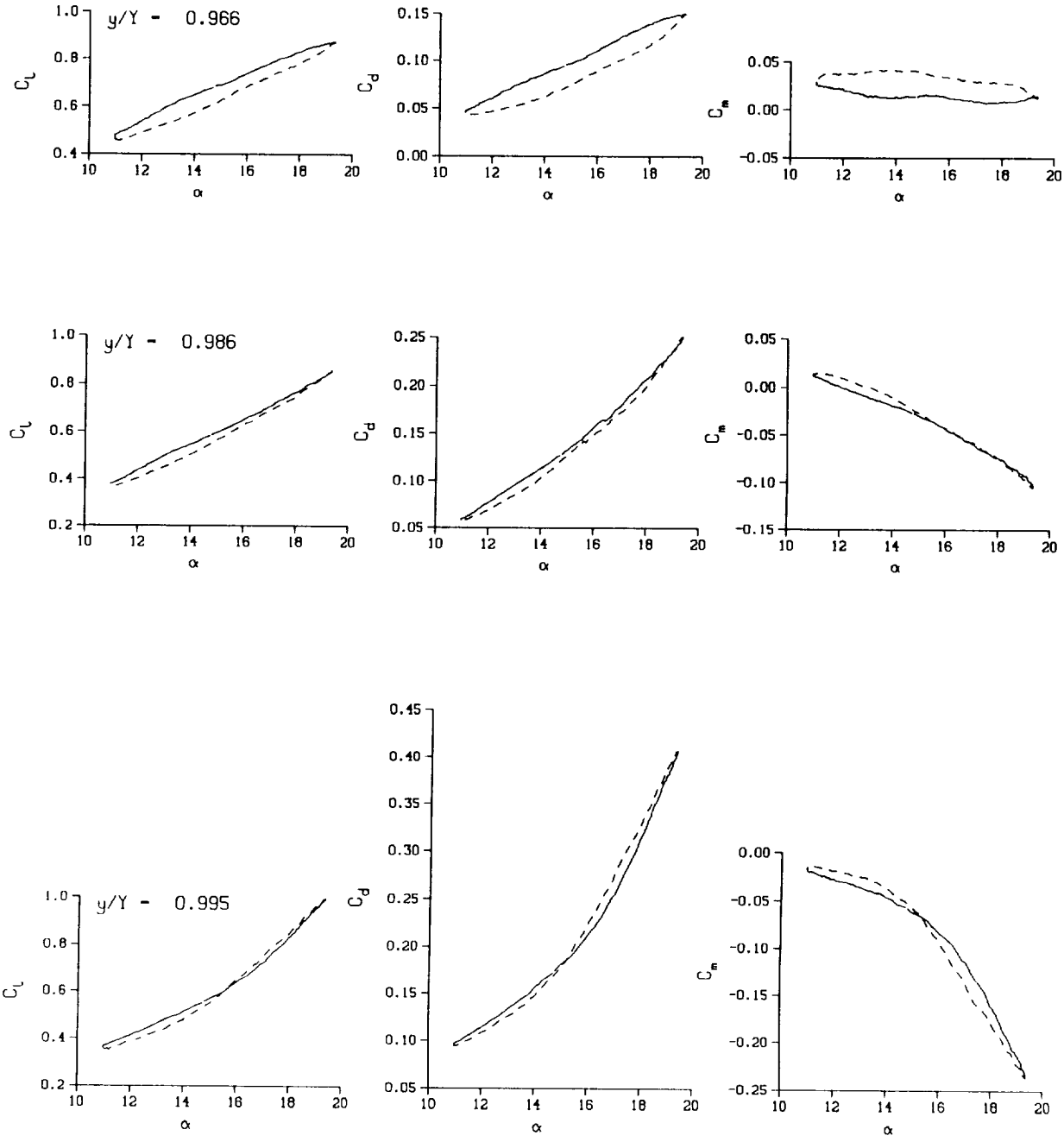

(c) v = 0.196. Concluded

Figure 99. Concluded.

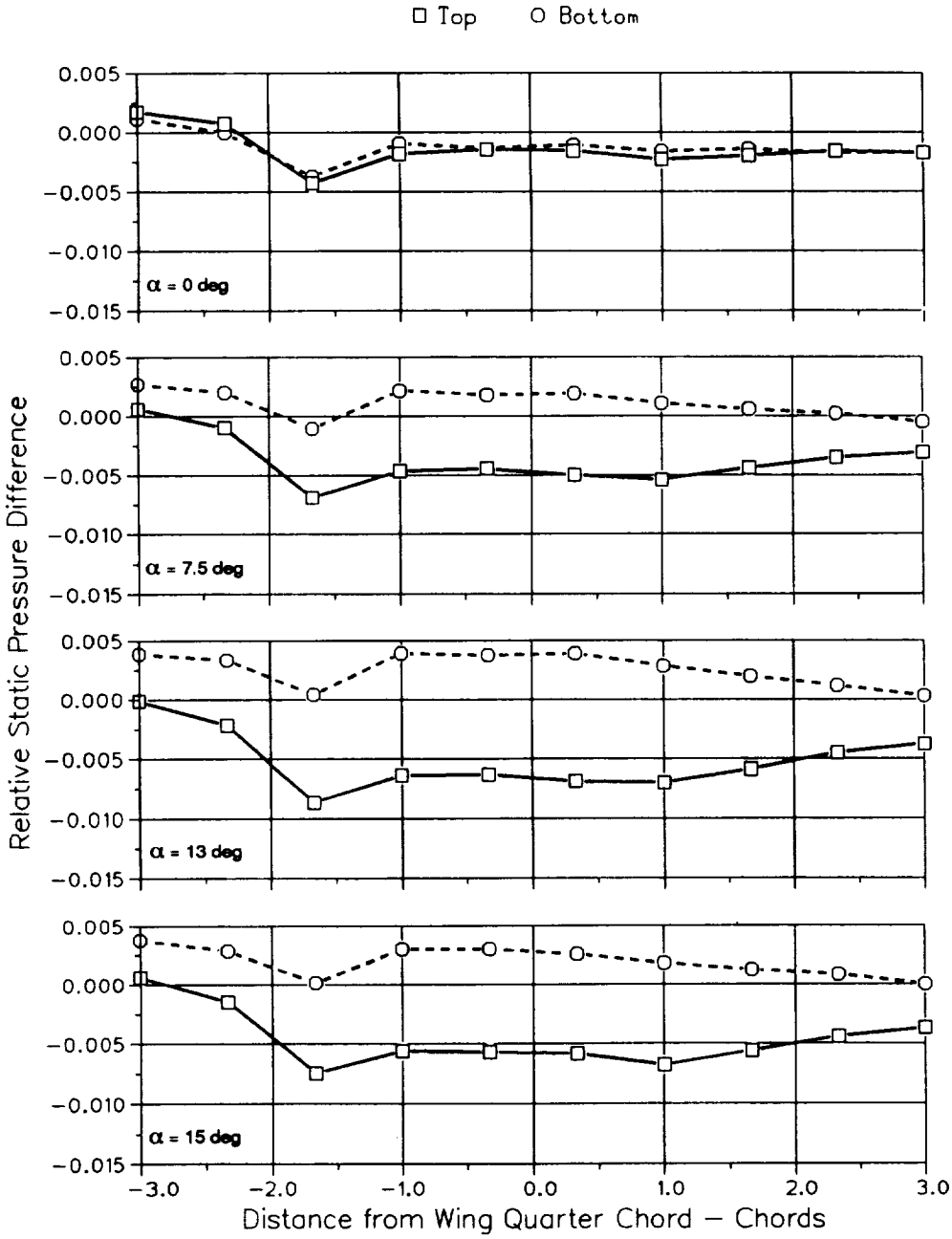

(a) Top and bottom boundary values

Figure 100. Static pressure survey; 2-D configuration.

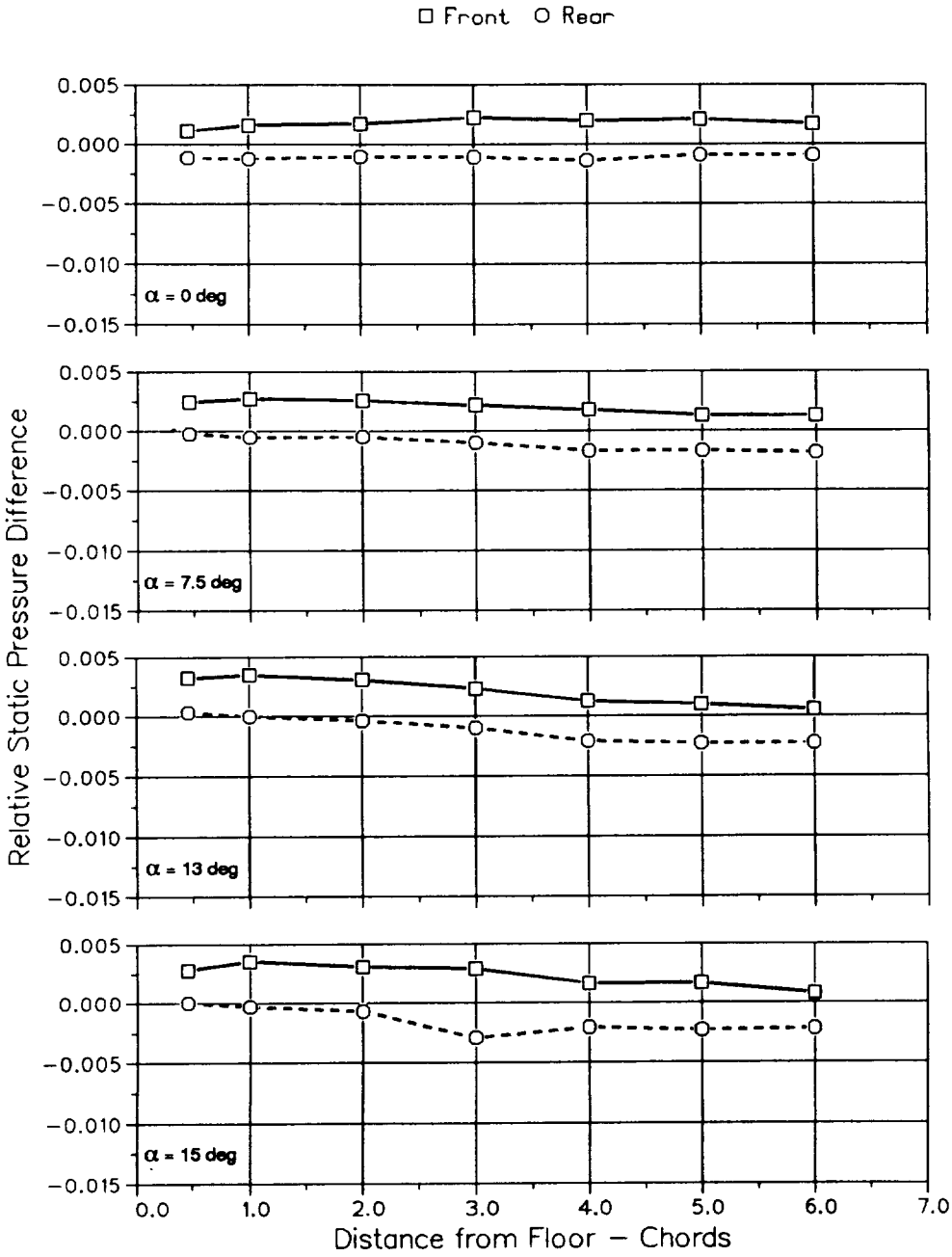

(b) Fore and aft boundary values

Figure 100. Concluded.

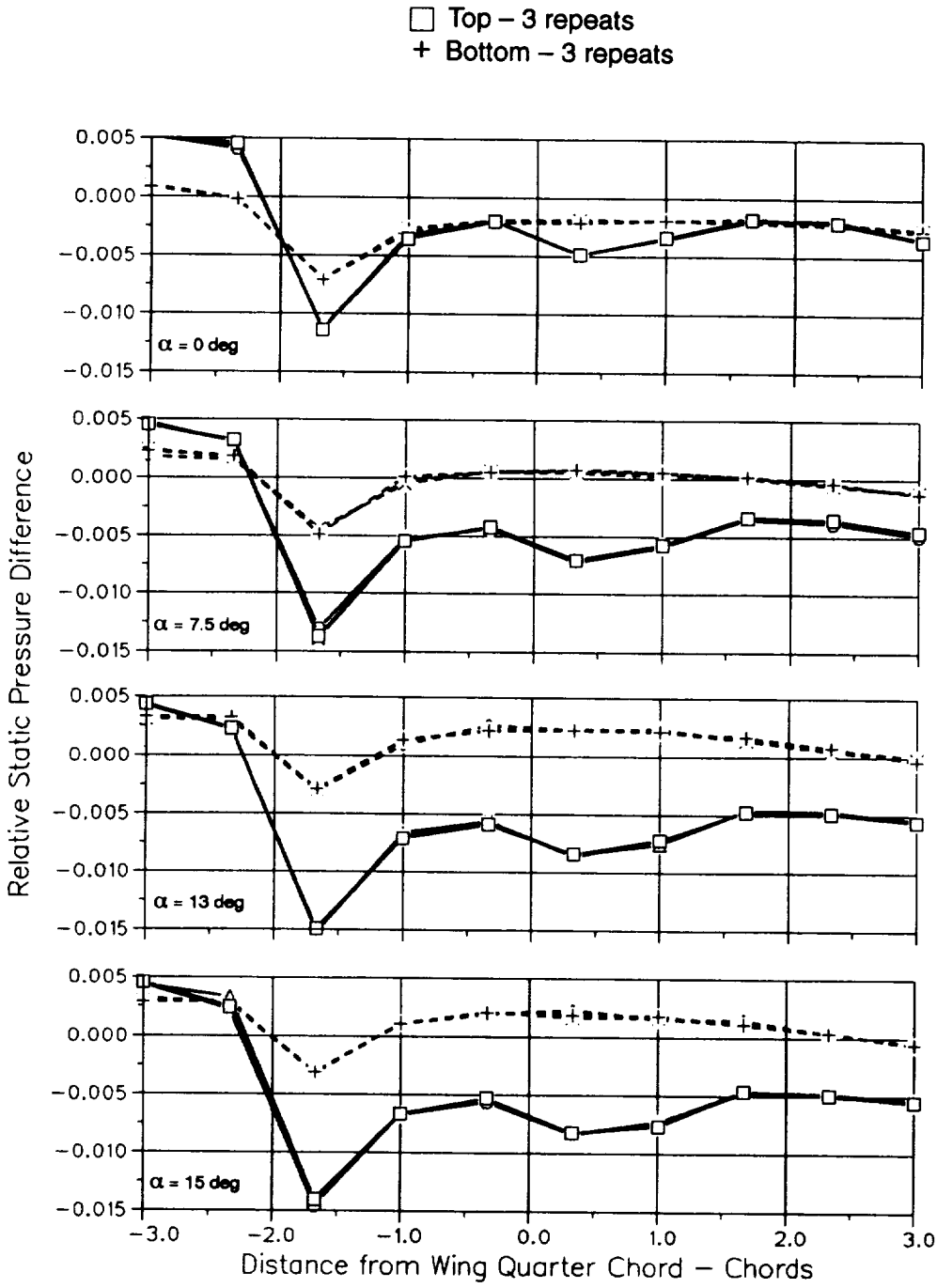

(a) Top and bottom boundary values

Figure 101. Static pressure survey; 3-D configuration; $\bar{y}$ = 0.075.

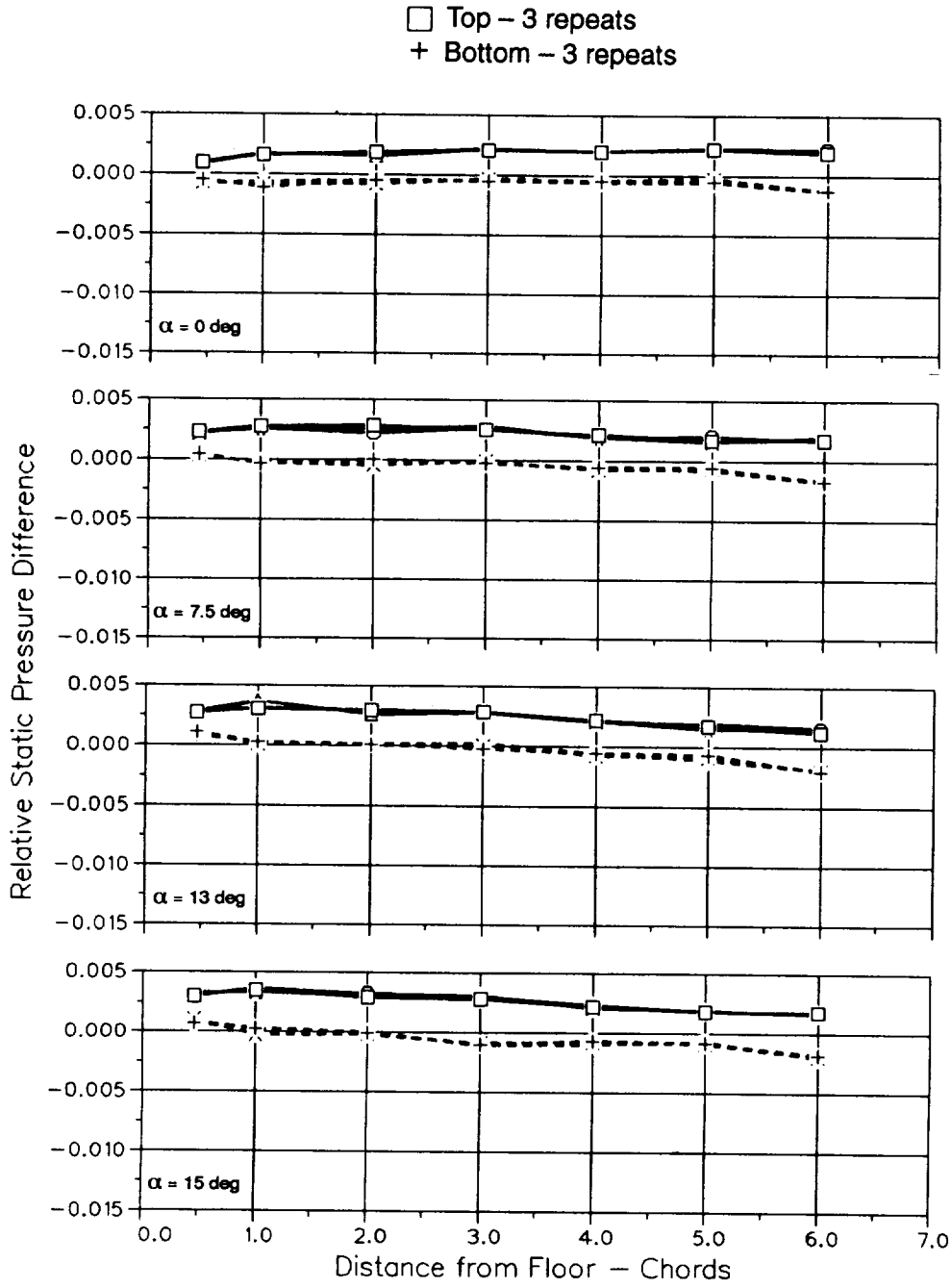

(b) Fore and aft boundary values

Figure 101. Concluded.

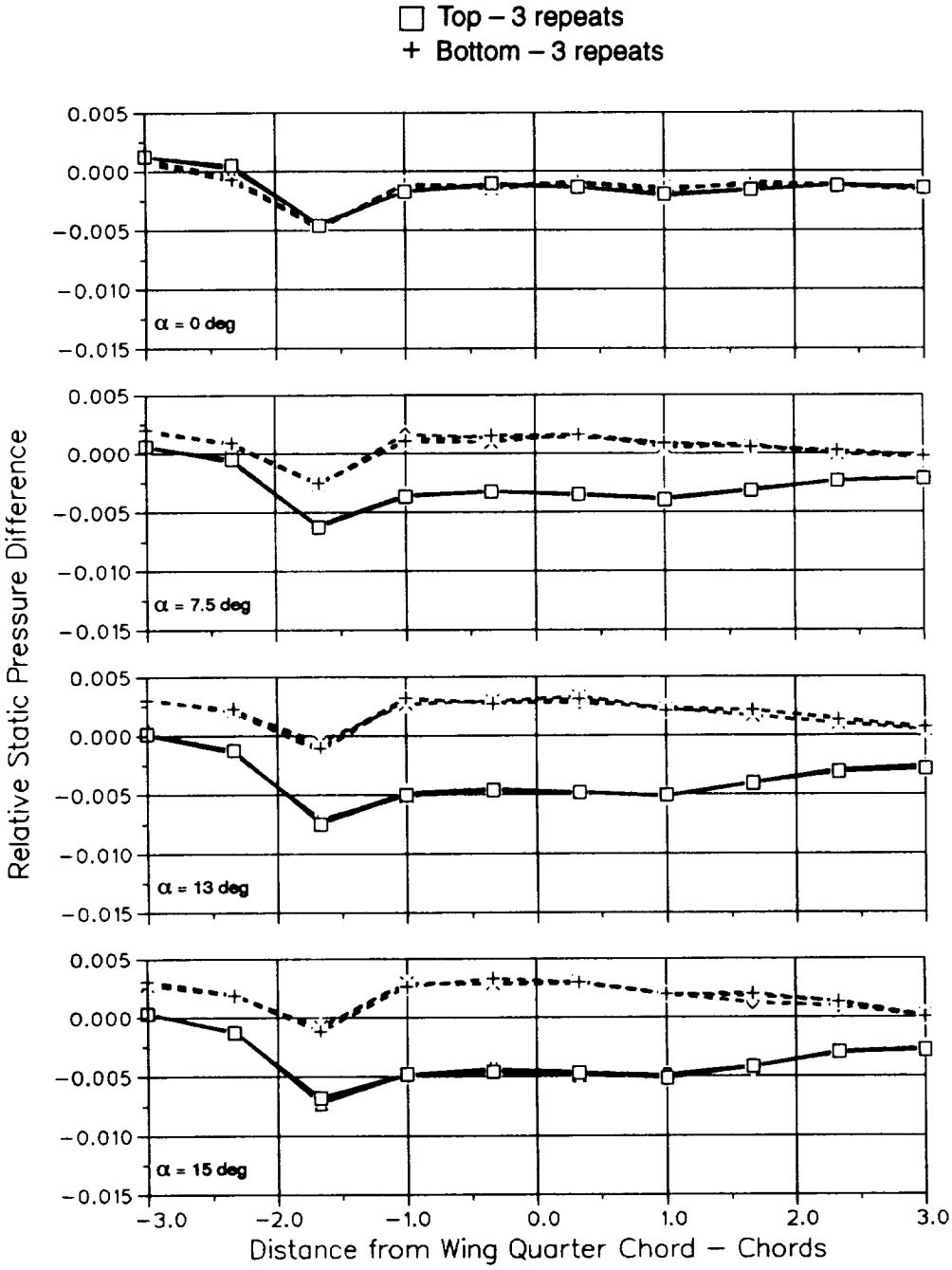

(a) Top and bottom boundary values

Figure 102. Static pressure survey; 3-D configuration; $\bar{y}$ = 0.479.

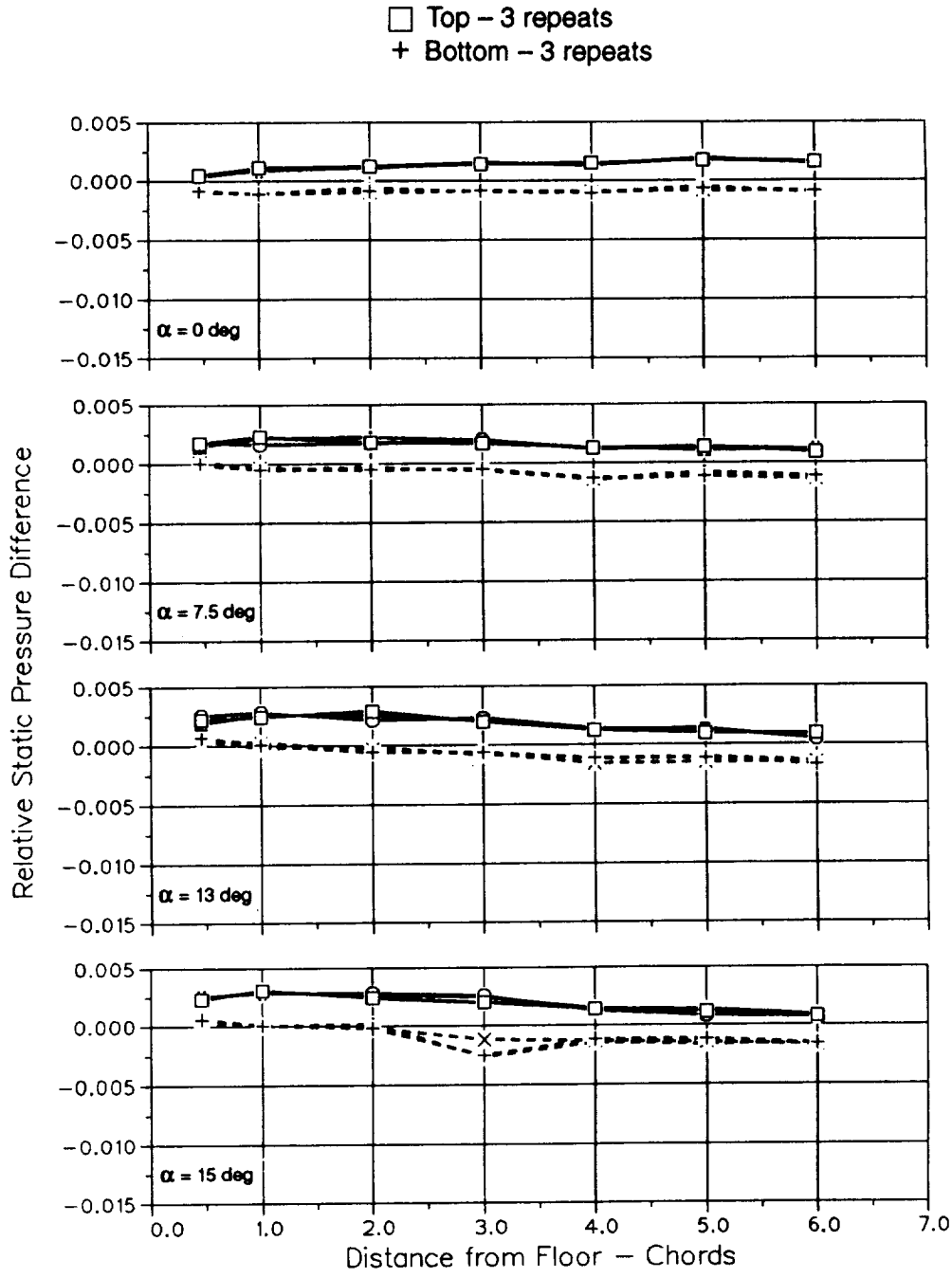

(b) Fore and aft boundary values

Figure 102. Concluded.

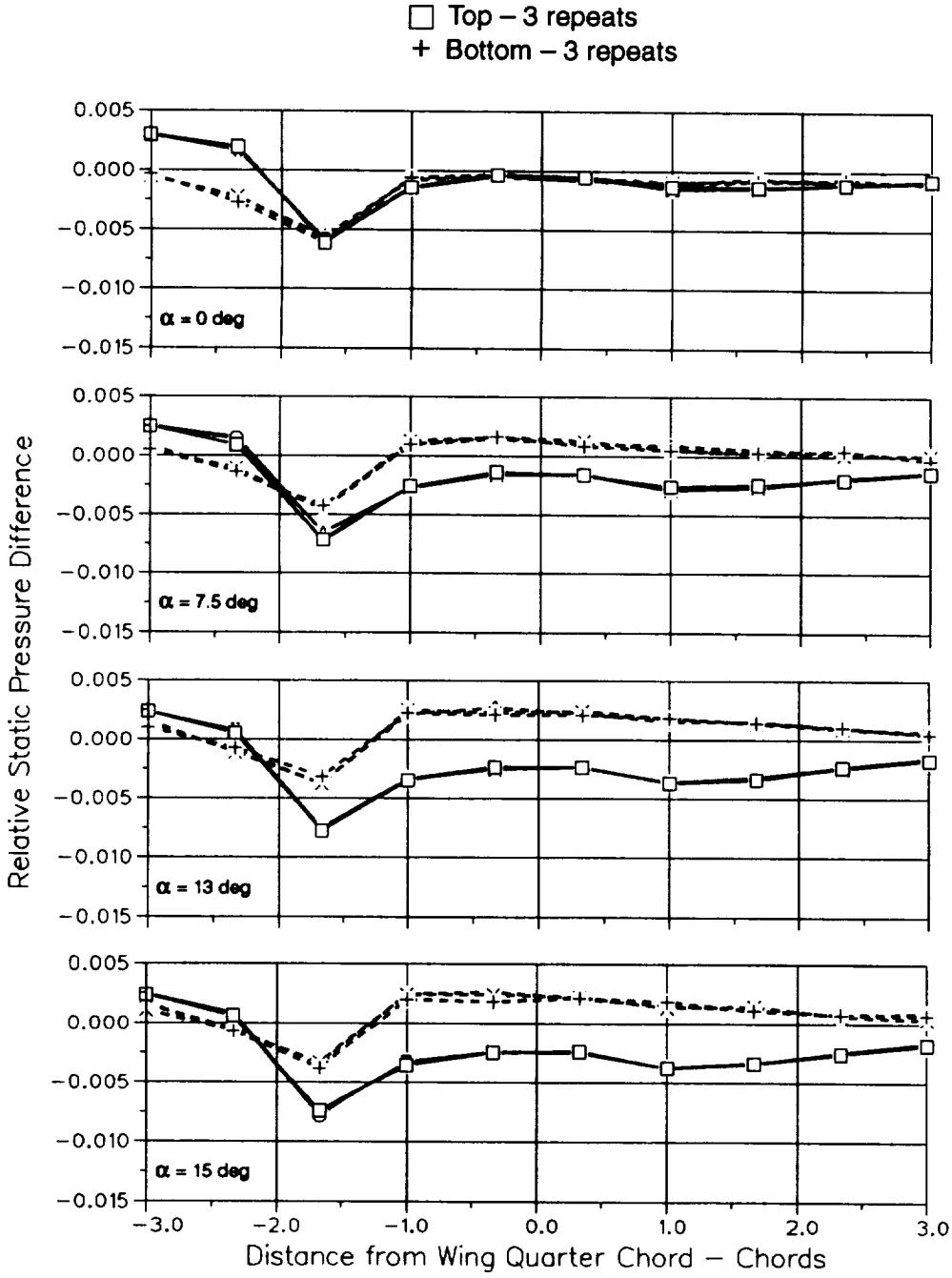

(a) Top and bottom boundary values

Figure 103. Static pressure survey; 3-D configuration; $\bar{y}$ = 0.892.

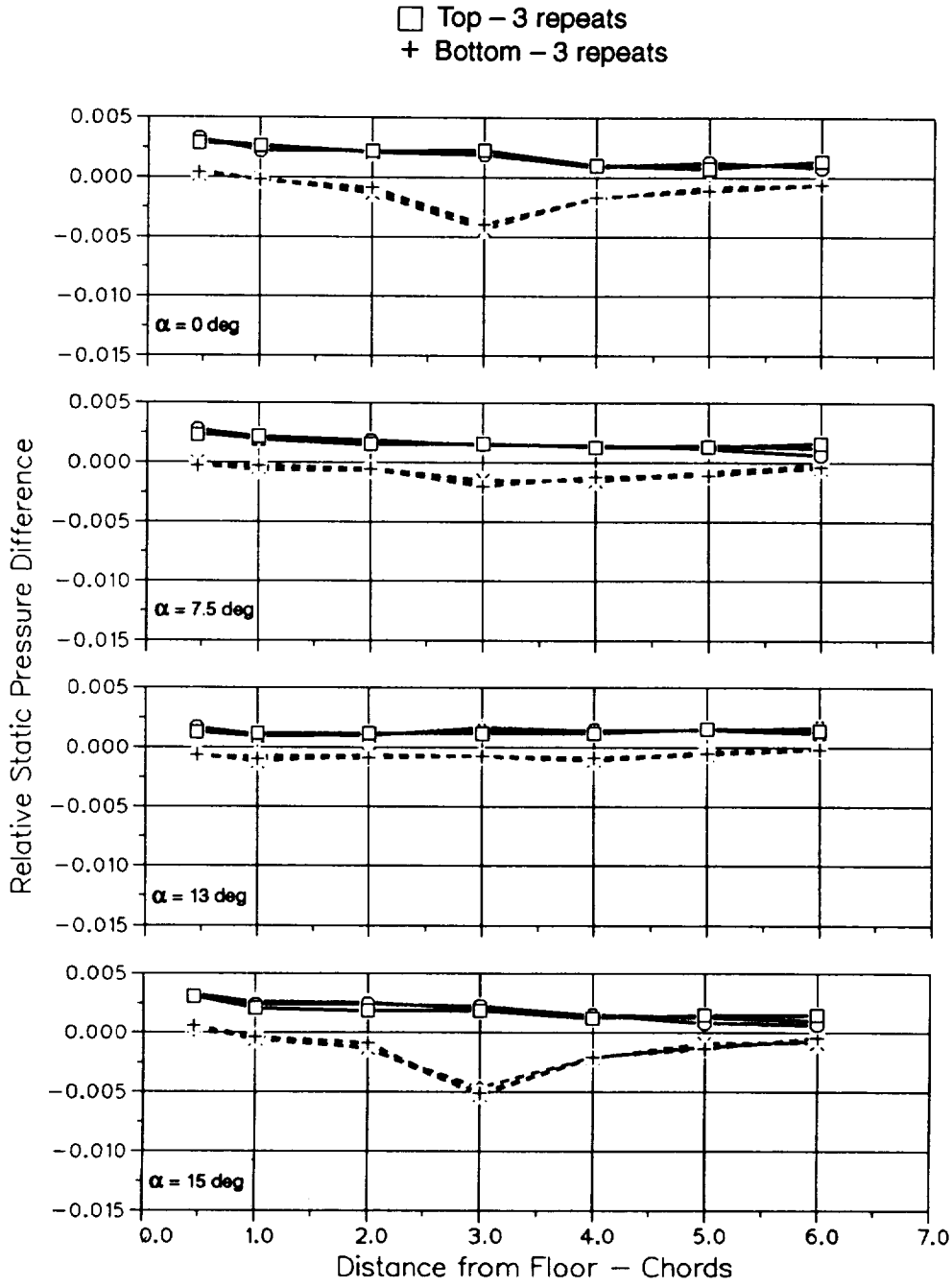

(b) Fore and aft boundary values

Figure 103. Concluded.

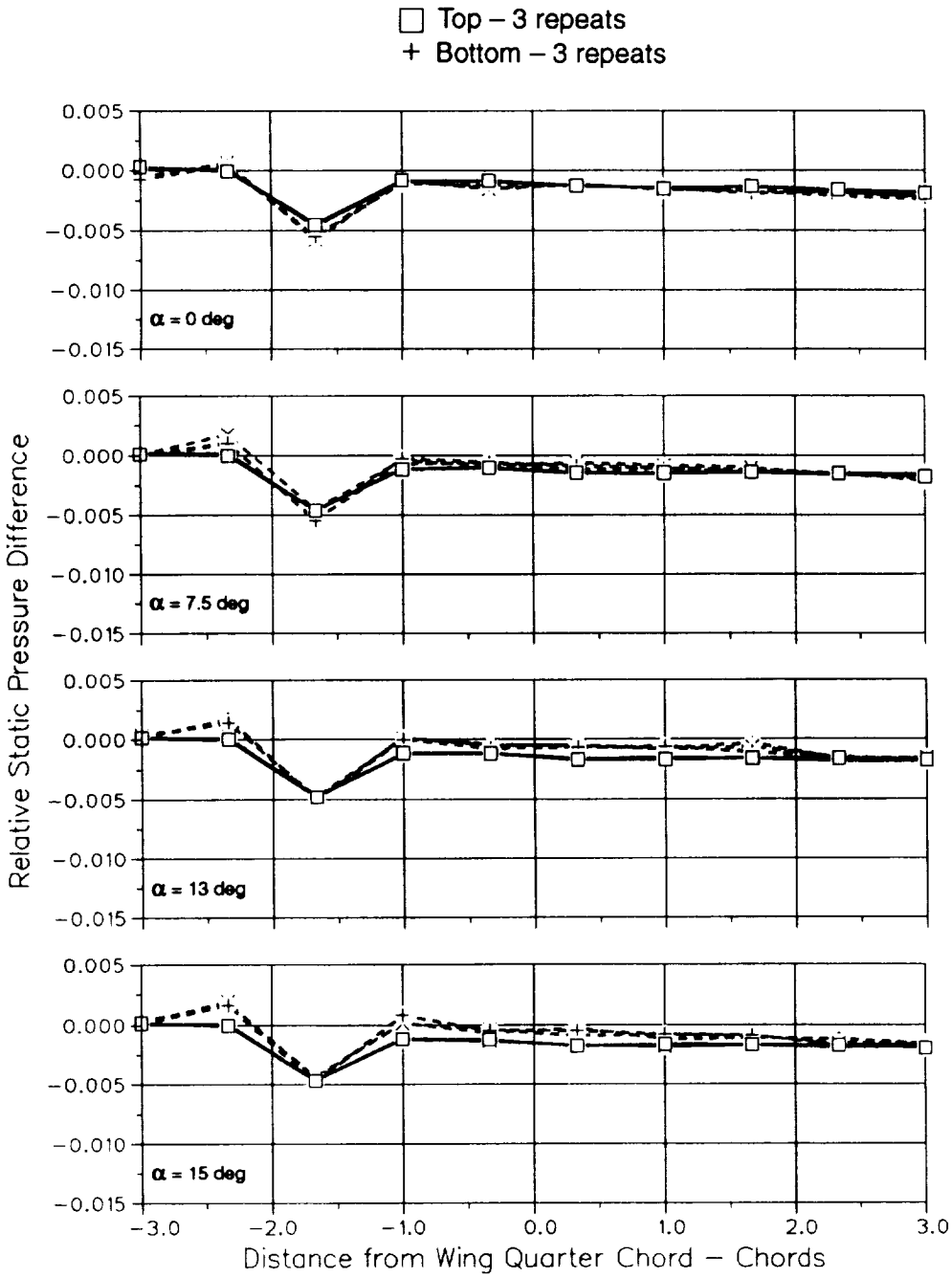

(a) Top and bottom boundary values

Figure 104. Static pressure survey; 3-D configuration; $\bar{y}$ = 1.671.

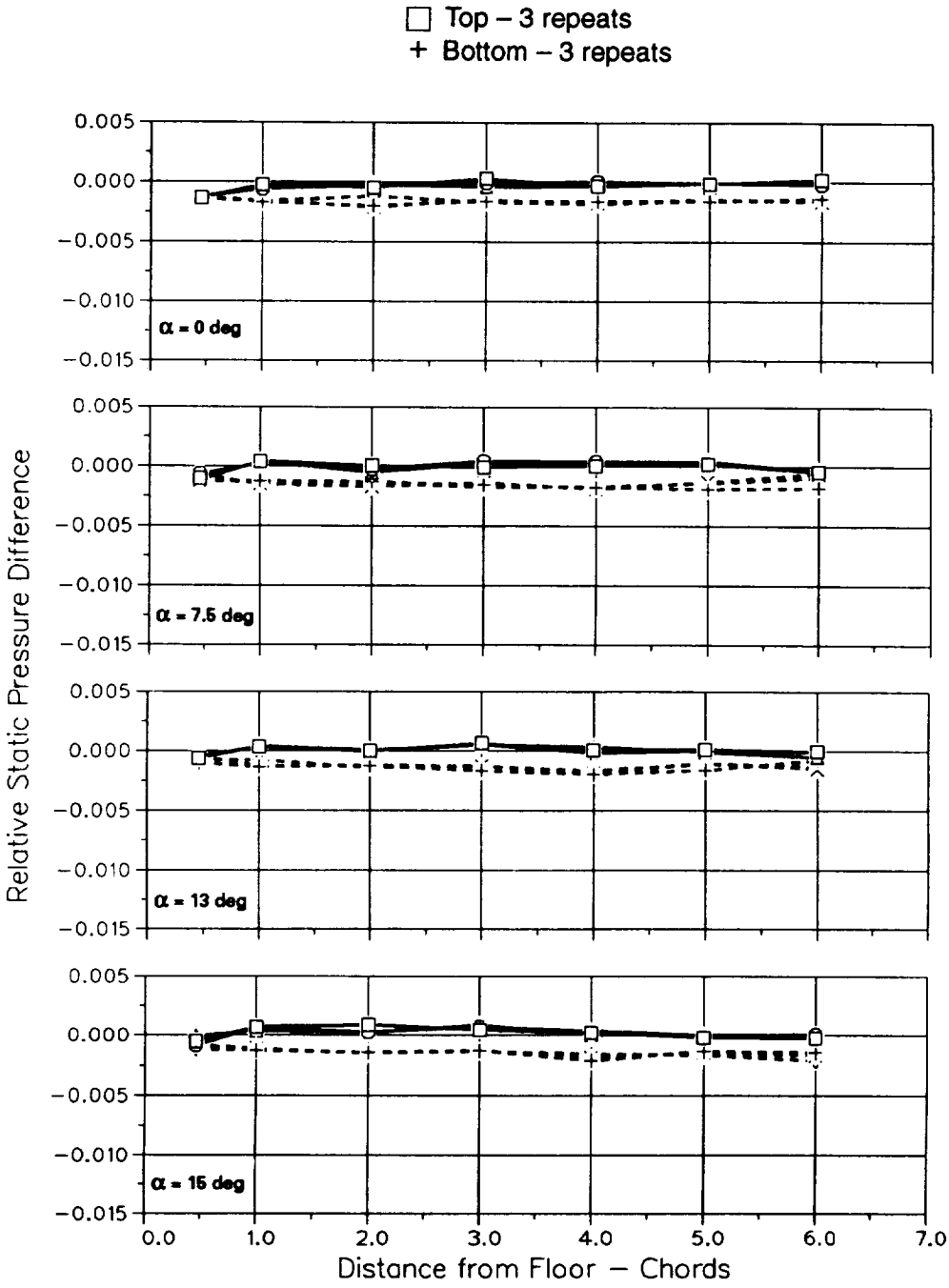

(b) Fore and aft boundary values

Figure 104. Concluded.

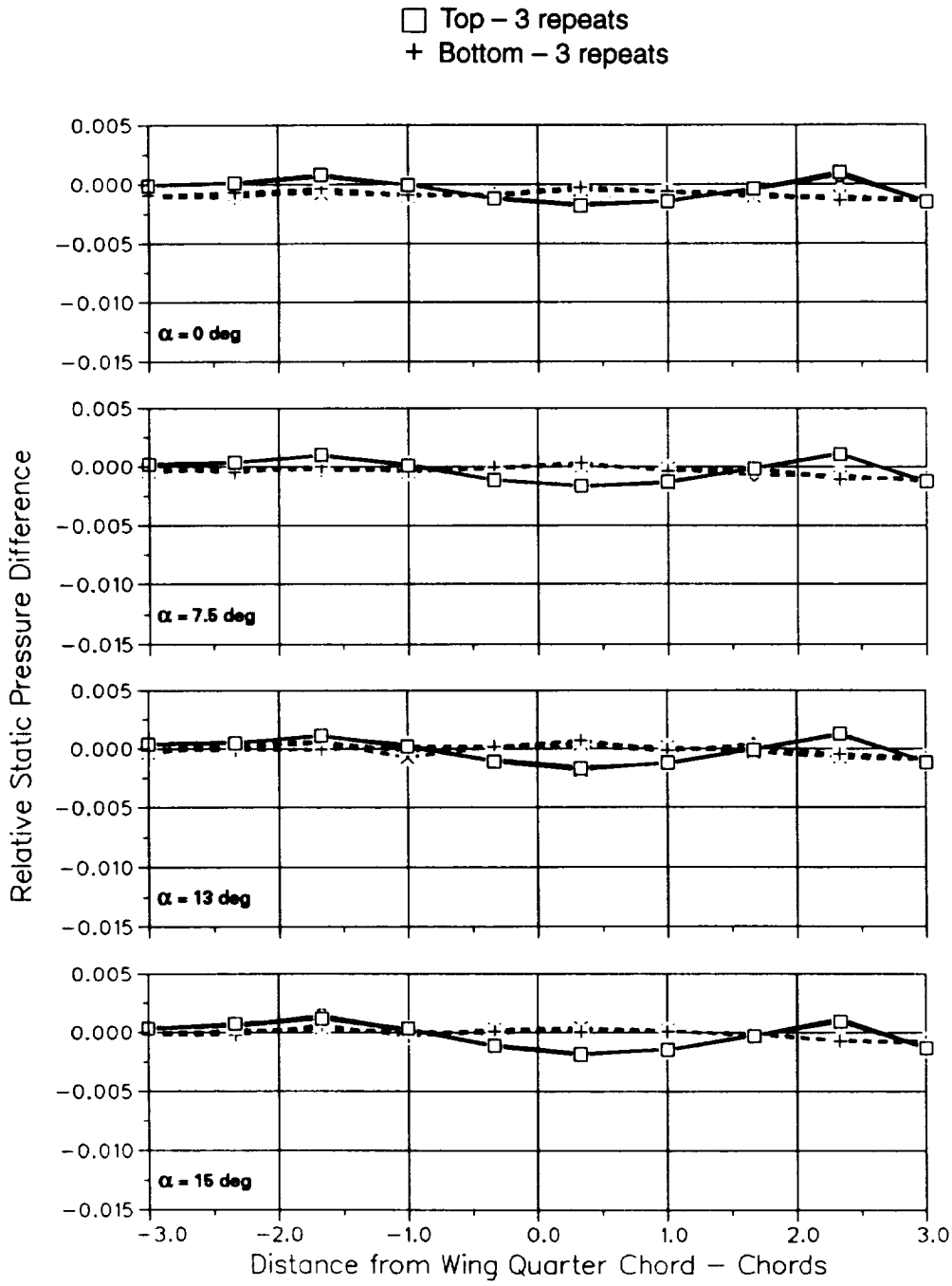

(a) Top and bottom boundary values

Figure 105. Static pressure survey; 3-D configuration; $\bar{y}$ = 1.800.

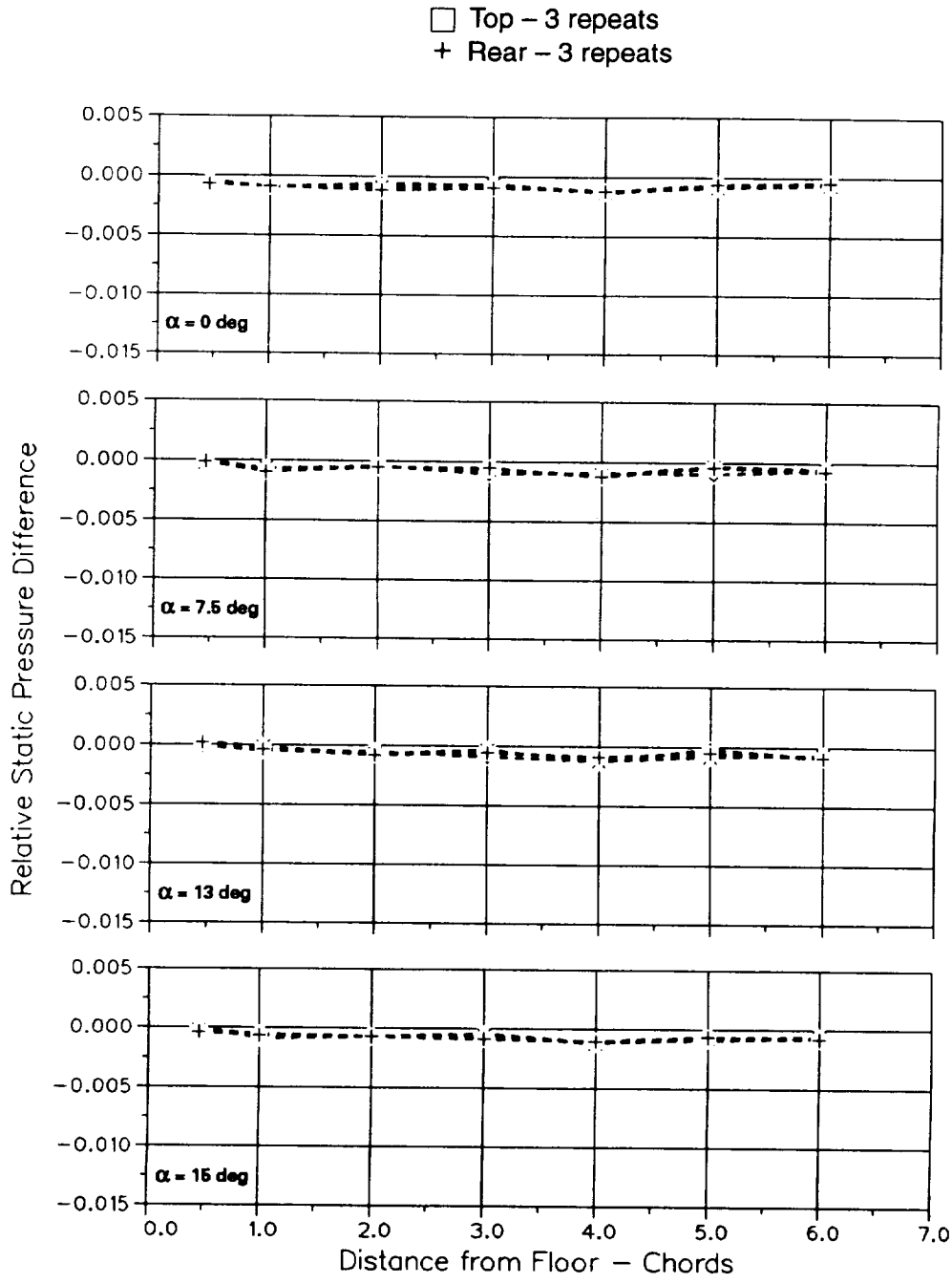

(b) Only aft boundary values

Figure 105. Concluded.

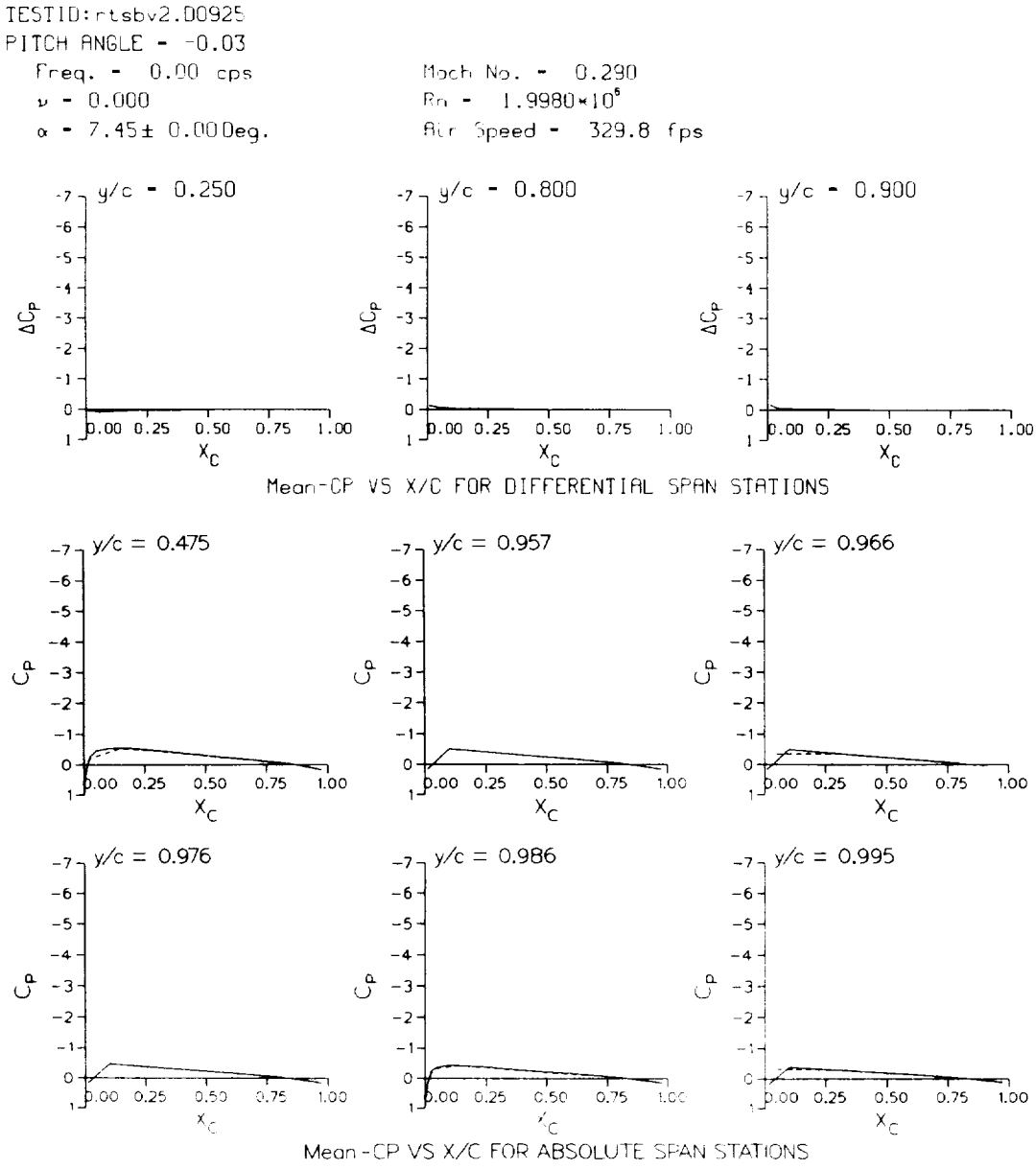

(a) α = 0.0 deg

Figure 106. Static pressure survey; chordwise pressure distributions.

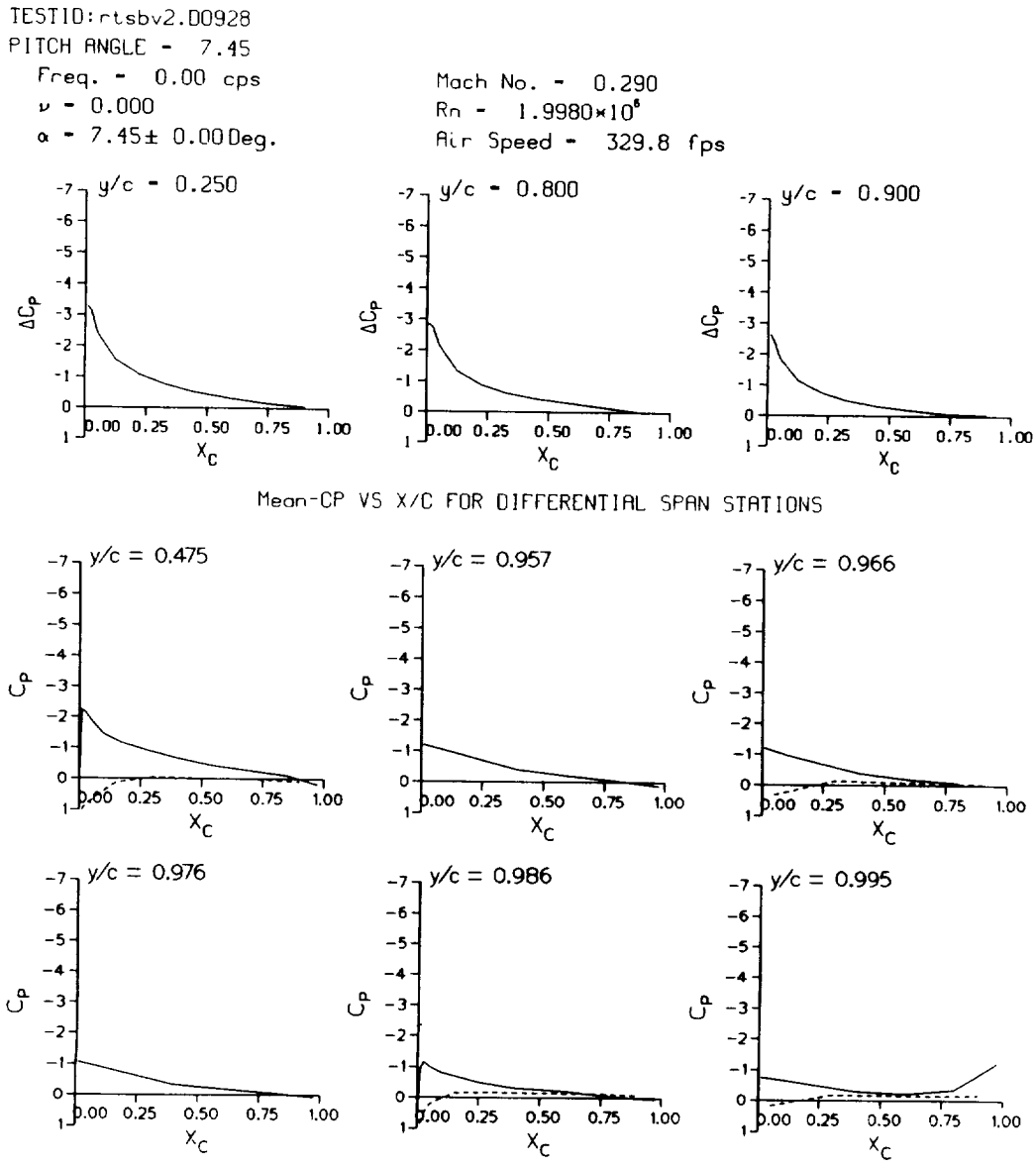

(b) α = 7.5 deg

Figure 106. Continued.

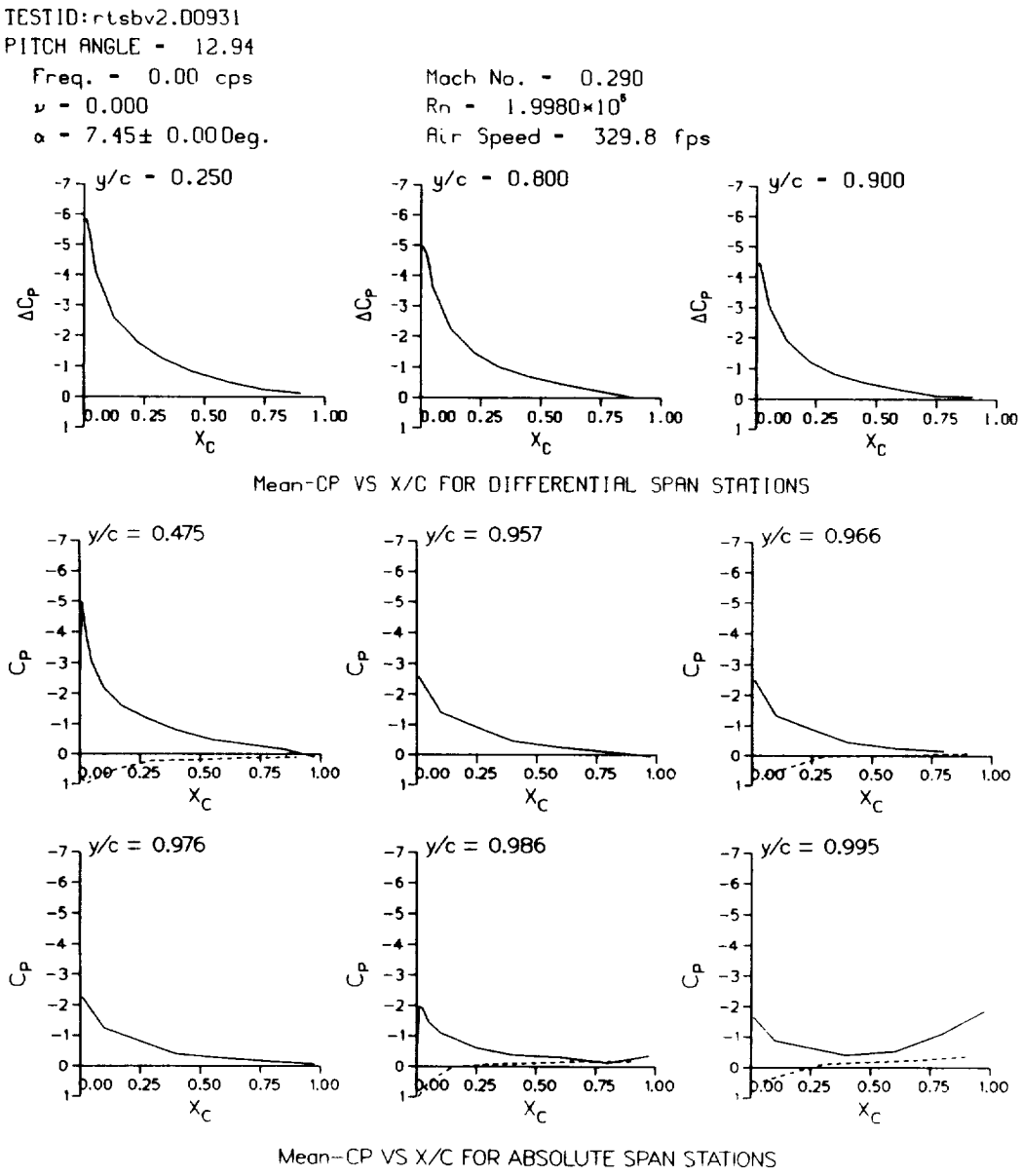

(c) α = 13.0 deg

Figure 106. Continued.

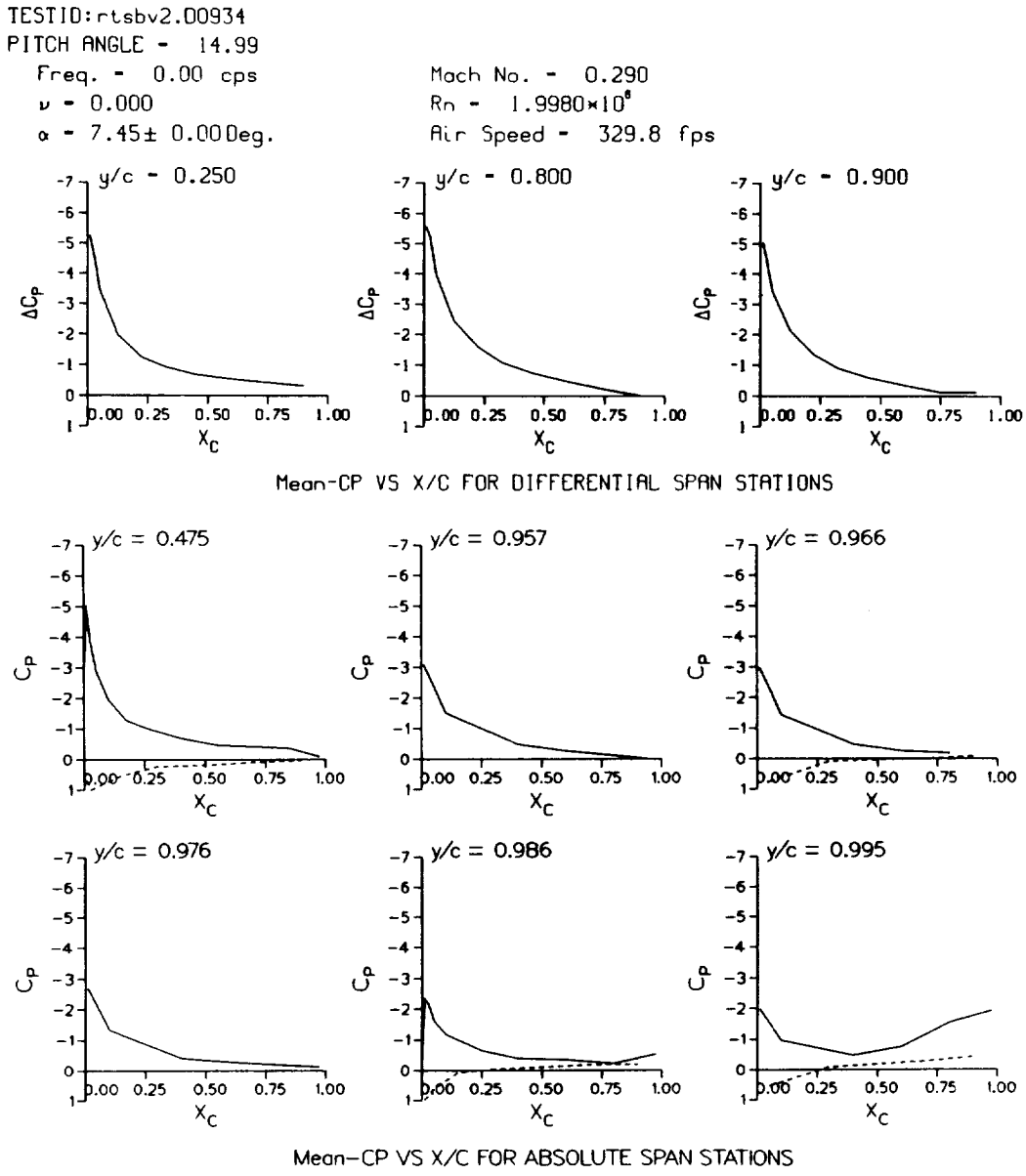

(d) α = 15.0 deg

Figure 106. Concluded.

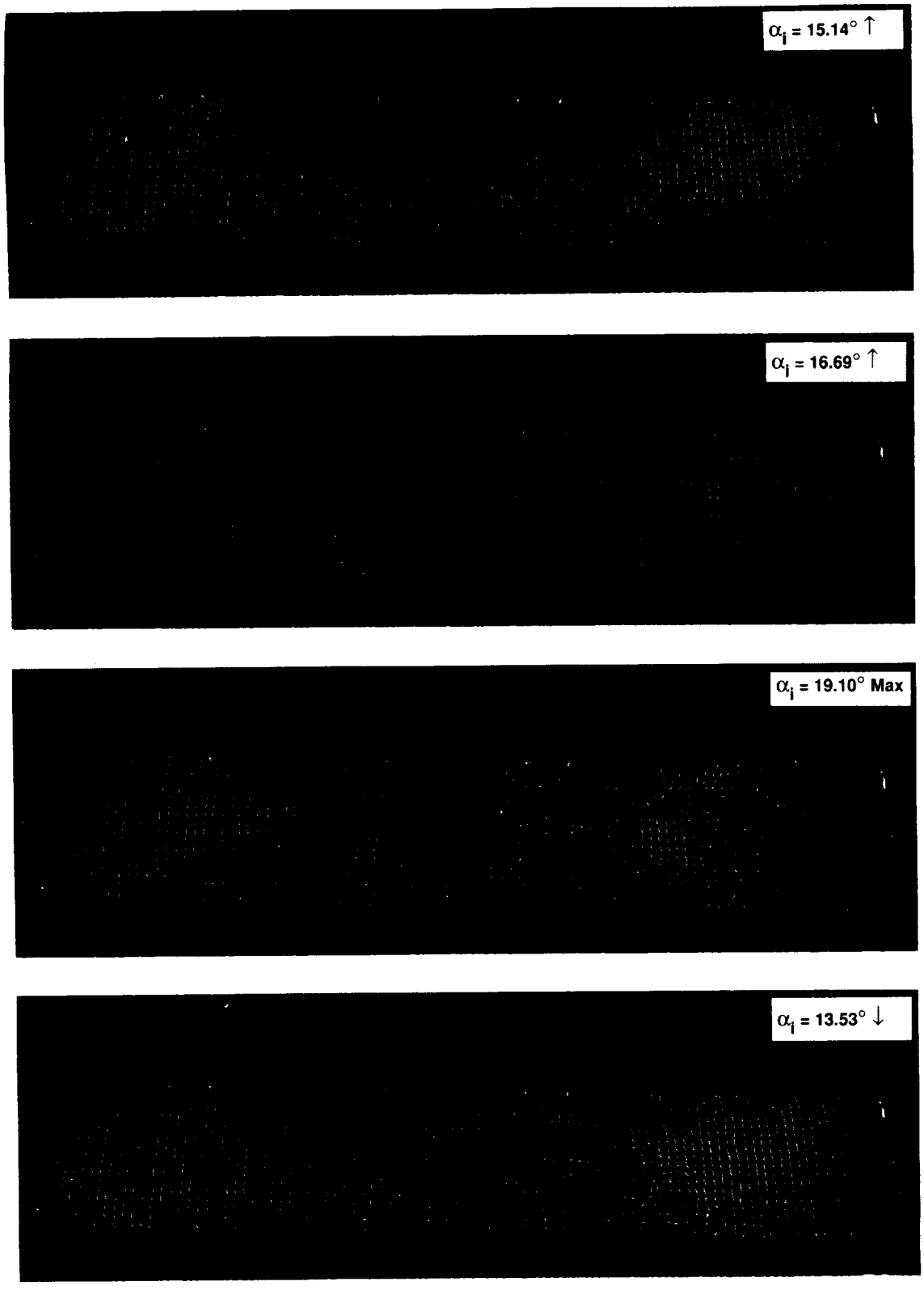

(a) $\alpha = 15 \pm 4$ deg. $v = 0.04$

Figure 107. Stalled surface flow; cycle-to-cycle variation of the flow patterns.

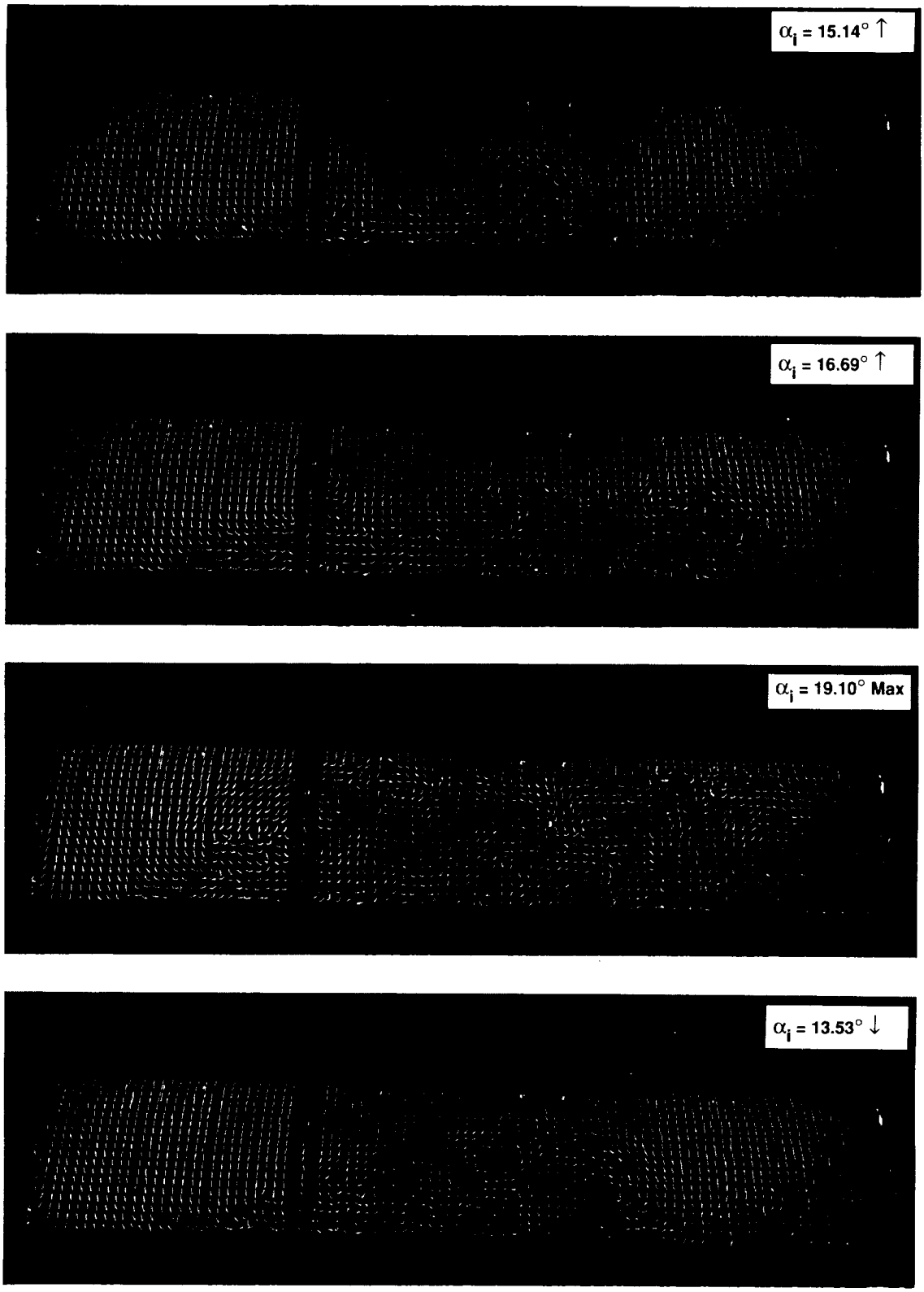

(b) α = 15 ± 4 deg. v = 0.04; repeat cycle

Figure 107. Concluded.

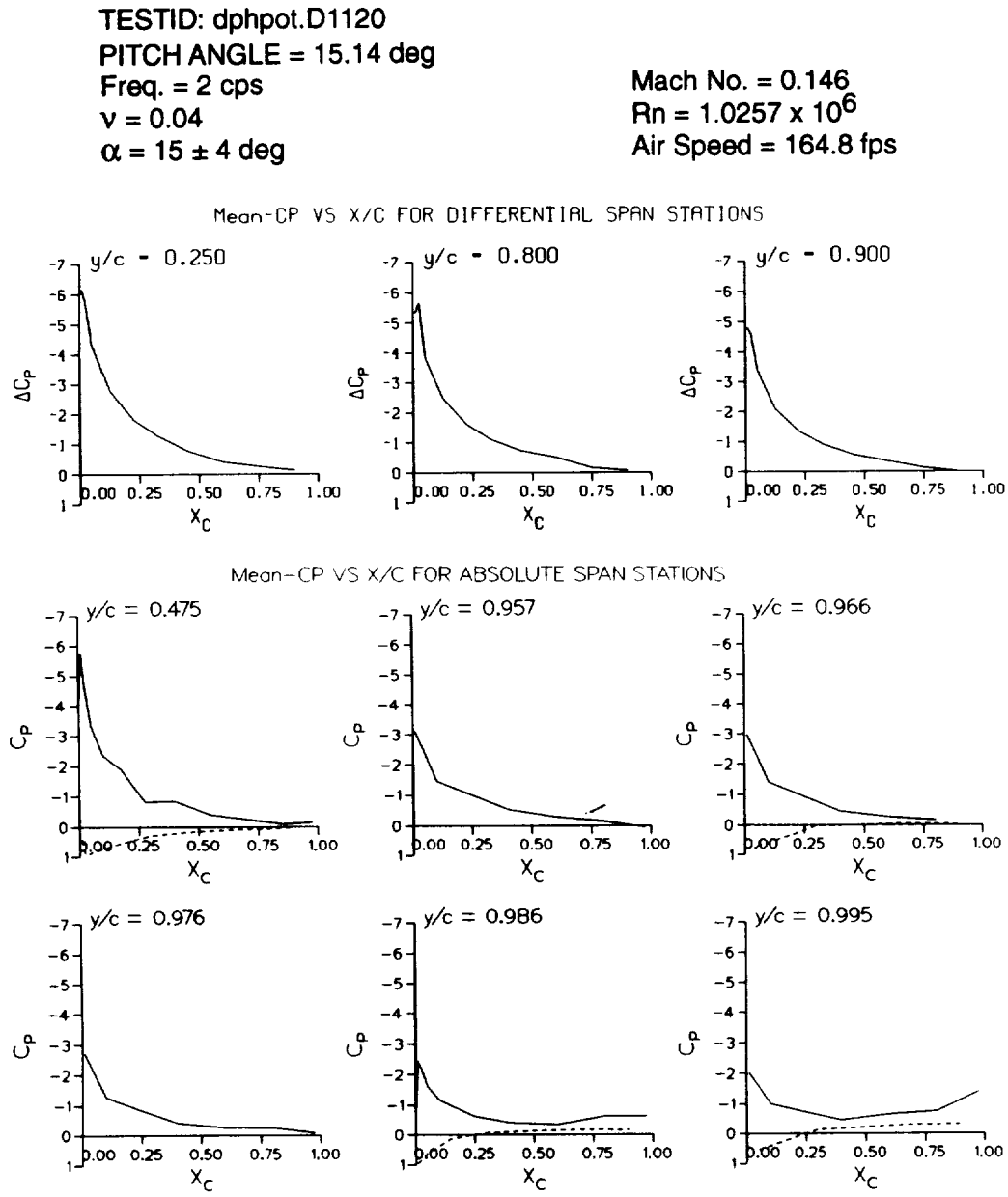

(a) α_i = 15.14 deg

Figure 108. Stalled surface flow; the instantaneous pressures corresponding to patterns of figure 107(a).

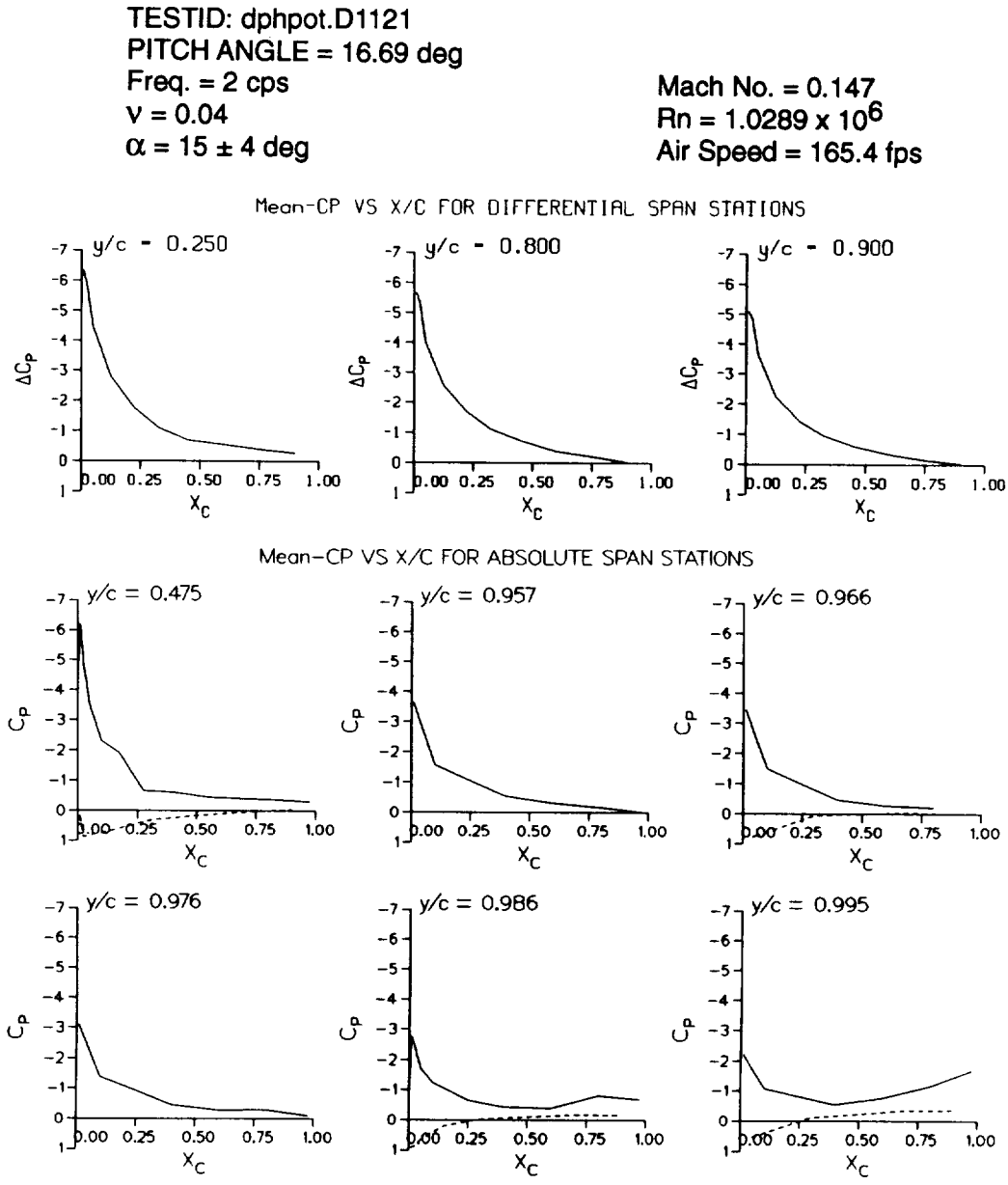

(b) α_i = 16.69 deg

Figure 108. Continued.

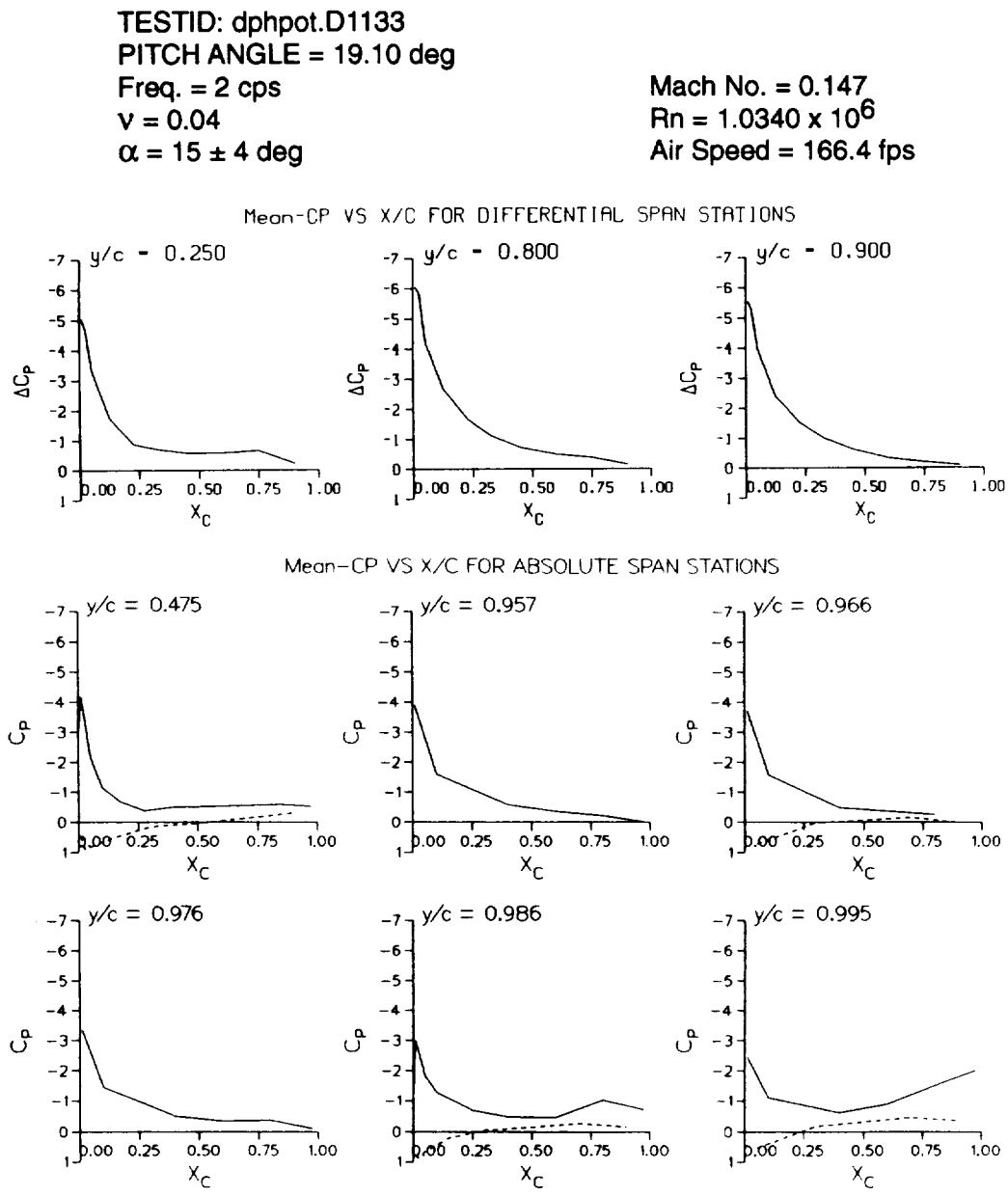

(c) α_i = 19.10 deg

Figure 108. Continued.

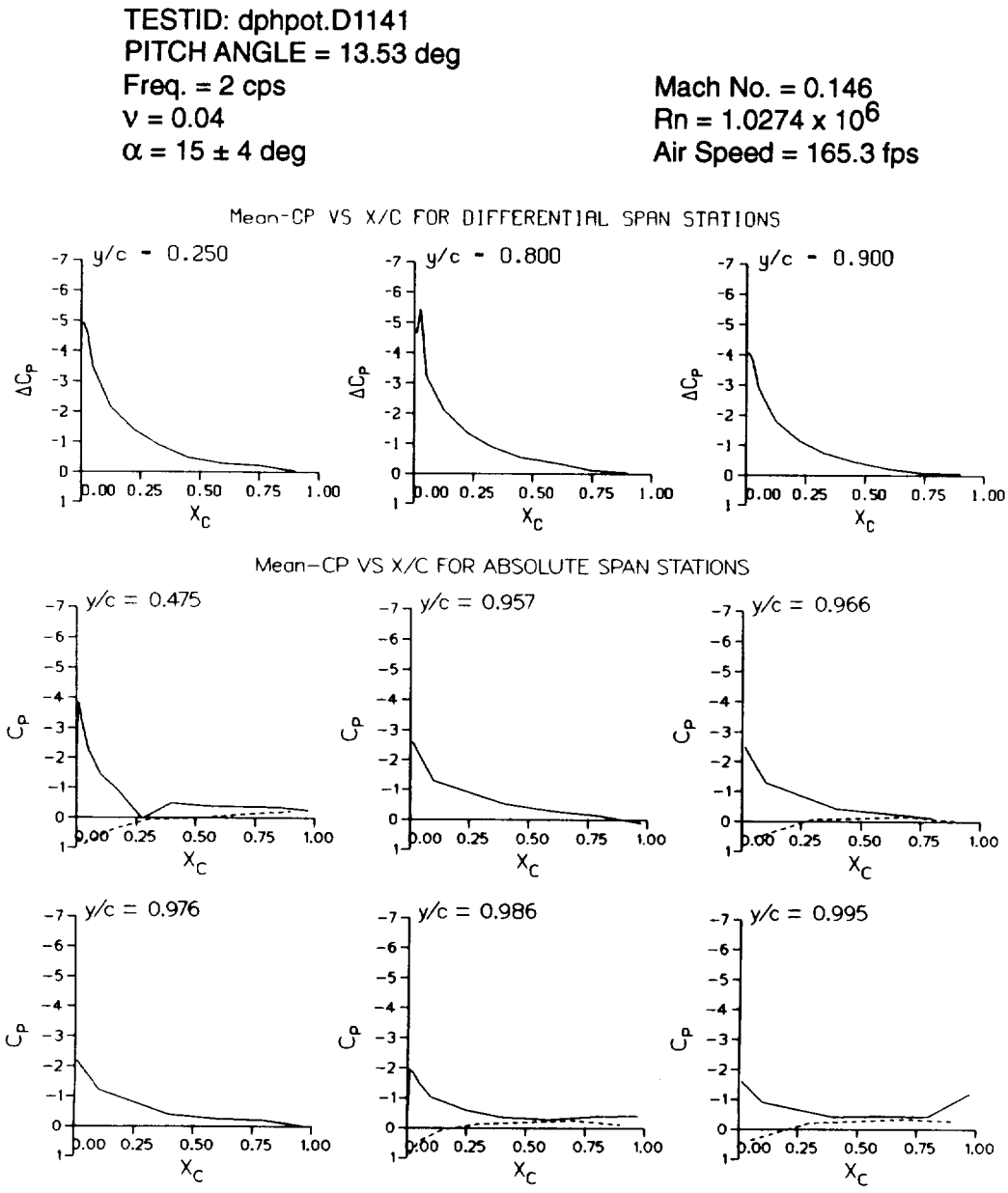

(d) α_j = 13.53 deg

Figure 108. Concluded.

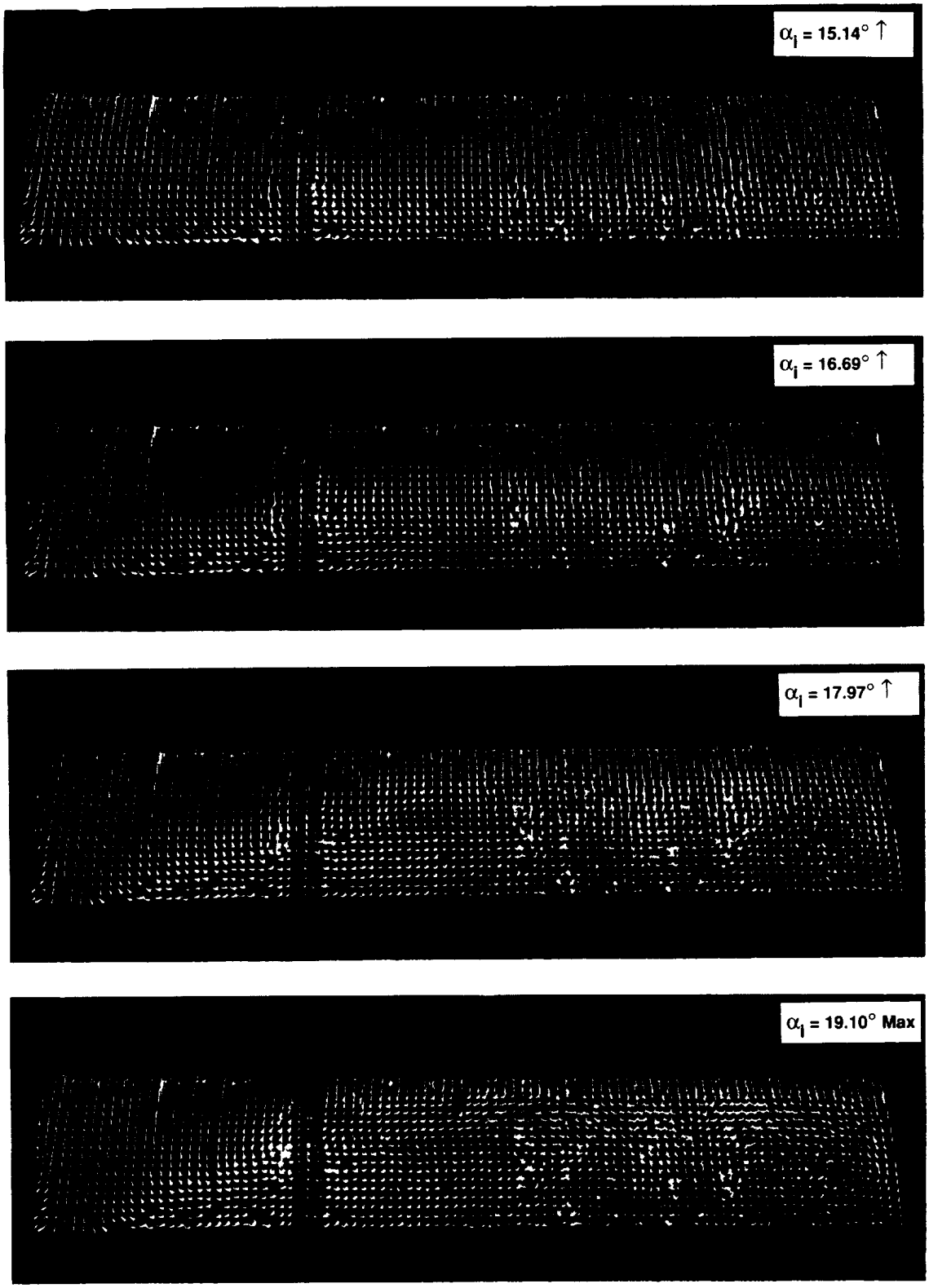

Figure 109. Stalled surface flow; cycle-average patterns; $\alpha = 15 \pm 4$ deg; $\nu = 0.04$.

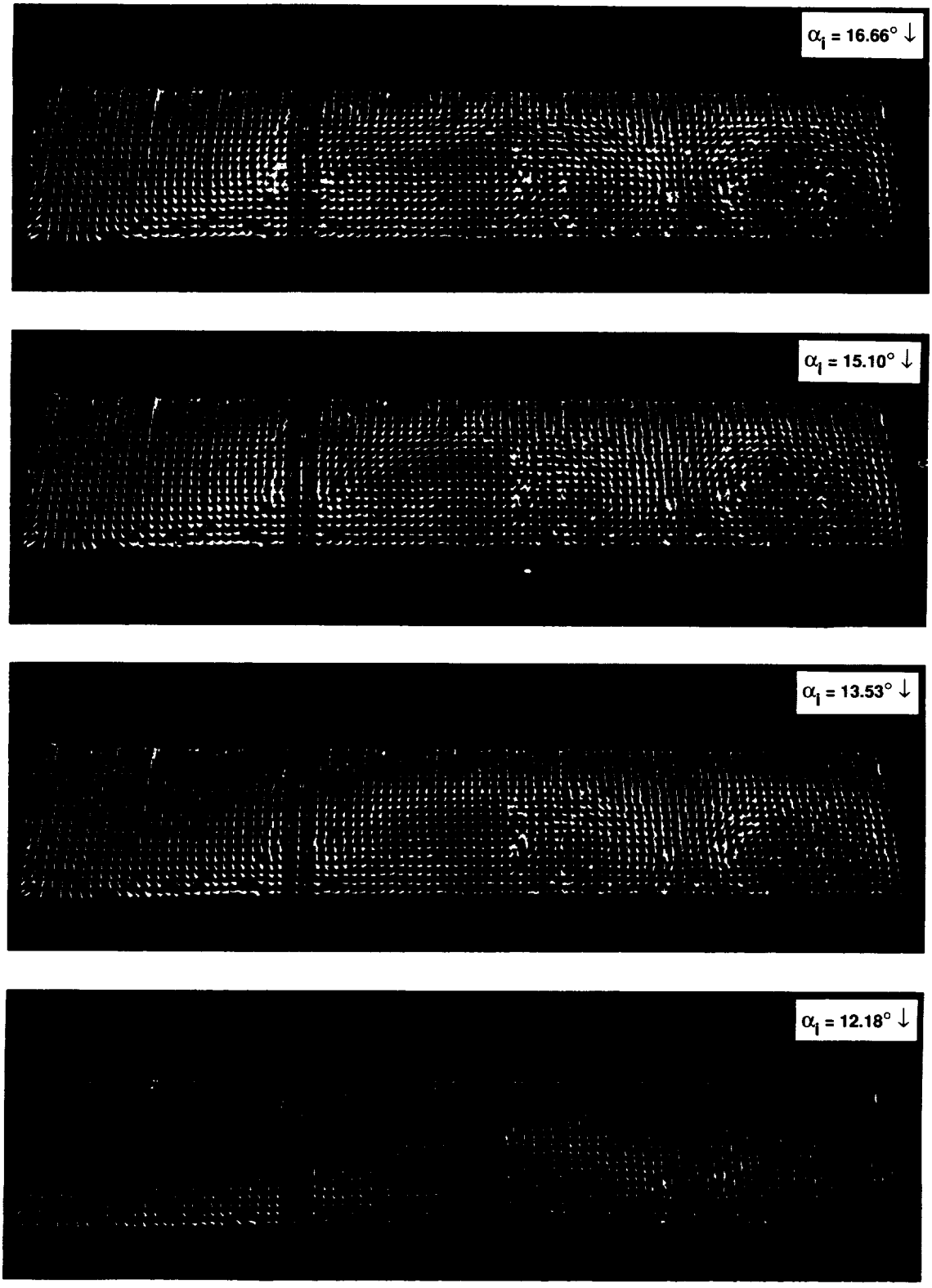

Figure 109. Concluded.

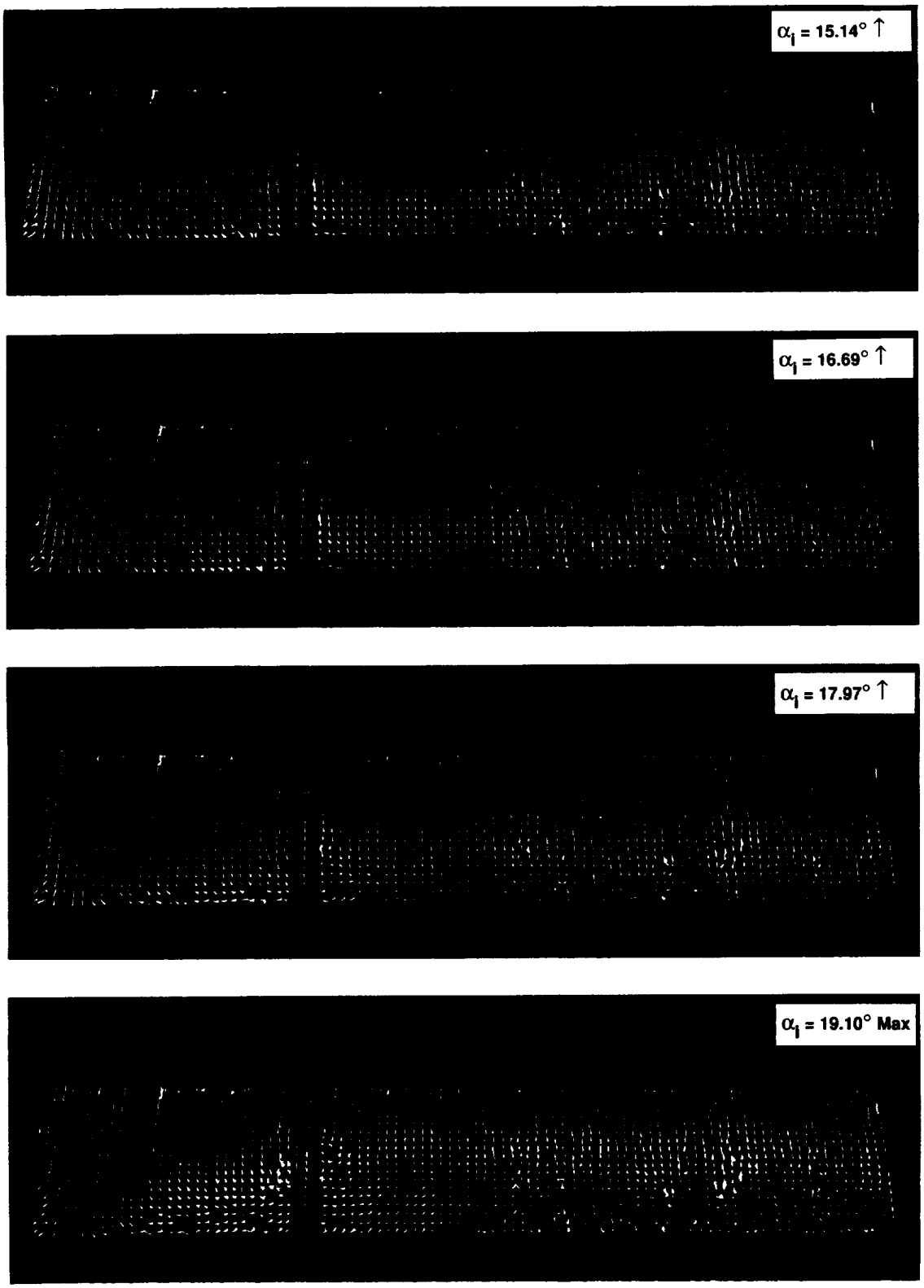

Figure 110. Stalled surface flow; cycle-average patterns; $\alpha = 15 \pm 4$ deg; $v = 0.20$.

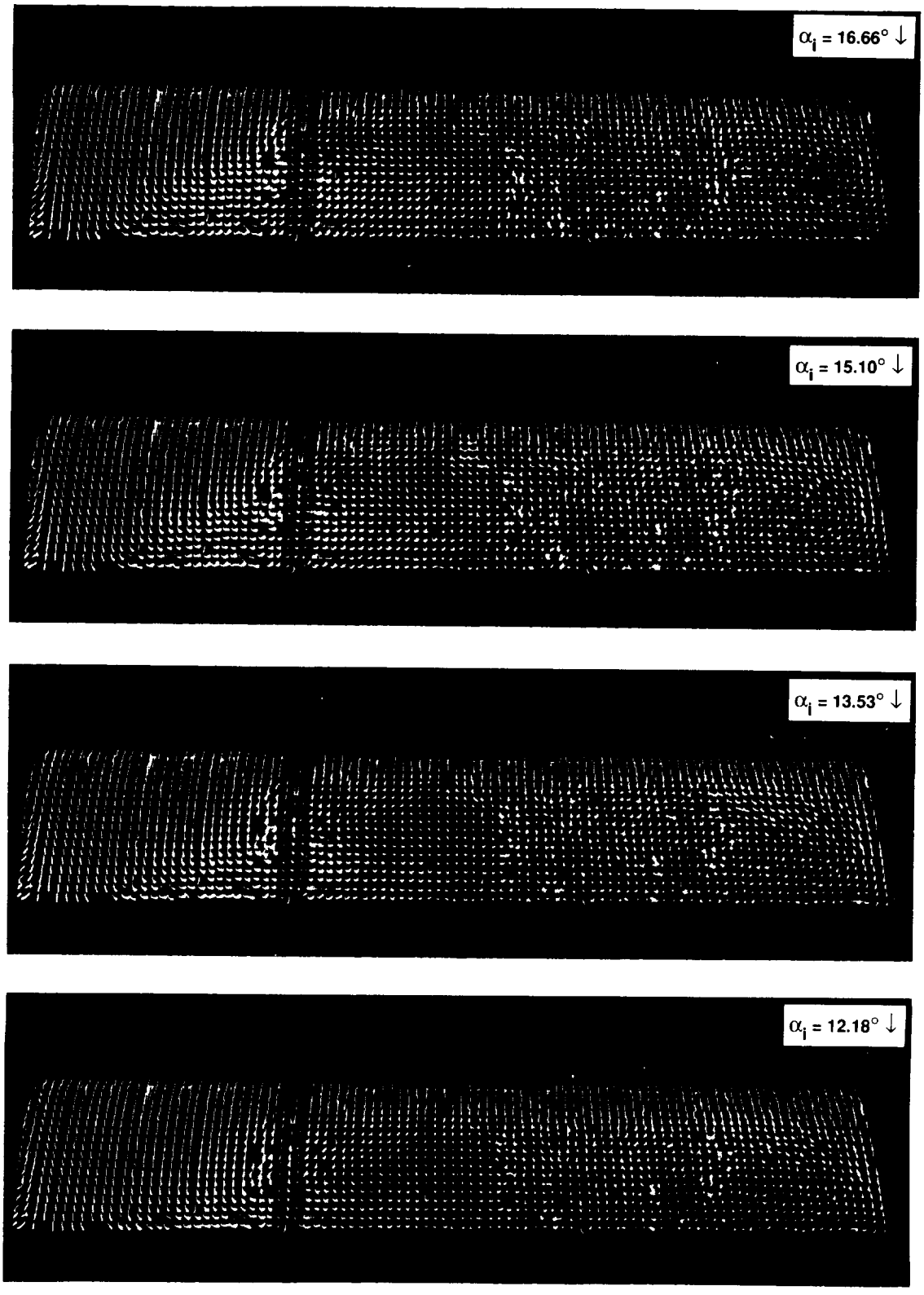

Figure 110. Concluded.

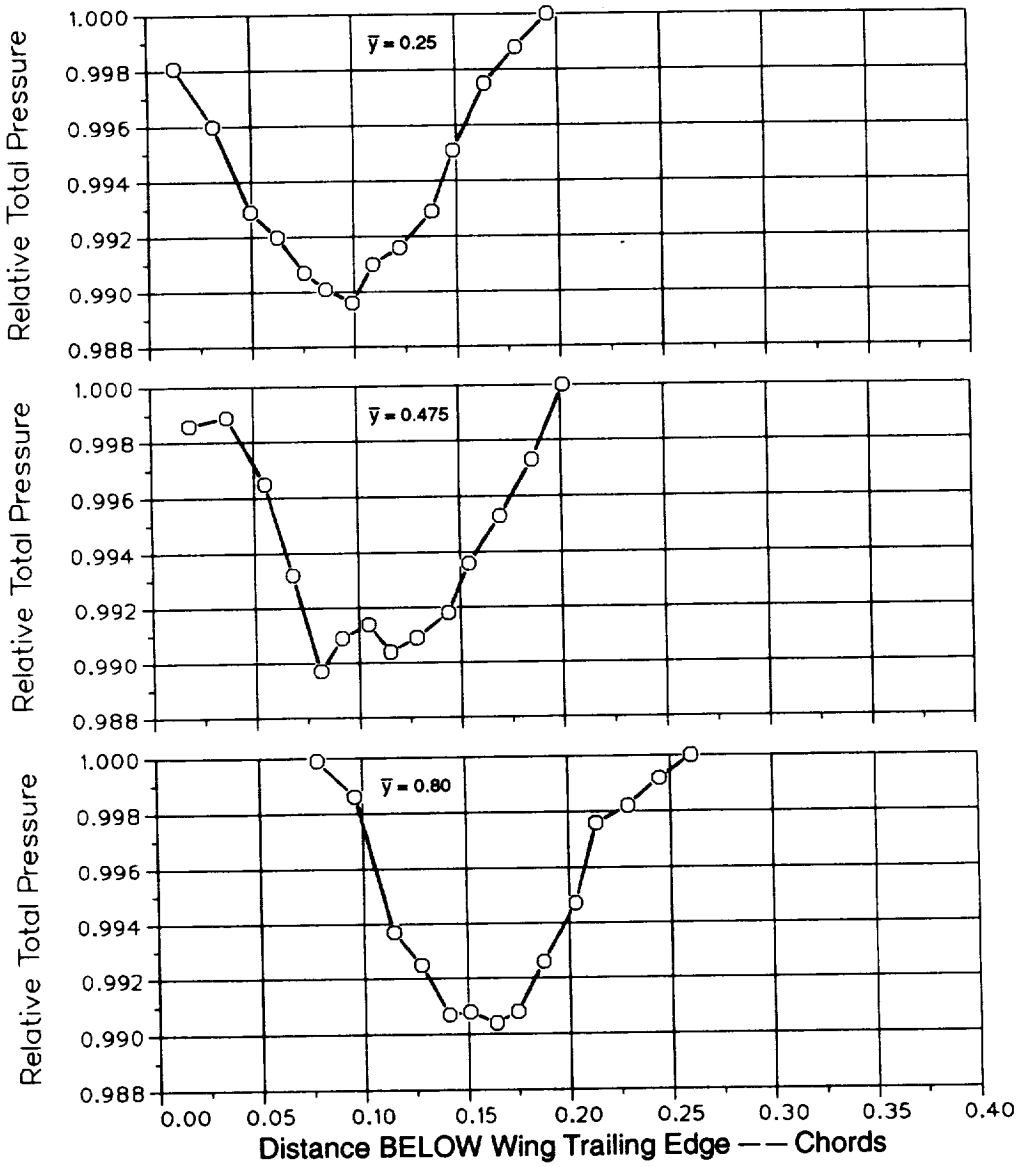

Figure 111. Wake survey data; α = 13 deg; $\bar{X}$ = 1.5.

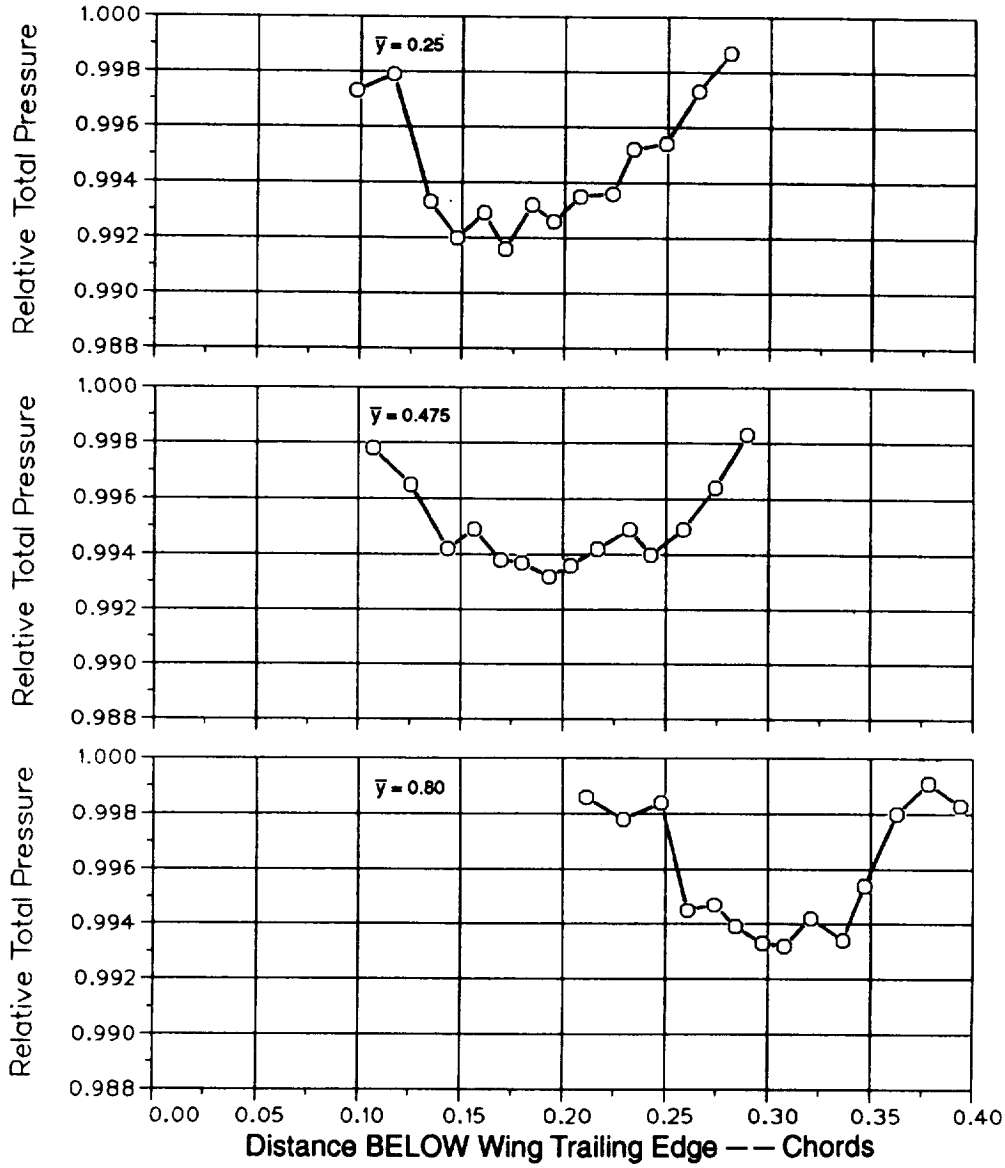

Figure 112. Wake survey data; α = 13 deg; $\overline{X}$ = 3.0.

APPENDIX

Data Base

The reduced data of this report, their cycle-averaged pressures, and the data base of raw data files are archived at the U.S. Aeroflightdynamics Directorate at NASA Ames Research Center. Inquiries about accessing these results should be addressed to the Directorate.

Data storage– The raw data acquired for each data point is stored in binary form on optical disks. Each data point file has a name identifying the test type and model configuration, and a name extension containing the sequential data point number (data point naming is defined in the Basic Data Set Description section of this report). The raw data file header contains the data point description parameters, the data acquisition parameters, and the run beginning zeros for each channel. It also holds the calibration constants, the voltage gain calibrations, and all the raw data samples for each channel for all repeats. Thus, each file is a low-level record of the data point except for the run end zeros. These were recorded as the beginning zeros of a dummy data point (with an ID of RTENDZ) taken at the end of the run. Each data point file, together with the end run zeros, contains all the information necessary to reduce the data point to engineering units at any desired level of detail.

Software– The interactive data reduction software opens the binary raw data file (described above) for the specified data point in the data base. It provides the user with the option to reduce and view the data point repetitively in any form from the most elementary to the fully integrated aerodynamic coefficients.

The following results can be produced for any individual pitch oscillation cycle or for the cycle-averaged results plus or minus a standard deviation:

1. The output of any individual pressure transducer, including the test section static and dynamic pressures, and the angle of attack transducer.
2. The chordwise distribution of C_p at any span station for any instant of time or phase angle in a pitch cycle.
3. The section aerodynamic coefficients versus α at any span station.
4. The spanwise distribution of the section aerodynamic coefficients at any instant of time or phase angle in a pitch oscillation cycle.
5. The wing aerodynamic coefficients versus α at any span station.

In addition to these graphical presentations, options exist to output most of the above forms as numerical results to a file for desired use, e.g., as input to post processing or plotting software.

Examples of data detail– Figures A-1 through A-8 present a graphic example of the kind of supporting detail available from the data base using the interactive data reduction software and are useful when interpreting the the cycle-averaged coefficient results.

The coefficient loops (i.e., section aerodynamic coefficients versus angle of attack for the cycle-averaged data) at a span station of 0.475 of data point RTPOT1.D0336 are presented in figure A-1. From these coefficient loops it is possible to obtain an overall view of all the surface pressures for this span station plotted over the cycle (fig. A-2). In this view, any point (phase angle) in the cycle can be selected via screen cross hairs for plotting the chordwise pressure distribution (fig. A-3) for this span location, or for all span locations (fig. A-4). A statistical view of the pressure at any one location can be obtained (fig. A-5). Here, the center curve is the cycle average, and the curves on either side of it are, respectively, the cycle average plus and minus a standard deviation. The upper and lower curves are, at each phase angle, the maximum and minimum over all the cycles. The information in this view shows how stalled flow unsteadiness varies throughout the cycle. For example, clearly the stall influence at this chord location becomes significant at a phase angle of about 70 deg, and the reattachment of the flow is complete at a phase angle of about 310 deg. Figure A-6 illustrates another view of the repeatability of this individual pressure where all the individual cycles are concatenated. The information in this view allows selection and plotting of any individual pressure cycle (e.g., cycle repeats numbers 5 and 8, fig. A-7) and production of the coefficient loops for these individual cycles (fig. A-8).

Lift Coefficient from Leading Edge Pressures

The procedure developed for the fit and interpolation of the leading pressure distributions described in the Data Reduction section implicitly locates the stagnation point. This interpolation procedure suggests a method for obtaining the local section C_l from leading edge pressure measurements.

The availability of the functional relationship between the stagnation point location and C_l for a given airfoil section (fig. 7) makes it possible to evaluate the magnitude of the local section C_l on any wing or rotating wing with the same airfoil, given as few as 2 (the minimum required for the fit procedure) leading edge pressure measurements. Note that while two measured pressures are the minimum required, more measurements increase the accuracy of the leading edge pressure fit and the determination of the stagnation point location.

The procedure is as follows: Experimentally calibrate the airfoil of the subject wing or rotor. Determine the

functional relationship of the stagnation point location to the section C_l (fig. 16) from a 2-D test of the airfoil section using the fit procedure. Use the wing or rotor leading edge pressures and the fit procedure to determine the stagnation point location. The stagnation point location is then used to determine the section C_l from the airfoil calibration.

The accuracy of this procedure has not been thoroughly investigated. However, within the context of this data set at the wing midspan location for $C_l \leq 1.0$, the procedure yields results within 4% at reduced frequencies up to 0.20. For $1.0 \leq C_l \leq 1.3$ on the nonlinear part of the lift curve attained under dynamic pitch operation, the results are within 9% when using linear extrapolation of the airfoil calibration.

The following limitations influencing accuracy need further investigation:

1. The procedure should only be valid below stall. However, a stalled airfoil has a bound circulation reflected in the stagnation point location.
2. The procedure may not be valid in highly 3-D regions of a wing, e.g., near the tip.
3. The fit procedure is based on the assumption of incompressible flow.

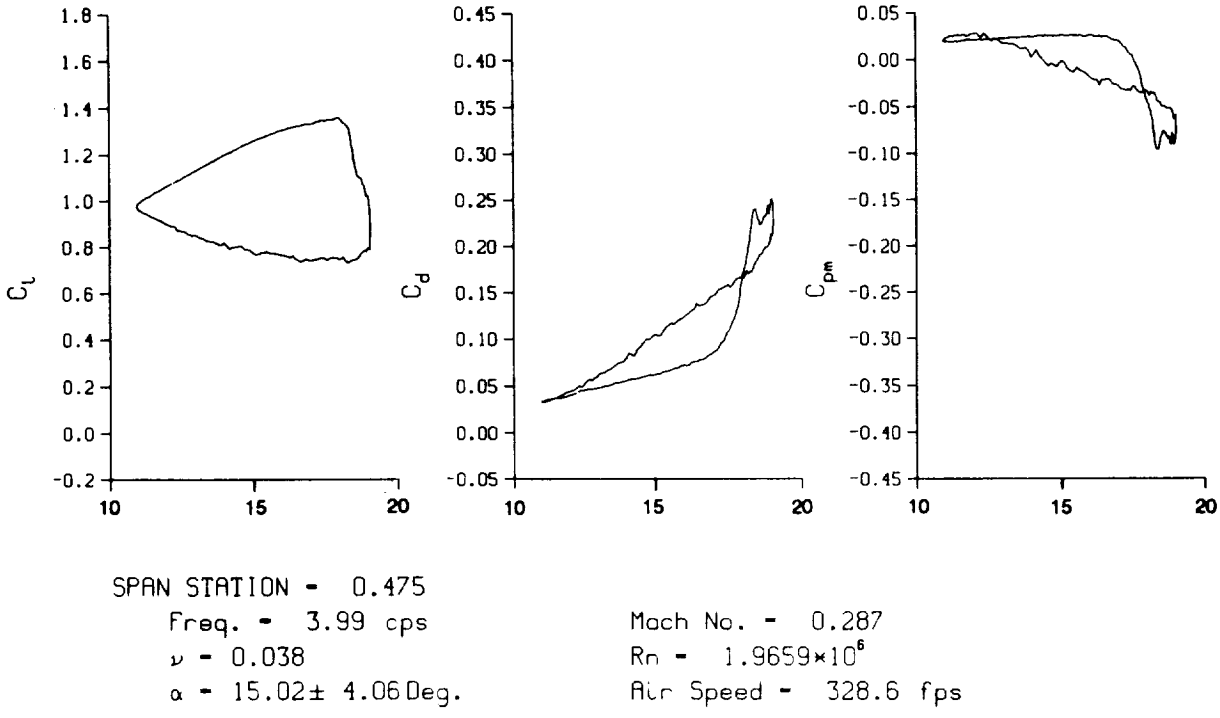

Figure A-1. Data view; aerodynamic coefficients versus α; cycle average.

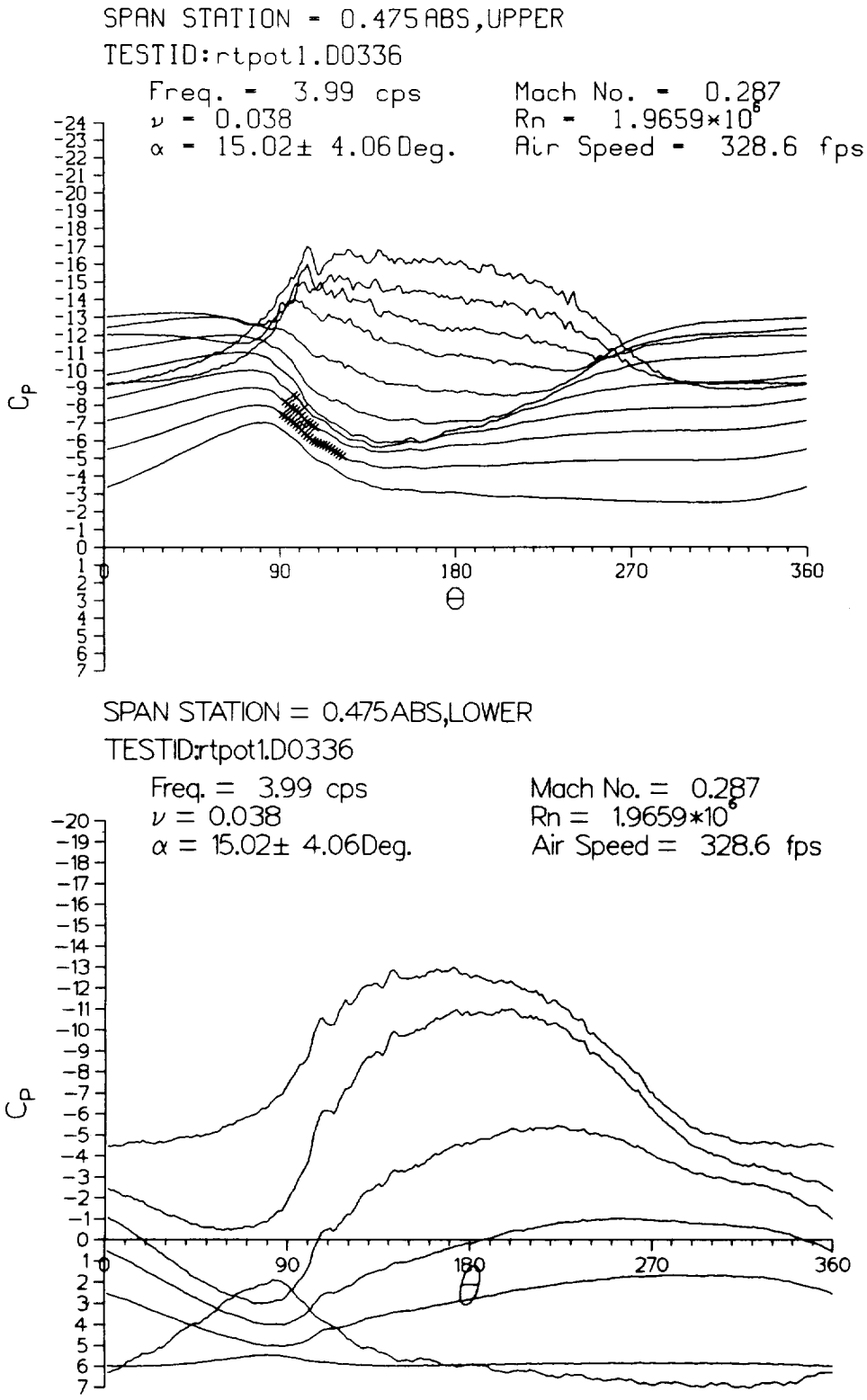

Figure A-2. Data view; all section pressures over cycle.

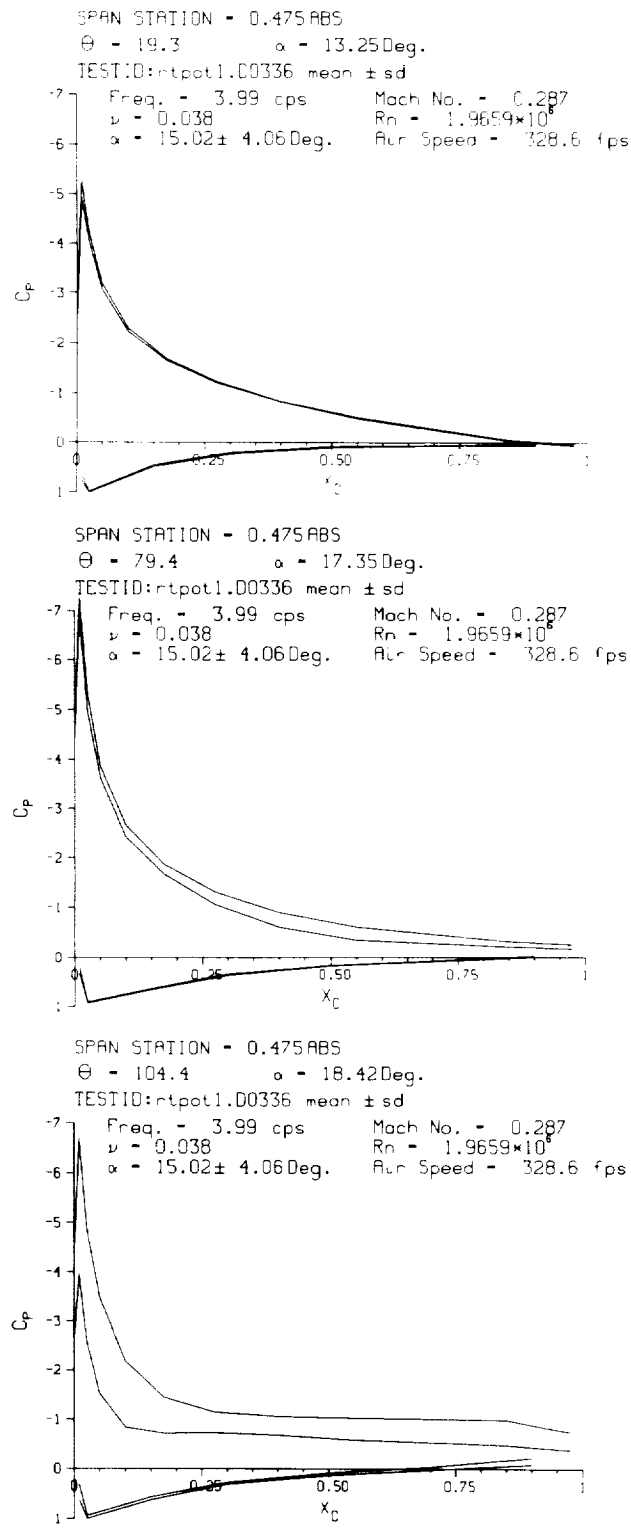

Figure A-3. Data view; individual chordwise pressures; any phase angle.

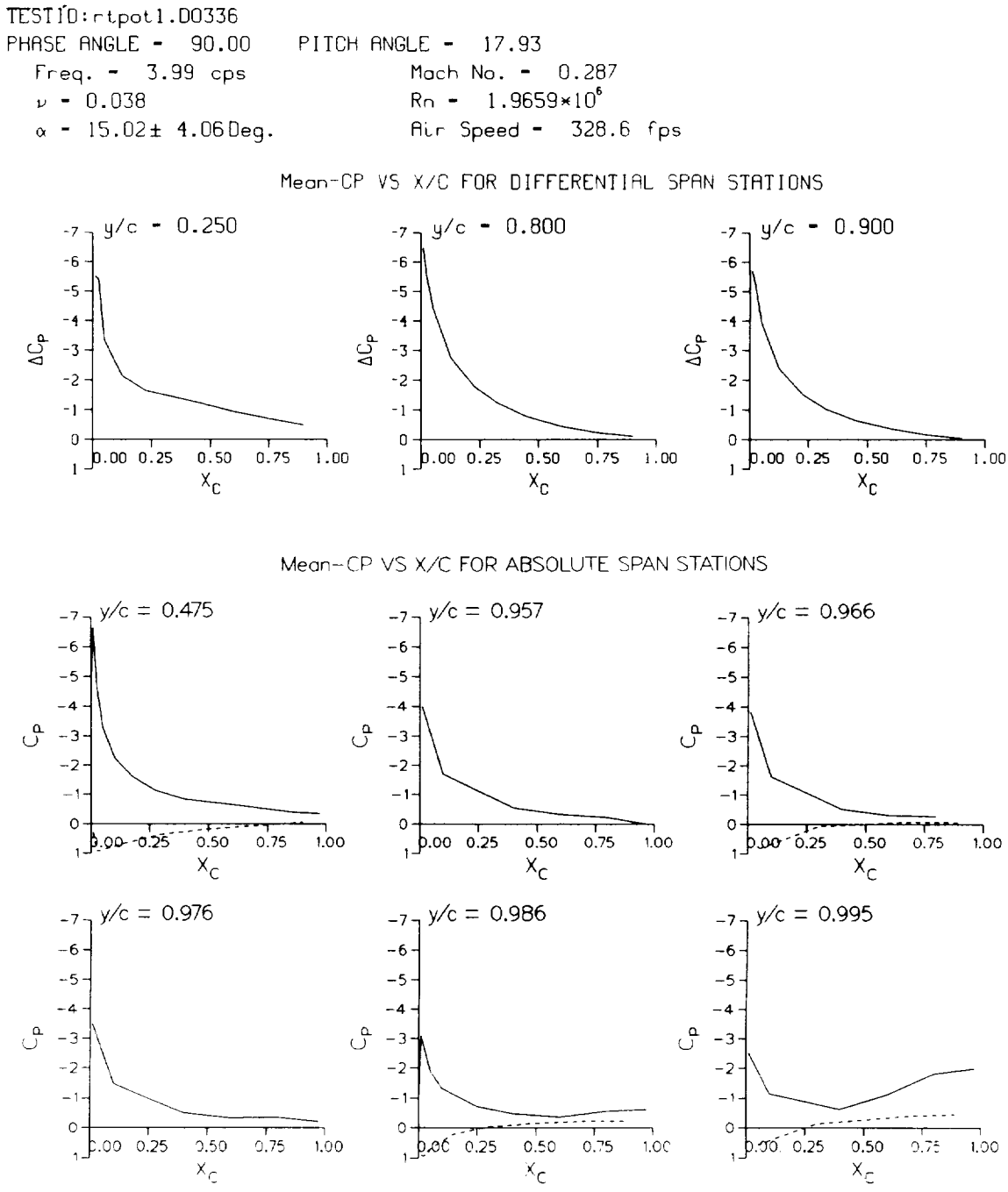

Figure A-4. Data view; all chordwise pressures; any phase angle.

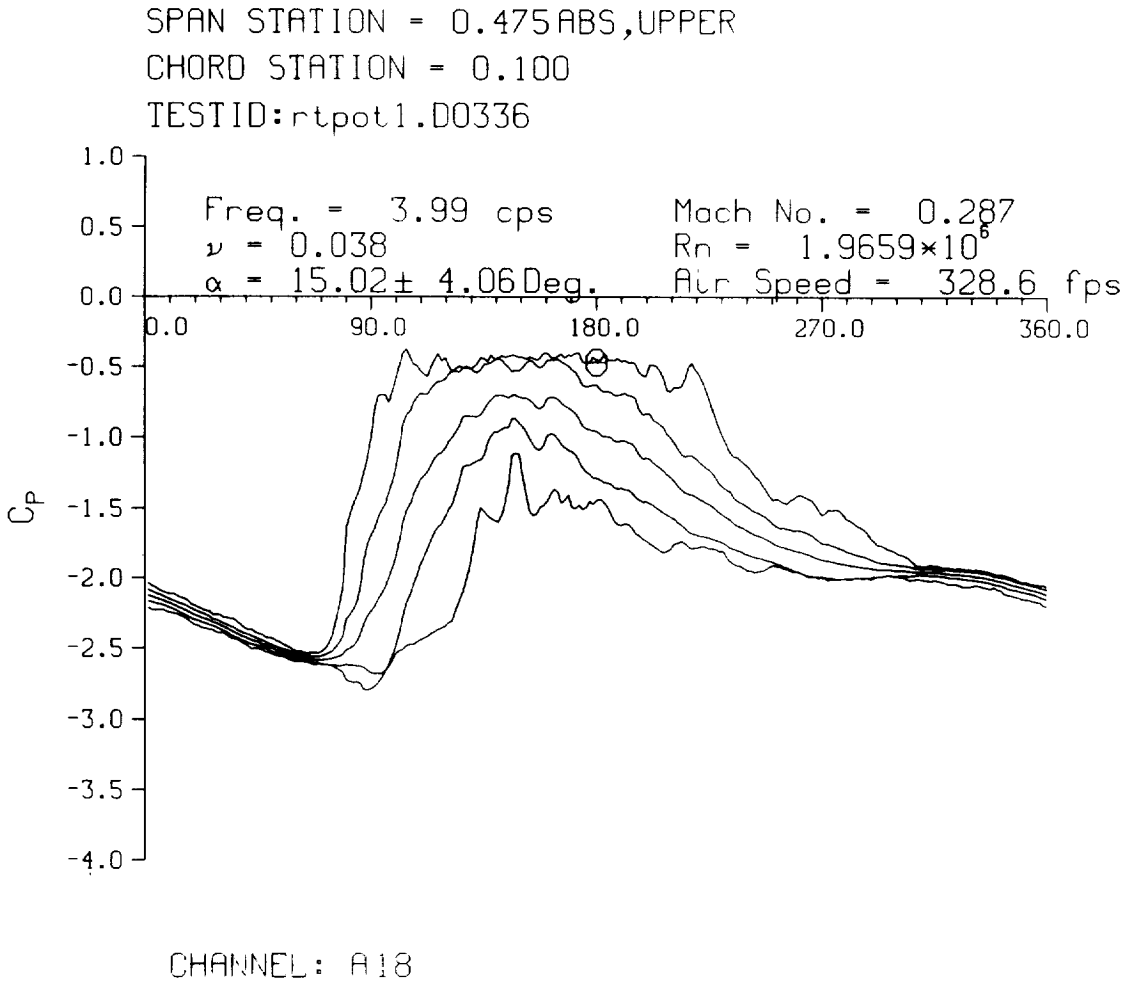

Figure A-5. Data view; individual pressure; statistical view.

SPAN STATION = 0.475 ABS, UPPER
CHORD STATION = 0.100
TESTID: rtpot1.D0336

Freq. = 3.99 cps	Mach No. = 0.287
ν = 0.038	Rn = 1.9659×10^6
α = 15.02 ± 4.06 Deg.	Air Speed = 328.6 fps

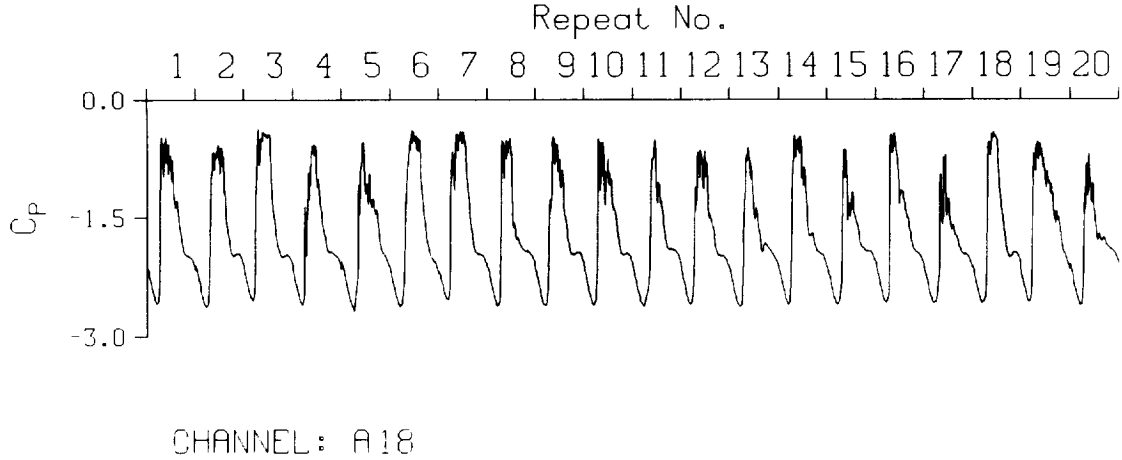

Figure A-6. Data view; individual pressure; all cycles concatenated.

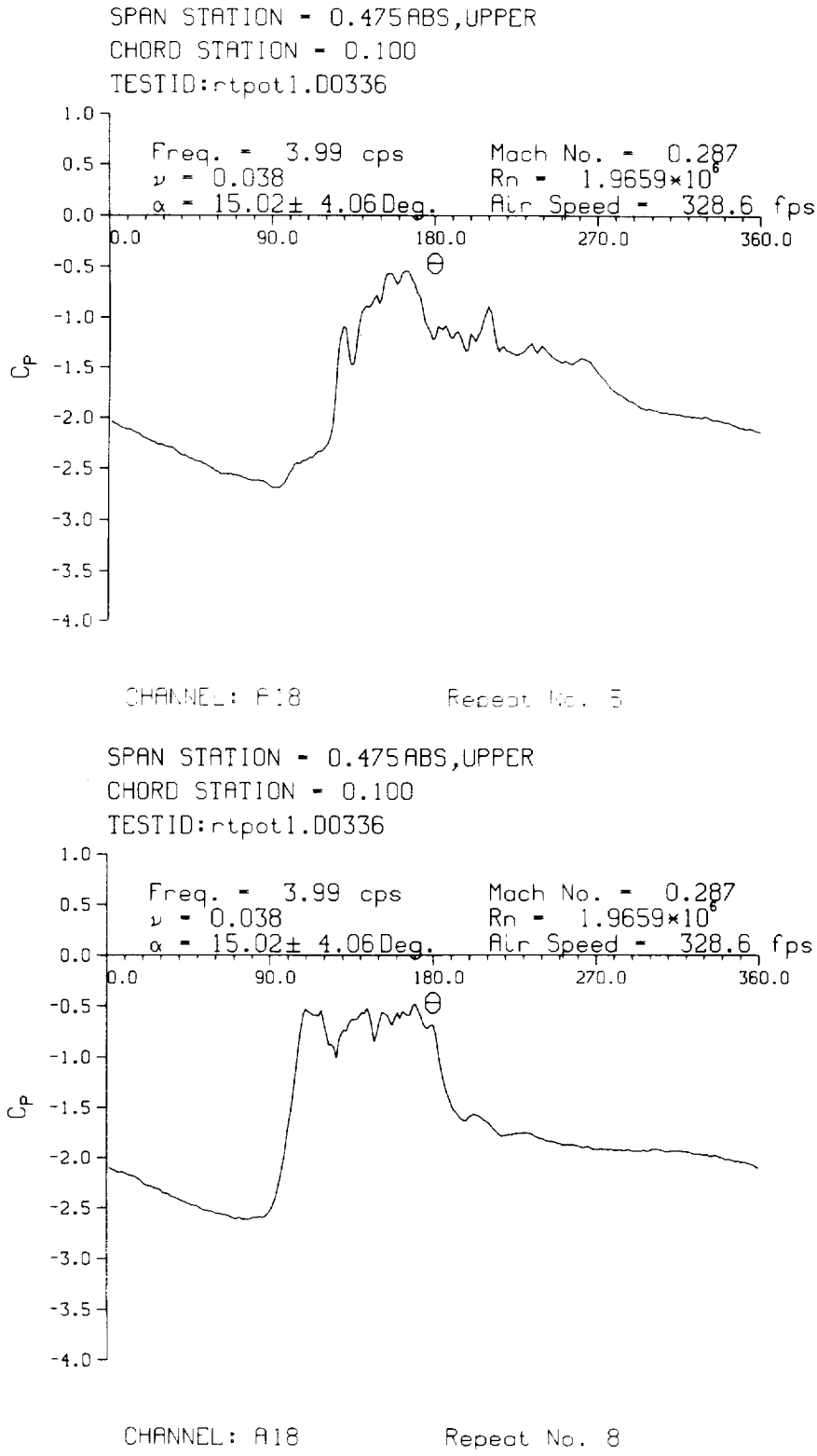

Figure A-7. Data view; individual pressure; single cycle.

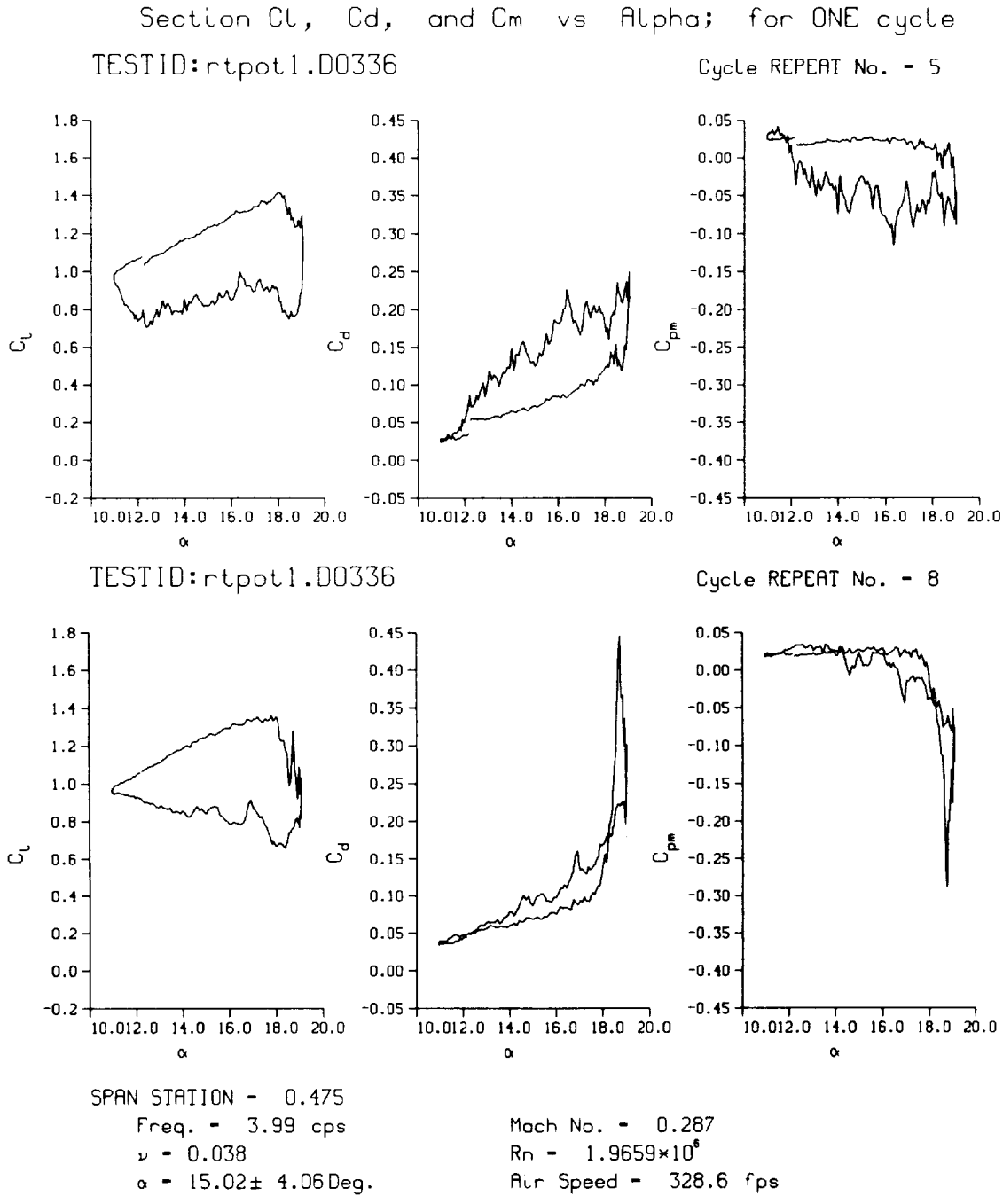

Figure A-8. Data view; aerodynamic coefficients versus α; single cycle.

REPORT DOCUMENTATION PAGE

Form Approved
OMB No. 0704-0188

1. AGENCY USE ONLY *(Leave blank)*	2. REPORT DATE	3. REPORT TYPE AND DATES COVERED
	September 1994	Technical Memorandum

4. TITLE AND SUBTITLE
2-D and 3-D Oscillating Wing Aerodynamics for a Range of Angles of Attack Including Stall

5. FUNDING NUMBERS
505-59-52

6. AUTHOR(S)
R. A. Piziali

7. PERFORMING ORGANIZATION NAME(S) AND ADDRESS(ES)
Ames Research Center, Moffett Field, CA 94035-1000 and
Aeroflightdynamics Directorate, U.S. Army Aviation and Troop Command, Ames Research Center, Moffett Field, CA 94035-1000

8. PERFORMING ORGANIZATION REPORT NUMBER
A-94053

9. SPONSORING/MONITORING AGENCY NAME(S) AND ADDRESS(ES)
National Aeronautics and Space Administration
Washington, DC 20546-0001 and U.S. Army Aviation and Troop Command, St. Louis, MO 63120-1798

10. SPONSORING/MONITORING AGENCY REPORT NUMBER
NASA TM-4632
USAATCOM TR-94-A-011

11. SUPPLEMENTARY NOTES
Point of Contact: Robert A. Ormiston, Ames Research Center, MS 215-1, Moffett Field, CA 94035-1000; (415) 604-5835

12a. DISTRIBUTION/AVAILABILITY STATEMENT
Unclassified-Unlimited
Subject Category – 02

12b. DISTRIBUTION CODE

13. ABSTRACT *(Maximum 200 words)*

A comprehensive experimental investigation of the pressure distribution over a semispan wing undergoing pitching motions representative of a helicopter rotor blade was conducted. Testing the wing in the nonrotating condition isolates the three-dimensional (3-D) blade aerodynamic and dynamic stall characteristics from the complications of the rotor blade environment. The test has generated a very complete, detailed, and accurate body of data. These data include static and dynamic pressure distributions, surface flow visualizations, two-dimensional (2-D) airfoil data from the same model and installation, and important supporting blockage and wall pressure distributions. This body of data is sufficiently comprehensive and accurate that it can be used for the validation of rotor blade aerodynamic models over a broad range of the important parameters including 3-D dynamic stall. This data report presents all the cycle-averaged lift, drag, and pitching moment coefficient data versus angle of attack obtained from the instantaneous pressure data for the 3-D wing and the 2-D airfoil. Also presented are examples of the following: cycle-to-cycle variations occurring for incipient or lightly stalled conditions; 3-D surface flow visualizations; supporting blockage and wall pressure distributions; and underlying detailed pressure results.

14. SUBJECT TERMS
2-D oscillating airfoil, 3-D oscillating airfoil, Wing and airfoil

15. NUMBER OF PAGES
570

16. PRICE CODE
A24

17. SECURITY CLASSIFICATION OF REPORT	18. SECURITY CLASSIFICATION OF THIS PAGE	19. SECURITY CLASSIFICATION OF ABSTRACT	20. LIMITATION OF ABSTRACT
Unclassified	Unclassified		